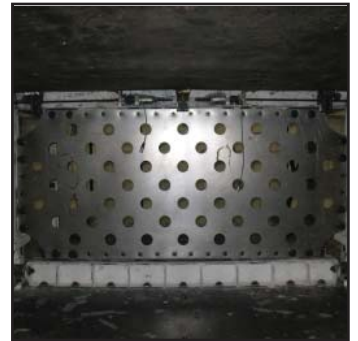
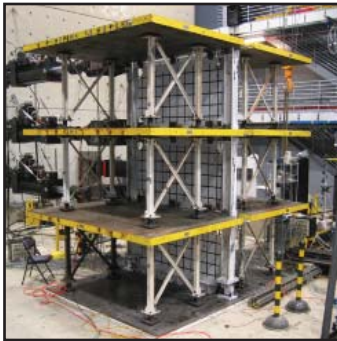


# Analytical and Experimental Investigation of Self-Centering Steel Plate Shear Walls

by  
Daniel M. Dowden and Michel Bruneau



Technical Report MCEER-14-0010

December 19, 2014

## NOTICE

This report was prepared by the University at Buffalo, State University of New York, as a result of research sponsored by MCEER. Neither MCEER, associates of MCEER, its sponsors, the University at Buffalo, State University of New York, nor any person acting on their behalf:

- a. makes any warranty, express or implied, with respect to the use of any information, apparatus, method, or process disclosed in this report or that such use may not infringe upon privately owned rights; or
- b. assumes any liabilities of whatsoever kind with respect to the use of, or the damage resulting from the use of, any information, apparatus, method, or process disclosed in this report.

Any opinions, findings, and conclusions or recommendations expressed in this publication are those of the author(s) and do not necessarily reflect the views of MCEER or other sponsors.

## Analytical and Experimental Investigation of Self-Centering Steel Plate Shear Walls

by

Daniel M. Dowden<sup>1</sup> and Michel Bruneau<sup>2</sup>

Publication Date: December 19, 2014

Submittal Date: October 6, 2014

Technical Report MCEER-14-0010

George E. Brown, Jr. Network for Earthquake Engineering Simulation (NEES)  
Program of the National Science Foundation  
NEESR Award Number CMMI-0830294

- 1 Research Engineer, Structural Engineering and Earthquake Simulation Laboratory, Department of Civil, Structural and Environmental Engineering, University at Buffalo, State University of New York
- 2 Professor, Department of Civil, Structural and Environmental Engineering, University at Buffalo, State University of New York

MCEER

University at Buffalo, State University of New York

212 Ketter Hall, Buffalo, NY 14260

E-mail: [mceer@buffalo.edu](mailto:mceer@buffalo.edu); Website: <http://mceer.buffalo.edu>

---



## Preface

MCEER is a national center of excellence dedicated to the discovery and development of new knowledge, tools and technologies that equip communities to become more disaster resilient in the face of earthquakes and other extreme events. MCEER accomplishes this through a system of multidisciplinary, multi-hazard research, in tandem with complimentary education and outreach initiatives.

Headquartered at the University at Buffalo, The State University of New York, MCEER was originally established by the National Science Foundation in 1986, as the first National Center for Earthquake Engineering Research (NCEER). In 1998, it became known as the Multidisciplinary Center for Earthquake Engineering Research (MCEER), from which the current name, MCEER, evolved.

Comprising a consortium of researchers and industry partners from numerous disciplines and institutions throughout the United States, MCEER's mission has expanded from its original focus on earthquake engineering to one which addresses the technical and socio-economic impacts of a variety of hazards, both natural and man-made, on critical infrastructure, facilities, and society.

The Center derives support from several Federal agencies, including the National Science Foundation, Federal Highway Administration, National Institute of Standards and Technology, Department of Homeland Security/Federal Emergency Management Agency, and the State of New York, other state governments, academic institutions, foreign governments and private industry.

*This report presents the results of an analytical and experimental study on a proposed self-centering steel plate shear wall (SC-SPSW) system. To investigate the behavior of SC-SPSWs, a multi-facility experimental program was developed and conducted. First, investigation of one-third scaled single-bay three-story frames was conducted at the Structural Engineering and Earthquake Simulation Laboratory at the University at Buffalo, consisting of quasi-static cyclic and dynamic shake-table testing. Second, a full-scale single-bay two-story specimen was conducted at the National Center for Earthquake Engineering in Taiwan subjected to an earthquake excitation loading using the pseudo-dynamic testing method. Furthermore, to assist in the design of SC-SPSWs, analytical models are developed in the computer programs SAP2000 and OpenSees. Additionally, also needed for the goal of practical implementation and design, fundamental knowledge on the kinematics of SC-SPSWs through detailed free body diagrams is established.*



## PREFACE

The Multidisciplinary Center for Earthquake Engineering Research (MCEER) is a national center of excellence in advanced technology applications that is dedicated to the reduction of earthquake losses nationwide. Headquartered at the University at Buffalo, State University of New York, the Center was originally established by the National Science Foundation in 1986, as the National Center for Earthquake Engineering Research (NCEER).

Comprising a consortium of researchers from numerous disciplines and institutions throughout the United States, the Center's mission is to reduce earthquake losses through research and the application of advanced technologies that improve engineering, pre-earthquake planning and post-earthquake recovery strategies. Toward this end, the Center coordinates a nationwide program of multidisciplinary team research, education and outreach activities.

MCEER's research is conducted under the sponsorship of two major federal agencies: the National Science Foundation (NSF) and the Federal Highway Administration (FHWA), and the State of New York. Significant support is derived from the Federal Emergency Management Agency (FEMA), other state governments, academic institutions, foreign governments and private industry.

*This report presents the results of an analytical and experimental study on a proposed self-centering steel plate shear wall (SC-SPSW) system. To investigate the behavior of SC-SPSWs, a multi-facility experimental program was developed and conducted. First, investigation of one-third scaled single-bay three-story frames was conducted at the Structural Engineering and Earthquake Simulation Laboratory at the University at Buffalo, consisting of quasi-static cyclic and dynamic shake-table testing. Second, a full-scale single-bay two-story specimen was conducted at the National Center for Research on Earthquake Engineering in Taiwan subjected to an earthquake excitation loading using the pseudo-dynamic testing method. Furthermore, to assist in the design of SC-SPSWs, analytical models are developed in the computer programs SAP2000 and OpenSees. Additionally, also needed for the goal of practical implementation and design, fundamental knowledge on the kinematics of SC-SPSWs through detailed free body diagrams is established.*





## ABSTRACT

Conventional lateral force resisting systems (LFRS) that comply with current building codes typically are designed for collapse prevention for a design level earthquake. Accordingly, significant structural damage is expected, leading to large residual drifts where yielded elements are difficult to repair or replace. Consequently, after a design level earthquake, demolition of the building may be required due to severe structural damage. An innovative self-centering steel plate shear wall (SC-SPSW) is proposed. The objective is to offer enhanced structural performance beyond conventional lateral systems by providing frame recentering and also to minimize structural damage of gravity frame components of the LFRS. The SC-SPSW combines the advantages of high initial stiffness and substantial energy dissipation provided by SPSW infill web plates, provides frame self-centering capability through the use of post-tensioned (PT) rocking frame joint connections, and concentrates hysteretic energy dissipation to replaceable infill web plates. In doing so, the SC-SPSW is intended to recover to its near pre-earthquake condition, after a moderate to significant earthquake, decreasing life-cycle costs.

To investigate and validate the behavior of the SC-SPSW system, an experimental program of one-third scaled single-bay three-story frames was developed and conducted, consisting of quasi-static cyclic and dynamic shake-table testing. SC-SPSWs detailed with three different beam-to-column rocking joints were investigated. A final complementary test was performed at the National Center for Research on Earthquake Engineering in Taiwan, where a full scale single-bay two-story specimen was subjected to an earthquake excitation loading using the pseudo-dynamic testing method. The experimental results show that SC-SPSWs systems can be a viable LFRS appropriate for buildings in regions of high seismicity. Furthermore, to assist in the design of SC-SPSWs, fundamental knowledge on the kinematics of SC-SPSWs through detailed free body diagrams are established, from which validated closed-form equations describing beam strength demands, tensile strain demands on the infill web plate, and unrestrained PT boundary frame expansion (aka beam-growth) of frames with PT rocking connections are provided in a form suitable for use as design tools.



## ACKNOWLEDGEMENTS

Financial support was provided by the National Science Foundation as part of the George E. Brown Network for Earthquake Engineering Simulation under award number CMMI-0830294. Steel donations were provided by the American Institute of Steel Construction (AISC). Additional financial support provided to the first author was provided by MCEER and is gratefully appreciated. Any opinions, findings, conclusions, and recommendations presented in this report are those of the writers and do not necessarily reflect the views of the sponsors.

This project was part of a collaborative research program with the University of Washington. Accordingly, the authors would like to acknowledge Tricia Clayton, Professor Jeffery Berman, and Professor Laura Lowes for their collaboration on this project. The authors also acknowledge Professor K.C. Tsai (National Taiwan University) and Chao-Hsien Li (National Center for Research on Earthquake Engineering, NCREE) for collaboration on the NCREE tests conducted in Taiwan. Furthermore, Professor Robert Tremblay and Marie Eve-Gagné of Ecole Polytechnique of Montreal are acknowledged for the collaboration on the frame NZP shake-table test conducted at the University at Buffalo.



# TABLE OF CONTENTS

SECTION	TITLE	PAGE
<b>1</b>	<b>INTRODUCTION</b>	<b>1</b>
1.1	General	1
1.2	Scope and Objectives	2
1.3	Overview of a Self-Centering Steel Plate Shear Wall	3
1.4	Outline	5
<b>2</b>	<b>LITERATURE REVIEW</b>	<b>9</b>
2.1	General	9
2.2	Steel Plate Shear Walls	9
2.2.1	Berman and Bruneau (2008)	10
2.2.2	Shishkin et al. (2009)	12
2.3	Steel Frame Beam-to-Column Rocking Connections	15
2.3.1	Christopoulos et al. (2002)	17
2.3.2	Garlock et al. (2005)	19
2.3.3	Rojas et al. (2005)	23
2.4	Frame Beam-to-Column Rocking Connections and Diaphragm Effects	28
2.4.1	Precast Concrete Construction: Zero beam-growth connections	29
2.4.2	Garlock and Li (2007)	32
2.4.3	Kim and Christopoulos (2009)	35
2.4.4	Iyama et al. (2009) and Wolski et al. (2009)	36
2.4.5	MacRae et al. (2010)	39
2.5	Other Relevant Self-Centering Systems	42
2.6	Relevance of Summarized Research	47
<b>3</b>	<b>KINEMATICS OF SELF-CENTERING STEEL PLATE SHEAR WALLS</b>	<b>49</b>
3.1	General	49
3.2	Basic Principles of Self-Centering SPSW Systems	50

## TABLE OF CONTENTS (cont'd)

SECTION	TITLE	PAGE
3.3	SPSW Self-Centering Configurations	53
3.3.1	Rocking about HBE Flanges	55
3.3.1.1	Free Body Force Diagram	55
3.3.1.2	Development of HBE Moments (rocking about HBE flanges)	64
3.3.1.2.1	HBE Moment Diagrams (rocking about HBE flanges)	68
3.3.1.3	Development of HBE Shears (rocking about HBE flanges)	75
3.3.1.4	Development of HBE Axial Force (rocking about HBE flanges)	76
3.3.1.5	Comparison with SAP2000 (rocking about flanges)	77
3.3.2	Rocking about HBE Centerline	84
3.3.2.1	Free Body Force Diagram	84
3.3.2.2	Development of HBE Moments (rocking about HBE centerline)	90
3.3.2.2.1	HBE Moment Diagrams (rocking about HBE centerline)	95
3.3.2.3	Development of HBE Shears (rocking about HBE Centerline)	99
3.3.2.4	Development of HBE Axial Force (rocking about HBE centerline)	100
3.3.2.5	Comparison with SAP2000 (rocking about HBE centerline)	101
3.3.3	Flange Rocking versus Centerline Rocking	107
3.3.4	NewZ-BREAKSS Rocking Connection	114
3.3.4.1	Free Body Force Diagram	116
3.3.4.2	Development of HBE Moments (NewZ-BREAKSS)	121
3.3.4.2.1	HBE Moment Diagrams (NewZ-BREAKSS)	127
3.3.4.3	Development of HBE Shears (NewZ-BREAKSS)	131
3.3.4.4	Development of HBE Axial Force (NewZ-BREAKSS)	132
3.3.4.5	Comparison with SAP2000 (NewZ-BREAKSS)	133
3.4	Infill Web Plate Strains Effects Due to HBE-to-VBE Gap Opening	138
3.5	Summary	146

## TABLE OF CONTENTS (cont'd)

SECTION	TITLE	PAGE
<b>4</b>	<b>EXPERIMENTAL PROGRAM AND TEST SPECIMEN DESIGN</b>	<b>149</b>
4.1	General	149
4.2	Quasi-Static Tests	150
4.2.1	Prototype Building	150
4.2.2	Static Tests – Specimen Design	152
4.2.2.1	Preliminary Design	152
4.2.2.2	Material Coupon Tests	157
4.2.2.3	Final Design	165
4.2.3	Analytical Results	173
4.2.3.1	Test Specimens	175
4.2.3.2	Frame Response Comparisons: General	181
4.2.4	Frame Response Investigation	183
4.2.4.1	Effects of Post-Tension Parameters	183
4.2.4.2	Frame Response Comparison: NZ versus CR	188
4.3	Shake Table	190
4.3.1	Prototype Building	190
4.3.2	Test Specimen Model Scaling	192
4.3.3	Quasi-Static versus Shake-Table Model Scaling	193
4.3.4	Spectral Response Evaluation	195
4.3.5	Analytical Results	201
<b>5</b>	<b>EXPERIMENTAL TEST SETUP</b>	<b>207</b>
5.1	General	207
5.2	Quasi-Static	207
5.2.1	Test Setup	207
5.2.2	Specimen Construction	214
5.2.3	Instrumentation	223
5.3	Shake-Table	230

## TABLE OF CONTENTS (cont'd)

SECTION	TITLE	PAGE
5.3.1	Test Setup	230
5.3.2	Instrumentation	233
<b>6</b>	<b>SCALED QUASI-STATIC EXPERIMENTAL RESULTS</b>	<b>241</b>
6.1	General	241
6.2	Experimental Loading Protocol and Observations	241
6.2.1	Actuator Loading: Displacement versus Force Control	242
6.2.2	Experimental Loading Protocol and General Observations	244
6.2.3	Observations – Infill Web Plate and Strips	252
6.2.4	Observations – Frame FRS	264
6.3	Flange Rocking (FR) Frame Experimental Results	266
6.3.1	FR: Global Response	266
6.3.2	FR: Boundary Frame Post-Tension Response	271
6.3.3	FR: Infill Web Plate and Strip Strain Gage Response	279
6.3.4	FR: HBE Strain Gage Response	282
6.3.5	FR: HBE Axial and Moment Demands	284
6.4	NewZ-BREAKSS (NZ) Frame Experimental Results	287
6.4.1	NZ: Global Response	287
6.4.2	NZ: Boundary Frame Post-Tension Response	292
6.4.3	NZ: Infill Plate and Strip Strain Gage Response	300
6.4.4	NZ: HBE Strain Gage Response	303
6.4.5	NZ: HBE Axial and Moment Demands	308
6.5	Centerline Rocking (CR) Frame Experimental Results	310
6.5.1	CR: Global Response	310
6.5.2	CR: Boundary Frame Post-Tension Response	315
6.5.3	CR: Infill Plate and Strip Strain Gage Response	325
6.5.4	CR: HBE Axial and Moment Demands	328
6.6	Frame Comparison	330



## TABLE OF CONTENTS (cont'd)

SECTION	TITLE	PAGE
6.7	Experimental versus Analytical: Base Shear versus Roof Drift	332
6.7.1	Experimental versus Analytical: Base Shear versus Roof Drift	332
6.7.2	Experimental versus Analytical: HBE Axial Force and Moments	340
6.8	Design Calculation of Post-Tension Area	343
6.9	Summary	351
<b>7</b>	<b>SCALED SHAKE-TABLE EXPERIMENTAL RESULTS</b>	<b>353</b>
7.1	General	353
7.2	Loading Protocol and Observations	353
7.2.1	Experimental Loading Protocol and General Observations	354
7.3	Dynamic Properties	365
7.3.1	Frame Dynamic Properties	365
7.3.2	Ground Motion Frequency Content	375
7.4	Flange Rocking (FR) Frame Shake-Table Experimental Results	378
7.4.1	FR: Global Response	378
7.4.2	FR: Boundary Frame Post-Tension Response	392
7.4.3	FR: HBE Strain Gage Response	398
7.5	NewZ-BREAKSS (NZ) Frame Shake-Table Experimental Results	402
7.5.1	NZ: Global Response	402
7.5.2	NZ: Boundary Frame Post-Tension Response	414
7.5.3	NZ: HBE Strain Gage Response	420
7.6	Flange Rocking Frame versus NewZ-BREAKSS Frame	424
7.7	NewZ-BREAKSS Frame with Perforated Infill Web Plate	426
7.7.1	NZP: Global Response	429
7.7.2	NZP versus NZW: Global Response	430
7.7.3	NZP: Boundary Frame Post-Tension Response	432
7.7.4	NZP: Experimental Infill Web Plate Observations	434
7.8	Infill Web Plate Deformations	434

## TABLE OF CONTENTS (cont'd)

SECTION	TITLE	PAGE
7.9	Experimental versus Analytical	445
7.10	Summary	450
<b>8</b>	<b>FULL SCALE PSEUDO-DYNAMIC TEST SPECIMEN DESIGN AND LOADING PROTOCOL</b>	<b>453</b>
8.1	General	453
8.2	Prototype Building Description	457
8.3	US-based and Taiwan-based Test Specimen Differences	458
8.4	Test Specimen Design	461
8.4.1	Maximum Base Shear Limit Consideration	462
8.4.2	Analytical Model and Cyclic Pushover Analysis	462
8.4.3	Tributary Seismic Mass for Prototype Frame	468
8.4.4	Selection of GMs and Loading Protocol	470
8.5	PT Boundary Frame Test – Loading Protocol	479
8.6	Analytical Results	481
8.7	PT Boundary Frame Characteristics with VBE PT Base	485
<b>9</b>	<b>FULL SCALE PSEUDO-DYNAMIC EXPERIMENTAL TESTS</b>	<b>491</b>
9.1	General	491
9.2	Specimen NZ fabrication and Construction	491
9.3	Test Setup	497
9.4	Instrumentation	501
9.5	Pseudo-Dynamic Loading Procedure	505
9.6	Free Vibration Tests	506
9.7	Experimental Observations	511
9.7.1	Experimental Observations – PSD Tests	511
9.7.2	Experimental Observations – Inelastic Cyclic Tests	519
9.8	PSD Experimental Results	523

## TABLE OF CONTENTS (cont'd)

SECTION	TITLE	PAGE
9.8.1	PSD Global Response	523
9.8.2	PSD Local Response	526
9.8.2.1	Boundary Frame Post-Tension Response	526
9.8.2.2	Boundary Frame Strain Gage Response	531
9.8.2.2.1	Boundary Frame Strain Gage Response - VBEs	531
9.8.2.2.2	Boundary Frame Strain Gage Response – HBEs	533
9.8.2.3	Boundary Frame Axial and Moment Demands	539
9.8.2.3.1	Boundary Frame Axial and Moment Demands - VBEs	540
9.8.2.3.2	Boundary Frame Axial and Moment Demands - HBEs	541
9.8.2.4	Boundary Frame Infill Web Plate Displacement Transducers	546
9.9	Inelastic Cyclic and Bare Frame Cyclic Experimental Results	549
9.9.1	Cyclic Global Response	549
9.9.2	Cyclic Local Response	551
9.10	Experimental versus Analytical Comparisons	554
9.11	PT Boundary Frame Expansion – Derivation of Beam-Growth	559
9.12	Comparison of UB Shake-Table and NCREE PSD Specimen Response	568
9.13	Summary	572
<b>10</b>	<b>SUMMARY, CONCLUSIONS, AND RECOMMENDATIONS</b>	<b>573</b>
10.1	Summary	573
10.2	Conclusions	575
10.3	Recommendations for Future Research	577
<b>11</b>	<b>REFERENCES</b>	<b>581</b>

## TABLE OF CONTENTS (cont'd)

SECTION	TITLE	PAGE
<b>APPENDIX</b>		
<b>A</b>	<b>INSTRUMENTATION DRAWINGS</b>	<b>587</b>
A1	Quasi-Static	587
A2	Shake-Table	623
<b>B</b>	<b>SUPPORTING INFORMATION ON QUASI-STATIC TEST FRAME FR ACTUATOR INTERACTION</b>	<b>645</b>
B.1	General	645
B.2	Investigation by Calculation	645

## LIST OF ILLUSTRATIONS

FIGURE	TITLE	PAGE
1-1	SC-SPSW idealized kinematics (flange-rocking frame)	4
1-2	SC-SPSW flange-rocking frame idealized force-displacement response: components	4
1-3	SC-SPSW flange-rocking frame idealized force-displacement response: (a) cycle 1; (b) cycle 2	5
2-1	VBE free body diagrams (Berman and Bruneau 2008)	12
2-2	Driver et al. (1997) SPSW: (a) specimen; (b) detailed model (Shishkin et al. 2009)	13
2-3	(i) PTED concept (ii) PTED idealized moment versus rotation response: (a) contribution of post-tension bars; (b) contribution of energy-dissipating bars; (c) combined response (Christopoulos et al. 2002)	18
2-4	Test setup: (a) ED bar (b) PTED conn. (Christopoulos et al. 2002)	19
2-5	(a) Schematic elevation of one floor of a post-tensioned frame; (b) connection detail (Garlock et al. 2005)	20
2-6	(a) Moment-rotation behavior; (b) deformation of a decompressed post-tensioned connection (Garlock et al. 2005)	21
2-7	Test setup (Garlock et al. 2005)	22
2-8	(a) Schematic elevation of one floor of a post-tensioned frame; (b) connection detail (Rojas et al. 2005)	23
2-9	Behavior of friction device (Rojas et al. 2005)	24
2-10	Moment-rotation behavior (Rojas et al. 2005)	25
2-11	Free body diagram of post-tensioned friction damped connection (Rojas et al. 2005)	26
2-12	Layout and structural system of prototype buildings (Rojas et al. 2005)	27
2-13	Frames used in analytical study (Rojas et al. 2005)	28
2-14	TCY gap frame connection (Srithan et al. 2000)	30

## LIST OF ILLUSTRATIONS (cont'd)

FIGURE	TITLE	PAGE
2-15	Hybrid Frame with draped unbonded tendons and metallic top hinge (Mesa 2010)	31
2-16	Hybrid Frame top hinge connection detail (Mesa 2010)	31
2-17	One floor of Self-Centering Moment Resisting Frame: (a) elevation view before lateral loading; (b) elevation view after lateral loading; (c) plan view of 3 collector-beam design; (d) 15-collector-beam design (Garlock and Li 2007)	33
2-18	Hypothetical beam force distribution in a 15 collector-beam design of a Self-Centering Moment Resisting Frame (Garlock and Li 2007)	35
2-19	Detailing between concrete slab and post-tensioned self-centering frame to eliminate the restraining effects of slab (Kim and Christopolous 2009)	36
2-20	Self-centering connections with different ED devices (Iyama et al. 2009)	37
2-21	Idealized moment-rotation response with different ED devices (Iyama et al. 2009)	38
2-22	Free body diagram of a BFFD connection (Iyama et al. 2009)	38
2-23	Sliding Hinge Joint Detail (MacRae et al. 2010)	40
2-24	Sliding of plates below beam during cyclic deformations (MacRae et al. 2010)	41
2-25	Concept of SCED systems (Christopolous et al. 2008)	44
2-26	Mechanics and hysteretic response of SCED systems (Christopolous et al. 2008)	44
2-27	Generic schematic of SCED with friction device (Christopolous et al. 2008)	45
2-28	Tested SCED prototype: (a) 3D view; (b) cross-section (Christopolous et al. 2008)	45
2-29	Setup for SCED frame assemblage tests (Christopolous et al. 2008)	46
2-30	Tensile force-deflection response of aramid type fibers (Christopolous et al. 2008)	46
3-1	Yield mechanism self-centering SPSW	50
3-2	Rocking mechanisms	53

## LIST OF ILLUSTRATIONS (cont'd)

FIGURE	TITLE	PAGE
3-3	Free body diagram of intermediate HBE	55
3-4	Resultant force free body diagram	56
3-5	Free body diagram vertical component	57
3-6	Partial free body diagram horizontal component	58
3-7	Partial free body diagram horizontal component at rocking connection	60
3-8	Complete force resultant free body diagram of HBE	63
3-9	SPSW infill corner cut-outs	65
3-10	Free body diagram along Zone 1	65
3-11	Free body diagram along Zone 2	66
3-12	Free body diagram along Zone 3	67
3-13	Moment diagram – Rocking about HBE flanges	70
3-14	Moment diagram - Vertical force component	71
3-15	Moment diagram - Horizontal force corner cut-out effects	71
3-16	Moment diagram - Horizontal force VBE component	72
3-17	Moment diagram - Post-tension force	72
3-18	Moment diagram – Story shear force	73
3-19	Moment diagram - No post-tension provided	74
3-20	Flange-rocking frame - Analytical model	77
3-21	Rocking about HBE flanges connection – Analytical model	79
3-22	Moment diagram – Rigid HBE	81
3-23	Moment diagram – Flexible HBE	81
3-24	Shear force diagram – Rigid HBE	82
3-25	Shear force diagram – Flexible HBE	82
3-26	Axial force diagram – Rigid HBE	83
3-27	Axial force diagram – Flexible HBE	83
3-28	Resultant force free body diagram	85
3-29	Free body diagram post-tension forces	86

## LIST OF ILLUSTRATIONS (cont'd)

FIGURE	TITLE	PAGE
3-30	Complete force resultant free body diagram of HBE	89
3-31	SPSW infill corner cut-outs	90
3-32	Free body diagram along Zone 1	91
3-33	Free body diagram along Zone 2	92
3-34	Free body diagram along Zone 3	93
3-35	Free body diagram along Zone 4	94
3-36	Free body diagram along Zone 5	95
3-37	Moment diagram – Rocking about HBE centerline	96
3-38	Moment diagram - Vertical force component	97
3-39	Moment diagram - Horizontal force corner cut-out effects	97
3-40	Moment diagram - Post-tension force	98
3-41	Centerline-rocking frame - Analytical model	102
3-42	Rocking about HBE centerline connection – Analytical model	103
3-43	Moment diagram – Rigid HBE	104
3-44	Moment diagram – Flexible HBE	104
3-45	Shear force diagram – Rigid HBE	105
3-46	Shear force diagram – Flexible HBE	105
3-47	Axial force diagram – Rigid HBE	106
3-48	Axial force diagram – Flexible HBE	106
3-49	Rocking connection comparison	108
3-50	Rocking connection comparison	109
3-51	Rocking connection comparison	110
3-52	Rocking connection comparison	111
3-53	Rocking connection comparison	111
3-54	NewZ-BREAKSS rocking connection	115
3-55	Resultant force free body diagram	116
3-56	Partial free body diagram horizontal component	117



## LIST OF ILLUSTRATIONS (cont'd)

FIGURE	TITLE	PAGE
3-57	Free body diagram post-tension forces	117
3-58	Reduced post-tension force on HBE	118
3-59	Complete force resultant free body diagram of HBE	120
3-60	SPSW infill corner cut-outs	121
3-61	Free body diagram along Zone 1	122
3-62	Free body diagram along Zone 2	123
3-63	Free body diagram along Zone 3	124
3-64	Free body diagram along Zone 4	125
3-65	Free body diagram along Zone 5	126
3-66	Moment diagram – NewZ-BREAKSS	127
3-67	Moment diagram - Vertical force component	128
3-68	Moment diagram - Horizontal force HBE component	128
3-69	Moment diagram - Horizontal force VBE component	129
3-70	Moment diagram - Post-tension force	129
3-71	Moment diagram – Story shear force	130
3-72	NewZ-BREAKSS frame - Analytical model	133
3-73	NewZ-BREAKSS connection – Analytical model	134
3-74	Moment diagram – Rigid HBE	135
3-75	Moment diagram – Flexible HBE	135
3-76	Shear force diagram – Rigid HBE	136
3-77	Shear force diagram – Flexible HBE	136
3-78	Axial force diagram – Rigid HBE	137
3-79	Axial force diagram – Flexible HBE	137
3-80	HBE-to-VBE joint gap formation	139
3-81	Panel sway kinematics	139
3-82	HBE-to-VBE rocking joint kinematics	141
3-83	Infill web plate corner cut-out dimensions	142

## LIST OF ILLUSTRATIONS (cont'd)

FIGURE	TITLE	PAGE
3-84	Corner infill web plate strain demands	145
3-85	Corner infill web plate strain components	146
4-1	Prototype building: quasi-static tests	150
4-2	(a) Prototype building site; (b) design response spectrum	151
4-3	Weld connection coupons: (a) coupons; (b) coupon details	159
4-4	Weld-coupon: (a) coupons; (b) fracture example; (c) approximate mechanical properties	160
4-5	22 GA web plate coupon: (a) test data; (b) analytical model	162
4-6	24 GA web plate coupon: (a) test data; (b) analytical model	163
4-7	26 GA web plate coupon: (a) test data; (b) analytical model	164
4-8	Test frame elevations	166
4-9	Test specimen elevation: (a) FR; (b) NZ; (c) CR	167
4-10	HBE-to-VBE joint details	168
4-11	Test specimen HBE-to-VBE joint detail: (a) FR; (b) NZ; (c) CR	169
4-12	Test frame with web strips	171
4-13	Test specimen with web strips	171
4-14	Foundation anchorage	172
4-15	Test specimen foundation anchorage: (a) side view; (b) front view	172
4-16	Analytical model frames: (a) FR; (b); NZ; (c) CR	174
4-17	OpenSees versus SAP2000: base shear versus roof drift	175
4-18	Quasi-static test analytical response: (a) infill web plate; (b) infill web strips	178
4-19	PT boundary frame versus Total response	179
4-20	Response components: (a) infill web plate; (b) PT boundary frame	180
4-21	PT boundary frame - Monotonic pushover comparison	182
4-22	PT boundary frame – $T_o$ Variable	185
4-23	PT boundary frame – $A_{pt}$ variable	187
4-24	NZ and CR comparison: (a) $T_o = 30\%x_{Apt}$ ; (b) $T_o = 0$	189

## LIST OF ILLUSTRATIONS (cont'd)

FIGURE	TITLE	PAGE
4-25	Prototype building: shake-table tests	191
4-26	Ground motion response spectrum	191
4-27	Synthetic ground motion: (a) prototype building; (b) scaled model building	192
4-28	Spectral response – prototype building comparison	198
4-29	Spectral response – prototype and model comparison	199
4-30	FR frame spectral response	200
4-31	NZ frame spectral response	201
4-32	Spectral acceleration response – scaled GM: (a) FR frame; (b) NZ frame	204
4-33	Spectral displacement response – scaled GM: (a) FR frame; (b) NZ frame	205
4-34	Analytical incremental dynamic response: (a) 2% damping; (b) 5% damping	206
5-1	GMF test specimen connection	208
5-2	Typical connections: (a) diaphragm; (b) lateral brace point	210
5-3	GMF base anchorage connection	211
5-4	GMF actuator connection	212
5-5	Actuator shoe: (a) Global view; (b) Close-up view	213
5-6	PT anchor details	218
5-7	Typical PT anchor: (a) stressing end; (b) dead end	218
5-8	PT stressing shoe	219
5-9	PT stressing aid	219
5-10	(a) Initial web plate weld; (b) Final web plate weld	220
5-11	Frame construction aid	221
5-12	Temporary foundation attachments	221
5-13	(a) Test specimen; (b) Construction aid; (c) Foundation connection	222
5-14	Quasi-static test specimen: (a) initial placement; (b) final setup	222
5-15	Quasi-static: Frame FR instrumentation	225
5-16	Quasi-static: Frame FR (NZ and CR similar) infill web strips strain gages	226
5-17	Quasi-static: Frame NZ instrumentation	227

## LIST OF ILLUSTRATIONS (cont'd)

FIGURE	TITLE	PAGE
5-18	Quasi-static: Frame CR instrumentation	228
5-19	Quasi-static: GMF instrumentation	229
5-20	Shake-table setup schematic	231
5-21	Shake-table setup final	232
5-22	Shake-table: Frame FR instrumentation	235
5-23	Shake-table: Frame FR (NZ similar) krypton sensors	236
5-24	Shake-table: Frame NZ instrumentation	237
5-25	Shake-table: GMF instrumentation	238
5-26	Shake-table: extension frame instrumentation	239
6-1	Actuator response	243
6-2	Specimen response	244
6-3	Quasi-static loading protocol	245
6-4	Infill web plate deformation	254
6-5	Infill web strip deformation	254
6-6	Infill web plate tearing - Legend	255
6-7	Frame FRW - infill web plate tearing: (a) Level 3; (b) Level 2; (c) Level 1	256
6-8a	Frame FRW – web plate tearing progression	257
6-8b	Frame FRW – web plate tearing progression	258
6-9	Frame NZW - infill web plate tearing: (a) Level 3; (b) Level 2; (c) Level 1	259
6-10	Frame CRW – infill web plate – stress arresting holes	261
6-11	Frame CRW - infill web plate tearing: (a) Level 3; (b) Level 2; (c) Level 1	262
6-12	Infill web plate tearing comparison: (a) Level 3; (b) Level 2; (c) Level 1	263
6-13	Level 1 Frame FR: (a) SW bot. flange; (b) SE bot. flange; (c) SW bot. flange	265
6-14	Level 2 Frame FR: (a) SW bot. flange; (b) SE top flange	265
6-15	Frame FR – global response	267
6-16	Frame FR – interstory response	270
6-17	Frame FRW – initial PT forces	272

## LIST OF ILLUSTRATIONS (cont'd)

FIGURE	TITLE	PAGE
6-18	Frame FRW – PT response	272
6-19	Frame FRW – select PT response: (a) Level 3; (b) Level 1	273
6-20	Frame FRB – initial PT forces	275
6-21	Frame FRB – PT response	275
6-22	Frame FRS – initial PT forces	276
6-23	Frame FRS – PT response	276
6-24	Frame FR – initial PT forces normalized by displacement step 1	278
6-25	Normalized initial PT force changes between FR tests	278
6-26	Frame FRW – infill web plate strains	280
6-27	Frame FRS – infill web strip strains	281
6-28	Frame FRS – HBE end strain versus gap rotation	283
6-29	Frame FRS – HBE axial force and moments	286
6-30	Frame NZ – global response	289
6-31	Infill web plate tearing effect on hysteresis response	290
6-32	Base shear versus roof drift: (a) NZW; (b) NZS; (c) 2% drift; (d) 6% drift	290
6-33	Frame NZ – interstory response	291
6-34	Frame NZW – initial PT forces	294
6-35	Frame NZW – PT response	294
6-36	Frame NZB – initial PT forces	295
6-37	Frame NZB – PT response	295
6-38	Frame NZS – initial PT forces	297
6-39	Frame NZS – PT response	297
6-40	Frame NZ – initial PT forces normalized by displacement step 1	298
6-41	Normalized initial PT force changes: (a) East end; (b) West end; (c) averaged	299
6-42	Frame NZW – infill web plate strains	301

## LIST OF ILLUSTRATIONS (cont'd)

FIGURE	TITLE	PAGE
6-43	Frame NZS – infill web strip strains	302
6-44	Frame NZW – HBE end strain versus gap rotation	305
6-45	Frame NZB – HBE end strain versus gap rotation	306
6-46	Frame NZS – HBE end strain versus gap rotation	307
6-47	Frame NZS – HBE axial force and moments	309
6-48	Frame CR – global response	311
6-49	Frame CR – interstory response	312
6-50	Frame CRB – residual base shear force	314
6-51	Frame CRB – residual base shear force adjusted	314
6-52	Frame CRW – initial PT forces	316
6-53	Frame CRW – initial PT forces normalized by displacement step 1	317
6-54	Frame CRW – PT response	318
6-55	Frame CRB – initial PT forces	319
6-56	Frame CRB – initial PT forces normalized by displacement step 1	320
6-57	Frame CRB – PT response	321
6-58	Frame CRS – initial PT forces	322
6-59	Frame CRS – initial PT forces normalized by displacement step 1	323
6-60	Frame CRS – PT response	324
6-61	Normalized initial PT force changes between CR tests	325
6-62	Frame CRW – infill web plate strains	326
6-63	Frame CRS – infill web strip strains	327
6-64	Frame CRS – HBE axial force and moments	329
6-65	Frame NZ versus CR – global response	331
6-66	Frame NZ versus CR – infill web response	331
6-67	Frame NZ: Experimental versus Analytical – global response	336
6-68	Frame CR: Experimental versus Analytical – global response	337
6-69	Frame FR: Experimental versus Analytical – global response	338

## LIST OF ILLUSTRATIONS (cont'd)

FIGURE	TITLE	PAGE
6-70	Analytical infill web plate compression: (a) uni-directional; (b) bi-directional	339
6-71	Frame NZS: Experimental versus Analytical – HBE axial force and moments	341
6-72	Frame CRS: Experimental versus Analytical – HBE axial force and moments	342
6-73	Analytical global response – Apt variable: (a) FRW; (b) NZW	344
6-74	PT boundary frame response: (a) generic condition; (b) design condition	349
6-75	NewZ-BREAKSS post-tension design example: (a) rigid frame sway mechanism; (b) joint moment strength; (c) frame lateral force distribution	350
6-76	NewZ-BREAKSS post-tension design example results	350
7-1	Infill web plate deformation: (a) Level 3; (b) Level 2; (c) Level 1	361
7-2	Infill web strip deformation: (a) Level 3; (b) Level 2; (c) Level 1	362
7-3	Frame FRW - infill web plate tearing	363
7-4	Frame NZW - infill web plate tearing	364
7-5	Sample white noise base excitation	365
7-6	Experimental versus Analytical – elastic fundamental period	366
7-7	FRW: (a) Transfer function elastic; (b) Transfer function inelastic; (c) Mode shapes	367
7-8	FRB: (a) Transfer function elastic; (b) Transfer function inelastic; (c) Mode shapes	368
7-9	FRS: (a) Transfer function elastic; (b) Transfer function inelastic; (c) Mode shapes	369
7-10	NZW: (a) Transfer function elastic; (b) Transfer function inelastic; (c) Mode shapes	370
7-11	NZB: (a) Transfer function elastic; (b) Transfer function inelastic; (c) Mode shapes	371

## LIST OF ILLUSTRATIONS (cont'd)

FIGURE	TITLE	PAGE
7-12	NZS: (a) Transfer function elastic; (b) Transfer function inelastic; (c) Mode shapes	372
7-13	Frame FRS - Logarithmic decay equivalent viscous damping	374
7-14	Frame FR - Target versus achieved acceleration response spectra	376
7-15	Frame NZ - Target versus achieved acceleration response spectra	377
7-16	Frame FR - original versus filtered hysteresis	379
7-17	Frame FRW - select global response	385
7-18	Frame FRB - select global response	386
7-19	Frame FRS - select global response	387
7-20	Frame FR - global response	388
7-21	Global response: (a) FRW versus FRB; (b) FRS versus FRB	389
7-22	Frame FR - story shear versus interstory drift	390
7-23	Frame FR - incremental dynamic response	391
7-24	Frame FRW – initial PT forces	394
7-25	Frame FRW – PT response	394
7-26	Frame FRB – initial PT forces	395
7-27	Frame FRB – PT response	395
7-28	Frame FRS – initial PT forces	396
7-29	Frame FRS – PT response	396
7-30	Frame FR – initial PT forces normalized by GM amplitude 1	397
7-31	Normalized initial PT force changes between FR tests	397
7-32	Frame FRW – HBE end strain versus gap rotation	399
7-33	Frame FRB – HBE end strain versus gap rotation	400
7-34	Frame FRS – HBE end strain versus gap rotation	401
7-35	Frame NZ - original versus filtered hysteresis	403
7-36	Frame NZW - select global response	407
7-37	Frame NZB - select global response	408



## LIST OF ILLUSTRATIONS (cont'd)

FIGURE	TITLE	PAGE
7-38	Frame NZS - select global response	409
7-39	Frame NZ - global response	410
7-40	Global response: (a) NZW versus NZB; (b) NZS versus NZB	411
7-41	Frame NZ - story shear versus interstory drift	412
7-42	Frame NZ - incremental dynamic response	413
7-43	Frame NZW – initial PT forces	415
7-44	Frame NZW – PT response	415
7-45	Frame NZB – initial PT forces	416
7-46	Frame NZB – PT response	416
7-47	Frame NZS – initial PT forces	417
7-48	Frame NZS – PT response	417
7-49	Frame NZ – initial PT forces normalized by GM amplitude 1	418
7-50	Normalized initial PT force change between NZ tests: (a) West; (b) East; (c) averaged	419
7-51	Frame NZW – HBE end strain versus gap rotation	421
7-52	Frame NZW: HBE end strain versus gap rotation – Select GMs	422
7-53	Frame NZB – HBE end strain versus gap rotation	422
7-54	Frame NZB: HBE end strain versus gap rotation – Select GMs	423
7-55	Frame NZS – HBE end strain versus gap rotation	423
7-56	Frame NZS: HBE end strain versus gap rotation – Select GMs	424
7-57	Frame FR versus NZ - incremental dynamic response	425
7-58	Frame NZP - frame elevation	427
7-59	Frame NZP - perforated infill web plate	427
7-60	Frame NZP – test setup	428
7-61	Frame NZP - global response	429
7-62	Frame NZP - incremental dynamic response	430
7-63	Frame NZP versus NZB: Global response - Select GMs	430

## LIST OF ILLUSTRATIONS (cont'd)

FIGURE	TITLE	PAGE
7-64	Frame NZP versus NZW - incremental dynamic response	431
7-65	Frame NZP versus NZW – Global Response – Select GMs	431
7-66	Frame NZP – PT response	433
7-67	Frame NZP – initial PT forces normalized by GM amplitude 1	433
7-68	Perforated infill web plate deformation	436
7-69	Post-testing bolt holes at infill web plate corners	436
7-70	Frame NZP - infill web plate tearing	437
7-71	Frame FRW and NZW – gap rotation versus interstory drift	438
7-72	Frame FRB and NZB – gap rotation versus interstory drift	439
7-73	Frame FRS and NZS – gap rotation versus interstory drift	440
7-74	Frame NZ: Gap rotation versus interstory drift – Level 1	441
7-75	Frame FRW and NZW - experimental versus theoretical	442
7-76	Frame FRB and NZB - experimental versus theoretical	443
7-77	Frame FRS and NZS - experimental versus theoretical	444
7-78	Frame NZP - experimental versus theoretical	445
7-79	Frame FRW - incremental dynamic response: (a) analytical; (b) experimental versus analytical	447
7-80	Frame NZW and NZP - incremental dynamic response: (a) analytical; (b) experimental versus analytical	448
7-81	Frame FRS and NZS - incremental dynamic response: (a) FRS; (b) NZS	449
8-1	Specimen NZ	455
8-2	(a) NewZ-BREAKSS joint detail; (b) VBE base rocking detail	456
8-3	NCREE Prototype Building	457
8-4	(a) VBE PT top detail; (b) VBE PT base kinematics	460
8-5	Infill panel web plate stress-strain coupons	464
8-6	Analytical model infill web plate axial hinge	465
8-7a	OpenSees model	467

## LIST OF ILLUSTRATIONS (cont'd)

FIGURE	TITLE	PAGE
8-7b	OpenSees model (alternate HBE-to-VBE)	467
8-8	Cyclic pushover analysis Specimen NZ versus FR	469
8-9	Pseudo-dynamic GMs	472
8-10a	Spectral acceleration response – original GMs	473
8-10b	Spectral acceleration response – PSD GMs	474
8-11a	Spectral displacement response – original GMs	475
8-11b	Spectral displacement response – PSD GMs	476
8-12	Analytical incremental dynamic response	483
8-13	Analytical sample roof drift history	483
8-14	Analytical base shear versus roof drift	484
8-15	PT boundary frame characteristics (for Eastward drift)	486
8-16	PT boundary frame comparisons	489
8-17	PT boundary frame variation in VBE $T_o$	489
8-18	(a) $T_o$ variable; (b) $A_{pt}$ variable	490
9-1a	Specimen NZ construction: Step 1 – assemble boundary frame	494
9-1b	Specimen NZ construction: Step 2 – install temporary HBE PT bars	494
9-1c	Specimen NZ construction: Step 3 – install web plates	495
9-1d	Specimen NZ construction: Step 4 – remove temporary HBE PT bars	495
9-1e	Specimen NZ construction: Step 5 – install HBE PT strands	496
9-2a	Test setup plan	500
9-2b	Test setup elevation	500
9-3	Test setup final	501
9-4	Displacement transducers	503
9-5	PT load cells	504
9-6	Boundary frame strain gages	504
9-7	PSD Free vibration tests	509
9-8	Test specimen dynamic properties	510

## LIST OF ILLUSTRATIONS (cont'd)

FIGURE	TITLE	PAGE
9-9	PSD ground motion loading protocol	512
9-10	PSD roof drift observation hold points	512
9-11	Infill web plate tearing – PSD tests	514
9-12	Infill web plate – inelastic cyclic tests	515
9-13	HBE-to-VBE flange separation	516
9-14	PT anchorage plate: observed twisting and detail (DSI Int.)	518
9-15a	2/50 GM select test photos	521
9-15b	End of test select photos	522
9-16	PSD global response	525
9-17	HBE PT force versus interstory drift and gap rotation versus interstory drift	528
9-18	VBE PT force versus roof drift and gap rotation versus interstory drift	528
9-19	HBE initial PT force history	529
9-20	VBE initial PT force history	531
9-21	West VBE: $\Delta$ Strains versus gap rotation	532
9-22	Strain effect schematic due to localized flange deformation	533
9-23	Level 2 HBE: End $\Delta$ Strains versus gap rotation	536
9-24	Level 2 HBE: 1/6 point $\Delta$ Strains versus gap rotation	537
9-25	Level 1 HBE: End $\Delta$ Strains versus gap rotation	538
9-26	Level 1 HBE: 1/6 point $\Delta$ Strains versus gap rotation	539
9-27	VBE bottom: $\Delta$ Axial force and $\Delta$ Moment versus gap rotation	541
9-28	Level 2: HBE end $\Delta$ Axial force and end $\Delta$ Moment versus gap rotation	542
9-29	Level 2: HBE 1/6 point $\Delta$ Axial force and interior $\Delta$ Moment versus gap rotation	542
9-30	Level 1: HBE end $\Delta$ Axial force and end $\Delta$ Moment versus gap rotation	543
9-31	Level 1: HBE 1/6 point $\Delta$ Axial force and interior $\Delta$ Moment versus gap rotation	543
9-32	HBE: $\Delta$ Axial force and $\Delta$ Moment distribution	544

## LIST OF ILLUSTRATIONS (cont'd)

FIGURE	TITLE	PAGE
9-33	Infill web plate axial deformation response	547
9-34	Experimental versus theoretical	548
9-35	Cyclic global response	550
9-36	Cyclic PT force response	552
9-37	L2 HBE: end total strains versus roof drift	553
9-38	L1 HBE: end total strains versus roof drift	553
9-39	PSD global response: experimental versus analytical	557
9-40	Incremental dynamic response: experimental versus analytical	558
9-41	Cyclic pushover response: experimental versus analytical	558
9-42	Frame beam-growth schematic	560
9-43	Frame beam-growth kinematics	562
9-44a	NewZ-BREAKSS connection Alt. detail 1	567
9-44b	NewZ-BREAKSS connection Alt. detail 2	568
9-45	UB versus NCREE - incremental dynamic response	569
9-46	UB versus NCREE - DBE response spectra	570
9-47	NCREE PSD spectral response	571
9-48	UB shake-table spectral response (scaled specimen)	572



## LIST OF TABLES

TABLE	TITLE	PAGE
4-1	Simultude scale factors	152
4-2	Similitude scale factors for prototype and shake-table model building	156
5-1	Quasi-static test instrumentation	223
5-2	Shake-table test instrumentation	234
6-1	Quasi-static test #1 loading protocol and observations	246
6-2	Quasi-static test #2 loading protocol and observations	247
6-3	Quasi-static test #3 loading protocol and observations	248
6-4	Quasi-static test #4 loading protocol and observations	249
6-5	Quasi-static test #5 loading protocol and observations	250
6-6	Quasi-static test #6 loading protocol and observations	250
6-7	Quasi-static test #7 loading protocol and observations	251
6-8	Quasi-static test #8 loading protocol and observations	251
6-9	Quasi-static test #9 loading protocol and observations	252
7-1	Shake-table test #1 loading protocol and observations	355
7-2	Shake-table test #2 loading protocol and observations	356
7-3	Shake-table test #3 loading protocol and observations	356
7-4	Shake-table test #4 loading protocol and observations	357
7-5	Shake-table test #5 loading protocol and observations	358
7-6	Shake-table test #6 loading protocol and observations	359
7-7	Shake-table test #7 loading protocol and observations	360
7-8	Shake-table rocking roof drift effects – Frame FRW	381
7-9	Shake-table rocking roof drift effects – Frame FRS	381
7-10	Shake-table rocking roof drift effects – Frame NZW	404
7-11	Shake-table rocking roof drift effects – Frame NZS	404
8-1	NCREE test loading protocol	478
8-2	NCREE test loading protocol – PT boundary frame	480
9-1	NCREE test observations	513





# SECTION 1

## INTRODUCTION

### 1.1 General

The field of earthquake engineering, for the development of lateral force resisting systems (LFRS), has significantly advanced in both research and the current state of practice in the past decades. Conventional LFRS steel systems that comply with current building codes and the AISC seismic specifications used in the United States are typically expected to suffer damage during an earthquake. Designed in accordance with prescribed detailing requirements proven by research to ensure ductile response (and protect occupants), these structural system are not expected to collapse during a severe earthquake, but will likely require repairs following a design level earthquake. Thus, although current conventional LFRS systems have shown to meet the code objective for standard buildings (collapse prevention), significant structural damage occurs (albeit controlled damage), rendering the function of the building possibly useless after a design level earthquake, and potentially leading to demolition of the building following the design level earthquake.

More recent research has demonstrated that it is possible to design steel structures to achieve greater performance objectives, by designing either specific energy dissipating elements or sacrificial structural components such to leave the remaining surrounding gravity frame essentially free of damage. However, to be fully successful, such strategies need to account for the interaction between the LFRS and the gravity frame (such as the transfer of diaphragm lateral forces to the LFRS, to name one). Such buildings could economically provide a level of protection designated as available for “immediate occupancy” following an earthquake. This strategy makes sense from a life-cycle cost perspective.

Towards that goal, researchers have proposed various LFRS systems, including steel and concrete moment frames with alternative beam-to-column moment rocking connections (e.g., Ricles et al. 2002, Christopoulos et al. 2002, Garlock et al. 2003, MacRae et al. 2010) and (e.g., Cheok and Lew 1991, MacRae and Priestley 1994, Stanton et al. 1997, Mesa 2010) respectively. In general, these LFRS systems incorporate a “structural fuse” concept (e.g., Vargas 2006),

where energy dissipation is provided by designated elements that are replaceable after the seismic event, while the surrounding structure is designed to remain essentially elastic. Furthermore, many of these connections characteristically provide self-centering of the building structure such that the residual building roof drift, after a design level seismic event, is within an acceptable out-of-plumb tolerance (e.g., typically less than 0.2% drift).

## **1.2 Scope and Objectives**

The research presented in this report proposes a new type of seismic structural system, known as a self-centering steel plate shear wall (SC-SPSW), compatible with the above higher performance objectives, that combines steel plate shear walls (SPSW), with a steel boundary frame, and with post-tensioned (PT) moment rocking connections. It is the objective of this research to validate this new LFRS system through experimental and analytical investigation, with the goal of facilitating practical implementation.

The SC-SPSW developed here combines the advantages of high initial stiffness and substantial energy dissipation capacity of conventional SPSWs (itself a seismic structural system accepted by current design standards, such as AISC 341-10), with the self-centering capability of steel moment PT rocking connections. Here the structural fuse is provided by the infill web plate (to be replaced after a moderate and/or design level earthquake), and the PT boundary frame consisting of column vertical boundary elements (VBE), beam horizontal boundary elements (HBE) and the PT monostrands (or alternatively rods) are designed to remain essentially elastic.

To investigate the behavior of the SC-SPSW system as an alternative LFRS for buildings located in moderate to high seismic regions, an experimental program of one-third scaled single-bay three-story frames was developed and conducted, consisting of quasi-static cyclic and dynamic shake-table testing. SC-SPSWs detailed with three different HBE-to-VBE rocking joints were investigated. A complementary test was performed at the National Center for Research on Earthquake Engineering (NCREE) in Taiwan, where a full scale single-bay two-story specimen was subjected to an earthquake excitation loading using the pseudo-dynamic testing method. Furthermore, to assist in the design of SC-SPSW, fundamental knowledge on the kinematics of SC-SPSWs through detailed free body diagrams are established, from which validated closed-

form equations describing HBE strength demands, tensile strain demands on the infill web plate, and unrestrained beam-growth of frames with PT rocking connections are provided in a form suitable for use as design tools.

### **1.3 Overview of a Self-Centering Steel Plate Shear Wall**

A SC-SPSW differs from a conventional SPSW in that the HBE-to-VBE rigid moment connections are replaced by PT rocking moment connections. This allows a joint gap opening to form between the VBE and HBE interface about a rocking point, leading to a PT elongation that then serves as the self-centering mechanism (a schematic of which is shown in figure 1-1). Furthermore, the base connection of the VBEs for a SC-SPSW should be detailed such to allow free rotation without the formation of a plastic hinge mechanism (in contrast to conventional SPSWs where typically a fixed VBE base connection is assumed). If a plastic hinge is able to form at the base of the VBE member, this could limit the self-centering potential of the PT boundary frame. Furthermore, providing a foundation detail free of damage would also use the SC-SPSW to its full potential. As a result, the only needed replaceable elements after a moderate or design level earthquake would be the infill web plates, as all other elements are designed to remain essentially elastic.

It then follows that the total hysteretic response of a SC-SPSW is provided by the combined elastic response of the PT boundary frame and the inelastic energy dissipation of the infill web plate (figure 1-2). Similar to self-centering moment frames (referenced earlier), the idealized PT boundary frame response loads and unloads along a bilinear elastic force-displacement curve; the initial frame stiffness is provided by the PT joint connection, up to the point of joint opening that defines the “decompression” moment. Once the decompression moment is exceeded, the PT boundary frame follows a second force-displacement path of lower lateral frame stiffness, dependent on the interaction of the axial stiffness of the PT and the HBE. It is this bilinear elastic response of the PT boundary frame, when combined with the inelastic hysteretic response of the energy dissipation elements, which provides the characteristic “flag-shaped” hysteretic response of self-centering LFRS systems. For a SC-SPSW system, the idealized cyclic hysteretic response obtained assuming a rigid boundary frame and an elastic-perfectly plastic tension-only hysteretic model of the infill web plate is shown in figure 1-3.

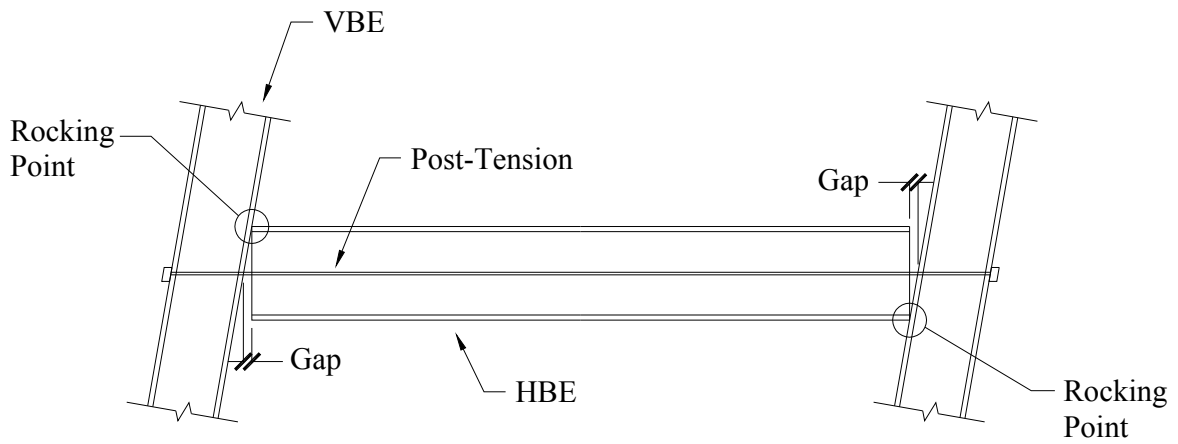


**FIGURE 1-1 SC-SPSW idealized kinematics (flange-rocking frame)**

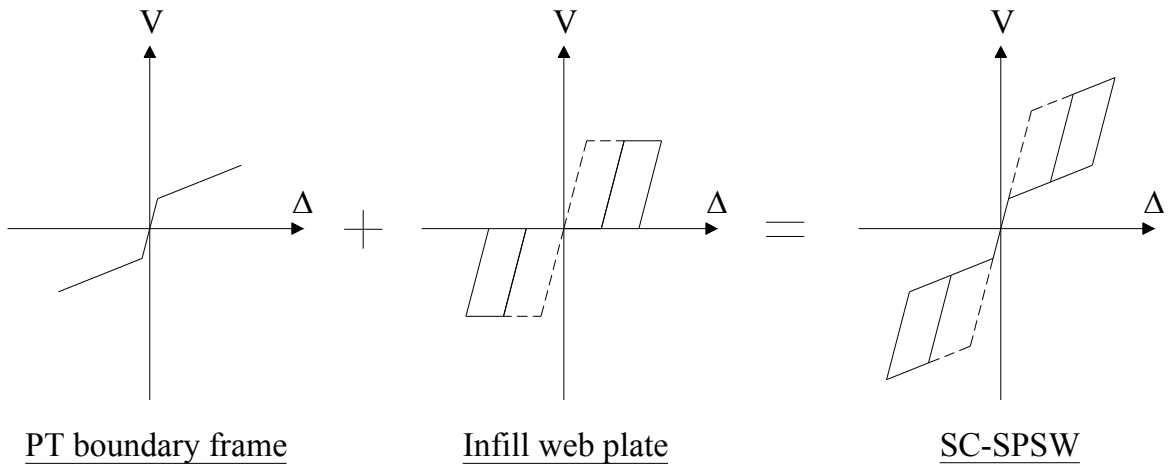


**FIGURE 1-2 SC-SPSW flange-rocking frame idealized force-displacement response: components**

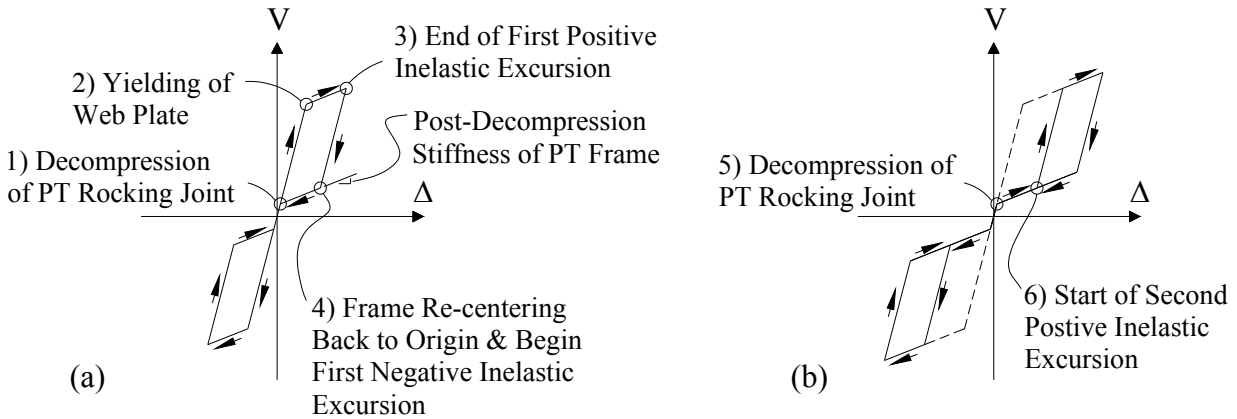


**FIGURE 1-3 SC-SPSW flange-rocking frame idealized force-displacement response: (a) cycle 1; (b) cycle 2**

Note that the idealized description presented above is for PT rocking joints that are detailed for rocking about the HBE flanges (i.e., a flange-rocking frame). Different PT rocking joints will have a similar flag-shaped hysteretic response but as a consequence of different kinematics (presented in Section 4). To prevent undesired interaction effects between the PT boundary frame and other elements of the structural system, such as the floor/roof diaphragms (as described in more detail in Section 2.4), in addition to this particular HBE-to-VBE rocking joint, a centerline rocking joint and a new proposed NewZ-BREAKSS rocking joint (Dowden and Bruneau 2011) are investigated for use in SC-SPSW systems as part of this research. These latter two HBE-to-VBE connections, given proper detailing, are intended to make possible immediate building occupancy following an earthquake.

## 1.4 Outline

This document includes ten sections (including this introduction) and two appendices A and B that contain the test specimen(s) instrumentation drawings and supportive information pertaining to observed undesired actuator interaction effects with the quasi-static flange-rocking frame tests. The remaining sections include the following general information:

- Section 2: A brief literature review is provided, covering past research that has some relevance to the topic at hand. Specifically, a select review of previous research related

to SPSWs, steel frame beam-to-column rocking connections, and frame rocking connection effects on diaphragms is presented.

- Section 3: The kinematics of SC-SPSW systems is investigated for three HBE-to-VBE rocking connections. Based on capacity design principles, closed form equations that describe the moment, shear and axial demand along the length of the HBE are obtained through detailed free body diagrams. Analytical models are then developed validating these equations. Furthermore, the effects of an HBE-to-VBE joint gap opening on the infill web plate tensile strain is investigated. Accordingly, detailed free body diagrams are developed leading to a closed-form equation that describes the tensile strains in the infill web plate for a given HBE-to-VBE joint rotation.
- Section 4: The experimental program and test specimen design are presented for both the quasi-static and shake-table tests along with preliminary analytical results. Furthermore, results are provided from monotonic pushover analyses conducted to identify the differences in frame response between the SC-SPSW frames detailed with different HBE-to-VBE rocking joints and the effects due to different PT parameters.
- Section 5: The experimental test setup is presented for both the quasi-static and shake-table tests which include: a description of the test setup, general construction sequence of the test frames, and instrumentation.
- Section 6: The loading protocol and experimental results along with comparison to analytical results for the quasi-static tests are presented. Furthermore, a simple design approach is presented for the calculation of HBE post-tension for a target residual drift.
- Section 7: The loading protocol and experimental results along with comparison to analytical results for the shake-table tests are presented.
- Section 8: The experimental program, loading protocol, and test specimen design is presented for the full-scale NCREE pseudo-dynamic test. Additionally, preliminary analytical results are provided. Furthermore, monotonic pushover analyses are conducted identifying frame response of a SC-SPSW detailed with a PT column base rocking detail (i.e., a different column base detail than used in the scaled tests).
- Section 9: Experimental results along with comparison to analytical results for the NCREE pseudo-dynamic test are presented. Furthermore, a derivation of beam-growth (as described in Section 2.4) using detailed free body diagrams is presented leading to a

closed-form equation that describes the beam-growth along the height of a frame for a given roof drift.

- Section 10: A summary of major findings, conclusions, and future research recommendations is provided.





## **SECTION 2**

### **LITERATURE REVIEW**

#### **2.1 General**

Significant advances in experimental and analytical research has been achieved in the past 30 years on steel plate shear walls (SPSW) and self-centering rocking systems. Accordingly, there is a significant amount of literature related to the subject matter. However, for brevity, only a narrow window of that past research is summarized, focusing here on issues closer to the specifics of the research presented in this report. As such, Section 2.2, 2.3, and 2.4, respectively, provide a select review of previous research related to SPSWs, steel frame beam-to-column rocking connections, and frame beam-to-column rocking connection effects on diaphragms. Furthermore, a non-rocking self-centering system is reviewed in Section 2.5.

#### **2.2 Steel Plate Shear Walls**

The use of SPSWs as the primary lateral force resisting system (LFRS) for building structures was implemented as early as in the 1970s. However, in these early applications, SPSWs were designed to dissipate hysteretic energy primarily through shear yielding, which either required thick infill web plates (i.e., unstiffened web plates) or the use of intermediate horizontal steel members to increase the shear buckling strength (i.e., stiffened web plates). At the time, there was apparently no available experimental data on the post-shear-buckling response of SPSWs.

To advance the knowledge of these LFRS systems, while also improving their cost efficiency for broader implementation by using thin unstiffened infill web plates and eliminating the need for thick infill web plates and intermediate horizontal stiffeners, subsequent analytical and experimental research in the early 1980s (Thorburn et al. 1983, Timler and Kulak 1983) investigated the post-shear-buckling response of SPSWs. This research validated the use of thin unstiffened infill web plates buckling in shear and developing tension field action to dissipate hysteretic energy (with tension field action similar to that investigated in plate girders by Wagner, 1931). Since this time, many researchers have expanded and refined the knowledge on SPSWs which has lead to codified design provisions (AISC 2010, CSA 2009). Much of that research is described in Bruneau and Sabelli (2007) and Bruneau et al. (2011), to name a few.

Note that design provision for SPSWs were first introduced in the 2005 AISC 341 Standard in the United States, and, previously, in the Canadian Steel Design Standard CAN/CSA S16.1 in 1994 (Bruneau and Sabelli, 2007).

As a result of the analytical and experimental research efforts culminating to codification of design requirements for SPSWs, significant knowledge is available on the seismic behavior of these systems. Although the present research is focusing on self-centering SPSWs, the mechanics of infill web plate behavior and its effects on the boundary frame in self-centering SPSWs is essentially no different than for conventional SPSWs. Therefore, only a few relatively recent studies on the analysis and design of the boundary frame elements of SPSWs that are particularly relevant to self-centering SPSW boundary frames are summarized below.

### **2.2.1 Berman and Bruneau (2008)**

The design intent of the AISC *Seismic Provision for Structural Steel Buildings* (AISC 2005b) for SPSWs (when subjected to a design basis earthquake) is that their horizontal boundary elements (HBEs) and vertical boundary elements (VBEs) should remain essentially elastic under the maximum forces generated by the tension field action of the fully yielded infill web plate, with the exception of plastic hinging at the ends of HBEs is permitted (and at the base of VBEs). Three design methods were presented in the commentary of the 2005 Edition of the AISC Seismic Provisions (2005b) to achieve this goal, but Berman and Bruneau (2008) identified the inaccuracies of some of these methods, leading to a new proposed VBE design procedure. The following is a brief description of the existing methods and the identified underlying deficiency.

- i. The first method, Combined Linear Elastic Computer Program and Capacity Design Concept (LE+CD), uses a linear elastic computer frame analysis of the boundary frame elements. Superposition of analysis results is then performed using different loading conditions with or without the infill web elements modeled with the boundary frame. Inconsistencies with respect to equilibrium were identified that did not ensure proper capacity design of the boundary elements.
- ii. The second method, Indirect Capacity Design (ICD) taken from the CSA-S16-02 (CSA, 2002) design standard, uses a linear elastic computer frame analysis that includes the

boundary frame elements and infill web plate elements. Capacity design of the VBEs is then approximated by increasing the moment and axial demand obtained from the linear elastic analysis by an amplification factor, based on a ratio of the expected shear strength of the infill web plate at the base of the wall divided by the factored lateral seismic force at the base of the wall. However, this amplification factor is calculated at the foundation level where the resulting amplification factor, may not accurately represent the conditions at the upper stories. Furthermore, the amplification factor does not consider the strength contribution of the surrounding boundary frame, which could have a substantial effect on the actual amplification factor.

- iii. The third method, nonlinear static pushover analysis, generally leads to a correct solution (on the basis of ensuring capacity design), but requires several iterations from a design perspective and is more complex in that it requires the modeling of nonlinear hinges in the frame and infill web elements. Hence, although the method is accurate, it can be time consuming.

Berman and Bruneau proposed an alternative procedure, using a fundamental plastic collapse mechanism and linear beam analysis to approximate the design actions for VBEs of SPSWs for given web plates and horizontal boundary member sizes. First, a model of the VBE on elastic supports is used to determine the axial forces in the HBEs and a plastic collapse mechanism is assumed to estimate the lateral seismic loads that cause full infill web plate yielding and plastic hinging of HBEs at their ends. A simple VBE free body diagram (shown in figure 2.1) is then used to determine the design VBE axial forces and moments. Although for design, several iterations may be necessary as initial parameters are assumed at the start of the procedure; this method does not involve nonlinear analysis or modeling of the entire SPSW frame. The results obtained using this procedure are typically in agreement with the nonlinear static pushover analysis (method iii), whereas the remaining procedures (method i and ii) have been shown to give significant inaccurate results in some instances.

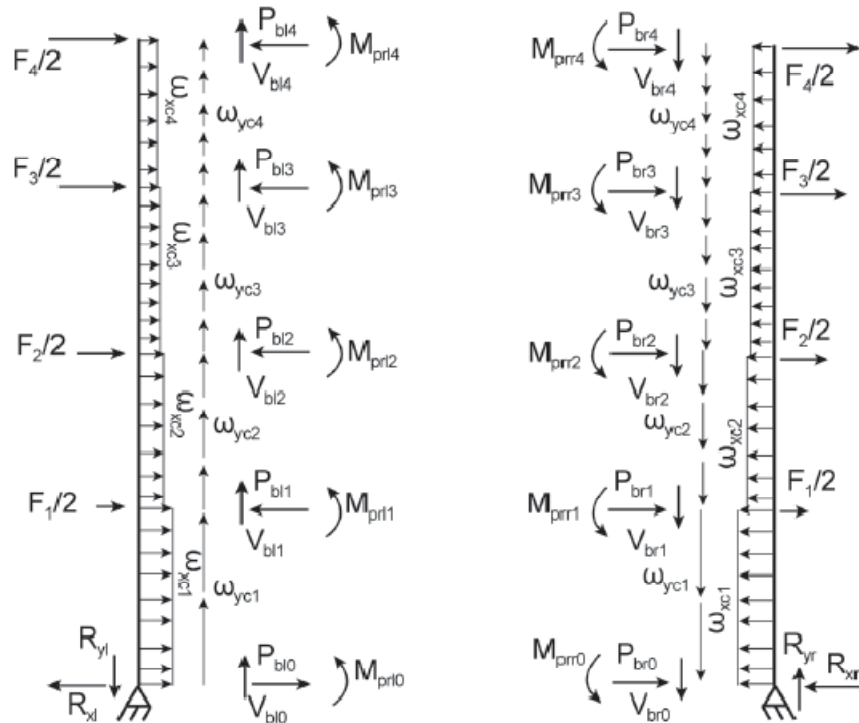


FIGURE 2-1 VBE free body diagrams (Berman and Bruneau 2008)

### 2.2.2 Shishkin et al. (2009)

Shishkin et al. (2009) proposed a refinement to the original strip model by Thorburn et al. (1983) to obtain a more accurate prediction of the inelastic behavior of SPSWs. For this purpose, a “detailed strip model” was first developed based on calibration with the experimental results from the Driver et al. (1998) test specimen using nonlinear monotonic pushover analysis. Material nonlinearities were incorporated by the designation of user defined flexural plastic hinges at the HBE-to-VBE connection at a distance of one-half depth of the member away from an assumed rigid panel zone (where flexural plastic hinges assigned to the VBEs were also reduced for the presence of axial forces), and tension-only axial plastic hinges for the infill web strips. Although the inclusion of plastic hinges had often been done in SPSW analyses using commercially available software, what was unique with the proposed detailed strip model was the use of a compression strut with a rigid-plastic hinge and deterioration infill web strips.

The proposed analytical model, for monotonic pushover analysis, is shown in figure 2-2b for a rightward drift condition. The compression strut (labeled as such in the figure) is placed in the

opposite orientation as the infill web strips, located at the corner-to-corner of the infill web panel, and has an equivalent cross-sectional area representing the whole infill web panel (i.e., assumes that the whole infill web plate contributes to compression resistance).

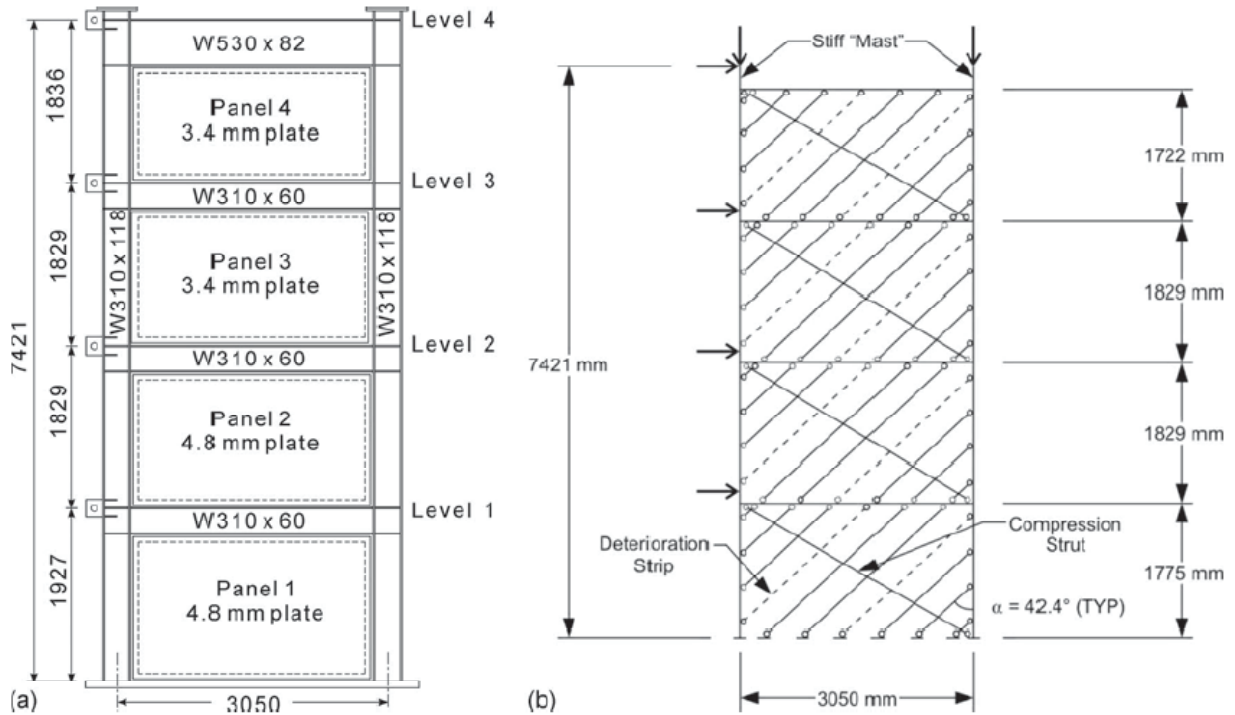


**FIGURE 2-2 Driver et al. (1997) SPSW: (a) specimen; (b) detailed model (Shishken et al. 2009)**

The deterioration strips (labeled as such in the figure are shown with the dashed line-type to further differentiate them from the typical tension-only infill strips shown, which have a solid line-type) were placed such that a deterioration strip was provided at opposite frame joint corners as shown in the figure. More specifically:

- i. The compression strut was added based on the observation that strip models (which are based on tension-only strips) tend to somewhat underestimate both the elastic stiffness and the ultimate capacity. This discrepancy was attributed to possible compression strength of the infill web plate (Driver et al. 1998). Furthermore, based on the empirical observations of Kulak et al. (2001) that considered both the capacity of the wall and energy dissipation characteristics in cyclically loaded models, the value of maximum

stress for the compression strut was set at 8% of the yield strength of the infill web plate; this was confirmed to be appropriate in a sensitivity analysis by Shishkin et al. (2005).

- ii. The deterioration strips were provided to simulate tearing of the infill web plate near the corners of the infill web plate. This was done in the strips by modifying the axial hinge definition to include degradation based on the empirical observations made by Driver et al. (1998a).

To further simplify the model, a sensitivity analysis on several parameters of the detailed model was performed. This led to the proposed simpler “modified strip model” (of geometry identical to that shown in figure 2-2), intended to be more appealing for use as a design tool. In this latter model, the flexural plastic hinges at the HBE-to-VBE locations were simplified to be rigid-perfectly plastic, all frame joint flexural plastic hinges were moved from a distance of half the depth of the member away from the column panel zone to the column panel zone boundary (i.e., effectively locating the beam plastic hinges at the end span of the beams, and providing a column plastic hinge at the top and bottom location of the column panel zone boundary), axial plastic hinges of the infill web strips were simplified to be rigid-perfectly plastic definitions, the layout of all the infill web strips used an average value of  $\alpha$  (i.e., the inclination angle of the diagonal tension field to the vertical), and the tension strips were spaced at equal intervals such that the strips in panels above and below the HBE shared the same nodes as suggested by Timler et al. (1998). A comparison of nonlinear pushover analysis of the detailed and modified strip models indicated that little accuracy was lost by using the simplified modeling assumptions.

The modified strip model was then used to simulate the nonlinear pushover response of a one-story SPSW test frame by Lubell et al. (2000), which was chosen because this frame was very different in geometry and had a much thinner infill web plate thickness than the Driver et al. (1998) frame. It was found that the peak capacity of the model pushover curve occurred at a considerably smaller top frame deflection than observed in the experiment, suggesting that deterioration in the modified strip model did not accurately replicate the deterioration observed in the Lubell et al. (2000) frame. This was attributed to the relatively thin infill web plate used in the Lubell et al. frame compared to that for the Driver et al. frame, for which Shishkin et al. suggested that thinner web plates would be less susceptible to tearing from out-of-plane web

plate buckling effects from tension-field action of the infill web plate. To assess the effectiveness of the model without considering the tearing failure mode, the deteriorating strip model was replaced by tension-only strips with similar non-deteriorating axial hinges used across the infill web plate. The pushover results obtained from this new analysis were found to be in good agreement with the experimental ones, indicating that the use of deteriorating strips predicted the same peak strength, but at a much smaller roof drift. The model was then re-analyzed without the compression strut (keeping the non-deteriorating strips) and the resulting initial elastic stiffness agreed well with that of the test specimen, but the predicted ultimate strength was underestimated by approximately 6%. From those analyses, Shishkin et al. concluded that for very thin infill web plates, the compression strut effect does not form in the early stage of loading, and that after approximately halfway through the initial yield portion of the envelope, the full compression strut effect starts to develop.

Furthermore, it was determined that although the global base shear versus roof drift response could be reasonably predicted with the modified strip model (by the inclusion or exclusion of the deteriorating web strips and/or compression strut, to create upper and lower bound peak responses), in general the proposed model over estimated the internal frame member forces, indicating that further improvement to the model can be made.

Finally, a parametric study was performed using nonlinear pushover analysis on the effects of  $\alpha$  using the modified strip model. One, four, and fifteen story frames were considered with varying panel aspect ratios and boundary frame flexibilities. Furthermore, for these parameters, an  $\alpha$  value of 38 and 50 degrees was considered. The results indicated that the nonlinear pushover response was relatively insensitive to the variation in  $\alpha$ , and it was proposed that a single value of 40 degrees could be used to simplify such future analyses.

### **2.3 Steel Frame Beam-to-Column Rocking Connections**

The development of post-tensioned (PT) rocking connections in steel frames in the early 2000s in the United States was influenced by prior research conducted by the National Institute of Standards and Technology (NIST) in 1987 (Cheok and Lew 1991) and the PREcast Seismic Structural Systems (PRESSSS) program in the early 1990s (MacRae and Priestley 1994). The

former was a four-phase research program tasked with developing guidelines for the design of precast concrete frame connections in regions of high seismicity. The latter was a multi-team three-phase research program, conducted in collaboration with Japanese researchers, on large scale seismic testing of pre-cast concrete buildings. These two research programs were quite extensive. A specific product of particular interest here is the connection that became known as the “hybrid” connection (e.g., Cheok et al. 1993, Cheok and Stone 1994, Stanton et al. 1997). This innovative connection provided frame recentering capabilities using continuous unbonded PT reinforcement located at the mid-depth of the beam and anchored to the outside of the supporting columns. Repeatable energy dissipation capability was provided to those connections by the use of bonded mild reinforcement, located at the top and bottom of the beam section at the column-to-beam rocking joint. Later, this beam-to-column rocking joint concept was adapted for use in steel moment frames as an alternative to moment connection (e.g., Ricles et al. 2002, Christopoulos 2002, Garlock 2002). In addition to frame recentering, the performance objective of these proposed steel framed systems also included limiting energy dissipation to replaceable hysteretic elements. Other similar self-centering steel moment frame systems used friction elements to dissipate energy (Rojas 2003, Kim and Christopoulos 2008). The proposed PT steel moment connections (some of which described below), with the exception of the energy dissipation element, are all similar in that prior to the connection reaching the decompression moment (a term to be clarified subsequently), the connection response is identical to that of a conventional steel moment connection.

As the current research aims to extend the knowledge developed for self-centering steel moment frames (using PT moment connections and the basic design philosophy of keeping the boundary frame essentially elastic) for use with SPSWs. As will be shown in subsequent Sections, for the SPSW application, the PT boundary frame construction is similar (for one of the three proposed self-centering SPSW configurations), but a pin connection is proposed at the base of the columns to the foundation, and the replaceable energy dissipation element is the infill web plate. Accordingly, the literature review summarized below in this section is limited to PT steel moment connections.



### 2.3.1 Christopoulos et al. (2002)

A post-tensioned steel moment frame detail, referred to as the post-tensioned energy dissipating (PTED) connection, was proposed by Christopoulos et al. (2002) and is shown in figure 2-3i. The PTED connection uses high strength PT bars located at mid-depth of the beams provided on each side of the beam web and energy dissipating (ED) bars located at the top and bottom beam flanges. The ED bars are threaded into couplers which are welded to the inside face of the beam flanges and column continuity plates. Additionally, the ED bars are encased by steel cylinders to limit buckling, enabling stable inelastic deformation in both tension and compression. Furthermore, flange reinforcing steel plates are welded to the beam flanges to control flange local yielding and buckling. Additionally, steel shim plates are provided at the beam-to-column flange rocking contact points to facilitate the beam flange rocking behavior about its flanges. Beam shear transfer is provided through coulomb-friction between the beam-to-column flange contact points from the clamping force provided by the PT. Christopoulos et al. indicated that dowel action of the ED and PT bars could also provide an alternative shear transfer mechanism in case of a loss of PT force between the beam-to-column contact points. Other alternative means of shear transfer mentioned included shear tabs with horizontal slotted holes or a flexible seat angle (as long as it could deform without developing any substantial moment restraint).

The idealized hysteretic behavior of the PTED connection is shown in figure 2-3ii in terms of moment versus joint rotation. The total flag-shaped hysteretic response shown (figure 2-3ii-c) is a result of the combination of the nonlinear elastic response of the PT boundary frame (figure 2-3ii-a) and the nonlinear inelastic response of the ED bars (figure 2-3ii-b). In particular, typical of such flange-rocking connections, the moment at point A in figure 2-3ii-a is referred to as the decompression moment, which depends on the distance from the beam-to-column flange rocking point to the centroid of the PT and the initial PT force provided. For joint rotations up to the decompression moment, no beam-to-column gap opening is present and the connection response is identical to that of a conventional steel moment frame connection. Furthermore, full recentering in the PTED connection is achieved only if the moment after the first half-cycle (indicated as  $M_E$  in figure 2-3ii-c) is positive. An analytical procedure based on an iterative beam sectional approach by Pampanin et al. (1999) was adopted and modified for use with the PTED connection that allows determination of the complete moment-rotation relationship.

Furthermore, using the determined moment-rotation relationship, a design procedure was developed for a target rotation along with the assumption that at the target rotation, it is assumed that neutral axis is located at a distance  $c$  (see figure 2-3i) equal to the beam flange thickness from the edge of the compression flange.

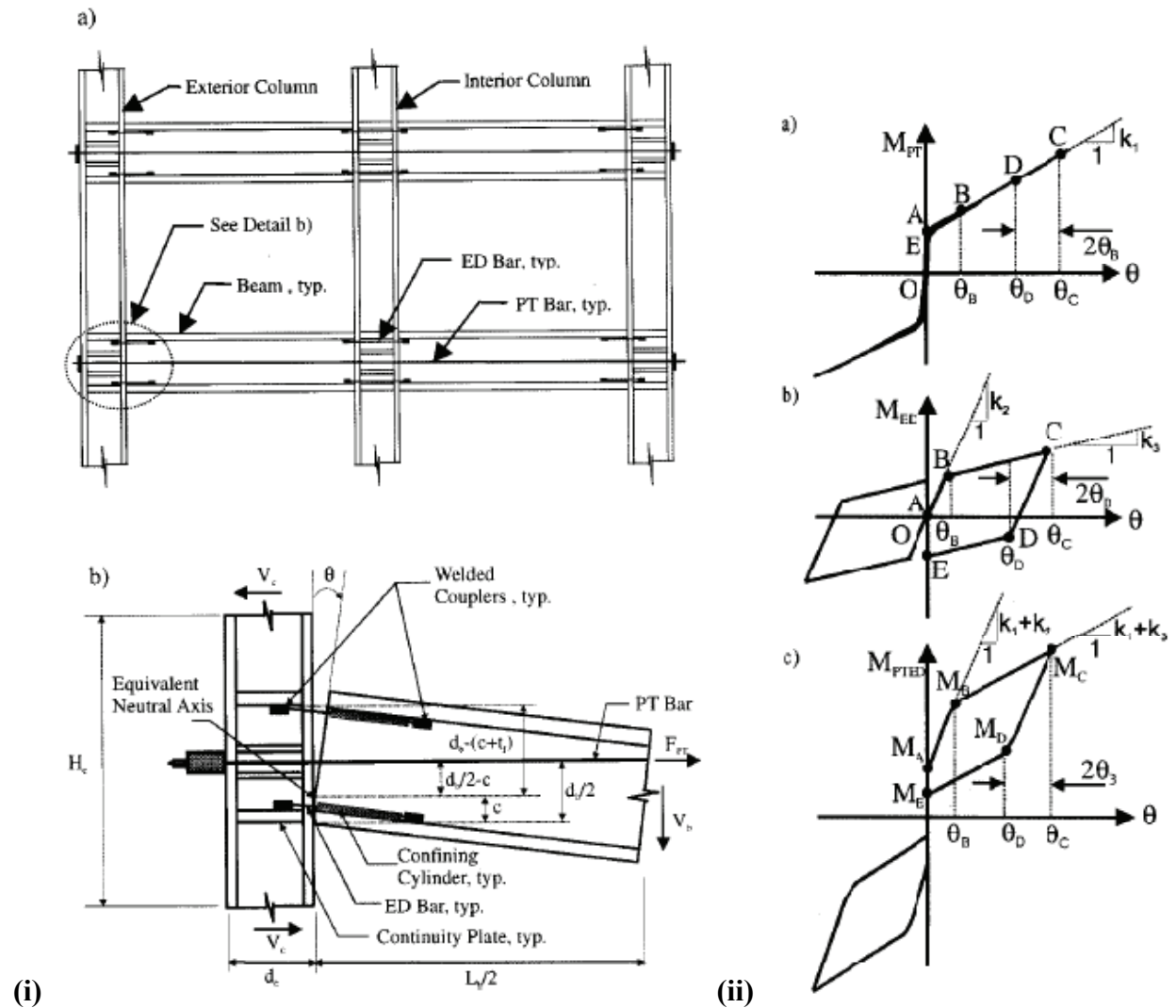


**FIGURE 2-3 (i) PTED concept (ii) PTED idealized moment versus rotation response: (a) contribution of post-tension bars; (b) contribution of energy-dissipating bars; (c) combined response (Christopoulos et al. 2002)**

To validate the analytical work and to investigate the response of the PTED connection experimentally, component testing of the ED bars was first investigated followed by quasi-static testing of a full-scale PTED connection subassembly. The test setup for both respective experiments is shown in figure 2-4. The experimental results for the ED component testing

showed that that the ED bar assemblage exhibited good energy dissipating response and could be incorporated in the PTED connection. The experimental results of the PTED connection subassembly showed that the proposed connection is able to undergo large deformations with stable energy dissipation characteristics, beam and column remain essentially elastic, and self-centering of the connection is achieved. Furthermore, the adequacy of the analytical models and design procedure developed to predict the experimental response was confirmed.

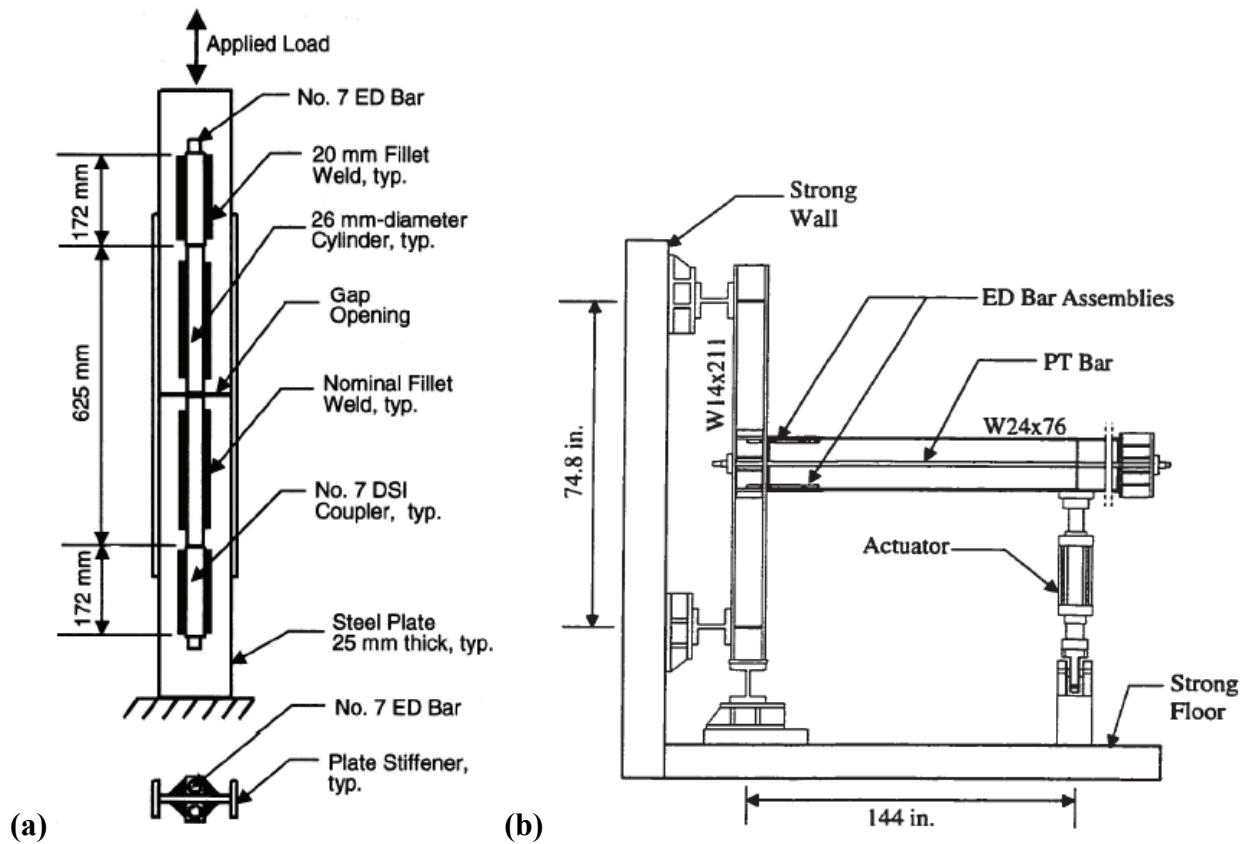
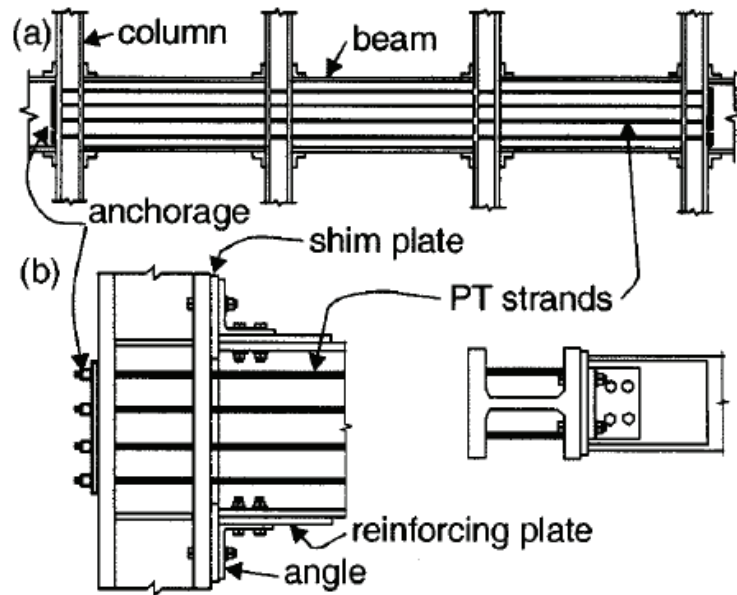


FIGURE 2-4 Test setup: (a) ED bar (b) PTED conn. (Christopoulos et al. 2002)

### 2.3.2 Garlock et al. (2005)

A slightly different post-tensioned steel moment frame connection proposed by Garlock et al. (2005) is shown in figure 2-5. The connection uses high strength bundled PT monostrands symmetrically placed such that the centroid of the PT grouping coincides with the centroid of the beam. Flange reinforcing steel plates are welded to the beam flanges to control flange local yielding and local buckling. Additionally, steel shim plates are provided at the beam-to-column

flange rocking contact points such that only the beam flange and flange reinforcement plates are in contact with the column flange. Energy dissipation is provided by bolted steel top-and-seat angles where hysteretic energy is dissipated through flexural plastic hinging of the angles. In particular, Garlock et al. (2003) showed that the steel angle in tension develops a mechanism by the formation of three plastic hinges (figure 2-6): namely one plastic hinge forms on the fillet of each angle leg, and another near the bolts connecting the angle to the column flange. Beam shear transfer is provided through coulomb-friction between the beam-to-column flange contact points; this friction resistance is proportional to the clamping force provided by the PT. In addition, although not their primary purpose, the top-and-seat angles provide a redundant load path for transfer of beam shear to the columns.



**FIGURE 2-5 (a) Schematic elevation of one floor of a post-tensioned frame; (b) connection detail (Garlock et al. 2005)**

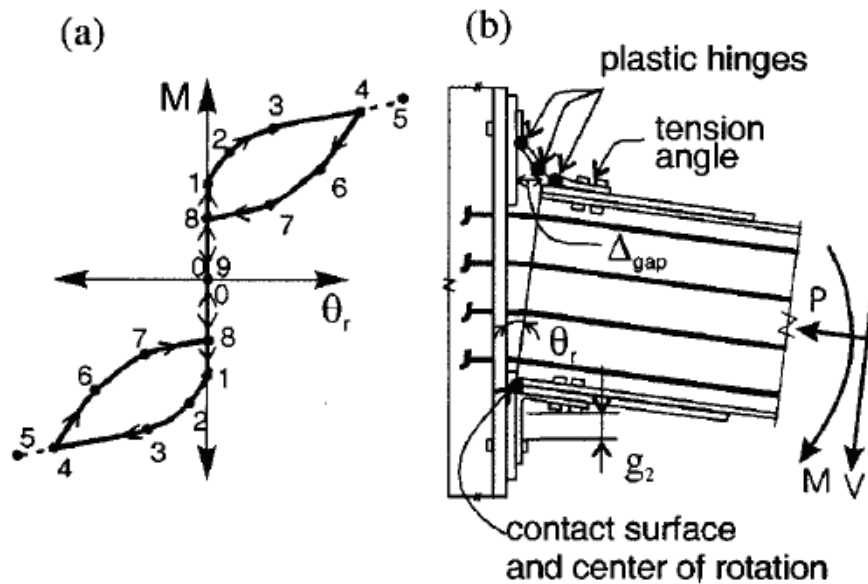


**FIGURE 2-6 (a) Moment-rotation behavior; (b) deformation of a decompressed post-tensioned connection (Garlock et al. 2005)**

The idealized hysteretic behavior of the connection is shown in figure 2-6 in terms of moment versus joint rotation, where for a positive joint rotation (behavior is the same in the negative direction, but with opposite signs):

- a) The connection behaves as a conventional steel moment frame connection up to event 1.
- b) The stiffness of the connection after decompression (event 1) is associated with the stiffness of the angles and the elastic axial stiffness of the PT strands. With continued loading, the steel angle in tension yields (event 2), with full plastic yielding of the steel angle in tension at event 3. If continued loading occurs, the PT strands will eventually yield at event 5.
- c) Unloading occurs at event 4 and the top-and-seat angles provide hysteretic energy dissipation up to event 8 where the gap between the beam-to-column flanges has closed. So long as the beam, column, and PT remained essentially elastic, self-centering will be achieved at event 8.

Component testing of the angles was performed and the yield mechanism (shown in figure 2-6) along with empirical formulas describing the actual strength of the angles was developed (Garlock et al. 2003). These relationships were then used to obtain closed-form equations to predict the connection response. Furthermore, based on force equilibrium and enforcing strain compatibility, a closed-form equation for the post-tension force in the strands was derived that included the axial stiffness effects due to axial shortening of both the PT strands and beam.

To validate the analytical work and to investigate the response of the connection experimentally, quasi-static testing of a full-scale connection subassembly was conducted. The subassembly test setup is shown in figure 2-7. The boundary conditions of the cruciform shaped test specimen were provided to simulate an interior moment frame joint of the prototype frame considered. The test matrix included six test specimens, where the parameters considered were the number of PT strands, the total initial PT force provided, and the length of the beam flange reinforcement plates. Furthermore, the parameters were chosen such that different failure limits states were targeted. Namely, angle fracture, PT strand yield, and beam local buckling.

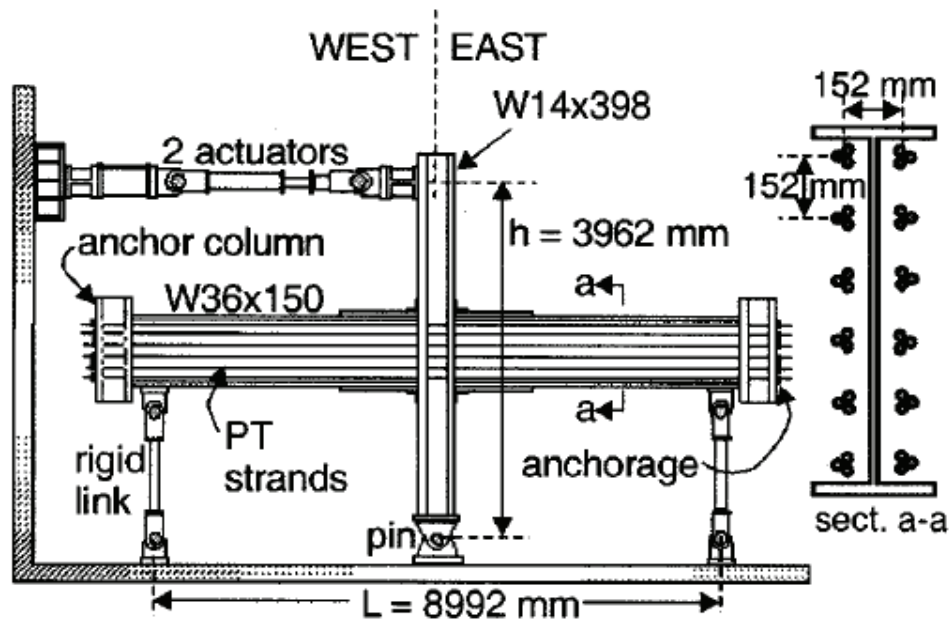


FIGURE 2-7 Test setup (Garlock et al. 2005)

The experimental results of the connection subassembly showed that the proposed connection was able to undergo large deformations with stable energy dissipation characteristics, beam and

column remained essentially elastic, and self-centering of the connection was achieved. Furthermore, the predictions using the closed-form equations that estimated the maximum connection moment and maximum PT strand force were found to be in good agreement with experimental results.

**2.3.3 Rojas et al. (2005)**

A post-tensioned friction damped connection (PFDC), shown in figure 2-8, was proposed by Rojas et al. (2005) as an alternative to conventional steel moment resisting frame connections. The connection uses high strength PT monostrands symmetrically placed such that the centroid of the PT grouping coincides with the centroid of the beam. Flange reinforcing steel plates are welded to the beam flanges to control flange local yielding and local buckling. Energy dissipation is provided by friction devices located at the top and bottom of the beam where a bolted connection is made to both the beam and column flanges. These devices consist of a friction plate sandwiched between two brass shim plates and modeled after experimental testing performed by Petty (1999) with a typical response shown in figure 2-9.

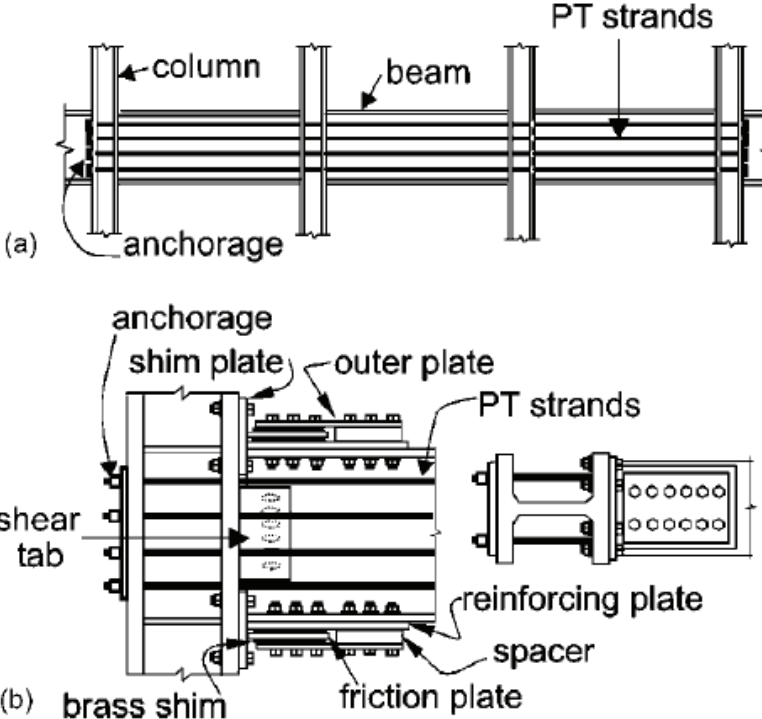
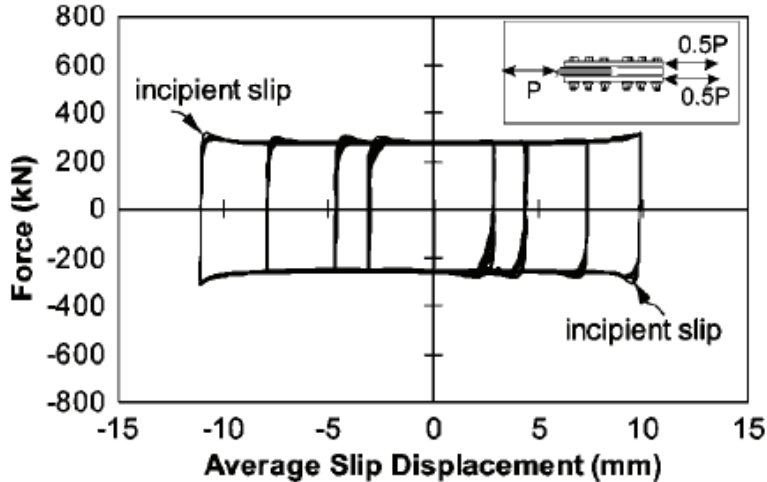


**FIGURE 2-8 (a) Schematic elevation of one floor of a post-tensioned frame; (b) connection detail (Rojas et al. 2005)**



Behavior of friction device [based on data from Petty (1999)]

**FIGURE 2-9 Behavior of friction device (Rojas et al. 2005)**

The friction plate is attached to the stem of a steel WT section where the flange of the WT is bolted to the column flange with standard holes and the stem of the WT is bolted to the beam flange with long-slotted holes. The WT flange also serves as a steel shim plate at the beam-to-column flange rocking contact points such that only the beam flange and flange reinforcement plates are in contact with the column flange. The slotted holes in the friction plate, attached to the WT stem, enable the beam flange and outer plate to slide relative to the friction plate in an unrestricted manner. Thus, stable energy dissipation is provided by the friction force generated between the friction plate and the brass shim plates by the sliding movement. Furthermore, gravity beam shear transfer is provided through the use of a shear plate welded to the column flange with a bolted connection to the beam web with long-slotted horizontal holes to allow relative beam-to-column joint rotation. However, it was reported that the beam vertical shear in excess of gravity shear is resisted by coulomb-friction between the beam-to-column flange contact points from the clamping force provided by the PT.

The idealized moment-relative rotation behavior of the connection is shown in figure 2-10 in terms of moment versus joint rotation, for a positive joint rotation (behavior is the same in the negative direction, but with opposite signs):



- a) The connection behaves as a conventional steel moment frame connection between events 0 to 2. Decompression of the beam-to-column joint occurs at event 1. However the applied moment continues to increase up to event 2 (the point of incipient gap opening) as the relative rotation of the beam is restrained by the resistance of the friction component.
- b) The stiffness of the connection after event 2 is associated with the elastic axial stiffness of the PT strands. With continued loading, elastic PT tensile strains develop producing an additional force, which contribute to resist the total applied moment. Yielding of the PT strands could occur at event 4.
- c) Unloading occurs at event 3 and the relative joint rotation remains constant (events 3 to 6) until the friction force under load reversal in the friction plates is overcome at event 6. So long as the beam, column and PT remain essentially elastic, self-centering will be achieved at event 7 when the beam tension flange is just in contact with the shim plate.
- d) Between events 7 to 8, the beam-to-column flanges are in full contact and full compression from the initially applied PT force is regained.

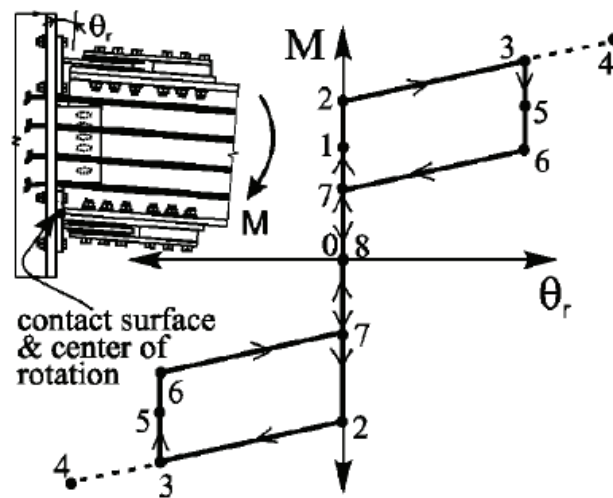


**FIGURE 2-10 Moment-rotation behavior (Rojas et al. 2005)**

Closed-form equations were developed to predict the connection moment capacity of a PFDC connection considering the free body diagram shown in figure 2-11. Furthermore, a performance based design approach was proposed based on the design objectives of:

- a) an immediate occupancy performance level for a building with PFDC-MRFs, to be achieved under the design basis earthquake (DBE), along with the additional condition that the PFDC-MRFs remain essentially elastic, and;
- b) a collapse prevention performance level, to be achieved under the maximum considered earthquake (MCE), with the additional condition that the PT strands and friction device components of the PFDC-MRFs remain elastic, but allowing some minor yielding to occur in the beams and columns.

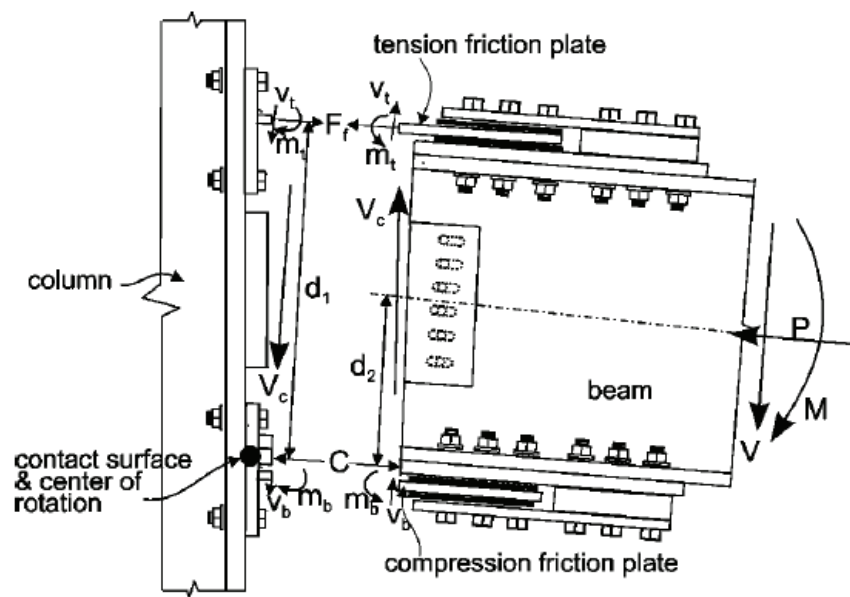


**FIGURE 2-11 Free body diagram of post-tensioned friction damped connection (Rojas et al. 2005)**

To validate the performance of the connection along with the goals of the proposed design objectives, nonlinear static and dynamic time history analysis was conducted on a six story prototype office building located in Los Angeles, CA located on stiff soil (note that experimental investigation of the proposed connection was not performed in the scope of work reported). The floor layout of the prototype building is shown in figure 2-12 and the prototype frame elevation

used to conduct the study is shown in figure 2-13. As noted in the figure, analyses were conducted on both a conventional moment frame system and the proposed PFDC-MRF system for comparison purposes. Furthermore, for the PFDC model, interaction effects between the floor diaphragm and the PFDC-MRF was also included in the analytical model via springs that model the strength and stiffness of three collector beams elements as shown in figure 2-12b. For the nonlinear dynamic time history analysis, an ensemble of eight ground motions were used for two sets of analysis, one set scaled for the DBE and a second for the MCE seismic hazard.

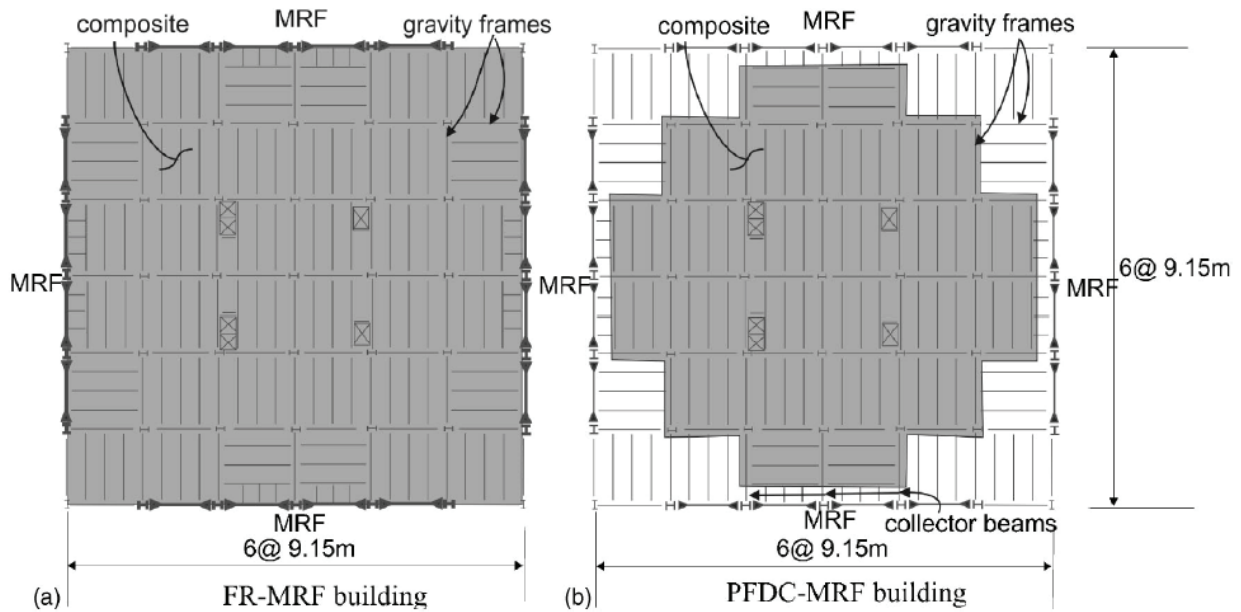


**FIGURE 2-12 Layout and structural system of prototype buildings (Rojas et al. 2005)**

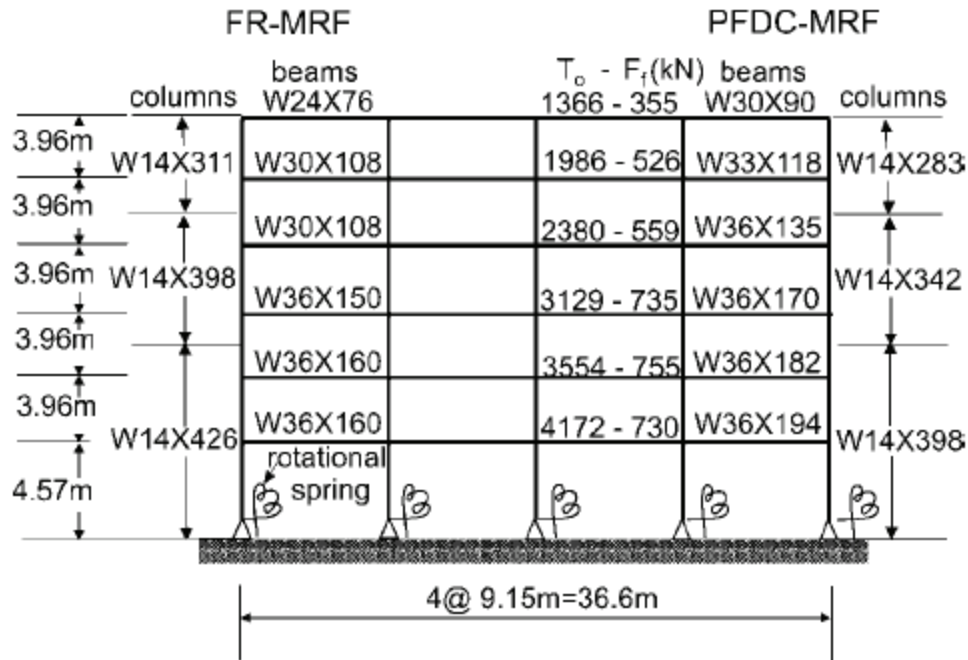


**FIGURE 2-13 Frames used in analytical study (Rojas et al. 2005)**

From the analytical study performed, the performance based design objectives for the PFDC-MRF were achieved. Furthermore, for the analytical studies conducted, the PFDC moment frames were deemed to perform better than special moment resisting moment frames with welded connections as inelastic deformation was limited only to the base of the PFDC-MRF columns and self-centering was achieved. Furthermore, the sensitivity of the PFDC connection and frame response to variability in the specified friction force provided in the friction device was investigated. It was determined that a change of either plus/minus 25% of the specified friction force of that used in the analytical study, did not significantly affect the response of the PFDC-MRF. This was attributed to the fact that the contribution of the friction force to the total connection moment resistance is on average 20%, which correlates to a deviation of connection moment resistance of only 4% based on a plus/minus 25% change investigated.

#### **2.4 Frame Beam-to-Column Rocking Connections and Diaphragm Effects**

The beam-to-column rocking joint detail used in previous research presented above is appealing for many reasons. However, a wide-spread concern with the practical implementation of these self-centering frames is the issue of “beam-growth” (a.k.a. frame beam-elongation, or PT

boundary frame expansion). This phenomenon occurs because the joint opening at each end of the beam (which is required in order induce PT tensile strains for recentering) manifests itself as an apparent increase in horizontal length of the beams (although physically the beam length remains essentially the same). This has the undesired effect of the beams pushing outward against the columns by the amount of the gap openings at the beam-to-column rocking joints. As a consequence, strength demands on the columns are increased (i.e., columns must flexurally deform to accommodate the beam-growth) as well as strain compatibility issues of the diaphragm connection to the beams arise (i.e., the diaphragm must slip/tear or deform to accommodate the beam-growth). This section presents some research on details that have been proposed to mitigate these effects in frames incorporating PT rocking joints.

#### **2.4.1 Precast Concrete Construction: Zero beam-growth connections**

In the PRESSS program, the issue of beam-growth was recognized. Accordingly, one of the beam-to-column joints proposed to eliminate beam-growth was the “TCY gap” connection shown in figure 2-14. In this beam-to-column connection, an initial gap is provided at the top of the beams while the bottoms of the beams are detailed to be in constant contact with the columns during frame drift. Beam-growth is then eliminated by the fact that, as joint rotation occurs, a gap opening and closing occurs simultaneously at the top of the beams, with a net gap opening of zero at each beam-to-column rocking joint location. Furthermore, energy dissipation is provided at the beam-to-column joint by bonded reinforcement provided at the top of the beams. Additionally, PT reinforcement is provided at the center of the beam-to-column contact bearing point, continuous along the length of the frame providing a clamping force keeping the frame assemblage together (but does not contribute to frame recentering since no appreciable gap opening is present for this layout). It is noted that although global beam-growth is eliminated (centerline-to-centerline dimension of columns remains constant, which reduces strength demands on the columns), local gap opening effects would still be present, leaving the diaphragm connection susceptible to damage if not accounted for by design and/or appropriate detailing.

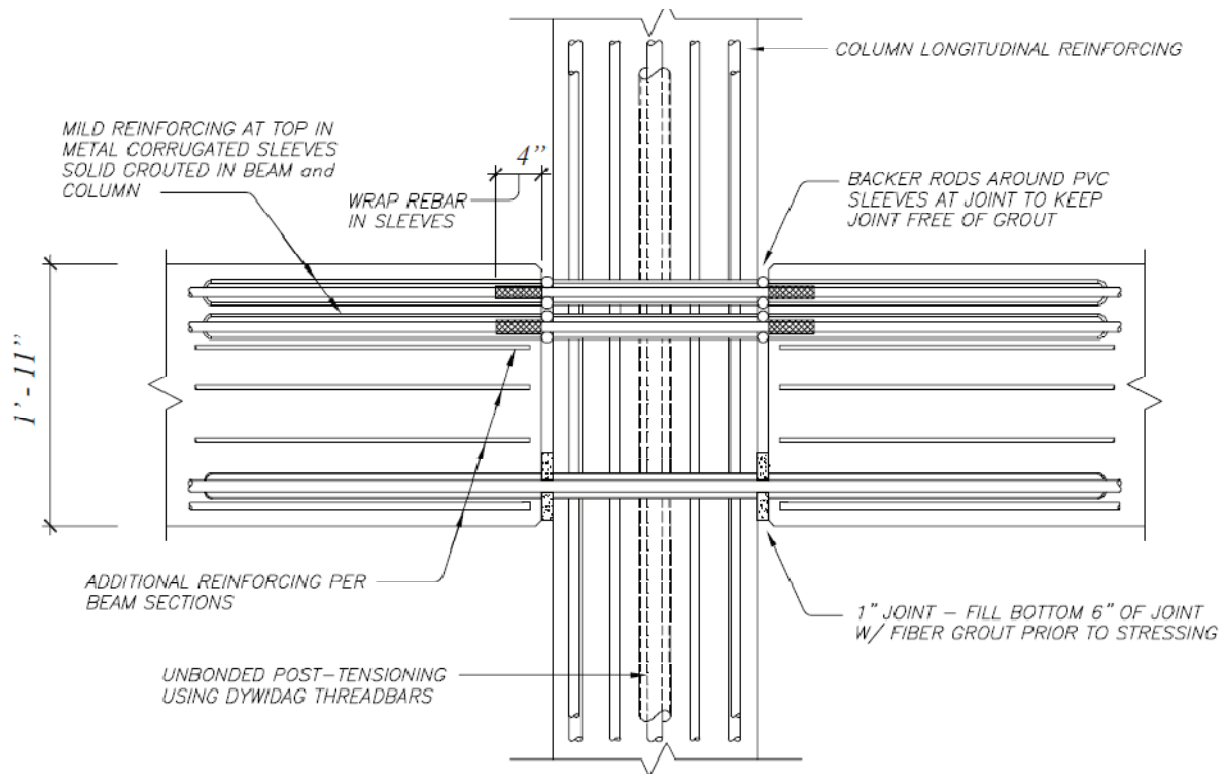


**FIGURE 2-14 TCY gap frame connection (Srithan et al. 2000)**

Evolving from the original TCY gap detail from the PRESSS program (by inverting it), top-hinging “non-gapping” connections have been investigated. One such configuration proposed by Mesa (2010) is shown in figure 2-15 and a schematic of the connection is shown in figure 2-16. In this detail, beam-growth is eliminated by the use of a metallic hinge cylinder at each ends of the beam. This hinge cylinder is part of an assemblage referred to as a “monohinge” which is cast in the concrete. The monohinge consist of three built-up steel plates (one horizontal top plate and two side plates) welded together. A steel cylinder with one-quarter removed, is then welded to the top plate. The monohinge sits on a steel corbel bracket and an uplift restrainer plate is then provided on top of the hinge cylinder. Hysteretic energy dissipation is provided by a mild steel reinforcement bar that is milled down to a specific diameter and then confined by a steel confining tube filled with epoxy to ensure energy dissipation in both tension and compression. These energy dissipation bars are threaded at each end to facilitate connection to the column and beam. In this joint detail, the use of the beam PT is provided to resist gravity loads and to provide additional damping to the system. Frame recentering is provided by a PT column base rocking connection.

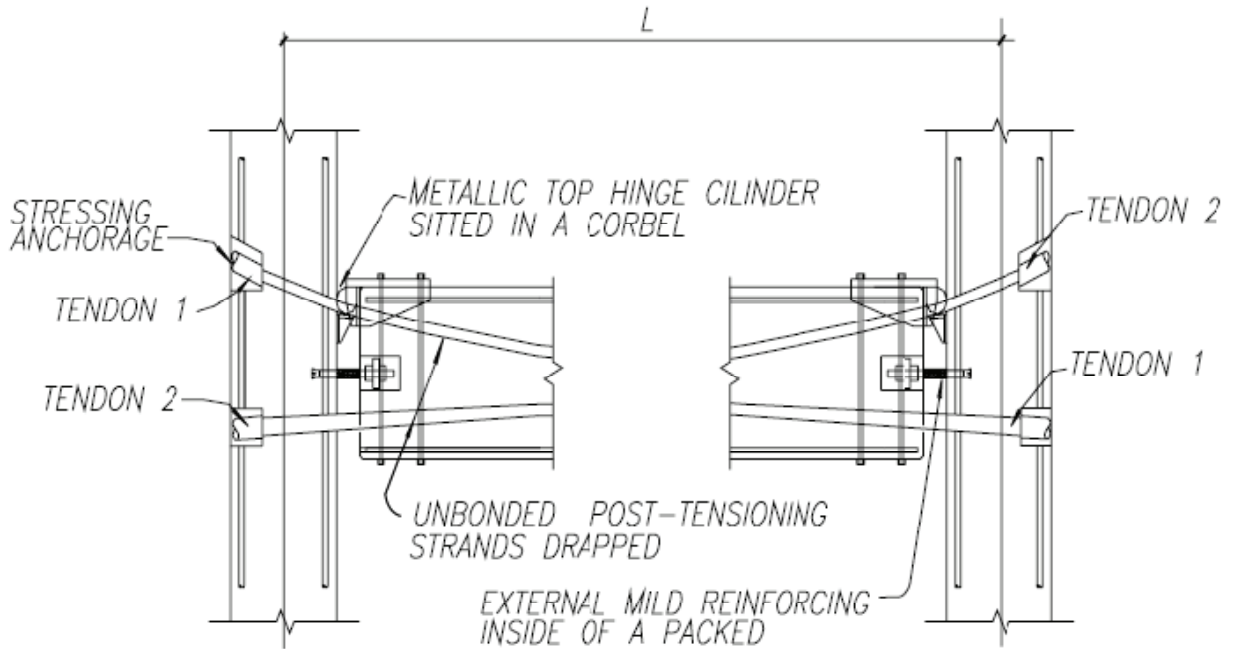


**FIGURE 2-15 Hybrid Frame with draped unbonded tendons and metallic top hinge (Mesa 2010)**

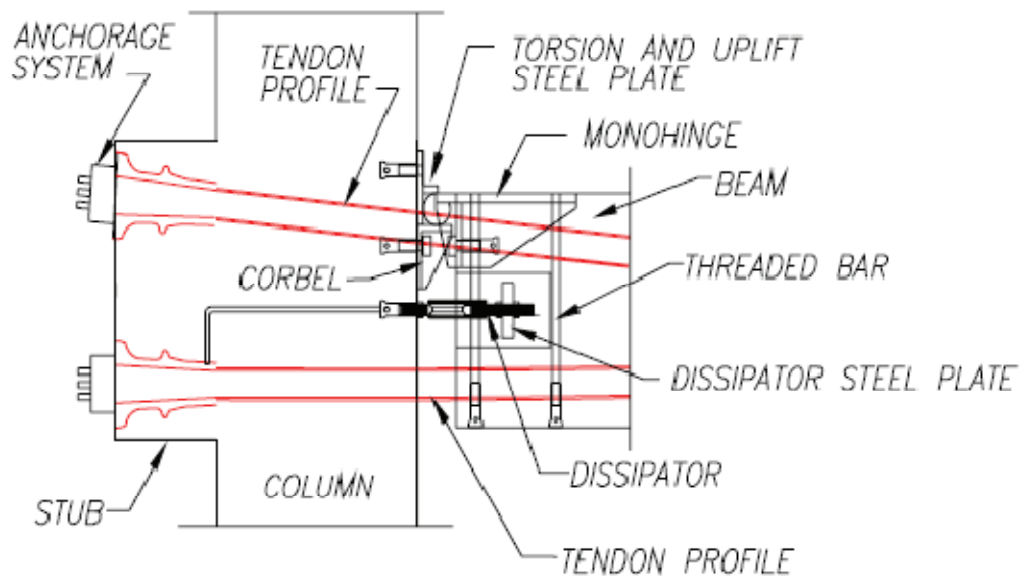


**FIGURE 2-16 Hybrid Frame top hinge connection detail (Mesa 2010)**

## 2.4.2 Garlock and Li (2007)

Garlock and Li (2007) proposed a method to account for diaphragm interaction effects associated with beam-growth that occurs with self-centering steel moment resisting frames (SC-MRF). The approach consists of using the floor/roof diaphragms as a drag-strut system to transfer seismic inertia forces to the SC-MRF. To accomplish this objective, special detailing of the slab connection and arrangement of gravity floor beams is required. To illustrate this, figure 2-17 shows two possible configurations for a four bay SC-MRF located along the building perimeter (i.e., in a 3 collector beam and a 15 collector beam configuration). Furthermore, as shown in figure 2-17b, it was recognized that for multi-bay frames, beam-growth elongations are cumulative from the middle beam spans to the exterior end spans.

To accommodate these beam-growth elongations, the proposed concept relies on two key considerations:

- First, as shown in figure 2-17, the steel collector beams provided are allowed to deform as horizontal cantilevers of length “b” (as indicated in the figure), whereas the composite slab deck (shown as the dark hatched floor regions in the figure) acts as the cantilever back-span. These collector beams are designed to transfer diaphragm forces to the SC-MRF through shear and flexural bending. The remaining beams not designated as collector beams are intended to move with the diaphragm through rotation at their flexible simple shear connections (at the beam ends).
- Second, the floor slab must be able to slide on the cantilevered portions of the collector beams, along the SC-MRF beams, and on the gravity beams not designated as collector beams (this “floating slab” region is shown as the non-hatched floor regions in the figure). To accomplish this latter requirement, a slide bearing detail, common of expansion joints, was proposed. It was noted that the connection at the steel collector beam to the SC-MRF beam must be designed to transfer the tributary floor diaphragm force, which can be significant and typically reaches the strength of the steel collector beam.



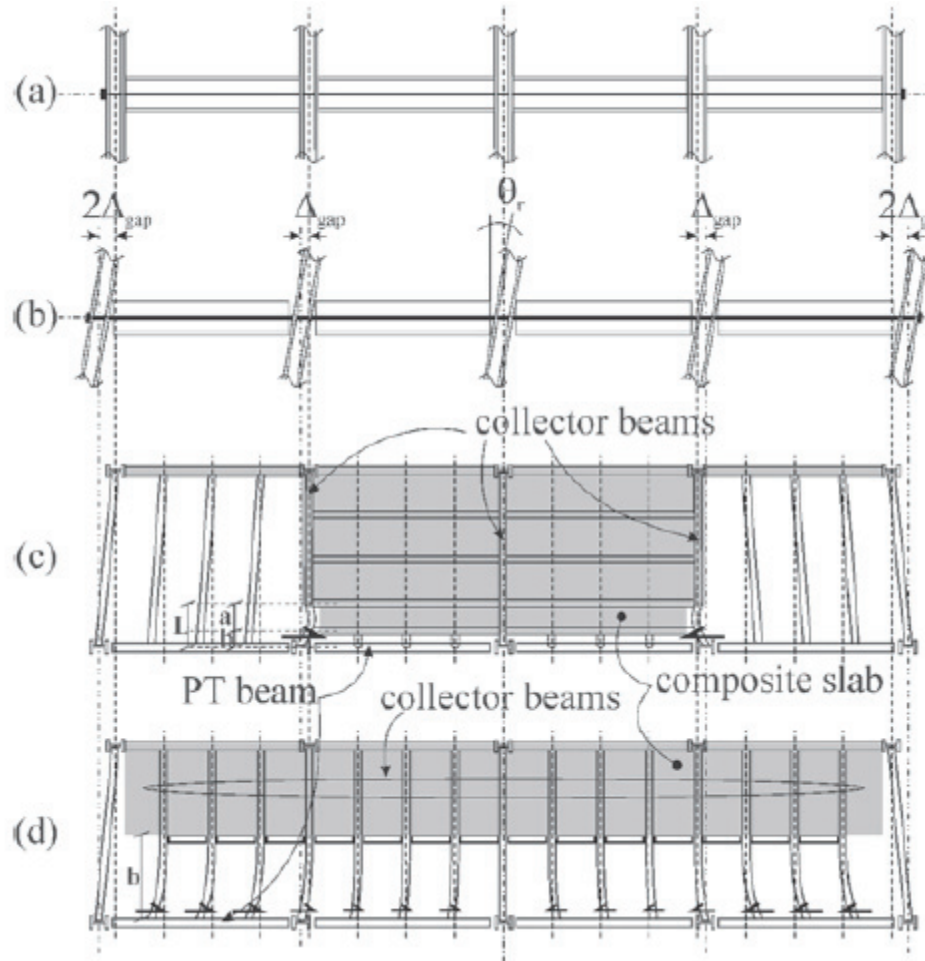


**FIGURE 2-17 One floor of Self-Centering Moment Resisting Frame: (a) elevation view before lateral loading; (b) elevation view after lateral loading; (c) plan view of 3 collector-beam design; (d) 15-collector-beam design (Garlock and Li 2007)**

The axial force demands on the SC-MRF beams including the diaphragm action described above are shown in figure 2-18, where  $T_o$  is the initial post-tension force provided,  $\Delta T$  is the PT axial force due to drift induced PT elongations,  $f^{cb}$  is restraining compression force from the steel collector beams,  $f^{if}$  is the tributary inertia forces of the SC-MRF beams, and  $f^{col}$  is axial force from the lateral deformation of the columns. The latter three components are related to beam-growth. Furthermore, as a simplification, for consideration of floor levels above the first floor, the latter component ( $f^{col}$ ) is ignored as it is assumed that beam-growth effects are similar along the story heights for this condition. With the axial force components due to beam-growth identified, closed-form equations were developed to approximate these axial force demands due to diaphragm floor interaction. Nonlinear dynamic time history analysis was then performed

using a suite of six ground motions and scaled for both a DBE and MCE level seismic hazard. The prototype frame investigated, consisted of a four-bay six-story prototype SC-MRF for the 3 collector beam and 15 collector beam configurations. The model included the interaction of the floor diaphragm with the SC-MRF using zero-length spring elements to characterize nonlinear force-deformation of the collector beams. In this study, the SC-MRF design remained constant while parameters of the floor diaphragm characteristics varied as represented by the number of collector beams, the collector beam stiffness, and the collector beam length. The closed-form equations were validated along with insight provided on the performance of the different collector beam configurations through the results of the nonlinear dynamic time history analysis.

Note that the fundamental concept of this proposed method to account for diaphragm interaction effects pertaining to beam-growth that occurs with SC-MRFs was also presented by Rojas (2003). These effects were included in the nonlinear dynamic time history analysis conducted for the PFDC-MRF presented in Section 2.3.3 and shown in figure 2.-2.

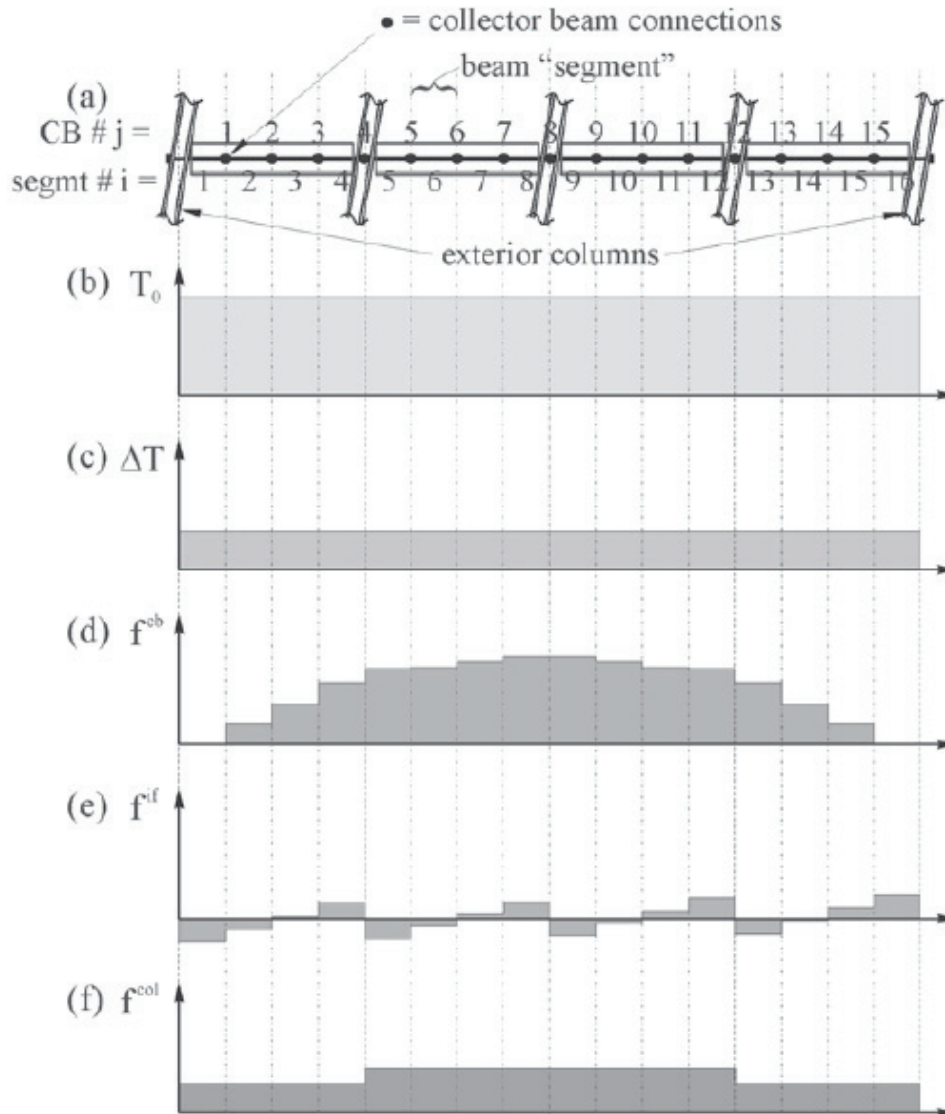


**FIGURE 2-18 Hypothetical beam force distribution in a 15 collector-beam design of a Self-Centering Moment Resisting Frame (Garlock and Li 2007)**

### 2.4.3 Kim and Christopoulos (2009)

Kim and Christopoulos (2009) proposed a slab detailing method to eliminate diaphragm interaction effects associated with beam-growth that occurs with SC-MRFs, as shown in figure 2-19. The proposed detailing involves allowing the floor slab to slide along SC-MRF column boundaries, to allow for gap openings at the SC-MRFs beam-to-column joints. To facilitate this, as shown in the figure, two of the four sides between girder spans (shown in Section A-A of the figure) are restrained by shear stud connectors while the other side moves with the PT frame expansion. To reduce friction along the sliding surface, teflon pads are placed underneath the

slab where sliding is allowed to occur. In the building orthogonal direction (Section B-B of the figure) similar detail is provided to allow for frame expansion for SC-MRF in that direction. The boundary of the restrained and unrestrained slab locations is filled with a flexible filler material and steel edge plates are provided at the ends of the two slab edges to protect them from crushing due to any potential racking effects. Furthermore, closed-form equations are presented to approximate axial force demands in the SC-MRF beams due to PT frame expansion (i.e., columns have to flexurally deform to accommodate beam-growth, which then generates additional axial compression forces on the SC-MRF beams). In particular, by incorporating the proposed “slab release” detail described, the component due to slab restraint interaction in the closed-form equations can be neglected.

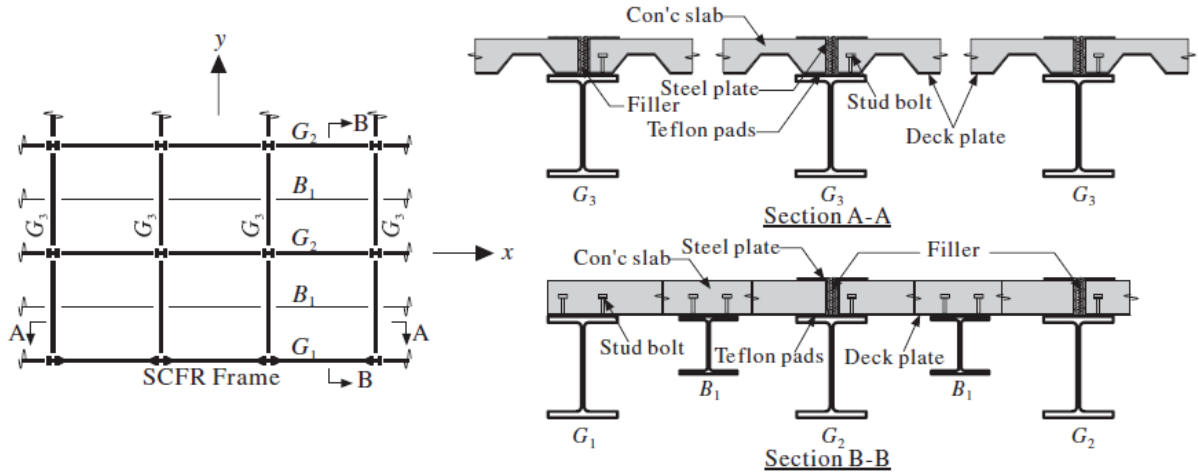


**FIGURE 2-19 Detailing between concrete slab and post-tensioned self-centering frame to eliminate the restraining effects of slab (Kim and Christopoulos 2009)**

#### 2.4.4 Iyama et al. (2009) and Wolski et al. (2009)

A bottom flange friction device (BFFD) connection was proposed as an alternative to the PFDC connection (presented in Section 2.3.3) for SC-MRFs by Iyama et al. (2009) and Wolski et al. (2009). The former presented results of nonlinear static and dynamic time history analyses results and the latter presented quasi-static experimental results of seven large scale subassembly tests. The work presented by Iyama et al. is more relevant to the current study, as it pertains more directly to the behavior of frame rocking connections and their interaction with the surrounding diaphragm.

The BFFD connection in comparison to the PFDC connection is shown in figure 2-20. The proposed BFFD friction device is attached only to the beam bottom flange to avoid interference with the floor slab. At the top beam flange, a restrainer angle with bolted connections is provided to prevent transverse and lateral movement of the beam at the column flange. The BFFD consists of a vertically oriented friction plate with slotted holes that is welded to the bottom of the beam flange. Built-up steel column angle sections are provided each side of the friction plate where a pre-tensioned bolted connection is provided to generate a clamping force for friction. Furthermore, brass shim plates are sandwiched between the column angles on both sides of the slotted plate for the same reason provided for the PFDC connection presented earlier.

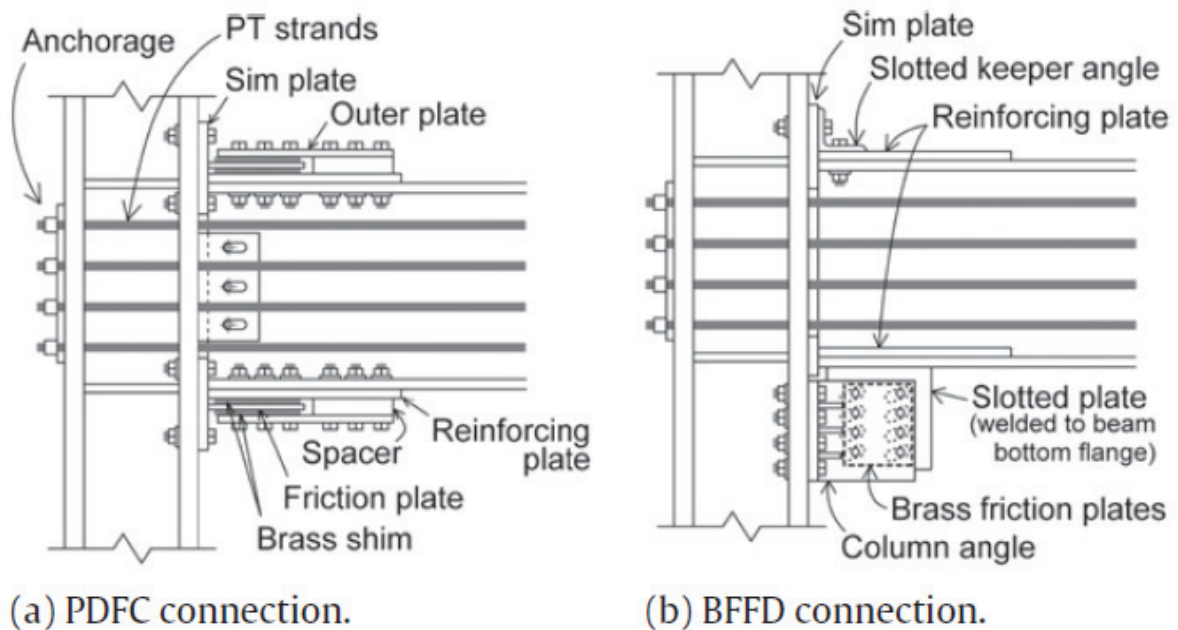


**FIGURE 2-20 Self-centering connections with different ED devices (Iyama et al. 2009)**

The idealized moment-relative rotation behavior of the BFFD connection is shown in figure 2-21b where for a positive joint rotation (sign convention indicated in the figure), the conceptual behavior is identical to the PFDC connection (shown in figure 2-21a), but the BFFD connection has a different behavior under positive and negative rotation as shown in the figure. The difference in response is due to the different lever arm,  $r$ , between the center of rotation and the friction force resultant,  $F_f$ , shown in the free body diagram of figure 2-22, which is dependent on the direction of joint rotation.

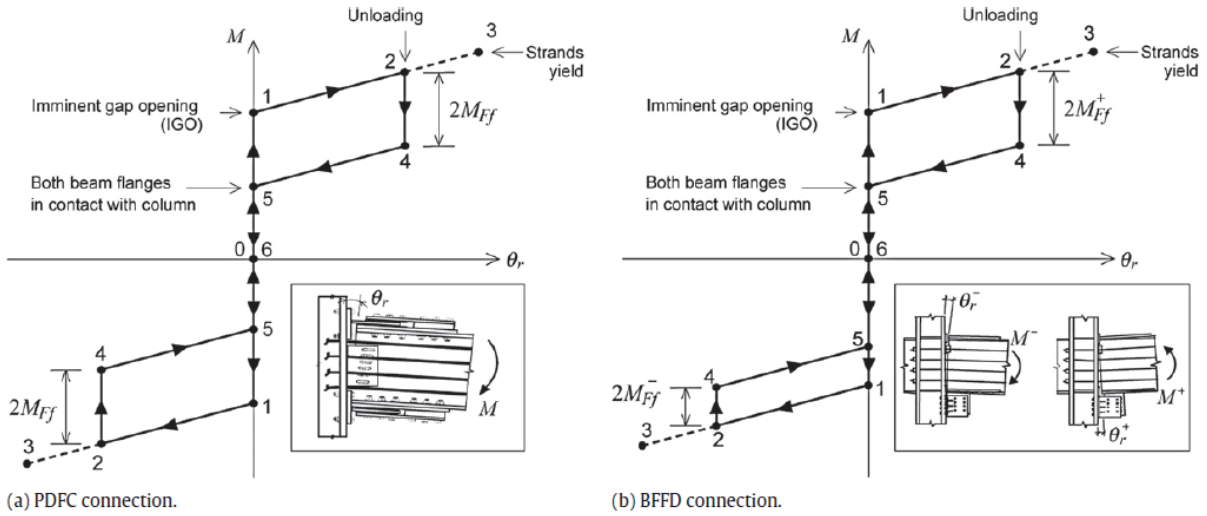


**FIGURE 2-21 Idealized moment-rotation response with different ED devices (Iyama et al. 2009)**

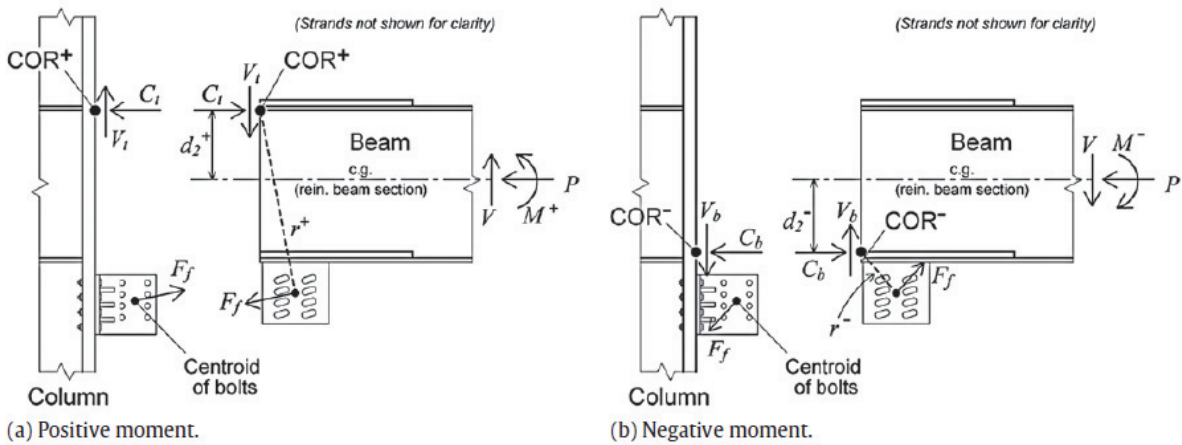


**FIGURE 2-22 Free body diagram of a BFFD connection (Iyama et al. 2009)**

Analytical models of the BFFD connection were developed where the model properties (i.e., stiffness of column angles, friction force in BFFD, material properties, etc.) were calibrated from experimental data presented by Wolski et al. (2009) such that the predicted analytical moment-rotation relationship matched that of the experimental results in order to validate the component connection. Nonlinear static and dynamic time history analyses were then conducted using the

identical prototype building and ground motions as in the study conducted by Rojas et al. (2005), to provide a direct comparison with the PFDC-MRF system. All parameters remained the same except for the modeling of the friction device and the value of the initially applied PT force, for which parameters were modified to approximately match the “positive rotation” design moment strength connection of the BFFD connection to that of the Rojas et al. (2005) frame. Furthermore, interaction effects between the floor diaphragm and the BFFD-MRF were also included in the analytical model using modeling parameters identical to those used by Rojas et al. (2005). It was determined that the lateral force capacity of the BFFD-MRF was approximately 90% of the PFDC-MRF for both the DBE and MCE levels for an “equivalently” equal frame. Additionally, the analytical study showed that the BFFD-MRF beam end moments and rotation demands were comparable to those predicted by design, and that maximum and residual deformations of the BFFD-MRF were similar to the PFDC-MRF.

#### **2.4.5 MacRae et al. (2010)**

MacRae et al. (2010) proposed a friction steel moment joint connection, referred to as a sliding hinge joint (SHJ) connection, to eliminate diaphragm interaction effects associated with beam-growth that occurs with typical beam-to-column joints that rock about the beam flanges. In this connection, the beam top flange maintains constant contact with the column flanges at each end (creating a fixed point of rotation), whereby a gap opening is allowed to form at the corresponding bottom beam flange locations. Energy dissipation is provided through the relative movement of friction plates that are clamped together with high strength pre-tensioned bolts. A schematic of the SHJ connection detail is shown in figure 2-23 and consists of the following components:

1. A beam clearance is provided between the column and beam flanges to provide an initial gap at the bottom beam flange. An empirical relationship was provided in determining this distance.
2. The beam top flange is connected (and kept in constant contact) with the column flange through a bolted top flange plate. The bolts are designed to accommodate the overstrength sliding action of the friction sliding components.

3. A shear plate welded to the column and bolted to the beam webs is provided to resist beam transverse loads. Furthermore, two sets of bolts are provided. For the condition shown in the figure, the top row is designed to resist the entire design shear load. The bottom row is designed only to dissipate energy through friction where a web cap plate with friction shims (not shown) is provided to facilitate this.
4. A steel bottom flange plate, welded to the column flange and bolted to the bottom of the beam flange is provided. Furthermore, as shown in the figure, friction shims are provided on both sides of the bottom flange plate. A steel bottom cap plate is then provided at the most outer layer.
5. All friction shims have standard bolt holes, where the steel “stationary” plates have long-slotted holes to allow relative movement of the shims. Furthermore, high strength pre-tensioned bolts are provided at all friction shim locations to provide a clamping compression normal force to generate the friction forces.

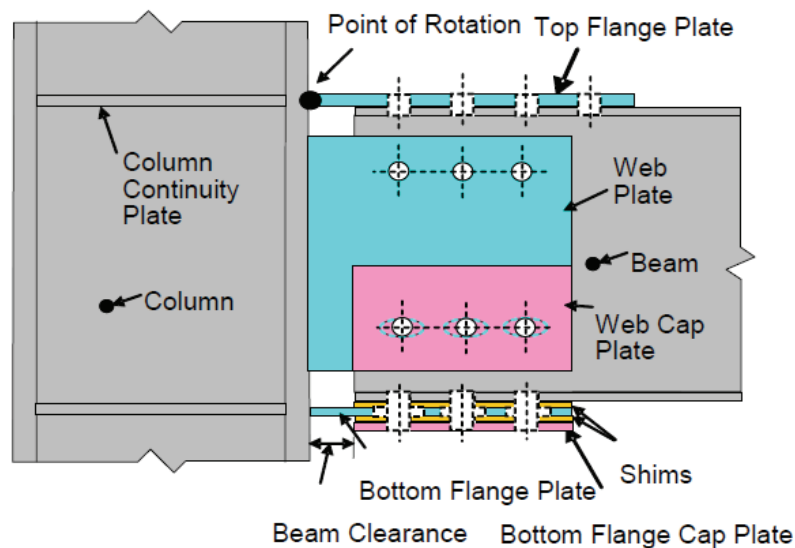


**FIGURE 2-23 Sliding Hinge Joint Detail (MacRae et al. 2010)**

The basic kinematics of the SHJ detail is shown in figure 2-24 for the bottom flange friction assemblage and the steps through a typical hysteretic loop are described as follows for the steps identified by the corresponding letters in the figure):

- (a) The column starts from rest.



- (b) As the top of the column moves in the rightward direction, slip occurs between the bottom of the beam flange and the bottom flange plate. At this stage, the bottom flange cap plate does not slide.
- (c) With increased gap opening, the bolt holes in the bottom flange move to such an angle that they provide sufficient force for slip to also occur between the bottom flange plate and the bottom flange cap plate. The slip on both friction plates leads to approximately double the friction force generated from that of stage (b) and shown diagrammatically in figure 2.24f.
- (d) When loading reverses, slip initially occurs only between the bottom of the beam flange and the bottom flange plate.
- (e) With increased gap opening in the reversed direction, the bolts again pull the bottom flange cap plate, initiating slip on both friction plates, thereby increasing the energy dissipation through friction from step (d).

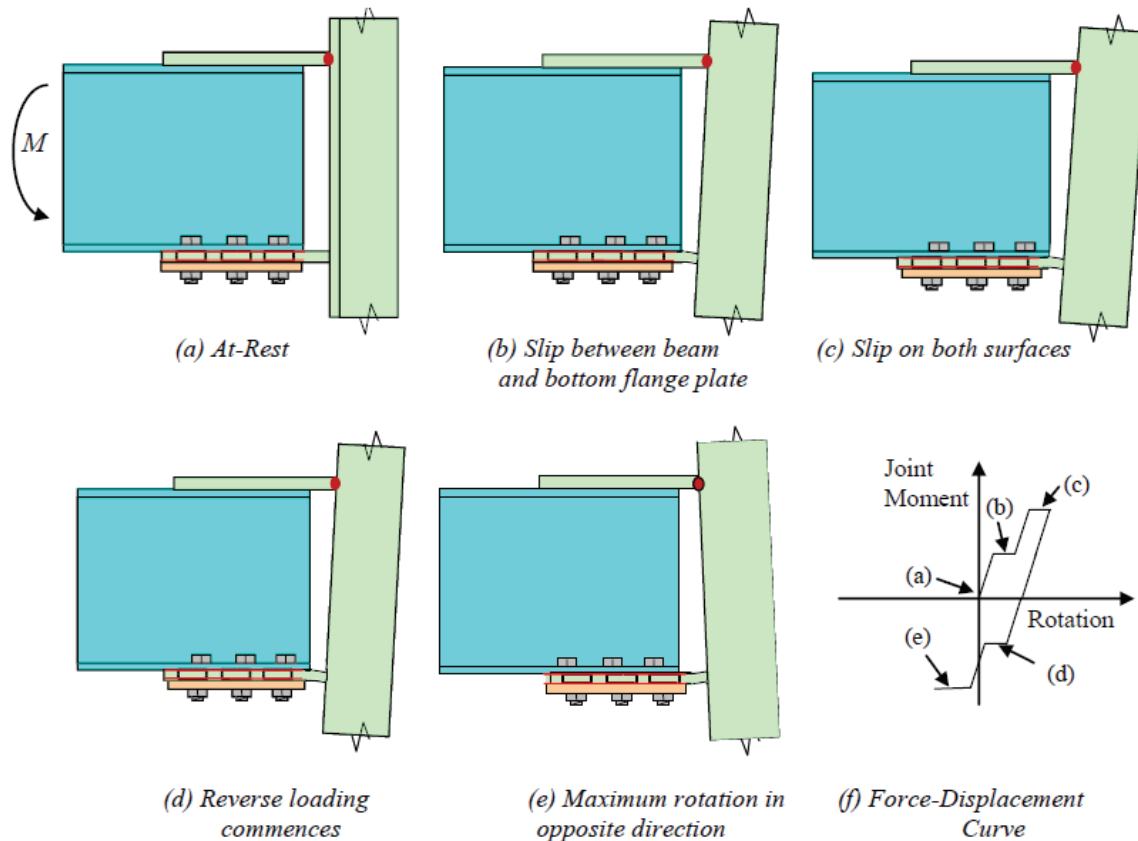


**FIGURE 2-24 Sliding of plates below beam during cyclic deformations (MacRae et al. 2010)**

Testing of a joint connection subassembly was performed to investigate the effect of various shim materials on the connection behavior. The test matrix consisted of six tests and the use of steel, brass, and aluminum friction plates was investigated. Results showed that all three can be used to provide satisfactory friction resistance and the connection remained elastic at design level displacements. Furthermore, although the proposed SJH connection does not incorporate any self-centering mechanism, MacRae et al. indicate that the experimental hysteresis response demonstrates a low possibility of large permanent residual displacements.

Closed-form equations were presented to evaluate the change in connection initial frictional moment resistance. Furthermore, closed-form equations were presented to account for moment-shear-axial interaction in the bolts, which has the effect of reducing the clamping force provided by each bolt (which in turn reduces the friction force). Finally, based on the cumulative research presented, a simple design methodology and example of its use was presented.

## **2.5 Other Relevant Self-Centering Systems**

Christopoulos et al. (2008) has proposed an innovative self-centering steel bracing system as an alternative to conventional steel brace lateral force resisting systems. Here the energy dissipation and PT element self-centering mechanism are provided in a diagonal steel brace element referred to as a self-centering energy dissipative (SCED) steel brace. Both the energy dissipation and the recentering mechanism of the PT are provided by the axial elongation of the bracing element due to interstory drift. The concept and hysteretic response is shown in figures 2-25 and 2-26 respectively. As shown in figure 2-25, the energy dissipation can be provided by either a friction, viscous, or yielding device (or any combination thereof) as shown in that figure. Furthermore, as shown in figure 2-26 for a friction device condition, the idealized flag shaped hysteretic response relies on relative movement of two independent structural members of the SCED steel brace. A generic schematic of the SCED detailed with a friction device is shown in figure 2-27. Furthermore, equations were developed to predict the SCED brace response.

The behavior of the SCED steel brace was investigated experimentally through full-scale quasi-static axial component testing of a single SCED brace element and quasi-static cyclic and dynamic testing of a SCED frame assemblage. For this purpose, a friction element was provided

for the energy dissipation component of the SCED brace system and aramid based fiber reinforced polymer (FRP) PT tendons were used for the self-centering component. The friction elements consisted of a nonasbestos-organic (NAO) material sandwiched between highly polished stainless steel plates, where pretensioned high-strength bolts provided the normal clamping force between the two different interfaces. The use of the FRP tendons (versus high strength steel tendons) was deemed necessary due to the large axial tensile strain demands expected for the PT tendons, due to elastic axial elongation generated from an interstory drift displacement. The schematic of the investigated SCED steel brace is shown in figure 2-28 and the test setup for the frame assemblage test is shown in figure 2-29. The experimental results performed as predicted by Christopolous et al. within the testing parameters considered.

Note that one challenge encountered by Christopolous et al. with the use of FRP tendons was obtaining the cyclic modulus of elasticity of the tendons. It was noted by Christopolous et al. that the mechanical properties typically reported by manufacturers of these composite materials, report properties based on monotonic tensile test results. As shown in figure 2-30, a stiffening effect occurs with composite materials when the material is prestretched and then subjected to cyclic loading at amplitudes lower than the prestretched level. This is due to the realignment of the fiber molecules and has an effect of reducing the elastic elongation of the material (i.e., due to a larger elastic modulus). To obtain the desired dynamic mechanical properties for design, Christopolous et al. conducted cyclic testing with a loading history expected of the tendons during the experimental investigation of the SCED steel brace.

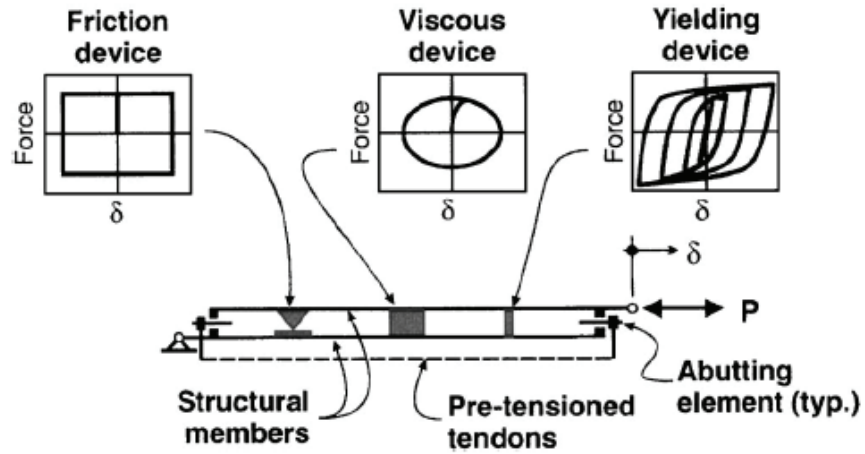


FIGURE 2-25 Concept of SCED systems (Christopolous et al. 2008)

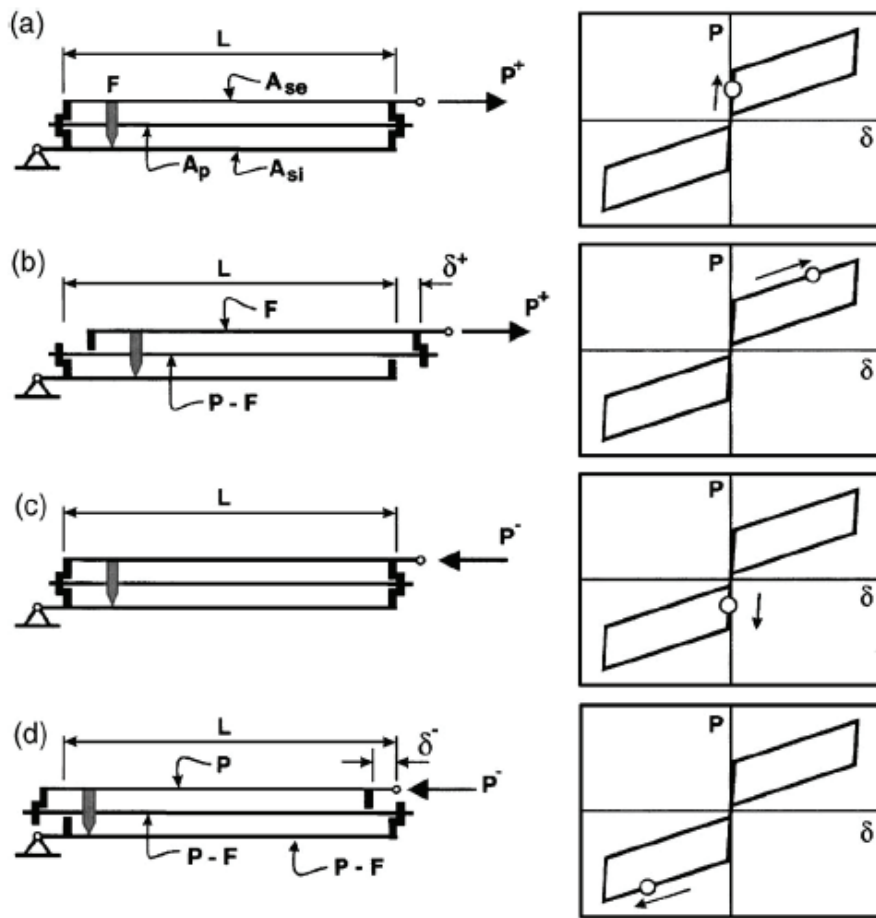


FIGURE 2-26 Mechanics and hysteretic response of SCED systems (Christopolous et al. 2008)

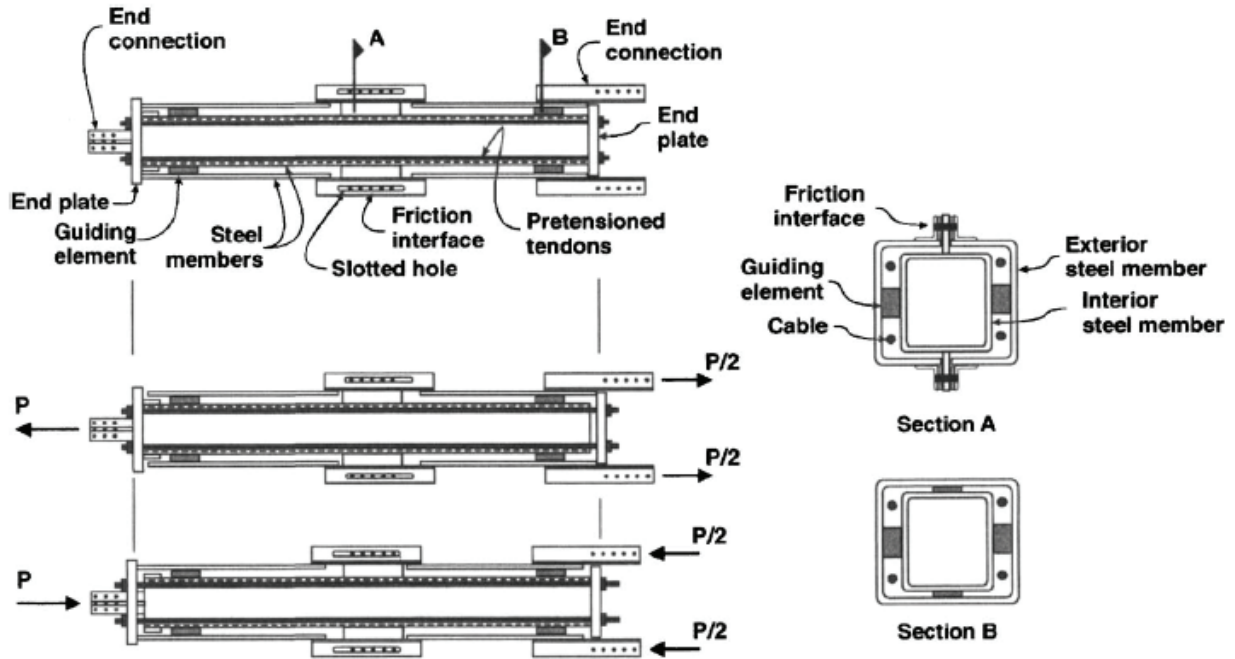


FIGURE 2-27 Generic schematic of SCED with friction device (Christopolous et al. 2008)

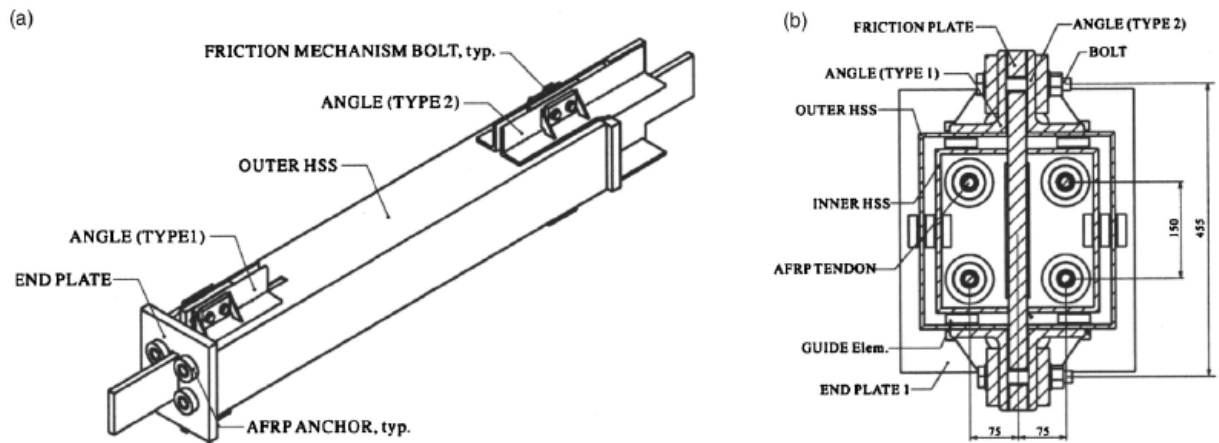


FIGURE 2-28 Tested SCED prototype: (a) 3D view; (b) cross-section (Christopolous et al. 2008)

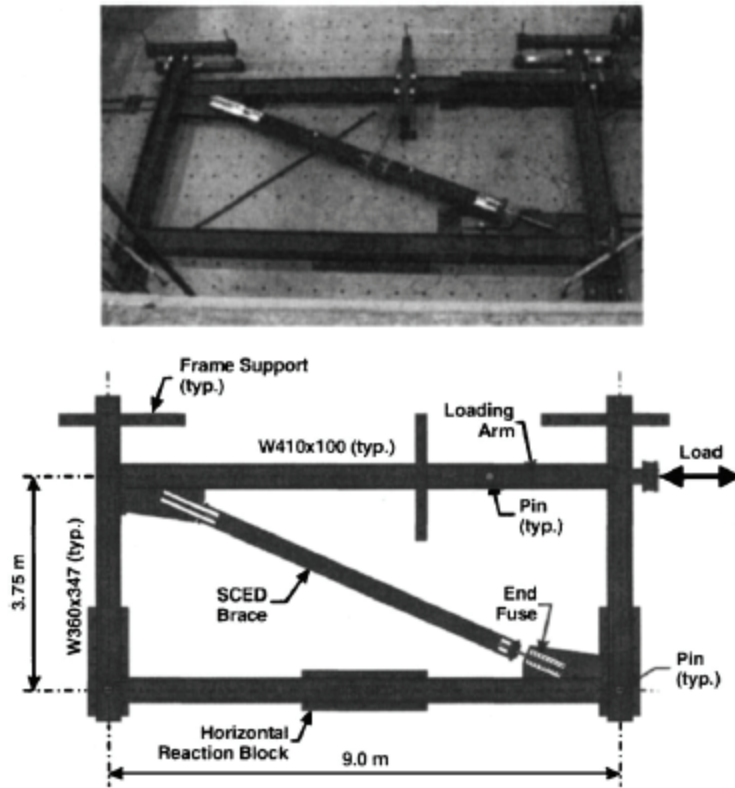


FIGURE 2-29 Setup for SCED frame assemblage tests (Christopolous et al. 2008)

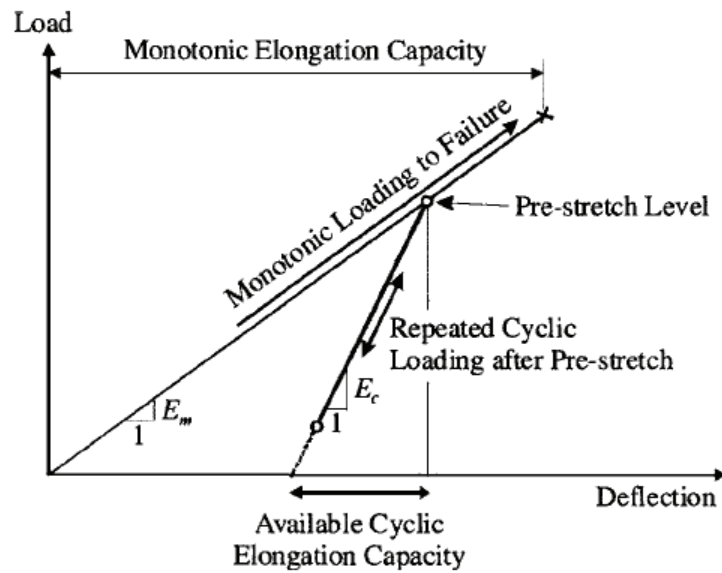


FIGURE 2-30 Tensile force-deflection response of aramid type fibers (Christopolous et al. 2008)

## 2.6 Relevance of Summarized Research

Although SPSW frames are relatively new to current design specifications (e.g., AISC 2005b and 2010b), research on SPSW frames is fairly mature (although in more recent years, new analytical methods and refinement of existing methods are being proposed to better predict SPSW response, of which just a few were presented Section 2.2). These systems offer significant stiffness, energy dissipation capability, and redundancy (i.e., combination of a steel moment frame with a steel infill web plate), which makes this system appealing for use in application for building seismic protection. However, along with other conventional LFRS systems, after a moderate to large earthquake, cumulative inelastic deformations in the LFRS can lead to significant residual building drifts, leaving the building permanently unusable.

As summarized above, past research has demonstrated the self-centering capabilities of moment frame systems having beam-to-column rocking connections. By incorporating similar self-centering beam-to-column connections in SPSWs and eliminating inelastic deformation in the primary LFRS members, the resulting new seismic structural system (proposed by the current research) would combine the benefits of both systems (i.e., significant energy dissipation with self-centering capability). However, as presented in Section 2.4, challenges arise with the use of these beam-to-column rocking connections, namely beam-growth and the corresponding undesired interaction effects with the floor/roof diaphragms. This creates significant challenges for practical implementation of these self-centering systems. Some of the methods proposed by other researchers for addressing these effects have been presented above. Furthermore, a self-centering steel brace system proposed by other researchers was presented in Section 2.5. The relevance of this research is that diaphragm interaction effects are not an issue since recentering is achieved through an interstory displacement. Additionally, this system also incorporated high-elongation FRP tendons which could be of some benefit in the current research presented in this report on self-centering SPSWs. Much remains to be investigated to make self-centering SPSW a viable concept. The research conducted toward that goal is presented in the subsequent Sections.





## SECTION 3

### KINEMATICS OF SELF-CENTERING STEEL PLATE SHEAR WALLS

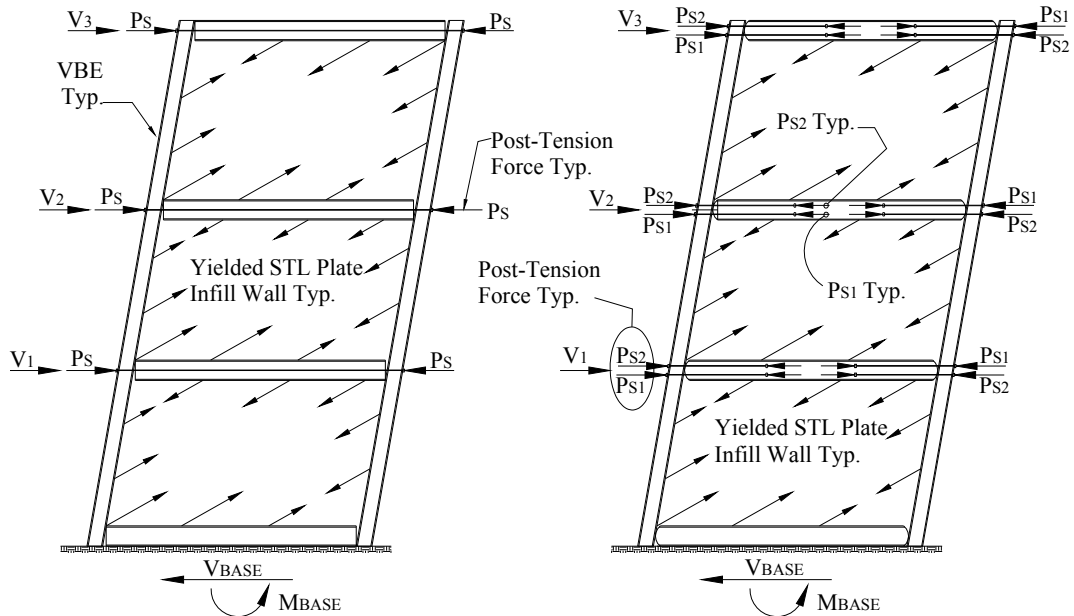
#### 3.1 General

The focus of this Section is to provide insight on the demands on HBEs in an SC-SPSW system. For this purpose, closed-form equations for the moment, shear and axial force diagrams along the HBE are obtained from a capacity design approach based on yielding of the SPSW web plate. Analytical comparisons are then performed using nonlinear pushover analysis to validate the fundamental equations derived from first principles. The insight and understanding gained on the fundamental behavior of SC-SPSWs presented in this Section is a key first step for the design of the test specimens in the experimental phase of this project, as well as contributing to the knowledge base of these systems. Investigation of three different HBE-to-VBE post-tension rocking connections is explored, of which all are further investigated in the experimental phase of this project. Note that the derivations of the closed-form equations presented in this Section for the HBE strength demands assume rigid VBES. In particular, the contribution of the flexibility of the VBES contributing to PT force losses is neglected. Consideration of VBE flexibility can be included by a nonlinear pushover analysis once the numerical model is established (for which the equations developed in the Section can be used to facilitate the initial design).

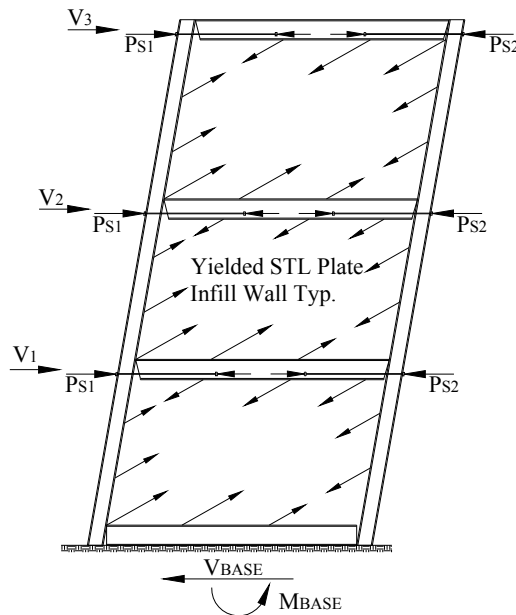
This Section begins with a short description on the yielding mechanism contributing to the global hysteretic response of SC-SPSWs in Section 3.2. Then, for each of the different HBE-to-VBE rocking joint connections, the development of HBE free body diagrams with loading components due to the yielding of the infill web plate is then used to establish moment, shear, and axial formulations in Section 3.3. Section 3.4 provides insight on the kinematics of the HBE-to-VBE joint connection and its effects on the tensile strain demands on the infill web plate. Finally, Section 3.5 concludes with a general summary.

### 3.2 Basic Principles of Self-Centering SPSW Systems

The primary energy dissipating mechanism of self-centering SPSW systems is achieved by the inelastic response of the infill web plate only, which yields through diagonal tension field action and resists the earthquake excitation through hysteretic energy dissipation.



(a) Rocking connection about HBE flanges (b) Rocking connection about HBE centerline



(c) Rocking connection about HBE top flanges (NewZ-BREAKSS Conn.)

FIGURE 3-1 Yield mechanism self-centering SPSW

Figure 3-1 shows free body diagrams of self-centering SPSW frames for three different HBE to VBE joint connections, with applied forces on the boundary frame associated with the yielding of the infill web plate; where HBE is the horizontal boundary element, VBE is the vertical boundary element,  $P_s$  is the post-tension axial force applied on the HBE associated with a HBE to VBE joint connection for which rocking (i.e., joint rotation) takes place about the HBE flanges,  $P_{s1}$  and  $P_{s2}$  is the post-tension axial force applied on the HBE associated with a HBE-to-VBE joint connection for which rocking takes place about the HBE centerline and top flanges,  $V$  is the externally applied lateral forces due to inertial seismic forces,  $V_{BASE}$  is the total base shear, and  $M_{BASE}$  is the total base overturning moment. The yield mechanism of the infill web plate shown is identical to a conventional SPSW system. However, the two differences that uniquely define the self-centering system from a conventional SPSW system are the absence of a HBE-to-VBE conventional welded or bolted moment-resisting rigid connection, which is replaced by a rocking connection, and the presence of an HBE post-tension axial force provided to re-center the SPSW boundary frame.

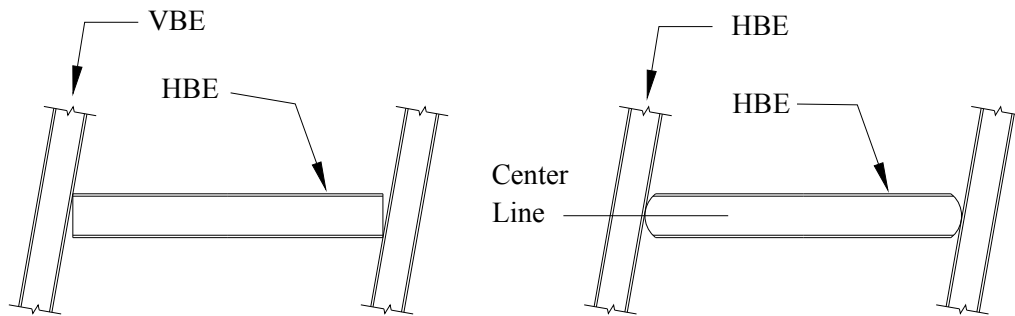
For reasons presented in Section 1, SPSW self-centering rocking connections should be designed to allow for free rotation at the HBE-to-VBE connection. Although this may appear to be counter intuitive from a conventional SPSW design approach, this is necessary to use post-tensioned elements as a re-centering mechanism. For this type of lateral force resisting system, the infill web plate is intended to reach significant plastic deformation during a design based earthquake. Concurrently both the HBE-and-VBE are designed to essentially remain elastic. To restore the building back to its original pre-earthquake vertical alignment, re-centering forces in the SPSW joint connections are developed during the earthquake due to the action of post-tensioning rods or tendons.

Typical cyclic behavior of SPSW systems with rocking connections can be described as follows. As the SPSW drifts laterally, the HBE-to-VBE rocking connection at each end of the HBE will open (or close depending on the rocking joint detail) and the resulting horizontal gaps at the opening joints will elongate the post-tension elements within their elastic range. Concurrently, the infill web plates dissipate hysteretic energy through inelastic action. Note that after repeated cycles of inelastic lateral drift, the SPSW lateral stiffness will be significantly reduced as

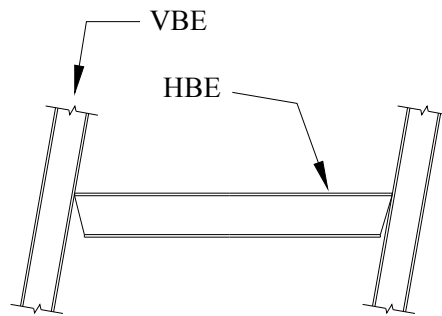
compared to the pre-earthquake condition. The lateral stiffness of the self-centering SPSW system is assumed to be provided by tension field action of the infill web plate only, while the compression stiffness of the infill web plate is assumed negligible. During each cycle of inelastic drift, the infill web plate will stretch. On the return drift cycle, as the SPSW drifts in the opposite direction the infill web plate will be in compression and will buckle until tension field action forces in the infill web plate can be developed in the opposite direction. Therefore, the infill web plates can only dissipate hysteretic energy if they progressively stretch more in each drift cycle. Furthermore, the HBE and VBE members are intended to remain elastic and no rigid frame action providing lateral resistance is developed at the rocking connections (although some lateral frame stiffness is provided by the rocking connection due to the presence of a post-tensioning force, this is typically small compared to the lateral stiffness of the infill web plate). Consequently, to re-center the SPSW frame back to its original vertical alignment, there will be negligible lateral stiffness of the SPSW system for the post-tension forces to overcome; the elastic tension force developed in the post-tension element will close the gap during each cycle of lateral drift, resulting in a re-centering action of the boundary frame. To better understand the behavior of a self-centering SPSW system (SC-SPSW), the moment, shear and axial force diagrams along the length of the HBE is developed based on first principles, which are reviewed in the sections to follow.

### 3.3 SPSW Self-Centering Configurations

The Structural Engineer can use many different approaches to enable the rocking mechanism at the HBE-to-VBE joint connections, of which three possibilities are shown in figure 3-2.



(a) Rocking connection about HBE flanges (b) Rocking connection about HBE centerline



(c) Rocking connection about HBE top flanges (NewZ-BREAKSS Conn.)

**FIGURE 3-2 Rocking mechanisms**

The first approach is rocking about the HBE flanges shown in figure 3-2a. In this configuration, only one HBE flange at opposite ends of the HBE is in contact with the VBE flange for a given lateral drift under imposed lateral forces. The use of this connection has been explored by many researchers in moment resisting frames, where the use of post-tension rocking moment connections was investigated to provide frame self-centering and hysteretic damage was limited to replaceable energy dissipating elements during earthquakes (e.g., Ricles et al. 2002, Christopoulos et al. 2002; Garlock et al. 2005; Rojas et al. 2005; to name a few). Validation of performance for these systems has been established based on analytical and experimental research and shows that these types of systems could be a viable alternative to conventional lateral force resisting systems.

However, the flange-rocking connection, although appealing for many reasons, requires careful and non-conventional floor diaphragm detailing to account for interaction effects of the PT boundary frame with the gravity system. In particular, issues with PT boundary frame expansion (Christopoulos 2002, Garlock 2002), often referred to as “beam-growth”, arise associated with the opening of the rocking beam joint. Garlock and Li (2008) and Iyama et al. (2009) proposed some innovative floor slab diaphragm details for specific plan layouts to accommodate this beam-growth that occurs in the PT boundary frames relative to the other gravity frames in building structures, and more challengingly when beam-growth develops in both orthogonal plan directions. Additional insight on the development of beam-growth in rocking connections is presented in Section 9.11 of this report. Apart from floor slab issues, in taller frames having larger columns, because columns must flexurally deform to accommodate beam-growth at subsequent stories, the large stiffness of these columns may become overwhelming and prevent beam-growth to the point where these systems may not work properly.

The second and third approaches shown seek to eliminate beam-growth. For the rocking point about the centerline of the HBE (figure 3-2b), only the centerline of the HBE is in contact with the VBE flange. Here, a pinned connection is used which provides restraint in the horizontal and vertical degree of freedom, but allows relative rotation between the HBE and VBE. As a result, beam-growth effects are eliminated since the HBE and VBE are kept in constant contact. Similarly, for the rocking point about the HBE top flanges (figure 3-2c), only the HBE top flanges are in contact with the VBE flange which also has the effect of eliminating beam-growth (the kinematics of which will be explained in Section 3.3.4).

The choice of HBE-to-VBE rocking joint detail presented above, will affect the free body diagram of the HBE. More significantly, it will affect the apparent moment distribution along the length of the HBE. However, all three approaches if detailed properly can be effective as rocking connections for frame re-centering. Accordingly, investigation of the HBE moment and force demands is developed for all three connections. It will be shown that each configuration has its own advantages and disadvantages. Regardless of which configuration the Structural Engineer chooses to use, one commonality is that it is critical that the post-tension elements be designed to remain essentially elastic for re-centering.

### 3.3.1 Rocking about HBE Flanges

#### 3.3.1.1 Free Body Force Diagram

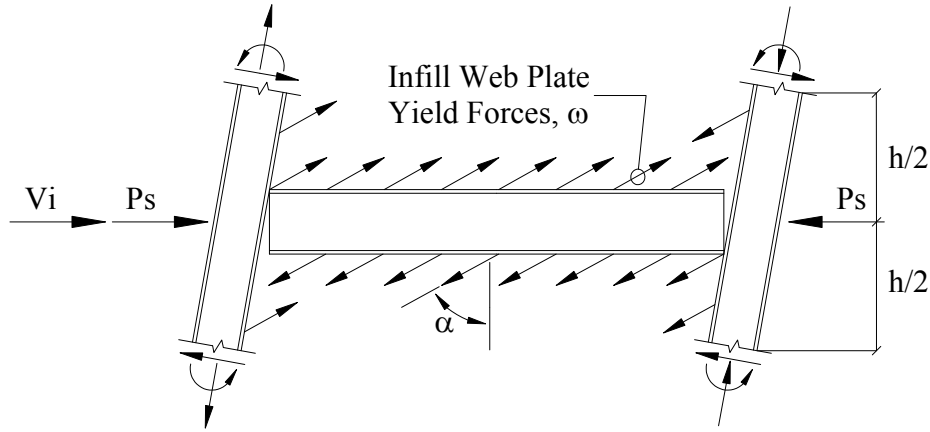


**FIGURE 3-3 Free body diagram of intermediate HBE**

Figure 3-3 shows a general free body diagram of an HBE and VBE elements located at an intermediate floor level of a SPSW frame once the infill web plate has fully yielded; where  $\omega$  is the diagonal tension yield force of the infill web plate (in units of force per length),  $\alpha$  is the angle of inclination of the diagonal tension field from the vertical axis,  $h$  is the story height and all other terms have been previously defined. The diagonal tension yield forces of the infill web plate can be resolved into vertical and horizontal components on the VBE (i.e.,  $\omega_{cy}$  and  $\omega_{cy}$ ) and HBE (i.e.,  $\omega_{by}$  and  $\omega_{by}$ ) as provided in (3-1) and (3-2) (Berman and Bruneau 2008) respectively:

$$\omega_{cx} = F_{yp} t (\sin \alpha)^2 \quad \omega_{cy} = \frac{F_{yp} t \sin 2\alpha}{2} \quad (3-1)$$

$$\omega_{bx} = \frac{F_{yp} t \sin 2\alpha}{2} \quad \omega_{by} = F_{yp} t (\cos \alpha)^2 \quad (3-2)$$

where  $F_{yp}$  is the yield stress of the infill web plate,  $t$  is the thickness of the infill web plate, and all other terms have been previously defined. More specifically, in all subsequent cases considered, the forces shown on free body diagrams are taken such that the infill web plate below the HBE is thicker than the infill web plate located above the HBE. This is a reasonable assumption as the lateral story shear is cumulative from the top story of the building to the

foundation, resulting in an interstory lateral shear strength demand larger from one story down to the next, requiring corresponding infill web plate thicknesses. Note that vertical HBE end reactions develop which would be resisted by a shear tab connection to the VBE; however for clarity, the shear tab is not shown in the free body diagram illustrated in figure 3-3 and in subsequent free body diagram figures.

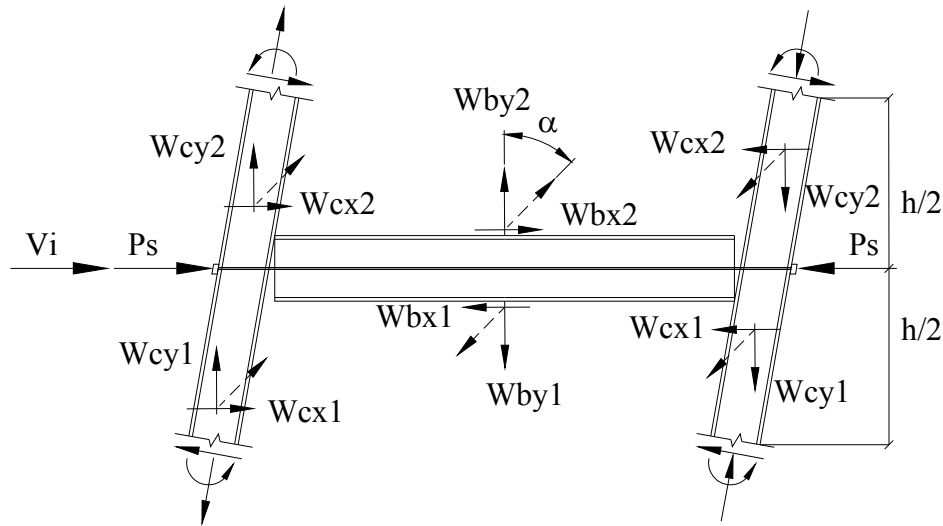


**FIGURE 3-4 Resultant force free body diagram**

Taking the forces shown on figure 3-3 and resolving the applied load distribution into horizontal and vertical resultant forces leads to the simplified free body diagram shown in figure 3-4; where  $W_{bx1}$  and  $W_{bx2}$  are the horizontal force resultants along the length of the HBE of the yielded infill web plate below and above the HBE respectively,  $W_{by1}$  and  $W_{by2}$  are the vertical force resultants along the length of the HBE of the yielded plate below and above the HBE respectively,  $W_{cx1}$  and  $W_{cx2}$  are the horizontal force resultants of the yielded infill web plate along the height of the VBE above and below the HBE respectively, and  $W_{cy1}$  and  $W_{cy2}$  is the vertical force resultant of the yielded plate along the height of the VBE above and below the HBE respectively, and all other terms have been previously defined. Note for the special condition when both infill web plates above and below the HBE are of the same thickness and have fully yielded, the vertical and horizontal force components from the infill web plates along the length of the HBE will cancel each other out, leaving only the force components  $P_s$ ,  $V_i$ ,  $W_{cx1}$  and  $W_{cx2}$  at the rocking point attributing to the required strength demand on the HBE where shown on figure 3-4; this will



become more apparent with the discussion that follows. The force resultants shown in figure 3-4 are further separated into individual components such that their influence on the HBE can be more clearly understood.

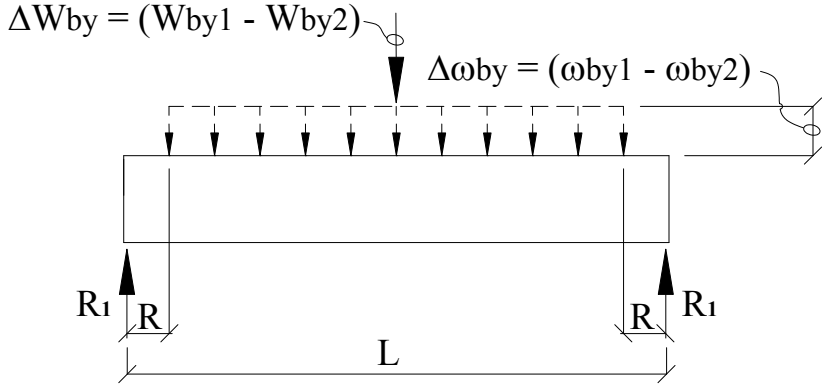


**FIGURE 3-5 Free body diagram vertical component**

First, figure 3-5 shows that the vertical components of the yielded infill web plate forces acting on the HBE above and below the HBE produces net vertical forces along the length of the HBE as a result of the different thickness of infill web plates assumed to be present. Recall that the subscripts 1 and 2 of the force components shown in figure 3-5 and subsequent figures denote that the magnitude of the horizontal and vertical resultants are not equal, the 2 corresponding to the level above the HBE, is assumed here to be the thinner of the two infill web plates considered. This results in a vertical end reaction at the ends of the HBE equal to:

$$R_1 = \frac{W_{by1} - W_{by2}}{2} \tag{3-3}$$

In figure 3-5,  $L$  is the HBE span length and  $R$  is the length of the infill web plate corner cut-out at each end of the HBE to accommodate the HBE-to-VBE joint rocking connection detailing. The corner cut-out  $R$ , is also provided to reduce the potential for corner tear out of the infill web plate due to high localized infill web plate strain effects due to opening of the rocking joint connection. This will be addressed with more clarity in Section 3.4.

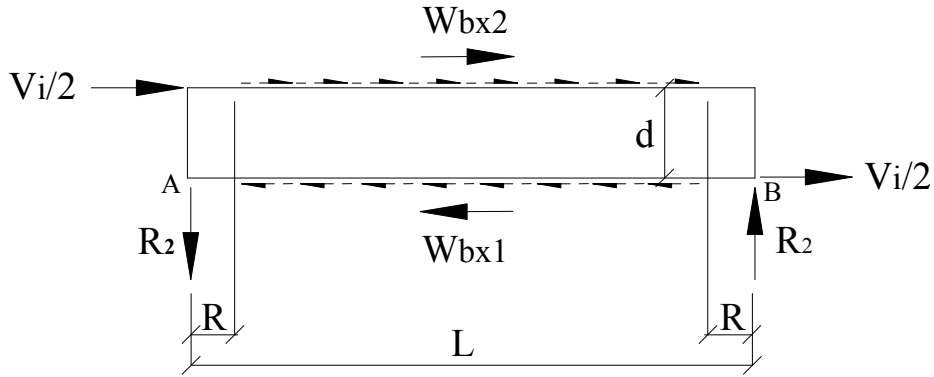


**FIGURE 3-6 Partial free body diagram horizontal component**

Next, the horizontal component of the yielded infill web plate forces acting along the length of the HBE above and below the HBE flanges is shown in figure 3-6 where  $V_i$  is the lateral seismic story shear force,  $W_{bx1}$  and  $W_{bx2}$  are the resultant horizontal yield force components below and above the HBE respectively,  $d$  is the depth of the HBE,  $R_2$  is the reaction force to maintain equilibrium and all other terms have been defined previously.

For the purpose of this discussion, it is assumed that the seismic story shear at each level,  $V_i$ , is distributed equally at each end of the HBE (i.e., the SPSW system being in the middle bay of a multi-bay frame and the story shear force is assumed to be equally distributed at the rocking points  $V_i/2$  at each end of the HBE) and any vertical reaction due to unbalanced loading from  $V_i$ , is assumed negligible. With the force components acting on the HBE identified in figure 3-6, from horizontal equilibrium of the HBE the horizontal force due to the applied lateral seismic story shear leads to the following expression for horizontal equilibrium:

$$V_i = W_{bx1} - W_{bx2} \quad (3-4)$$

Equation (3-4) can be re-expressed in terms of the design SPSW properties, by replacing the resultant forces by the equivalent force per unit length quantities and their expression provided in (3-2), which results in the following:

$$V_i = (\omega_{bx1} - \omega_{bx2})(L - 2R) = \frac{1}{2}(t_1 - t_2)F_{yp}(L - 2R)\sin(2\alpha) \quad (3-5)$$

where in (3-5),  $t_1$  and  $t_2$  are the infill web plate thicknesses below and above the HBE respectively, and all other terms have been previously defined. From (3-5) it is shown that, from a capacity design approach, the design story shear forces along the length of an HBE of a self-centering SPSW is a function of only the net horizontal yield forces of the infill web plates along the length of the HBE. Recall that some lateral resistance is provided by the stiffness of the PT boundary frame with rotational joint stiffness provided by the post-tensioning elements. However, for condition of the applied story shear force distributed equally at each end of the frame, the contribution of lateral force resisted by the frame is resisted through shear directly by the VBEs. Thus, (3-5) represents the portion of the total base shear contribution provided by the infill web plate only. Typically the portion of the total base shear contribution provided by the PT boundary frame will be small compared to that of the infill web plate and since the PT boundary frame is designed to remain essentially elastic, the hysteretic energy dissipation is provided by the infill web plate only. Note that the horizontal component of the yield force due to the infill web plate is the same as for a conventional SPSW system. Accordingly in keeping with the same terminology used in the *AISC Design Guide 20 Steel Plate Shear Walls* (Sabelli and Bruneau 2007), the horizontal force component due to yielding of the infill web plate  $V_i$ , is equivalent to the terminology  $P_{HBE(web)}$  used in the *design guide*.

To determine the vertical reaction at the ends of the HBE to maintain equilibrium, by taking the summation of moments about point  $B$ , leads to the reaction force  $R_2$  as:

$$R_2 = \frac{V_i}{2} \left( \frac{d}{L} \right) + W_{bx2} \left( \frac{d}{L} \right) = \left( \frac{W_{bx1} - W_{bx2}}{2} \right) \left( \frac{d}{L} \right) + W_{bx2} \left( \frac{d}{L} \right) = (W_{bx1} + W_{bx2}) \left( \frac{d}{2L} \right) \quad (3-6)$$

Note that in figure 3-6, if no corner cut-out is provided (i.e.,  $R = 0$ ), than the couple formed by the reaction  $R_2$  and the horizontal forces along the length of the HBE balance out in such a manner that no moment is induced along the HBE. In this special case, the moment induced to the HBE is the unbalanced moment from the story shear force (i.e.,  $V_i/2$ ) applied at the rocking point.

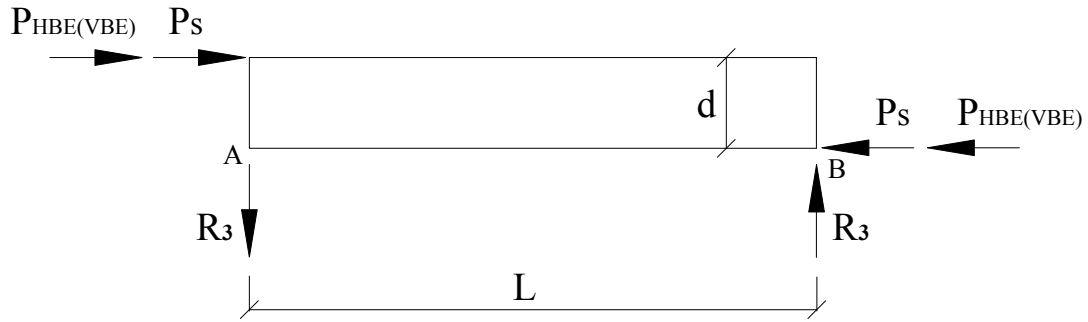


**FIGURE 3-7 Partial free body diagram horizontal component at rocking connection**

To determine the remaining vertical reactions at the ends of the HBE, figure 3-7 shows the horizontal components that produce reactions at the rocking points from force components developed outside of the HBE (i.e., externally applied). The two horizontal components that produce reactions at the rocking points is the force along the height of the VBE due to the yielding of the infill web plate (i.e.,  $W_{cx1} + W_{cx2}$ ) and the axial force due to the post-tension element anchored to the outside of the VBE flange (i.e.,  $P_s$ ). Note that the axial force component due to the VBE is the same as for a conventional SPSW system. Accordingly, in keeping with the same terminology used in the *design guide* (Sabelli and Bruneau 2007), the axial force component from the VBE consisting of  $(W_{cx1} + W_{cx2})$  is equivalent to the terminology  $P_{HBE(VBE)}$ . Furthermore, the horizontal reaction components,  $W_{cx1}$  and  $W_{cx2}$ , from the VBE can be thought of as an additional post-tensioning force as it produces a compression force in the HBE due to the yielding mechanism of the infill web plate (i.e., the yield forces generated by the inelastic action of the infill web plate will pull the columns towards the geometric center of the SPSW with the HBE members behaving as a compression strut resisting these forces). Figure 3-7 reveals that the eccentricity between the horizontal rocking reactions produces a force couple. This couple can be resolved into an equivalent resistive force couple consisting of vertical reactions at the ends of the HBE, equal to:

$$R_3 = (P_s + W_{cx1} + W_{cx2}) \left( \frac{d}{L} \right) \quad (3-7)$$

For the post-tension element component,  $P_s$  in (3-7), consists of an initial post-tension force,  $P_o$ , applied at the time of construction of the SPSW system and remains for the life of the building structure (minus force losses due to post-tension relaxation and any long-term stress losses if applicable), and an incremental force,  $\Delta P$ , due to post-tension elongation when the building drifts and the SPSW joint connections open due to rocking action at the HBE-to-VBE joints during an earthquake. The drift induced elongation of the post-tension elements at the HBE-to-VBE joint connection producing the incremental force  $\Delta P$ , for the condition of the post-tension elements located at the mid-depth of the HBE, is as follows:

$$\Delta_{drift} = 2 \left( \frac{\phi_{drift} d}{100 \cdot 2} \right) = \frac{\phi_{drift} d}{100} \quad (3-8)$$

where  $d$  is the depth of the HBE and  $\phi_{drift}$  is the target joint rotation (in percent) due to frame drift at the HBE-to-VBE joint connection. Although (3-8) is formulated for the post-tension elements located at the mid-depth of the HBE, the post-tension elements can be designed and placed in alternate configurations along the depth of the HBE for the same target  $P_s$ , without affecting the overall analysis results of the HBE. For example, multiple layers of post-tension elements maybe required for design. In such a configuration, the elongation of the post-tension elements will vary in each layer. For this condition, the largest stress and strains reached should not exceed the permissible value in each layer. However, (3-8) remains valid if the layers are symmetrically distributed about the HBE center of gravity. Because, in that case, the average elongation and post-tensioning summed over all layers is equal to that which would occur for a single centrally located layer.

Note that the axial loads generated on the HBE can be substantial and stress losses due to post-tension relaxation should also be considered when designing the post-tensioning elements of the SC-SPSW system. Equilibrium of axial forces in the post-tension elements requires that the increase in tension forces in the post-tension elements equals the increase in compressive forces on the HBE (Garlock 2002). For SC-SPSW systems, for equal story force at each end of the HBE (i.e.,  $V_i/2$  each end of the SPSW frame), the post-tension force losses are attributed to the HBE axial shortening under the axial compression force from the VBE and the axial

compression force due to the post-tension elongation during lateral drift (recall that  $V_i/2$  here is transferred directly into the VBE's through shear). It then follows that the axial shortening of the HBE due to the compression forces of the post-tension and the VBE is equal to the following:

$$\Delta_{loss} = \frac{P_{PT} L_{HBE}}{A_{HBE} E_{HBE}} + \frac{P_{HBE(VBE)} L_{HBE}}{A_{HBE} E_{HBE}} = \frac{P_{PT}}{k_{HBE}} + \frac{P_{HBE(VBE)}}{k_{HBE}} \quad (3-9)$$

where  $L_{HBE}$  is the length of the HBE,  $L_{PT}$  is the length of the post-tension elements,  $A_{HBE}$  is the cross section area of the HBE,  $A_{PT}$  is the area of post-tension, and  $E_{HBE}$  and  $E_{PT}$  are the modulus of elasticity of the HBE and post-tension respectively,  $k_{HBE}$  is the axial stiffness of the HBE,  $P_{PT}$  is the axial compression force on the HBE from the post-tension elements,  $P_{HBE(VBE)}$  is the axial compression force on the HBE from the VBE. Solving (3-9) for  $P_{PT}$  leads to the following:

$$P_{PT} = k_{HBE} \Delta_{loss} - P_{HBE(VBE)} \quad (3-10)$$

Accordingly, the net effective axial tension force in the post-tension elements is the elongation due to drift minus the axial shortening of the HBE and is calculated as follows:

$$P_{PT} = \left( \frac{A_{PT} E_{PT}}{L_{PT}} \right) (\Delta_{drift} - \Delta_{loss}) = k_{PT} (\Delta_{drift} - \Delta_{loss}) \quad (3-11)$$

Finally, equating (3-10) and (3-11), and solving for  $\Delta_{loss}$  leads to the amount of post-tension relaxation that should be considered as indicated in (3-12).

$$\Delta_{loss} = \frac{P_{HBE(VBE)}}{k_b + k_{PT}} + \left( \frac{k_{PT}}{k_b + k_{PT}} \right) \Delta_{drift} \quad (3-12)$$

The resulting equation for  $P_s$ , which includes losses due to HBE axial shortening, thus follows:

$$P_s = P_o + \Delta P = P_o + \frac{A_{PT} E_{PT}}{L_{PT}} (\Delta_{drift} - \Delta_{loss}) \quad (3-13)$$

Alternatively, substituting (3-12), (3-13) can be expressed as:

$$P_s = P_o + \left( \frac{k_b k_{PT}}{k_b + k_{PT}} \right) \Delta_{drift} - \frac{k_{PT}}{k_b + k_{PT}} P_{HBE(VBE)} \quad (3-14)$$

Note that in (3-13), only post-tension force losses are applied to  $\Delta P$ . Although some axial shortening will occur upon application of  $P_o$ , the initial post-tensioning force applied at time of construction, this axial shortening component is permanently locked into the HBE during stressing. Consequently, only axial shortening during lateral drift is considered in the post-tension force loss as indicated.

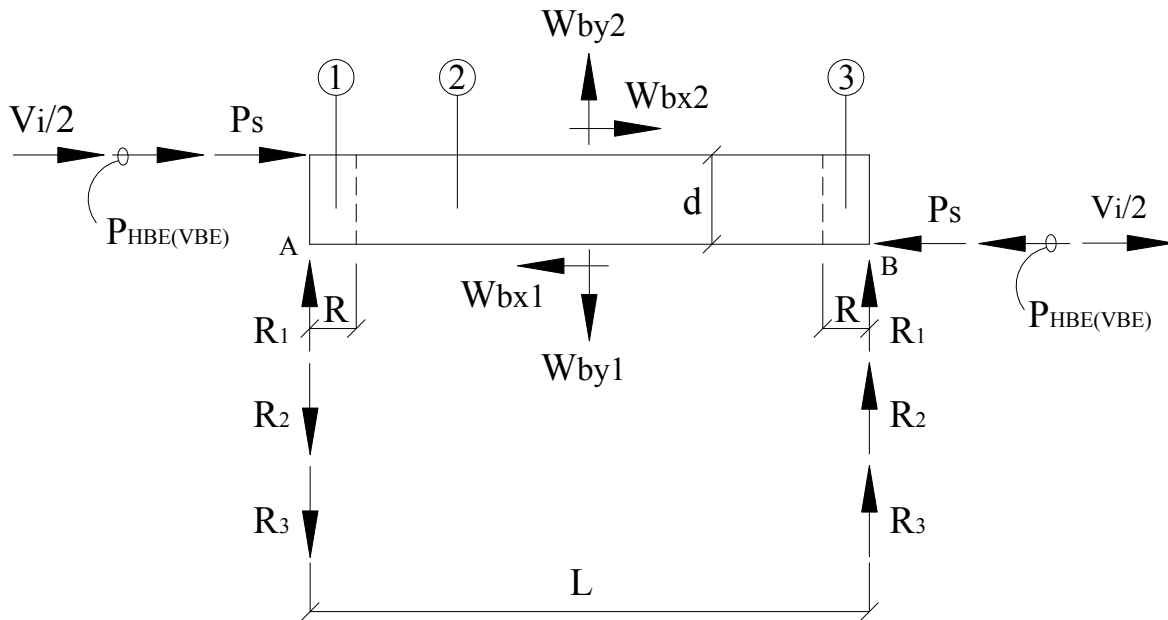


**FIGURE 3-8 Complete force resultant free body diagram of HBE**

Superimposing all of the above force components identified to be acting on the HBE element, figure 3-8 shows the resulting free body diagram of an HBE for the condition when the infill web plate above and below the HBE flanges have fully yielded (for a rightward drift condition). To simplify the free body diagram shown, the horizontal compression reactions at the rocking connection at the HBE flanges are combined into a single variable  $C$  and in terms of force resultants is:

$$C = \frac{V_i}{2} + P_{HBE(VBE)} + P_s \quad (3-15)$$

where recall that  $P_{HBE(VBE)}$  is the summation of  $W_{cx1}$  and  $W_{cx2}$ . Furthermore, the vertical end shear components have been combined and designated as reaction  $R_a$  and  $R_b$  for the left and right end vertical reactions respectively. Substituting (3-3), (3-6) and (3-7) for  $R_1$ ,  $R_2$ , and  $R_3$  respectively into (3-16) and (3-17), results in the following equations in terms of force resultants:

$$R_a = R_1 - R_2 - R_3 = \frac{W_{by1} - W_{by2}}{2} - (W_{bx1} + W_{bx2}) \frac{d}{2L} - (P_s + W_{cx1} + W_{cx2}) \frac{d}{L} \quad (3-16)$$

$$R_b = R_1 + R_2 + R_3 = \frac{W_{by1} - W_{by2}}{2} + (W_{bx1} + W_{bx2}) \frac{d}{2L} + (P_s + W_{cx1} + W_{cx2}) \frac{d}{L} \quad (3-17)$$

Note that the vertical gravity loads normally present for an actual building are not considered here; although typically small compared to the other effects acting on the HBE, they could easily be incorporated in the analysis presented above. Also note that the yield mechanism of a SC-SPSW system results in a shear demand in the HBE and vertical joint connection forces (i.e., maximum reaction force  $R_b$ ) that can be quite large. It is critical that the designer be cognizant on the effects of these forces when designing the HBE-to-VBE shear connections.

### 3.3.1.2 Development of HBE Moments (rocking about HBE flanges)

The moment distribution to be used in the design of an HBE incorporating self-centering components can be determined from the free body diagram of figure 3-8 for the case of rocking about the HBE flanges. Development of the moment, shear, and axial force diagrams along the HBE must recognize that the infill web plate geometry at the joint connection has an impact on the results and needs to be considered. As previously discussed, a rocking type connection is necessary to achieve the self-centering mechanism, which allows free joint rotation of the HBE relative to the VBE and allows elongation of the post-tension elements during lateral drift. These details require access above and below the HBE at the joint for connection detailing. Consequently, radius infill web plate cut-outs have been provided at the joint connections to facilitate construction of these configurations. As discussed earlier, the corner cut-outs are also



provided to reduce the potential for corner tear out of the infill web plate due to high localized infill web plate strain effects due to opening of the rocking joint connection. Past experimental and analytical tests have shown radius corner cut-outs do not significantly affect the performance of conventional SPSW systems (Bruneau et al. 2009).

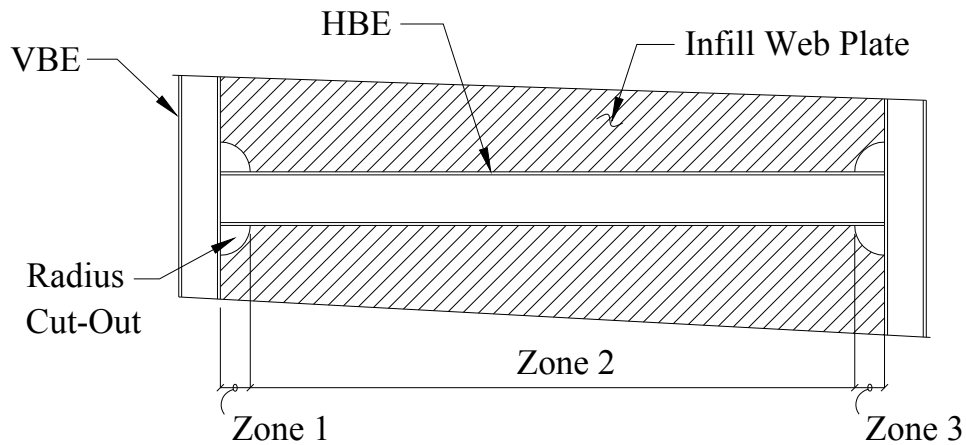


**FIGURE 3-9 SPSW infill corner cut-outs**

Therefore, in developing the subsequent moment diagrams, three zones along the HBE are considered; the two segments of HBE where the infill web plate is cut-out and not in contact with the HBE flange; and the segment of the HBE between the infill web plate corner cut-outs where the infill web plate is in contact with the HBE flange. These zones, for the purpose of discussion, are designated as Zone 1, Zone 2, and Zone 3 as indicated on figure 3-9.

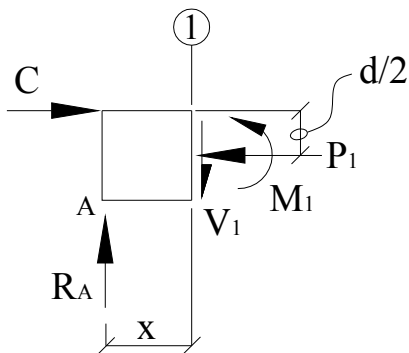


**FIGURE 3-10 Free body diagram along Zone 1**

The resulting free body diagram for the HBE segment along Zone 1 is shown in figure 3-10. Because of the corner cut-out in the infill web plate, the internal moment is obtained from the vertical end reaction and the horizontal reaction force at the rocking connection. Taking moment equilibrium at the HBE section Cut 1 gives (3-18) in terms of force resultants.

$$M_1 = \frac{Cd}{2} + R_a x \quad (3-18)$$

Substituting (3-15) and (3-16), and the equivalent force per unit length quantities for the resultant forces (i.e., (3-1) and (3-2)), into (3-18), the resulting moment relationship expressed in terms of the infill web plate yield forces per unit length along the HBE along Zone 1 is:

$$M_1 = P_s \left( \frac{d}{2} - \frac{d}{L} x \right) + (\omega_{by1} - \omega_{by2}) \left( \frac{L}{2} x - Rx \right) + (\omega_{bx1} + \omega_{bx2}) \left( \frac{dR}{L} x - \frac{d}{2} x \right) + (\omega_{cx1} + \omega_{cx2}) \left( \frac{d^2}{2L} x + \frac{dR}{L} x + \frac{dh}{4} - \frac{dh}{2L} x - \frac{d^2}{4} - \frac{dR}{2} \right) + (\omega_{bx1} - \omega_{bx2}) \left( \frac{dL}{4} - \frac{dR}{2} \right) \quad (3-19)$$

Next, considering any HBE section at some point along Zone 2, the internal moment can be obtained by taking moment equilibrium at the arbitrary HBE section Cut 2.

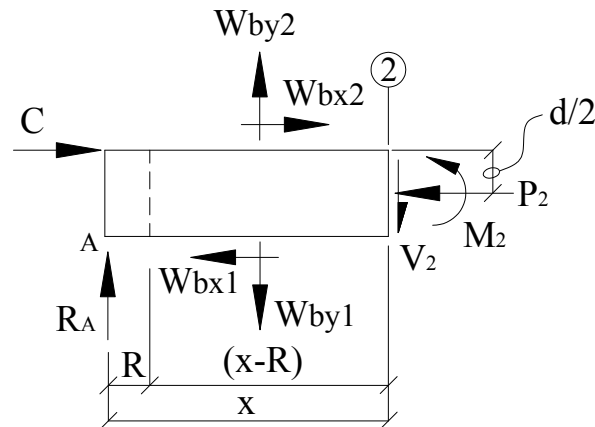


**FIGURE 3-11 Free body diagram along Zone 2**

The free body diagram along Zone 2 is shown in figure 3-11. As can be seen from the free body diagram, in addition to the vertical end reaction and the horizontal reaction at the rocking point connection, additional force components from the infill web plate contribute to the HBE moment. Taking moment equilibrium at the HBE section Cut 2, (3-20) in terms of force resultants is obtained.

$$M_2 = R_a x + C \frac{d}{2} + (W_{by2} - W_{by1}) \left( \frac{x-R}{2} \right) + (W_{bx1} + W_{bx2}) \frac{d}{2} \quad (3-20)$$

Substituting (3-15) and (3-16), and the equivalent force per unit length quantities for the resultant forces into (3-20), the resulting moment relationship expressed in terms of the infill web plate yield forces per unit length along the HBE along Zone 2 is:

$$M_2 = P_s \left( \frac{d}{2} - \frac{d}{L} x \right) + (\omega_{by1} - \omega_{by2}) \left( \frac{L}{2} x - \frac{x^2}{2} - \frac{R^2}{2} \right) + (\omega_{bx1} + \omega_{bx2}) \left( \frac{dR}{L} x - \frac{dR}{2} \right) + (\omega_{cx1} + \omega_{cx2}) \left( \frac{dR}{L} x + \frac{dh}{4} + \frac{d^2}{2L} x - \frac{dh}{2L} x - \frac{d^2}{4} - \frac{dR}{2} \right) + (\omega_{bx1} - \omega_{bx2}) \left( \frac{dL}{4} - \frac{dR}{2} \right) \quad (3-21)$$

Likewise, for the HBE moment along Zone 3, where again the corners of the infill web plate has been cut-out, the free body diagram can be drawn to obtain the moment relationship along the length of the HBE along Zone 3.

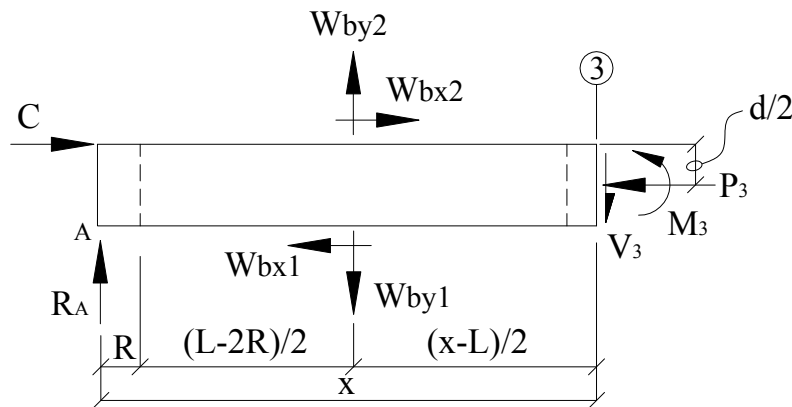


**FIGURE 3-12 Free body diagram along Zone 3**

Taking moment equilibrium at the HBE Cut 3 shown in figure 3-12, (3-22) in terms of force resultants is obtained.

$$M_3 = R_a x + C \frac{d}{2} + (W_{by2} - W_{by1}) \left( x - \frac{L}{2} \right) + (W_{bx1} + W_{bx2}) \frac{d}{2} \quad (3-22)$$

Substituting (3-15) and (3-16), and the equivalent force per unit length quantities for the resultant forces into (3-22), the resulting moment relationship expressed in terms of the infill web plate yield forces per unit length along the HBE along Zone 3 is:

$$\begin{aligned} M_3 = & P_s \left( \frac{d}{2} - \frac{d}{L} x \right) + (\omega_{by1} - \omega_{by2}) \left( \frac{L^2}{2} - LR - \frac{L}{2} x + Rx \right) \\ & + (\omega_{bx1} + \omega_{bx2}) \left( \frac{dR}{L} x + \frac{dL}{2} - dR - \frac{d}{2} x \right) \\ & + (\omega_{cx1} + \omega_{cx2}) \left( \frac{dR}{L} x + \frac{dh}{4} + \frac{d^2}{2L} x - \frac{dh}{2L} x - \frac{d^2}{4} - \frac{dR}{2} \right) + (\omega_{bx1} - \omega_{bx2}) \left( \frac{dL}{4} - \frac{dR}{2} \right) \end{aligned} \quad (3-23)$$

Note that significant axial and shear forces can be generated in the HBE member due to the plastic yielding of the infill web plate and the effects of post-tension forces. Consequently combined axial, shear and flexural loading interaction should be considered and the corresponding reduced plastic moment capacity of the HBE should be used based on an appropriate plastic stress combination model (e.g., Bruneau et al. 2011). Finally, if no infill web plate corner cut-outs were to be provided, the HBE analysis can be simplified to the use of the analysis results presented for Zone 2 only.

### 3.3.1.2.1 HBE Moment Diagrams (rocking about HBE flanges)

With the moment relationship along the HBE now established, the moment diagram of an HBE can be plotted for a SPSW system incorporating a post-tension self-centering mechanism. However, clearly, the magnitude of the moments depends on the geometry, materials, and properties of an actual SC-SPSW system (i.e., infill web plate design properties, amount of post-tensioning force, depth of HBE, etc.). These parameters are the result of an iterative design process. A proposed design approach (and design example) for this structural system is

developed in Dowden et al. (2012). For completeness, the design approach is provided for reference as follows:

1. Select initial boundary element sizes and web plate thickness (of many possible approaches, this could be done by designing a conventional SPSW, although other approaches are acceptable too).
2. Design the self-centering connection with the least PT forces that would result in the maximum moment occurring at the HBE ends at the target drift.
3. Select post-tension to ensure that the PT rods remain elastic at least up to 4% drift.
4. Select the initial PT force applied to the self-centering connection to be also large enough to provide an adequate decompression moment to overcome gravity loads and possible wind loads.
5. Select the least cross section areas of PT rods that satisfy the previous conditions.
6. Consider the effect of PT on reducing the HBE plastic moment as well as the effect of PT losses due to axial shortening to assess the adequacy of the HBE.
7. Iterate as needed to reduce the HBE size, ensuring that the HBE moment capacity reduced due to axial and shear forces remains adequate.

Note that the above design procedure is applicable only for the HBE-to-VBE flange-rocking joint, where it is observed that the PT can have an effect of shifting the location of maximum HBE moment. This is not possible for use with the centerline rocking connection and difficult to achieve for the NewZ-BREAKSS rocking connection due to the kinematics of a frame detailed with these rocking connections (to be presented subsequently). However, a general procedure is presented in Section 6.8 for the calculation of the minimum amount of PT to ensure recentering at a target residual drift, which is applicable for all rocking connections presented in this report. Note that this general procedure was not available (nor used) during development of the experimental program, as the SPSW models at the time assumed infill plates modeled using tension-only strips, with the consequence that any value of initial pretension can achieve the recentering objective.

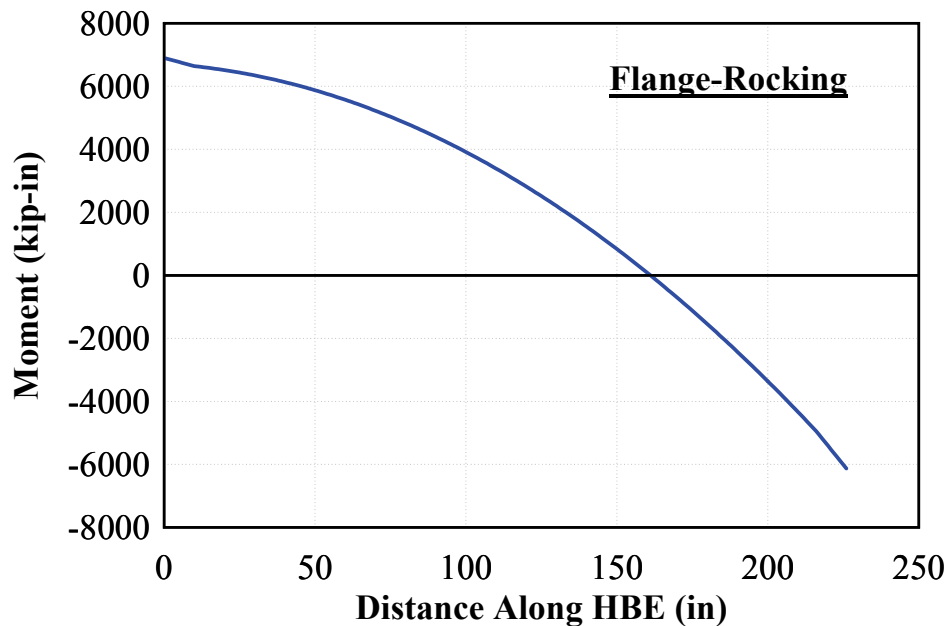


**FIGURE 3-13 Moment diagram – Rocking about HBE flanges**

The moment demands on an HBE for a frame detailed with the flange-rocking joint are presented subsequently. Furthermore, for illustrative purposes only, to avoid abstract complexities in keeping the problem parametric, all results here are presented in terms of an example. The model used for this example consisted of an intermediate level W18 HBE with a clear span of 226 inches and a story height of 153 inches of a single bay frame. The SPSW web plates consisted of an approximate 14 Gauge and 18 Gauge infill web plate thicknesses below and above the HBE respectively with a corner cut-out radius of 10 inches. Area of post-tension steel was provided to produce a target maximum moment of approximately 60% of the full HBE plastic moment capacity at a 2% drift with an initial post-tensioning force of approximately 30% of the assumed yield strength of the PT. A yield stress of 30 ksi was assumed for the infill web plates, an ultimate tensile strength of 150 ksi for the PT elements, and ASTM A572 steel for the boundary frame. The resulting moment diagram is shown in figure 3-13. However, the relevant importance here is the HBE moment distribution effects of the different components contributing to the moment equations (3-18) to (3-23). To better understand the relative contributions of various terms to the resulting HBE moment distribution, the composite moment diagram shown in figure 3-13, which would be obtained from a specific design example, is decomposed into its individual components to observe each respective influence on the HBE.

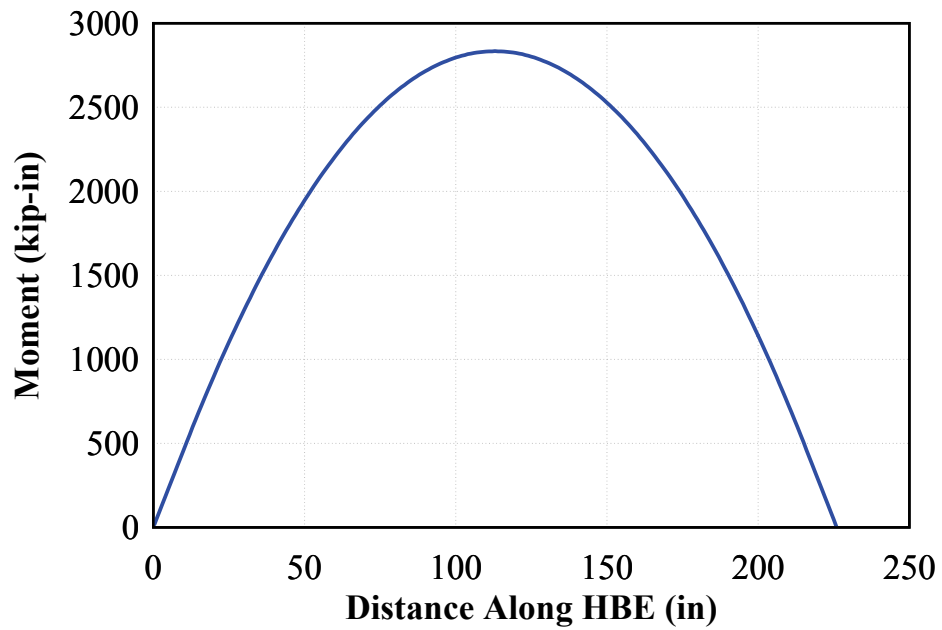


**FIGURE 3-14 Moment diagram - Vertical force component**

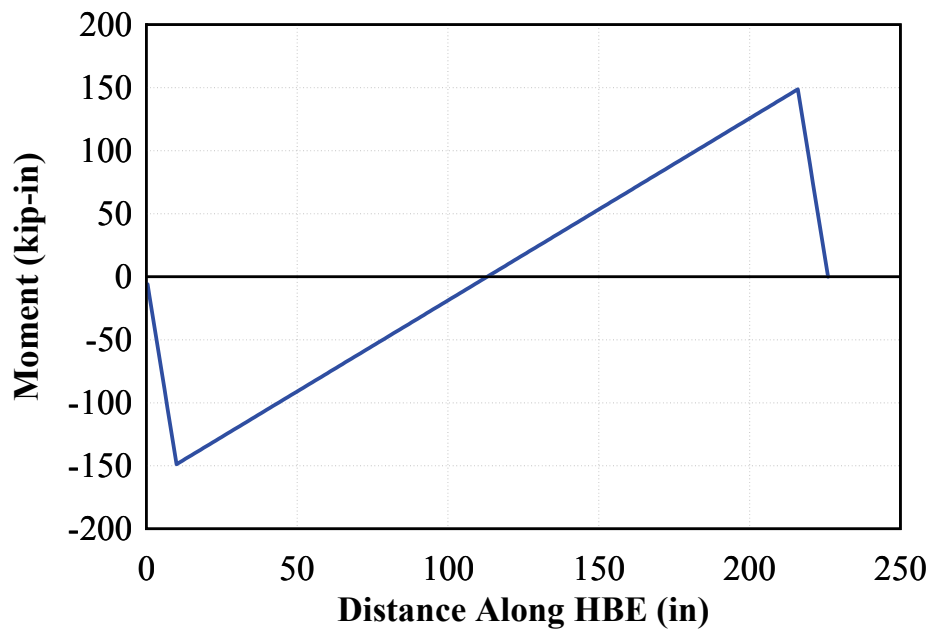


**FIGURE 3-15 Moment diagram - Horizontal force corner cut-out effects**

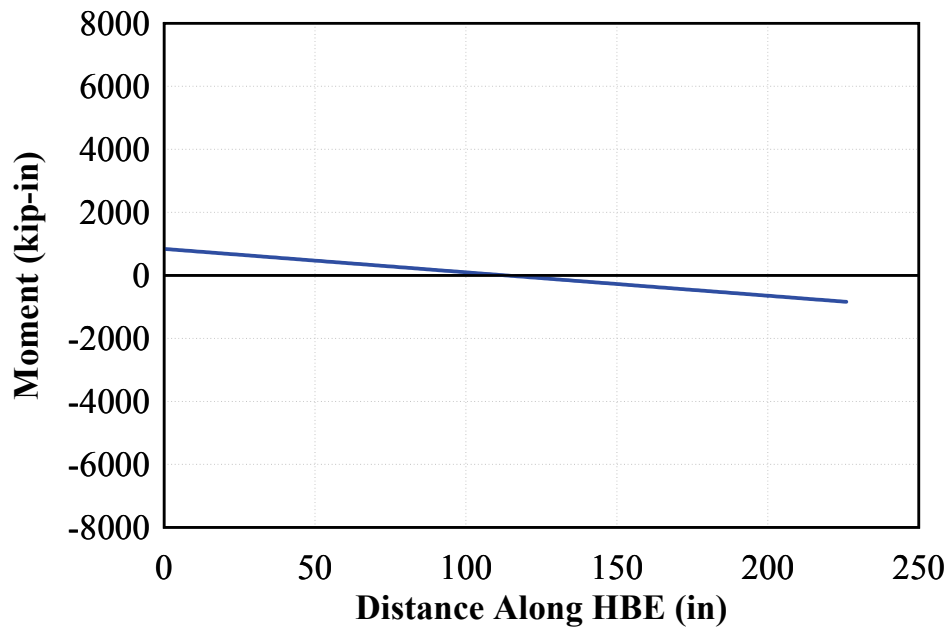


**FIGURE 3-16 Moment diagram - Horizontal force VBE component**

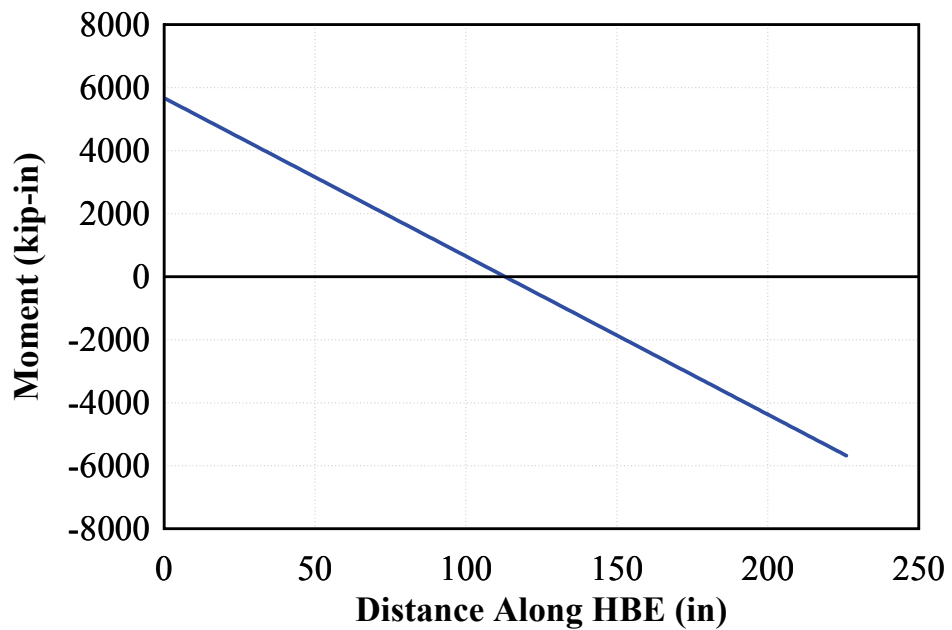


**FIGURE 3-17 Moment diagram - Post-tension force**



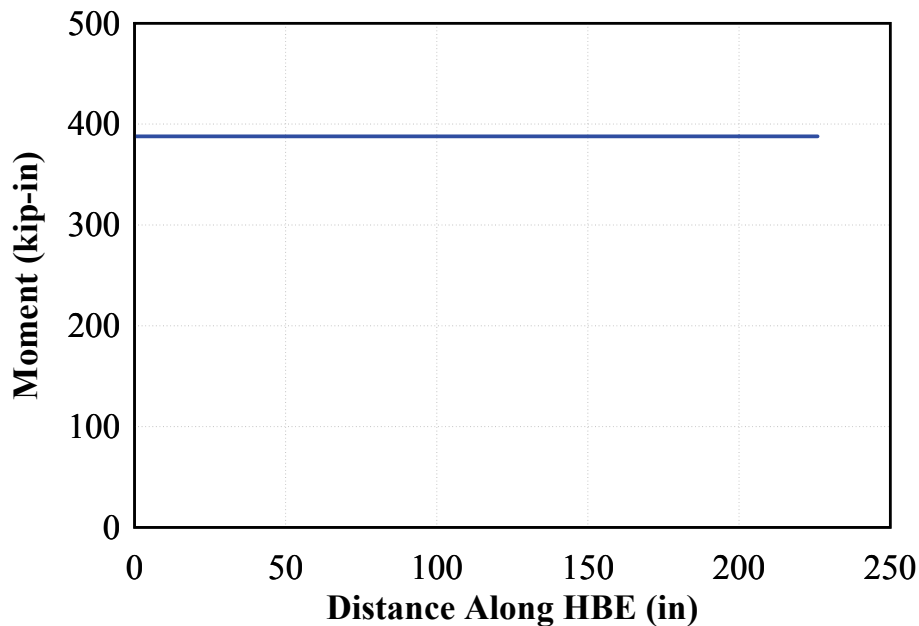


**FIGURE 3-18 Moment diagram – Story shear force**

From the moment equations presented above, it can be observed that the moment along the length of an HBE due to the yielding of the infill web plates can be decomposed into five primary components; the vertical yield force component along the length of the HBE (i.e.,  $W_{by1}$  and  $W_{by2}$ ), the horizontal yield force component (i.e.,  $W_{bx1}$  and  $W_{bx2}$ ) along the length of the HBE due to effects of providing corner cut-outs, the eccentric axial reaction at the rocking connection due to the horizontal yield force components of the infill web plate along the height of the VBE (i.e.,  $W_{cx1}$  and  $W_{cx2}$ ), the eccentric axial reaction at the rocking connection due to the post-tensioning element (i.e.,  $P_s$ ), and the applied eccentric axial story shear at the rocking connection (i.e.,  $V_i$  which also relates to  $W_{bx1}$  and  $W_{bx2}$ ). The moment diagrams corresponding to each of these components are plotted on figures 3-14 to 3-18, respectively.

On figure 3-14, although barely visible, note that the ends of the moment diagram are linear and not parabolic. This is because corner cut-outs are provided in the infill web plate at each end of the HBE. At these locations the shear is constant along the length of the radius plate cut-out, leading to a linear moment distribution along the length of the HBE at these locations. Also note that the moment contribution from the horizontal component of infill web plate at yield (figure 3-15) is a result of the corner cut-outs of the infill web plate. Incidentally, if the steel plate infill

was extended over the full length of the HBE (i.e. no corner cut-outs of the infill web plate at the HBE-to-VBE joint connection), (3-21) would be applicable for the full length of the HBE.

It is observed from the moment diagrams of figure 3-16 and 3-17 that for rocking about the HBE flanges, the horizontal reactions at the rocking point will always generate double curvature moments at the ends of the HBE. Furthermore, the moment diagrams are of identical shape, only the moment magnitudes are different. Generally, the contribution of the moment due to the effects of the VBE being pulled toward each other by the yielding of the infill web plate (figure 3-16 for this example), is not as significant as the HBE moment produced by the applied post-tension force (figure 3-17 for this example). The contribution to the HBE moment from the VBE horizontal reaction at the rocking point, will always be additive to the HBE moment produced by the post-tensioning component.

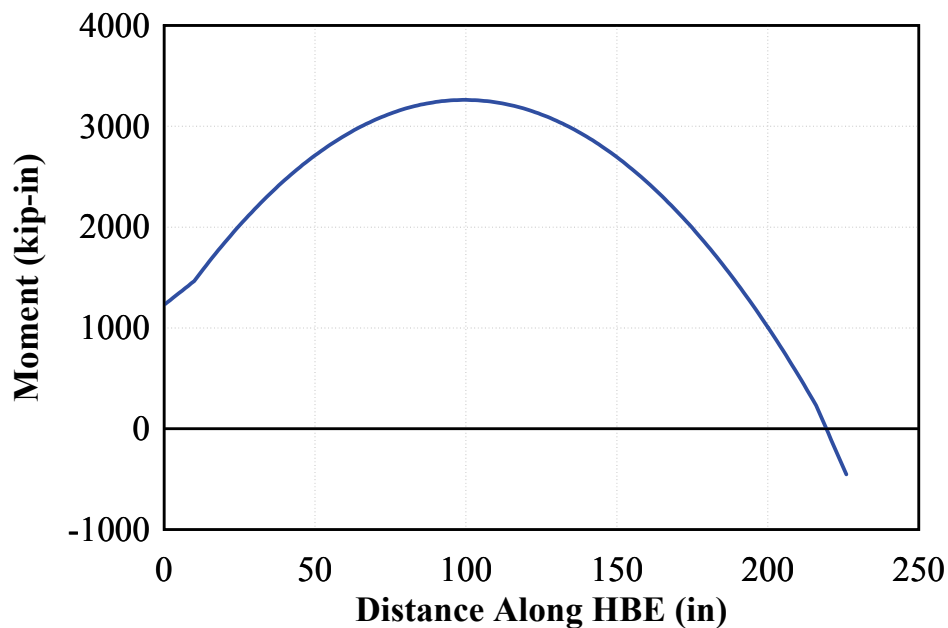


**FIGURE 3-19 Moment diagram - No post-tension provided**

To observe the effects that the post-tension has on the HBE moment of a SC-SPSW system, the composite moment diagram shown in figure 3-19 has been developed for the same example SPSW system used to obtain the moment diagram of figure 3-13, but without adding the post-tension component to the total moment diagram. Without the post-tension component it can be

seen that the maximum moment occurs close to the HBE mid-span. As presented in Dowden et al. (2012), having the maximum moment occur near the mid-span of the HBE is not desirable. The relevance here is the post-tension force effects on the HBE for the SC-SPSW system under consideration. Comparing figures 3-13 and 3-19, it is observed that, in addition to acting as a self-centering mechanism, the post-tension force can be designed to shift the point of maximum moment towards the ends of the HBE (although at the cost of increased HBE moment demand).

### 3.3.1.3 Development of HBE Shears (rocking about HBE flanges)

The shear distribution to be used in the design of an HBE incorporating self-centering components can be determined using the same free body diagrams developed earlier for the HBE moments. Similarly, due to the presence of infill web plate corner cut-outs, three zones along the length of the HBE are considered. From the free body diagram for the HBE segment along Zone 1, shown in figure 3-10, the corresponding shear force is the reaction  $R_a$  described in (3-16). Substituting (3-1) and (3-2) in place of the resultant infill web plate yield force components leads to the shear force distribution along HBE segment Zone 1 as follows:

$$V_1 = R_a = \frac{(\omega_{by1} - \omega_{by2})(L - 2R)}{2} - \frac{(\omega_{bx2} + \omega_{bx1})(L - 2R)}{2L} d - (\omega_{cx1} + \omega_{cx2}) \left( \frac{h}{2} + \frac{d}{2} - R \right) \left( \frac{d}{L} \right) - P_s \left( \frac{d}{L} \right) \quad (3-24)$$

Next, from the free body diagram for the HBE segment along Zone 2, shown in figure 3-11, the corresponding shear force is reduced by the vertical component of the infill web plate yield forces. The shear force distribution along HBE segment Zone 2 follows:

$$V_2 = R_a - (\omega_{by1} - \omega_{by2})(x - R) \quad (3-25)$$

Similarly, from the free body diagram for the HBE segment along Zone 3, shown in figure 3-12, the corresponding shear force distribution along HBE segment Zone 3 follows:

$$V_3 = R_a - (\omega_{by1} - \omega_{by2})(L - 2R) \quad (3-26)$$

### 3.3.1.4 Development of HBE Axial Force (rocking about HBE flanges)

The axial force distribution to be used in the design of an HBE incorporating self-centering components can be determined using the same free body diagrams developed earlier for the HBE moments. Similarly, due to the presence of infill web plate corner cut-outs, three zones along the length of the HBE are considered. From the free body diagram for the HBE segment along Zone 1 (figure 3-10), the corresponding axial force is the horizontal reaction  $C$  at the rocking point described in (3-15). Substituting (3-1) and (3-2) in place of the resultant infill web plate yield force components leads to the axial force along HBE segment Zone 1 as follows:

$$P_1 = C = \frac{(\omega_{bx1} - \omega_{bx2})(L - 2R)}{2} + (\omega_{cx1} + \omega_{cx2})\left(\frac{h}{2} - \frac{d}{2} - R\right) + P_s \quad (3-27)$$

Next, from the free body diagram for the HBE segment along Zone 2, shown in figure 3-11, the corresponding axial force is reduced by the horizontal component of the infill web plate yield forces. The axial force distribution along HBE segment Zone 2 follows:

$$P_2 = C - (\omega_{bx1} - \omega_{bx2})(x - R) \quad (3-28)$$

Similarly, from the free body diagram for the HBE segment along Zone 3, shown in figure 3-12, the corresponding axial force distribution along HBE segment Zone 3 follows:

$$P_3 = C - (\omega_{bx1} - \omega_{bx2})(L - 2R) \quad (3-29)$$

### 3.3.1.5 Comparison with SAP2000 (rocking about flanges)

The programs SAP2000 (CSI 2009) and OpenSees (Mazzoni et al. 2009) were both used for the analyses presented in this report. The former is a commercially available software program used in practice by design professionals. The latter is an open-source code mainly used by the research community. Both have their particular advantages. Accordingly, both programs were used interchangeably throughout this report depending on the particular task performed. The analytical results presented in this Section were obtained using SAP2000. However, to keep things organized for presentation purposes (to keep relevant material descriptions together), modeling description will be presented for both programs where applicable.

To validate the formulations describing the distribution of moment, shear, and axial forces developed, comparisons were made to non-linear pushover analysis. The analytical model used consisted of a single bay, single story frame with a bay width of 20 feet and story height of 10 feet with material properties noted earlier in the first example. The infill web plate has a 14-gauge thickness. A PT area of 5.1 square inches is provided with an initial PT force of approximately 25% of the assumed yield strength of the PT. Furthermore, it is assumed that the boundary frame remains elastic. A strip model approach (Sabelli and Bruneau 2007) was used for the analytical modeling of the SPSW infill web plate and shown in figure 3-20.

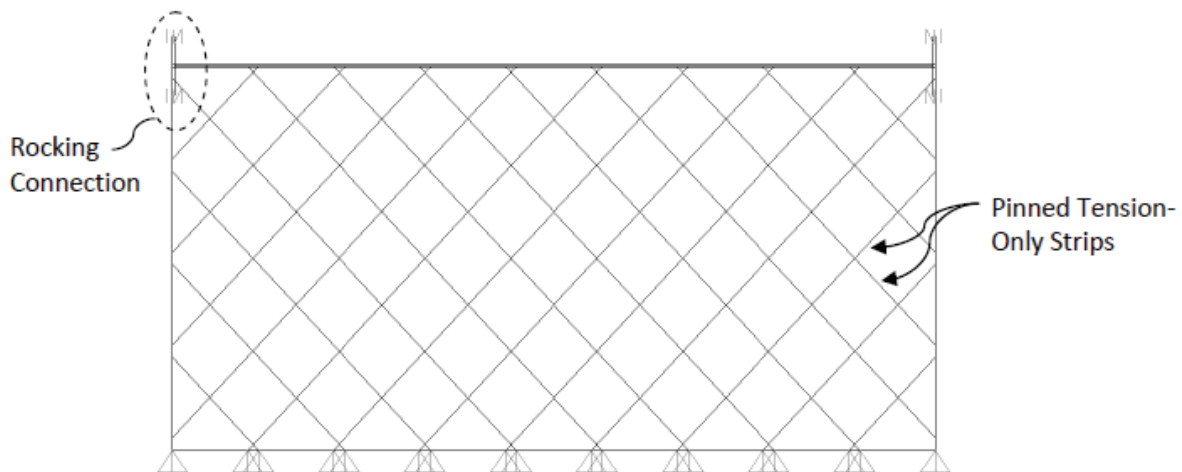


**FIGURE 3-20 Flange-rocking frame - Analytical model**

The hysteretic behavior of SPSW systems is yielding of the infill web plate through tension field action. Accordingly, the infill web plate is modeled by using a series of tension-only strips. In SAP2000, each of the strips is assigned an axial plastic hinge model to account for non-linear hysteretic behavior. The post-tension elements along the length of the HBE are modeled as tension-only members where temperature loading was used to simulate initial post-tensioning forces. Here temperature loading was used to simulate post-tension forces which allowed modeling the PT elements as simple frame elements. The VBE frame members are considered to be rigid (for the results presented here; otherwise the actual VBE section would be used). For the HBE, both rigid and flexible section properties are considered; for the rigid HBE condition, negligible post-tension force losses will occur whereas for the flexible HBE, which considers the actual axial stiffness of the HBE, post-tension force losses due to HBE axial shortening will occur. For modeling in OpenSees, the strips are assigned an axial plastic hinge using the *Hysteretic Material* definition. The PT elements are modeled with the *Steel02 Material Giuffre-Menegotto-Pinto* definition. This latter material definition allows simulation of initial applied PT forces by inputting an initial stress value.

In SAP2000, the rocking connection is modeled using *Gap Link* elements. A rigid frame element was used as a link to model the depth of the HBE to capture the rocking motion about the HBE flanges. Joint constraints in the translational vertical global DOF and in-plane rotational DOF (HBE strong axis bending) were provided at key nodes. For modeling in OpenSees, stiff compression only springs (using the *Elastic-No Tension Material* definition) are used at the HBE-to-VBE contact flange locations in combination with the use of nodal constraints and *rigidlink beams*. The connection models used in SAP2000 and OpenSees described are shown in figure 3-21.

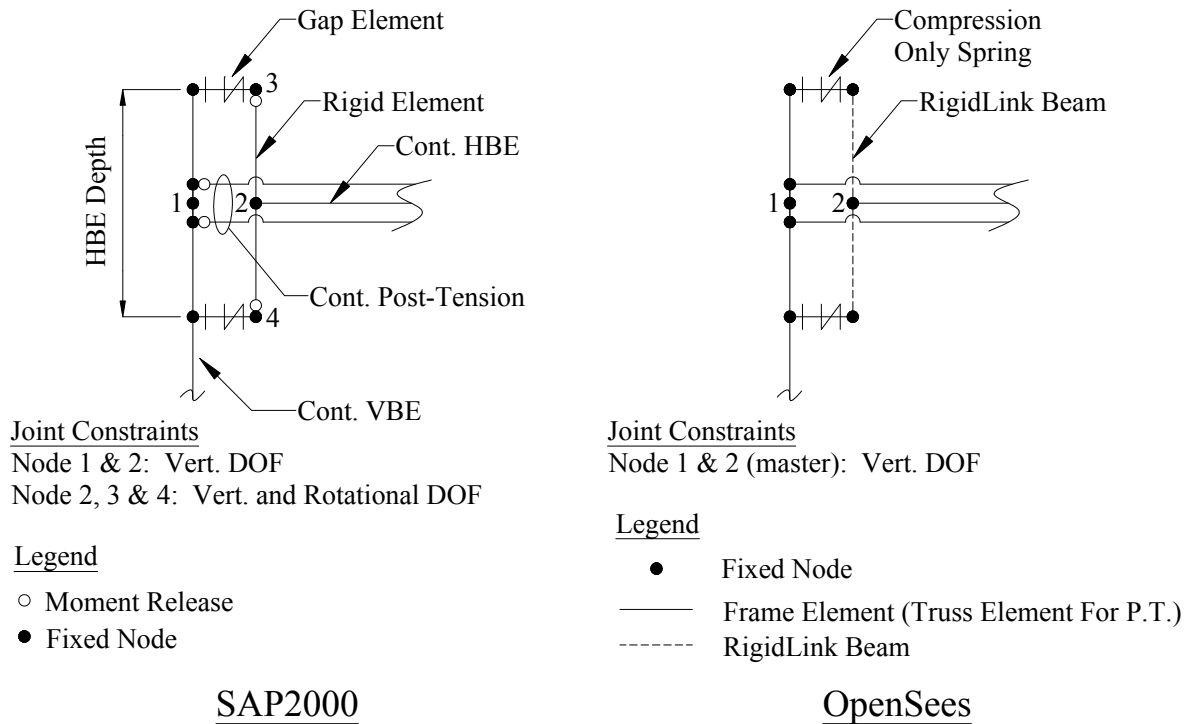


**FIGURE 3-21 Rocking about HBE flanges connection – Analytical model**

Note that the design conditions of the HBE for comparison to the analytical SAP2000 model used here is different than that presented earlier for the development of the moment, shear and axial formulations. Here the analytical model used for this example consisted of a single bay, single story frame with a bay width of 20 feet and story height of 10 feet. The SPSW web plate consisted of a thickness of approximately 14 gauge light gauge infill web plate. A post-tension area of 5.109 square inches was provided. An initial post-tensioning force of approximately 25% and 30% of the assumed yield strength of the PT was provided for the flexible HBE and rigid HBE respectively. The relevant importance here is not the design of the SC-SPSW system, but to validate the formulations developed earlier with numerical analysis using SAP2000.

Figures 3-22 to 3-27 below provide comparisons of the moment, shear and axial force distributions along the length of the HBE using the formulations developed to that with the numerical model of the SAP2000 analysis for a rightward 3% drift condition. Comparisons are presented for conditions ignoring post-tension force losses due to axial shortening and for conditions considering HBE axial shortening. Note that since the SAP2000 model uses a finite

amount of strips to represent the infill web plate, the shear and axial force diagrams obtained from the SAP2000 analysis are stepped as compared to the continuous force diagrams using the theoretical formulations. The comparisons show that the moment, shear and axial formulations developed earlier are comparable to the results obtained from SAP2000.



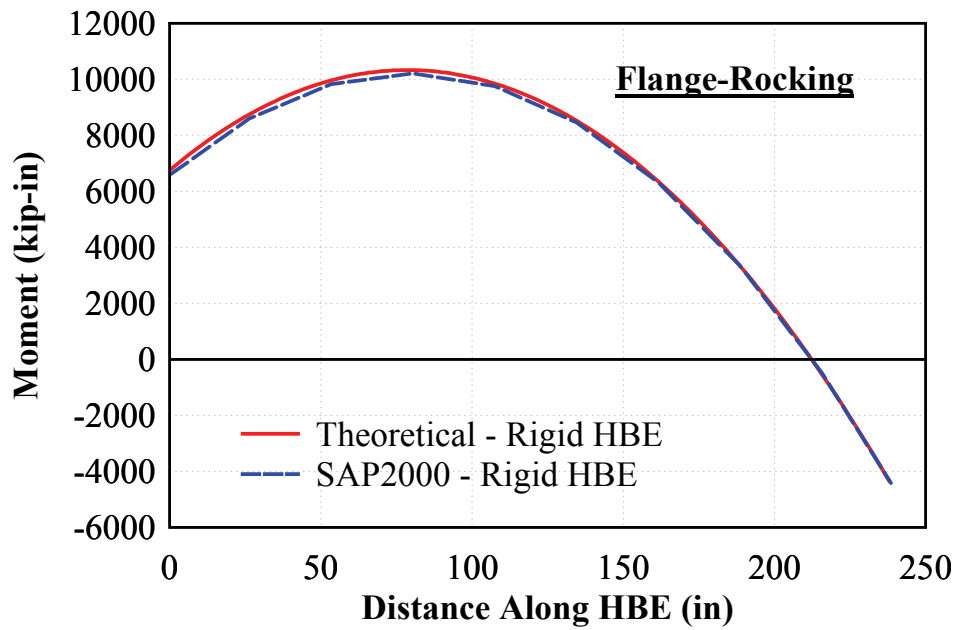


FIGURE 3-22 Moment diagram – Rigid HBE

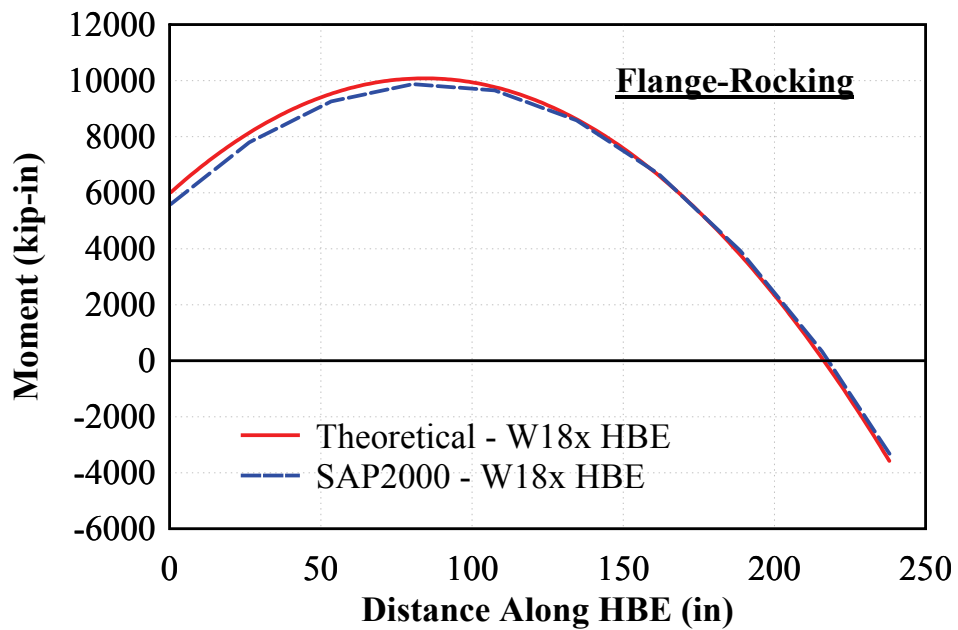


FIGURE 3-23 Moment diagram – Flexible HBE

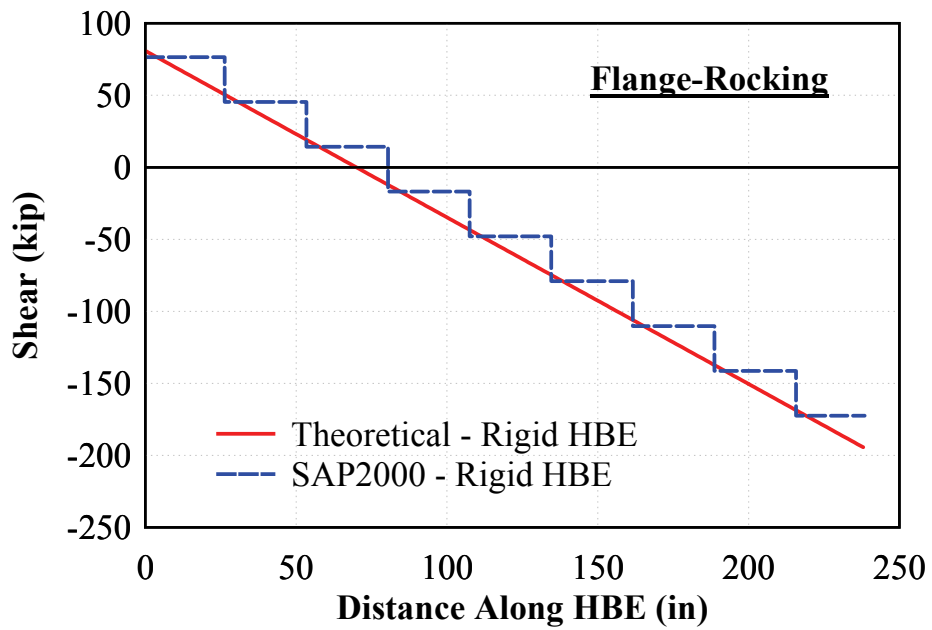


FIGURE 3-24 Shear force diagram – Rigid HBE

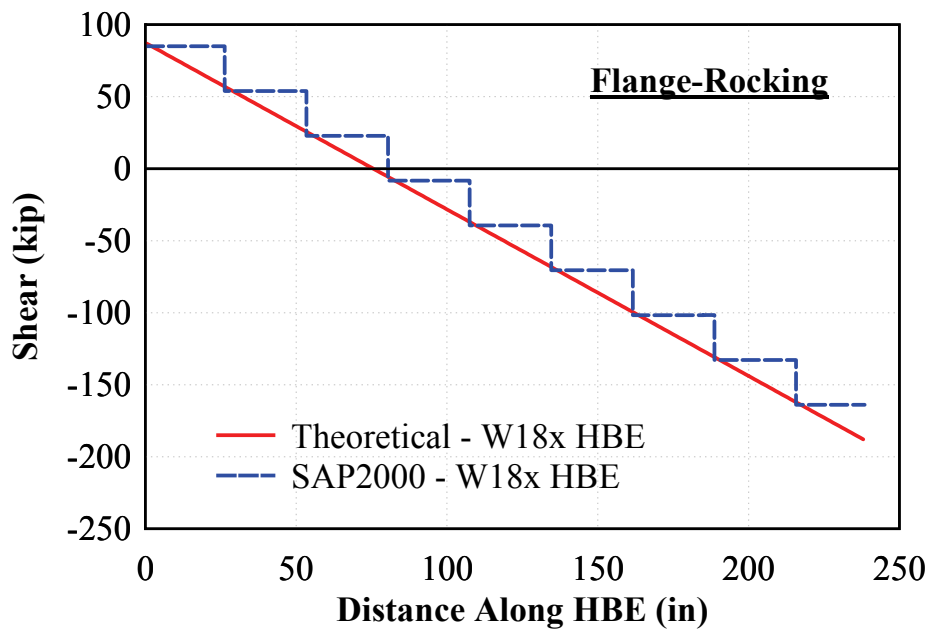
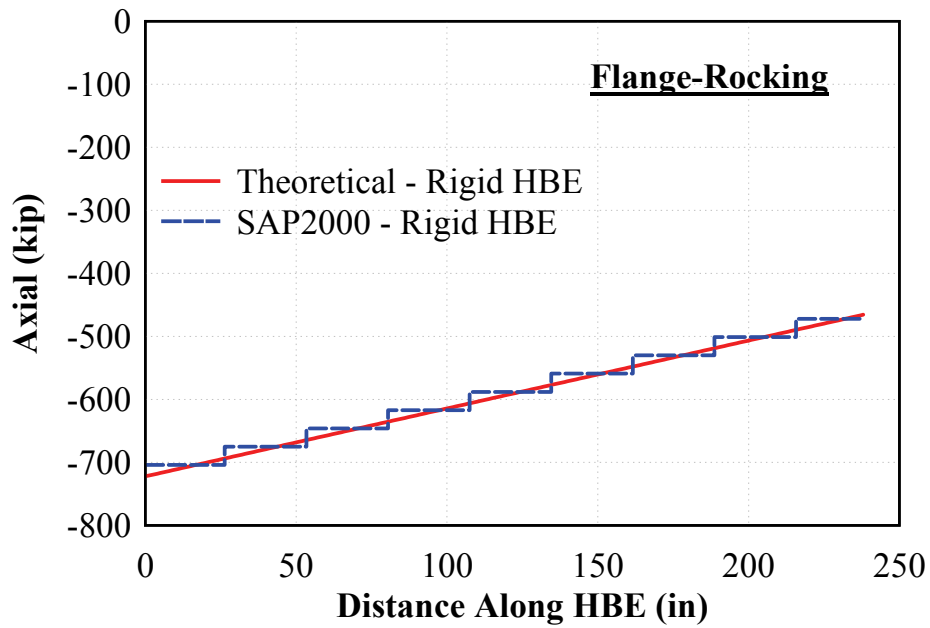
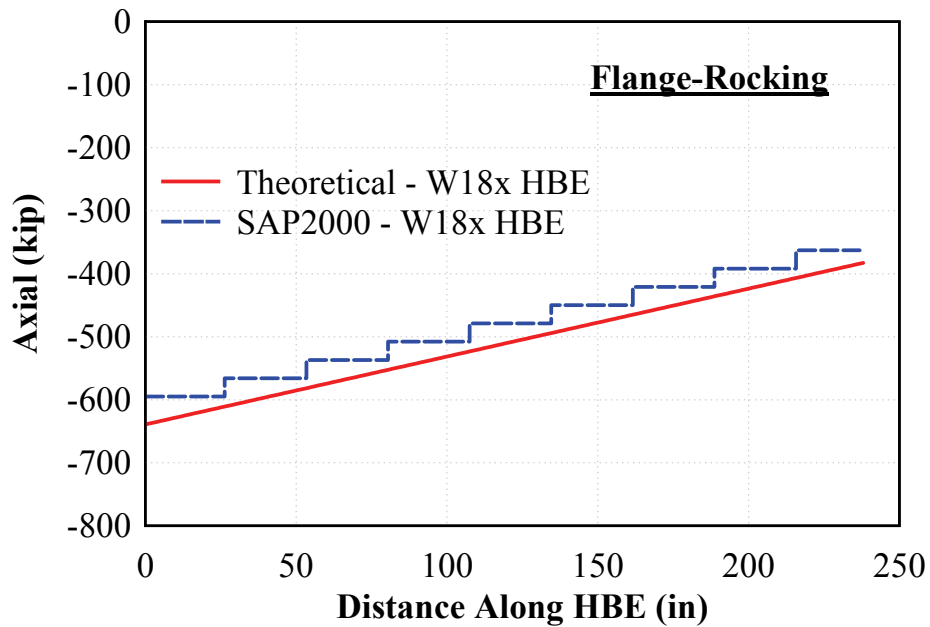


FIGURE 3-25 Shear force diagram – Flexible HBE



**FIGURE 3-26 Axial force diagram – Rigid HBE**



**FIGURE 3-27 Axial force diagram – Flexible HBE**

### **3.3.2 Rocking about HBE Centerline**

#### **3.3.2.1 Free Body Force Diagram**

Connections that use post-tension elements to generate self-centering forces can be of any geometry as long as drift induced elongations in the post-tension elements can be achieved. However, the moment distribution along the length of the HBE for rocking about the HBE centerline is significantly different than that of a rocking connection about the HBE flanges. To demonstrate this, new free body diagrams must first be developed, from which the corresponding moment, shear and axial force diagrams will be developed.

Recall that the development of self-centering forces is achieved by elongation of the post-tension elements due to opening of the HBE to VBE joint connection during lateral drift. As was previously shown, for rocking about the HBE flanges, this is easily achieved. However, for rocking about the HBE centerline, two conditions for the post-tension elements must be met.

First, the post-tension elements need to be located above and below the HBE centerline (i.e., the center of rotation) for their elongation to be possible. Second, the post-tension elements need to be anchored to the HBE and cannot be continuous across the length of the HBE (as was done for rocking about the HBE flanges); without such an adequate anchorage point, the post-tension elements will simply shift laterally with the boundary frame without experiencing any drift induced elongations (since the center of joint rotation on the HBE remains in full contact with the VBE). In other words, as one joint opens, the opposite end joint closes leading to a net elongation of zero if the post-tension element were placed continuous, as was done for rocking about the HBE flange condition. However, it is because of this behavior that beam-growth effects are eliminated for this rocking connection type. Note that the location of the PT anchor point along the HBE will depend on the strain demands of the PT elements at a maximum target drift. The anchor location should be provided to ensure that the PT strains remain elastic up to that drift demand.

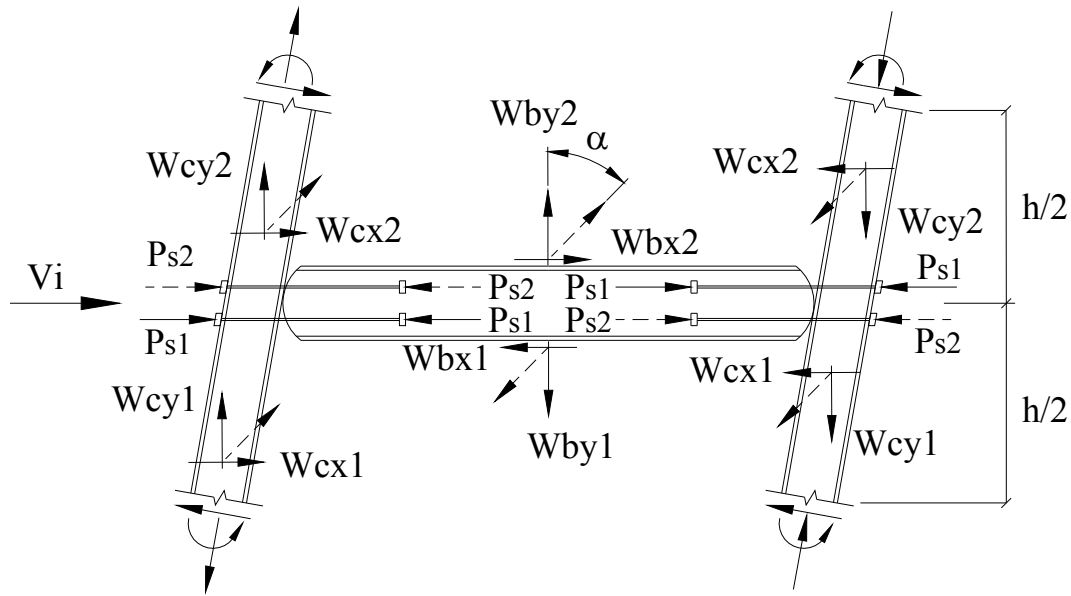


**FIGURE 3-28 Resultant force free body diagram**

Imposing the above conditions on the post-tension elements, the free body diagram of resultant forces on the boundary frame can be drawn as shown in figure 3-28 (for a rightward drift); where  $P_{s1}$  (shown by solid arrows) is the post-tension force that increases due to elongation during lateral drift and  $P_{s2}$  (shown by dashed arrows) is the post-tension force that reduces from “relaxation” due to lateral drift, and all other terms have been previously defined.

The force resultants shown in figure 3-28 can be further separated into individual components so that their influence on the HBE can be more understood. The influence of the vertical and horizontal force components ( $W_{by}$  and  $W_{bx}$ ) due to the inelastic yield forces of the infill web plate acting on the HBE is identical to that for the case of rocking about the HBE flange condition (i.e., figures 3-5 and 3-6, and remain identical in this case with the exception of the rocking point location). Furthermore, for a capacity design approach, the design story shears remain expressed by (3-5). For the condition of rocking about the HBE centerline, three differences from the case of rocking about the HBE flanges arise:

- i. Because the center of rotation is located at the neutral axis of the HBE, the influence of the horizontal forces due to the column pull-in (i.e.,  $P_{HBE(VBE)}$ ) does not contribute to the primary HBE moments.
- ii. Because the center of rotation is located at the neutral axis of the HBE, the influence of the story shear force (i.e.,  $V_i$ ) does not contribute to the primary HBE moments.
- iii. The moment distribution effects from the post-tension differ due to the intermediate anchorage point along the length of the HBE.

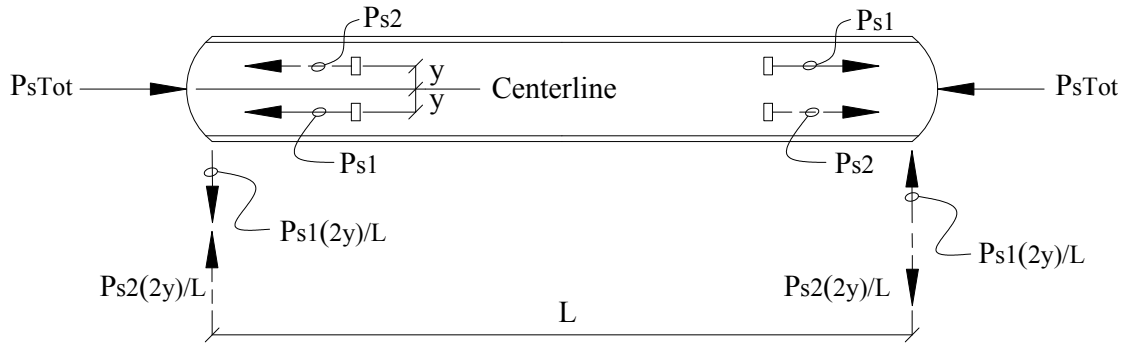


**FIGURE 3-29 Free body diagram post-tension forces**

Figure 3-29 is a free body diagram of an HBE with the post-tension forces expressed for a rightward drift. To further clarify the effects of  $P_{s1}$  and  $P_{s2}$ , recall that each  $P_s$  component is composed of two forces; the initial post-tension force  $P_o$ , applied prior to drift, and the force induced due to post-tension elongation during building drift,  $\Delta P$ . For the condition shown, from geometry, elongation of post tension will occur in  $P_{s1}$  while “relaxation” of the post-tension element  $P_{s2}$  will occur resulting in the following post-tension forces on the HBE:

$$P_{s1} = P_o + \Delta P = P_o + \frac{A_{PT1} E_{PT1}}{L_{PT1}} (\Delta_{drift} - \Delta_{loss}) \quad (3-30)$$

$$P_{s2} = P_o - \Delta P = P_o - \frac{A_{PT2} E_{PT2}}{L_{PT2}} (\Delta_{drift} + \Delta_{loss}) \quad (3-31)$$

From (3-30) and (3-31) it is observed that an increase in force  $P_{s1}$  results in a simultaneous decrease in force of  $P_{s2}$  (and vice versa for lateral drift in the opposite direction). It is also

observed that if the force  $\Delta P$  equals  $P_o$ ,  $P_{s2}$  will become fully “relaxed” and this force component will vanish. In other words, for the condition when  $\Delta_{net}$  (i.e.,  $\Delta_{drift}$  less  $\Delta_{loss}$ ) is equal to or greater than  $\Delta_o$ ,  $P_{s2}$  will equal zero. Consequently, the effectiveness of  $P_{s2}$  depends on the amount of initial post-tension force  $P_o$  as well as the maximum drift reached. In (3-30) and (3-31),  $\Delta_{loss}$  is the axial shortening that occurs along the HBE span length between the end of the HBE to the post-tension anchor point location on the HBE. To calculate the loss in post-tension force from HBE axial shortening, the same procedure for rocking about the HBE flange is used (and repeated for clarity), except that here the post-tension force losses due to HBE axial shortening occur due to the axial shortening of a partial HBE span segment. Thus it then follows that the HBE axial shortening is calculated as:

$$\Delta_{loss} = \frac{P_{PT} L_1}{A_{HBE} E_{HBE}} + \frac{P_{HBE(VBE)} L_1}{A_{HBE} E_{HBE}} \quad (3-32)$$

where  $L_1$  is the length of the HBE that corresponds to HBE-to-VBE rocking point to the location of the post-tension anchor,  $P_{PT}$  is the total post-tension force acting at the rocking point (i.e.,  $P_{s1}$  and  $P_{s2}$ ) and all other terms have been previously defined. Solving (3-32) for  $P_{PT}$  leads to the following:

$$P_{PT} = \frac{A_{HBE} E_{HBE}}{L_1} \Delta_{loss} - P_{HBE(VBE)} \quad (3-33)$$

Accordingly, the net effective axial tension force in the post-tension elements is the elongation due to drift minus the axial shortening of the HBE that occurs along the length of the post-tension elements and is calculated as follows:

$$P_{PT} = \left( \frac{A_{PT} E_{PT}}{L_{PT}} \right) (\Delta_{drift} - \Delta_{loss}) = k_{PT} (\Delta_{drift} - \Delta_{loss}) \quad (3-34)$$

Finally, equating (3-33) and (3-34), and solving for  $\Delta_{loss}$  leads to the amount of post-tension relaxation that should be considered and is calculated as:

$$\Delta_{loss} = \frac{P_{VBE(HBE)}}{k_{PT} + \frac{A_{HBE} E_{HBE}}{L_1}} + \left( \frac{k_{PT}}{k_{PT} + \frac{A_{HBE} E_{HBE}}{L_1}} \right) \Delta_{drift} \quad (3-35)$$

Furthermore, the relationship for the post-tension elongation due to lateral drift,  $\Delta_{drift}$ , must be re-defined since the center of rotation has changed. In figure 3-29,  $y$  is the distance from the centerline of the HBE to the centerline of the post-tension elements, resulting in the following relationship for post-tension elongation due to lateral drift:

$$\Delta_{drift} = \frac{\phi_{drift}}{100} y \quad (3-36)$$

Additionally, from observation of figure 3-29, the horizontal forces  $P_{S1}$  and  $P_{S2}$  will also produce vertical reactions at the left and right ends of the HBE, as provided in (3-37) and (3-38) respectively:

$$R_4 = (P_{s2} - P_{s1}) \frac{2y}{L} \quad (3-37)$$

$$R_5 = (P_{s1} - P_{s2}) \frac{2y}{L} \quad (3-38)$$



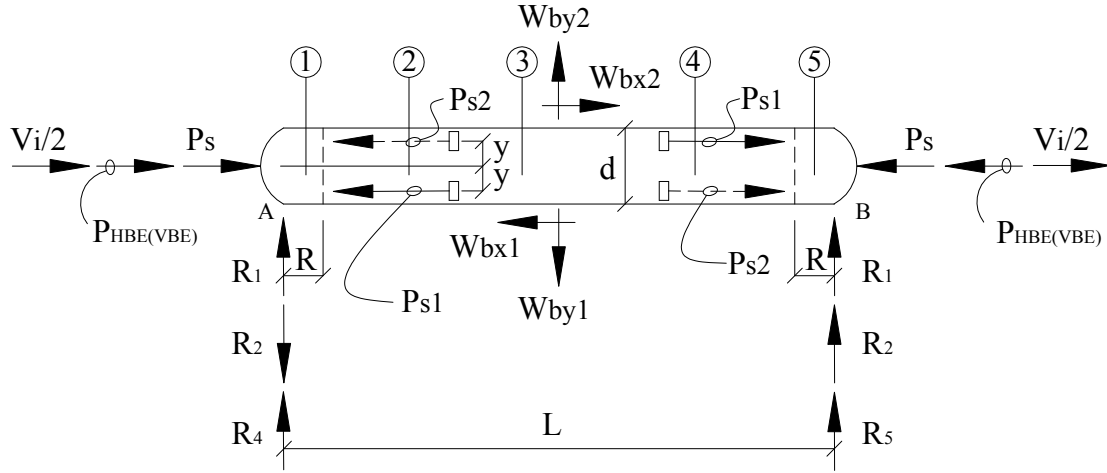


**FIGURE 3-30 Complete force resultant free body diagram of HBE**

Superimposing all of the force components identified to be acting on the HBE, figure 3-30 shows the resulting free body diagram of an HBE when the infill web plate above and below the HBE flanges have fully yielded for a rightward drift (neglecting gravity forces). As done previously, the horizontal compression reactions at the rocking connection and the vertical end reactions at the HBE centerline are combined into single variables  $C$ ,  $R_a$  and  $R_b$  respectively to simplify the free body diagrams leading to the HBE axial force in terms of force resultants is:

$$C = \frac{V_i}{2} + P_{HBE(VBE)} + (P_{s1} + P_{s2}) \quad (3-39)$$

where recall that  $P_{HBE(VBE)}$  is the summation of  $W_{cx1}$  and  $W_{cx2}$ . Next for the HBE vertical reactions, substituting (3-3), (3-6), (3-37) and (3-38) for  $R_1$ ,  $R_2$ ,  $R_4$ , and  $R_5$  respectively into (3-40) and (3-41), results in the following equations in terms of force resultants for the left and right end HBE vertical reactions,  $R_a$  and  $R_b$  respectively:

$$R_a = R_1 - R_2 + R_4 = \frac{W_{by1} - W_{by2}}{2} - (W_{bx1} + W_{bx2}) \frac{d}{2L} + (P_{s2} - P_{s1}) \frac{2y}{L} \quad (3-40)$$

$$R_b = R_1 + R_2 + R_5 = \frac{W_{by1} - W_{by2}}{2} + (W_{bx1} + W_{bx2}) \frac{d}{2L} + (P_{s1} - P_{s2}) \frac{2y}{L} \quad (3-41)$$

### 3.3.2.2 Development of HBE Moments (rocking about HBE centerline)

The moment distribution to be used in the design of an HBE incorporating self-centering components can be determined from the free body diagram of figure 3-30 for the case of rocking about the HBE centerline. For reasons described previously, radius corner cut-outs have also been provided at the joint connections and are considered in the HBE analysis.

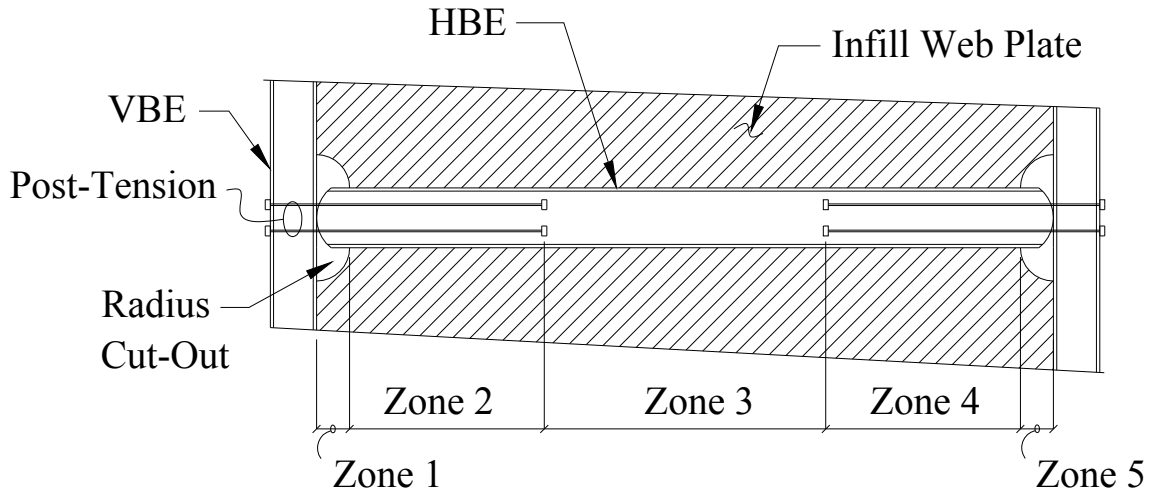


**FIGURE 3-31 SPSW infill corner cut-outs**

Five zones along the HBE are considered here; the two segments of HBE where the infill web plate is cut-out and is not in contact with the HBE flange; the two segments of the HBE between the infill web plate corner cut-out and the post-tension anchor where the infill web plate is in contact with the HBE flange; and the segment of the HBE between the post-tension anchor points along the length of the HBE. These zones, for the purpose of discussion, are designated as Zone 1, Zone 2, Zone 3, Zone 4, and Zone 5 as indicated on figure 3-31.

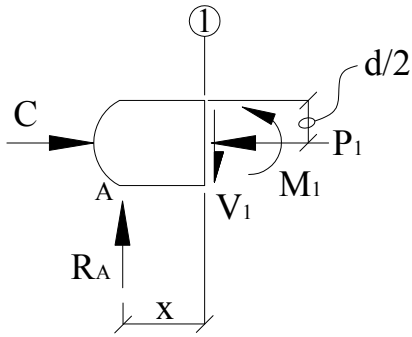


**FIGURE 3-32 Free body diagram along Zone 1**

The resulting free body diagram for the HBE segment along Zone 1 is shown in figure 3-32. For rocking about the HBE centerline, the influence of the axial force,  $C$ , does not contribute to the HBE moment (unlike the condition for rocking about the HBE flanges presented earlier). Taking moment equilibrium at the HBE section Cut 1, the moment relationship in terms of force resultants is:

$$M_1 = R_a x \quad (3-42)$$

Substituting (3-40), along with the equivalent force per unit length quantities for the resultant forces defined earlier into (3-42), the resulting moment relationship expressed in terms of the infill web plate yield forces per unit length along the HBE along Zone 1 is:

$$M_1 = (P_{s2} - P_{s1}) \left( \frac{2y}{L} \right) x + (\omega_{by1} - \omega_{by2}) \left( \frac{L}{2} x - Rx \right) + (\omega_{bx1} + \omega_{bx2}) \left( \frac{dR}{L} x - \frac{d}{2} x \right) \quad (3-43)$$

Next, considering any HBE section at some point along Zone 2, the internal moment can be obtained by taking moment equilibrium at the arbitrary section Cut 2.

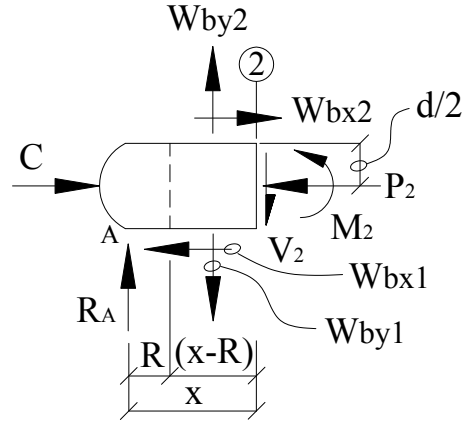


**FIGURE 3-33 Free body diagram along Zone 2**

The free body diagram along Zone 2 is shown in figure 3-33. Taking moment equilibrium at the HBE section Cut 2, the moment relationship in terms of force resultants is:

$$M_2 = R_A x + (W_{by2} - W_{by1}) \left( \frac{x-R}{2} \right) + (W_{bx1} + W_{bx2}) \left( \frac{d}{2} \right) \quad (3-44)$$

Substituting (3-40), along with the equivalent force per unit length quantities for the resultant forces defined earlier into (3-44), the resulting moment relationship expressed in terms of the infill web plate yield forces per unit length along the HBE along Zone 2 is:

$$M_2 = (P_{s2} - P_{s1}) \left( \frac{2y}{L} \right) x + (\omega_{by1} - \omega_{by2}) \left( \frac{L}{2} x - \frac{x^2}{2} - \frac{R^2}{2} \right) + (\omega_{bx1} + \omega_{bx2}) \left( \frac{dR}{L} x - \frac{dR}{2} \right) \quad (3-45)$$

Next, considering any HBE section at some arbitrary point along Zone 3 the internal moment can be obtained by taking moment equilibrium at the arbitrary HBE section Cut 3.

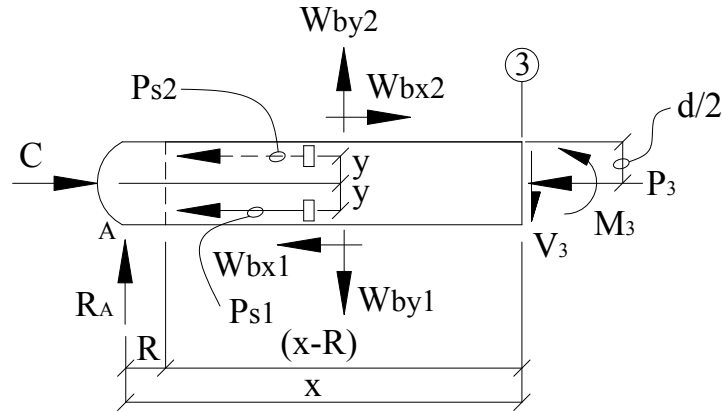


**FIGURE 3-34 Free body diagram along Zone 3**

The free body diagram along Zone 3 is shown in figure 3-34. Taking moment equilibrium at the HBE section Cut 3, the moment relationship in terms of force resultants is:

$$M_3 = R_a x + (P_{s1} - P_{s2})(y) + (W_{by2} - W_{by1})\left(\frac{x-R}{2}\right) + (W_{bx1} + W_{bx2})\left(\frac{d}{2}\right) \quad (3-46)$$

Substituting (3-40), along with the equivalent force per unit length quantities for the resultant forces defined earlier into (3-46), the resulting moment relationship expressed in terms of the infill web plate yield forces per unit length along the HBE along Zone 3 is:

$$M_3 = (P_{s2} - P_{s1})\left(\frac{2}{L}x - 1\right)y + (\omega_{by1} - \omega_{by2})\left(\frac{L}{2}x - \frac{x^2}{2} - \frac{R^2}{2}\right) + (\omega_{bx1} + \omega_{bx2})\left(\frac{dR}{L}x - \frac{dR}{2}\right) \quad (3-47)$$

Next, considering any HBE section at some point along Zone 4 the internal moment can be obtained by taking moment equilibrium at the arbitrary HBE section Cut 4.

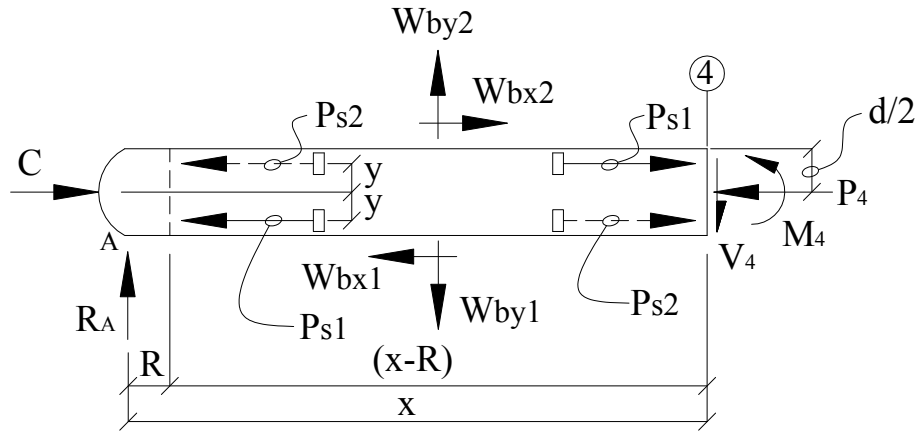


**FIGURE 3-35 Free body diagram along Zone 4**

The free body diagram along Zone 4 is shown in figure 3-35. Taking moment equilibrium at the HBE section Cut 4, the moment relationship in terms of force resultants is:

$$M_4 = R_a x + (P_{s1} - P_{s2})(2y) + (W_{by2} - W_{by1})\left(\frac{x-R}{2}\right) + (W_{bx1} + W_{bx2})\left(\frac{d}{2}\right) \quad (3-48)$$

Substituting (3-40), along with the equivalent force per unit length quantities for the resultant forces defined earlier into (3-48), the resulting moment relationship expressed in terms of the infill web plate yield forces per unit length along the HBE along Zone 1 is:

$$M_4 = (P_{s2} - P_{s1})\left(\frac{x}{L} - 1\right)2y + (\omega_{by1} - \omega_{by2})\left(\frac{L}{2}x - \frac{x^2}{2} - \frac{R^2}{2}\right) + (\omega_{bx1} + \omega_{bx2})\left(\frac{dR}{L}x - \frac{dR}{2}\right) \quad (3-49)$$

Finally, the remaining unknown moment to be solved is the HBE moment along Zone 5, where again the infill web plate has been cut-out to facilitate the HBE to VBE joint rocking connection. Considering any HBE section at some point along Zone 5, the internal moment can be obtained by taking moment equilibrium at the arbitrary HBE section Cut 5.

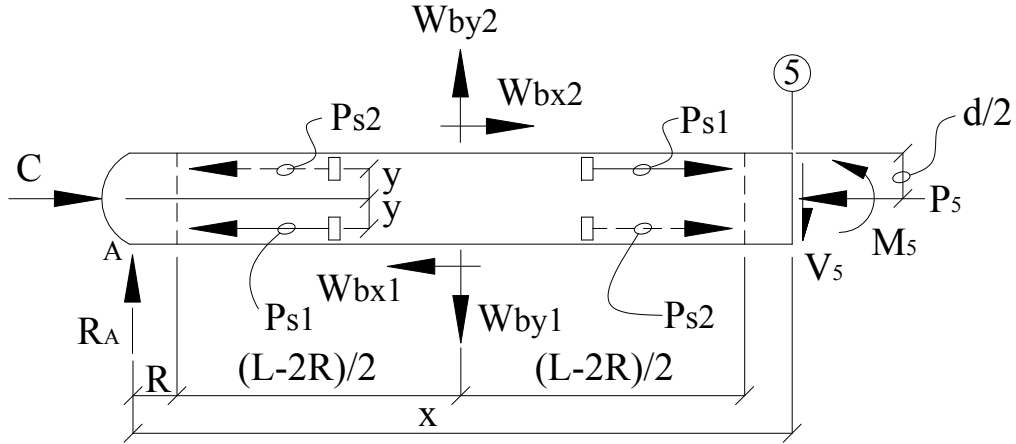


**FIGURE 3-36 Free body diagram along Zone 5**

The free body diagram along Zone 5 is shown in figure 3-36. Taking moment equilibrium at the HBE section Cut 5, the moment relationship in terms of force resultants is:

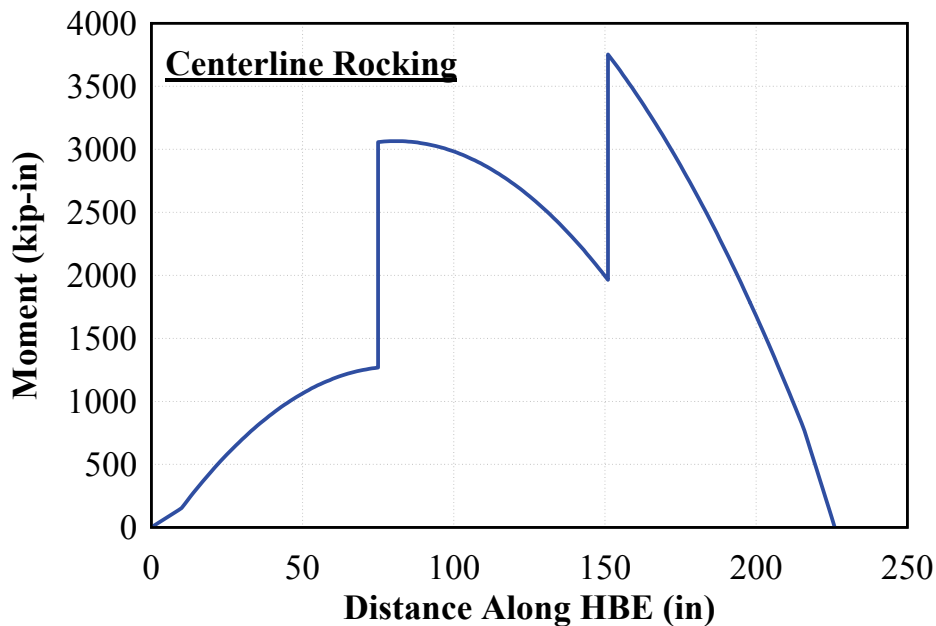
$$M_5 = R_a x + (P_{s1} - P_{s2})(2y) + (W_{by2} - W_{by1})\left(x - \frac{L}{2}\right) + (W_{bx1} + W_{bx2})\left(\frac{d}{2}\right) \quad (3-50)$$

Substituting (3-40), along with the equivalent force per unit length quantities for the resultant forces defined earlier into (3-50), the resulting moment relationship expressed in terms of the infill web plate yield forces per unit length along the HBE along Zone 5 is:

$$M_5 = (P_{s2} - P_{s1})\left(\frac{x}{L} - 1\right)2y + (\omega_{by1} - \omega_{by2})\left(\frac{L^2}{2} - LR - \frac{L}{2}x + Rx\right) + (\omega_{bx1} + \omega_{bx2})\left(\frac{dR}{L}x + \frac{dL}{2} - dR - \frac{d}{2}x\right) \quad (3-51)$$

### 3.3.2.2.1 HBE Moment Diagrams (rocking about HBE centerline)

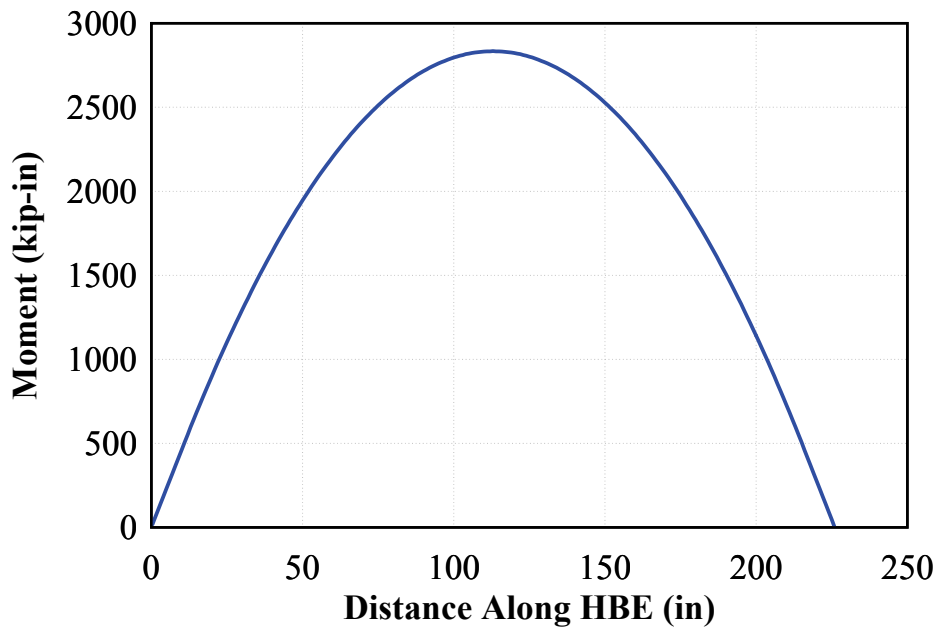
With the moment relationship along the HBE established, the moment diagram of an HBE can be plotted for a SPSW system incorporating a post-tension self-centering mechanism with rocking about the HBE centerline. For illustrative purposes, the same SPSW design parameters used for rocking about the HBE flanges are used to establish the moment diagrams.



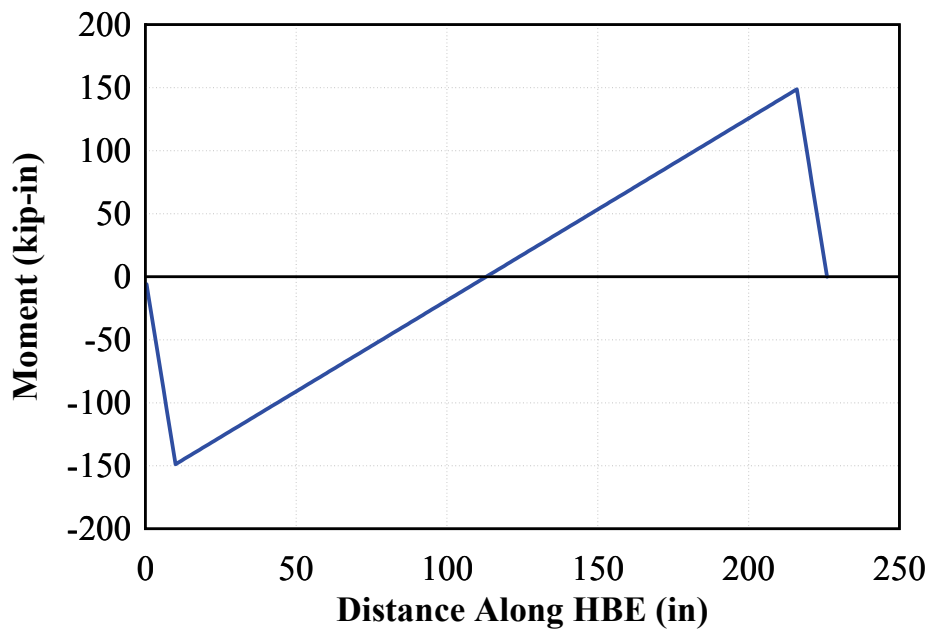
**FIGURE 3-37 Moment diagram – Rocking about HBE centerline**

Figure 3-37 is the moment distribution for a W18 HBE with the same total area of post-tension elements provided at each end of the HBE (but distributed equally among the top and bottom PT elements at each end) as was used for the condition of rocking about the HBE flanges, and located at a distance  $y$  of 6 inches above and below the HBE centerline. As shown in figure 3-37, the resulting moment diagram is significantly different to the one obtained for the corresponding rocking about the HBE flanges (figure 3-13). Note the vertical jumps in the moment diagram, which correspond to the anchorage points of the post-tension elements to the web of the HBE; the height of these vertical offsets in the moment diagrams at the post-tension anchorage points are of the same magnitude since identical post-tension forces are anchored at those locations. Furthermore there is zero moment at the HBE ends due to the pinned joint connection and that the rocking point occurs at the neutral axis of the HBE. To better understand the HBE moment distribution, the composite moment diagram shown in figure 3-37 is decomposed into its individual components.





**FIGURE 3-38 Moment diagram - Vertical force component**



**FIGURE 3-39 Moment diagram - Horizontal force corner cut-out effects**

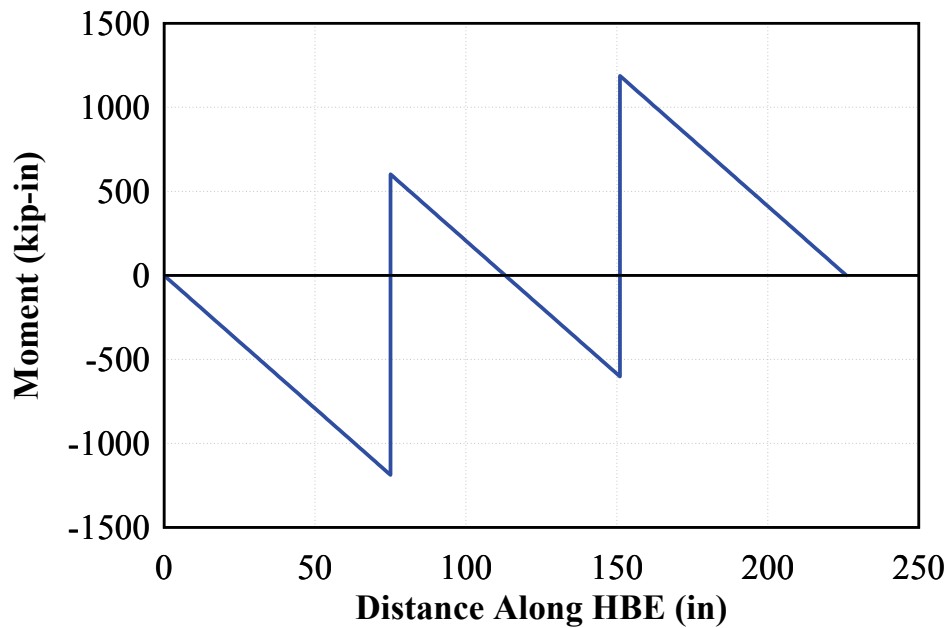


**FIGURE 3-40 Moment diagram - Post-tension force**

The resulting contribution of the moment along the length of the HBE are separated into three primary components for the condition of rocking about the HBE centerline; the vertical force component along the length of the HBE (i.e.,  $W_{by1}$  and  $W_{by2}$ ), the horizontal yield force component (i.e.,  $W_{bx1}$  and  $W_{bx2}$ ) along the length of the HBE due to effects of providing corner cut-outs, and the eccentric axial force of the post-tensioning element (i.e.,  $P_s$ ). Each of these contributing moment diagrams are shown in figures 3-38 to 3-40.

As was discussed earlier, the contribution to moment due to the vertical and horizontal force components of the yielded infill web plate wall are identical to that of rocking about the HBE flange condition as shown in figures 3-38 and 3-39 (compared with figures 3-14 and 3-15). Furthermore, as indicated earlier, the component due to the column pull-in and the lateral story shear force do not contribute to the moment along the HBE since rotation (i.e., rocking point) is about the neutral axis of the HBE.

Of significance is the moment distribution effect due to the post-tension elements. Because the post-tension elements are eccentrically anchored to the HBE, a concentrated moment is applied at that location. Also, due to an idealized HBE-to-VBE pin connection for the centerline-rocking

frame, the HBE moment reduces to zero at the ends of the HBE from the point of force application on the HBE (i.e., the post-tension anchorage point). As a result, these eccentrically applied moments (figure 3-40), located at some distance away from the ends of the HBE, create the vertical jumps observed on the moment diagram at the post-tension anchorage points shown on figure 3-37.

Note that for the HBE moment diagram shown on figure 3-37, the total area of post-tension used for rocking about the HBE flanges was divided equally at each end of the HBE between the top and bottom post-tension locations (i.e.,  $P_{s1}$  and  $P_{s2}$ ) as noted earlier. This was done to maintain the same total area of post-tension at each end of the HBE for the two rocking connection types. Although the influence of the post-tension on the HBE for each rocking condition is different with respect to the rocking connection type, for discussion purposes, this was done to compare the HBE moment diagrams in terms of the same amount of total area of post-tension used. In other words, the resulting HBE moment diagram in figure 3-37 (rocking about the HBE centerline) is based on an HBE design with the same total area of post-tension elements at each end of the HBE as that for the moment diagram of figure 3-13 (rocking about the HBE flanges).

### 3.3.2.3 Development of HBE Shears (rocking about HBE Centerline)

The shear distribution to be used in the design of an HBE incorporating self-centering components can be determined using the same free body diagrams developed earlier for the HBE moments. Similarly, due to the presence of infill web plate corner cut-outs, five zones along the length of the HBE are considered. From the free body diagram for the HBE segment along Zone 1, shown in figure 3-32, the corresponding shear force is the reaction  $R_a$  described in (3-40). Substituting (3-1) and (3-2) in place of the resultant infill web plate yield force components leads to the shear force along HBE segment Zone 1 as follows:

$$V_1 = R_a = \frac{(\omega_{by1} - \omega_{by2})(L - 2R)}{2} - \frac{(\omega_{bx2} + \omega_{bx1})(L - 2R)}{2L}d - (P_{s2} - P_{s1})\frac{2y}{L} \quad (3-52)$$

Next, from the free body diagram for the HBE segment along Zone 2, 3, and 4 shown in figures 3-33 to 3-35, the corresponding shear force is reduced by the vertical component of the infill web

plate yield forces. The shear force along the HBE segments along these Zones follows where  $x$  is the distance from the end of the HBE:

$$V = R_a - (\omega_{by1} - \omega_{by2})(x - R) \quad (3-53)$$

Similarly, from the free body diagram for the HBE segment along Zone 5, shown in figure 3-36, the corresponding shear force along HBE segment Zone 5 follows:

$$V_5 = R_a - (\omega_{by1} - \omega_{by2})(L - 2R) \quad (3-54)$$

### 3.3.2.4 Development of HBE Axial Force (rocking about HBE centerline)

The axial force distribution to be used in the design of an HBE incorporating self-centering components can be determined using the same free body diagrams developed earlier for the HBE moments. Similarly, due to the presence of infill web plate corner cut-outs, three zones along the length of the HBE are considered. From the free body diagram for the HBE segment along Zone 1 (figure 3-32), the corresponding axial force is the horizontal reaction  $C$  at the rocking point described in (3-39). Substituting (3-1) and (3-2) in place of the resultant infill web plate yield force components leads to the axial force along HBE segment Zone 1 as follows:

$$P_1 = C = \frac{(\omega_{bx1} - \omega_{bx2})(L - 2R)}{2} + (\omega_{cx1} + \omega_{cx1})\left(\frac{h}{2} - \frac{d}{2} - R\right) + (P_{s1} + P_{s2}) \quad (3-55)$$

Next, from the free body diagram for the HBE segment along Zone 2 shown in figure 3-33, the corresponding axial force is reduced by the horizontal component of the infill web plate yield forces. The axial force along the HBE segment Zone 2 follows:

$$P_2 = C - (\omega_{bx1} - \omega_{bx2})(x - R) \quad (3-56)$$

Next, from the free body diagram for the HBE segment along Zone 3 shown in figure 3-34, the corresponding axial force is reduced by the horizontal component of the infill web plate yield

forces and post-tension forces at the HBE anchor locations. The axial force along the HBE segment Zone 3 follows:

$$P_3 = C - (\omega_{bx1} - \omega_{bx2})(x - R) - (P_{s1} + P_{s2}) \quad (3-57)$$

Next, from the free body diagram for the HBE segment along Zone 4 shown in figure 3-35, the corresponding axial force is reduced by the horizontal component of the infill web plate yield forces and post-tension forces at the HBE anchor locations. The axial force along the HBE segment Zone 4 follows:

$$P_4 = C - (\omega_{bx1} - \omega_{bx2})(x - R) \quad (3-58)$$

Similarly, from the free body diagram for the HBE segment along Zone 5, shown in figure 3-36, the corresponding axial force along HBE segment Zone 5 follows:

$$P_5 = C - (\omega_{bx1} - \omega_{bx2})(L - 2R) \quad (3-59)$$

### 3.3.2.5 Comparison with SAP 2000 (rocking about HBE centerline)

The formulations describing the distribution of moment, shear and axial forces developed above were compared to non-linear pushover analysis using SAP2000. The analytical model used consisted of a single bay, single story frame with a bay width of 20 feet and story height of 10 feet and is shown in figure 3-41. The same model parameters described for the flange-rocking frame presented in Section 3.2.1.5 apply. However, the infill web plate thickness was reduced to a 23-gauge plate to accentuate the effects of the PT on the HBE moment diagram. For the case of modeling in OpenSees, the previously described method also applies. However, the PT elements are now modeled with the *Elastic-Perfectly Plastic Gap Material* definition which allows for tension-only behavior. Recall that for the centerline-rocking connection, PT elements at the closing joint locations will always relax. Unlike the material definition used for the flange-rocking connection described earlier, the latter material definition can be modeled as tension-only. Furthermore, this material definition allows the user input of an initial negative strain to simulate the initial applied PT forces.

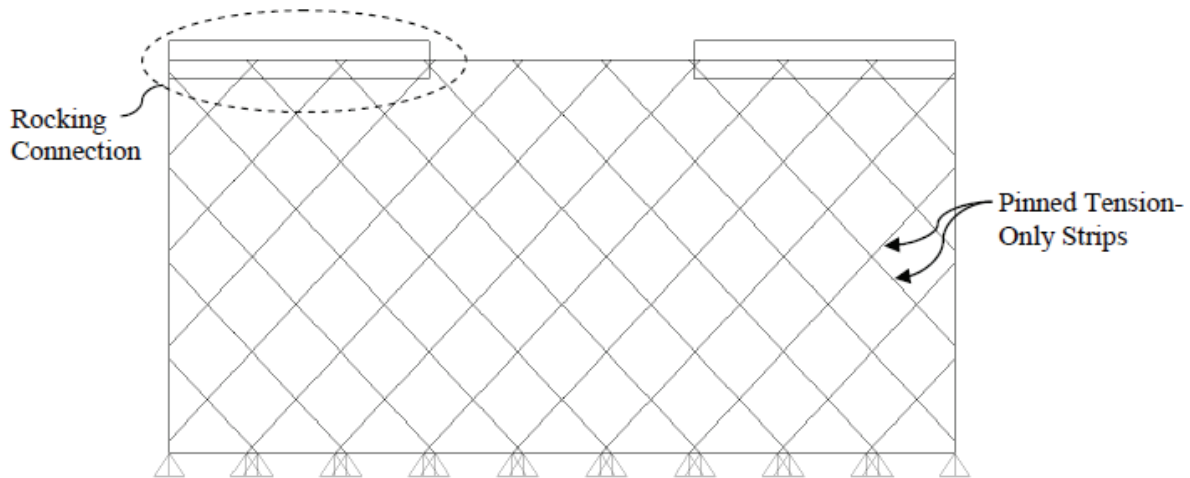


**FIGURE 3-41 Centerline-rocking frame - Analytical model**

For the rocking connection, in SAP2000 a rigid beam element was used as a link to model the post-tension anchor points to the HBE to capture the applied moment during rocking motion about the HBE centerline. Joint constraints in the translational vertical global DOF and in-plane rotational DOF (HBE strong axis bending) were provided at key nodes. For the case of modeling in OpenSees, *rigidlink beams* are used. Furthermore, a rotational hinge with negligible stiffness is provided at the ends of the HBES to simulate a pin connection, as OpenSees does not currently have a moment release command. The connection models used in SAP2000 and OpenSees described are shown in figure 3-42.

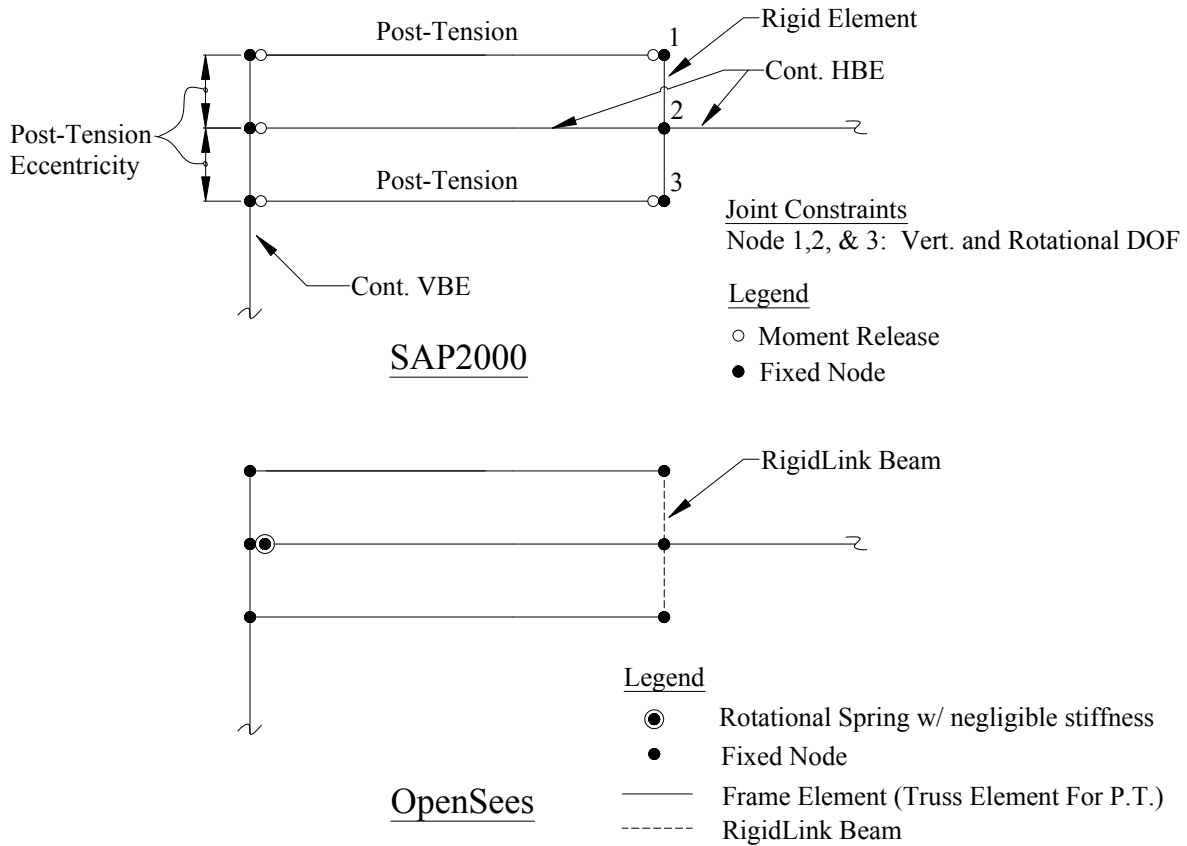


**FIGURE 3-42 Rocking about HBE centerline connection – Analytical model**

Figures 3-43 to 3-48 below provide comparisons of the moment, shear and axial force distributions along the length of the HBE using the formulations developed earlier to that with the analytical model of the SAP2000 analysis. Comparisons are presented for conditions ignoring post-tension force losses due to axial shortening and for conditions considering HBE axial shortening. Note that since the SAP2000 model uses a finite amount of strips to represent the infill web plate, the shear and axial force diagrams obtained from the SAP2000 analysis are stepped as compared to the continuous force diagrams using the theoretical formulations.

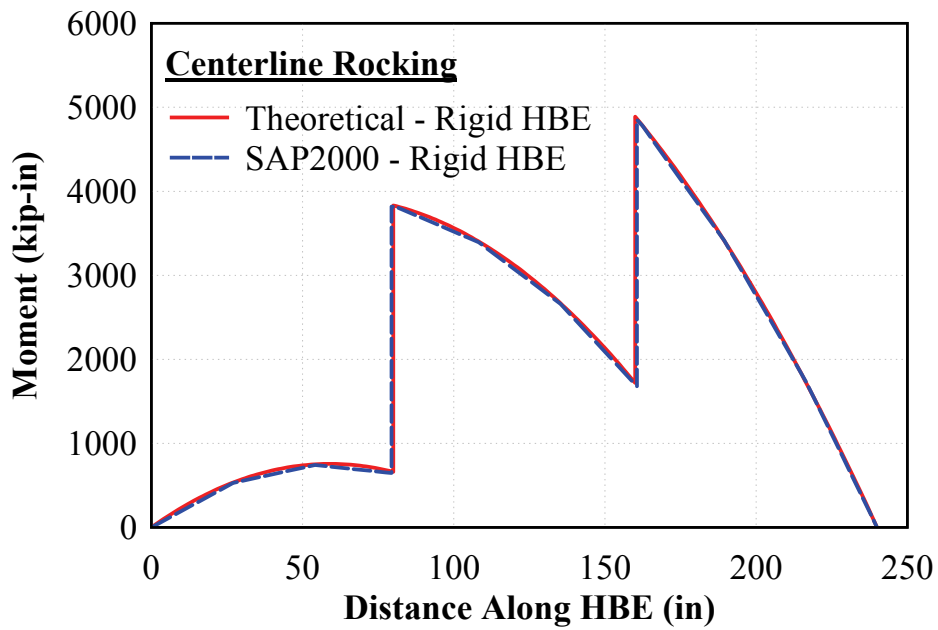


**FIGURE 3-43 Moment diagram – Rigid HBE**

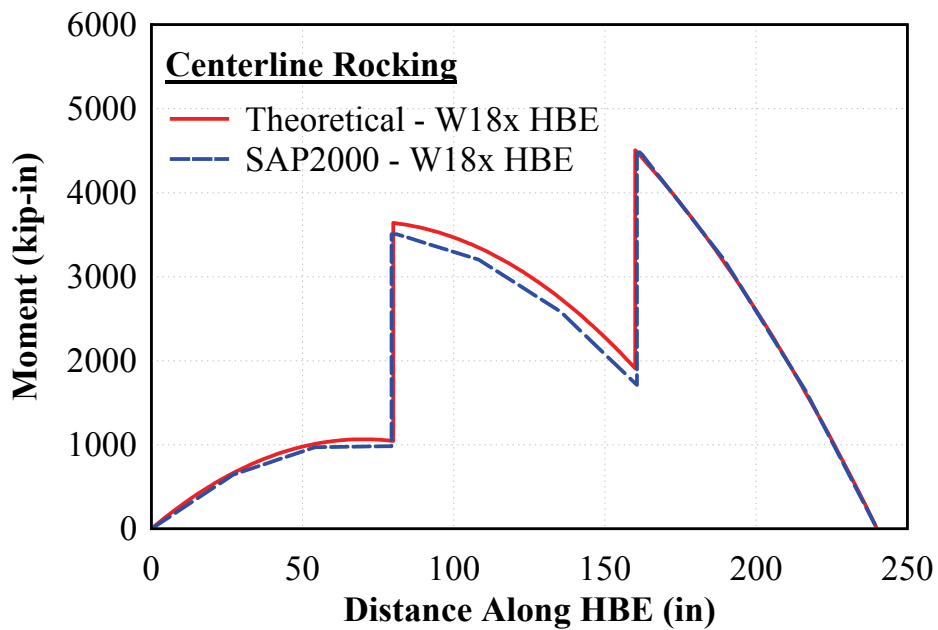


**FIGURE 3-44 Moment diagram – Flexible HBE**



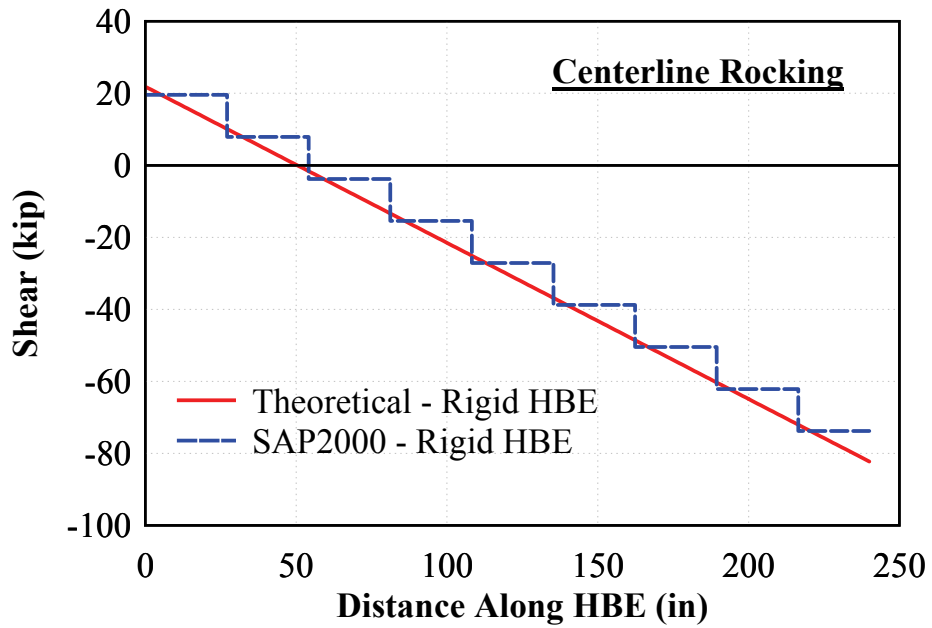


FIGURE 3-45 Shear force diagram – Rigid HBE

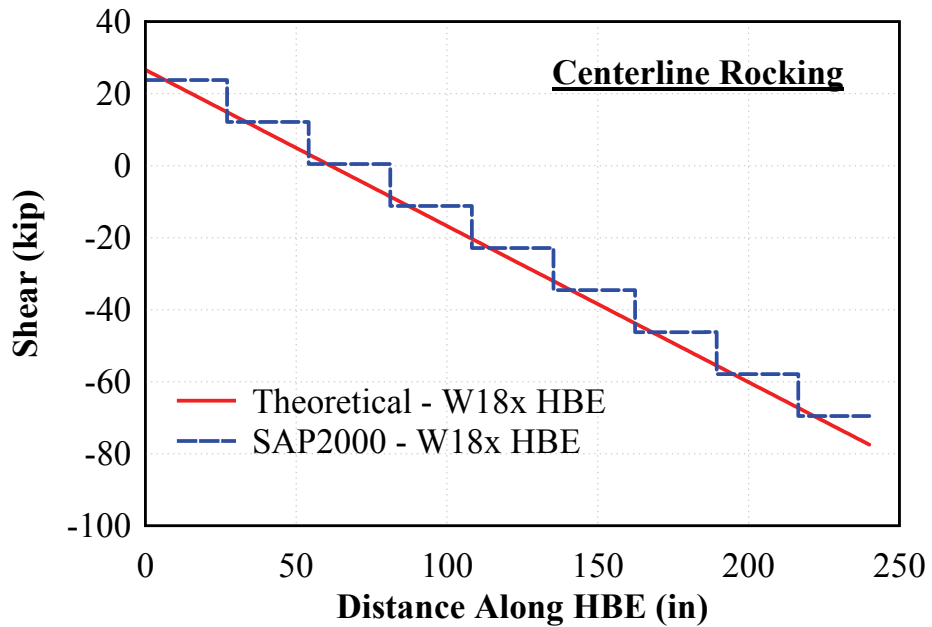


FIGURE 3-46 Shear force diagram – Flexible HBE

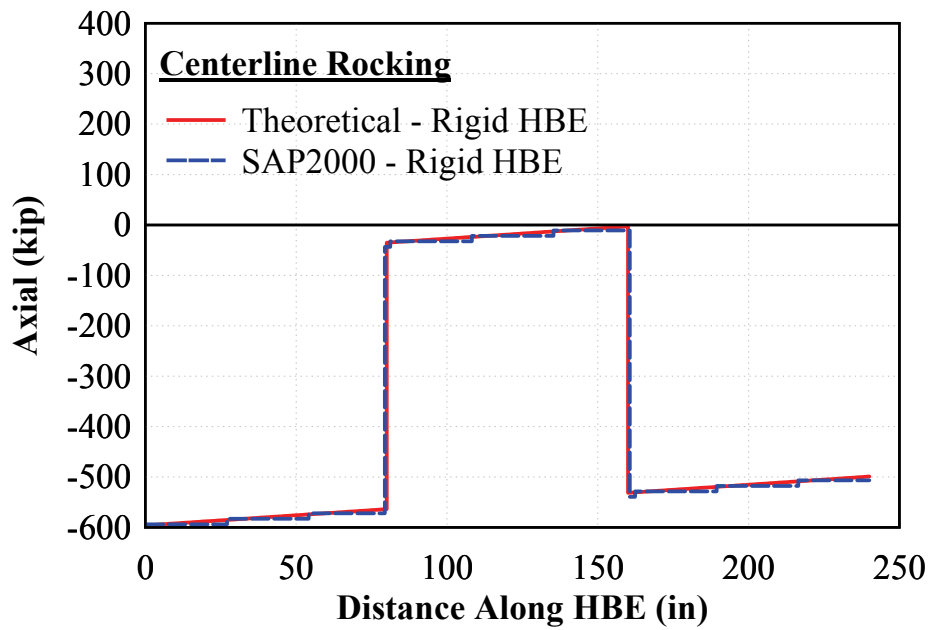


FIGURE 3-47 Axial force diagram – Rigid HBE

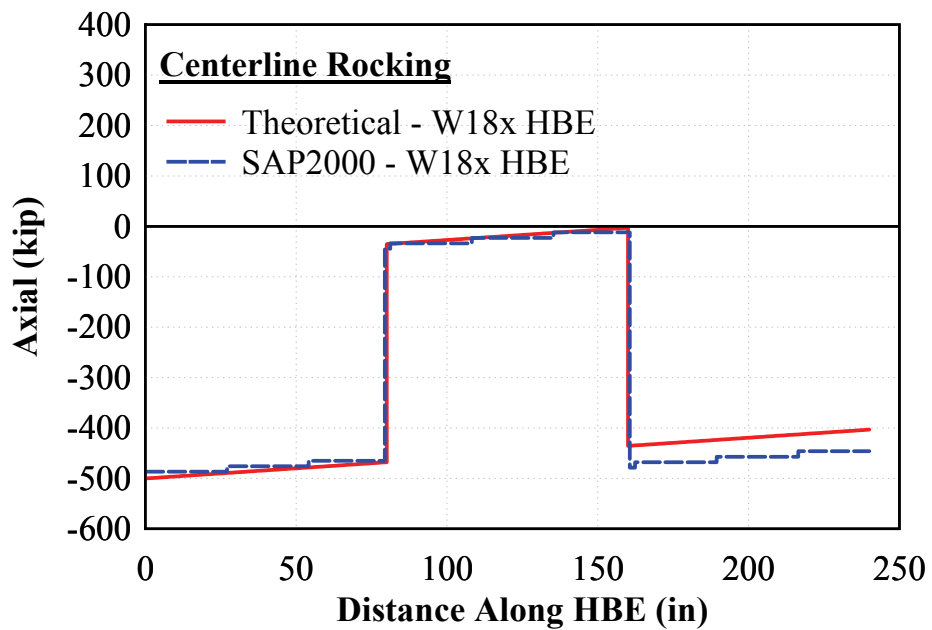
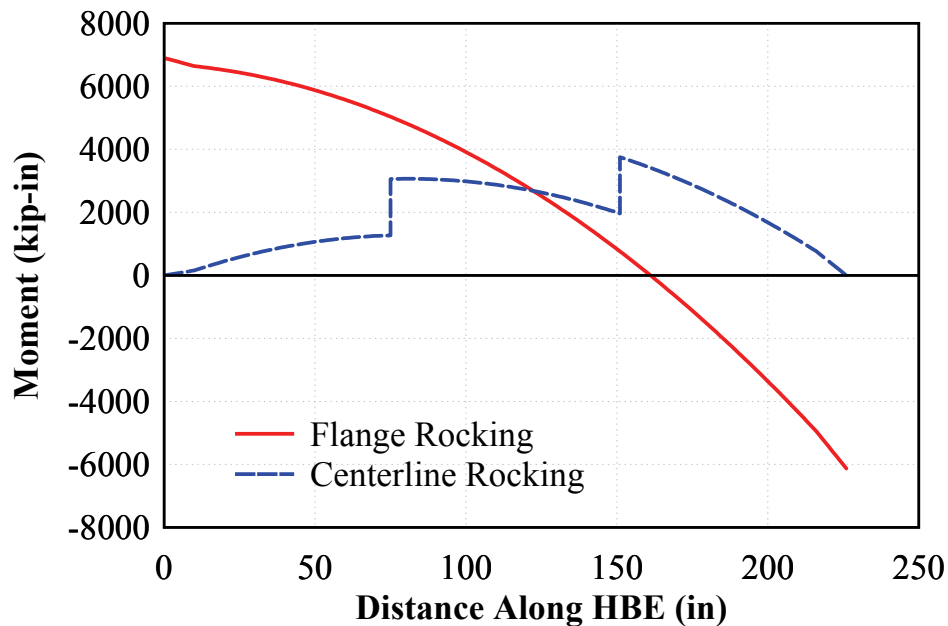


FIGURE 3-48 Axial force diagram – Flexible HBE

Note that in figure 3-48 for the flexible HBE condition which considers post-tension losses due to HBE axial shortening, there is an increase in axial force in the SAP2000 Pushover analysis along the 2/3 span length of the HBE as compared to the theoretical results. The theoretical formulations do not consider HBE curvatures as some vertical beam deflection will occur due to the development of the infill plate tension strips pulling down on the HBE. As a result, some differences with the analytical SAP2000 model are anticipated as compared to the theoretical formulations developed based on first principles, which although considers axial shortening of the HBE, does not consider changes in vertical curvature of the HBE, which will affect the rotations at the ends of the HBE. The increase in axial force observed in figure 3-48, is due to an increase in post-tension force in the SAP2000 analysis which accounts for the axial and vertical flexibility of the HBE. Compared to figure 3-47 which assumes a rigid boundary frame, the SAP2000 analysis and are in good comparison with the corresponding theoretical formulations along the full length of the HBE.

### **3.3.3 Flange Rocking versus Centerline Rocking**

Free body diagrams and moment diagrams for rocking connections about the HBE flange and rocking about the HBE centerline have been presented. It has been shown that the moment distribution along the length of the HBE is significantly different for the two connection types for the design parameters used.



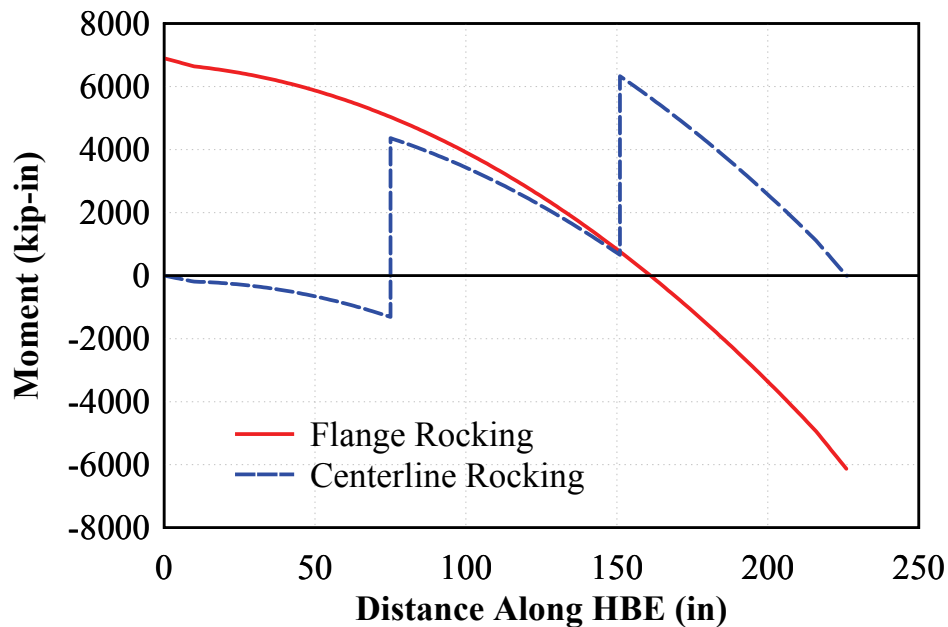
**FIGURE 3-49 Rocking connection comparison**

Figure 3-49 shows the resulting moment diagram for both configurations. The commonality for both configurations is the moment distribution effects from the vertical and horizontal components of the infill web plate at yield along the length of the HBE (figures 3-14, 3-15, 3-38, and 3-39). However, the remaining force effects on the moment distribution along the length of the HBE for the two connections are significantly different for the condition shown, as observed by the moment diagrams in figure 3-49.

As mentioned previously, the moment diagrams shown in figure 3-49 are for a HBE design with the same total area of post-tension at each end of the HBE. However, although the total area of post-tension is the same for the two rocking connection types compared, the amount of post-tension effective in producing self-centering forces for rocking about the HBE centerline is half of that for the condition for rocking about the HBE flanges as was discussed earlier. Furthermore, the eccentricity of the post-tension force is different for the two rocking conditions. For rocking about the HBE flanges, the effective moment lever arm of the post-tension is equal to half the depth of the HBE. For rocking about the HBE centerline, it is equal to the distance  $y$  (figure 3-29). Additionally, for rocking about the HBE centerline, recall that there are two

different post-tensioning reaction force conditions possible, which will affect the moment contribution depending on whether  $\Delta_{net}$ , is less than or equal to  $\Delta_o$ .

Regardless of these differences, the HBE moment for the two rocking connection types will be different for practical design purposes, due to the location of the post-tensioning elements and the HBE-to-VBE rocking point. However, in the following for comparison purposes, for the case of rocking about the HBE centerline, the post-tension force and the eccentricity parameters are changed to produce the same applied moment as that for the case for rocking about the HBE flanges. This provides additional insight into the behaviors of the two configurations.



**FIGURE 3-50 Rocking connection comparison**

Figure 3-50 show both moment diagrams for an HBE for rocking about the HBE flange and for rocking about the HBE centerline condition with the same post-tension force and eccentricity. It can be observed that the moment diagrams are relatively similar between the post-tension anchor points (i.e., Zone 3 on figure 3-31) with a moderate difference in slope. For the HBE end segments outside of Zone 3, the moment diagram is parallel but vertically shifted due to the eccentricity of the post-tension anchor point locations on the HBE span. It will be shown that as the post-tension anchor points along the length of the HBE are further moved towards their

respective HBE ends, the trace of the moment diagram between the anchor points continues on a relatively similar path to that of the condition for rocking about the HBE flange condition.

The difference in slope between the two moment diagrams between the post-tension anchor points can be explained by reviewing the moment diagram component contributions. Recall for the case of rocking about the HBE flanges, there are two additional components that contribute to the moment distribution along the length of the HBE that are not applicable for rocking about the HBE centerline condition. Namely, the horizontal reaction at the rocking point from the VBE (figure 3-16) and the horizontal reaction at the rocking point from the applied story shear (figure 3-18); these components are not contributing factors to the moment distribution along the length of the HBE as they occur at the center of rotation of the HBE.

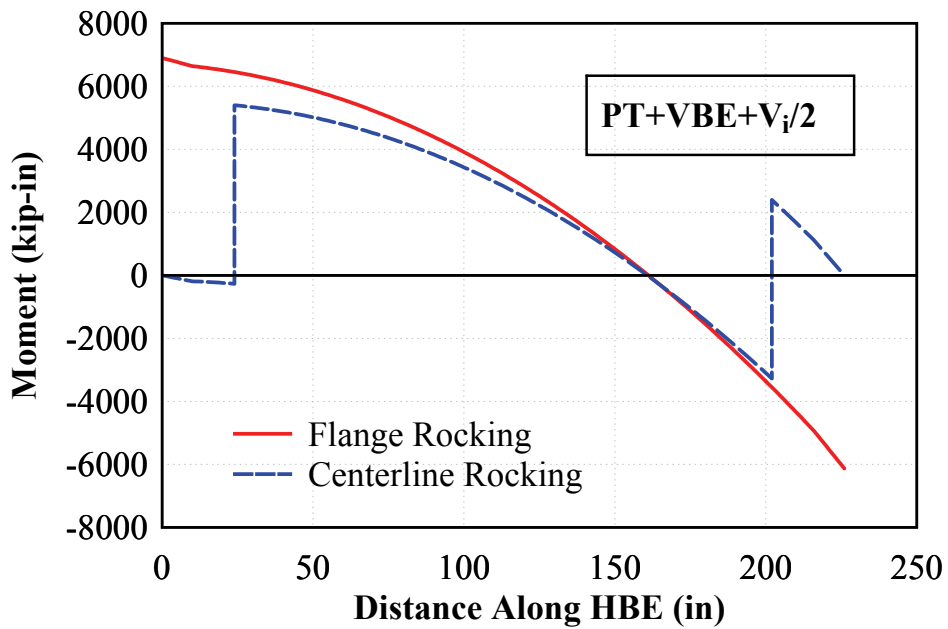


**FIGURE 3-51 Rocking connection comparison**

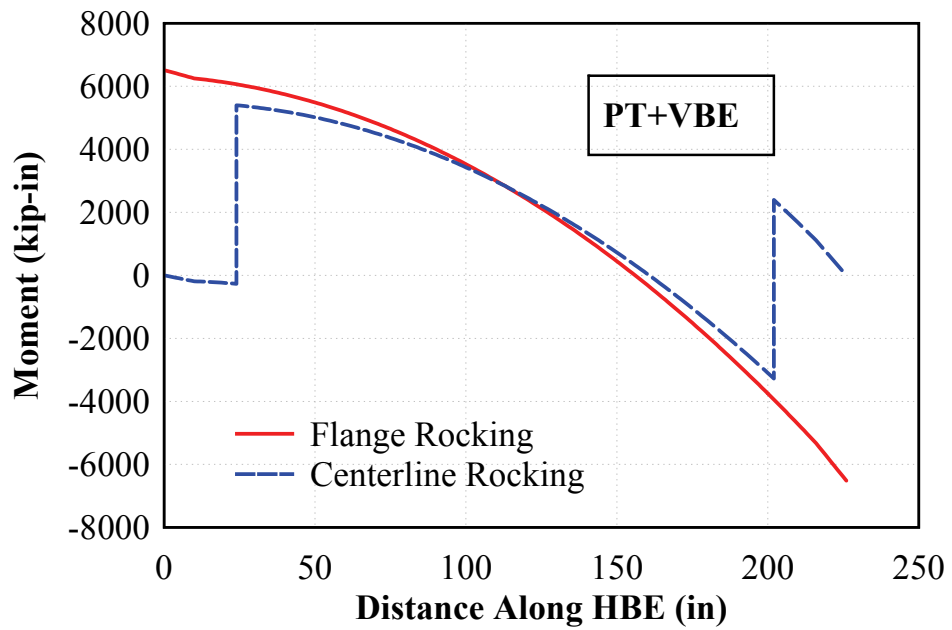


FIGURE 3-52 Rocking connection comparison

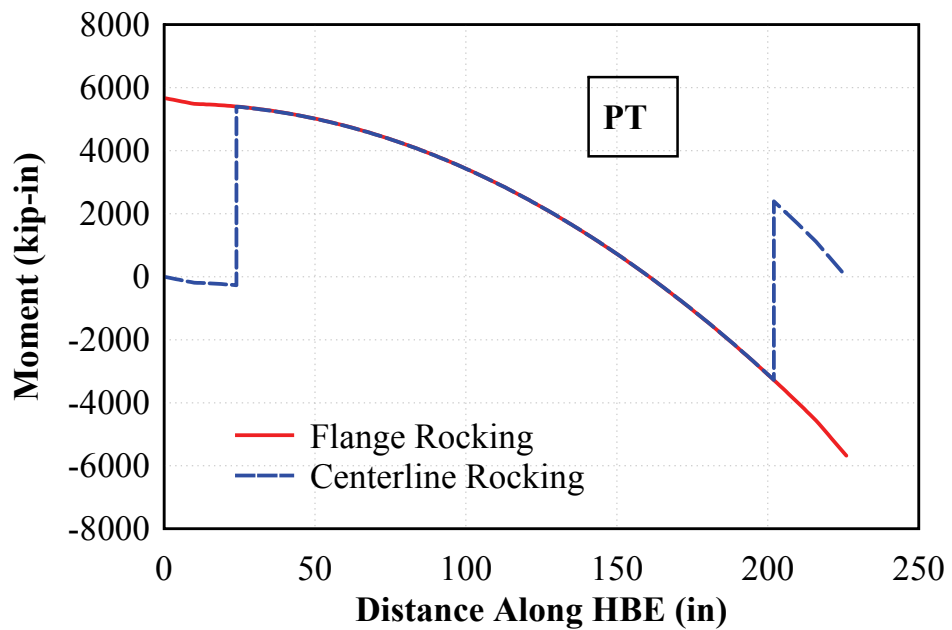


FIGURE 3-53 Rocking connection comparison

Figures 3-51 to 3-53 show the progression of moment diagrams showing the differences between the two rocking conditions as non-common moment components between the two rocking conditions are progressively removed. In these figures, the moment diagram for rocking about the HBE centerline does not change, only the moment diagram for rocking about the HBE flanges is modified. First, as a base comparison, figure 3-51 is the moment diagrams with no modifications. This represents the design condition considering all components of the moment diagram (i.e.,  $PT + VBE + V_i/2$ ) for rocking about the HBE flanges. Note that figure 3-51 is the same condition as shown in figure 3-50 but moving the post-tension anchor locations closer to the end supports of the HBE. Next, figure 3-52 shows the comparison if the story shear component,  $V_i$ , is removed from the moment diagram. Finally, figure 3-53 shows the comparison if the VBE component is additionally removed, leaving only contributions to the moment diagram from the post-tension elements. It is observed that the influence of the moment diagram by the post-tension mechanism is the same for both rocking conditions, and for this special case considered (same post-tension force and eccentricity), results in identical moment diagrams between the post-tension anchor points from influence of the post-tension elements.

For discussion purposes only, if the post-tension force (i.e.,  $P_s$ ), eccentricity and anchorage location of the post-tension elements were identical for both rocking connection types, the moment diagrams along the full length of the HBE would converge to the same solution for the moment contribution due to post-tension forces. However, there are physical limitations that will typically result in large differences in the HBE moment distribution for the two rocking conditions:

- a) For rocking about the HBE flanges, the post-tension anchorage point will always be at the ends of the HBE, and for rocking about the HBE centerline, the post-tension anchorage point will always occur at some location along the span of the HBE, resulting in differences in the moment diagrams in the segments between the ends of the HBE to the post-tension anchorage point.
- b) The location of the post-tension elements for rocking about the HBE centerline need to be provided below the HBE flange at a distance adequate enough for installation and



stressing, resulting in differences in the post-tension eccentricities, leading to differences in moment magnitudes.

- c) If the design post-tension force for condition of rocking about the HBE flanges is used for the condition for rocking about the HBE centerline, the total area of post-tension elements would double at each end of the HBE for the latter case. Depending on the post-tension design parameters for the condition of rocking about the HBE flanges, this may lead to excessive quantities of post-tension elements that may be impractical to field install, leading to constructability issues.

Aside from these physical limitations, for the practical application, although the HBE moment diagrams may be significantly different for rocking about the HBE flanges versus rocking about the HBE centerline, from observation of figure 3-53, the effects of the post-tensioning along Zone 3 (figure 3-31) for rocking about the centerline and effects of post-tensioning along Zone 2 (figure 3-9) for rocking about the flanges is similar for both connection types. Furthermore, figure 3-53 provides an internal check on the validity of the moment equations developed for both rocking connection types; that for a given moment due to the eccentric application of post-tension, the resulting moment diagram due to post-tension force effects, should yield the same moment diagram regardless of the rocking configuration for equivalent post-tension parameters that result in the same HBE moment demands.

A few final observations are possible from the above. First, recognizing that for rocking about the HBE flanges, the development of post-tension self-centering forces is the primary reason for adding the post-tension elements, it is observed that with the addition of post-tensioning forces, the maximum moment can be shifted from approximately the middle of the HBE to its ends as shown in figure 3-49. However, the disadvantage of shifting the maximum moment to the ends of the HBE is that it substantially increases the moment demand on the HBE. Although intentionally increasing the moment demand on the HBE may appear to be counter intuitive, the rationale behind this approach is to prevent potential in-span plastic hinges to form by shifting the maximum moments to the ends of the HBE. Providing a minimum amount of post-tensioning to shift the maximum moment demand to the ends of the HBE also will lead to a larger decompression moment required to open the HBE-to-VBE joint; potentially improving the

performance of the SC-SPSW system under serviceability conditions under gravity, wind and low level earthquake demands.

By comparison, for rocking about the HBE centerline, it appears that the addition of post-tension only serves the purpose of self-centering. Unlike rocking about the HBE flanges, no moments are developed at the ends of the HBE, as shown in figure 3-49. Consequently no moment frame action can occur and shifting of maximum moment to the HBE ends cannot be achieved. Since the post-tension elements can only be used to develop self-centering forces, there is no need to provide more post-tension beyond what is needed to act as a self-centering mechanism. Furthermore, recall that the VBE horizontal reactions (i.e.,  $P_{HBE(VBE)}$ ) and the lateral story shear force (i.e.,  $V_i$  or namely  $P_{HBE(WEB)}$ ) at the rocking points do not contribute to the moment demand for rocking about the centerline condition. Consequently, the moment demand along the length of the HBE can be significantly less as compared to that of rocking about the HBE flange condition.

### **3.3.4 NewZ-BREAKSS Rocking Connection**

Inspired by a type of moment-resisting connection developed and implemented in New Zealand (Clifton 1996 & 2005, MacRae et al. 2007, Clifton et al. 2007), to achieve the advantages of a post-tensioned rocking moment connection system without beam-growth, a type of rocking connection is proposed. However, while this report illustrates how a rocking connection of the type proposed here could be detailed for SPSW systems, it is presented with the understanding that, with minor changes, it could also be a workable solution for rocking moment resistant frames as a method to eliminate beam-growth issues, while providing in both cases the benefit of frame re-centering while eliminating the need for special detailing of the diaphragm to accommodate beam-growth.

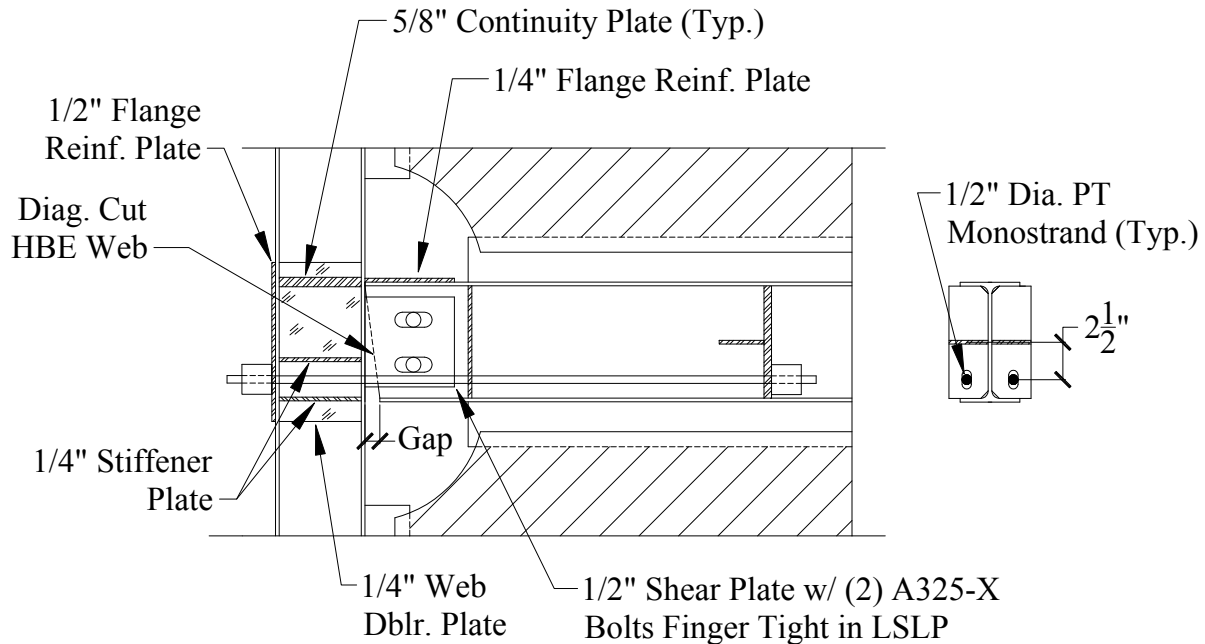


**FIGURE 3-54 NewZ-BREAKSS rocking connection**

For convenience, the proposed connection is called the “New Zealand-inspired – Buffalo Resilient Earthquake-resistant Auto-centering while Keeping Slab Sound (NewZ-BREAKSS) Rocking Connection”. This proposed rocking connection is shown in figure 3-54 for the particular detail that would be used in a self-centering SPSW system (the detail shown is for the UB 1/3 scale test frame presented in Section 4). The proposed rocking connection eliminates the beam-growth typically encountered in the previously researched connections that rock about both of their beam flanges, by instead maintaining constant contact of the HBE top flange with the VBES during lateral drift. By doing so, when one of the rocking joint “opens”, the rocking joint at the opposite end of the HBE “closes”. As a result, the net gap opening (due to beam-growth) is zero over the full length of the beam (similar to that described for the centerline-rocking connection). Furthermore, this connection provides a large moment arm from the rocking point to the centroid of the post-tension for maximizing the PT elongation desired for self-centering connections.

### 3.3.4.1 Free Body Force Diagram

The corresponding HBE moment, shear, and axial force diagrams are presented. However, due to the differences in kinematics from the previous rocking connections, new free body diagrams must first be developed. Similar to the centerline-rocking connection, the post-tension elements need to be anchored to the HBE. Furthermore, the location of the PT anchor point along the HBE will depend on the strain demands of the PT elements at a maximum target drift, and should be located to ensure that the PT strains remain elastic up to that drift demand.

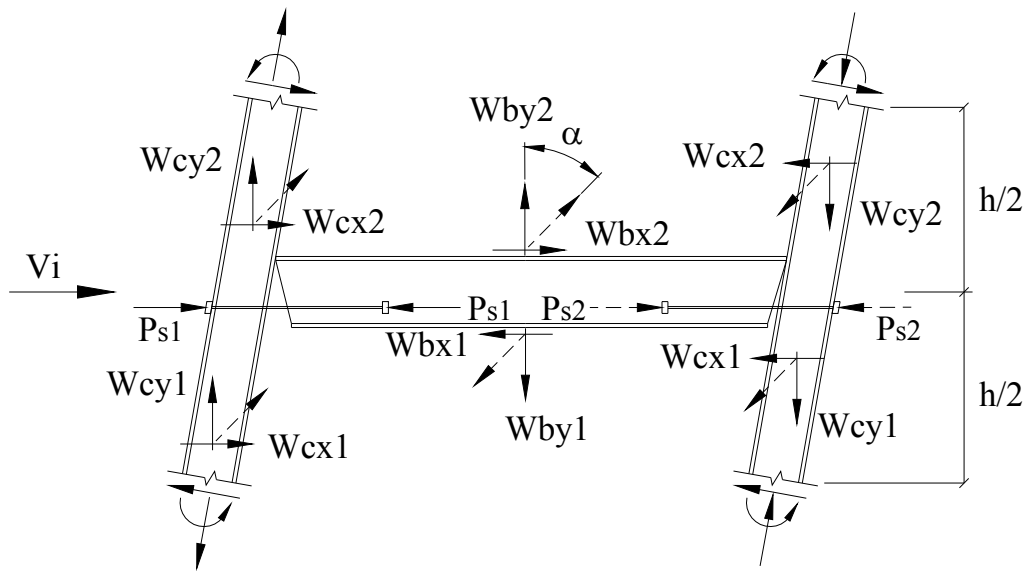


**FIGURE 3-55 Resultant force free body diagram**

Accordingly, the free body diagram of resultant forces on the boundary frame are shown in figure 3-55 (for a rightward drift); where  $P_{s1}$  (shown by solid arrows) is the post-tension force that increases due to elongation during lateral drift and  $P_{s2}$  (shown by dashed arrows) is the post-tension force that reduces from “relaxation” due to lateral drift, and all other terms have been previously defined.

The force resultants shown in the figure can be further separated into individual components. The influence of the vertical components (i.e.,  $W_{by}$ ) due to the inelastic yield forces of the infill web plate acting on the HBE is identical to that for the previous rocking connections. However,

the effect of the horizontal component (i.e.,  $W_{bx}$ ) is different due to the location of the rocking point.

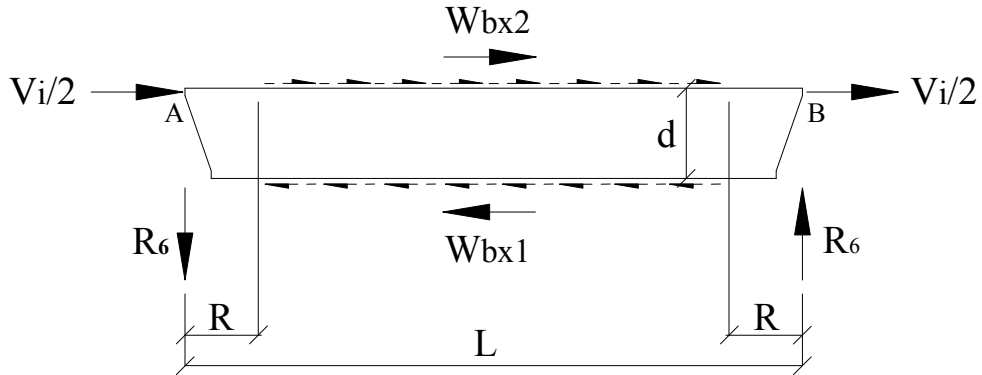


**FIGURE 3-56 Partial free body diagram horizontal component**

The free body diagram for the horizontal component of the infill web plate forces acting along the length of the HBE above and below the HBE flanges is shown in figure 3-56. It can be observed that the vertical HBE reactions are different than that of the other rocking connections presented earlier. For this reason, the reaction is defined as  $R_6$  and can be obtained by moment equilibrium at point  $B$  leading to:

$$R_6 = W_{bx1} \left( \frac{d}{L} \right) \quad (3-60)$$

Furthermore, the effects on the HBE from the post-tension also require a new free body diagram.

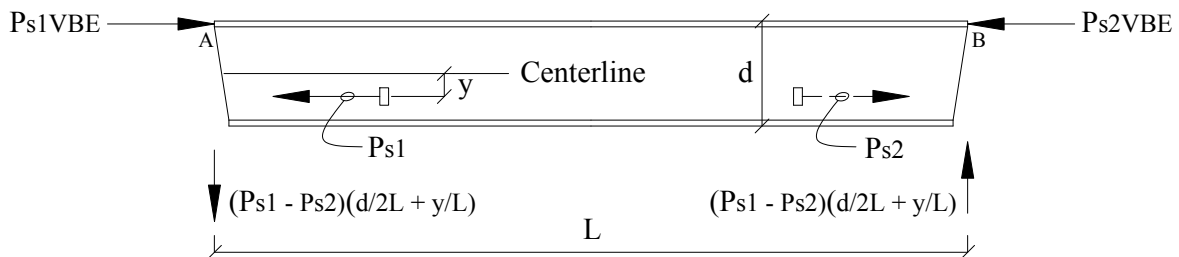


**FIGURE 3-57 Free body diagram post-tension forces**

Figure 3-57 is the corresponding free body diagram of an HBE with the post-tension forces expressed for a rightward drift. Similar to the centerline-rocking connection, for the condition shown, elongation of post-tension will occur in  $P_{s1}$  while “relaxation” of the post-tension element  $P_{s2}$  will occur. Accordingly, the response of the post-tension is identical to (3-30) and (3-31). However, the post-tension force losses due to axial shortening are different. Specifically, the contribution of the post-tension force acting on the HBE flange is different. A schematic of this is shown in figure 3-58 for a single story frame.

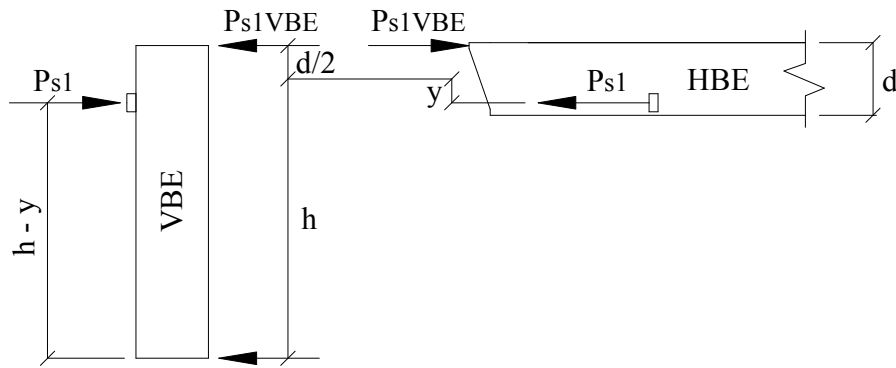


**FIGURE 3-58 Reduced post-tension force on HBE**

It is observed that the post-tension force along the HBE span between the rocking point and post-tension anchor located on the HBE will be less than the force in the post-tension element itself. Note that as a result, to maintain internal force equilibrium due to the post-tension force effects, the HBE mid-span section between anchor points is in tension. To calculate the total loss in post-tension force from HBE axial shortening, the same procedure for the centerline-rocking is applied (which is repeated here for clarity), except that here the post-tension force losses due to HBE axial shortening contribution from the post-tension arise from  $P_{s1}VBE$ , as shown in the figure. It then follows that the HBE axial shortening is calculated as:

$$\Delta_{loss} = \frac{(P_{PT} \cdot SF) L_1}{A_{HBE} E_{HBE}} + \frac{P_{HBE(VBE)} L_1}{A_{HBE} E_{HBE}} \quad (3-61)$$

where  $SF$  is some scale factor (presented subsequently),  $P_{PT}$  is the force in the post-tension element (i.e.,  $P_{s,l}$ ) and all other terms have been previously defined. Solving (3-61) for  $P_{PT}$  leads to the following:

$$P_{PT} = \frac{1}{SF} \left( \frac{A_{HBE} E_{HBE}}{L_1} \Delta_{loss} - P_{HBE(VBE)} \right) \quad (3-62)$$

Accordingly, the net effective axial tension force in the post-tension elements is the elongation due to drift minus the axial shortening of the HBE that occurs along the length of the post-tension elements and is calculated as follows:

$$P_{PT} = \left( \frac{A_{PT} E_{PT}}{L_{PT}} \right) (\Delta_{drift} - \Delta_{loss}) = k_{PT} (\Delta_{drift} - \Delta_{loss}) \quad (3-63)$$

Finally, equating (3-62) and (3-63) and solving for  $\Delta_{loss}$  leads to the amount of post-tension relaxation that should be considered and is calculated as:

$$\Delta_{loss} = \frac{P_{VBE(HBE)}}{k_{PT}^* + \frac{A_{HBE} E_{HBE}}{L_1}} + \left( \frac{k_{PT}^*}{k_{PT}^* + \frac{A_{HBE} E_{HBE}}{L_1}} \right) \Delta_{drift} \quad (3-64)$$

where the axial stiffness of the post-tension term is modified such that:

$$k_{PT}^* = \left( \frac{A_{PT} E_{PT}}{L_{PT}} \right) \cdot SF = k_{PT} \cdot SF \quad (3-65)$$

and from figure 3-58, the scale factor can be approximated as:

$$SF = \left( \frac{h-y}{h+0.5d} \right) \quad (3-66)$$

Furthermore, where all terms have been previously defined, the relationship for the post-tension elongation due to lateral drift,  $\Delta_{drift}$ , is:

$$\Delta_{drift} = \frac{\phi_{drift}}{100} \left( \frac{d}{2} + y \right) \quad (3-67)$$

Additionally, as previously shown in figure 3-57, the horizontal forces  $P_{s1}$  and  $P_{s2}$  also produce vertical reactions at the left and right ends of the HBE that are different than previously defined. For this reason, the reaction is defined as  $R_7$  and is obtained by moment equilibrium at point  $B$  shown in the figure, leading to:

$$R_7 = (P_{s1} - P_{s2}) \left( \frac{d}{2L} + \frac{y}{L} \right) \quad (3-68)$$

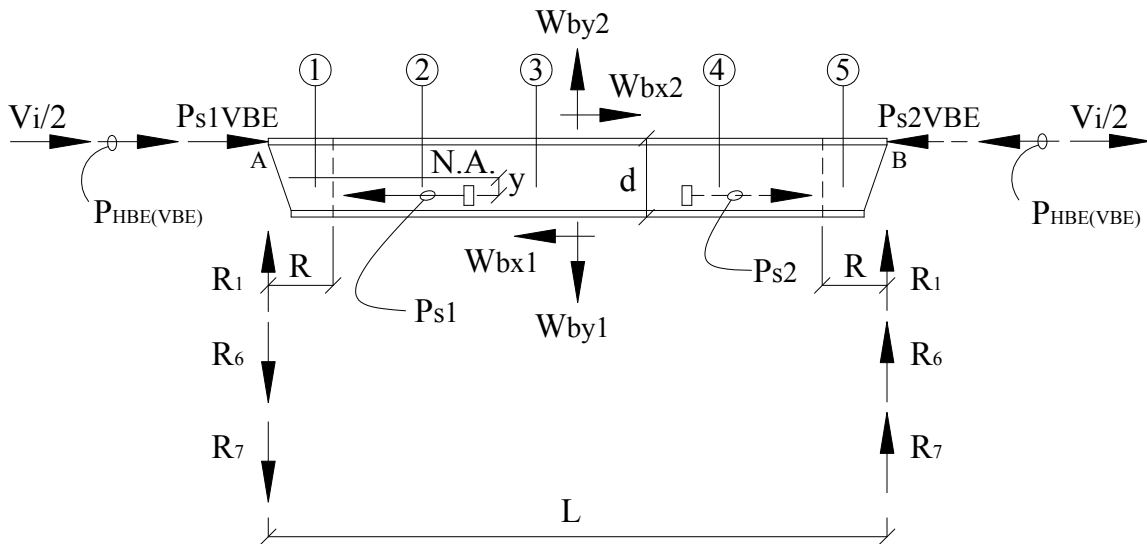


**FIGURE 3-59 Complete force resultant free body diagram of HBE**

Superimposing all of the force components identified to be acting on the HBE, figure 3-59 shows the resulting free body diagram of an HBE when the infill web plate above and below the HBE flanges have fully yielded for a rightward lateral drift (neglecting gravity forces). As done previously, the horizontal compression reactions at the rocking connection and the vertical end reactions at the HBE centerline are combined into single variables  $C$ ,  $R_a$ , and  $R_b$ , respectively, to



simplify the free body diagrams, leading to the HBE axial force in terms of force resultants, where:

$$C = \frac{V_i}{2} + P_{HBE(VBE)} + P_{s1(VBE)} \quad (3-69)$$

Next for the HBE vertical reactions, substituting (3-3), (3-60) and (3-68) for  $R_1$ ,  $R_6$ , and  $R_7$  respectively into (3-70) and (3-71), results in the following equations in terms of force resultants for the left and right end HBE vertical reactions,  $R_a$  and  $R_b$ , respectively:

$$R_a = R_1 - R_6 - R_7 = \frac{W_{by1} - W_{by2}}{2} - (W_{bx1}) \frac{d}{L} - (P_{s1} - P_{s2}) \left( \frac{d}{2L} + \frac{y}{L} \right) \quad (3-70)$$

$$R_b = R_1 + R_6 + R_7 = \frac{W_{by1} - W_{by2}}{2} + (W_{bx1}) \frac{d}{L} + (P_{s1} - P_{s2}) \left( \frac{d}{2L} + \frac{y}{L} \right) \quad (3-71)$$

### 3.3.4.2 Development of HBE Moments (NewZ-BREAKSS)

The moment distribution to be used in the design of an HBE incorporating self-centering components can be determined from the free body diagram of figure 3-59. For reasons described previously, radius corner cut-outs have also been provided at the joint connections and are considered in the HBE analysis.

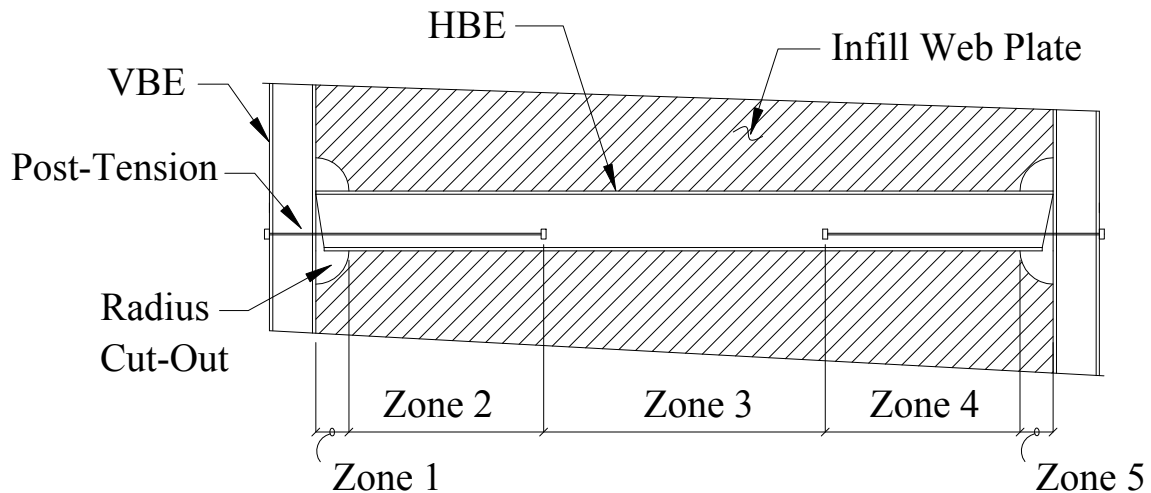
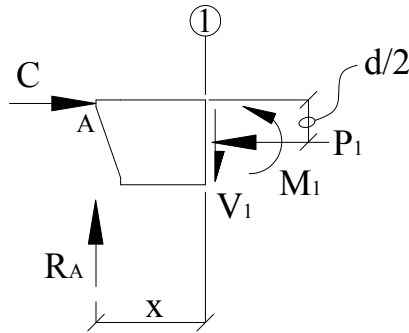


FIGURE 3-60 SPSW infill corner cut-outs

Five zones along the HBE are considered here: the two segments of HBE where the infill web plate is cut-out and is not in contact with the HBE flange; the two segments of the HBE between the infill web plate corner cut-out and the post-tension anchor where the infill web plate is in contact with the HBE flange, and; the segment of the HBE between the post-tension anchor points along the length of the HBE. These zones, for the purpose of discussion, are designated as Zone 1, Zone 2, Zone 3, Zone 4, and Zone 5, as indicated on figure 3-60.



**FIGURE 3-61 Free body diagram along Zone 1**

The resulting free body diagram for the HBE segment along Zone 1 is shown in figure 3-61. Taking moment equilibrium at the HBE section Cut 1, the moment relationship in terms of force resultants is:

$$M_1 = R_a x + C \left( \frac{d}{2} \right) \quad (3-72)$$

Substituting (3-69) and (3-70), along with the equivalent force per unit length quantities for the resultant forces defined earlier into (3-72), the resulting moment relationship expressed in terms of the infill web plate yield forces per unit length along the HBE along Zone 1 is:

$$\begin{aligned} M_1 = & P_{s1(VBE)} \left( \frac{d}{2} \right) - P_{s1} \left( \frac{d}{2L} x + \frac{y}{L} x \right) + P_{s2} \left( \frac{y}{L} x + \frac{d}{2L} x \right) + (\omega_{by1} - \omega_{by2}) \left( \frac{L}{2} x - Rx \right) \\ & + (\omega_{cx1} + \omega_{cx2}) \left( \frac{dh}{4} - \frac{d^2}{4} - \frac{dR}{2} \right) + \omega_{bx1} \left( \frac{2dR}{L} x - dx \right) + V_i \left( \frac{d}{4} \right) \end{aligned} \quad (3-73)$$

Next, considering any HBE section at some point along Zone 2, the internal moment can be obtained by taking moment equilibrium at the arbitrary section Cut 2.

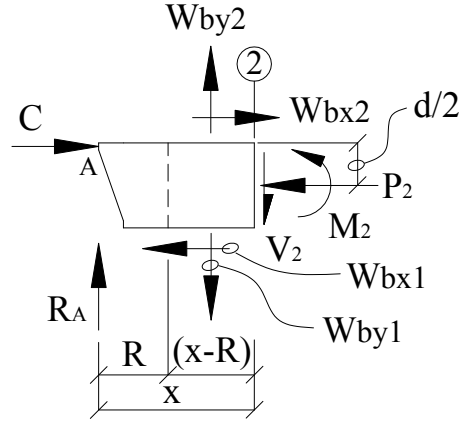


**FIGURE 3-62 Free body diagram along Zone 2**

The free body diagram along Zone 2 is shown in figure 3-62. Taking moment equilibrium at the HBE section Cut 2, the moment relationship in terms of force resultants is:

$$M_2 = R_a x + C \left( \frac{d}{2} \right) + (W_{by2} - W_{by1}) \left( \frac{x-R}{2} \right) + (W_{bx1} + W_{bx2}) \left( \frac{d}{2} \right) \quad (3-74)$$

Substituting (3-69) and (3-70), along with the equivalent force per unit length quantities for the resultant forces defined earlier into (3-74), the resulting moment relationship expressed in terms of the infill web plate yield forces per unit length along the HBE along Zone 2 is:

$$\begin{aligned} M_2 = & P_{s1(VBE)} \left( \frac{d}{2} \right) - P_{s1} \left( \frac{d}{2L} x + \frac{y}{L} x \right) + P_{s2} \left( \frac{y}{L} x + \frac{d}{2L} x \right) \\ & + (\omega_{by1} - \omega_{by2}) \left( \frac{L}{2} x - \frac{x^2}{2} - \frac{R^2}{2} \right) + (\omega_{cx1} + \omega_{cx2}) \left( \frac{dh}{4} - \frac{d^2}{4} - \frac{dR}{2} \right) \\ & + \omega_{bx1} \left( \frac{2dR}{L} x - \frac{d}{2} x - \frac{dR}{2} \right) + \omega_{bx2} \left( \frac{d}{2} x - \frac{dR}{2} \right) + V_i \left( \frac{d}{4} \right) \end{aligned} \quad (3-75)$$

Next, considering any HBE section at some arbitrary point along Zone 3. the internal moment can be obtained by taking moment equilibrium at the arbitrary HBE section Cut 3.

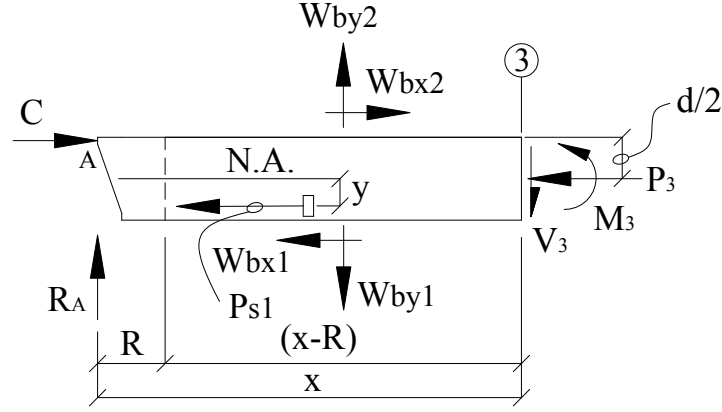


**FIGURE 3-63 Free body diagram along Zone 3**

The free body diagram along Zone 3 is shown in figure 3-63. Taking moment equilibrium at the HBE section Cut 3, the moment relationship in terms of force resultants is:

$$M_3 = R_a x + C \left( \frac{d}{2} \right) + P_{s1} (y) + (W_{by2} - W_{by1}) \left( \frac{x-R}{2} \right) + (W_{bx1} + W_{bx2}) \left( \frac{d}{2} \right) \quad (3-76)$$

Substituting (3-69) and (3-70), along with the equivalent force per unit length quantities for the resultant forces defined earlier into (3-76), the resulting moment relationship expressed in terms of the infill web plate yield forces per unit length along the HBE along Zone 3 is:

$$\begin{aligned} M_3 = & P_{s1(VBE)} \left( \frac{d}{2} \right) + P_{s1} \left( y - \frac{d}{2L} x - \frac{y}{L} x \right) + P_{s2} \left( \frac{y}{L} x + \frac{d}{2L} x \right) \\ & + (\omega_{by1} - \omega_{by2}) \left( \frac{L}{2} x - \frac{x^2}{2} - \frac{R^2}{2} \right) + (\omega_{cx1} + \omega_{cx2}) \left( \frac{dh}{4} - \frac{d^2}{4} - \frac{dR}{2} \right) \\ & + \omega_{bx1} \left( \frac{2dR}{L} x - \frac{d}{2} x - \frac{dR}{2} \right) + \omega_{bx2} \left( \frac{d}{2} x - \frac{dR}{2} \right) + V_i \left( \frac{d}{4} \right) \end{aligned} \quad (3-77)$$

Next, considering any HBE section at some point along Zone 4, the internal moment can be obtained by taking moment equilibrium at the arbitrary HBE section Cut 4.

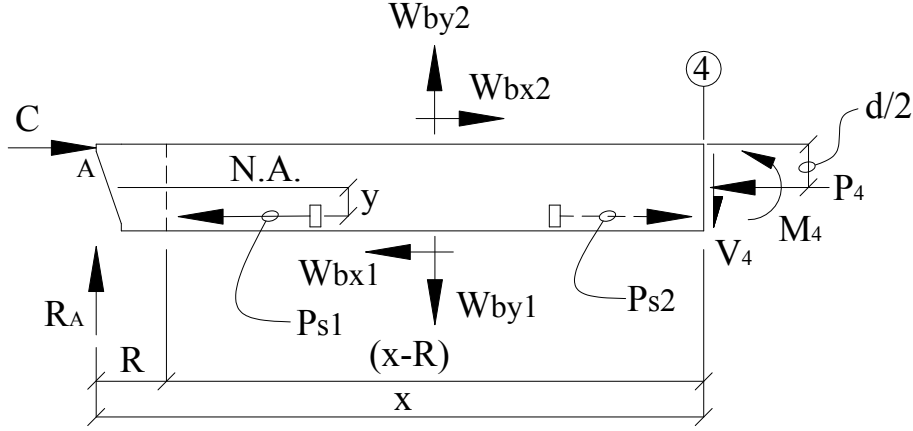


**FIGURE 3-64 Free body diagram along Zone 4**

The free body diagram along Zone 4 is shown in figure 3-64. Taking moment equilibrium at the HBE section Cut 4, the moment relationship in terms of force resultants is:

$$M_4 = R_a x + C \left( \frac{d}{2} \right) + (P_{s1} - P_{s2})(y) + (W_{by2} - W_{by1}) \left( \frac{x-R}{2} \right) + (W_{bx1} + W_{bx2}) \left( \frac{d}{2} \right) \quad (3-78)$$

Substituting (3-69) and (3-70), along with the equivalent force per unit length quantities for the resultant forces defined earlier into (3-78), the resulting moment relationship expressed in terms of the infill web plate yield forces per unit length along the HBE along Zone 4 is:

$$\begin{aligned} M_4 = & P_{s1WBE} \left( \frac{d}{2} \right) + P_{s1} \left( y - \frac{d}{2L} x - \frac{y}{L} x \right) + P_{s2} \left( \frac{y}{L} x + \frac{d}{2L} x - y \right) \\ & + (\omega_{by1} - \omega_{by2}) \left( \frac{L}{2} x - \frac{x^2}{2} - \frac{R^2}{2} \right) + (\omega_{cx1} + \omega_{cx2}) \left( \frac{dh}{4} - \frac{d^2}{4} - \frac{dR}{2} \right) \\ & + \omega_{bx1} \left( \frac{2dR}{L} x - \frac{d}{2} x - \frac{dR}{2} \right) + \omega_{bx2} \left( \frac{d}{2} x - \frac{dR}{2} \right) + V_i \left( \frac{d}{4} \right) \end{aligned} \quad (3-79)$$

Finally, the remaining unknown moment to be solved is the HBE moment along Zone 5, where again the infill web plate has been cut-out to facilitate the HBE to VBE joint rocking connection. Considering any HBE section at some point along Zone 5, the internal moment can be obtained by taking moment equilibrium at the arbitrary HBE section Cut 5.

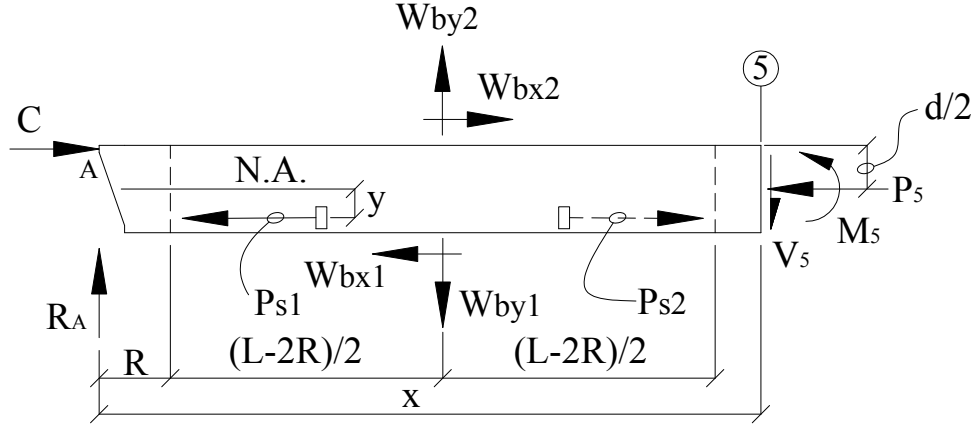


**FIGURE 3-65 Free body diagram along Zone 5**

The free body diagram along Zone 5 is shown in figure 3-65. Taking moment equilibrium at the HBE section Cut 5, the moment relationship in terms of force resultants is:

$$M_5 = R_a x + C \left( \frac{d}{2} \right) + (P_{s1} - P_{s2})(y) + (W_{by2} - W_{by1}) \left( x - \frac{L}{2} \right) + (W_{bx1} + W_{bx2}) \left( \frac{d}{2} \right) \quad (3-80)$$

Substituting (3-69) and (3-70), along with the equivalent force per unit length quantities for the resultant forces defined earlier into (3-80), the resulting moment relationship expressed in terms of the infill web plate yield forces per unit length along the HBE along Zone 5 is:

$$\begin{aligned} M_5 = & P_{s1(VBE)} \left( \frac{d}{2} \right) + P_{s1} \left( y - \frac{d}{2L} x - \frac{y}{L} x \right) + P_{s2} \left( \frac{y}{L} x + \frac{d}{2L} x - y \right) \\ & + (\omega_{by1} - \omega_{by2}) \left( \frac{L^2}{2} + Rx - \frac{L}{2} x - LR \right) + (\omega_{cx1} + \omega_{cx2}) \left( \frac{dh}{4} - \frac{d^2}{4} - \frac{dR}{2} \right) \\ & + \omega_{bx1} \left( \frac{2dR}{L} x - dx + \frac{dL}{2} - dR \right) + \omega_{bx2} \left( \frac{dL}{2} - dR \right) + V_i \left( \frac{d}{4} \right) \end{aligned} \quad (3-81)$$

### 3.3.4.2.1 HBE Moment Diagrams (NewZ-BREAKSS)

With the moment relationship along the HBE established, the moment diagram of an HBE can be plotted for a SPSW system incorporating a post-tension self-centering mechanism with the NewZ-BREAKSS connection. For illustrative purposes, the same SPSW design parameters used for the previous examples are used to establish the moment diagrams.

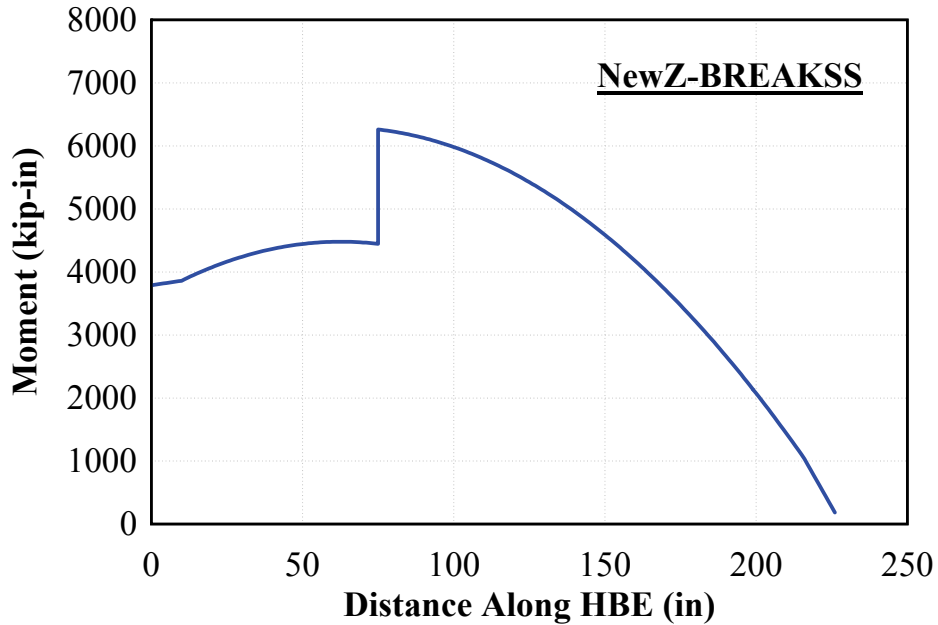


**FIGURE 3-66 Moment diagram – NewZ-BREAKSS**

Figure 3-66 is the moment distribution for a W18 HBE with half of the area of post-tension elements used for the condition of rocking about the HBE centerline (since for this condition the eccentric distance to the centroid of the PT increased from 6 inches to 15 inches, and reducing the post-tension area compensates for the increased post-tension force demand due to drift), and located at a distance  $y$  of 6 inches below the HBE centerline. From observation of the moment distribution, it can be seen that the PT force at the “opened” joint results in a vertical step in the moment diagram at the post-tension anchor point (similar to the centerline-rocking frame). However, the post-tension at the “closing” joint has become fully relaxed at this particular drift, and therefore no vertical step in the moment diagram is present at that location (which would not be the case otherwise).

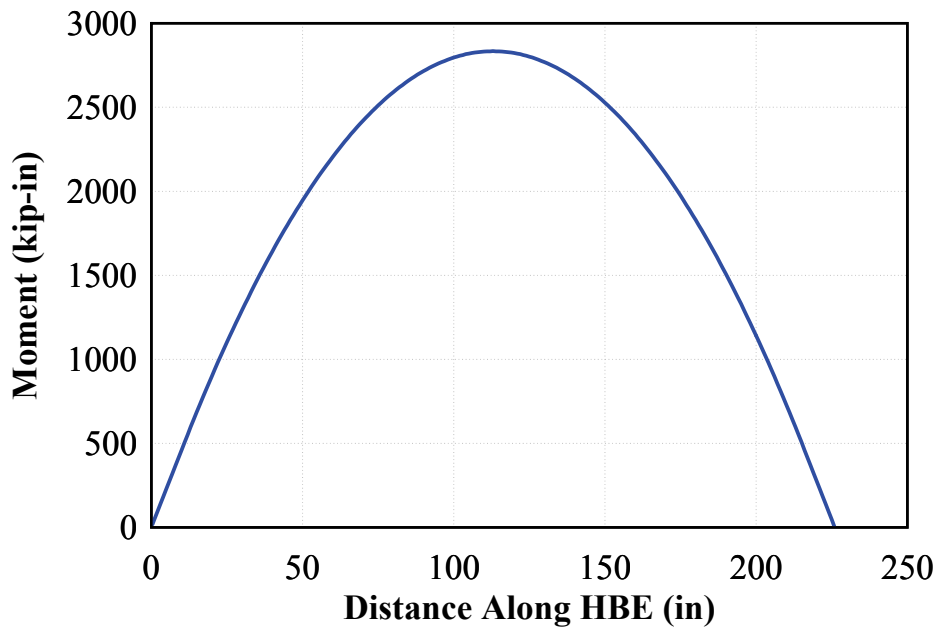


**FIGURE 3-67 Moment diagram - Vertical force component**

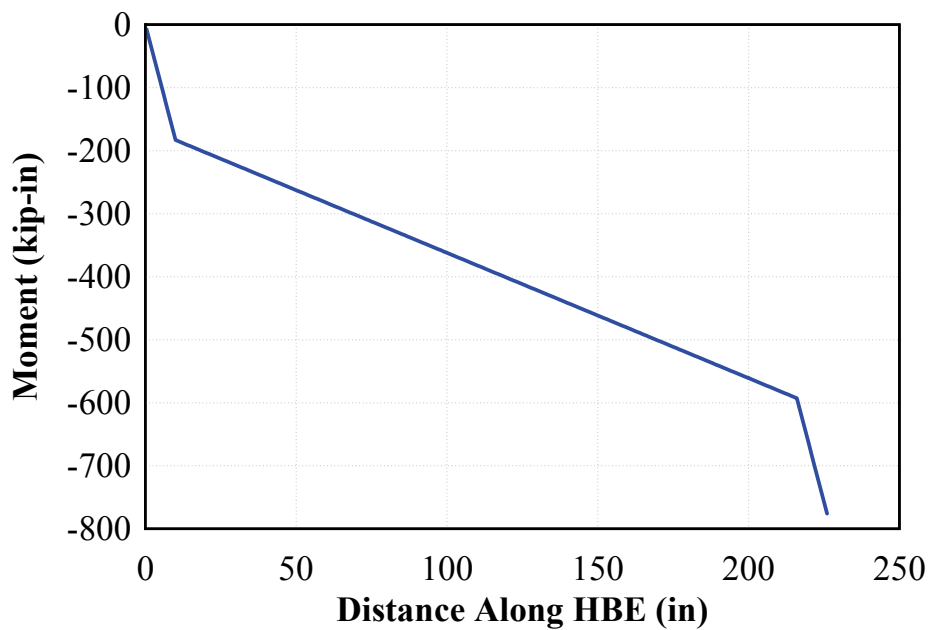


**FIGURE 3-68 Moment diagram - Horizontal force HBE component**



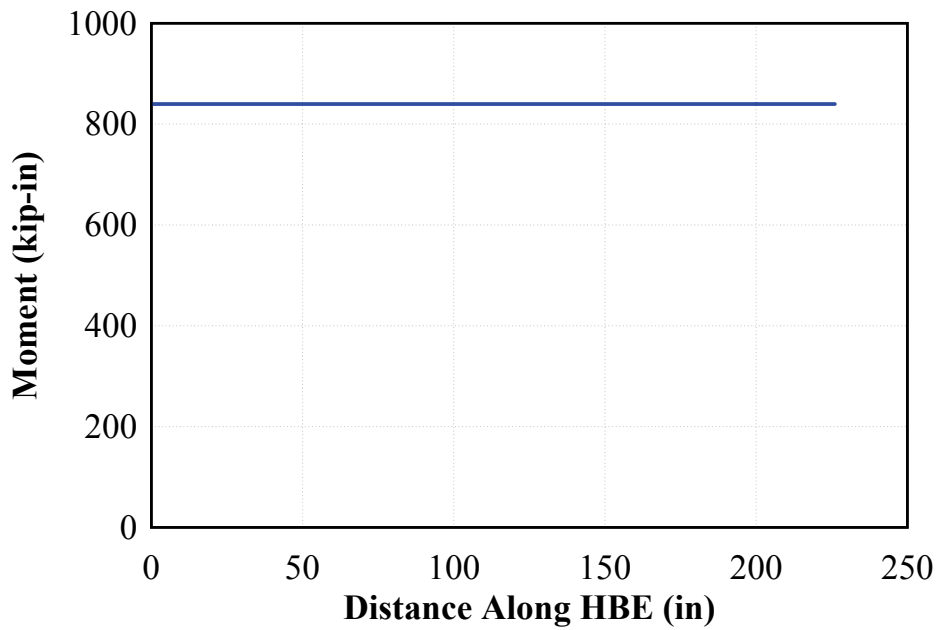


**FIGURE 3-69 Moment diagram - Horizontal force VBE component**

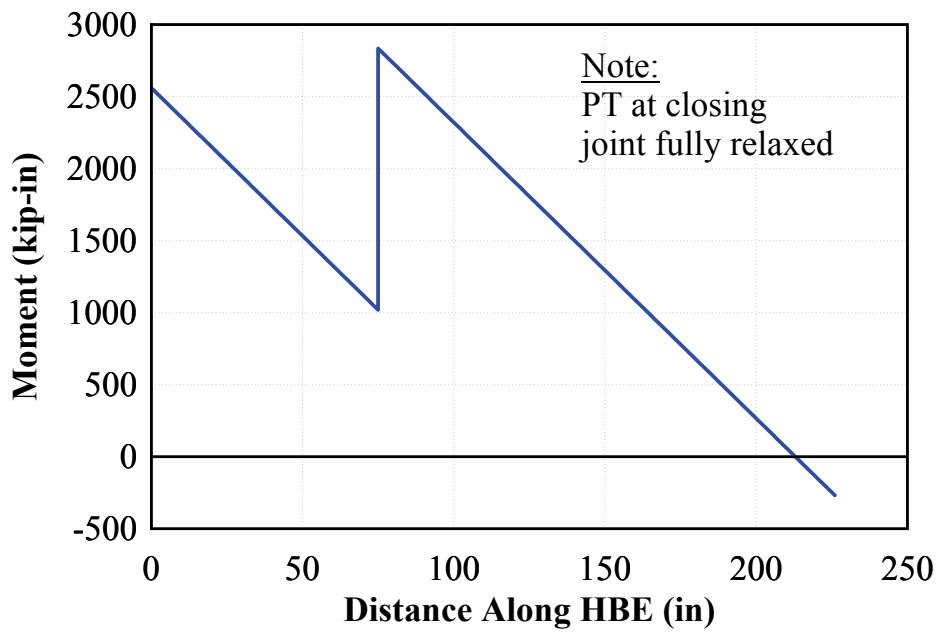


**FIGURE 3-70 Moment diagram - Post-tension force**

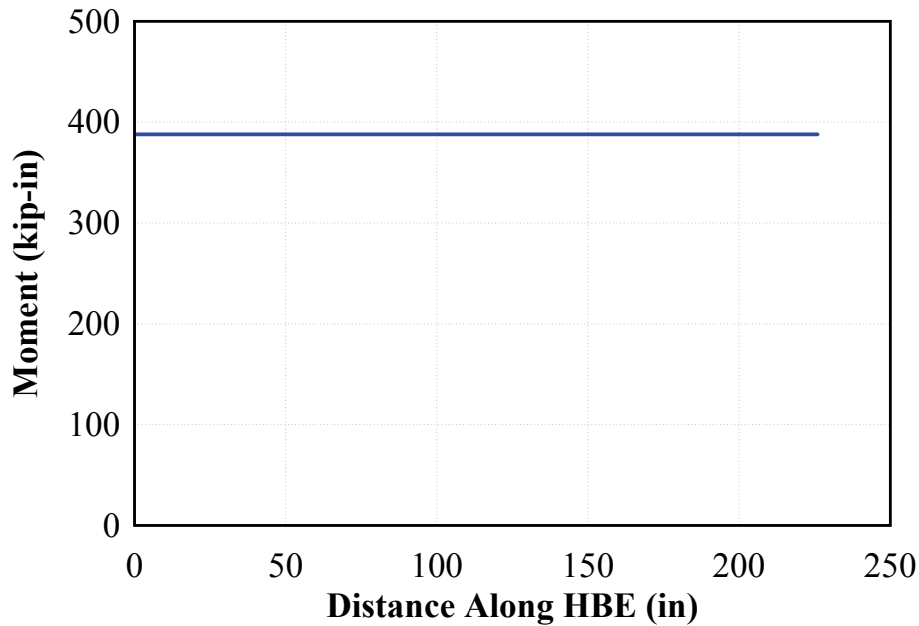


**FIGURE 3-71 Moment diagram – Story shear force**

The moment along the length of the HBE, shown in figure 3-66, can be decomposed into individual components similar to that presented for the flange-rocking frame, consisting of the following:

1. Vertical force component along the length of the HBE (i.e.,  $W_{by1}$  and  $W_{by2}$ ).
2. Horizontal force component (i.e.,  $W_{bx1}$  and  $W_{bx2}$ ) along the length of the HBE.
3. Horizontal force component from the VBE (i.e.,  $W_{cx1}$  and  $W_{cx2}$ ).
4. Horizontal force component from the story shear force (i.e.,  $V_i$ ).
5. Horizontal component from the post-tension (i.e.,  $P_s$ ).

Recall that for the centerline-rocking connection, only components #1, #2 and, #5 contributes to the HBE moments since the remaining components are applied at the centroid of the HBE. The individual moment diagrams for the components indicated above as a result of the NewZ-BREAKSS connection are shown in figures 3-67 to 3-71 respectively. Similar general observations presented earlier for the flange-rocking and centerline-rocking connections also apply here, with two notable differences:

- i. Component #2 vanishes for the flange-rocking and centerline-rocking connections, for a corner cut-out radius condition of  $R = 0$ . As an example, for the flange-rocking frame, for Zone 2, in (3-21), for  $R = 0$ , the terms  $\omega_{bx}$  drop out. For the NewZ-BREAKSS connection, this component is always present since the reaction  $R_\delta$ , only includes the horizontal force components of the infill web plate along the bottom flange (figure 3-56), which has an effect of the  $\omega_{bx}$  terms always present in the moment equations.
- ii. Component #3 is constant for the NewZ-BREAKSS connection, whereas for the other connections it decreases linearly. This is due the fact that the NewZ-BREAKSS connection remains in contact with the VBEs at the HBE top flanges only. Hence, there is no vertical end reactions induced on the HBEs from the  $\omega_{cx}$  components.

### 3.3.4.3 Development of HBE Shears (NewZ-BREAKSS)

The shear distribution to be used in the design of an HBE incorporating self-centering components can be determined using the same free body diagrams developed earlier for the HBE moments. Similarly, due to the presence of infill corner cut-outs, five zones along the length of the HBE are considered. From the free body diagram for the HBE segment along Zone 1, shown in figure 3-60, the corresponding shear force is the reaction  $R_a$  described in (3-70). Substituting (3-1) and (3-2) in place of the resultant infill yield force components into (3-70) leads to the shear force along HBE segment Zone 1 as follows:

$$V_1 = R_a = \frac{(\omega_{by1} - \omega_{by2})(L - 2R)}{2} - \frac{(\omega_{bx1})(L - 2R)}{L}d - (P_{s1} - P_{s2})\left(\frac{d}{2L} + \frac{y}{L}\right) \quad (3-82)$$

Next, from the free body diagram for the HBE segment along Zone 2, 3, and 4 shown in figure 3-62 to 3-64, the corresponding shear force is reduced by the vertical component of the infill plate yield forces. The shear force along the HBE segments along these Zones follow, where  $x$  is the distance from the end of the HBE:

$$V = R_a - (\omega_{by1} - \omega_{by2})(x - R) \quad (3-83)$$

Similarly, from the free body diagram for the HBE segment along Zone 5, shown in figure 3-65, the corresponding shear force along HBE segment Zone 5 follows:

$$V_5 = R_a - (\omega_{by1} - \omega_{by2})(L - 2R) \quad (3-84)$$

#### 3.3.4.4 Development of HBE Axial Force (NewZ-BREAKSS)

The axial force distribution to be used in the design of an HBE incorporating self-centering components can be determined using the same free body diagrams developed earlier for the HBE moments. Similarly, due to the presence of infill corner cut-outs, three zones along the length of the HBE are considered. From the free body diagram for the HBE segment along Zone 1, the corresponding axial force is the horizontal reaction  $C$  at the rocking point described in (3-69). Substituting (3-1) and (3-2) in place of the resultant infill yield force components into (3-69) leads to the axial force along HBE segment Zone 1 as follows:

$$P_1 = C = \frac{(\omega_{bx1} - \omega_{bx2})(L - 2R)}{2} + (\omega_{cx1} + \omega_{cx2})\left(\frac{h}{2} - \frac{d}{2} - R\right) + P_{s1(VBE)} \quad (3-85)$$

Next, from the free body diagram for the HBE segment along Zone 2 shown in figure 3-62, the corresponding axial force is reduced by the horizontal component of the infill plate yield forces. The axial force along the HBE segment Zone 2 follows:

$$P_2 = C - (\omega_{bx1} - \omega_{bx2})(x - R) \quad (3-86)$$

Next, from the free body diagram for the HBE segment along Zone 3 shown in figure 3-63, the corresponding axial force is reduced by the horizontal component of the infill plate yield forces and post-tension forces at the HBE anchor locations. The axial force along the HBE segment Zone 3 follows:

$$P_3 = C - (\omega_{bx1} - \omega_{bx2})(x - R) - (P_{s1} + P_{s2}) \quad (3-87)$$

Next, from the free body diagram for the HBE segment along Zone 4 shown in figure 3-64, the corresponding axial force is reduced by the horizontal component of the infill plate yield forces and post-tension forces at the HBE anchor locations. The axial force along the HBE segment Zone 4 follows:

$$P_4 = C - (\omega_{bx1} - \omega_{bx2})(x - R) \quad (3-88)$$

Similarly, from the free body diagram for the HBE segment along Zone 5, shown in figure 3-65, the corresponding axial force along HBE segment Zone 5 follows:

$$P_5 = C - (\omega_{bx1} - \omega_{bx2})(L - 2R) \quad (3-89)$$

### 3.3.4.5 Comparison with SAP2000 (NewZ-BREAKSS)

The formulations describing the distribution of moment, shear and axial forces developed above were compared to non-linear pushover analysis using SAP2000. The analytical model used consisted of a single bay, single story frame with a bay width of 20 feet and story height of 10 feet and is shown in figure 3-72. The same model parameters described for the centerline-rocking frame presented in Section 3.3.2.5 apply (for both SAP2000 and OpenSees). However, the post-tension area was reduced by 25% since the distance from the rocking point to the centroid of the post-tension elements increases from 6 inches to 15 inches for the same reason noted earlier for the prior example (Section 3.3.4.2.1).

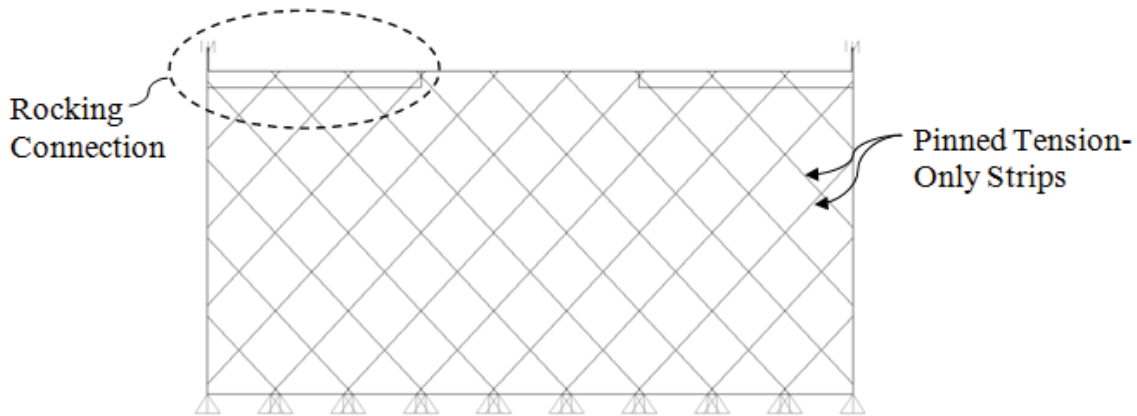


**FIGURE 3-72 NewZ-BREAKSS frame - Analytical model**

For the rocking connection, in SAP2000 a rigid beam element was used as a link to model the post-tension anchor points to the HBE to capture the applied moment during rocking motion about the HBE centerline. Joint constraints in the translational vertical global DOF and in-plane (HBE strong axis bending) rotational DOF were provided at key nodes. For the case of modeling in OpenSees, *rigidlink beams* are used in lieu of joint constraints (with the exception of modeling the HBE to VBE shear transfer). The connection models used in SAP2000 and OpenSees described are shown in figure 3-73.

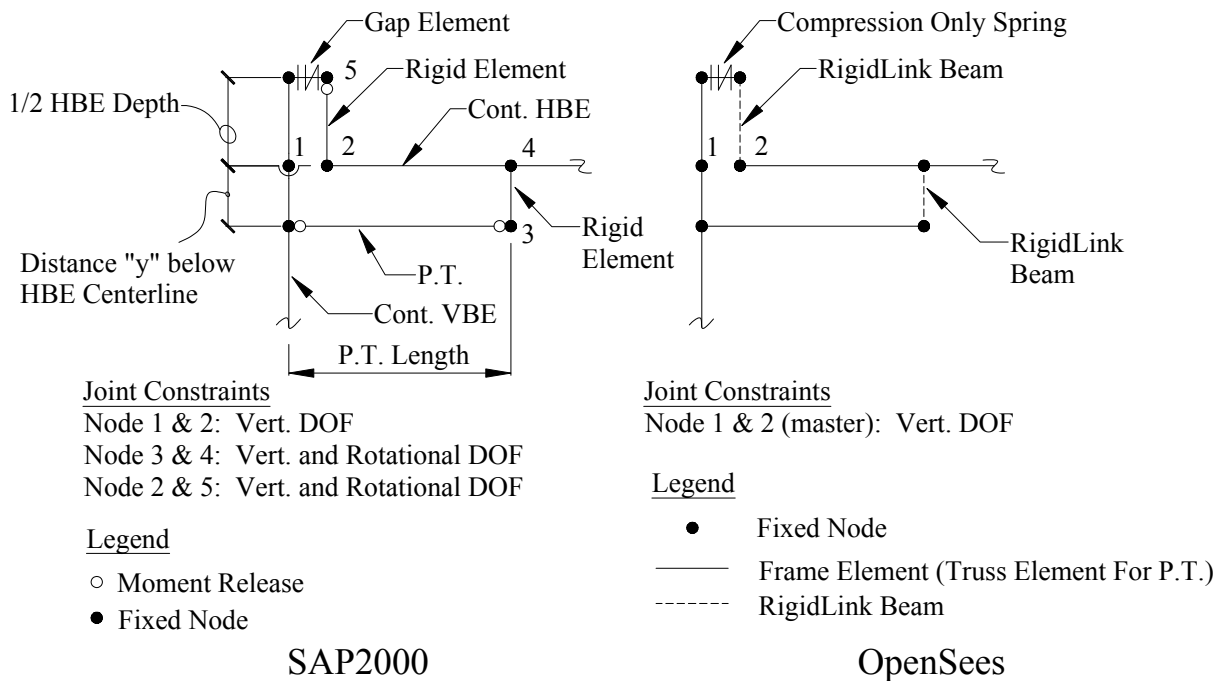


**FIGURE 3-73 NewZ-BREAKSS connection – Analytical model**

Figures 3-74 to 3-79 below provide comparisons of the moment, shear and axial force distributions along the length of the HBE using the formulations developed earlier to that with the analytical model of the SAP2000 analysis. Comparisons are presented for conditions ignoring post-tension force losses due to axial shortening and for conditions considering HBE axial shortening. Note that since the SAP2000 model uses a finite amount of strips to represent the infill web plate, the shear and axial force diagrams obtained from the SAP2000 analysis are stepped as compared to the continuous force diagrams using the theoretical formulations.

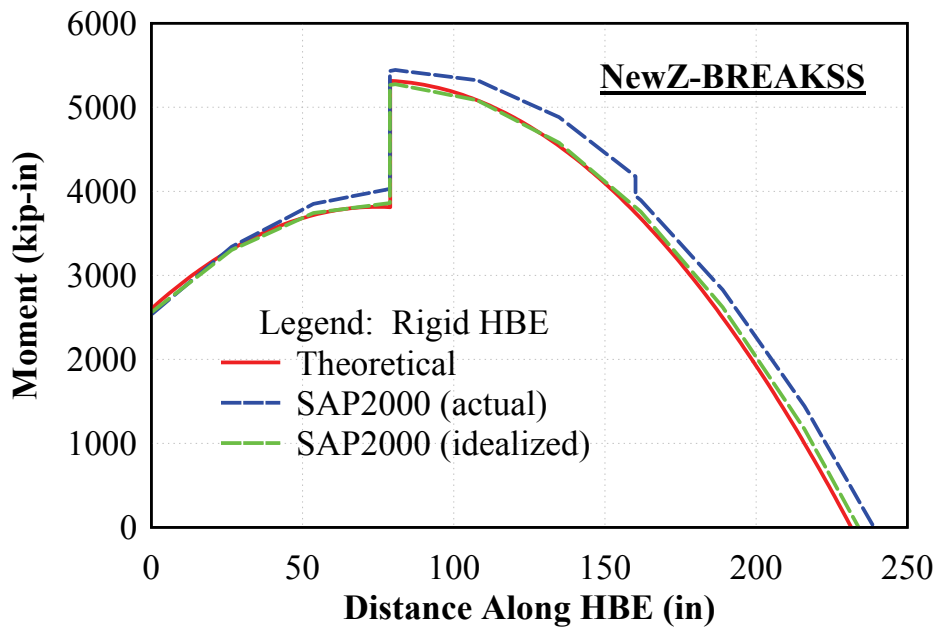


**FIGURE 3-74 Moment diagram – Rigid HBE**

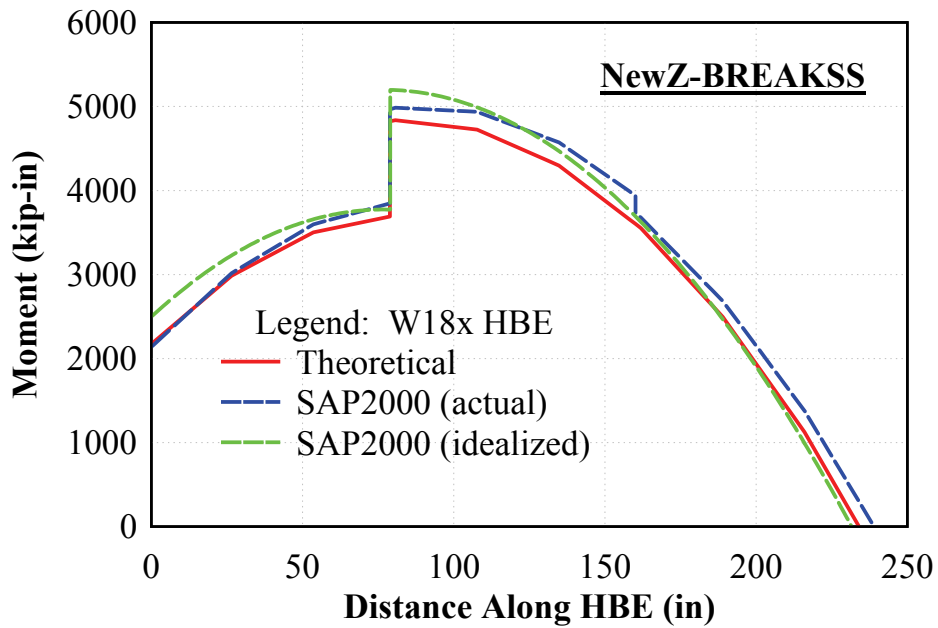


**FIGURE 3-75 Moment diagram – Flexible HBE**

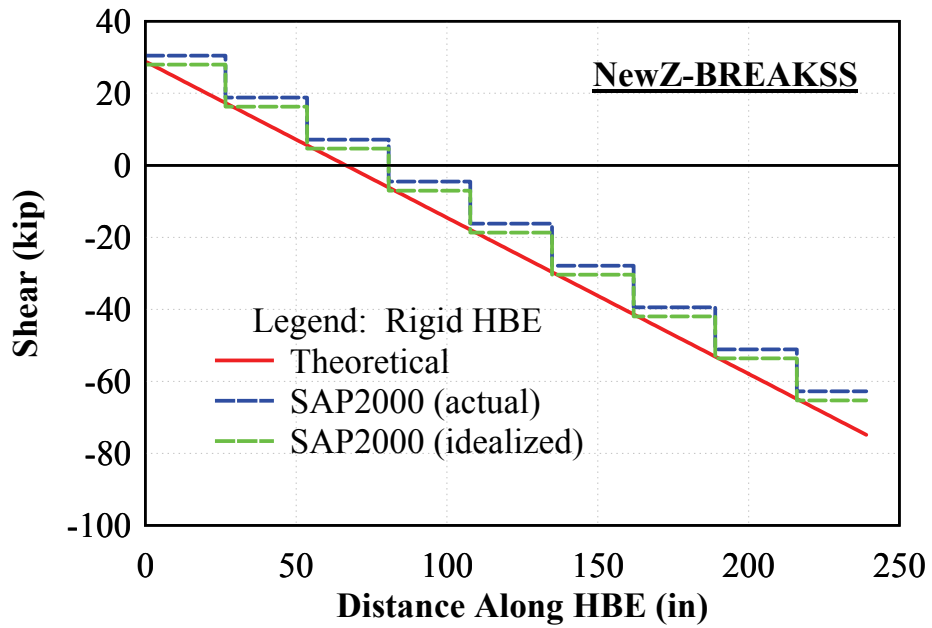


FIGURE 3-76 Shear force diagram – Rigid HBE

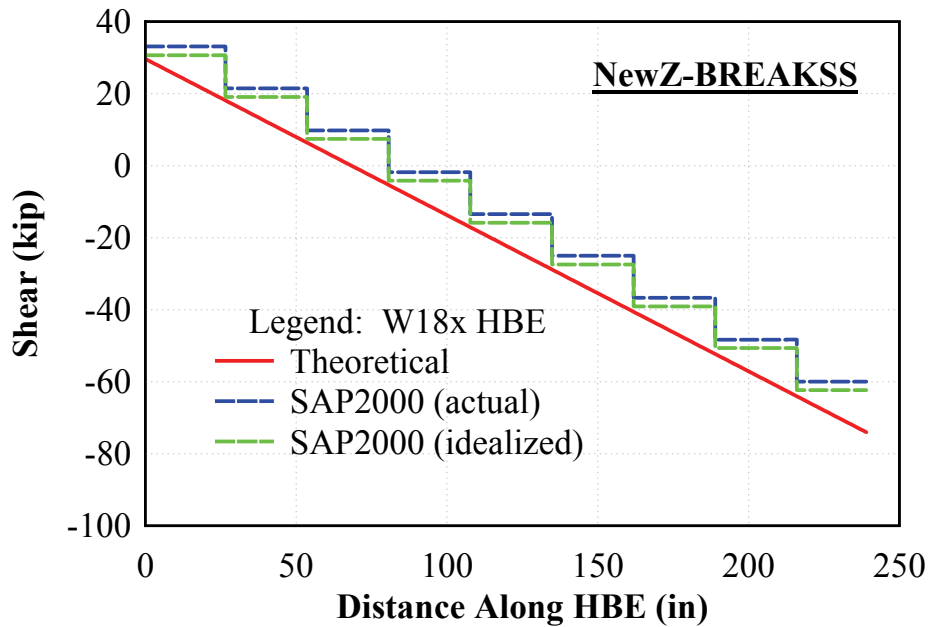
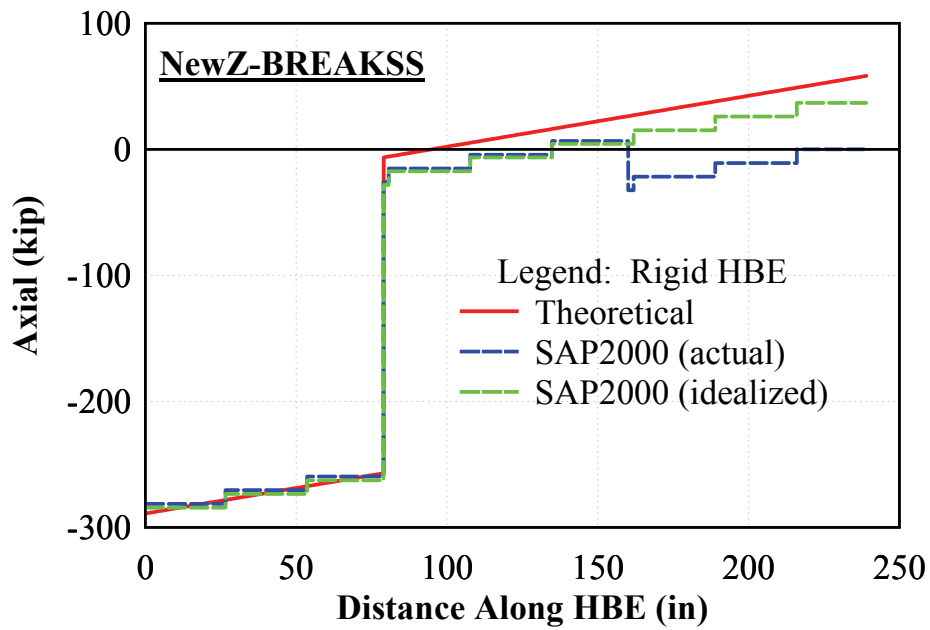
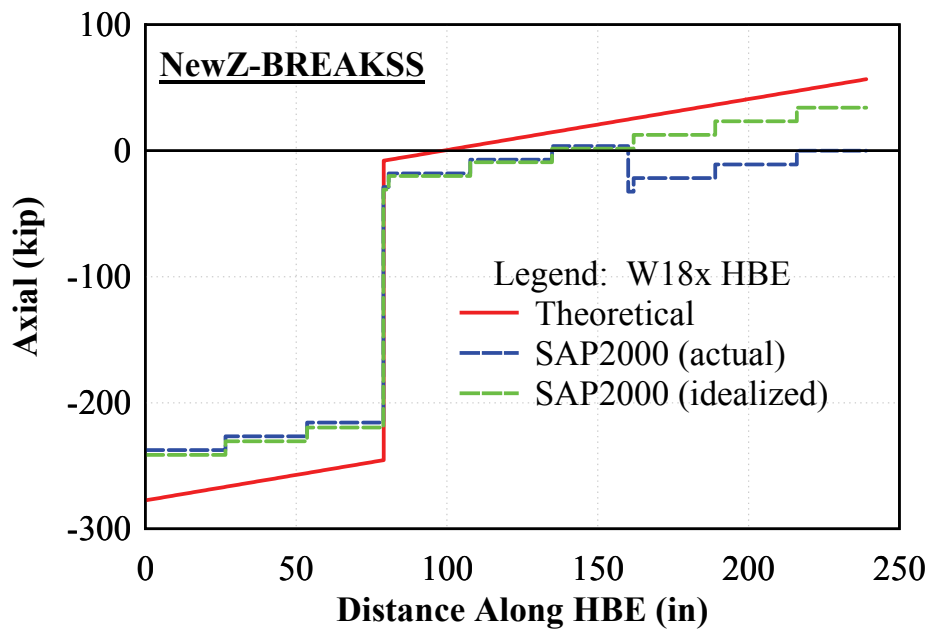


FIGURE 3-77 Shear force diagram – Flexible HBE





**FIGURE 3-78 Axial force diagram – Rigid HBE**



**FIGURE 3-79 Axial force diagram – Flexible HBE**

Note that the theoretical formulations are compared to two different SAP2000 curves labeled “actual” and “idealized”, where for the condition of a rigid HBE, the “idealized” curve matches the theoretical one almost perfectly for the moment and shear diagrams. The difference between the two different analytical models is that the “idealized” curves assume a pinned connection at the HBE-to-VBE flange contact rocking point. The “actual” model uses the compression-only element shown in figure 3-73, which models more accurately the real condition of the joint detail. To further clarify, the derivations presented above assume that the effects on the post-tension (i.e., terms  $P_{s1}$  and  $P_{s2}$ ) are exactly equal; which is essentially true for the rigid HBE condition if the HBE is pin connected to the VBEs. However, with the use of the compression-only element, some differences arise in response, since now the compression force at the closing joint can reduce (from the global effects captured by the analytical frame model that is not considered in the theoretical formulations), leading to small differences in the kinematics governing the axial tension in the post-tension elements.

Note that results from the SAP2000 analysis and the corresponding theoretical formulations compare reasonably along the full length of the HBE. The most notable difference is with the axial force diagram for the flexible HBE condition, where it is observed that the theoretical formulations are on the conservative side. As was observed in the previous rocking connection comparisons, these differences arise since the analytical formulations do not consider the vertical curvature of the HBE (i.e., the infill web strips pulling down on the HBE), which affects the rotations at the ends of the HBE, and in turn affects the axial forces in the post-tension elements. As a final observation (not made previously) on the SAP2000 moment and axial diagram curves, note that the post-tension force at the closing joint has not fully relaxed, as there is a vertical step in the response curves.

### **3.4 Infill Web Plate Strains Effects Due to HBE-to-VBE Gap Opening**

As mentioned earlier, radius corner cut-outs are provided at the infill web plate corner locations. The primary purpose of this detail is to remove the portion of the infill web plate at the corner locations that would otherwise be subjected to excessive tensile strains during lateral frame drift due to the opening of the rocking joint (as schematically shown in figure 3-80).

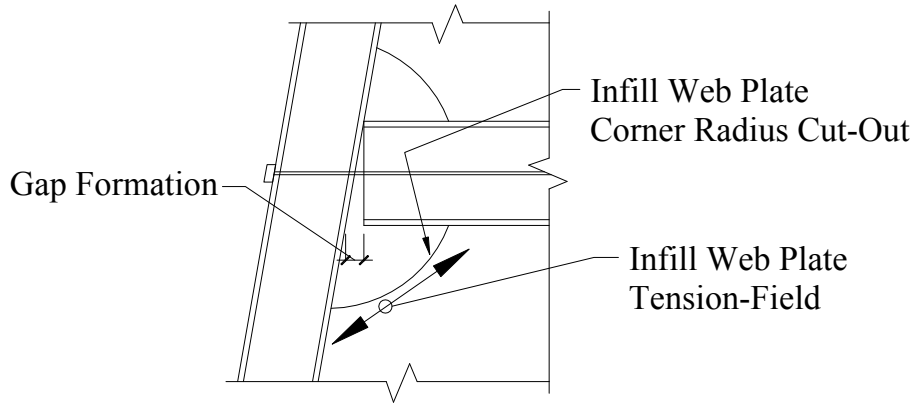


**FIGURE 3-80 HBE-to-VBE joint gap formation**

To determine the appropriate value of the radius corner cut-out to use in design, a review of the kinematics of the joint detail under frame sway is necessary and is performed below. First, it is instructive to review the kinematics of the infill web plate without the effects of the HBE-to-VBE gap openings.

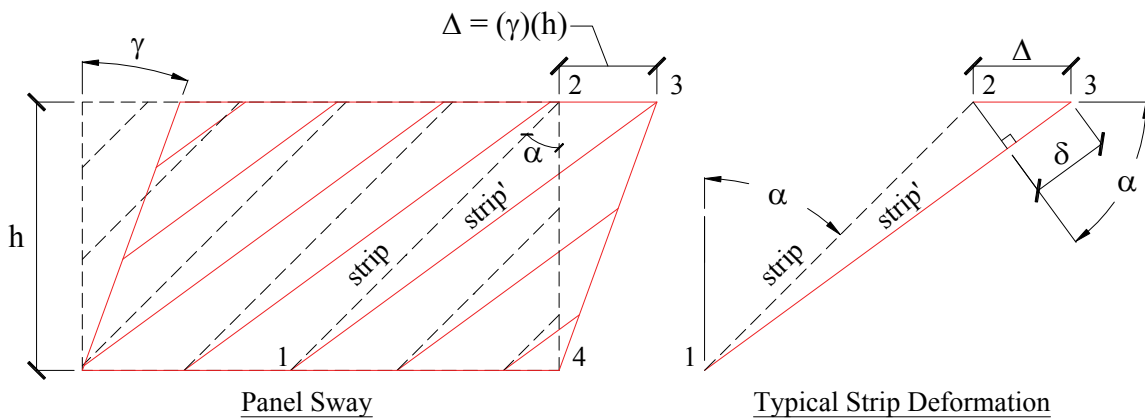


**FIGURE 3-81 Panel sway kinematics**

Figure 3-81 shows, in a panel sway mechanism, the tensile strain demands in the infill web plate for a given lateral drift. As shown, the infill web plate is idealized by discrete strips with pin connections on the boundary frame members, where:  $h$  is the story height,  $\gamma$  is the drift rotation,  $\Delta$  is the lateral drift,  $\alpha$  is the angular dimension to the vertical axis of the undeformed strips, and  $\delta$  is the axial tensile deformation. For the panel sway mechanism, without the effects of the HBE-to-VBE gap openings, and for rigid HBEs and VBEs, the axial tensile strains are equal in

all strip elements. The axial tensile strain for this condition can be determined by considering the infill web strips 1-2 and 1-3 shown in the figure, which represents a single strip before and after frame drift, respectively. From geometry, the axial tensile deformation is:

$$\delta = \Delta \sin \alpha \quad (3-90)$$

The undeformed length of strip 1-2 (using the geometry of triangle 1-2-4) is:

$$L_{strip1-2} = \frac{h}{\cos \alpha} \quad (3-91)$$

The tensile strain response of strip 1-3 due to lateral drift is then:

$$\varepsilon_{drift} = \frac{\delta}{L_{strip1-2}} = \frac{\Delta \sin \alpha \cos \alpha}{h} \quad (3-92)$$

Next, substituting the drift quantity and using the sine double-angle identity, (3-92) can be expressed as:

$$\varepsilon_{drift} = \frac{(\gamma h) \sin 2\alpha}{2h} = \frac{\gamma \sin 2\alpha}{2} \quad (3-93)$$

Figure 3-82 shows the geometry and parameters necessary to establish the kinematic relationships governing the infill web plate tensile strains when also including the HBE-to-VBE gap openings in the calculation of strains.

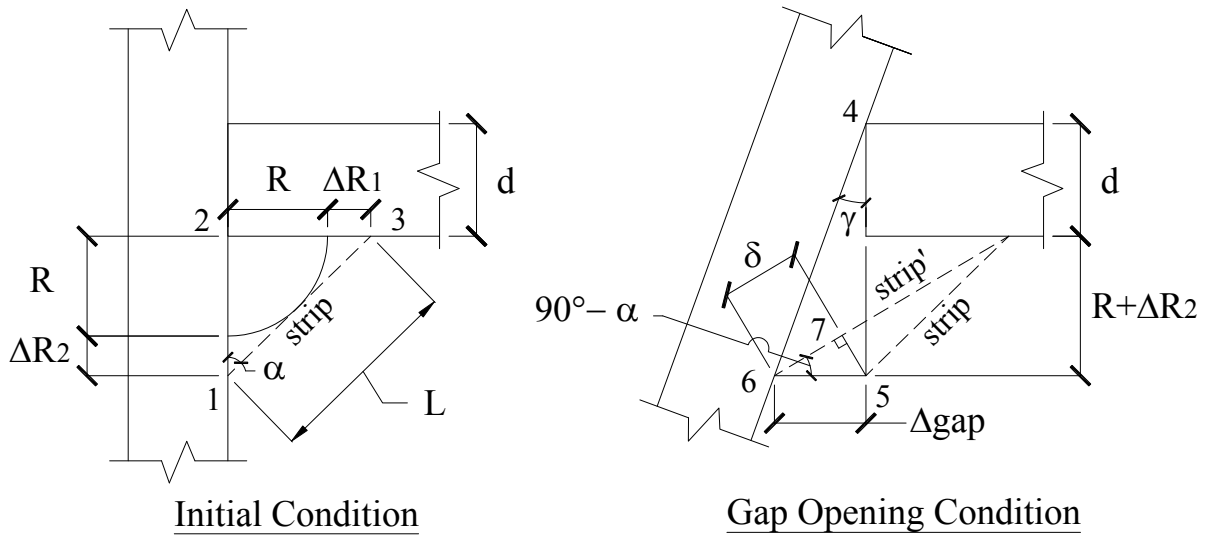


**FIGURE 3-82 HBE-to-VBE rocking joint kinematics**

In figure 3-82,  $R$  is the radius length of the corner cut-out,  $L$  is the length of the adjacent infill web strip to the corner (shown idealized),  $\alpha$  is the angle of inclination of the tension field to the vertical axis,  $\Delta R$  are differential lengths dependent on the value  $\alpha$ ,  $\Delta gap$  is the HBE-to-VBE gap opening,  $d$  is the depth of the HBE, and  $\gamma$  is the gap opening rotation. To determine the total cumulative axial tensile strain of the strip adjacent to the tip of the radius cut-out, the following relationships are established from geometry.

The length  $L$  is obtained from the initial condition geometry (triangle 1-2-3) as:

$$L = \frac{R + \Delta R_1}{\sin \alpha} \quad (3-94)$$

Next, the axial tensile deformation of the infill web strip due to gap opening is (using the geometry of triangle 5-6-7):

$$\delta = (\Delta_{gap}) \cos(90 - \alpha) \quad (3-95)$$

The gap opening can then be calculated (using geometry of triangle 4-5-6) as:

$$\Delta_{gap} = \gamma(d + R + \Delta R_2) \quad (3-96)$$

It is also observed that (using the geometry of triangle 1-2-3):

$$\tan \alpha = \frac{(R + \Delta R_1)}{(R + \Delta R_2)} \quad (3-97)$$

Next, the differential term  $\Delta R_2$  is established (for reasons to be made clear subsequently). To proceed, figure 3-83 shows the additional information needed to determine this quantity.

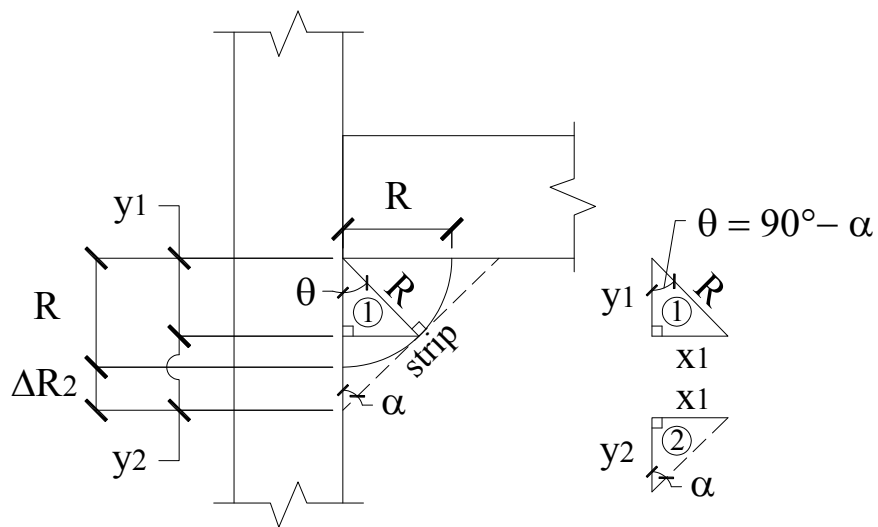


**FIGURE 3-83 Infill web plate corner cut-out dimensions**

It then follows, using triangle 1 in figure 3-83, along with the cosine double-angle identity, the parameter  $x1$  is:

$$x1 = R \cos(90 - \alpha) = R \sin \alpha \quad (3-98)$$

Furthermore from the same triangle 1, the term  $y_1$  can be determined as follows:

$$y_1 = R \sin \alpha \quad (3-99)$$

Next, from the geometry of triangle 2 in figure 3-83, substituting (3-98) for  $x_1$  and solving for  $y_2$  leads to:

$$y_2 = \frac{R \cos \alpha}{\tan \alpha} \quad (3-100)$$

Furthermore, in figure 3-83 it is observed that:

$$\Delta R_2 + R = y_1 + y_2 \quad (3-101)$$

from which substituting (3-99) and (3-100) for  $y_1$  and  $y_2$  respectively in (3-101) and solving for  $\Delta R_2$  leads to:

$$\Delta R_2 = y_1 + y_2 - R = R \sin \alpha + \frac{R \cos \alpha}{\tan \alpha} - R \quad (3-102)$$

The resulting infill web plate tensile strain can then be expressed as:

$$\varepsilon = \frac{\delta}{L} = \frac{\Delta_{gap} \sin \alpha}{\left( \frac{R + \Delta R_1}{\sin \alpha} \right)} \quad (3-103)$$

Substituting the terms for  $\Delta_{gap}$  and  $(R + \Delta R_1)$  using (3-96) and (3-97) into (3-103), it then follows:

$$\varepsilon = \frac{\gamma (d + R + \Delta R_2) \sin^2 \alpha}{(R + \Delta R_2) \tan \alpha} \quad (3-104)$$

Next, substituting in  $\Delta R_2$  from (3-102) and simplifying leads to:

$$\varepsilon = \frac{\gamma \left( d + \frac{R \cos \alpha}{\tan \alpha} + R \sin \alpha \right) (\sin \alpha \cos \alpha)}{R \left( \frac{\cos \alpha}{\tan \alpha} + \sin \alpha \right)} \quad (3-105)$$

Finally, (3-105) can be further simplified by the substitution of the sine double-angle identity, which then results in the following expression:

$$\varepsilon_{Total} = \frac{\gamma \sin 2\alpha}{2} \left( \frac{\frac{d}{R} \tan \alpha + \cos \alpha + \sin \alpha \tan \alpha}{\cos \alpha + \sin \alpha \tan \alpha} \right) \quad (3-106)$$

Equation (3-106) represents the total tensile strain demand on the infill web plate for HBE-to-VBE rocking connections. In comparison to (3-93), it is observed that the effect of the gap opening leads to a magnification factor by a quantity equal to the expression in the bracketed portion of (3-106). To illustrate the effects of the magnification factor (due to joint gap opening) in comparison to (3-93), for the case of  $\alpha = 45$  degrees, (3-106) results in the following:

$$\varepsilon_{Total} = Component1 + Component2 = \frac{\gamma d \sqrt{2}}{4R} + \frac{\gamma}{2} \quad (3-107)$$

where, in (3-107), *Component1* is the contribution of tensile strain from the gap opening and *Component2* is the contribution from lateral frame drift (i.e., panel sway described by (3-93)). To further illustrate, figure 3-84 shows the axial strain demand for several different lateral drift conditions. It is observed, that the closer the infill web plate is to the corner (corresponding to a smaller  $R$ ), the larger the strain demands. In particular, if  $R = 0$ , the theoretical strain is infinite.



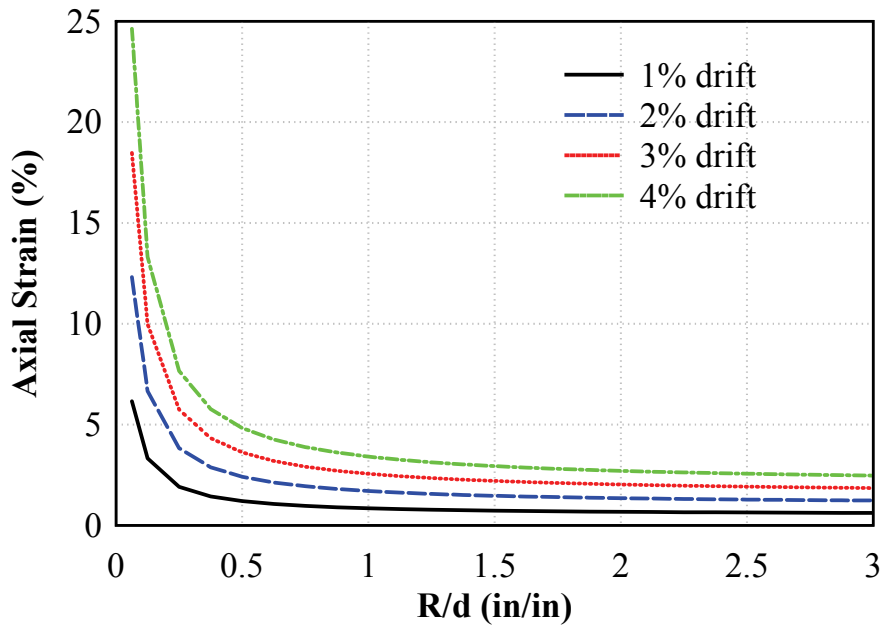


**FIGURE 3-84 Corner infill web plate strain demands**

Furthermore, figure 3-85 shows the total axial tensile strain, together with the strain corresponding to each component, for a 4% drift condition. It is observed that the concentration of strains in the infill plate due to the use of a rocking connection is a localized phenomenon, with values approaching those for the pure panel sway mechanism away from the rocking connection gap opening. Note that in the examples presented, the gap rotation was assumed to be equal to the drift rotation which assumes rigid sway behavior; which is a reasonable assumption (more exact joint rotation could be obtained from a rigorous frame analysis). Nonetheless, the above equations provide an approach to select the radius of the corner cut-outs. As an example, the test specimens for this research were detailed with an  $R/d$  ratio of approximately 1. For the condition shown in figure 3-84 (i.e.,  $\alpha = 45$  degrees) for the case of 2% roof drift (which would represent an approximate roof drift for a design level earthquake), (3-106) predicts a maximum theoretical infill web plate tensile strain of approximately 1.7%.

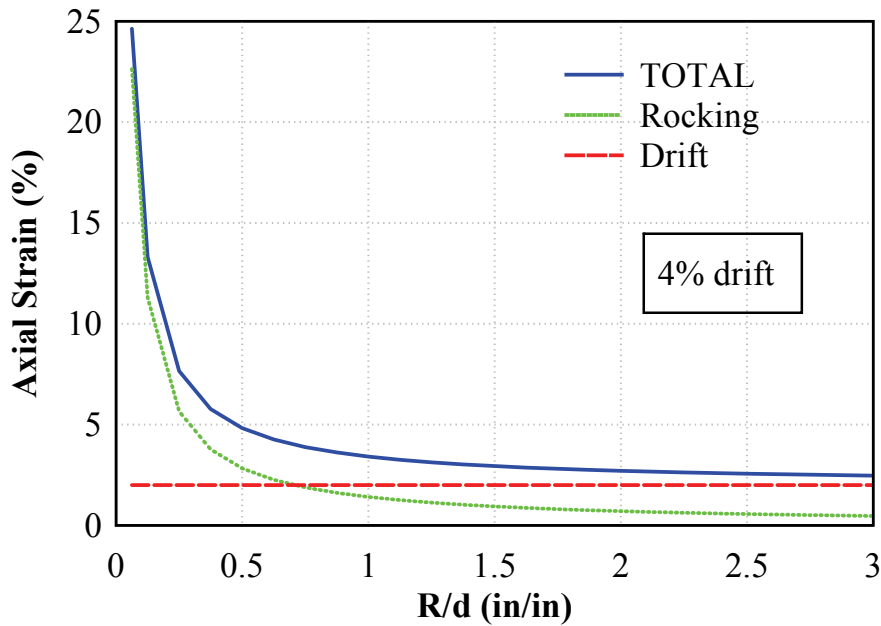


**FIGURE 3-85 Corner infill web plate strain components**

Finally, note that the above strain equations were derived using free body diagrams of the flange-rocking connection. However, these equations are applicable to any rocking configuration, as only the distance from the rocking contact point to the HBE flange needs to be modified in those equations for them to be applicable to the other types of connections. For example, for the centerline-rocking frame,  $d/2$  (half-depth of the HBE) would be used in lieu of  $d$  in the above equations. For the NewZ-BREAKSS connection, no changes to the equations are required since it follows the same kinematics when the HBE-to-VBE gap is present.

### 3.5 Summary

Information on the fundamental behavior of HBEs in a SC-SPSW frame was presented. In particular, three different rocking connections were investigated, of which two are intended to eliminate the beam-growth effects associated with the flange-rocking connection. The closed-form equations derived for these connections, based on detailed free body diagrams, provide insight on the kinematics of self-centering steel frames incorporating these details. Additionally, comparisons of results using these equations were made with results from nonlinear pushover analysis obtained with the program SAP2000, and results were comparable.

Furthermore, the effect of rocking connections on the tensile strain of the infill web plate was addressed. It was shown that strain demands near the corners of infill web plates are subject to significantly larger tensile strains as a consequence of the HBE-to-VBE gap opening. The kinematics of the HBE-to-VBE joint was established, leading to a simple closed-form equation quantifying the infill web plate strain response, which can then be used to calculate the desirable radius of the cut-outs at the corner of the infill web plates.



## SECTION 4

### EXPERIMENTAL PROGRAM AND TEST SPECIMEN DESIGN

#### 4.1 General

The purpose of the experimental program conducted in this research was to investigate the behavior of self-centering steel plate shear walls (SC-SPSW). More specifically, this experimental test phase was intended to verify and validate analytical models, provide a database of experimental data (to be made publicly available), and provide observations on local and global behavior in a physical model.

The experimental test program at the Structural Engineering and Earthquake Simulation Laboratory (SEESL) at the University at Buffalo (UB) was conducted in two phases. First, quasi-static cyclic tests were conducted, followed by dynamic shake-table tests. The physical specimens and test setup for each phase were identical (i.e., dimensions, material sections and properties, etc.); only the loading parameters were different. As a consequence of this single design, after the quasi-static phase was completed, the entire test setup was moved to sit on the shake-table (the inherent mass of the test setup provided the required mass to generate the necessary inertia forces for the shake-table tests). Note that the beams (i.e., HBES) and columns (i.e., VBEs) of the boundary frame were designed to remain essentially elastic and were re-used for the shake-table tests; only the infill web plates and post-tension (PT) elements were replaced (with the new components being identical to those used in the quasi-static tests). For this purpose, and to ensure consistency in material mechanical properties to facilitate comparison in specimen responses, the infill web plate and post-tension strands for both test phases were ordered at the same time.

This chapter presents the prototype building and general procedure used in the design of the test specimens, the different configurations and characteristics of the test specimens investigated, and analytical results for the quasi-static tests (Section 4.2). Furthermore, design parameters, similitude scaling, prototype building as it relates to the dynamic tests, and analytical results are presented for the shake-table test phase (Section 4.3).

## 4.2 Quasi-Static Tests

### 4.2.1 Prototype Building

The prototype building used for this project was based on the 3-story prototype building used in the SAC Steel Project (FEMA 2000) and shown in figure 4-1. It is representative of a standard office building with typical structural steel framing construction situated on stiff soil (Site Class D per ASCE 7-10 definition) and assumes a total of six lateral force resisting frames in each primary building direction. Note that the site for the prototype building used for this project is also located in Los Angeles, CA (similar to the original Los Angeles site SAC building). However, the earthquake spectral response acceleration parameters used are based on the 2009 NEHRP seismic hazard maps to reflect more current code standards. The corresponding design basis earthquake (DBE) response spectrum is shown in figure 4-2, where  $S_{DS}$  and  $S_{D1}$  are the design spectral response acceleration parameters at short periods and 1 second period respectively for a damping of 5%.

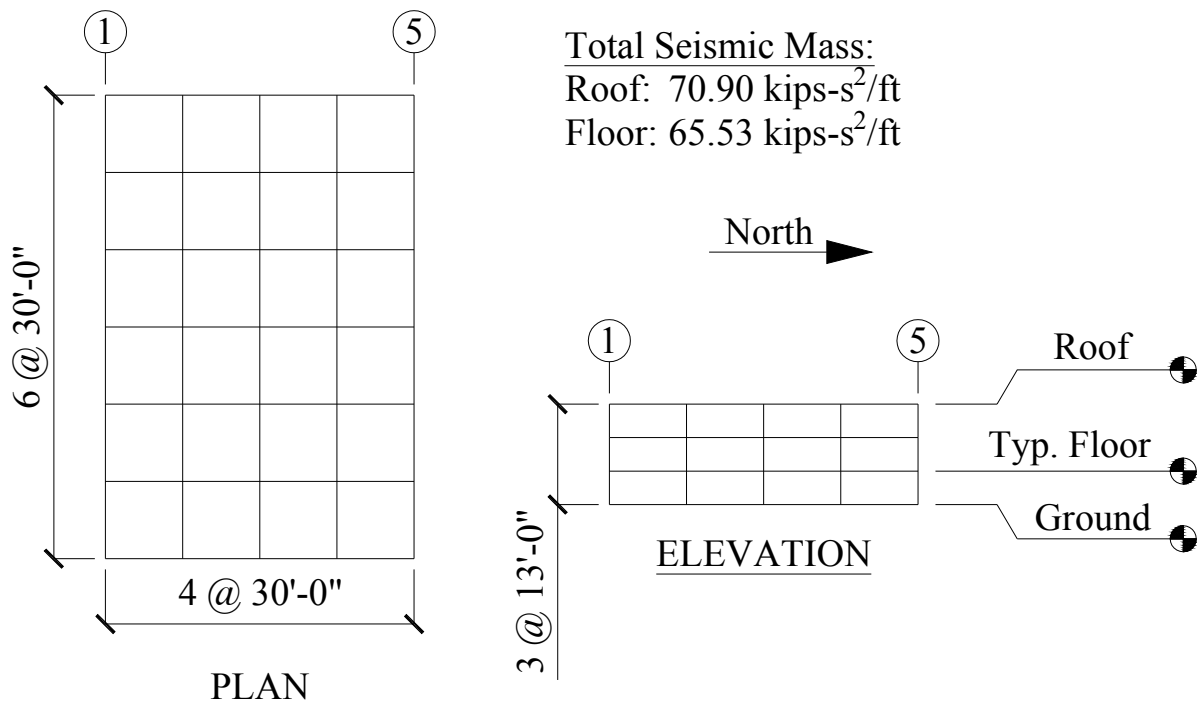


FIGURE 4-1 Prototype building: quasi-static

# USGS "DesignMaps" Summary Report

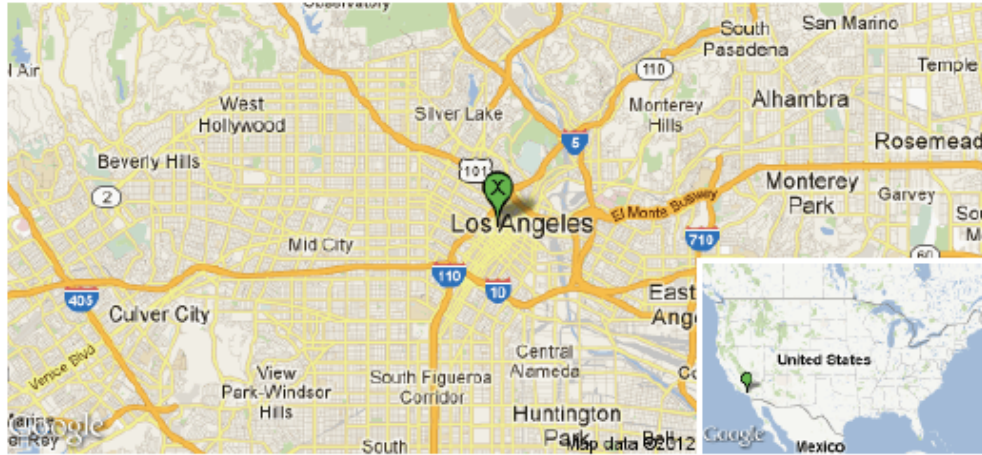
## User-Specified Input

**Building Code Reference Document** 2009 NEHRP Recommended Seismic Provisions  
(which makes use of 2008 USGS hazard data)

**Site Coordinates** 34.05101°N, 118.25436°W

**Site Soil Classification** Site Class D - "Stiff Soil"

**Risk Category** I/II/III



## Design Spectrum 5% Damping Los Angeles, CA

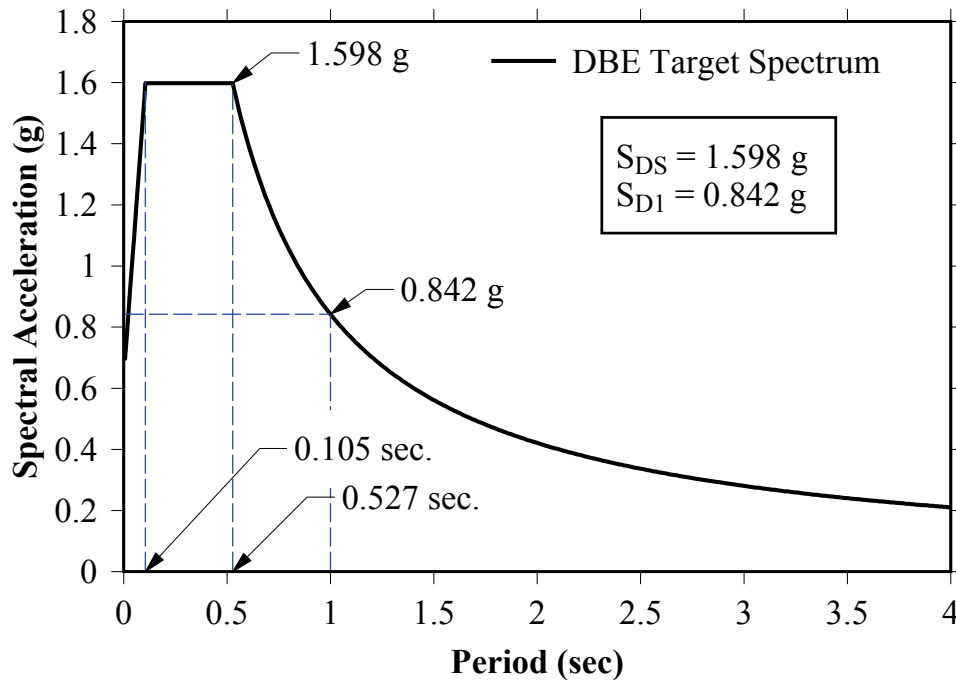


FIGURE 4-2 (a) Prototype building site; (b) design response spectrum

## 4.2.2 Static Tests – Specimen Design

### 4.2.2.1 Preliminary Design

For the quasi-static tests, a single-bay three-story frame representing a typical lateral frame of the prototype building was experimentally investigated. However, the prototype frame was scaled to a smaller model frame in order to facilitate testing. For these tests, a scale factor of three (i.e., one-third scale of the prototype) was selected for the model, which also brought it within the testing capabilities for the shake-table tests. The test specimen(s) section members were then a result of geometrically scaling the section properties of the prototype frame design. The applicable similitude relationships and values used are shown in table 4-1 where the scale factor,  $\lambda$  = prototype quantity/model quantity.

**TABLE 4-1 Simultude scale factors**

	Quantity	Scale Factor	Value
Geometry	Linear Dimension, $L$	$\lambda_L$	3
	Plastic Modulus, $Z$	$\lambda_L^3$	27
	Moment of Inertia, $I$	$\lambda_L^4$	81
	Area, $A$	$\lambda_L^2$	9
Material Property	Elastic Modulus, $E$	$\lambda_E = 1$	1
	Density, $\rho$	$\lambda_E/(\lambda_L\lambda_a)$	1
	Mass, $m$	$\lambda_p\lambda_L^3$	9
	Stress, $\sigma$	$\lambda_\sigma = 1$	1
	strain, $\varepsilon$	$\lambda_\varepsilon = 1$	1
Loading	Force, $f$	$\lambda_E\lambda_L^2$	9
	Gravitational Acceleration, $g$	$\lambda_g = 1$	1
	Acceleration, $a$	$(\lambda_E\lambda_L^2)/\lambda_m$	1
	Velocity, $v$	$(\lambda_L\lambda_a)^{1/2}$	1.73
	time, $t$	$(\lambda_L/\lambda_a)^{1/2}$	1.73
	Frequency, $\omega$	$(\lambda_L/\lambda_m)^{1/2}$	0.58
	Critical Damping, $\xi$	$\lambda_\xi = 1$	1



As an initial design step, since design code provisions are not currently available for SC-SPSWs, the lateral frames for the prototype building were assumed to be conventional steel plate shear walls (CSPSW) and the boundary frame members designed using the *indirect capacity design approach* per the *AISC Seismic Provision for Structural Steel Buildings* (AISC 2005b). Accordingly, only general steps used for the design of the specimen are presented here (i.e., information on the use of the design approach can be found in the reference noted). The equivalent lateral force procedure per ASCE 7-10 was performed to obtain the design seismic forces using the following parameters:  $R$  = response modification factor for CSPSWs = 7;  $I$  = importance factor = 1;  $S_{DS}$  = design response acceleration parameter at short periods = 1.598g;  $W$  = frame tributary seismic weight =  $(201.96 \text{ kips-sec}^2/\text{ft}) \cdot (32.2 \text{ ft/sec}^2) \cdot (1/6 \text{ frames}) = 1084 \text{ kips}$ . The tributary design base shear for the prototype frame was then calculated to be 248 kips using (4-1).

$$V = C_s W = \frac{S_{DS}}{\left(\frac{R}{I_e}\right)} W \quad (4-1)$$

Next, the vertical distribution of the base shear force along the height of the prototype frame at each level was calculated using:

$$F_x = C_{vx} V \quad (4-2)$$

and,

$$C_{vx} = \frac{w_x h_x^k}{\sum_{i=1}^n w_i h_i^k} \quad (4-3)$$

where  $C_{vx}$  = vertical distribution factor,  $k$  = exponent related to the structure period = 1 for the prototype building,  $w$  is the portion of the total effective seismic weight  $W$  assigned to Level  $i$  or  $x$ , and  $h$  is the height from the base to Level  $i$  or  $x$ . From (4-2) the resulting story shears were found to be 129 kips, 208 kips, and 248 kips at Level 3, 2, and 1 respectively.

Using the calculated design story shears, the thickness of the infill web plates was determined assuming that the infill web plates resist 100% of the story shears at each level. Furthermore for sizing purposes, ASTM A36 was assumed for the infill web plate material (as it is commonly available in practice). The required thickness of the infill web plates was then calculated using the design shear strength equation according to the AISC Seismic Provisions as follows:

$$t_{required} = \frac{V_u}{\phi(0.42F_{yp}L_{cf} \sin 2\alpha)} \quad (4-4)$$

where  $\phi$  = strength reduction factor = 0.9,  $F_{yp}$  = nominal yield strength of web plate = 36 ksi,  $L_{cf}$  = clear distance between VBE flange of frame = 240 inches; and  $\alpha$  = angle of web yielding tension field measured from the vertical in units of radians. For preliminary purposes,  $\alpha$  was assumed to be 45 degrees. Using (4-4) the required infill web plates was determined to be the ones corresponding to 18 gage (GA), 14 GA, and 13 GA at Level 3, 2, and 1, respectively, for the prototype frame.

Next, a monotonic nonlinear pushover analysis, using a strip model (Sabelli and Bruneau 2007), was performed. The infill web strips (of thickness determined above) were assigned elastic-perfectly plastic nonlinear axial hinges. The boundary frame members were assumed to be ASTM A992 and were designed using the AISC LRFD design procedures (AISC 2005a). Note that for SC-SPSWs, the boundary frame should be designed to remain essentially elastic for reasons discussed in Section 3. Accordingly, the CSPSW boundary frame members were designed (through iterative process) to remain elastic at 4% roof drift. The final boundary frame members selected were W24x162, W24x131, and W24x162 for Level 3, 2, and 1 HBEs, respectively; for the VBEs a W18x234 was selected.

Finally, the boundary frame members and the infill web plate thicknesses determined from the CSPSW prototype frame were geometrically scaled to obtain the corresponding model frame. For this purpose, the plastic section modulus,  $Z_x$ , was scaled for the boundary frame members and the gage thickness was scaled for the infill web plates. An analytical model of the SC-SPSW model frame was then developed and checked to ensure that the model frame boundary elements

remained elastic at a minimum of 4% drift. Note that much of the above sizing was done based on a C-SPSW prototype frame, which does not require PT elements. Consequently, since PT elements are needed for the model SC-SPSW frame, these were sized based on detailing constraints of the test specimen, and geometrically scaled up for the corresponding SC-SPSW prototype frame. The resulting design of the model frame consisted of W8x18, W8x15, and W8x18 for Level 3, 2, and 1 HBEs, respectively, W6x25 for the VBEs, ASTM A992 material for all boundary frame members; 26 GA, 24 GA and 22 GA at Level 3, 2, and 1, respectively, for the infill web plates; and 1/2 in diameter ASTM A416 grade monostrands for the PT. The boundary frame members (i.e., HBEs and VBEs) were donated by the American Institute of Steel Construction (AISC) for this project.

Note that the infill web plates of the prototype frame were assumed to be A36 (for hot-rolled steel); however, A36 plates were not available for the small thicknesses of the corresponding infill web plates for the model frame, and A1008 (for cold-rolled steel) was used instead. Furthermore, for the model frame, although 28 GA was required at Level 3, 28 GA material stock was not found to be available through suppliers, and 26 GA was used instead. A summary of the prototype and model frame along with target and achieved scale factors are shown in table 4-2.

**TABLE 4-2 Similitude scale factors for prototype and shake-table model building**

	Quantity		Prototype	Model	Target Scale Factor	Actual Scale Factor	
Building Dimensions	Bay Spacing (in.)		270	90	3	3	
	L3 Story Ht. (in.)		150	50.75	3	3	
	L2 Story Ht. (in.)		150	50.75	3	3	
	L1 Story Ht. (in.)		156	42.875	3	4	
Seismic Weights	Level 3 (kips)		153	17	9	9	
	Level 2 (kips)		153	17	9	9	
	Level 1 (kips)		153	17	9	9	
Beams	Level 3	<u>W24x162</u> $Z_x$ (in <sup>3</sup> )	468	<u>W8x18</u> 17	27.0	27.5	
		$A$ (in <sup>2</sup> )	47.7	5.26	9.0	9.1	
	Level 2	<u>W24x131</u> $Z_x$ (in <sup>3</sup> )	370	<u>W8x15</u> 13.6	27.0	27.2	
		$A$ (in <sup>2</sup> )	38.5	4.44	9.0	8.7	
	Level 1	<u>W24x162</u> $Z_x$ (in <sup>3</sup> )	468	<u>W8x18</u> 17	27.0	27.5	
		$A$ (in <sup>2</sup> )	47.7	5.26	9.0	9.1	
	Columns	<u>W18x234</u> $Z_x$ (in <sup>3</sup> )		549	<u>W6x25</u> 18.9	27.0	29.0
		$A$ (in <sup>2</sup> )		68.8	7.34	9.0	9.4
Infill Web Plates	Level 3	t (in.)	0.0478 (18 GA)	0.0179 (26 GA)	3	2.7	
	Level 2	t (in.)	0.0747 (14 GA)	0.0239 (24 GA)	3	3.1	
	Level 1	t (in.)	0.0897 (13 GA)	0.0299 (22 GA)	3	3	
Post-Tension Strands	Level 3	$A$ (in <sup>2</sup> )	2.754	0.306	9	9	
	Level 2	$A$ (in <sup>2</sup> )	2.754	0.306	9	9	
	Level 1	$A$ (in <sup>2</sup> )	2.754	0.306	9	9	

#### 4.2.2.2 Material Coupon Tests

The connection of the infill web plate to the boundary frame for SPSW construction is typically provided by a welded connection to a “fish” plate on the boundary frame. Furthermore, for full scale frames, typically the infill web plates are usually sufficiently thick to be hot-rolled steel plate material stock. In contrast, for the scaled test specimens, the infill web plates were much thinner and consisted of cold-formed steel. At the early stages of the test phase, there was a concern that the designed infill web plate thicknesses for the model specimen were too thin to allow effective welded connections; the perceived potential problems were that the weld material could burn through the edge of the infill web plate without adequately fusing to the base material, and/or that the edge of the plates would become too brittle in the heat-affected zone, leading to a significant reduction in ductility of the infill web plates.

To investigate the validity of these concerns, coupons were cut from a 26 GA sheet (it being the thinnest of the three infill web plates for the SC-SPSW model) and welded to steel tabs, as shown in figure 4-3. These weld-coupons were then tested in a uniaxial testing machine (in tension) to observe the failure modes. The weld-coupon specimens after testing are shown in figure 4-4, side-by-side along with an untested reference coupon for visual comparison. It is observed that all of the coupons exhibited good ductility (as visually assessed from total elongation and, in some cases, cross-section changes). Coupons “A” and “B” fractured in the heat-affected zone at the weld connection; a close-up view is shown in figure 4-4b for coupon “A”. Coupons “C” and “D” fractured away from the heat-affected weld connection (i.e., the ideal failure mode), as shown also in the figure.

Due to the larger width of the coupons, an extensometer could not be fitted on the coupons to accurately measure and collect data on elongation, but approximate elongation properties of the coupons were estimated as shown in figure 4-4c. The rough estimate calculations for maximum strain were obtained by measuring the approximate total length of the elongated coupon after fracture and dividing by the original length. Of significance is that the approximate ultimate strain prior to fracture was 12.5% for coupon “B” and 20% for the remaining three coupons (as tabulated in figure 4-4); these values are much higher than the anticipated tensile strains of the infill web plate expected in the experiments (i.e., less than 5% elongation was anticipated for the

tests). Also, prior to the uniaxial tension tests, the thickness and width of each coupon was measured in order to calculate an approximate cross-sectional area. The peak forces in the coupon tests were recorded, from which the approximate ultimate tensile stresses were calculated. It was observed that the ultimate tensile stress of the coupons ranged from approximately 31.6 to 34.4 ksi, all close but less than the assumed 36 ksi tensile stress used to design the boundary frame members. Note that the coupon ends were at a horizontal (i.e., perpendicular to the longitudinal axis of the coupons tested in uniaxial tension). In hindsight, additional coupons could have been tested with ends at a 45 degree angle from the longitudinal axis of the coupons, to closer simulate the stress conditions at the weld connection once the diagonal tension-field has formed in the infill web plates (for an assumed  $\alpha = 45$  degrees), but it is believed that this would not have led to significant differences in the results.

Overall, the above data obtained from the weld-coupon tests showed that a welded connection of the infill web plate was possible, while not significantly affecting the infill web plate ductility for the thin web plates to be used in the test specimens. It also confirmed that the demands from the yielding infill web plates supplied would remain within the design limits of the boundary frame (assuming the new infill plates to be ordered are close in mechanical properties to those obtained from these preliminary coupon tests). Accordingly, the infill web plate panels for the test specimens were ordered (for both quasi-static and shake-table test phases) from a local supplier (from whom the sheet for the weld-coupons was obtained) and final design/detailing commenced as planned.

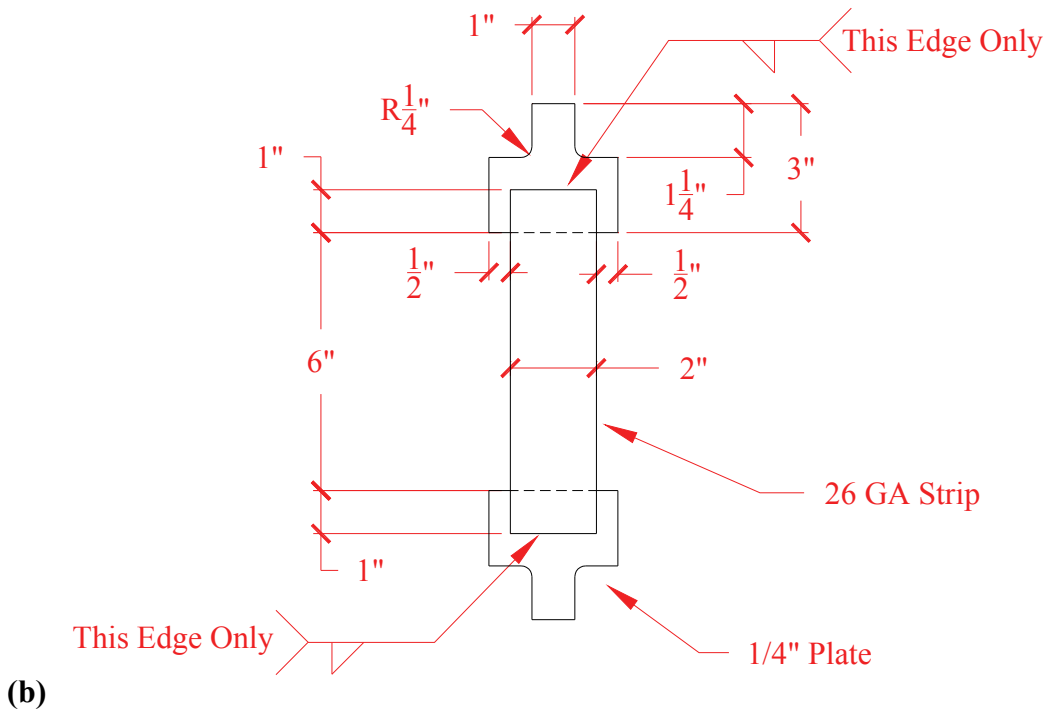
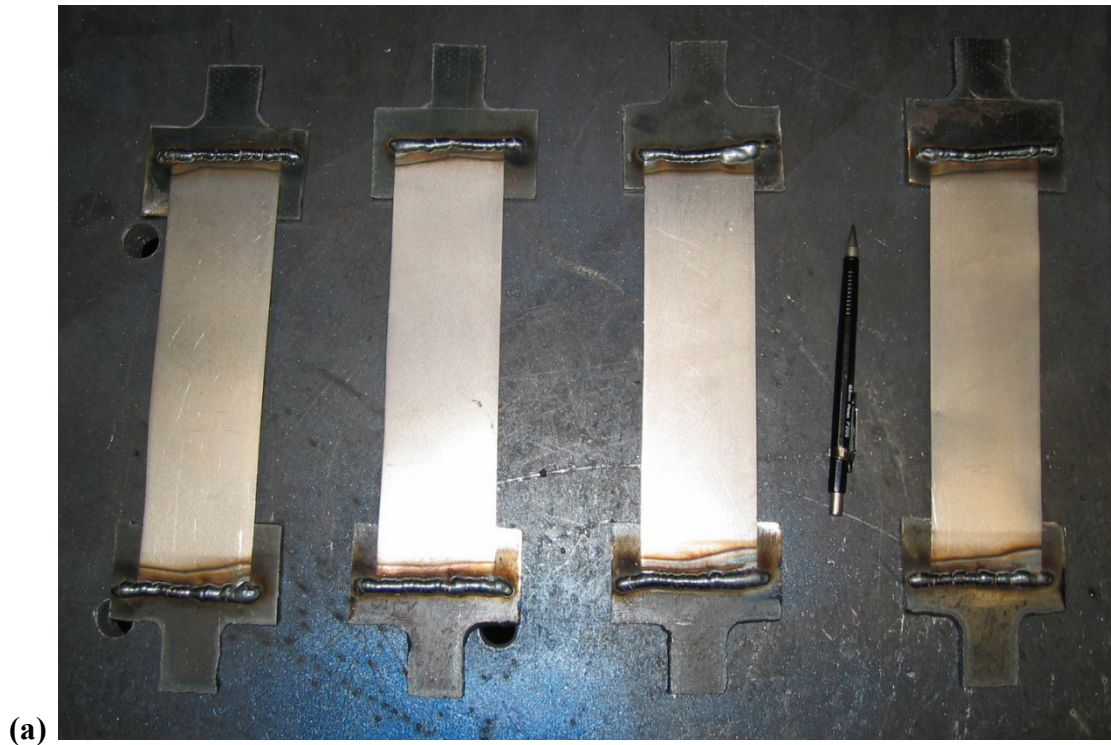
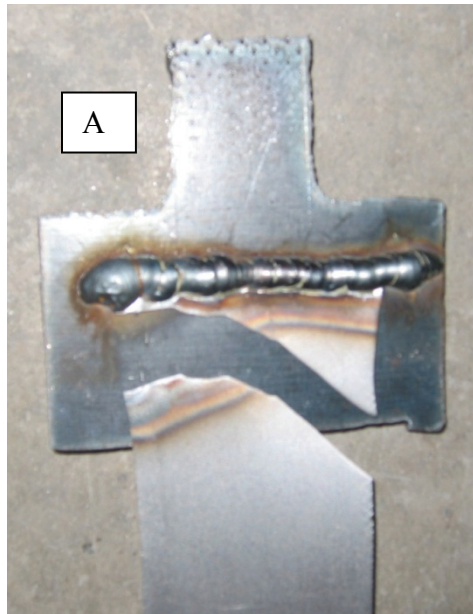
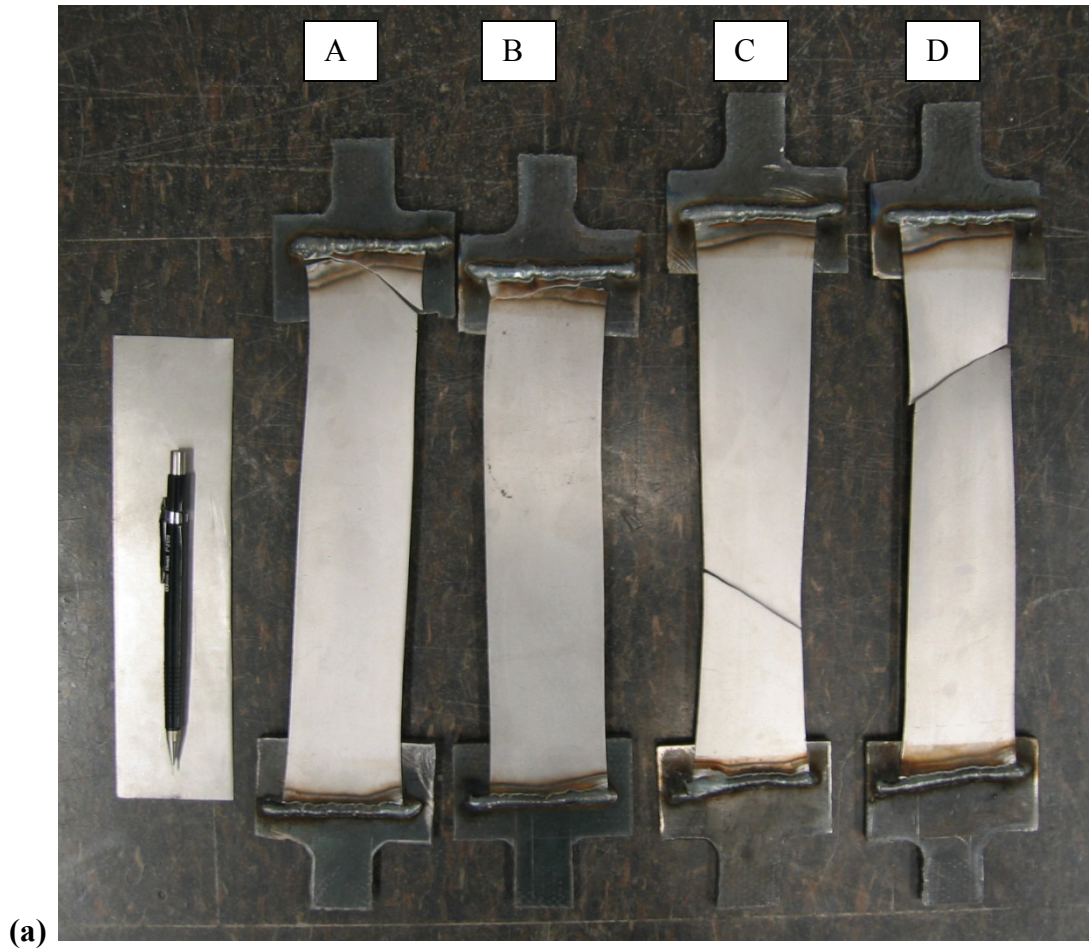


**FIGURE 4-3 Weld connection coupons: (a) coupons; (b) coupon details**



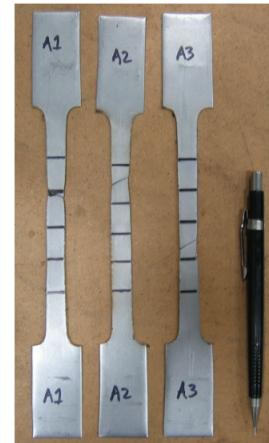
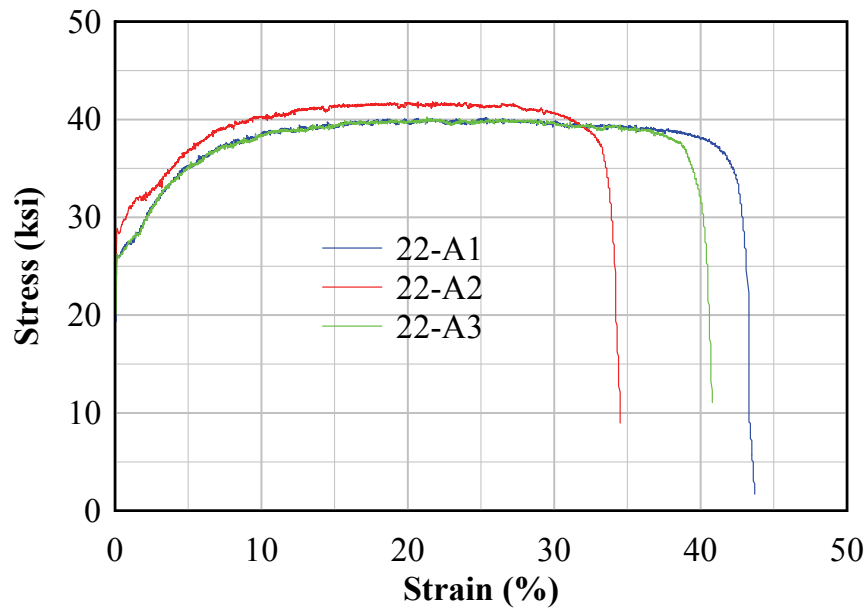
Specimen	$T_{max}$ (kip)	$\Delta_{max}$ (kip)	$F_u$ (ksi)	$\epsilon_{max}$ (%)
A	1.23	1.75	34.4	21.9
B	1.13	1	31.6	12.5
C	1.2	1.75	33.5	21.9
D	1.2	1.75	33.5	21.9

(b) (c)

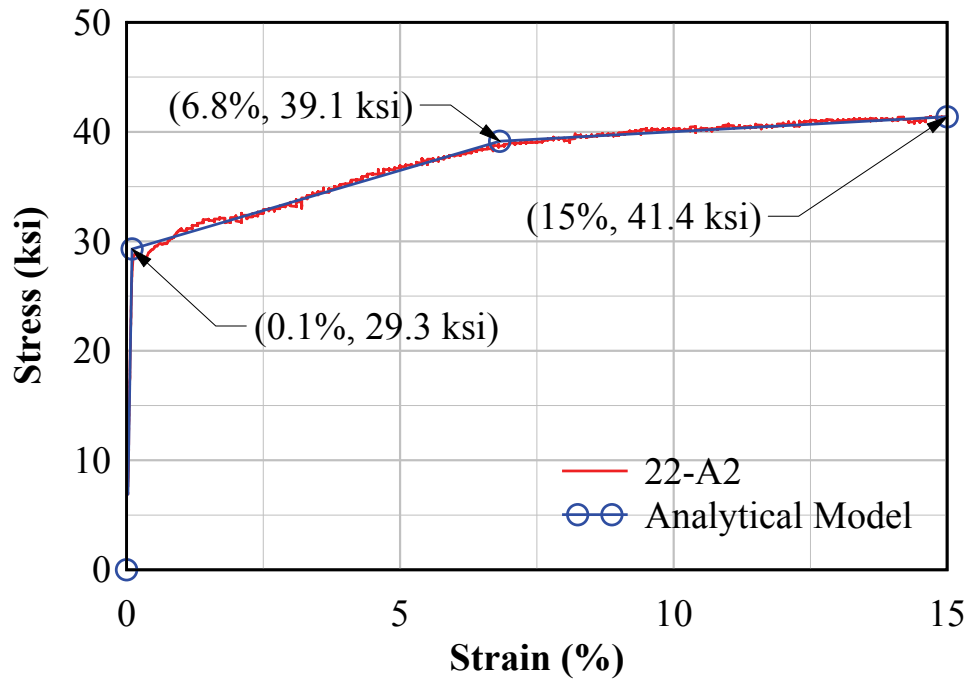
**FIGURE 4-4 Weld-coupon: (a) coupons; (b) fracture example; (c) approximate mechanical properties**



For reasons presented above, the infill web plate mechanical properties obtained in the weld-coupon tests were crude and the testing procedure did not conform to any specific ASTM standard. Consequently, to obtain mechanical properties for use in analytical models specific for the test specimens, additional coupon testing was conducted per ASTM E8. Three coupons were taken from each batch of the 22 GA, 24 GA and 26 GA sheets received from the steel supplier for a total of nine coupon tests. The results are shown in figures 4-5a, 4-6a, and 4-7a for the 22 GA, 24 GA, and 26 GA sheets respectively, along with the photos of the fractured coupons. Note that each of the coupons was marked with horizontal reference lines to visually observe the fracture location, where the topmost and bottommost reference lines indicate the attachment points of the extensometer. Coupons 24-B1, 24-B3, and 26-C3 fractured outside of the extensometer gage length as observed in the figures and were rejected (as it gave incomplete stress-strain curves). From the remaining results, the coupon from each gage thickness that fractured between the extensometer connection points and exhibited the largest strength (i.e., as it represents an upperbound response) was chosen to define the stress-strain model for use in the analytical models. In general, as observed in the figures, for the anticipated tensile strain range for infill web plates of the test specimens (i.e., less than 5% strain), the variation between coupon to coupon is not significant. Figures 4-5b, 4-6b, and 4-7b show the multi-linear stress-strain curves (and the coupon data) used in the analytical models for the infill web plates.

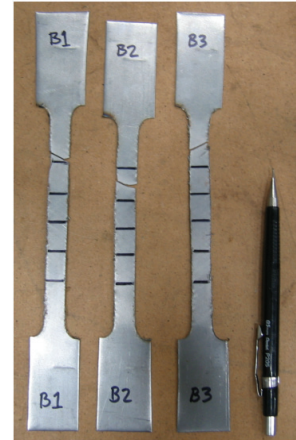
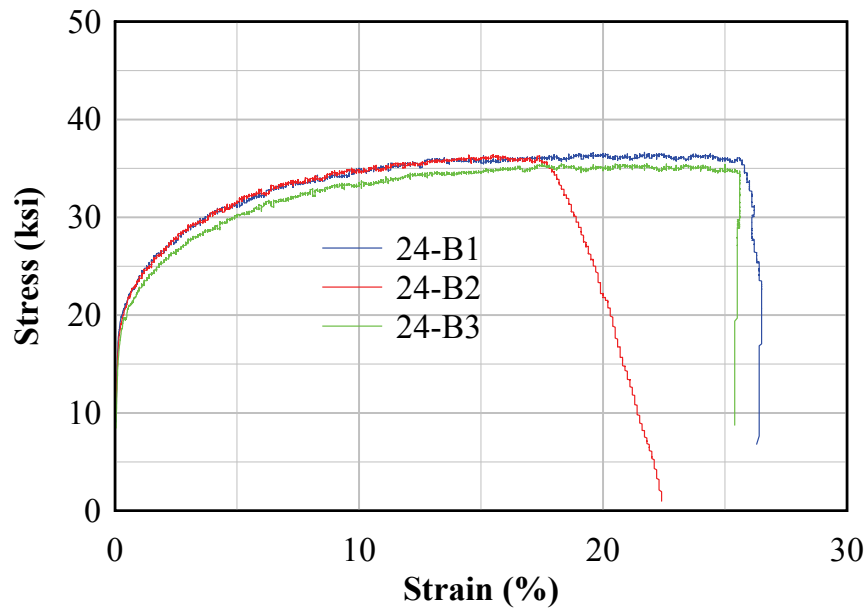


(a)

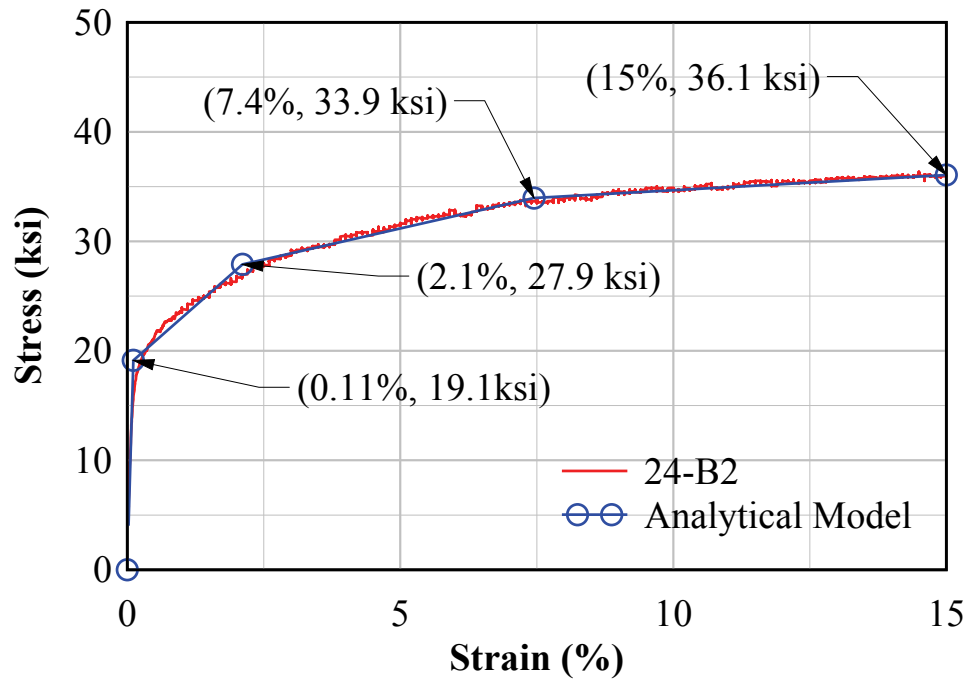


(b)

FIGURE 4-5 22 GA web plate coupon: (a) test data; (b) analytical model

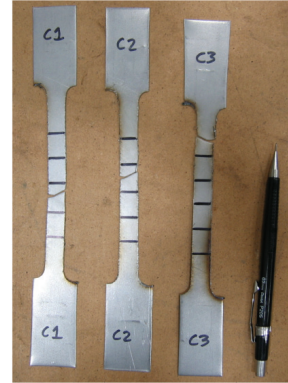
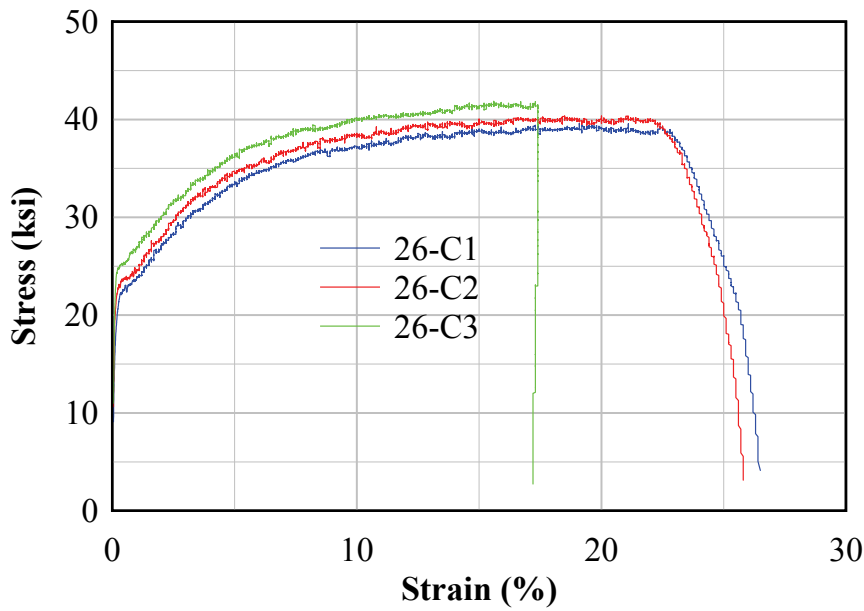


(a)

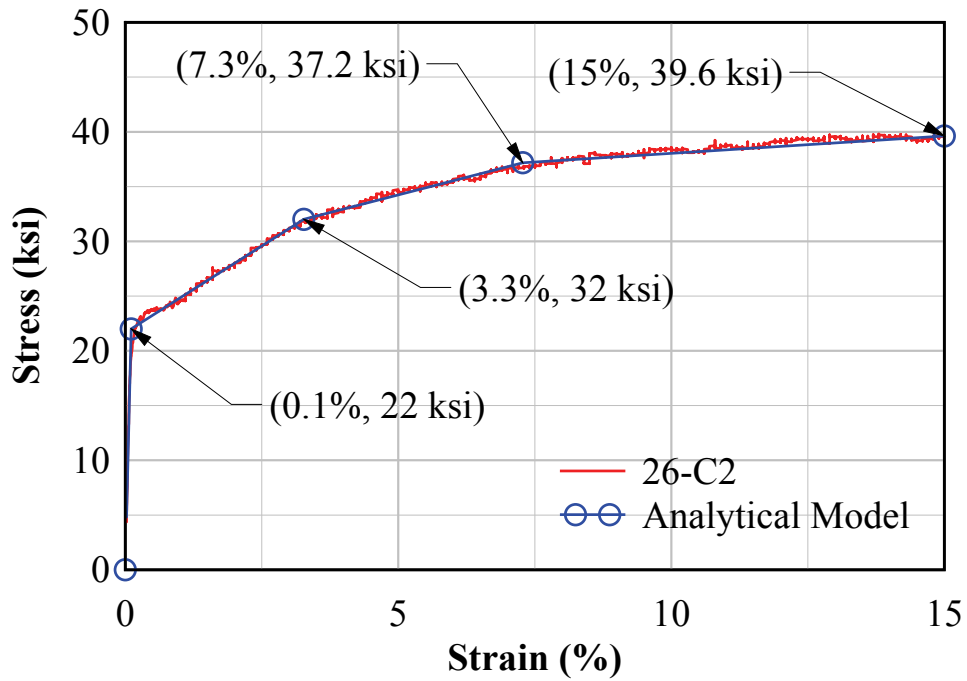


(b)

FIGURE 4-6 24 GA web plate coupon: (a) test data; (b) analytical model



(a)



(b)

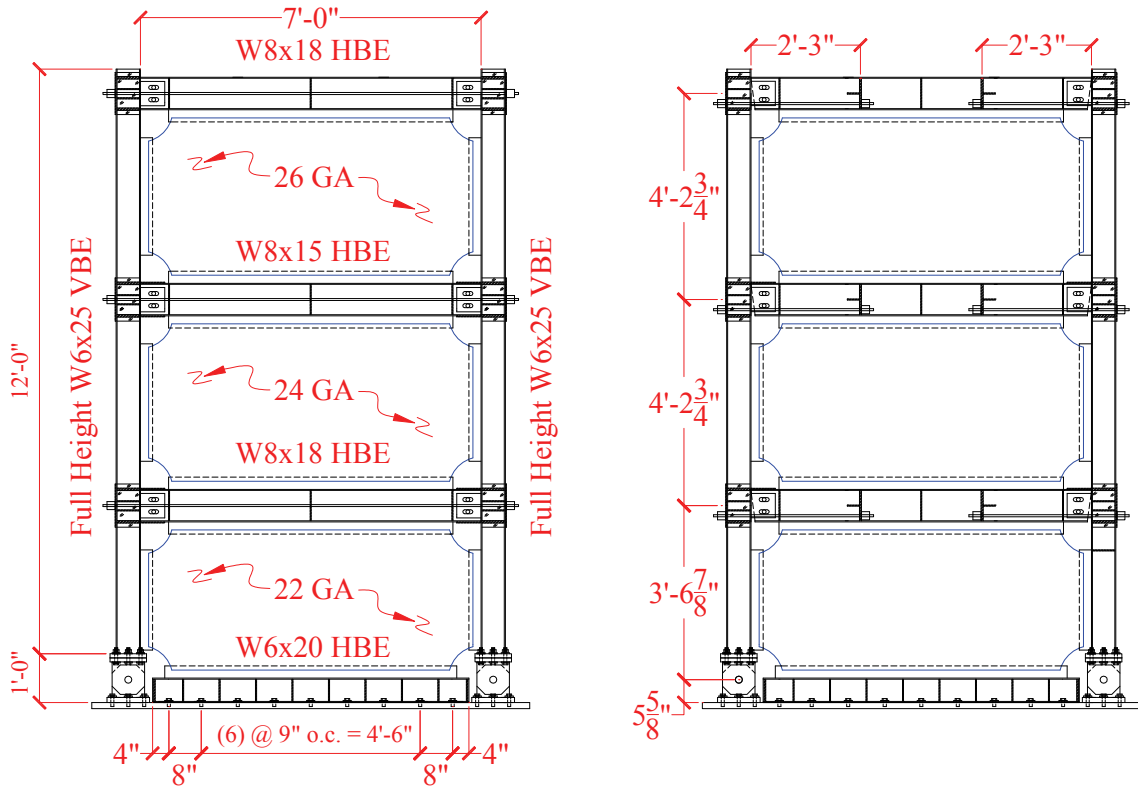
FIGURE 4-7 26 GA web plate coupon: (a) test data; (b) analytical model

Finally, it is observed from the stress-strain curves for the infill web plates used in the experiments, that the stress capacity at 5% strain (corresponding to an upperbound limit on the maximum anticipated strains of the infill web plates during testing) was approximately 36 ksi, 32 ksi, and 35 ksi for the 22 GA, 24 GA, and 26 GA coupons, respectively, which are all below the ultimate tension stress of 36 ksi that was used for the boundary frame design. Coupon tension tests for the boundary frame members and PT strands were not performed as it was expected that these components would remain essentially elastic.

#### **4.2.2.3 Final Design**

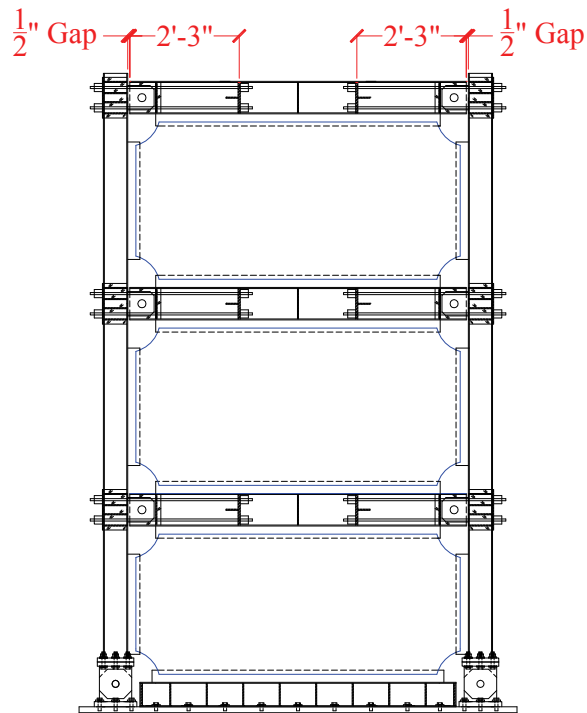
Three different HBE-to-VBE rocking connections were presented in chapter 3 for potential implementation in SC-SPSW systems. For the quasi-static tests, all three were investigated. The final designed test specimen schematics are shown in figure 4-8 and elevation photos of the test specimens in figure 4-9. Steel fabrication was performed off site by a local steel fabricator and then delivered to the SEESL lab where all remaining work was performed (e.g., frame construction, post-tensioning, weld connections of infill web plate, etc.). Details of the three different HBE-to-VBE rocking connections, designated as FR (flange-rocking), NZ (NewZ-BREAKSS), and CR (centerline-rocking), are shown in figures 4-10 and 4-11.

Note that while the floor heights of the test specimens were scaled appropriately, the bay dimension of the test specimens was not at a one-third scale of the prototype frame presented in Section 4.2.1, but actually at one-fourth scale. This was done on purpose to be able to use an existing modular frame test setup (which will be described in Section 5). As a consequence, the distance between the VBEs was dictated by the use of that modular system. For the quasi-static tests, this adjustment does not necessarily distort the test results, as the tests are conducted in displacement control, without being influenced by the characteristics of the prototype building; in that case, the primary purpose of the prototype building was to provide a basis for member sizing and no direct comparison is made to the prototype building (i.e., investigation of the behavior of an SC-SPSW was the primary purpose of the quasi-static tests). On the contrary, this does have an effect on the shake-table tests and will be addressed in Section 4.3.1.



Flange Rocking (FR) Frame

NewZ-BREAKSS Rocking (NZ) Frame



Centerline Rocking (CR) Frame

**FIGURE 4-8 Test frame elevations**

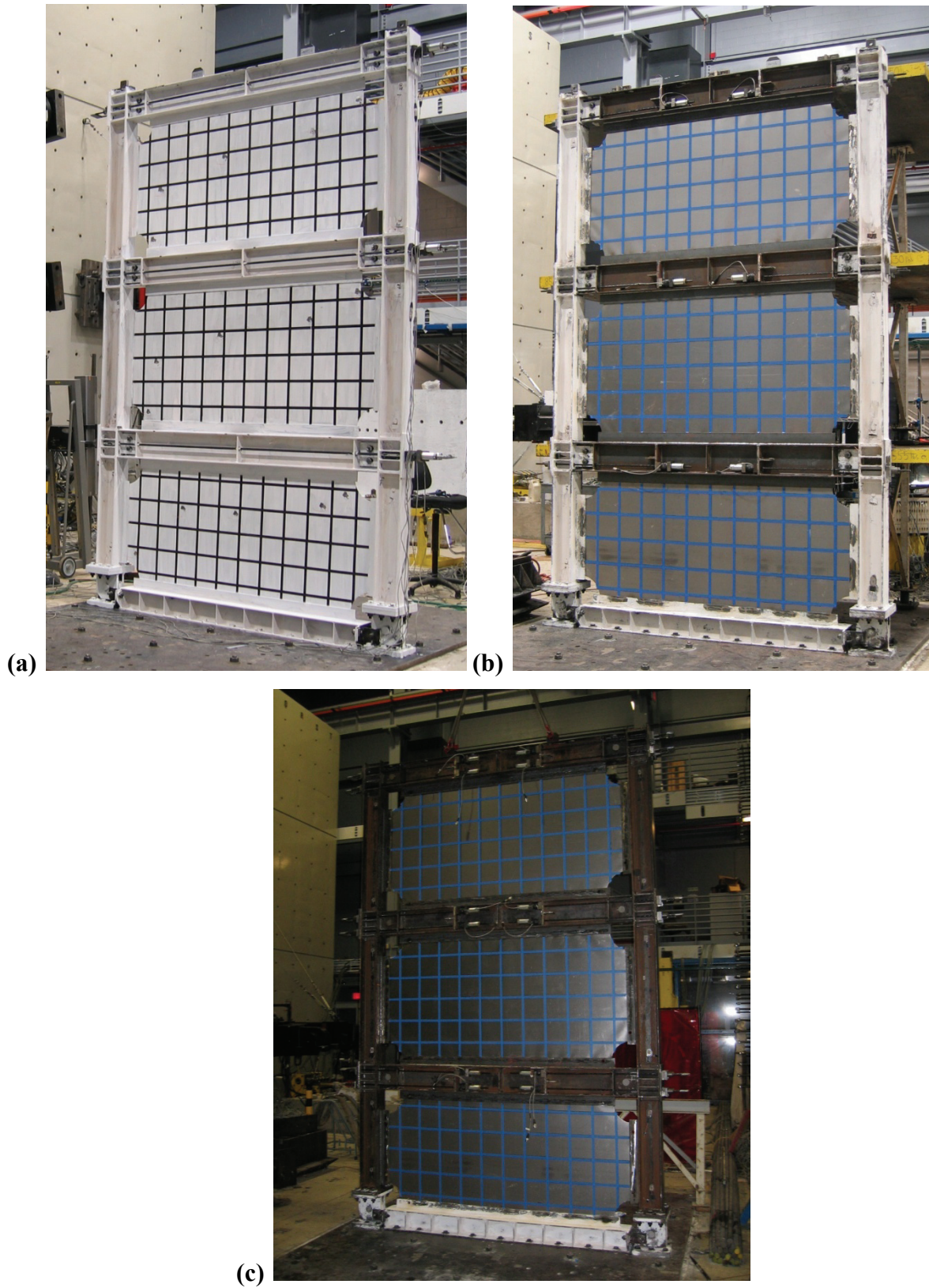
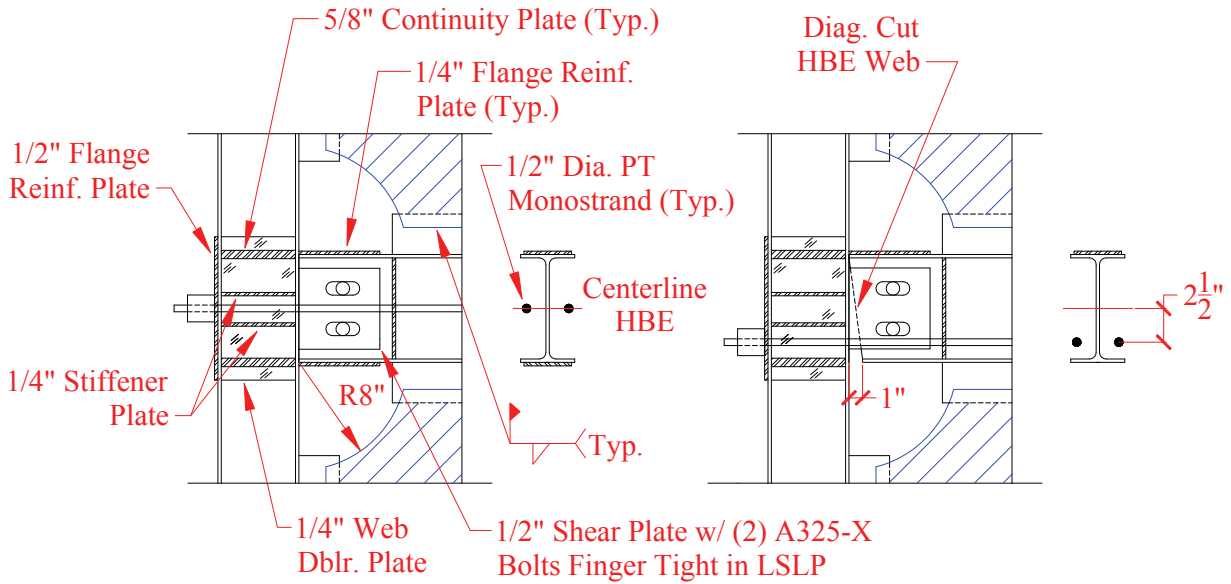


**FIGURE 4-9 Test specimen elevation: (a) FR; (b) NZ; (c) CR**



Flange Rocking (FR)

NewZ-BREAKSS (NZ)

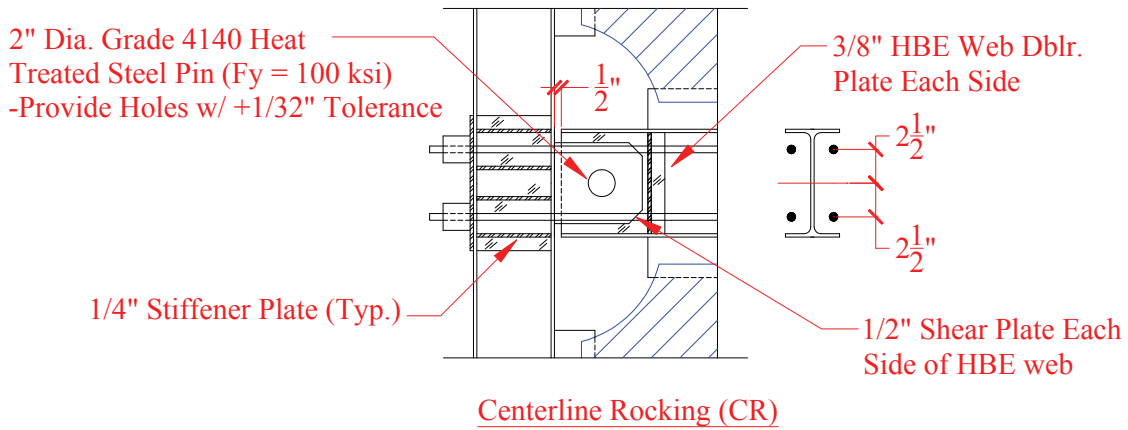


**FIGURE 4-10 HBE-to-VBE joint details**



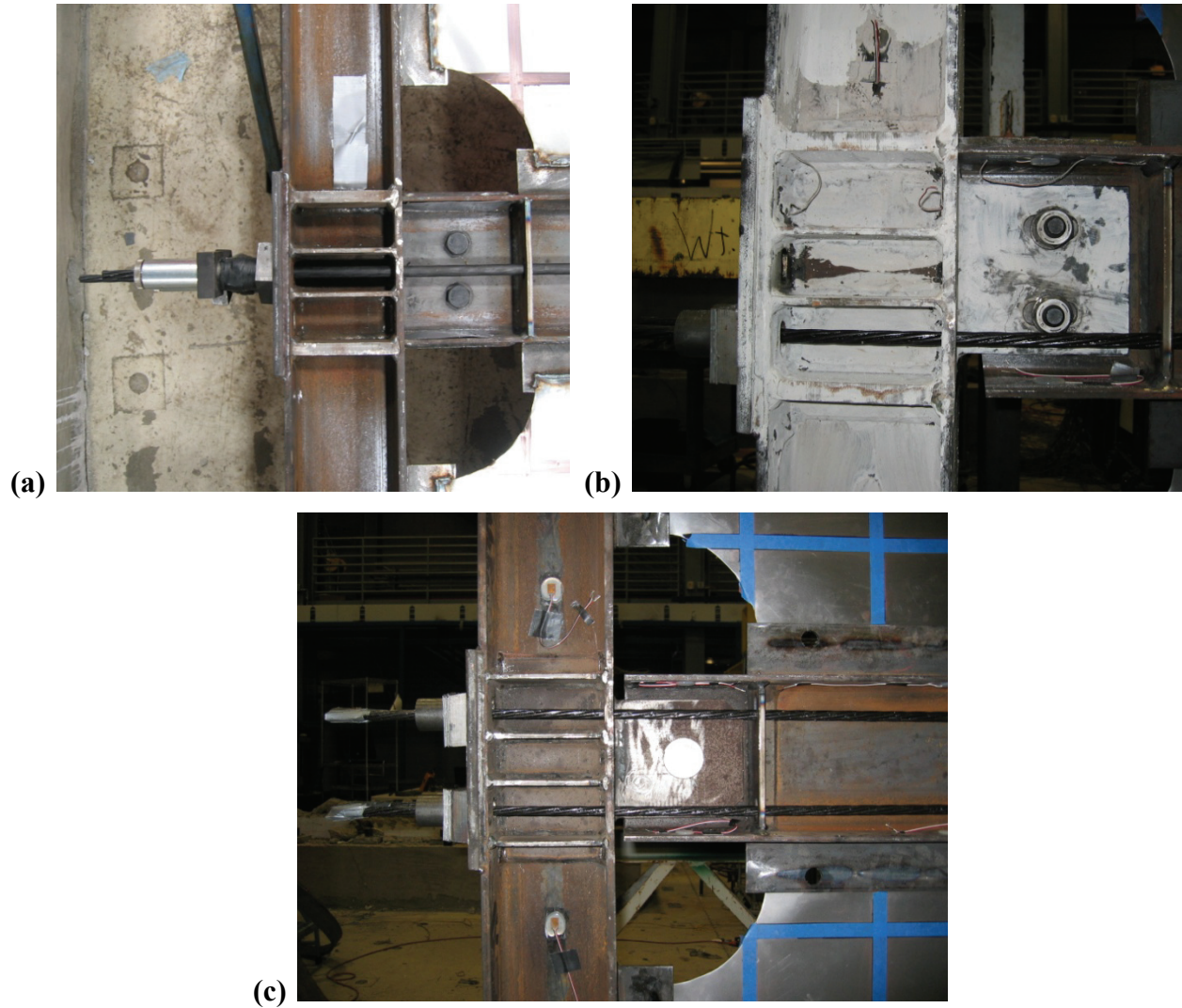
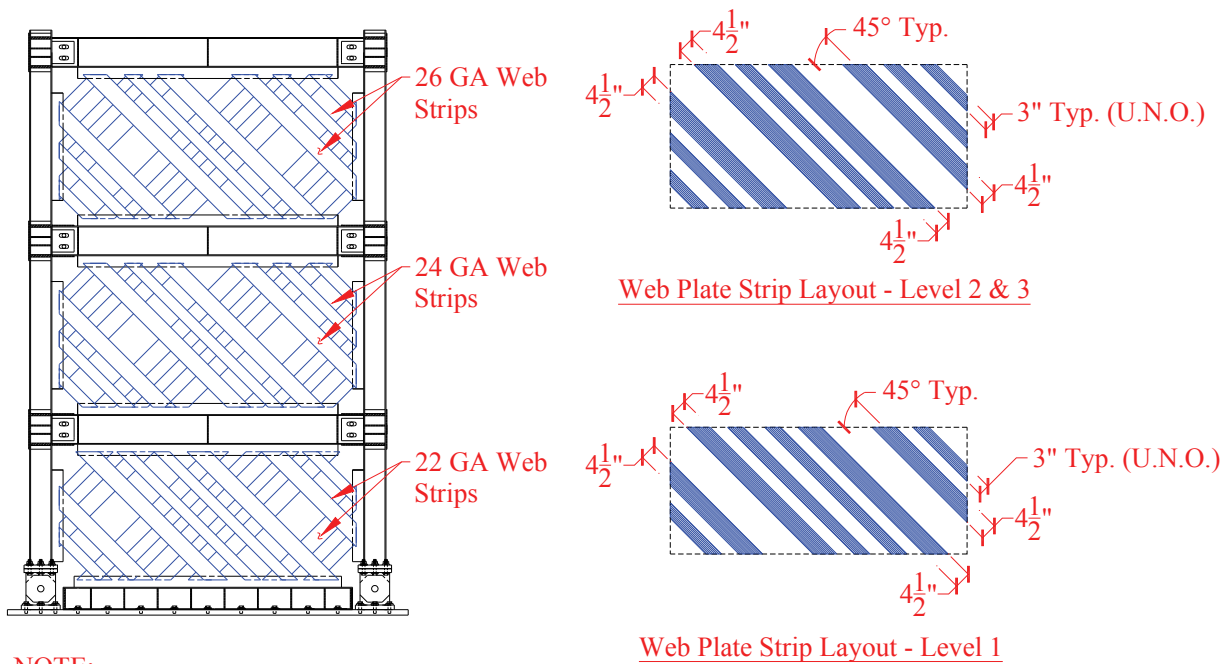


**FIGURE 4-11 Test specimen HBE-to-VBE joint detail: (a) FR; (b) NZ; (c) CR**

Furthermore, for each HBE-to-VBE rocking connection, three different frame configurations were investigated, namely:

1. A full infill web plate configuration (i.e., solid panel), which is the typical construction of SPSW system used in practice.
2. A case without infill web plates, to investigate the response of the PT boundary frame alone.
3. An infill web strip configuration (i.e., individual strips) of the type shown in figures 4-12 and 4-13.

This last configuration was originally conceived as a way to investigate SC-SPSW response while having a better knowledge of the demands from tension-field action, because when using infill web strips instead of solid infill web plates, the angle-of-inclination of the tension field can be precisely known. Here, the gage thickness of the infill web strips at each level was chosen to match that of the corresponding frame using the infill web plates. At the foundation level, a clevis and pin connection was provided at the VBE base to allow free rotation without the formation of a plastic hinge (for reasons discussed in Section 1). Furthermore, an anchor beam bolted to the foundation anchor plate was provided for connection of the infill web plates. Details and photos are shown in figures 4-14 and 4-15, respectively. To differentiate the different infill web plate configuration for each test specimen, the following acronyms will be used (and appended to the “frame type” designation/label): W = full infill web plate, B = no infill web plate, corresponding to a bare frame condition, and S = infill web strips. As examples of frame designations/labels: FRW = flange-rocking frame with infill web plate, NZB = NewZ-BREAKSS frame with no infill web plate, CRS = centerline rocking frame with infill web strips.



NOTE:  
FR Frame Shown; NZ & CR Frames Similar

**FIGURE 4-12 Test frame with web strips**

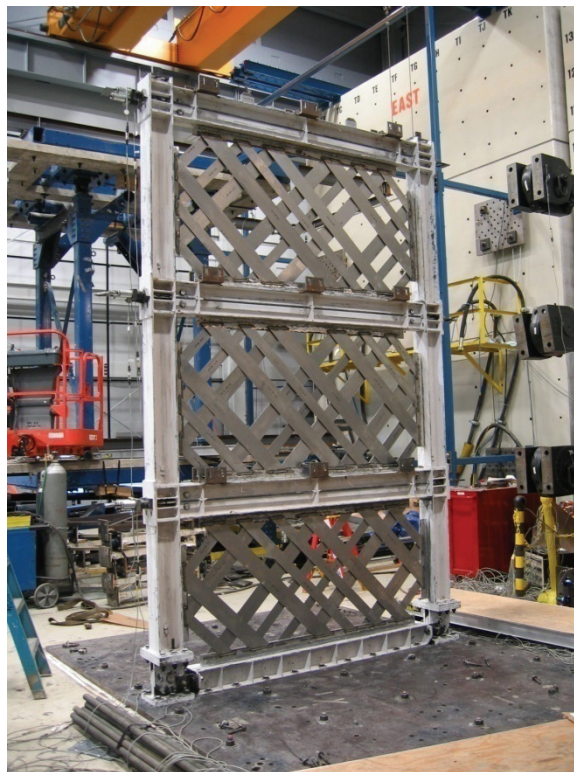


**FIGURE 4-13 Test specimen with web strips**

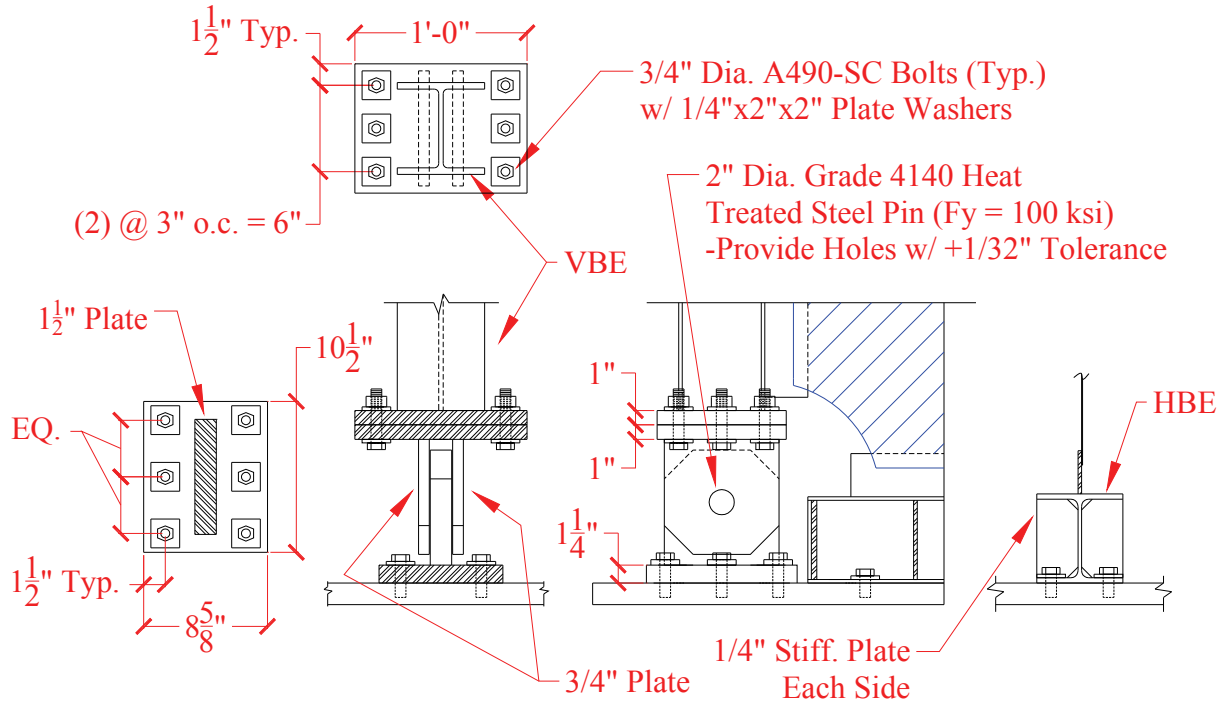


**FIGURE 4-14 Foundation anchorage**

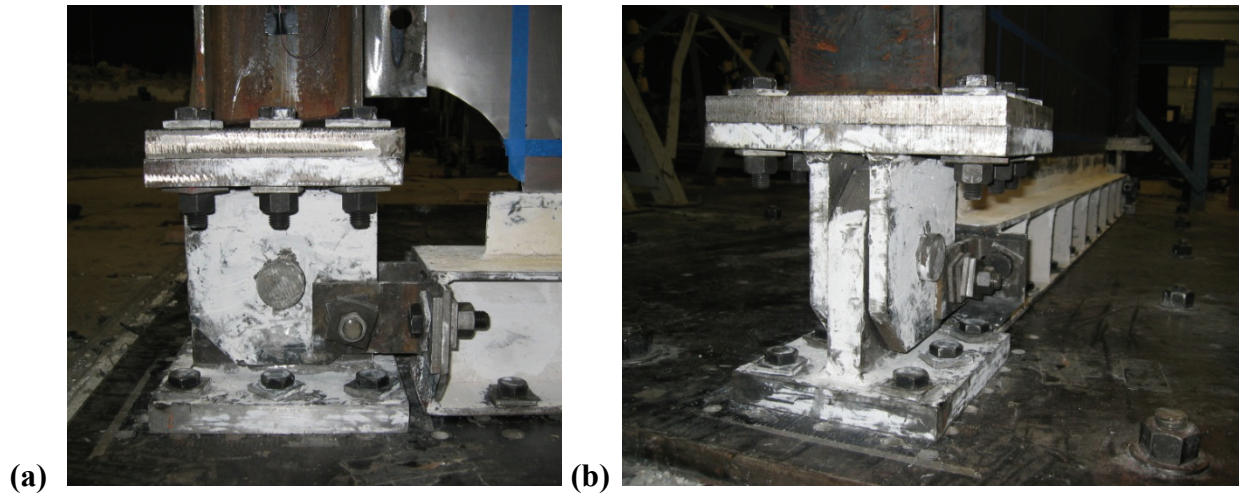


**FIGURE 4-15 Test specimen foundation anchorage: (a) side view; (b) front view**

Note that some elements of the boundary frames were detailed to be shared between different frame configurations. More specifically: i) the FR and NZ frames shared the same VBEs between test series; and ii) all three frames shared the VBE clevis and pin base connection and HBE anchor beam. Hints of that re-use of members can be seen in figure 4-9, which show some SC-SPSW frames having already white washed members after being assembled: The FR frame tests were conducted first, followed by the NZ frame tests that re-used the same VBEs (already white washed from previous test series), and finally the CR frame tests that reused the VBE clevis and pin base, and the anchor beam. Furthermore, note that all boundary frames were reused for the different infill configurations; only the infill web plates/strips were removed and replaced between each subsequent test.

### **4.2.3 Analytical Results**

The programs OpenSees (Mazzoni et al. 2009) and SAP2000 (CSI 2009) were used for analytical modeling of the test specimens. The former is an open-source code mainly used by the research community. The latter is a commercially available software program used in common practice by design professionals. Both have their particular advantages. Accordingly, both programs were used interchangeably depending on the particular task performed. The analytical models of the test specimens are shown in figure 4-16 using a tension-only strip model approach for the SPSW web plate (Sabelli and Bruneau 2007). The specifics of the modeling parameters of each SC-SPSW frame type were presented in Section 3. To provide some comparison of the software programs, a cyclic nonlinear static analysis of the model specimens was performed and is shown in figure 4-17. The results are comparable; the minor differences for the particular models are due to the inherencies of each program. Unless specifically noted otherwise, all analytical results presented are performed using OpenSees.

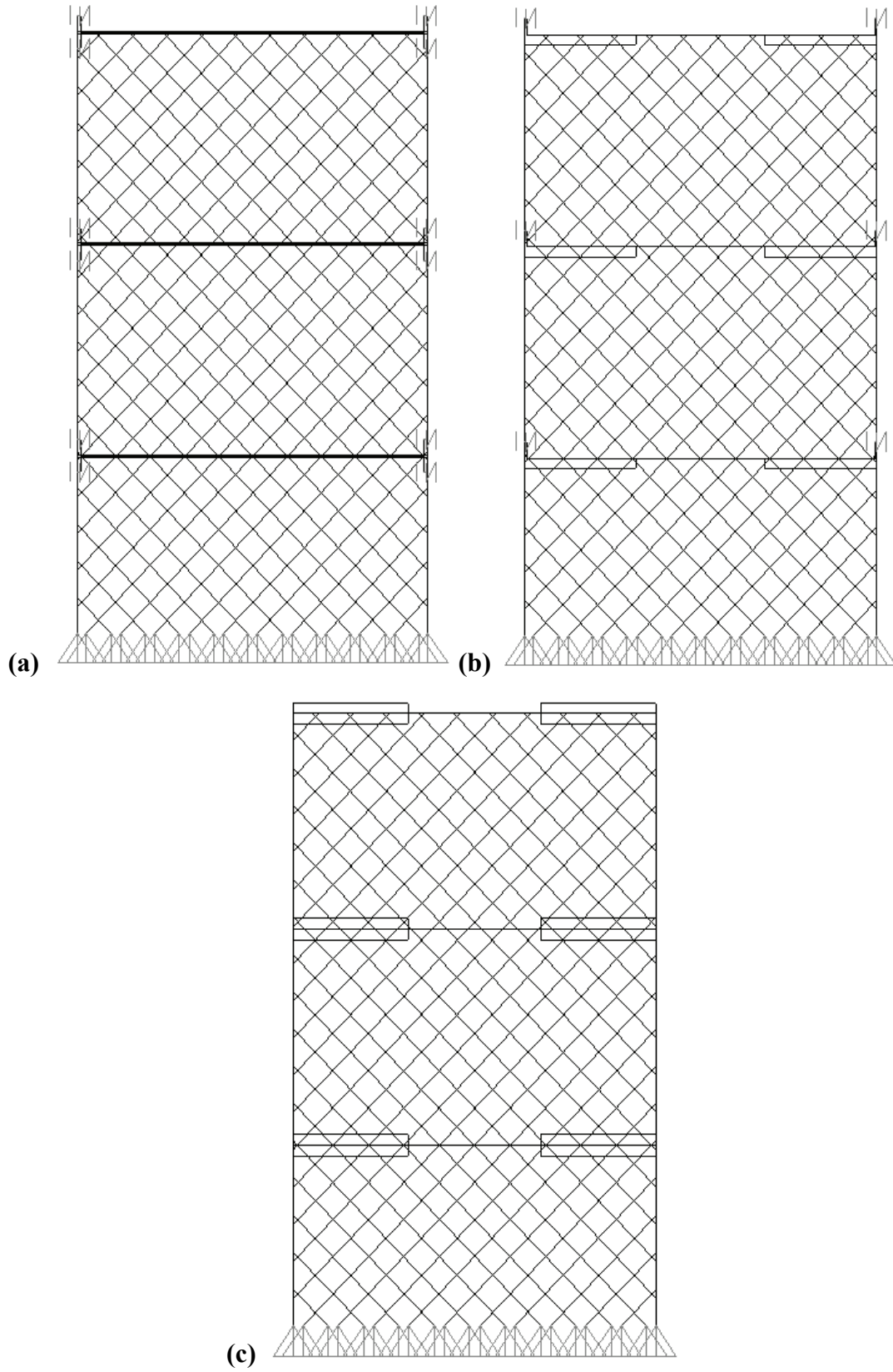


**FIGURE 4-16 Analytical model frames: (a) FR; (b); NZ; (c) CR**

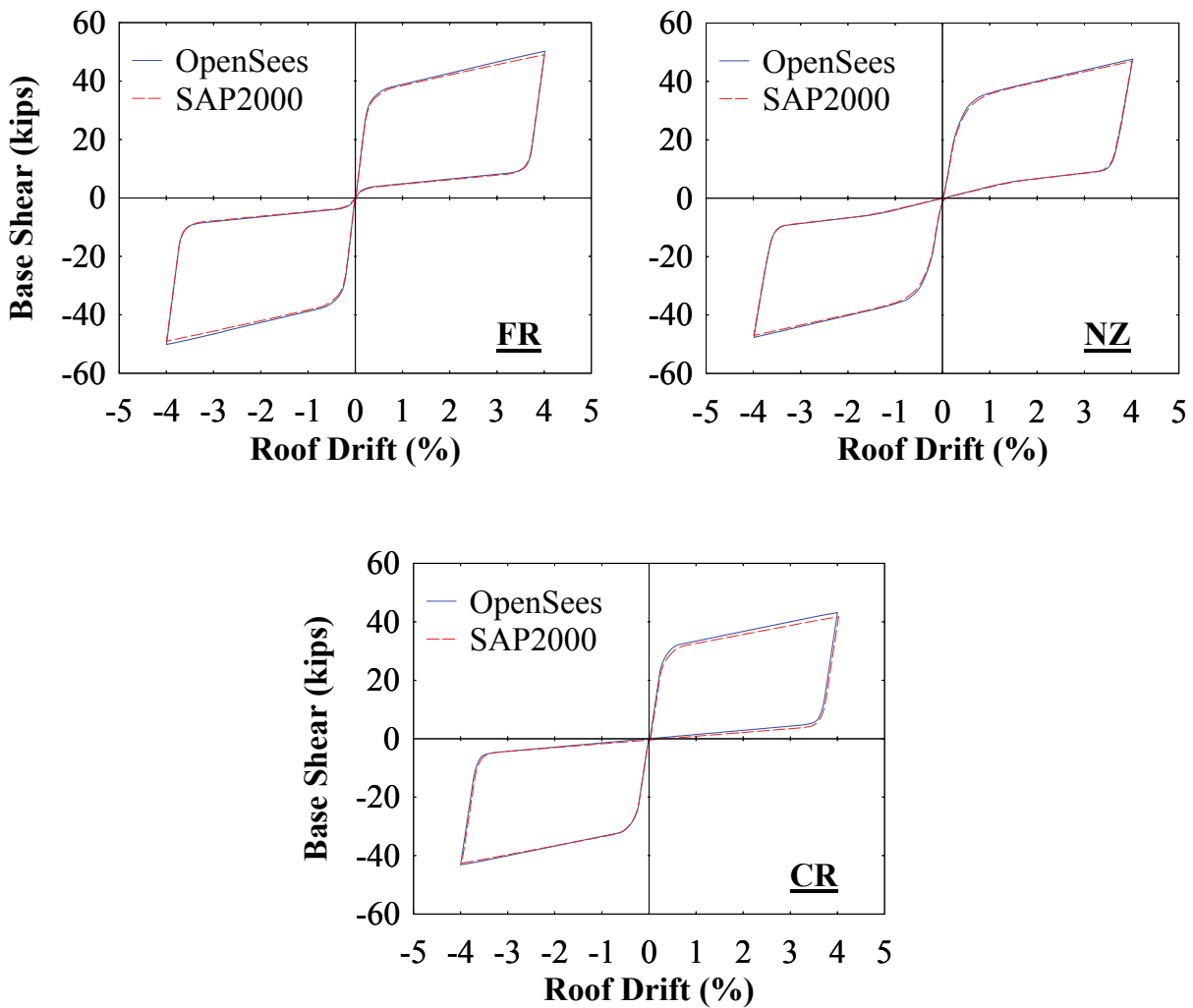


**FIGURE 4-17 OpenSees versus SAP2000: base shear versus roof drift**

#### 4.2.3.1 Test Specimens

The analytical hysteretic response for the quasi-static test frames are shown in figure 4-18 for a 4% roof drift (as a representation of a typical response) for both the infill web plate and strip configuration. An initial post-tensioning force,  $T_0$ , of approximately 20% of the PT yield strength was targeted for the FR and NZ frames where the PT yield strength,  $F_{yPT}$ , was assumed to be 90% of the ultimate tensile strength,  $F_{uPT}$ , of the PT strands; for the CR frame approximately 30% was provided. The larger initial PT force provided for the CR frame is a reflection of the smaller eccentricity of the PT from the rocking point, compared to the other two frames. As shown in figure 4-10, the distance from the rocking point to the centerline of the PT

elements is approximately 4.25 in., 6.5 in., and 2.5 in. for the FR, NZ, and CR frames, respectively. The smaller eccentric distance to the PT for the CR frame was controlled by detailing constraints of the boundary frame members. In particular, the eccentricity of 2.5 in. provided was the most that could be provided to accommodate the PT anchorage detail located on the HBE webs; a larger eccentric distance would have been provided if detailing constraints had allowed it. To help compensate for this shortcoming, a larger initial PT force was provided. Since the PT force demand generated during frame drift was calculated to be smaller in the CR frame (due to smaller eccentric distance to PT), the larger initial PT force could be provided without concern of (potentially) yielding the PT elements at large drifts compared to the other frames. Furthermore, in the analytical models, no superimposed gravity loads was applied on the frame (i.e., to reflect the testing conditions).

As observed from the analytical predictions in figure 4-18, for a tension-only strip model, re-centering is perfectly achieved given that the point on the hysteresis curve at zero drift also corresponds to a base shear demand of zero (as should be expected when modeling hysteretic elements as tension-only members). Note that the strength of the frames having infill web strips is approximately half of the corresponding frame with a solid infill web plate. Since thicknesses of infill web strips was identical to those of their corresponding solid infill web plates, the base shear strength of the frames with infill web strips is proportional to the width of infill covered by the strips (i.e., approximately 50% of the solid infill web plates was removed as a result of the space left between the strips). Furthermore, note that in these analytical models, all of the hysteretic response is provided by the infill web plate (i.e., boundary frame members were modelled as elastic, since they were designed as such).

Since the three frames analyzed were identical except for the differences in the HBE-to-VBE joint connection and the corresponding PT configuration, the noticeable differences in system response between the three frames arise from the different effect of the PT boundary frames. To highlight these differences, figure 4-19 shows the PT boundary frame response (which is bilinear elastic) superimposed with the total response, and figure 4-20 shows the individual response of the infill web plate and boundary frame separately.



In figure 4-20a, response of the infill web plates, although not significantly different, are not identical for all the frames (even though the infill web strip model layout and mechanical properties themselves are). It is observed that the NZ and CR frames closely match; differences are most noticeable in the initial stiffness, where in fact the NZ frame is slightly stiffer for the design parameters used. However, the web plate response for the FR frame is noticeably different than both the NZ and CR frames, with slightly larger initial stiffness and strength. These differences arise due to the HBE-to-VBE joint kinematics of the different boundary frames (Section 3.4). In particular, the corner strains for the FR and NZ frame are larger than the CR frame at the opening joint location as the distance from the rocking point to the connection of the web plate is largest (i.e., depth of HBE for FR and NZ frames, and one-half depth of HBE for CR frame); these larger strains lead to larger strength demands of the infill web plate at those locations. Furthermore, overall strength demands on the infill web plate are larger for the FR frame than for the NZ frame since the FR frame has an opening joint each end of the HBEs, and NZ frame only has one for any given drift.

From figure 4-20b, with respect to response of the PT boundary frame alone, it is observed that the FR and NZ frames are bilinear elastic; while the CR response is linear elastic (but in some circumstances can be bilinear as will be shown subsequently). Furthermore, the CR frame is approximately half the strength of the FR and NZ frames; this will be addressed in Section 4.2.4.2.

Given that the observed differences in overall SC-SPSW behavior are related to the response of the PT boundary frame (i.e., since the response of the infill web plate is essentially the same for all three different frames), and the fact that the PT boundary frame responses shown in figure 4-20b depend on the specifics of particular designs and can change depending on the PT parameters provided, some sensitivity analyses were conducted to assess how some parameters affect behavior. These are presented in the following sections.

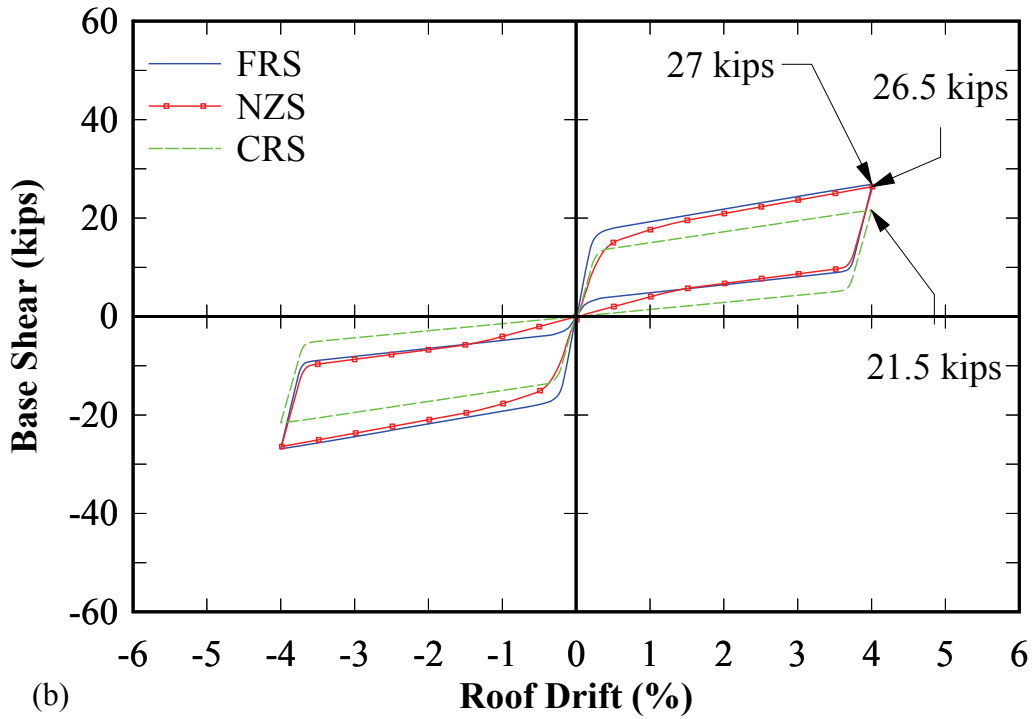
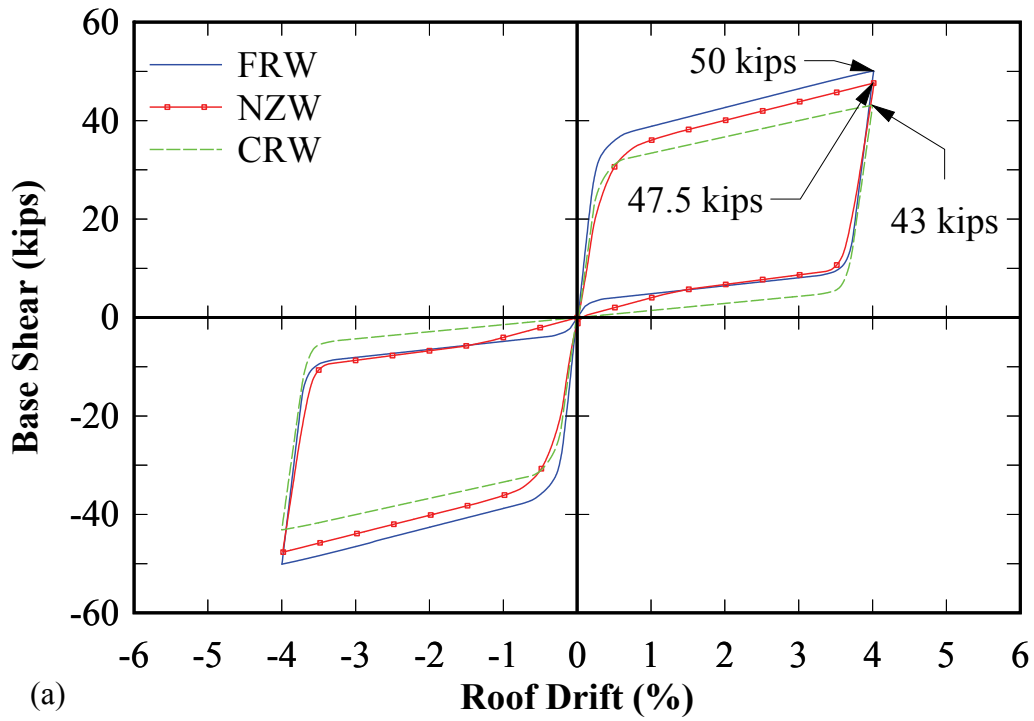
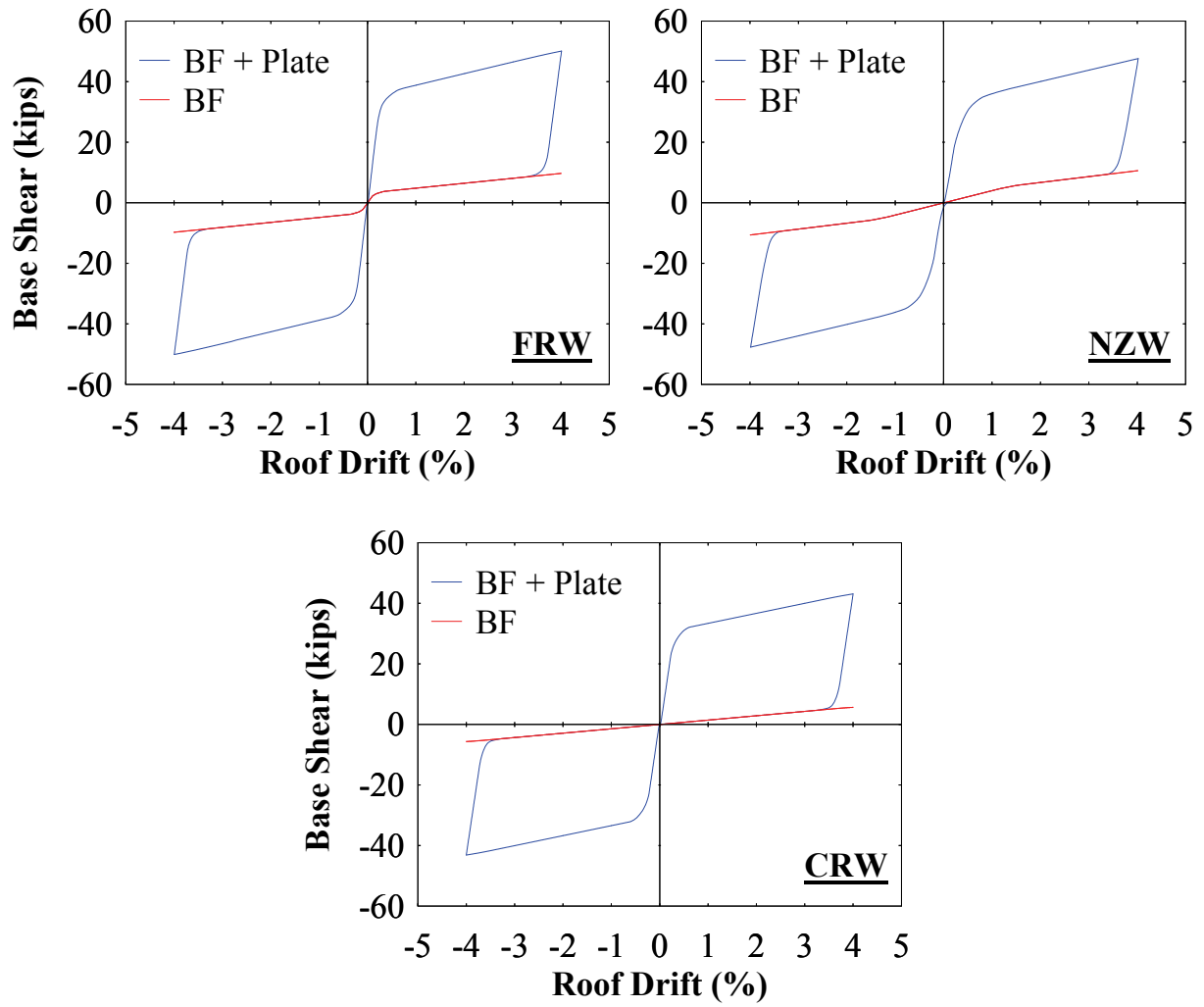
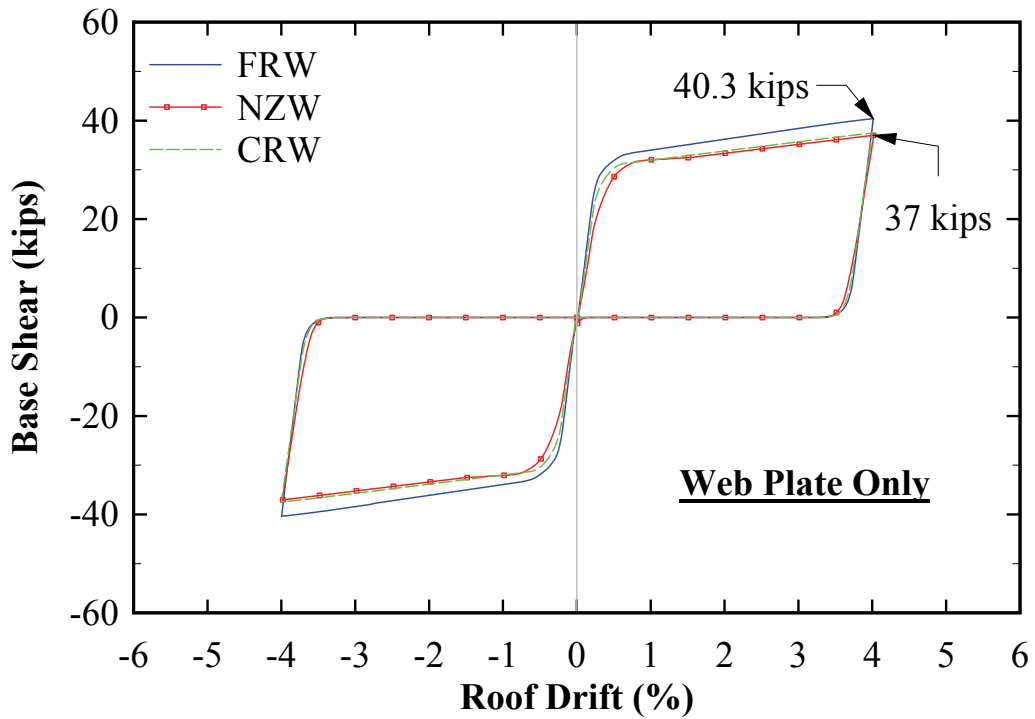


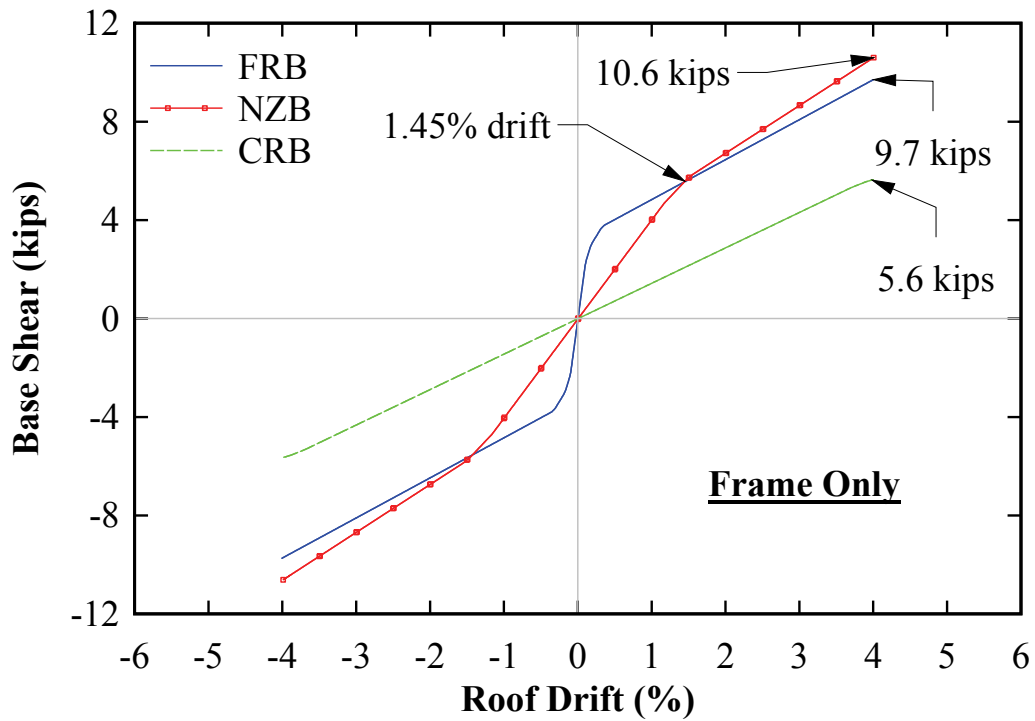
FIGURE 4-18 Quasi-static test analytical response: (a) infill web plate; (b) infill web strips



**FIGURE 4-19 PT boundary frame versus Total response**



(a)



(b)

FIGURE 4-20 Response components: (a) infill web plate; (b) PT boundary frame

#### 4.2.3.2 Frame Response Comparisons: General

To further illustrate these differences and highlight general characteristics in behavior, monotonic pushover curves for the three different PT boundary frames are shown in figure 4-21 (note that these pushover curves are for the same frames, with same design parameters, as those for which the response curves were presented in figures 4-18 to 4-20). The following observations are made:

- 1) The FR frame has a bilinear behavior, with the two linear stiffnesses,  $K_1$  and  $K_2$ . The first stiffness occurs when the HBE-to-VBE joints are in full contact compressed together by the initial PT force provided as part of the frame design; upon lateral frame loading, the initial PT force decreases as a result of decompression of the HBE-to-VBE joints during frame drift. The second stiffness occurs when the HBE-to-VBE joint just opens and the initial PT force is no longer present, where the presence of an initial PT force and a lever arm from the PT centroid to the HBE-to-VBE rocking point generates a moment, commonly referred to as the decompression moment (also see Section 2.3.1). From this point (when the decompression moment is zero), all subsequent PT force demands are from strand elongation due to increased drift.
- 2) The NZ frame is also bilinear, however with different stiffnesses,  $K_3$  and  $K_4$ . Along the initial stiffness, upon loading, the initial PT force with increase and decrease as a function of HBE-to-VBE joint opening and closing, respectively. The second stiffness occurs when the PT at the closing joint becomes fully relaxed.
- 3) The CR frame also has a bilinear response with different stiffnesses  $K_5$  and  $K_6$ , developing for same reasons as those described for the NZ frame. In figure 4-21, the monotonic pushover analysis was extended up to 5% drift to reach the point when the PT at the closing joints became fully relaxed (corresponding to development of the second stiffness). Note that for the CR frame, at each end of the HBE, there exist both an elongating and shortening PT element (i.e., the PT at the top and one at the bottom of the HBE acting in opposite manner). Also note that this bilinear response was not observed in figures 4-18 to 4-20 for the CR frame because the boundary frame was not subjected to sufficiently large drifts in those figures.

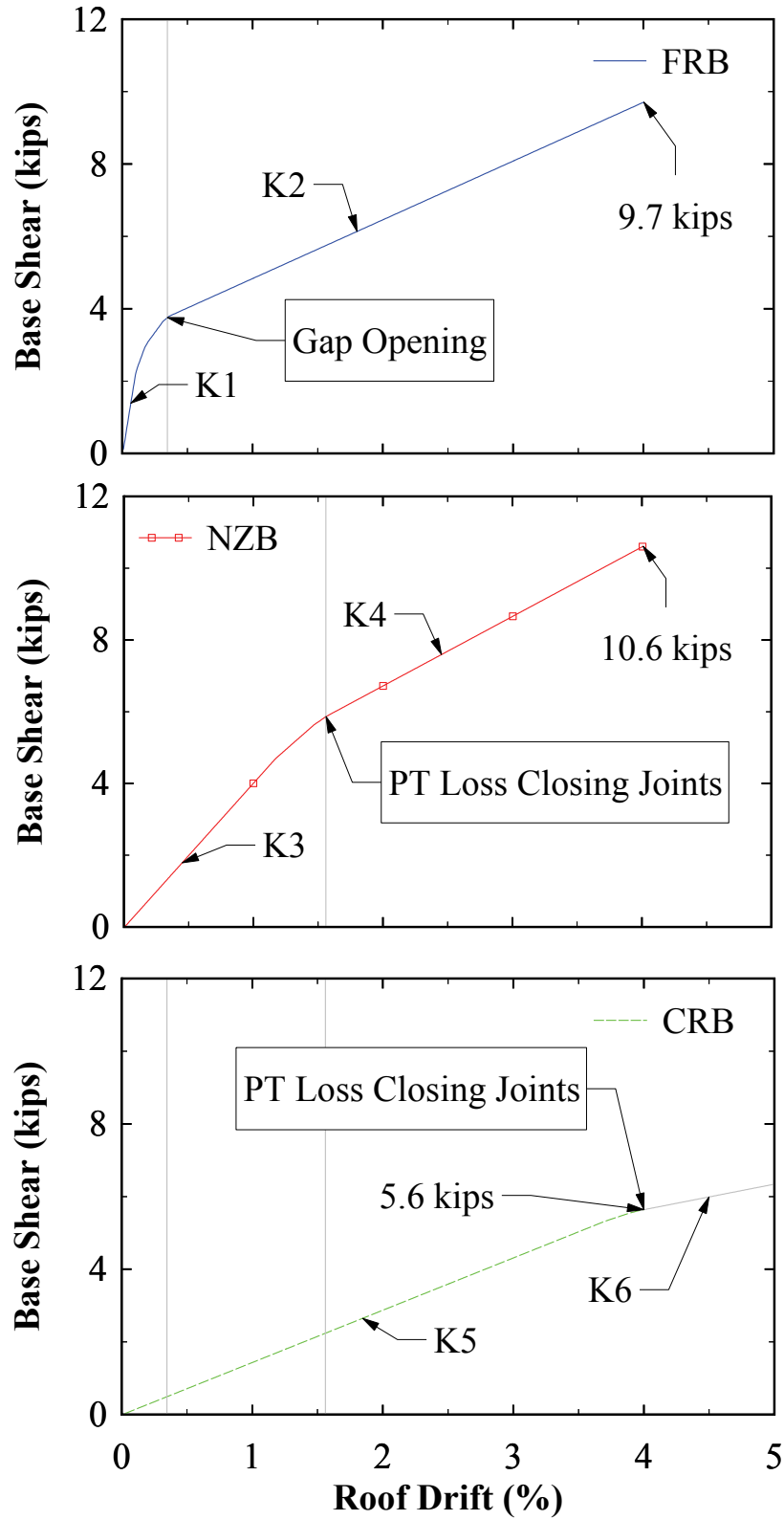


FIGURE 4-21 PT boundary frame - Monotonic pushover comparison

For the FR and NZ curves presented, the quantity of PT strands and initial PT force provided are identical. For this reason, a side-by-side comparison (of those curves shown in figure 4-21) can be made for these two frames for this condition. It is observed that the initial stiffness of the FR frame is the larger of the two (i.e.,  $K1 > K3$ ). This is due to the presence of the decompression moment effects inherent with the FR frame. However, for the second stiffness, the NZ frame is stiffer (i.e.,  $K4 > K2$ ) due to the fact that the PT strands on the NZ frame are shorter. With respect to frame recentering, a large initial stiffness provides a more efficient use of the PT, given that a SC-SPSW subjected to hysteretic loading unloads back to the origin displacement following the bilinear elastic stiffness of the boundary frame (figure 4-19). To illustrate, by comparison of recentering, starting from the peak positive drift position, the NZ frame response closely matches that of the FR frame at the second stiffness (i.e., the curve segments are almost on top of each other), down to approximately 1.45% drift when the NZ frame quickly loses stiffness and strength due to the lower initial stiffness (figure 4-20b). Thus, from figure 4-20b, it is observed that the FR frame provides the best recentering ability for the full cyclic response as a result of its larger initial stiffness. Note that for the CR frame, even though the initial PT force provided was the largest (for the same number of PT strands), it has the lowest stiffness and strength of the three frames. This is due to the much smaller eccentricity of the PT strands, as noted earlier, and its effects will be addressed in Section 4.2.4.2.

#### **4.2.4 Frame Response Investigation**

##### **4.2.4.1 Effects of Post-Tension Parameters**

To investigate the effects of various PT parameters on the response of the boundary frame, the variation in frame response when changing the initial PT force ( $T_0$ ) and the quantity of PT strands ( $A_{pt}$ ) is presented, using the UB test frames as an example for illustration purposes. In the following figures, response curves for the condition labeled  $1 \times T_0$  and  $1 \times A_{pt}$  corresponds to the PT design parameters used in the UB specimens (as a reference). In this investigation, note that: 1) all other design parameters (i.e., member sections, distance of PT eccentricity to the rocking point, etc.) remain the same, as changing those would require other design changes, and; 2) practical considerations of construction tolerances are not considered, as only the consequences of relative change in response are of interest here. Furthermore, this investigation

is only made for the PT boundary frame, with the understanding that the total response is a superposition of the effects of the PT boundary frame and the infill web plate (figure 4-20).

In figure 4-22, the variation in response due to  $T_0$  as the parametric variable is presented, with all other parameters held constant. Note that if significant PT yield occurs for a given  $T_0$ , no additional parametric curves are presented for that frame, as only the elastic response of the boundary frame is of interest here (i.e., no yielding of PT elements; which would alter the frame response). It is observed that with  $T_0 = 0$  kips (i.e.,  $0 \times T_0$ ), the frame response moves along a single elastic curve; it is the presence of an initial PT force that defines the bilinear frame response. This observation was made earlier, but is shown here for reference. Also note that the second stiffness for the different frames considered is equal to their respective stiffness for  $0 \times T_0$  (since the second stiffness represents the condition when the initial PT force effects are no longer present). Of significance, it is observed that the magnitude of  $T_0$  defines the location of the transition point between the two response stiffnesses (as shown in figure 4-21). More specifically, increasing the initial applied PT force results in: 1) a positive shift of that transition point along the horizontal axis, resulting in an increase of the initial stiffness range of response which has the largest stiffness along the bilinear response curve, and; 2) a positive shift of that transition point along the vertical axis, contributing more strength to the hysteretic response of the entire system. Note that for the CR curves, responses for the cases  $1 \times T_0$  and  $2 \times T_0$  are identical (both curves are on top of each other), but this is largely because drifts considered were not large enough to develop the second stiffness for the original CR frame design (i.e., the  $1 \times T_0$  condition). Consequently, since  $T_0$  only affects the location of the transition point between the stiffness on the bilinear response curve, increasing  $T_0$  has no effect up to the drift condition shown in figure 4-22. Also note that the strength for  $3 \times T_0$  response is less than at  $2 \times T_0$ ; this is due to the fact that PT yielding occurred for the former case.



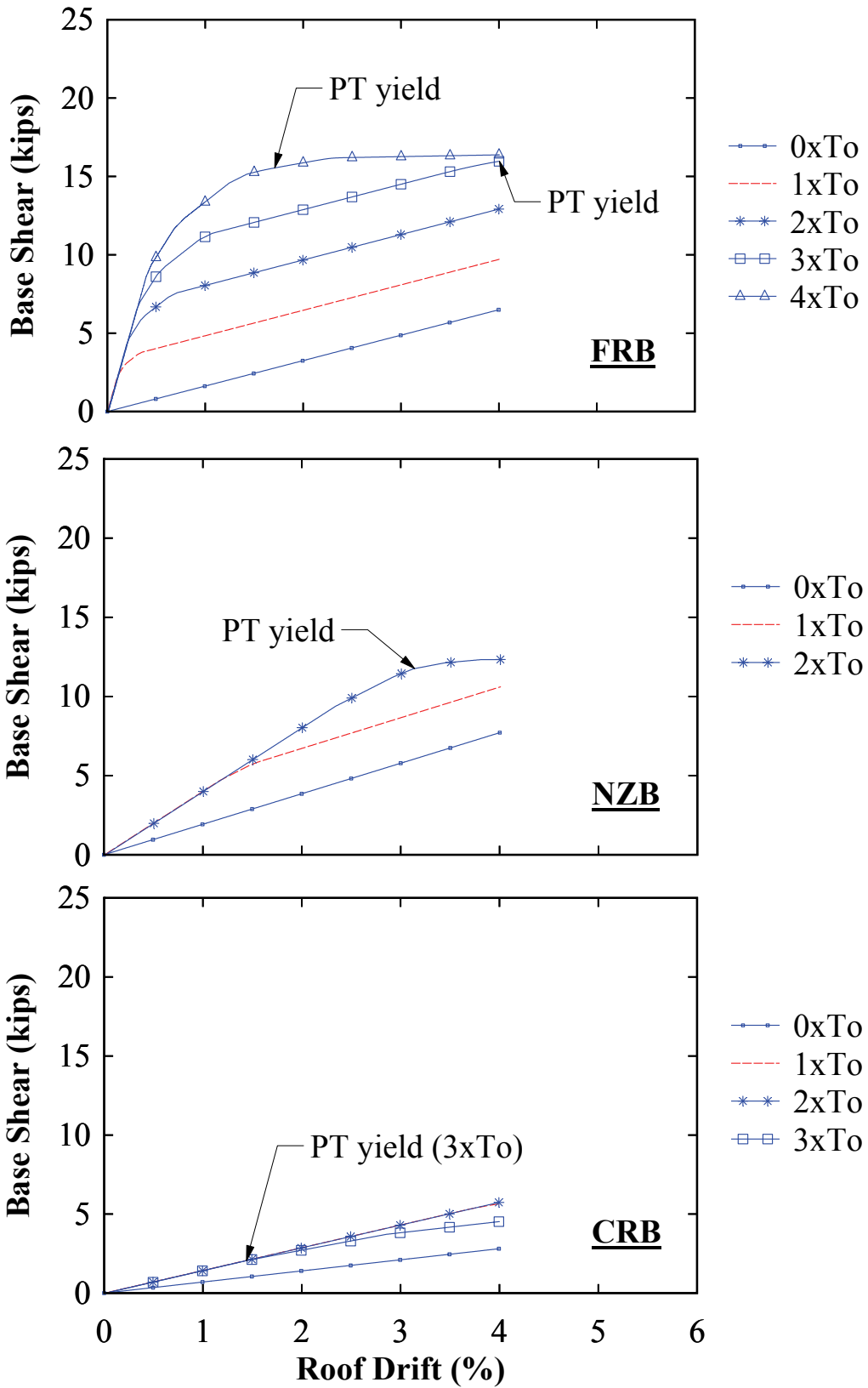


FIGURE 4-22 PT boundary frame –  $T_o$  Variable

Note that for a quasi-static cyclic response, complete recentering is achieved when the system unloads following its hysteretic curve to the axis origin (i.e., zero base shear demand and drift). Alternatively, if the system unloads along its hysteretic curve and intersects the horizontal axis prior to reaching the zero base shear condition, recentering is not achieved (although the corresponding residual drift may or may not be significant). As mentioned earlier, increasing  $T_o$  provides an improved frame recentering response and greater lateral strength, but taking non-linear response into account, it is observed from figure 4-22 that significant PT yielding occurred for the  $2xT_o$  and  $4xT_o$  cases for the NZ and FR frames, respectively; this is because increasing the initial PT force limits the amount of additional elongation the PT elements can achieve prior to yielding; as a result, this limits the amount of post-tensioning that can be used if it is desirable to ensure elastic response up to a specified target drift.

In figure 4-23, the variation in response due to  $A_{pt}$  as the parametric variable is presented, with all other parameters held constant. It is observed that the quantity of PT strands (or rods) affects the stiffness (i.e., slopes) of the response curves (as would be expected). Furthermore, as  $A_{pt}$  increases, the effects of the second linear branch (i.e., condition when  $T_o$  reduces to zero) becomes more dominate over the first linear branch. This is due to a reduction in  $T_o$  in each corresponding PT strand (i.e.,  $T_o$  remains constant, however  $T_o$  per strand decreases proportional to the increase in  $A_{pt}$ ). As a consequence, not only does increasing  $A_{pt}$  affect both branches of the stiffness of the boundary frame response curves, it also shifts the transition point between the two linear branches towards the axis origin (whereas increasing  $T_o$  shifts it away). The one exception is the response curve for the FR frame, where it is observed that only the second linear branch is affected. Recall that the first linear branch for the FR frame is dependent only on  $T_o$ ; the second linear branch occurs when the HBE-to-VBE joint connection fully decompresses from the clamping force provided by  $T_o$  (which is a constant parameter for the curves shown). In comparison to figure 4-22, a significant increase in stiffness can be achieved without concern of yielding the PT elements for a target drift; however at the expense of larger strength demands on the boundary frame than consideration of  $T_o$  alone.

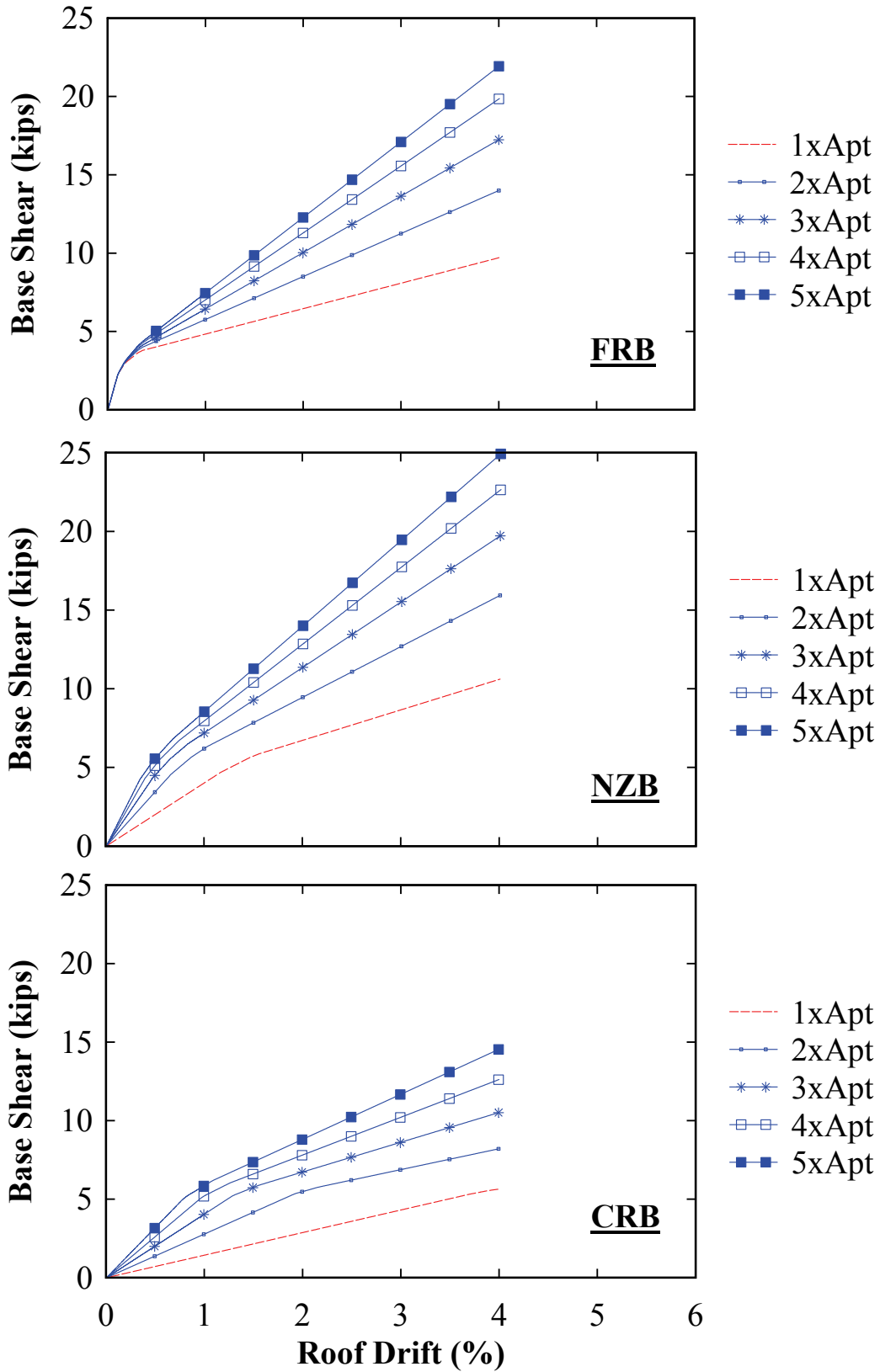
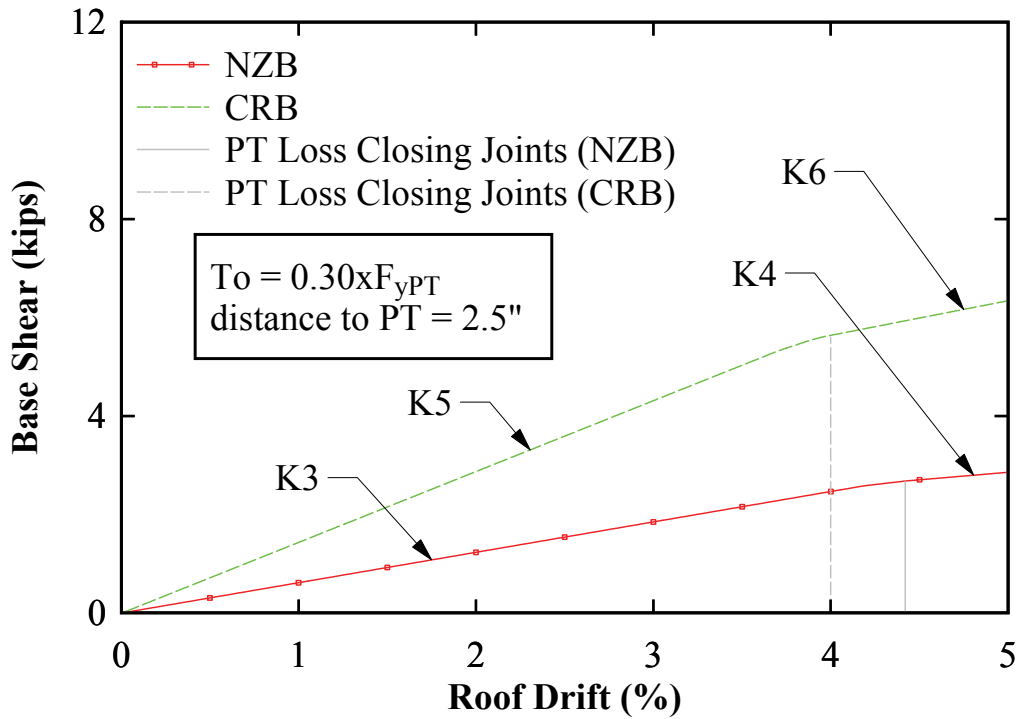


FIGURE 4-23 PT boundary frame – Apt variable

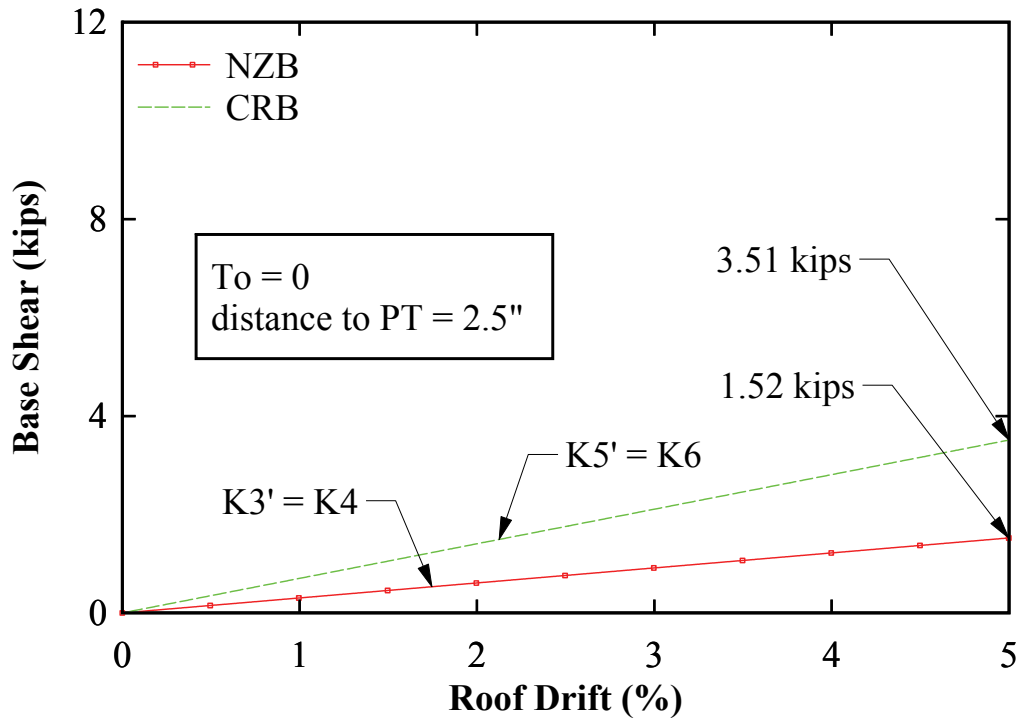
#### **4.2.4.2 Frame Response Comparison: NZ versus CR**

The NZ and CR frames are similar in that there is no decompression moment (as defined in Section 4.2.3.2) to overcome prior to HBE-to-VBE joint opening (i.e., the HBE-to-VBE joint opens immediately upon frame drift). By contrast, the FR frame behaves as a rigid frame until the decompression moment from the PT effects is overcome. Consequently, the kinematics of the NZ and CR frames is essentially identical (but local responses are different).

Interestingly, it was observed that in figure 4-20b the boundary frame strength of the CR frame was significantly less compared to the NZ frame. Although this is true of the test specimens, it is not representative of the CR frame in general. As noted in Section 4.2.3.1 the eccentricity to the PT for the CR test specimen is much smaller due to detailing constraints (2.5 in. versus 6.5 in.); this is the reason for the strength differences. To provide some perspective, if the PT eccentricity and initial force of the CR and NZ frames were made equal, the CR frame stiffness would be approximately two times larger than the NZ frame. This larger stiffness in the CR frame arises for the reason that the CR frame has both an opening and closing joint at each HBE-to-VBE joint, whereas the NZ frame there is not (presented in Section 3). To illustrate this, the NZ frame parameters were modified to match those of the CR frame and the monotonic pushover curves are shown in figure 4-24 for comparison, where these effects can be observed more clearly.



(a)



(b)

FIGURE 4-24 NZ and CR comparison: (a)  $T_o = 30\% \times A_{pt}$ ; (b)  $T_o = 0$

### **4.3 Shake Table**

As mentioned earlier, the test specimen boundary frames from the quasi-static tests were reused for the shake-table tests; only the infill web plates and PT elements were replaced (with identical components as in the quasi-static tests). Note that although the PT elements were designed to remain elastic, these elements were replaced for the shake-table tests. Furthermore, only the FR and NZ frames were investigated during the shake-table testing program. Similar to the quasi-static tests, each frame type was tested with a full infill web plate, PT bare frame, and an infill web strip configuration.

Furthermore, for the NZ frame, a perforated infill web plate configuration (Purba and Bruneau 2007) with bolted connections to the boundary frame was investigated. This work was performed in collaboration with researchers from Ecole Polytechnique of Montreal and is presented in Section 7.7.

#### **4.3.1 Prototype Building**

The prototype building for the scaled shake-table tests used the same DBE response spectra as the quasi-static prototype building (figure 4-2), but has different building parameters as shown in figure 4-25; for reasons described in the following sections. Furthermore, a spectra-compatible synthetic ground motion (GM) was used targeting the DBE response spectra. The corresponding GM spectrum is shown in figure 4-26 and is observed to be comparable to the DBE target spectrum. This ground motion was generated using the Target Acceleration Spectra Compatible Time Histories (TARSCTHS) code, by Papageorgiou et al. (1999) and is shown in figure 4-27. The test setup (presented in Section 5) provided a fixed seismic weight of approximately 51 kips. The specimen weight capacity of the shake-table is approximately 90 kips and the maximum acceleration that the shake-table can reproduce is approximately 1.0 g for a 51 kip specimen. Accordingly, the quasi-static prototype building could not be used for the shake-table tests and had to be modified to not exceed these constraints, as clarified below.

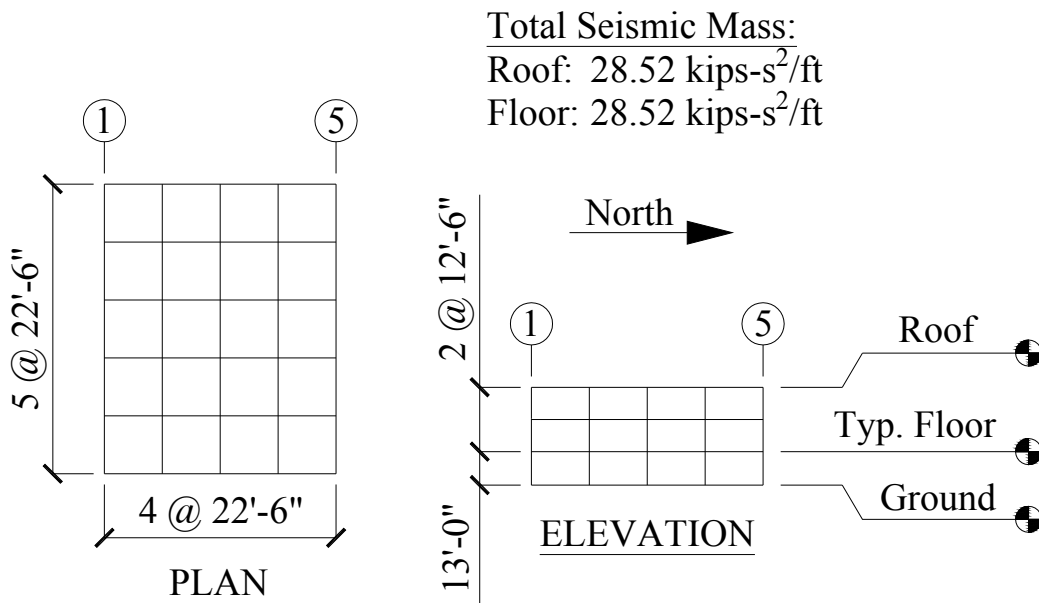


**FIGURE 4-25 Prototype building: shake-table tests**

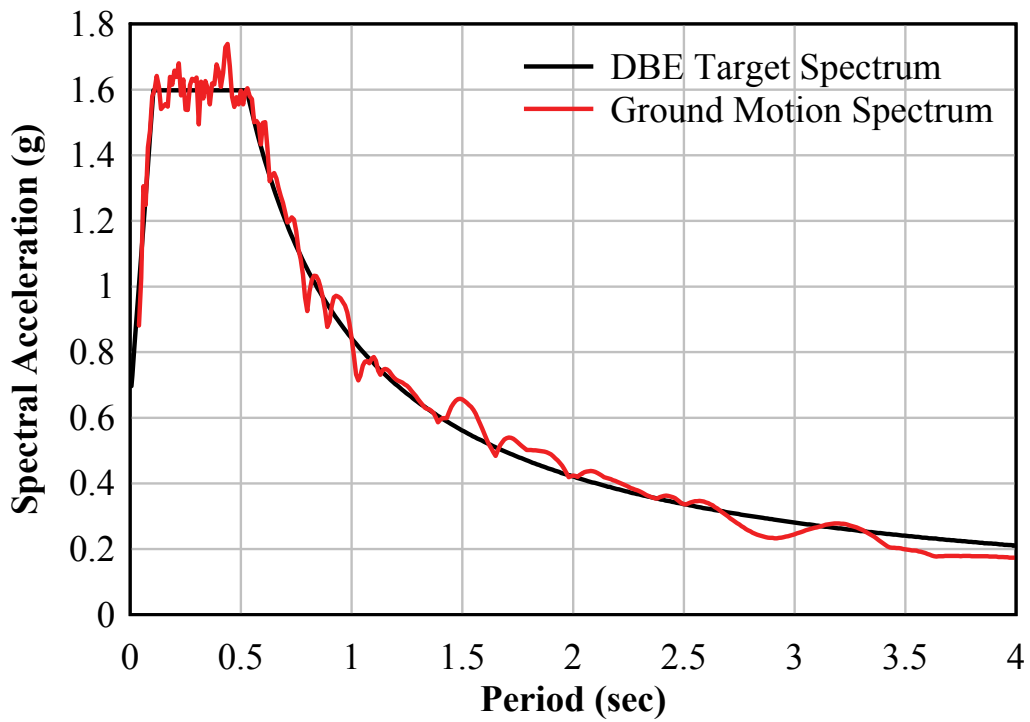


**FIGURE 4-26 Ground motion response spectrum**

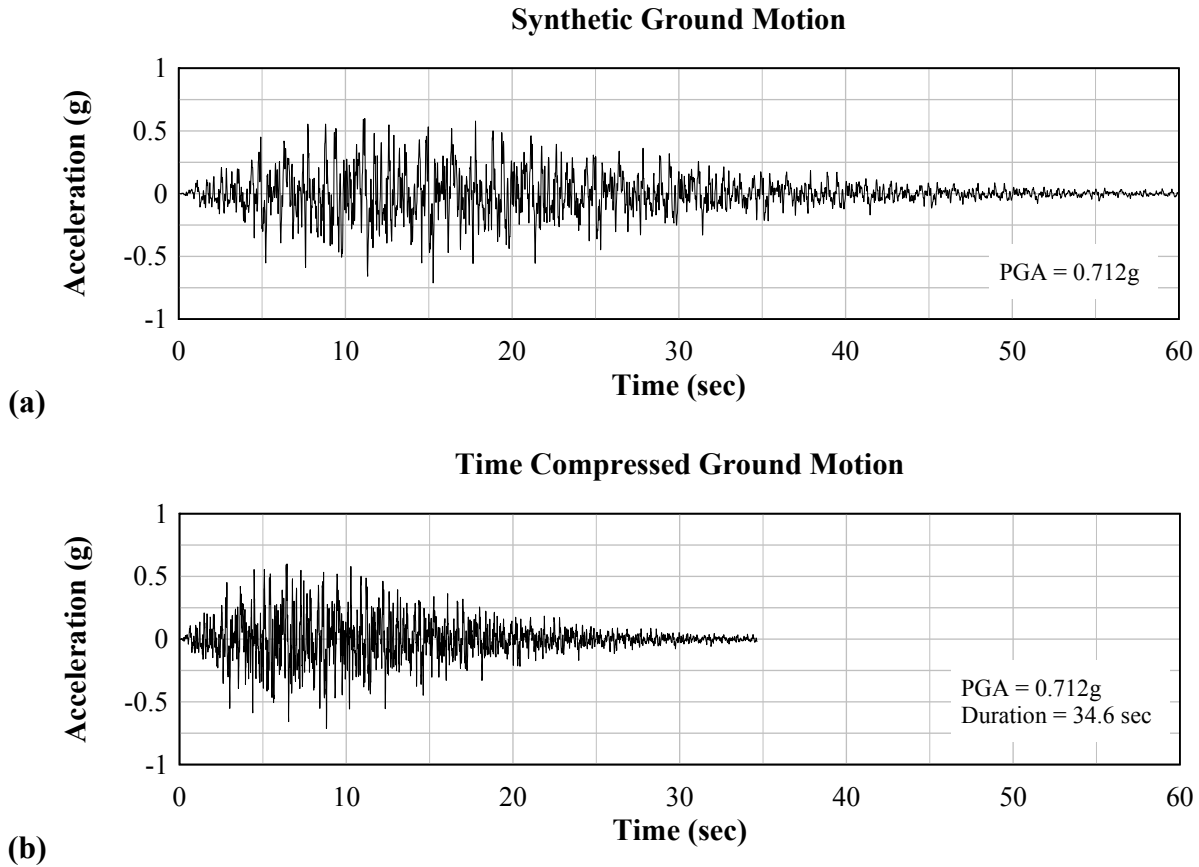


**FIGURE 4-27 Synthetic ground motion: (a) prototype building; (b) scaled model building**

**4.3.2 Test Specimen Model Scaling**

The similitude scale factors were presented in table 4-1. For scaled-dynamic tests, the parameter on density is a key factor in influencing the similitude relationships between the prototype building and the scaled model building. In particular, from table 4-1, the scale factor for density is  $\lambda_\rho = \lambda_E/\lambda_L\lambda_a$  and the required scale factor for the case at hand is calculated to be  $= 1/(3)(1) = 1/3$  if the acceleration field is assumed to be the same between the prototype and model. However, as shown in the table, the actual scale factor for density is 1 (since this is a physical constraint and cannot be modified). Furthermore, the assumed relationship of the acceleration field (i.e.,  $\lambda_a$ ) between the prototype and model building also has an influence on the scaled dynamic testing parameters. Hence, in order to maintain proper similitude between the quasi-static prototype and the shake-table model, further scale factor adjustments would be necessary, either on the model mass or ground motion. However, here, in lieu of these adjustments, the



prototype building was modified to match the existing test setup (which has a total seismic frame tributary weight of approximately 51 kips) to provide a comparable similitude match.

In particular, from table 4-1, using the scale factor relationship for the acceleration field (while enforcing  $\lambda_a = 1$ ) and solving for the required mass leads to  $\lambda_m = \lambda_E \lambda_L^2 / \lambda_a = (1)(3)^2 / 1 = 9$ . Thus, the required tributary seismic frame weight of the prototype frame is  $W_p = 9W_m = (9)(51 \text{ kips}) = 459 \text{ kips}$  or  $459 \text{ kips} / 3 \text{ levels} = 153 \text{ kips/level}$ . Furthermore, a total of six lateral frames were assumed for the prototype building (to match that of the original prototype SAC building). The column bay spacing was then determined from the 7'-6" column spacing of the test specimen (which was controlled by the test setup conditions), leading to a column spacing of 22'-6" in the prototype building. Finally, the overall building footprint was determined by matching the distributed floor dead load of the SAC building of 86 psf (this is the contribution used for seismic mass calculation). Thus leading to  $(153 \text{ kips})(6 \text{ frames}) / (112.5 \text{ ft})(90 \text{ ft}) = 90.7 \text{ psf}$  per level.

Note that although it is convenient to associate the shake-table tests to a full-scale prototype building to provide some level of reference, the primary objective of these tests was to observe the behavior of SC-SPSWs subjected to dynamic earthquake simulation loadings. The loading protocol is presented in Section 7, but relevant to this section is that it follows an incremental dynamic pushover format. In particular, shake-table testing of the specimen(s) is planned to continue up to the safe operating capacity of the shake-table and/or test specimen. Thus, the definition of a prototype building as it pertains to these tests is not necessarily critical due to the manner in which the tests were to be conducted.

### **4.3.3 Quasi-Static versus Shake-Table Model Scaling**

This section provides additional information on why the shake-table prototype building parameters were selected differently from the quasi-static tests. It was identified above that the scale factor for density is violated between the prototype and scaled model buildings. To compensate, one approach would have been to add additional seismic weight to the model building (i.e., to the test setup). Using similitude rules it then follows that the additional weight required to the model frame would be:

$$\begin{aligned}
\Delta W &= W_p \left( \frac{\lambda_L - 1}{\lambda_L^3} \right) \\
&= \left[ (\lambda_p \lambda_L^3) W_m \right] \left( \frac{\lambda_L - 1}{\lambda_L^3} \right) \\
&= \left[ (1)(3)^3 W_m \right] \left( \frac{3-1}{3^3} \right) \\
&= 2W_m
\end{aligned} \tag{4-5}$$

where  $W_p$  = prototype seismic weight,  $W_m$  = model seismic weight, and all other terms are defined in table 4-1. Thus, in order to satisfy correct scaling of the one-third scale shake-table tests using the quasi-static prototype building, an additional mass of  $2(51 \text{ kips}) = 102 \text{ kips}$  or  $2(17 \text{ kips per level}) = 34 \text{ kips per level}$  would have been needed. As noted earlier, the maximum specimen weight capacity of the shake-table is 88 kips, which is less than the total weight of 153 kips that would have been required for this option; therefore, it was not a viable solution for matching the quasi-static prototype building.

Another approach would have been to modify the horizontal acceleration field (i.e.,  $\lambda_a$ ) of the model frame. This option is only possible due to the arrangement of the test setup (to be presented in Section 5) in that the superimposed seismic mass is supported vertically by an independent gravity frame system and only horizontal acceleration effects are transferred to the test specimen. As a consequence of the horizontal and vertical acceleration fields being decoupled, different scale factors could be used in respective directions. It then follows that the actual scale factor for seismic mass =  $\lambda_m$  = prototype mass / model mass =  $(1084 \text{ kips/g}) / (51 \text{ kips/g}) = 21.2$ . This leads to a scale factor for the horizontal acceleration field =  $\lambda_a = (\lambda_E \lambda_L^2) / \lambda_m = (1)(9) / 21.2 = 0.424$ , which would have required that the ordinate of the input ground motion used in the shake-table tests be scaled by 2.36. Given that the peak ground acceleration (PGA) of the GM is 0.712 g, this would have resulted in a value of  $(2.36)(0.712 \text{ g}) = 1.68 \text{ g}$ , which is approximately 50% larger than the capacity of the shake-table. Thus, amplitude scaling the GM was also not an option. For these reasons, the prototype building for the shake-table tests was modified.

#### 4.3.4 Spectral Response Evaluation

Modifying the prototype building parameters (from the original prototype building for which the specimen design was originally based to the one use for the shake table tests) has an effect on the interpretation of the seismic performance and response of the test specimens. To determine these effects, a spectral response evaluation was performed. This method is a simplified analyses technique based on equating the seismic demand expressed in terms of response spectra parameters with the inelastic capacity described in terms of force-deformation (Reinhorn 1997). The spectral demand curve is expressed in terms of spectral accelerations (ordinate values) versus spectral displacements (abscissa values). The spectral capacity curve is the strength of the test specimen and is obtained from a monotonic pushover analysis of the specimen and then converted to a spectral capacity.

This analysis technique is used to evaluate the approximate inelastic response of single-degree-of-freedom (SDOF) systems. However, of interest here is obtaining an approximation of the response modification factor,  $R$ , for comparison between the quasi-static and shake-table prototype buildings. For this purpose, only the elastic spectral demand in conjunction with the spectral capacity curve is used. Furthermore, note that for SDOF systems, the spectral capacity curve is the same as the monotonic pushover curve. However, for multi-degree-of-freedom (MDOF) systems, the monotonic pushover curve must be further modified for conversion to a spectral capacity curve (since response spectra are based on a SDOF system).

Using the method presented by Reinhorn (1997) for transformation from a MDOF to an approximate SDOF system, where  $i$  = floor level and  $j$  = mode number, the transformation of the base shear to a spectral capacity,  $Q(u)^*$ , is:

$$Q^*(u) = \frac{S_a(\omega_o, \xi_o)}{g} = \left[ \frac{Q(u)}{W} \right] \left( \frac{1}{\Gamma_1^2} \right) \bullet srss \left( \gamma_j^2 S_{aj} \right) \quad (4-6)$$

where  $S_a(\omega_o, \xi_o)$  = the spectral demand,  $g$  = gravitational acceleration,  $Q(u)$  = base shear,  $W$  = total seismic weight,  $\Gamma_1$  = first mode participation factor, and  $srss$  is a short description of the square root of the sum of the squares superposition and has the following general form:

$$srss(x_j) = \sqrt{\sum_{j=1}^M x_j^2} \quad (4-7)$$

where the terms forming  $x_j$  are defined as the ratios to the respective properties of the first mode, such that: (i) the modal ratios are defined as  $\gamma_j = \Gamma_j/\Gamma_1$  and  $f_{ij} = \phi_{ij}/\phi_{i1}$  and (ii) the spectral ratios for the various modes are defined as  $s_{aj} = S_a(\omega_j, \xi_j)/S_a(\omega_1, \xi_1)$  and  $s_{dj} = S_d(\omega_j, \xi_j)/S_d(\omega_1, \xi_1)$  for spectral accelerations and displacements, respectively. In similar fashion the transformation of the displacements to a spectral displacement capacity,  $u^*$ , where  $S_d$  = the spectral displacement demand is:

$$u^* = S_d(\omega_o, \xi_o) = \frac{u_i}{\phi_{i1}\Gamma_1} \bullet srss \left( f_{ij} \gamma_j s_{dj} \right) \quad (4-8)$$

Equations (4-6) and (4-8) include higher mode contributions in the transformation of a MDOF system to an equivalent SDOF spectral capacity curve. However the transformation equations can be further simplified as it can be recognized for *regular structures* that first mode characteristics are dominant and higher modes can be neglected as a reasonable approximation. Accordingly, letting  $M = 1$  in the *srss* summation in the aforementioned equations leads to:

$$Q^*(u) \cong \left[ \frac{Q(u)}{W} \right] \left( \frac{1}{\Gamma_1^2} \right) \quad \text{and} \quad u^* \cong \frac{u_i}{\phi_{i1}\Gamma_1} \quad (4-9)$$

Note that (4-6) to (4-9) are formulated using mass normalized modes for all calculations such that  $\phi_j^T M \phi_j = 1$  where the superscript  $T$  represented a transposed vector and  $M$  is the mass matrix. Alternatively, (4-9) can be expressed in more familiar terms using non-mass-normalized mode shapes. The modal participation factor,  $\Gamma_1$ , and the total effective modal mass,  $M_1^*$ , for the fundamental mode can be expressed accordingly, where  $m_j$  = mass at floor level  $j$ ,  $N$  = the number of floors, and  $\phi_{j1}$  is the  $j$ th-floor element of the fundamental mode  $\phi_1$ , as:

$$\Gamma_1 = \frac{\sum_{j=1}^N m_j \phi_{j1}}{\sum_{j=1}^N m_j \phi_{j1}^2} \quad \text{and} \quad M_1^* = \frac{\left( \sum_{j=1}^N m_j \phi_{j1} \right)^2}{\sum_{j=1}^N m_j \phi_{j1}^2} \quad (4-10)$$

$$Q^*(u) \cong \left[ \frac{Q(u)}{W} \right] \left( \frac{1}{M_1^*} \right) \quad \text{and} \quad u^* \cong \frac{u_i}{\phi_{i1} \Gamma_1} \quad (4-11)$$

Using (4-10) in (4-11) leads to an alternate form in terms of modes shapes directly obtained from the eigenvalue analysis used to obtain the free vibration dynamic properties. Note that the formulation for spectral displacement demand is unchanged; however, the change is inherent with the mode shape and participation factor terms.

The spectral analysis results for the quasi-static and shake-table prototype frames are shown in figure 4-28 for comparison. The prototype frames are SC-SPSWs with the NewZ-BREAKSS HBE-to-VBE joint connection with design parameters indicated in table 4-2. Furthermore, the spectral demand curve is based on the synthetic GM (figure 4-27a) for the site for an assumed 2% viscous damping. Recall that the strength of the prototype frame is identical for both buildings, with only the frame tributary seismic weight modified, as indicated in the figure. The approximate response modification factors are calculated to be  $R = 1.19/0.13 = 9.1$  and  $R = 2.33/0.71 = 3.3$  for the quasi-static and shake-table prototype respectively. Therefore, the specimens for the quasi-static tests have an  $R$  factor approximately 2.76 times greater than those for the shake-table specimens.

These results indicate that the seismic response of the shake-table specimens are expected to exhibit less inelastic drifts than the case if the prototype building parameters of the quasi-static tests could have been enforced for the shake-table tests (i.e., if the capacity of the shake-table was not an issue). Thus, the quasi-static and shake-table tests must be considered independent of each other, and results from each test phase stand on their own. However, although a direct comparison of prototype response between those two test phases is not possible, the two phases complement each other, and together, enhance knowledge on the behavior of SC-SPSWs. Approximation of the  $R$  factor for the shake-table model specimen is also useful as it relates to

the selected GM used for the loading protocol; which will be valuable in interpreting the seismic response of the shake-table test specimens.

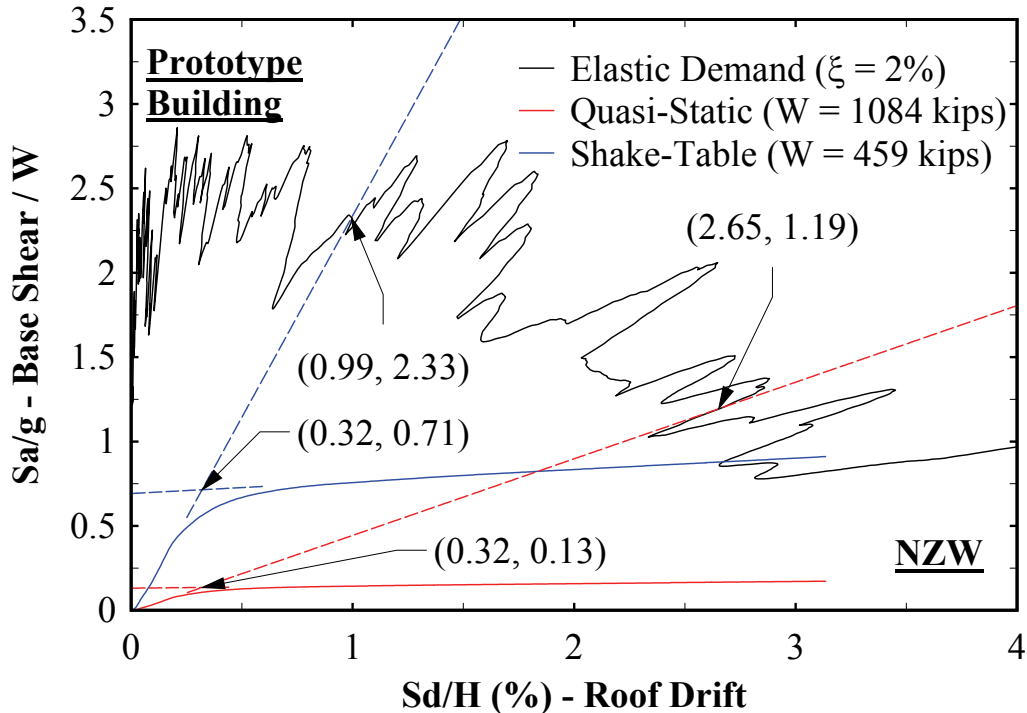


**FIGURE 4-28 Spectral response – prototype building comparison**

Furthermore, as a check on the similitude used for the shake-table tests, in figure 4-29 the spectral analysis for the model specimen is compared with the prototype. The results are comparable providing an indication that correct similitude scaling between the prototype and model frame was used. The observed differences in the spectral capacities are due to the Level 1 story height in the model specimen compared to the prototype frame. That is, in figure 4-8, the model story height at Level 1 is 42.875 in., which was reduced from 50.75 in.. This was done to take into consideration the distance to the center of rotation of the clevis and pin VBE base connection. As a result of this height adjustment, it turns out that the actual geometric scale factor is approximately 4 at the Level 1 story, as indicated in table 4-2. As a consequence, the model specimen frame stiffness is expected to be larger than the prototype frame (i.e., since it is more squat at Level 1). This is reflective of the differences in the spectral capacity curves shown. Furthermore, the spectral demand curves are essentially identical but do not perfectly lie

on top of each other. In part, this is a result of the scaling effects on the time scale for the model GM. Recall that the model GM was time compressed by the scale factor of  $1/(3)^{1/2}$ , which leads to a time step for the data that does not have a whole multiple, leading to some truncation error due to rounding effects.

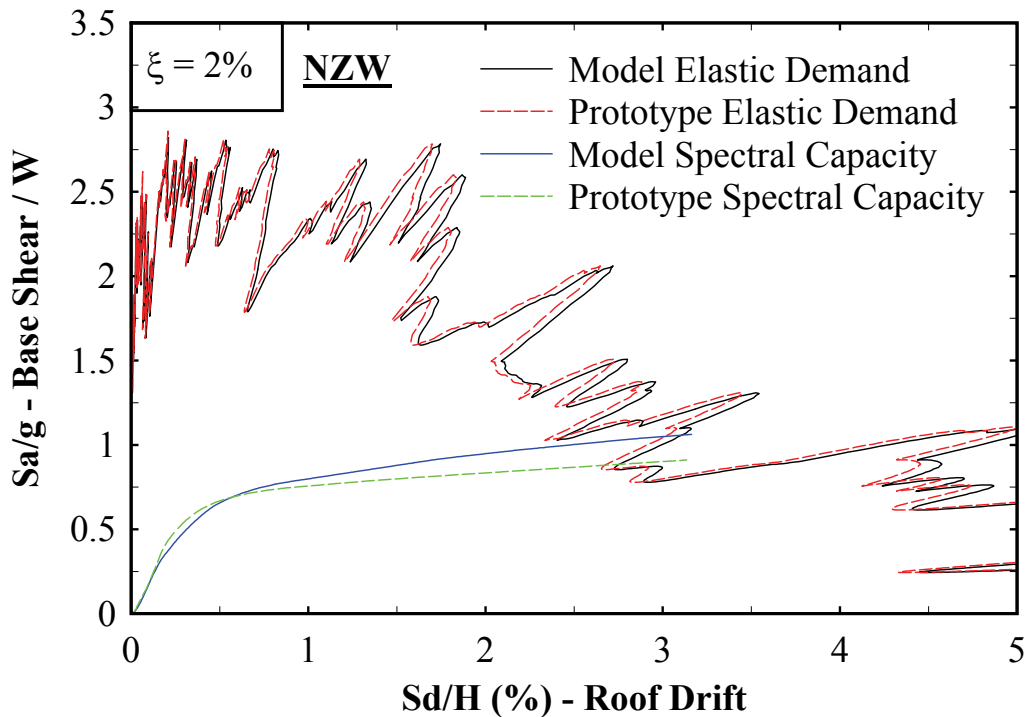


**FIGURE 4-29 Spectral response – prototype and model comparison**

Finally, to provide some perspective in regards to the shake-table test specimens, the spectral analysis for the FR and NZ model frames are shown in figures 4-30 and 4-31 respectively for both infill web plate and strip configurations. Based on an assumed 2% viscous damping response spectra (for the time compressed synthetic GM shown in figure 4-27b), approximate response modification factors are calculated to be  $R = 2.55/0.75 = 3.4$  and  $R = 2.27/0.35 = 6.5$  for the web plate and strip configuration respectively for the FR frame. Correspondingly,  $R = 2.41/0.74 = 3.25$  and  $R = 1.71/0.35 = 4.9$  for the web plate and strip configuration respectively for the NZ frame. By comparison, both FRW and NZW are essentially identical and are comparable to the  $R$  factor for the prototype. FRS and NZS comparisons are reasonably close given that some judgment was made in choosing the data points for the elastic and inelastic

linear regression curves used to determine  $R$ . Furthermore, the effect of using the same gage thickness of plates for the strips as the infill web plates is also observed by the larger  $R$  factors determined for FRS and NZS.

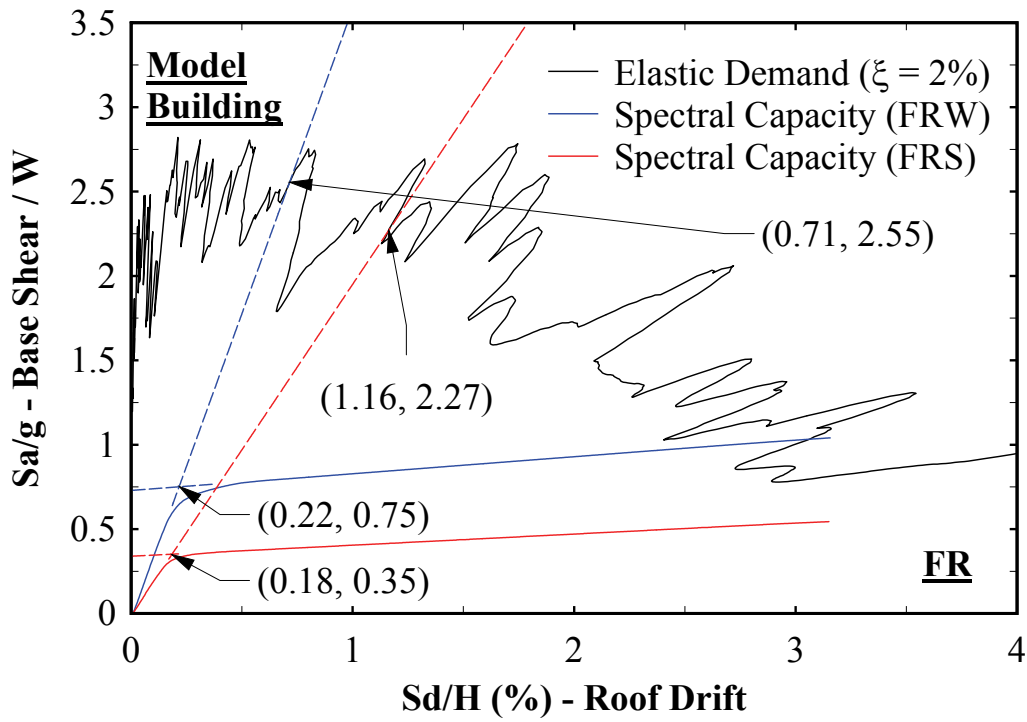


FIGURE 4-30 FR frame spectral response



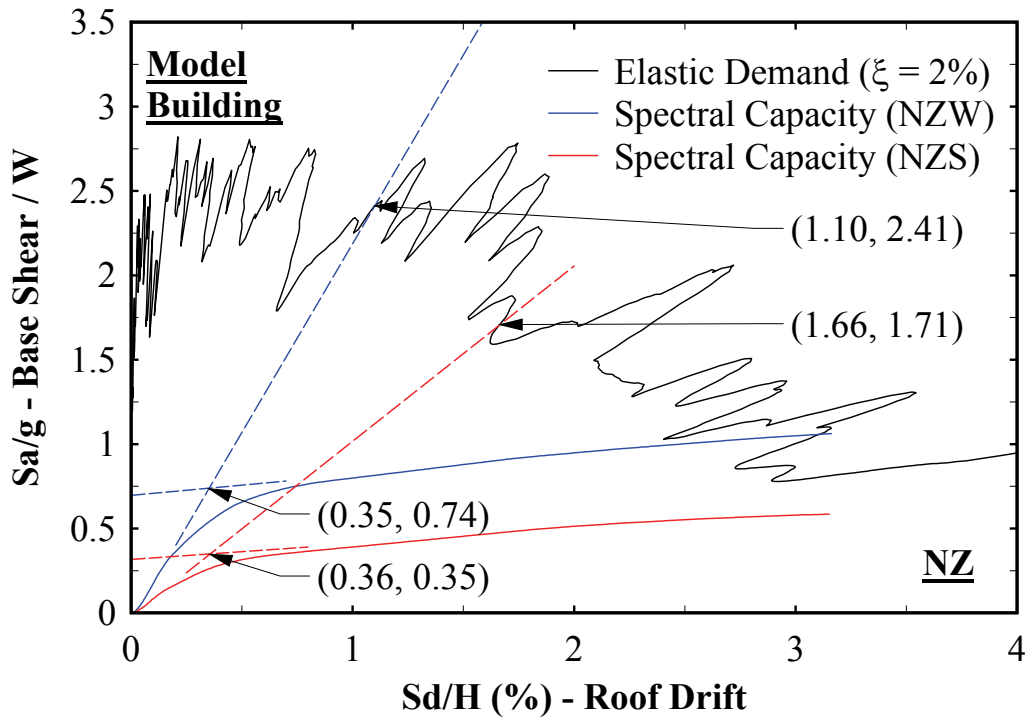


FIGURE 4-31 NZ frame spectral response

#### 4.3.5 Analytical Results

Typically a suite of GMs would be used for design to take into consideration the variability of individual GM characteristics, with the objective of obtaining a median and/or average response matching the DBE response spectra. For testing purposes this is not practical (i.e., one design level GM loading per test specimen). Therefore, the loading protocol (presented in Section 7) consisted of scaling the amplitude of the synthetic GM, beginning with low level amplitude intensities, and for subsequent ground motions with increased scaled amplitudes.

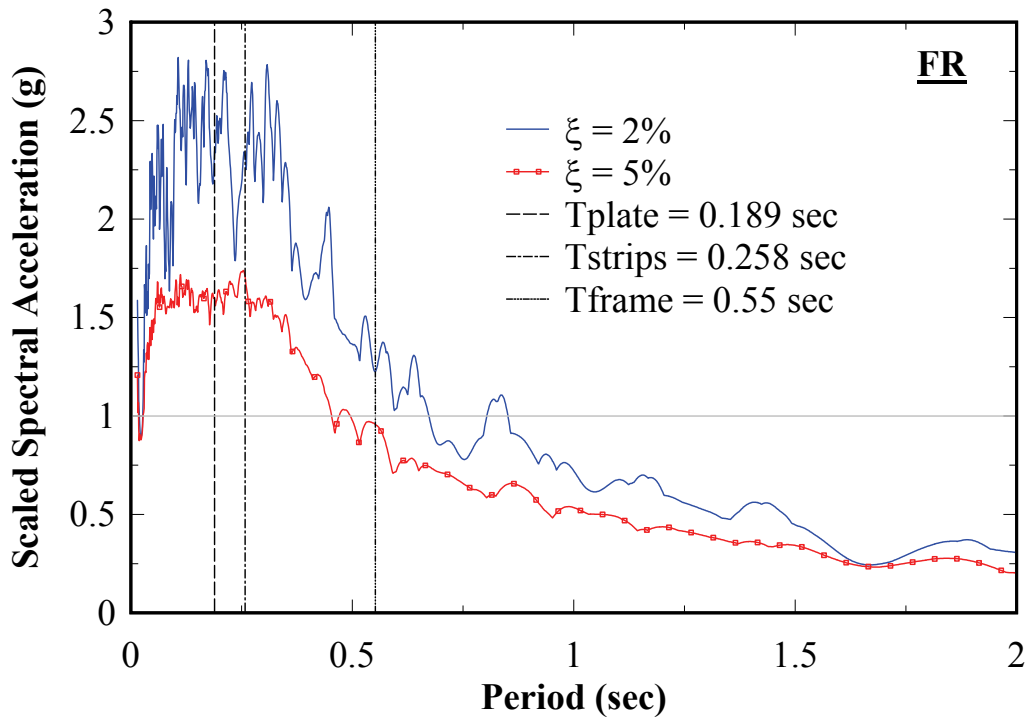
The corresponding response spectra for acceleration and displacement demands are shown in figures 4-32 and 4-33 respectively. Spectra are provided for 2% and 5% viscous damping to provide an approximate lower and upperbound response. Furthermore, the fundamental elastic periods obtained from the analytical models are provided for the infill web plate, infill web strip, and bare frame conditions for reference. Note that the bare frame period for each specimen provides an approximate upperbound response. This is because the behavior of the test specimen is approximately bounded by the elastic period of the SC-SPSW and that of the PT bare frame.

In figure 4-32, it is observed that the elastic response of the infill web plate and strip configurations are comparable (as they are both on the constant acceleration branch of the DBE response spectra). Additionally, note that the elastic spectral acceleration demands are over 1 g, the approximate capacity of the shake-table. However, this assumes that the initial GM excitation will use 100% of the GM amplitude values at the start of the test; which will not be the case for reasons noted above. Also, it is observed in figure 4-32 that without the presence of the infill web plate, the PT boundary frame periods are significantly different for the FR and NZ frames (for the PT design parameters).

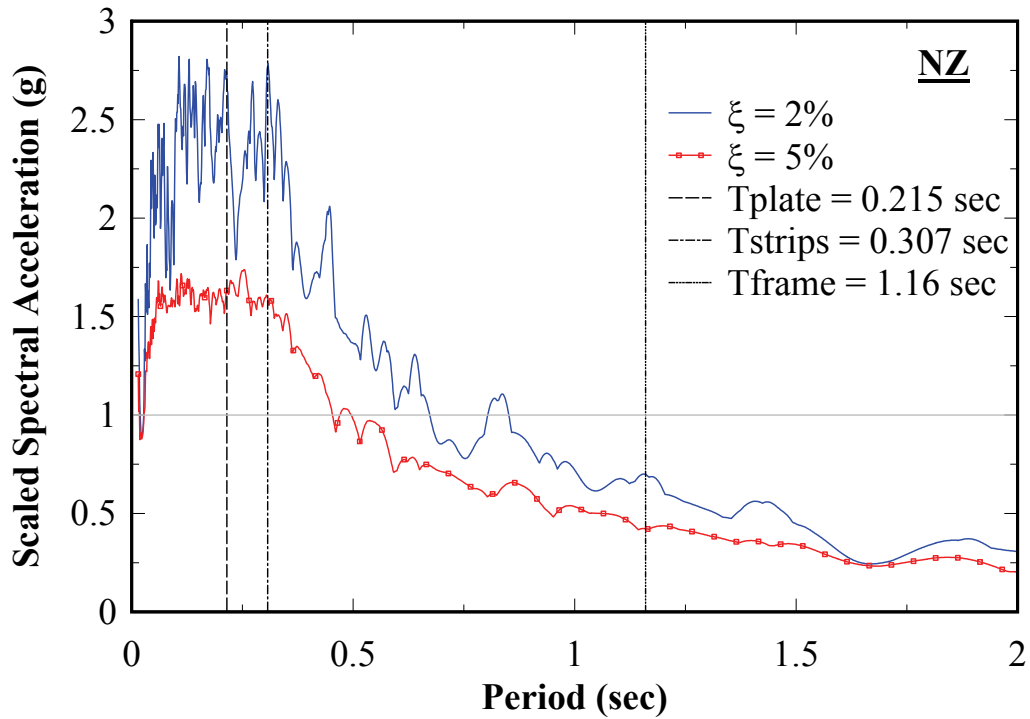
Results from incremental dynamic analyses of response for the test specimens are shown in figure 4-34. The analytical model parameters are identical to those of the quasi-static analysis but with different initial PT forces,  $T_0$ . An initial post-tensioning force of approximately 40 to 45% of the PT yield strength was targeted for the FR and NZ frames. This value, larger than for the quasi-static tests, was used since the drift demands for the shake-table tests were anticipated to be much smaller. Furthermore, the scaled GMs were arbitrarily selected at 25% increments to obtain a general response. Note that each point on the analytical incremental dynamic curve does include the cumulative inelastic deformation history from the previous scaled GM (as would be the case for the shake-table tests). In the analytical model, this was done by concatenating the appropriate scaled GMs and providing a segment of free vibration between each to approximately “reset” the initial velocity and acceleration conditions to zero between GMs (as would be the case for the shake-table tests). For example, for the 50% GM result shown in figure 4-34, the GM loading in the analysis consisted of a single GM file that first included the 25% GM, followed by 10 seconds of free vibration, followed by the 50% GM.

In general, it is observed that the strength of the FR frame is slightly larger. However, the drift demands are noticeably larger for the NZ frame. Both of these observations are due to the differences in dynamic response of the PT boundary frames. Furthermore, for reasons presented earlier, frames with the infill web strips have a strength of approximately half, and a drift demand of approximately twice, those of their corresponding specimens with infill web plates. Also note that for the 2% damping condition (approximate upperbound), the maximum acceleration demand is 1.04 g for the FRW frame; which is less than the elastic spectral

acceleration demand in figure 4-32, and comparable to the limits of the shake-table capacity (as a result of the cumulative inelastic response up to the 100% scaled GM). This last observation is provided to show that the upperbound analytical response of the test specimens is within the testing constraints of the shake-table capacity, contrary to what is observed on the acceleration response spectra at the elastic SC-SPSW frame periods.

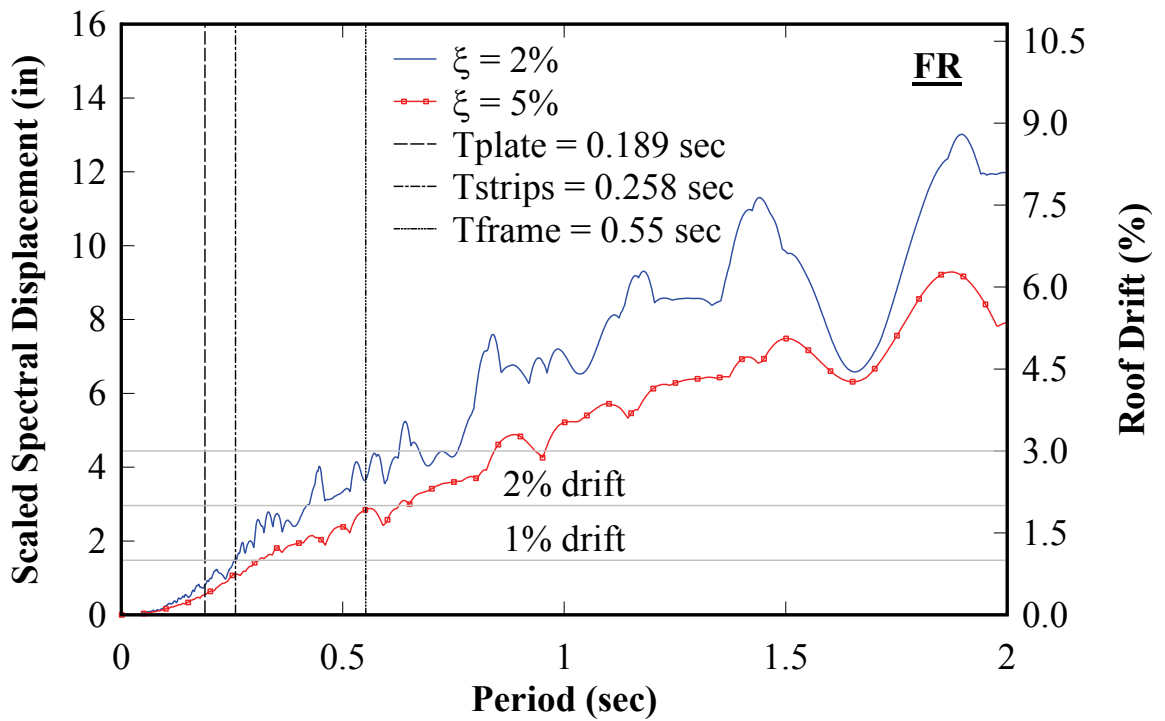


(a)

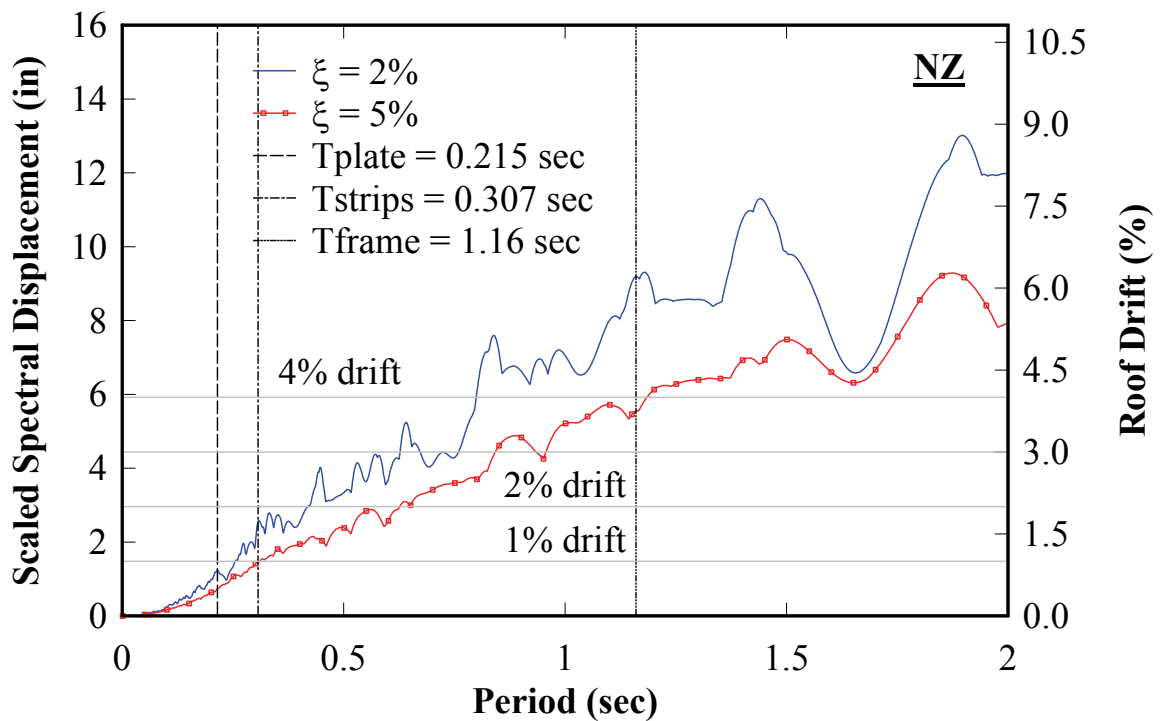


(b)

**FIGURE 4-32 Spectral acceleration response – scaled GM: (a) FR frame; (b) NZ frame**

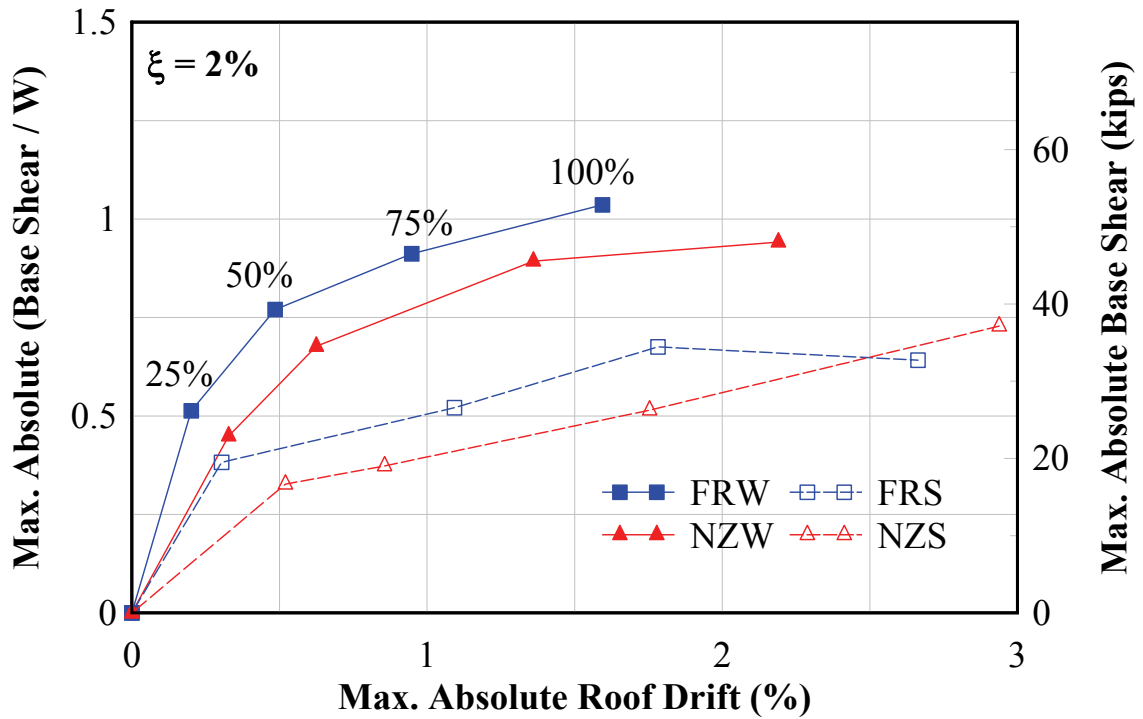


(a)

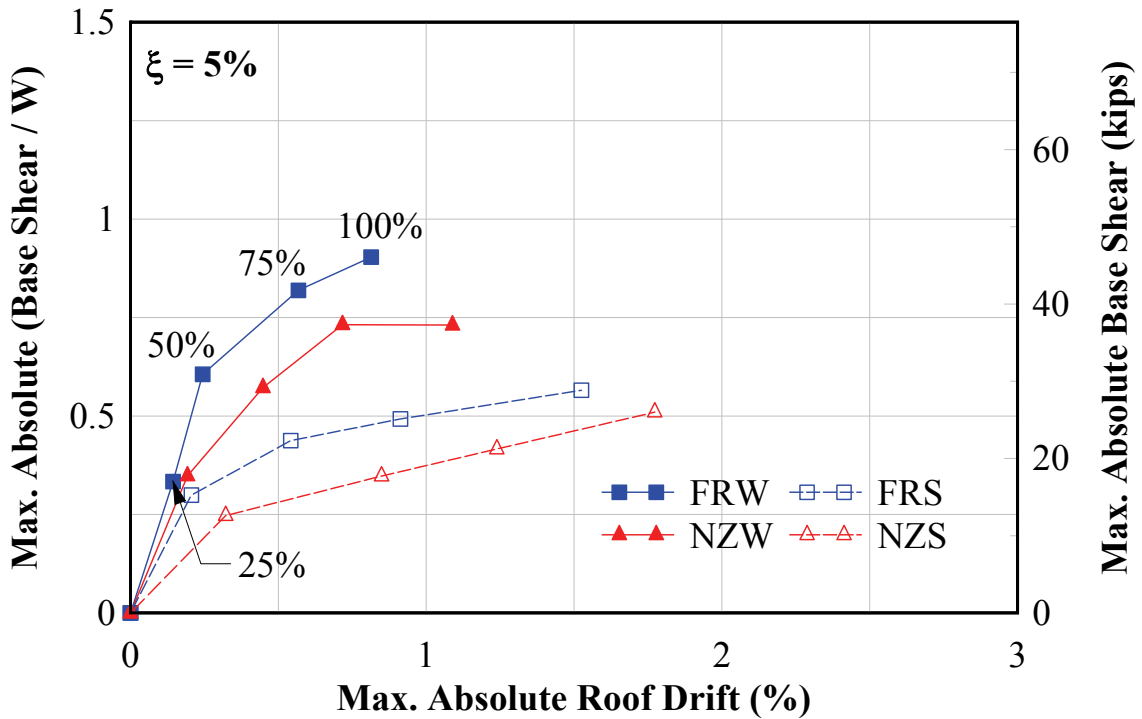


(b)

FIGURE 4-33 Spectral displacement response – scaled GM: (a) FR frame; (b) NZ frame



(a)



(b)

**FIGURE 4-34 Analytical incremental dynamic response: (a) 2% damping; (b) 5% damping**

## SECTION 5

### EXPERIMENTAL TEST SETUP

#### 5.1 General

This chapter presents the experimental test setup, instrumentation and equipment used for the quasi-static (Section 5.2) and shake-table (Section 5.3) tests conducted.

#### 5.2 Quasi-Static

##### 5.2.1 Test Setup

The test setup used an existing modular lateral bracing system developed at UB for the experimental testing of scaled specimens (Kusumastuti 2005). The modular bracing system, hereafter referred to as the Gravity Mass Frame (GMF) system, was originally developed for dynamic shake-table testing. However, due to its versatile design, it can be adapted for use in quasi-static testing without any significant modifications – as was done for these tests.

The GMF system was designed to be a self-contained structure that can support its own weight (e.g., imposing no gravity loads to the specimen tested), has lateral stiffness and stability in its primary transverse direction, but has essentially no lateral stiffness in its longitudinal direction. The system can be thought of as a set of “floor/roof diaphragms” provided by 3.5” thick steel plates with an approximate weight of 8.5 kips per plate, each supported by four S3x5.7 columns. Transverse lateral stiffness of the system is provided by L1.5x1.5x1/4 X-bracing connected to each pair of gravity columns at each floor plate. The negligible longitudinal stiffness is achieved by the use of “rocker plates” at the top and bottom of all gravity columns (note that no GMF lateral bracing is provided in the longitudinal direction). These rocker plates have a spherical surface with 10” radius on one side and a flat surface on the opposite face. Horizontal forces that develop at the gravity columns are resisted by friction between the rockers and the GMF weight. However, for safety, 3/8” diameter dowels (a.k.a. thru-rods) are provided at each rocker plate location. These thru-rods would keep the rocker plates above and below the steel floor plate together, up to some drift level, if the horizontal friction force were to be exceeded at the gravity column rocker plates. Note that these rods, are placed loosely thru oversized holes and hence do

not provide any lateral restraint under the anticipated test conditions. The schematic of the test setup and photo of the column rocker plates are shown in figure 5-1.

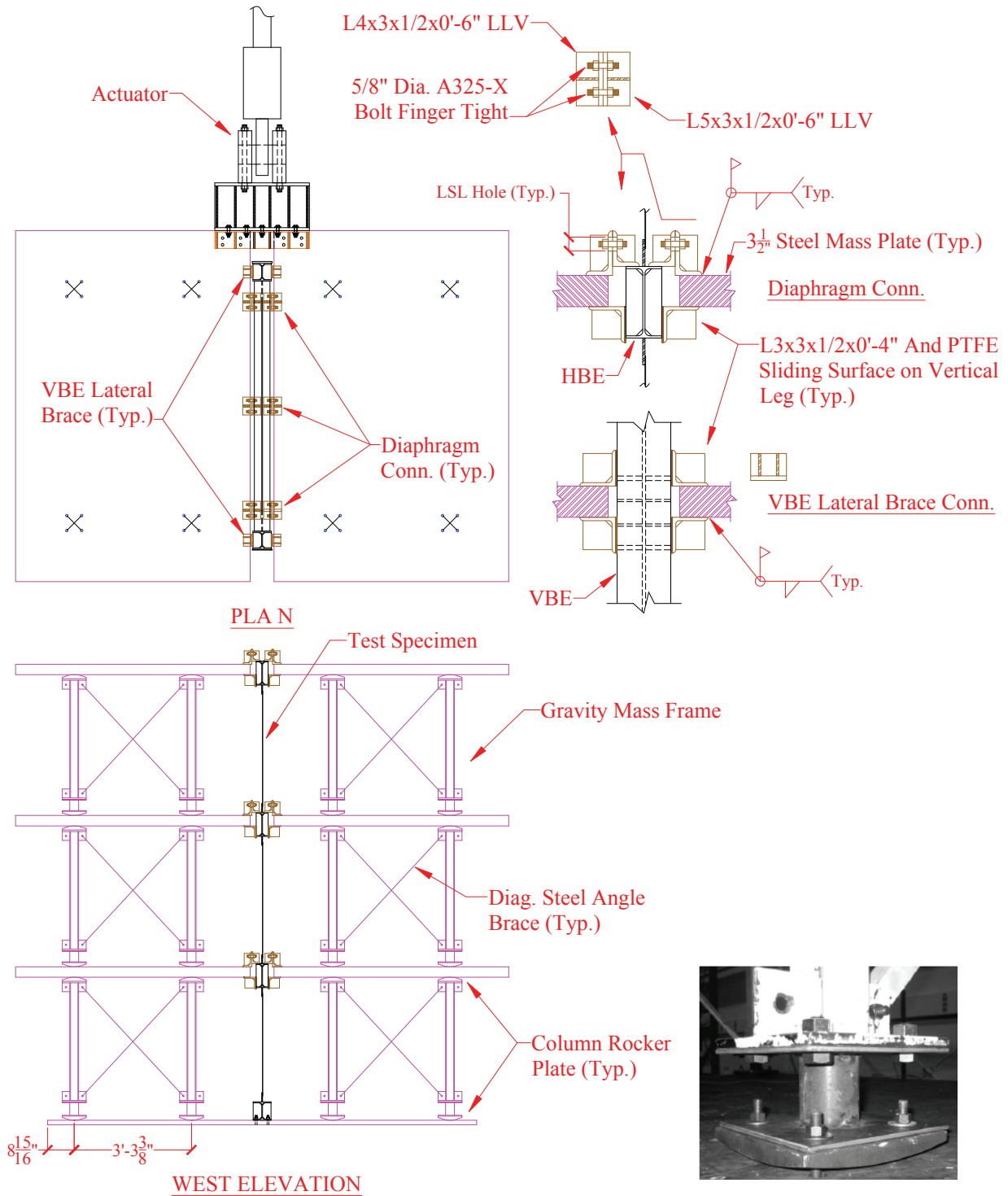


**FIGURE 5-1 GMF test specimen connection**



As indicated in the figure, two sets of GMFs were used, one on each side of the test specimen. In this configuration, the test specimen is the lateral force resisting system (LFRS) in the longitudinal direction and the GMF provides lateral bracing to the test specimen in the transverse direction. The diaphragm connections were made using back-to-back double-angles, one welded on the diaphragm plate and the other to the test specimen (figure 5-2a). Connection of the two angles was made by a finger-tight bolted connection. To reduce bolt slip in the lateral direction upon loading from the actuators, a  $+1/32$ " bolt hole tolerance was used. Furthermore, to accommodate some rotation at the diaphragm connections, the bolt holes were long-slotted in the vertical direction. Note that for this particular test setup, only connecting the floor plate diaphragm to the HBEs allowed the HBE-to-VBE rocking joints to rotate freely (i.e., opening and closing of gap mechanism), which would not have been the case if the diaphragm connection had been made to the VBEs instead.

Furthermore, the VBEs and HBEs were braced at each floor level with L3x3 angles (e.g., figure 5-2b shown at VBE). At the interfaces of these brace points, Teflon shims were provided to reduce friction during testing. At the foundation level, the GMF and test specimen sat on a 12'-0"x9'-0"x1.5" thick steel base plate that was anchored to the strong floor with 1-1/8" post-tensioned all-thread anchor rods, as schematically shown in figure 5-3. Also shown in the figure, the VBE clevis and pin base plates assembly, as well as the HBE anchor beam were anchored to the foundation plate using threaded bolts into tapped holes. Note that oversized holes were used at all bolt connections to the foundation plate to accommodate construction tolerance; hence all foundation bolts were designed as slip-critical.

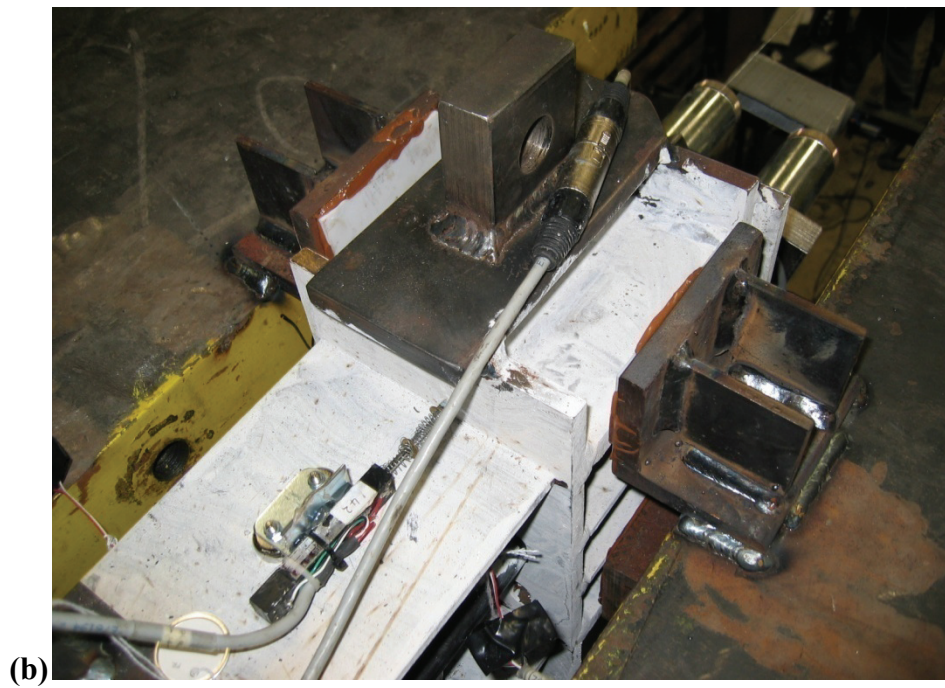
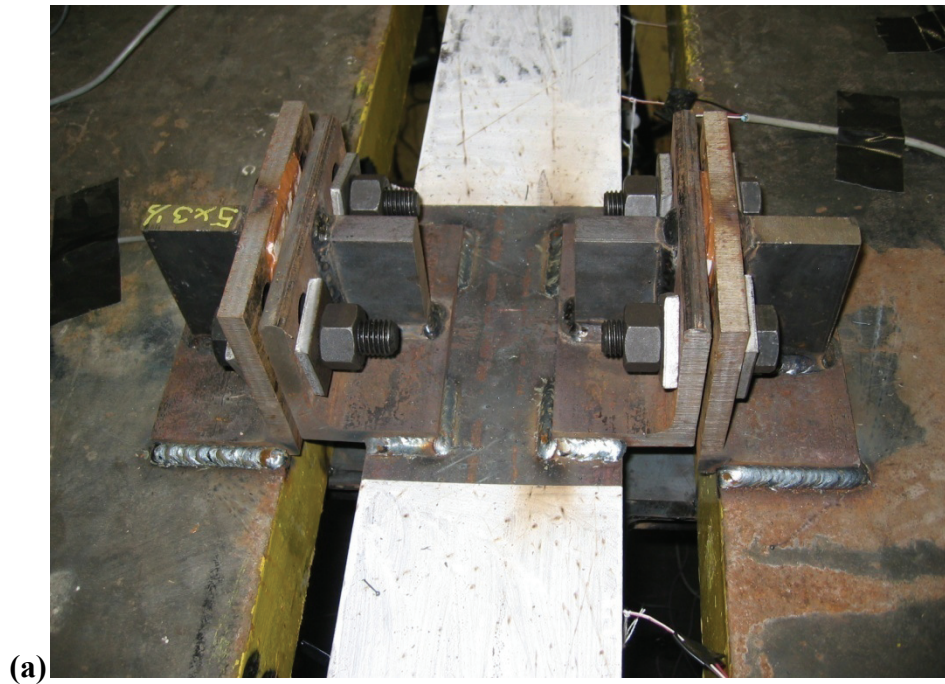


**FIGURE 5-2 Typical connections: (a) diaphragm; (b) lateral brace point**

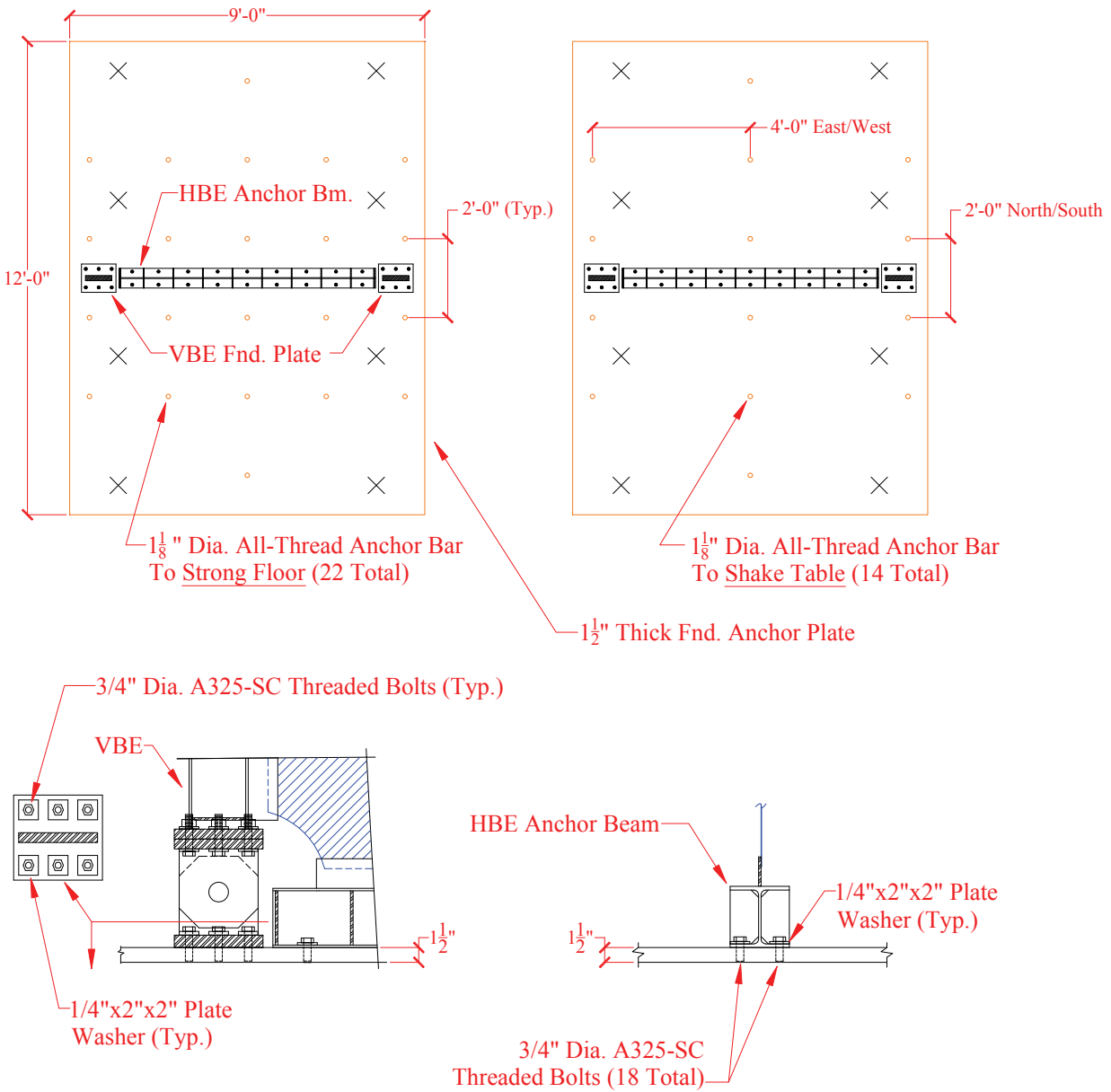


**FIGURE 5-3 GMF base anchorage connection**

The test setup used a total of three MTS 244.51 actuators for lateral loading, one located at each floor level. These actuators are high-performance dynamic actuators with an individual capacity of 220 kips. Although the dynamic capability and the capacity limit of these actuators far exceed the requirements of what was needed for these quasi-static tests, these were the only set of three identical actuators currently available in SEESL's inventory at the time of testing; consistency in actuator characteristics was desired to allow the actuators to run in synchronicity during the tests.

The connection of the actuators to the GMF is shown in figure 5-4. A built-up steel beam (also referred to as the “actuator shoe”) connection was used to attach the actuators to the GMF floor plates, as shown by photos in figure 5-5.

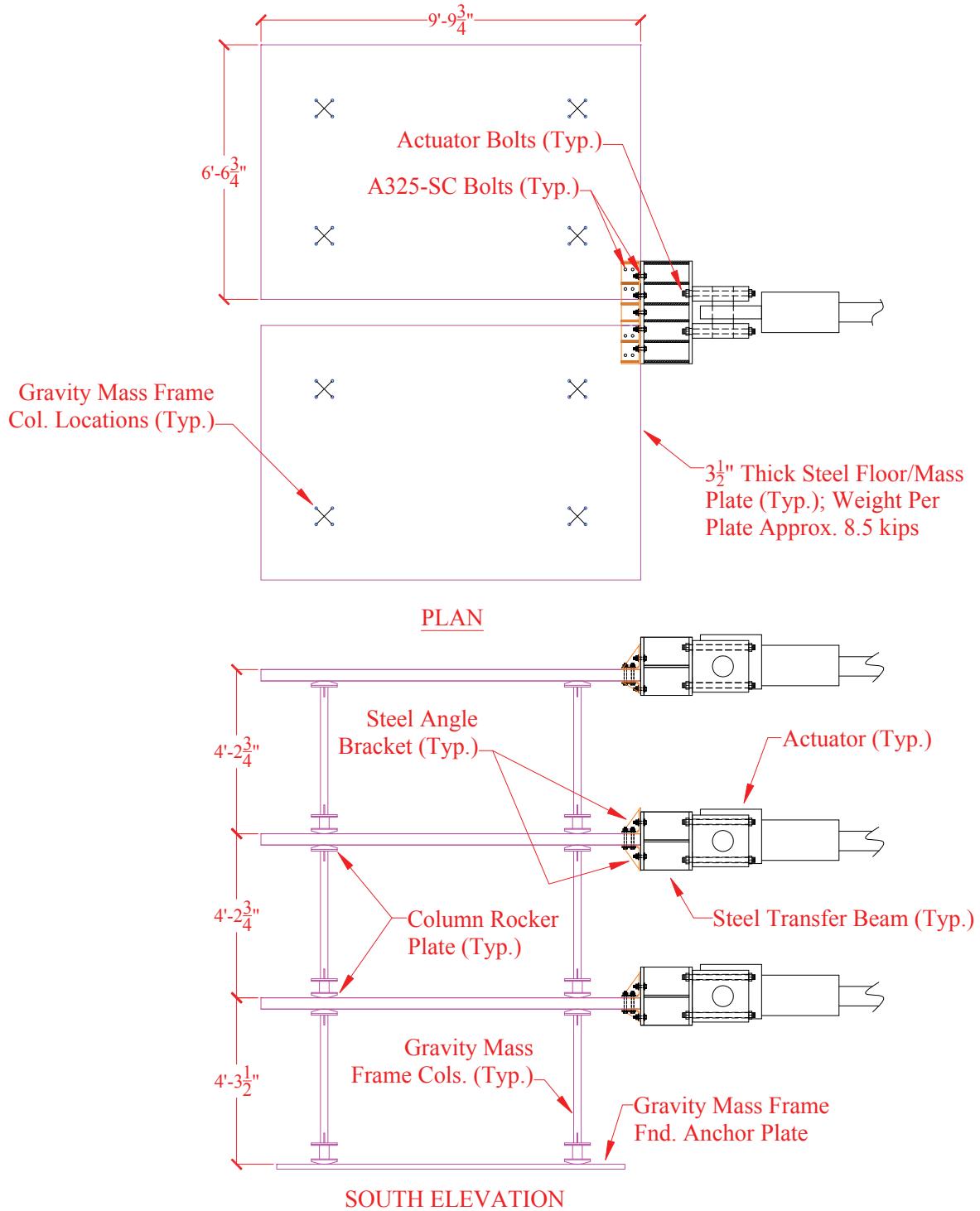


**FIGURE 5-4 GMF actuator connection**



(a)



(b)

**FIGURE 5-5 Actuator shoe: (a) Global view; (b) Close-up view**

### 5.2.2 Specimen Construction

This section highlights some key points related to construction of the specimens and test setup. In particular, the PT anchorage details, the procedure for application and removal of initial post-tension (PT) force, special considerations for PT stressing of frames NZ and CR, installation of the infill web plates, and placement of the built specimen are described below:

1. The PT anchorage details are shown in figures 5-6 and 5-7. Barrel chuck PT anchors were used at both the stressing and “dead” anchorage ends of the PT strands. At the stressing end, “single-use” barrel chucks were used with a 1 in. thick “U” shaped steel shim plate (for reasons to follow). At the dead end, “multi-use” barrel chucks were used. PT load cells were used to monitor PT forces during stressing operations and were located at the dead end anchorage locations. The load cells were positioned between two 1/2 in. thick steel bearing plates to facilitate uniform transfer of the PT anchor force to the load cells.
2. The post-tensioning of the PT strands was performed prior to the installation of the infill web plates. The initial target PT force for frame FR and NZ was approximately 20% of the PT yield strength for each monostrand; for frame CR, it was approximately 30% (note that these are the same target values used in the nonlinear static monotonic and cyclic analyses results presented in Section 4). Stressing operations of PT monostrands can only “pull” on the PT strands and the effects cannot be reversed. To provide a method in which the effects of PT stressing can be reversed (i.e., removal of strand PT force), a PT stressing “shoe” was used; this detail, shown in figure 5-8, was based on a similar one used by Winkley (2011). This stressing shoe is a temporary assemblage used only for stressing/de-stressing operations and the general PT stressing procedure used is as follows:
  - a. A 1 in. thick “U” shaped steel plate spacer is provided between the PT anchor and the VBE flange. The reason for this spacer plate will be made clear in step “g”.
  - b. The stressing shoe is put in place, PT strands are “fished” through the front bearing plate of the shoe, and the stressing jack is put in place in bearing on the front plate of the shoe.

- c. The stressing jack then stresses the PT strands by reacting on the shoe which then transfers the strand PT force to the boundary frame; at this stage, the PT anchor at the stressing location does nothing.
  - d. During PT stressing, the strands elongate and a gap forms between the “U” bearing plate where then steel shims are inserted to fill the gap at a target strand PT force, which is monitored by reading the PT load cell values. The shoe was fabricated allowing access from the sides, top, and bottom to facilitate the placement of these bearing shims.
  - e. The stressing jack was then released and PT force transfers from the stressing shoe to the PT anchors at the stressing location. The resulting PT force is read from the load cell readings.
  - f. If the target PT force is exceeded, the stressing jack re-engages the PT strand and pulls on the strand until a gap forms and individual steel shims can be removed. Then the stressing jack is released, once again transferring the PT force to the PT anchors where the load cell reading is re-evaluated. If the PT target force is under the target, the procedure is repeated but now steel shims are added. This process continues until the approximate initial PT target force has been achieved.
  - g. After the test is complete, to de-tension the PT monostrands, the shoe is put back in position at the stressing anchorage location, and the strands are pulled until the 1 in. thick “U” shaped steel plate spacer can be removed. Once all shims are removed, the stressing jack releases and the strands become fully relaxed as the PT anchor will not re-engage the VBE flange due the initial gap provided by the 1 in. thick shim plate.
3. PT stressing was performed at one individual PT strand location at a time. For frames NZ and CR, special attention had to be given for the stressing operation. For these details an initial gap exists at the ends of the HBEs (for frame NZ it is at the bottom flange, and for frame CR it is at both top and bottom flanges). Furthermore, the PT strands are anchored on the HBEs. As a consequence, temporary restraining plates were provided to facilitate stressing of the PT strands shown in figure 5-9. If these temporary plates are not provided, the HBE-to-VBE joint will close (due to the initial gap) pulling the frame out-of-square during stressing operations. Once all PT strands had been stressed to their

approximate target force, the temporary restraining plates were then removed. In principle, some redistribution of PT forces on the boundary frame can occur during removal of the restraining plates, but with all tendons stressed and the boundary frame “locked” into position, additional adjustments can always be made to the boundary frame PT strands (which is made possible by the use of the stressing shoe detail presented above). However, note that for the UB specimens, the redistribution of the boundary frame PT forces upon removal of the restraining plates was observed to be negligible. Note that, as an alternative to providing a temporary restraining plate, the PT strands could have been stressed in complete tandem (i.e., for each PT strand location, the opposite-hand PT strand could have been stressed simultaneously).

4. After the PT strands on the boundary frame had been stressed the installation of the infill web plates followed. The first step was tack-welding the infill web plates to the boundary frame (figure 5-10a). This served as a temporary connection keeping the infill web plates at each level in-place on the boundary frame during construction. Furthermore, it was a method to uniformly distribute the infill web plate shrinkage effects during welding. The second step involved providing the continuous weld connection between tack-welds; to also help distribute the shrinkage effects, the welding was done in staggered segments along the perimeter of the infill web plates, until a continuous weld was provided along the infill web plate perimeter (figure 5-10b). All welding was done in the flat position.
5. To facilitate construction of the final built specimen and to hoist the specimen in place on the strong floor, a temporary connection of the HBE anchor beam to the base of the VBE clevis and pin assembly was required (i.e., since this anchor beam is not connected to the VBEs in the test setup). This was accomplished as shown in figure 5-11. This “construction aid” connection consisted of an L5x3 angle each side of the HBE anchor beam web with bolted connections to the clevis and pin side plates. The construction of the boundary frame then followed:
  - a. The HBE anchor beam and VBE clevis and pin supports were loosely bolted on the foundation plate, after which the L5x3 construction aid connections were made. This ensured that the clevis and pin and HBE anchor beam, temporarily



behaved as a single component, facilitating alignment with the existing anchor bolt holes on the foundation plate (figure 5-12).

- b. Next, the remaining portions of the boundary frame were loosely bolted together and hoisted such that the VBEs aligned with the clevis and pin support attached to the foundation plate. The VBEs were then lowered in contact with the clevis and pin support and the bolted connections were made.
  - c. Once the VBEs were securely attached, the anchor bolts were removed and the whole frame assembly was hoisted and placed flatwise on temporary cribbing for remainder of work.
  - d. The frame was checked for square, adjustments were made as necessary, and all shear plate bolt connections were then torqued with a pneumatic gun to lock the frame in position, now the boundary frame is ready for installation of the PT and infill web plates.
  - e. After installation of the PT and infill web plates, the frame was hoisted back onto the foundation plate where all anchor bolt connections were made (figure 5-13). Note that all anchor bolts were in oversized holes to accommodate construction tolerance. Accordingly all anchor bolts were designed and installed as slip-critical.
6. With the specimen in place. The frame was checked for out-of-plumb (in transverse direction) and adjustments were made accordingly. Next, the GMF was installed, followed by connection of the actuators to the GMF floor plates. Finally, the construction angles connecting the clevis and pin and HBE anchor beam together were removed prior to testing (figure 5-14).

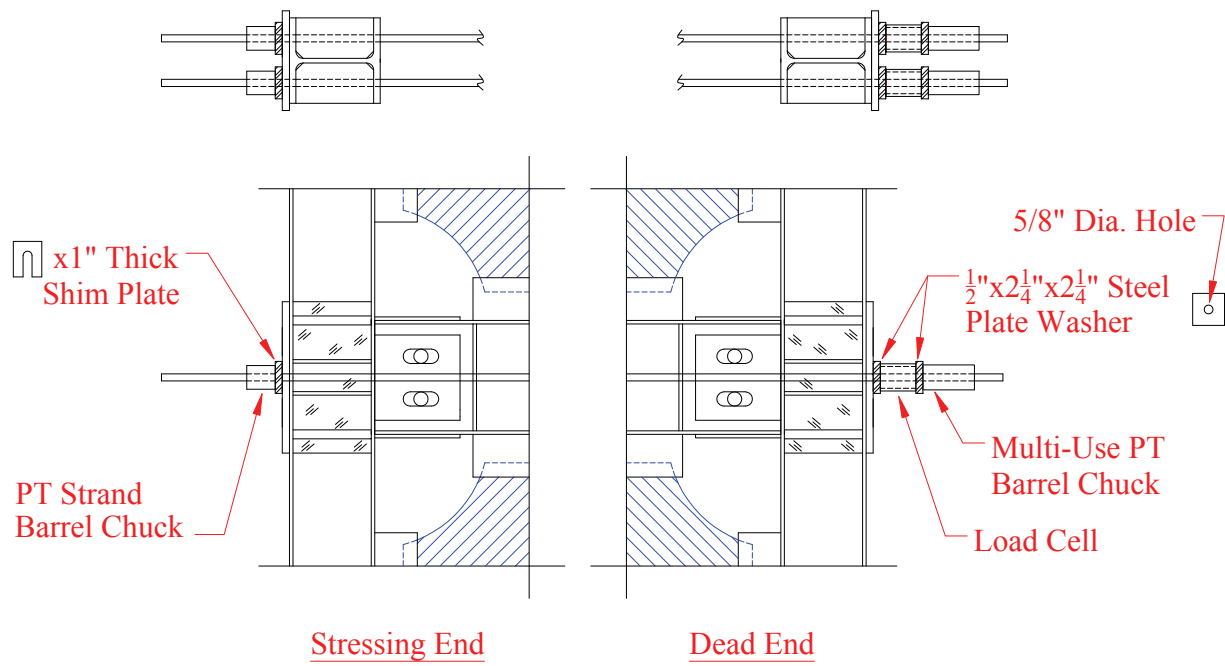


**FIGURE 5-6 PT anchor details**

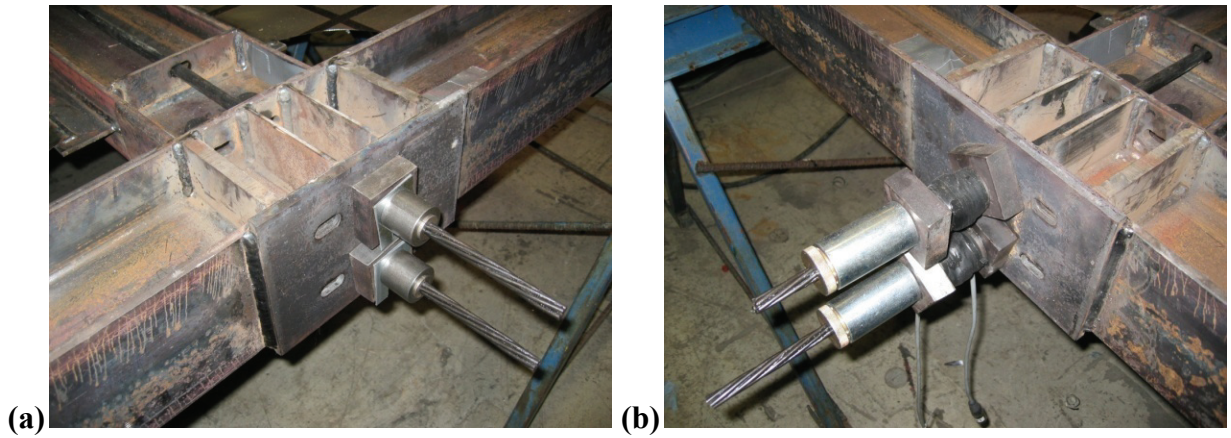


**FIGURE 5-7 Typical PT anchor: (a) stressing end; (b) dead end**

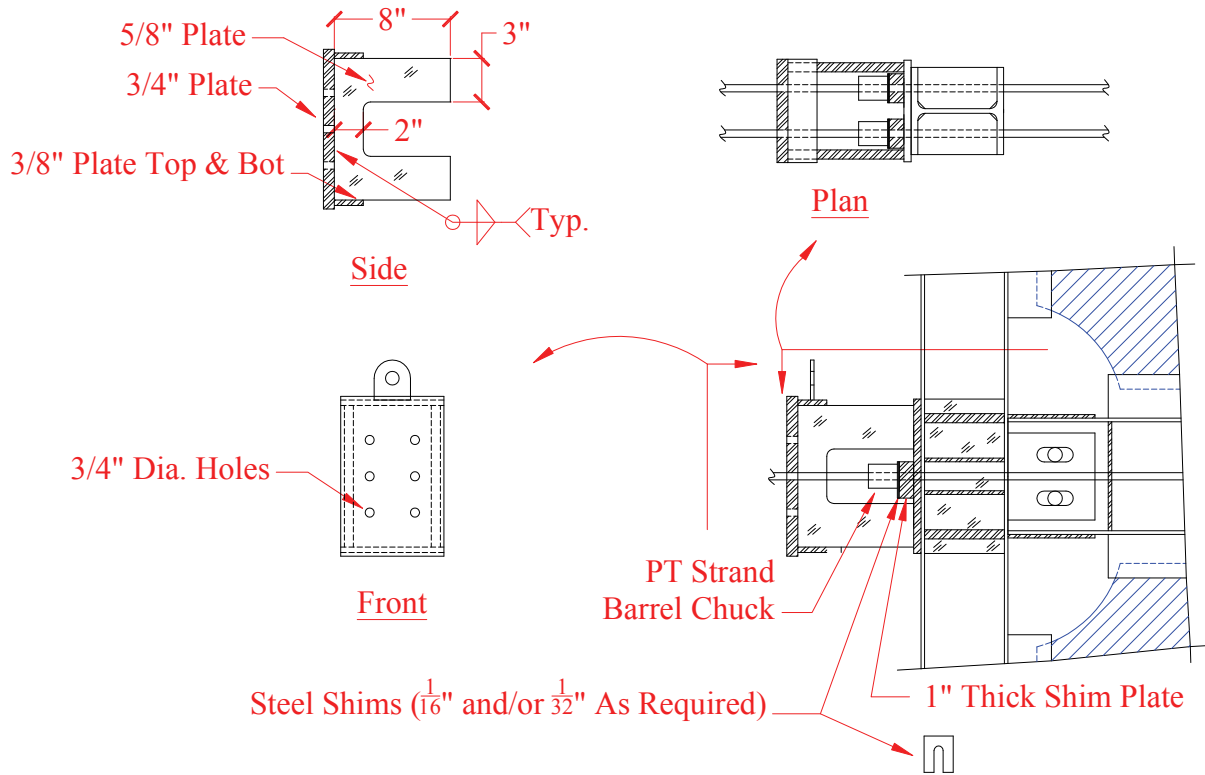


**FIGURE 5-8 PT stressing shoe**

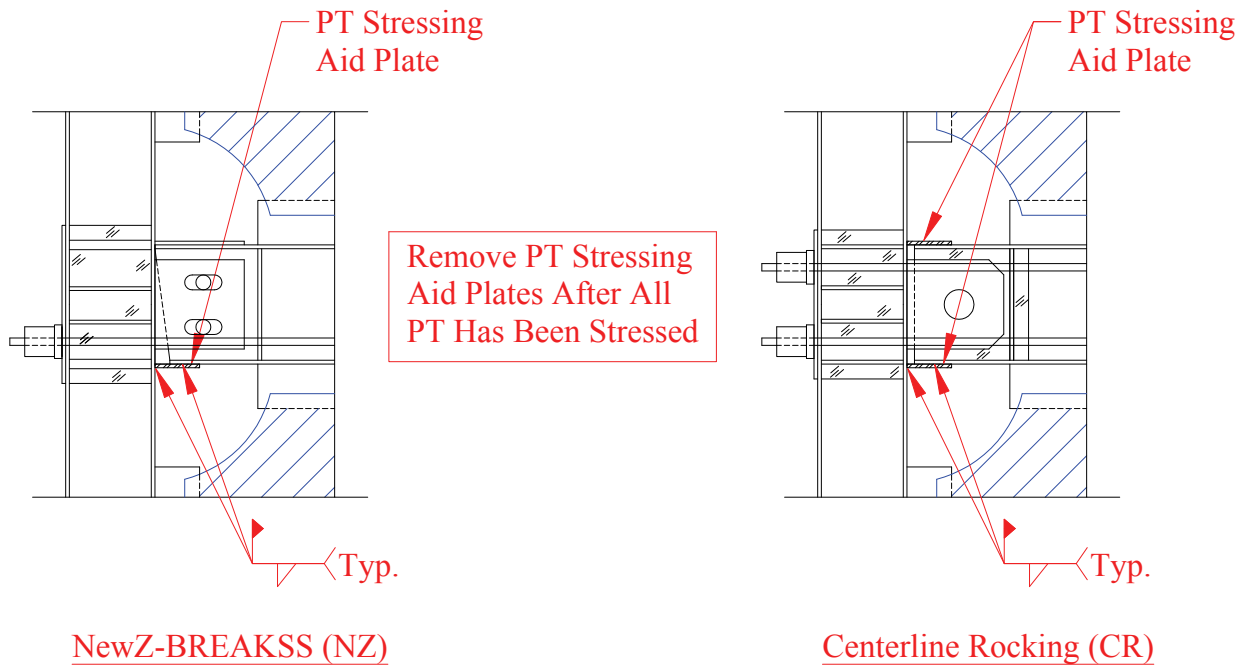
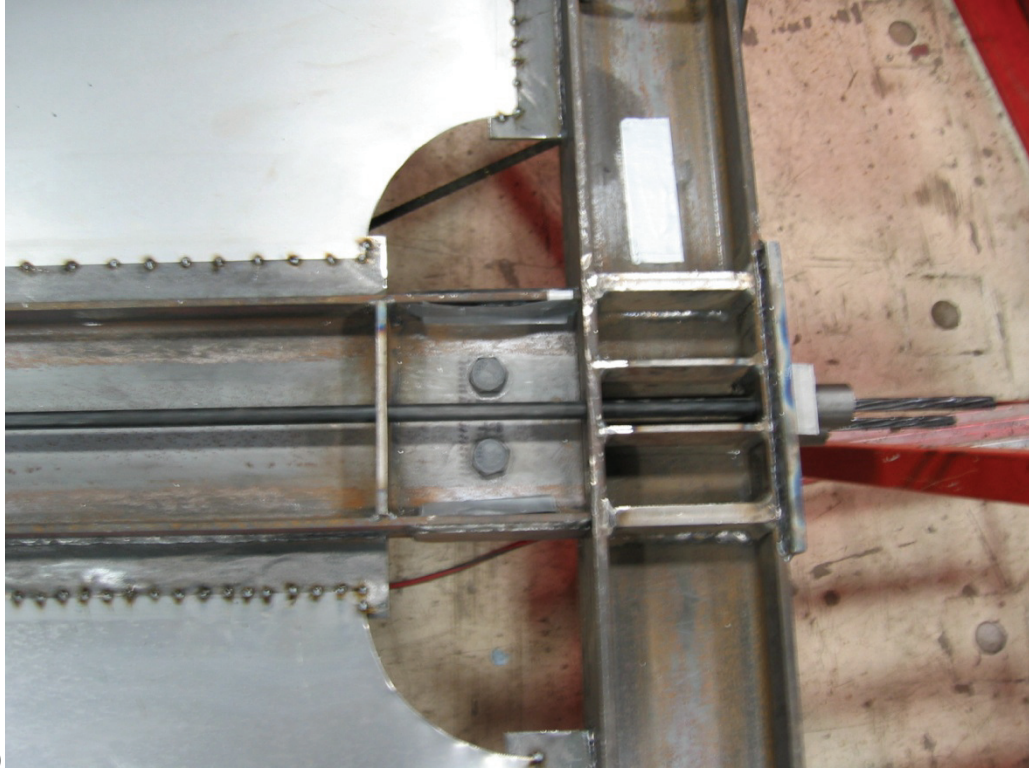
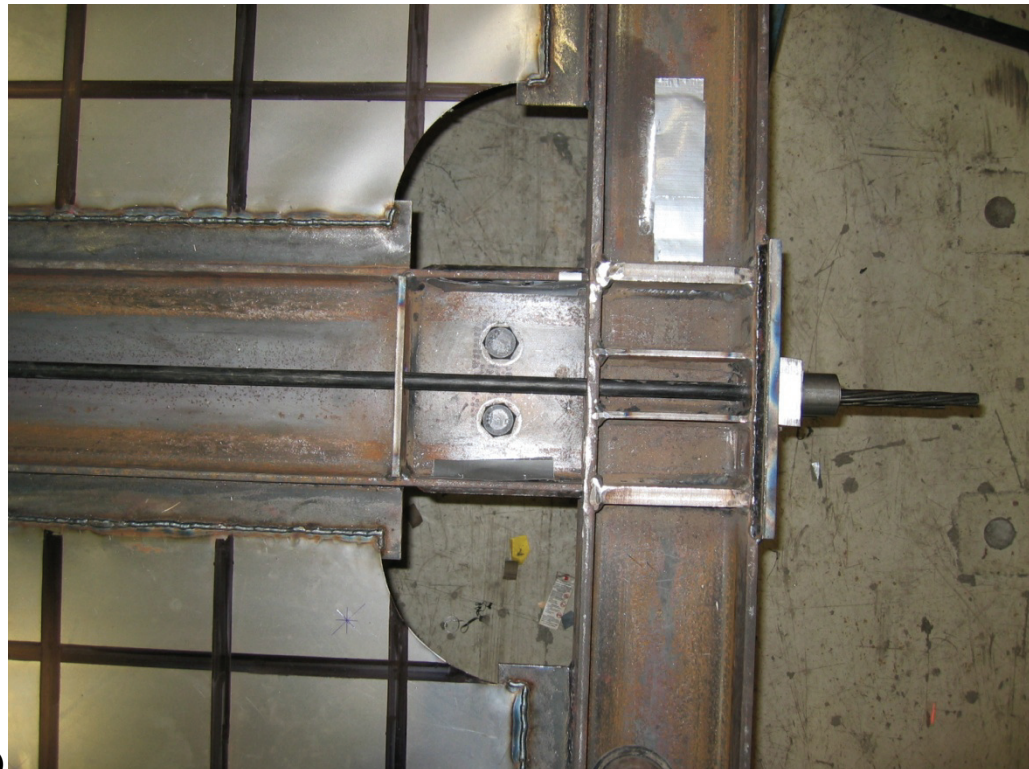


**FIGURE 5-9 PT stressing aid**



(a)



(b)

**FIGURE 5-10 (a) Initial web plate weld; (b) Final web plate weld**

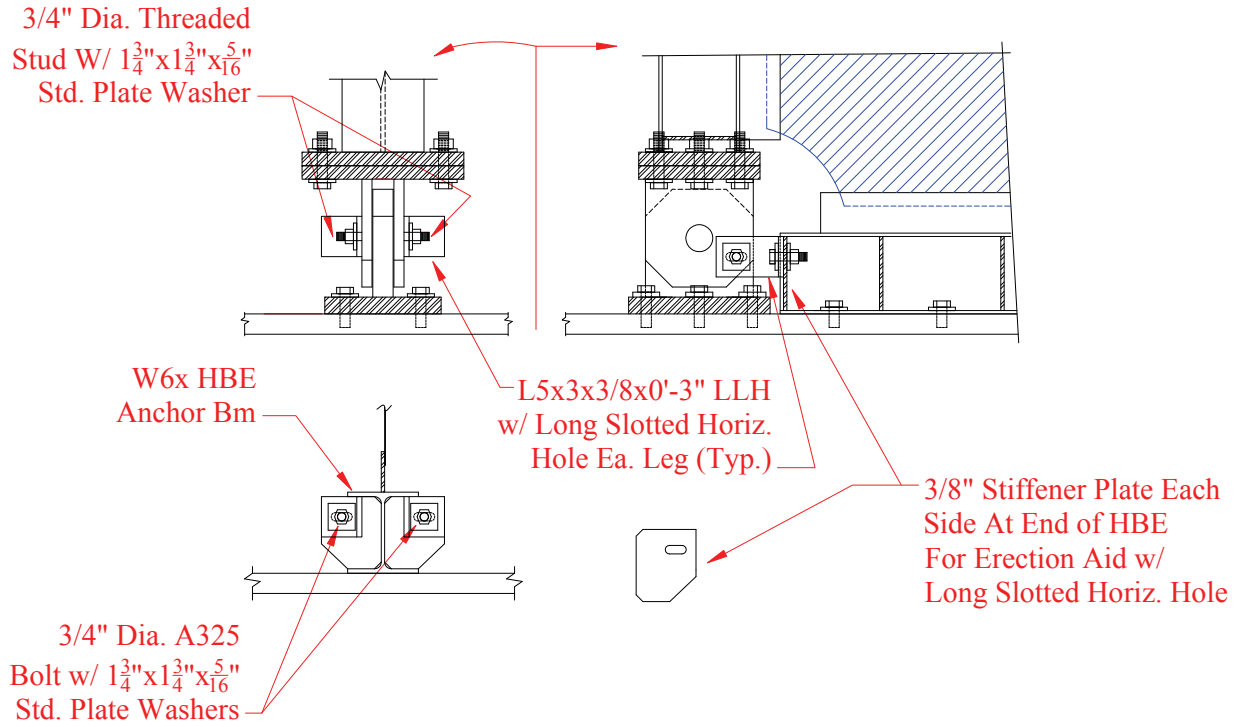


**FIGURE 5-11 Frame construction aid**

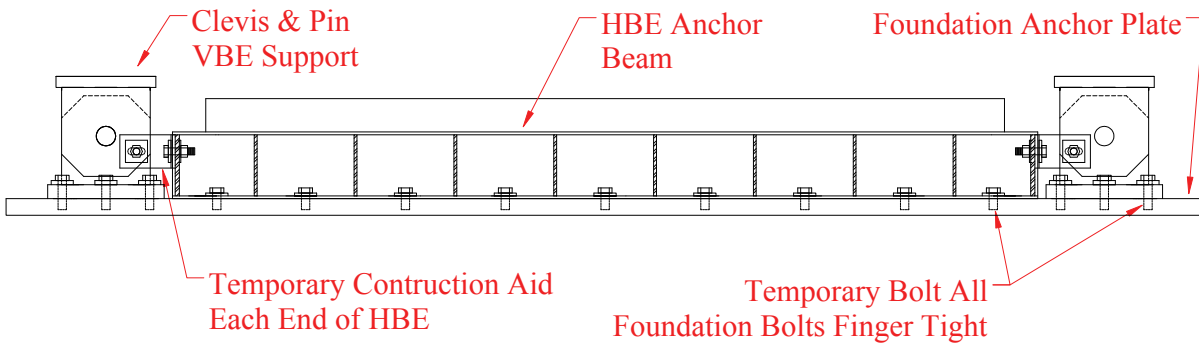


**FIGURE 5-12 Temporary foundation attachments**

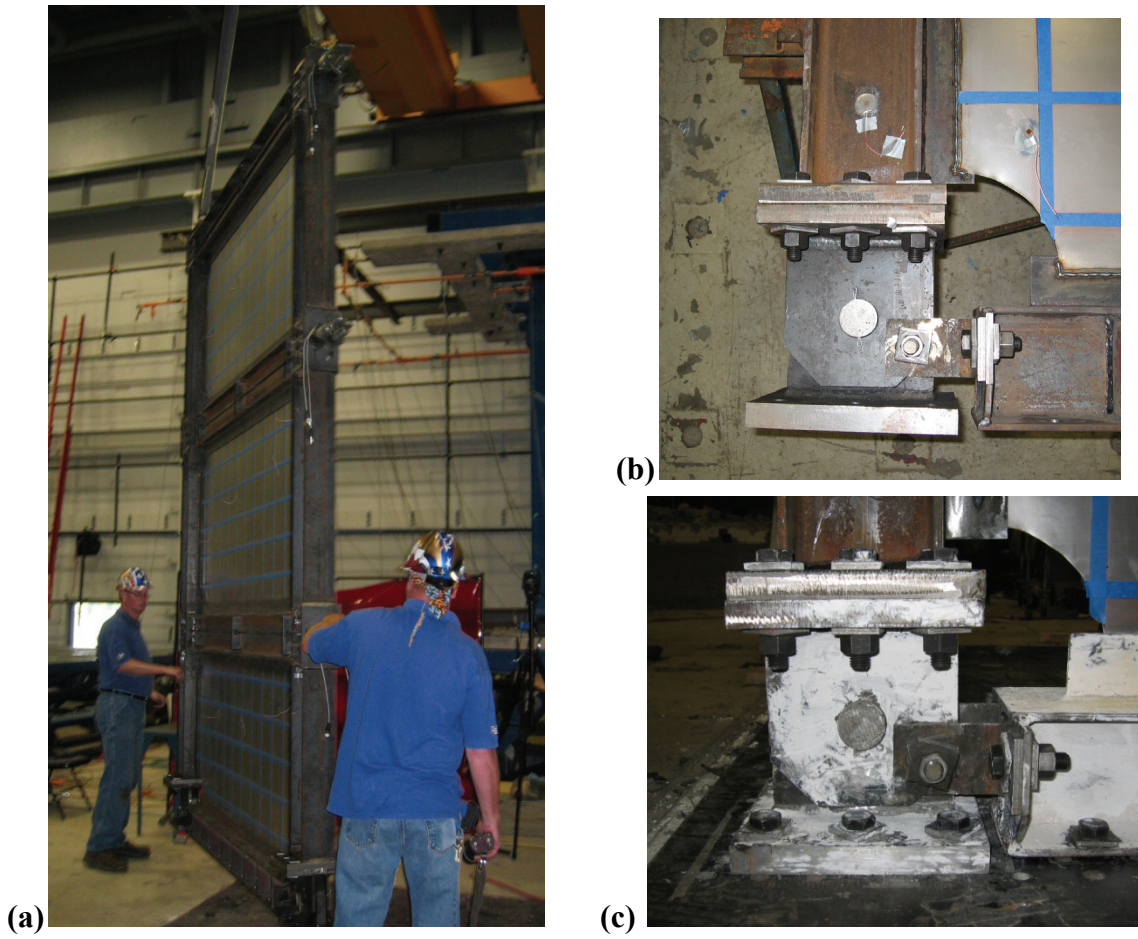


**FIGURE 5-13 (a) Test specimen; (b) Construction aid; (c) Foundation connection**

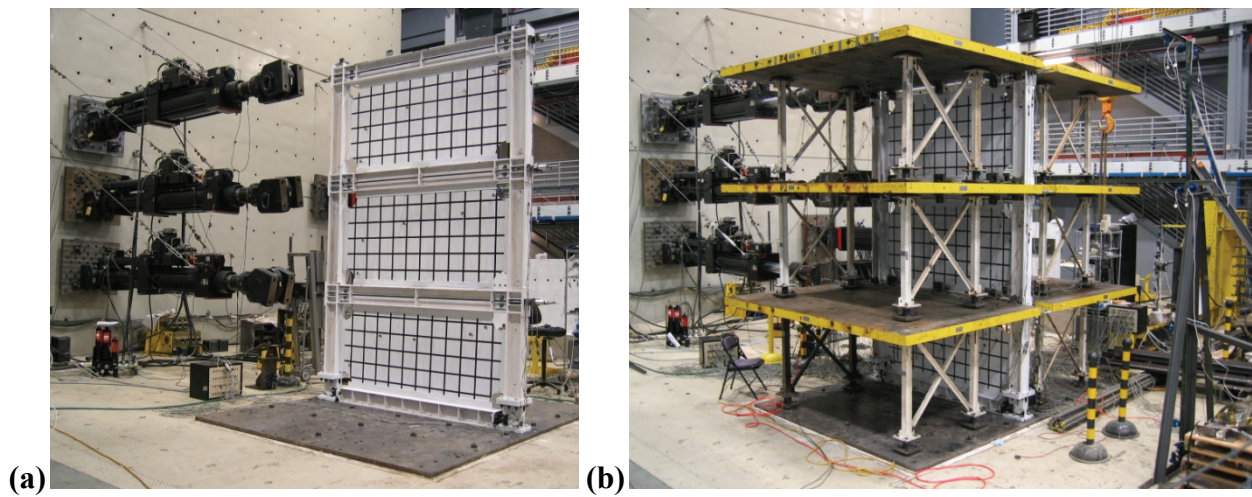


**FIGURE 5-14 Quasi-static test specimen: (a) initial placement; (b) final setup**

### 5.2.3 Instrumentation

Instrumentation sensors used to record local and global response are shown in figures 5-15 to 5-18 for the specimens and figure 5-19 for the GMF. For clarity, only the sensor symbol (indicating sensor type) is shown as indicated by the Legend provided in the figures. The complete instrumentation drawings for each test specimen, including sensor names, are provided in Appendix A of this report. For reference, a break-down of the total number of sensors used for each test specimen is provided in table 5-1.

**TABLE 5-1 Quasi-static test instrumentation**

Test	Sensor					Total
	SP	LP	LC	SG	SGR	
FRW	14	12	6	108	12	152
FRB	14	12	6	78	12	122
FRS	14	12	6	104	12	148
NZW	14	12	12	93	12	143
NZB	14	12	12	78	12	128
NZS	14	12	12	104	12	154
CRW	14	12	24	93	12	155
CRB	14	12	24	78	12	140
CRS	14	12	24	104	12	166

Test Nomenclature:

FR - flange rocking frame  
 NZ - NewZ-BREAKSS frame  
 CR - Centerline rocking frame  
 W - infill web plate  
 B - bare frame  
 S - infill web strip

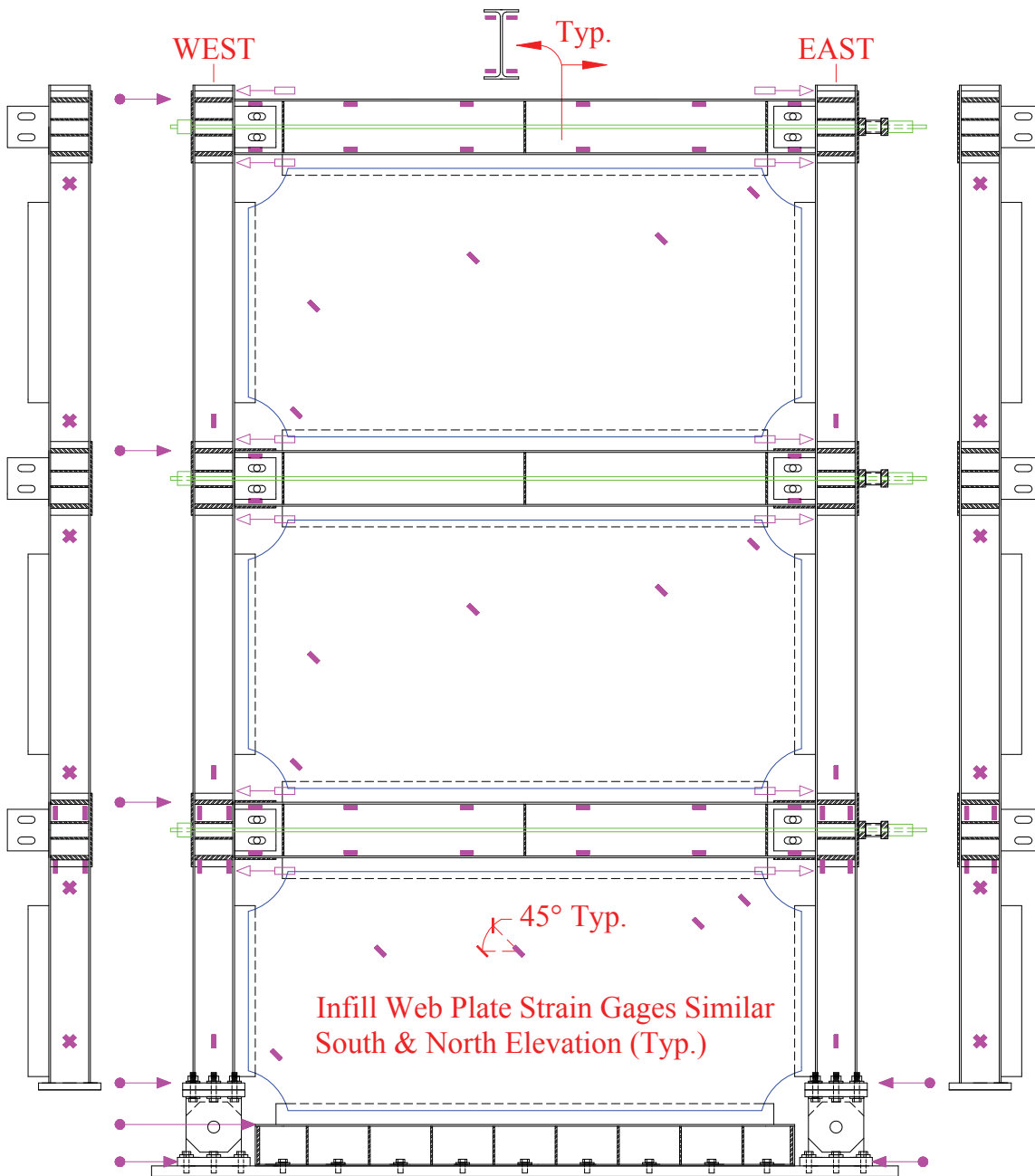
Sensor Nomenclature:

SP - string potentiometer  
 LP - linear potentiometer  
 LC - load cell  
 SG - linear strain gage  
 SGR - strain gage rosette

In general, the instrumentation for all three frame types was identical. Minor differences observed in the figures are due to the characteristics of each frame type. Displacement transducers in the form of string potentiometers (string pots) were provided to record global displacements on the specimen and the GMF floor plates; linear potentiometers were provided at the top and bottom flanges at the ends of the HBEs to collect data that could be used to calculate relative HBE-to-VBE gap rotations. All string pots were attached to a fixed reference point to obtain the actual displacement of the recorded element (i.e., no string pots were attached to the

reaction wall and the displacement transducers of the actuators were not used – other than for internal actuator controls). The actuator forces were recorded by the load cell in each actuator. PT load cells were provided at the PT dead end anchorage location to record PT force response. Furthermore, although the boundary frame was designed to remain essentially elastic, strain gages were provided to verify this at a few locations and obtain strain data for conversion into axial and moment demands at particular locations along the boundary frame. All uniaxial strain gages were on quarter bridge circuits and strain rosettes were on full bridge circuits.

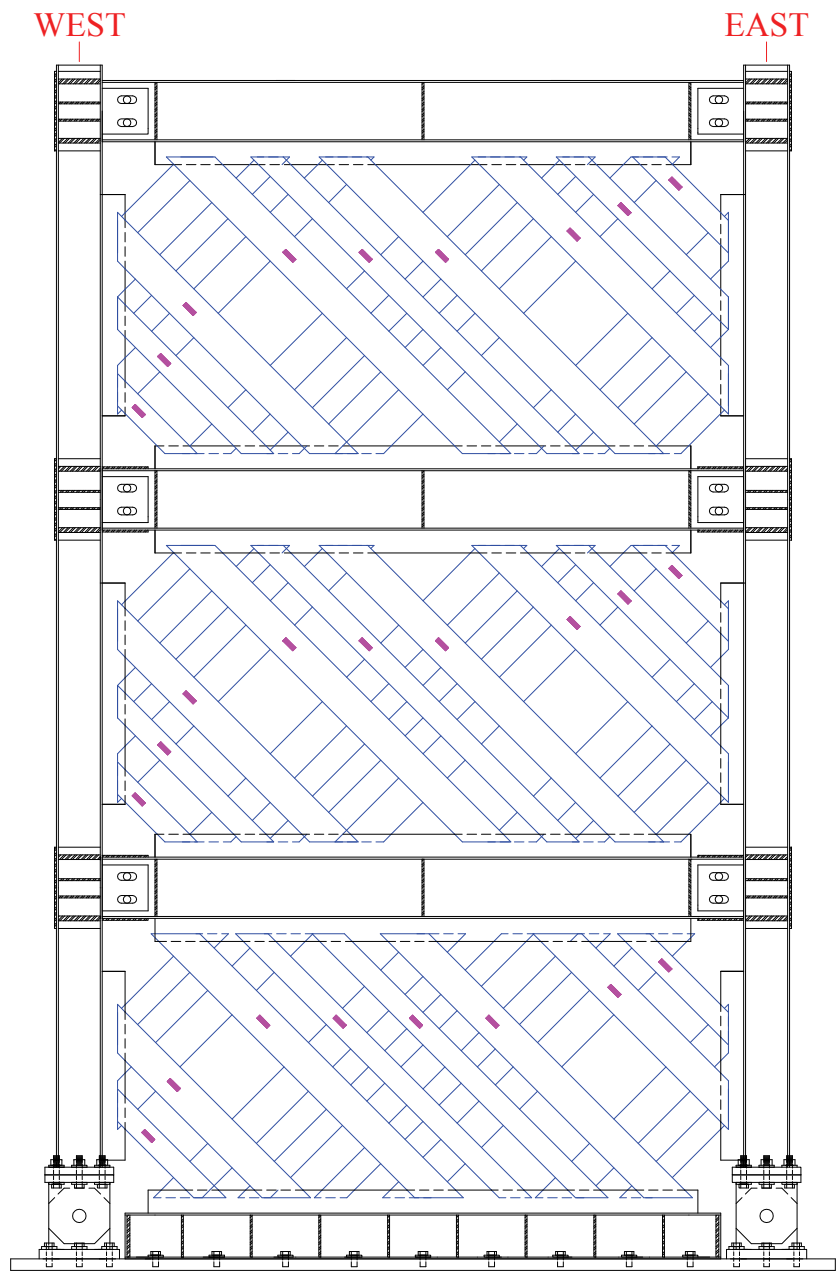




**LEGEND:**

- Uniaxial Strain Gage
- ← Linear Potentiometer
- ▨ PT Load Cell
- \* Shear Rosette Strain Gage
- String Potentiometer

**FIGURE 5-15 Quasi-static: Frame FR instrumentation**



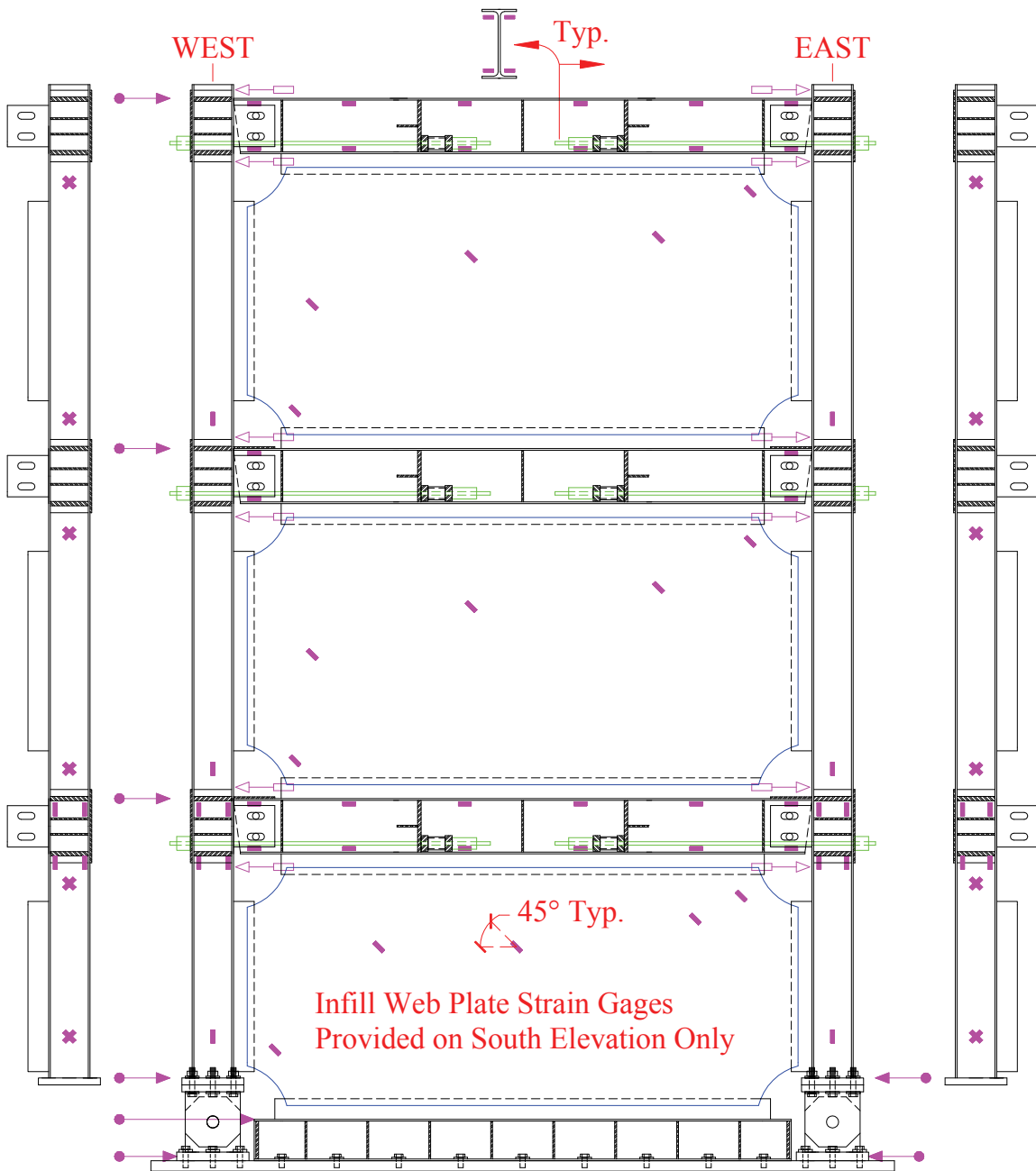
**LEGEND:**

- Uniaxial Strain Gage

**NOTE:**

FR Frame Shown;  
 NZ and CR Infill  
 Web Strips Similar

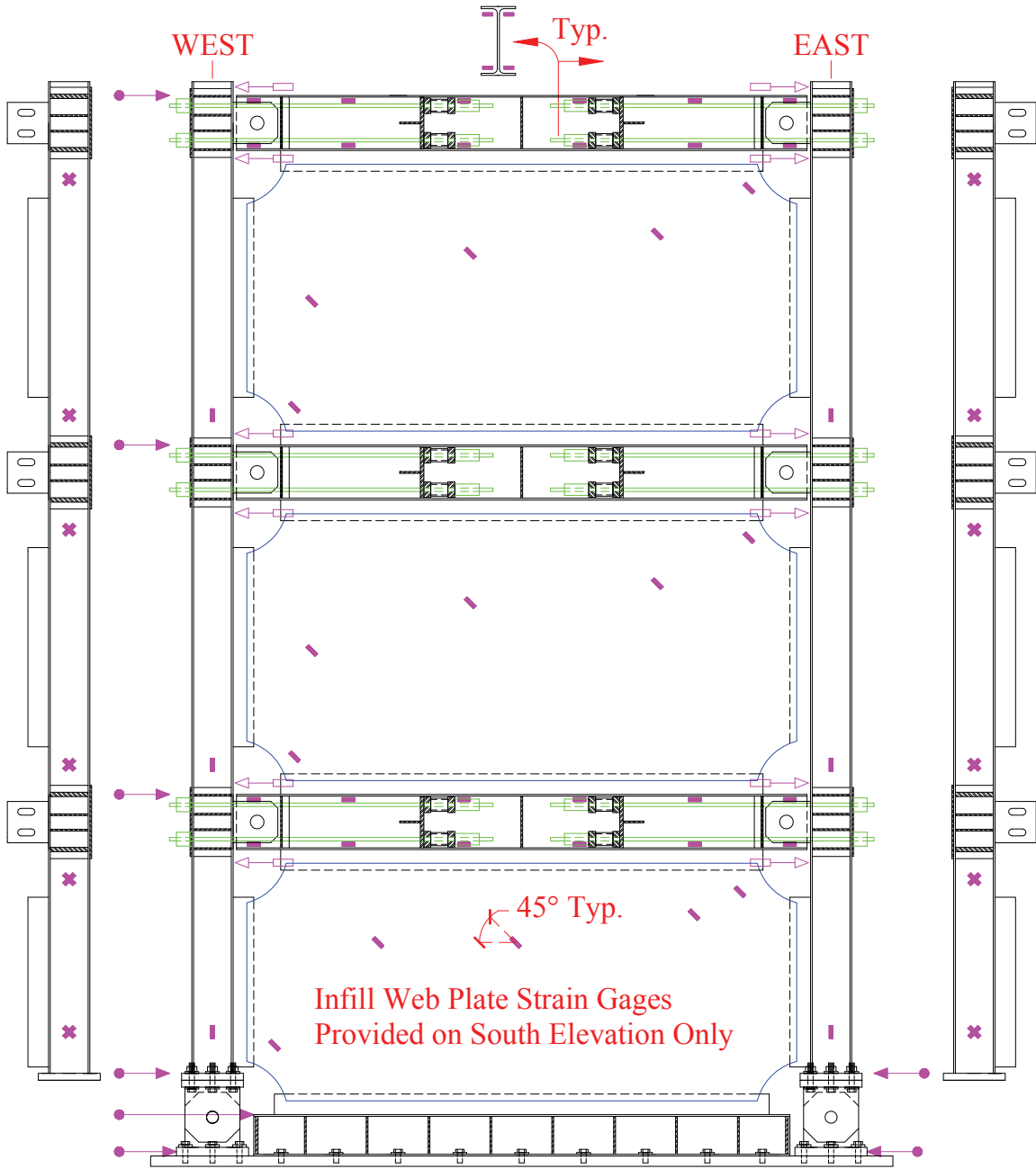
**FIGURE 5-16 Quasi-static: Frame FR (NZ and CR similar) infill web strips strain gages**



**LEGEND:**

- Uniaxial Strain Gage
- ◁ Linear Potentiometer
- ▨ PT Load Cell
- \* Shear Rosette Strain Gage
- String Potentiometer

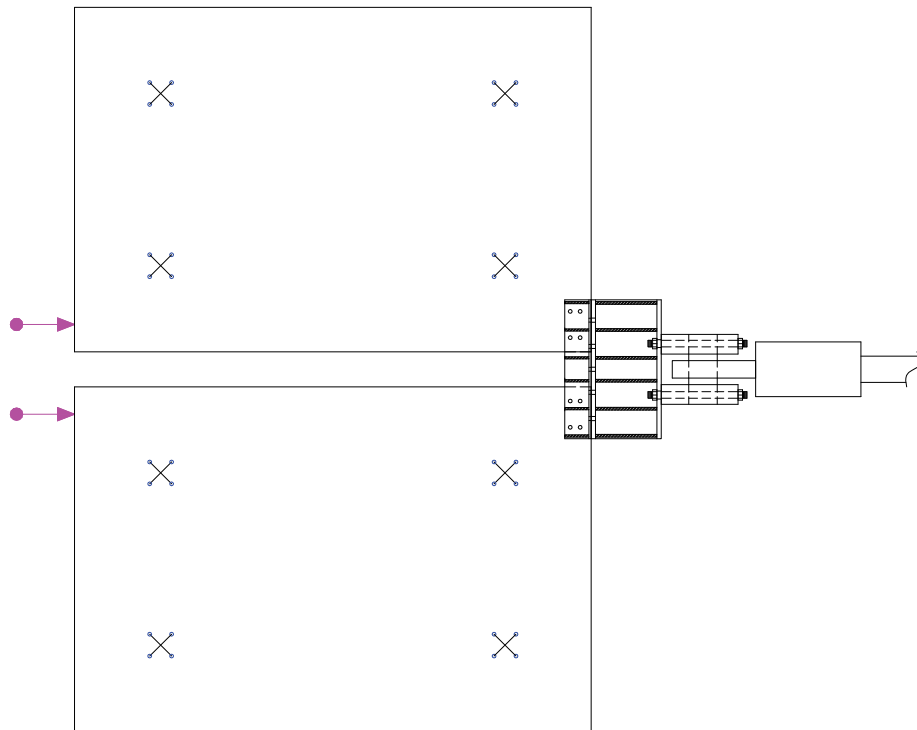
**FIGURE 5-17 Quasi-static: Frame NZ instrumentation**



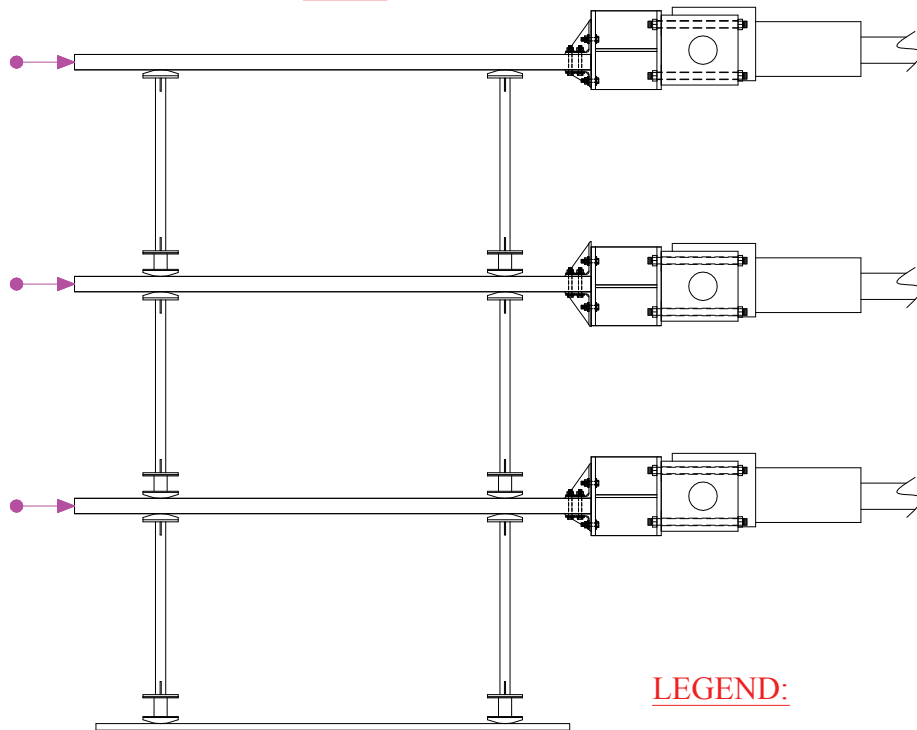
**LEGEND:**

- Uniaxial Strain Gage
- ◁ □ Linear Potentiometer
- ▨ PT Load Cell
- ✖ Shear Rosette Strain Gage
- ◁ ● String Potentiometer

**FIGURE 5-18 Quasi-static: Frame CR instrumentation**



PLAN



SOUTH ELEVATION

LEGEND:

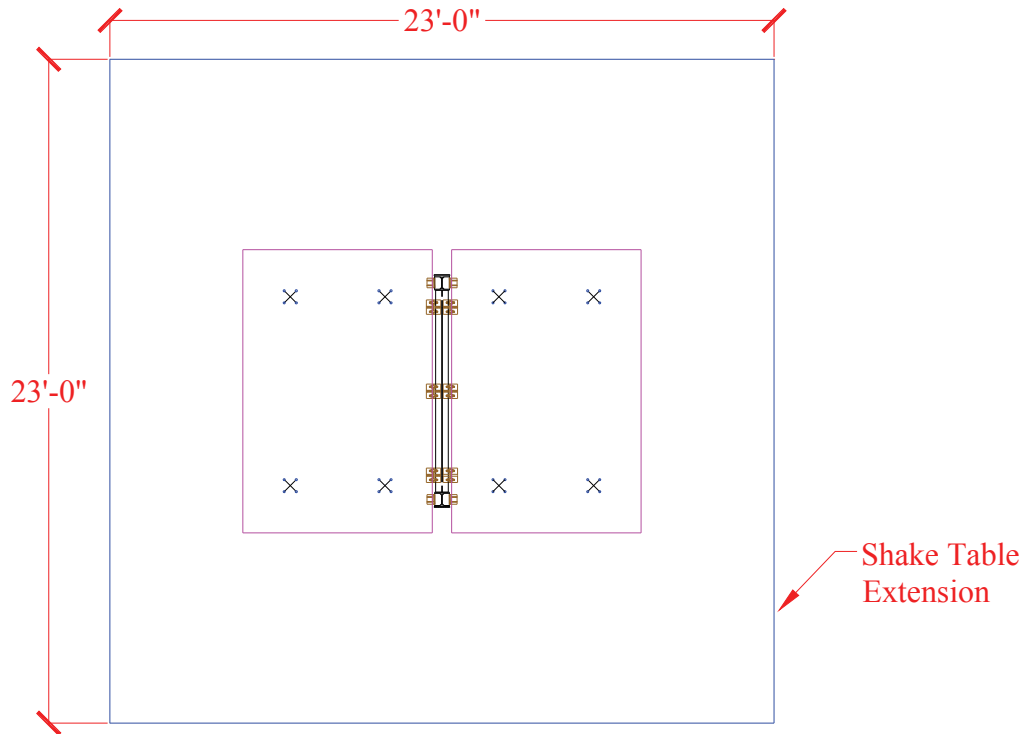
←● String Potentiometer

**FIGURE 5-19 Quasi-static: GMF instrumentation**

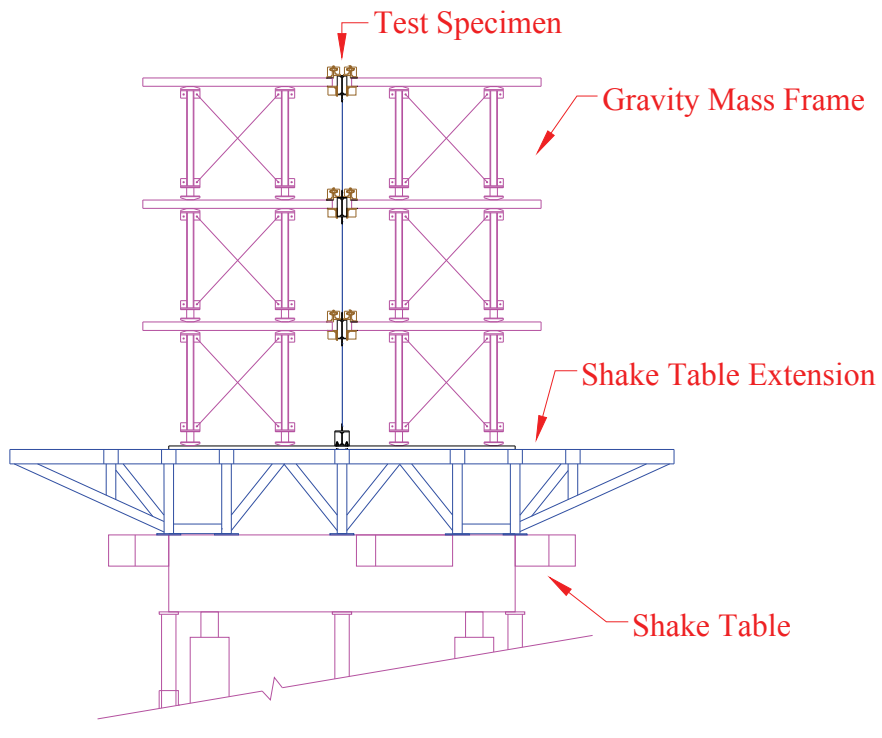
## **5.3 Shake-Table**

### **5.3.1 Test Setup**

The shake-table used at SEESL for these experiments has 6-degrees-of-freedom, can support a superimposed specimen weight of up to approximately 88 kips, has a maximum rated overturning resistance of approximately 335 kip-ft, and can reproduce a base acceleration of approximately 1.15 g for a 44 kip specimen. The test setup on the shake-table is shown in figures 5-20 and 5-21. The use of the GMF system is identical to that presented for the quasi-static tests; the only difference is that, for the shake table tests, the steel floor plates provide the seismic mass needed to generate the inertia forces (which corresponds to a seismic weight of approximately 17 kips per floor level). As was mentioned in Section 4.3, only the FR and NZ frames were tested on the shake-table, with replacements of the infill web plate and PT material that matched that of the quasi-static tests. Other than the change in loading (i.e., shake-table testing instead of quasi-static testing), the only other difference was that the initial PT forces used were different than those used for the quasi-static tests; for both frames subjected to shake table testing, an initial target PT force of approximately 40-45% of the PT yield strength for each monostrand was used (note that these are the same target values used in the nonlinear dynamic time history analyses results presented in Section 4).



PLAN



EAST / WEST ELEVATION

**FIGURE 5-20 Shake-table setup schematic**

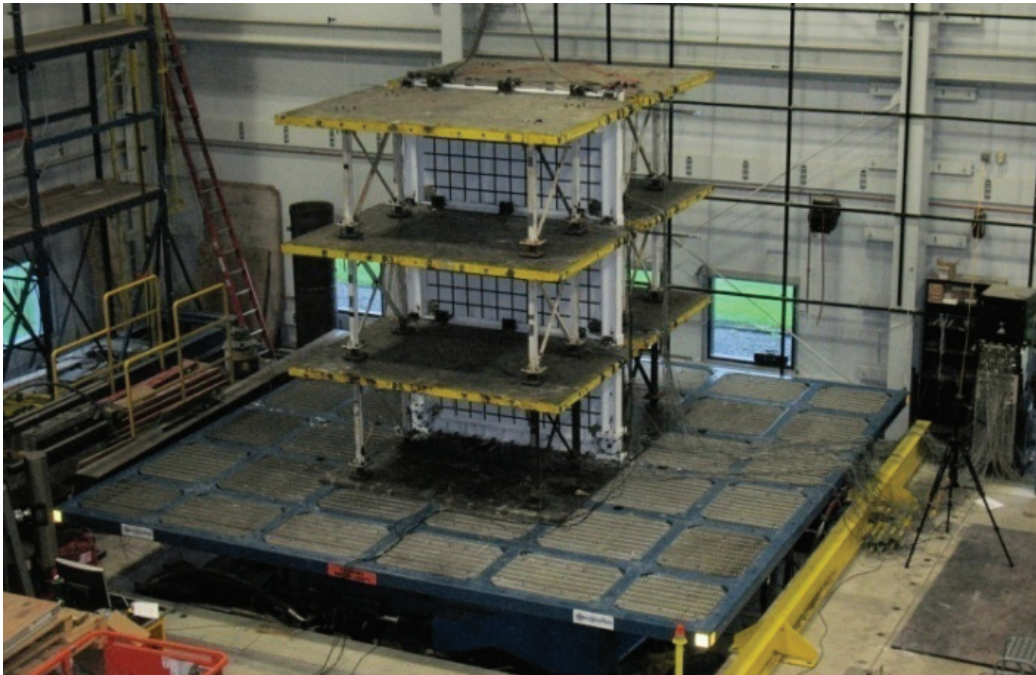


**FIGURE 5-21 Shake-table setup final**



### 5.3.2 Instrumentation

In addition to the instrumentation sensors used for quasi-static tests, accelerometers and krypton sensors were also provided for the shake-table tests. The accelerometers were provided on both the test specimen and the shake-table. Krypton sensors were provided as a redundant sensor (in addition to the string pots used) for data collection of global linear frame displacements. The instrumentation layout for the sensors is shown in figures 5-22 to 5-24 for the specimens, figure 5-25 for the GMF, and figure 5-26 for the shake-table. Note that similarly to what was presented for the quasi-static instrumentation drawings, only the sensor symbols are shown and the complete instrumentation drawings for each test specimen is provided in Appendix A. For reference, a break-down of the total number of sensors used for each test specimen is provided in table 5-2.

Note that for the shake-table tests, uniaxial strain gages on the HBEs were omitted, except for the gages at their ends. Furthermore, strain gages on the infill web plates and strips were also omitted. All other instrumentation sensor locations from the quasi-static tests essentially remained unchanged, except for additional string pots added to the floor mass plates to record torsional effects, and string pots added to the Level 1 infill web plate location to obtain data on approximate infill web plate deformations.

**TABLE 5-2 Shake-table test instrumentation**

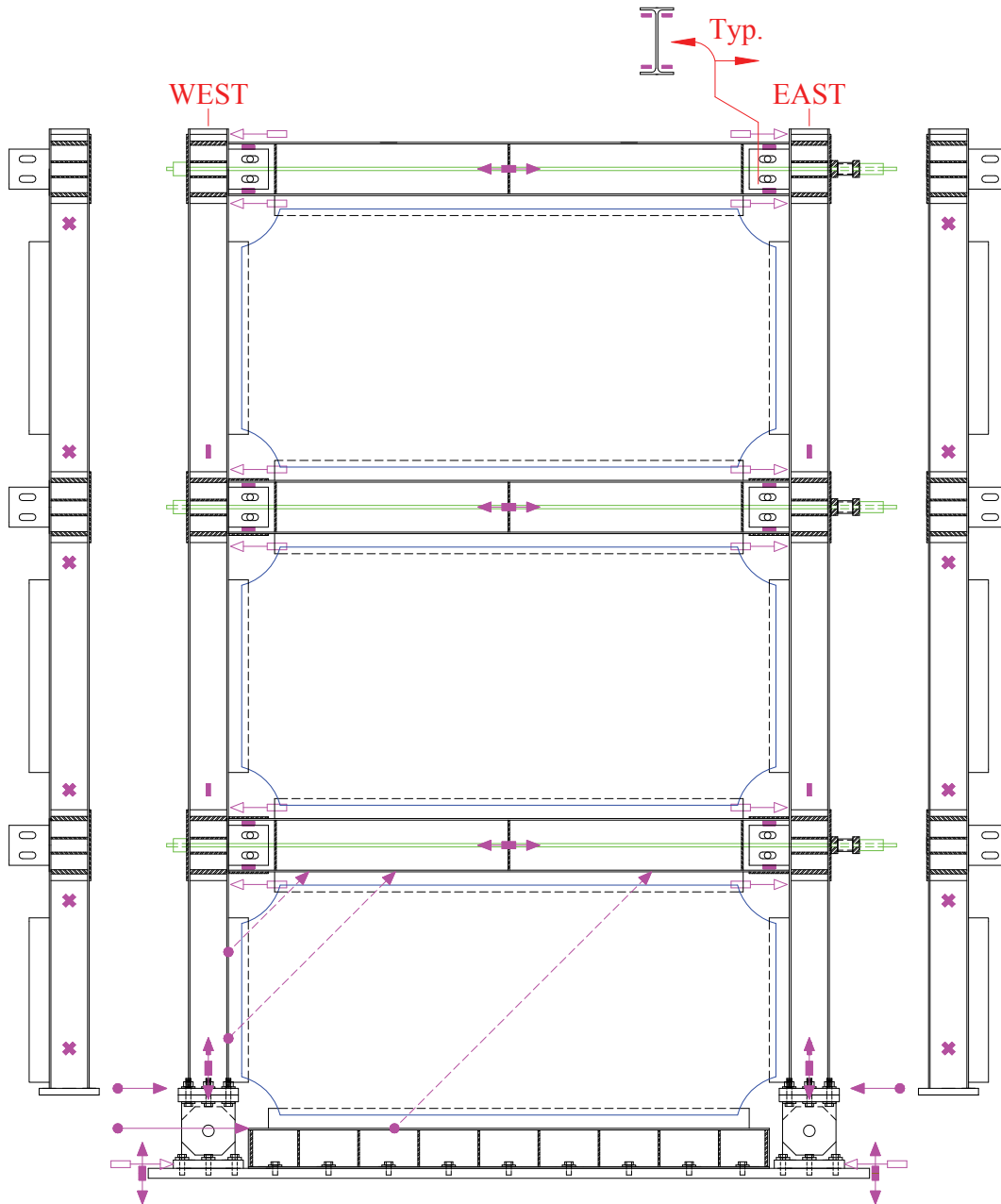
Test	Sensor							Total
	SP	LP	LC	SG	SGR	A	K	
FRW	21	14	6	30	12	26	14	123
FRB	21	14	6	30	12	26	14	123
FRS	21	14	6	30	12	26	14	123
NZW	21	14	12	30	12	26	14	129
NZB	21	14	12	30	12	26	14	129
NZS	21	14	12	30	12	26	14	129
NZP	21	14	12	30	12	26	14	129

Test Nomenclature:

FR - flange rocking frame  
 NZ - NewZ-BREAKSS frame  
 W - infill web plate  
 B - bare frame  
 S - infill web strip  
 P - perforated infill web plate

Sensor Nomenclature:

SP - string potentiometer  
 LP - linear potentiometer  
 LC - load cell  
 SG - linear strain gage  
 SGR - strain gage rosette  
 A - accelerometer  
 K - krypton



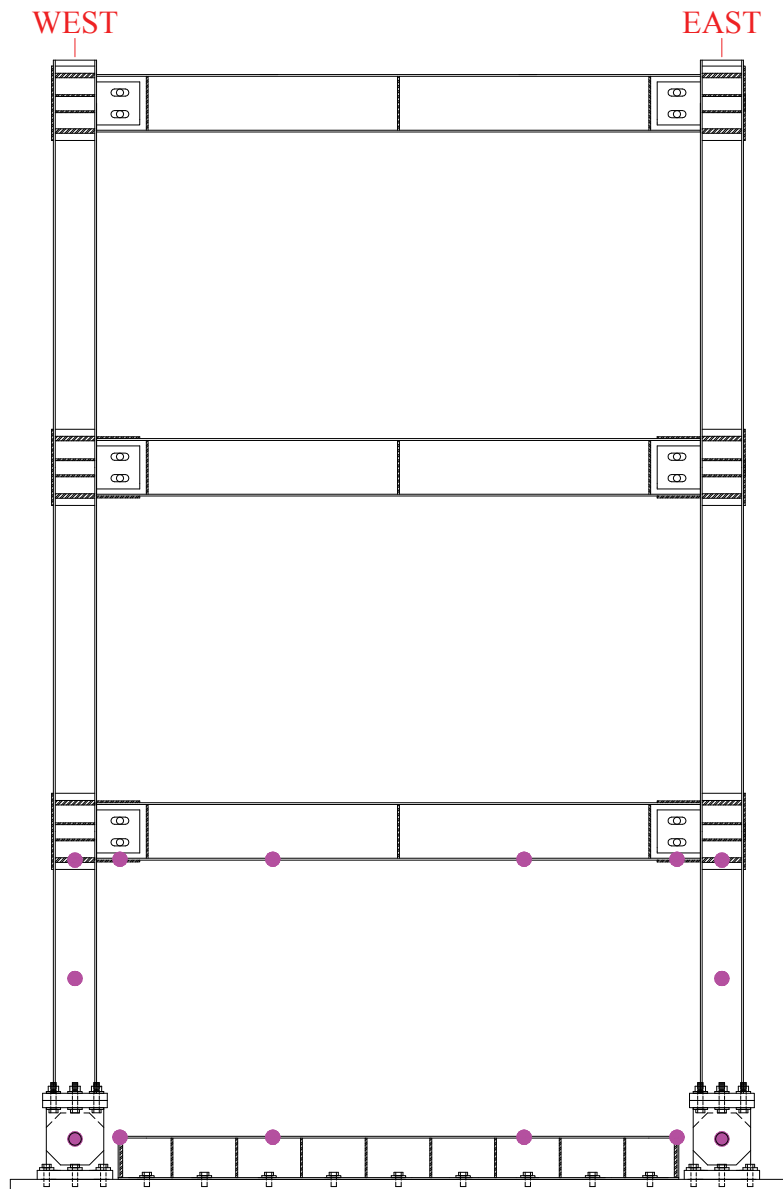
**LEGEND:**

- |     |   |   |                           |   |              |
|-----|---|---|---------------------------|---|--------------|
| ◁ □ | Linear Potentiometer                                    | - | Uniaxial Strain Gage      | ▣ | PT Load Cell |
| ● ← | String Potentiometer                                    | * | Shear Rosette Strain Gage |   |              |
| ↔   | Accelerometer (X = Long., Y = Transverse, Z = Vertical) |   |                           |   |              |

**NOTE:**

Full Infill Web Plate Shown; FR Bare Frame & FR Infill Web Plate Strips Similar

**FIGURE 5-22 Shake-table: Frame FR instrumentation**



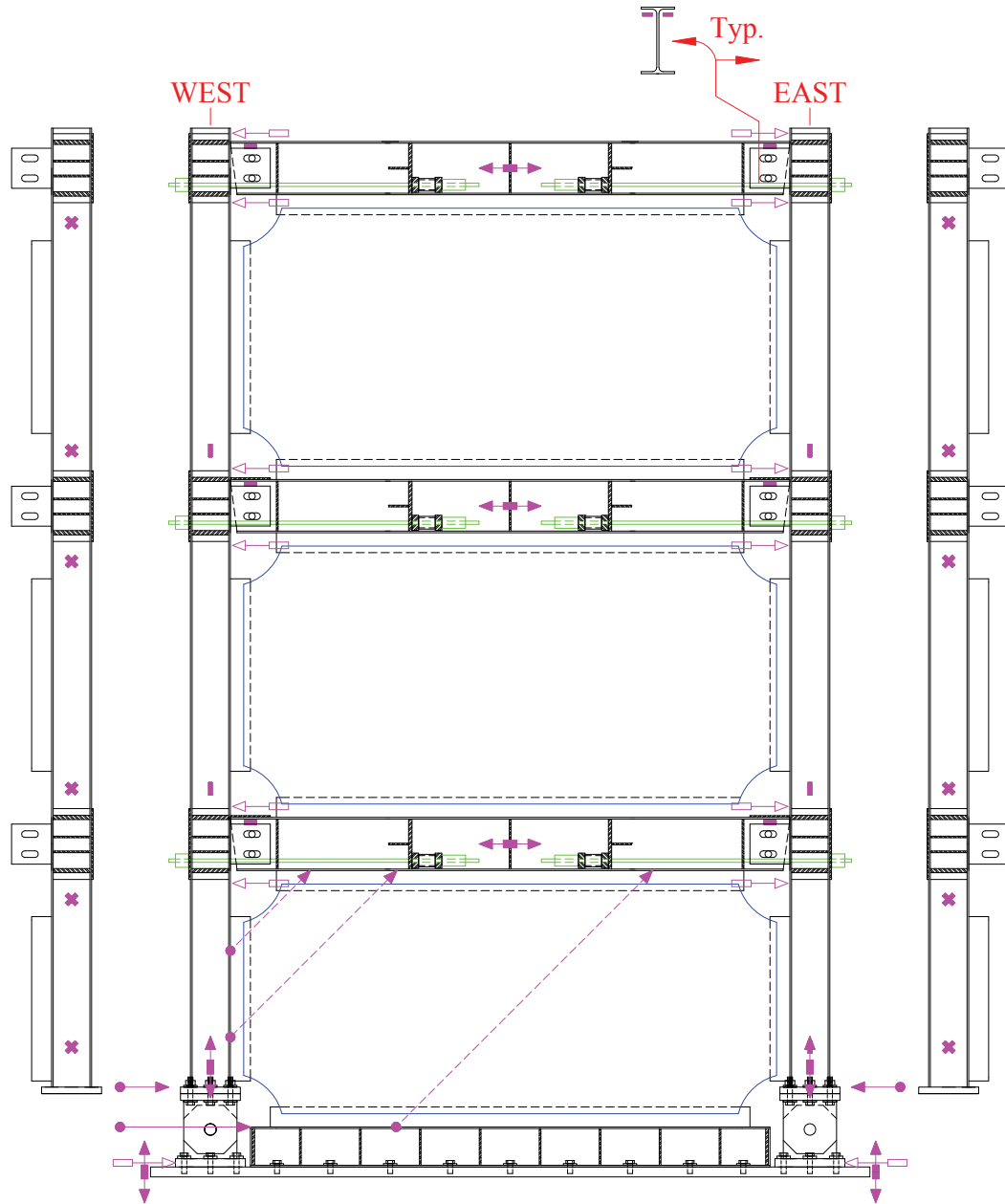
LEGEND:

- Krypton

NOTE:

FR Frame Shown; NZ Frame Similar

**FIGURE 5-23 Shake-table: Frame FR (NZ similar) krypton sensors**



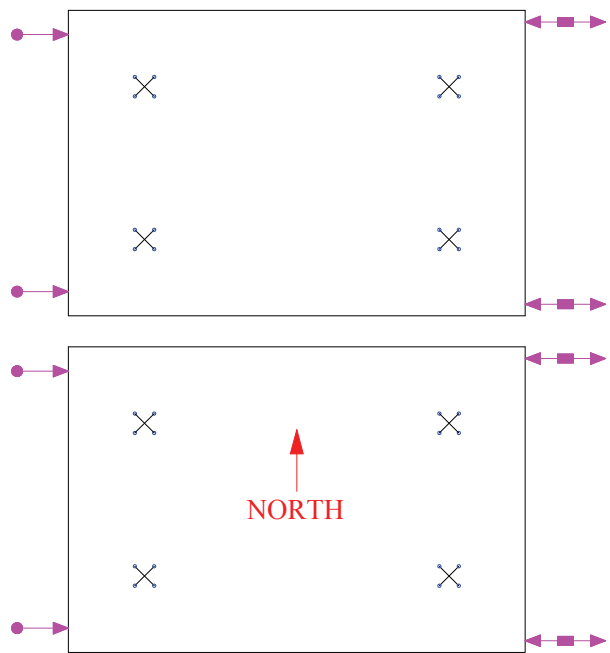
**LEGEND:**

- |    |   |   |                           |   |              |
|----|---|---|---------------------------|---|--------------|
| ←□ | Linear Potentiometer                                    | — | Uniaxial Strain Gage      | ▨ | PT Load Cell |
| ←● | String Potentiometer                                    | * | Shear Rosette Strain Gage |   |              |
| ↔  | Accelerometer (X = Long., Y = Transverse, Z = Vertical) |   |                           |   |              |

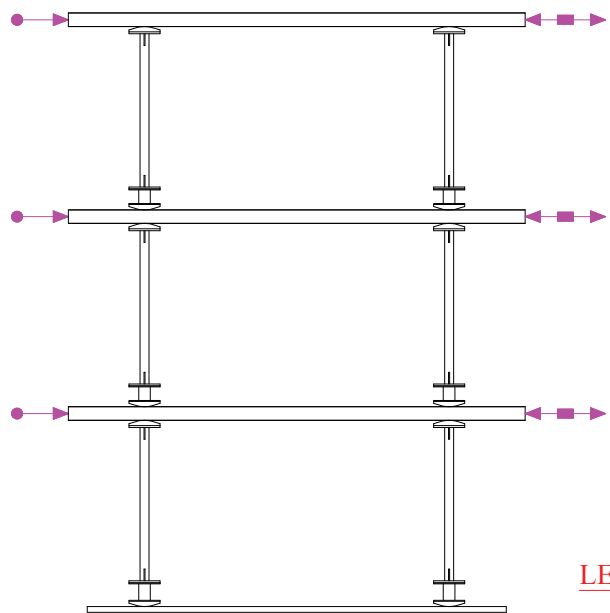
**NOTE:**

Full Infill Web Plate Shown; NZ Bare Frame, NZ Infill Web Plate Strips & NZ Perforated Infill Web Plate Similar

**FIGURE 5-24 Shake-table: Frame NZ instrumentation**



PLAN



SOUTH ELEVATION

LEGEND:

- ←● String Potentiometer
- ←■→ Accelerometer (X = Long., Y = Transverse, Z = Vertical)

**FIGURE 5-25 Shake-table: GMF instrumentation**

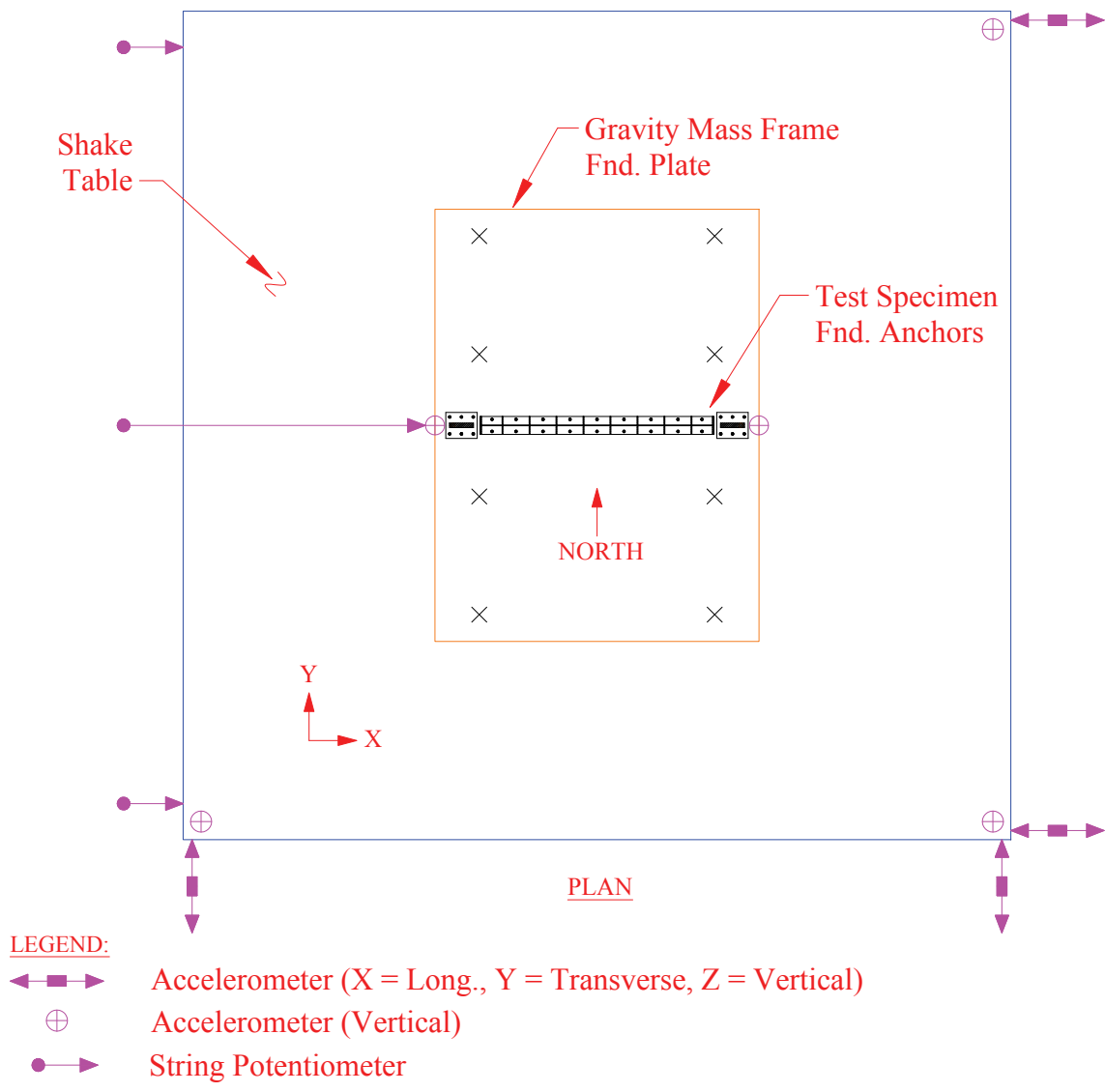


**FIGURE 5-26 Shake-table: extension frame instrumentation**





## SECTION 6

### SCALED QUASI-STATIC EXPERIMENTAL RESULTS

#### 6.1 General

This chapter presents the experimental results for the one-third scaled quasi-static tests. In particular, the loading protocol and observations are provided in Section 6.2. Furthermore, the experimental results for frame FR, NZ and CR are provided in Sections 6.3, 6.4 and 6.5 respectively. A comparison in global response is made for frames NZ and CR in Section 6.6 (a direct comparison to frame FR is not made due to the different actuator loading scheme used for reasons presented subsequently). Furthermore, experimental versus analytical comparisons are presented in Section 6.7, a simplified design approach for calculating the required area of post-tension (PT) at HBE-to-VBE joints to ensure frame recentering to a target residual roof drift is presented in Section 6.8, followed by a general summary of results and conclusions in Section 6.9.

#### 6.2 Experimental Loading Protocol and Observations

The specimens for quasi-static testing were presented in Section 4. For convenience, recall that the following nomenclature is used to differentiate each test specimen, where the following acronyms is appended to the “frame type” (i.e., FR, NZ, CR): W = full infill web plate, B = no infill web plate = PT boundary frame = bare frame condition, and S = infill web strips. For example, FRW = flange-rocking frame with infill web plate, NZB = NewZ-BREAKSS frame with no infill web plate, CRS = centerline rocking frame with infill web strips, and so on. The sequential order of tests performed was as follows: FRW, FRB, FRS, NZW, NZB, NZS, CRW, CRB and CRS. Additionally, for experimental results presented subsequently, a positive drift corresponds to a Westward drift direction (moving away from the reaction wall).

Finally, it is noted that each PT boundary frame type was constructed only once. Using frame FR as an example, after the FRW was performed, the infill web plate was removed with the test setup in place “as is”, and test FRB was conducted. After this test on the PT boundary frame, the entire test setup was then taken down (with removal of any external instrumentation) for installation of the infill web strips. Thus, for each frame type (i.e., FR, NW or CR), the test setup

construction and break-down was repeated twice. In particular, through each frame test sequence (i.e., FRW, FRB and FRS) no alterations were made to the PT elements from the initial frame construction. The significance of this being that any PT losses is cumulative and carries over to each subsequent test (the consequence of this approach will be addressed in subsequent sections where applicable).

### **6.2.1 Actuator Loading: Displacement versus Force Control**

For the first three tests conducted on frame FR, a displacement control scheme at all three actuator levels was used. The displacement shape was based on an approximate first mode shape pattern normalized by the top story level in the proportion of 1, 0.7, and 0.3 for Level 3, 2, and 1, respectively. This displacement shape was obtained from a nonlinear pushover analysis, conducted in displacement control (at the top story level) with a lateral story force distribution pattern along the height of the frame, based on a first-mode distribution defined in ASCE 7-10. However, during the test, it was found that the use of this displacement control scheme lead to undesired actuator interaction across the story heights. In particular, at times, the forces applied by the actuators at Levels 1 and 2 were acting in opposite directions and approximately similar in magnitude, indicating that these actuators were “fighting” each other to maintain the enforced lateral displacement shape at each floor level. Similar interaction effects were observed at Level 3 and 2, but not as dominantly as at the lower levels. As a consequence, the global base shear versus roof drift response exhibited a negative stiffness, which was concerning (as will be presented in Section 6.3). This effect was observed during the early elastic displacement steps of the test protocol. At that stage, negative stiffness due to P-Delta effects of the weight of the test setup floor mass plates was unlikely. After further checks on the instrumentation and actuator signals, it was determined that the response was not due to instrument errors and testing continued, although no explanation was found for the peculiar actuator response (hoping the behavior would correct itself at larger forces and drift amplitudes).

For the subsequent FRB test, the actuator displacement control scheme used for the previous FRW test was maintained. A similar negative stiffness in global response with the FRB test was also observed. To further investigate the source of this puzzling actuator response, after the completion of the bare frame test, additional cycles were conducted investigating an alternative

combined force-and-displacement control scheme. This was done by enforcing an actuator displacement control at Level 3 and corresponding slaved actuator force control at Level 1 and 2 (with the actuator force at Level 3 being the master). The comparison of actuator response between the two schemes is shown in figure 6-1. The undesired interaction effects of the actuators can be clearly observed for the displacement control scheme. On the contrary, for the combined force-and-displacement control scheme, the sign and proportion of the actuator forces is more representative of the anticipated first mode response, and the presence of actuator interaction was eliminated.

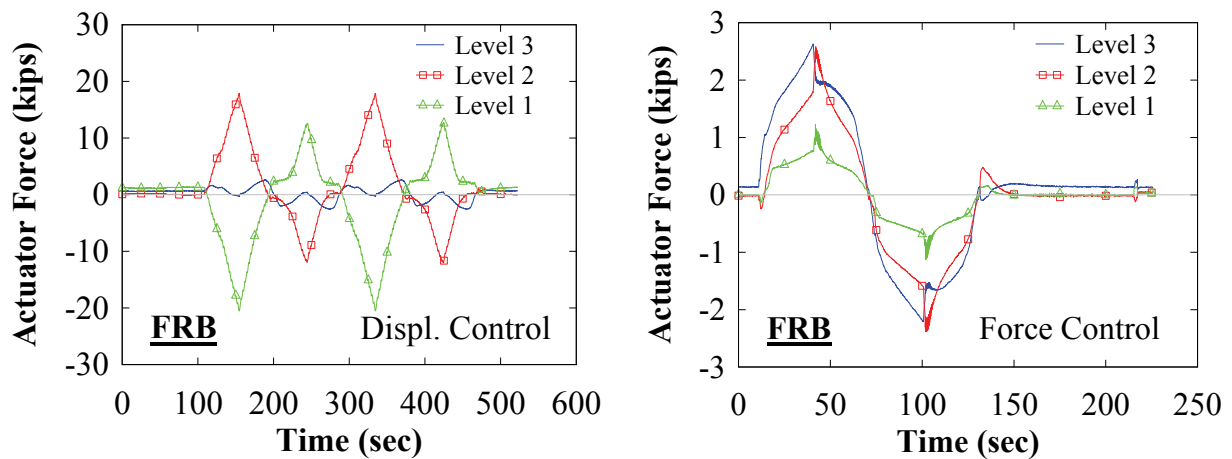


**FIGURE 6-1 Actuator response**

The corresponding story shear versus interstory drift is shown in figure 6-2. Results show that the negative stiffness observed for the FR frame was a consequence of the displacement shape imposed to the specimen using the aforementioned actuator displacement control scheme, which lead to the undesirable actuator interaction observed across the stories. As shown in figure 6-2, this artifact disappeared when a combined force-and-displacement control scheme was used. For the remaining NZ and CR tests, the alternative scheme was used with an actuator force load pattern distribution of 1, 0.658, and 0.316 at Level 3, 2, and 1, respectively; based on the approximate first mode distribution of story forces defined in ASCE 07-10. Note that although the FRS test was conducted after the FRB test for which it was identified that the actuator interaction was due to an artifact of the displacement control scheme, for continuity purposes in

order to provide some comparison with the previous FR tests, the displacement control scheme was maintained for the FRS test.

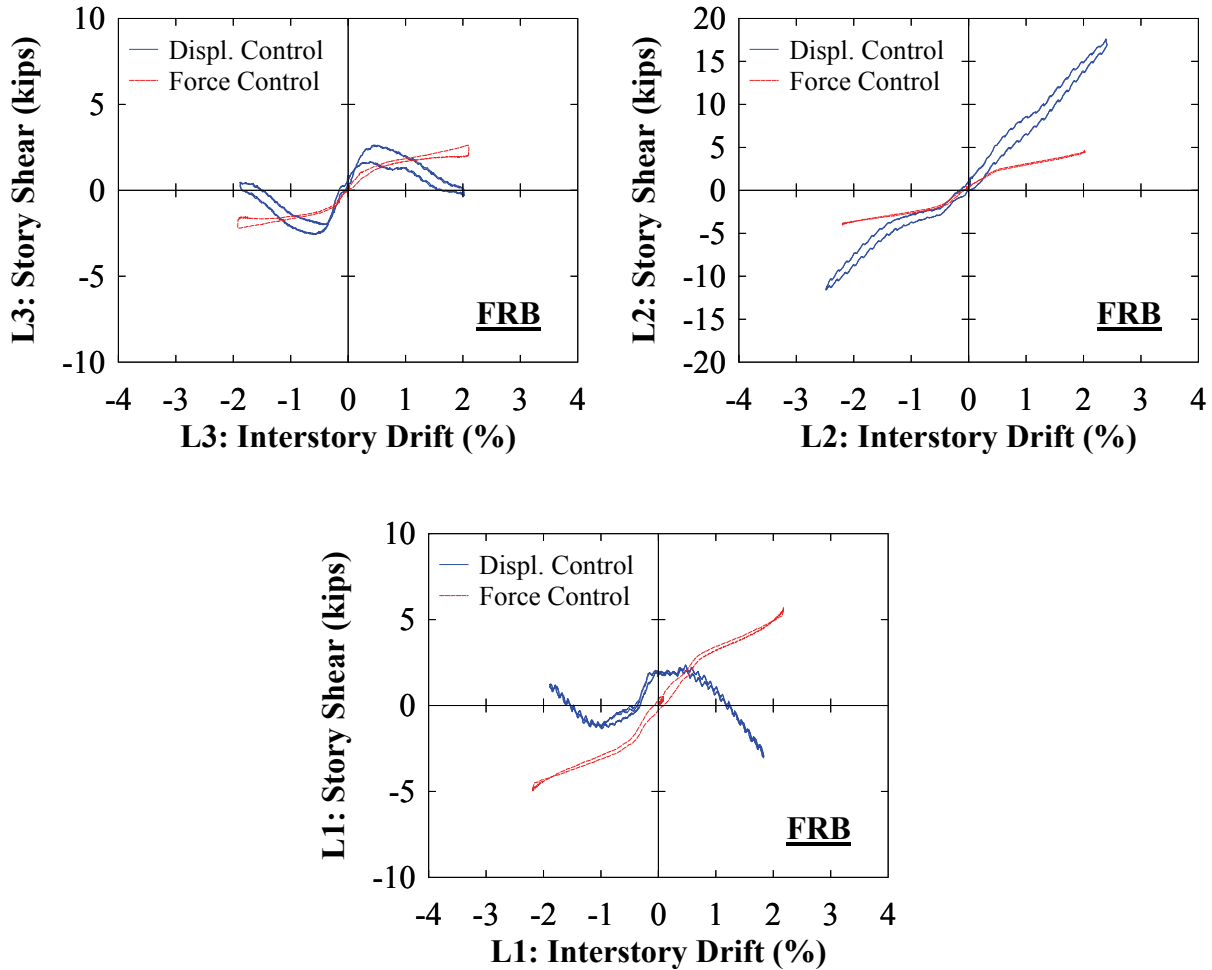
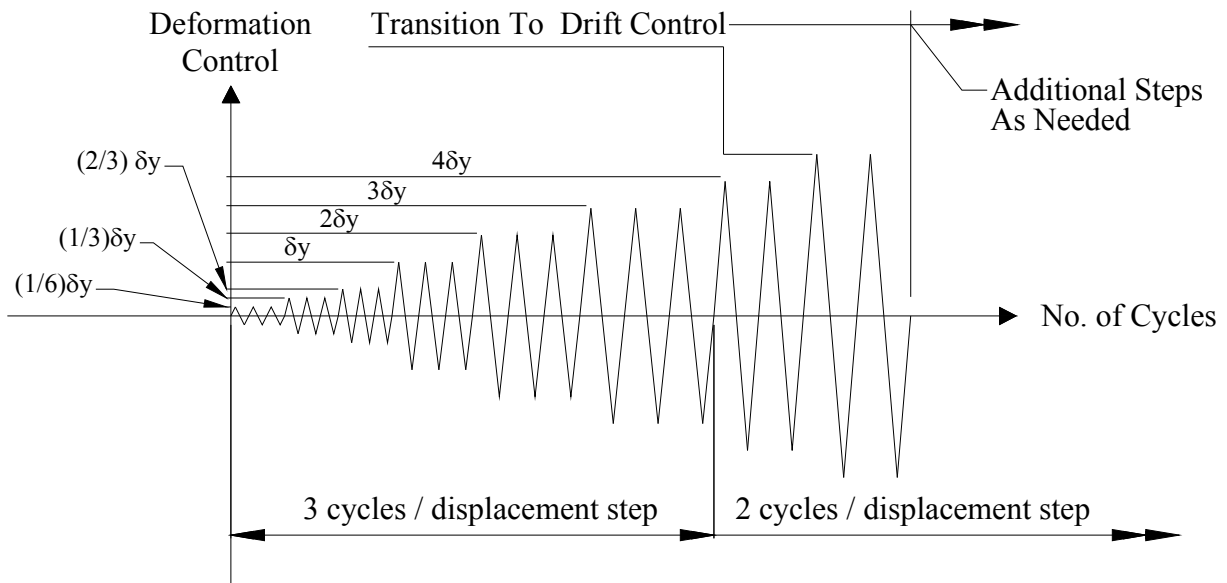


FIGURE 6-2 Specimen response

### 6.2.2 Experimental Loading Protocol and General Observations

The cyclic loading protocol used to conduct the quasi-static tests was adapted from the ATC 24 (ATC 1992) loading protocol. This document specifies that specimens should be subjected to three cycles at each displacement step up to three times the yield displacement,  $\delta_y$ , after which only two cycles are necessary at each displacement step. The first displacement step should be at 1/3 of the yield displacement, the second step at 2/3, and each subsequent step should be at increasing multiples of that displacement (i.e.,  $1\delta_y$ ,  $2\delta_y$ ,  $3\delta_y$ , etc.). For the UB tests, the ATC 24

loading protocol was modified by reducing the first step to  $1/6^{\text{th}}$  of the yield displacement, to better capture the elastic response of the test specimens. Additionally, after the displacement step at  $4\delta_y$ , the target actuator displacements were changed from ductility values to drift values (i.e., becoming 2% drift, 2.5% drift, etc.). This is shown graphically in figure 6-3. The approximate yield displacement target for the top level actuator for each test was obtained from nonlinear pushover analysis results and corresponds to the effective yield of the test specimen (see figures 4-30 and 4-31 for an example of effective yield). The loading protocol resulting from each test, along with general observations made during testing, is shown in tables 6-1 through 6-9.



**FIGURE 6-3 Quasi-static loading protocol**

**TABLE 6-1 Quasi-static test #1 loading protocol and observations**

Frame FRW					
Displacement Step	Num. of Cycles	Ductility $\Delta_3/\delta_y$	Roof Displacement, $\Delta_3$ (in)	Roof Drift (%)	Observations
1	3	0.17	0.072	0.05	-
2	3	0.33	0.142	0.09	Audible crinkling in web plate
3	3	0.67	0.289	0.19	-
4	3	1	0.431	0.28	Changed to load rate of 4 min/cycle to see if it would help with the level 1 actuator force. No change.
5	3	2	0.863	0.56	No problems with the level 1 load cell could be determined and testing commenced. This cycle, large popping noise occurred.
6	3	3	1.294	0.85	-
7	2	4	1.726	1.13	tearing of plate at corner cut outs observed.
8	2	-	2.295	1.5	-
9	2	-	3.060	2.0	-
10	2	-	3.825	2.5	-
11	2	-	4.590	3.0	-
12	2	-	6.120	4.0	-

**TABLE 6-2 Quasi-static test #2 loading protocol observations**

Frame FRB					
Displacement Step	Num. of Cycles	Ductility $\Delta_3/\delta_y$	Roof Displacement, $\Delta_3$ (in)	Roof Drift (%)	Observations
1	3	0.17	0.07	0.046	-
2	3	0.33	0.14	0.092	-
3	3	0.67	0.29	0.190	-
4	3	1	0.43	0.281	-
5	3	2	0.60	0.393	-
6	3	3	1.29	0.843	-
7	2	4	1.73	1.131	-
8	2	-	2.30	1.5	-
9	2	-	3.06	2.0	-
10	2	-	3.83	2.5	-
11	2	-	4.59	3.0	-
12	2	-	6.12	4.0	-

**TABLE 6-3 Quasi-static test #3 loading protocol and observations**

Frame FRS					
Displacement Step	Num. of Cycles	Ductility $\Delta_3/\delta_y$	Roof Displacement, $\Delta_3$ (in)	Roof Drift (%)	Observations
1	3	0.17	0.100	0.07	-
2	3	0.33	0.198	0.13	-
3	3	0.67	0.402	0.26	yielding occurring on hysteresis plots
4	3	1	0.600	0.39	noticeable sag in strips
5	3	2	1.201	0.78	-
6	3	3	1.801	1.18	lost strain gage S1 @ level 2
7	2	4	2.401	1.57	-
8	2	5.1	3.060	2.0	-
9	2	6.4	3.825	2.5	-
10	2	7.6	4.590	3.0	-
11	2	8.9	5.355	3.5	-
12	2	10.2	6.120	4.0	-
13	2	11.5	6.885	4.5	-
14	2	12.7	7.650	5.0	-



**TABLE 6-4 Quasi-static test #4 loading protocol and observations**

Frame NZW					
Displacement Step	Num. of Cycles	Ductility $\Delta_3/\delta_y$	Roof Displacement, $\Delta_3$ (in)	Roof Drift (%)	Observations
1	3	0.17	0.090	0.061	-
2	3	0.33	0.180	0.122	-
3	3	0.67	0.362	0.245	-
4	3	1	0.540	0.365	No tearing of the web plate observed. Yielding of web plate is observed.
5	3	2	1.080	0.730	No tearing of the web plate observed
6	3	3	1.620	1.095	Some minor tearing at the corners of the web plate is observed.
7	2	4	2.160	1.459	-
8	2	5.5	2.960	2.0	See Section 6.4.2
9	2	6.9	3.70	2.5	See Section 6.4.2
10	2	8.2	4.44	3.0	See Section 6.4.2

**TABLE 6-5 Quasi-static test #5 loading protocol and observations**

Frame NZB					
Displacement Step	Num. of Cycles	Ductility $\Delta_3/\delta_y$	Roof Displacement, $\Delta_3$ (in)	Roof Drift (%)	Observations
1	3	0.167	0.09	0.06	-
2	3	0.33	0.18	0.12	-
3	3	0.67	0.36	0.24	-
4	3	1	0.54	0.36	-
5	3	2	1.08	0.73	-
6	3	3	1.62	1.09	-
7	2	4	2.16	1.46	-
8	2	5.5	2.96	2.0	-
9	2	6.9	3.70	2.5	-
10	2	8.2	4.44	3.0	-

**TABLE 6-6 Quasi-static test #6 loading protocol and observations**

Frame NZS					
Displacement Step	Num. of Cycles	Ductility $\Delta_3/\delta_y$	Roof Displacement, $\Delta_3$ (in)	Roof Drift (%)	Observations
1	3	0.167	0.085	0.057	-
2	3	0.33	0.169	0.114	-
3	3	0.67	0.340	0.230	-
4	3	1	0.507	0.343	-
5	3	2	1.014	0.685	-
6	3	3	1.521	1.028	-
7	2	4	2.028	1.370	-
8	2	5.8	2.960	2.0	-
9	2	7.3	3.700	2.5	-
10	2	8.8	4.440	3.0	-
11	2	11.7	5.920	4.0	-
12	2	13.2	6.670	4.5	-
13	2	14.6	7.400	5.0	-
14	2	16.1	8.140	5.5	-
15	2	17.5	8.880	6.0	-

**TABLE 6-7 Quasi-static test #7 loading protocol and observations**

Frame CRW					
Displacement Step	Num. of Cycles	Ductility $\Delta_3/\delta_y$	Roof Displacement, $\Delta_3$ (in)	Roof Drift (%)	Observations
1	3	0.167	0.072	0.049	-
2	3	0.33	0.144	0.097	-
3	3	0.67	0.299	0.202	Minor infill web plate yielding.
4	3	1	0.433	0.293	-
5	3	2	0.866	0.585	-
6	3	3	1.299	0.878	-
7	2	4	1.732	1.170	-
8	2	6.8	2.960	2.0	Complete separation of infill web plate along level 1 East columns
9	2	8.5	3.700	2.5	-
10	2	10.3	4.440	3.0	-
11	2	13.7	5.920	4.0	-

**TABLE 6-8 Quasi-static test #8 loading protocol and observations**

Frame CRB					
Displacement Step	Num. of Cycles	Ductility $\Delta_3/\delta_y$	Roof Displacement, $\Delta_3$ (in)	Roof Drift (%)	Observations
1	3	0.167	0.072	0.049	-
2	3	0.33	0.144	0.097	-
3	3	0.67	0.299	0.202	-
4	3	1	0.433	0.293	-
5	3	2	0.866	0.585	-
6	3	3	1.299	0.878	-
7	2	4	1.732	1.170	-
8	2	-	2.960	2.0	-
9	2	-	3.700	2.5	-
10	2	-	4.440	3.0	-
11	2	-	5.920	4.0	-

**TABLE 6-9 Quasi-static test #9 loading protocol and observations**

Frame CRS					
Displacement Step	Num. of Cycles	Ductility $\Delta_3/\delta_y$	Roof Displacement, $\Delta_3$ (in)	Roof Drift (%)	Observations
1	3	0.167	0.064	0.043	-
2	3	0.33	0.129	0.087	Replaced LPB3TFW cable 722 with cable 723. Reset/rebalanced LC1 channel as it was not reading
3	3	0.67	0.259	0.175	-
4	3	1	0.386	0.261	-
5	3	2	0.772	0.522	-
6	3	3	1.158	0.782	-
7	2	4	1.544	1.043	-
8	2	5.8	2.220	1.5	-
9	2	7.7	2.960	2.0	-
10	2	9.6	3.700	2.5	-
11	2	11.5	4.440	3.0	-
12	2	15.3	5.920	4.0	-
13	2	19.2	7.400	5.0	-
14	2	23.0	8.880	6.0	-
15	2	26.8	10.360	7.0	-
16	2	30.7	11.840	8.0	-
17	2	34.5	13.320	9.0	-

### 6.2.3 Observations – Infill Web Plate and Strips

A typical infill web plate panel showing the visual condition before and after testing is shown in figure 6-4 for frame FRW (results for frames NZW and CRW are similar). Similarly, the infill web strip configuration is shown in figure 6-5 for frame FRS (results for frames NZS and CRS are similar). The progression of infill web plate tearing at the weld connection along the boundary frame fish plates was monitored between displacement steps. Figure 6-6 is the legend

and nomenclature used to record web plate tearing for frames FRW, NZW and CRW (when applicable). Frames FRS, NZS and CRS were tested up to 5%, 6%, and 9% drift, respectively, and no tearing of the infill web strips occurred. Additionally, for the frames with the infill web plate, the formation of the tension field and buckling of the infill web plate during testing was audibly loud. On the contrary, there was no audible noise during the yielding and buckling of the infill web strips.

The results of web plate tearing for frame FRW are shown in figure 6-7. It is observed that noticeable web plate tearing initiated at approximately 2% drift. Increased web plate tearing was moderate up to approximately 2.5% drift, where thereafter at 3%, an “unzipping” effect occurred along the East VBE web plate boundary, leading to complete separation of the web plates at Level 1 and 2. At 4% drift, a similar effect occurred in the West VBE at Levels 1 and 2. Additionally, complete separation at the bottom of Level 3 infill web plate occurred. A sample progression of observed infill web plate tearing is shown in figure 6-8, arbitrarily chosen at the Southwest corner location of the Level 2 infill web plate. Note that the diagonal tear perpendicular to the radial corner cut-out shown in the figure was atypical and was not observed at any other locations or tests.

The results for infill web plate tearing for frame NZW are shown in figure 6-9 and are comparable to those for frame FRW at 3% drift at Level 1. At Level 2 and 3, the infill web plate tearing for frame NZW was typically less than frame FRW. Observations of the initiation and propagation of infill web plate tearing at the corners were similar to those for frame FRW. In general, it was observed that tearing initiates from the corner locations of the infill web plates. It was shown analytically in Section 3 that the tensile strains are at a maximum at the corners of the infill web plate for rocking connections; thus observation of web plate tearing initiating from these locations is consistent with the kinematics derived earlier.



**FIGURE 6-4 Infill web plate deformation**



**FIGURE 6-5 Infill web strip deformation**

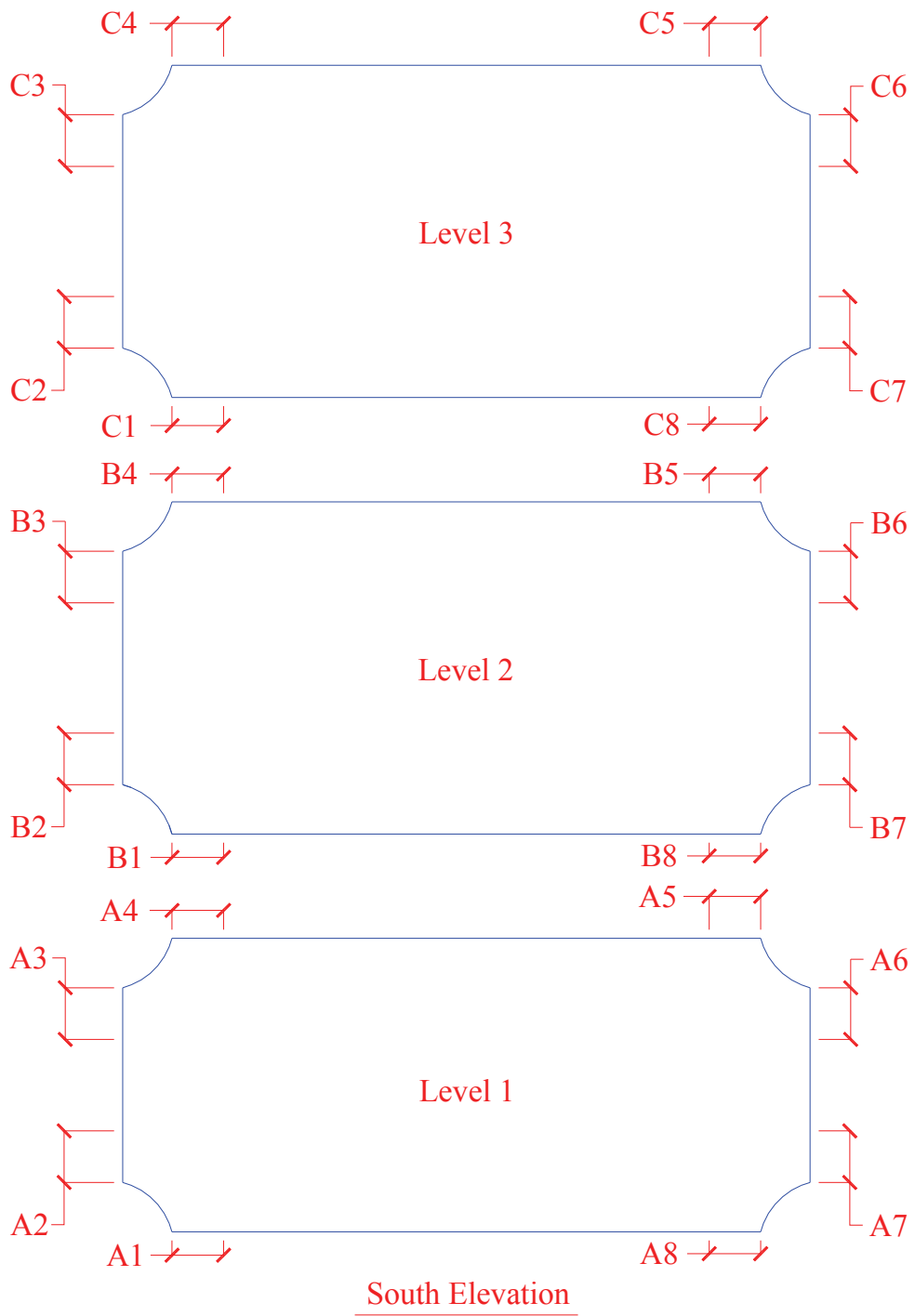
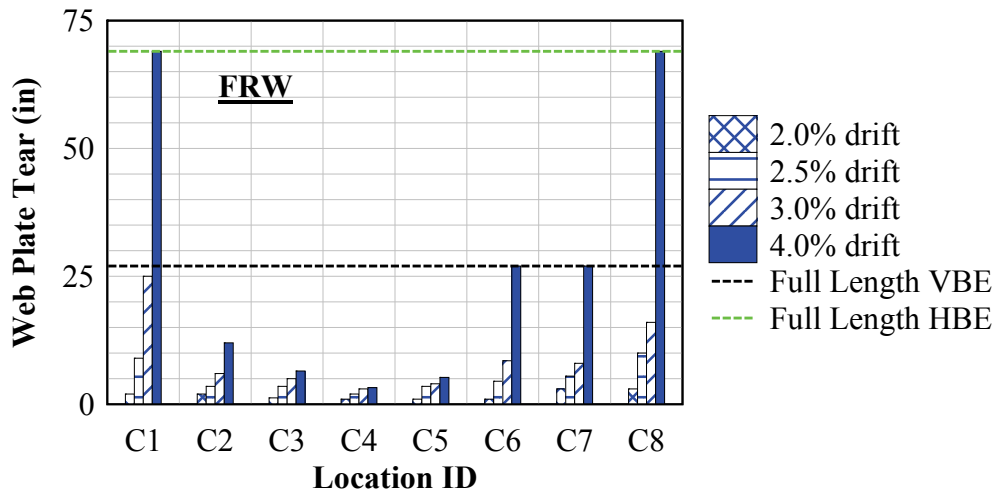
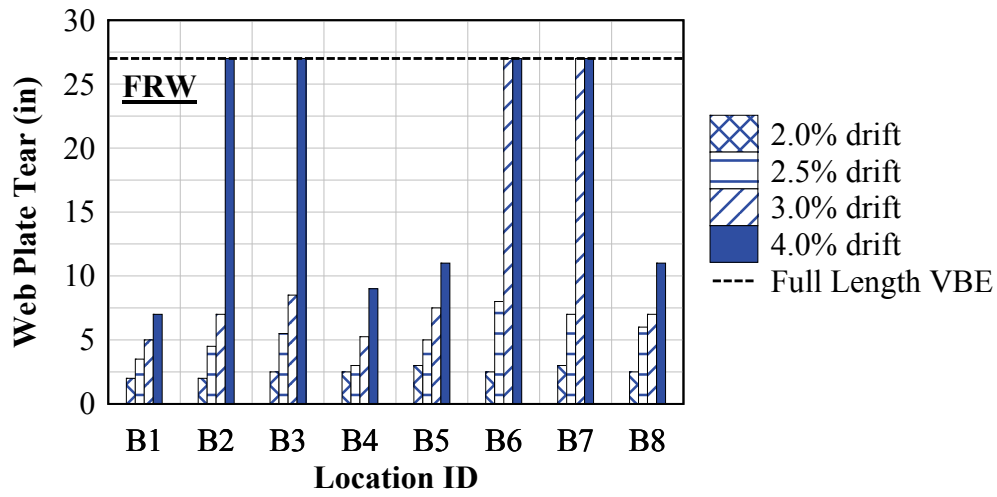


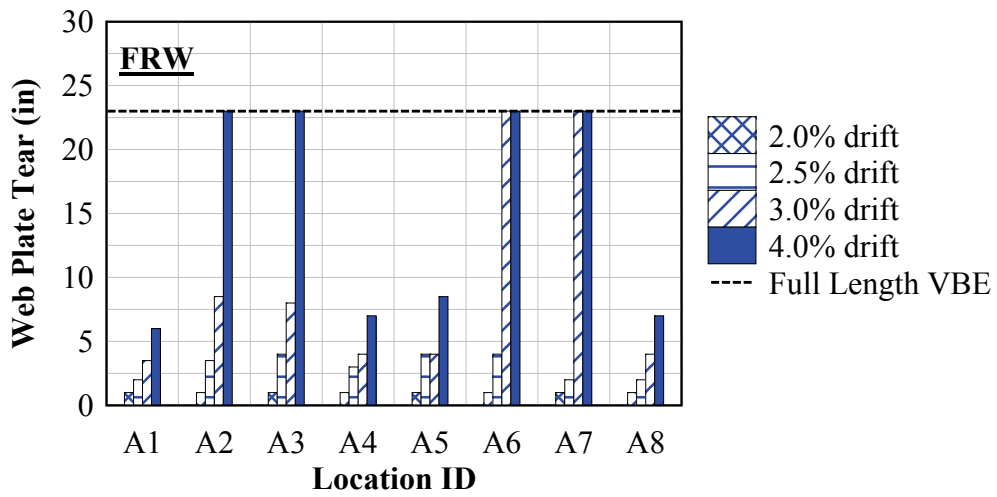
**FIGURE 6-6 Infill web plate tearing - Legend**



(a)



(b)



(c)

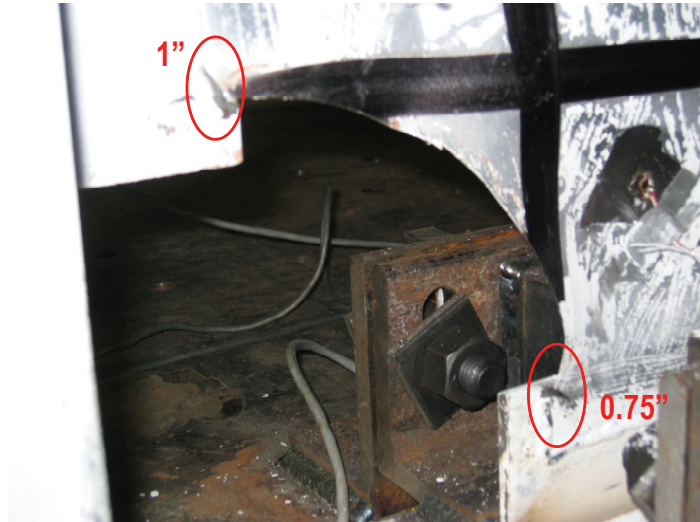
FIGURE 6-7 Frame FRW - infill web plate tearing: (a) Level 3; (b) Level 2; (c) Level 1



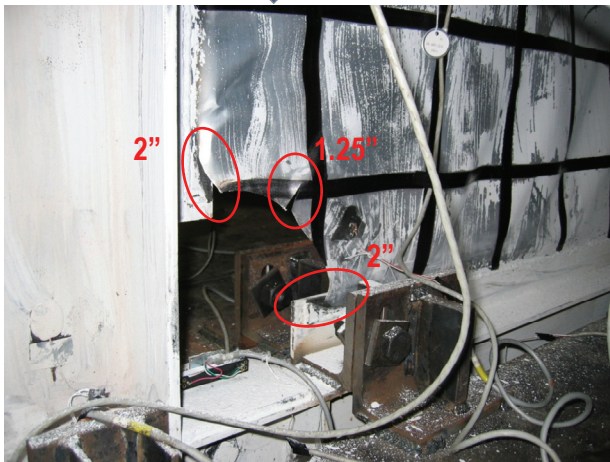
Note:

Excursion  $4\Delta_y$  (1.13% drift) initial corner “tearing” was observed at corners.

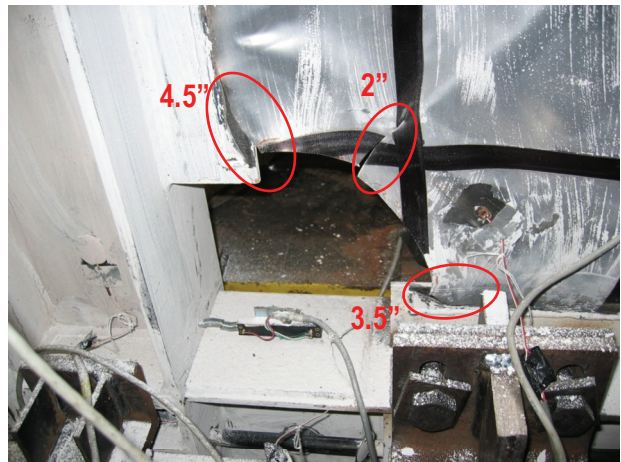
Subsequent photos will follow progression of tearing at Level 2 SW lower corner



Level 2 Plate Tearing  
SW Corner – 1.5% Drift

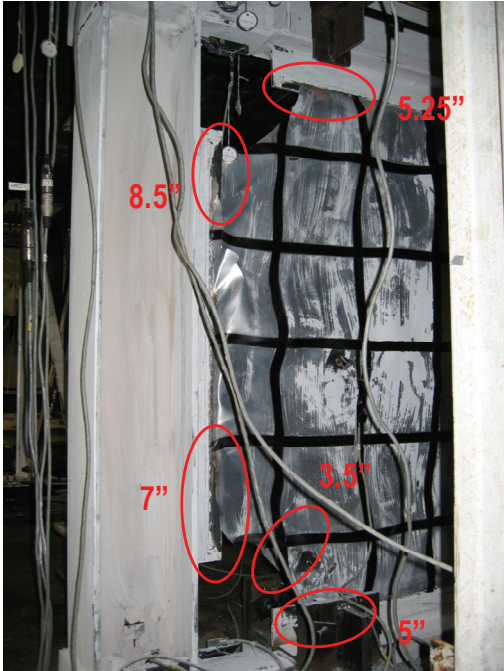


Level 2 Plate Tearing  
SW Corner - 2% drift

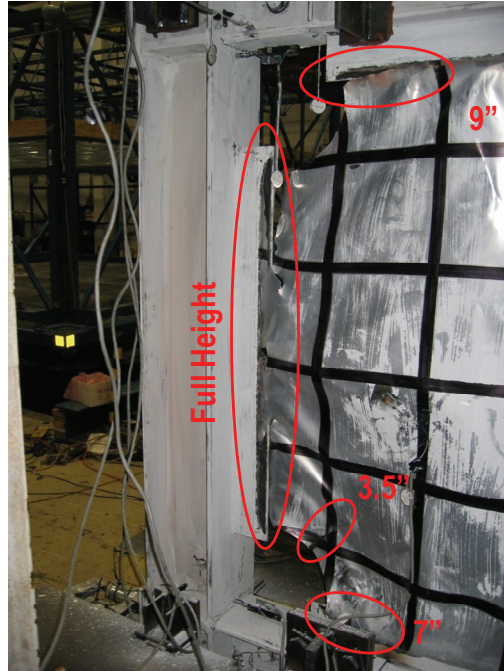


Level 2 Plate Tearing  
SW Corner - 2.5% drift

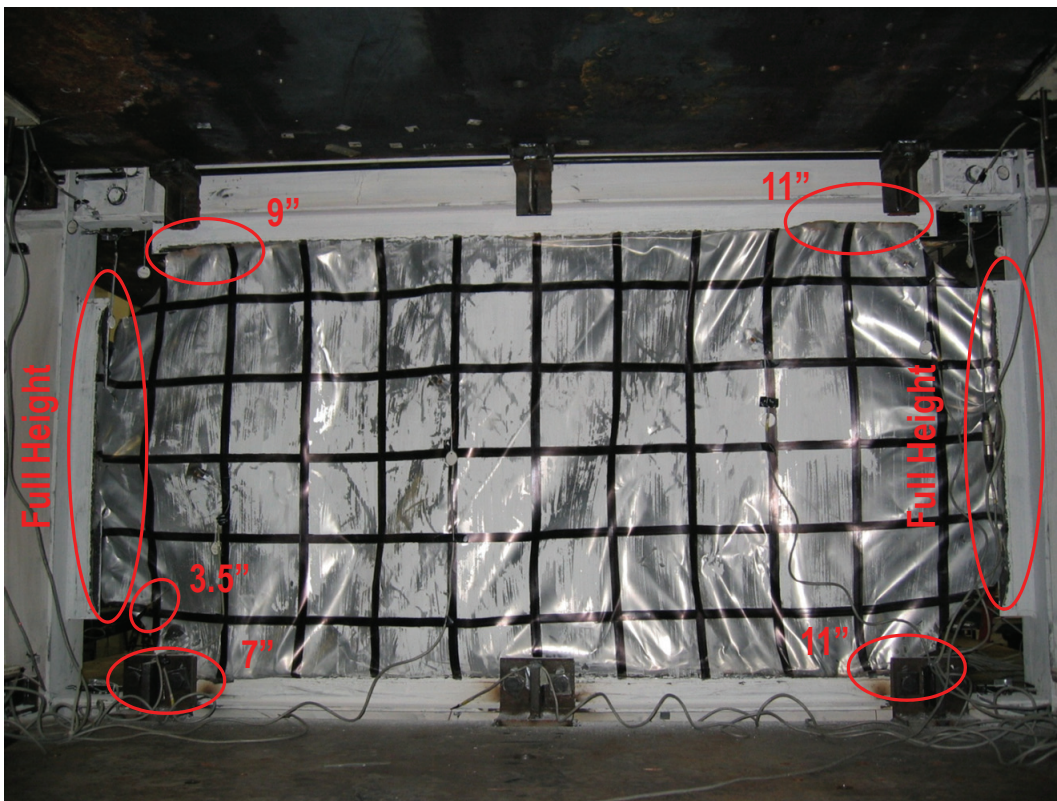
**FIGURE 6-8a Frame FRW – web plate tearing progression**



Level 2 Plate Tearing - SW End - 3% drift

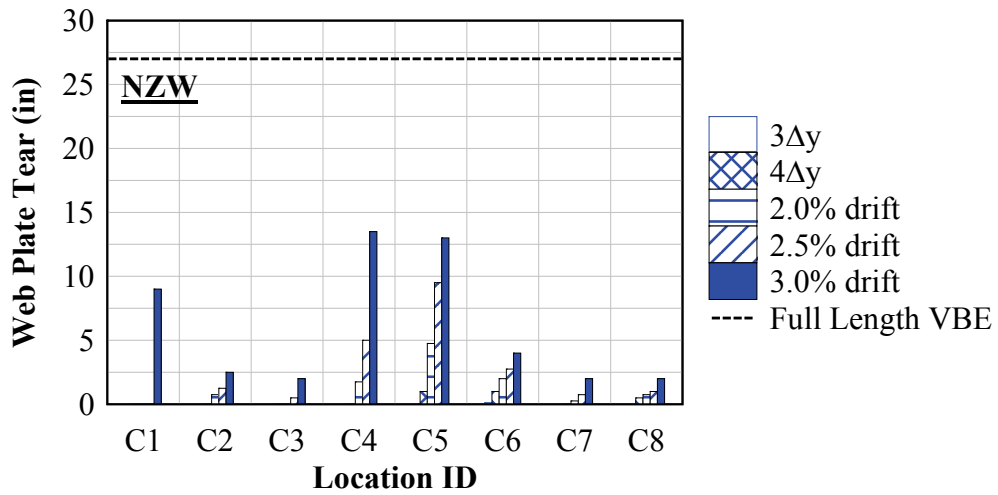


Level 2 Plate Tearing – SW End - 4% drift

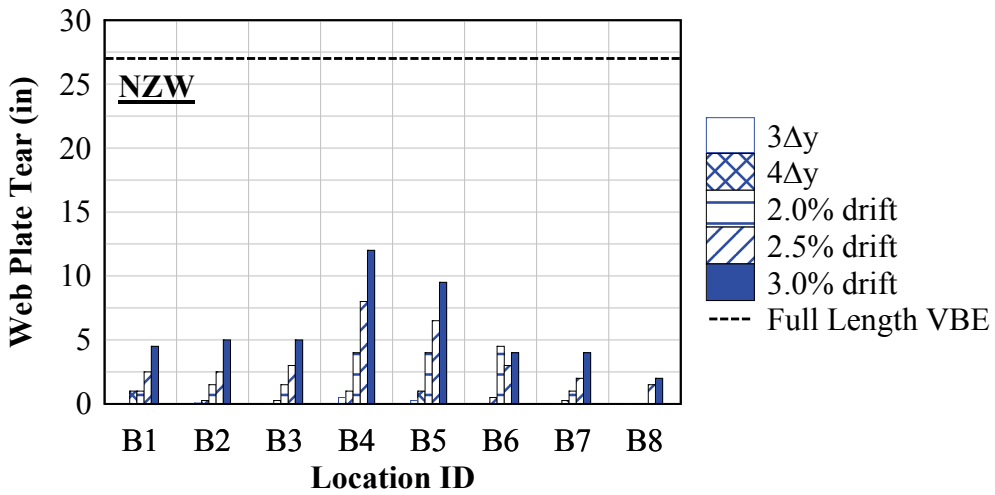


Level 2 Plate Tearing – South Elev. - 4% Drift

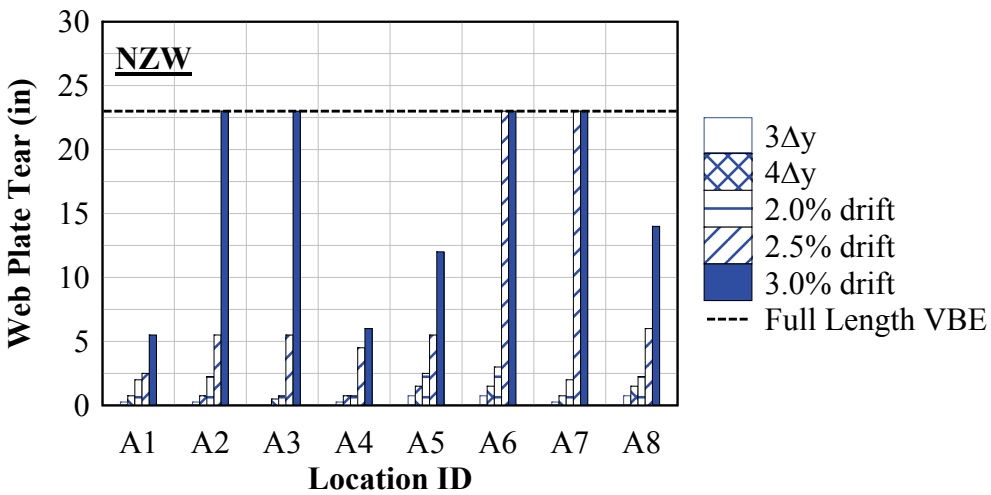
**FIGURE 6-8b Frame FRW – web plate tearing progression**



(a)



(b)



(c)

FIGURE 6-9 Frame NZW - infill web plate tearing: (a) Level 3; (b) Level 2; (c) Level 1

For the CRW test, 3/4" diameter "crack arresting" holes were provided approximately 3 inches from the ends of the infill web plate corners, as shown in figure 6-10 for a typical corner joint location. The motivation in providing these holes was to investigate the potential of delaying the infill web plate tearing unzipping effect observed in the previous tests. Additionally, because the weld connection coupon tests results (presented in Section 4) showed that two of the four coupons fractured in their heat-affected zone (figure 4.4), the crack-arresting holes were located such as to remove the heat-affected zone within the infill web plate (shown in the close-up view in figure 6-10). Additionally, the decision to locate the holes 3" away from the start of the weld connection was based on the judgment that the first few inches of the weld connection could be weaker, being closer to a boundary edge where larger internal residual stresses developed due to the welded connection. The results of the infill web plate tearing are shown in figure 6-11 for frame CRW. Additionally, comparisons are made with frame FRW and NZW in figure 6-12 for displacement steps at 2%, 2.5%, and 3% drift (which represent the common displacement steps between the three frame tests). As observed, in comparison to frame FRW and NZW, adding the holes actually did not appear to have a significant influence in delaying the infill web plate tearing progression.

From comparison of all three frames, it is observed that regardless of the frame type, infill web plate tearing was minor to moderate up to approximately 2% to 2.5% drift, and in general, the majority of the infill web plate stays connected with the boundary frame. For larger drifts (beyond 2.5%), the infill web plate connection was susceptible to unzipping leading to substantial and/or complete tearing of the infill web plate from the boundary frame. In particular, separation from the VBEs was more susceptible than on the HBEs.

Finally, in comparison of frame FRW and NZW (direct comparison to CRW cannot be made since the gap opening eccentricity is different and the crack-arresting holes were not provided for the other frames), it is observed that frame NZW had the least infill web plate tearing. This might be attributable to the differences in rocking connection type. That for the FR rocking joints, both the top and bottom corners (i.e., above and below the HBE flange) of the infill web plate alternatively undergo large tension locally due to opening and closing of the distance between the HBE and VBE flange. That is, in any given direction of drift, a gap opening forms

at the top or bottom of the HBE at each joint, and in doing so will always induce tensile strain demands on the infill web plate corner connections. On the other hand, for the NZ rocking joint, the infill web plate is affected predominately at the bottom of the HBEs (since the top flange of the HBE is designed to maintain constant contact with VBE flange). As a result, the overall tensile strain demands on the infill web plate for frame NZW will be smaller compared to frame FRW, and in part, this is reflected by the differences in the infill web plate tearing observed. However, to validate this behavior, a finite element analysis would need to be performed (this is not within the current scope of work and could be investigated in future research).

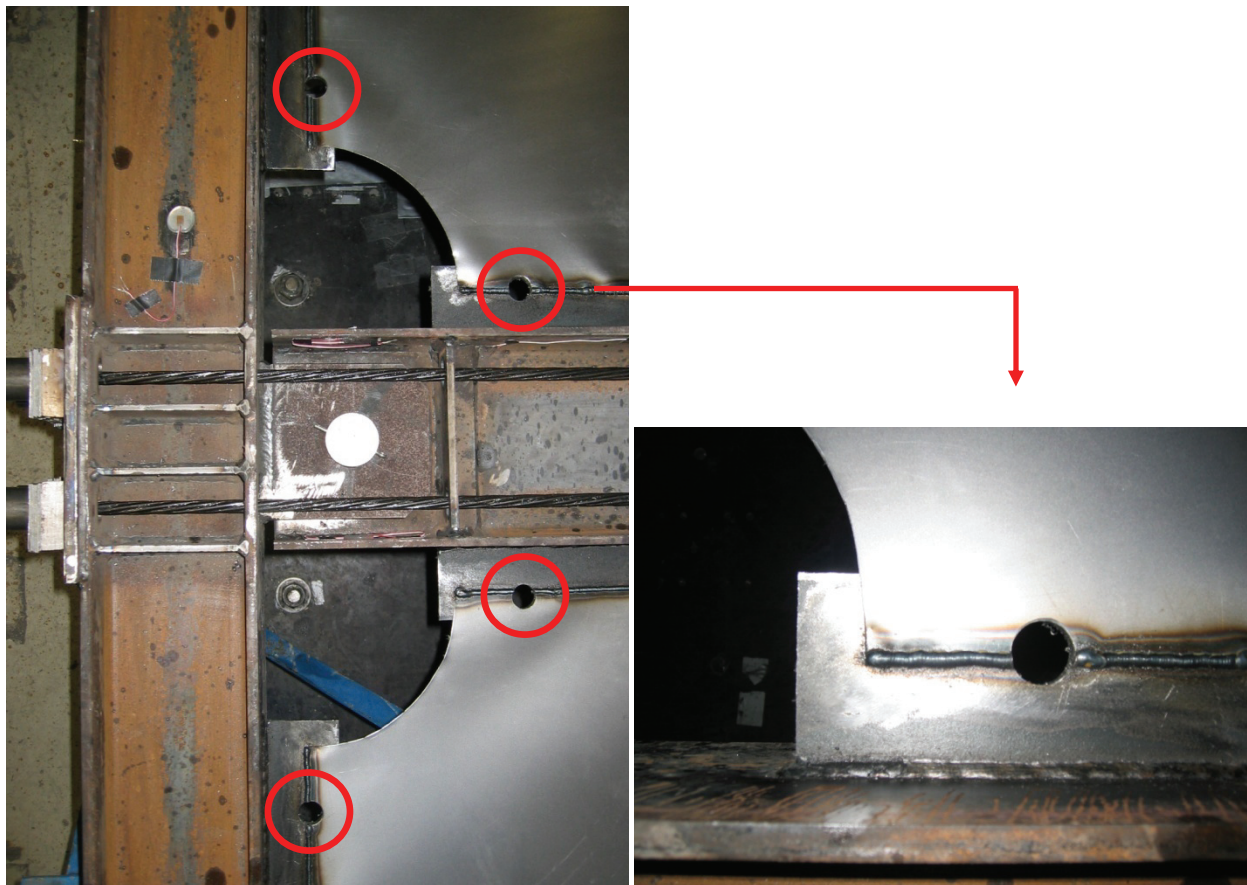
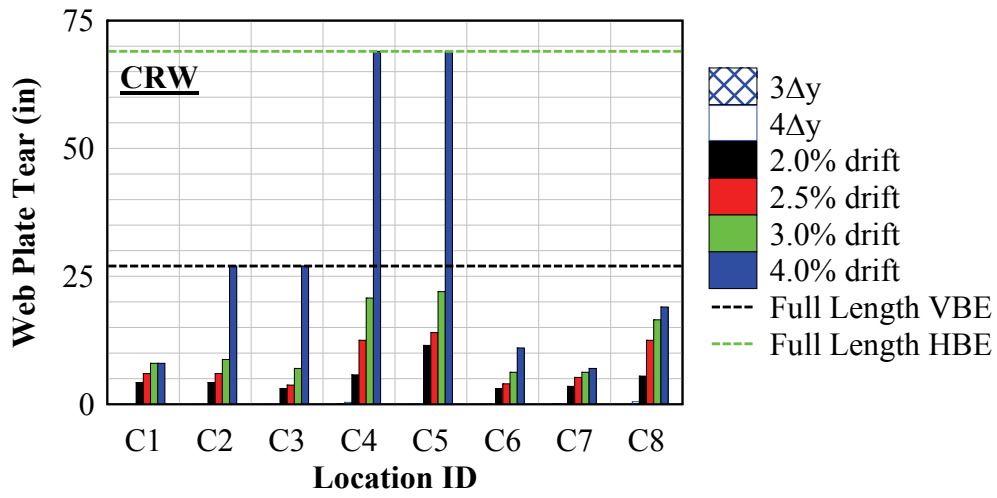
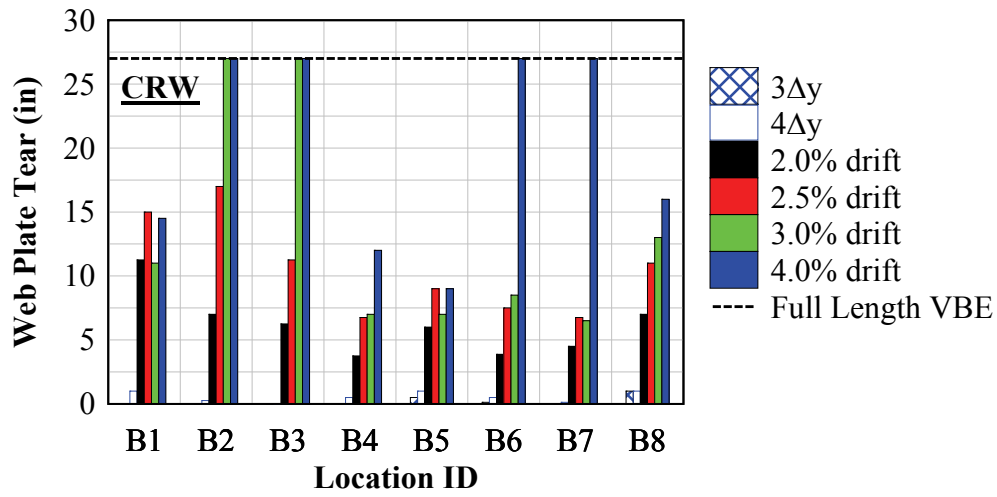


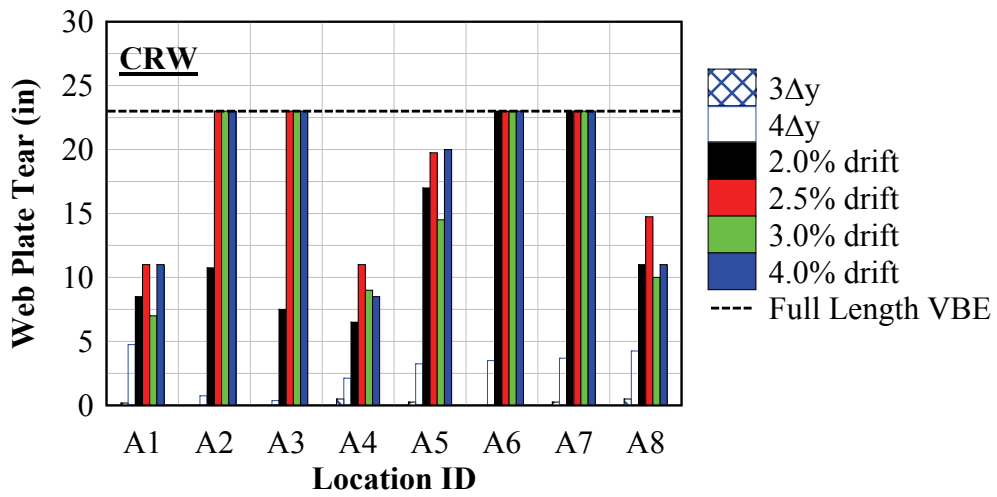
**FIGURE 6-10** Frame CRW – infill web plate – stress arresting holes



(a)

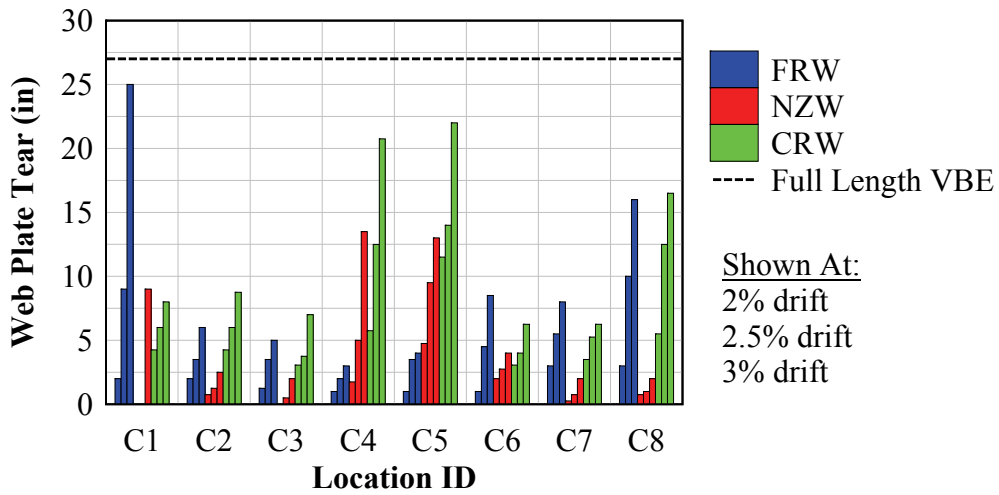


(b)

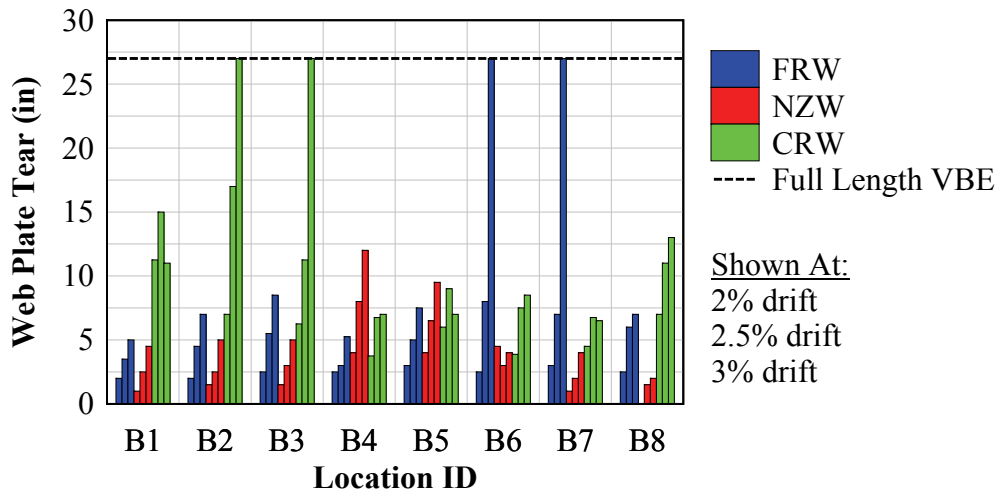


(c)

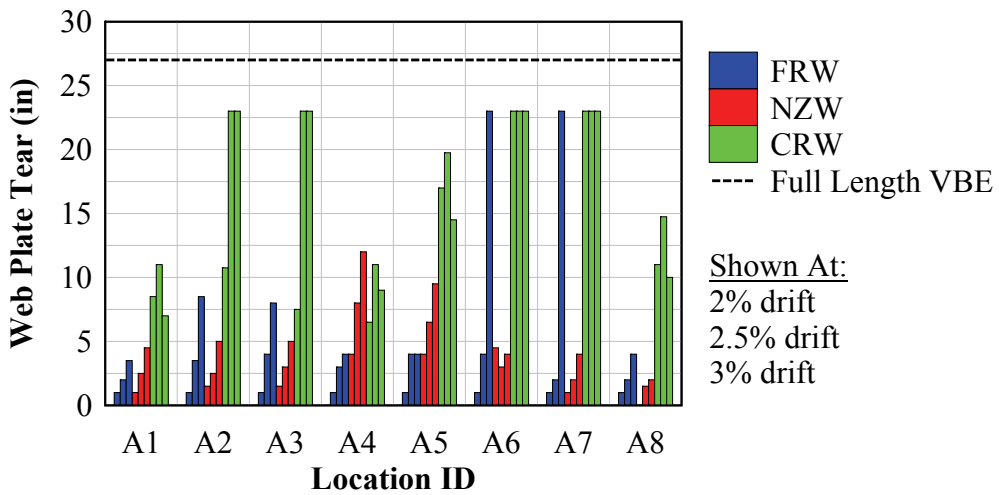
FIGURE 6-11 Frame CRW - infill web plate tearing: (a) Level 3; (b) Level 2; (c) Level 1



(a)



(b)



(c)

FIGURE 6-12 Infill web plate tearing comparison: (a) Level 3; (b) Level 2; (c) Level 1

#### **6.2.4 Observations – Frame FRS**

This section provides additional observations made during testing that only apply to frame FRS. Some local yielding was observed at the HBE flange reinforcement plates provided at the ends of the HBEs; this is shown in figures 6-13 and 6-14 at Level 1 and 2, respectively. Two likely causes for this follow.

First, the story forces developed were significantly larger than the analytical predictions at Level 1 and 2 due to the unforeseen actuator interaction affects described earlier. As will be presented in Section 6.3, at 5% drift for frame FRS, Level 2 story shear was approximately 80 kips, whereas the predicted total base shear demand for frame FRW (which represents the upperbound base shear demand) was anticipated to be approximately 50 kips. In terms of story forces (i.e., actuator forces), this is equivalent to approximately 70 kips of load reversal between Levels 2 and 1 for the FRS test.

Second, the flange reinforcement plates were welded to the HBE flanges only along the plate perimeter (three sided weld on plate). From the figures, it is apparent that yielding occurred due to local buckling of the flange reinforcement plate. In hindsight, this could have been prevented if plug welds had also been provided. However, in general, the observed local yielding was minor and was not detrimental to the performance of the test specimen.



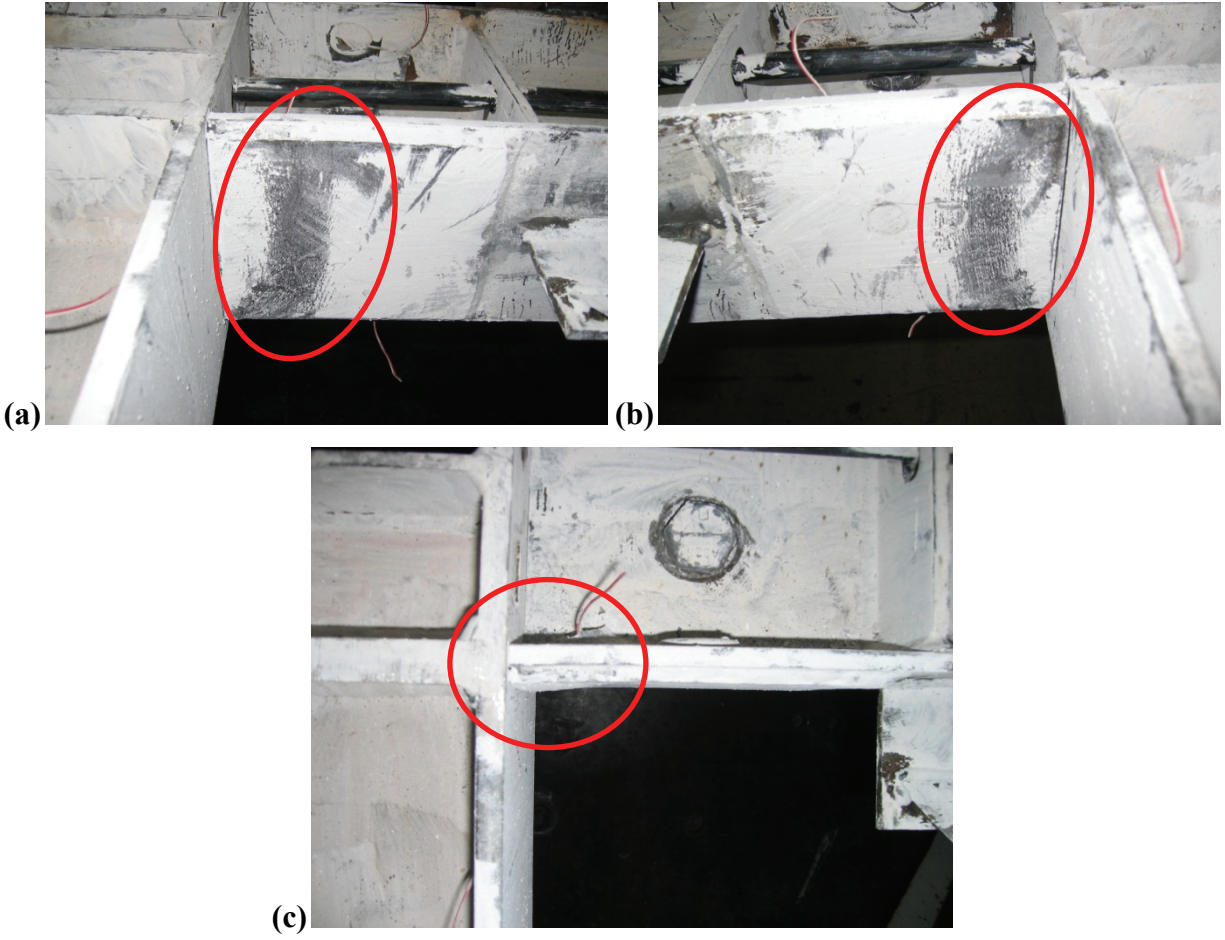


**FIGURE 6-13 Level 1 Frame FR: (a) SW bot. flange; (b) SE bot. flange; (c) SW bot. flange**

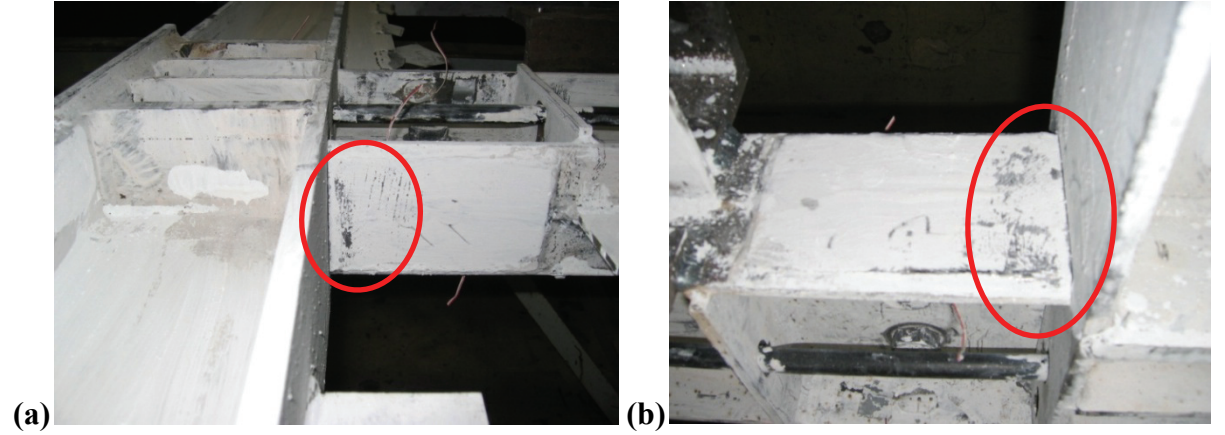


**FIGURE 6-14 Level 2 Frame FR: (a) SW bot. flange; (b) SE top flange**

## **6.3 Flange Rocking (FR) Frame Experimental Results**

### **6.3.1 FR: Global Response**

The global response in terms of base shear versus roof drift is shown in figure 6-15 for the different FR frame web plate configurations. As presented earlier, the negative stiffness observed is an artifact of using displacement control at all floor level actuators. Due to this effect, the global force versus drift response is distorted and only relative comparisons between the FR tests are presented, rather than rigorous comparisons to the NZ and CR frames (although the global response observed for the FR tests is not representative of the actual response in the prototype frame, some of the recorded information on the SC-SPSW behavior presented in this section remains of interest and of relevance). Note that the figure includes a plot of the ratio of the residual base shear normalized by the maximum base shear at each displacement step (hereinafter referred to as the residual base shear ratio) that will be used subsequently to provide observations on the effects of the infill web plate on frame response.

As presented in Section 4, the base shear strength of frame FRS is approximately half that of frame FRW. Additionally, frame FRB's response is essentially elastic and its base shear strength contribution is small compared to that provided by the frames with infill web plate or strips. Note that some energy dissipation (although negligible) is observed in the PT boundary frame given that the response is not perfectly linear; this is attributed to friction and slip inherent in the test setup and HBE-to-VBE joint connections. Furthermore, from the hysteretic response shown in figure 6-15, it is observed that strength degradation occurs at approximately 2% drift for frame FRW; this is due to tearing of the infill web plate from the boundary frame. In contrast, for frame FRS, no strength degradation is observed; this is consistent with the observation that no tearing of the infill web strips at the welded connection to the fish plates occurred during testing.

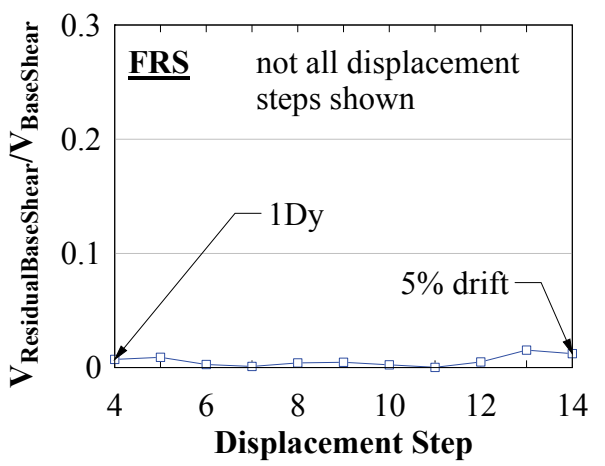
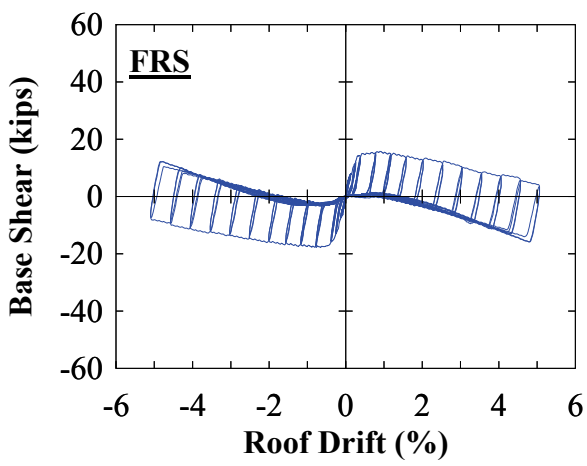
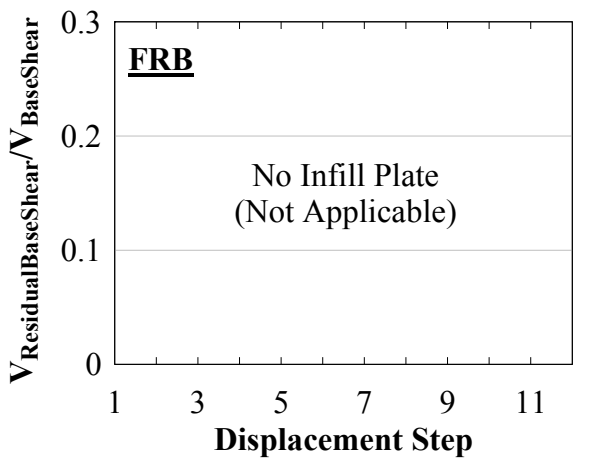
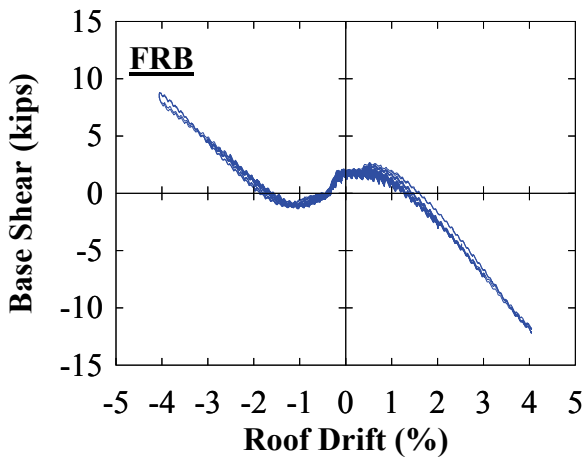
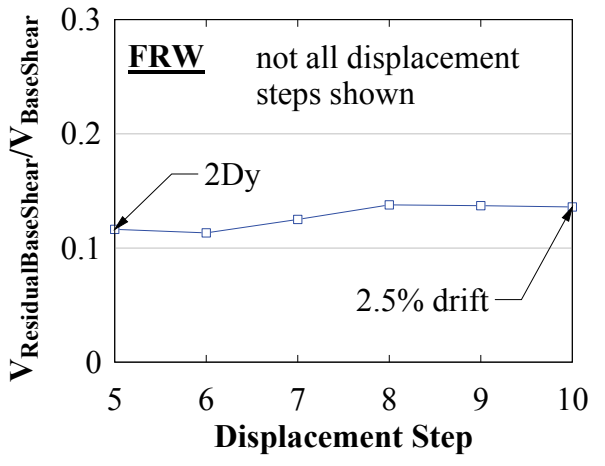
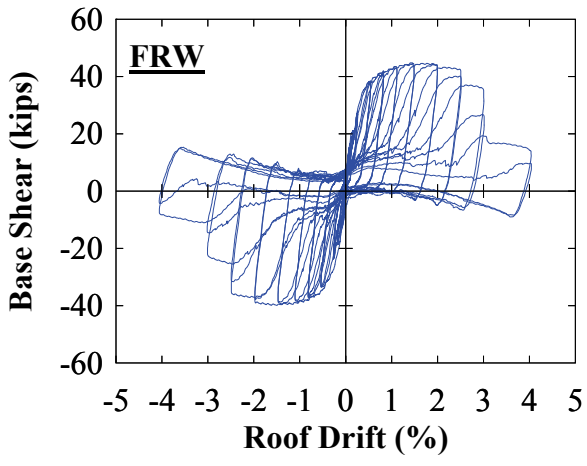
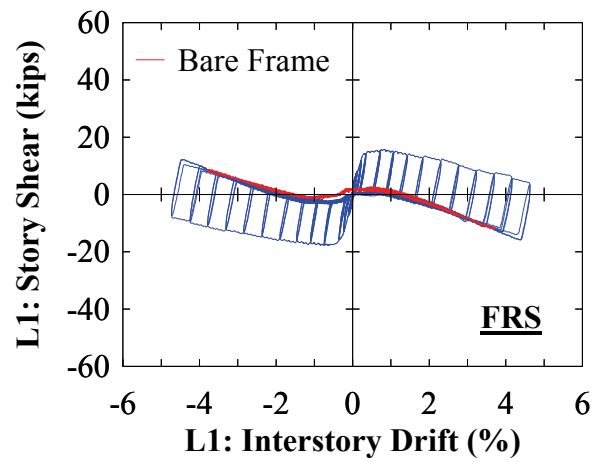
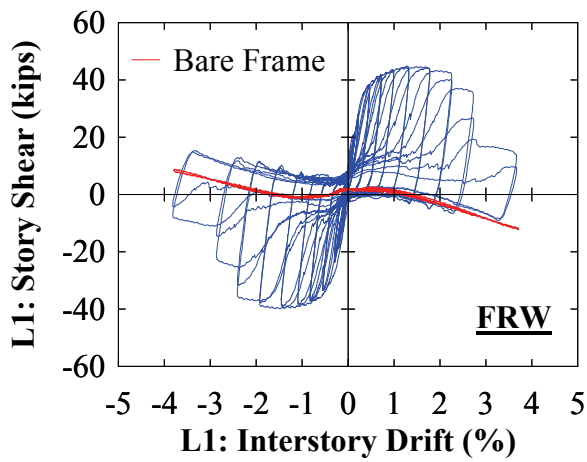
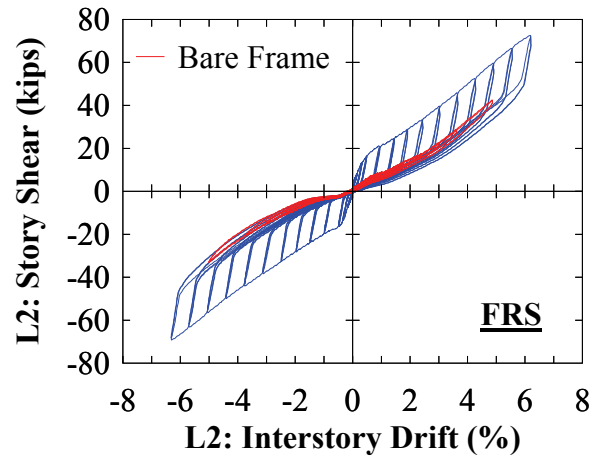
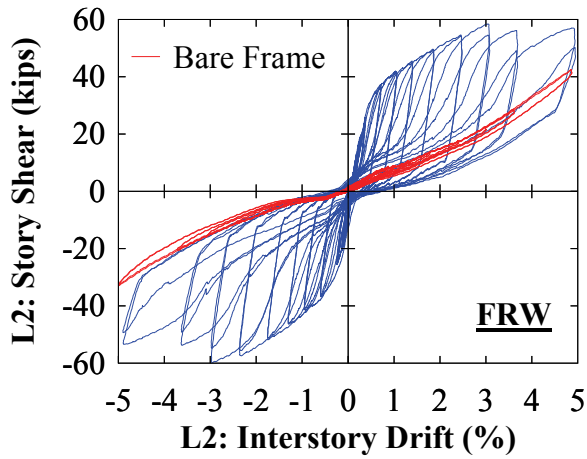
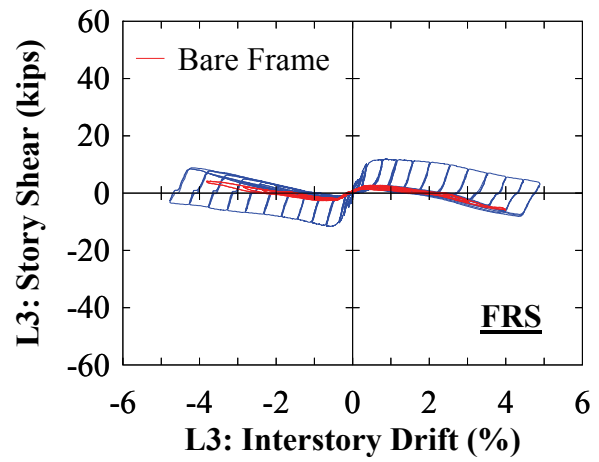
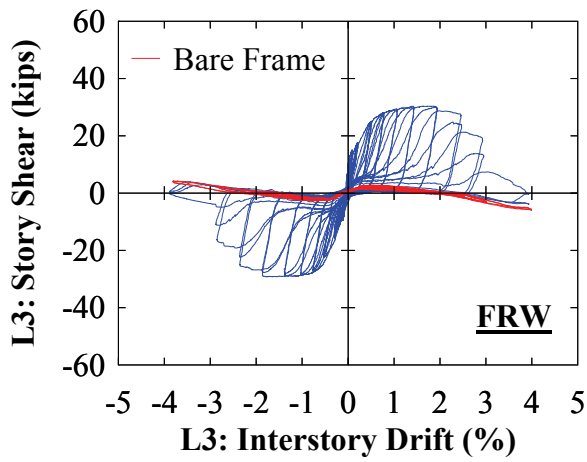


FIGURE 6-15 Frame FR – global response

Additionally, it is observed that for frame FRW, the base shear is not zero at the location of zero drift, indicating the presence of a residual base shear. In comparison, by visual inspection of the hysteretic response curves for frame FRB and FRS, the residual base shear is essentially zero. This is quantified by the residual base shear ratio at the particular displacement steps shown in figure 6-15 for frame FRW and FRS. Note that these ratios for the FR tests are distorted for the same reasons as the hysteresis curves themselves, but do provide a relative comparison between frame FRW and FRS. Additionally, only shown are results for the displacement steps where it has been observed that significant yielding in the infill web plate has occurred. Given that there is no infill web plate for frame FRB, and frame FRS is comparable at the zero drift location, the residual base shear can be attributed to the presence of the infill web plate. This indicates that contrary to the infill strips that essentially behave as tension-only members, the infill web plate contributes some compression strength. This compression strength of the infill web plate is attributed to the random folding of the infill web plate as it is pushed through the zero drift point after some cycles. More specifically, when the infill web plate yields, it develops a sort of “corrugated” shape upon reaching plastic deformations that exceed the previous deformations reached, which can then provide some stiffness in compression (equivalent to a temporary compression-strut). This observation of SC-SPSWs with full infill web plates was also observed by Clayton (2013) and an investigation of this phenomenon was performed by Webster (2013).

The residual base shear ratio also serves as an indicator of frame re-centering. That is if the frame perfectly re-centers, the residual base shear ratio would be zero. Consequently, for static loading, it is apparent that the infill web plate affects the re-centering response due to its compression-strut effect as the infill web plate becomes significantly deformed at large inelastic cycles. Additionally, although it cannot be observed for the FR frames (due to the artificial negative stiffness response), the residual drift corresponds to the point on the roof drift axis where the base shear is equal to zero. For frame FRS, it is observed that this frame essentially re-centers perfectly (based on observation of the residual base shear ratio). The residual base shear observed for frame FRS is due to the hysteretic response of the PT boundary frame. That is if the test setup and HBE-to-VBE joint connections were friction free, the residual base shear ratio for the frame FRS would be zero.

Finally, the story shear versus interstory drift response is shown in figure 6-16 for frame FRW and FRS with the response of FRB superimposed. The interstory response is consistent with the observations made above. In particular, the energy dissipation provided by the boundary frame is insignificant, there exists a compression effect of the infill web plate, and infill web strips behave essentially as tension-only members. Also observed are the effects of the actuator interaction across the stories. The fact that actuator forces at Level 1 act in the opposite direction of those at Level 2 results in a significant reduction of story shear force at Level 1 (this is more evident in the FRS test). Some actuator interaction (i.e., actuator forces acting in opposite directions) is also developed between the Level 3 and 2 actuators due to the negative stiffness observed at Level 3.



**FIGURE 6-16 Frame FR – interstory response**

### 6.3.2 FR: Boundary Frame Post-Tension Response

The target initial PT force,  $T_o$ , for frame FR was approximately 20% of the PT yield strength,  $T_{yPT}$ , where the yield strength of the PT was taken as approximately 90% of the ultimate PT tensile strength. Corresponding PT forces normalized by  $T_{yPT}$ , for the achieved initial PT force (shown by displacement step 1) and at the start of subsequent displacement steps is shown in figure 6-17. Any reduction in value between displacement steps indicates loss in PT forces attributed to PT relaxation and anchor wedge seating. Additionally, as noted in the figure, only one of two load cells at Level 1 and 2 were operable. It is observed that minor PT force losses initiated at around displacement step 6 (i.e.,  $3\delta_y$  for test FRW) and increases with subsequent displacement steps.

The global PT force versus interstory drift response is shown in figure 6-18. It is observed that the PT force is proportional to the interstory drift. Additionally, as annotated on the Level 3 response curve, from the start to the end of the test, observation of PT force loss is indicated by a vertical downward shift along the PT force axis (where ‘‘To’’ Start’ refers to the beginning of the test and ‘‘To’’ End’ is at the completion of the test). Furthermore, it is observed that the PT response is nonlinear (even though the PT elements remained elastic). This is due to the effects of the infill web plate on the boundary frame. In particular, the infill web plate affects the opening and closing of the HBE-to-VBE gap leading to a nonlinear PT response. Also, figure 6-18 is a superposition of response of all displacement steps, which includes the cumulative effects of the PT force losses from the start to end of the test. To provide a more accurate representation of the nonlinear response, it is more appropriate to look at the individual displacement steps. Accordingly, figure 6-19 shows two different displacement steps where it is observed that the nonlinear response is not as significant as that shown in figure 6-18. It is also observed in figure 6-19a that there is an initial transition at the start of the displacement step where the PT force remains relatively constant. This transition is associated with the gap opening due to frame drift at the HBE-to-VBE joint (i.e., an increase in PT force does not occur until the HBE-to-VBE gap forms for frames with FR joint connections). In comparison in figure 6-19b at the 2.5% drift displacement step, the initial transition is not as evident, indicating the gap formation at the HBE-to-VBE joint at these locations occur earlier than at Level 3 for the displacement steps shown.

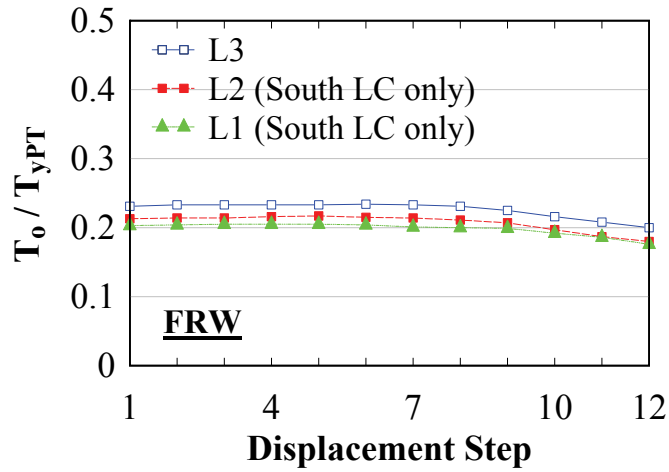


FIGURE 6-17 Frame FRW – initial PT forces

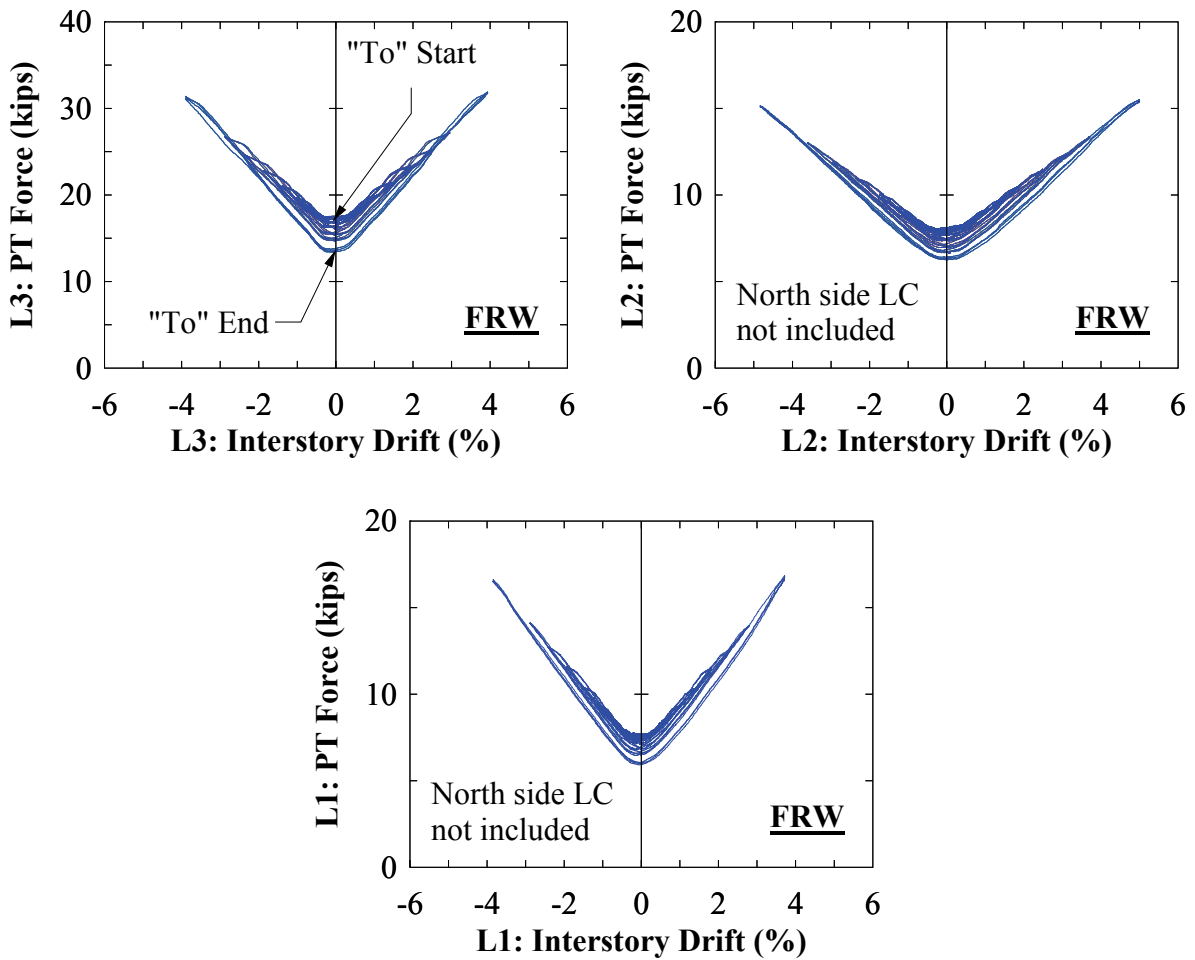
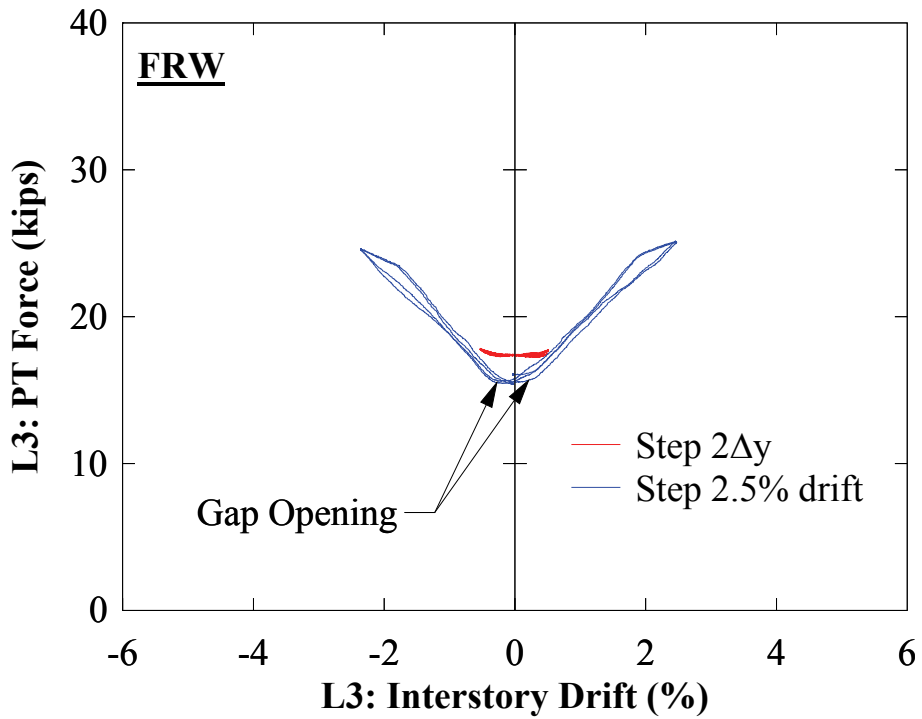
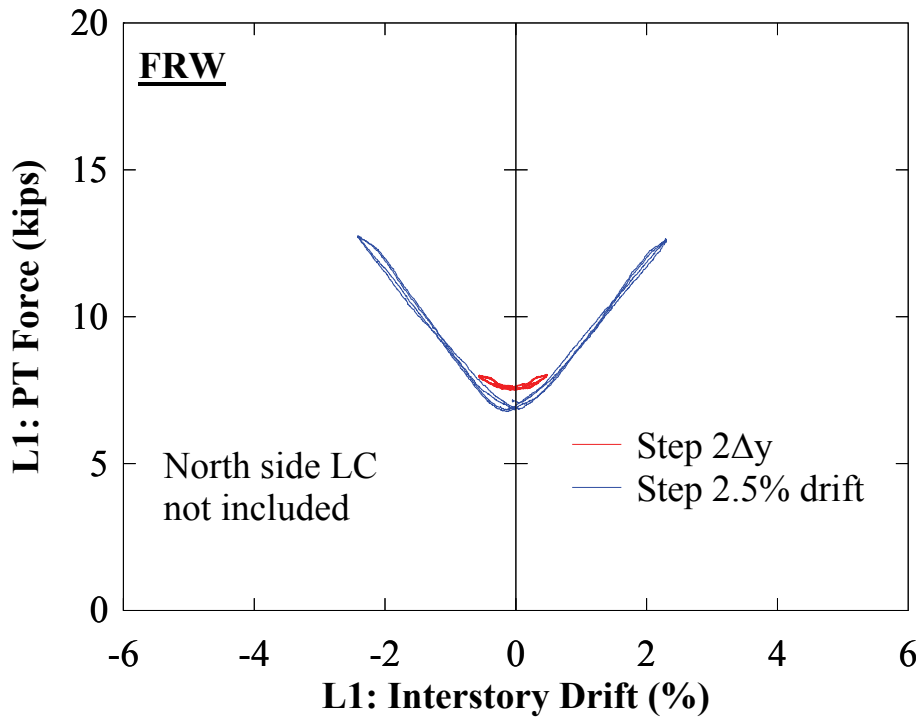


FIGURE 6-18 Frame FRW – PT response





(a)



(b)

FIGURE 6-19 Frame FRW – select PT response: (a) Level 3; (b) Level 1

The initial PT force and response history for frame FRB is shown in figures 6-20 and 6-21, respectively. For frame FRS, these are shown in figures 6-22 and 6-23, respectively (note that unlike test FRW and FRB, all PT load cells were functioning in those cases). Observations on behavior for those frames are similar to those made for frame FRW. Additionally, for the PT boundary frame test, it is observed that the initial PT forces remain essentially constant between displacement steps. This is reasonable as the test FRB was an elastic test and the loading protocol of test FRW was repeated; so the PT was not “stretched” further than tested earlier. Similarly, the initial PT forces for frame FRS remain relatively constant throughout the test, for the same reason that previous displacement steps were also repeated for frame FRS. The only exception is that the maximum drift in the last displacement step, for test FRS, was increased up to 5% drift (i.e., more than in all prior tests), where it can be observed in figure 6-22 that the initial PT force does decrease slightly. It is noted that the initial PT forces shown for frame FRS should start at the values recorded when the frame FRB test ended. However, it is observed in figure 6-22 that the initial PT forces start at slightly higher values than what is shown for the last displacement step in figure 6-20. Prior to test FRS, the test setup was taken down completely in order to install the infill web strips and re-install instrumentation, and it appears that there was some unexplained fluctuation in initial PT load cell readings that occurred during that process. In contrast, such fluctuation was not observed between the FRW and FRB tests as test FRB was conducted the day after test FRW (after removal of the infill plates, with all instrumentation remaining in place).

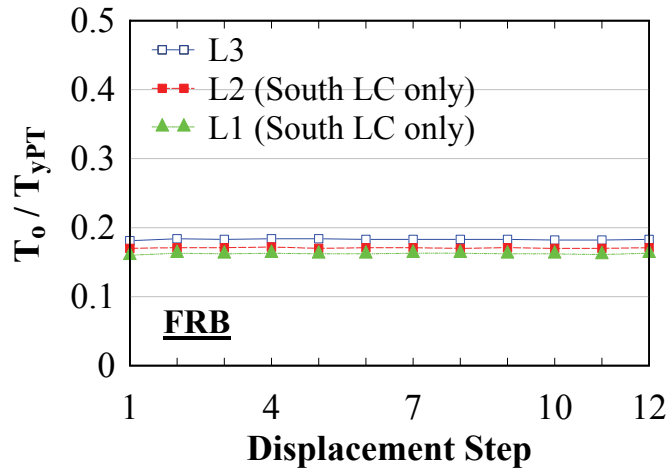


FIGURE 6-20 Frame FRB – initial PT forces

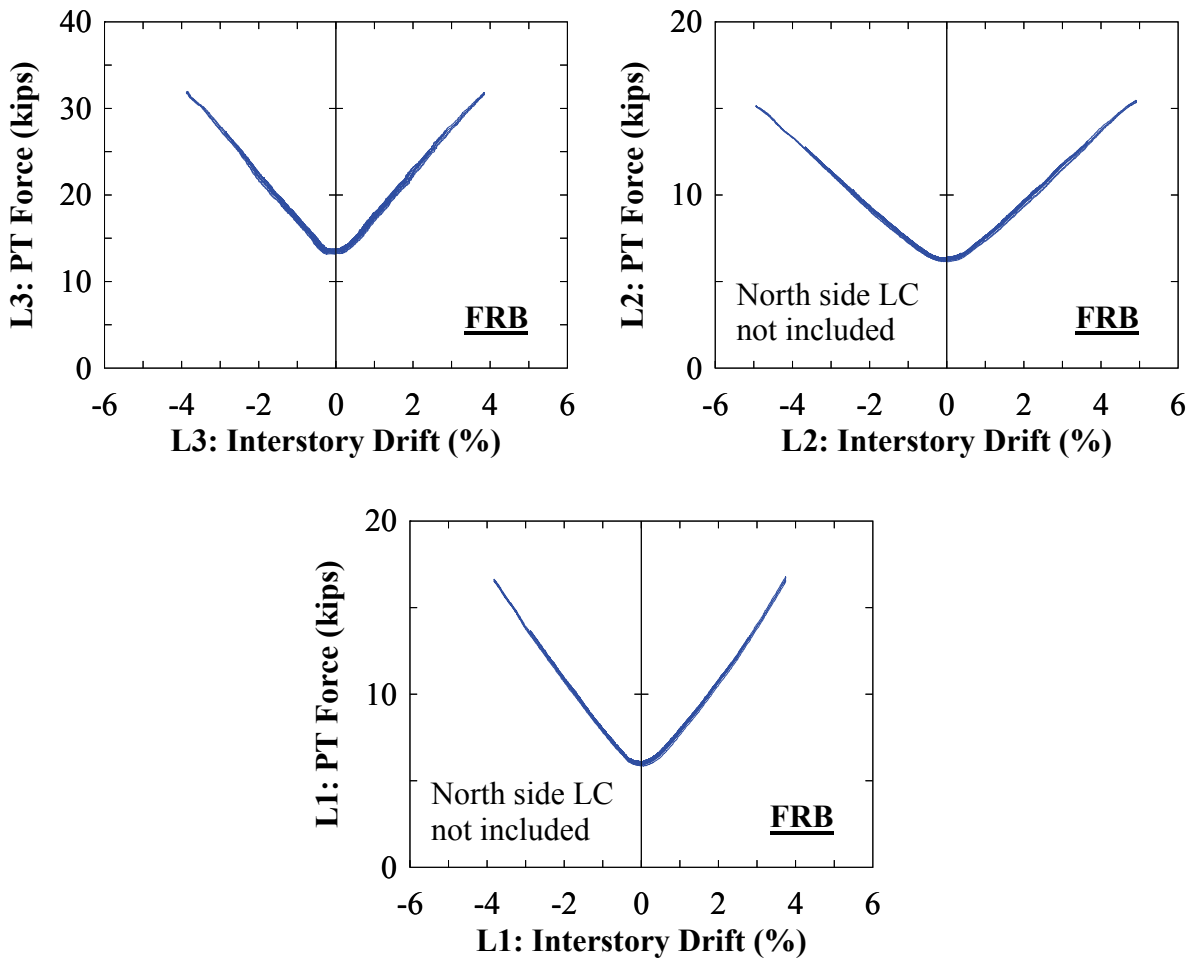


FIGURE 6-21 Frame FRB – PT response

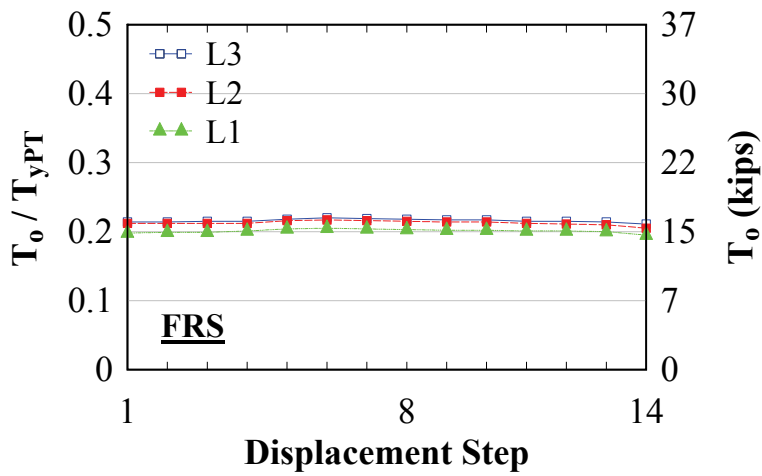


FIGURE 6-22 Frame FRS – initial PT forces

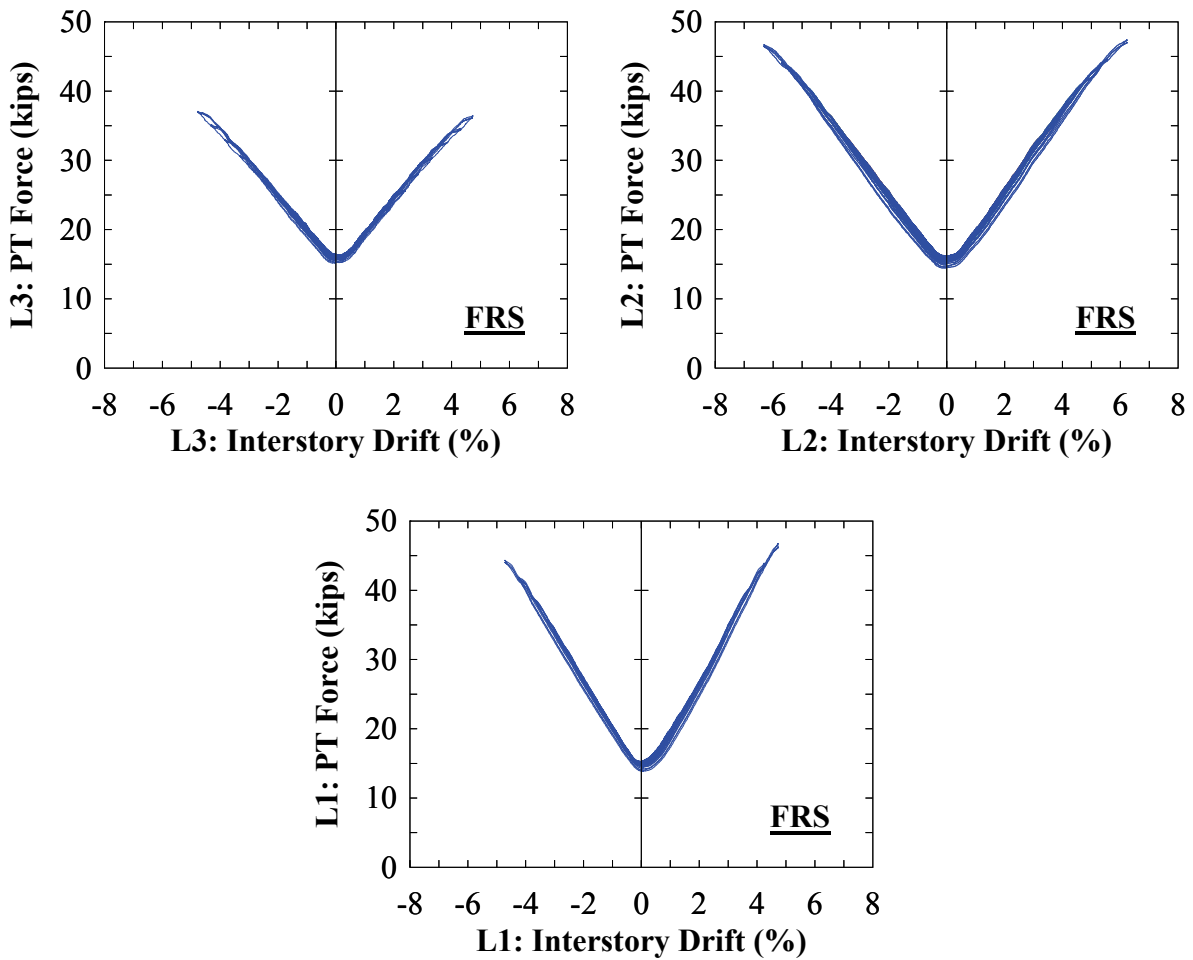


FIGURE 6-23 Frame FRS – PT response

To provide a more meaningful account of the PT force losses, figure 6-24 shows the PT force at the end of displacement step normalized by the initial PT force at the start of displacement step 1 for each test. It is observed that for test FRW, a PT force loss of approximately 20% occurred. For reasons presented earlier, relative PT force losses for test FRB are insignificant. For test FRS, relative PT force losses ranged between 5 to 8% (and as presented earlier, PT force losses are less for FRS compared to FRW since the displacement steps were repeated). As an additional comparison, figure 6-25 shows the effects of PT force losses relative between frame tests where  $T_o$  is the PT force at the end of each frame test and  $T_{start}$  is the initial PT force at the start of test FRW (i.e., at the start of the first test). As observed, the largest PT force loss occurs during the first test FRW. Additional minor losses accumulate during the second test FRB. However, with the third test FRS, as mentioned above, some fluctuation in initial load cell reading was evident, affecting the results shown in the figure for that test. Thus, considering only the first two tests, the total PT loss was approximately 20%.

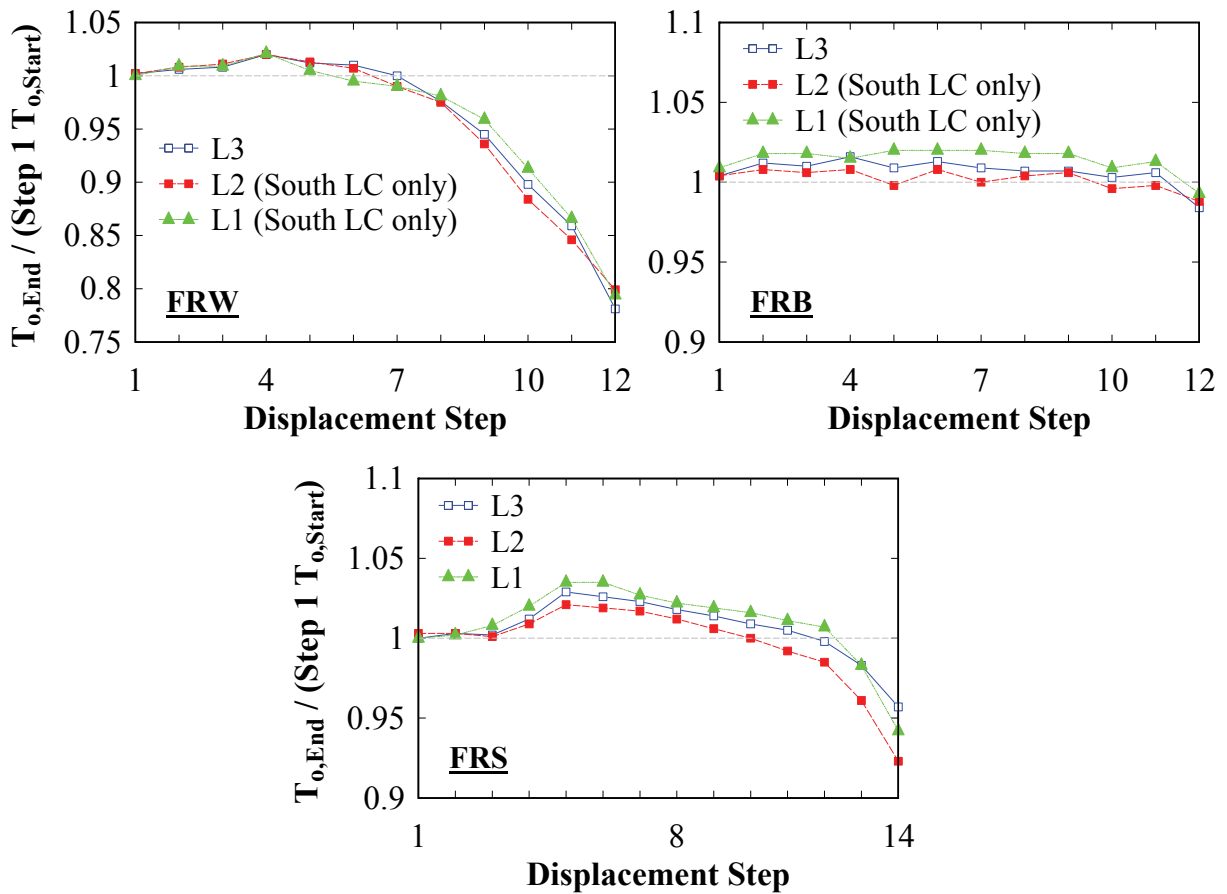


FIGURE 6-24 Frame FR – initial PT forces normalized by displacement step 1

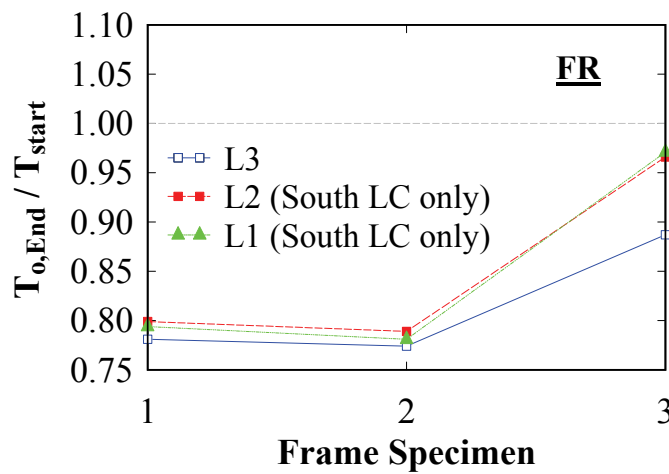


FIGURE 6-25 Normalized initial PT force changes between FR tests

### **6.3.3 FR: Infill Web Plate and Strip Strain Gage Response**

The South elevation infill web plate tensile strain response for selected displacement steps (for a frame drift in the positive drift direction) is shown in figure 6-26, where WP3, WP2 and WP1 refer to the Level 3, 2 and 1 infill web plates, respectively. Additionally, the strain values of interest are the marker symbols representing each strain gage provided; the continuous line between the markers is only a reference line. Furthermore, the plotted distance indicated in each curve is the horizontal distance from the West edge of the infill web plates, where the relative vertical location can be referenced in the instrumentation drawings presented in Section 5. Also note that a point of zero strain location indicates that the strain gage delaminated from the infill web plate surface during the test and hence is no longer valid.

It is observed that in general, the strains at the corner locations (at the far left and right point locations in the plots) have higher strains than those further removed from that location. Additionally, for the strain gages located between the far left and right end locations (representing the interior locations of the infill web plate), it is observed that the strains are approximately equal, indicating uniform distribution of infill web plate yielding (which is reflective of a strain distribution in an idealized sway panel mechanism). Similar response is observed with the infill web strip strain distribution shown in figure 6-27. Furthermore, tensile strains in the infill web strips are larger than those observed with the infill web plate, but that may simply be a consequence of the fact that strain gages were oriented axially with the infill web strips direction (at a 45 degree angle) but not necessarily in the correct tension field action direction for the infill web plates.

The distributions of infill web plate/strip tensile strains observed are consistent to those presented in Section 3, in that, for rocking connections, larger infill web plate tensile strains occur near the HBE-to-VBE joints due to the formation of a gap opening. In particular, the equations in Section 3 were derived assuming the kinematics of the infill web strips (i.e., no redistribution of strains). Thus, those theoretical equations provide an upperbound value for use in design.

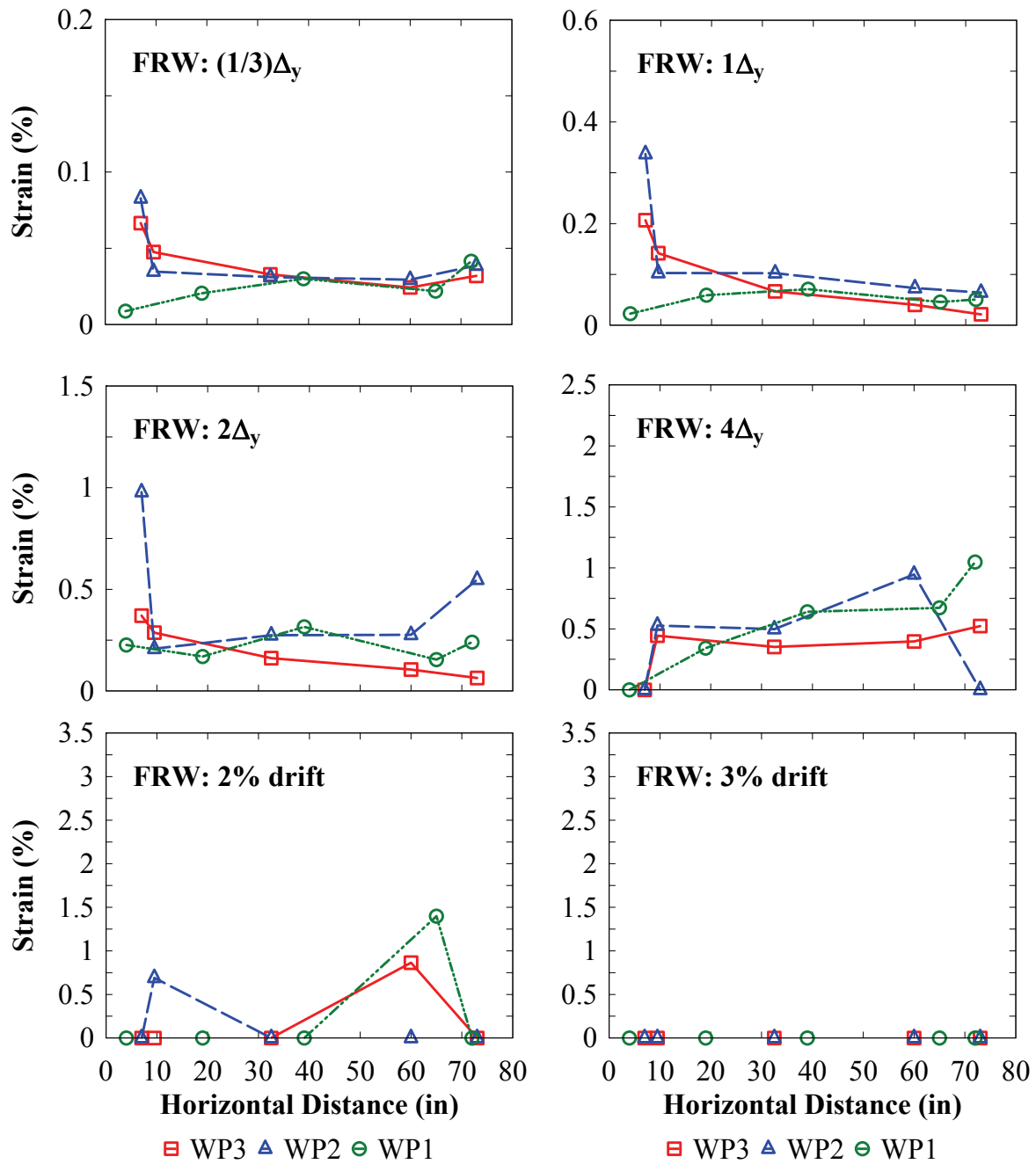


FIGURE 6-26 Frame FRW – infill web plate strains



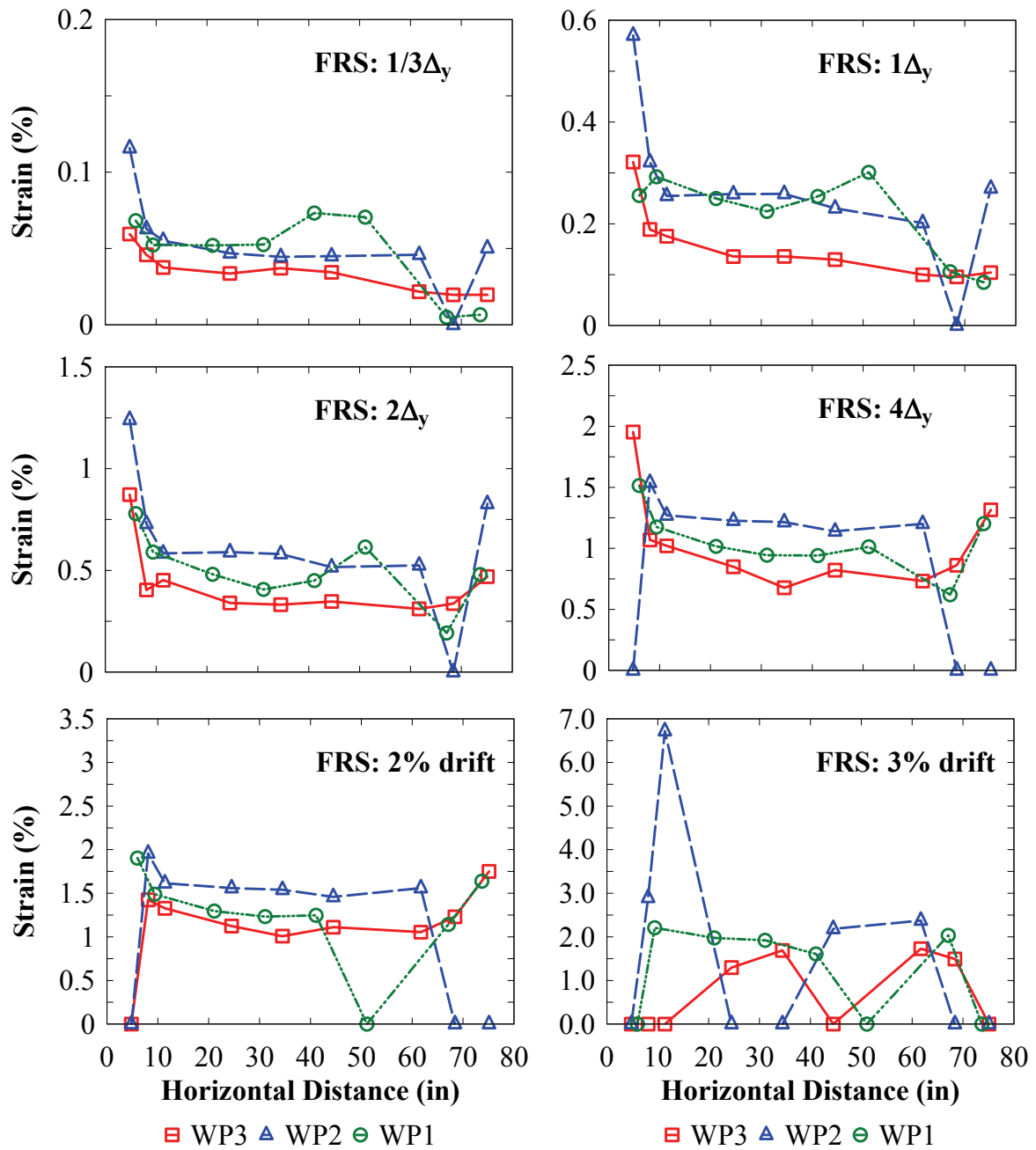
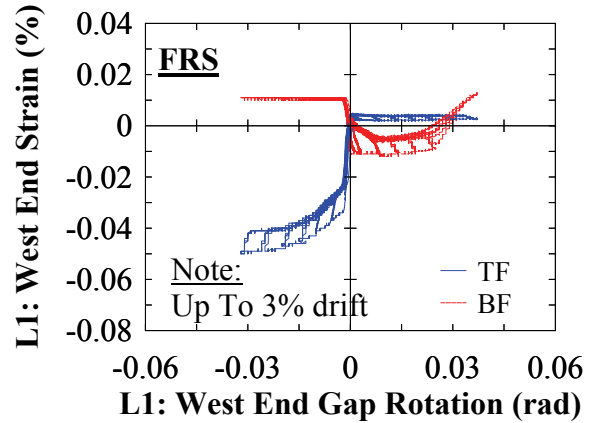
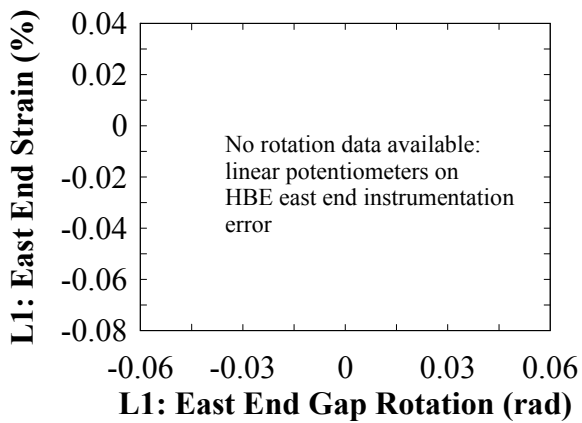
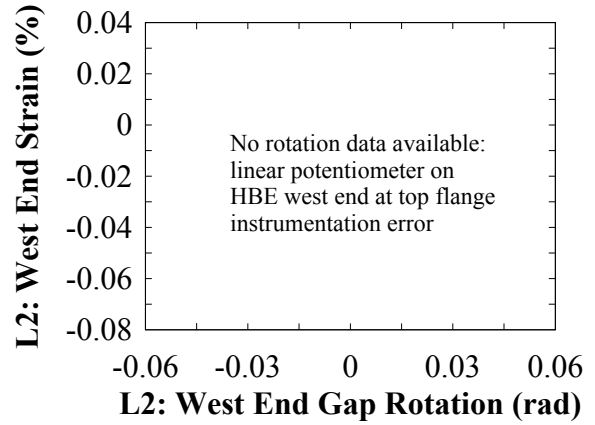
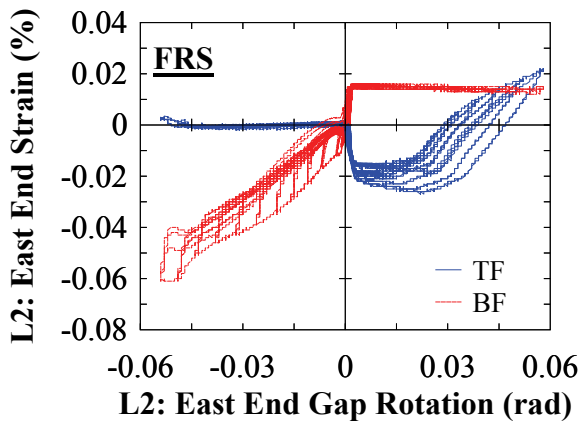
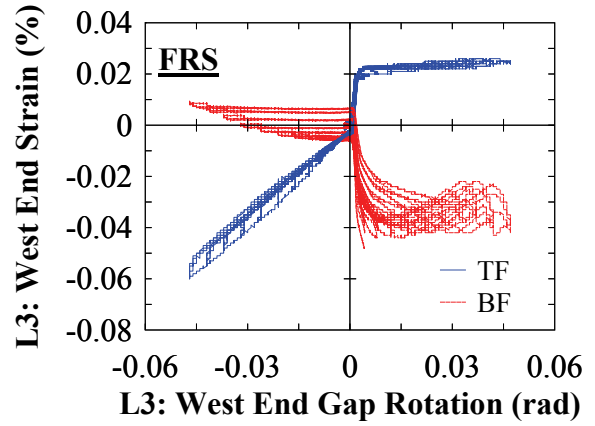
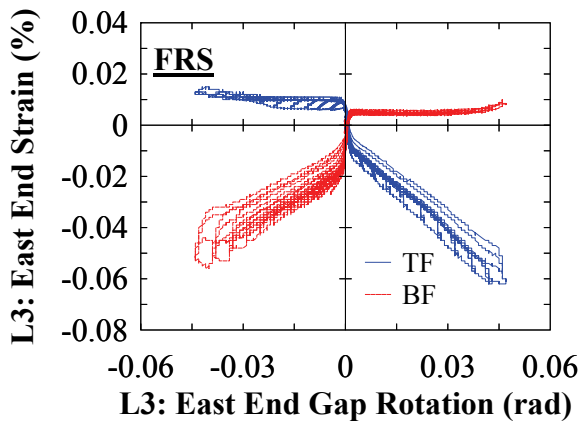


FIGURE 6-27 Frame FRS – infill web strip strains

#### **6.3.4 FR: HBE Strain Gage Response**

The HBE end strain versus gap rotation is shown in figure 6-28 for frame FRS; note that frame FRW and FRB results are not presented due to strain gage instrumentation error (where the error was not with the sensor themselves but the data acquisition system related to those particular sensors). Additionally, the sign convention for positive gap rotation is gap opening at the bottom flange at the East end of the HBEs and a corresponding gap opening at the top flange at the West end of the HBEs. This corresponds to a positive drift moving away from the reaction wall.

It is observed that depending on the drift direction, the strains at the top or bottom flanges are either in compression or zero (but not simultaneously in compression or zero); where zero strain is indicated by the horizontal line segment of the response curves (and further clarified subsequently). This is a reflection of the kinematics of the FR frame. As an example, for a positive drift condition, once the HBE-to-VBE joints have opened, at the East HBE end, the top flange is in compression (in bearing with the VBE flange) and the bottom flange is no longer in contact with the VBE flange (due to gap opening). Correspondingly, at the opposite end of the HBE, the top flange is not in contact (due to gap opening) and the bottom flange is in compression (in bearing with the VBE flange). At the flange location not in contact with the VBEs, there are no external forces present on the boundary surface leading to zero strains observed at that location. Note that the zero strain condition corresponding to the horizontal line segment does not coincide with the zero strain axes as it should (except for the top flange at Level 2 HBE East end condition where it is shown at approximately zero). This indicates that there is a vertical offset error with the strain gage readings by that amount.



**FIGURE 6-28 Frame FRS – HBE end strain versus gap rotation**

It is also observed that the response in compression differs at some locations. In particular there is a dipping effect such that the strains increase in compression, then a reduction in compression strain is observed for increased joint rotation. This phenomenon appears to be due to changes in compression stress trajectory at the HBE-to-VBE flange contact points. That is, as the frame drift increases, the joint rotation increases, changing the orientation of the resultant contact compression force between the HBE-to-VBE flanges. In doing so, the resultant compression force redistributes forces to the HBE web leading to a reduction of compression stress in the HBE contact flange. However, to validate this behavior, a finite element analysis of that local detail would need to be performed (this is not within the current scope of work and could be investigated in future research).

### **6.3.5 FR: HBE Axial and Moment Demands**

The axial force and moment demand for selected displacement steps is shown in figure 6-29 for a positive drift condition (i.e., rightward direction on figure). Additionally, the values of interest are at the marker symbols representing the locations where the strain gages were provided; the continuous line between the markers is only a reference line. This is more relevant for the moment plots, as the moment is not a linear relationship between marker symbols. Furthermore, the plotted distance indicated in each curve is the horizontal distance from the East end of the HBE. Also recall that there exists some vertical offset error with the strain gage data noted above. The resulting axial and moment values presented include this offset error, since these values are obtained by a linear combination of the strain gage data. As a consequence, the results shown are not necessarily the actual values. However, this does not preclude providing a relative comparison between the curves themselves.

In general, from observation of the axial force curves, the maximum axial compression force occurs at the East end of the HBE and reduces along the length in the Westward direction. The reduction in axial force is due to the horizontal component of the infill strips acting on the HBEs where these net forces oppose the compression force at the HBE-to-VBE contact point (which is consistent with results presented in Section 3). Additionally, from observation of the HBE moments at Level 3, the effects of the PT on response between increased displacement steps can be observed with some clarity. In particular for the  $2/3\Delta_y$  displacement step, it can be observed

that the response is dominated by the vertical component of the infill web plate. This is supported by figure 6-19a where it is observed that for  $2\Delta_y$ , the PT force response is essentially constant, indicating that the HBE-to-VBE joint has not opened. Accordingly the contribution of moment from the PT is negligible (as there is no eccentric PT moment if the HBE-to-VBE joint has not opened for HBE-to-VBE joints with FR connections). For the larger 2% and 4% drifts, as observed, the effects of the PT shifts the point of maximum moment to the HBE ends (which is consistent with results presented in Section 3).

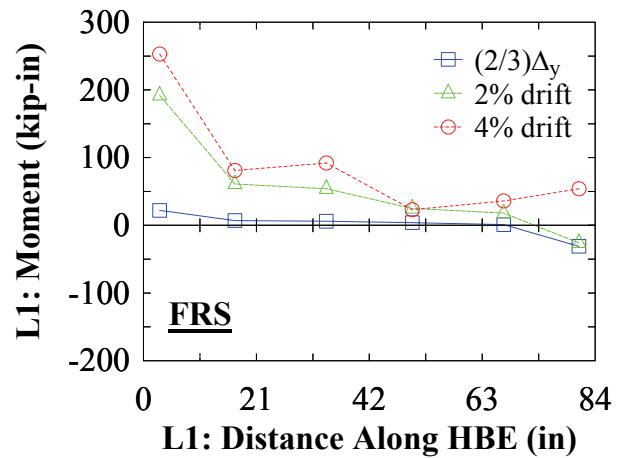
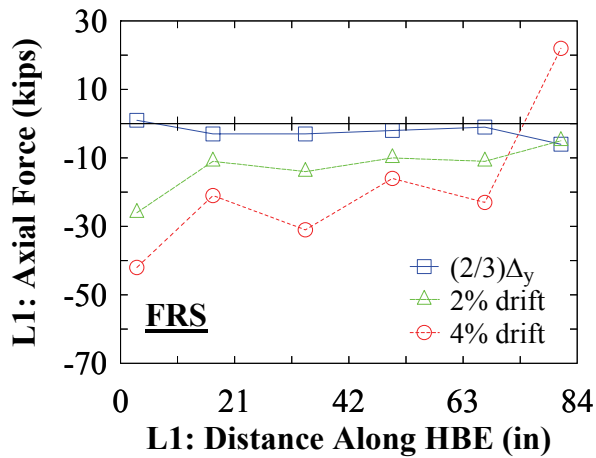
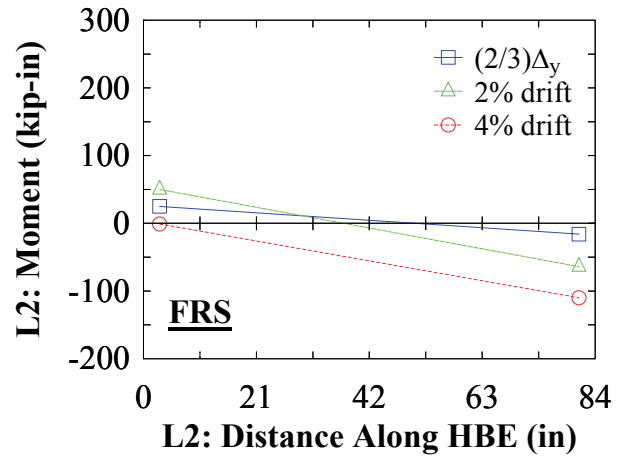
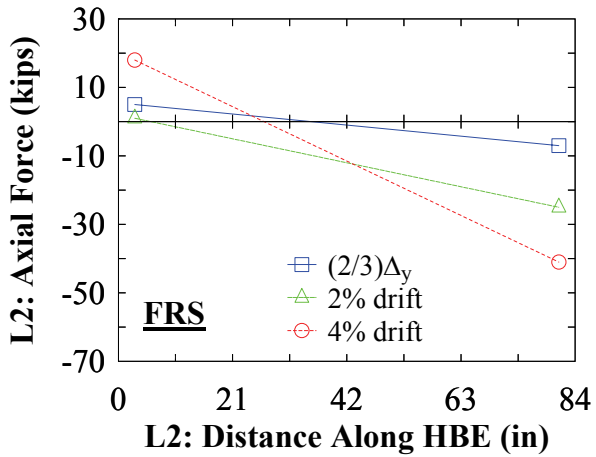
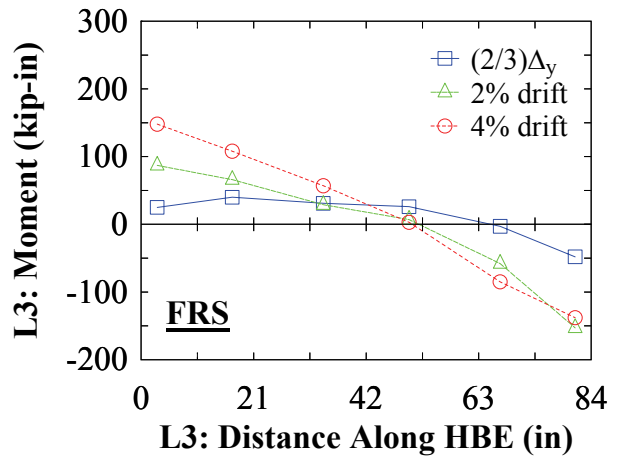
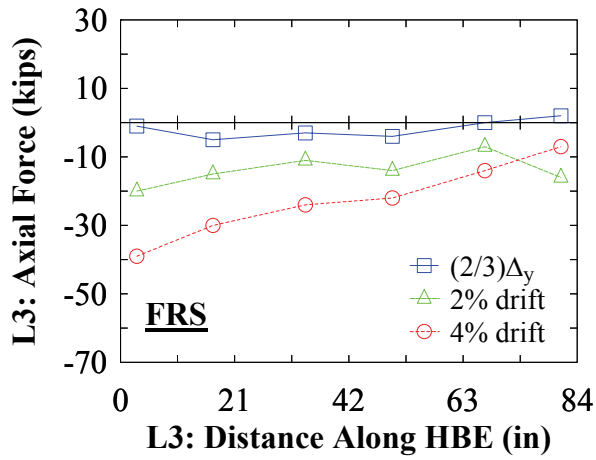


**FIGURE 6-29 Frame FRS – HBE axial force and moments**

## **6.4 NewZ-BREAKSS (NZ) Frame Experimental Results**

Many of the general observations and explanations provided for the FR frames also apply to the NZ frames. Although some overlap in observation will be presented for the NZ frames, observations will be provided concisely without detailed explanation. Any response that is unique to the NZ frames or which will provide additional clarity to the FR frame results will be presented in detail.

### **6.4.1 NZ: Global Response**

The global response in terms of base shear versus roof drift is shown in figure 6-30 for the different NZ frame web plate configurations. As observed, using a combined force-and-displacement control scheme on the actuators eliminated the undesired actuator interaction observed with the previous FR tests. From observation of the residual base shear ratio, the frame NZW does not perfectly recenter due to the effects of the infill web plate. On the contrary, frame NZS re-centers essentially perfectly. Additionally, for frame NZW, the strength degradation effects of the infill web plate separation can be observed by the separation of peaks of individual hysteresis loops. This is further annotated in figure 6-31 and indicates strength degradation after 2% drift. This is in agreement with the visual inspections made during the test and progression of web plate tearing summarized in figure 6-9 which shows that noticeable web plate tearing initiated between the 2% and 2.5% drift steps.

For frame NZB, it is noted that a slight change in frame stiffness is observed due to the complete relaxation of the PT at the closing joints. This observation is not readily apparent due to the effects of friction inherent in the system (i.e., if the test setup and frame connections were friction free, the hysteretic curve would be exactly bi-linear elastic). However, to help clarify this, annotation is provided in the figure highlighting this transition. In particular, the stiffness change occurs at approximately 1.6% drift (indicated by the vertical dashed reference line in the figure) and similar response occurs in the negative drift direction. Additionally, after the test the setup was taken down, inspection of the slip-critical bolts that connected the actuator shoe assemblage to the GMF plates revealed that the threads of those bolts were deformed at some locations. This indicates that the bolts had slipped and gone into bearing. This explains the

small spikes in the hysteretic curves shown and annotated in figure 6-30; these spikes occur at the peaks of the cycles and are more pronounced at larger drifts.

Furthermore, the hysteretic response for frame NZW and NZS is shown in figures 6-32a and 6-32b, respectively, for two consecutive displacement steps. It is observed that the hysteretic loops overlap for frame NZW. In contrast, for frame NZS, consecutive loops occur adjacent to one another with no overlapping. Additionally, figures 6-32c and 6-32d, only shows the latter displacement step (i.e., 2% and 6% drift for frame NZW and NZS respectively), which shows more clearly the effects of repeating only a single displacement step. The comparisons show that infill web plates do provide some energy dissipation at repeated cycles. However, the infill web strips provide no additional energy dissipation at repeated cycles, providing further support that they behave as tension-only elements.

Finally, the story shear versus interstory drift response is shown in figure 6-33 for frame NZW and NZS with the response of NZB superimposed. The interstory response is consistent with the observations made above. Note that in comparison of frame NZS with the superimposed frame NZB response, the NZB curve does not lay on top of the NZS curve. Since it has been observed that the infill web strips behave as essentially tension-only elements, the NZB and NZS plots should overlap almost seamlessly (as it was observed earlier for frame FRS). The reason for the differences observed here, is that PT yielding occurred at Level 1 and 2 for test FRS; this will be presented in more depth in the subsequent section.



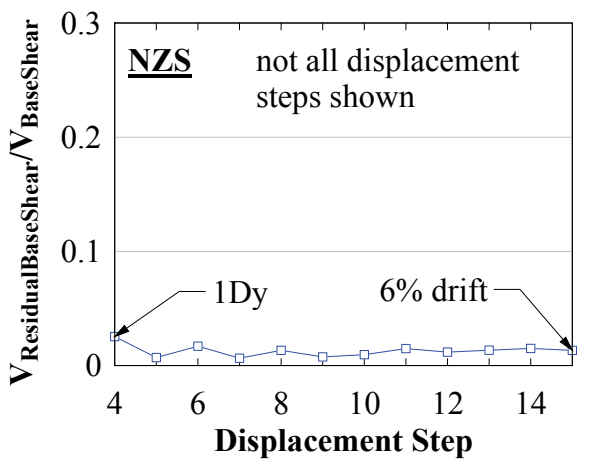
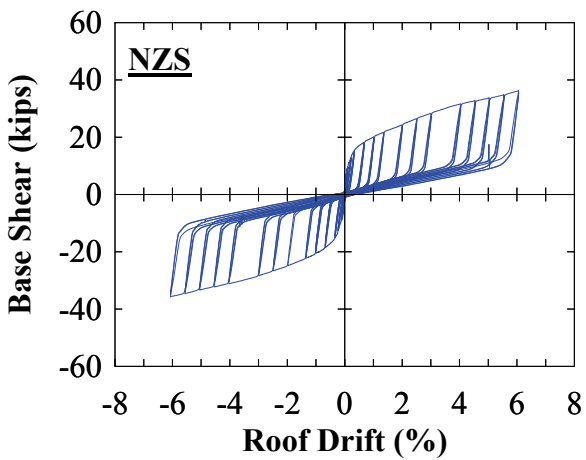
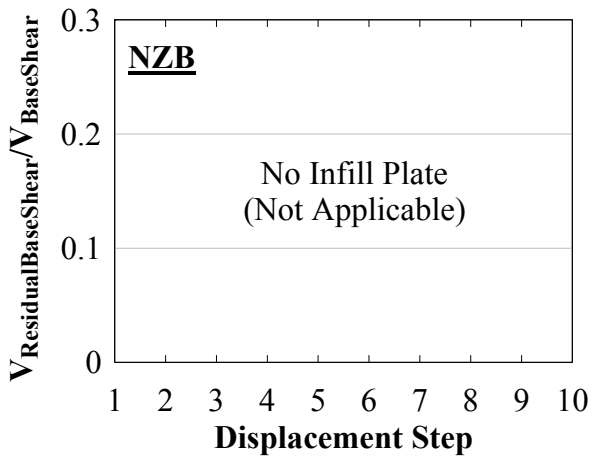
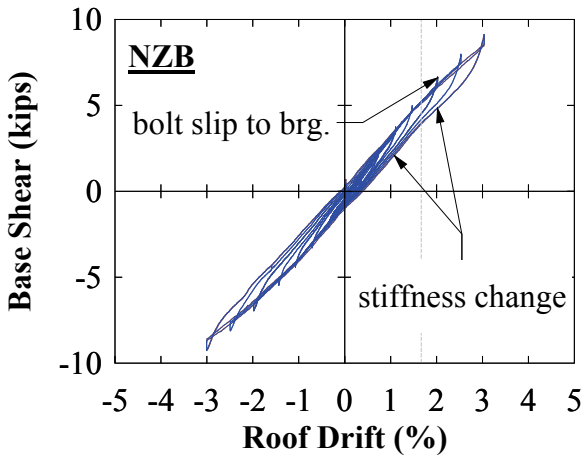
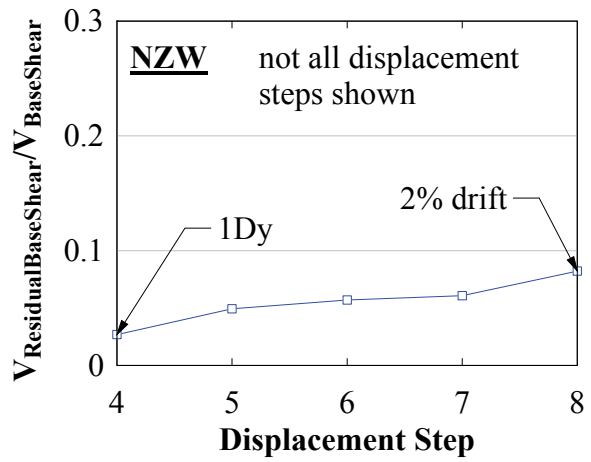
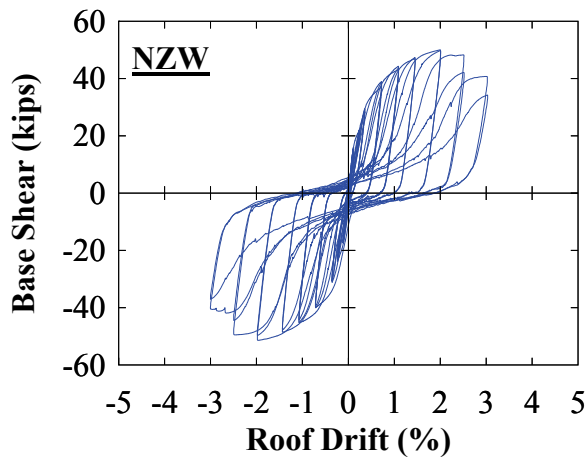


FIGURE 6-30 Frame NZ – global response

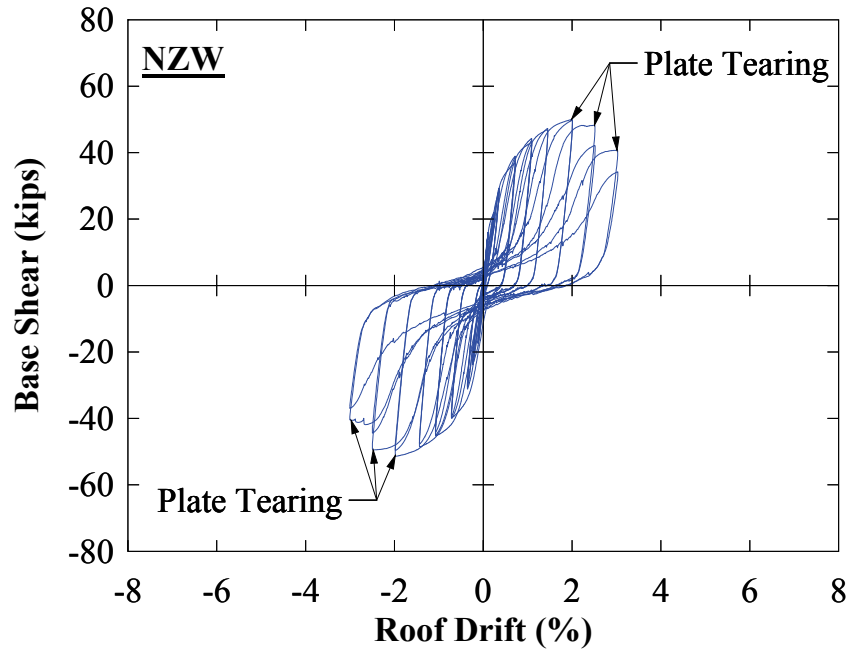


FIGURE 6-31 Infill web plate tearing effect on hysteresis response

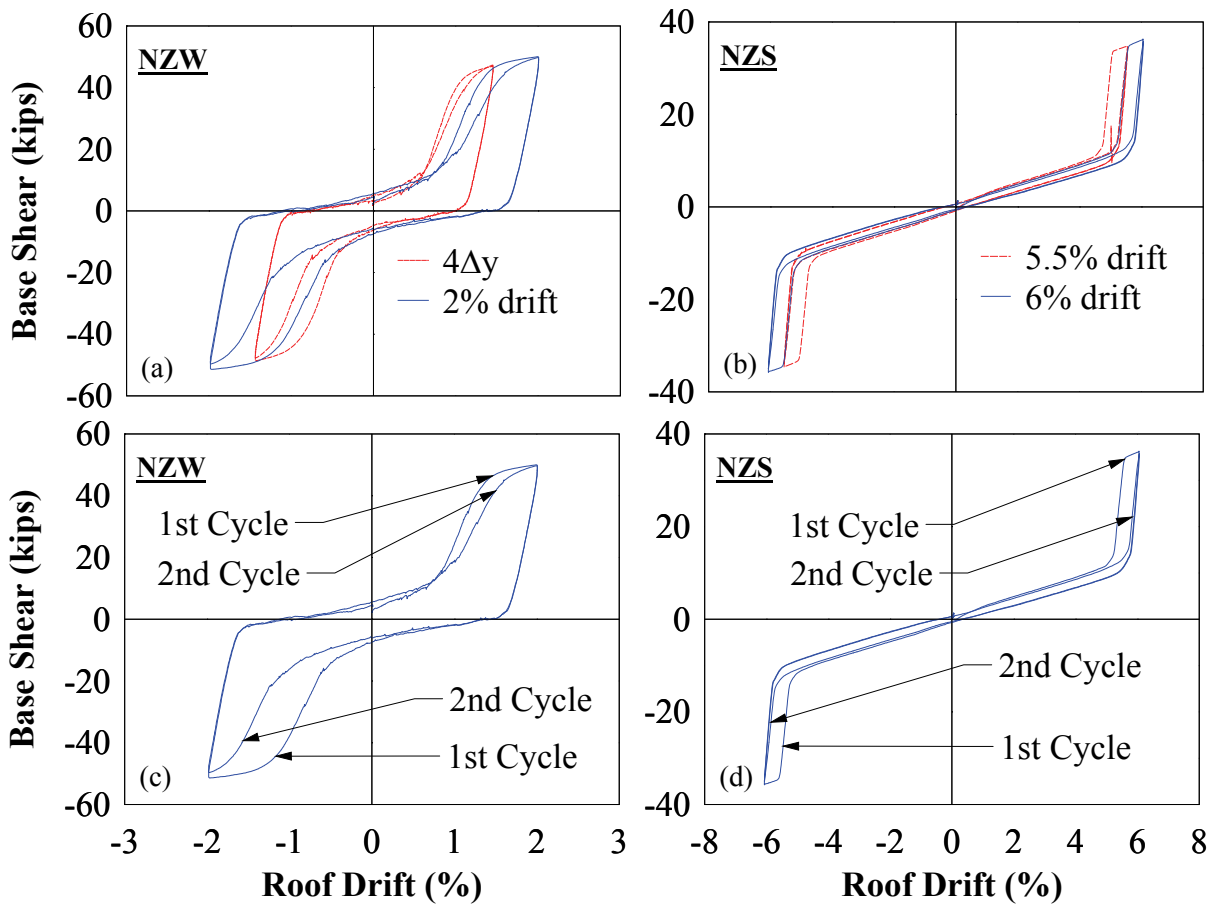
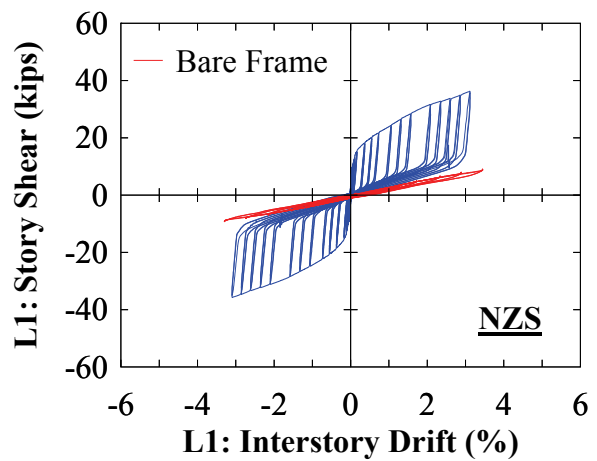
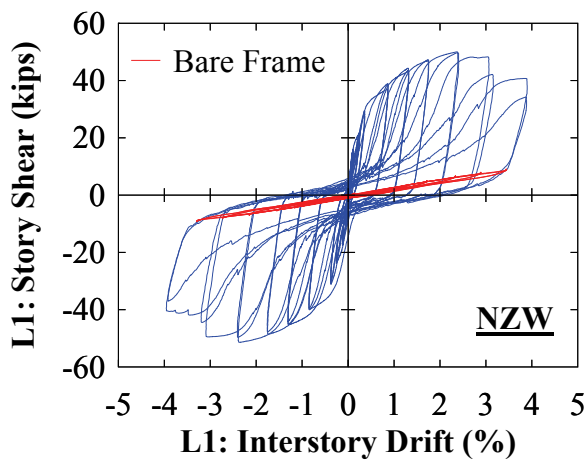
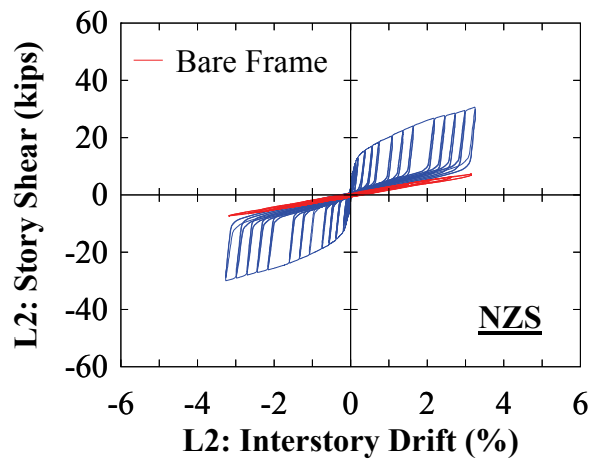
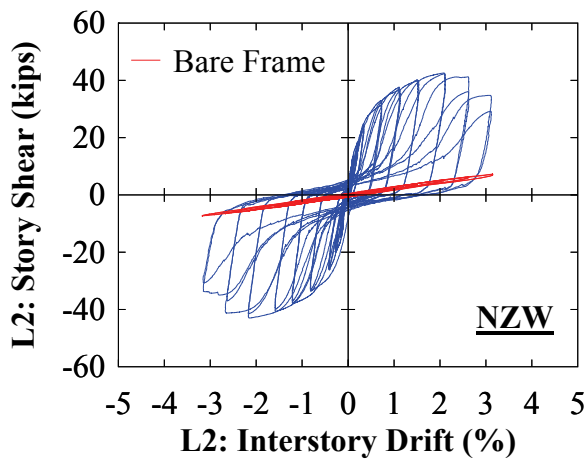
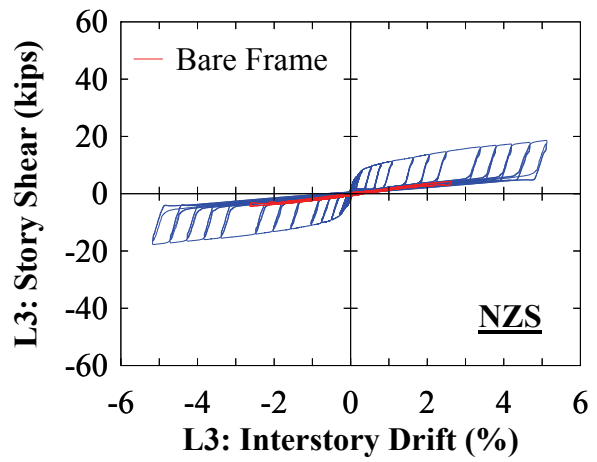
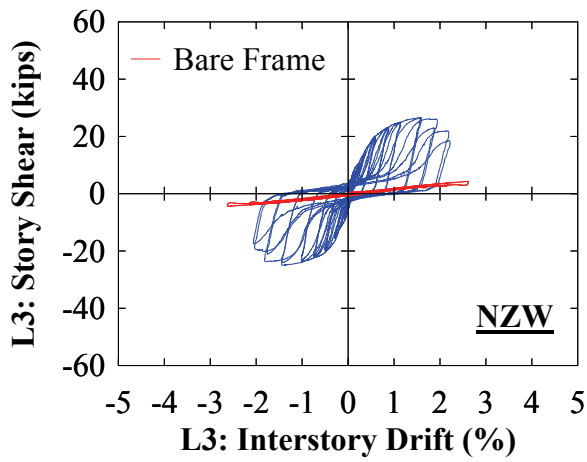


FIGURE 6-32 Base shear versus roof drift: (a) NZW; (b) NZS; (c) 2% drift; (d) 6% drift



**FIGURE 6-33 Frame NZ – interstory response**

#### **6.4.2 NZ: Boundary Frame Post-Tension Response**

The target initial PT force for frame NZ was approximately 20% of the PT yield strength. The achieved initial PT force and subsequent changes at the start of each displacement step is shown in figure 6-34. It is observed that at displacement step 4, a change in the initial PT force from the previous displacement step becomes readily apparent. In particular, there is a reduction in the East end PT force and a corresponding increase at the West end of approximately the same magnitude. This pattern continues up to displacement step 6 where thereafter a reduction in the initial PT force continues at both ends of the HBEs. The response at the West end is counter intuitive as it would be expected that the PT force at the start of each displacement step would remain relatively constant or decrease from the previous test displacement step. However, since the PT elements are separate at each ends of the HBEs, redistribution of PT forces occur, and in part, leading to the PT response shown.

The global PT force versus interstory drift response is shown in figure 6-35. As observed, the increase of PT force is proportional to the interstory drift at the opening joint locations. Correspondingly, at the closing joint locations, a decrease in PT force occurs. In particular, at approximately 2% interstory drift, the PT at the closing joint becomes fully relaxed. Additionally, the PT force response is nonlinear due to the effects of the infill web plates and PT force losses between displacement steps (described earlier for frame FRW).

Furthermore, it is observed in figure 6-35 that the East end PT response changes abruptly at Level 1 and 2. To clarify, during visual inspection after displacement step 9 (i.e., 2.5% drift), it was observed that the steel shims placed during the PT stressing operations at the East end PT load cell (sensor name LC9) at Level 2 HBE at the south side of the HBE web, fell out at this displacement step. The reason for this is that the “U” shaped steel shims were inadvertently placed upside down during PT stressing, and as consequence fell out once the PT strands became fully relaxed. Upon observation, three shims were put back in place to fill the gap to the extent possible for the next displacement step (but not all shims could be put back in place). Similarly, for the same reason, after displacement step 10 (i.e., 3% drift), it was observed that the steel shims fell out at the same location but at the North side load cell (sensor name LC10). The effect of the loss of the steel shims is also reflected in figure 6-34 at displacement step 9 by the large

drop in initial PT force. At the end of test NZW, the frame was pushed laterally (in order to fully relax the PT strands at the closing joints) such as to reinstall all the shims that fell out during the test. However, as will be discussed subsequently, it appears that not all steel shims that fell out were replaced. Additionally, during this process, an additional 1/32" steel shim was added to the PT load cell locations at the West end of the Level 1 HBE as a measure to regain some of the PT force losses that occurred during the test.

The initial PT force and response history for frame NZB is shown in figures 6-36 and 6-37, respectively. As a first observation, there appears to be a discrepancy with the East end initial PT force at displacement step 1 with the previous NZW test. To clarify, it is observed that the initial PT force at the start of displacement step 1 for test NZB starts at approximately half the value of that at displacement step 8 shown in figure 6-34 for test NZW (which corresponds to the displacement step just prior to when it was first visually observed that the steel shims fell out). Although some differences would not be unexpected due to fluctuation in PT load cell readings between test setups, the difference between the two is significant; which suggests that all steel shims were not necessarily replaced in the previous NZW test, as initially thought. One other noticeable observation is that in comparison to the frame FRB response, there is more nonlinear behavior (due to friction). To clarify, recall that for frame FR, the HBE-to-VBE joints remain closed until the initial PT force is overcome. However, for frame NZ, the HBE-to-VBE joints immediately open (and close) due to the initial gap provided at the bottom ends of the HBE. As a result, more energy dissipation is provided through friction since the bolts at the HBE shear plate connections must slip earlier to accommodate joint rotation. As an aside, since it will affect the results of PT force losses between NZ tests made subsequently, it is noted that at the end of test NZB, additional steel shims were added at some load cell locations as a measure to recover some of PT force losses. Namely, one 1/32" steel shim was added at the South-side West and East ends of Level 2 PT load cells and two 1/32" steel shims added at the South-side East-end of Level 1 PT load cell (these locations correspond to sensors LC5, LC9 and LC4 respectively).

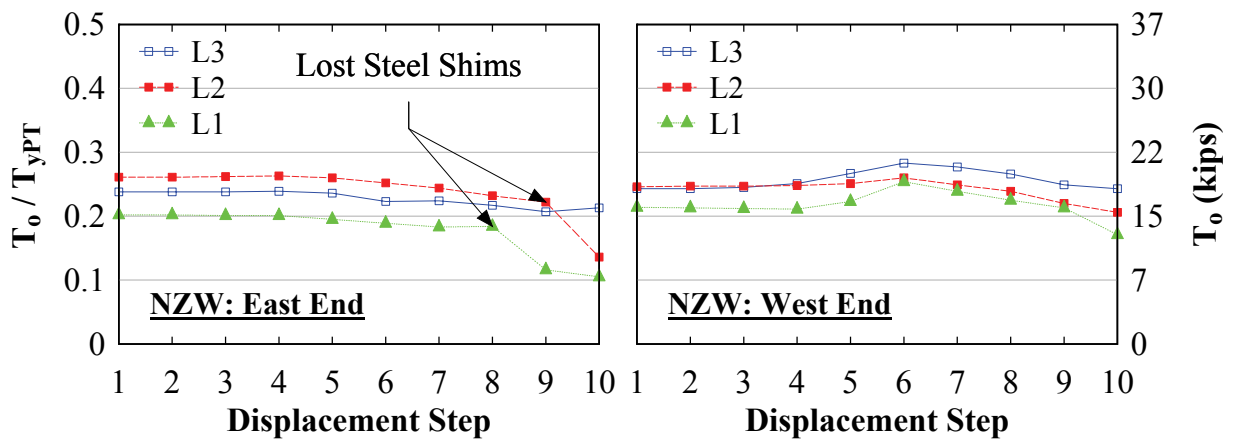


FIGURE 6-34 Frame NZW – initial PT forces

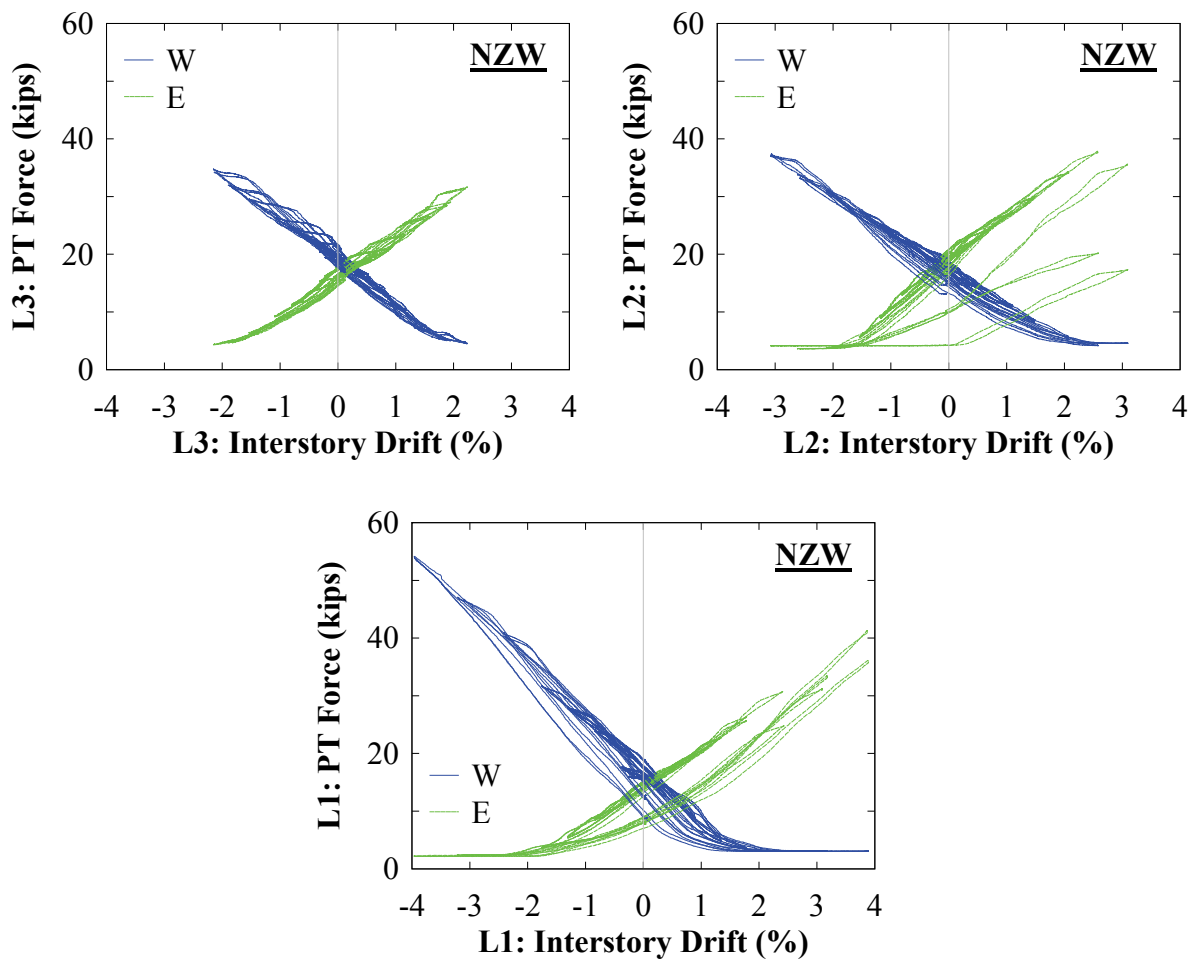


FIGURE 6-35 Frame NZW – PT response

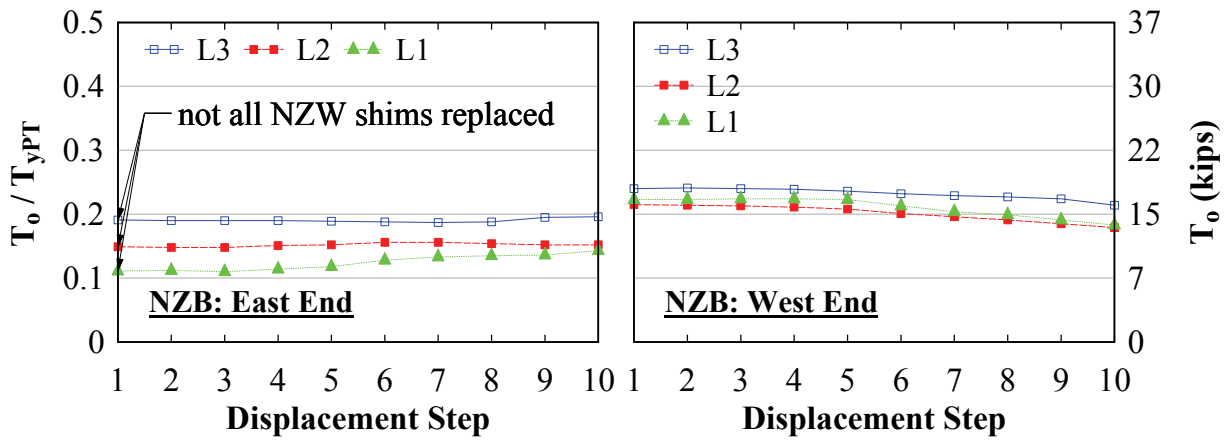


FIGURE 6-36 Frame NZB – initial PT forces

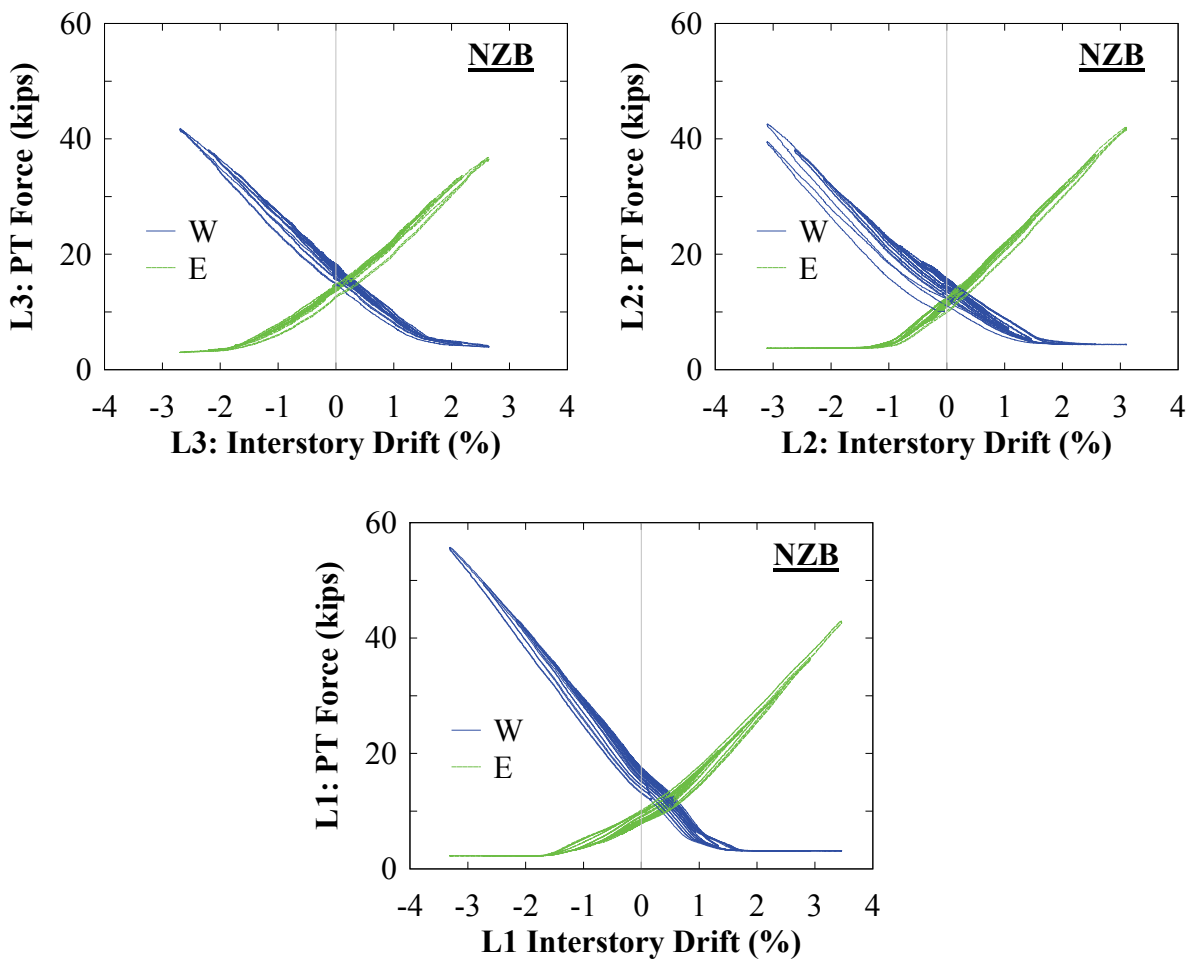


FIGURE 6-37 Frame NZB – PT response

The initial PT force and response history for frame NZS is shown in figures 6-38 and 6-39 respectively. The PT versus interstory drift response should be similar to frame NZB; since the infill strips behave as tension-only elements. However it is observed that there is a significant increase in nonlinear response with the NZS test results. This was due to PT yielding noted earlier. In figure 6-38, at displacement step 11 at the West end Level 1 PT, a rapid reduction in initial PT forces is observed with subsequent displacement steps. This is the point at which PT yielding first initiated (i.e., displacement step 11 which corresponds to 4% drift). In particular, at the end of test FRS, it was visually observed that PT yielding occurred in all PT elements at Level 1 HBE except for the HBE East-end-North-side PT location (sensor name LC3), and PT yielding occurred at Level 2 at both the East end PT elements (sensor name LC9 and LC10).

The normalized initial PT forces for each displacement step are shown in figure 6-40 for each of the NZ tests, which show the change in initial PT forces from the start of the test with more clarity. The observations made above related to the initial PT force at the start of each displacement step, also apply to the normalized results shown. Additionally, the comparison of the normalized initial PT forces between NZ tests is shown in figures 6-41a and 6-41b. Note that for comparison purposes, for frame NZW, displacement step 7 was used, corresponding to the condition prior to the displacement step during which the steel shims fell out. Additionally, for frame NZS, displacement step 10 was used, corresponding to the displacement step prior to the first observation of PT yielding. The average of the West and East end normalized values at each level is shown in figure 6-41c. From the average results, it is observed that cumulative PT force losses across the story heights were approximately 10% after test NZW; after test NZB, cumulative losses ranged between 20 to 50%, and after test NZS, they ranged between 5 to 25%. The results show a large initial PT force loss between test NZW and NZB at Level 2, which is counter intuitive. However, this appears to be because not all steel shims were replaced at the end of test NZW, as described earlier. Additionally, it is observed that some initial PT forces are recovered between tests NZB and NZS. This is due to the addition of steel shims at the end of test NZB, as noted above. In hindsight, the steel shims should not have been added in order to more accurately track changes in PT force loss effects.



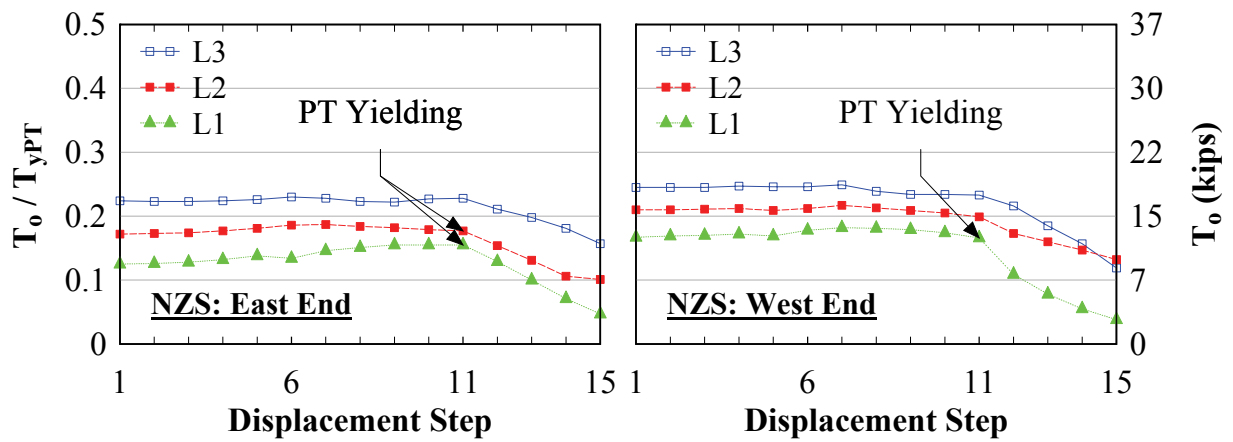


FIGURE 6-38 Frame NZS – initial PT forces

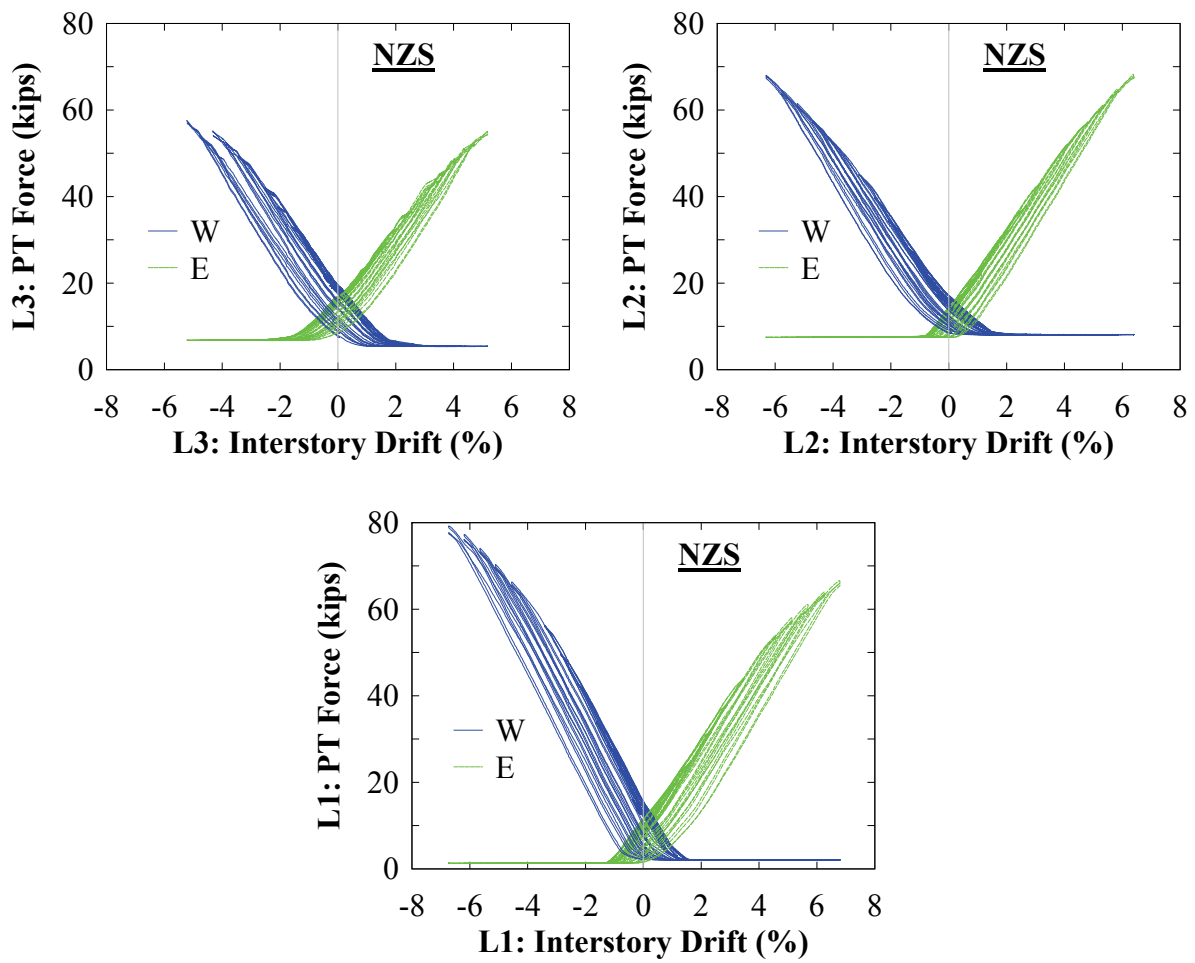


FIGURE 6-39 Frame NZS – PT response

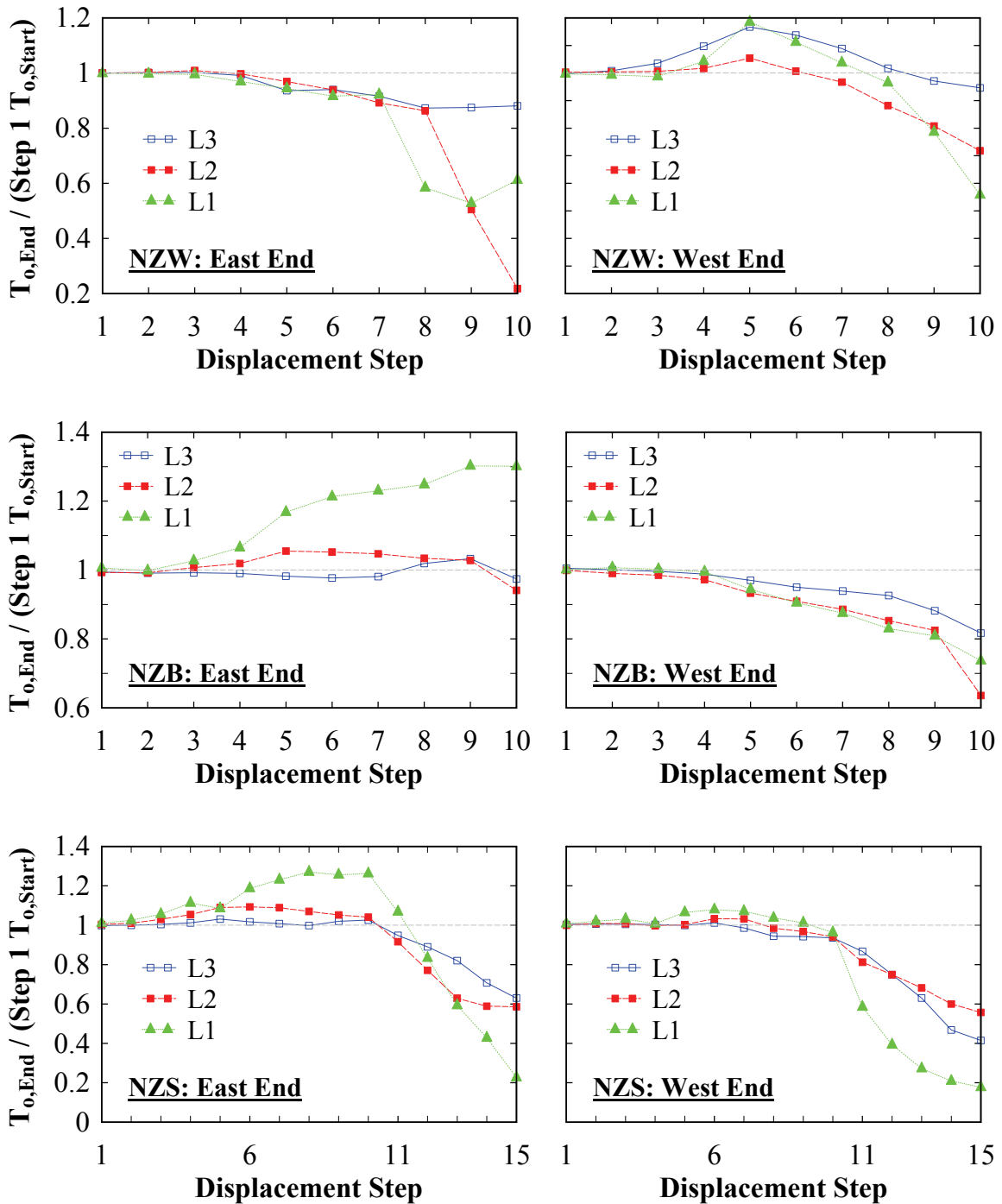
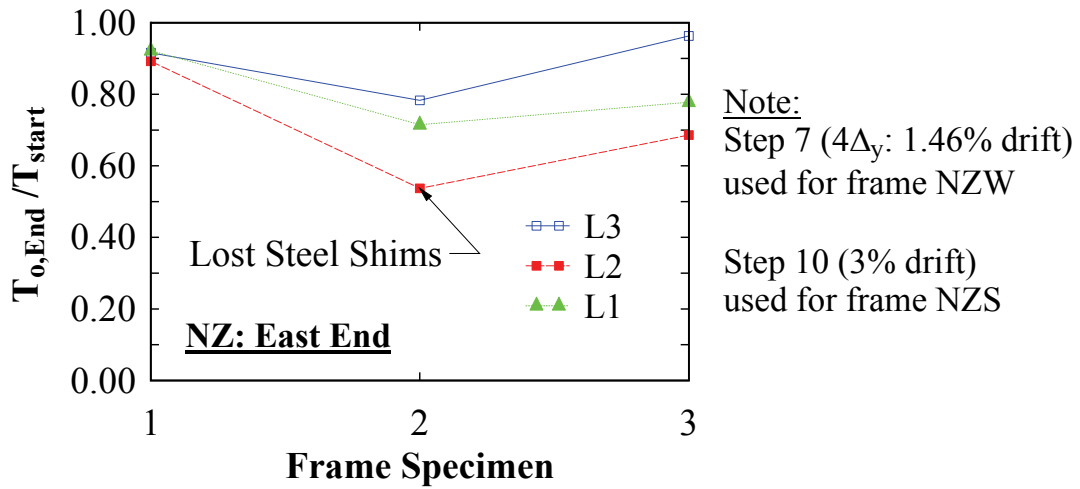
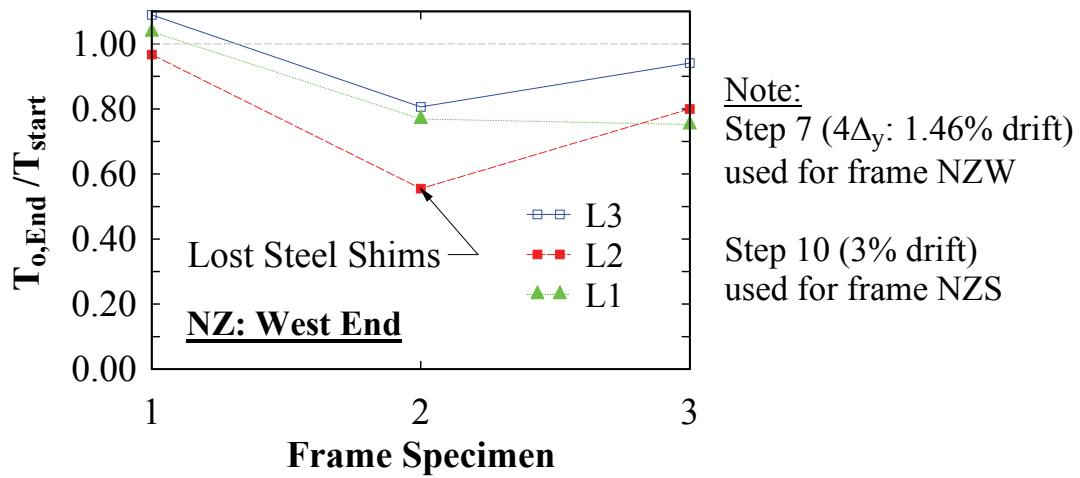


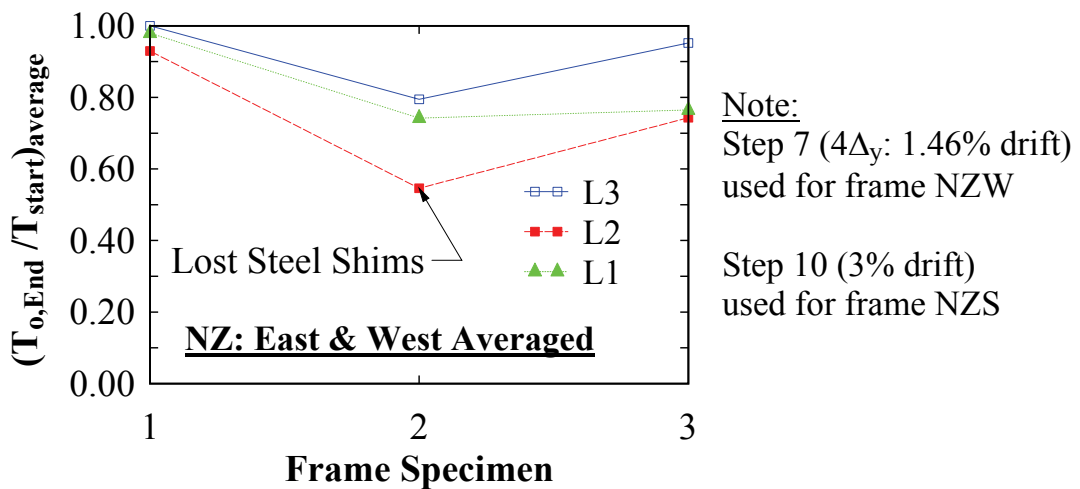
FIGURE 6-40 Frame NZ – initial PT forces normalized by displacement step 1



(a)



(b)



(c)

**FIGURE 6-41 Normalized initial PT force changes: (a) East end; (b) West end; (c) averaged**

### **6.4.3 NZ: Infill Plate and Strip Strain Gage Response**

The South elevation infill web plate and strip tensile strain response for selected displacement steps is shown in figures 6-42 and 6-43 respectively. Observations presented in Section 6.3.3 for frame FRW and FRS also apply to frame NZW and NZS. However one additional observation is that the strains near the corner locations for frame NZW are, in general, much larger than for frame NZS. The reason for this is not clear, but possibly the consequence of a localized effect at the corner locations with the infill web plate; this doesn't occur for the infill strips, as each individual strip yields more uniformly along the length of the strips. To understand this behavior, a finite element analysis of that local detail would need to be performed (this is not within the current scope of work and could be investigated in future research).

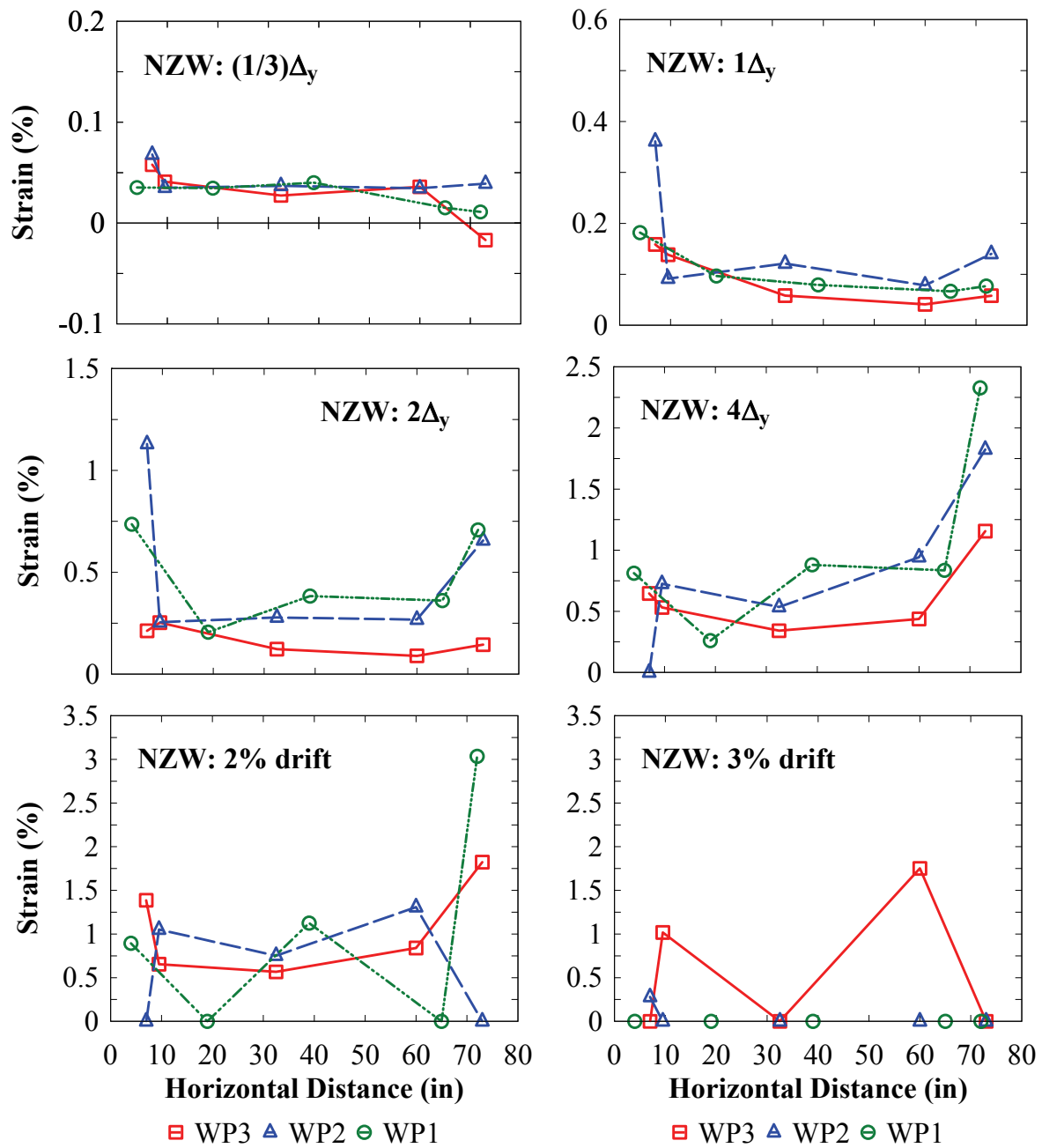


FIGURE 6-42 Frame NZW – infill web plate strains

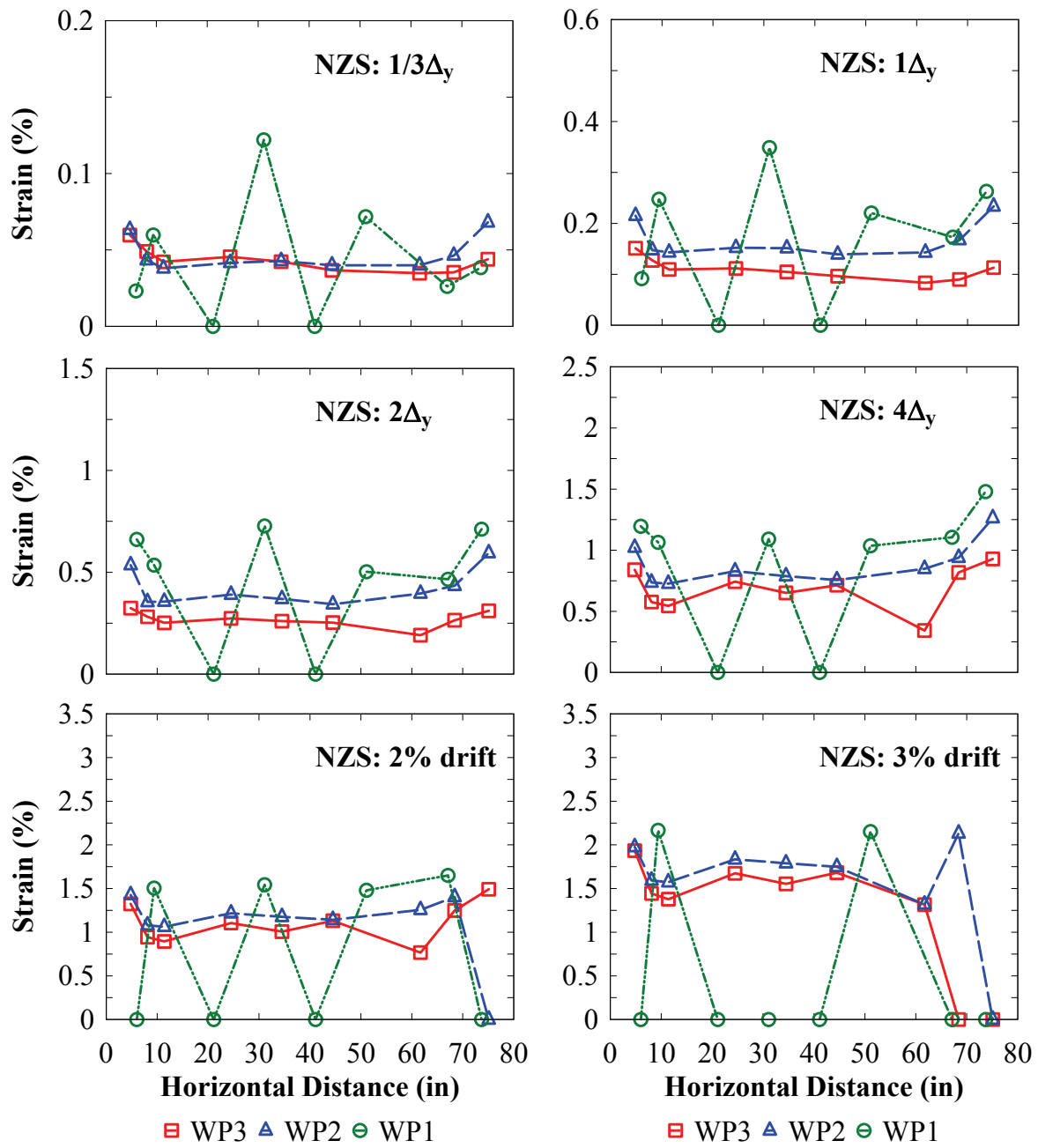


FIGURE 6-43 Frame NZS – infill web strip strains

#### 6.4.4 NZ: HBE Strain Gage Response

The HBE end strain versus gap rotation response is shown in figures 6-44 to 6-46 for frames NZW, NZB, and NZS, respectively. Note that the sign convention for positive joint rotation is for an increase in opening at the bottom flange gap at the East end of the HBEs and a corresponding closing of the gap at the bottom flange at the West end of the HBEs. Additionally, it is observed that at the zero gap rotation axis location, the strains in the top flanges are positive indicating that the flanges are in tension, which is incorrect (since the top flanges are initially in compression at the start of the test from the PT forces provided). This indicates that there is a vertical offset error with the strain gage readings at the top flanges, and the subsequent information is presented with that understanding.

From the strain response shown, it is observed that the strains at the bottom flanges are essentially zero for the reason that they are never in contact with the VBE flanges (for reasons mentioned earlier for frame FRS). At the top flanges, a nonlinear response is observed which is due to the effects of the infill web plate and strips. That is without the presence of the infill web plate and strips, the strain response is essentially nonlinear elastic by observation of results shown for frame NZB in figure 6-45. In particular, the HBE-to-VBE gap rotation is not directly proportional to the interstory drift due to the restraining effects of the infill web plate and strips.

Furthermore, by observation of the strain response for frame NZB shown in figure 6-45 (frame NZW and NZS are similar), in the positive drift direction (negative direction similar but mirrored response), it is observed that from the response curve shown in the figure, that at the East end of the HBEs, corresponding to the opening joint locations (for a positive drift condition considered here), the compression in the top flange increases; this is largely due to an increase in PT forces as a result of an increase in the HBE-to-VBE gap rotation at these joint locations (since there is no infill web plate present). Correspondingly, at the HBE West end, corresponding to the closing joint locations, a reduction in compression strain is observed; this is due to decrease in PT forces as a result of a reduction in the HBE-to-VBE gap rotation at these joint locations. It is observed that at the closing joint locations (West end of HBEs), the response curve is bilinear. The first stiffness corresponds to the condition when the PT elements are in tension, and the second stiffness occurs when the PT elements are fully relaxed. It is observed that the curve

segment with the second stiffness is at or near horizontal, indicating that the HBE flange is just in contact with the VBE flange, and no significant contact compression forces are present. If the HBE and VBE flanges were to separate at the rocking contact point, the second branch would be exactly horizontal. It is observed that at Level 1, the second branch has a slight negative slope, indicating presence of contact forces between the HBE and VBE flanges. However, at Levels 2 and 3 it is not as clear and it appears to be horizontal, indicating the possibility that flange separation has occurred. Furthermore, as noted earlier, there is a vertical offset error with the strain gage data. This offset error is approximately the tension strain value corresponding to the near horizontal segment of the strain gage data; since this represents the point at which the HBE and VBE flanges are just in contact or have separated. This phenomenon will be addressed in further detail in Section 9, where the experimental results regarding this observation is not as ambiguous.

Similar to what was observed with frame FRS, at the opening joint locations, the compression strains increase and then decrease with further joint rotation (i.e., the dipping effect). This is more apparent for frame NZS in the negative drift direction. Also note that this effect is not dominant in frames NZW and NZB, but not entirely unexpected as these tests were only conducted up to 3% drift. By comparison, frame NZS was taken up to 6% drift, and these effects are more pronounced due to larger joint rotations. One additional difference compared with frame FRS, there is also a similar dipping effect at the closing joint location (most noticeable at the Level 2 West-end top flange location), but interestingly the resultant contact force here is oriented in the opposite direction (i.e., not downward into the HBE web, but upwards away from the HBE web), which at large rotations also appears to have the effect of inducing localized tension stresses on the top flange at the HBE-to-VBE contact point. However, it is also understood that at the HBE end locations, there are also localized strain effects from the HBE shear plate reactions that may also contribute to the nonlinear response observed.



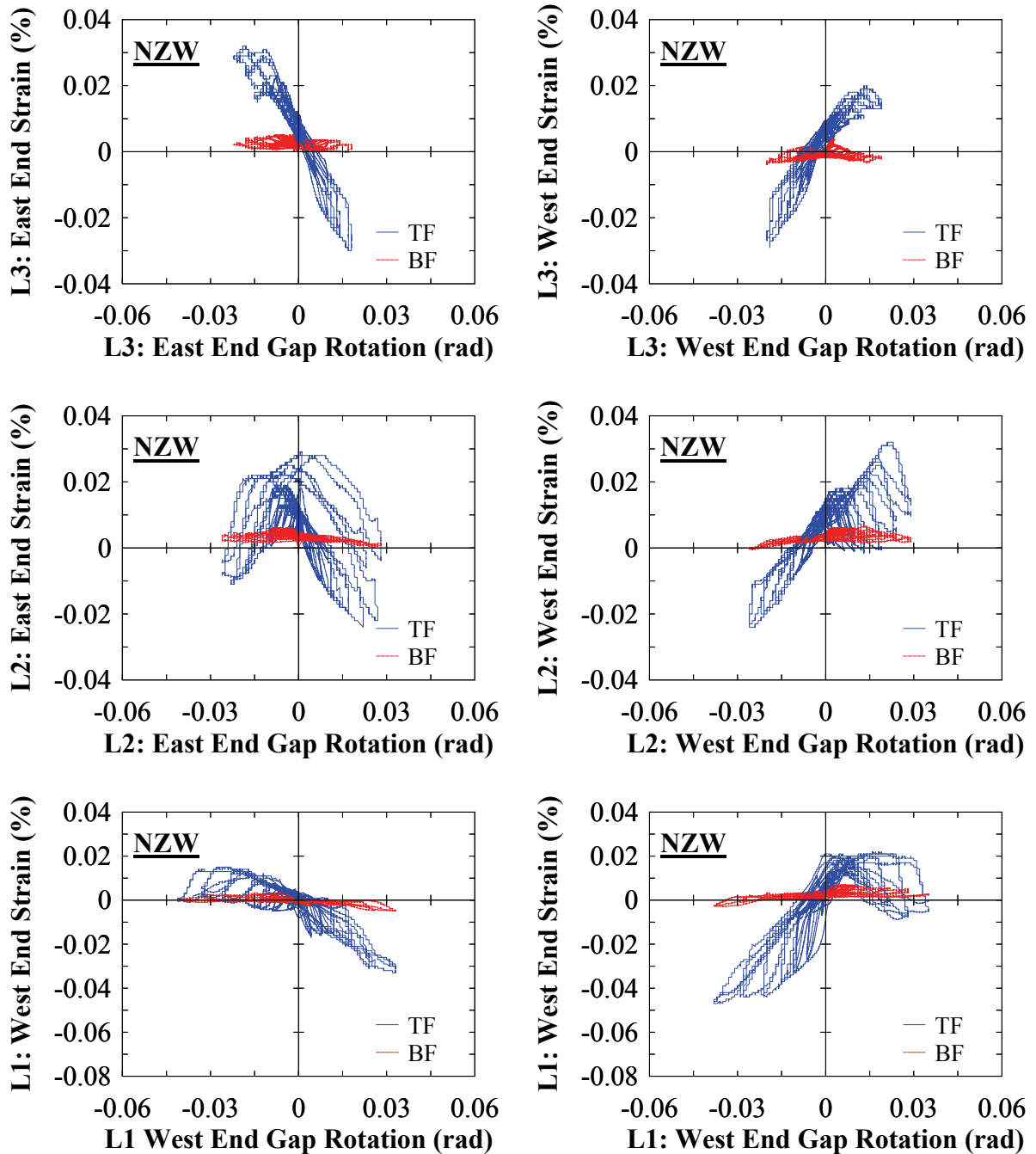
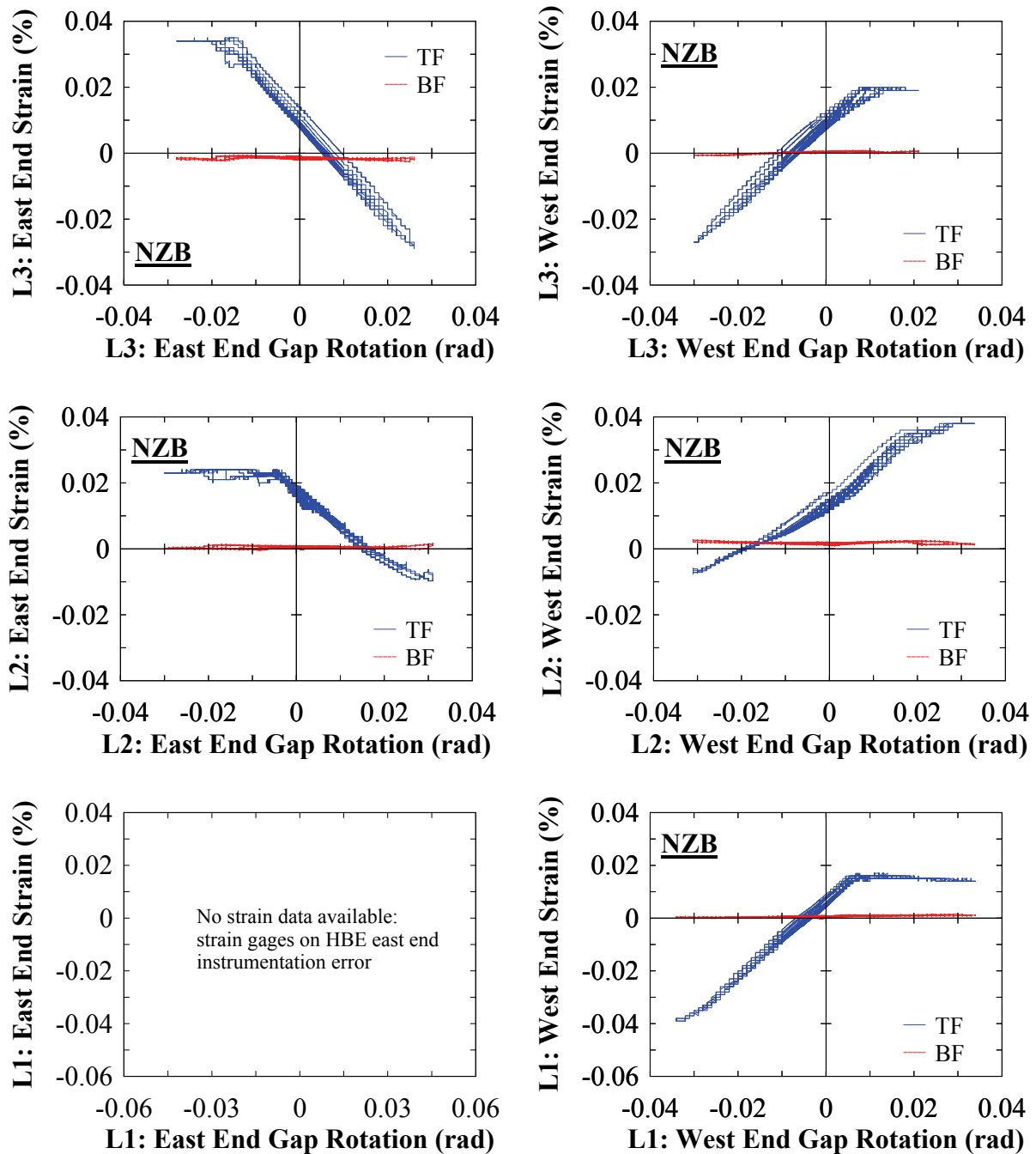


FIGURE 6-44 Frame NZW – HBE end strain versus gap rotation



**FIGURE 6-45 Frame NZB – HBE end strain versus gap rotation**

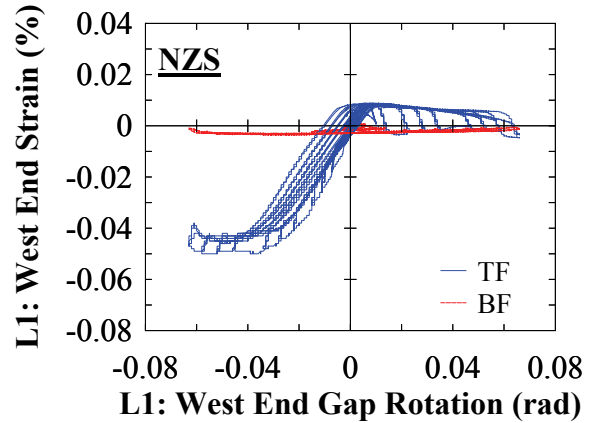
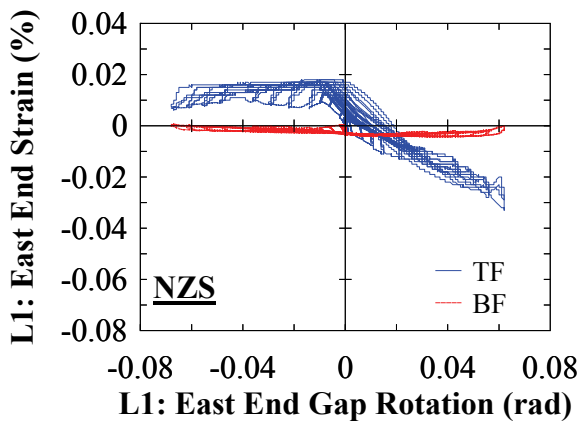
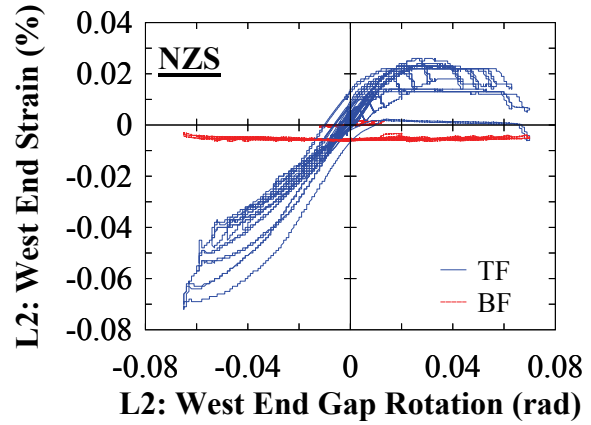
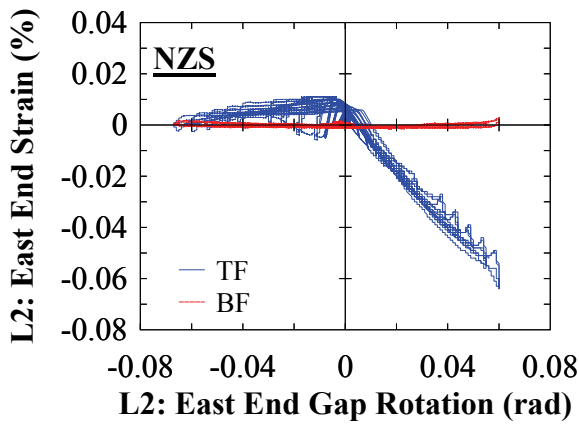
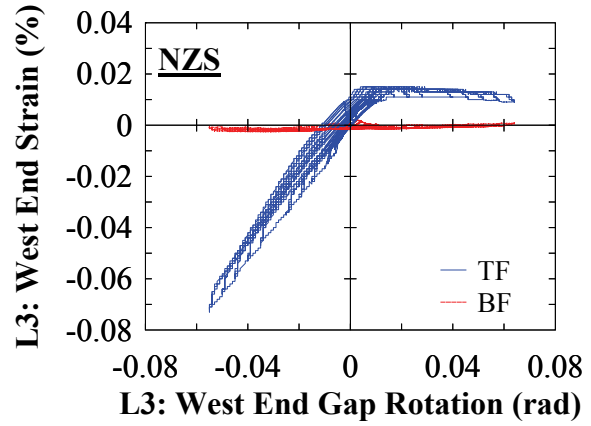
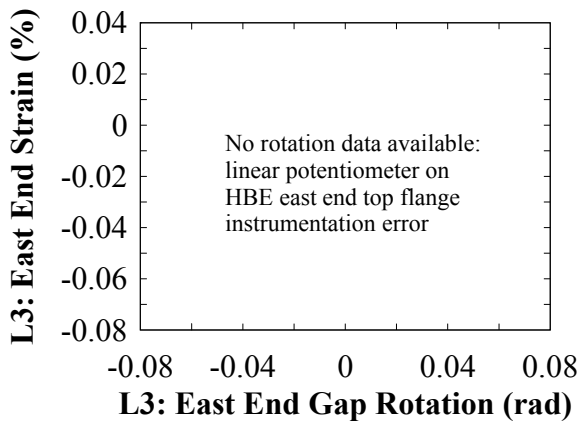


FIGURE 6-46 Frame NZS – HBE end strain versus gap rotation

#### 6.4.5 NZ: HBE Axial and Moment Demands

The axial force and moment demand for frame NZS at selected displacement steps is shown in figure 6-47 for a positive drift condition (i.e., rightward direction on figure). The formatting and nomenclature is similar to that presented for frame FRS in Section 6.3.5. Furthermore, shown in the plots are vertical dashed reference lines that mark the approximate location of the PT anchors on the HBEs. Additionally, the resulting axial and moment values presented also include the strain gage offset error noted above.

Similar observations made earlier for frame FRS also are applicable for frame NZS. Additionally, the effect of the PT anchored on the HBE is observed by the vertical step in the axial force values between the PT anchors. In particular at displacement step  $2/3\Delta_y$ , no significant discontinuity of axial forces is observed since PT elements at each ends of the HBE are still both in tension. In contrast, as observed at 2% and 4% drift, the PT at the closing joint is fully relaxed and the PT at the opening joint has increased. One notable exception is at Level 1 at the far left end, where the axial force should be the largest. Contrary to the axial forces, the effects of the PT on the HBE moments are not as clear. A comparison of analytical versus experimental is presented in Section 6.7.

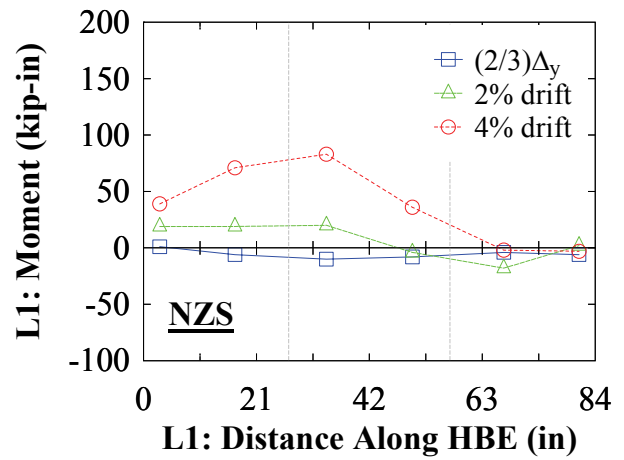
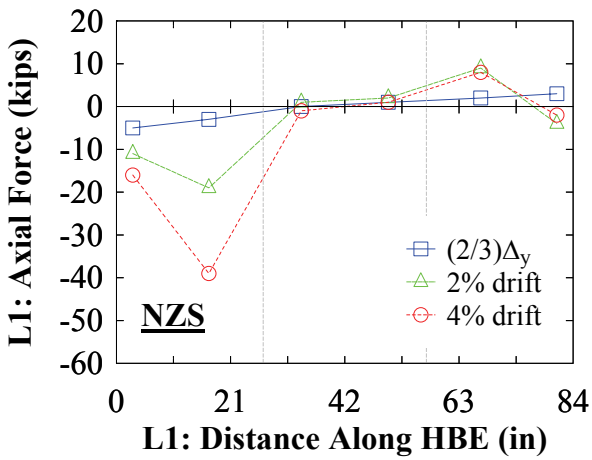
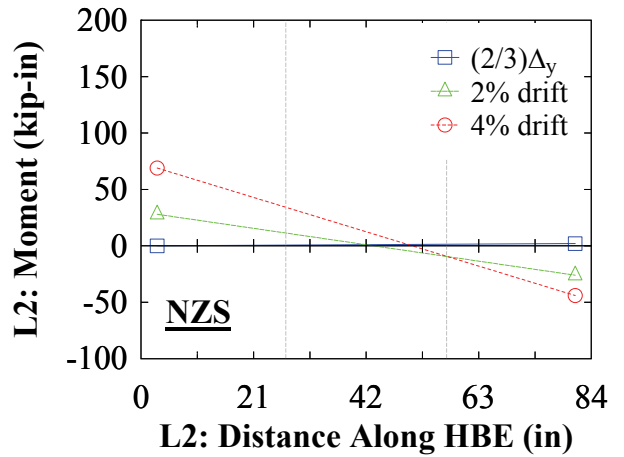
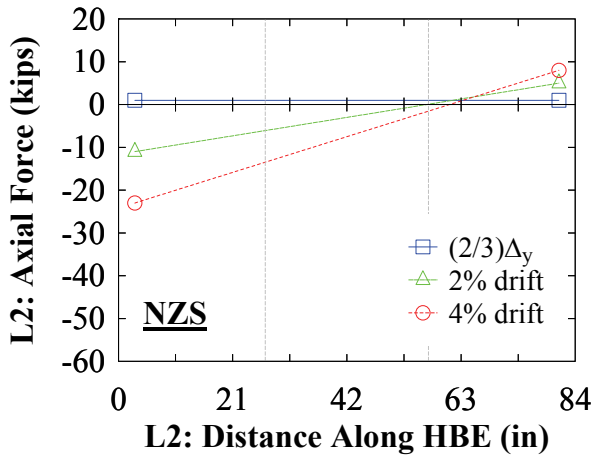
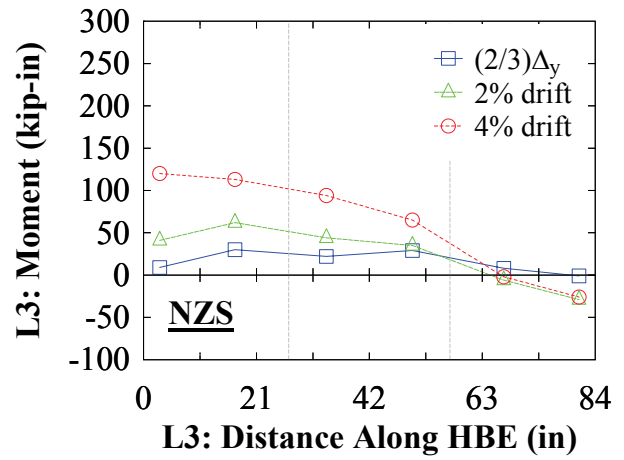
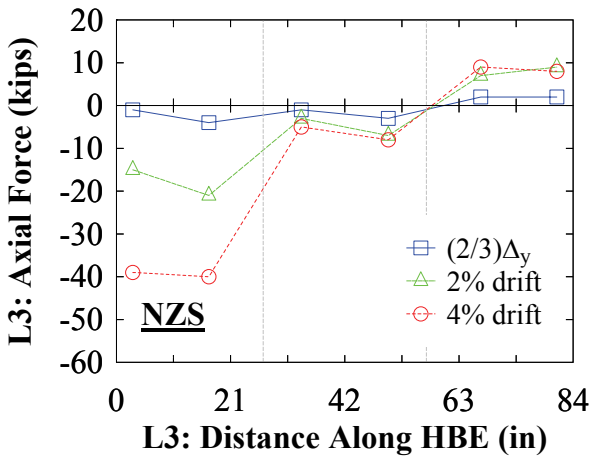


FIGURE 6-47 Frame NZS – HBE axial force and moments

## **6.5 Centerline Rocking (CR) Frame Experimental Results**

Many of the general observations and explanations provided for the FR and NZ frames also apply to the CR frames. Although some overlap in observations may be presented, these observations will be provided concisely without detailed explanation. Any response that is unique to the CR frames or observation that provides additional clarity to the FR and NZ frame results will be presented in detail.

### **6.5.1 CR: Global Response**

The global response in terms of base shear versus roof drift, and the story shear versus interstory drift are shown in figures 6-48 and 6-49 respectively for the CR frames. The general response is similar to frame NZ and previous observations made are also applicable; any significant differences are due to the individual characteristics of each PT boundary frame (which was presented in Section 4). A comparison of response for frames NZ and CR is made in Section 6.6.

However, one notable difference that deserves clarification is the one related to the comparison of the residual base shear ratios with frame NZ (note that direct comparison to frame FR is not relevant due to the actuator interaction observed for that frame). Recall that for perfect recentering, this ratio would be zero. For frame NZW and NZS, the approximate average ratio value is 5.5% and 1.3%, respectively, as shown earlier. For frame CRW and CRS, the approximate average value is 7% and 6.8%, respectively. In comparison, the ratio for CRW is consistent to that observed with frame NZW, in that there is a residual base shear force due to the compression-strut effect of the infill web plate. On the contrary, the ratio for CRS indicates that there is also a compression strength of the infill web strips for frame CRS. However, by visual inspection of the hysteretic response, it clear that the infill web strips behave as tension-only elements and recentering is essentially achieved.

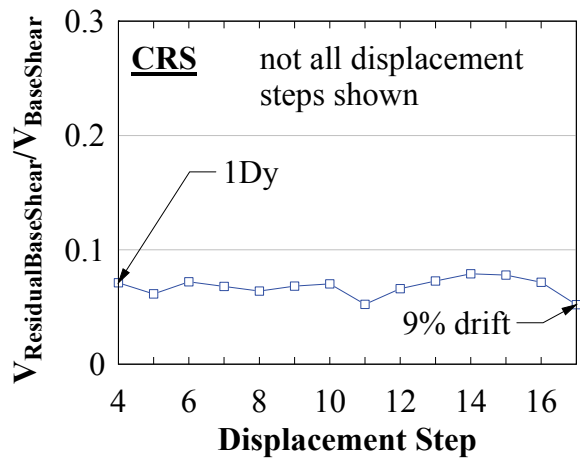
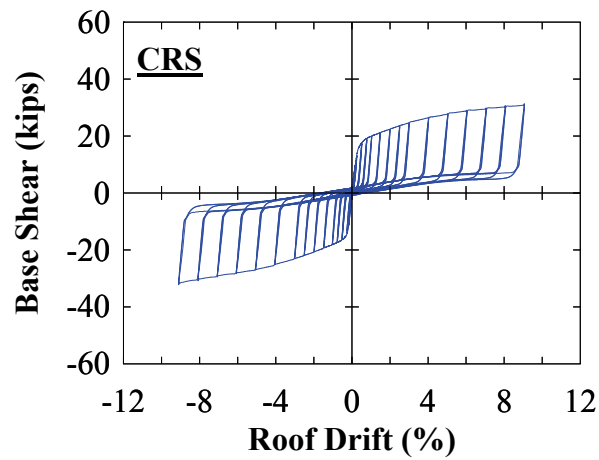
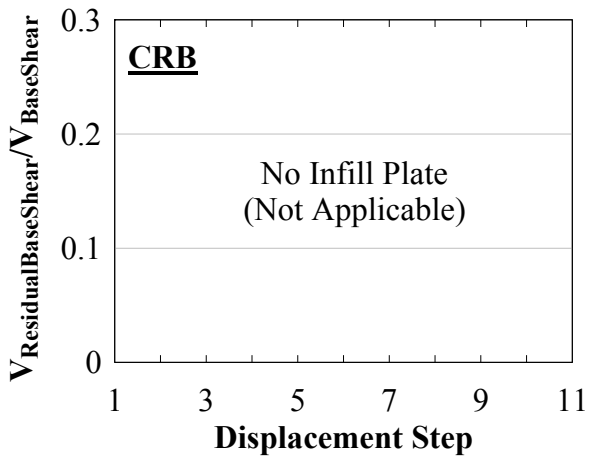
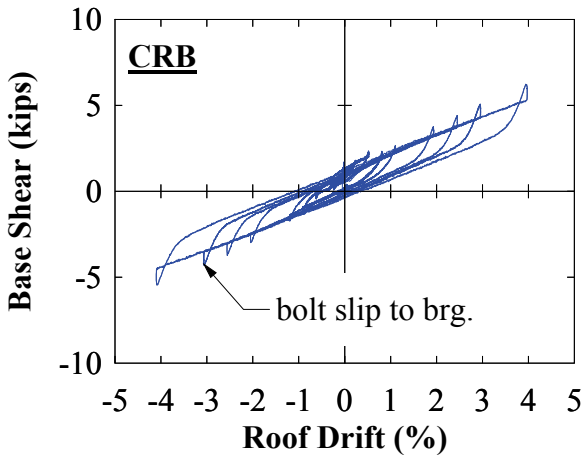
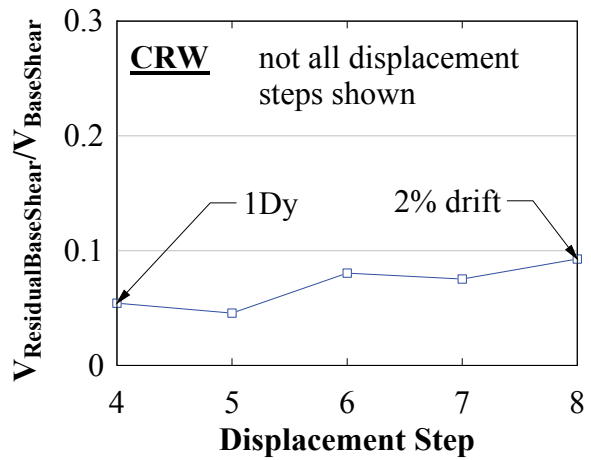
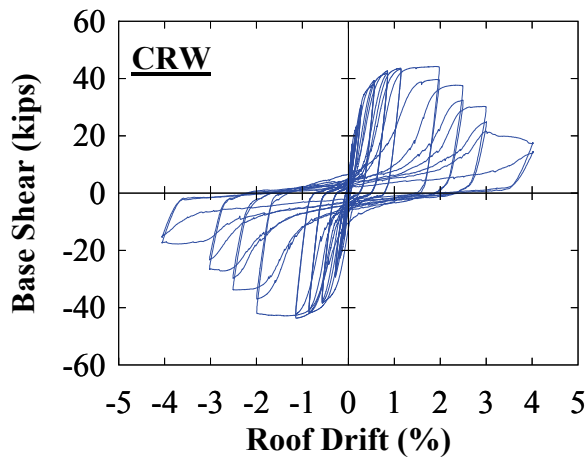


FIGURE 6-48 Frame CR – global response

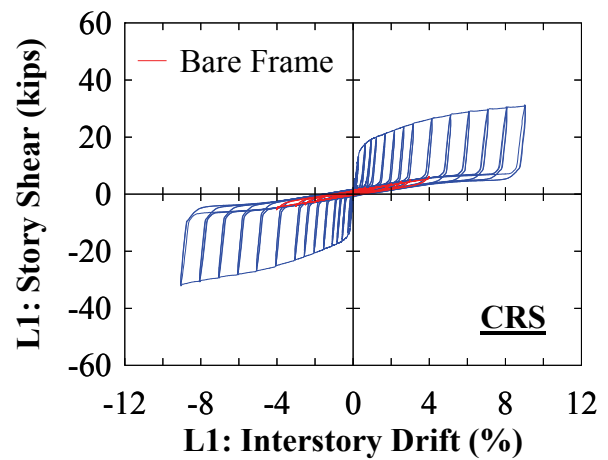
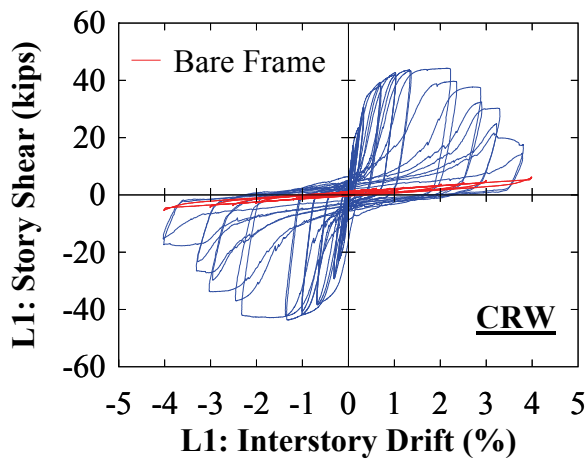
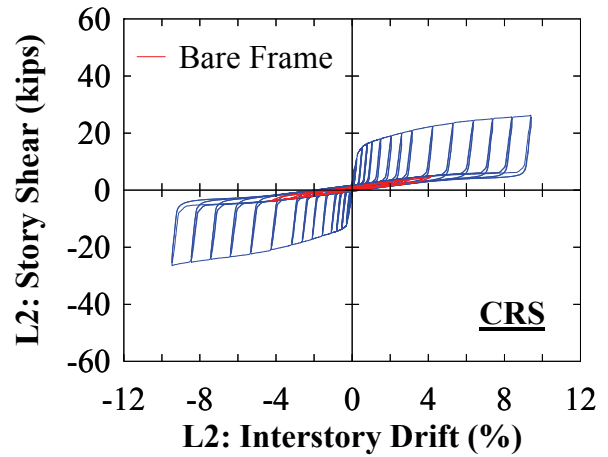
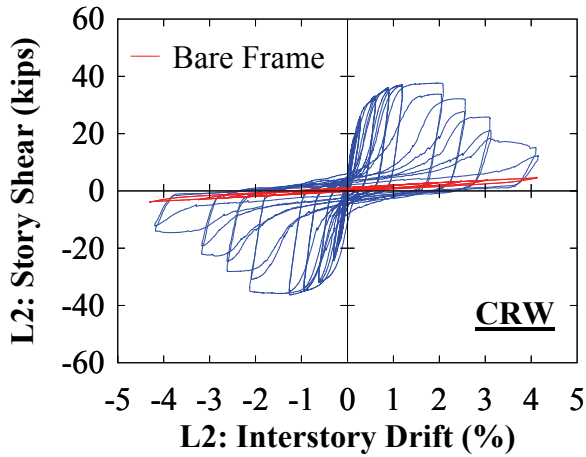
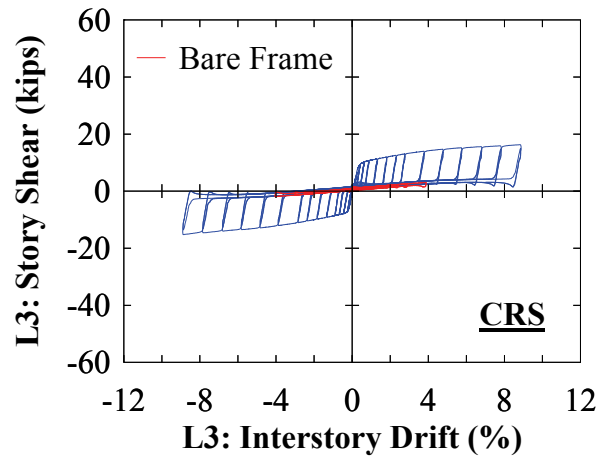
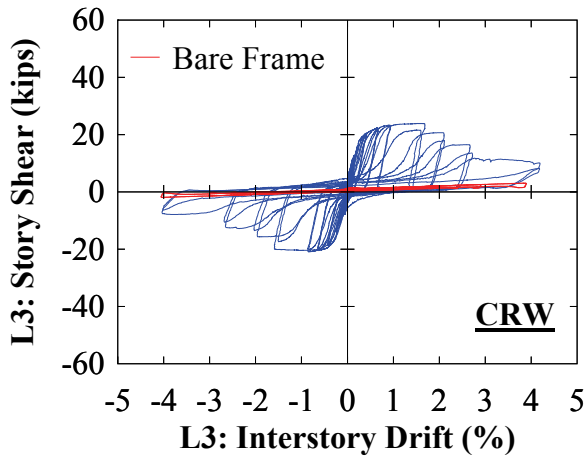


FIGURE 6-49 Frame CR – interstory response



To provide an explanation, at the end of test CRB, after the actuator connections to the GMF were removed (allowing the frame to return to its natural equilibrium), a noticeable Eastward lean of the frame was observed (which was not apparent for the FR and NZ frames). It is also noted that test CRB was conducted the day after test CRW without any changes to the test setup (only the infill web plate was removed). Thus, the cumulative PT force losses of test CRW and CRB appeared to have created an unbalance of initial PT forces that produced a noticeable residual base shear, at the zero-drift location. In particular, because the HBE-to-VBE joints are true pin connections, the CR frame is more sensitive to unbalanced residual PT force effects than frames FR and NZ. Additionally, frame CR has PT elements above and below the shear pins at each ends of the HBEs. Consequently, effects include not only unbalanced PT force effects at each ends of the HBEs, but also unbalanced PT force effects of PT elements located above and below the HBE shear pins, further compounding the effect.

To further clarify, figure 6-50 shows the residual base shear for test CRB. It is observed that there is an increasing trend in residual base shear. Between the breakdown of test CRB and the test setup for frame CRS, no changes to the PT boundary frame were made. Thus, the last residual base shear value in the CRB test represents an initial residual base shear at the start of test CRS (since the test started in the zero-drift location). Accordingly, the original residual base shear ratios presented for CRS are misleading since it includes the effects of an unbalance of PT force at the zero-drift location. A more accurate representation of the residual base shear for frame CRS is shown in figure 6-51, where the residual base shear from the unbalance of PT forces at the end of test CRB has been removed, and results are comparable to that observed with frame NZS.

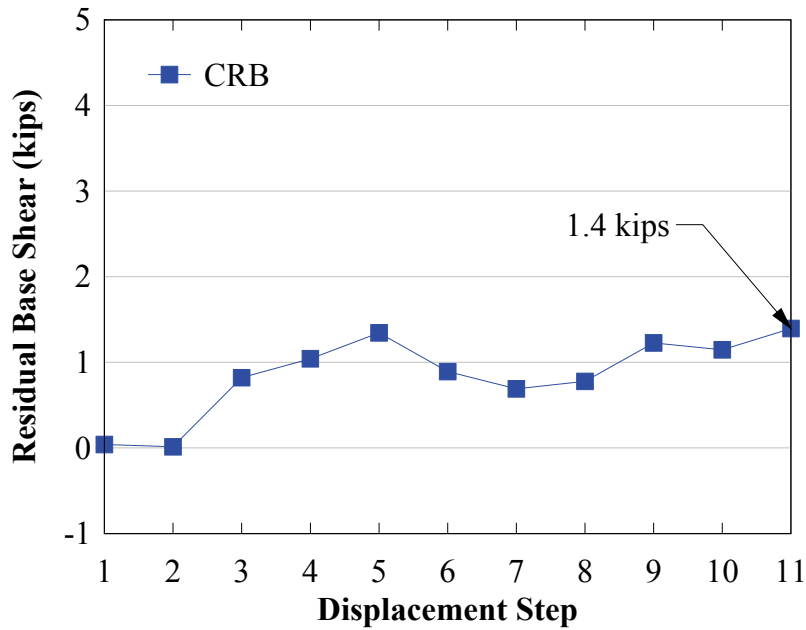


FIGURE 6-50 Frame CRB – residual base shear force

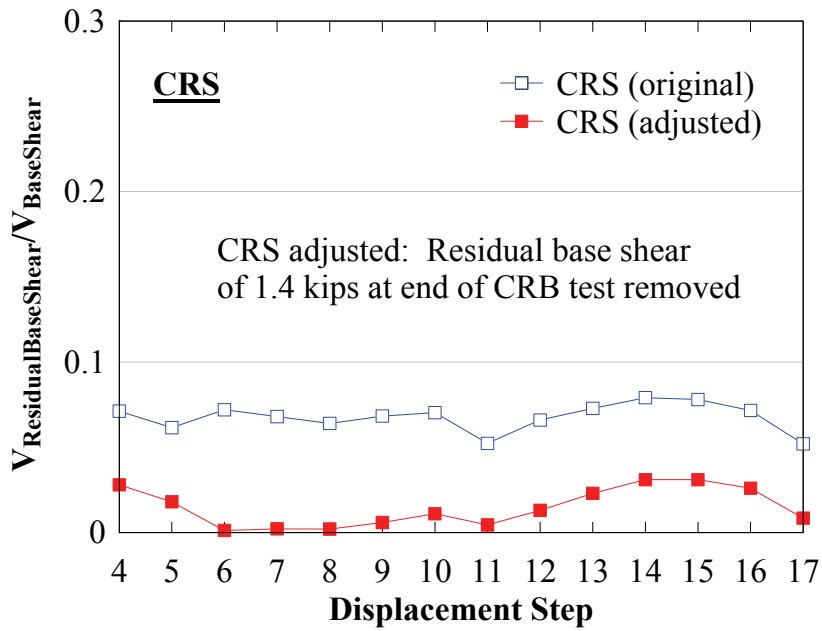


FIGURE 6-51 Frame CRB – residual base shear force adjusted

### 6.5.2 CR: Boundary Frame Post-Tension Response

The target initial PT force for frame CR was approximately 30% of the PT yield strength. The achieved initial PT force and subsequent changes at the start of each displacement step is shown in figure 6-52 for frame CRW. Additionally, the corresponding initial PT force at the end of each displacement step, normalized by the initial PT force at the start of displacement step 1, is shown in figure 6-53. It is observed the CR frame appears to be more sensitive to PT redistribution behavior than frames FR and NZ, as the relative changes are more erratic (for reasons presented above). Additionally, initial PT force values increase for subsequent displacement steps, which is consistent with the presence of a residual base shear due to an unbalance of initial PT force at the zero-drift location (i.e., PT forces are not at an “at rest” condition at the end of the displacement step). Furthermore, the corresponding global PT force versus interstory drift response is shown in figure 6-54. Individual PT elements have a similar response to PT elements as frame NZ. It is observed that none of the PT elements reached a state of full relaxation. In comparison to frame NZW, for frame CRW, the distance to the rocking point is much smaller and a larger initial PT force was provided, delaying this effect.

Given that some non-negligible unbalance of PT forces are present at the start of test CRS, it would be reasonable to expect that an initial frame lean should have been observed during the test setup (for reasons presented above). However, recall that during PT stressing, the frame was “locked” into position by PT stressing aid plates at the HBE-to-VBE joints (figure 5-9) and by temporary construction aid angles at the base of the VBEs to the HBE anchor beam (figures 5-11 and 5-12). After PT stressing was performed, the PT stressing aid plates were removed but the construction aid angles were kept in place preventing rotation of the VBE columns. Incidentally, at the end of test CRB, when the residual lean was observed after removal of the actuator connections, the frame was put back into vertical-in-plane plumb by pushing at the top of the frame with the Level 3 actuator. Once the frame was plumb, the construction aid angle connections at the base of the VBEs were made, preventing rotation of the VBEs. The test setup was then taken down for preparation of frame CRS.

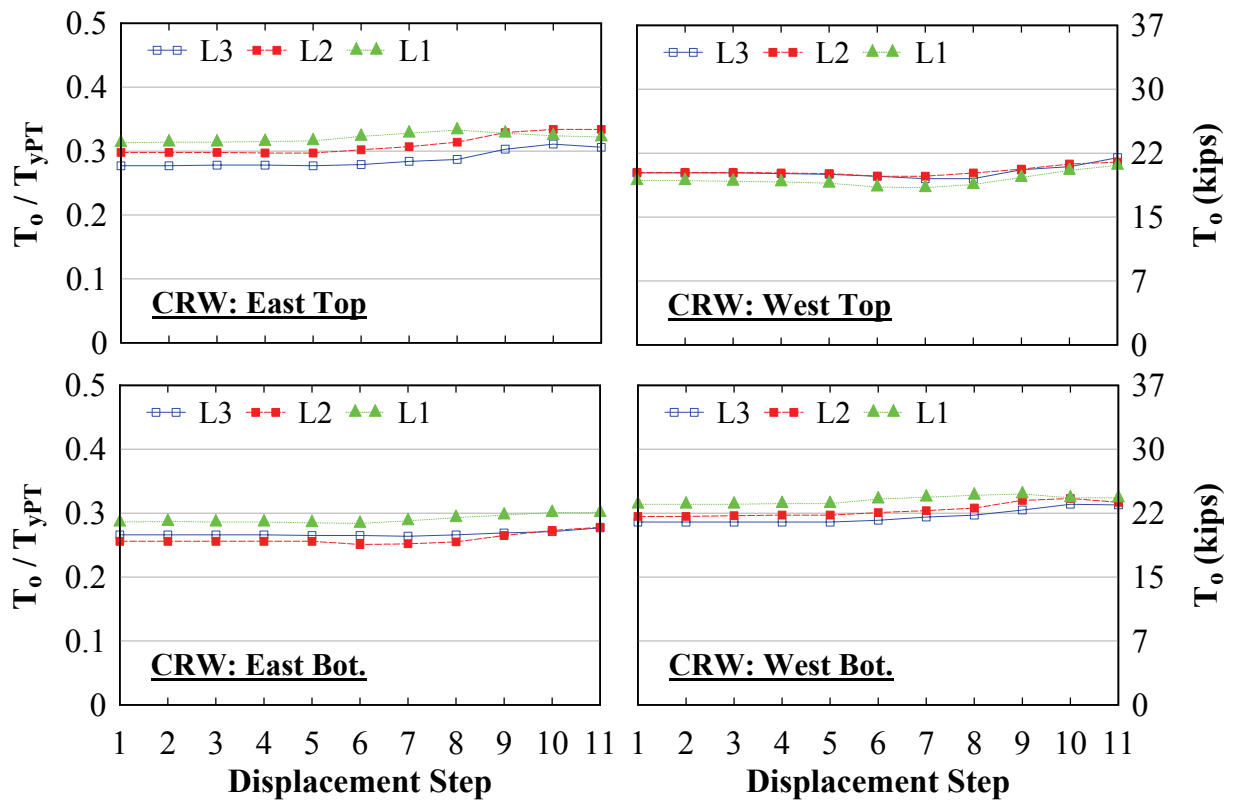


FIGURE 6-52 Frame CRW – initial PT forces

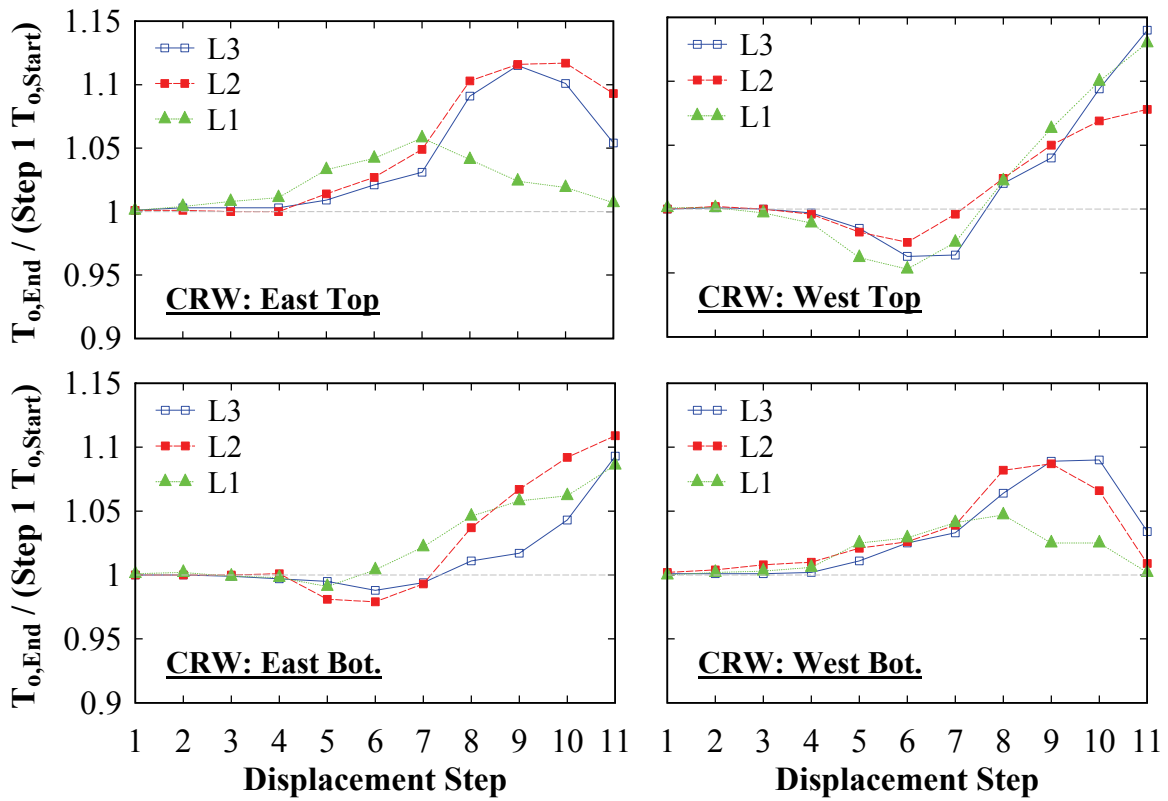
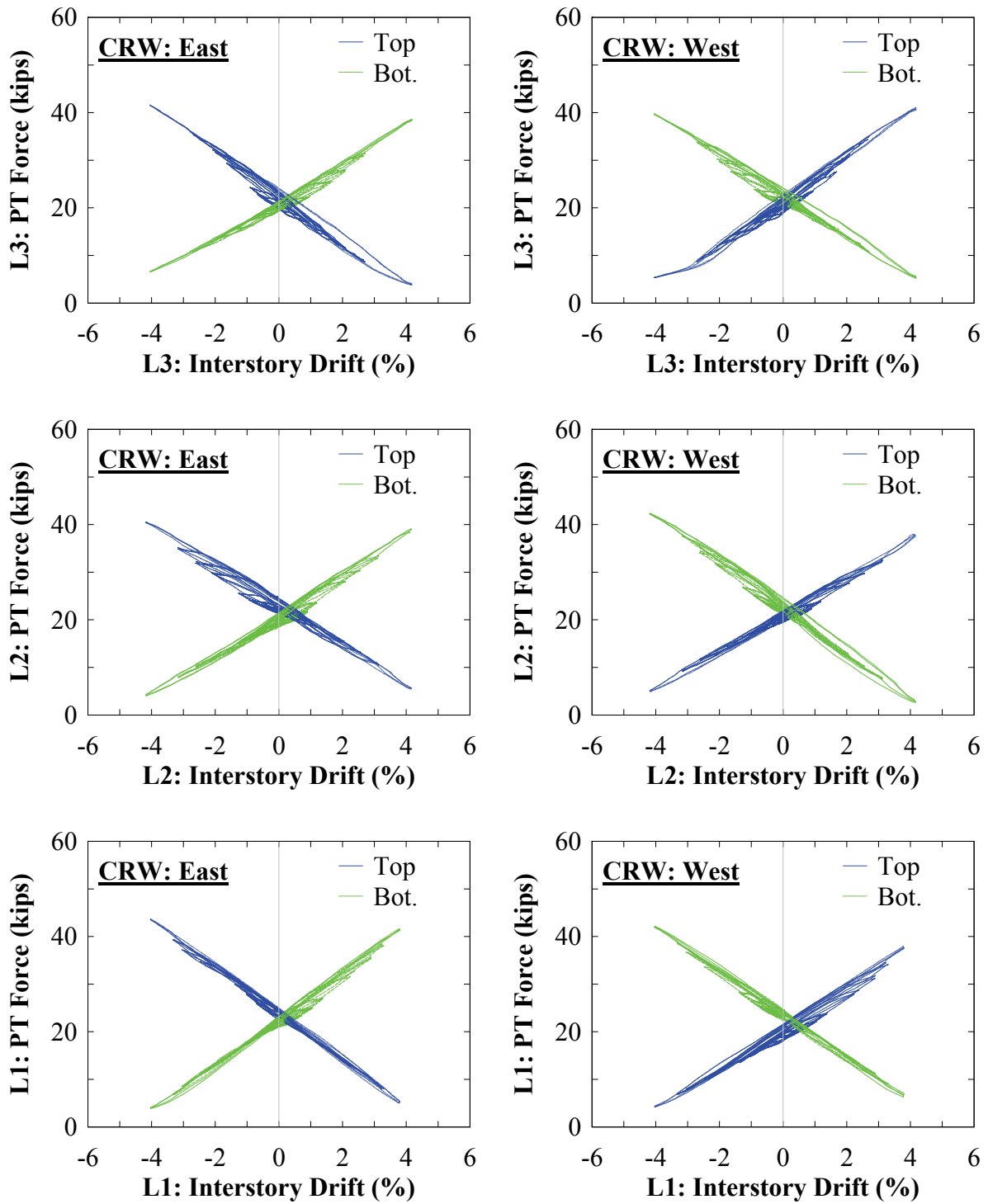


FIGURE 6-53 Frame CRW – initial PT forces normalized by displacement step 1



**FIGURE 6-54 Frame CRW – PT response**

The initial PT force, the corresponding initial PT force at the end of each displacement step normalized by the initial PT force at the start of displacement step 1, and the PT force versus interstory drift response for frame CRB, are shown in figures 6-55 to 6-57, respectively. For frame CRS, the corresponding response are shown in figures 6-58 to 6-60. The general observations made previously for the FR, NZ, and CRW frames also apply here. Additionally for frame CRS, it is observed that at approximately 5% interstory drift, full PT relaxation occurred at the closing joints. Furthermore, at the end of test CRS, PT force losses are observed up to approximately 40% at some locations; PT force losses for tests CRW and CRB were not significant in comparison. Additionally, cumulative PT force losses from start to end of the CR tests is shown in figure 6-61; these are within 10% of those for test CRW and CRB, where it is also observed that, at some locations, increases in initial PT forces occurred with these tests (due to redistribution of PT forces for reasons noted earlier). For test CRS, the initial PT force losses dropped significantly, down by nearly 50% at some locations. However, the large PT force losses observed are not entirely unexpected as test CRS went up to 9% drift (where earlier CR tests only went up to 4% drift).

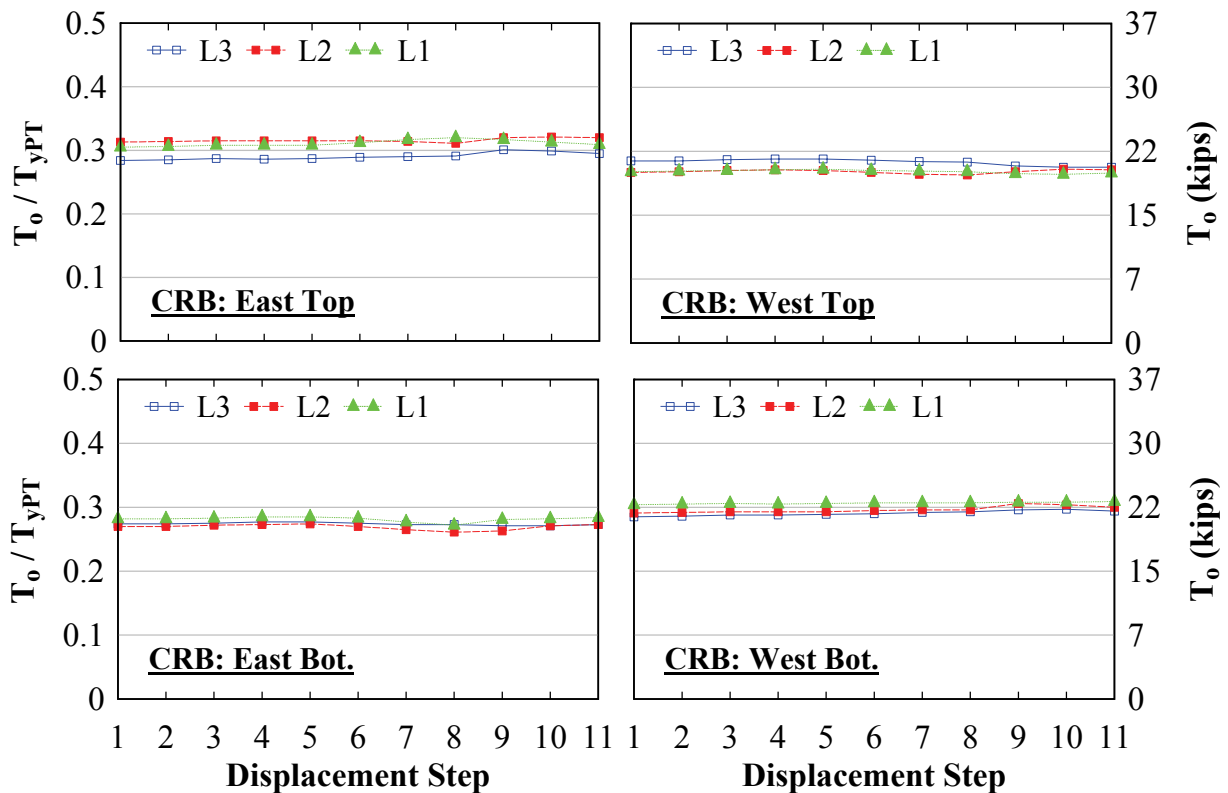


FIGURE 6-55 Frame CRB – initial PT forces

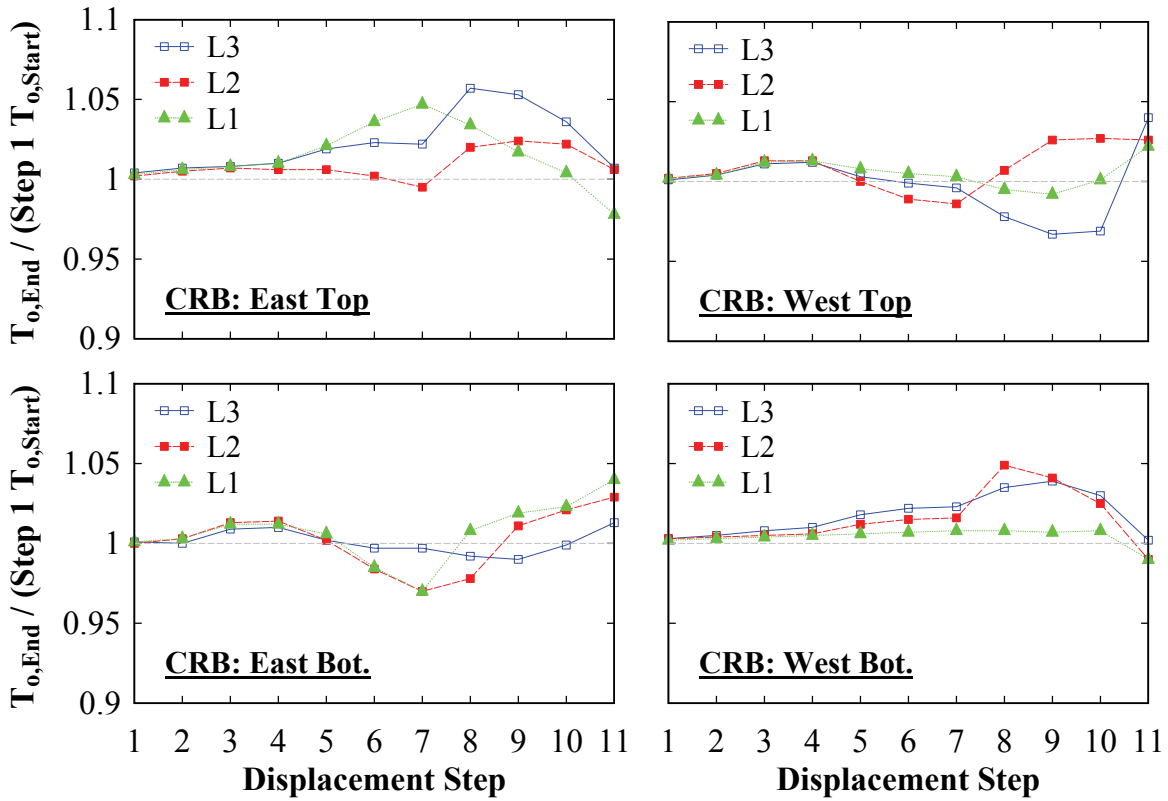
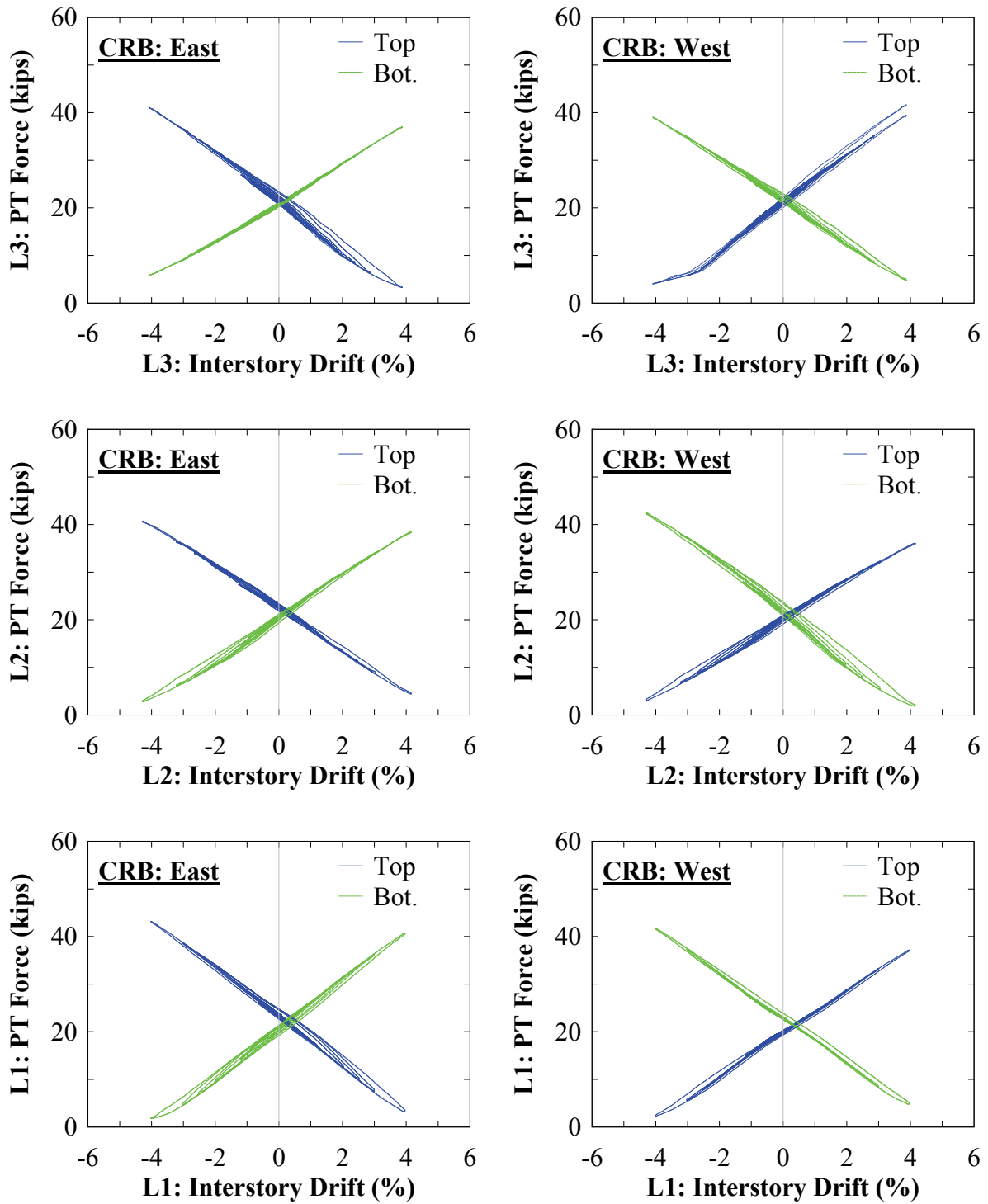


FIGURE 6-56 Frame CRB – initial PT forces normalized by displacement step 1





**FIGURE 6-57 Frame CRB – PT response**

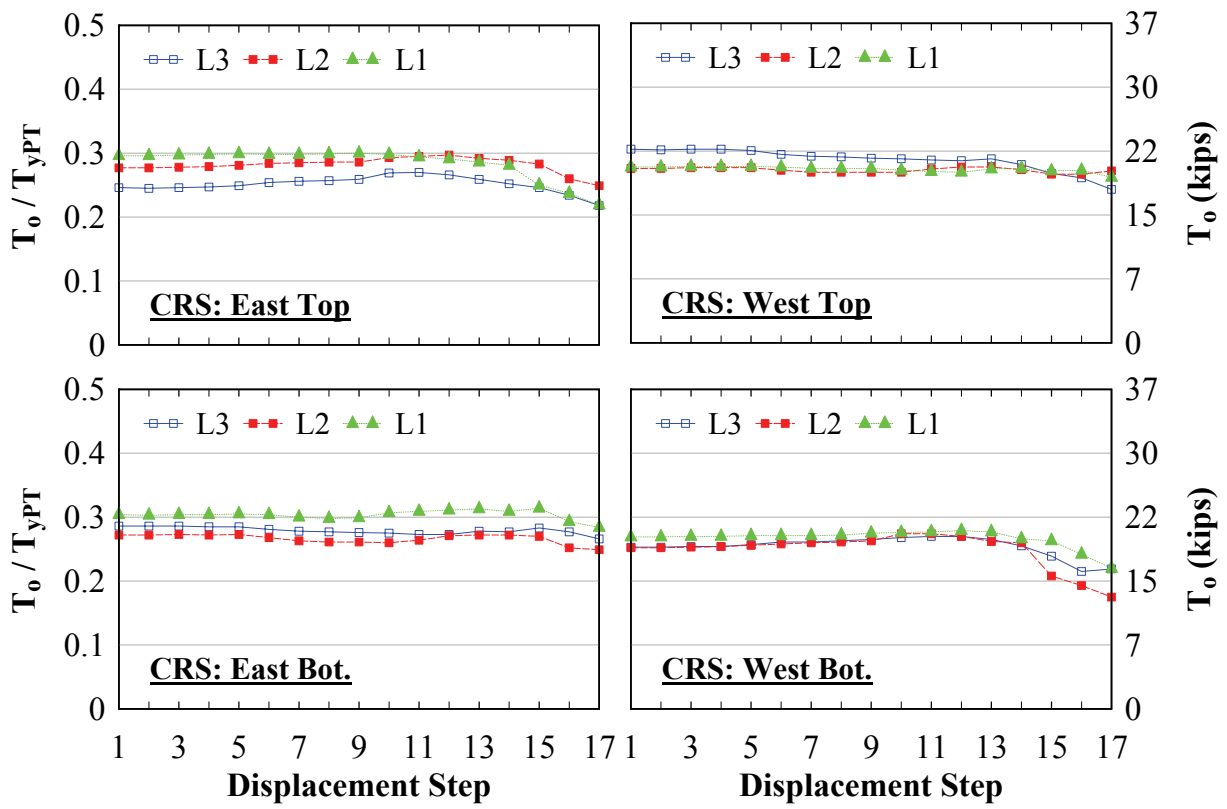


FIGURE 6-58 Frame CRS – initial PT forces

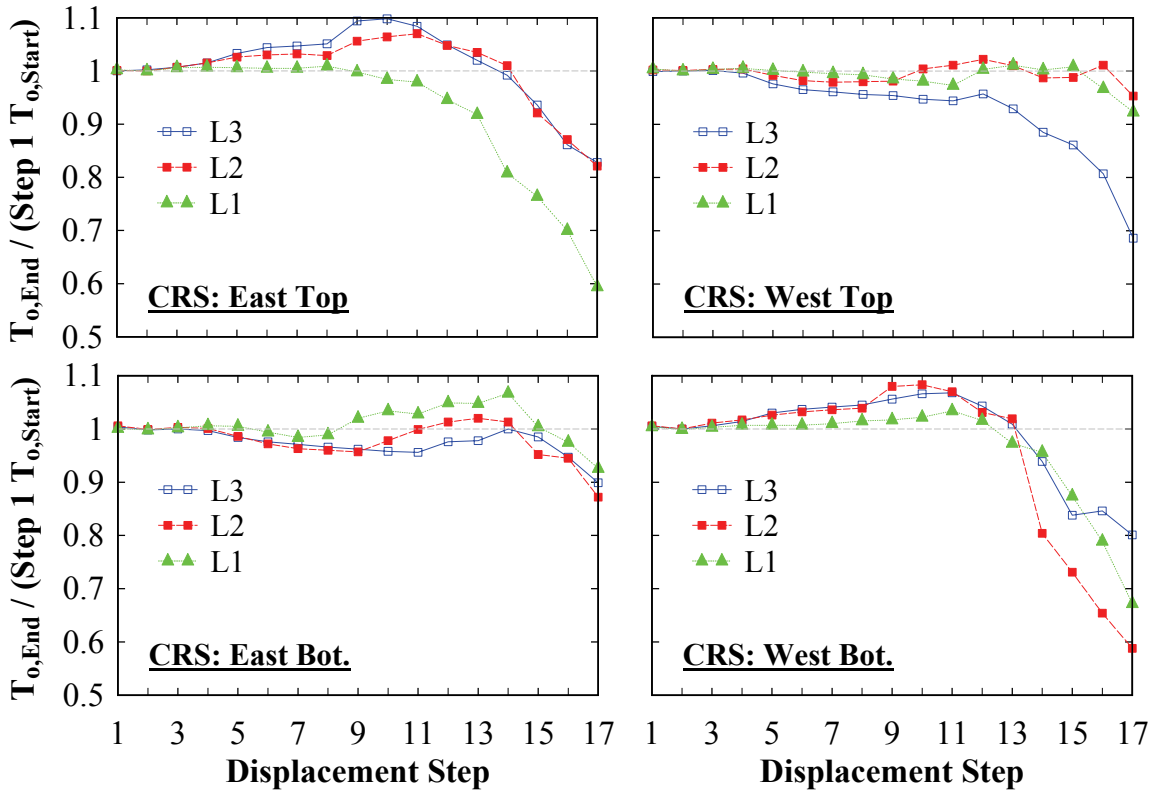
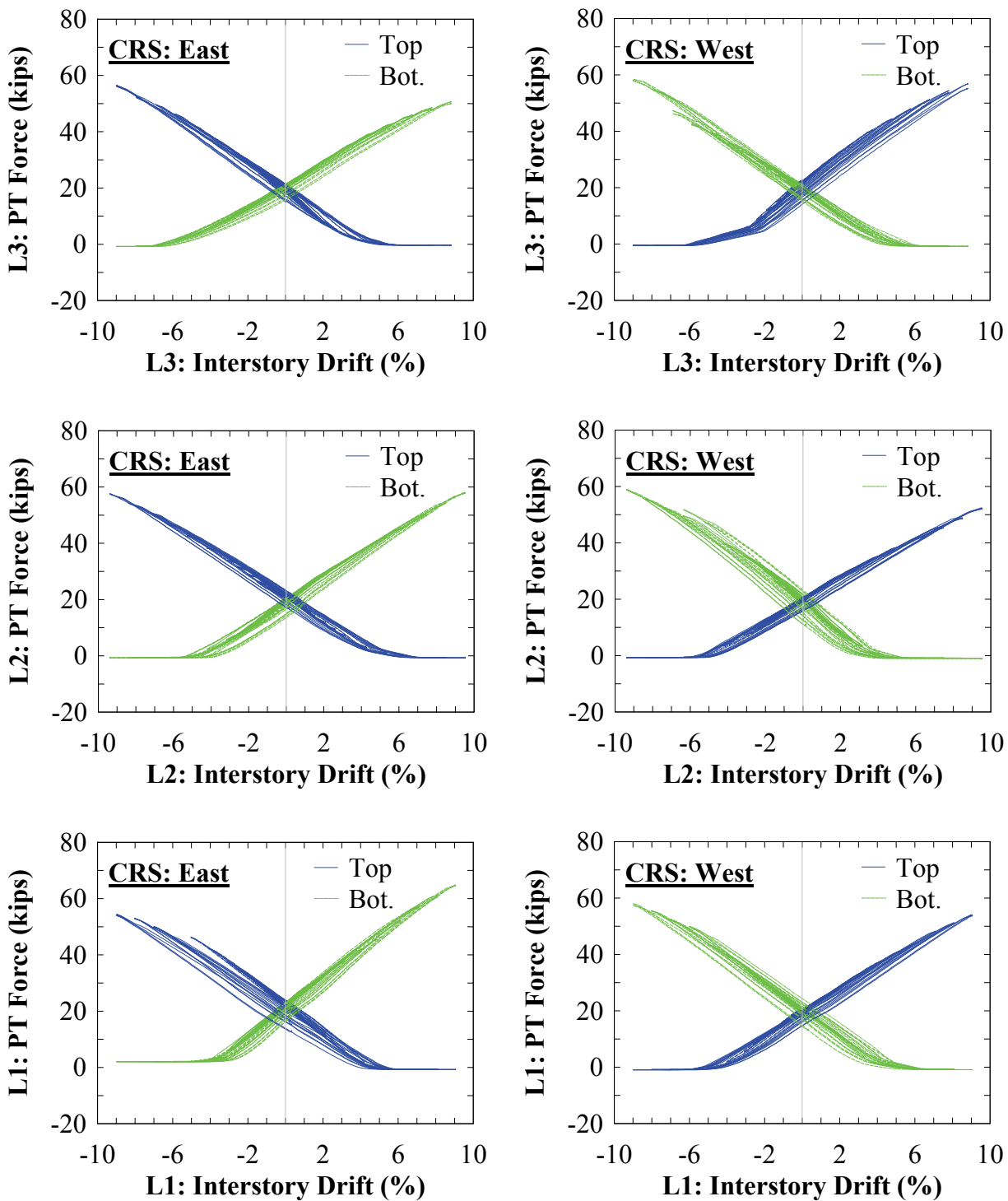


FIGURE 6-59 Frame CRS – initial PT forces normalized by displacement step 1



**FIGURE 6-60 Frame CRS – PT response**

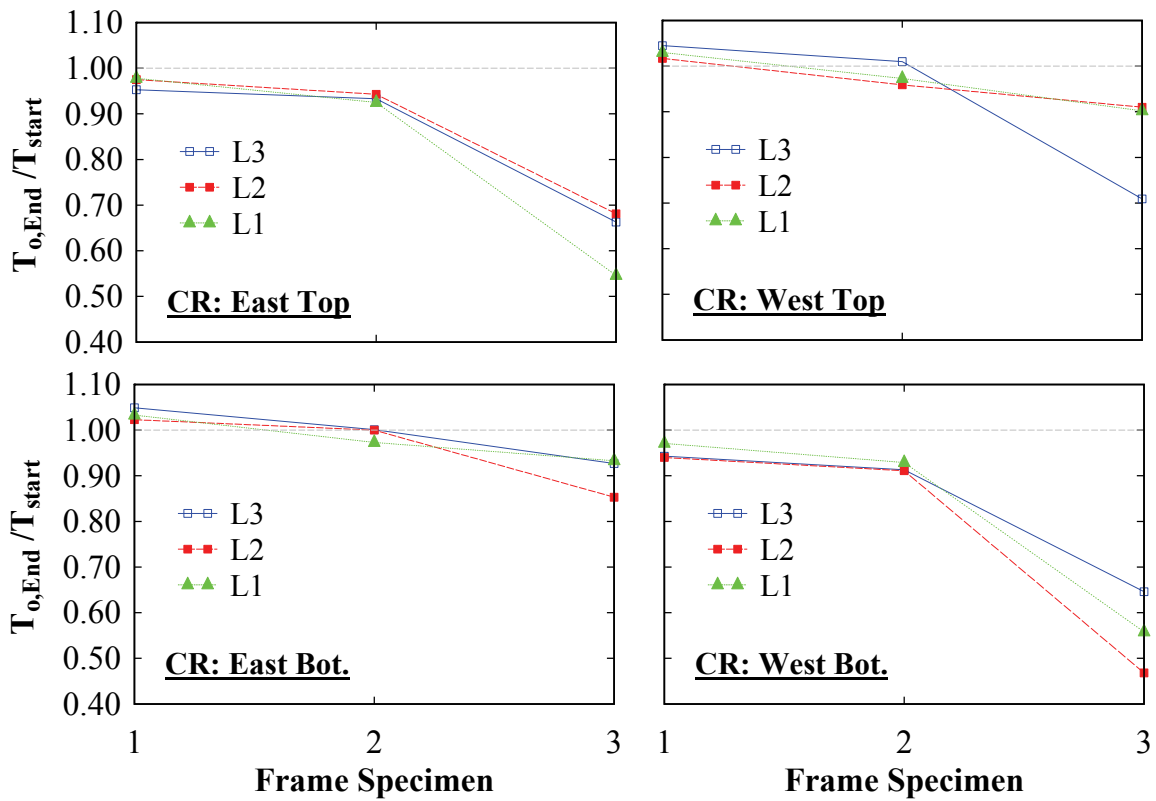


FIGURE 6-61 Normalized initial PT force changes between CR tests

### 6.5.3 CR: Infill Plate and Strip Strain Gage Response

The South elevation infill web plate and strip tensile strain response for selected displacement steps is shown in figures 6-62 and 6-63 respectively. Similar observations to those presented in Section 6.3.3 and 6.4.3 for frames FR and NZ also apply here.

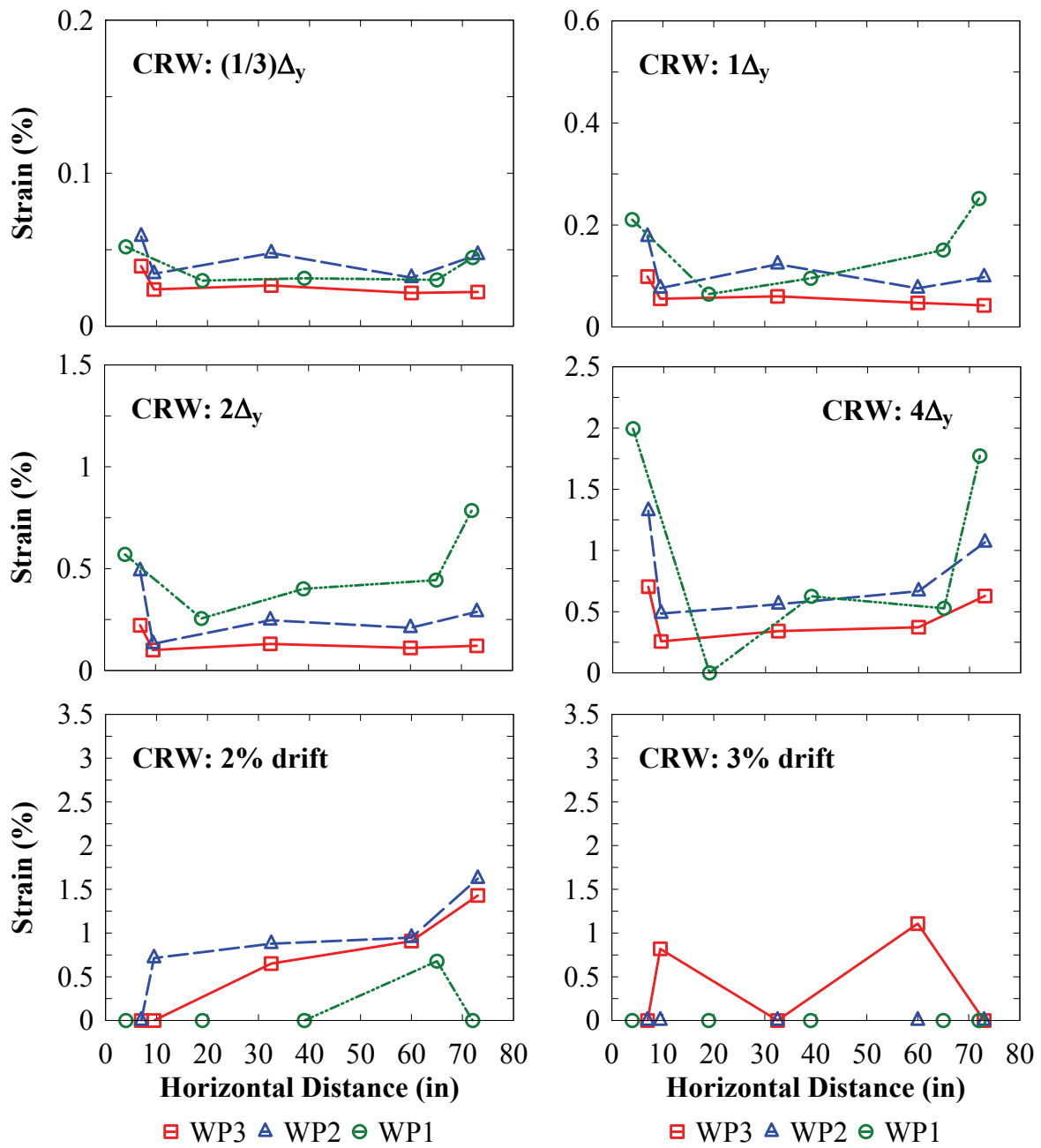


FIGURE 6-62 Frame CRW – infill web plate strains

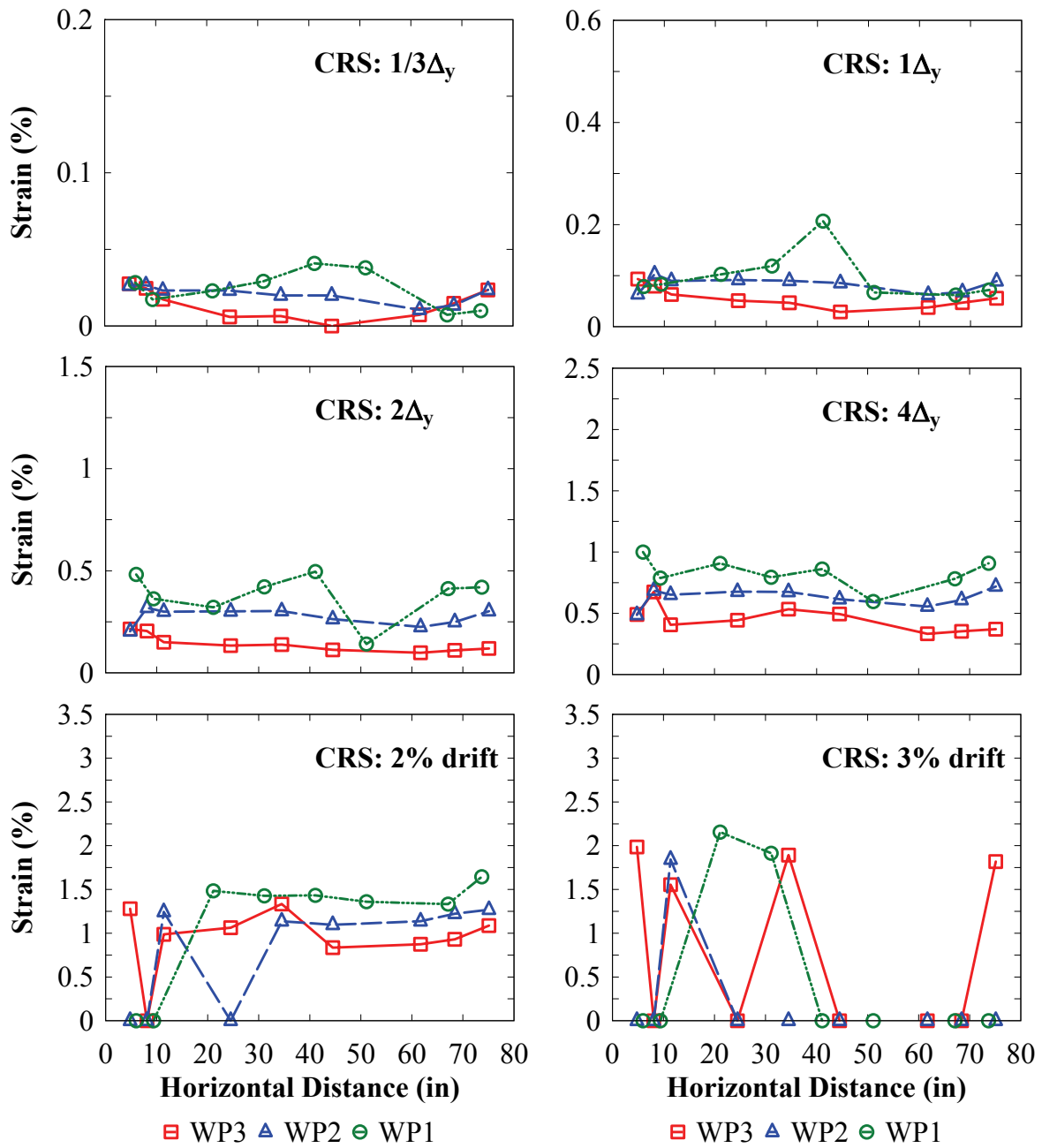
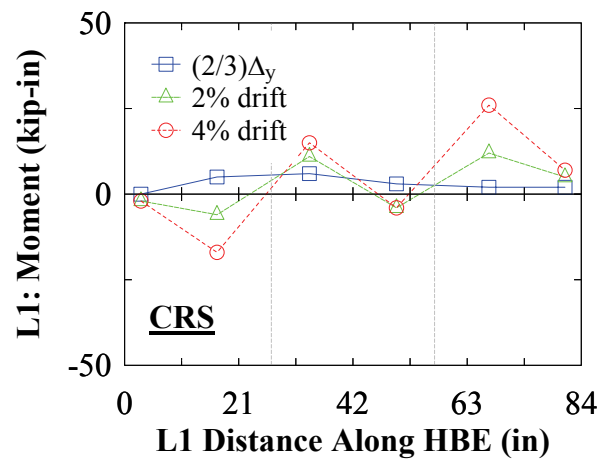
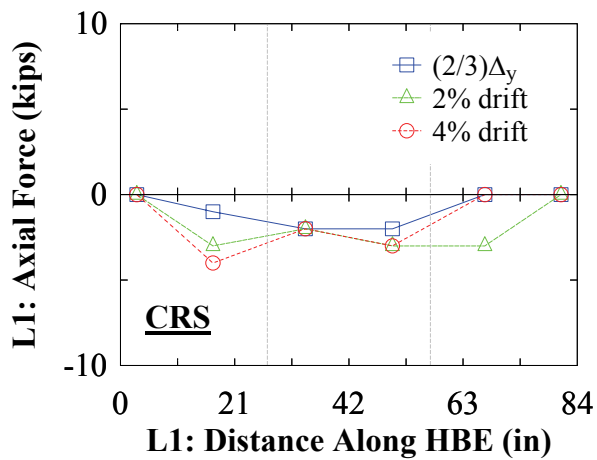
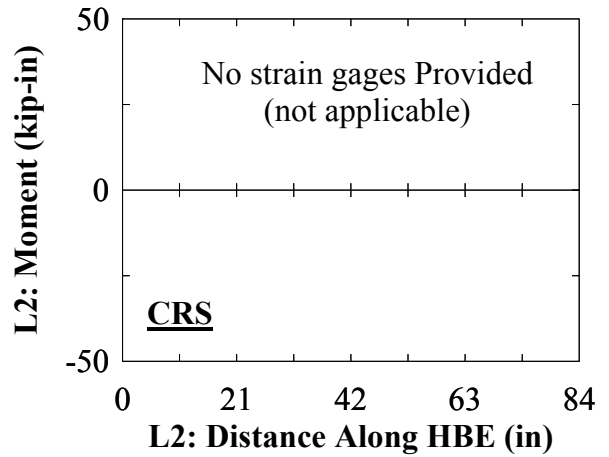
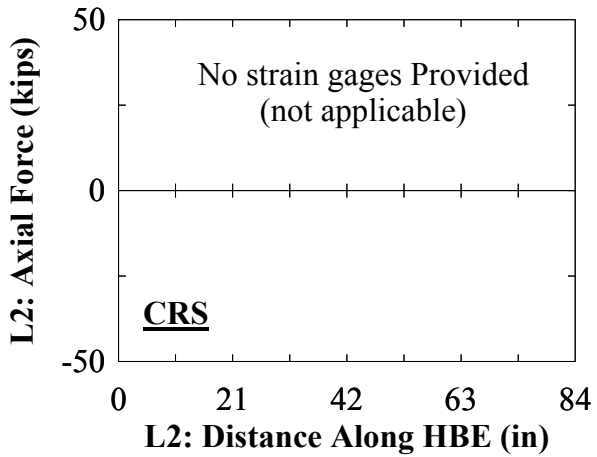
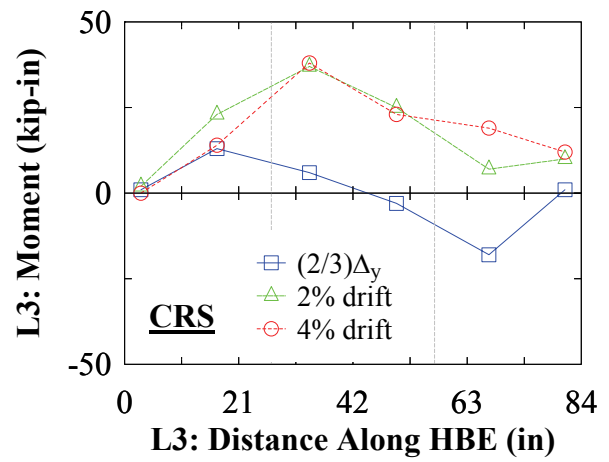
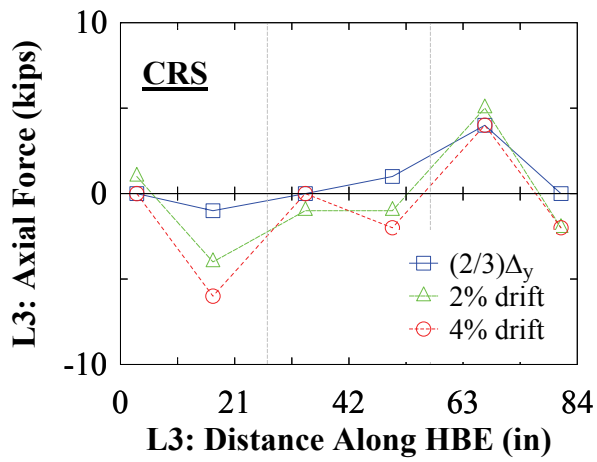


FIGURE 6-63 Frame CRS – infill web strip strains

#### **6.5.4 CR: HBE Axial and Moment Demands**

Similar in format to that was presented earlier for frames FRS and NZS, the axial force and moment demand for frame CRS are shown in figure 6-64. It is observed that the moments at the ends of the HBEs are approximately zero, which is appropriate for the HBE-to-VBE pin connections. Additionally, it is observed that the axial force at the far left end of the HBE is shown to be zero; however, this should be the location of maximum HBE axial compression force. Other than these two observations, additional interpretation of results is not readily apparent for the data shown. A comparison of analytical versus experimental results is presented in Section 6.7.





**FIGURE 6-64 Frame CRS – HBE axial force and moments**

## 6.6 Frame Comparison

The global base shear versus roof drift response for frame NZ and CR are shown in figure 6-65 for results up to the maximum roof drift reached by frame NZ; note that frame FR is not included due to the different displacement control actuator loading procedure used. In general, the response of the two frames is similar. The primary difference lies in the respective contribution of the PT boundary frame to total response, where it is observed that frame NZB is stiffer than frame CRB. In this case, frame NZB is stiffer since the distance provided from the rocking point to the centroid of the PT elements is greater. Recall that for the UB frames, this condition was governed by detailing constraints.

Furthermore, for the infill web plate and PT boundary frame tests, both frame NZ and CR have the same sequence of displacement steps shown in the figure. However, for the infill web strip tests, the displacement steps are the same up to 4% drift, where thereafter whole drift increments were used for frame CRS (i.e., 5%, 6%), and half drift increments for frame NZS (i.e., 4.5%, 5%, etc.). This is reflected by the differences in individual hysteresis loops shown over these displacements steps. Moreover, figure 6-66 shows the response at an individual displacement step where the effects of the PT boundary frame and different loading steps (i.e., whole versus half drift increments) can be observed with additional clarity.

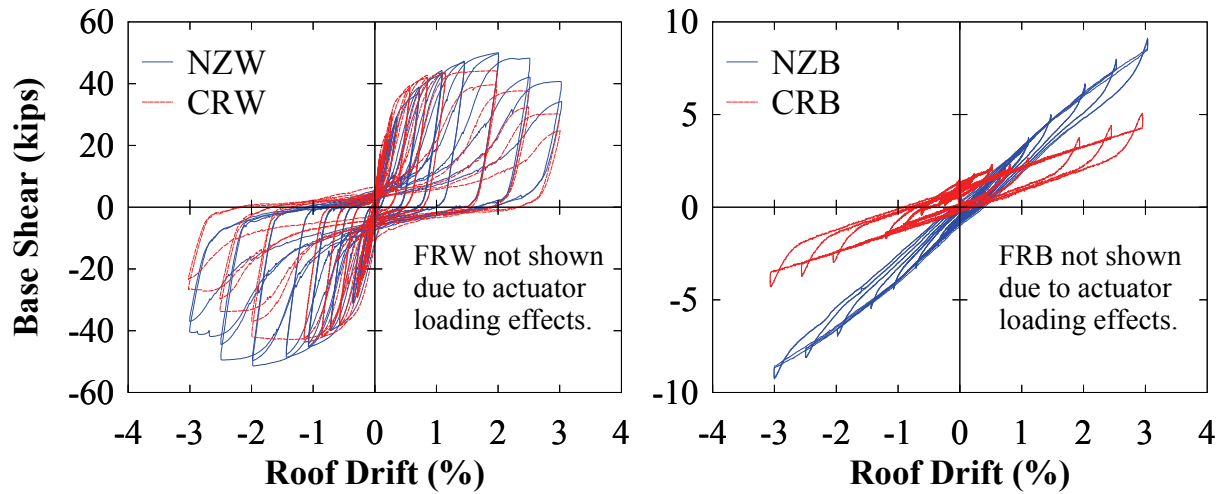


FIGURE 6-65 Frame NZ versus CR – global response

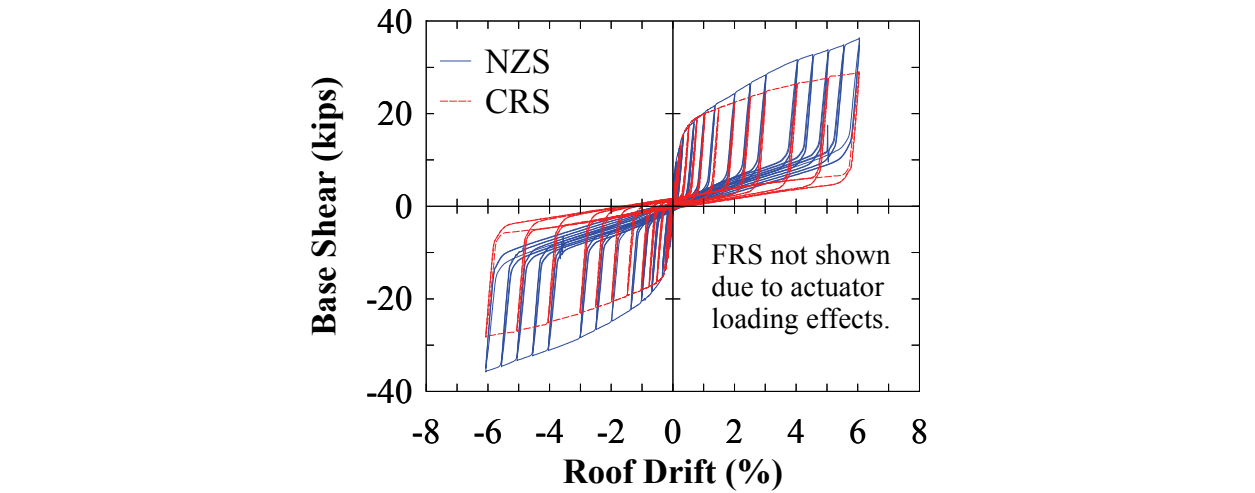


FIGURE 6-66 Frame NZ versus CR – infill web response

## **6.7 Experimental versus Analytical**

### **6.7.1 Experimental versus Analytical: Base Shear versus Roof Drift**

The experimental base shear versus roof drift results show that some compression strength is developed by the infill web plates. Past researchers have reported the contribution of compression strength to the total infill web plates strength (Driver 1997), and proposed a modified strip model (Shishkin et al. 2009) to consider the compression strength of the infill web strips. However, the supporting research was limited and based on CSPSWs where the hysteretic response of the infill web plate is coupled with that of the rigid boundary frame. For SC-SPSWs, the hysteretic response is essentially provided by the infill web plate only, providing a more definitive account of the compression effects of the infill web plate. This was observed by the presence of a residual base shear at the zero-drift location presented earlier. Comparisons to analytical results using OpenSees (OS) is shown in figures 6-67 to 6-69 for frames NZ, CR, and FR, respectively. The analytical comparisons include both a tension-only (TO) and a combined tension-compression (TC) hysteretic model for the infill web strips for comparison. The latter TC model considers the compression strength of the infill web plate using the approach presented by Clayton (2013). Additionally, for each TO or TC hysteretic model, based on trial-and-error, different parameters were considered in order to calibrate the analytical models with the experimental results. Furthermore, as shown in the figures, only the analytical model that best matches those results is superimposed with the experimental results for clarity. As indicated in the figures, analytical results shown are for the following models:

- TO-1: Tension-Only model. This is the model used to generate the preliminary results presented in Section 4 and is the widely accepted method used to model CSPSWs using the strip model approach (Sabelli and Bruneau 2007).
- TO-2: Tension-Only model plus superimposed additional base shear due to  $P-\Delta$  effects of the gravity mass frame (GMF) floor mass plates used in the test setup. Additional clarifications on the effects due to  $P-\Delta$  will be presented subsequently, hereinafter referred to as “GMF effects”.
- TC-1: Tension-Compression model that considers 10% compression in direction of frame drift and 20% compression in recentering direction. Additional clarifications on

the 10%/20% nomenclature will be presented subsequently, hereinafter referred to as “#%/#%” where # is some number.

- TC-2: Tension-Compression model for 10%/20% plus GMF effects.
- TC-3: Tension-Compression model for 20%/20%.
- TC-4: Tension-Compression model for 20%/20% plus GMF effects.
- TC-5: Tension-Compression model for 10%/10%.
- TC-6: Tension-Compression model for 10%/10% plus GMF effects.

The GMF effects noted above refer to the physical pulling and pushing of the GMF gravity weight acting on the actuators from P- $\Delta$  effects. Note that although P- $\Delta$  effects can be considered in the analysis, it is typically handled as a geometric non-linearity within the framework of the program and only has the effect of reducing the stiffness matrix of the analytical model. For the physical test setup, to maintain external force equilibrium due to P- $\Delta$  effects, the weight of the GMF test setup has an additive story force effect on the actuator load cells. To further clarify, as an approximation, if the total weight,  $P$ , of the GMF is lumped at the roof level with height,  $h$ , and the top of frame is laterally displaced a distance,  $\Delta$ , equilibrium requires a horizontal force-couple,  $V$ , at the foundation and roof level such that:

$$Vh = P\Delta \quad (6-1)$$

For assumed axially rigid members, the rotation at the base of the VBEs is proportional to the frame drift,  $\gamma$ , and (6-1) can be expressed as:

$$Vh = P \left[ \left( \frac{\gamma}{100} \right) h \right] \quad (6-2)$$

From which the additional base shear due to the external effects of the GMF is approximated as:

$$V = P \left( \frac{\gamma}{100} \right) \quad (6-3)$$

To provide some perspective on this contribution, using the total weight of the GMF mass plates (which is approximately  $P = 51$  kips), for a roof drift of 4%, the corresponding additional base shear is  $V = (51 \text{ kips})(0.04) = 2$  kips. This added effect is relatively small and has a negligible effect on the frames having infill web plates (where the base shears are relatively large and the maximum roof drifts in the tests are relatively small). In contrast, this has a noticeable effect on the frames with the infill web strips (where the total base shear is relatively small and the maximum roof drifts in the tests are large).

Additionally, for the TC web strip axial hinge models, hysteretic compression of the infill web strips is modeled as some percentage of the tensile yield strength of the corresponding infill web strips. Furthermore, in the nomenclature used above (i.e., #%/#%), the first number indicates a compression strength in the direction moving away from the zero-drift location. The second number indicates compression strength in the direction upon return to the zero-drift location (i.e., during frame recentering). To illustrate, the NZW frame is used as an example and shown in figure 6-70 for two conditions. First, figure 6-70a only considers compression strength in the infill web in the recentering direction, indicated as 0%/20%, where the latter number indicates 20% of the tensile yield strength of the infill web plate. Second, figure 6-70b considers compression strength in the infill web plate in both directions, indicated as 20%/20%, where in this example the compression strength is the same in each direction.

The analytical results that were most comparable to the experimental results were the TC-4 (20%/20%) and TC-6 (10%/10%) models shown in the figures, where the comparisons are in good agreement. The former considers a compression stress of 20% of the yield strength of the infill web plate in both directions and the latter considers 10% in both directions. However, it is observed in the PT boundary frame experimental results that some energy dissipation is provided; attributed to friction and slip inherent in the test setup. As was observed earlier, the hysteretic response of infill web strips are essentially tension-only. Consequently, the infill web strip “compression” strength observed is due to the hysteretic response of the PT boundary frame (due to friction). Accordingly, for the infill web plate, if the hysteretic response of the PT boundary frame is neglected, this suggests that the actual contribution of compression strength from the infill web plates is closer to 10%. Interestingly, this value is comparable to the value of

8% used by Shishkin et al. (2009) in the reference noted above. Furthermore, the residual base shear ratios for the infill web plates presented earlier were generally closer to 10%, even though 20% was used in the analytical model for the results shown. However, the experimental ratios presented is a ratio of the maximum base shear and the residual base shear for a given displacement step. Accordingly, the effects of the PT boundary frame are included in both base shear values and effects minimized once a ratio is taken, leaving only the dominant effects of the infill web plate.

Additionally, it is observed in the frame NZS comparison shown, the residual base shear for the analytical results is noticeably larger in comparison to the experimental. In particular, for the different analytical comparisons presented, the Tension-Only results do not perfectly recenter. This is due to PT yielding effects in the analytical model. Although PT yielding was also observed in the NZS test, the occurrence and extent of PT yielding are dissimilar between the analytical and experimental comparisons, leading to a larger disparity between the comparisons. It is also noted that for frame FR, the analytical comparisons shown are based on the comparison results obtained from the NZ and CR frames, since the FR experimental results is not representative of the prototype frame response, due to the actuator interaction effects.

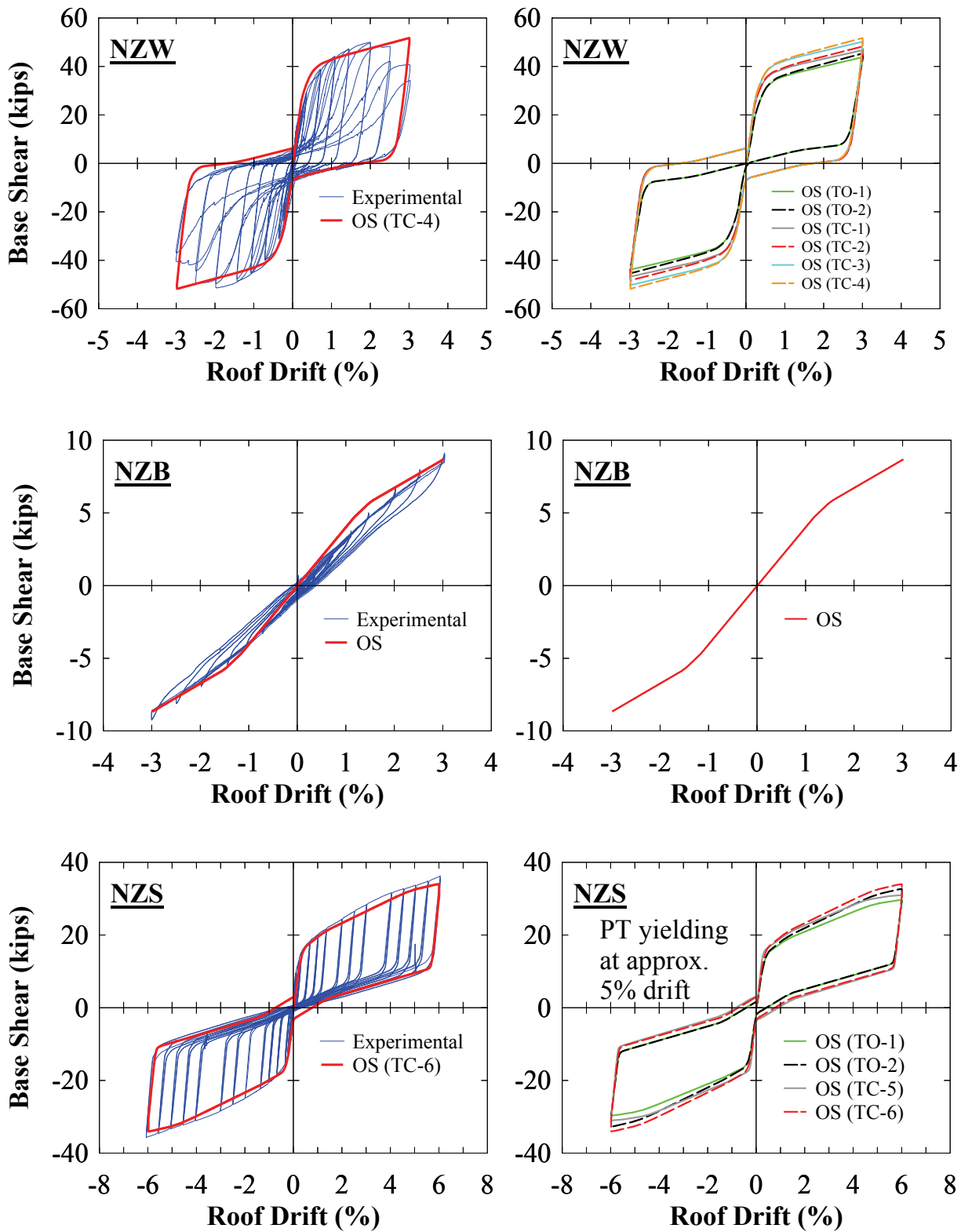


FIGURE 6-67 Frame NZ: Experimental versus Analytical – global response



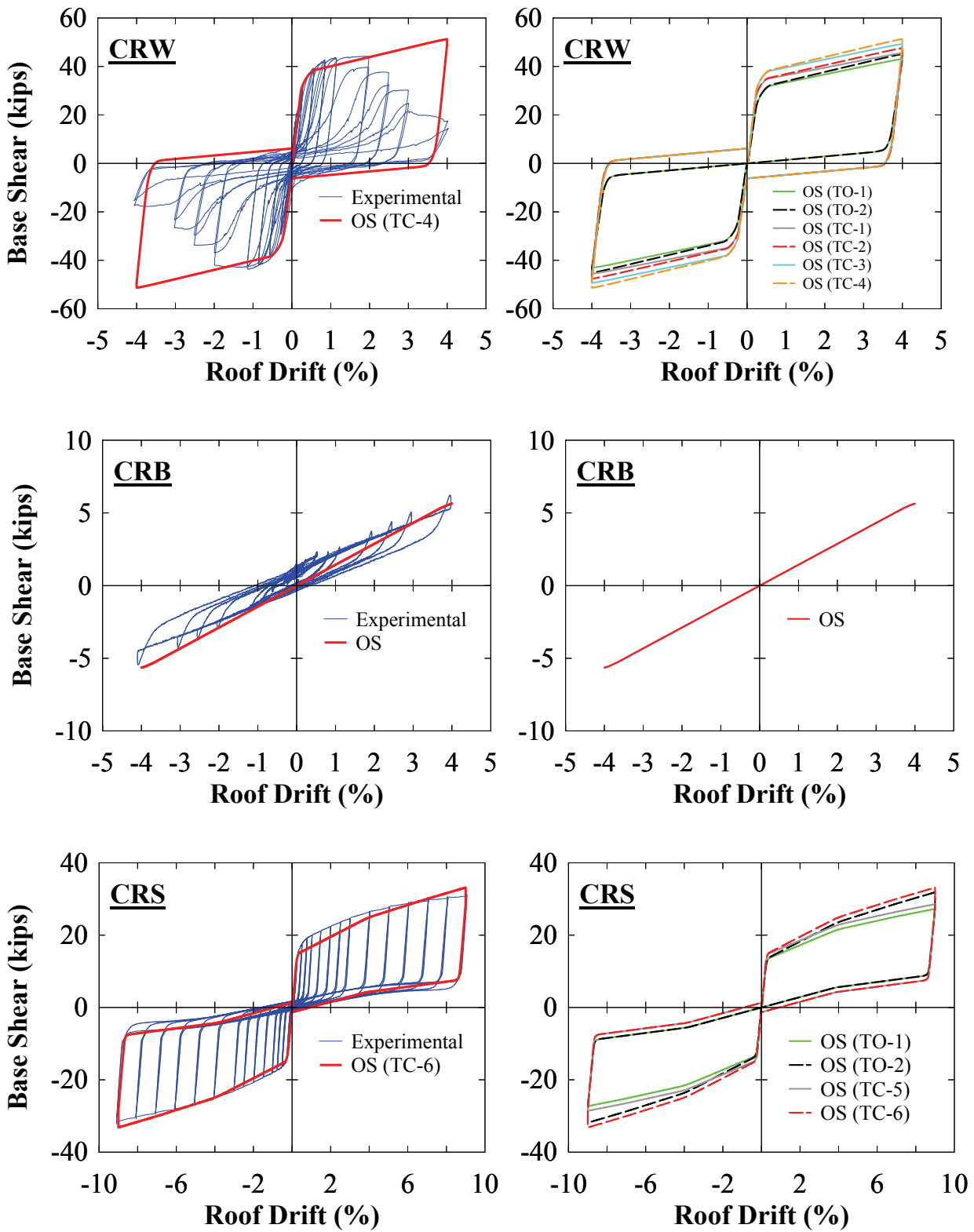


FIGURE 6-68 Frame CR: Experimental versus Analytical – global response

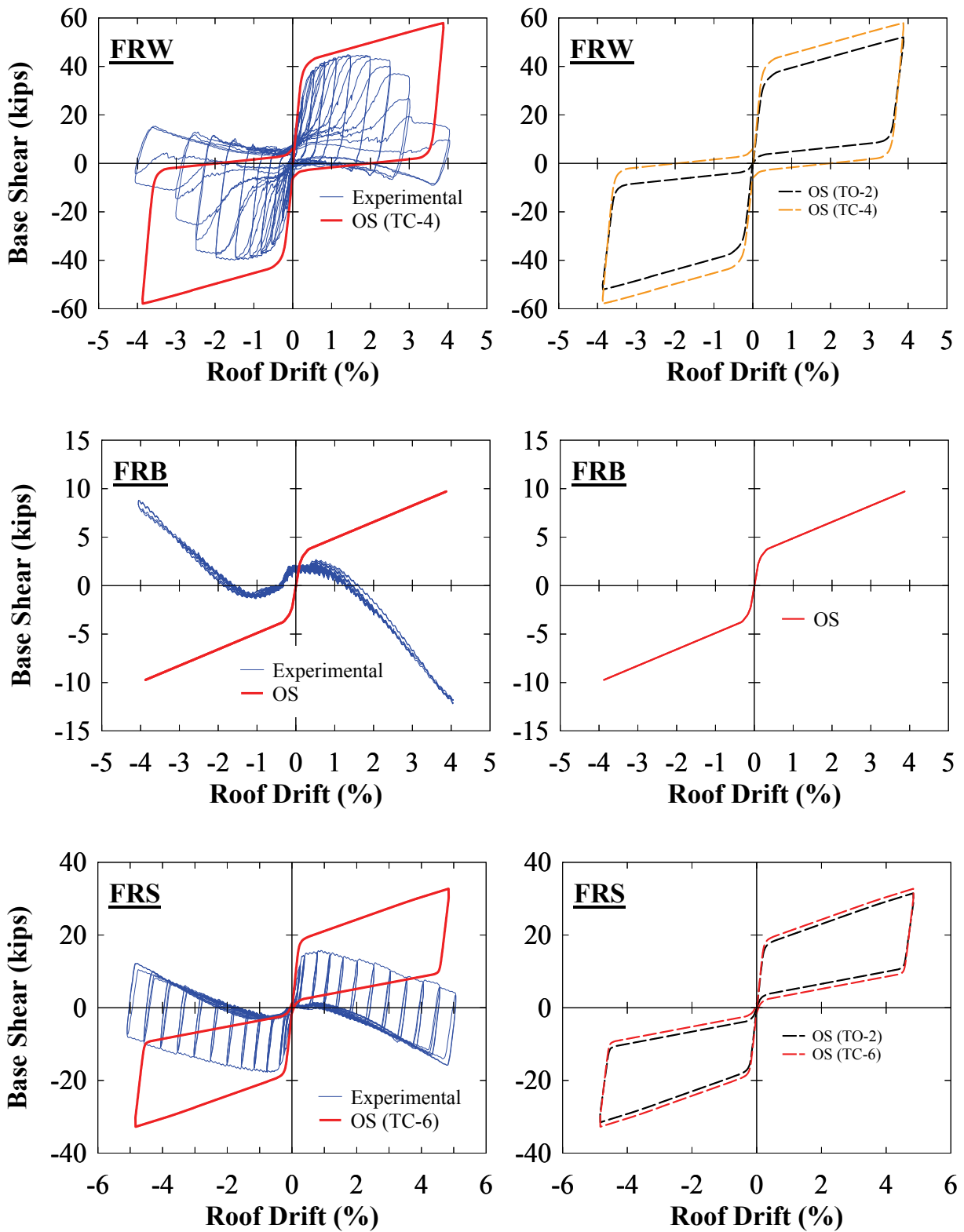
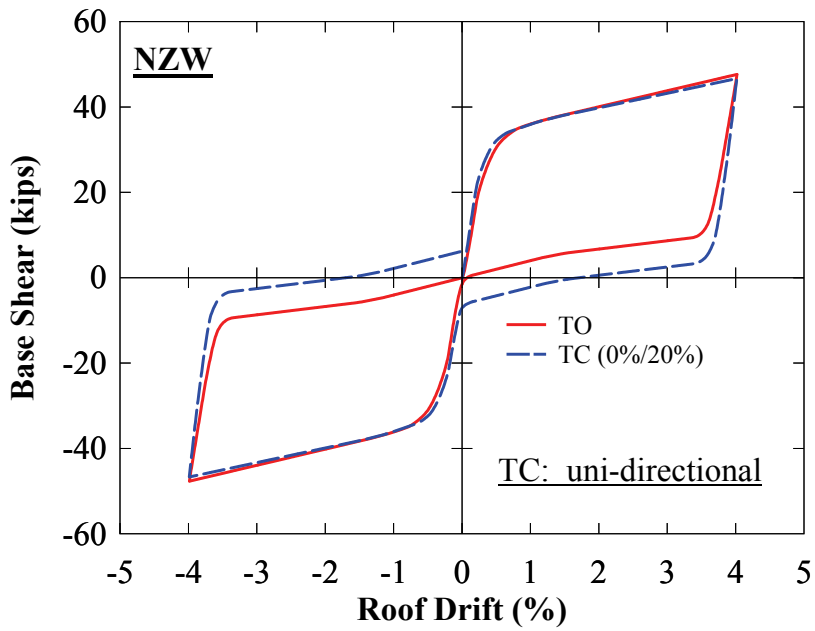
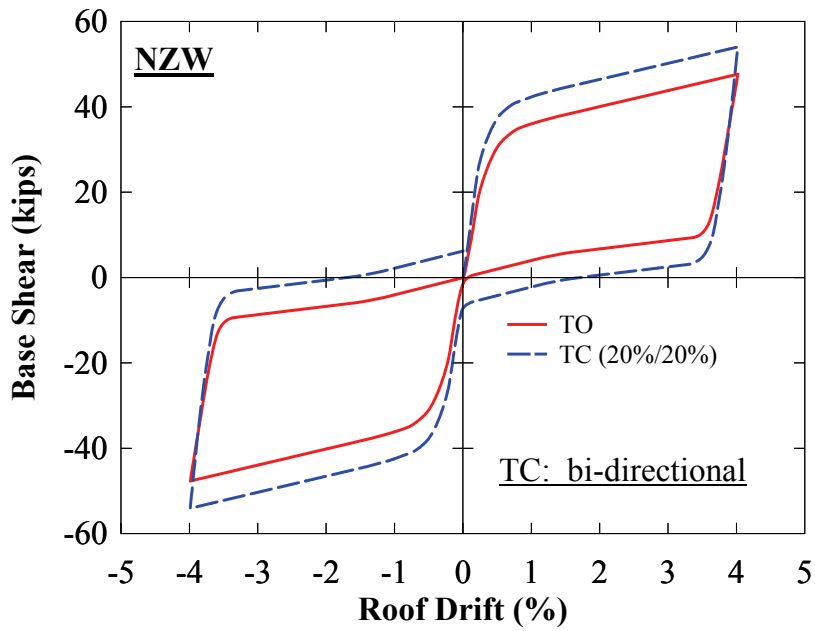


FIGURE 6-69 Frame FR: Experimental versus Analytical – global response



(a)



(b)

**FIGURE 6-70 Analytical infill web plate compression: (a) uni-directional; (b) bi-directional**

### **6.7.2 Experimental versus Analytical: HBE Axial Force and Moments**

From the experimental results presented earlier, the HBE axial force and moment demands for frame NZS and CRS are compared with analytical results using OpenSees. The comparisons are made at the 2% drift displacement step and shown in figures 6-71 and 6-72, respectively (note that a comparison to frame FRS is not provided due to the actuator interaction effects). The OpenSees model uses the Tension-Only (TO) hysteretic model for the infill web strips; which is appropriate as the experimental results show that the infill web strips are essentially tension-only.

In general, it is observed that the comparisons are significantly different. The experimental quantities are much smaller than the analytical results. In particular, the axial force quantities calculated from the strain gage data is significantly lower where the HBE-to-VBE axial force should be the largest (i.e., far left end point in the curves). It is apparent that the particular distribution of strain gages provided does not accurately capture the total response along the HBEs. That is the strain gage data are dominated by local strain effects. As an example, the strain readings at the bottom flange at the ends of the HBEs for frame NZS is essentially zero, which captures the local physical behavior for reasons presented earlier. Additionally, for frame CRS, the strain readings at the ends are essentially zero because the HBE-to-VBE axial force is transferred through the pin in the HBE webs, and the strain gages were located on the flanges directly above and below the shear pin. Such local physical responses are not captured by the idealized OpenSees model. Additionally, the distribution of strain gages does not accurately capture the localized stress effects at the PT anchor points on the HBEs. Finally, the disparity in results is also partly attributable to the fact that the experimental results are affected by vertical offset error of unknown magnitude in the strain data collected.

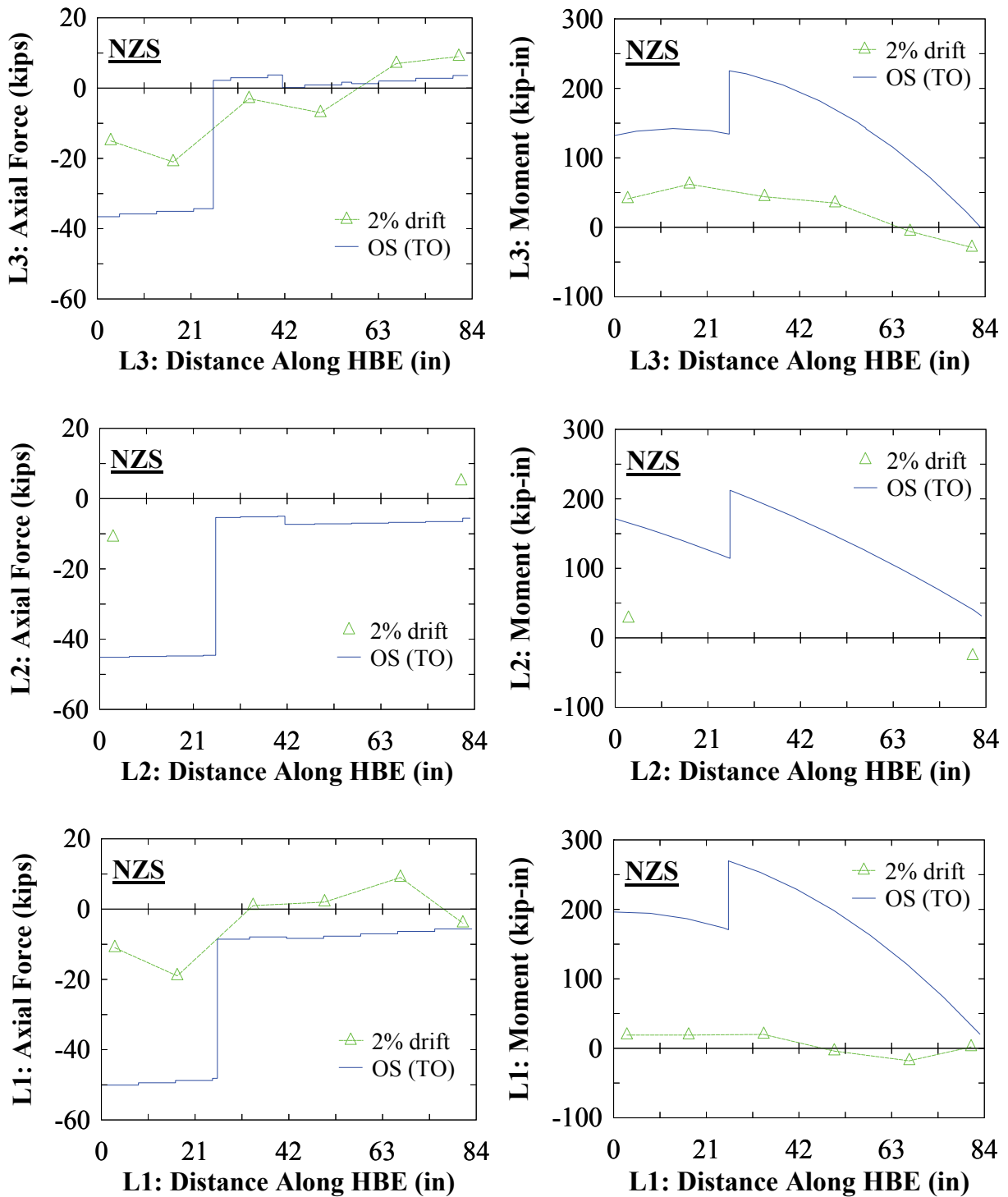
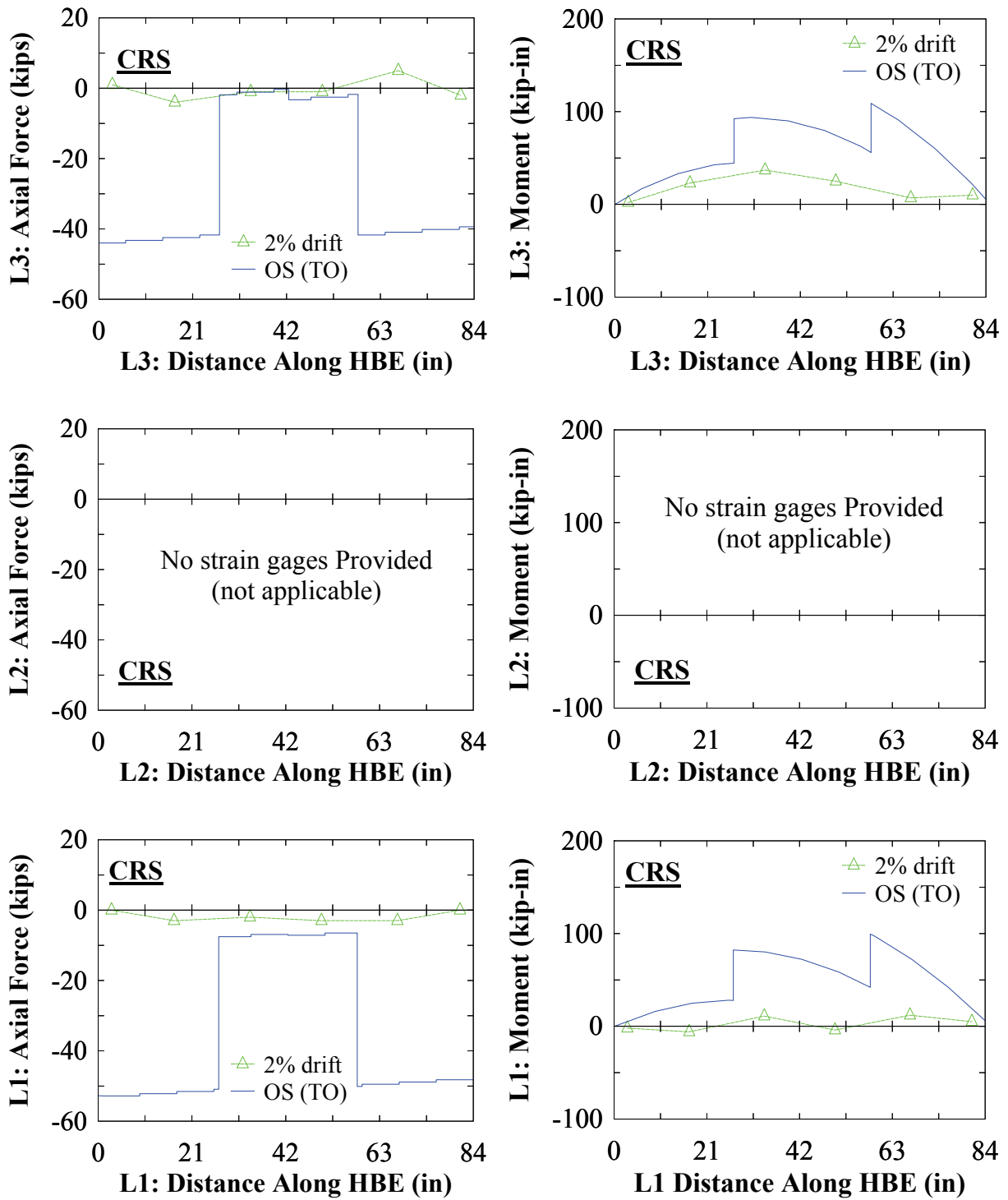


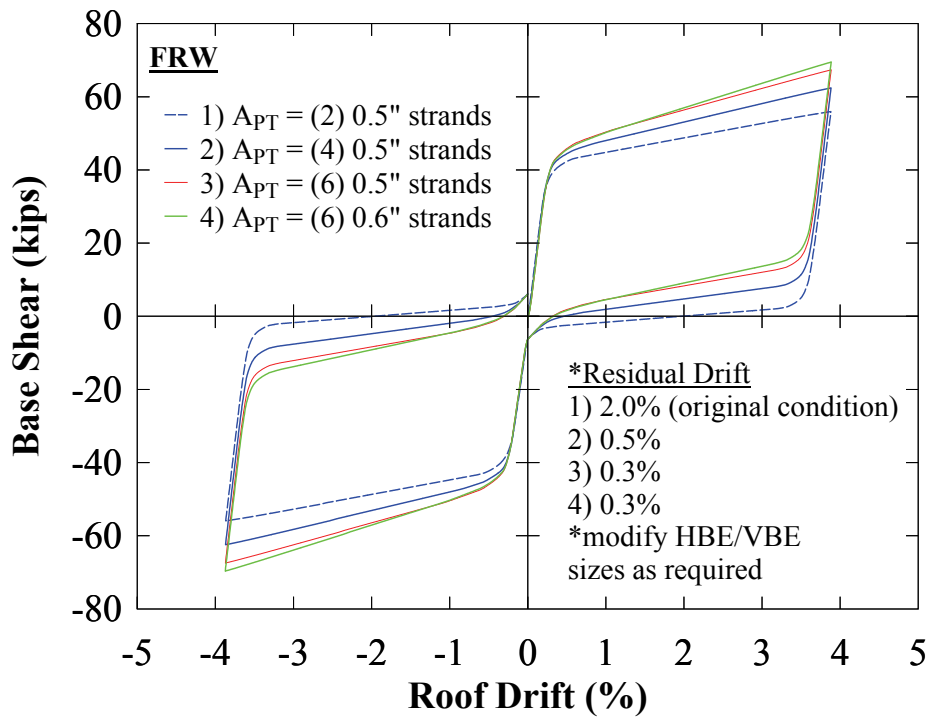
FIGURE 6-71 Frame NZS: Experimental versus Analytical – HBE axial force and moments



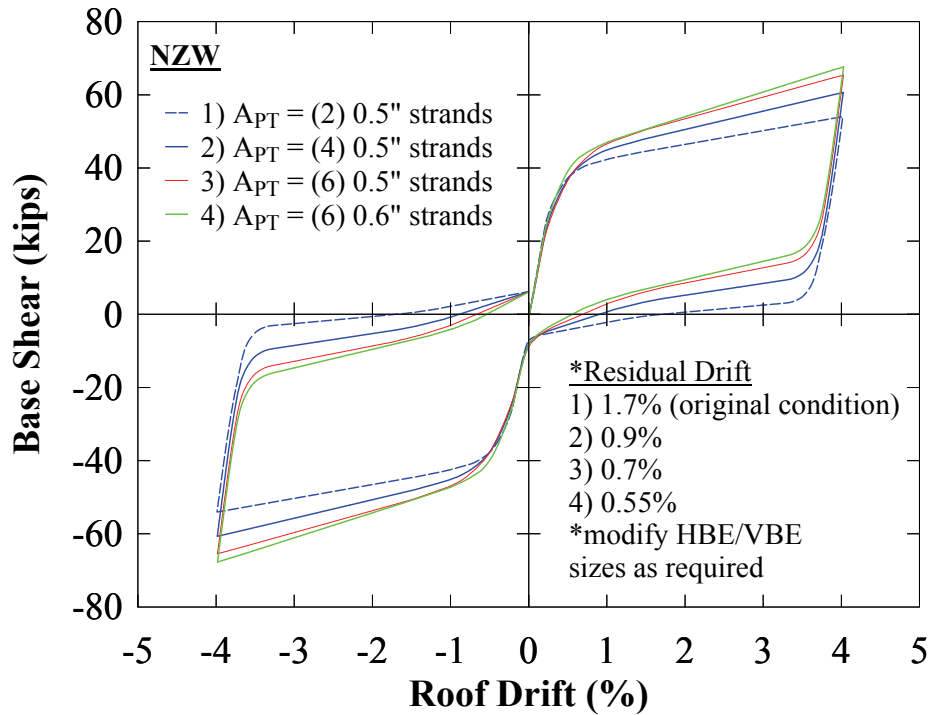
**FIGURE 6-72 Frame CRS: Experimental versus Analytical – HBE axial force and moments**

## **6.8 Design Calculation of Post-Tension Area**

At the time of test specimen design, the effects of the infill web plate on recentering for static loading conditions were not fully known. Although recentering was not achieved for the frames with the infill web plates, consideration of the infill web plate effects can be incorporated into the frame design by changing the PT parameters, as presented in Section 4. To illustrate, figure 6-73 shows alternate PT configurations for frames FRW and NZW (by arbitrarily increasing the PT area to show its effect), where it is shown that a significant reduction in residual drift can be achieved compared to the original design. Note that only the quantity of PT strands was increased as indicated for illustrative purpose only; the boundary frame was assumed to remain elastic. Accordingly, the frame member sections would require modification as warranted, commensurate with increased strength demands on the boundary elements due the increase in PT forces.



(a)



(b)

FIGURE 6-73 Analytical global response –  $A_{pt}$  variable: (a) FRW; (b) NZW



A simplified design approach for determination of the calculation of PT area is developed for a particular frame configuration and shown below. First, recall that the force-displacement response of the PT boundary frame is bilinear elastic regardless of the rocking joint detail used (for reasons presented in Section 4) and the subsequent method presented is applicable for all three frame types FR, NZ and CR. Also, it is realized that the compression strength of the infill web plate has an effect of vertically shifting the PT boundary frame response by an amount  $\beta$ , which is the assumed compression effect of the infill web plate as shown in figure 6-74a for a positive drift condition. Correspondingly, the residual drift then occurs at some point  $\lambda$  as shown in that same figure. It then follows that, for a given  $\beta$ , the design effective frame stiffness  $K1$  or  $K2$  can be obtained for a target residual drift  $\lambda$ , as shown in figure 6-74b, where the effective frame stiffness is calculated by (6-4). The approximate PT area at each joint can then be obtained by designing the PT elements for an effective frame stiffness condition (given by (6-4)) from a frame analysis by the method of virtual work.

$$K_{eff} = \frac{\beta}{\lambda} \quad (6-4)$$

This can be illustrated by an example using frame NZW. Consider the rightward drift shown in figure 6-75 where:  $V$  is the total base shear;  $h_i$  is the story heights;  $W_i$  is the frame tributary effective seismic weight,  $C_i$  is the distribution of base shear along the frame height,  $\theta$  is the frame drift rotation assumed for a rigid boundary frame,  $M_{conn}$  is the strength of the HBE-to-VBE PT rocking joint,  $P_s$  is the total PT force in the PT elements at each HBE-to-VBE joint; and  $y$  is the distance from the rocking point to the centroid of the PT elements. For simplicity in this example, assuming that the story heights are all equal to  $h$ , and floor seismic weights are all equal to  $W$ , it then follows from the principle of virtual work that:

The external work is,

$$W_E = (C_3V)[\theta(3h)] + (C_2V)[\theta(2h)] + (C_1V)[\theta(h)] \quad (6-5)$$

And the internal work is,

$$W_I = \sum M_{conn} \theta \quad (6-6)$$

Next, setting (6-5) equal to (6-6), then substituting the  $C_i$  distribution factors shown in figure 6-75c and solving for  $V$ , leads to the approximate strength of the PT boundary frame as:

$$V = \frac{6}{14} \left( \frac{\sum M_{conn}}{h} \right) \quad (6-7)$$

Furthermore, since the design approach presented here uses an effective global frame stiffness to obtain the approximate area of PT for a given  $\beta/\lambda$  ratio, the height to the resultant of the total story shear force,  $H$ , is required and is determined by equilibrium of the resultant overturning moment of the resultant story forces (i.e., base shear  $V$ ), equated to the overturning moment due to the story forces such that:

$$(V)(H) = (C_1 V)(h) + (C_2 V)(2h) + (C_3 V)(3h) \quad (6-8)$$

Substituting the  $C_i$  distribution factors shown in figure 6-75c and solving for  $H$  leads to:

$$H = \frac{14}{6} h \quad (6-9)$$

Next, the equation for the effective PT boundary frame strength can be written as shown in (6-10), where  $\Delta_{eff}$  is the lateral displacement at height  $H$  indicated by (6-9).

$$\begin{aligned} V &= (K_{eff})(\Delta_{eff}) \\ &= (K_{eff})(\theta H) \\ &= (K_{eff})(\theta) \left( \frac{14}{6} h \right) \end{aligned} \quad (6-10)$$

Furthermore, substituting (6-7), for  $V$  into (6-10), then solving for  $K_{eff}$  leads to:

$$K_{eff} = \left( \frac{6}{14h} \right)^2 \left( \frac{\sum M_{conn}}{\theta} \right) \quad (6-11)$$

In (6-11),  $M_{conn}$  is the post-tension force,  $P_s$ , multiplied by the moment lever arm  $y$  from the rocking point to the centroid of the PT elements. Recall, from Section 3, that  $P_s$  includes both an initial PT force and a drift induced PT force which also considers PT force losses, such that:

$$M_{conn} = \left[ P_o + \frac{A_{PT} E_{PT}}{L_{PT}} (\Delta_{drift} - \Delta_{loss}) \right] (y) \quad (6-12)$$

To keep the equations manageable for the purpose of initial calculations, the PT force loss term is neglected in (6-12) here (for final design, this effect could be accounted for using a nonlinear pushover analysis). Thus, by substituting (6-12) into (6-11), replacing the summation term with  $N_{conn}$  (i.e., total number of  $M_{conn}$  considered in frame strength), and solving for  $A_{PT}$  leads to the following:

$$A_{PT} = \left( \frac{K_{eff}}{N_{conn}} \right) \left[ \left( \frac{14h}{6y} \right)^2 \left( \frac{L_{PT}}{E_{PT}} \right) \right] - \left( \frac{P_o}{y} \right) \left( \frac{L_{PT}}{E_{PT}} \right) \left( \frac{1}{\theta} \right) \quad (6-13)$$

Next, substituting (6-4) into (6-13) for a target  $K_{eff}$ , (6-13) can be re-written as follows:

$$A_{PT} = \left( \frac{1}{N_{conn}} \right) \left( \frac{\beta}{\lambda} \right) \left[ \left( \frac{14h}{6y} \right)^2 \left( \frac{L_{PT}}{E_{PT}} \right) \right] - \left( \frac{P_o}{y} \right) \left( \frac{L_{PT}}{E_{PT}} \right) \left( \frac{1}{\theta} \right) \quad (6-14)$$

Equation (6-14) provides the required area of PT, for the case of an axially rigid HBE at an HBE-to-VBE joint, for a target effective stiffness,  $\beta/\lambda$ , for the lateral force distribution shown in figure 6-75. For frame configurations other than shown, the virtual work calculation in determining the strength of the PT boundary frame,  $V$ , would need to be modified accordingly. Additionally, (6-14) is “exact” for the condition  $P_o = 0$ , but this term can conservatively be assumed to be zero for the purpose of an initial calculation. A nonlinear cyclic pushover analysis could be conducted to obtain the approximate value of  $\beta$ , for a frame model considering some

compression strength of the infill web plate. Alternatively, an approximation could be obtained from a nonlinear monotonic pushover analysis of a tension-only model by assuming some percentage of the peak base shear value. As presented earlier, the analytical models could consider approximately 10 to 20% of the tensile yield strength of the infill web plate for the compression strength of the infill web plates.

For this example, from a nonlinear cyclic pushover analysis,  $\beta$  is obtained to be approximately 6.75 kips for the frame NZW considered. Additionally, as shown in figure 6-75a, the condition when full relaxation occurs at the closing joints is assumed (i.e.,  $N_{conn} = 3$ ) which corresponds to setting  $K_{eff}$  to  $K_2$  (shown in figure 6-74b). Furthermore, a target residual drift of 0.2% is selected, such that  $\lambda$  is equal to  $(0.002)(148 \text{ in.}) = 0.296$  inches, and  $P_o$  is conservatively taken to be zero. Equation (6-14) indicates that 2.22 in. square of PT is required. The resulting global hysteretic response is shown in figure 6-76, which indicates a residual roof drift of approximately 0.24%, comparable to the target 0.2%; also shown in the figure are the results for the original PT configuration for reference. Furthermore, only the area of PT strands was increased in this example (i.e., for the results shown in figure 6-76); the boundary frame was assumed to remain elastic. Accordingly, the frame member sections would require modification as warranted, commensurate with increased strength demands on the boundary elements due the increase in PT forces.

Note that the design approach presented is based on the observation that for static cyclic loading conditions for progressive increase in roof drifts, frame recentering is affected by the compression effects of a solid infill web plate configuration. However, as will be shown in Sections 7 and 9, frame recentering is not affected by the infill web plate compression effects for dynamic earthquake loadings. Accordingly, this general design approach may still be applied (as it will provide a conservative upperbound design condition on the post-tension); it is not necessarily warranted for frames subjected to earthquake loadings.

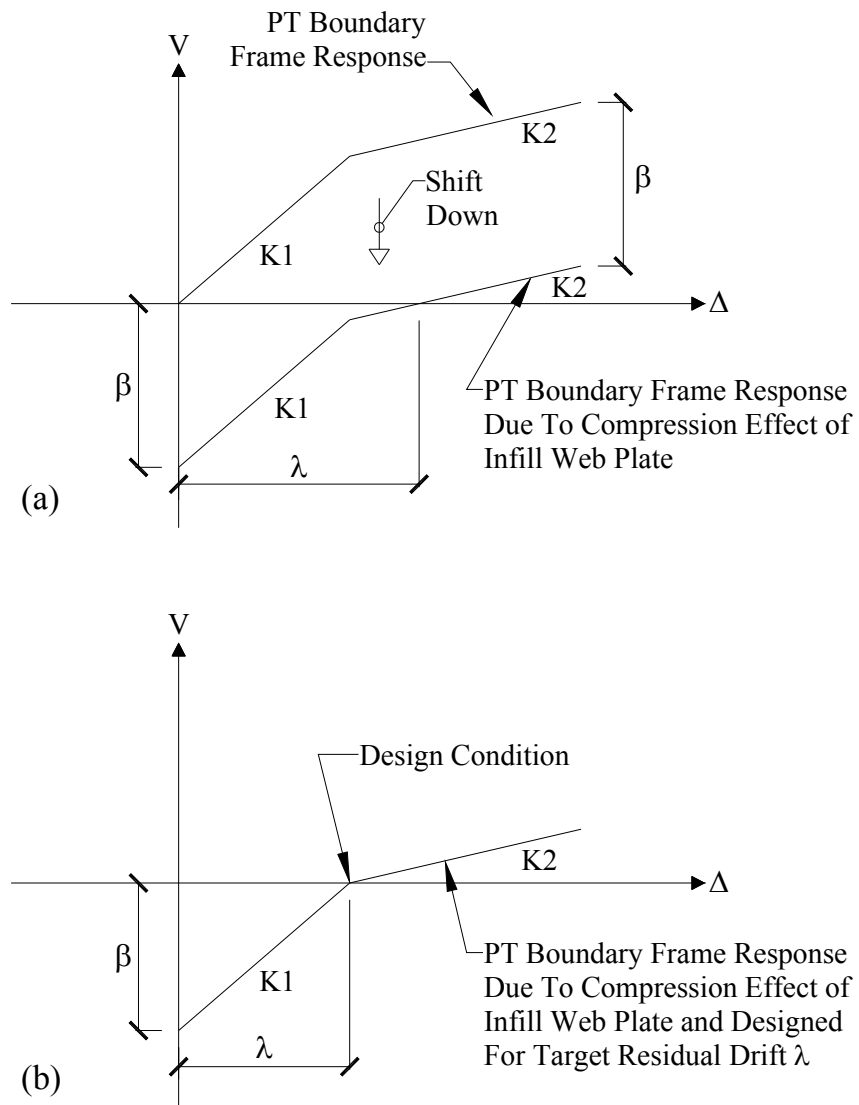


**FIGURE 6-74 PT boundary frame response: (a) generic condition; (b) design condition**

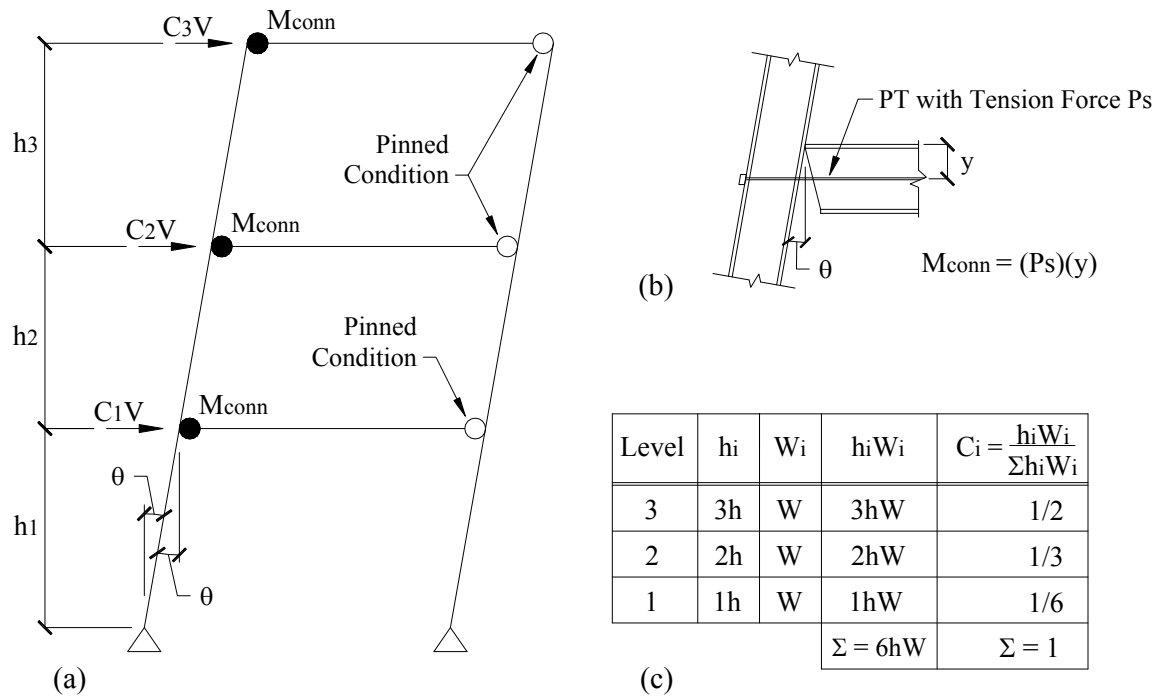


**FIGURE 6-75 NewZ-BREAKSS post-tension design example: (a) rigid frame sway mechanism; (b) joint moment strength; (c) frame lateral force distribution**

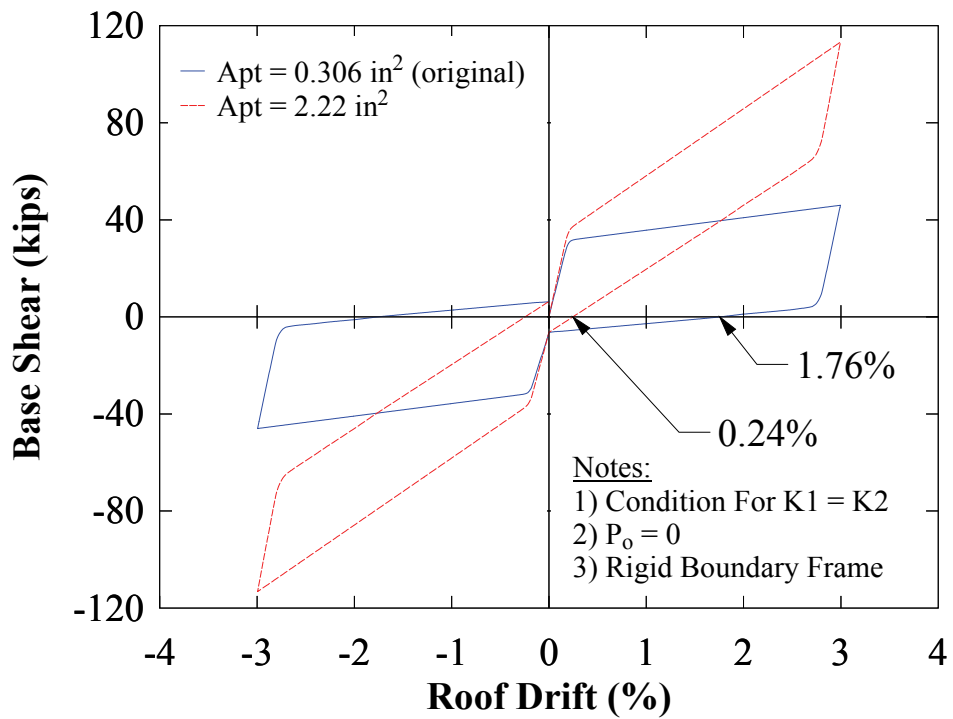


**FIGURE 6-76 NewZ-BREAKSS post-tension design example results**

## 6.9 Summary

The quasi-static tests provided valuable observations on the behavior of SC-SPSW having infill web strip or infill web plate configuration, as well as on the response of the PT boundary frame by itself. Additional insight on the infill web plate behavior as it deforms due to tension-field action was also obtained. In particular, results suggest that the infill web plate has some compression strength that contributes to energy dissipation and also has an effect on frame re-centering when subjected to the static cyclic loading protocol considered here. On the contrary, infill web strips essentially behave as tension-only members. Furthermore, infill web strips are not susceptible to tearing from the boundary frame compared to infill web plates. It was also observed, that infill web plates provide some energy dissipation during repeated cycles at the same drift. In contrast, infill web strips only provide energy dissipation for increased axial yielding beyond the previous inelastic excursion, per a characteristic tension-only behavior.

Additionally, PT force losses were observed; however, this is common with the use of PT monostrands. These tests also showed that the CR frame is more sensitive to unbalanced PT force effects than frames FR and NZ, for at rest conditions, due to the inherent instability of HBE-to-VBE pin connections. Furthermore, full relaxation of PT elements at the closing joint for the NZ frame was observed and did not have a detrimental effect on frame response. Finally, experimental and analytical results of global frame response (i.e., base shear versus roof drift) were found to be comparable. In particular, the analytical models that best matched the experimental results included bi-directional compression strength of the infill web plate of approximately 20% and 10% of the tensile yield strength of the infill plate for the infill web plate and for the infill web strip configurations, respectively. However, note that the 10% used for the infill web strip was intended to account for the hysteretic response of the PT boundary frame (due to friction). By inference, this suggests that the actual compression strength of the infill web plate is approximately 10% of the tensile yield strength of the infill web plate.





## SECTION 7

### SCALED SHAKE-TABLE EXPERIMENTAL RESULTS

#### 7.1 General

This chapter presents the experimental results for the one-third scaled shake-table tests. In particular, the loading protocol and observations are provided in Section 7.2. The dynamic frame properties are presented in Section 7.3. The results for frame FR and NZ are provided in Sections 7.4 and 7.5, respectively, and a comparison of global response between frame types is provided in Section 7.6. Furthermore, results from a final test performed with frame NZ using a perforated infill web plate and an alternative bolted connection is presented in Section 7.7. Also, the response of the infill web plate and strips are highlighted in Section 7.8. A comparison between experimental and numerical results is presented in Section 7.9 and a general summary of results is provided in Section 7.10.

Note that many of the general observations on response and explanations for the FR and NZ frames provided for the quasi-static tests (in Section 6) also apply for the shake-table test results. When overlap in observations exists, observations for the shake-table tests will be provided concisely without detailed explanation. Any response that is unique to the shake-table tests, or that provides additional evidence and/or clarifies the response observed in the quasi-static tests, will be presented in further details. Furthermore, the nomenclature used to present the shake-table results is identical to that defined earlier for the quasi-static tests.

#### 7.2 Loading Protocol and Observations

The specimens for shake-table testing were presented in Section 4. The nomenclature used to differentiate each test specimen was defined previously, except for the additional letter used in one of the acronyms used in the shake-table tests, namely “P” referring to the test with a perforated infill web plate at Level 1 (Levels 2 and 3 same as frame NZW). The tests were performed sequentially as follows: FRW, FRB, FRS, NZW, NZB, NZS, and NZP. Furthermore, in all shake-table experimental results, a positive drift corresponds to an Eastward drift direction (note that this is an opposite sign convention to the one used for the quasi-static tests).

Also note that, similarly to what was done for the quasi-tests, each PT boundary frame type was constructed only once. This means that, through each frame test sequence (i.e., FRW, FRB and FRS), no alterations were made to the PT elements from the initial frame construction; as such, PT losses are cumulative and carry over to each subsequent test of each sequence.

### **7.2.1 Experimental Loading Protocol and General Observations**

As presented in Section 4, a spectra-compatible synthetic ground motion (GM) was generated for use in the shake-table tests. The loading protocol consisted of amplitude scaling the GM, starting with low level amplitude intensities followed by subsequent ground motions with increased scaled amplitudes. Furthermore, for the frames with infill web plates and strips, the tests concluded with the GM scaled to a level representing a moderate level aftershock, to investigate frame response after the infill web plates/strips have yielded significantly. To quantify changes in dynamic properties, white noise identification tests were conducted prior to each GM amplitude and at the conclusion of each test series. Testing continued by scaling GM up to the safe operating limits of the shake-table, determined by monitoring the overturning moment and base shear demands of the test specimen. Accordingly, the loading protocol was modified as needed during the course of each test for safety reasons. Additionally, periodic pauses were performed between GM amplitudes to monitor infill web plate damage and to make general visual observation assessments of the test specimens. However, for safety reasons, the shake-table hydraulics was shut down prior to providing visual assessments between GM amplitudes. Consequently, the number of visual inspections provided for each test was limited, due to time constraints.

The resulting loading protocols with general observations are provided in tables 7-1 through 7-7 for each test conducted. Figures 7-1 and 7-2 shows the general deformation at each level for an infill web plate and infill web strip condition, at the start and end of a typical test; results are similar for both frame FR (shown) and NZ. Furthermore, limited field measurements of the infill web plate tearing from the boundary frame were made, and are provided in figures 7-3 and 7-4 for frame FRW and NZW respectively. It is observed that infill web plate tearing was minor. However, maximum roof drifts for these two tests did not exceed 2%. As a reference, recall that moderate to significant web plate tearing was not observed until after approximately 2% to 2.5%

for the quasi-static tests. In comparison, no tearing of the infill web strips occurred (which was also the case for the quasi-static tests).

**TABLE 7-1 Shake-table test #1 loading protocol and observations**

Test Frame FRW					
GM Amplitude	Label	Excitation	PGA		Observations
			% GM	g	
1	frw1wn1	WN	-	0.1	integrated accelerometer ABX3 at level HBE and checked with against L3 string pots as a spot check, results are comparable
1b	frw1wn1b	WN	-	0.15	approx. f1 = 2.9 Hz level 3
2	frw2e010	EQ	10	0.07	-
3	frw3e025	EQ	25	0.178	-
4	frw4wn2	WN	-	0.15	approx. f1 = 2.25 Hz
5	frw5e050	EQ	50	0.356	-
6	frw6wn3	WN	-	0.15	approx. f1 = 1.7 Hz
7	frw7e075	EQ	75	0.534	-
8	frw8wn4	WN	-	0.15	approx. f1 = 1.25 Hz
9	frw9e100	EQ	100	0.712	-
10	frw10wn5	WN	-	0.15	approx. f1 = 1.1 Hz
11	frw11e120	EQ	120	0.854	-
12	frw12wn6	WN	-	0.15	approx. f1 = 1.1 Hz
13	frw13e140	EQ	140	0.997	tightened all bolts on diaphragm connections; some pin holes observed in level 1 web plate
14	frw14wn7	WN	-	0.15	-
15	frw15e050	EQ	50	0.356	-
16	frw16wn8	WN	-	0.15	-

**TABLE 7-2 Shake-table test #2 loading protocol and observations**

Test Frame FRB					
GM Amplitude	Label	Excitation	PGA		Observations
			% GM	g	
1	frb1wn1	WN	-	0.1	approx. f1 = 1.31 Hz
2	frb2e010	EQ	10	0.07	-
3	frb3e025	EQ	25	0.178	resonance occurred and had to stop shake TABLE manually
4	frb4wn2	WN	-	0.1	approx. f1 = 1.12 Hz

**TABLE 7-3 Shake-table test #3 loading protocol and observations**

Test Frame FRS					
GM Amplitude	Label	Excitation	PGA		Observations
			% GM	g	
1	frs1wn1	WN	-	0.05	no trigger on pacific DAQ; approx.: f1 = 3.7 Hz; f2 = 11.6 Hz; f3 = 28 Hz
2	frs2wn2	WN	-	0.05	repeat WN to solve trigger issue - trigger working
3	frs3e010	EQ	10	0.07	-
4	frs4wn3	WN	-	0.05	approx.: f1 = 3.44 Hz; f2 = 11.3 Hz; f3 = 27 Hz
5	frs5e025	EQ	25	0.178	-
6	frs6wn4	WN	-	0.05	approx.: f1 = 3 Hz; f2 = 11 Hz; f3 = 27 Hz
7	frs7e050	EQ	50	0.356	-
8	frs8wn5	WN	-	0.05	approx.: f1 = 1.4 Hz; f2 = 6.7 Hz; f3 = none defined
9	frs9e075	EQ	75	0.534	-
10	frs10wn6	WN	-	0.05	approx.: f1 = 1.25 Hz; f2 = none defined
11	frs11e100	EQ	100	0.712	manual shut off of shake TABLE (shake TABLE in resonance)
12	frs12wn7	WN	-	0.05	approx.: f1 = 1.12 Hz
13	frs13e025	EQ	25	0.178	manual shut off of shake TABLE (shake TABLE in resonance)
14	frs14wn8	WN	-	0.05	approx.: f1 = 1 Hz

**TABLE 7-4 Shake-table test #4 loading protocol and observations**

Test Frame NZW					
GM Amplitude	Label	Excitation	PGA		Observations
			% GM	g	
1	nzw1wn1	WN	-	0.1	approx.: f1 = 4.19 Hz; f2 = 15.4 Hz
2	nzw2e010	EQ	10	0.07	-
3	nzw3wn2	WN	-	0.1	t = 40 sec (manual trigger); f1 = 4.06 Hz; f2 = 15.06 Hz
4	nzw4e025	EQ	25	0.178	automatic trigger working
5	nzw5wn3	WN	-	0.1	approx.: f1 = 3.81 Hz; f2 = 14.8 Hz
6	nzw6e050	EQ	50	0.356	-
7	nzw7wn4	WN	-	0.1	approx.: f1 = 3.81 Hz; f2 = 14.3 Hz
8	nzw8e075	EQ	75	0.534	-
9	nzw9wn5	WN	-	0.1	approx.: f1 = 3.06 Hz; f2 = 13.25 Hz
10	nzw10e100	EQ	100	0.712	-
11	nzw11wn6	WN	-	0.1	approx.: f1 = 1.94 Hz; f2 = not defined
12	nzw12e120	EQ	120	0.854	-
13	nzw13wn7	WN	-	0.1	approx.: f1 = 1.38 Hz; tightened diaphragm bolts
14	nzw14e140	EQ	140	0.997	-
15	nzw15wn8	WN	-	0.1	f1 - no change
16	nzw16e140	EQ	140	0.997	-
17	nzw17wn9	WN	-	0.1	approx. f1 = 1.1 Hz (stopped testing for the day and resume next day)
18	nzw18wn10	WN	-	0.1	resume testing; f1 = no change
19	nzw19e050	EQ	50	0.356	-
20	nzw20wn11	WN	-	0.1	f1 = no change

**TABLE 7-5 Shake-table test #5 loading protocol and observations**

Test Frame NZB					
GM Amplitude	Label	Excitation	PGA		Observations
			% GM	g	
1	nzb1wn1	WN	-	0.1	approx.: f1 = 0.875 Hz; f2 = 6.19 Hz
2	nzb2e010	EQ	10	0.07	-
3	nzb3e015	EQ	15	0.107	-
4	nzb4e020	EQ	20	0.142	-
5	nzb5e025	EQ	25	0.178	approx.: $\Delta 3 = 2.25'' = 1.5\%$ top story drift
6	nzb6e030	EQ	30	0.214	approx.: $\Delta 3 = 2.8'' = 1.9\%$ top story drift
7	nzb7e035	EQ	35	0.249	approx.: $\Delta 3 = 3.25''$ ; 2.2% top story drift
8	nzb8e040	EQ	40	0.285	approx.: $\Delta 3 = 4''$ ; 2.7% top story drift
9	nzb9e045	EQ	45	0.228	approx.: $\Delta 3 = 4.25''$ ; 2.87% top story drift
10	nzb10e050	EQ	50	0.356	approx.: $\Delta 3 = 5''$ ; 3.38% top story drift
11	nzb11wn2	WN	-	0.1	approx.: f1 = 0.75 Hz; f2 = no change

**TABLE 7-6 Shake-table test #6 loading protocol and observations**

Test Frame NZS					
GM Amplitude	Label	Excitation	PGA		Observations
			% GM	g	
1	nzs1wn1	WN	-	0.05	approx.: f1 = 3.6 Hz; f2 = 13.6 Hz
2	nzs2e005	EQ	5	0.036	-
3	nzs3wn2	WN	-	0.05	approx.: f1 = 3.44 Hz; f2 = 13.31 Hz
4	nzs4e013	EQ	13	0.093	-
5	nzs5wn3	WN	-	0.05	f1 = no change; f2 = no change
6	nzs6e025	EQ	25	0.178	-
7	nzs7wn4	WN	-	0.05	approx.: f1 = 3.25 Hz; f2 = 13 Hz
8	nzs8e038	EQ	38	0.271	-
9	nzs9wn5	WN	-	0.05	approx.: f1 = 1.75 Hz; f2 = 9 Hz (noticeable shift in transfer function)
10	nzs10e050	EQ	50	0.356	lost video feed on top east camera; 0.85% approx. top story drift
11	nzs11wn6	WN	-	0.05	parked TABLE to inspect - looks fine - all bolts still snug; approx.: f1 = 1.375 Hz; f2 = 5.87 Hz
12	nzs12e060	EQ	60	0.427	approx. 1.52% top story drift
13	nzs13wn7	WN	-	0.05	approx.: f1 = 1.25 Hz; f2 = no change
14	nzs14e070	EQ	70	0.498	approx. 2% top story drift
15	nzs15wn8	WN	-	0.05	approx. f1 = 1.06 Hz; f2 = no change
16	nzs16e090	EQ	90	0.641	approx. 2.43% top story drift
17	nzs17wn9	WN	-	0.05	approx. f1 = no change; f2 = no change
18	nzs18e100	EQ	100	0.712	approx. 3.38% top story drift
19	nzs19wn10	WN	-	0.05	approx.: f1 = 0.94 Hz; f2 = 6-7 Hz; stop test due to time and resume next day
20	nzs20e038	EQ	38	0.271	resume testing; approx. 2% top story drift
21	nzs21wn11	WN	-	0.05	f1 = no change; f2 = no change

**TABLE 7-7 Shake-table test #7 loading protocol and observations**

Test Frame NZP					
GM Amplitude	Label	Excitation	PGA		Observations
			% GM	g	
1	nzp1wn1	WN	-	0.10	approx.: f1 = 3.5 Hz; f2 = 16 Hz; f3 = 30.6 Hz
2	nzp2e015	EQ	15	0.11	-
3	nzp3wn2	WN	-	0.10	no change in frequencies
4	nzp4e025	EQ	25	0.178	integrated accelerometer ABX3 at level HBE and checked with against L3 string pots as a spot check, results are comparable
5	nzp5wn3	WN	-	0.10	approx.: f1 = 3.44 Hz; f2 = 15 Hz; f3 = 29.5 Hz
6	nzp6e050	EQ	50	0.356	-
7	nzp7wn4	WN	-	0.10	approx.: f1 = 3.25 Hz; f2 = 14.5 Hz; f3 = not present
8	nzp8e075	EQ	75	0.534	-
9	nzp9wn5	WN	-	0.10	approx.: f1 = 2.25 Hz; f2 = 12.8 Hz
10	nzp10e100	EQ	100	0.712	approx. 0.85% top story drift
11	nzp11wn6	WN	-	0.10	approx.: f1 = 1.5 Hz, f2 = 10 Hz
12	nzp12e0120	EQ	120	0.854	approx. 1.4% top story drift
13	nzp13wn7	WN	-	0.10	approx. f1 = 1.25 Hz
14	nzp14e0140	EQ	140	0.997	approx. 1.52% top story drift
15	nzp15wn8	WN	-	0.05	approx. f1 = no change
16	nzp16e0140	EQ	140	0.997	approx. 3% top story drift
17	nzp17wn9	WN	-	0.10	no change in frequencies
18	nzp18e050	EQ	50	0.356	approx. 1.68% top story drift
19	nzp19wn10	WN	-	0.10	-
20	nzp20e100	EQ	100	0.712	approx. 2.7% top story drift
21	nzp21e120	EQ	120	0.854	approx. 3% top story drift
22	nzp22wn11	WN	-	0.10	-



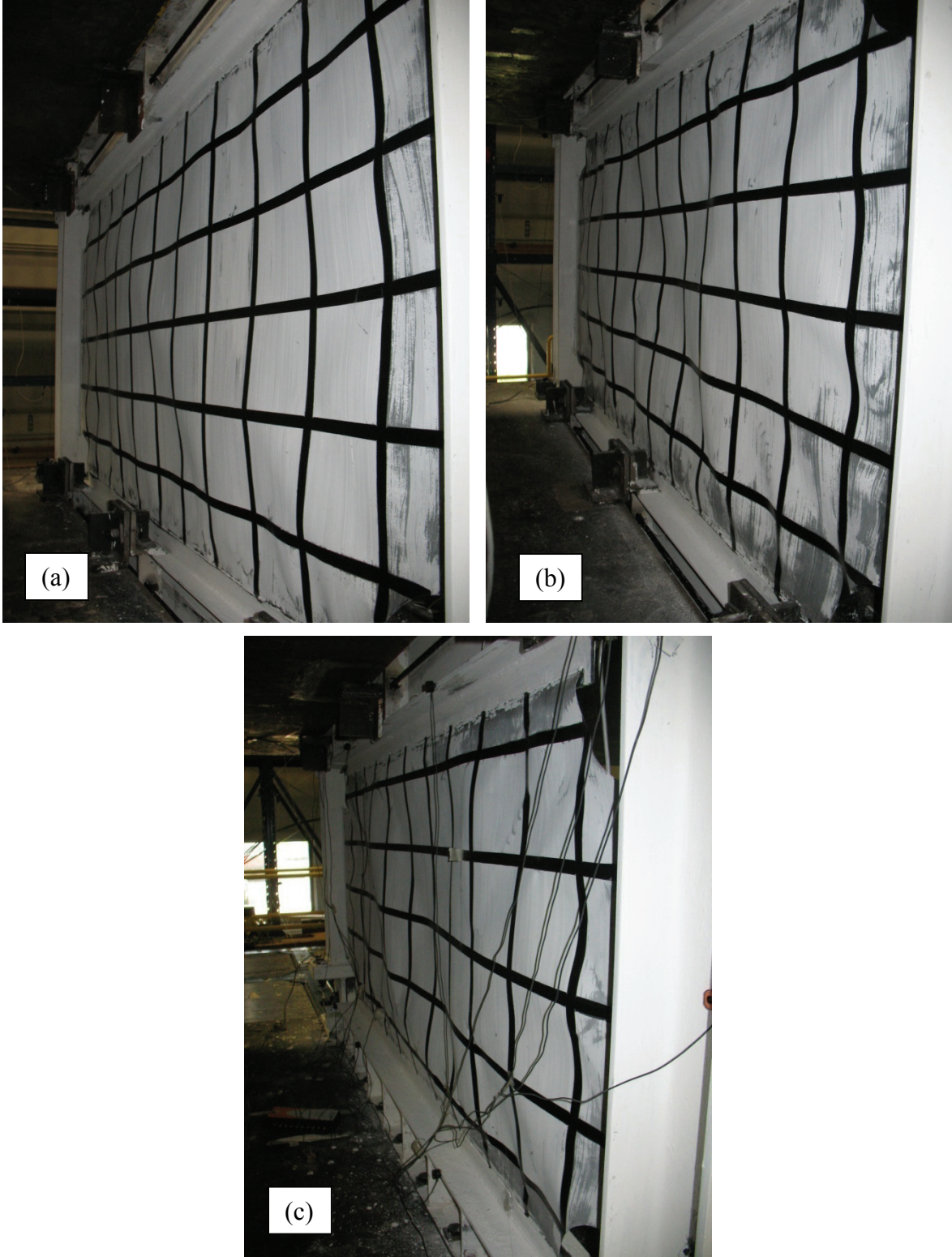


**FIGURE 7-1 Infill web plate deformation: (a) Level 3; (b) Level 2; (c) Level 1**

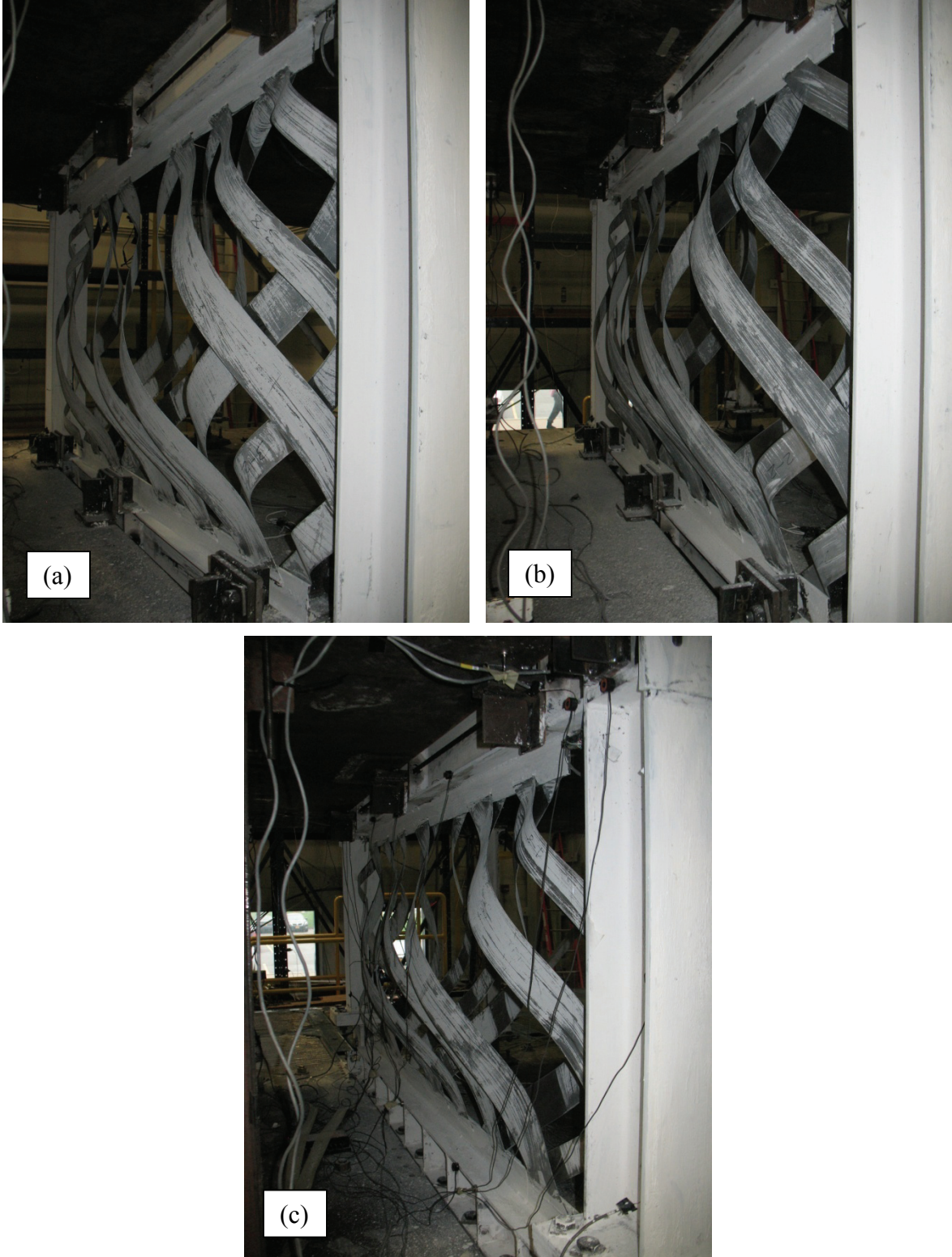
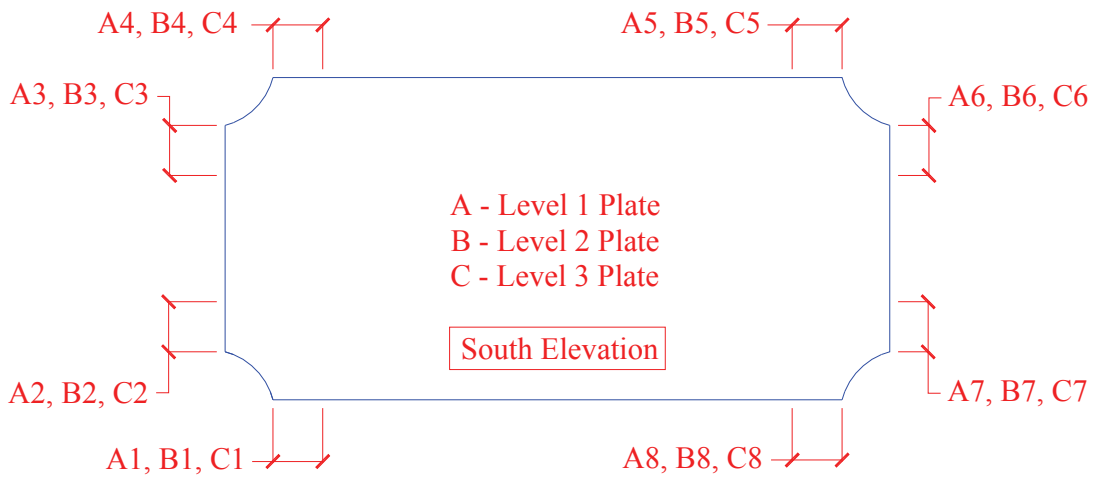


**FIGURE 7-2 Infill web strip deformation: (a) Level 3; (b) Level 2; (c) Level 1**



Web Plate Tearing Legend

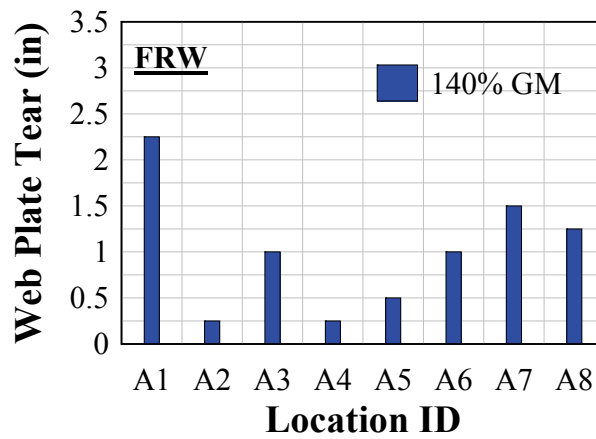
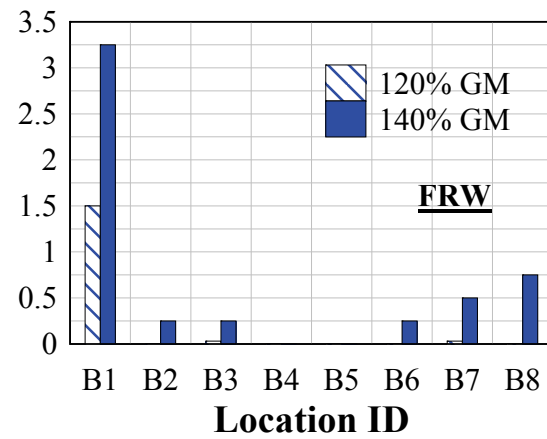
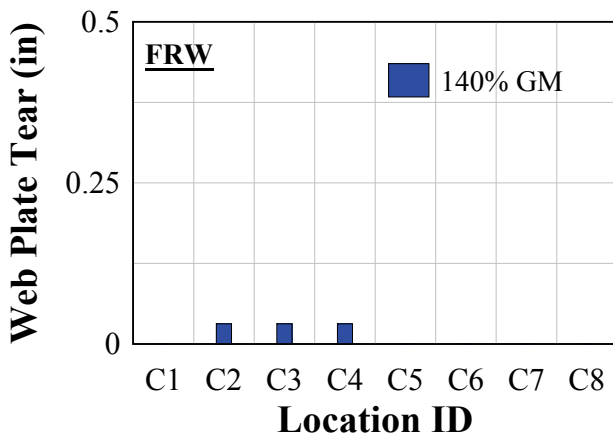
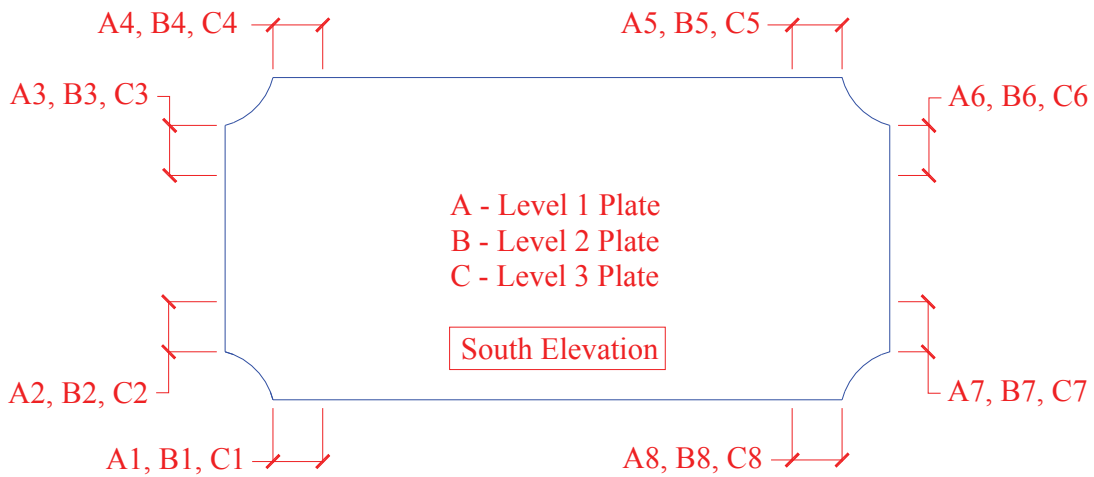


**FIGURE 7-3 Frame FRW - infill web plate tearing**



Web Plate Tearing Legend

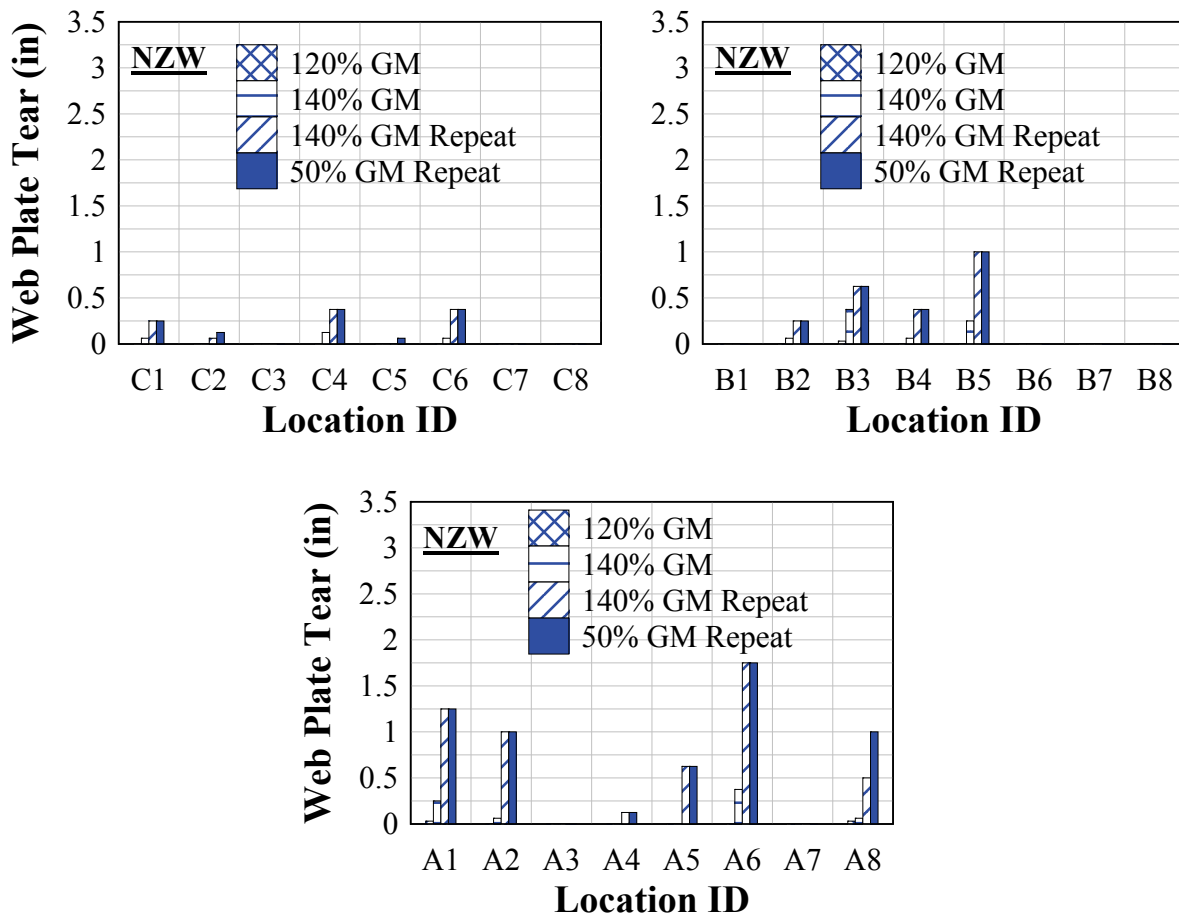
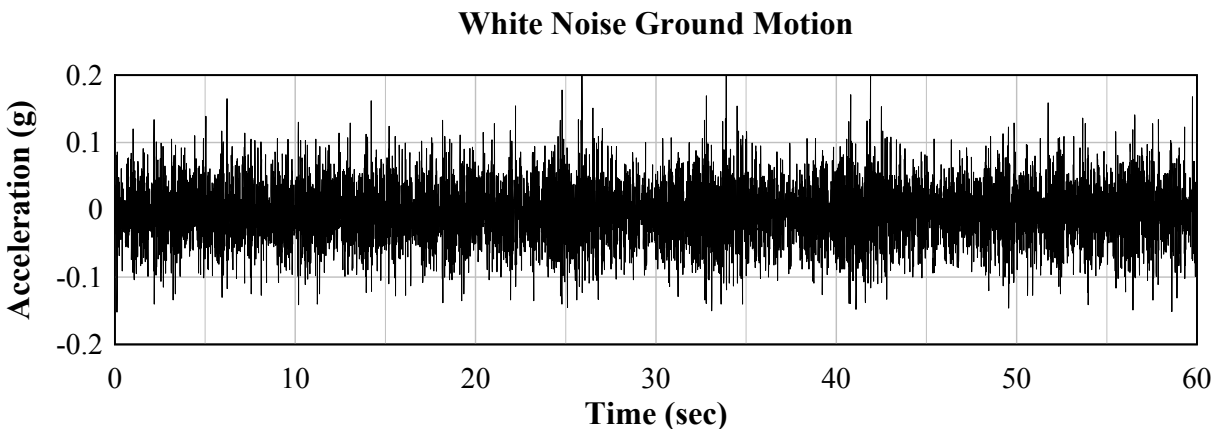


FIGURE 7-4 Frame NZW - infill web plate tearing

### 7.3 Dynamic Properties

#### 7.3.1 Frame Dynamic Properties

The dynamic properties of the test frames were obtained by conducting white noise identification tests as indicated in the loading protocols referenced above. A sample white noise base excitation is shown in figure 7-5. The excitation is a superposition of an indefinite number of random signals, the goal being to excite all significant frequencies that may contribute to frame response. For each white noise test, the corresponding acceleration response in the time domain was then used to obtain the transfer function characterizing the response of the test specimen in the frequency domain, where a transfer function is defined as the Fourier Transform of a story level acceleration time history (i.e., the output) normalized by the Fourier Transform of the base acceleration time history (i.e., the input). The dominant natural frequencies (or inversely the periods) were then identified as the peaks of the resulting transfer functions. Furthermore, the mode shapes were obtained by the relative ratio of the corresponding peaks of the respective story level transfer functions, where the sign was obtained by the direction of the corresponding phase angle values.



**FIGURE 7-5 Sample white noise base excitation**

The fundamental natural periods for the initial elastic conditions is shown in figure 7-6 along with the analytical values presented in Section 4. It is observed that the experimental values are comparable for frames NZW, NZS, and FRS. However, there is a larger disparity in comparison with the experimental results with frames NZB, FRB and FRW. Furthermore, it is also observed

that the period for frame FRW is larger than frame NZW, which should not have been the case for the frame design parameters. These latter discrepancies in expected results could not be rigorously explained with the available data, in spite of best efforts.

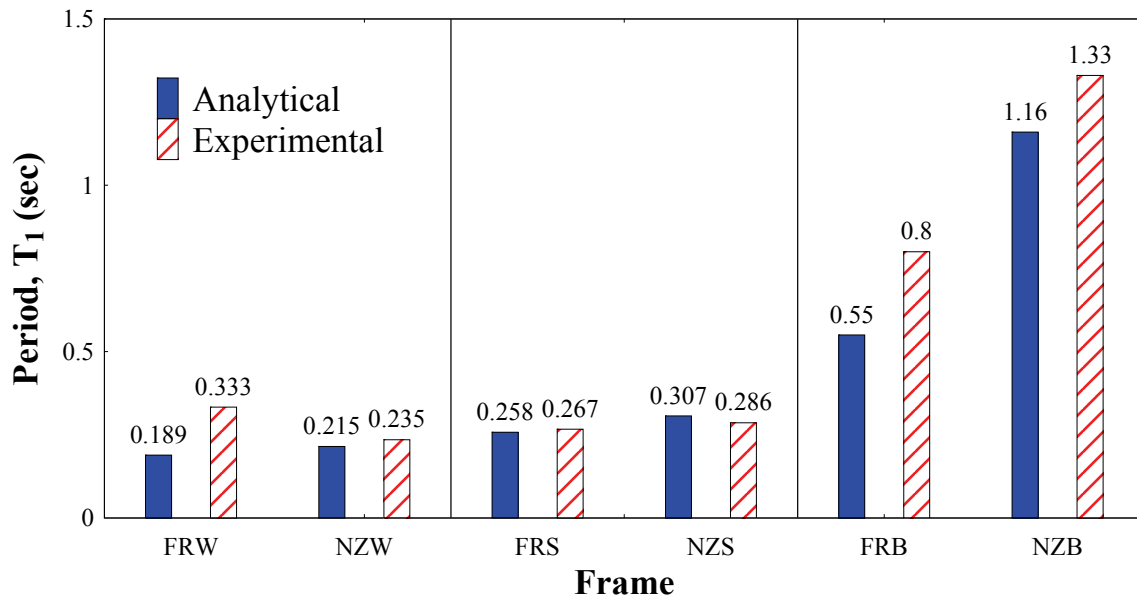
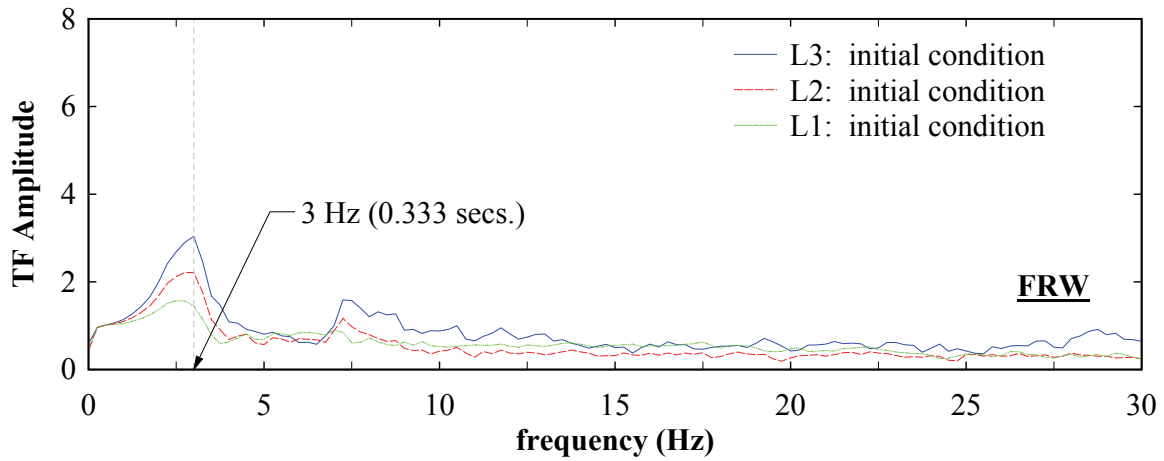
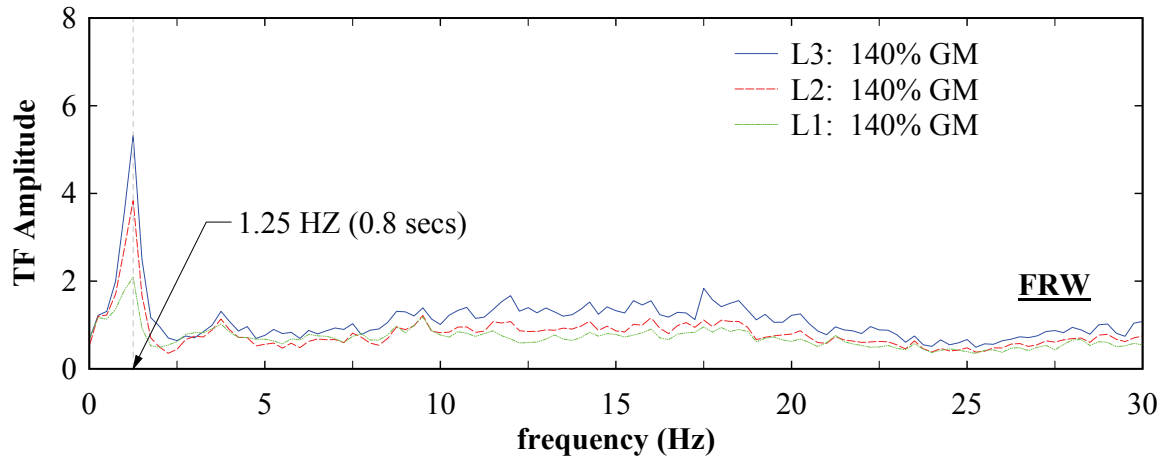


**FIGURE 7-6 Experimental versus Analytical – elastic fundamental period**

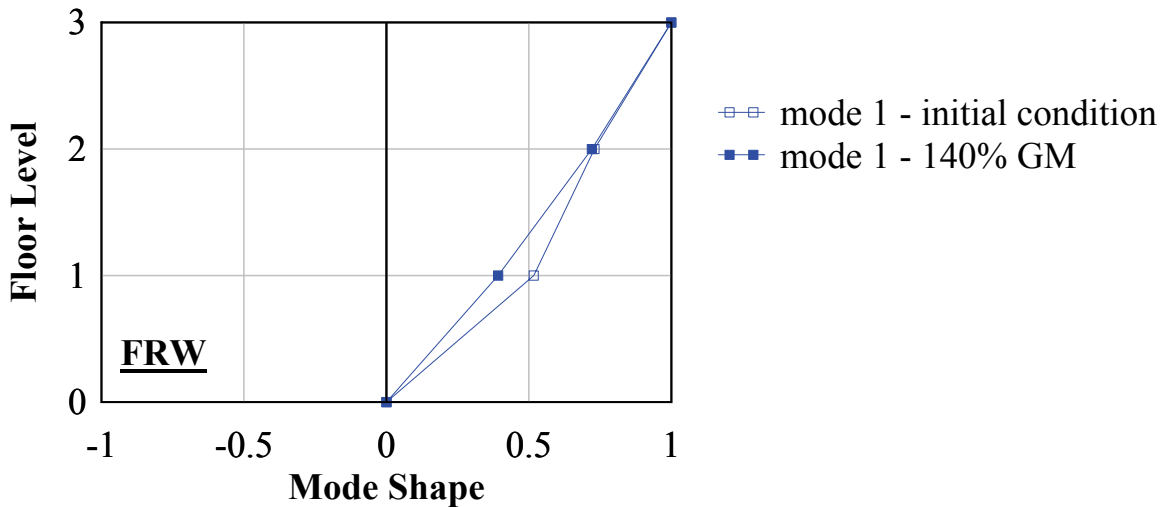
The transfer functions at each story level and corresponding mode shapes for the different test specimens are shown in figures 7-7 to 7-12. The results are shown for the initial elastic condition and after the first largest intensity GM amplitude noted in the figures (i.e., the “first” since some GM amplitudes were repeated). Note that there is no period change for frame FRB, which is expected given that all FRB tests were elastic tests. Furthermore, for frame FRW and FRS, after significant yielding of the infill web plate/strips, the dynamic response of the frame becomes dominated by that of the PT boundary frame alone (i.e., as evidenced by the progressive shift of the fundamental period, between GM amplitudes, towards that of frame FRB). Similarly, for frame NZB, there is no change in the fundamental period for that test. However, for frame NZW and NZS, the fundamental period at significant infill web plate/strip yield are both less than that of frame NZB; indicating that there is still some reserve strength of the infill web plates/strips. With further yielding (subject to additional GMs of larger amplitude intensity), it is expected that the period shift of frame NZW and NZS would further approach and eventually closely match that of frame NZB.



(a)

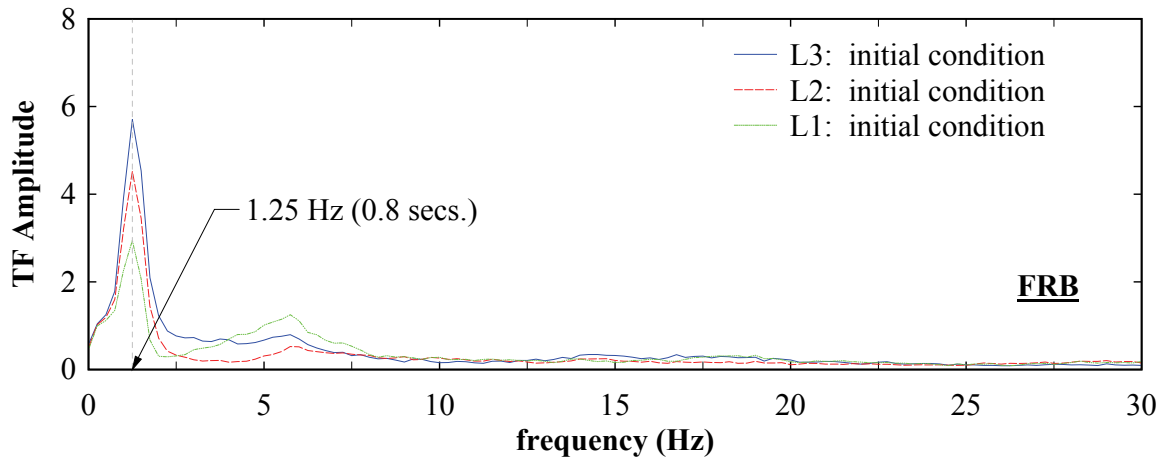


(b)

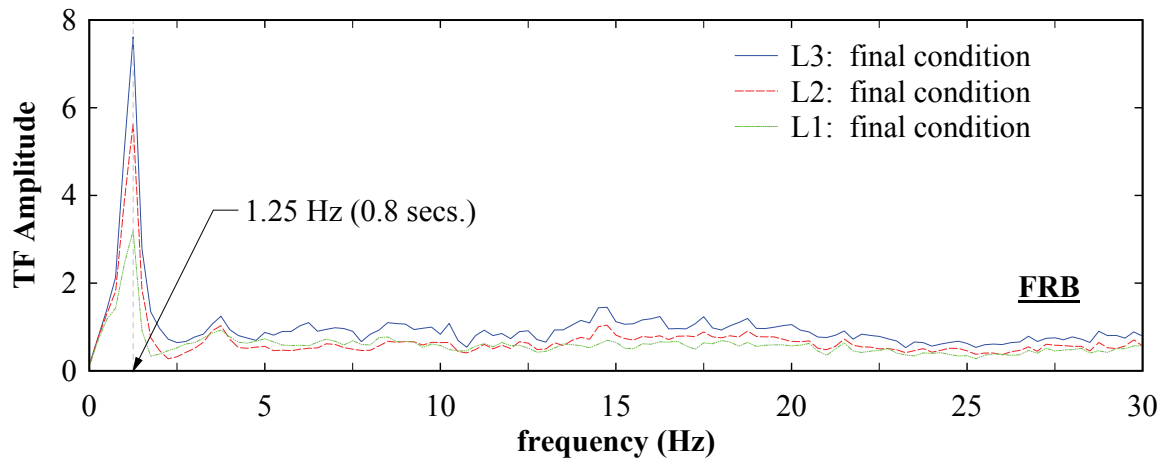


(c)

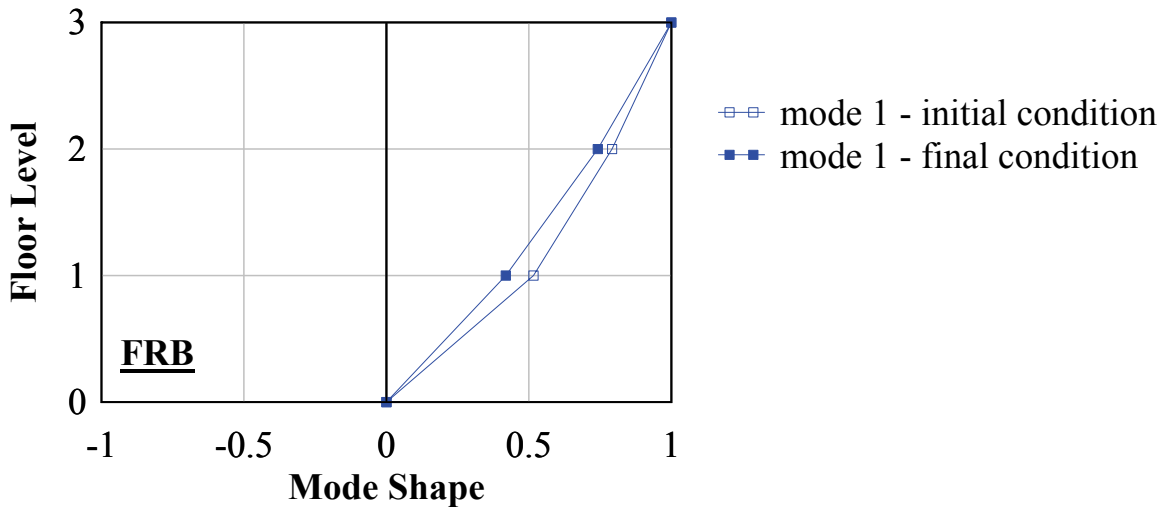
**FIGURE 7-7 FRW: (a) Transfer function elastic; (b) Transfer function inelastic; (c) Mode shapes**



(a)



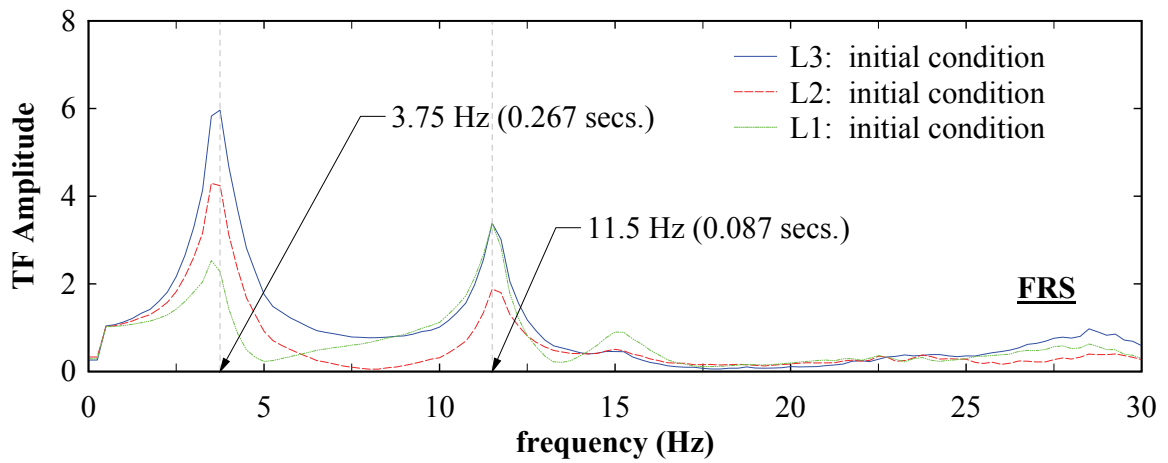
(b)



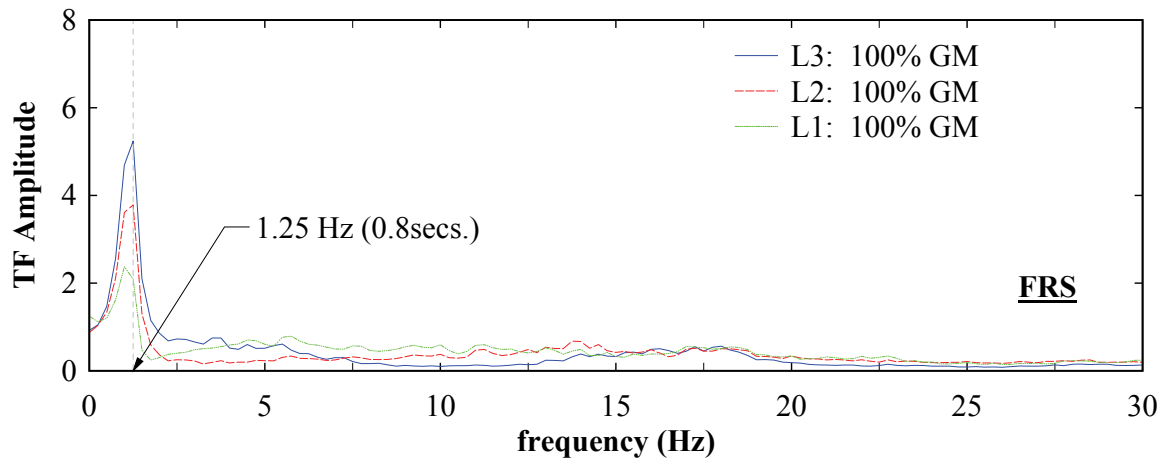
(c)

**FIGURE 7-8 FRB: (a) Transfer function elastic; (b) Transfer function inelastic; (c) Mode shapes**

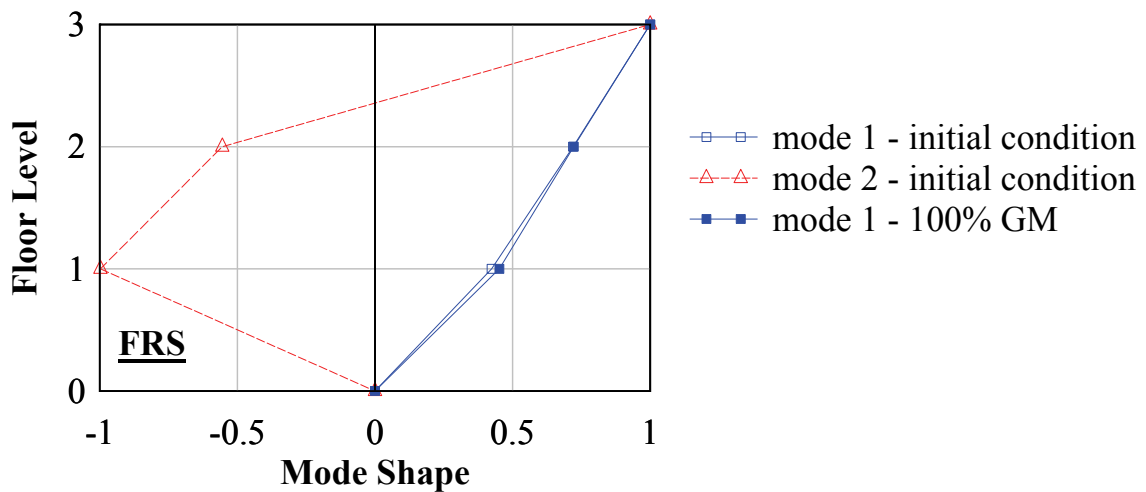




(a)

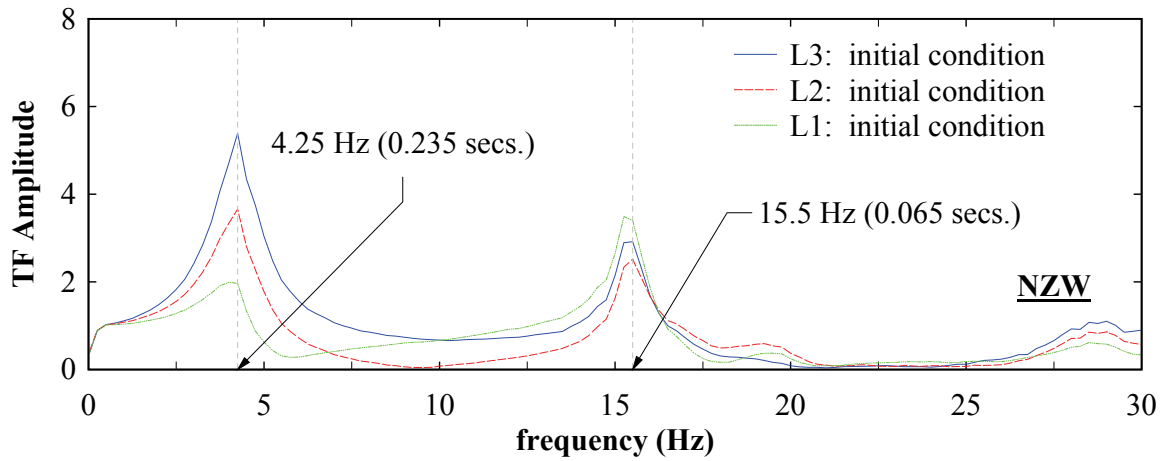


(b)

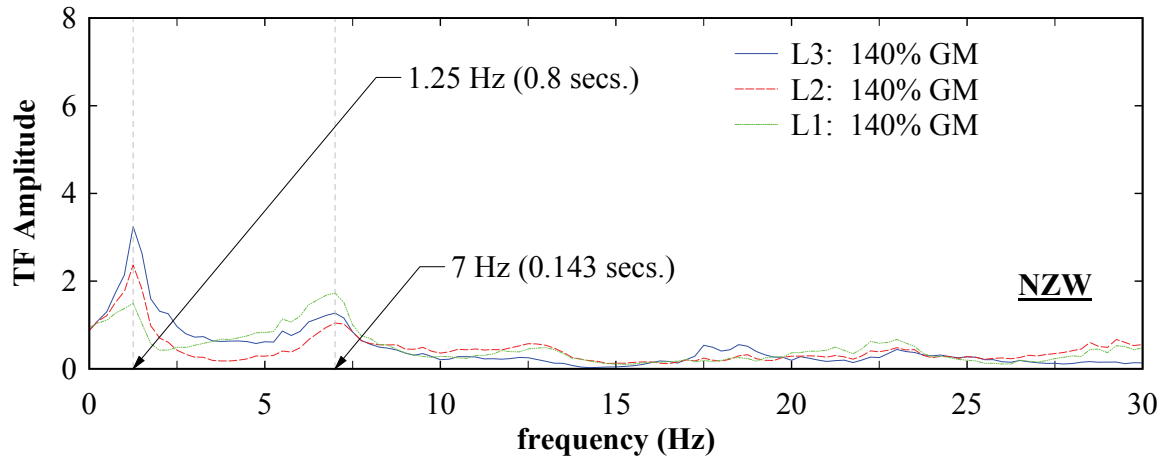


(c)

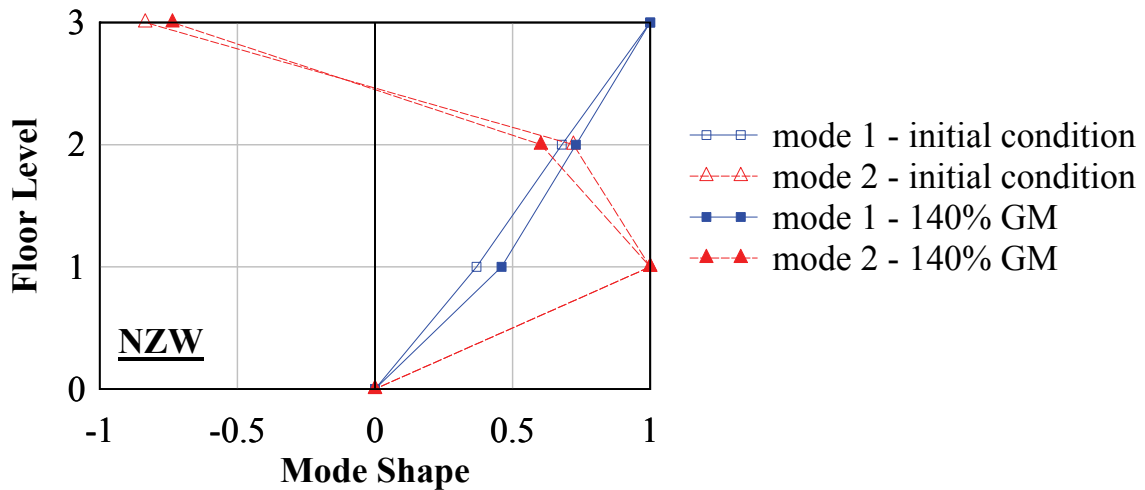
FIGURE 7-9 FRS: (a) Transfer function elastic; (b) Transfer function inelastic; (c) Mode shapes



(a)

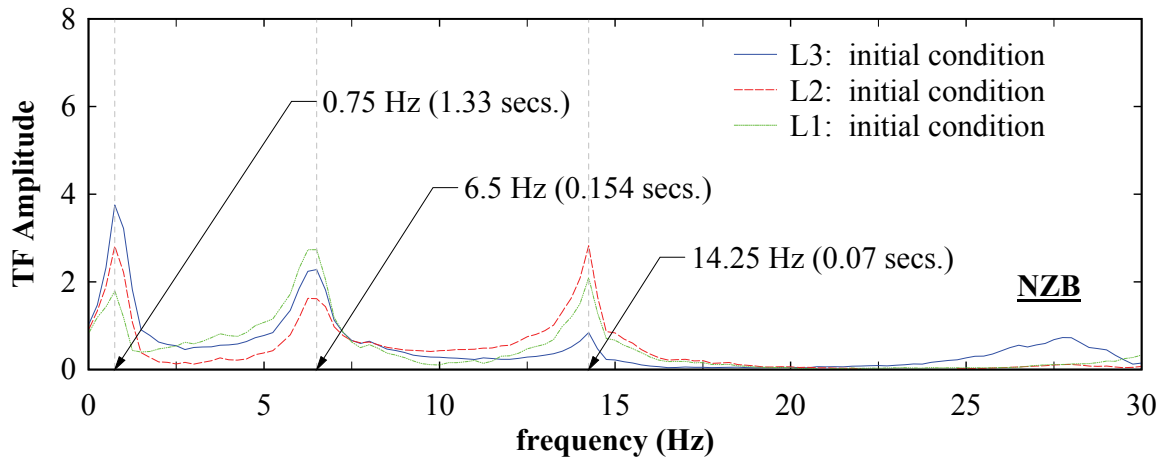


(b)

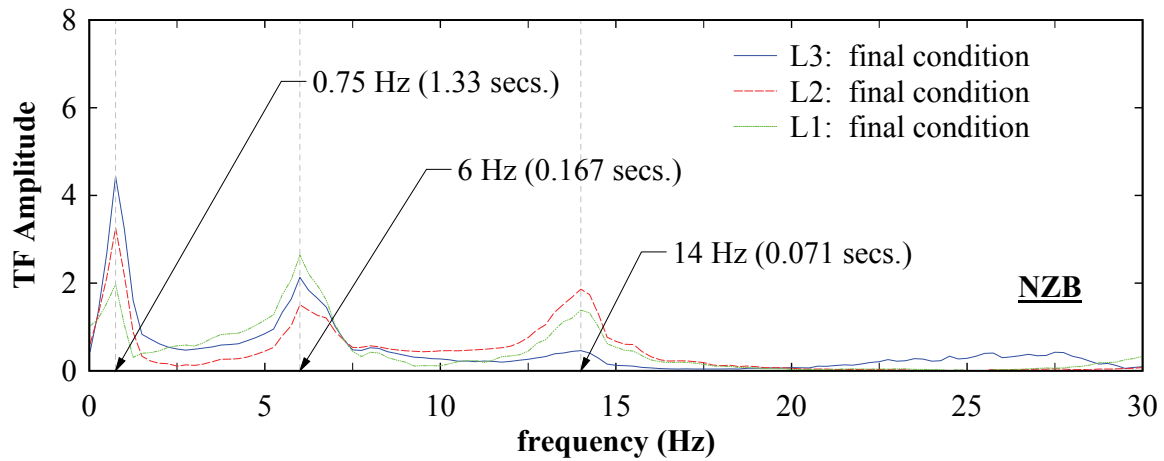


(c)

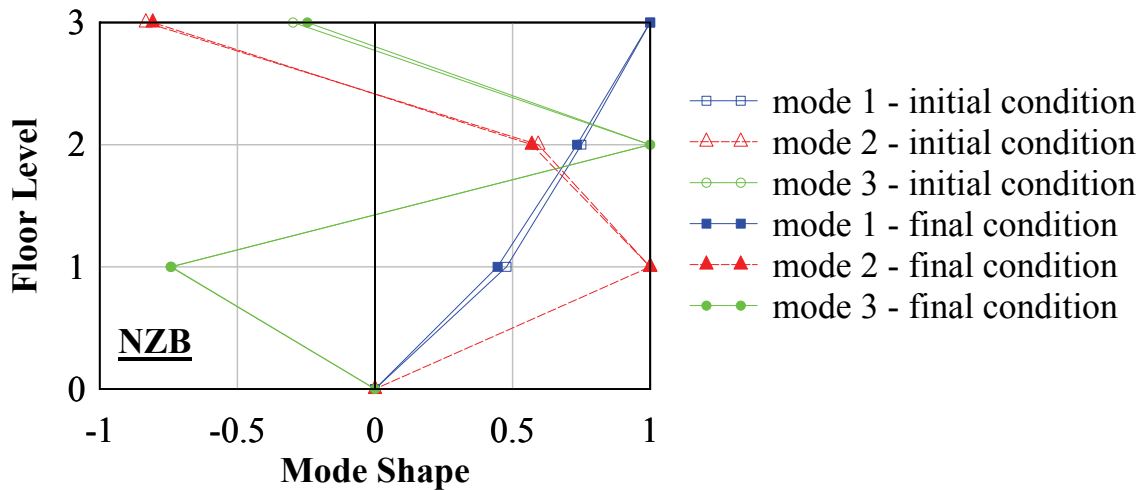
**FIGURE 7-10 NZW: (a) Transfer function elastic; (b) Transfer function inelastic; (c) Mode shapes**



(a)

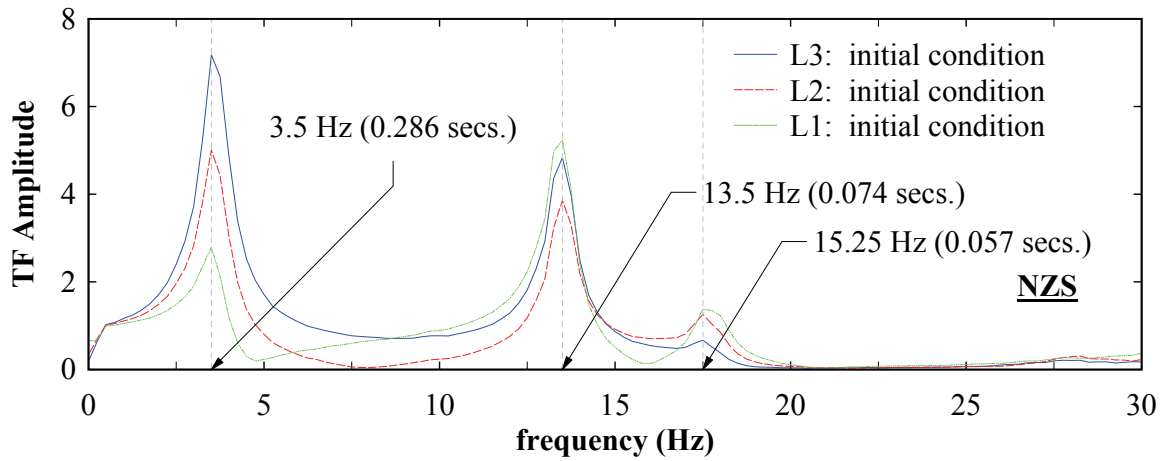


(b)

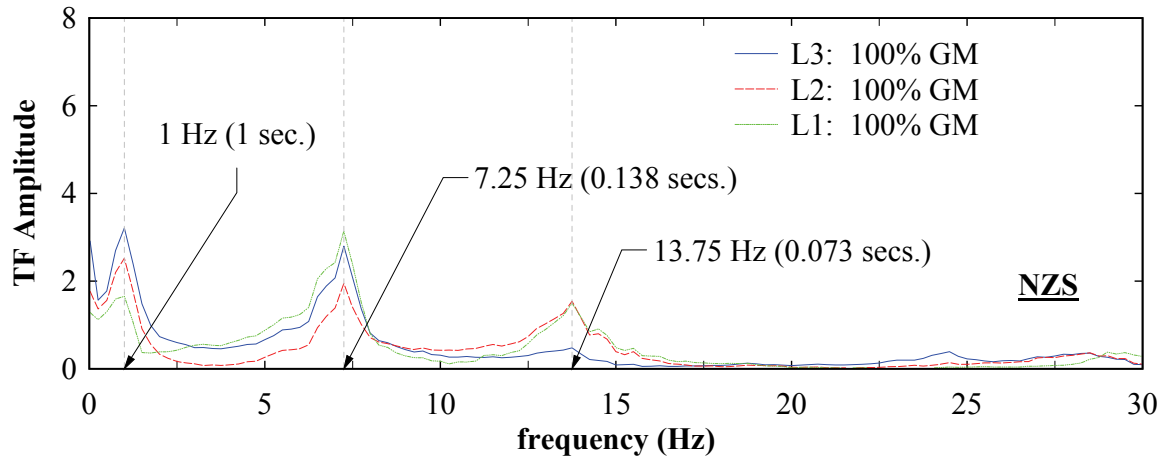


(c)

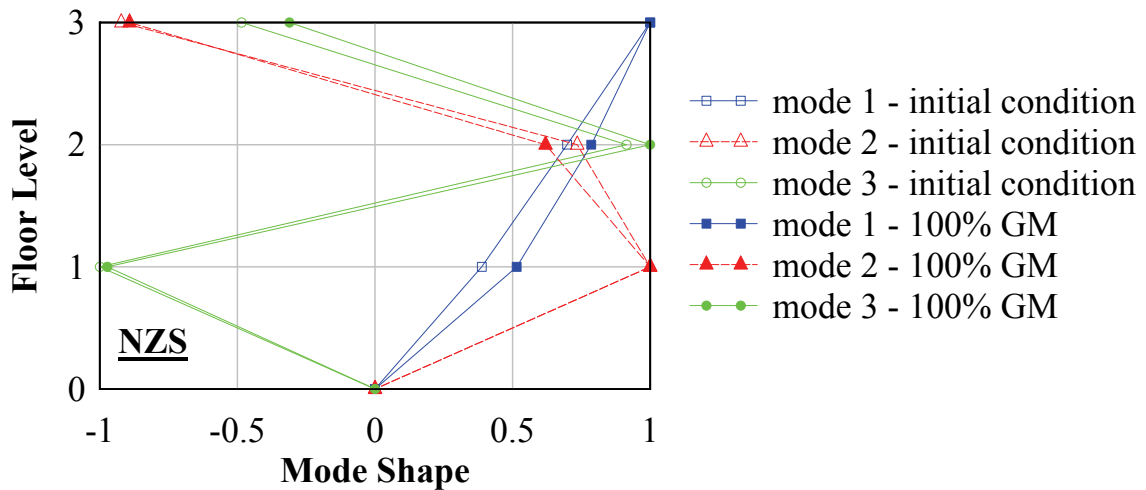
**FIGURE 7-11 NZB: (a) Transfer function elastic; (b) Transfer function inelastic; (c) Mode shapes**



(a)



(b)



(c)

**FIGURE 7-12 NZS: (a) Transfer function elastic; (b) Transfer function inelastic; (c) Mode shapes**

Furthermore, the equivalent viscous damping ratios were calculated using the half-band width method (Chopra, 2007). It was found that the calculated values were significantly larger than what would be deemed appropriate for bare steel structures, where the damping ratio is generally in the range of 1 to 3%. In particular, the average initial condition elastic damping ratio calculated was approximately 15% for the frames with infill web plates and strips. For the bare frame tests, an average initial condition elastic damping ratio of approximately 25% was calculated. The large discrepancy with the experimental values calculated, in part, could be attributed to the frequency resolution used to calculate the transfer functions. In particular, if the peak of the calculated transfer function is lower than the actual peak, an overestimation of the damping ratio can occur (as the transfer function curve for the lower peak could be wider).

However, another possibility could be attributed to the effects of the shake-table extension frame in effecting the damping of the total system (i.e., test frame and setup plus table-extension frame). To provide some evidence of this, as noted in table 7-3, resonance (in rocking) of the shake-table and the test specimen occurred at GM amplitude 11 and 13 for frame FRS. As a consequence, manual shut-off of the shake-table was initiated. This occurrence has the benefit that usable free vibration data was collected while the shake-table was essentially at rest. Accordingly, figure 7-13 shows the roof drift history along with the corresponding acceleration time history of the shake-table extension for GM amplitude 13. As shown in the figure, using the portion of decay when the acceleration of the table extension is essentially zero, a damping ratio of approximately 3.4% was calculated using the logarithmic decay (Chopra, 2007). In comparison, the corresponding damping ratio calculated for the white noise base excitation that directly followed this test, was calculated to be approximately 25% using the half-band width method (which corresponds to the bare frame damping ratio noted above). Thus, it is concluded that the transfer function includes the acceleration response of both the test specimen and the shake-table extension. Note that for the typical earthquake test (where resonance did not occur), free vibration data was collected at the end of the input GM. However, the extent of free vibration data was sparse and deemed not reliable for calculations (otherwise this method would have been used to obtain all approximate equivalent viscous damping ratios).

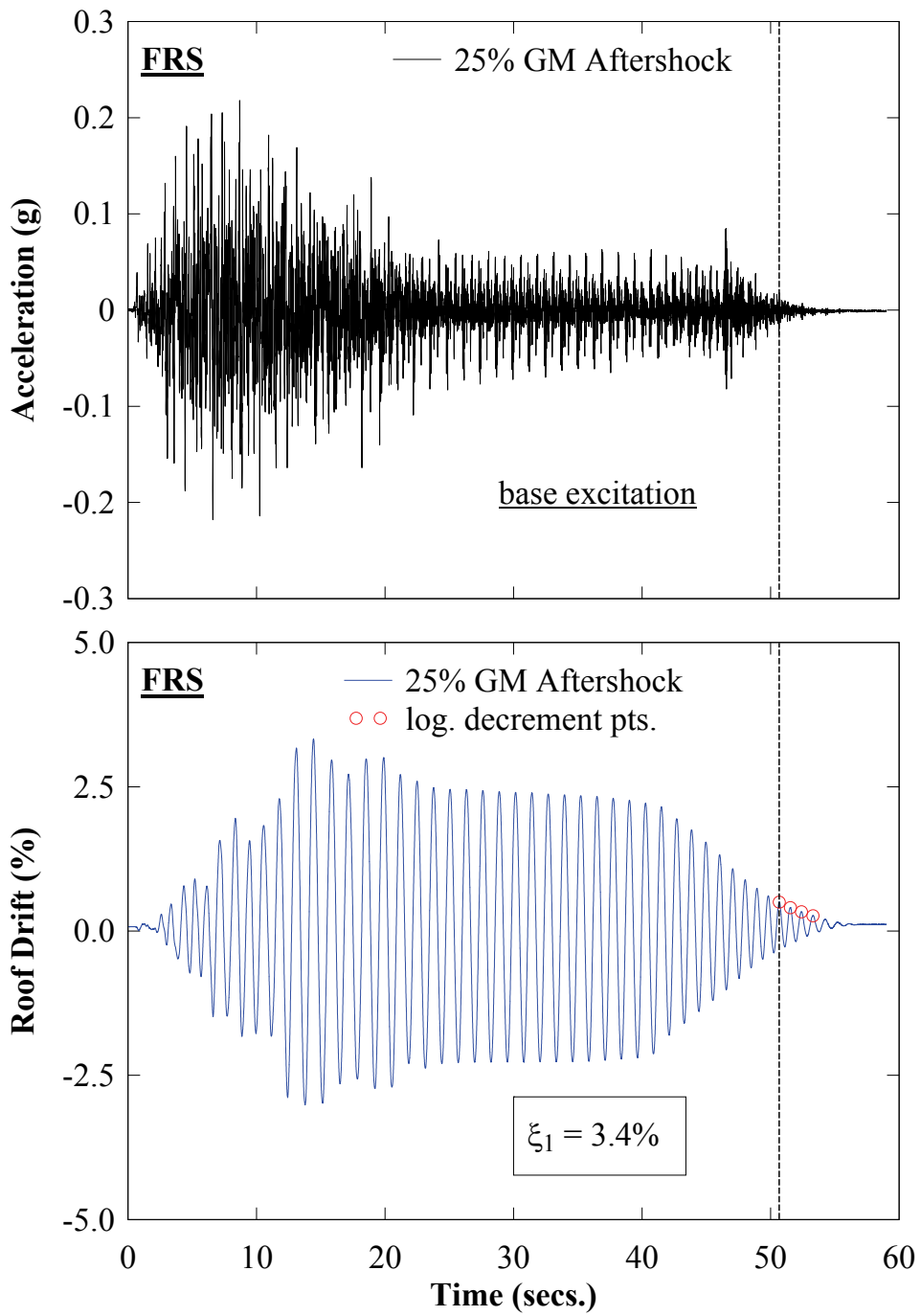
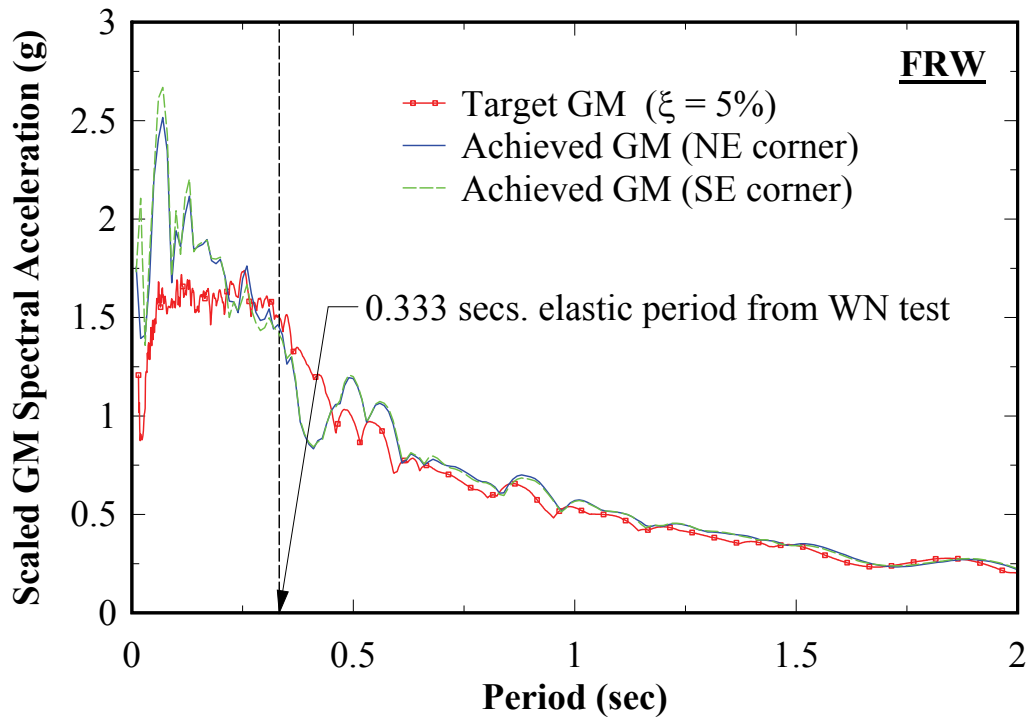


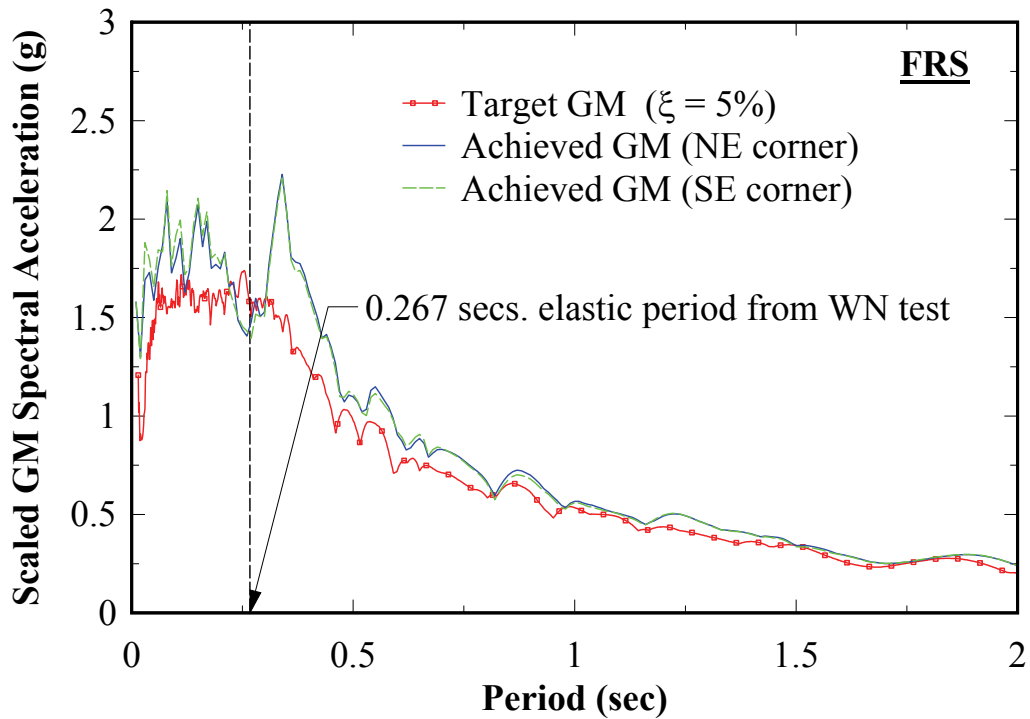
**FIGURE 7-13 Frame FRS - Logarithmic decay equivalent viscous damping**

### **7.3.2 Ground Motion Frequency Content**

A comparison of the target and achieved acceleration response is shown in figures 7-14 and 7-15 for the FR and NZ frames respectively for the 100% GM, assumed to be generally representative of the fidelity achieved in all tests. The comparison is provided in terms of acceleration response spectra. For this purpose, 5% damping is used, since this is the original criteria (and input parameter) that was used to generate the synthetic GM. The achieved acceleration response is taken from the accelerometer sensors located at the NE and SE corners of the shake-table extension, corresponding to the acceleration in the longitudinal frame direction (reference figure 5-26). Furthermore, the initial elastic fundamental period obtained from the corresponding white noise identification tests is superimposed for reference. In general, it is observed that the target and achieved spectra compare reasonably well in the anticipated period range of the test specimens (i.e., in the range of periods larger than the initial fundamental period shown). Additionally, it is observed that there were no significant GM base excitation torsional effects (here defined by multiplying the horizontal distance between the accelerometers by the difference in horizontal acceleration response of the two sensors, for a rotation about a vertical axis), since the acceleration response at opposite corners of the shake-table extension frame were essentially identical.



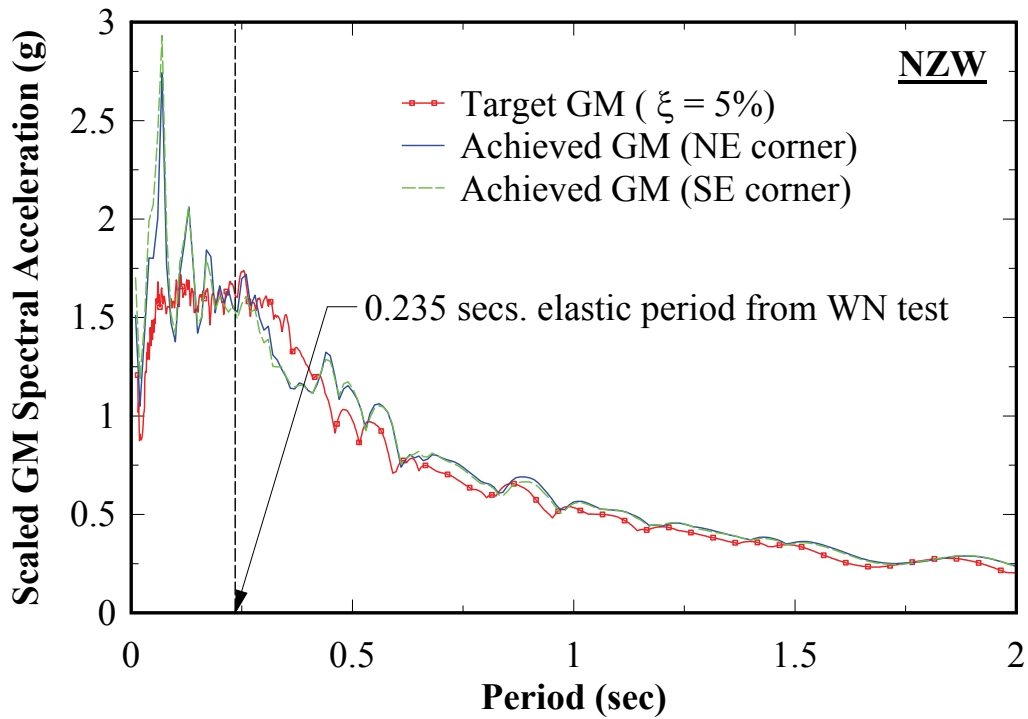
(a)



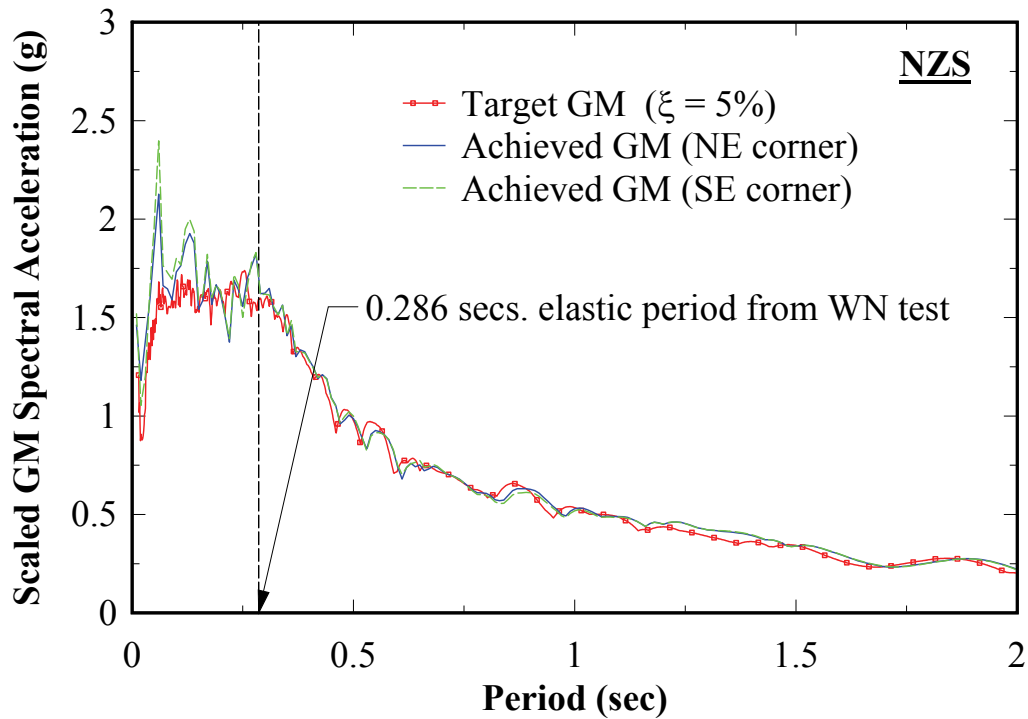
(b)

**FIGURE 7-14 Frame FR - Target versus achieved acceleration response spectra**





(a)



(b)

**FIGURE 7-15 Frame NZ - Target versus achieved acceleration response spectra**

## **7.4 Flange Rocking (FR) Frame Shake-Table Experimental Results**

### **7.4.1 FR: Global Response**

The global response in terms of base shear versus roof drift is presented, where the base shear was obtained as the summation of the total acceleration response at each story level, multiplied by the approximate mass at each corresponding level. Furthermore, the original acceleration data was modified using a low-pass filter with a cut off frequency of 20 Hz. The acceleration data was filtered due to the presence of undesired high frequency content observed using the original accelerometer data. The cut off frequency was chosen to ensure that the first two modes were present. This was based on a modal analysis performed on the analytical model, indicating that the modal participating mass ratio at the second mode was approximately 95%. Additionally, from the transfer functions presented earlier, at the roof level, it was also observed that the effects of the third mode are insignificant. A sample comparison of the global hysteretic response with the original and filtered data at the 50% and 100% GM for frame FRW, and 100% GM for frame FRS is shown in figure 7-16.

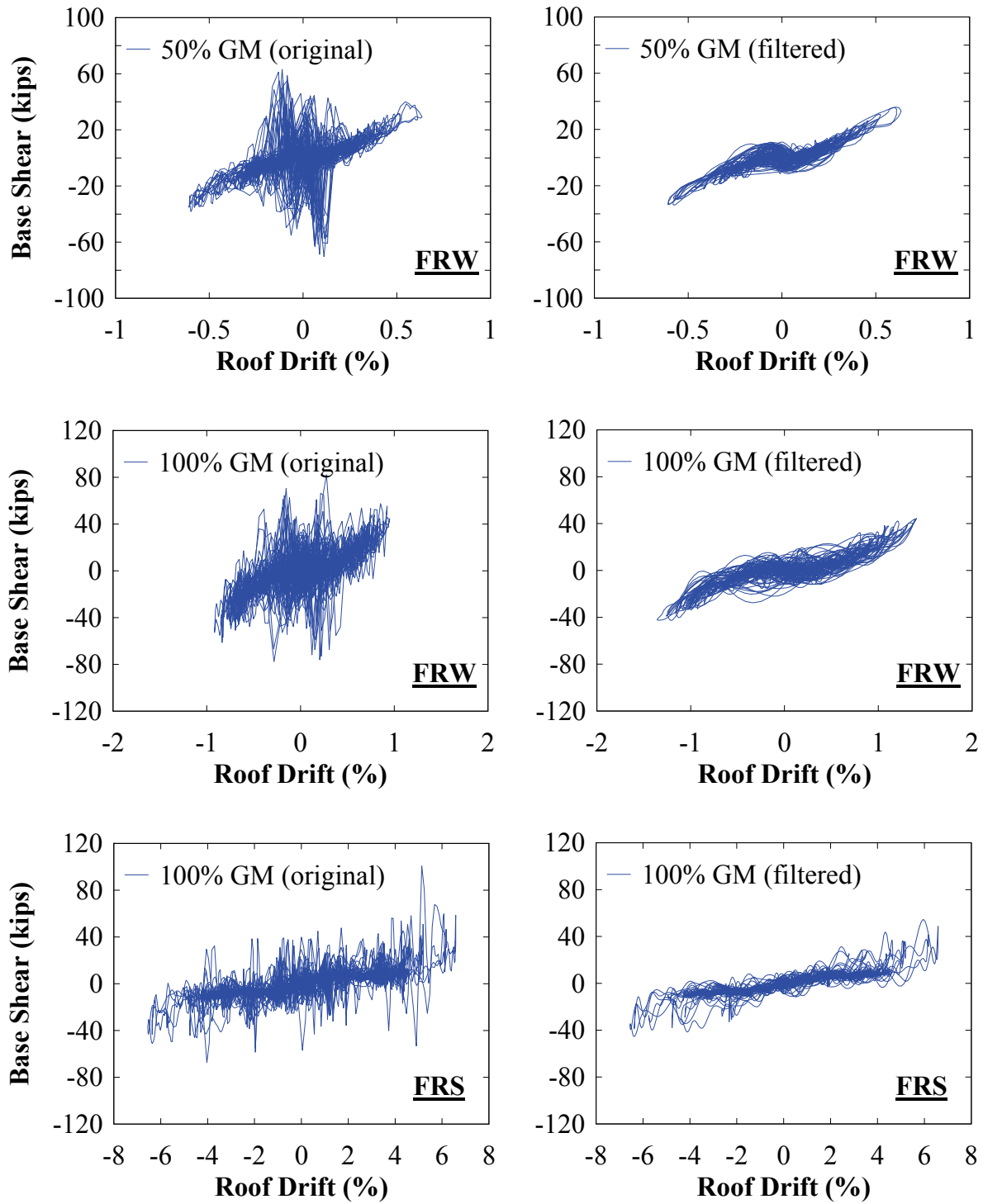


FIGURE 7-16 Frame FR - original versus filtered hysteresis

Furthermore, although the base excitation for the shake-table tests is in the primary longitudinal direction of the test specimen (i.e., in the horizontal West/East direction), some rotation about an axis perpendicular to the plane of the test specimen developed due to rocking effects of the shake-table as result of resisting the base reactions of the test specimen. As a consequence, the total linear displacements recorded by the string potentiometers used to measure story displacements, also include a horizontal component due to rotation of the shake-table, which is further compounded by the use of the extension frame. To further clarify, the additional horizontal displacement at the top of the test specimen due to rotation of the shake-table would be  $\Delta = (\theta)(h + d)$  where  $\theta$  is the recorded rotation of the shake-table in units of radians,  $h$  is the height of the test specimen from its base, and  $d$  is the depth of the extension frame and is approximately 36 inches. Accordingly, with the assumption of rigid body rotation as an approximation, the effects of the shake-table rotation as it translates to an additional horizontal displacement of the test specimen (i.e.,  $\Delta$ ), was removed from the string potentiometer data. By doing this, the frame drift response is more of a representation of effects due to inelastic deformation, and also provides a more appropriate comparison with analytical results (as the analytical models assume a rigid foundation). For reference, the shake-table rotation, together with corresponding absolute and corrected peak roof drifts are shown in tables 7-8 and 7-9, respectively, for frame FRW and FRS. Peak rotations of the shake-table typically ranged between 0.05 to 0.10 degrees, with a maximum of 0.15 degrees for FRW. As shown in this table, in some cases, rocking of the shake-table provided a noticeable increase in apparent roof drift, which is why the corrected drift values are used in this report.

**TABLE 7-8 Shake-table rocking roof drift effects – Frame FRW**

Frame FRW				
% GM	TABLE Rotation (deg)	Peak Roof Drift (%)		Comparison Ratio
		Original	Rocking Removed	Original/Rocking Removed
10	0.01	0.09	0.08	1.19
25	0.04	0.32	0.22	1.44
50	0.04	0.64	0.49	1.30
75	0.15	0.93	0.59	1.56
100	0.11	0.95	0.69	1.37
120	0.03	1.28	1.33	0.96
140	0.03	1.75	1.61	1.09
50	0.06	1.48	1.43	1.03

**TABLE 7-9 Shake-table rocking roof drift effects – Frame FRS**

Frame FRS				
% GM	TABLE Rotation (deg)	Peak Roof Drift (%)		Comparison Ratio
		Original	Rocking Removed	Original/Rocking Removed
10	0.01	0.10	0.07	1.31
25	0.03	0.25	0.19	1.34
50	0.04	0.74	0.61	1.23
75	0.08	1.96	1.79	1.10
100	0.10	6.59	6.34	1.04
25	0.02	3.33	3.27	1.02

The global base shear versus roof drift response using the filtered accelerations and removal of rotational effects of the shake-table is shown in figures 7-17, 7-18, and 7-19 at select GM amplitudes for frames FRW, FRB, and FRS respectively; note that, hereinafter, it is understood that the modified sensor data as noted is used in the presentation of all results, unless noted otherwise. The corresponding roof drift history is also provided to visually assess frame recentering. Given the typical code-specified 0.2% out-of-plumb construction tolerance, a maximum value of 0.2% residual roof drift was used here as the criterion for frame recentering. For convenience, this threshold is indicated by the horizontal dashed lines provided in the roof drift history figure, to facilitate visual assessment of whether recentering was achieved. It is also noted, that for tests FRB and FRS, resonance occurred with the shake-table and test specimen,

which is reflected in the roof drift response shown. At these GM amplitudes, the shake-table was shut-down manually before the full GM excitation history was complete.

The concatenation of all GM amplitude results of the global base shear versus roof drift response is shown in figure 7-20, along with the residual drifts at each GM amplitude for frame FR. In comparison results for frame FRW and FRS, the effect of the compression strength of the infill web plate is observed to provide a more uniform distribution of energy dissipation (i.e., by observation of the “fatness” of the hysteresis curve near the zero-drift location, recognizing that some of it may be due to the noise in the data). In contrast, for frame FRS, there is less energy dissipation near the zero-drift location due to the tension-only response of the infill web strips. To further clarify, figure 7-21 shows the respective response with the results of frame FRB superimposed, where the hysteretic response provided by the infill web plates/strips is that portion not overlapping the response of frame FRB. In particular, it is also observed in the figure, that the frame stiffness is dominated by the PT boundary frame for frame FRS, whereas the infill web plate provides substantial stiffness observed for frame FRW that overshadows the stiffness of the PT boundary frame. Furthermore, near the zero-drift axis, the hysteretic response is dominated by the PT boundary frame for frame FRS, whereas there is noticeably more energy dissipation for frame FRW.

Of significance, frame recentering is not affected by the compression strength of the infill web plates, as it was observed in the figure 7-20 for frame FRW, that recentering is achieved for all GM amplitudes (i.e. residual drift is less than 0.2% drift). This may be due to the fact that the inertia forces that develop help to overcome the compression stiffening effect observed in the static tests, but also because of the many smaller cycles of excitations that follow large cycles and occur after development of the compression strut effect (i.e., due to the buckled plate taking the form of a sort of corrugated shape when drifts exceed previously achieved values). Note also that the residual drifts shown in the figure are taken as the initial point of the subsequent white noise test that directly followed the earthquake test, where the frame is at complete rest, corresponding to the true residual drift. That is, in the roof drift response history plots shown earlier, although it is shown that recentering is achieved, the residual roof drift shown is at the point where instrumentation data collection was stopped (although the test specimen had not

come to a complete rest). Hence, the values shown in those plots are slightly larger than the true residual drift (shown in figure 7-20). Furthermore, for reference, the story shear versus interstory drift is shown in figure 7-22 for frame FRW and FRS, which provides a slightly cleaner hysteretic response more representative of a first mode response (i.e., for the global base shear versus roof drift plots, the effects of higher modes is more prevalent).

The incremental dynamic response is shown in figure 7-23 where the maximum absolute base shear versus roof drift is plotted for each GM amplitude; note that this point does not necessarily correspond to the same point (i.e., the maximum absolute base shear may occur at a drift smaller than the absolute maximum roof drift and vice versa). Also shown is the fundamental period for each GM amplitude obtained from the transfer function of the white noise tests conducted between GM amplitudes. For frame FRW, the maximum roof drift was approximately 1.6% which is relatively small compared to the 2% or 4% roof drift, respectively, typically expected for a DBE or MCE level earthquake. However, for perspective, recall that the prototype building (affecting the model frame) was adjusted due to operating limitations of the shake-table presented in Section 4. Furthermore, it is observed that at GM amplitude 4, the fundamental period remains constant and matches the fundamental period of frame FRB; which shows more clearly that after significant yielding of the infill web plate, the dynamic response of the frame at low amplitudes of vibration is dominated by the PT boundary frame, as noted earlier.

For frame FRB, which was designed to remain essentially elastic, it is observed that the incremental dynamic pushover response curve is bi-linear. This indicates that at the 10% GM amplitude tests, the HBE-to-VBE joints remained closed (i.e., no gap opened at the frame joints, effectively making the PT boundary frame stiffness similar to that of a rigid moment frame); the same joints opened during the 25% GM amplitude tests, producing elastic PT elongations, resulting in the secondary reduced PT boundary frame stiffness. Furthermore, the period remains constant; indicative of an elastic response, as expected of the PT boundary frame.

For frame FRS, the maximum roof drift was approximately 6.3%, which is approximately four times that of the maximum drift corresponding to frame FRW; this was due to the unexpected occurrence of resonance noted earlier. In light of this occurrence, this showed that the PT boundary frame was able to fully recenter for drift levels much larger than drifts anticipated at

MCE level events. Furthermore, after the last GM amplitude, an increase in period occurred, from 0.8 (period of the PT boundary frame) to 1 seconds. This may have been a consequence of a slight loosening of connections during resonance response, but this was not investigated.

Furthermore, it is also observed (figure 7-23) that the period shift for frame FRS to the value matching the fundamental period of frame FRB occurred at the end of GM amplitude 3 (50% GM). In particular, this is the point on the incremental dynamic response curve where noticeable yielding occurred (by visual observation of the curve's change in slope). Consequently, with subsequent white noise base excitation (at low vibration amplitudes), the response of the frame was dominated by the PT boundary frame response, since the infill web strips were no longer taut with the frame and they behaved essentially as tension-only elements. In other words, up to the point of minor infill web strip yielding, the fundamental period was relatively constant (i.e., close to the elastic period); once moderate yielding of the infill web strips occurred, the period shifted abruptly to that of the PT boundary frame (at low vibration amplitudes) for all subsequent GM amplitudes.



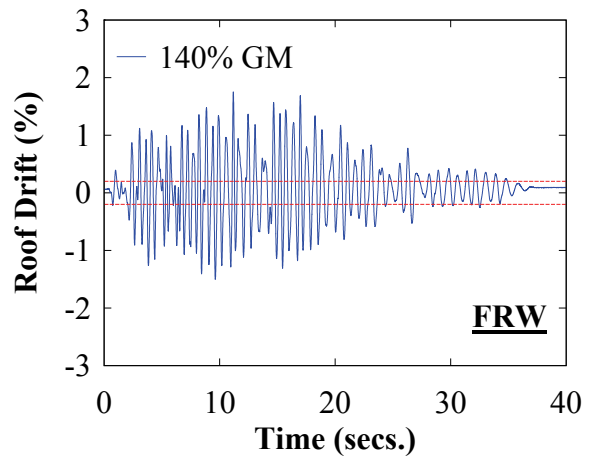
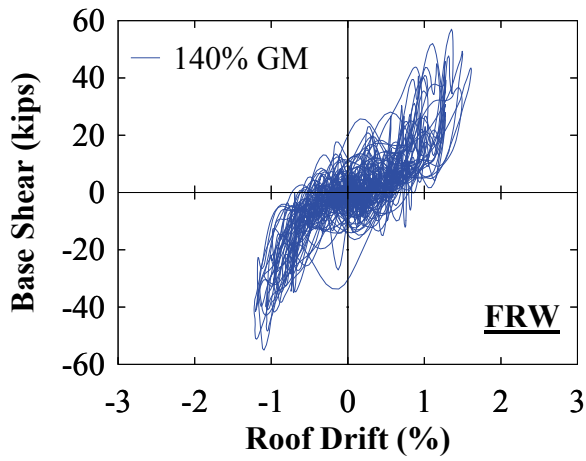
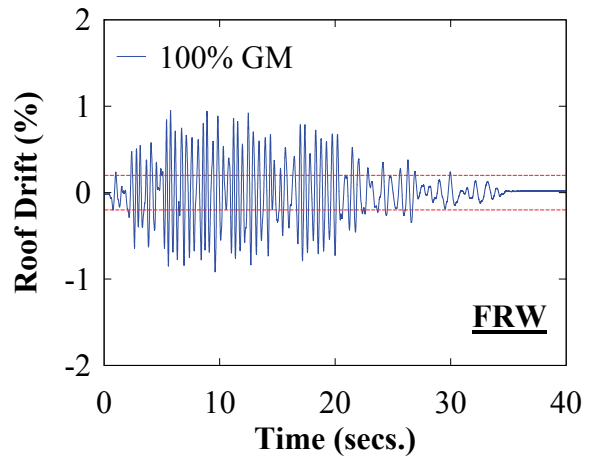
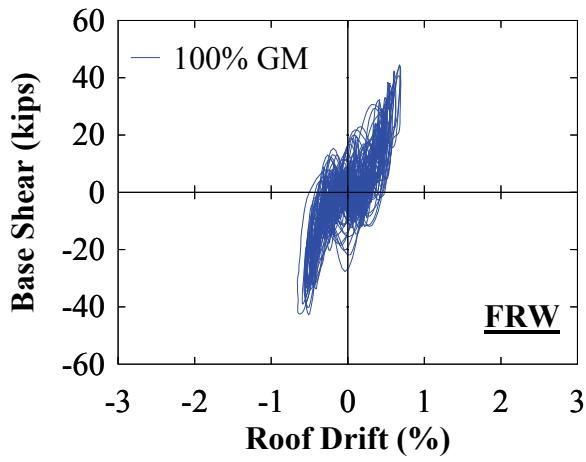
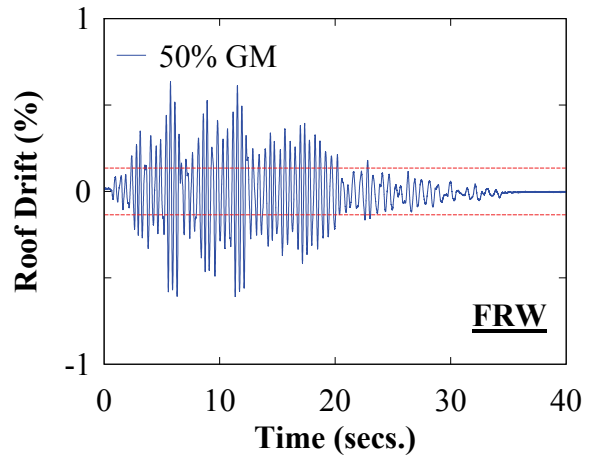
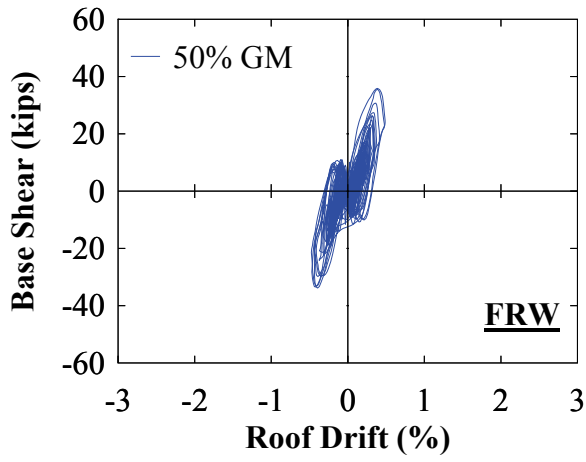


FIGURE 7-17 Frame FRW - select global response

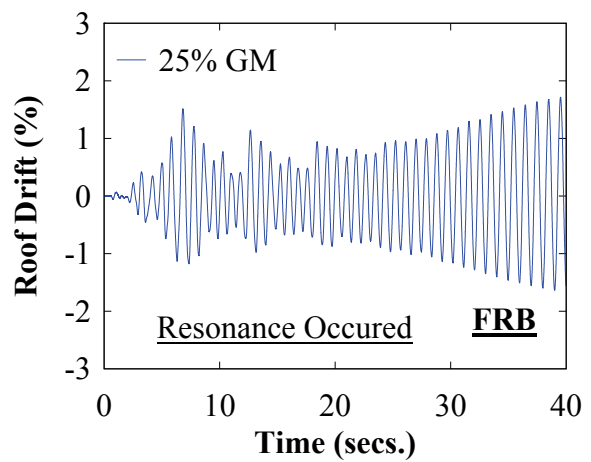
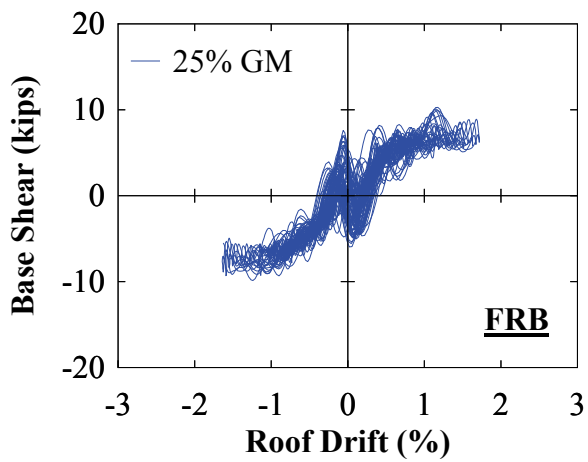
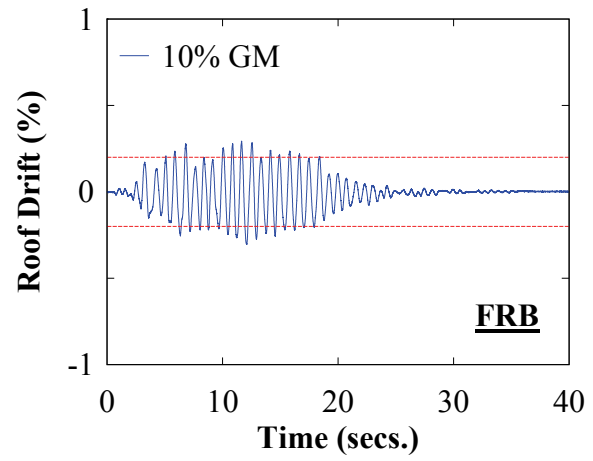
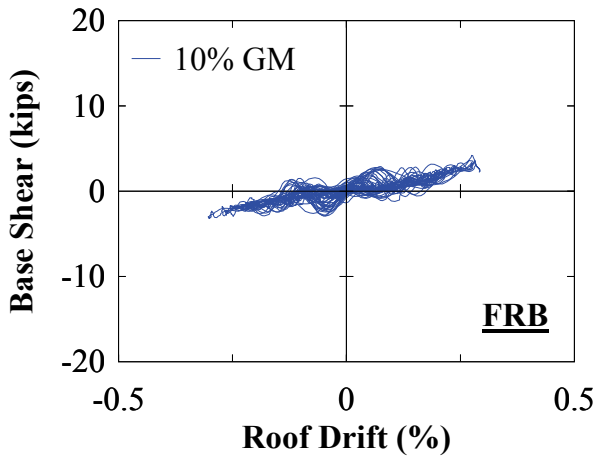
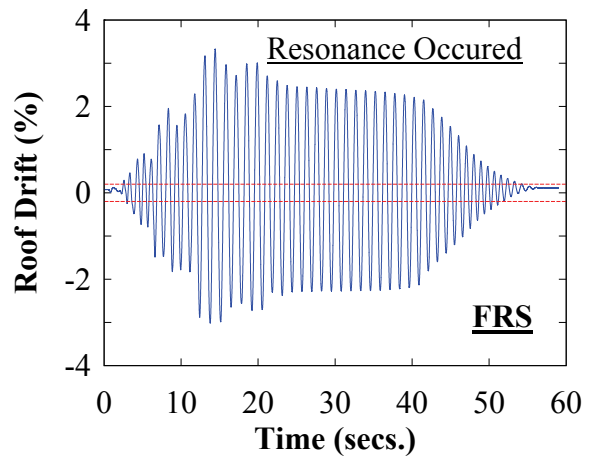
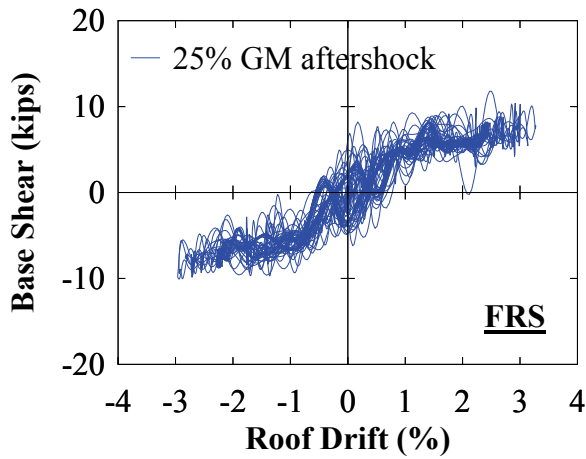
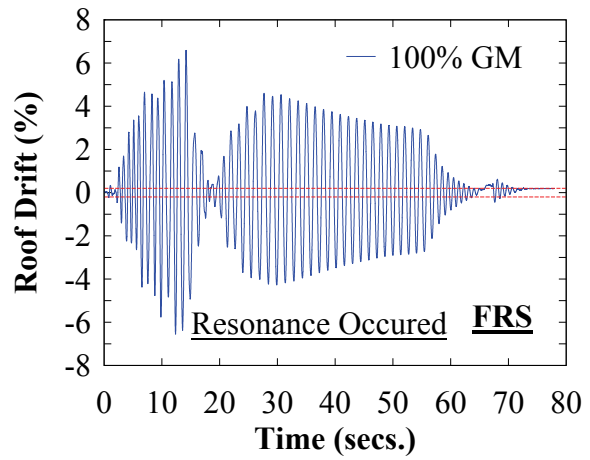
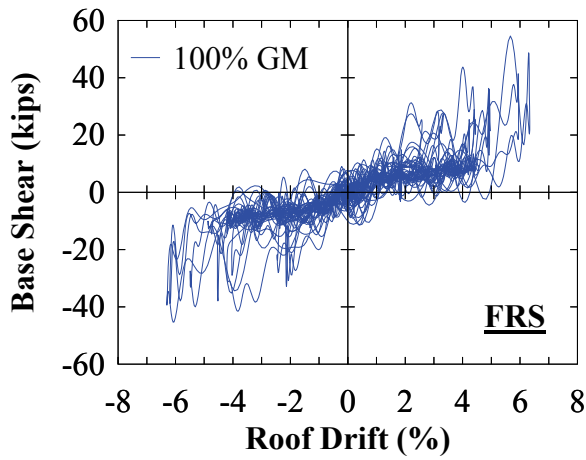
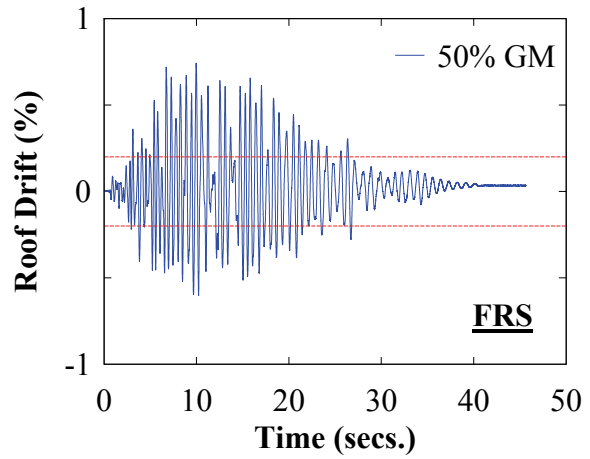
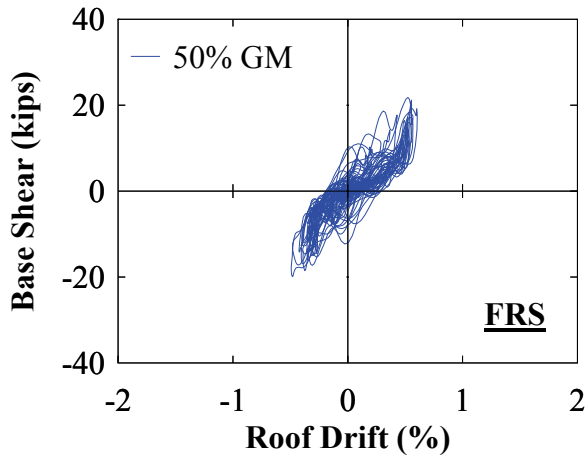


FIGURE 7-18 Frame FRB - select global response



**FIGURE 7-19 Frame FRS - select global response**

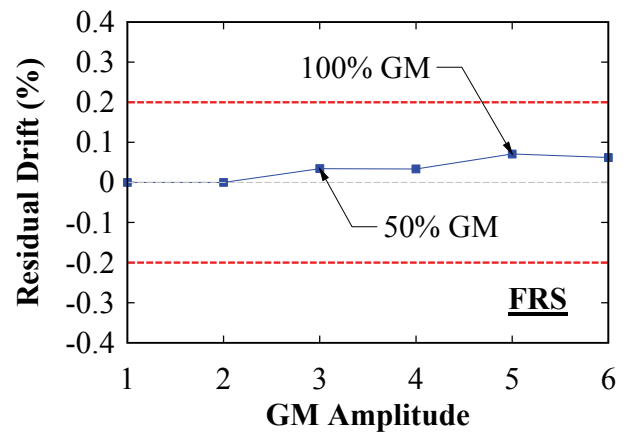
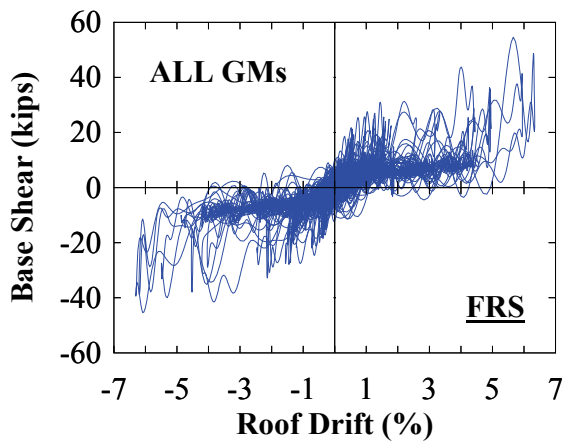
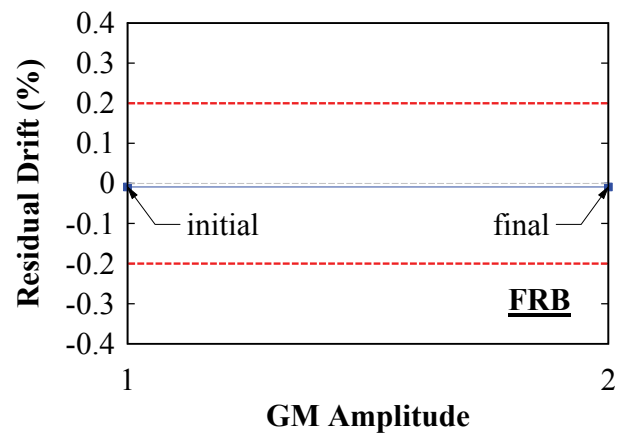
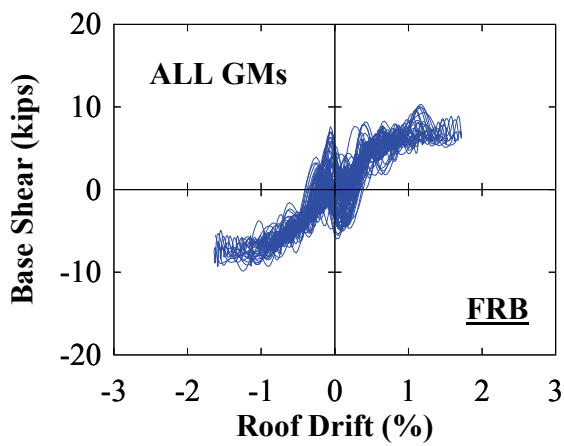
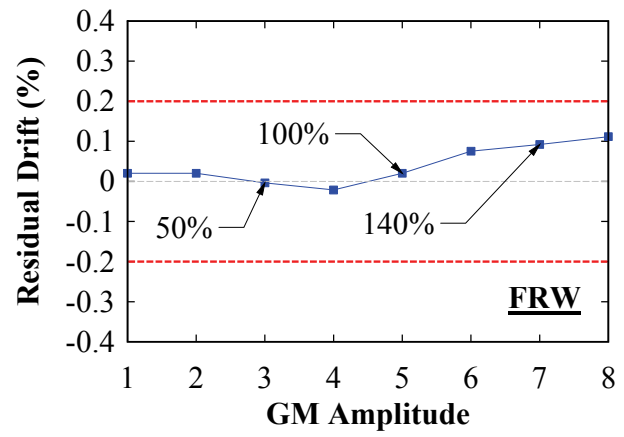
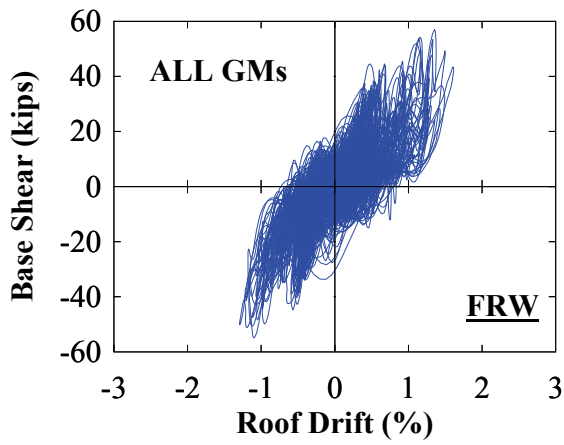
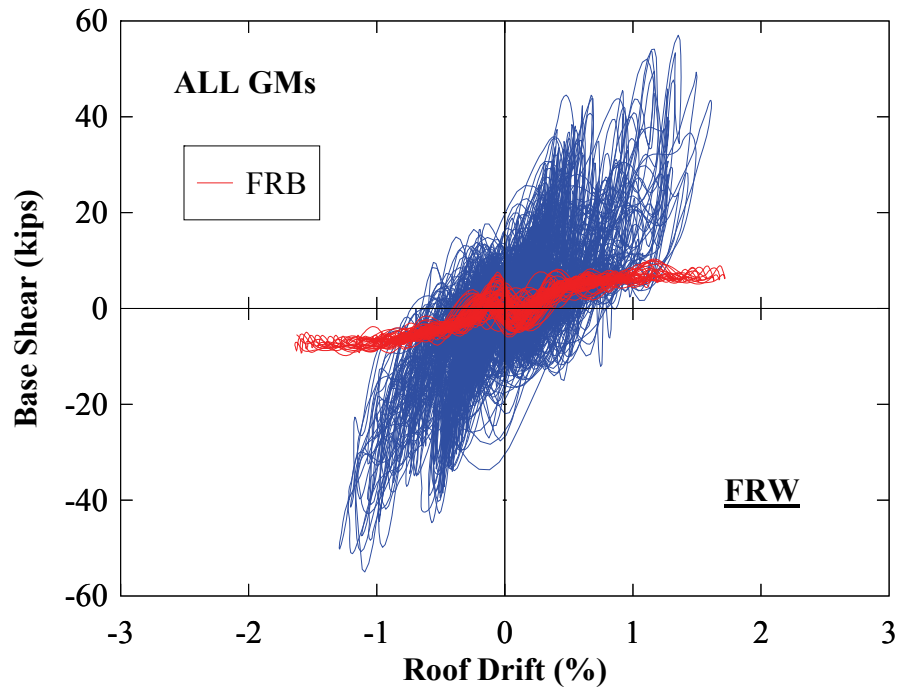
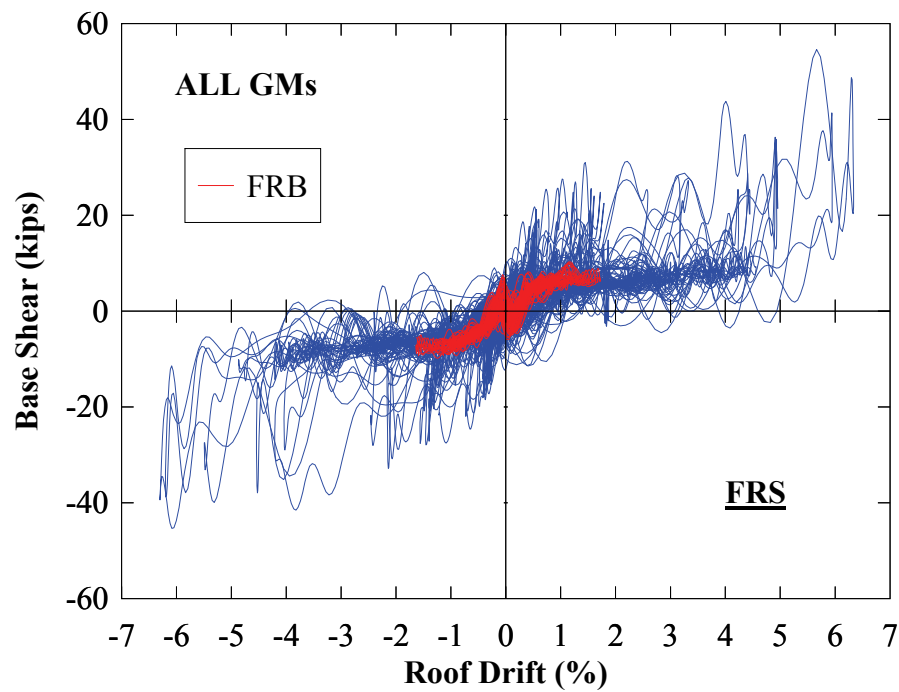


FIGURE 7-20 Frame FR - global response



(a)



(b)

FIGURE 7-21 Global response: (a) FRW versus FRB; (b) FRS versus FRB

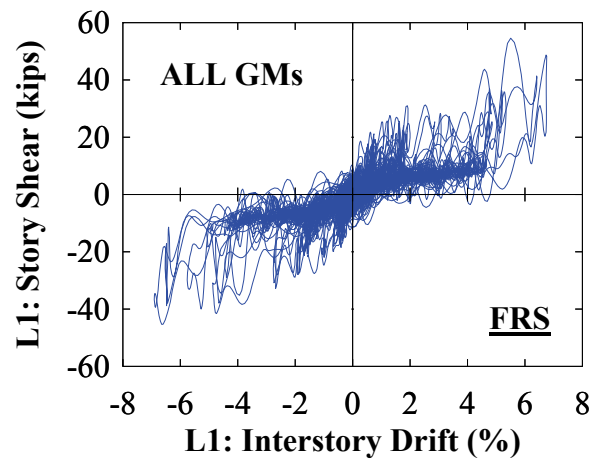
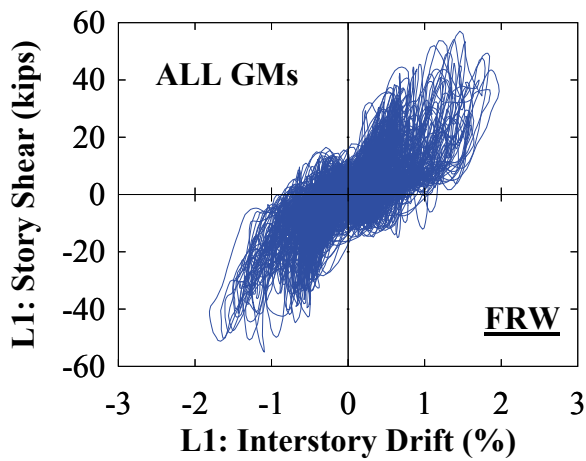
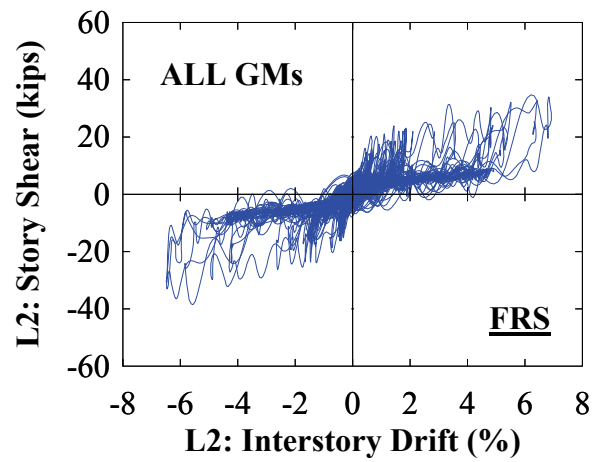
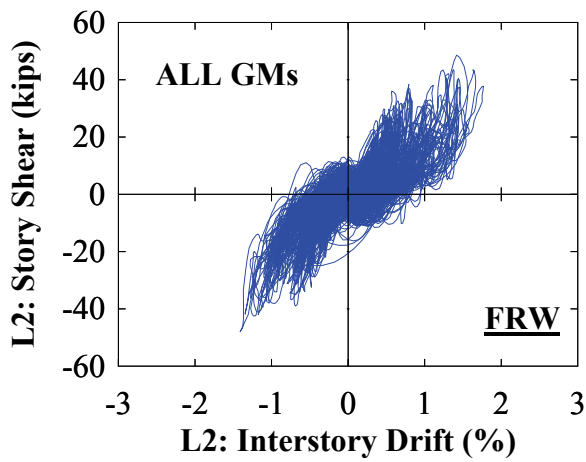
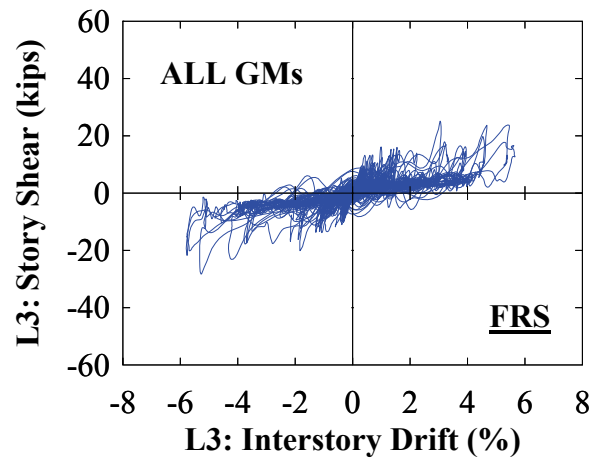
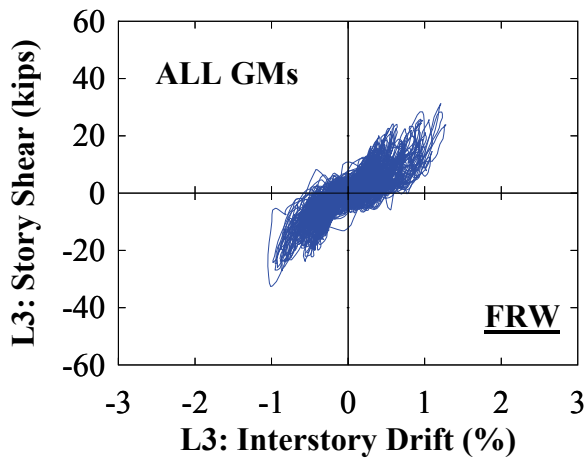
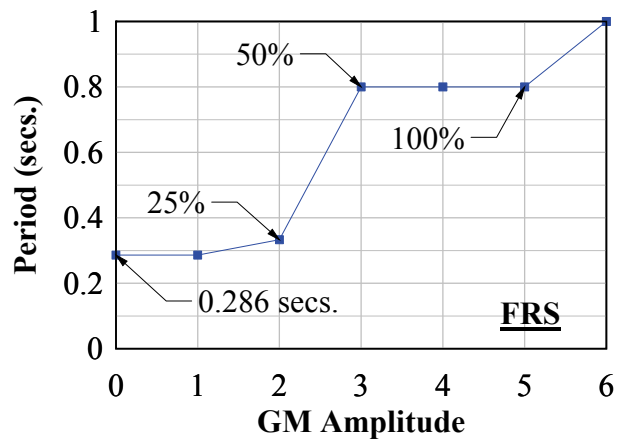
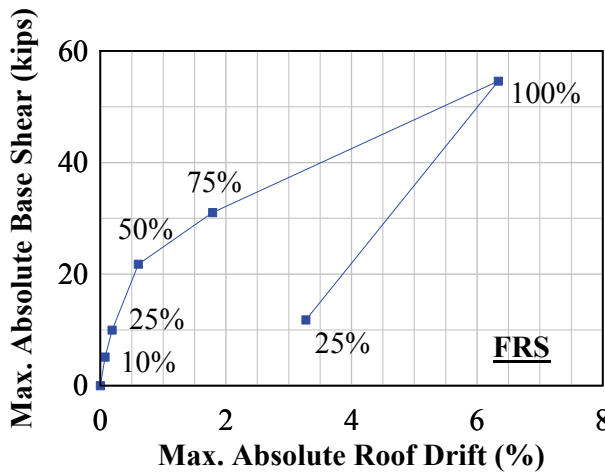
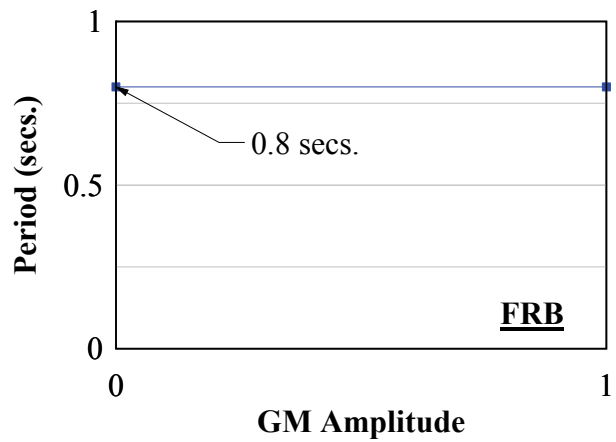
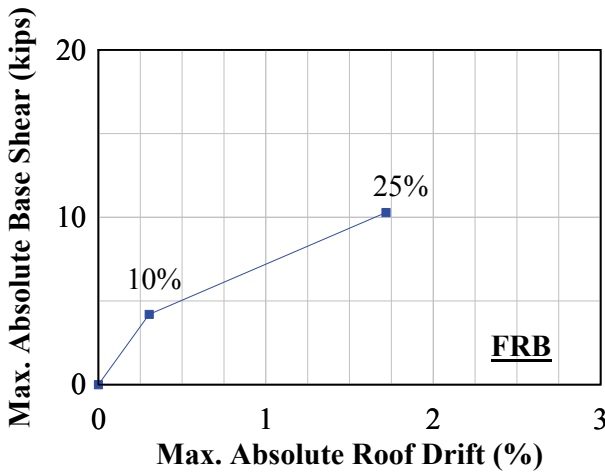
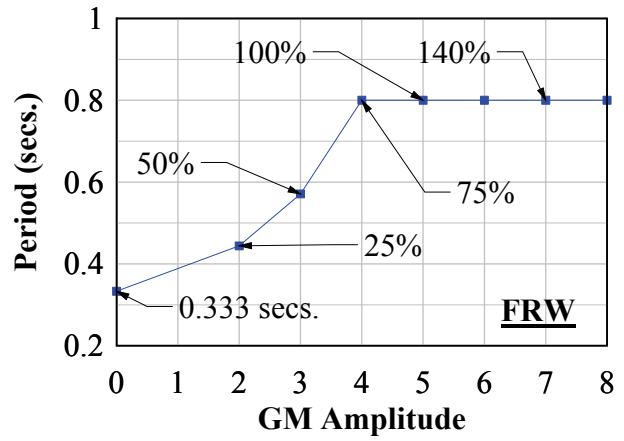
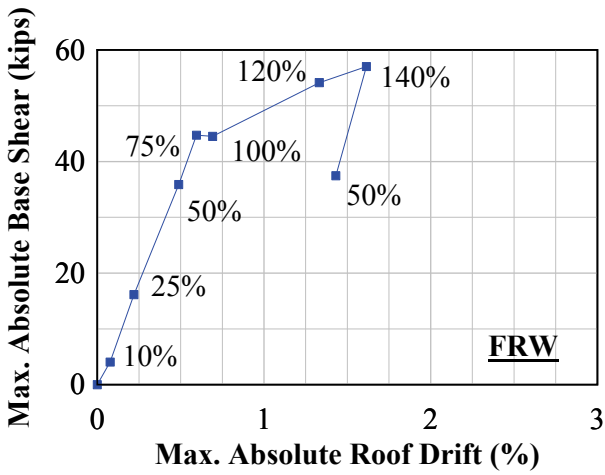


FIGURE 7-22 Frame FR - story shear versus interstory drift



**FIGURE 7-23 Frame FR - incremental dynamic response**

#### **7.4.2 FR: Boundary Frame Post-Tension Response**

The target initial PT force for frame FR was approximately 40 to 45% of the PT yield strength. The normalized achieved initial PT force and corresponding values at the start of subsequent GM amplitudes is shown in figure 7-24 for frame FRW, where it is observed that PT force losses were insignificant. The corresponding global PT force versus interstory drift response is shown in figure 7-25 and the response is similar to that observed for the quasi-static tests. However, some differences are apparent. Recall that the target initial PT force for the shake-table test was almost twice that of the quasi-static tests. Consequently, the transition associated with the gap opening due to drift at the HBE-to-VBE joint required a larger frame drift excursion prior to the formation of a gap at the HBE-to-VBE flanges. This is observed by a longer “flat” segment of the PT response curve; note that, at Level 3, that curve is almost fully horizontal, indicating that the HBE-to-VBE gap opening was relatively small at that level. Furthermore, it is observed that the nonlinear response, in part due to the effects of the infill web plate, is larger as a result of the abrupt and erratic dynamic loading compared to that of the gradual cyclic static loading condition.

The initial PT force and response history for frame FRB is shown in figures 7-26 and 7-27, respectively. In comparison to frame FRW, the response without the infill web plate is essentially nonlinear elastic and similar at all floor levels. This provides some clarity on the effects of the infill web plate observed with frame FRW. In particular, the infill web plate has a restraining effect on the HBE-to-VBE joint gap response leading to a nonlinear response; in absence of the infill web plate, a nonlinear elastic response is observed.

For frame FRS, the initial PT force and response history is shown in figures 7-28 and 7-29, respectively. The initial PT forces remain essentially constant between GM amplitudes with the exception of GM amplitude 5, where resonance first occurred. Furthermore, the drift at GM amplitude 5 was approximately 6.3%, whereas the maximum roof drift in the previous GM amplitude was approximately 1.8%. As a consequence, a significant loss of initial PT force occurred as a result of the abrupt increase in roof drift. Additionally, from figure 7-29 it is observed that the PT response is nonlinear (whereas for the static tests, the response was essentially nonlinear elastic). However, the occurrence of the abrupt loss in initial PT force



observed at GM amplitude 5, has the effect of amplifying the nonlinear response (due to PT force losses); this is shown by the downward vertical shift of the PT force along the vertical axis (at zero drift) in figure 7-29 (for reasons presented in Section 6 for frame FRW). Overall, the response is similar to that of frame FRB; although some nonlinear response is provided by the effects of the infill tension strips on the boundary frame, it is insignificant in comparison to the effects of the infill web plate.

Finally, the relative change of initial PT forces (representing the PT force losses), within each frame type (i.e., FRW, FRB and FRS) and cumulative PT force losses between the frame types is shown in figures 7-30 and 7-31, respectively. It is observed that the relative PT force losses were less than 5% for test FRW and FRB. For test FRS, relative losses were insignificant until the occurrence of resonance where a PT force loss of approximately 10 to 20% occurred across the story levels. Furthermore, the total cumulative PT force losses were negligible for test FRW, being less than 5% for test FRB, and a maximum of approximately 20% for test FRS. Note that, in the figures shown, the initial PT force value (i.e.,  $T_{o,End}$ ) is taken as the last collected data point at the end of each GM amplitude. As noted earlier, some free vibration response (although minor) was present when instrumentation data collection stopped. Consequently, the last collected data point for the PT load cells is not necessarily the absolute “at rest” condition. However, for the purpose of providing general observations of the relative PT force changes from the start of the test to the end, this effect on PT load cell values is negligible.

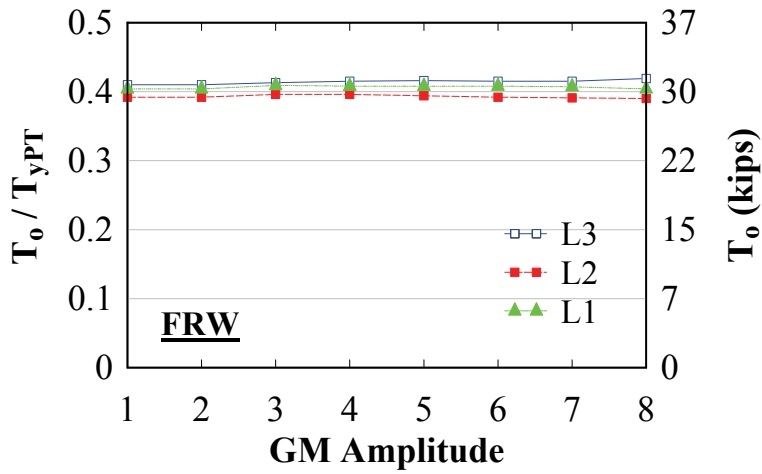


FIGURE 7-24 Frame FRW – initial PT forces

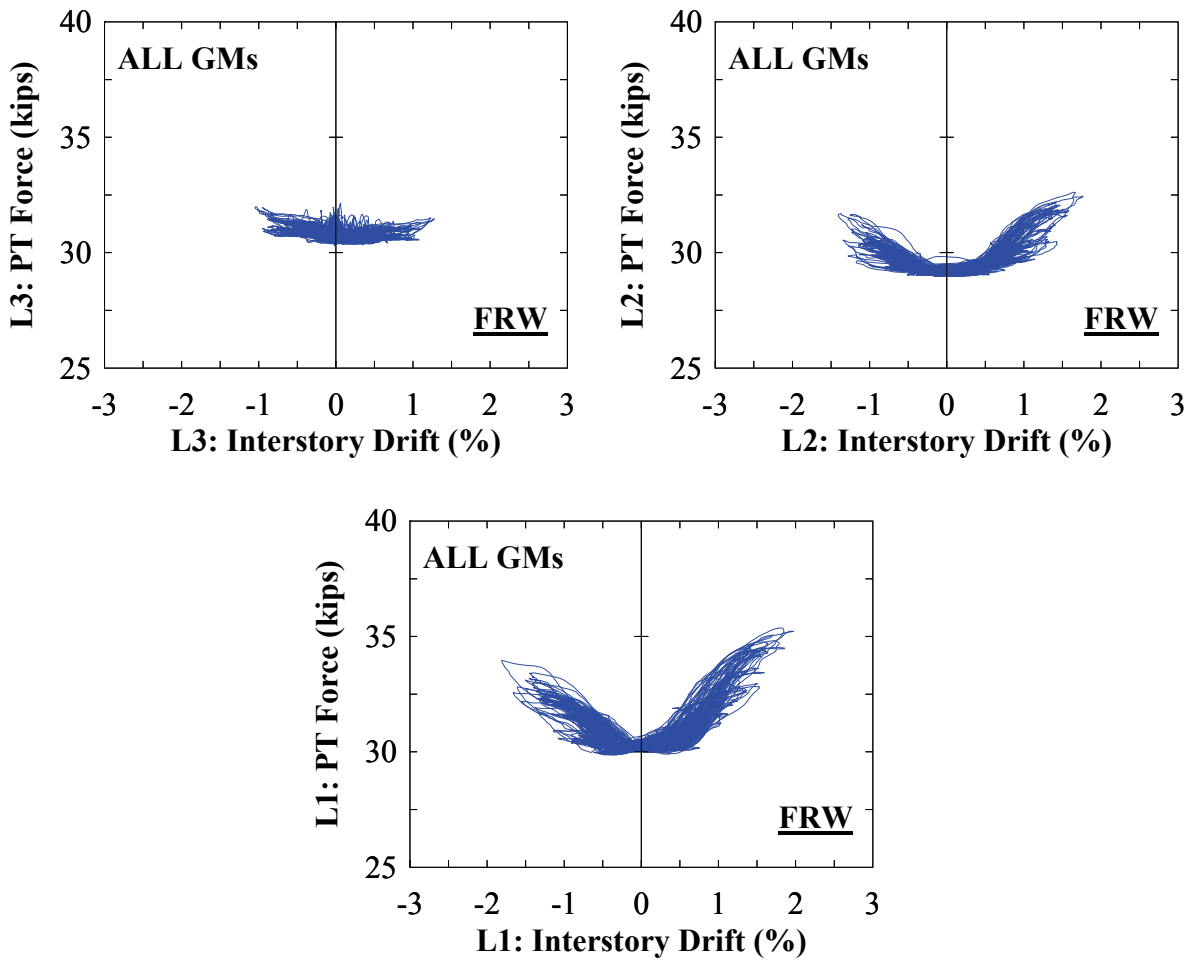


FIGURE 7-25 Frame FRW – PT response

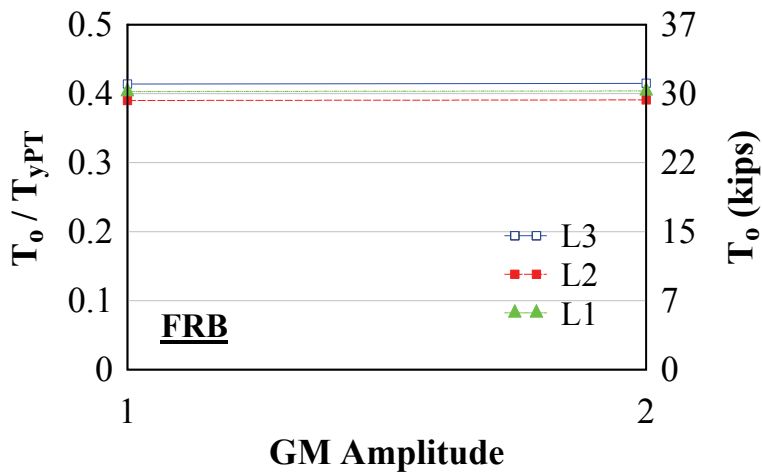


FIGURE 7-26 Frame FRB – initial PT forces

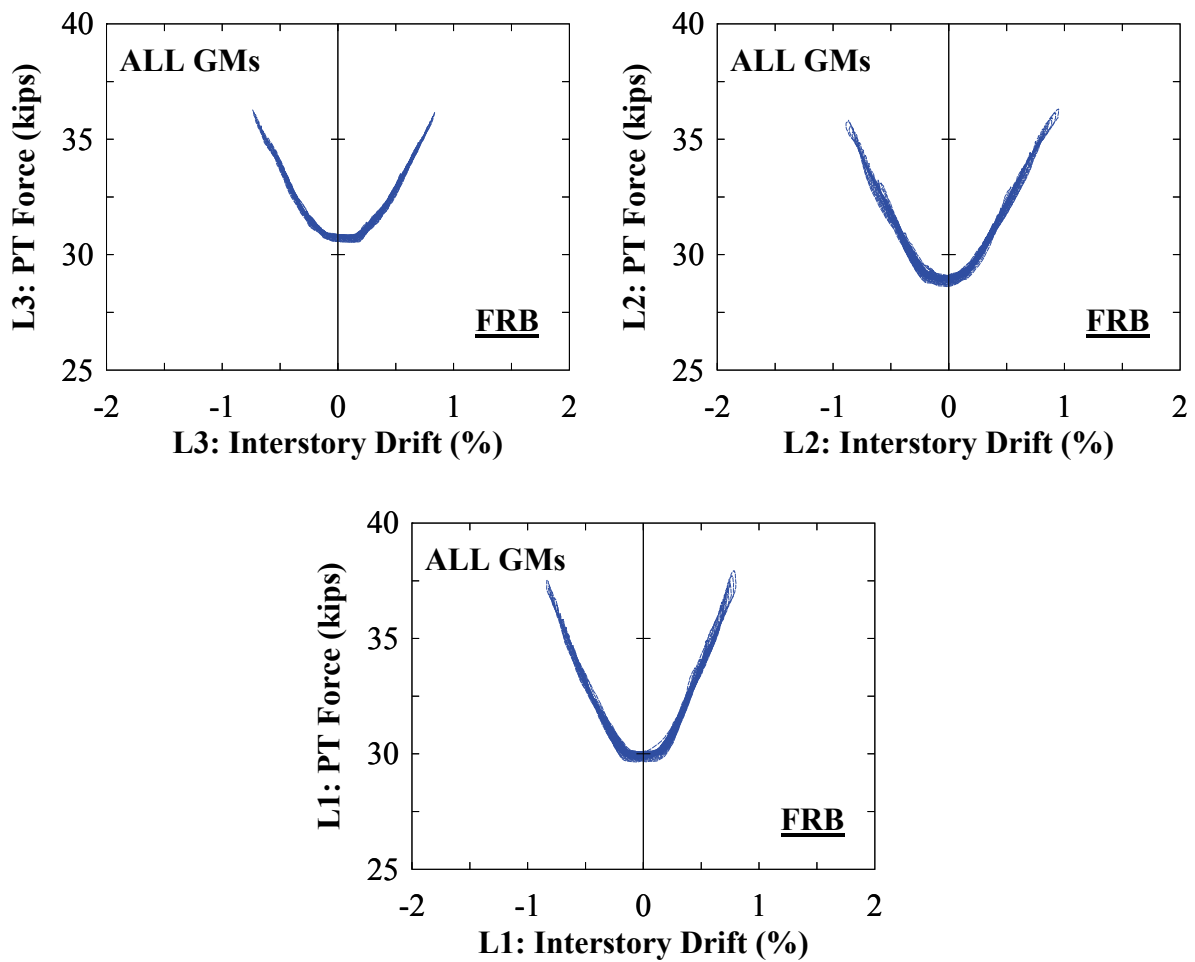


FIGURE 7-27 Frame FRB – PT response

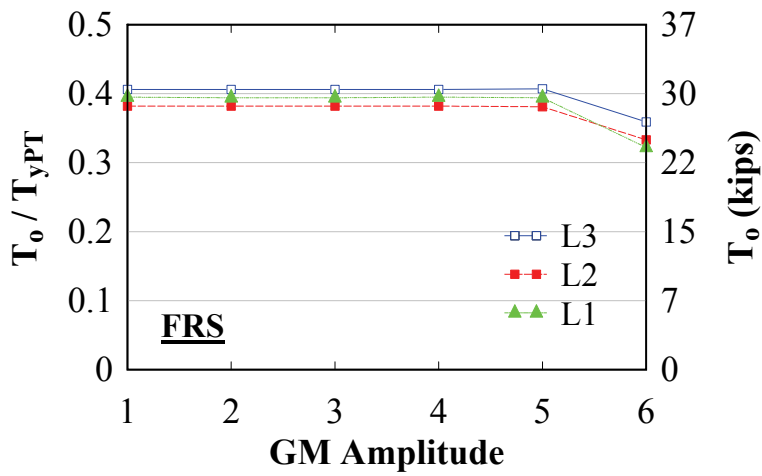


FIGURE 7-28 Frame FRS – initial PT forces

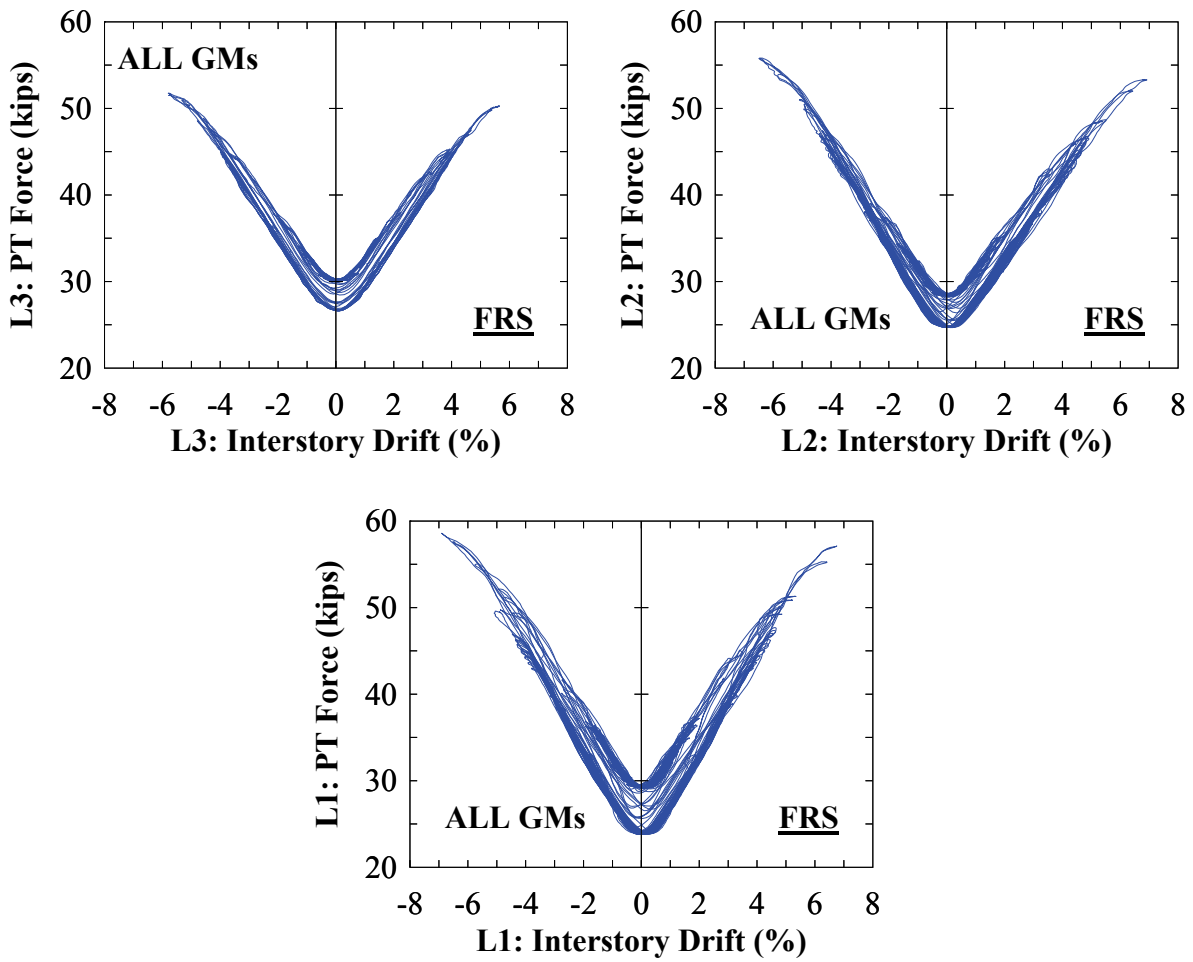


FIGURE 7-29 Frame FRS – PT response

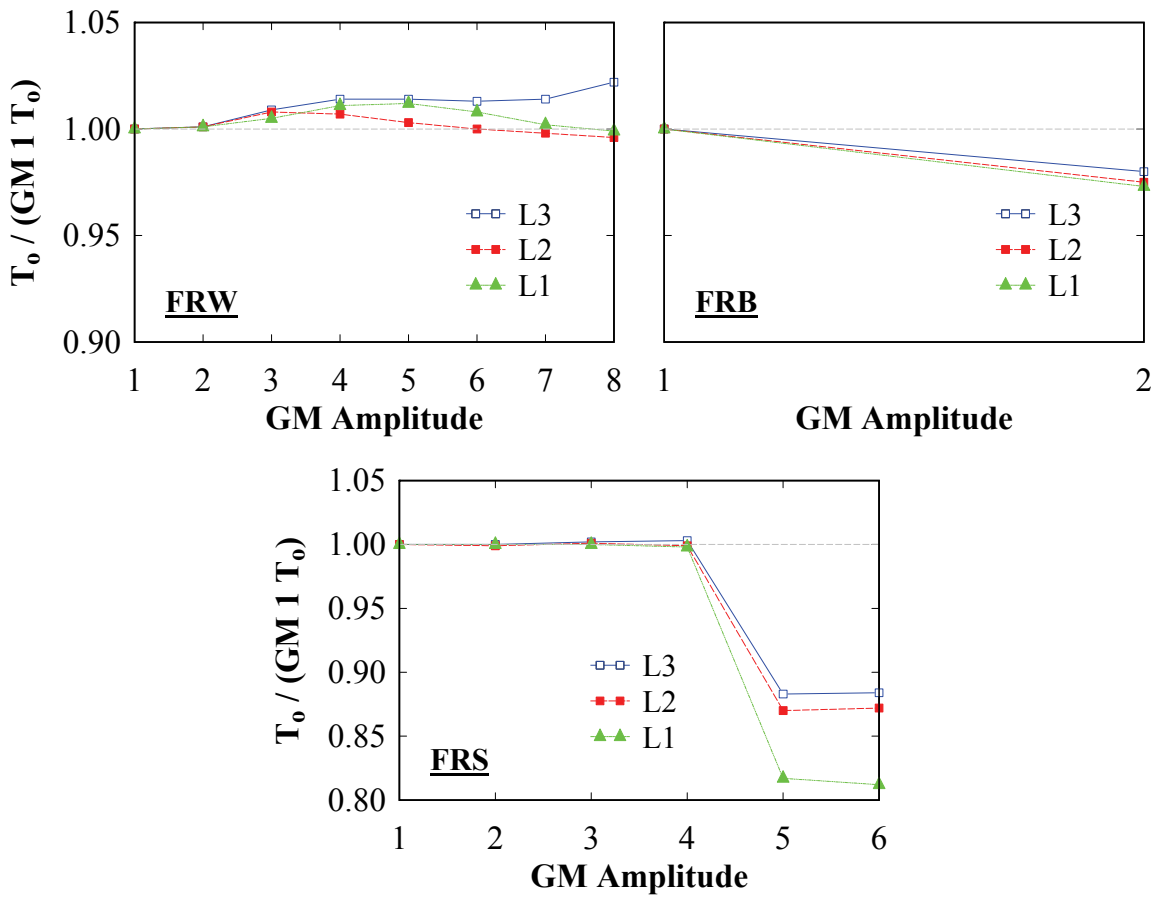


FIGURE 7-30 Frame FR – initial PT forces normalized by GM amplitude 1

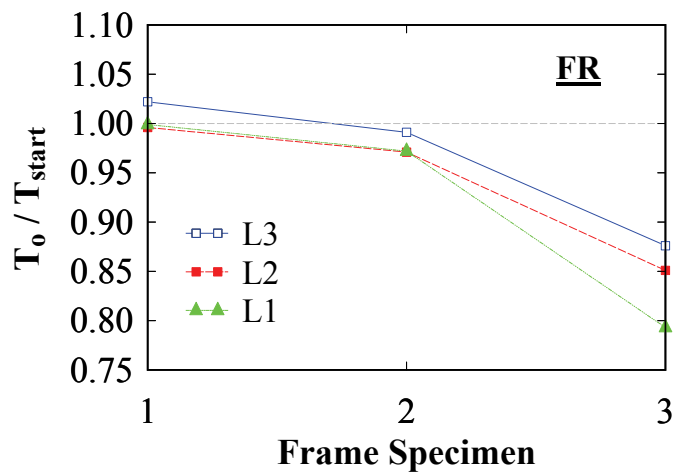


FIGURE 7-31 Normalized initial PT force changes between FR tests

### 7.4.3 FR: HBE Strain Gage Response

The HBE end strain versus gap rotation is shown in figures 7-32, 7-33, and 7-34 for frame FRW, FRS, and FRS, respectively. Furthermore, the sign convention for positive gap rotation is gap opening at the bottom flange at the West end of the HBEs, and a corresponding gap opening at the top flange at the East end of the HBEs (opposite sign convention than the one used for the quasi-static tests). This corresponds to a sign convention of a positive drift in the Eastward direction.

The strain gage response for frame FRB and FRS is similar to what was observed for the quasi-static test FRS (recall that quasi-static test results were not presented for frame FRW or FRB due to complications with the data acquisition system for the particular strain gage sensors). That is, when HBE-to-VBE gap opening occurs, the strain at the HBE flange at the gap location is zero, as indicated by the horizontal segments of the strain response curves. Furthermore, as was the case in the static tests, a vertical offset error is observed in the strain gage data. Additionally, the “dipping” effect is also present. That is, the compression strains initially increase at the HBE contact bearing flange, then there is transition in which a reduction in compression strain is observed for increased joint rotation. Note that for frame FRS, at the Level 1 and 2 West-end locations, some drifting in the strain gage data occurred; which is reflected by the “vertical separation” of the strain versus gap rotation response shown in figure 7-34.

Furthermore, particular for frame FRB, it is observed that the response is essentially nonlinear elastic. Consequently, the nonlinear response of frame FRW and FRS is due to the effects of the infill web plate and strips. Similarly to what was observed with the PT response history, the infill web plate effects are more significant (i.e., larger strain versus gap rotation loops) compared to the infill web strips. In particular, it is also observed that the “dipping” effect in the strain response is also observed with frame FRB. This indicates that this is a localized phenomenon dependent on the kinematics of the frame, and not directly related to the presence of infill web plates or strips.

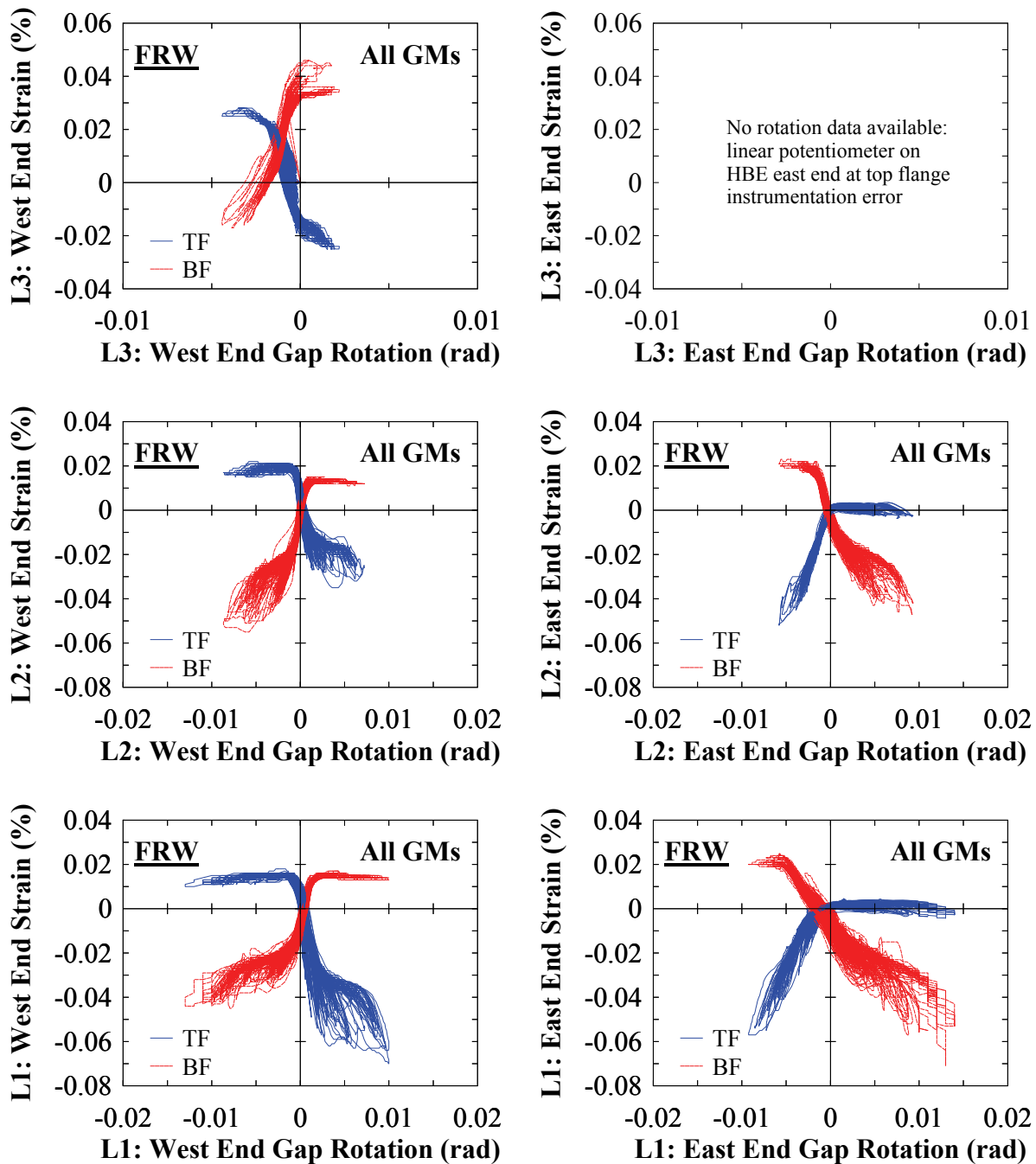
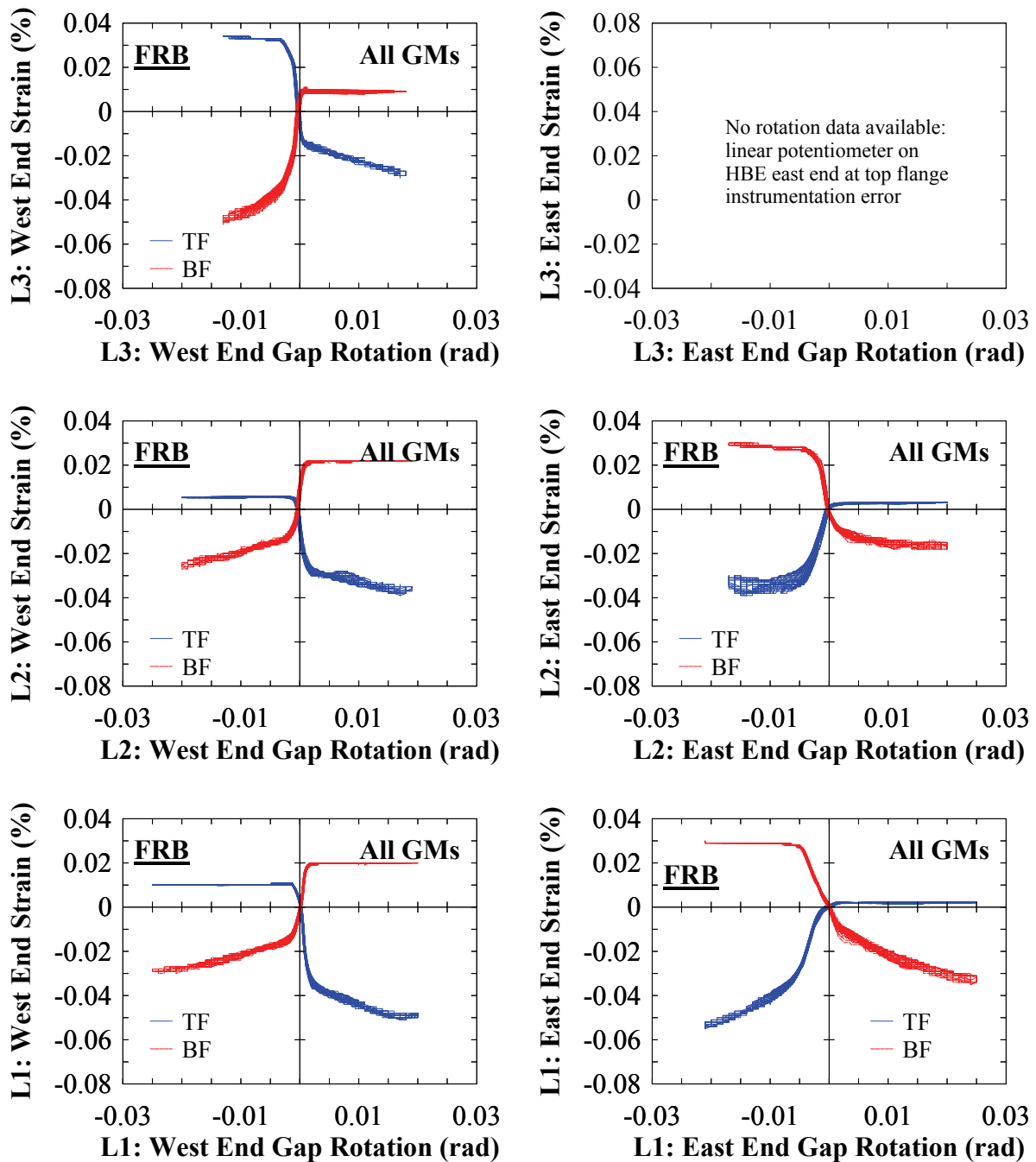


FIGURE 7-32 Frame FRW – HBE end strain versus gap rotation



**FIGURE 7-33 Frame FRB – HBE end strain versus gap rotation**



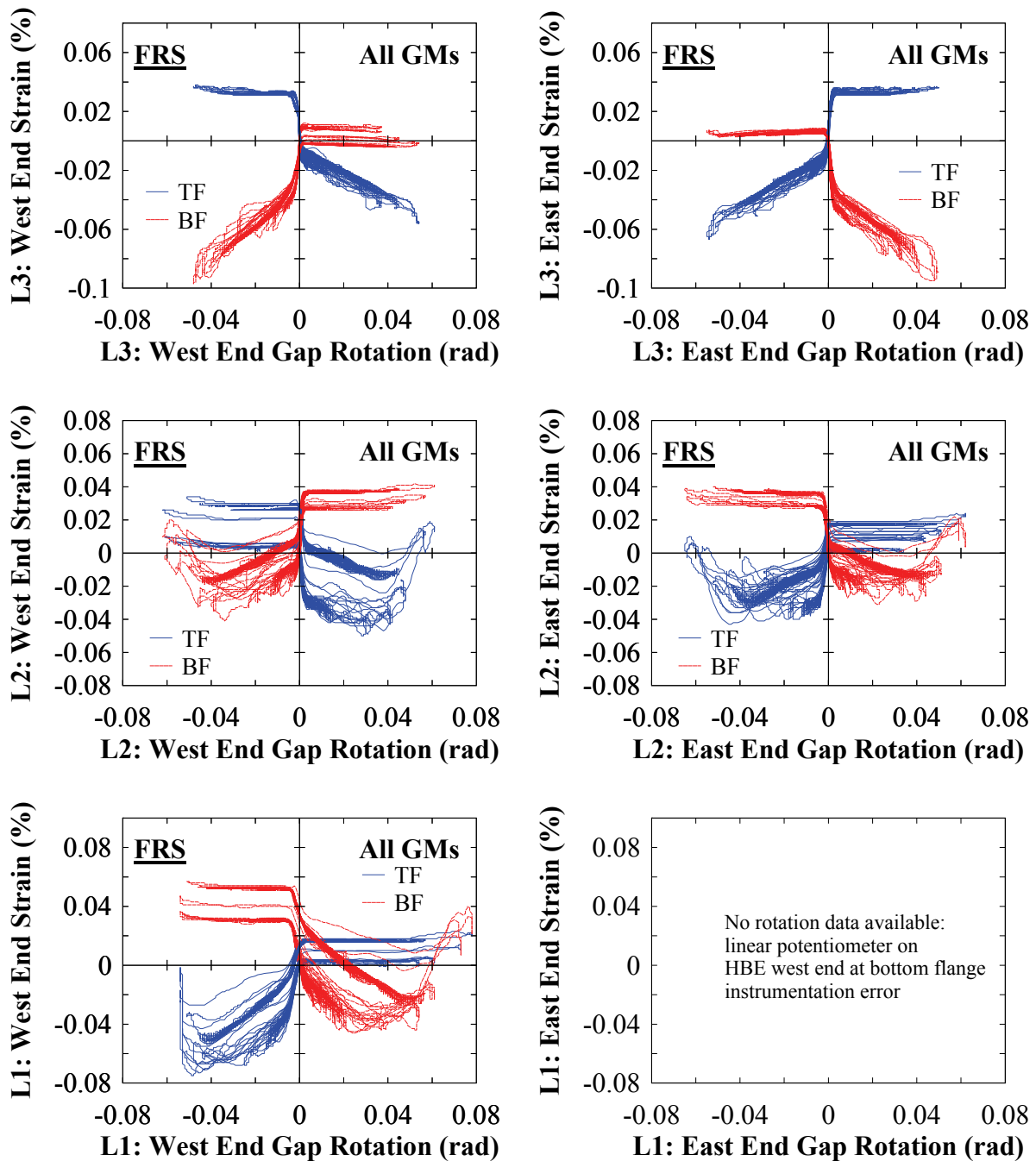


FIGURE 7-34 Frame FRS – HBE end strain versus gap rotation

## **7.5 NewZ-BREAKSS (NZ) Frame Shake-Table Experimental Results**

### **7.5.1 NZ: Global Response**

For reasons presented for Frame FR, the original acceleration data was modified using a low-pass filter with a cut off frequency of 20 Hz, and the roof drift data was also modified to remove rocking effects due to the shake-table. A sample comparison of the hysteretic response with the original and filtered data at the 50% and 100% GM for frame NZW, and 100% GM for frame NZS is shown in figure 7-35. It is noted that the undesired frequency content effects observed for frame FR is not as significant for frame NZ. This suggests that the effects of HBE-to-VBE gap opening and closing (which generates an impact force at the HBE-to-VBE flanges) that occurs only in frame FR may have been the primary reason for the recorded acceleration spikes (observed near the zero-drift axis, where the opening and closing of the gap occurred). In frame NZ, such effects are minimized since an initial gap is provided at the HBE bottom flanges and the HBE top flanges remain in contact with the VBEs. However, for consistency in comparing results for frame FR and NZ response, the cut off frequency of 20 Hz was maintained. For reference, the shake-table rotation, together with corresponding absolute and corrected peak roof drifts are shown in tables 7-10 and 7-11, respectively, for frame NZW and NZS.

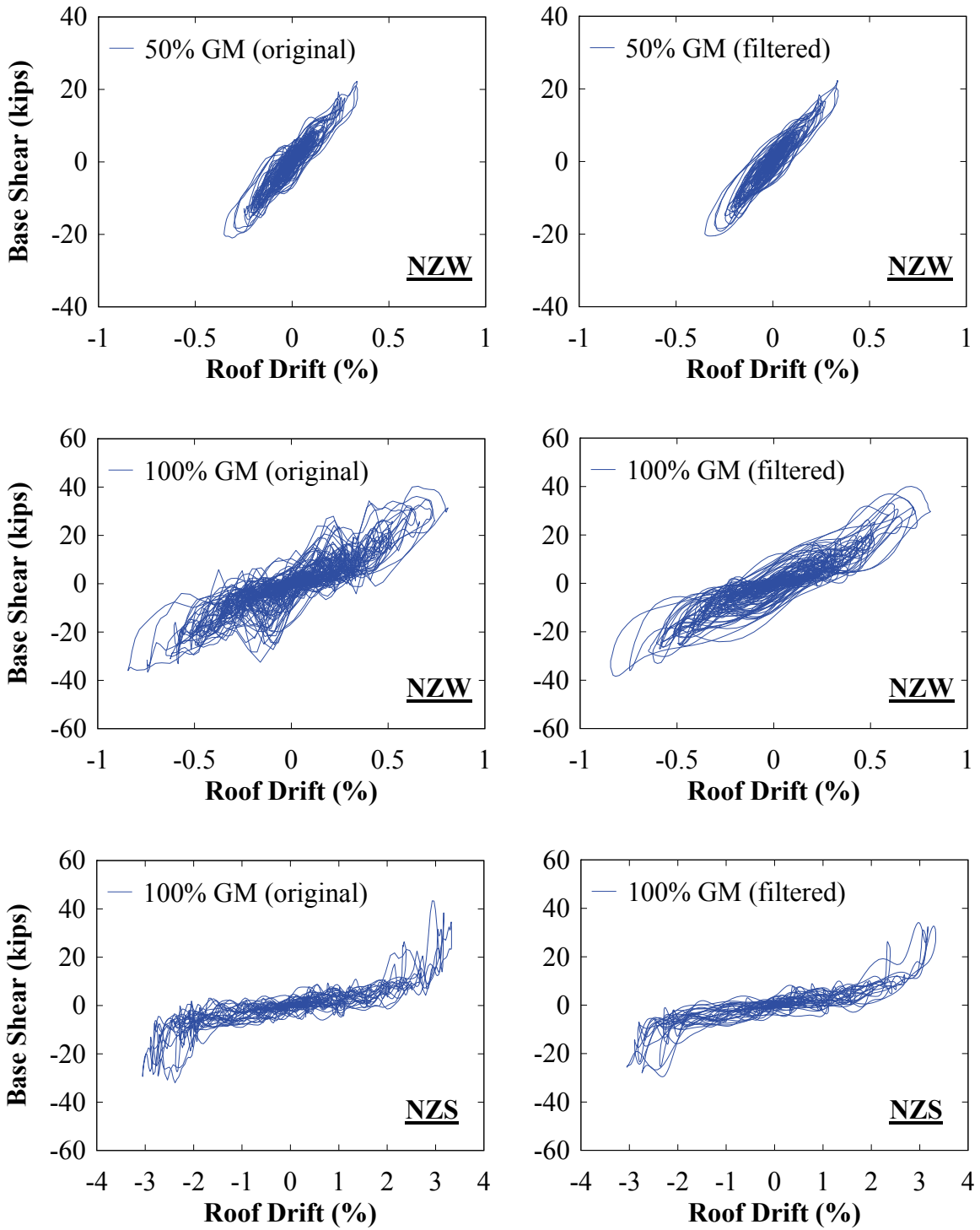


FIGURE 7-35 Frame NZ - original versus filtered hysteresis

**TABLE 7-10 Shake-table rocking roof drift effects – Frame NZW**

Frame NZW				
% GM	TABLE Rotation (deg)	Peak Roof Drift (%)		Comparison Ratio
		Original	Rocking Removed	Original/Rocking Removed
10	0.00	0.08	0.06	1.23
25	0.01	0.19	0.13	1.48
50	0.06	0.35	0.20	1.76
75	0.08	0.58	0.40	1.45
100	0.13	0.84	0.56	1.51
120	0.10	1.17	0.89	1.32
140	0.02	1.40	1.35	1.04
140	0.04	2.03	1.93	1.05
50	0.09	1.18	1.36	0.87

**TABLE 7-11 Shake-table rocking roof drift effects – Frame NZS**

Frame NZS				
% GM	TABLE Rotation (deg)	Peak Roof Drift (%)		Comparison Ratio
		Original	Rocking Removed	Original/Rocking Removed
5	0.01	0.05	0.04	1.39
13	0.01	0.15	0.12	1.26
25	0.02	0.26	0.20	1.31
38	0.05	0.44	0.33	1.34
50	0.06	0.73	0.59	1.24
60	0.05	1.46	1.34	1.09
70	0.08	2.04	1.85	1.10
90	0.06	2.47	2.33	1.06
100	0.07	3.33	3.17	1.05
38	0.02	2.02	1.98	1.02

The global base shear versus roof drift and the corresponding roof drift response history is shown in figures 7-36, 7-37, and 7-38 at select GM amplitudes for frames NZW, NZB, and NZS, respectively. From the roof drift histories, it is observed that frame recentering is achieved for the GM amplitudes shown. Furthermore, the concatenation of all GM amplitudes results is shown in figure 7-39. It is observed that recentering is achieved for all GM amplitudes, further indicating that for dynamic loadings, recentering of the frame is not affected by the compression strength of the infill web plate. Furthermore, similar to frame FR, it appears that the compression strength contribution of the infill web plate does provide additional energy dissipation and stiffness, as evidenced by the strength and stiffness of the system's hysteretic loops at 0% drift upon displacement reversals (as shown in figure 7-40). Additionally, the story shear versus interstory drift is shown in figure 7-41 for frames NZW and NZS.

The incremental dynamic response is shown in figure 7-42. For frame NZW, the maximum roof drift was approximately 1.9%, which is comparable to the 2% roof drift typically expected for a DBE level earthquake. In comparison, the maximum roof drift for frame FRW was 1.6%. However, recall that the 140% GM for test NZW was repeated (for the purpose of attaining a larger roof drift). For perspective, the maximum roof drift at the first 140% GM for frame NZW was approximately 1.3%.

For frame NZS, the maximum roof drift was approximately 3.2%, which is two times the maximum drift corresponding to frame NZW. However, recall that the stiffness of frame NZS is approximately half that of frame NZW. Furthermore, as it has been shown, the infill strips are tension-only. Consequently, the dynamic response for frame NZS for drift excursions less than the previously maximum attained value is dominated by the PT boundary frame. Furthermore, for both frame NZW and NZS, the fundamental period observed is less than the value of frame NZB, indicating that there is still some contribution to stiffness by the infill web plates/strips. However, this is peculiar for frame NZS (i.e., that the period for NZS is smaller than NZB), as the frame period at the white noise base excitations after significant infill web strip yield, should closely match that of frame NZB (i.e., the infill web strips are no longer taut with the boundary frame). To provide an explanation, recall that the response of the shake-table frame extension is coupled with the test specimen. Consequently, the dynamic properties obtained from the transfer

functions include the effects of the frame extension. Accordingly, interpretation of the periods must include that into consideration. However, the general trend observed matches what would be expected, namely that the period was relatively constant up to the end of GM amplitude 3 (i.e., 25% GM), until yielding occurred, after which an abrupt change in period (approaching that of the PT boundary frame) was observed and remained relatively constant thereafter.

Finally, it is observed that the maximum roof drift for frame NZB was approximately 3.1%; indicating that the PT boundary frame response is stable at relatively large drifts. Furthermore, it is observed that the incremental dynamic response curve is essentially linear and the period remains constant; indicative of a linear response expected of the PT boundary frame.

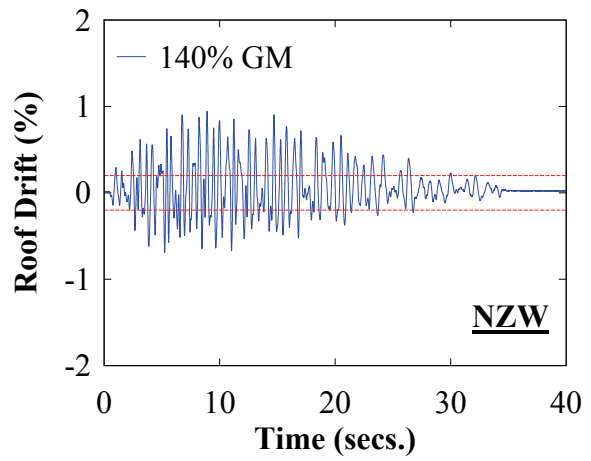
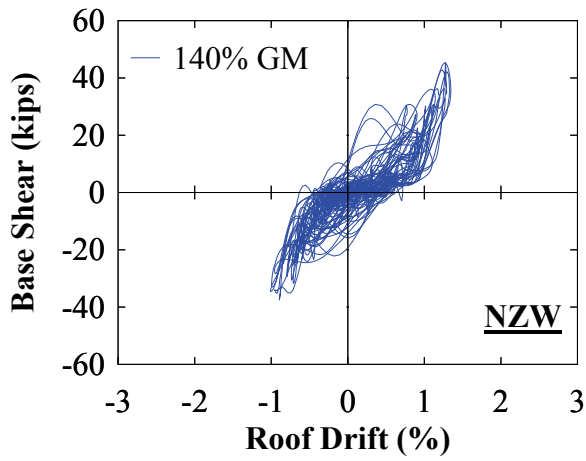
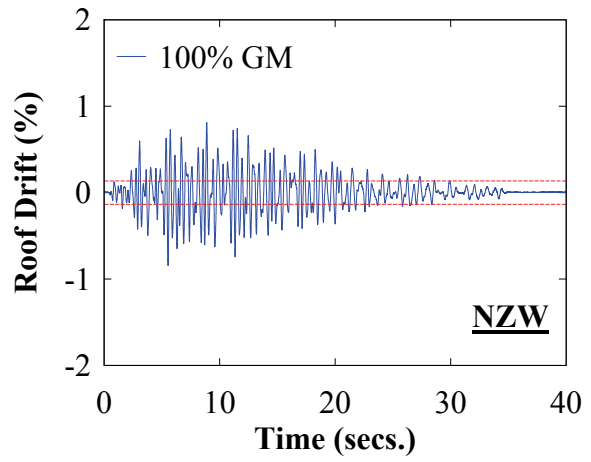
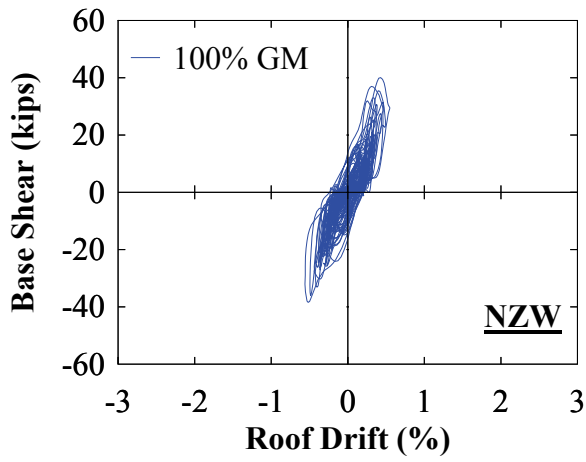
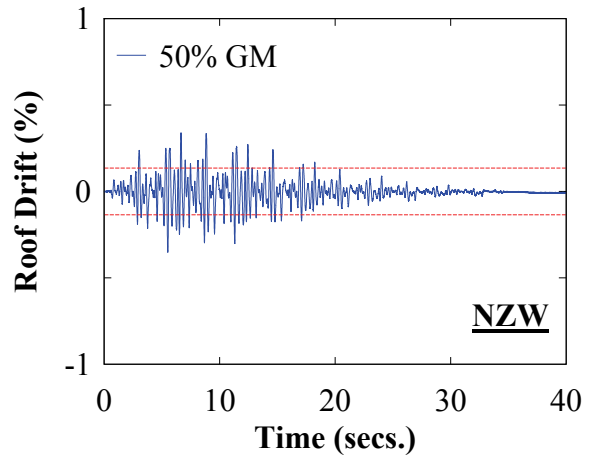
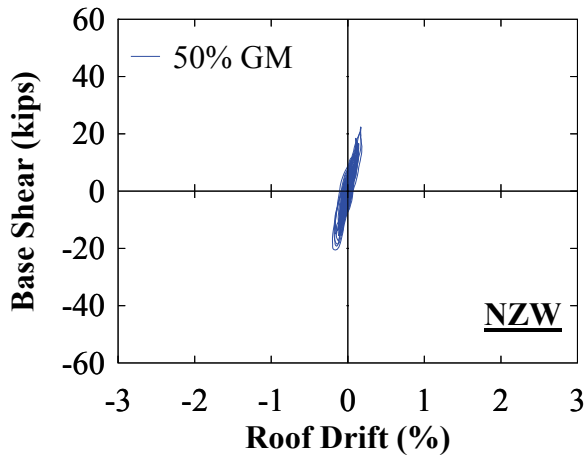
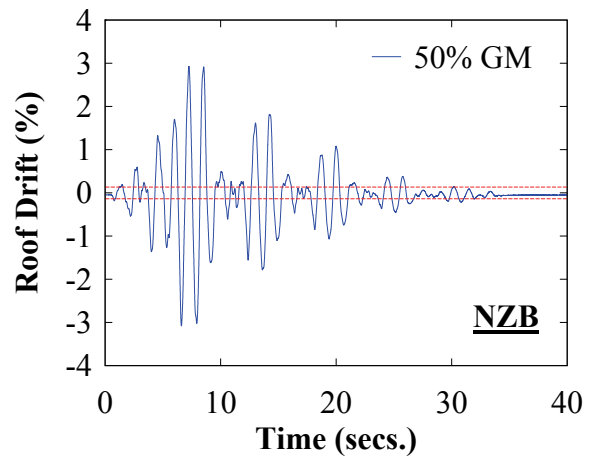
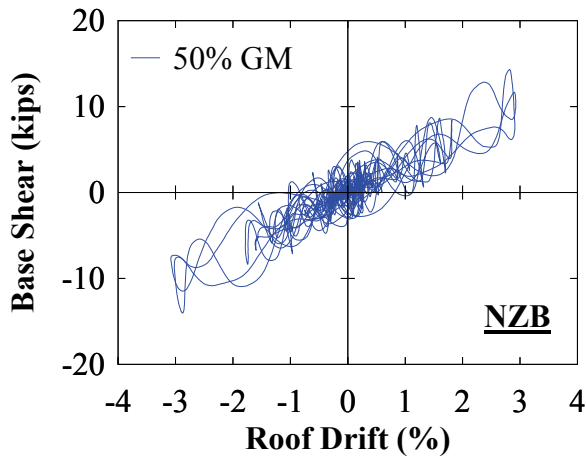
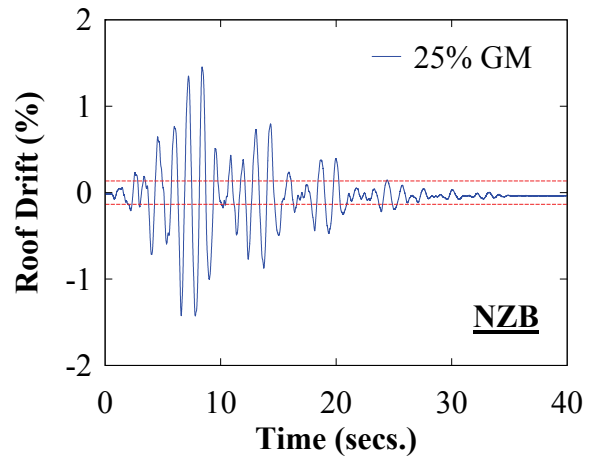
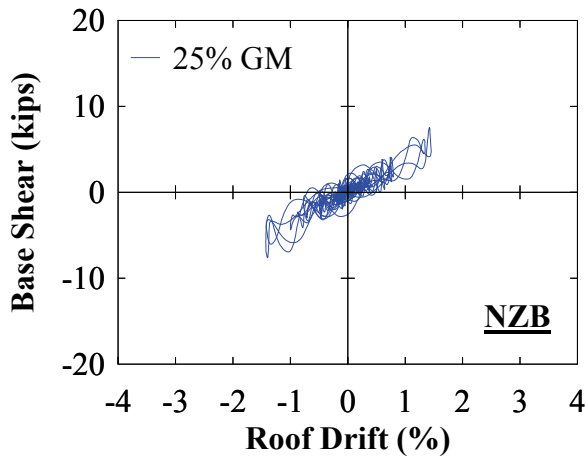
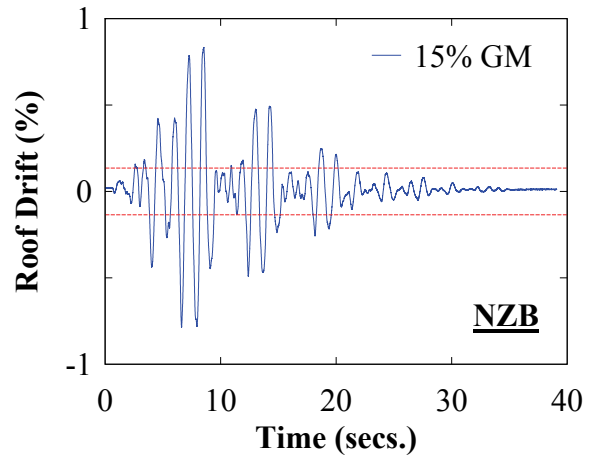
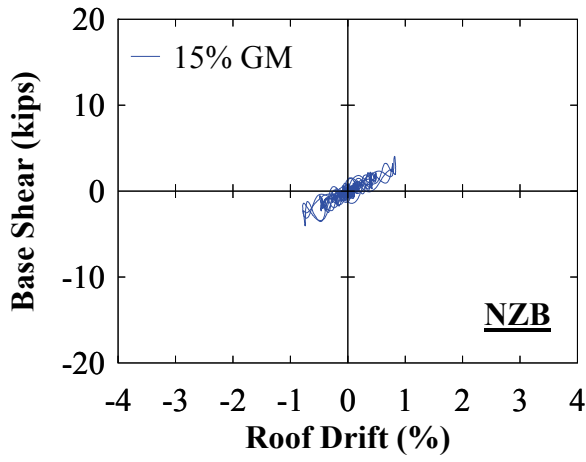
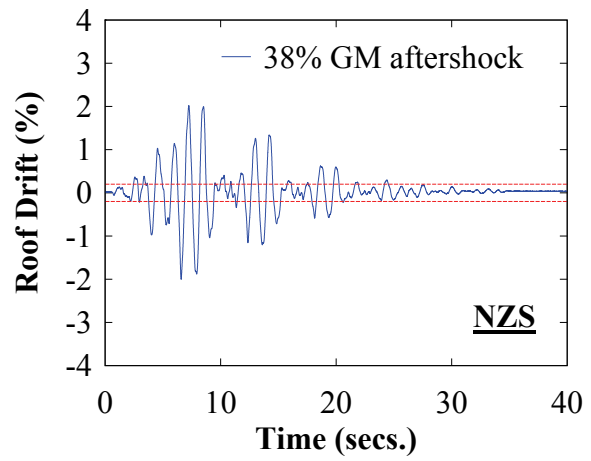
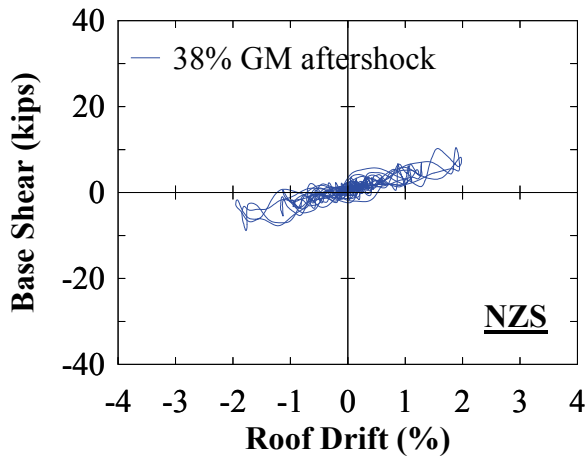
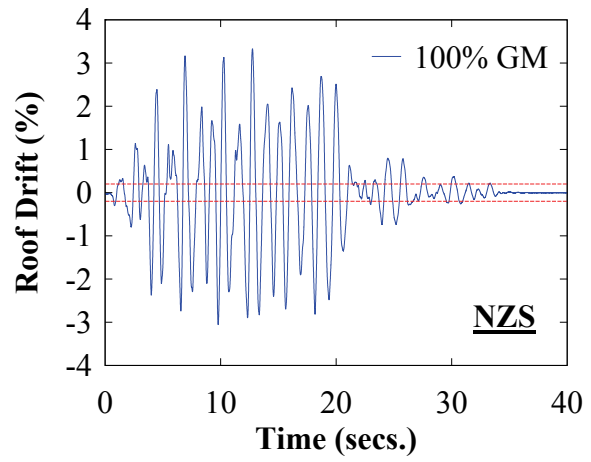
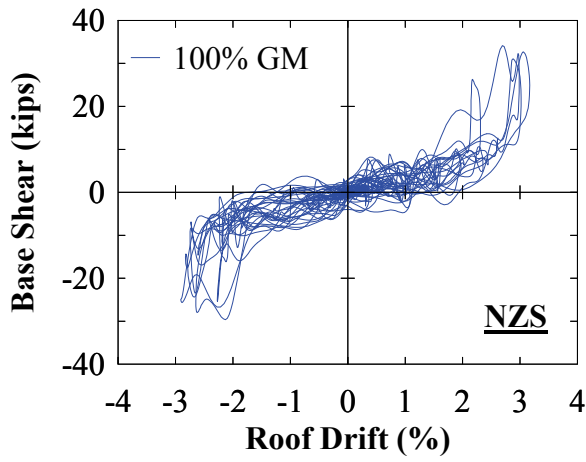
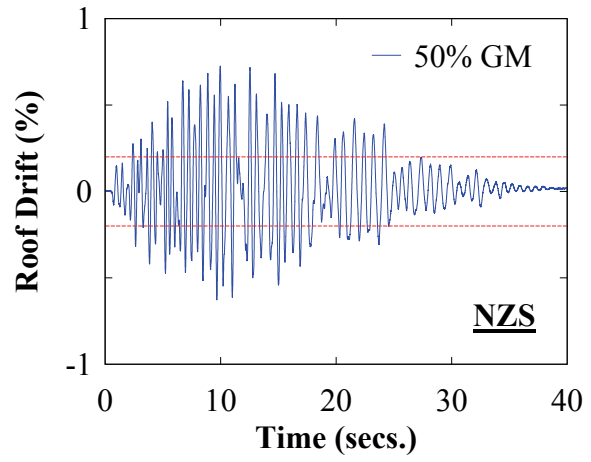
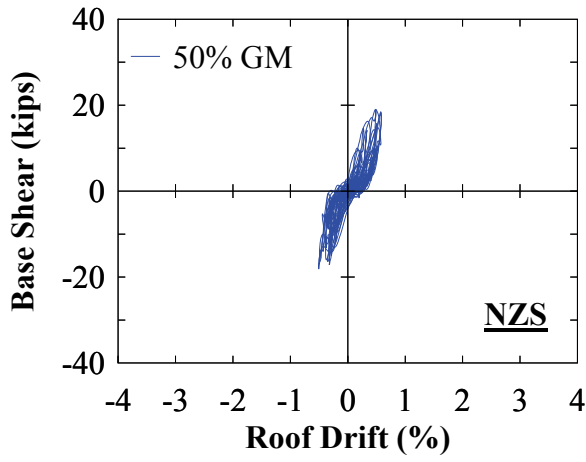


FIGURE 7-36 Frame NZW - select global response



**FIGURE 7-37 Frame NZB - select global response**





**FIGURE 7-38 Frame NZS - select global response**

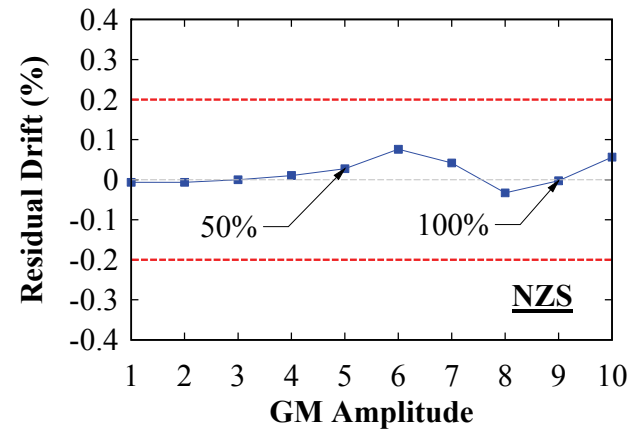
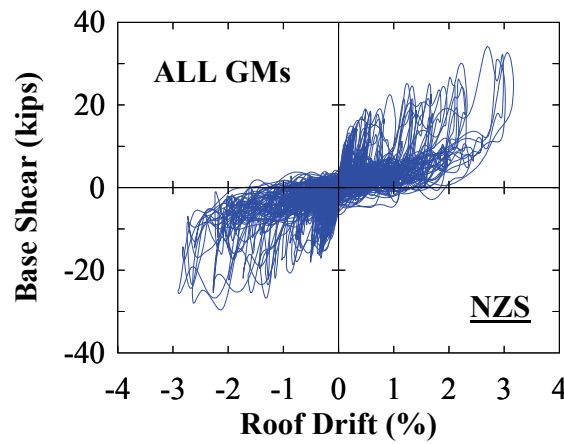
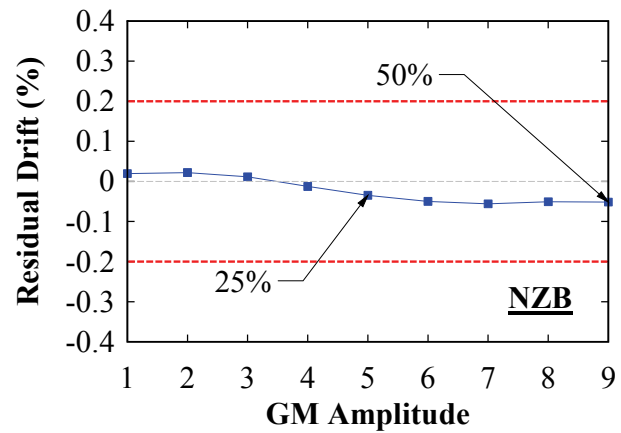
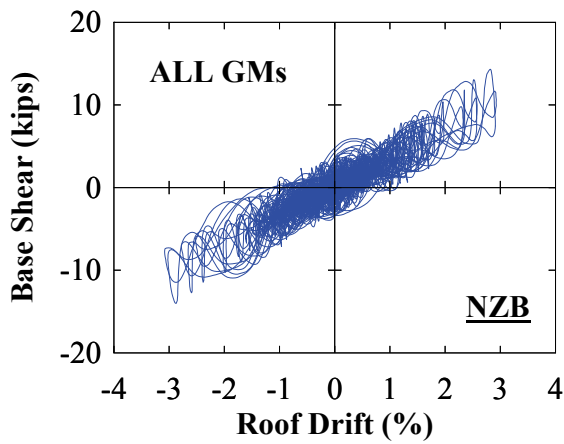
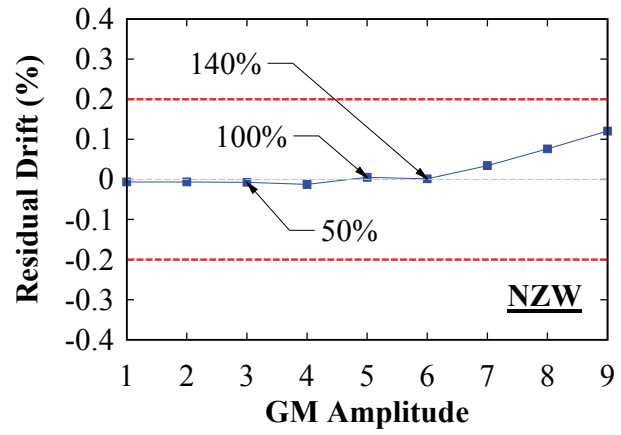
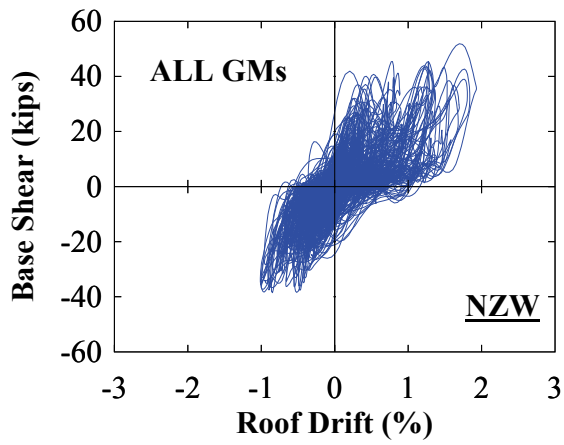
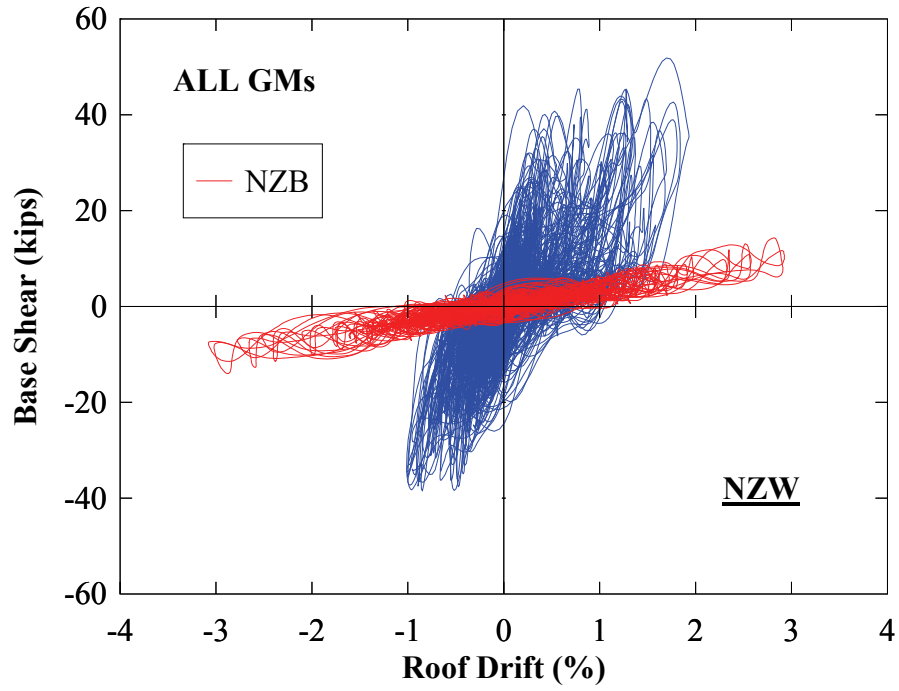
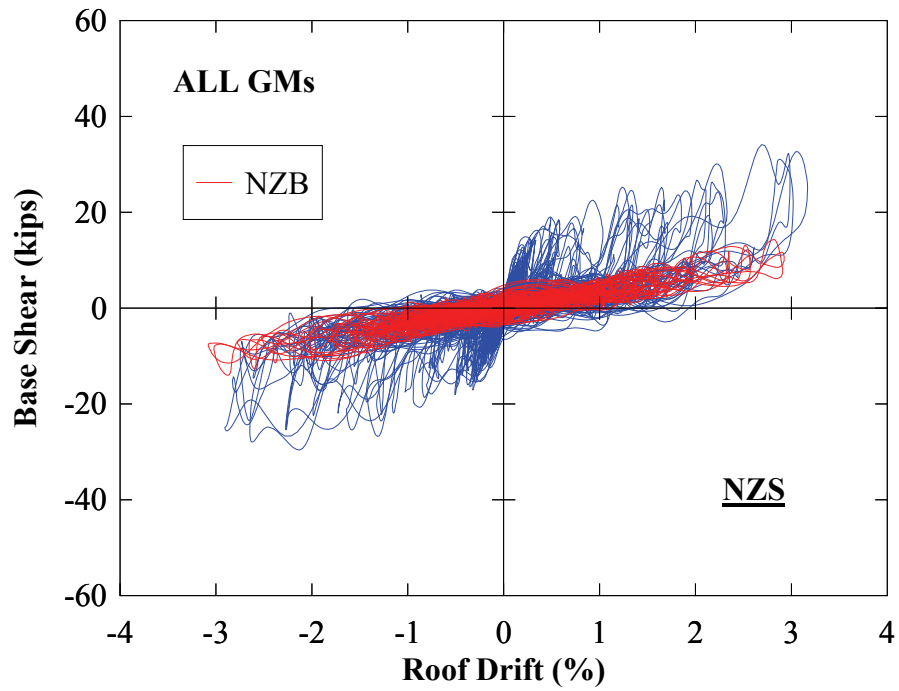


FIGURE 7-39 Frame NZ - global response



(a)



(b)

**FIGURE 7-40 Global response: (a) NZW versus NZB; (b) NZS versus NZB**

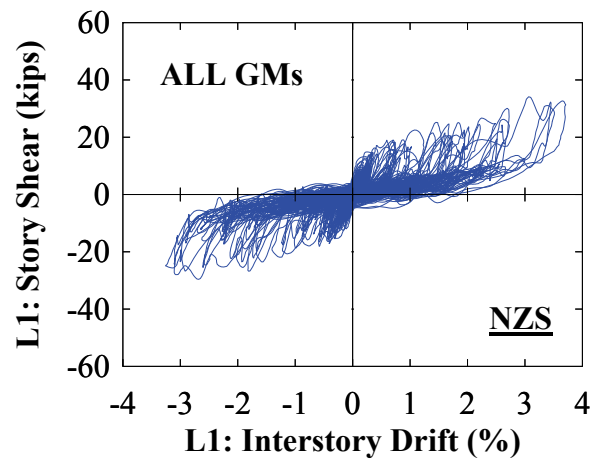
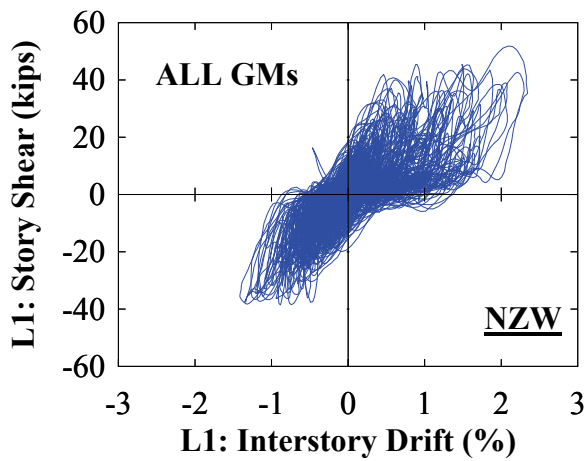
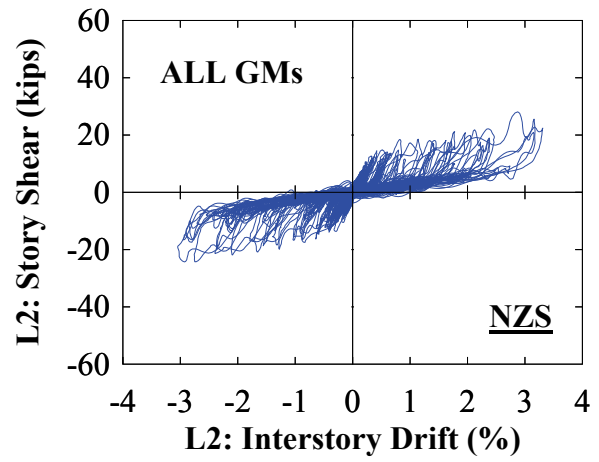
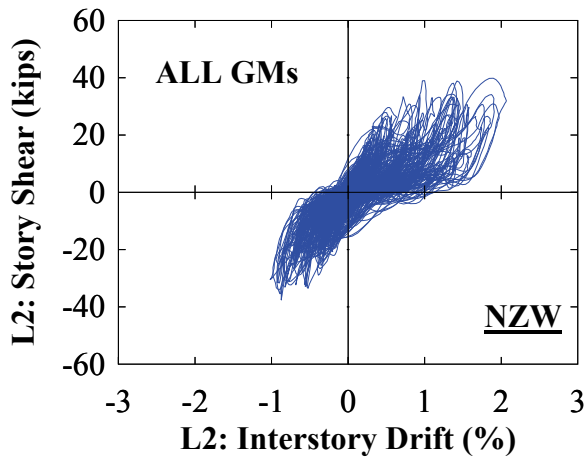
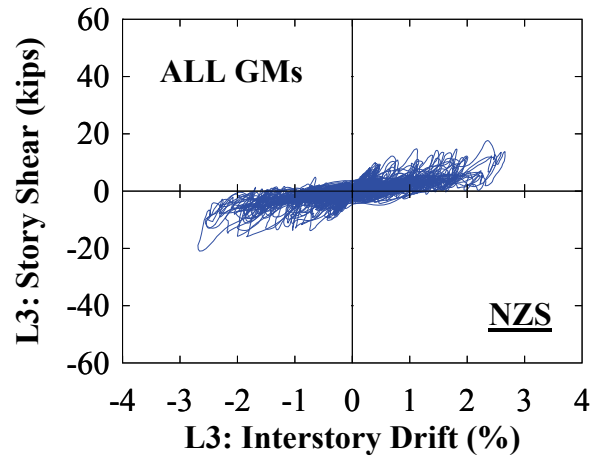
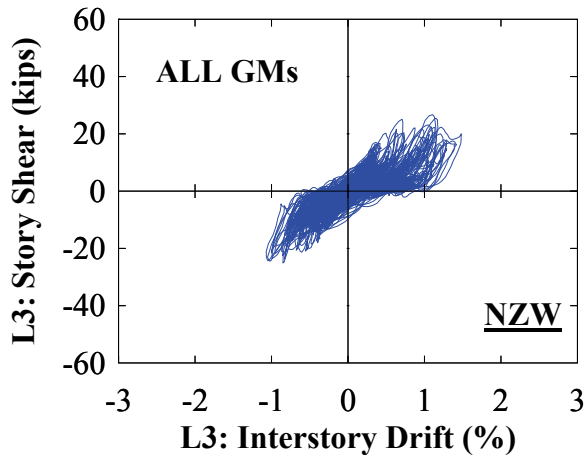


**FIGURE 7-41 Frame NZ - story shear versus interstory drift**

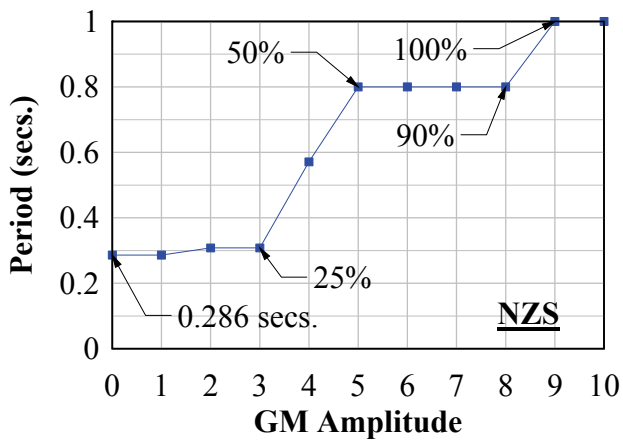
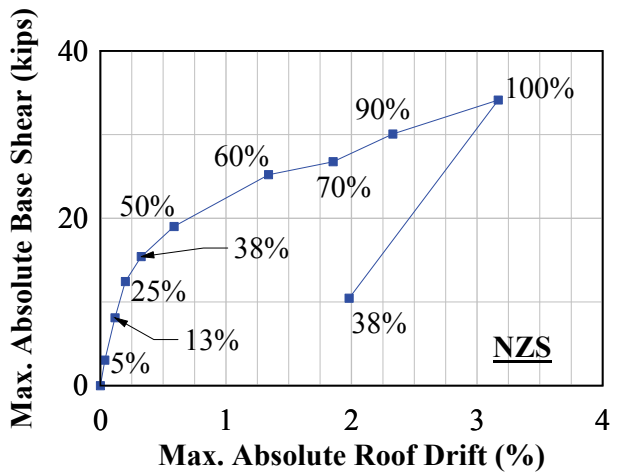
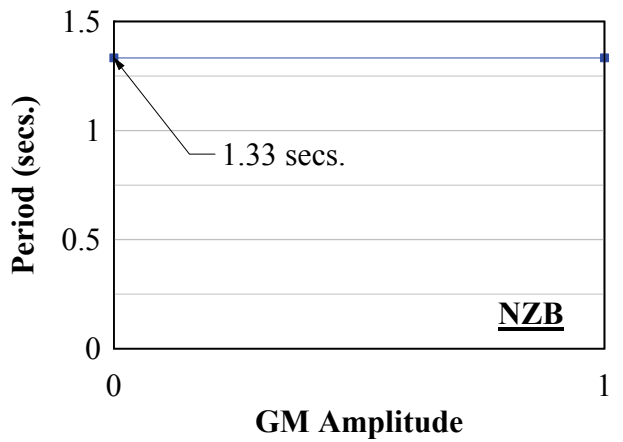
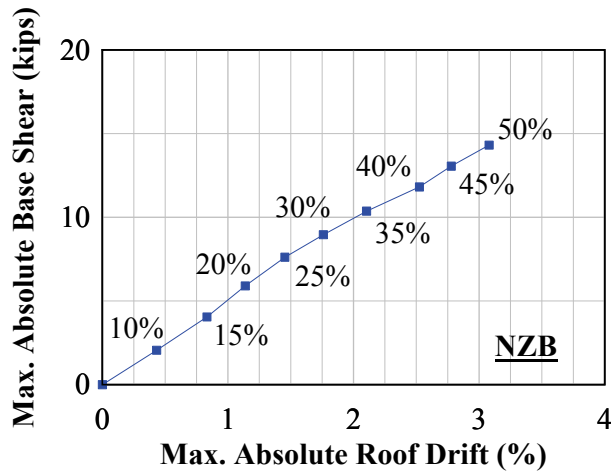
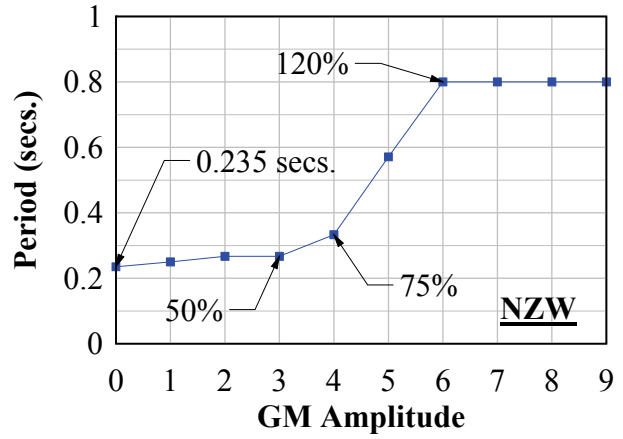
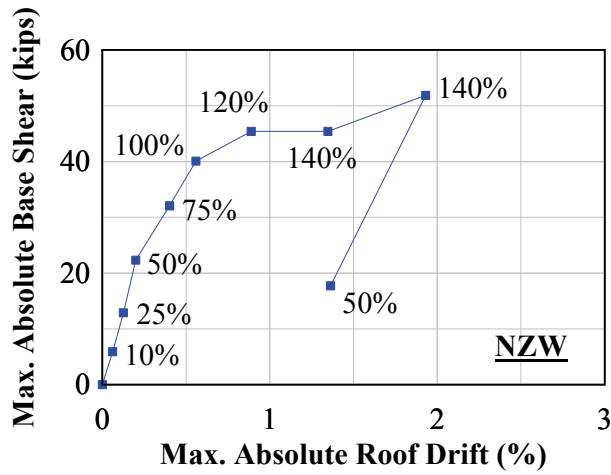


**FIGURE 7-42 Frame NZ - incremental dynamic response**

### **7.5.2 NZ: Boundary Frame Post-Tension Response**

The target initial PT force for frame NZ was approximately 40 to 45% of the PT yield strength. The normalized achieved initial PT force and values at the start of subsequent GM amplitudes are shown in figure 7-43. The PT response is shown in figure 7-44 for frame NZW. The general observations on response observed in the static tests and the response to dynamic loadings observed for frame FR made previously are similar here for frame NZW.

The corresponding response(s) for frame NZB are provided in figures 7-45 and 7-46. Interestingly it is observed that there is a noticeable loss in PT forces between GM amplitudes. It appears that with the absence of the infill web plate or strips, the PT boundary frame is more susceptible to PT force losses. To clarify, during the dynamic frame response for frame NZW, the frame drift is predominantly dependent on the response of the infill web plate. That is for a given drift, the restoring force is provided mainly by the energy dissipation of the infill web plates. In contrast, for the boundary frame, the PT elements alone provide resistance to the inertia forces. In doing so, it appears that this may have had an influence on PT anchor wedge seating, leading to a larger reduction in PT forces observed between GM amplitudes. For comparison, note that for frame FRB subjected to two GM amplitudes up to approximately 1.7%, PT force losses were negligible, whereas frame NZB was subjected to nine GM amplitudes up to approximately 3.1% drift. Furthermore, the initial PT force and response history is shown in figures 7-47 and 7-48, respectively for frame NZS. In particular, the initial PT forces remain essentially constant between GM amplitudes, providing additional evidence of the PT force losses presented for frame NZB (i.e., PT losses due to increased anchor wedge seating).

Finally, the normalized relative PT force losses are shown in figures 7-49 and 7-50. It is observed that the relative PT force losses were less than 5% for test NZW, approximately 10 to 20% across the story levels for frame NZB, and less than 5% for frame NZS. The average total cumulative PT force losses was within 10% for frame NZW, 10 to 25% across the story levels for frame NZB, and 10 to 30% across the story levels for frame NZS.

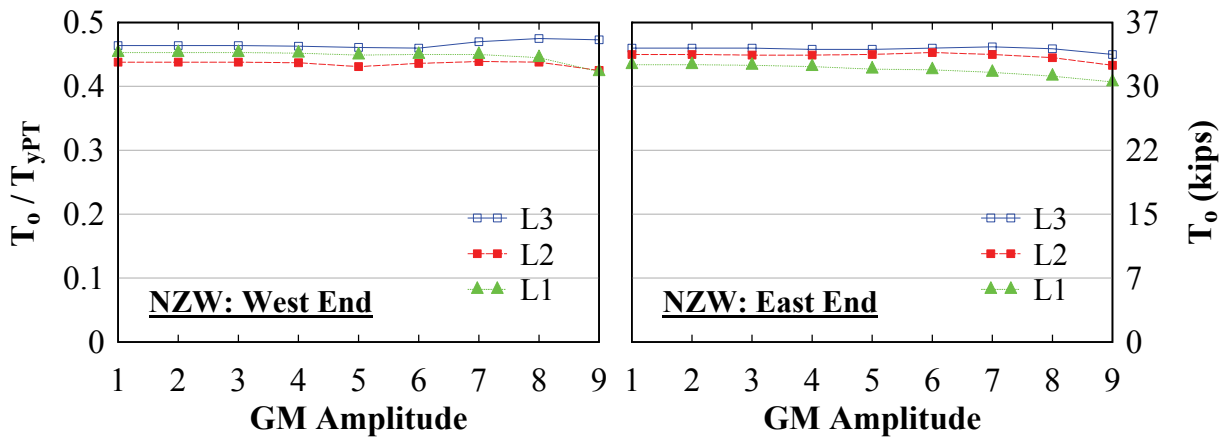


FIGURE 7-43 Frame NZW – initial PT forces

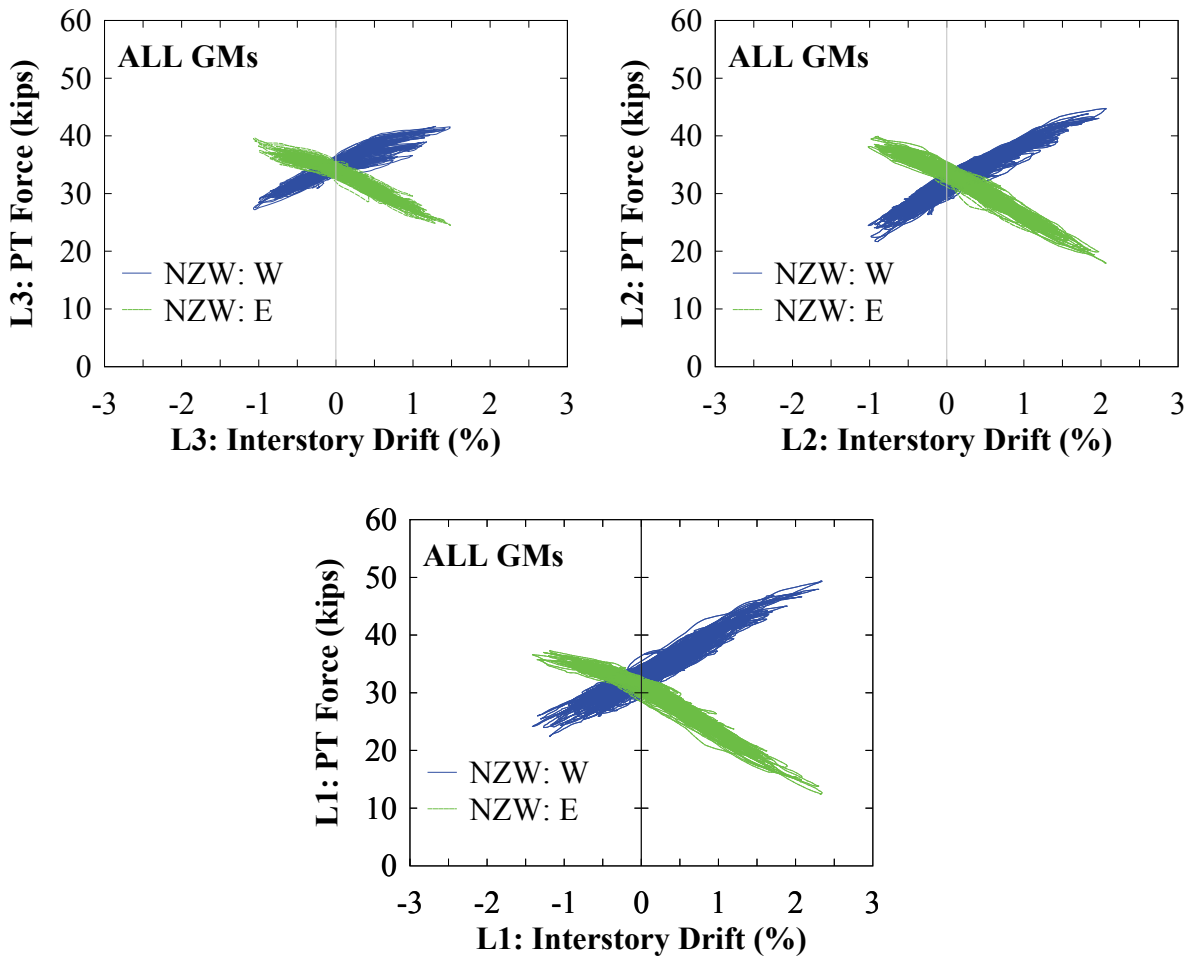


FIGURE 7-44 Frame NZW – PT response

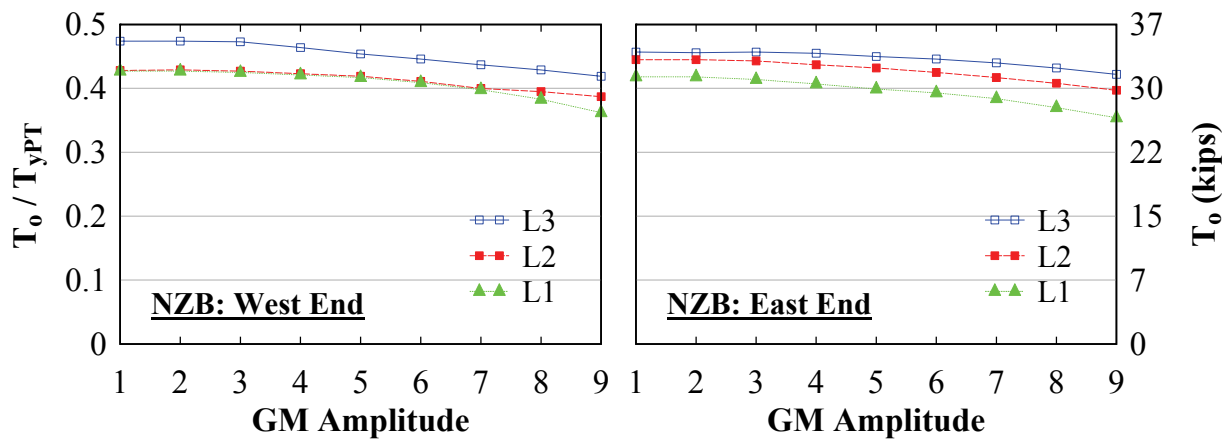


FIGURE 7-45 Frame NZB – initial PT forces

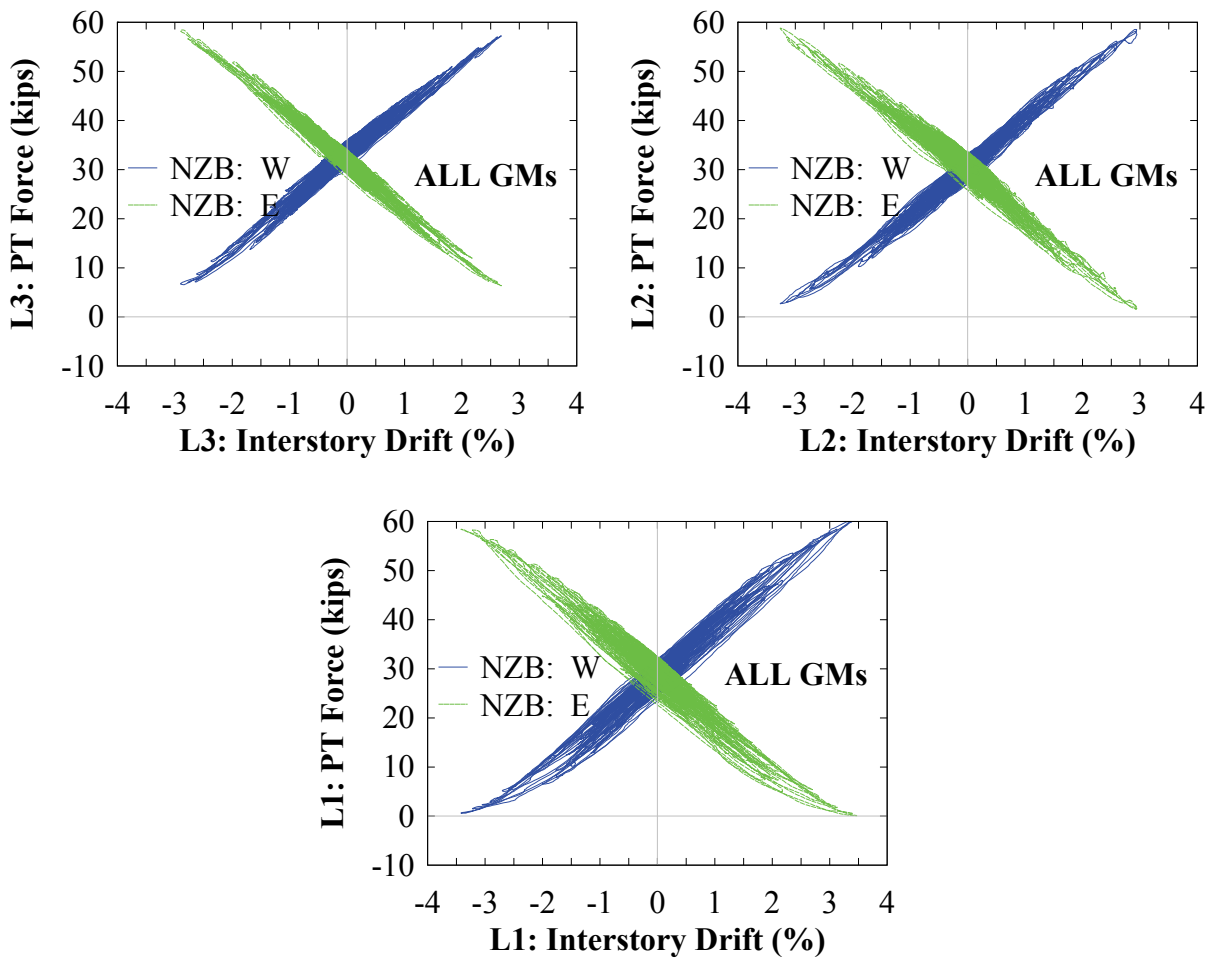


FIGURE 7-46 Frame NZB – PT response



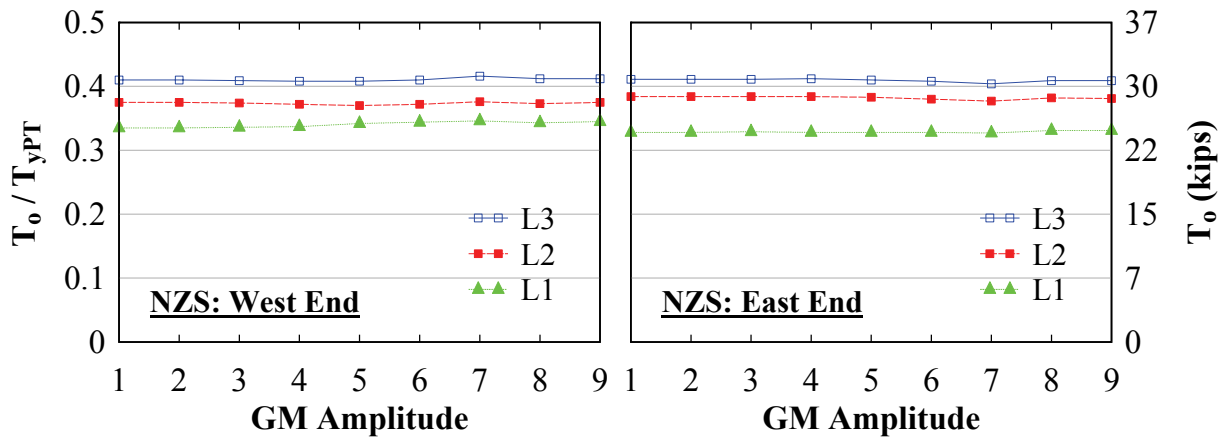


FIGURE 7-47 Frame NZS – initial PT forces

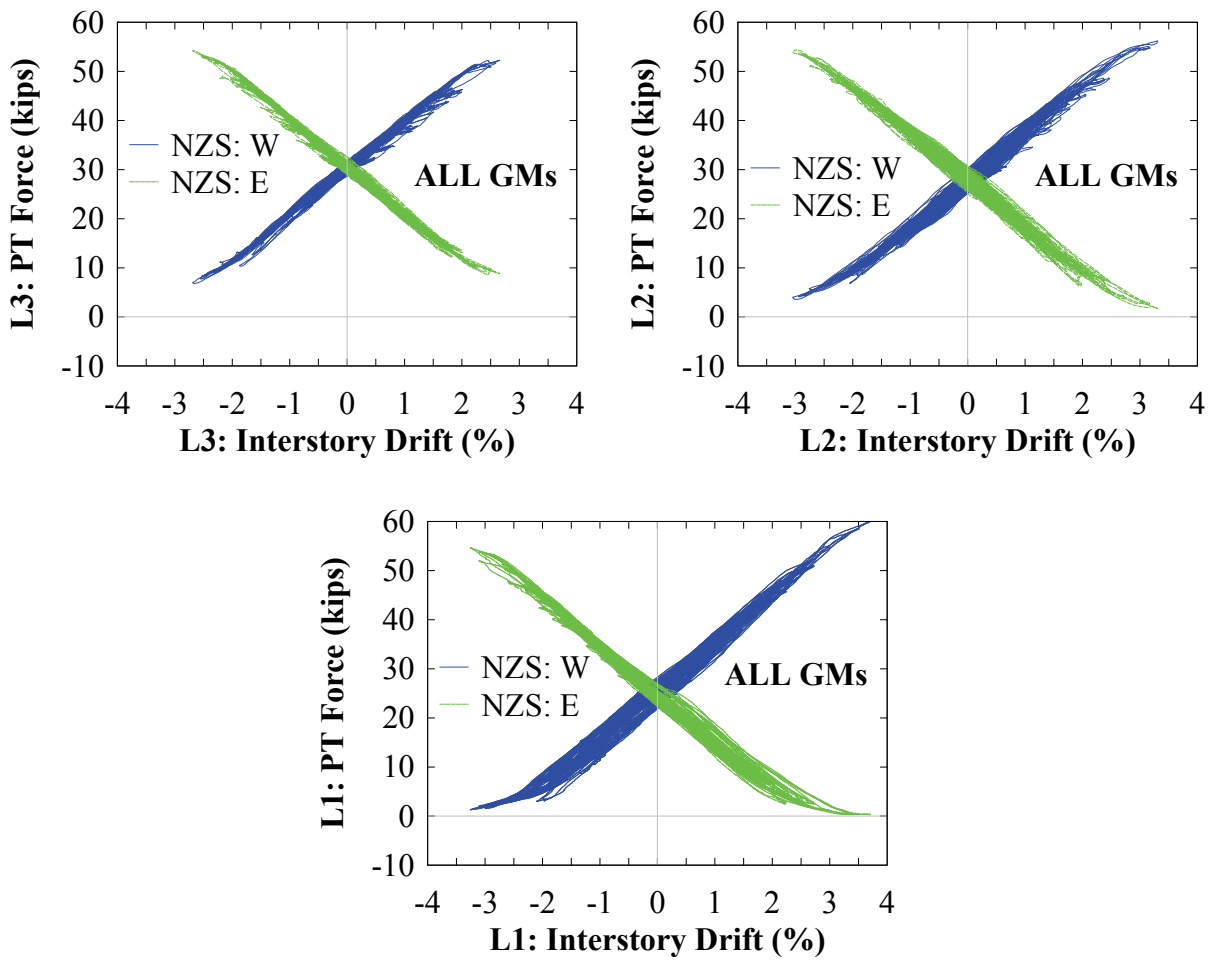


FIGURE 7-48 Frame NZS – PT response

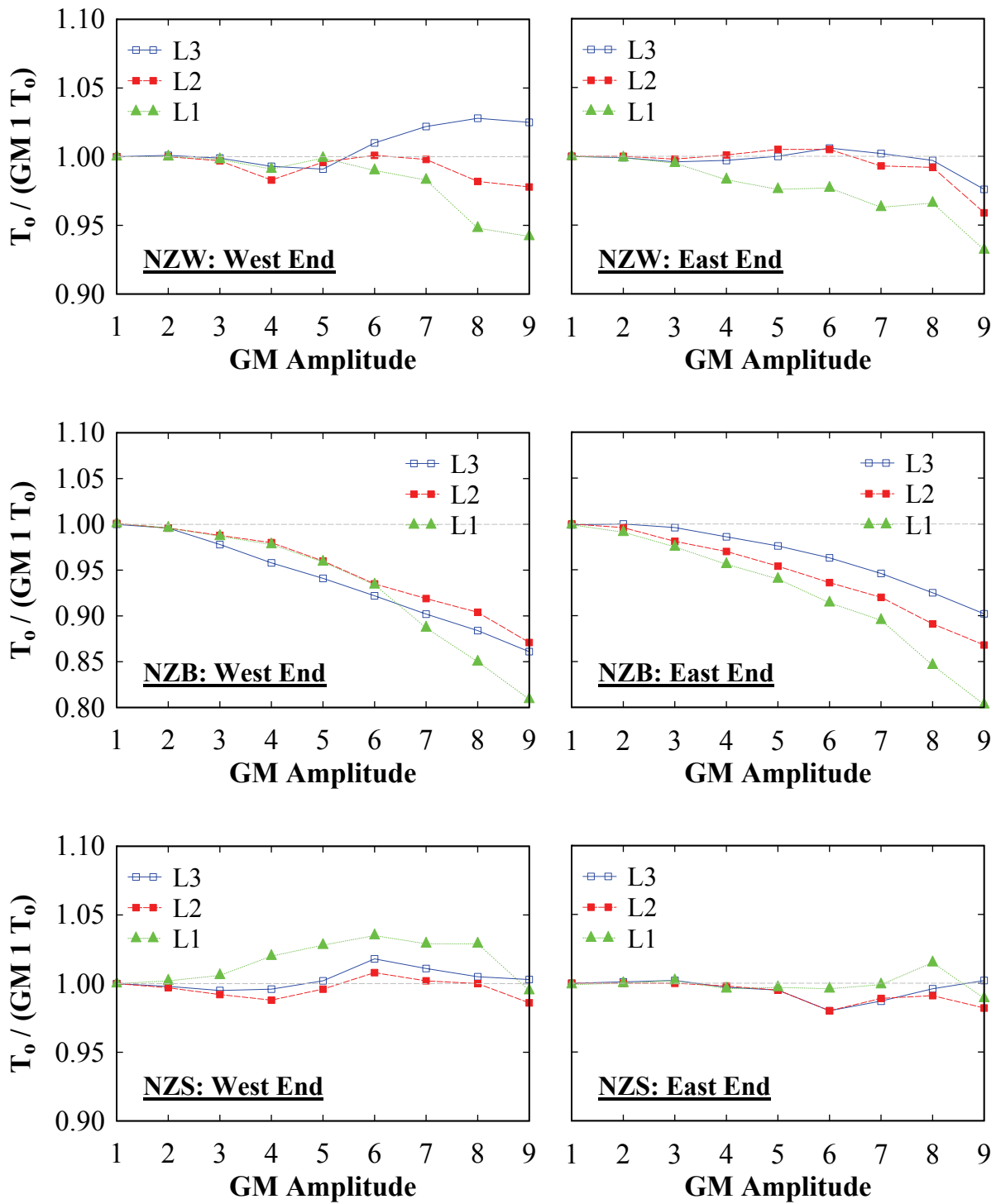


FIGURE 7-49 Frame NZ – initial PT forces normalized by GM amplitude 1

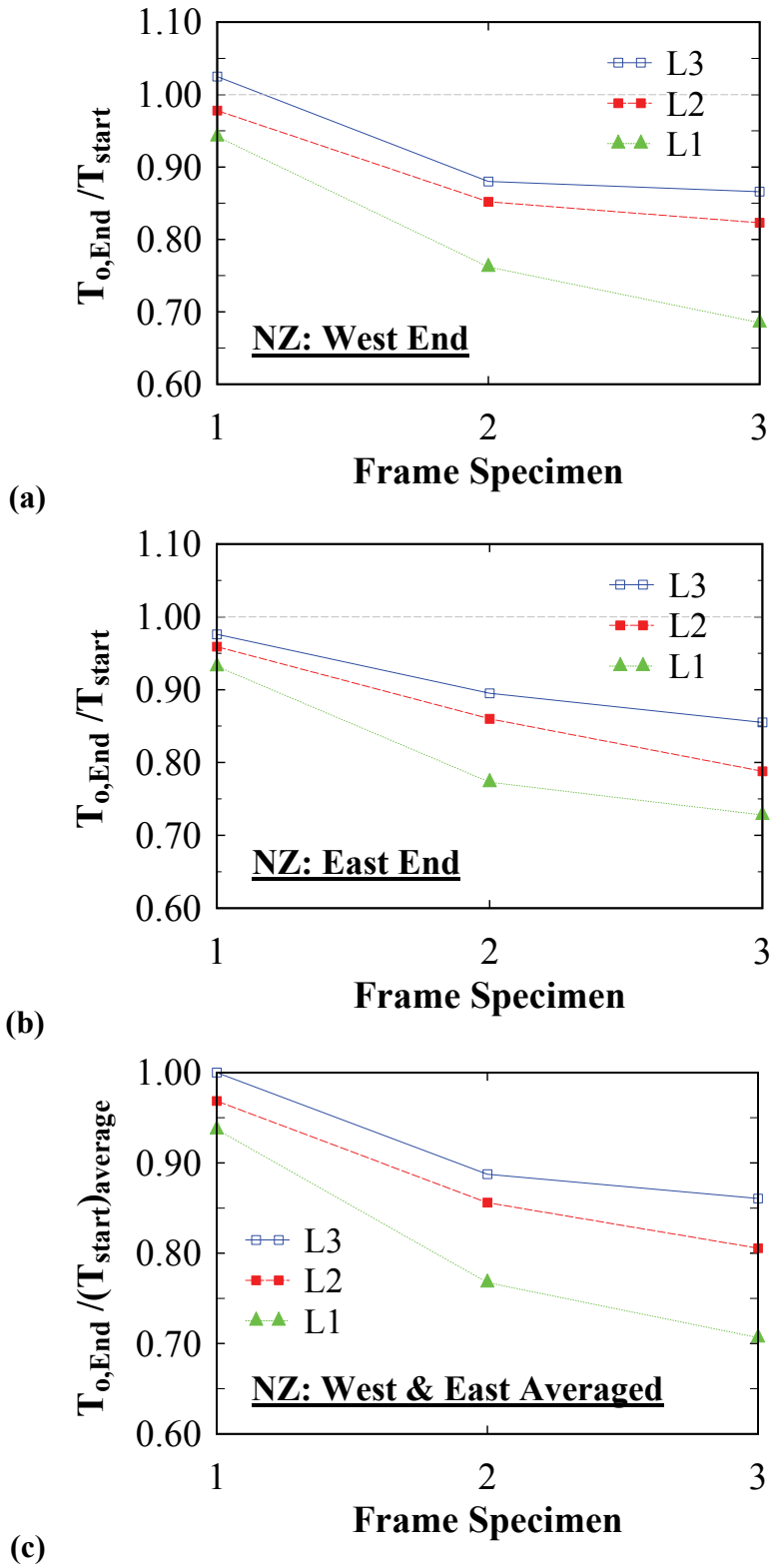


FIGURE 7-50 Normalized initial PT force change between NZ tests: (a) West; (b) East; (c) averaged

In general, it has been observed that PT force losses for frame NZ were larger than frame FR. In part this could be attributed to the fact that the PT strands for frame NZ have the potential to become fully relaxed at relatively large drifts. In doing so, some vertical slip of the PT anchor could occur, affecting the initial PT forces in the strands. Furthermore, PT loss effects due to anchor wedge seating will affect frame NZ more than frame FR. To clarify, if the PT elongation loss effects due to anchor wedge seating is  $\Delta_{loss}$ , and assumed equal for both frames, the PT force loss is equal to  $P = (AE/L) \Delta_{loss}$  where  $AE/L$  is the PT axial stiffness. Since the PT strand length,  $L$ , is shorter for frame NZ, the PT force losses due to anchor wedge seating will be larger.

### 7.5.3 NZ: HBE Strain Gage Response

The HBE end strain versus gap rotation response is shown in figures 7-51 to 7-56; plots provided include the concatenation of all GMs at each corresponding story level, and also of select individual GMs at Level 1 to provide some clarity of the typical response for a single GM amplitude. Note that only the strain gage response at the top flange is presented. The bottom flange strain gages were not used in these tests, due to lack of availability of channels in the data acquisition system at the time of test setup. However, this is not a loss given that it was observed during the quasi-static tests that the bottom flange strains were zero at these locations since there is no contact with the VBE flanges. Here, the sign convention for positive gap rotation is gap opening at the bottom flange at the West end of the HBEs, and a corresponding gap closing at the bottom flange at the East end of the HBEs. This corresponds to a sign convention of a positive drift in the Eastward direction.

The strain gage response is similar to what was observed for the quasi-static tests. However, the nonlinear response for frame NZW is more pronounced due to the erratic nature of dynamic loading (in contrast to slow cyclic loading of the static tests). Additionally, the vertical offset error is also observed in the strain gage data. Furthermore, the “dipping” effect is present and also observed with the NZB test, providing further evidence that this phenomenon is not due to the infill web plate/strips. Furthermore, the response of frame NZB and NZS are essentially nonlinear elastic; indicating that the nonlinear response observed with frame NZW is mainly due to the compression effects of the infill web plate. It is noted that the response curves with the concatenation of GMs for frame NZB and NZS appear to be nonlinear. However, the

corresponding figures with individual GMs show otherwise (i.e., response is essentially nonlinear elastic). In particular, the appearance of nonlinear response for frames NZB and NZS, is due to the vertical shifting between the individual GM amplitude response curves, which upon superposition of all GM amplitude responses, gives the appearance of nonlinear behavior.

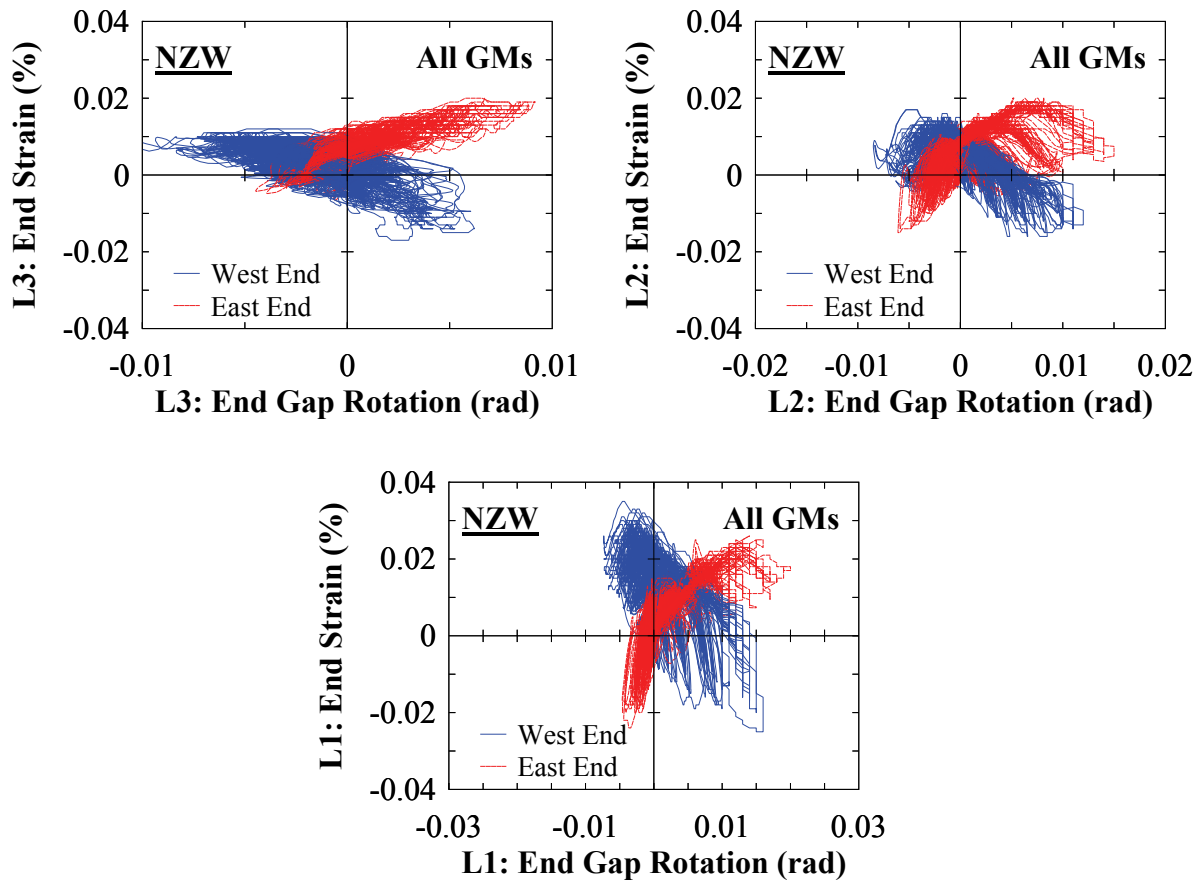


**FIGURE 7-51 Frame NZW – HBE end strain versus gap rotation**

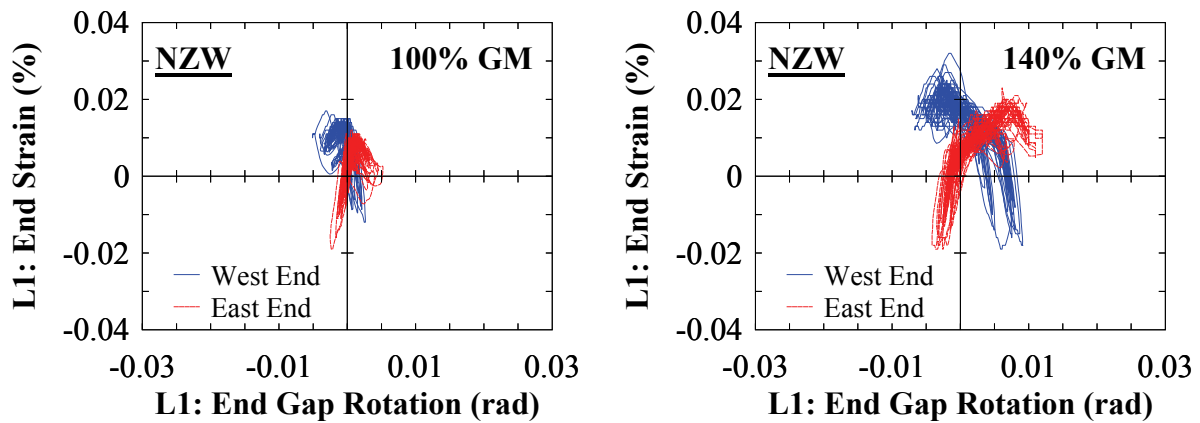


**FIGURE 7-52 Frame NZW: HBE end strain versus gap rotation – Select GMs**

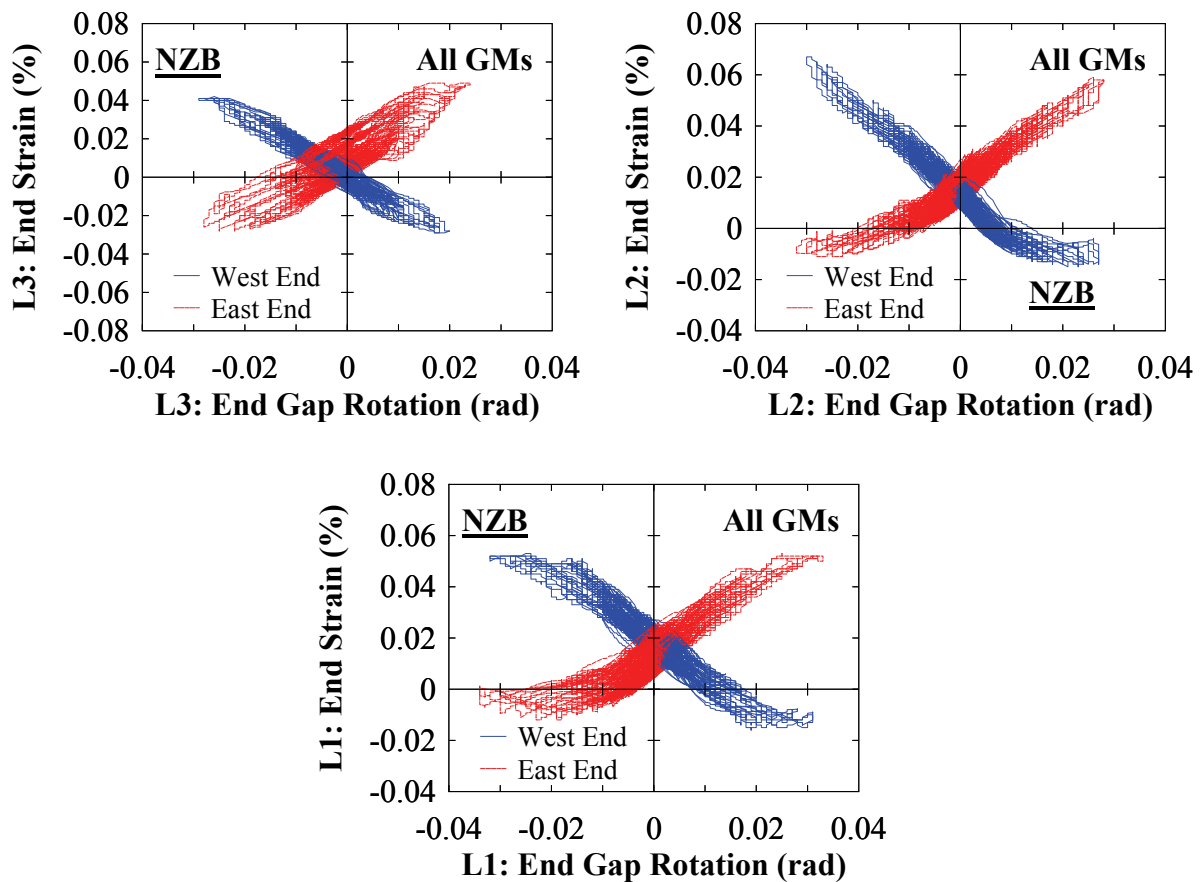


**FIGURE 7-53 Frame NZB – HBE end strain versus gap rotation**

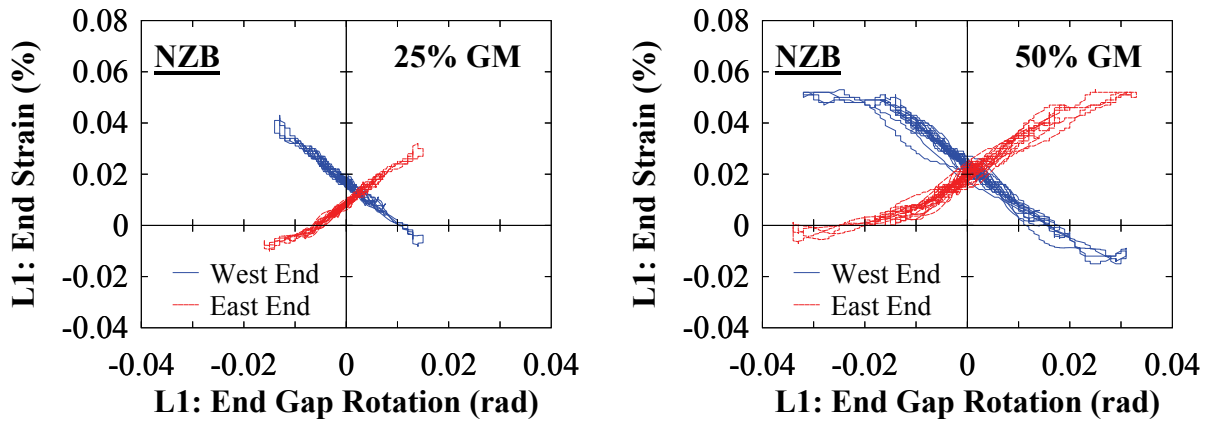


**FIGURE 7-54 Frame NZB: HBE end strain versus gap rotation – Select GMs**

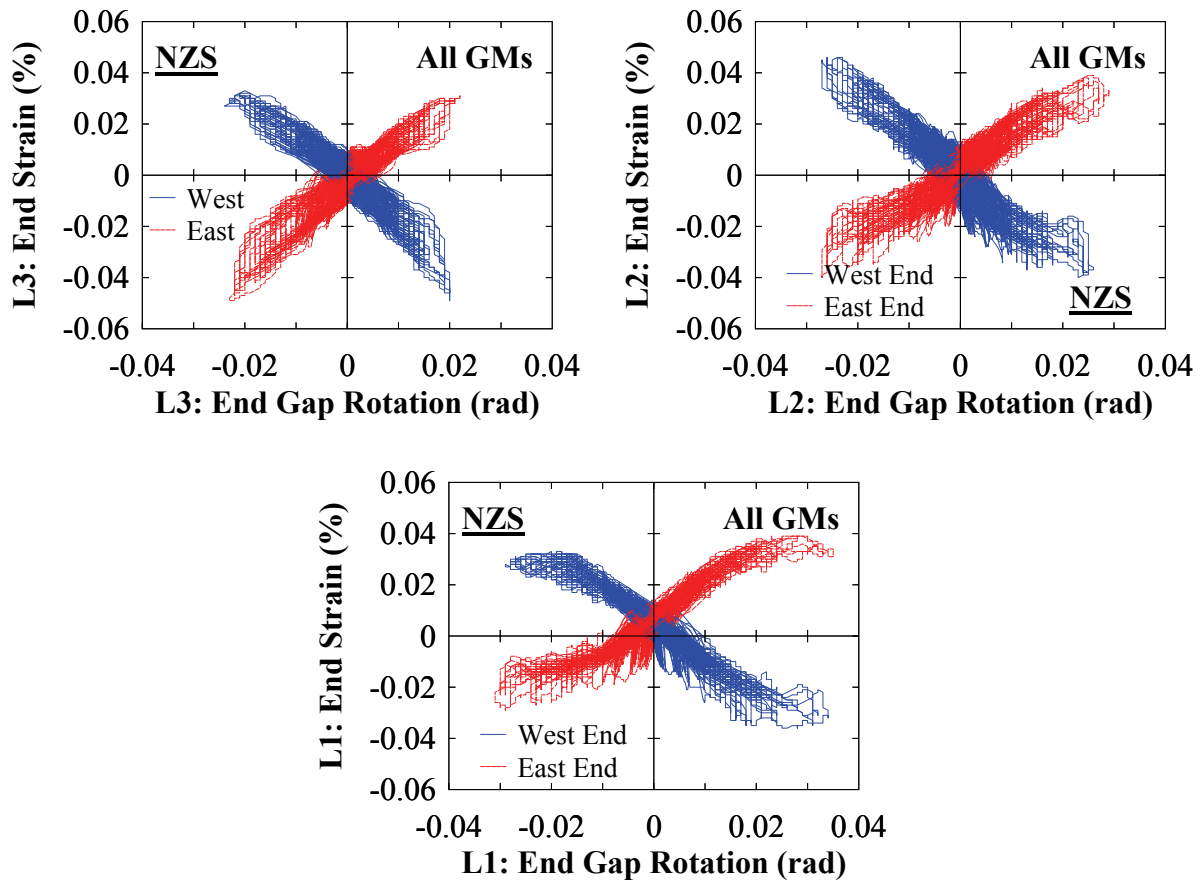


**FIGURE 7-55 Frame NZS – HBE end strain versus gap rotation**

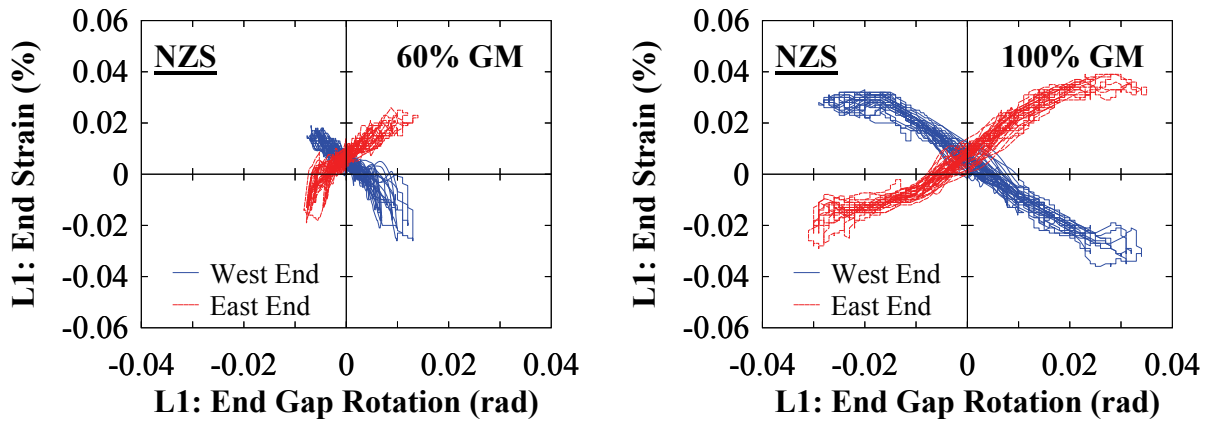


**FIGURE 7-56 Frame NZS: HBE end strain versus gap rotation – Select GMs**

### 7.6 Flange Rocking Frame versus NewZ-BREAKSS Frame

The incremental dynamic response for frame FR and NZ presented earlier are superimposed and shown in figure 7-57 for comparison. Note that for frame FRW and NZW, only results up to 140% GM are shown, as thereafter frame NZW repeated the 140% GM, where FRW did not. Observations on the differences in elastic fundamental period were provided in Section 7.3.1 and general observations on the incremental changes in period shifts were made in previous sections, particular for each test frame. However, for convenience, recall that the fundamental periods calculated using the transfer functions are affected by the frequency resolution, but mainly that the response includes the effects of the shake-table frame extension. Thus, it is understood that the periods shown are only an approximate representation of the periods of the test specimens.

The comparison of the incremental dynamic pushover response curves provides a more accurate and informative representation of the response of the test specimens. One significant difference in response between the two frames having infill web strips occurs at the 100% GM, but this difference is due to the resonance that occurred for frame FRS. Furthermore, for frame FRW, the base shear demand and roof drift are noticeably larger than the corresponding values for frame NZW for the 120% and 140% GM. This is slightly peculiar as frame NZW, in theory, should have a larger roof drift for the same loading history, than frame FRW with all parameters being equivalently equal. Aside from the observations noted, the absolute base shear demands and peak roof drifts are comparable for frame FR and NZ.



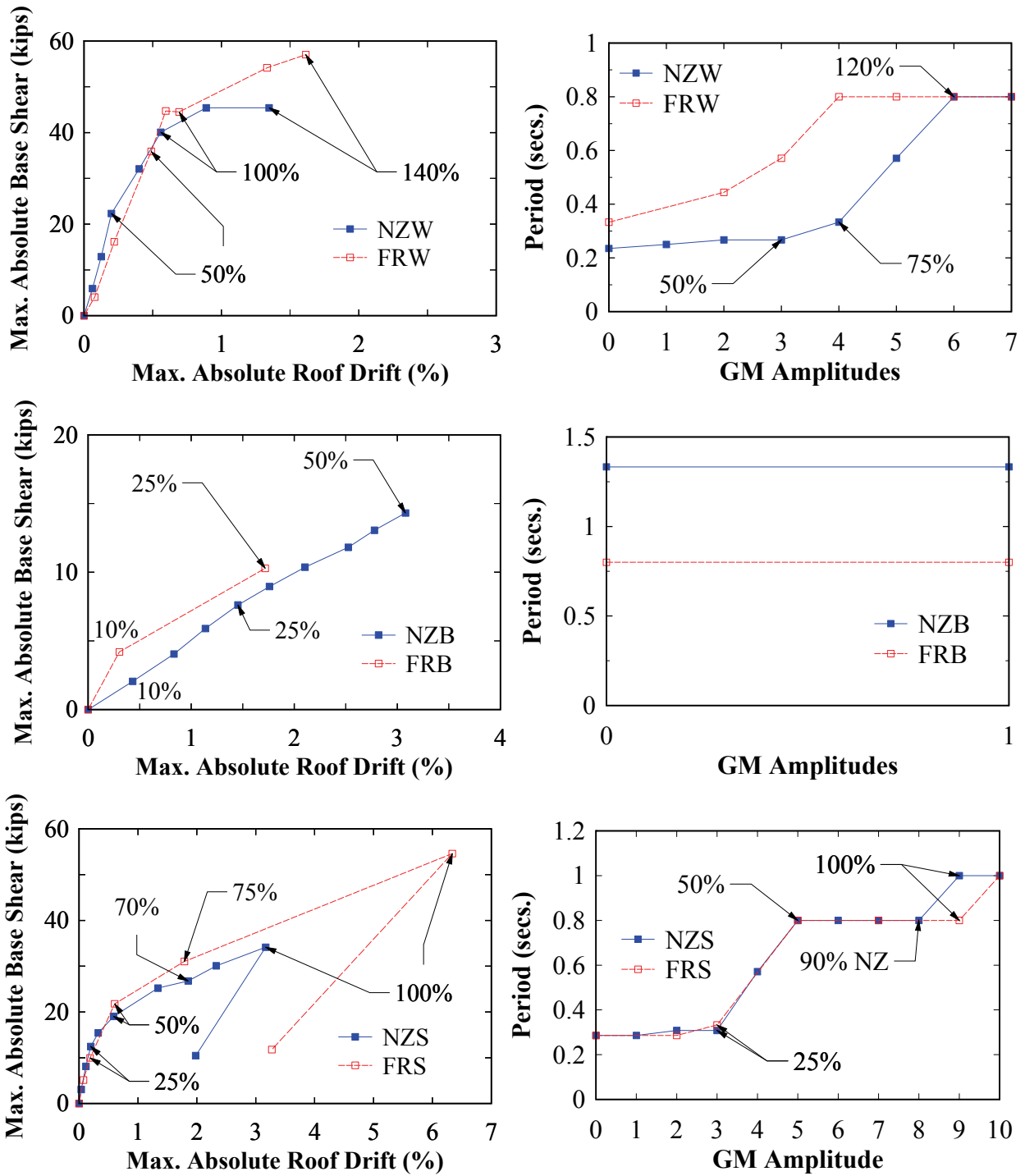
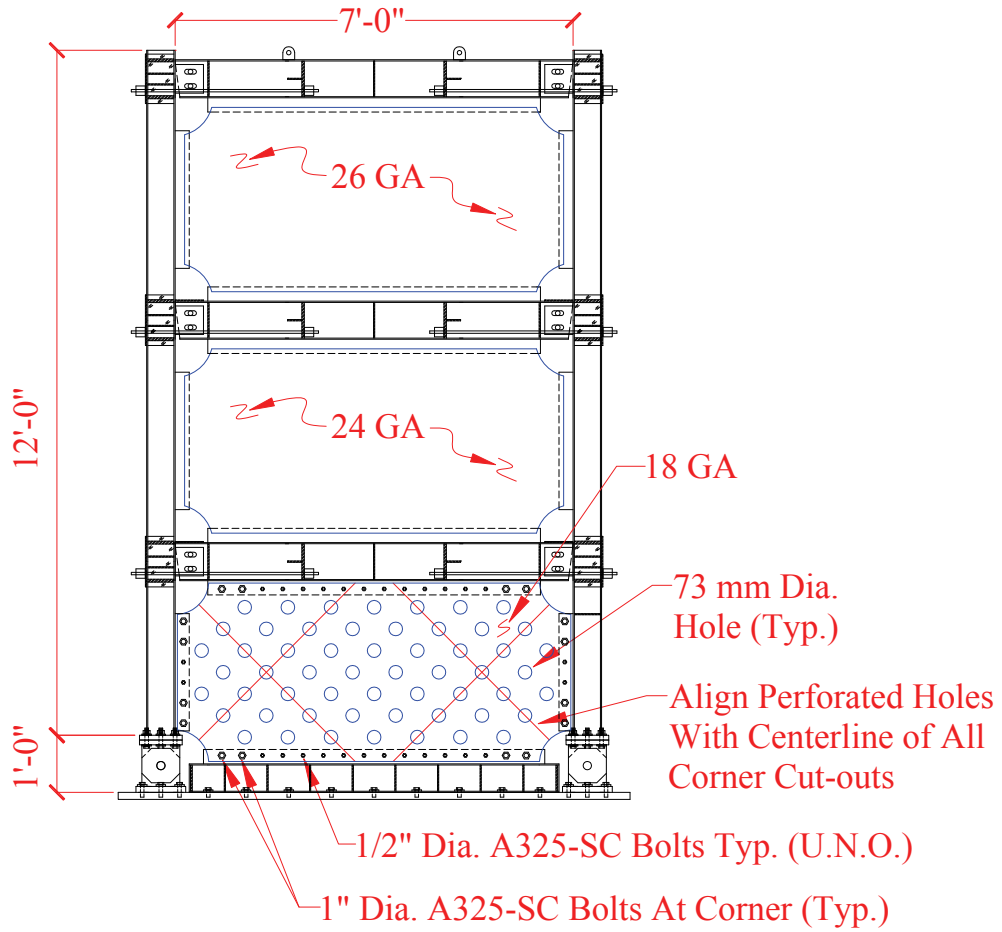


FIGURE 7-57 Frame FR versus NZ - incremental dynamic response

## 7.7 NewZ-BREAKSS Frame with Perforated Infill Web Plate

A final test was performed with frame NZ, using a perforated infill web plate at Level 1 with an alternative bolted connection to the boundary frame (i.e., frame NZP). The investigation of this alternative bolted connection was performed in collaboration with Robert Tremblay (Professor) and Marie Eve-Gagné (graduate research assistant) of Ecole Polytechnique of Montreal, who developed the equations for the strength of the bolted infill connection. The perforated infill web plate was designed to be approximately equivalent to a solid 22 GA infill web plate used in the previous tests conducted at UB. Thus, the target goal was to have frames NZW and NZP be approximately equivalent.

For use in frames with HBE-to-VBE rocking connections, it is important that the location of the perforated holes be aligned with the corner cut-outs; since the radial corners are themselves a natural perforation in the plate (i.e., in the form of a quarter circle). Furthermore, no changes were made to Levels 2 and 3 from the previous tests due to time constraints (because new holes had to be drilled in the existing NZ boundary frame for the bolted connections). The bolted connections were designed as slip-critical, relying on pre-tensioning of the bolts to prevent slip through friction. Additionally, larger diameter bolts were provided at the corner cut-out locations where the tensile strains in the infill web plate are the largest, to provide additional clamping force. A schematic of the test frame is shown in figure 7-58, the installed perforated infill web plate is shown in figure 7-59, and the test setup is shown in figure 7-60.



**FIGURE 7-58 Frame NZP - frame elevation**

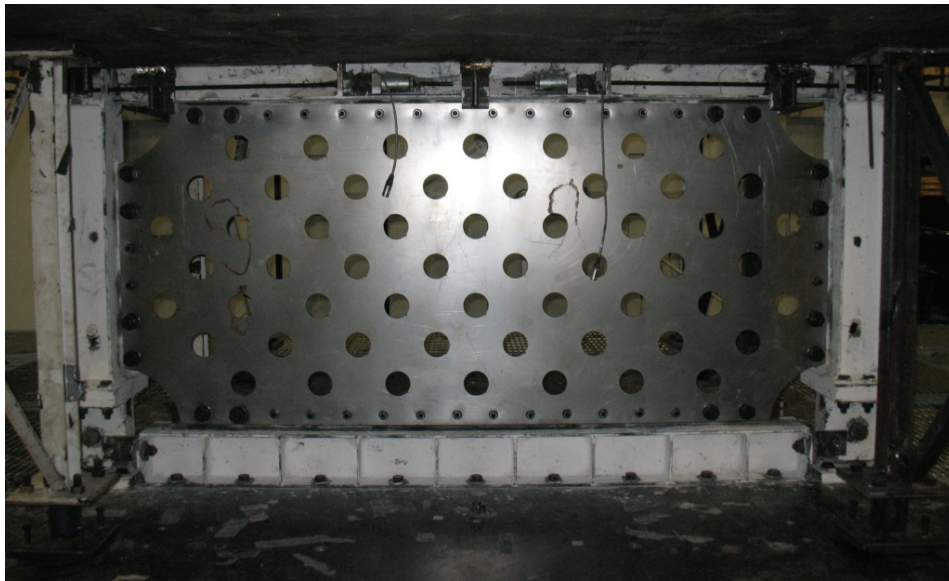


**FIGURE 7-59 Frame NZP - perforated infill web plate**

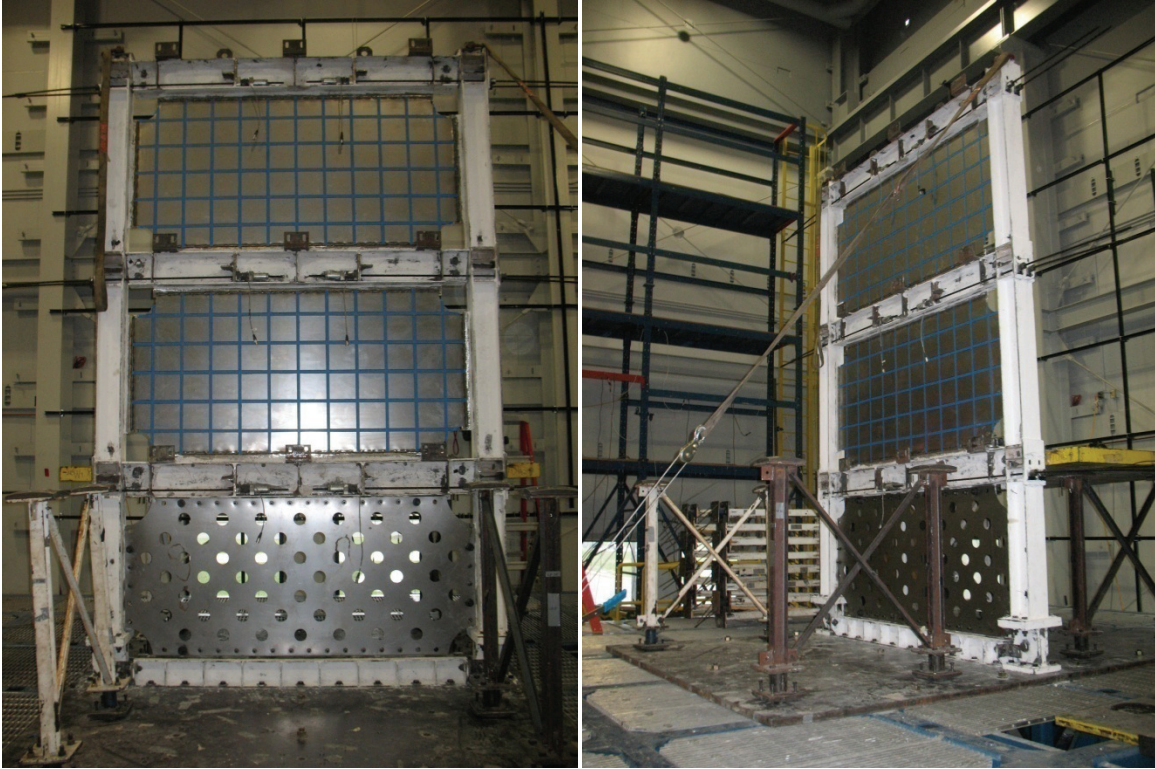


**FIGURE 7-60 Frame NZP – test setup**

### 7.7.1 NZP: Global Response

The base shear versus roof drift and the residual drifts for all GM amplitudes are shown in figure 7-61. Furthermore, the corresponding incremental dynamic pushover response and change in fundamental period are shown in figure 7-62. Similar to previous tests, recentering was achieved for all GM amplitudes. It is also observed that after the 140% GM repeat, there was a decrease trend in the residual drift (figure 7-61). Coincidentally, the subsequent roof drifts are less than the previously attained peak roof drift (at the 140% GM repeat). This confirms that the compression strut effects of the infill web plate during recentering is reduced at peak drifts less than those previously achieved (when there is no incremental yielding of the infill web plates). Although the loading protocol matched that of the NZW test up to the 50% GM “aftershock”, it also included repeat 100% and 120% GM strong aftershocks. For these large amplitude repeat GMs, it is observed that significant strength was still achieved. Furthermore, the frame response for these GM amplitudes is shown in figure 7-63 along with the results of previous test NZB for comparison. It is observed that there still some energy dissipation provided, and that frame stiffness (at low excitation amplitudes) after significant yielding of the infill web plates was provided predominantly by the PT boundary frame.

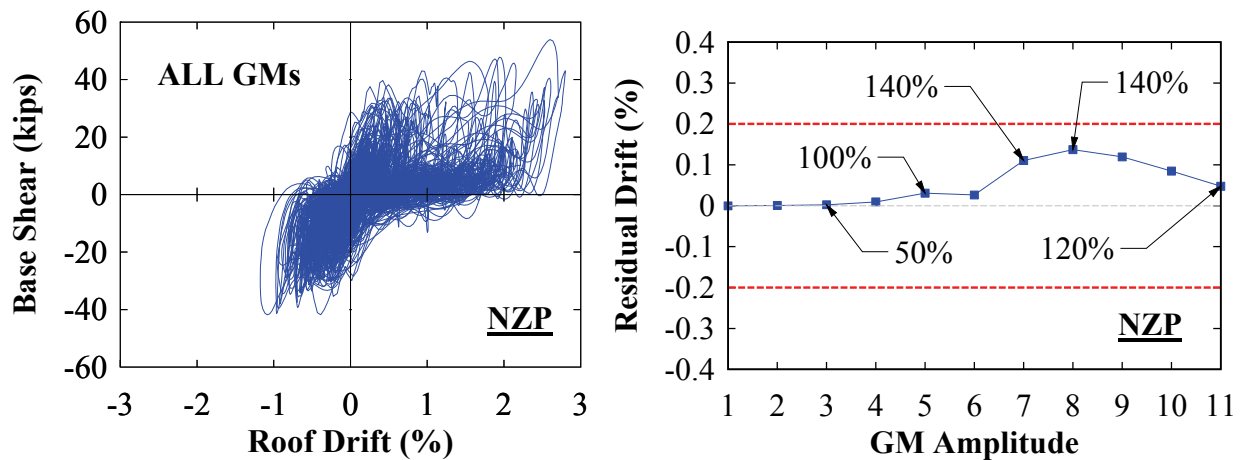


FIGURE 7-61 Frame NZP - global response

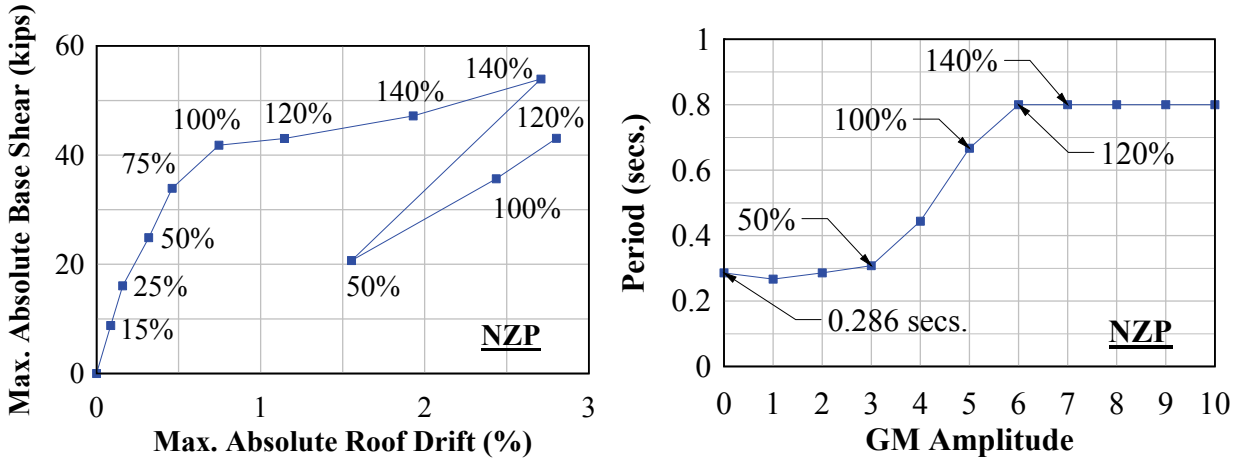


FIGURE 7-62 Frame NZP - incremental dynamic response

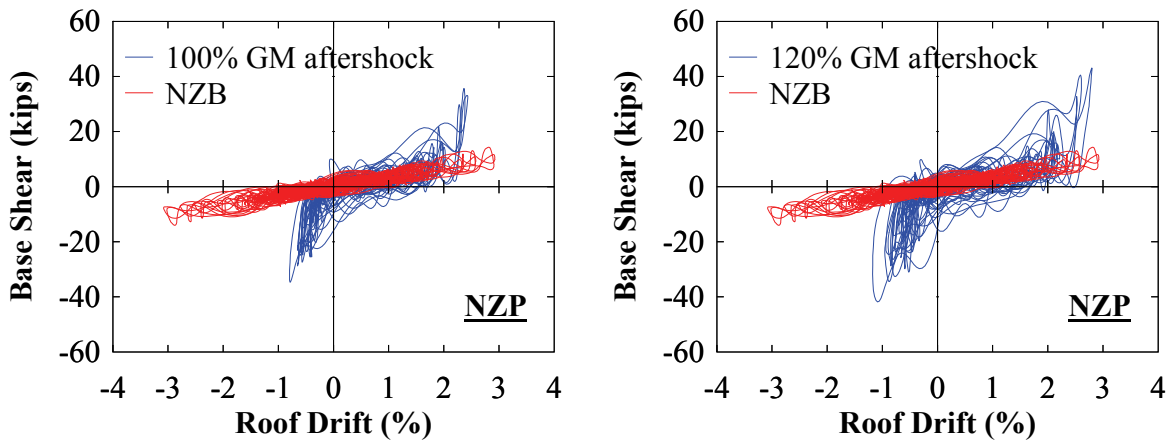


FIGURE 7-63 Frame NZP versus NZB: Global response - Select GMs

### 7.7.2 NZP versus NZW: Global Response

A comparison of the incremental dynamic response of frames NZP and NZW is shown in figure 7-64. As presented earlier, the two frames are approximately equivalent and the response should be similar. It is observed that the peak base shear demand and roof drifts are almost identical up to the 120% GM. Thereafter, it is observed that roof drifts are noticeably larger for frame NZP (i.e., at the first 140% GM), but the corresponding peak base shear demand remains approximately the same between the two frames. Furthermore, the individual story shear versus interstory drift at Level 1 is shown in figure 7-65 for the 100% and 140% GM, which provides a more direct comparison of response history between the two frames. Note that in the figure, for

convenience, dashed reference lines are provided that locate the peak base shear and roof drift responses. It is observed that the overall general response history is comparable with the difference of increased roof drift noted for the 140% GM.

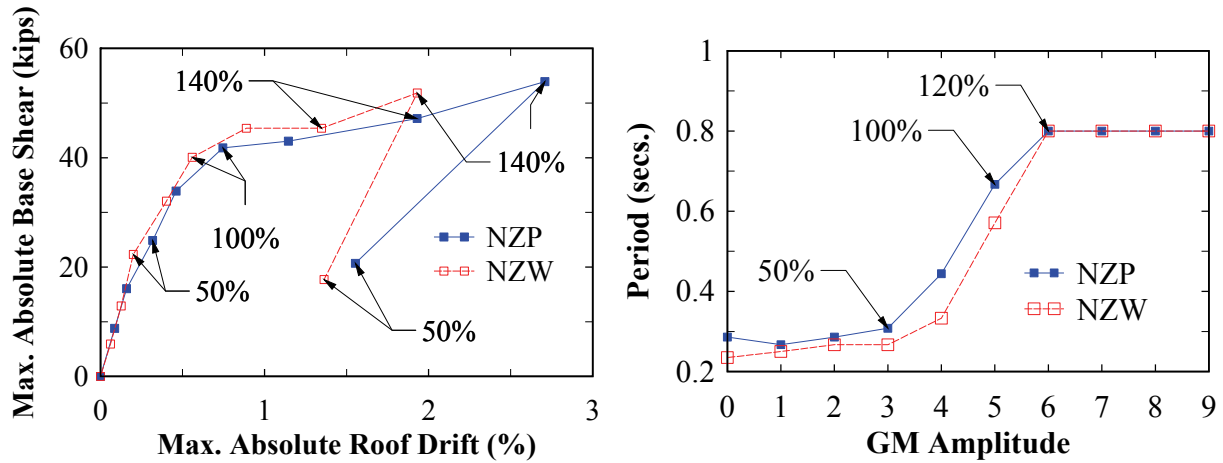


FIGURE 7-64 Frame NXP versus NZW - incremental dynamic response

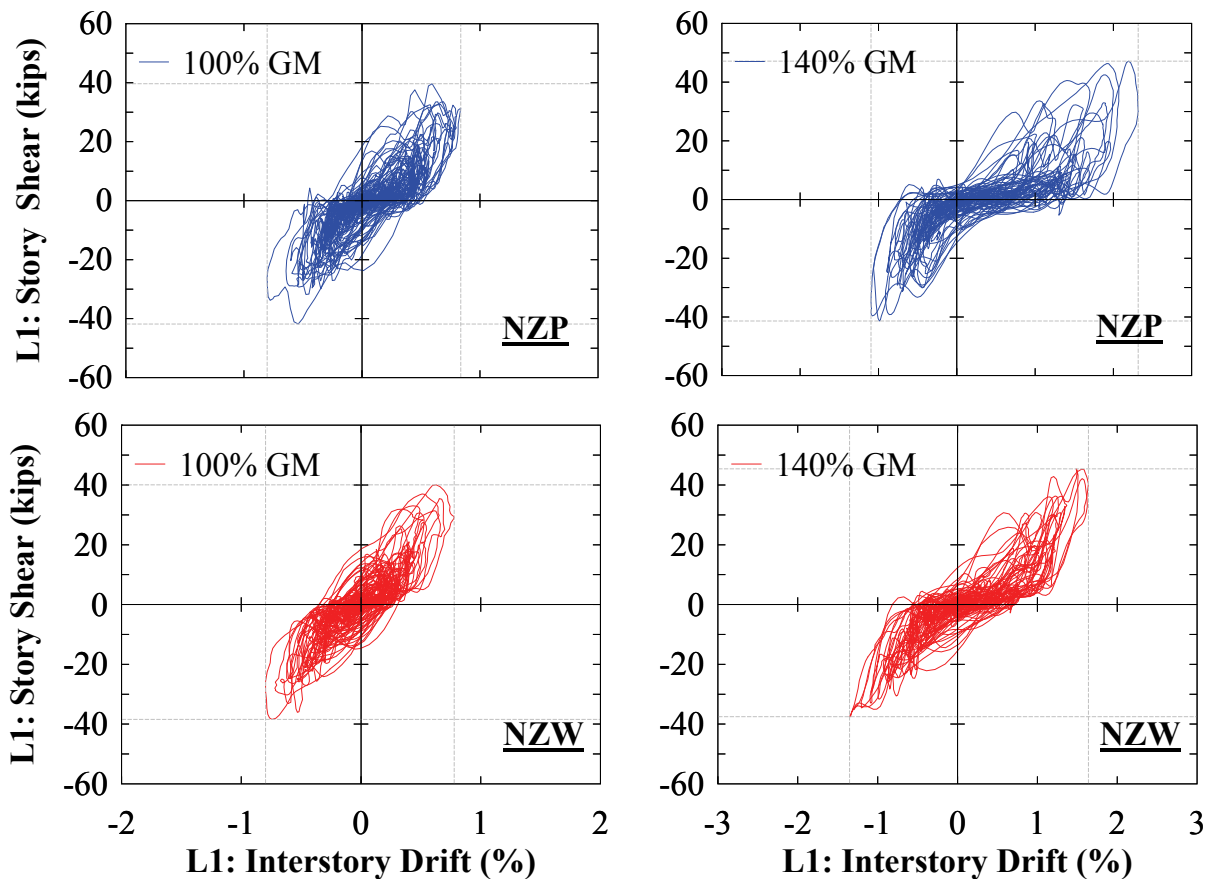


FIGURE 7-65 Frame NXP versus NZW – Global Response – Select GMs

It is apparent, that the difference in response after the 100% GM is attributed to the perforated holes provided at the Level 1 infill web plate for frame NZP. In particular, the compression strut effect of the infill web plate upon significant yield is significantly less in the perforated infill compared to the solid infill web plate. However, to quantify and validate this behavior, a finite element analysis of frame comparison would need to be performed (this is not within the current scope of work and could be investigated in future research).

### **7.7.3 NZP: Boundary Frame Post-Tension Response**

The PT response history is shown in figure 7-66 and the overall response for frame NZP is similar to that for frame NZW. It is noted that the initial PT forces at the start of test NZP include the cumulative PT force losses from the previous NZ tests. This is because the PT boundary frame used for test NZP was used “as is” after test NZS. Furthermore, the normalized change in initial PT forces between GM amplitudes is shown in figure 7-67. In comparison to frame NZW, the response is slightly more erratic. However, this is attributed to the larger range of residual drift response observed for frame NZP. That is, for any given residual drift, depending on the drift direction, a gap at an HBE-to-VBE joint will open and the opposite end of the HBE will close, thus affecting the “at rest” initial PT force values.



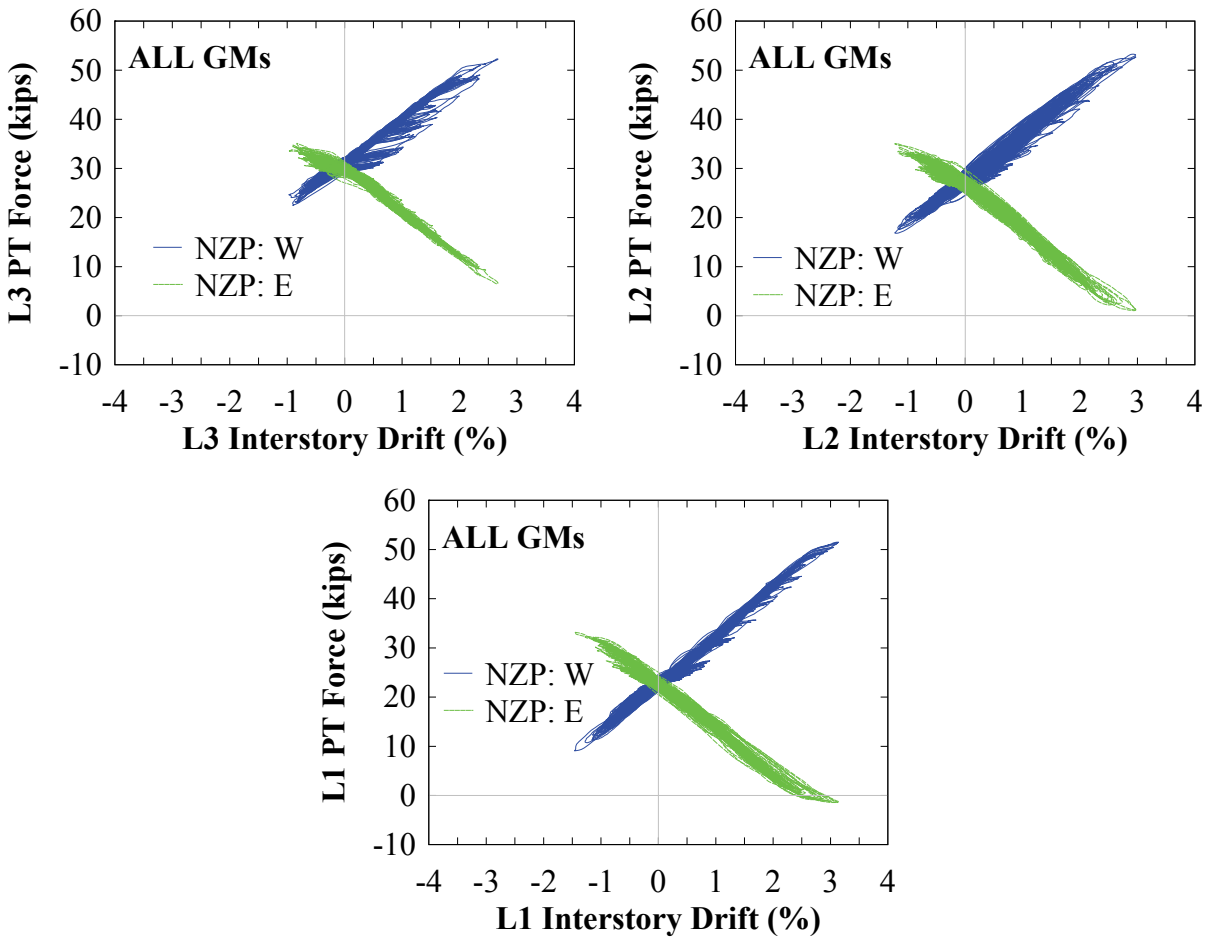


FIGURE 7-66 Frame NZP – PT response

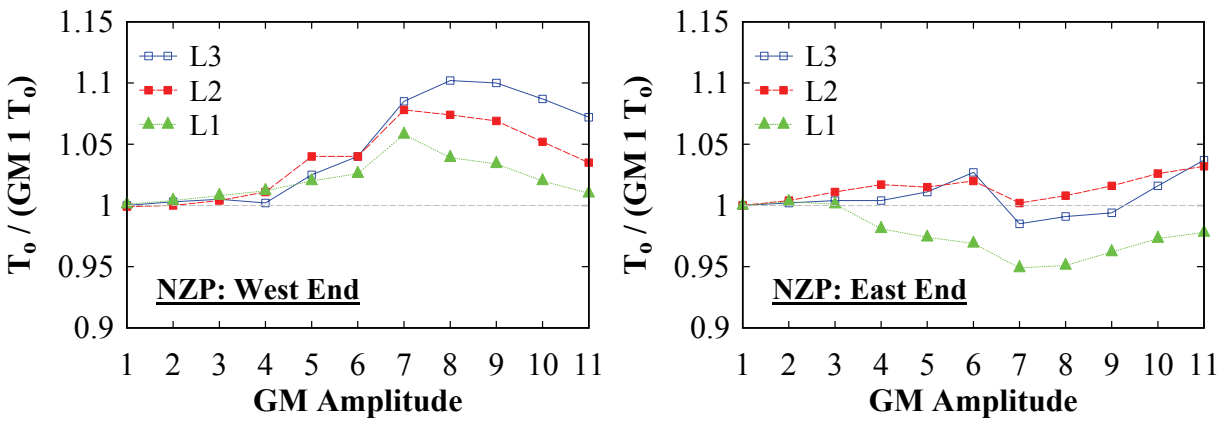


FIGURE 7-67 Frame NZP – initial PT forces normalized by GM amplitude 1

#### **7.7.4 NZP: Experimental Infill Web Plate Observations**

The deformation of the perforated infill web plate at the start and finish of test NZP is shown in figure 7-68. Furthermore, after completion of the test, the perforated infill web plate was removed to inspect the bolt holes for signs of bolt slip. No indication of bolt slip was observed, as there was no localized plate deformation present at the bolt holes. In particular, no bolt slip was observed at the corner locations of the infill web plate, shown in figure 7-69, where the bolt force demands are the largest. Accordingly, this is analogous to no tearing of the infill web plate from the boundary frame for a welded connection. In contrast, some minor infill web plate tearing occurred at Levels 2 and 3, as documented in figure 7-70.

#### **7.8 Infill Web Plate Deformations**

The primary purpose of this section is to compare the experimental results of the infill web plate/strip deformations with that of the analytical formula describing this quantity, (3-106) in Section 3. For this purpose, recall that string potentiometers were provided at Level 1, placed at a 45 degree angle at three locations along the infill web plate/strip location, namely: (1) at the corner cut-out; (2) near the corner cut-out, and; (3) far removed from the corner cut-out (reference figures 5-22 and 5-24).

First, since (3-106) is dependent on the total gap rotation, the interstory drift versus gap rotation is investigated to check the assumption of rigid sway behavior that was used in the derivation, which allows the simplification of setting the gap rotation equal to the interstory drift. Accordingly, the response on these parameters for frame FR and NZ are shown in figures 7-71, 7-72, and 7-73, for the infill web plate, bare frame, and infill web strips, respectively. Also provided is the corresponding comparison for frame NZP with the other NZ frame infill web configurations, shown in figure 7-74. For the frames with the infill web plates, it is observed that the response is nonlinear due to the presence of the infill web plate. Consequently, the interstory drift and gap rotation are not exactly proportional. In particular, the infill web has a restraining effect on opening and closing of the HBE-to-VBE joint gap; which in part, is responsible for the nonlinear response observed.

In comparison, for the bare frame and frames with infill web strips (figures 7-72 and 7-73), the interstory drift versus gap rotation response is nearly proportional, but not exactly since some nonlinear behavior is present (as there is some “fatness” in the response curves indicating that the loading and unloading along the curves are different). However, the nonlinear effects are negligible. Furthermore, for frame NZP (figure 7-74), it is observed the nonlinear response falls somewhere in between frame NZW and NZS (i.e., the compression strength of the perforated infill web plate is less than a solid web plate but more than web strips). Note that for frame FR, there is a slight lag (horizontal segment) prior to an increase in gap rotation (i.e., effects of the decompression moment described in Section 4.2.3.2); this response curve segment occurs when the HBE-to-VBE gap has not formed. In contrast, for frame NZ, the response is immediate because of the initial gaps provided at the HBES’ bottom flange.

The results just presented, indicate that (3-106) provides an approximate solution for predicting the tensile strain demands (although it was understood in the derivation, but the above validates the assumption). To check the accuracy of (3-106), the experimental versus analytical axial deformation response at the approximate locations of the string potentiometers, are provided in figures 7-75 to 7-78. Furthermore, each frame type is provided in the same figure for comparison (i.e., FRW vs. NZW, FRB vs. NZB, etc.). It is also noted that for frame FRS, for the linear potentiometer at the bottom flange at the West end Level 1 HBE, an instrumentation error occurred. Hence, no gap rotation data could be collected there as indicated in the figure. Similar to what was observed for the interstory drift versus gap rotation, there is a slight horizontal lag for the FR frames due to the presence of a decompression moment that is not present for frame NZ. From the comparisons shown, in general, the experimental and analytical results are in good agreement.

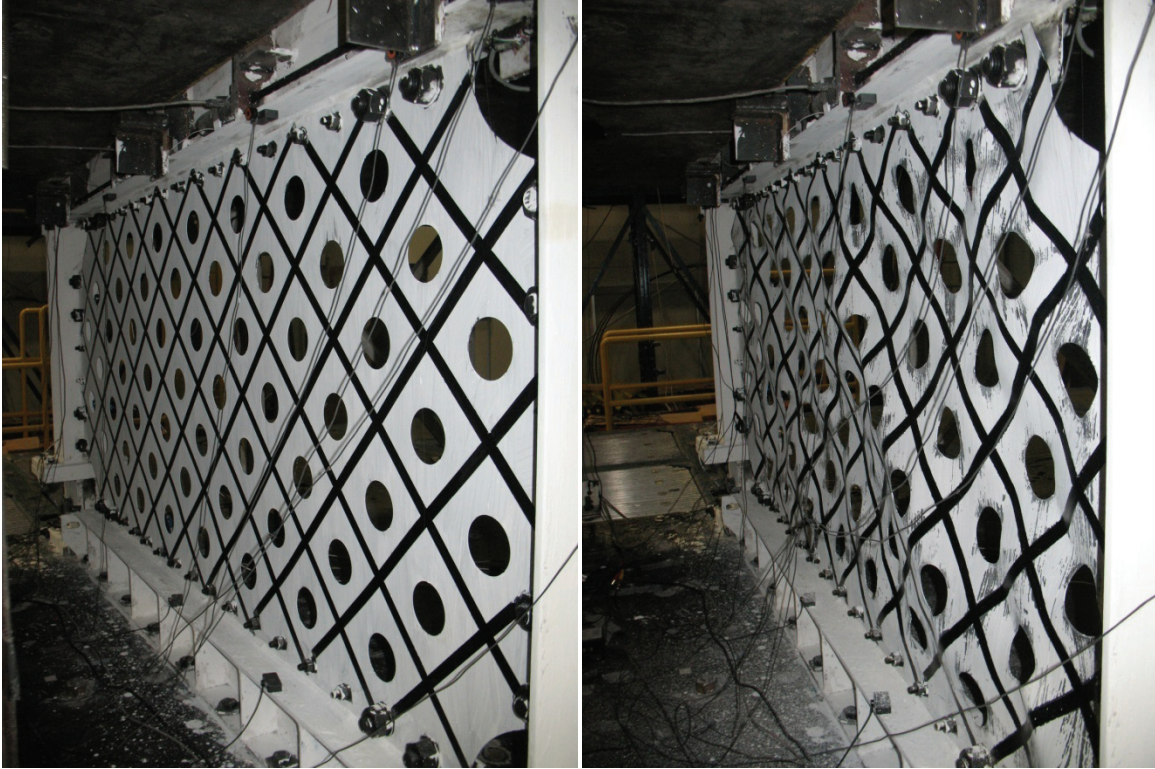
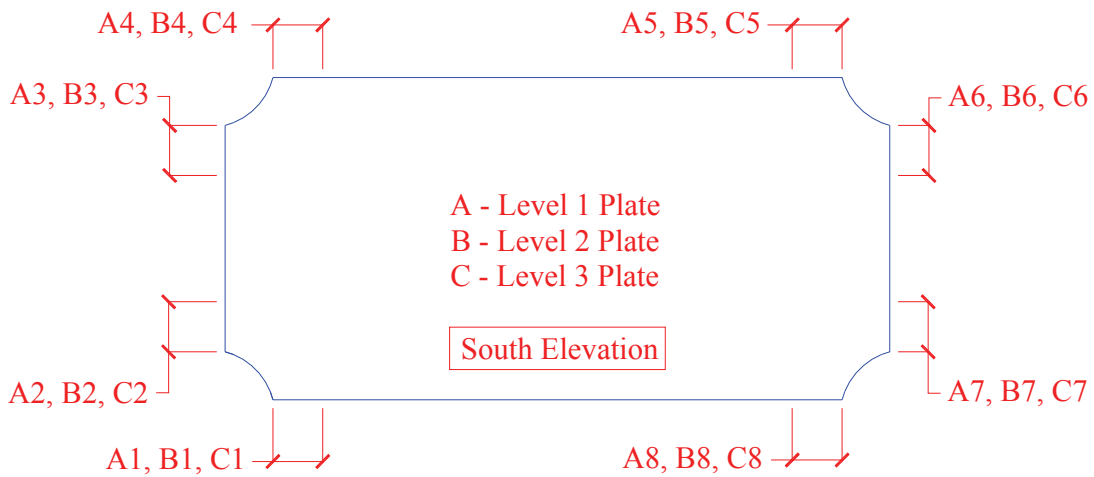


**FIGURE 7-68 Perforated infill web plate deformation**



**FIGURE 7-69 Post-testing bolt holes at infill web plate corners**



**Web Plate Tearing Legend**

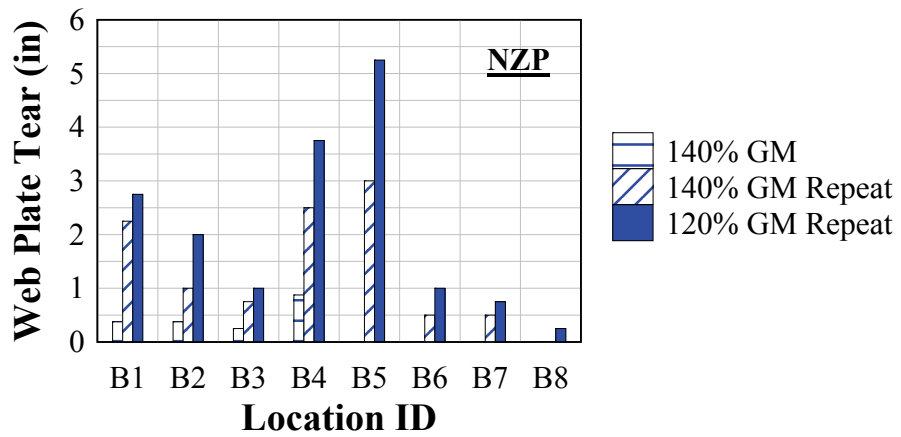
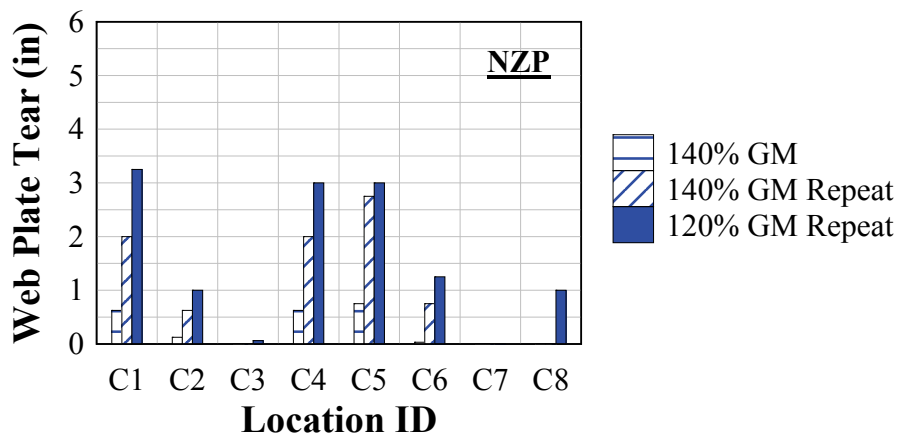


**FIGURE 7-70 Frame NZP - infill web plate tearing**

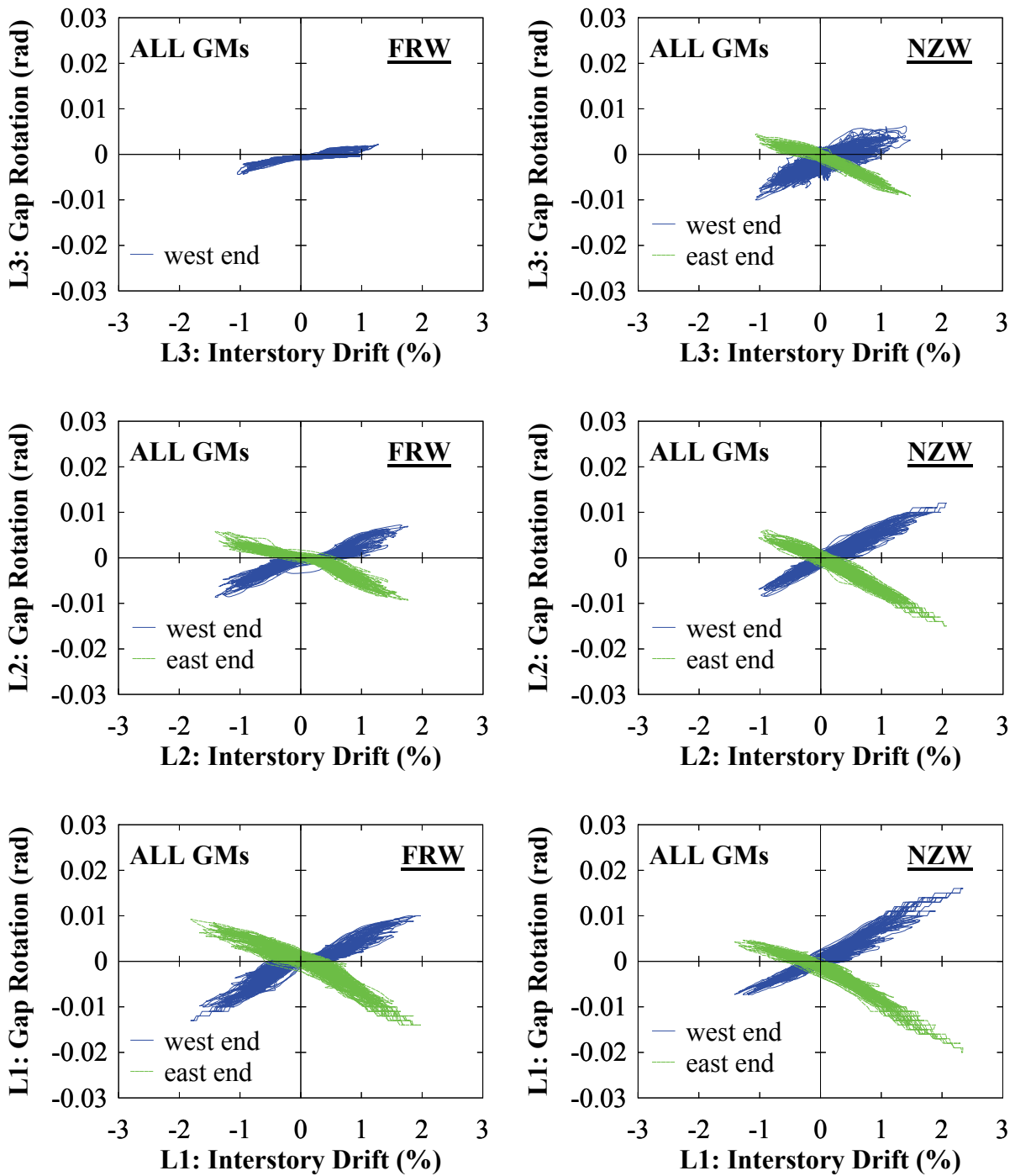


FIGURE 7-71 Frame FRW and NZW – gap rotation versus interstory drift

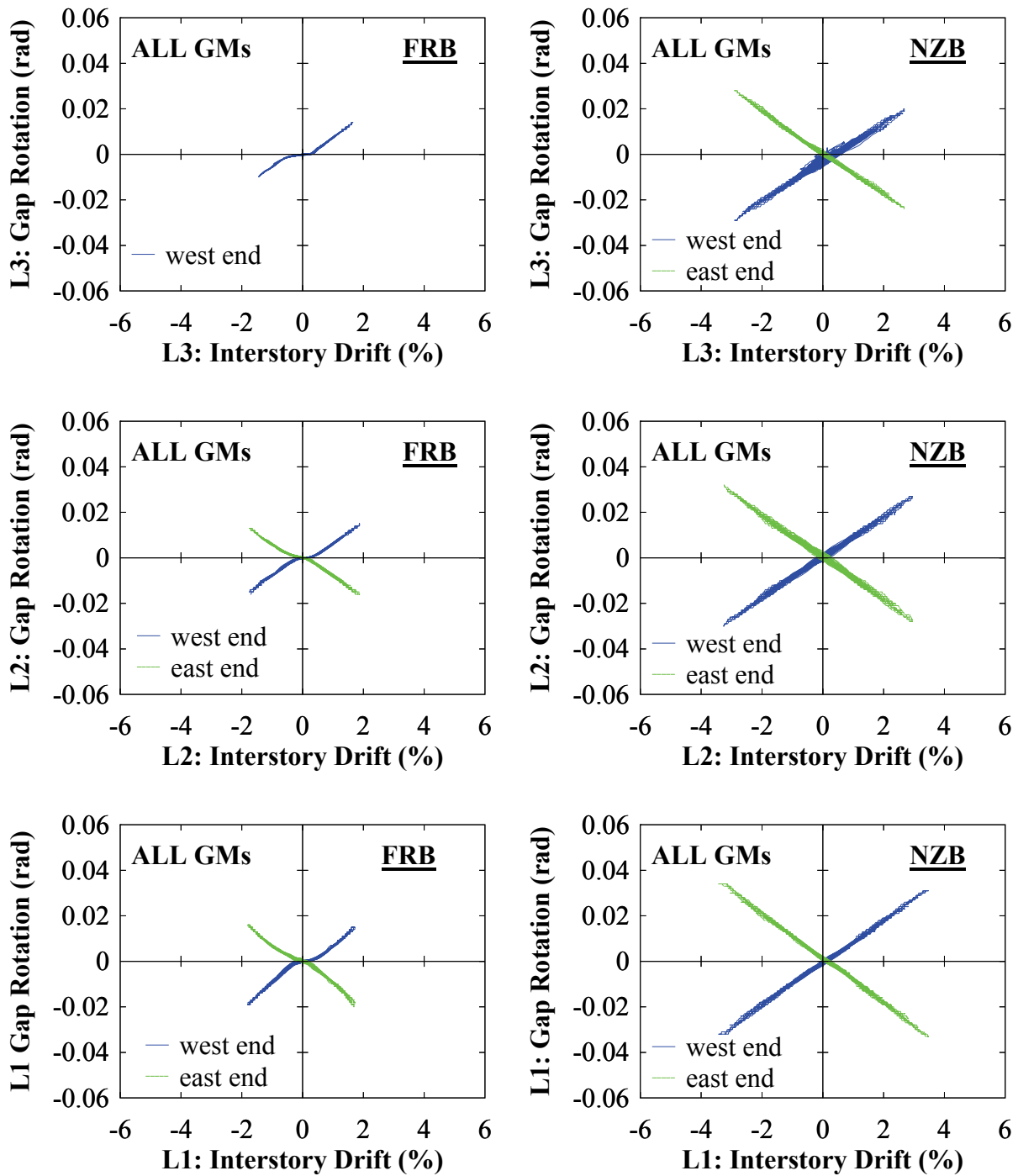
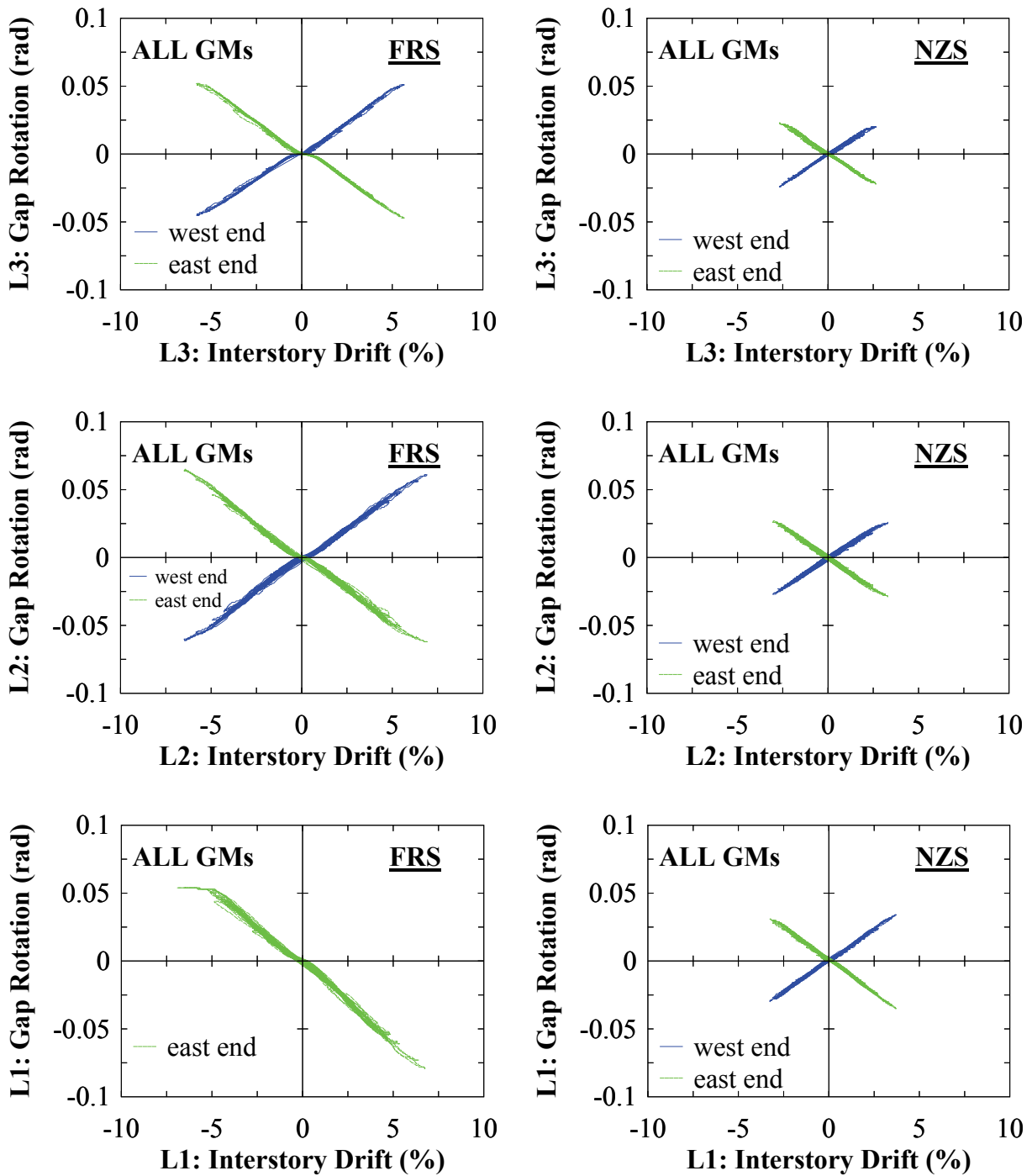
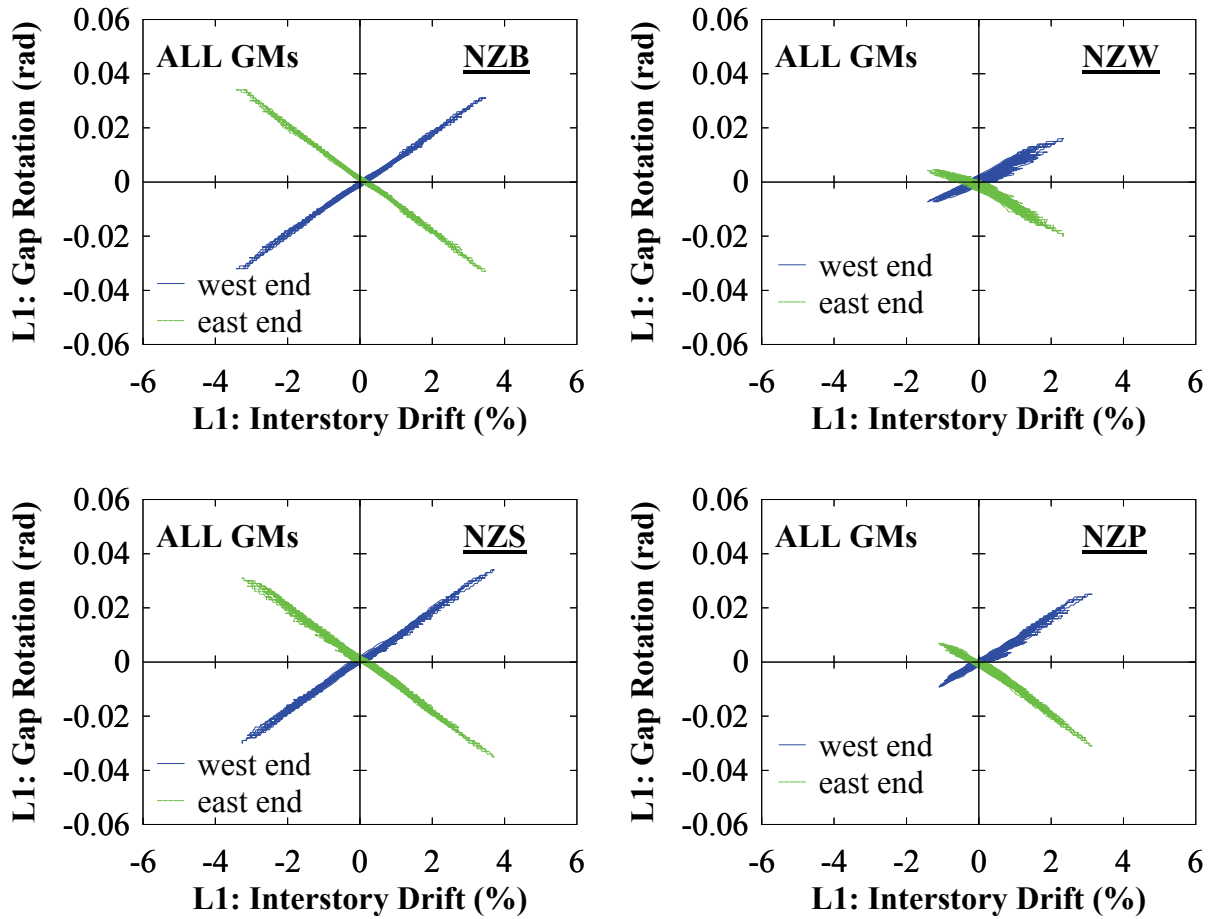


FIGURE 7-72 Frame FRB and NZB – gap rotation versus interstory drift



**FIGURE 7-73 Frame FRS and NZS – gap rotation versus interstory drift**





**FIGURE 7-74 Frame NZ: Gap rotation versus interstory drift – Level 1**

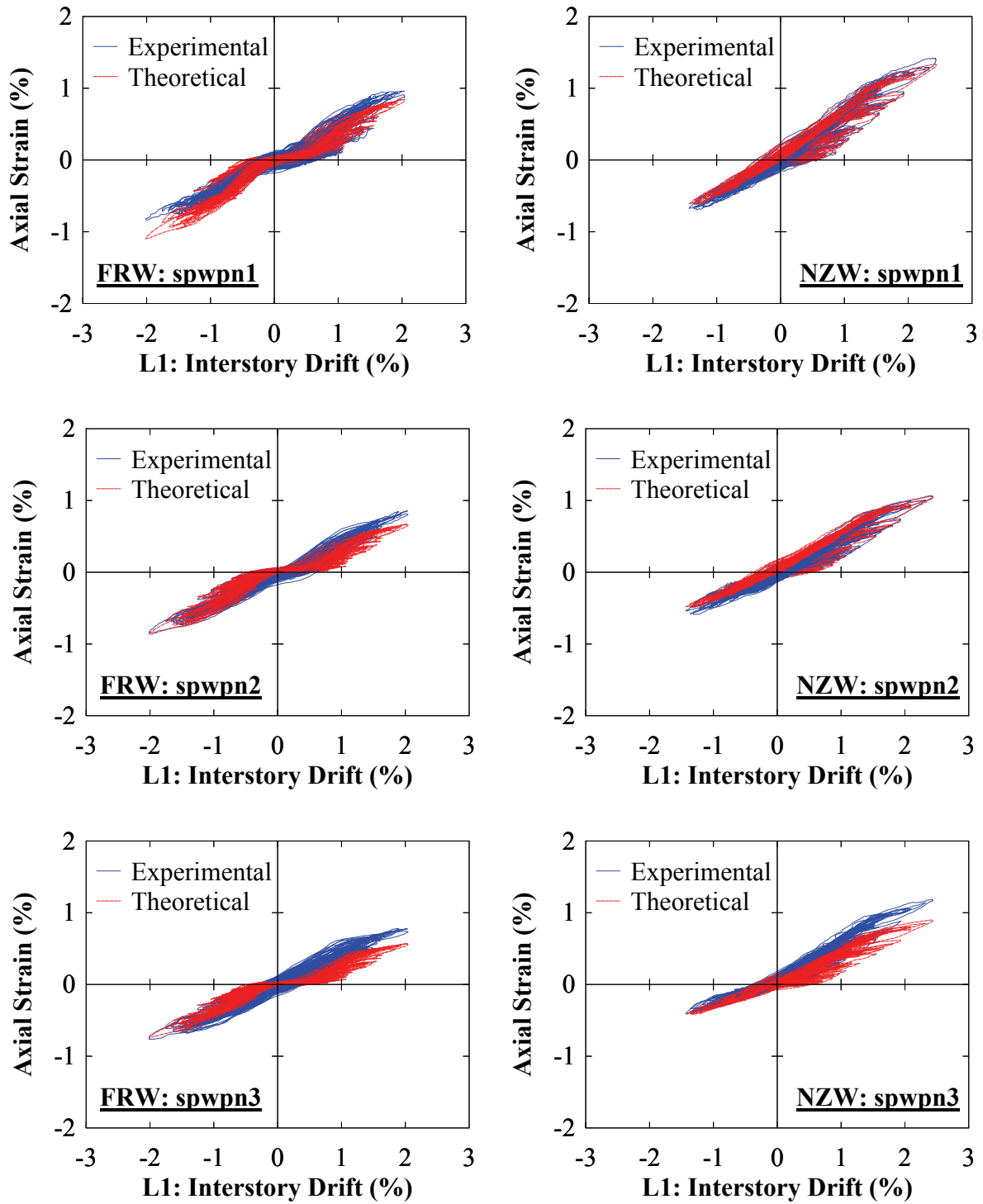


**FIGURE 7-75** Frame FRW and NZW - experimental versus theoretical

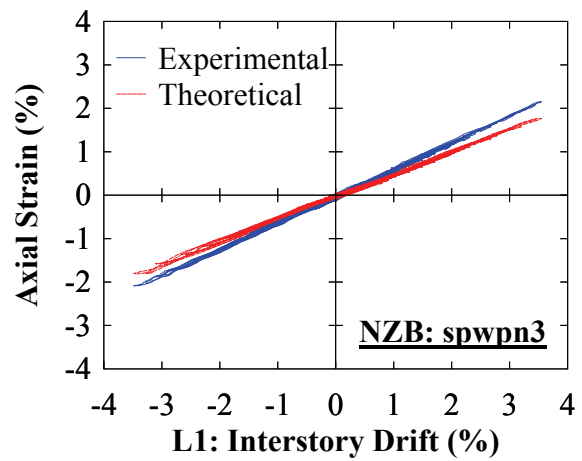
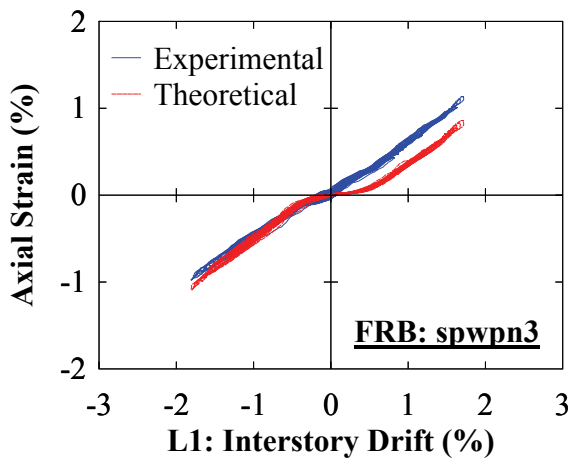
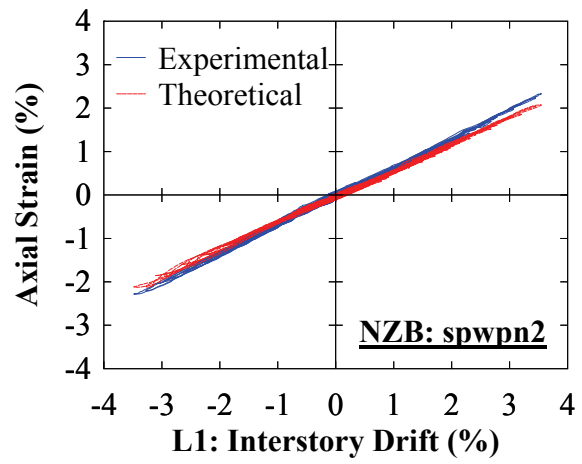
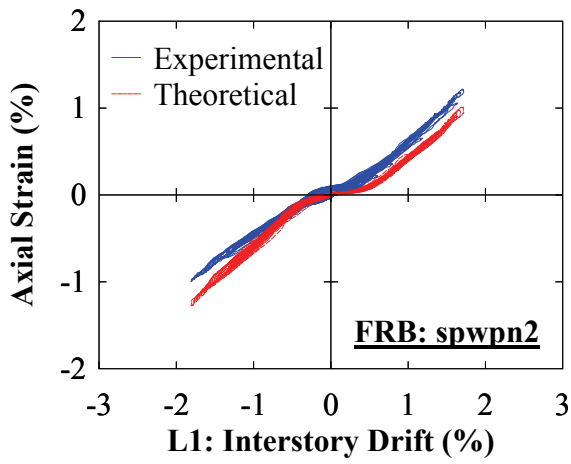
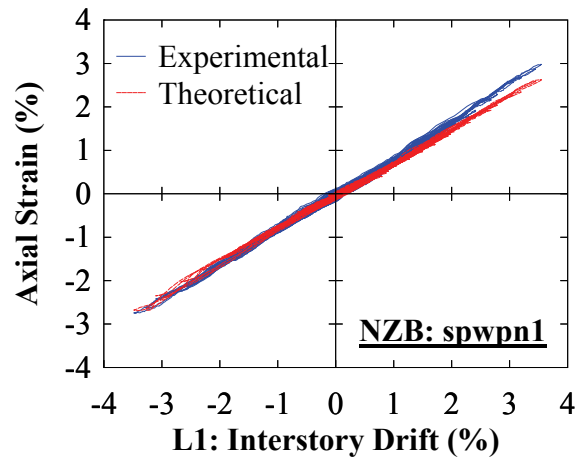
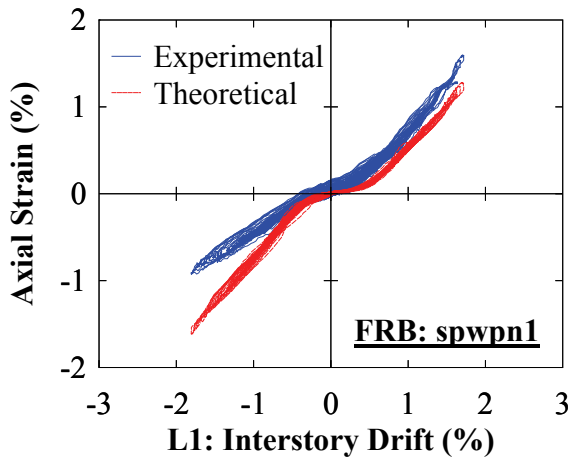


FIGURE 7-76 Frame FRB and NZB - experimental versus theoretical

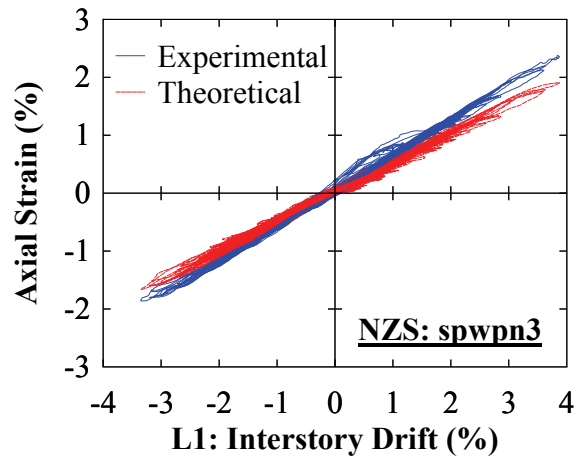
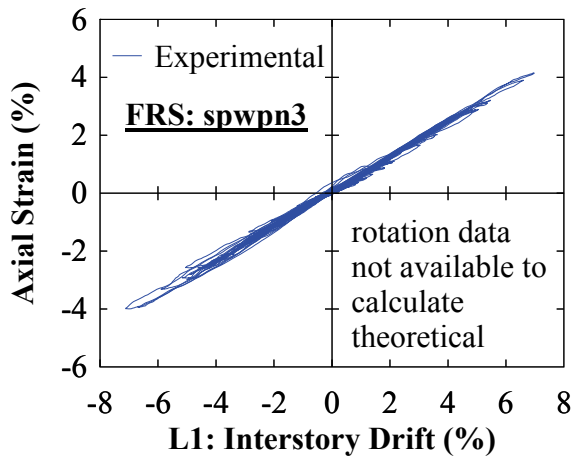
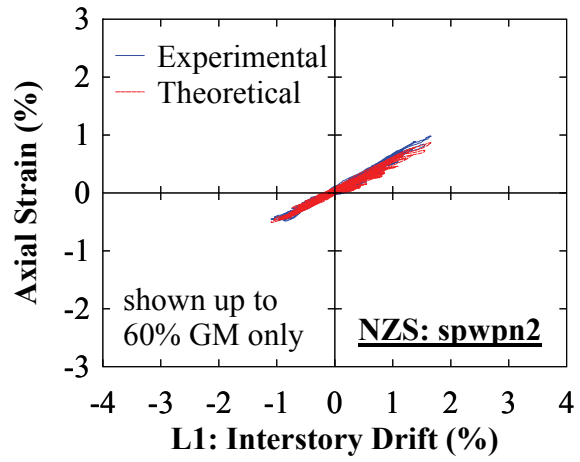
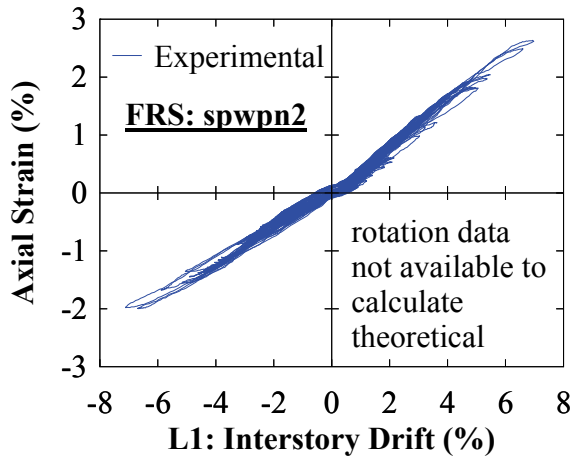
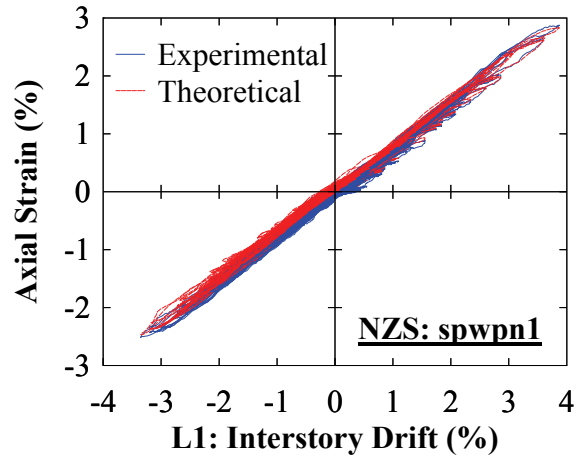
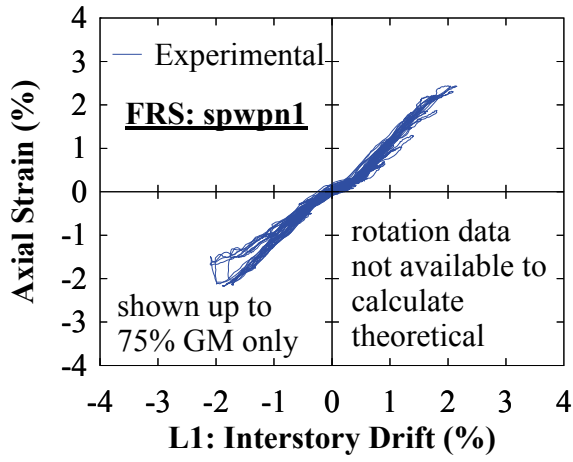
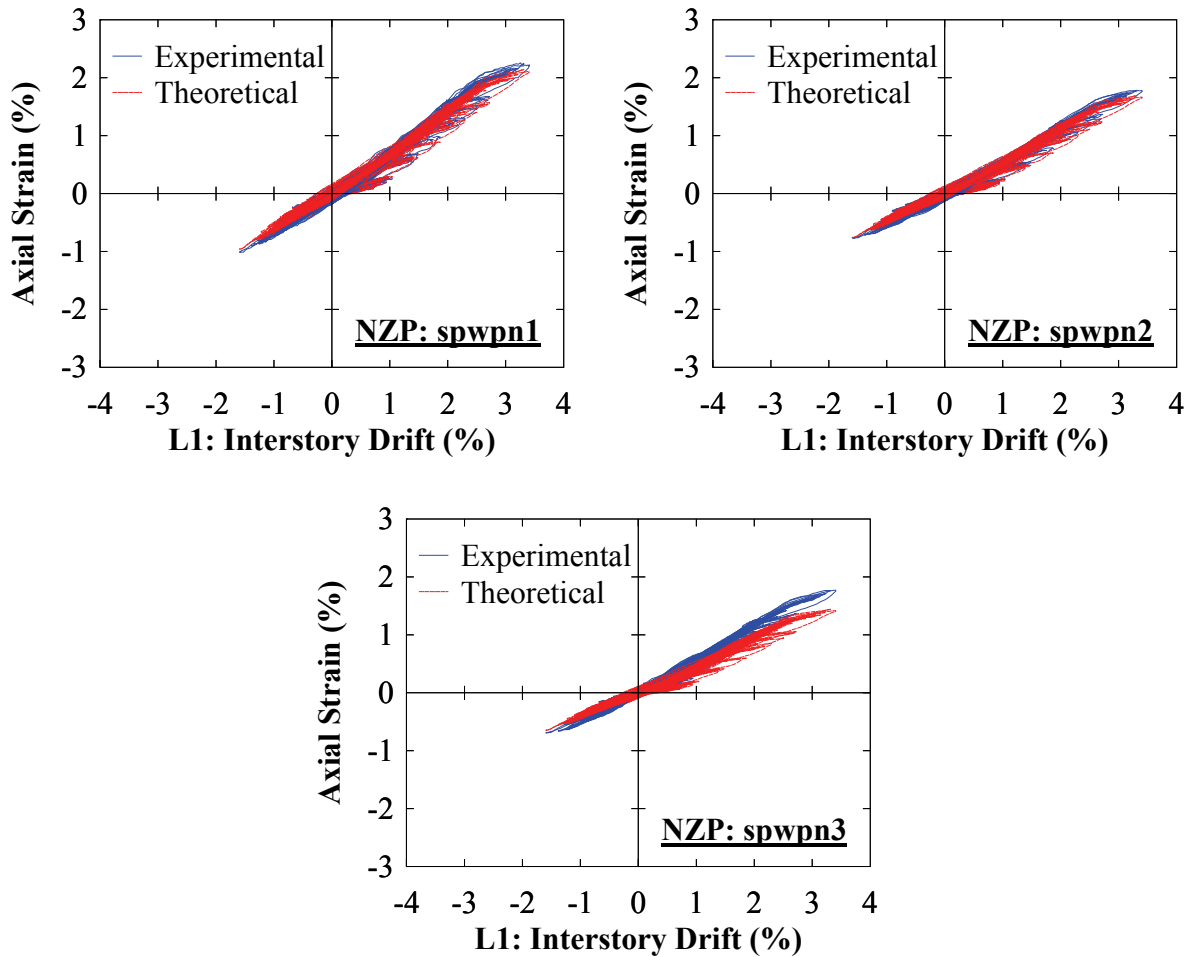


FIGURE 7-77 Frame FRS and NZS - experimental versus theoretical



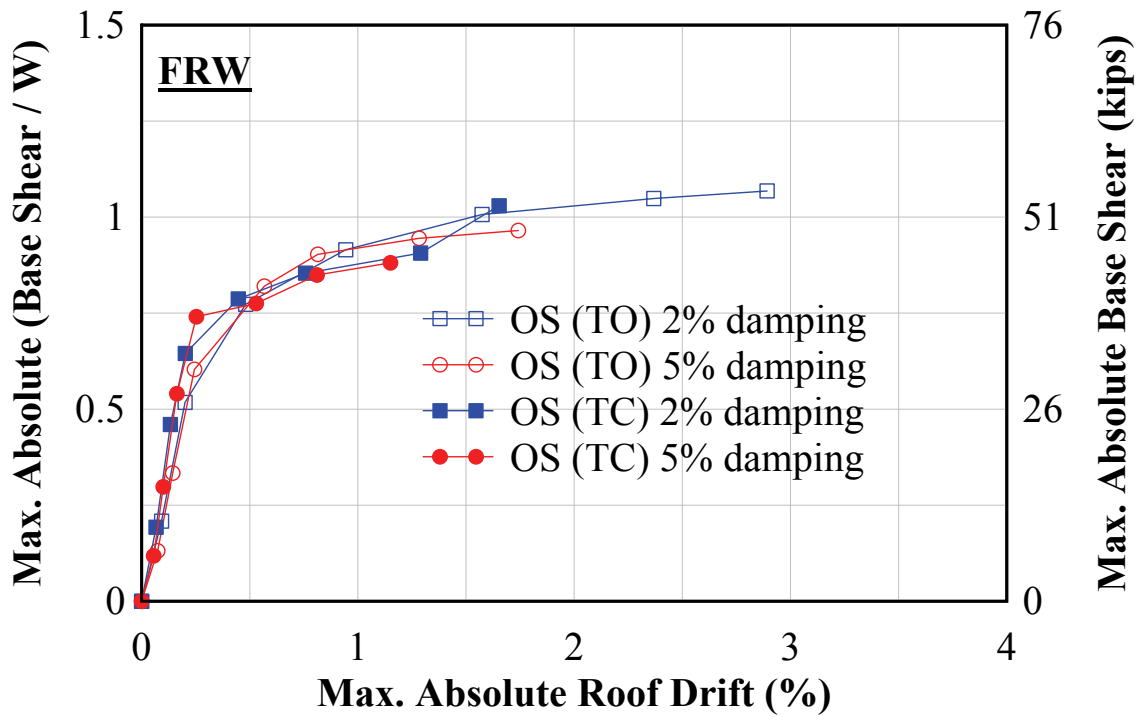
**FIGURE 7-78 Frame NWP - experimental versus theoretical**

### 7.9 Experimental versus Analytical

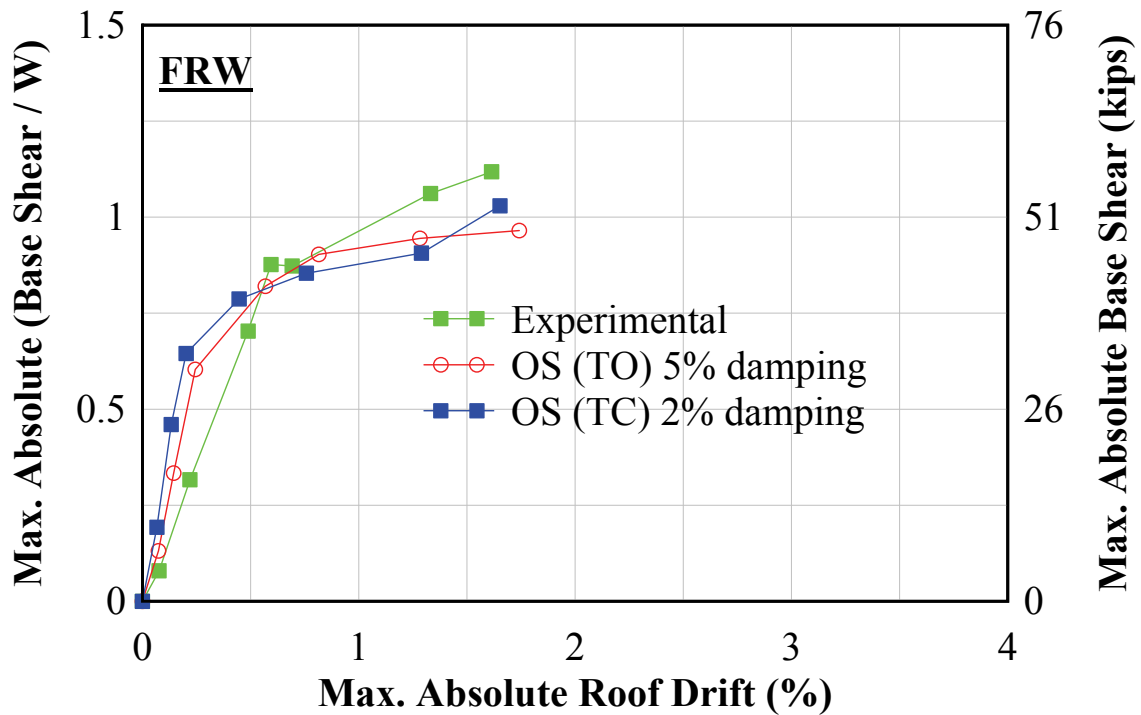
Incremental dynamic pushover results from OpenSees analyses are provided for comparison with the experimental, in figures 7-79, 7-80, and 7-81 for frames FRW, NZW (NWP), FRS, and NZS, respectively. The comparisons are made only up to the largest intensity GM (i.e., repeat GMs and aftershock GMs are not included). Note that each point on the analytical incremental dynamic curve includes the cumulative inelastic deformation history from the previous scaled GM (as explained in Section 4.3.5). Furthermore, for the infill web plate comparison, both a Tension-Only (TO) and Tension-Compression (TC) response of the infill web plate was considered in the analyses, using a lower bound and upper bound equivalent viscous damping ratio in each case. Furthermore, one difference in the TC model used for the dynamic response from the one used in the quasi-static cyclic comparisons, here the TC model was considered as

uni-directional (see figure 6-70a), versus bi-directional (see figure 6-70b) used for the quasi-static comparisons (uni-directional and bi-directional TC models were explained in Section 6.7.1). The reason being that a uni-directional model is slightly more conservative, as the infill web plate is still modeled as tension-only for a frame drift moving away from the zero-drift location (i.e., larger drift response). Additionally, for the TC model, 20% of the tensile yield strength of the infill web plate was used to model the compression strength in the infill web in the recentering direction (similar to the model used for the quasi-static comparisons). Note that for clarity, only results for the analytical model for each TO and TC damping condition that best compares with the experimental results are shown superimposed in the figures.

From the comparisons shown, the TO model with large damping (i.e., 5%) and the TC model with low damping (i.e., 2%) provide results comparable to the experimental ones. Furthermore, for the frames with infill web strips, the TO model with small damping (i.e., 2%) provides the best comparison. Furthermore, it is observed that the comparisons with the infill web strips, in general, provide a better match to the experimental results than those of the corresponding frames with infill web plates. This provides further evidence that the infill web strips are tension-only. Additionally, for frame NZP, the response actually better matches the TO model, indicating that there is less effects of compression in a perforated infill web plate. From the results shown, the analytical models are able to provide a reasonable prediction of the absolute maximum base shear and peak roof drift demands for the parameters shown.

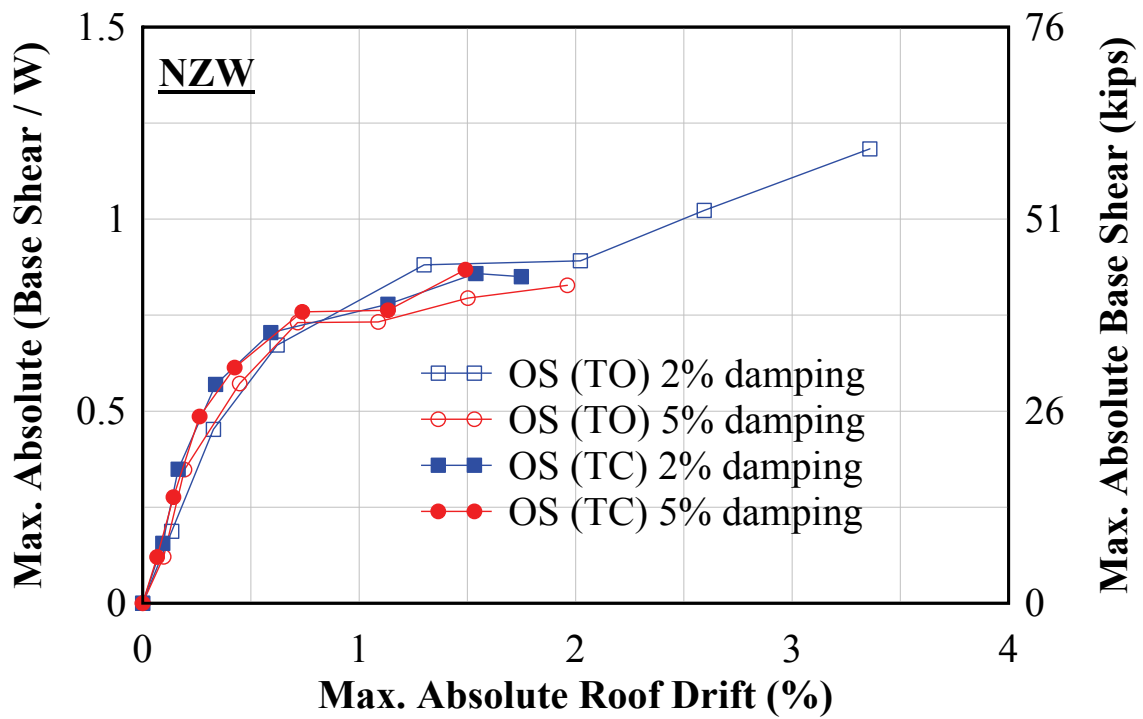


(a)

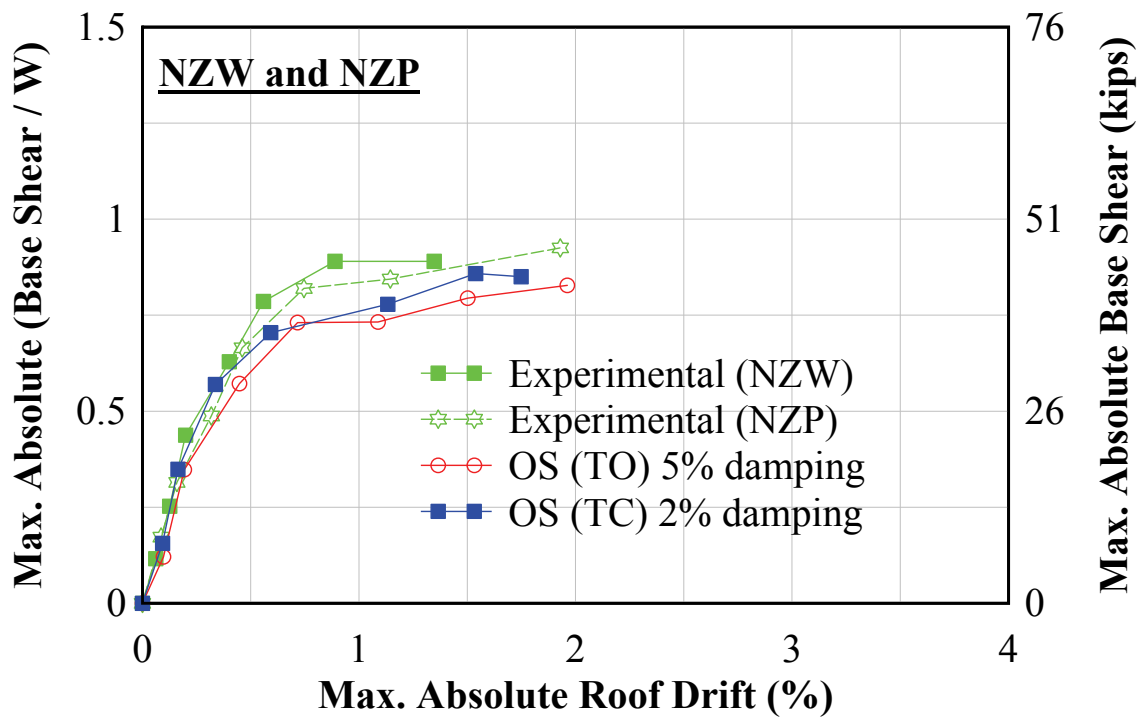


(b)

FIGURE 7-79 Frame FRW - incremental dynamic response: (a) analytical; (b) experimental versus analytical



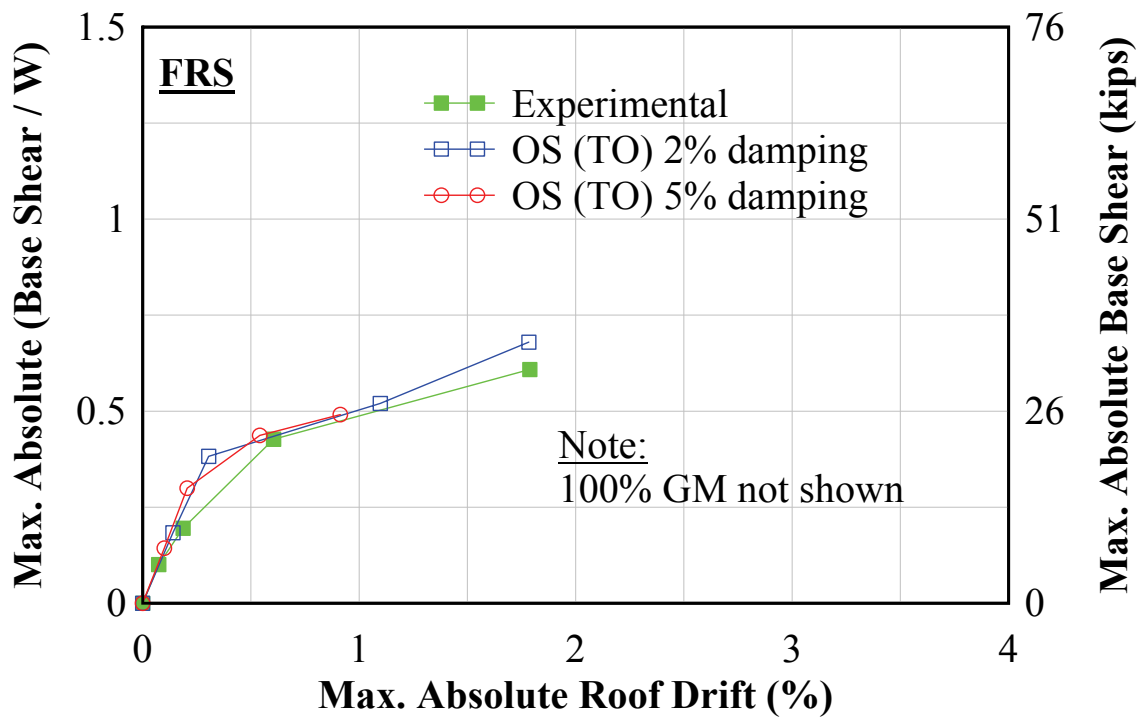
(a)



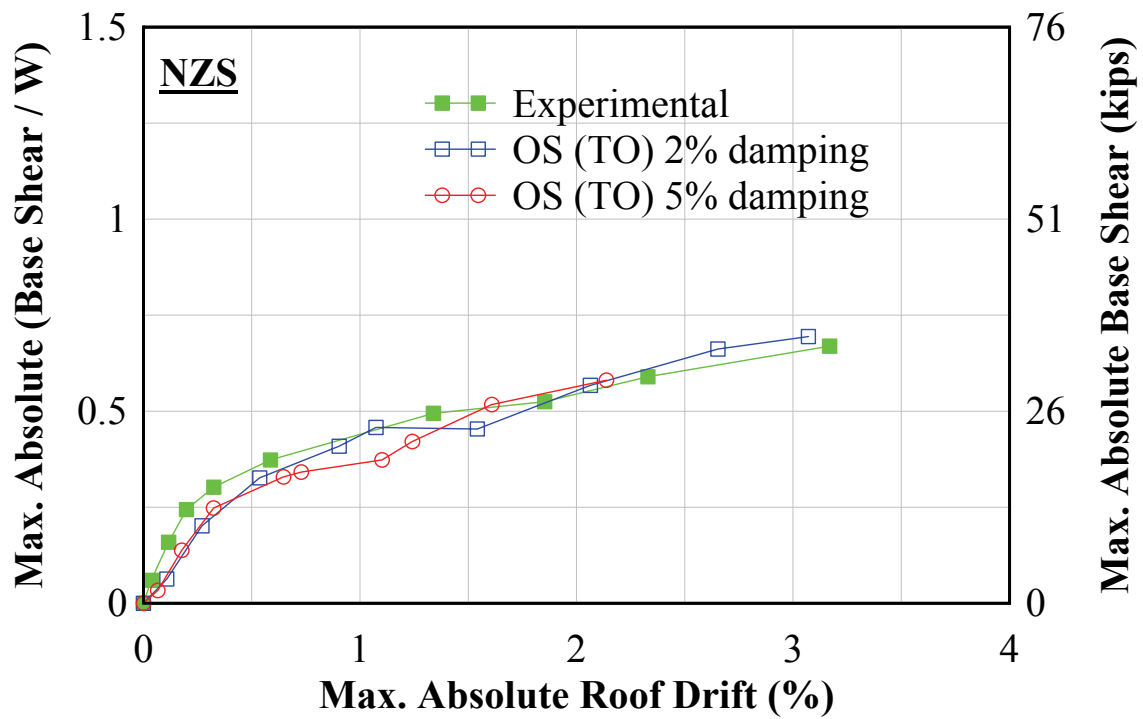
(b)

**FIGURE 7-80** Frame NZW and NZP - incremental dynamic response: (a) analytical; (b) experimental versus analytical





(a)



(b)

FIGURE 7-81 Frame FRS and NZS - incremental dynamic response: (a) FRS; (b) NZS

## 7.10 Summary

The shake table tests conducted have provided key insights into the seismic response of SC-SPSW systems. In particular, frame recentering was found to not be sensitive to compression stiffening of the infill web plate for dynamic loadings, contrary to what had initially been observed during the quasi-static tests. However, the compression effect of the infill web plate does provide some additional energy dissipation, whereas the infill web strips are tension-only and provide negligible energy dissipation; this is similar to what had been observed during the quasi-static tests. Furthermore, dynamic tests revealed that the negative stiffness effects observed with frame FR during the quasi-static tests is artificial, as both frame FR and NZ performed as intended. In other words, boundary frames remained elastic and recentering was achieved in all GM amplitudes. For frame FRW and NZW, the infill web plate separation from the boundary frame was observed to be minor. However, the maximum roof drift was approximately 1.6% and 1.9% for frame FRW and NZW respectively. Additionally, the maximum roof drift was approximately 6% and 3% respectively for frame FRS and NZS, showing that at MCE level drifts the PT boundary frame performed well, and no fracture or plate tearing of the infill web strips from the boundary frame occurred.

Furthermore, a perforated infill web plate with an alternative bolted connection was investigated using the NZ PT boundary frame (i.e., frame NZP). In general, the response was comparable to frame NZW. However, it was observed that the perforated infill web plate has less compression effect on the global response; indicated by larger drifts. For example, the maximum roof drift was approximately 2.7% at the 140% repeat GM amplitude, where at the corresponding GM amplitude for frame NZW it was 1.9%. No bolt slip or tearing of the infill web plate occurred at the bolted connections on the boundary frame, whereas some minor plate tearing was observed at Levels 2 and 3 infill web plates.

Similarly to the quasi-static tests, non-negligible PT force losses were also observed (but expected with the use of monostrands). Furthermore, full relaxation of PT elements at the closing joint for the NZ frame was observed and did not have a detrimental effect on frame response or frame recentering. Also, the fundamental equations derived for the kinematics of web plate behavior was found to be in agreement with the experimental results.

Finally, comparisons of experimental to analytical results were made on global response, in terms of absolute maximum base shear and peak roof drifts. For comparison with the frames with an infill web plate, both a uni-directional TC model and a TO model for the infill web plate were considered. The TC model providing the best comparison used a compression strength for the infill web plate of 20% of the tensile yield strength of the infill plate, with 2% damping. For the TO model, it was found that 5% damping provided reasonable comparisons on peak response. Lastly, the TO model with 2% damping also compared reasonably well with the frames with the infill web strips.



## SECTION 8

### FULL SCALE PSEUDO-DYNAMIC TEST SPECIMEN DESIGN AND LOADING PROTOCOL

#### 8.1 General

Full scale pseudo-dynamic (PSD) testing of a self-centering steel plate shear wall (SC-SPSW) system was performed at the National Center for Research on Earthquake Engineering (NCREE) in the summer of 2012 as part of this research project. The NCREE tests were conducted with Professor K.C. Tsai (National Taiwan University) and Chao-Hsien Li (Assistant Research Fellow at NCREE), in collaboration with the US-based researchers leading this NSF NEESR project. These tests complemented the full scale subassembly and scaled system experiments conducted at the University of Washington (UW) and at the University at Buffalo (UB) respectively, by providing additional proof-of-concept applied to a full scale SC-SPSW. Furthermore, the NCREE tests allow the opportunity to implement new ideas culminating from the UW and UB research in a final experiment. The additional experimental results were intended to further enhance the fundamental understanding of the behavior and seismic performance of SC-SPSWs, by increasing the database of experimental test data available to researchers and practitioners for experimental comparisons to predicted response from analytical models in a full scale test specimen. Additionally, testing of specimens at full-scale at NCREE was also intended to provide additional insight into potential issues that may arise that might not otherwise have been readily apparent in previous subassemblage and scaled specimens (which will be addressed in Section 9, experimental results and observations, where applicable).

A unique aspect of this test phase is the collaborative nature of how these tests were designed and conducted. The UW and UB researchers jointly designed a SC-SPSW frame to be tested at NCREE, each team investigating a different self-centering connection detail. For convenience, the two different test specimens are named Specimen FR and Specimen NZ based on the HBE-to-VBE detail used. Specimen FR, investigated by the UW researchers, was detailed with a PT rocking joint connection that rocks about the top and bottom flanges of the HBES. Specimen NZ, investigated by the UB researchers, was detailed with the NewZ-BREAKSS rocking connection that rocks about the top flanges only. The experiments at UW and UB have shown

both types of connections to be viable for implementation in SC-SPSW systems. However each type of connection is uniquely different, leading to differences in response, and thus two SC-SPSW specimens were investigated for testing at NCREE.

Other than the differences between the HBE-to-VBE details and the amount of initial post-tensioning forces applied to PT elements (described later in Section 9), the two test specimens are physically identical (i.e., identical member sizes, dimensions, material properties, etc.). This allowed redundancy in steel fabrication and reusability of the testing setup between the two tests (i.e., actuator connections, use of lateral bracing system, instrumentation, etc.). Specimen NZ frame elevation and typical connection details are shown in figure 8-1 and figure 8-2, respectively. Furthermore, in general, the same loading protocol was used for both test specimens. Aside from reducing some complexity involved with these tests through redundancy, using two physically similar specimens and loading protocol provided an opportunity to compare behavior of an SC-SPSW detailed with two uniquely different HBE-to-VBE connections through full scale testing. Finally, although this was a collaborative project, only the results of Specimen NZ are presented herein since this was the one detailed by the UB researchers.

This chapter describes the prototype building used for the PSD tests (Section 8.2), highlights differences between the US-based and the Taiwan-based test specimens (Section 8.3), presents the general procedure used in the design of the test specimen and determination of the loading protocol (Section 8.4), presents the loading protocol for the PT boundary frame cyclic tests that was performed after completion of the PSD testing phase (Section 8.5), presents preliminary analytical results for the PSD tests (Section 8.6), and provides insight on the behavior of PT boundary frames with different VBE base connections (Section 8.7).

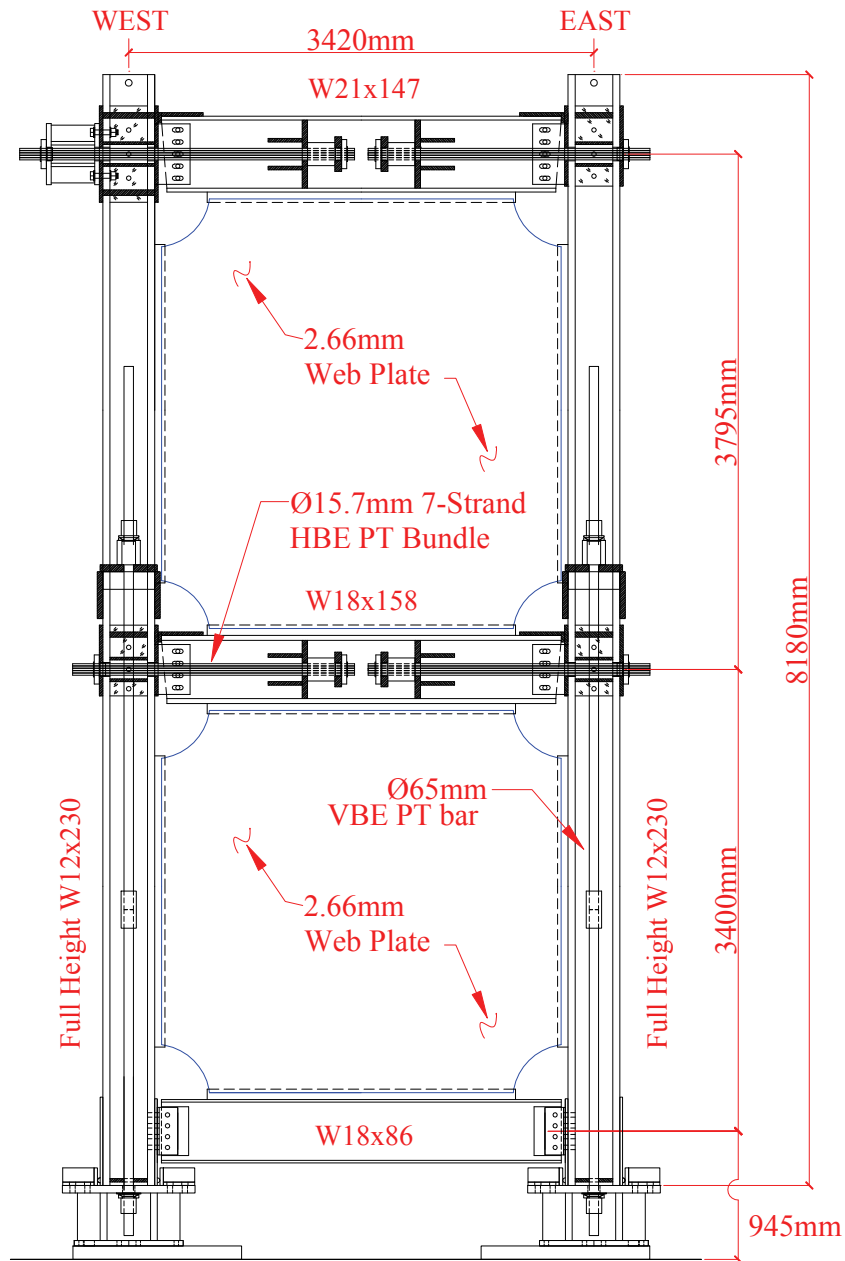


**FIGURE 8-1 Specimen NZ**

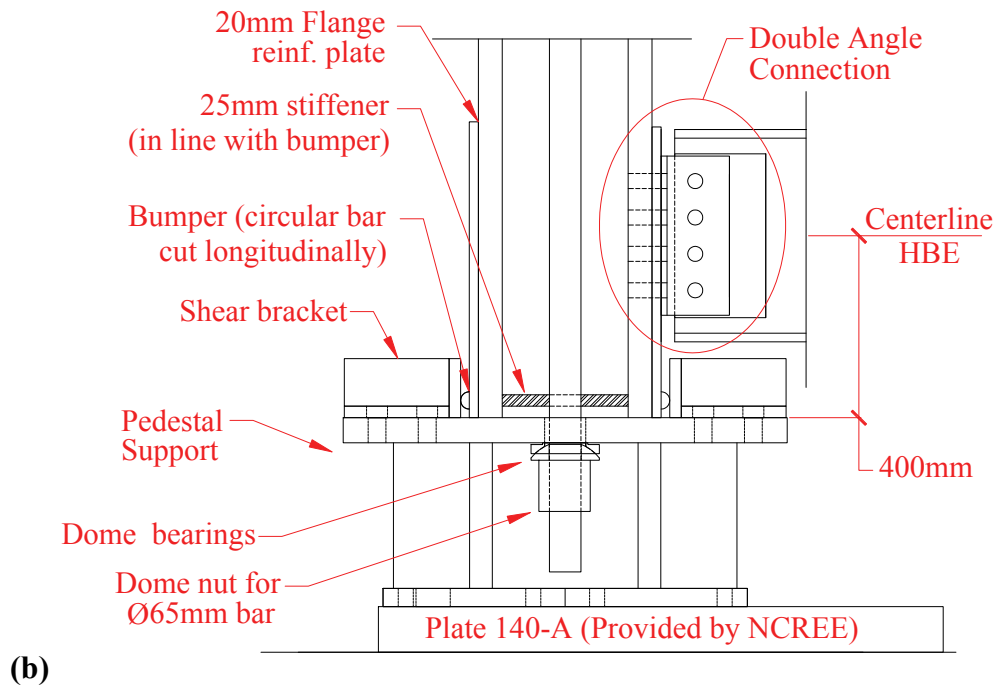
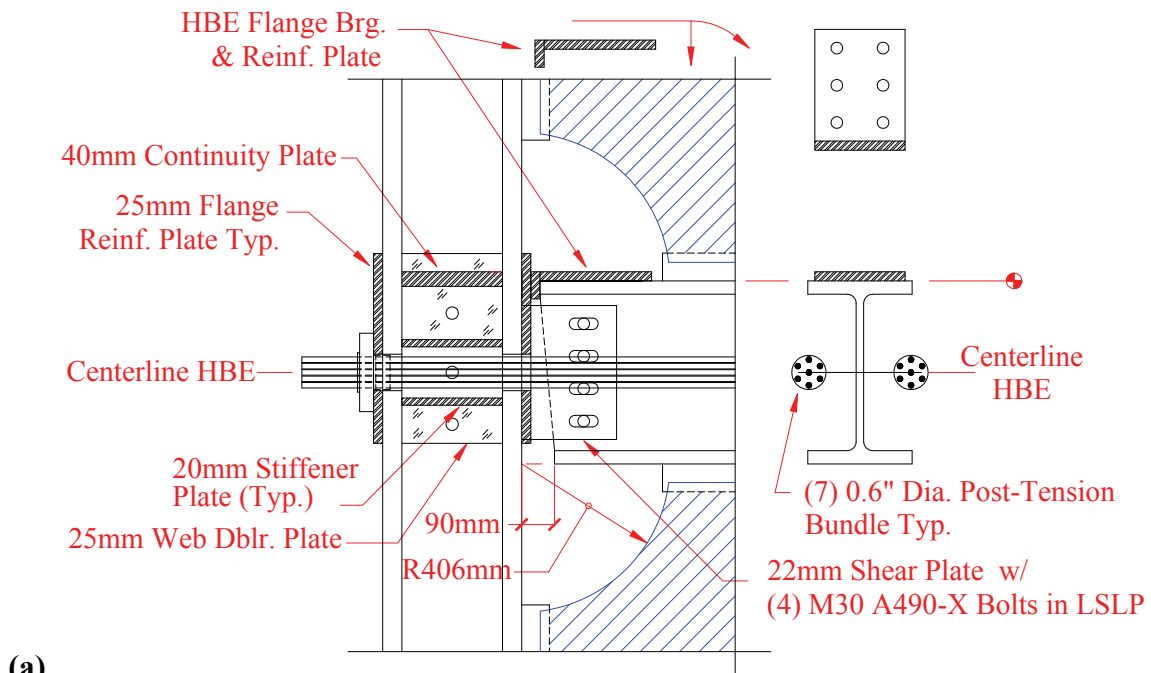


**FIGURE 8-2 (a) NewZ-BREAKSS joint detail; (b) VBE base rocking detail**



## 8.2 Prototype Building Description

The design of the test specimen was based on a modification of the 3-story prototype building used in the SAC Steel Project (FEMA 2000) for the Los Angeles, CA site. This prototype building has a 120'-0" x 180'-0" building footprint with 30'-0" on center bays in each direction and story heights of 13'-0". It is representative of a standard office building with typical structural steel framing construction situated on stiff soil (Site Class D per ASCE7-10 definition). For purposes of the NCREE tests, due to height limitations at the NCREE testing site, only the first two levels of the 3-story SAC building were used with a modification of story heights to 12'-6". The design floor and roof seismic mass of 65.53 kips-s<sup>2</sup>/ft (0.9568 kN-s<sup>2</sup>/mm) was used, which corresponds to the typical floor mass of the original SAC prototype building. Note that the original SAC prototype building roof mass is 70.90 kips-s<sup>2</sup>/ft (1.035 kN-s<sup>2</sup>/mm). Also, for the NCREE test, the total building mass was lumped at the roof level due to the limitation that only one actuator could be used for those tests. The final configuration of the 2-story prototype building used for the NCREE tests is shown in figure 8-3.

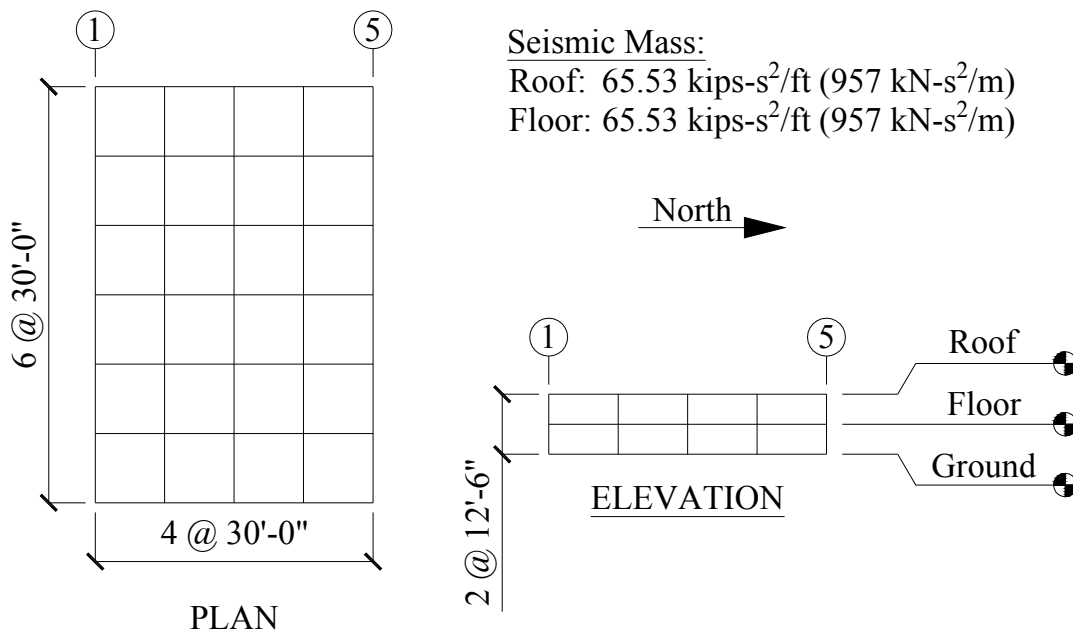


**FIGURE 8-3 NCREE Prototype Building**

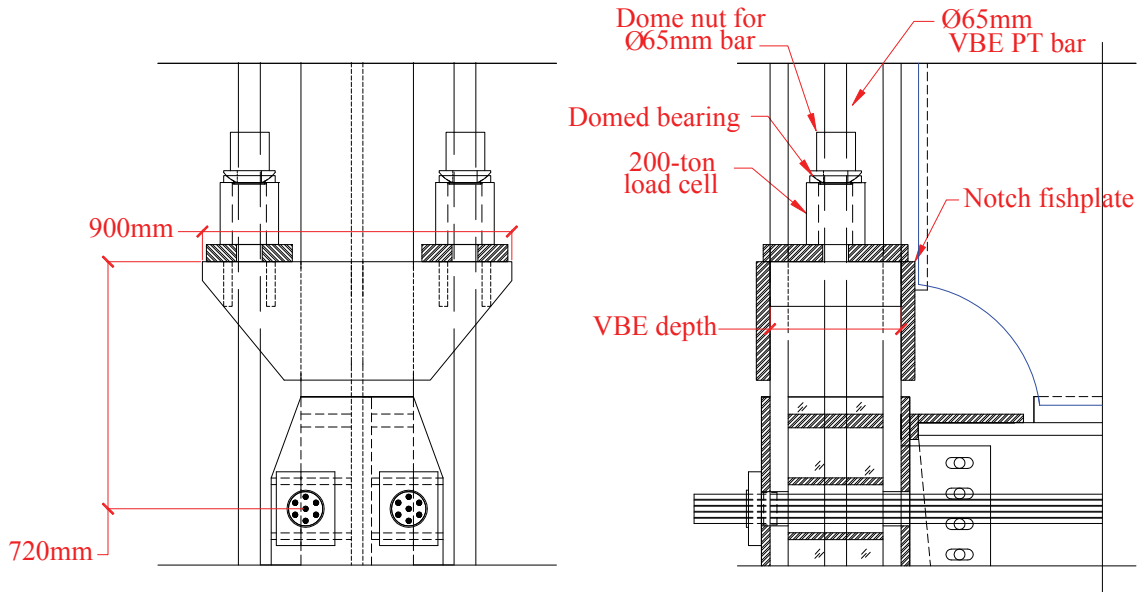
### **8.3 US-based and Taiwan-based Test Specimen Differences**

For the two-story prototype building, a prototype of the proposed SC-SPSW lateral force resisting system was designed (as representative of a typical lateral frame in the building). Note that since a full-scale specimen was to be tested, the specimen and SC-SPSW prototype are the same. Also, some of the design freedom inherent in new construction was constrained by the fact that the experimental test setup used an existing modular lateral bracing and anchorage system provided by NCREE for loading of the test frame (to be discussed in further detail in Section 9). Accordingly, limitations of the test setup had to be considered and influenced the final design.

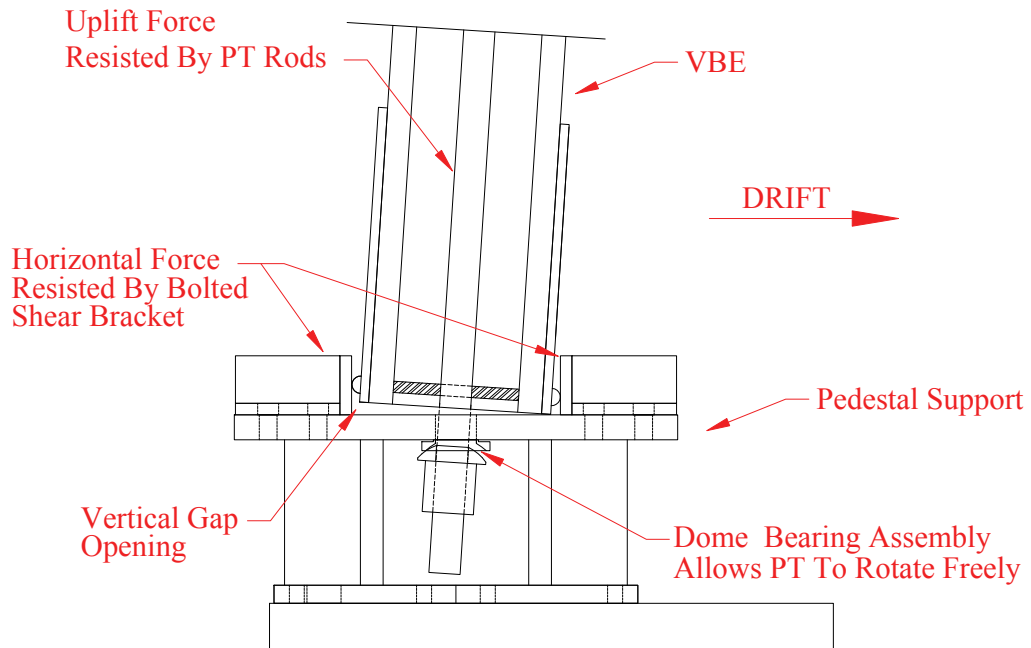
To provide proper perspective for the eventual comparison of results between the behavior of the Taiwan (NCREE) and U.S. (UB and UW) specimens, three notable differences between the NCREE tests and the previous SC-SPSW tests at UW and UB are outlined below. First, the NCREE SC-SPSW frame specimens used a Low Yield Strength (LYS) steel for the infill web panels which is not commonly available in the United States. This material, also referred to as Low Yield Point (LYP) steel, is manufactured in two different grades, namely,  $F_y = 100$  MPa (14.5 ksi) and 225 MPa (33 ksi). In addition to having low yield strength, this LYS material also possess high elongation properties, achieving up to 40%-50% elongation prior to fracture, and does not have a definite yield plateau prior to strain hardening. The use of this material for seismic applications is attractive since it provides significant energy dissipation due to the low yield ratio and high ductile properties. Other prior tests of SPSW systems at NCREE (e.g., Vian 2005, Qu 2008, Li et al. 2012) typically used LYS infill web plates. Accordingly, for this collaborative project, given the readily available infill web plates on site at NCREE, LYS web plates were also used for the test specimen.

Second, the VBE base connection detail used for the NCREE specimens was different than the ones used in previous SC-SPSW tests. The UW tests used a pin and roller connection for their subassembly testing. While this type of boundary condition typically would not be used in practice, for purposes of the UW subassembly testing, the boundary condition was justified. The UB tests used a clevis and pin base connection for the scaled system testing providing a true pin connection (for reasons discussed in Section 1). Such pin connections can be found in bridge

construction, space frame structures, and although not as common also have been used in building applications where connections are architecturally exposed. In contrast to the UB system tests, the NCREE specimens were detailed with a post-tensioned VBE base rocking detail to allow free rotation indicative of a pin base boundary condition. This type of base connection had previously been used by Chi and Liu (2012) for self-centering steel moment frames also tested at NCREE. In this detail, the uplift force is provided by PT rods and the horizontal shear forces are resisted by a shear bracket type detail, allowing the base of the VBE to rock about its flanges, with a vertical gap opening at edges of the column base during rocking. A schematic of this detail along its basic kinematics is shown in figure 8-4. An advantage of using this rocking type detail is that the VBE PT rods provide additional self-centering capabilities. Furthermore, inherent in the detail is relatively good erection tolerances and stability for frame placement. However, some challenges in using this detail arise due to: (i) the additional complexity in detailing the PT anchorage connections (as well as PT stressing); (ii) the fact that the axial compression demands to the VBE will be significantly larger, and; (iii) the vertical gap opening, introducing column-growth (i.e., similar to beam-growth discussed earlier but now in the vertical direction), at the base of the VBEs, which must be accommodated by a vertical displacement of the gravity beams/floor framing into the VBEs. Aside from the advantages and disadvantages of this VBE base detail, incorporating a VBE base detail not yet explored in previous tests of SC-SPSWs provided an opportunity to further broaden the knowledge and potential of SC-SPSWs.



(a)



(b)

**FIGURE 8-4 (a) VBE PT top detail; (b) VBE PT base kinematics**

Third, a difference existed in the way the ground level infill web plate transferred loads to the foundation. In practical application, the infill web plate at the ground level would typically be anchored to the foundation directly; this was done for the UB tests through the use of an HBE foundation anchor beam. However for the NCREE tests, the ground level infill web plate was anchored to an elevated HBE transfer beam for reasons that will be discussed subsequently. This transfer beam was not post-tensioned at this level as it was deemed to not be necessary, and its end connections were detailed to allow relatively restraint-free rotation. Given this difference, the NCREE test frame configuration more closely represents an intermediate level along the height of a multi-story frame (minus post-tensioning of the bottom HBE). The HBE transfer beam connection was detailed with a double-angle bolted shear connection of the type commonly used for gravity frames where beams are idealized as simply supported. The simple shear plate connection with long-slotted-horizontal holes used in the HBE-to-VBE PT detail could also have been used to allow joint rotation, since it has already proven to be a successful detail in the UW and UB tests, but the use of a different shear connection detail provided the opportunity to expand on the use of alternative connection details. A gap was provided between the HBE transfer beam and the VBE flanges to allow rotation of the connection through flexure of the double-angle shear connections. Consequently, it was anticipated that some mild to moderate yielding of the double angle connection would occur due to the large rotational demands of a PT rocking joint connection. Because of this yielding, it was understood that the alternative double-angle connection may require repair or replacement after a design level earthquake.

#### **8.4 Test Specimen Design**

Four steps were taken to design the prototype frame: 1) Determination of a maximum base shear limit based on the constraints of the existing test setup; 2) Initial design performing cyclic pushover analysis with consideration of the maximum base shear limit in previous step; 3) Determination of the tributary seismic mass of the prototype frame, needed for analytical earthquake simulations and for performing the PSD experimental tests, based on a design base shear calculated using the Equivalent Lateral Force Procedure as defined in ASCE7-10, and; 4) Selection of ground motions (GM) to be used in the loading protocol, and verification of final design using non-linear time-history analysis. These are described in the subsequent sections.

#### **8.4.1 Maximum Base Shear Limit Consideration**

The first step consisted of determining the maximum base shear that could be safely achieved in the test setup. In early coordination with the NCREE team, the general configuration of the foundation anchorage of the prototype frame to the strong floor was established. In order to use the existing lateral bracing and foundation anchorage system, an elevated HBE anchor beam configuration similar to previously tested SPSWs at NCREE (e.g., Vian 2005, Qu 2008, Li et al. 2012) was adopted. This configuration requires that the base shear and overturning moments be entirely transferred to the strong floor through the base connection of the VBEs. Furthermore, each VBE base detail was designed to resist 100% of the total base shear (in combination with the corresponding maximum anticipated axial and flexural forces). For SC-SPSW frames, the horizontal base shear reaction is not equally distributed at each VBE support but is predominantly directed towards a single support, depending on drift direction (for a single bay frame configuration), so designing each VBE base connection for 100% of the total base shear was deemed to be not excessively conservative, but appropriate. The controlling condition governing the maximum base shear limit was then determined to be the VBE base connection to the strong floor and not the actuator capacity. In particular, the slip-critical bolts anchoring the VBE base detail to the strong floor steel bearing plate was the controlling factor in determining the maximum base shear limit of the test setup. Subsequent analyses and design considerations would be performed being cognizant of this limitation.

#### **8.4.2 Analytical Model and Cyclic Pushover Analysis**

Material properties specified for the SC-SPSW frame consisted of A572 Grade 50 ( $F_y = 345$  MPa) for the boundary frame members, LYS 225 ( $F_y = 33$  ksi) steel panels for the infill web plates, A416 Grade 270 ( $F_u = 1860$  MPa) for the HBE post-tension strands and  $F_y = 150$  ksi (1030 MPa) for the VBE threaded post-tension rods. Furthermore, the yield strength of the A416 post-tension strands was taken to be approximately 90% of  $F_u$ . As an initial starting point, a design base shear was approximated from the experimental results of a conventional SPSW (CSPSW) cyclic test (Li et al. 2012) that was tested at NCREE in the previous fall of 2011. This test frame, referenced as Specimen NC, had similar geometric frame dimensions, used similar LYS 225 infill web plate material, and finally used the same lateral bracing and anchorage system as the SC-SPSW test. Given the similarities of the two frames, using the experimental

results of Specimen NC as a reference point helped to ensure that the SC-SPSW tests would remain within the constraints of the existing NCREE test setup. The initial target design base shear was then calculated to be approximately 1500 kN (337 kips) based on a base shear demand at 2% drift for Specimen NC.

However, since Specimen NC is a CSPSW, the 1500 kN base shear it developed resulted from the combined strengths of the rigid moment boundary frame and the infill web plate. For SC-SPSWs, the PT boundary frame does not contribute significantly to the total base shear strength. Furthermore, hysteretic energy dissipation in a SC-SPSW is only provided by the infill web plates. Accordingly, for design purposes, the infill web plate was assumed to resist 100% of the base shear. Assuming web yielding inclination angle of  $\alpha = 45$  degrees, the required thickness of the infill web plate was then calculated using the panel design shear strength equation specified in the provisions of the AISC seismic design provisions (AISC 2005b) for SPSWs. Preliminary boundary frame members were then determined based on a capacity design approach, combining the demands from the plastic response of the infill web plates and the elastic PT force demands, at 4.5% drift (the maximum anticipated drift demand for the NCREE tests), based on results from a nonlinear push-over analysis. The initial selection of PT elements was based on detailing constraints of the test specimen (i.e., reflecting local construction practices) and ensuring that the combined effects of the PT boundary frame and infill web plate stiffness always remained positive in the presence of design gravity column loads (based on nonlinear cyclic pushover analysis results). Note that the final test setup of the NCREE tests did not include gravity design loads on the VBEs. However during the initial design process a design gravity load of approximately 5% of the axial compression strength of the VBE was considered due to the potential of including VBE gravity loads in the test setup. An initial PT force of approximately 20% to 30% of the yield strength of the PT tendons was targeted for the HBEs, and 10% to 15% of the yield strength of the PT threaded rods for the VBEs.

The mechanical properties of the infill web plate were based on coupon tension tests of the material stock at NCREE that were to be used for the test. The coupon tests were performed using a 10 tonf material testing machine located at the National Taiwan University (NTU) structural laboratory adjacent to the NCREE laboratory. The results of the stress-strain plots are

shown in figure 8-5. The width of the reduced segment of the coupons was 20 mm. The coupons were extracted in the longitudinal (L), transverse (T) and 45 degree (D) directions with respect to the plate roll direction. Accordingly the names of the individual stress-strain plots are labeled 20-D1, 20-D2, 20-L and 20-T. The characteristics of the LYS material discussed earlier can be observed in the plots. Furthermore, it is observed that for the coupons taken, differences in the mechanical properties are not significant for the different orientations in the panel. For design purposes and in the analytical models used to predict response of the test specimen, the mechanical properties for coupon 20-L were used as it provided an upper bound representation of the expected strength of the infill web plate. The resulting backbone of the axial hinge property used in the analytical model for design is shown in figure 8-6. Note that in the stress-strain curve shown in the figure, the proportional limit used to define the analytical model was adjusted such that the modulus of elasticity would equal 200 GPa (29,000 ksi) for structural steel (for this purpose, the yield stress obtained from the coupon test was maintained and the yield strain was adjusted accordingly). Coupon tension tests for the boundary frame and PT members were not performed as it was expected that these members would remain essentially elastic.

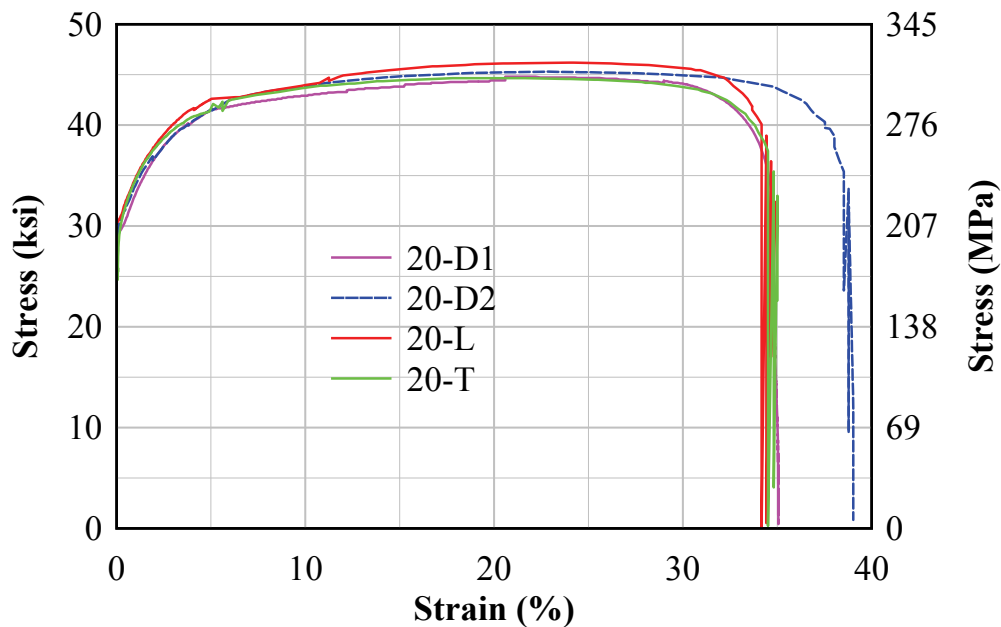


**FIGURE 8-5 Infill panel web plate stress-strain coupons**



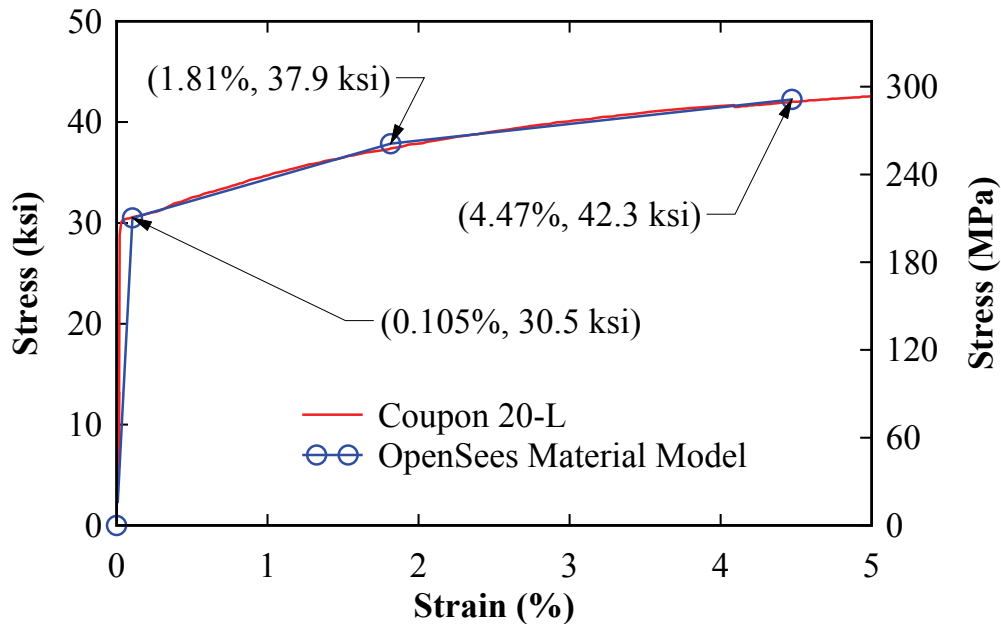
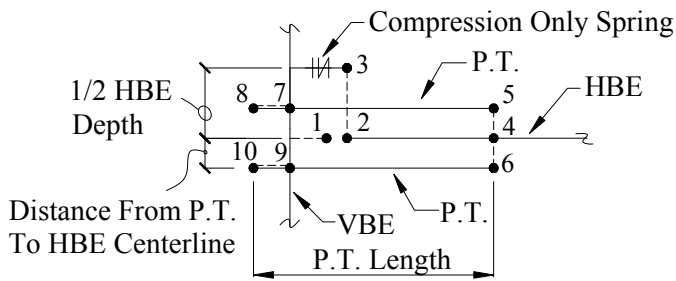


**FIGURE 8-6 Analytical model infill web plate axial hinge**

The program OpenSees (Mazzoni et al. 2009) was used to model and perform numerical simulations of the test specimen response. A strip model approach (Sabelli and Bruneau 2007) was used for analytical modeling of the SPSW web plate, as shown in figure 8-7a. Each of the strips was assigned a tension-only axial plastic hinge using the *Hysteretic Material* definition in OpenSees to match the tri-linear backbone from the coupon test result. PT elements were modeled with the *Elastic-Perfectly Plastic Gap Material* model for tension-only behavior with an initial negative strain to simulate the initial applied PT forces. The boundary frame was modeled using elastic frame members, which is reasonable since the boundary frame was designed to remain essentially elastic. Rigid offsets were used for the infill web plate panel connection to the boundary frame to better represent the response of the infill web strips. Furthermore, for the same reasons as the infill web strips, rigid offsets were used at the end of the PT anchorage locations on the VBEs to better match the actual length of the PT elements. Also note that at the PT anchorage for the top beam West end PT members, the rigid offset for the PT anchorage on the VBE also accounts for the depth of the actuator transfer beam (see figure 8-1). To model the rocking behavior at the HBE-to-VBE joint connections and at the VBE base connection, stiff compression-only springs (using the *Elastic-No Tension Material*

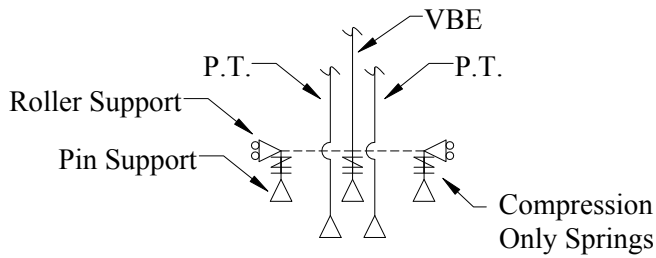
definition in OpenSees) were used at the contact locations in combination with the use of nodal constraints and rigid offsets.

Note that figure 8-7a provides a simplified model of the HBE-to-VBE flange rocking detail where only a single compression-only spring is used to represent the top flange. However the real rocking behavior rocks about the depth of the top flange (plus flange thickness of flange reinforcement plate if provided). As a consequence some beam-growth is present that is not captured with the simplified representation shown. To include the actual rocking behavior, a compression-only spring is needed at the top and bottom of the rocking flange as shown in figure 8-7b as an alternate model. It is noted however that the alternate model doubles the number of required nonlinear compression-only springs and, as a consequence, will increase computational computer run time. Consequently for purpose of design, the more effective simplified representation was used. Formulations describing and obtaining design parameters due to beam-growth effects are developed in Section 9, which can be used in combination with the simplified model.



**Joint Constraints**

- Node 1 & 2 (master): Vert. DOF
- Node 2 (master) & 3: Vert. and Rot. DOF
- Node 4 (master), 5 & 6: Vert. and Rot. DOF
- Node 7 (master) & 8: Vert. and Rot. DOF
- Node 9 (master) & 10: Vert. and Rot. DOF



**Legend**

- Constrained Node
- Frame Element (Truss Element For P.T.)
- Rigid Element

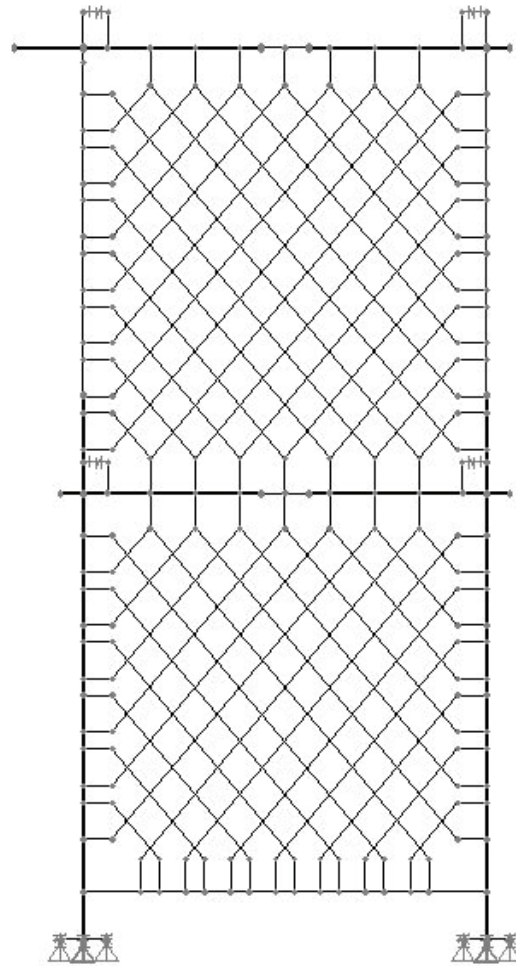
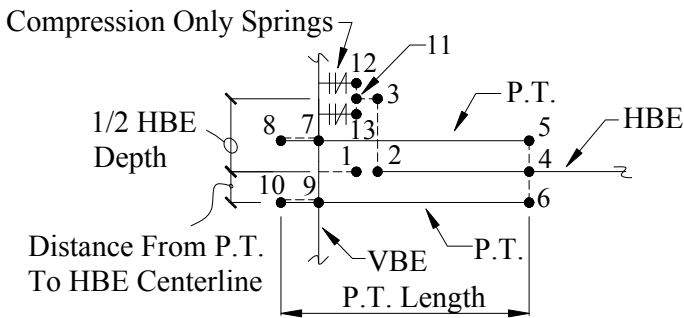


**FIGURE 8-7a OpenSees model**



**Joint Constraints**

- Node 1 & 2 (master): Vert. DOF
- Node 2 (master) & 3: Vert. and Rot. DOF
- Node 4 (master), 5 & 6: Vert. and Rot. DOF
- Node 7 (master) & 8: Vert. and Rot. DOF
- Node 9 (master) & 10: Vert. and Rot. DOF
- Node 11 (master), 12 & 13: Vert. and Rot. DOF
- Node 3 (master) & 11: Vert. and Rot. DOF

**Legend**

- Constrained Node
- Frame Element (Truss Element For P.T.)
- Rigid Element

Captures rocking behavior at HBE-to-VBE flange contact points.

**FIGURE 8-7b OpenSees model (alternate HBE-to-VBE)**

### 8.4.3 Tributary Seismic Mass for Prototype Frame

For pseudo-dynamic testing procedures a seismic mass is required for numerical simulation during the experiment. The tributary seismic mass for the prototype frame was calculated using the equivalent lateral force procedure as defined in ASCE7-10. The design base shear was then calculated using:

$$V = C_s W = \frac{S_{DS}}{\left( \frac{R}{I_e} \right)} W \quad (8-1)$$

where the parameters and values used in this design are:  $R$  = response modification factor = 7;  $I$  = importance factor = 1;  $S_{DS}$  = design response acceleration parameter at short periods = 1.07g, and;  $W$  = total building seismic weight = 18772 kN (4220 kips). Note that the design spectral acceleration  $S_{DS}$  value was taken from the 10% in 50 year probability response spectra for 5% damping at a period of 0.3 seconds for the SAC Steel Project prototype building for the Los Angeles site described earlier. Using the above equation, the total design base shear for the prototype building was calculated to be 2869 kN (645 kips). Recall that the maximum lateral load that could be applied to the specimen was approximated to be 1500 kN (as explained in Section 8.4.2), and because this was considered to be an actual maximum force (i.e., taken directly from a real test specimen response), the ultimate strength of each prototype frame was taken to be equal to 1500 kN. Current code practice requires the use of an overstrength factor for design of key components of the lateral force resisting frames where applicable. The overstrength factor is an attempt to take into consideration the actual strength of the lateral force resisting frame due to various effects, such as strain hardening of the primary yielding components. For SPSWs, the overstrength factor is specified as  $\Omega_o = 2$  per ASCE7-10. The NCREE specimens were expected to be tested at the maximum considered earthquake (MCE) level, with the infill web plates expected to yield far into the strain hardening range. Accordingly, for determination of the seismic tributary mass for the prototype frame, the ultimate strength of each frame (1500 kN) was reduced by the overstrength factor, to obtain a design level strength of 750 kN per frame. Ignoring torsional effects (i.e., assuming the layout of the frames and distribution of mass to be symmetric), dividing the total base shear demand by the

design strength of each frame indicated that four SC-SPSW frames were required in the 2-story prototype building considered. Thus, the tributary seismic mass for the prototype frame was taken to be the total building mass divided by four frames, namely 473,000 kg per frame.

However, some correction factor was needed to be able to compare the frames to be tested for Specimen FR and Specimen NZ. For reasons discussed in Section 4, for all other parameters being equal (in particular, the PT parameters), SC-SPSWs detailed with the NewZ-BREAKSS rocking connection have a reduced PT boundary frame stiffness when compared with a SC-SPSW detailed with a flange rocking detail. For the NCREE frames, from nonlinear cyclic pushover analysis, the strength of Specimen NZ was determined to be approximately 80% that of Specimen FR, as shown in figure 8-8. Since the intent was to use the same prototype building and loading protocol for both test specimens, this required that for the 2-story prototype building, five SC-SPSW NewZ-BREAKSS frames be used. Accordingly, the tributary seismic mass used in the pseudo-dynamic tests for Specimen NZ was approximately 75% that of Specimen FR, which equates to 354,750 kg.

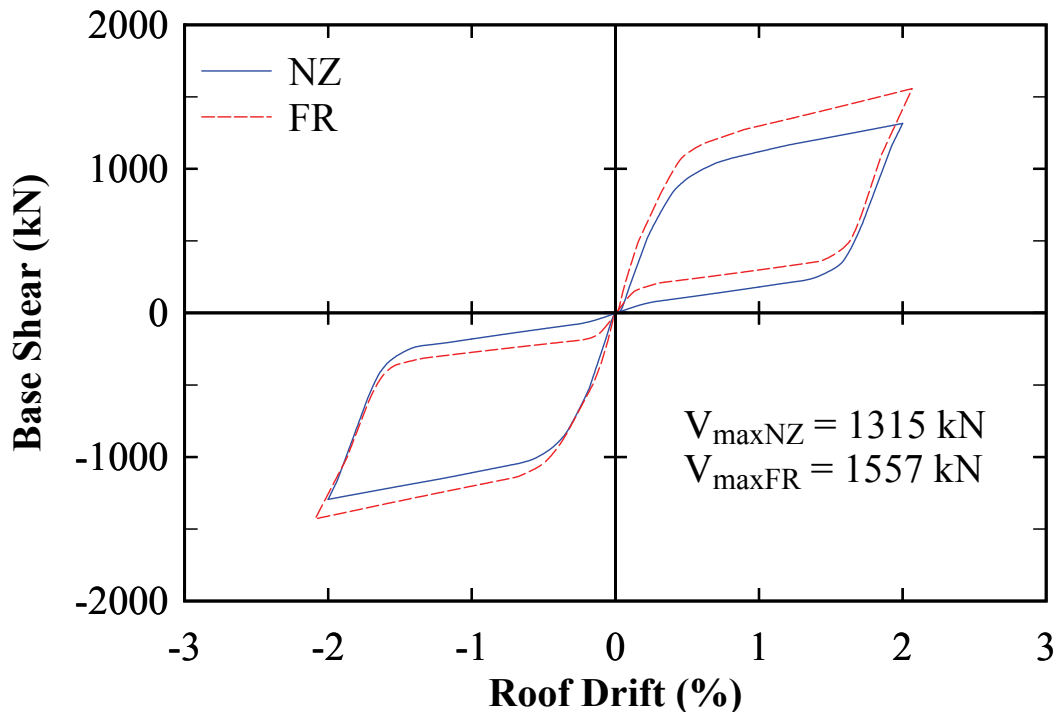


FIGURE 8-8 Cyclic pushover analysis Specimen NZ versus FR

#### 8.4.4 Selection of GMs and Loading Protocol

Three different ground motions (GMs) were selected from the suite of LA SAC ground motions for use in the pseudo-dynamic tests. One GM was selected from each of the three following seismic hazard levels: 1) 50% probability of being exceeded in 50 years (50/50); 2) 10% probability of being exceeded in 50 years (10/50); and 3) 2% probability of being exceeded in 50 years (2/50). The 50/50 ground motion represents a low level frequent event, the 10/50 GM representing the design basis earthquake (DBE), and the 2/50 GM representing a maximum considered earthquake (MCE). Using these GMs, the test frames were designed to meet target performance-based design objectives (POs) for SC-SPSWs proposed by Clayton et al. (2012) for each of the different seismic hazard levels such that:

- 50/50: System recentering is achieved and no repair is required following a seismic event. Minor yielding in the infill web plate may occur, but system remains essentially elastic.
- 10/50: System recentering is achieved and only the infill web plate requires replacement following a seismic event. Boundary frames and PT elements remain essentially elastic. Building drift should be limited to a 2% code-based drift limit per ASCE7-10.
- 2/50: Primary objective is collapse prevention. Residual drift may occur. To prevent lateral instability, the PT elements and boundary frame should remain essentially elastic, although some minor yielding would be acceptable. A target drift limit for this PO was established as 4%.

Typically, a suite of GMs would be used for design to take into consideration the variability of individual GM characteristics for a specific seismic hazard, with the objective of the median and/or average response meeting the POs. However, for testing purposes, only a single GM for a particular seismic hazard is practical. A numerical simulation study using OpenSees was performed by Clayton (2013) to select ground motions compatible with both Specimen FR and Specimen NZ, leading to predicted analytical SC-SPSW responses meeting the approximate drift criteria of the POs. Only historical GMs were considered for this purpose (i.e. synthetic GMs were ignored). The selected GMs were chosen to be LA42, LA01 and LA23 representing the 50/50, 10/50 and 2/50 seismic hazards respectively. Furthermore, LA23 was modified by scaling

the amplitude of the GM record by a factor of 1.3. This was done to increase the analytically predicted drift response to be closer to the 4% drift level of the 2/50 PO. The selection of GMs was also cognizant of the drift limits of the test setup, which was determined to be 4.5% based on physical constraints of the HBE flange lateral brace retainers at the top level HBE. Accordingly, to help ensure that the test specimen drift response would be within the constraints of the test setup, a small damping ratio was assumed (1% damping) for analytical predictions using OpenSees; providing for an upperbound drift response. Finally, for testing purposes, due to testing time constraints, only the strong portion of the record was used for the pseudo-dynamic tests. The selected GMs showing the truncated and retained portion of the record used in the PSD tests are shown in figure 8-9.

The acceleration and displacement response spectra for the selected GMs are shown in figure 8-10 and figure 8-11 respectively for a 2% and 5% damping ratio. Note that response spectra are provided for both the original GMs and the modified PSD GMs for completeness. It is observed that differences in the 10/50 and 2/50 spectra for the PSD GM compared to the original GM are negligible. For the 50/50 the differences are more noticeable but not significant. However the test specimen is expected to remain essentially elastic for the 50/50 PSD GM and differences with the original GM spectra at the approximated elastic period (i.e.,  $T_{initial}$ ) are negligible. For convenience, provided in the displacement response spectra are horizontal gridlines identifying the 2% and 4% drift condition (for reference to the target drift POs). Also shown in the spectra plots is the approximate predicted fundamental period range for Specimen NZ ranging from the initial elastic period,  $T_{initial}$ , to the period of the PT boundary frame,  $T_{BareFrame}$ . Note that for an SC-SPSW, the period range bounded by  $T_{initial}$  and  $T_{BareFrame}$  provides an approximate predicted lower and upper bound of acceleration and displacement response; that is after significant inelastic infill web plate deformations, the response of the SC-SPSW will be dominated by the PT boundary frame for lesser amplitudes of deformations. From observation of the acceleration spectra, for a 2% damping condition in the period range of interest, the 10/50 and 2/50 GMs in general will result in a larger strength demand than required by the code based spectrums. Thus, on the basis of those observations, the selected GMs were deemed to be appropriate for use in the pseudo-dynamic tests.

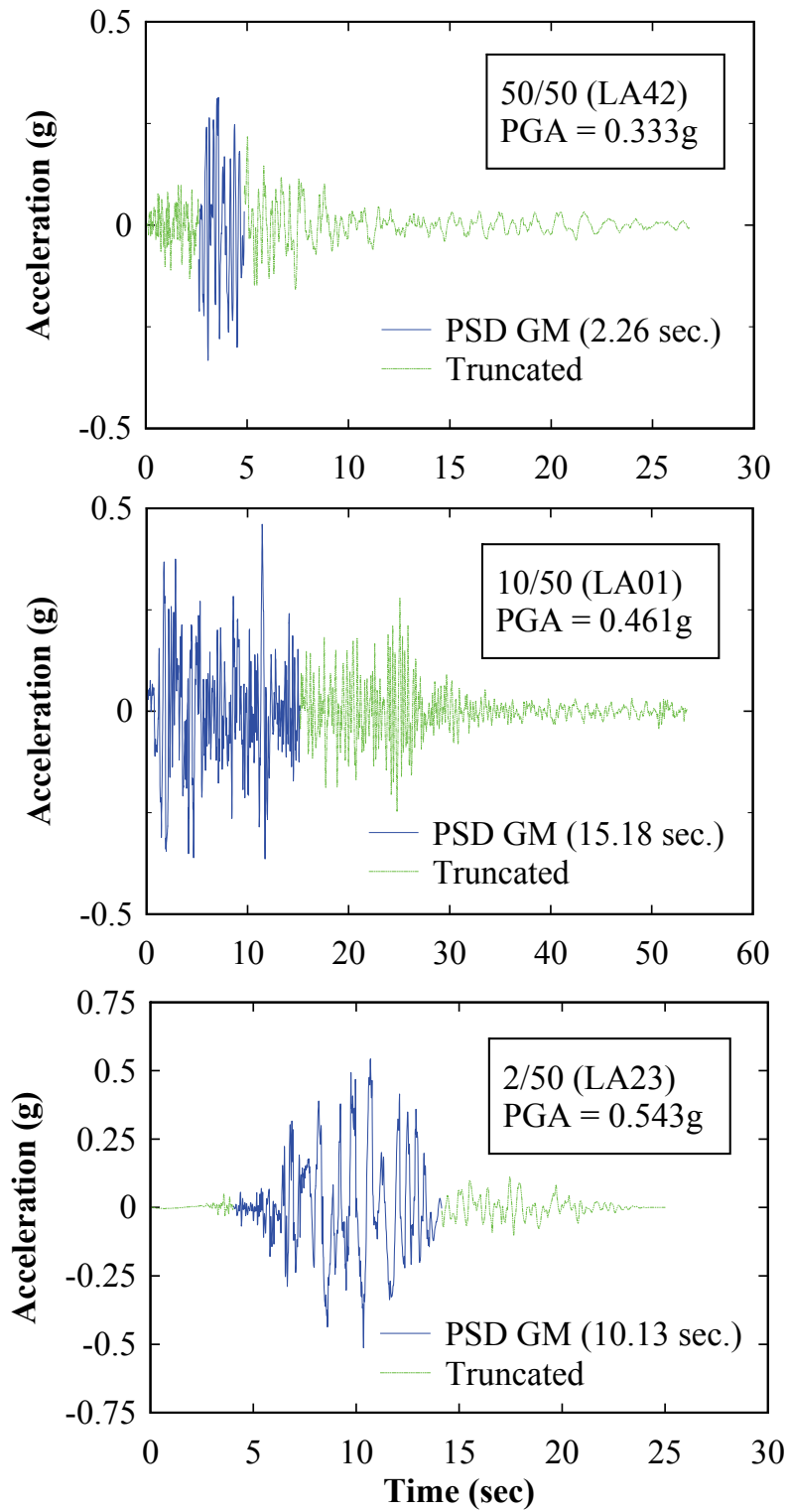


**FIGURE 8-9 Pseudo-dynamic GMs**



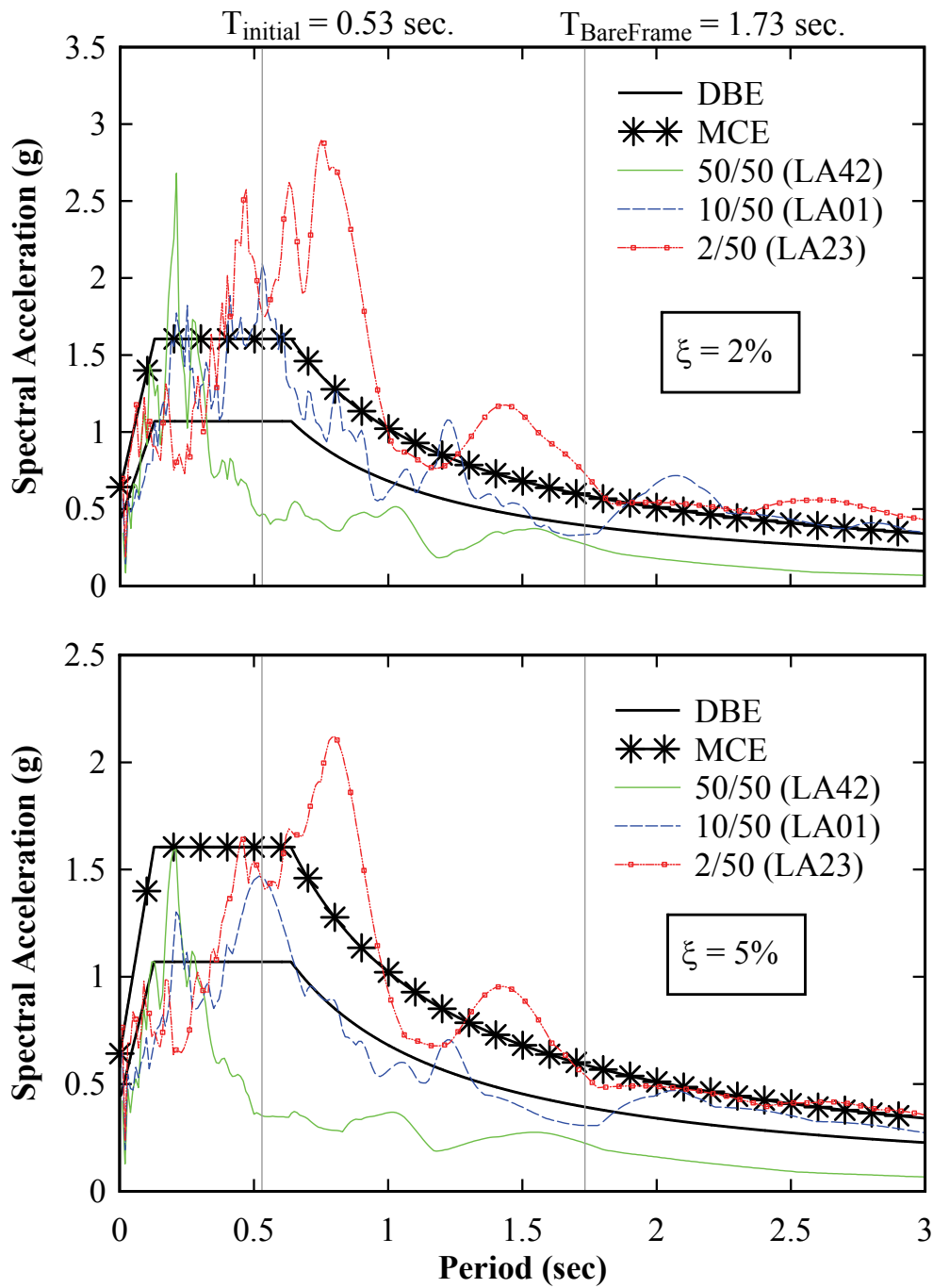


FIGURE 8-10a Spectral acceleration response – original GMs

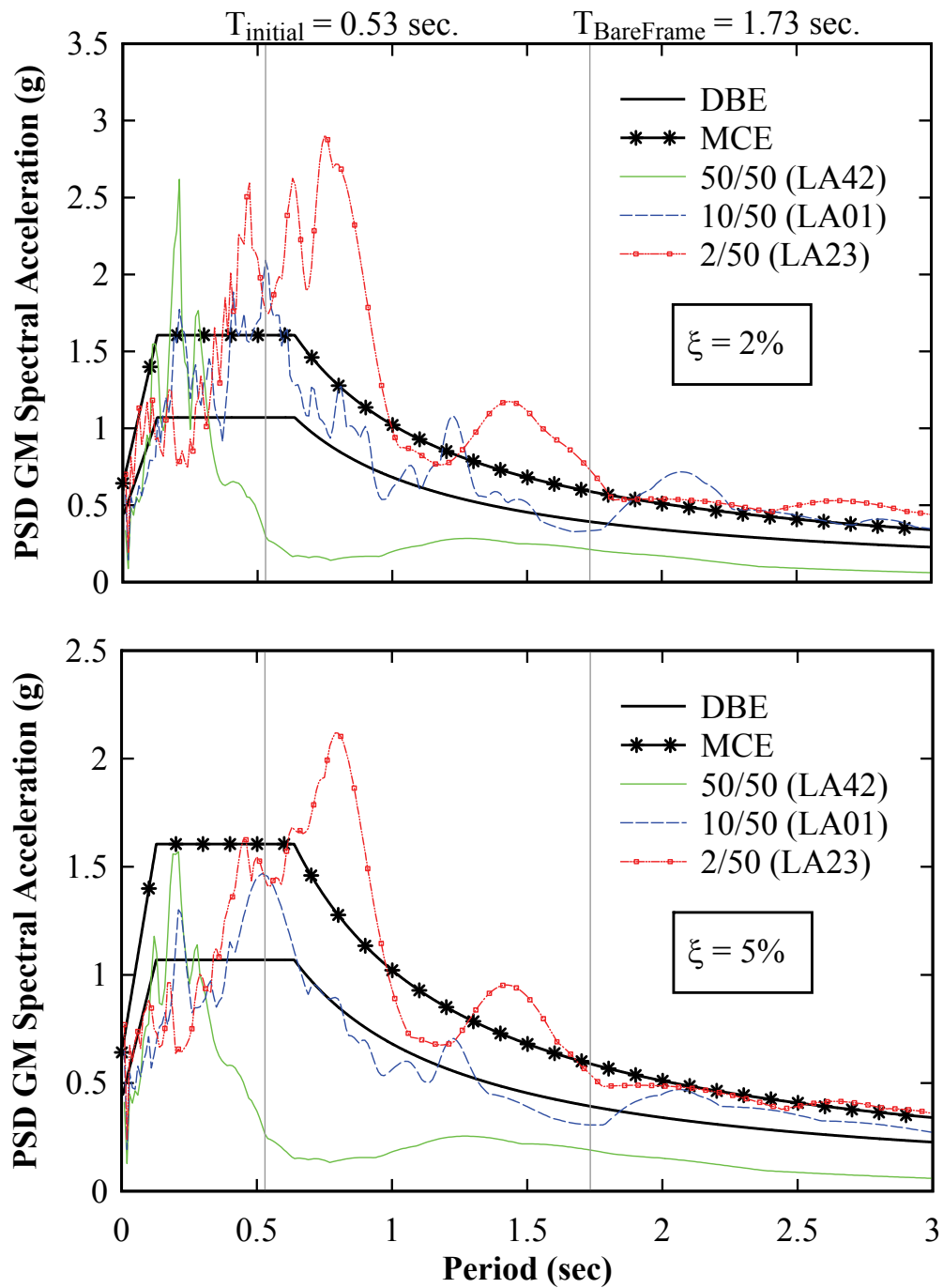


FIGURE 8-10b Spectral acceleration response – PSD GMs

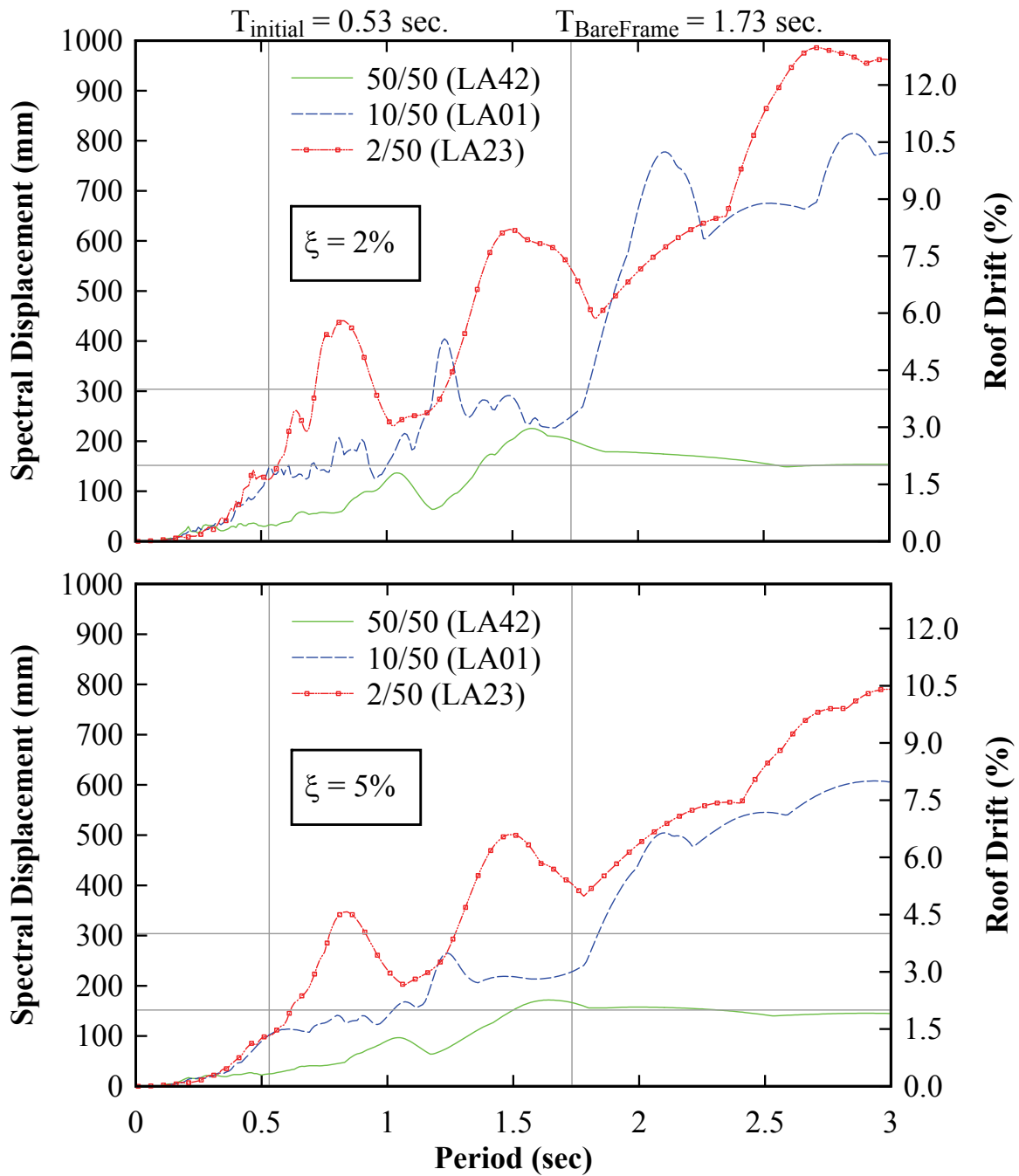


FIGURE 8-11a Spectral displacement response – original GMs

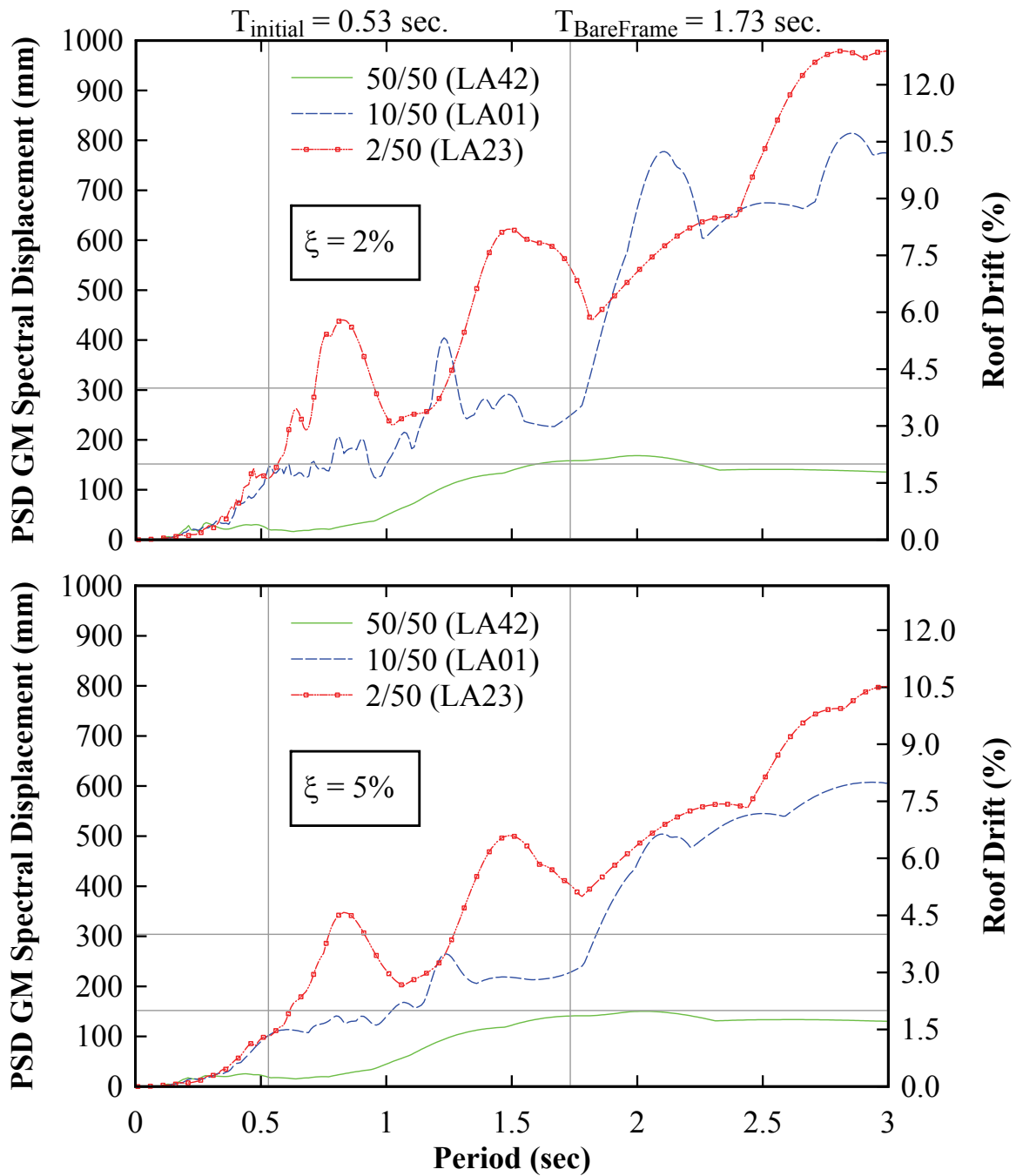


FIGURE 8-11b Spectral displacement response – PSD GMs

As noted, the response of a SC-SPSW is bounded by  $T_{\text{initial}}$  and  $T_{\text{BareFrame}}$ , which leads to a significant range in drift demand. By observation of the spectral displacements, the drift demand at the MCE level for the bare frame condition is approximately 5% and 7% drift for a damping ratio of 2% and 5% respectively. By definition, the bare frame condition implies complete absence of the infill web plate, which gives the most conservative estimate of drift. Unless a complete separation of the infill web plate occurs (at all or most of the floor levels) during a seismic event, the infill web plate will continue to provide some stiffness and energy dissipation. Experimental results in past research show that even with moderate levels of infill web plate separation from the boundary frame, partial tension field action can still develop and hysteretic behavior of the web plate can still be achieved. However, it is plausible that after a DBE or MCE level event, low level aftershocks representative of the 50/50 GM could occur prior to the replacement of the infill web plates. Conservatively assuming tension-only behavior of the infill web plate for discussion purposes, the stiffness of the SC-SPSW web plate for a 50/50 GM aftershock would be negligible (as the plate would only contribute stiffness at drifts exceeding the previously reached maximum drift response) and only the PT boundary frame would contribute to frame stiffness in that case. In this scenario, from the response displacement spectra for the 50/50 GM, the drift demand assuming only PT boundary frame response is about 2.5%, which, although large, would likely be sufficient to protect the building from collapse until the infill web plates could be replaced. Finally, as noted earlier, the building response is also dependent on the characteristics of the GMs. The variability of acceleration and displacement response can be observed in the response spectra for the selected GMs. Note that, unlike a DBE response spectrum that includes a constant acceleration range at the maximum spectral acceleration (independent on building period), the actual building acceleration response is dependent on the characteristics of the GM and change in building period during the earthquake.

The complete loading protocol history also included a number of different quasi-static cyclic and free vibration tests. An initial elastic cyclic test and PSD free vibration test was performed prior to the PSD earthquake tests to obtain elastic properties of the frame, to check the instrumentation, and to obtain approximate elastic dynamic properties of the total system (i.e., including effects of the test setup). For the PSD tests, a free vibration phase was recorded after termination of the GM records (made possible by appending a zero ground acceleration segment

at the end of the GM record) to observe free vibration decay and to obtain an approximate residual drift. Furthermore, quasi-static cyclic tests were added at the end of the PSD tests to: 1) ensure that the specimen was tested to a minimum of 4% drift, which is the drift PO for the MCE level; 2) impose drift cycles up to the maximum 4.5% drift limit of the test setup, to test the specimen beyond MCE level if necessary; and 3) repeat quasi-static cycles beyond the previous displacement history of PSD tests to possibly trigger and observe the ultimate failure mode of the specimen.

**TABLE 8-1 NCREE test loading protocol**

Loading Sequence	Cyclic		Free Vibration		PSD			
	No. of Cycles	Top Story Drift (%)	$U_o$ (mm)	Duration (sec.)	Seismic Hazard	GM	GM Duration (sec.)	Free Vibration (sec.)
1	2	0.15	-	-	-	-	-	-
2	-	-	10	16.42	-	-	-	-
3	-	-	-	-	50/50	LA42	2.26	5.41
4	-	-	-	-	10/50	LA01	15.18	4.82
5	-	-	-	-	2/50	LA23	10.13	7.06
6	1	2.5	-	-	-	-	-	-
7	1	3	-	-	-	-	-	-
8	1	3.5	-	-	-	-	-	-
9	1	4	-	-	-	-	-	-
10	4	4.5	-	-	-	-	-	-

The loading protocol for the test is summarized in table 8-1 where  $U_o$  is the applied initial top story displacement for free vibration. Also note that for the PSD tests, *GM Duration* is the total time of the GM record used for the tests, and *Free Vibration* is the additional time appended to the GM Duration. The time durations and added free vibration indicated are the values corresponding to the ground motion records during the test, not the actual time it took to execute the PSD tests (which runs the earthquakes in “slow motion” at an incremental time step  $\Delta t$ ).

## **8.5 PT Boundary Frame Test – Loading Protocol**

For Specimen NZ, the opportunity was provided to perform additional tests on the PT boundary frame upon completion of the PSD and inelastic cyclic tests. This was done by cutting out the existing infill web plates. Obtaining data on response of the PT boundary frame alone helps better understand the overall SC-SPSW behavior response, since the PT boundary frame essentially does not contribute to hysteretic energy dissipation. Similar to the previous PSD tests, free vibration tests were conducted to obtain dynamic properties of the total system. However, only cyclic tests were conducted on the PT boundary frame since it provides for more meaningful observations for direct comparison to the cyclic SC-SPSW behavior response for a similar drift history (i.e., a direct comparison of PT boundary frame response to that of the SC-SPSW behavior response using the PSD earthquake simulations would not be logical given their different periods and dynamic response). The loading protocol for the PT boundary frame test is summarized in table 8-2 where the parameters have been defined earlier.

**TABLE 8-2 NCREE test loading protocol – PT boundary frame**

PT BOUNDARY FRAME				
Loading Sequence	Cyclic		Free Vibration	
	No. of Cycles	Top Story Drift (%)	U <sub>o</sub> (mm)	Duration (sec.)
1	-	-	20	8.29
2	2	0.5	-	-
3	1	2.5	-	-
4	1	3	-	-
5	1	3.5	-	-
6	1	4	-	-
7	1	4.5	-	-

PT BOUNDARY FRAME - Bracing Released				
Loading Sequence	Cyclic		Free Vibration	
	No. of Cycles	Top Story Drift (%)	U <sub>o</sub> (mm)	Duration (sec.)
1	-	-	20	20.92
2	2	0.5	-	-
3	2	2.5	-	-

Note that two different bare frame tests were performed. The first series of tests were conducted directly after the completion of the PSD tests with no adjustments to the lateral bracing system of the test setup. For the second series of tests (differentiated as “bracing released”), the lateral bracing system was adjusted such that the specimen almost touched the lateral HBE braces. The purpose was to investigate the effects, if any, of the lateral bracing system to the damping response during the PSD earthquake simulations (due to friction between the specimen and the lateral bracing system).



## 8.6 Analytical Results

The analytical predictions for Specimen NZ showing the absolute maximum base shear and drift response at each PSD test is shown in figure 8-12 in the form of an incremental dynamic response (IDR) curve. Each data point represents the absolute maximum response (i.e., in either positive or negative drift direction) for a given PSD earthquake simulation (i.e., 50/50, 10/50 and 2/50). Results are provided for both a 1% and 5% damping ratio in an attempt to predict an upper and lower bound response. Mass proportional damping type was used in the analytical model as the test specimen was loaded by an actuator at a single location representing a single-degree-of-freedom (SDOF) system in the horizontal direction. To match the experimental setup, a single lumped mass in the horizontal degree-of-freedom was applied at the top of the West VBE (location of actuator connection). Furthermore, an initial PT force of approximately 25% and 15% of the PT yield strength was used for the HBE and VBE PT elements, respectively, matching the experimental PT load cell values of the specimen at the start of the PSD tests. The 25% was targeted for the HBE PT to avoid PT yielding at drift levels up to 4.5%. The 15% was targeted for the VBE PT based on not exceeding the designed load cell capacity at 4.5% drift. Note however, that over the course of the PSD testing, some PT force losses occurred due to PT relaxation and anchor wedge seating between GM tests (see Section 9) that cannot be readily captured in the analytical predictions. Additionally, although the results are for a particular seismic hazard, the GMs used in the analytical predictions were concatenated to create a single GM, with the individual GM seismic hazard separated by periods of zero acceleration to allow for free vibration. Sufficient amount of free vibration time was included in the GM record to allow the analytical model to return to approximate “at rest” conditions prior to the subsequent individual GM excitation.

A roof displacement history sample plot for all seismic hazards for a 1% damping condition is shown in figure 8-13; which includes the free vibration response between individual seismic hazard GM records. The roof displacement history, shown for this approximate upper bound response, closely matches the PO target drifts, indicating that the selected GMs are appropriate (for small damping) for use in the loading protocol. Although the PO is independent of damping, this upper bound prediction provides some assurance that the response of the specimen will be

within the constraints of the test setup noted earlier. Also note that recentering in the analytical model was achieved, as the residual drift obtained were below the 0.2% drift recentering criteria.

The individual base shear versus roof drift plots for the 10/50 and 2/50 GMs are shown in figure 8-14 (note that the 50/50 response is essentially elastic and not shown). Observation of the hysteresis response shows that perfect recentering is obtained from the analytical model; which is expected with tension-only modeling of the infill web strips. However, as observed in the quasi-static tests conducted at UB, frames with full infill web plates do not perfectly recenter, due to compression stiffening effects of the infill web plate (as a result of geometric web plate distortion due to tension field action). As discussed in Section 3, research by Webster (2013) was underway to propose a new material model (for use in OpenSees) for the infill web plates to capture this behavior, but no such substantiated material models for use in analysis were available for the modeling of SPSW web plates at the time of the NCREE tests. This was not believed to be a significant problem given that experimental results from the UB shake table experimental results showed that recentering is not sensitive to this phenomenon when subjected to earthquake excitations (as opposed to quasi-static loading).

Additional observation of the hysteresis plots in figure 8-14 show a noticeable asymmetry for the 2/50 GM response with a 5% damping condition. For all other plots (i.e., with different GMs and damping), the response is essentially symmetric in comparison. However, earthquake ground motion displacement responses are not necessarily balanced in the positive and negative drift directions. Accordingly, the hysteretic response does not necessary have to exhibit similar drifts in both directions. The dynamic response is sensitive to not only the frequency content of the GM, but also the dynamic characteristics of the SC-SPSW frame.

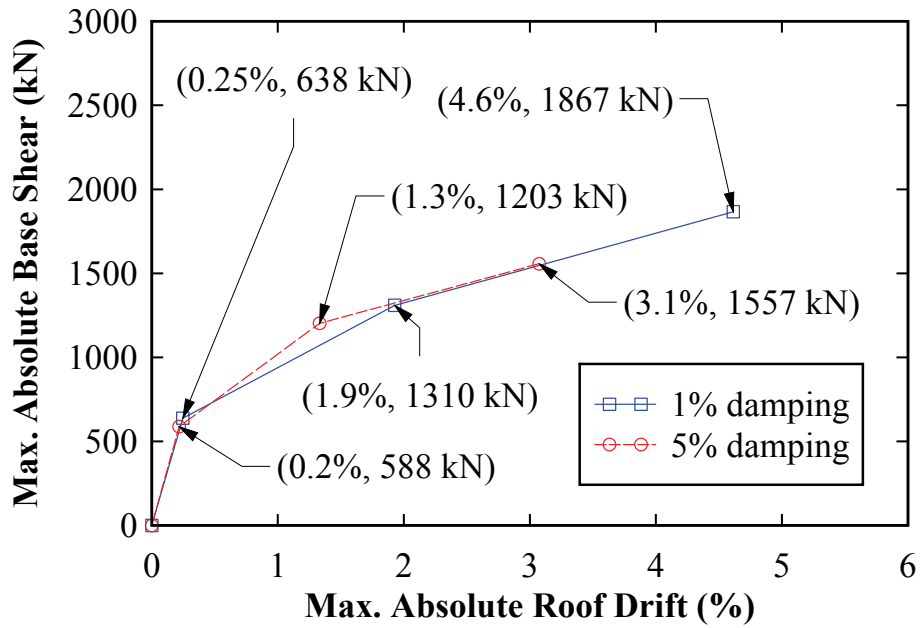


FIGURE 8-12 Analytical incremental dynamic response

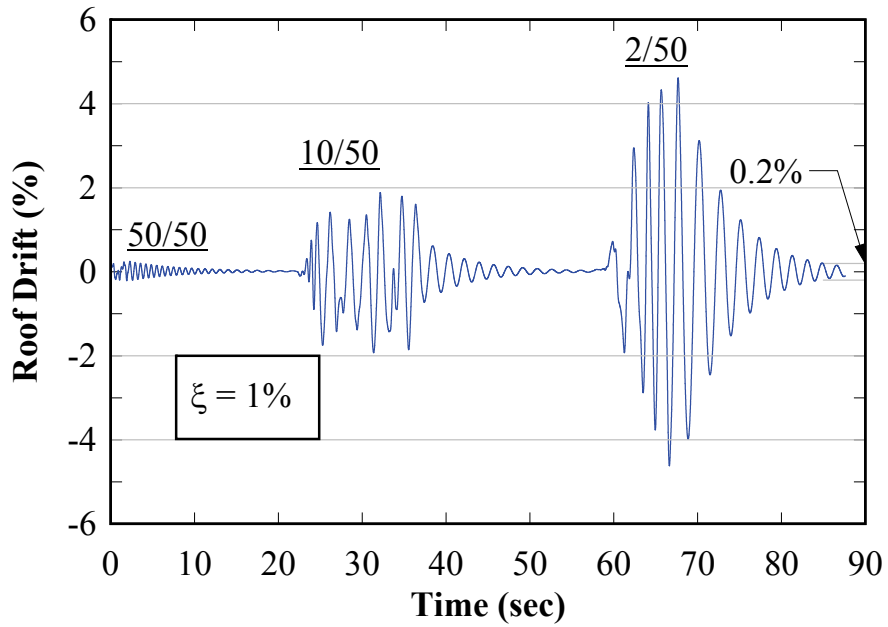
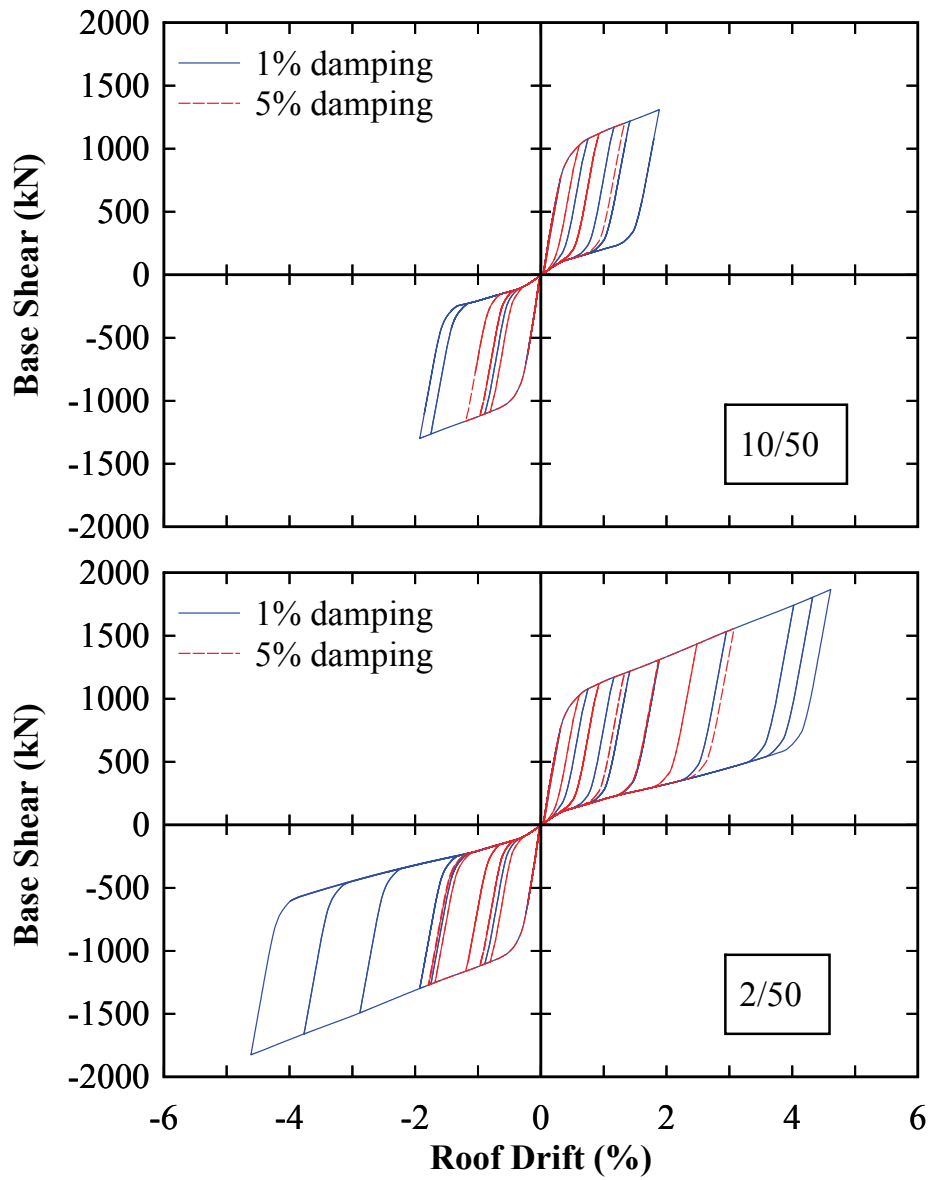


FIGURE 8-13 Analytical sample roof drift history



**FIGURE 8-14 Analytical base shear versus roof drift**

## 8.7 PT Boundary Frame Characteristics with VBE PT Base

As mentioned earlier, one of the primary motivations for using a VBE PT base connection for the NCREE tests was to provide a possible alternative connection detail to the pin connection previously used for the UB tests (solely for the sake of providing more design options, as the pin detail remains an effective solution for use in a SC-SPSW system). For illustrative purposes, monotonic pushover analyses was performed on the PT boundary frame of Specimen NZ with an arbitrary initial PT force of approximately 30% and 15% of the PT yield strength used for the HBE and VBE PT elements, respectively. The results are provided in figure 8-15 along with the corresponding PT force versus roof drift plots. It is observed that the addition of the VBE PT component leads to a tri-linear response such that: 1) initial stiffness  $K_1$  occurs when the initial PT force on the VBE PT element is present and both the West and East end HBE PT are in tension; 2) secondary stiffness  $K_2$  occurs when both the West and East VBE PT force overcomes the initial applied VBE PT forces, and both the West and East end HBE PT are still in tension; 3) third stiffness branch  $K_3$  occurs when the East end HBE PT force at the closing joint has fully relaxed. Other characteristic behavior also observed is a lag in the initial horizontal branch of the VBE PT force plots. Note that the East VBE is the compression column for resisting the foundation overturning moment for an Eastward drift condition shown; hence the initial horizontal branch for this column is longer since in order to engage the VBE PT in tension, the axial force in the VBE must first overcome the axial compression force from the overturning moment. Furthermore, the initial portion of the HBE PT force curves is parabolic (although difficult to see in the figure); once the initial PT force is exceeded the response is linear (similar is true for the VBE PT response). Finally, although the same PT design was used at each of the HBE levels, the stiffness is different at each level as observed by the PT force versus roof drift plots. In part, this is a reflection of the losses of PT forces due to differences in HBE axial shortening (i.e., the HBE sections are different at each level). Similar is true for the VBE PT stiffness but the effects of the axial shortening is due to the differences in the axial forces in the columns from the overturning moment demands (i.e., the VBE sections are the same but the axial shortening affects will be of opposite sign). Thus, the response of the PT boundary frame is defined by a combination and complex interaction of the amount of PT strands provided and the corresponding initial PT force applied.

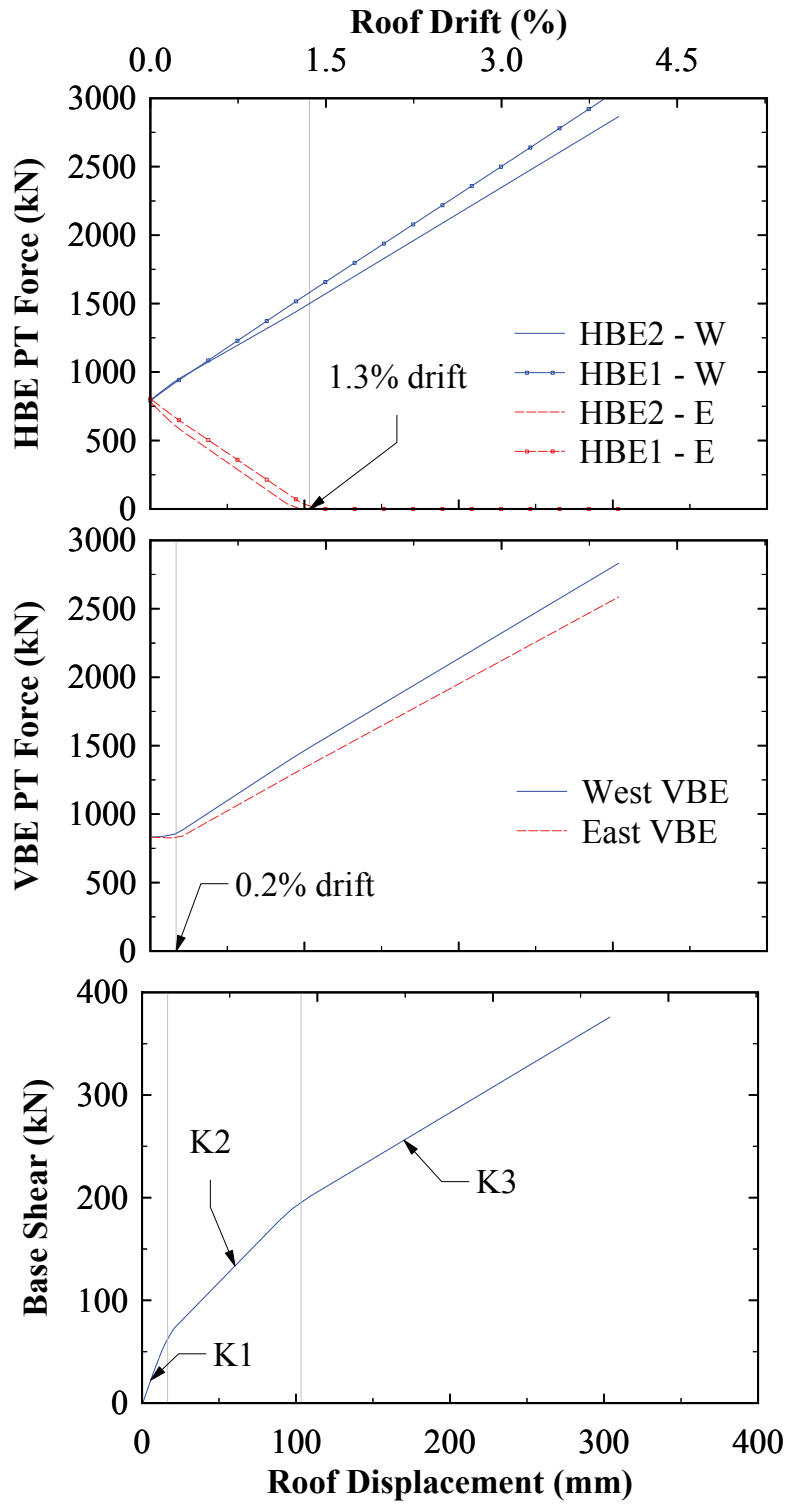


FIGURE 8-15 PT boundary frame characteristics (for Eastward drift)

It is intuitive that the addition of a VBE PT rocking detail will provide additional recentering stiffness. To illustrate this, additional monotonic pushover analyses were performed on the PT boundary frame considering two different base conditions: 1) zero initial VBE PT force for the base connection model presented above; and 2) a pin connection at the VBE base eliminating the VBE PT elements. For the HBEs, an initial PT force of approximately 30% of the HBE PT yield strength was used for both conditions. Also, recall that the NewZ-BREAKSS PT boundary frame response using a pin VBE base connection is bi-linear, with an initial stiffness that includes contribution of PT elements at both ends of the HBE and a secondary stiffness that only includes contribution of the PT at the opening joints when the PT at the closing joints are fully relaxed. The resulting pushover curves are compared with that of the original condition (i.e., the pushover curve shown in figure 8-15) and shown in figure 8-16, where  $T_y$  noted in the figure is the assumed yield stress of the PT strands.

Comparing the tangent stiffness values, K2 to K5, indicates that the addition of the VBE PT alone (i.e., without any initial PT force), increases the PT boundary frame stiffness by approximately  $K2/K4 = 1.25$  and  $K3/K5 = 1.5$  over the value for the case with the pinned VBE base (for the example problem shown). This corresponds to an increase in base shear strength of approximately 105 kN (24 kips) over the range of response shown in figure 8-16. Relative to the total base shear demand, this increase in strength and stiffness is not substantial. However, it is observed that with the addition of an initial VBE PT force component ( $T_o = 15\%T_y$  for example shown), an increase in the initial stiffness of the PT boundary frame by approximately  $K1/K2 = 2.7$  and  $K1/K4 = 3.3$  is achieved over the case with VBE  $T_o = 0$  and with the pinned VBE base respectively (for the example problem shown). Furthermore, the variation of VBE  $T_o$  does not increase the stiffness K1, but simply extends the range of stiffness K1 with a small increase in base shear strength, as shown in figure 8-17. For example, results in this figure show that increasing the initial VBE PT force from 15% to 30%, extends the drift range with stiffness K1 from approximately 0.2% to 0.5% drift, with an increase in base shear strength of approximately 40 kN (9 kips). Note that although increasing the initial VBE PT forces does not change the tangent stiffness values (i.e., K1, K2, K3, etc...), it still provides an increase in recentering response by the increase in base shear strength (i.e., by increasing the secant stiffness global

response). Consequently, the use of a VBE PT rocking detail with an initial PT force can have an appreciable increase in recentering stiffness.

Note that the above comparisons were made by only changing the VBE base connection conditions, to illustrate the effect that this single parameter has on the response. In actual designs of a SC-SPSW using a pin VBE base connection, the HBE PT elements would be modified for a given target response. In particular, the PT boundary frame stiffness would be modified by increasing the quantity of PT elements and/or increasing the initial HBE PT forces, thereby increasing the recentering stiffness of the SC-SPSW as appropriate. Figure 8-18 shows the effect of each separately; where Pin indicates a PT boundary frame modeled using pinned VBE base connections and the VBE PT  $T_o$  curves correspond to the PT boundary frame modeled with the VBE PT base rocking connection. Also recall that the curve for VBE  $T_o = (15\%)(T_y)$  shown, represents approximately the actual conditions of Specimen NZ for comparison purposes; where the 1.3% drift indicates the point at which the HBE PT becomes fully relaxed at the closing joint.

For reasons discussed earlier, the option of increasing the initial HBE PT forces in individual PT strands does not provide any significant advantages. Although, as shown in figure 8-18a, a small benefit is gained by the extension of the range of the first initial stiffness branch, this is at the cost of reducing the drift limit of the frame in order to prevent yielding of the PT elements. Therefore, as shown in figure 8-18b, increasing the quantity of PT elements is the most effective way of increasing the recentering stiffness of the PT boundary frame. However, this is now achieved at the cost of increased strength demands on the HBES from the additional PT elements (note that the plots shown in figure 8-18b assumes elastic behavior and frame members are not resized in this example), and possible constraints in accommodating more PT elements from a constructability stand point. A satisfactory design solution, regardless of the type of VBE base connection used, will involve providing a PT joint detail that is constructible and cost effective, by seeking an optimum combination of number of PT strands and applied initial PT forces to meet the design objectives.



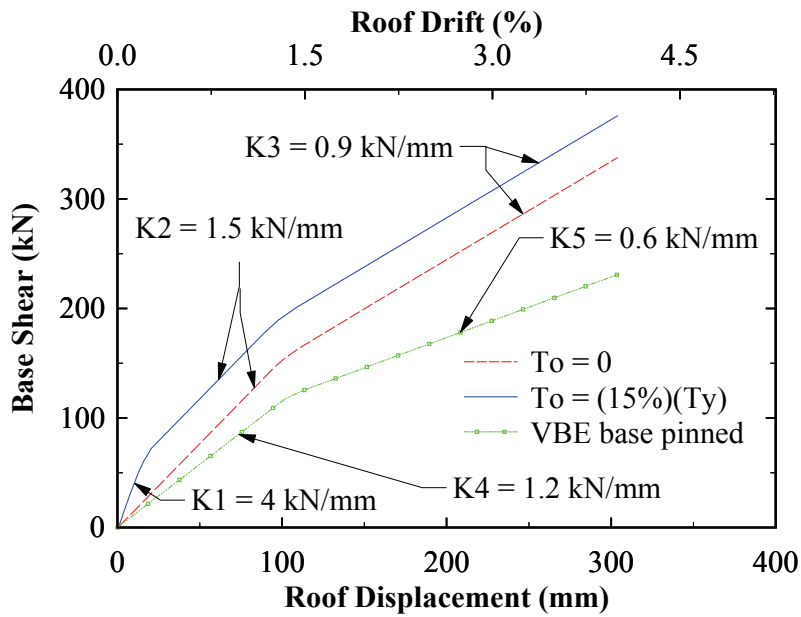


FIGURE 8-16 PT boundary frame comparisons

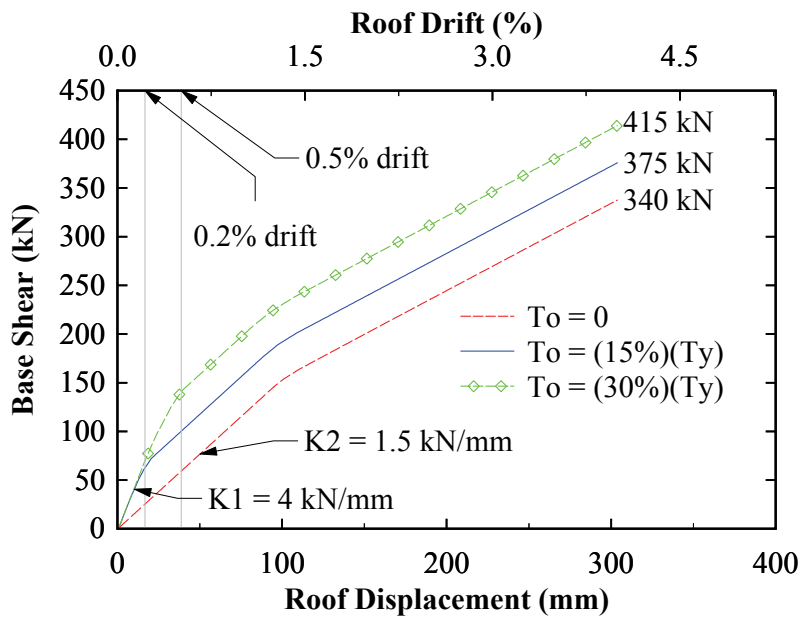
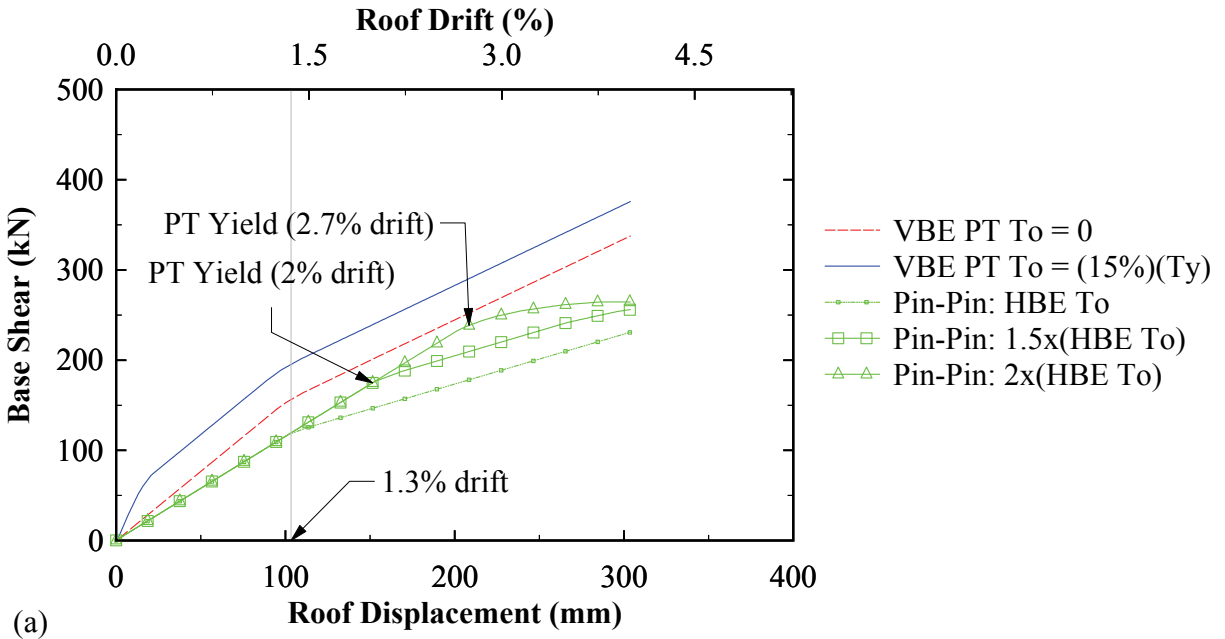
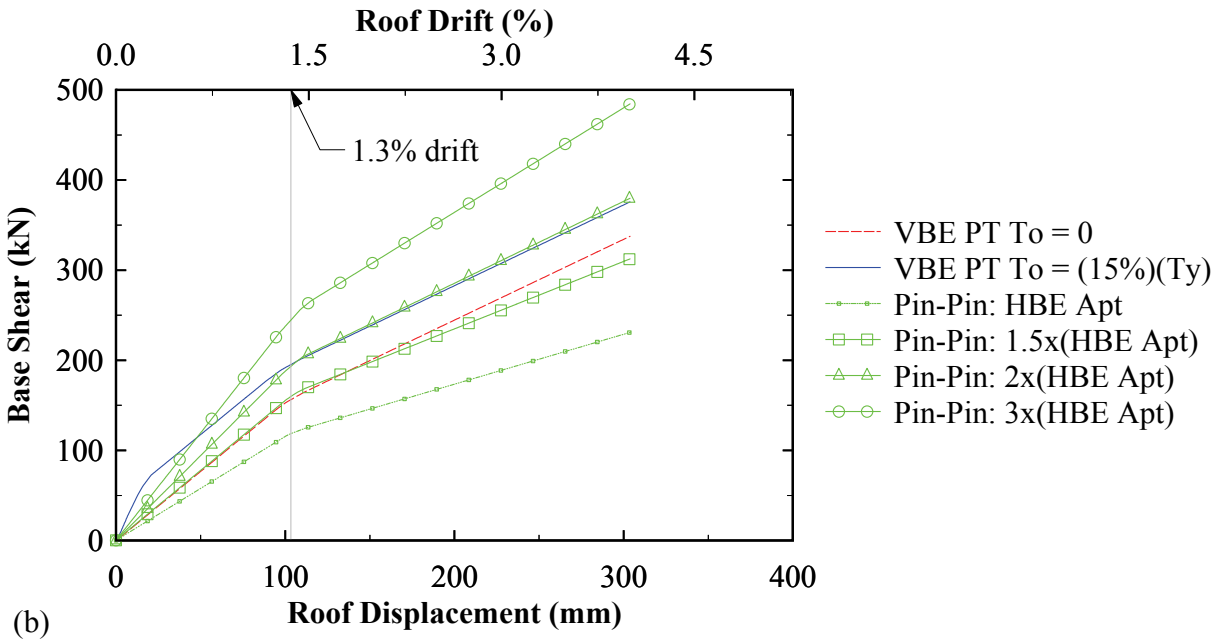


FIGURE 8-17 PT boundary frame variation in VBE  $T_o$



(a)



(b)

FIGURE 8-18 (a)  $T_o$  variable; (b)  $A_{pt}$  variable

## **SECTION 9**

### **FULL SCALE PSEUDO-DYNAMIC EXPERIMENTAL TESTS**

#### **9.1 General**

The PSD tests were conducted using the NCREE research facility's 1.4 m thick strong floor (to which the specimen was anchored) and 1.2 m thick (box design) reaction post-tensioned stepped wall system (on which the actuator reacted to apply loads to the specimen). This chapter describes the test specimen fabrication and construction (Section 9.2), the test and loading setup (Section 9.3), instrumentation used during the tests to collect data (Section 9.4), the PSD loading procedure (Section 9.5), the PSD free vibration tests performed and results (Section 9.6), and the visual condition assessment observations made during the experimental tests (Section 9.7). It also presents the experimental results of the PSD tests (Section 9.8), the experimental results of the cyclic static inelastic and bare frame tests (Section 9.9), a comparison of analytical results with the experimental (Section 9.10), some insights on the development of beam-growth effects for frames with PT rocking connections (Section 9.11), a comparison of the UB shake-table and NCREE PSD test results (Section 9.12), and a summary of findings from the NCREE test (Section 9.13).

#### **9.2 Specimen NZ fabrication and Construction**

The steel shapes used to fabricate the boundary frame were donated by the American Institute of Steel Construction (AISC) and shipped from the United States to the NCREE lab in Taiwan via ocean cargo barge. The post-tensioning (PT) rods and strands were supplied by the Dwidag-Systems International (DSI) distributor in Taiwan, and the infill web panels were supplied by the China Steel Corporation. All steel fabrication was done in Taiwan by a local steel fabrication shop under supervision of the NCREE team in coordination with the US-based team. Upon completion of all fabrication the individual HBE and VBE frame members and plates were delivered to the NCREE site where all assembly work was accomplished.

The construction of the test specimen, shown in figure 9-1, consisted of the following five general steps:

- 1) Assembly of the boundary frame: The VBEs were first placed flatwise on the floor supported by temporary cribbing, and the HBEs were then loosely bolted in place.
- 2) Alignment using temporary PT: After ensuring that the boundary frame was square and HBE-to-VBE flanges were in contact (to the extent possible without the aid of mechanical leverage), temporary full length PT rods anchored to the outside of the VBE flanges were placed along the length of the top and middle HBEs. Then the rods were stressed clamping the HBEs and VBEs together ensuring full contact at the HBE-to-VBE joint connections, and snug tight bolted connections at the HBE shear plates were then made using a pneumatic gun.
- 3) Installation of the infill web plate panels: A welded connection of the infill web plate panels to the steel boundary frame fish plates (a connection typical of SPSWs) was made. Note that each of the infill web plate panels consisted of three separate subpanels spliced together using complete penetration welds to create the full infill web panel and that the splice locations were grinded smooth, providing a seamless flush panel surface.
- 4) Removal of the temporary PT rods.
- 5) Installation of the PT strands specific for the test specimen: Here the middle HBE was stressed first, followed by the top HBE. After all PT strands were stressed, individual strand locations were additionally stressed as needed to reach the individual strand target initial design PT force (approximately 25% of the yield strength of the each individual monostrand). Finally, the stressing of the PT strands to the target initial PT force was achieved by monitoring forces in the HBE PT loads cells.

Note that during design of the test specimen, the actual stressing sequence to be followed for construction of the PT boundary frame was not known. As such, the PT boundary frame was designed considering the worst case stressing scenario, which corresponds to first fully stressing each 7-strand PT bundle on one side of the HBE web (producing an unbalanced weak-axis bending of the HBE until the other PT strand bundle on the opposite side of the HBE web is stressed). Additionally, it was recognized that in the NewZ-BREAKSS connection detail, because the bottom HBE flange is not in contact with the VBE flange, the gap between the VBE

flange and HBE web will want to close if PT stressing is performed one strand at a time (as was done with the UB tests). Consequently, similar to the UB NewZ-BREAKSS tests, a temporary PT stressing plate aid was provided; this detail for Specimen NZ is shown in figure 9-1e. This temporary plate prevents closing of the gap until all HBE PT strands have been stressed. In the UB tests, when all HBE PT stressing had been performed, attaining an essentially balanced condition, the temporary plates were then removed.

However, for the NCREE test, it turned out that PT stressing of an individual PT strand at each end of an HBE was always performed simultaneously to PT stressing of its equivalent counterpart strand at the other end of the HBE (i.e., the two PT strands were stressed in tandem). For this PT stressing method in complete tandem, the temporary stressing plate would not have been necessary (because the corresponding strand elongations at each of the stressing jacks during PT stressing are essentially equal), and the shims served more for safety in case unforeseen problems occurred during stressing, such as a significant loss in pressure in one of the stressing jacks, that would have pulled the frame significantly out-of-square as a result of the unbalanced PT forces, and could have induced some damage to the infill plates (which were installed prior to PT stressing).

As for the VBE PT rods, PT stressing was performed after the test specimen was put in its final testing position, because the VBE base pedestal connection was already in its' final position (and anchored to the strong floor) for reasons to be presented subsequently.



**FIGURE 9-1a Specimen NZ construction: Step 1 – assemble boundary frame**

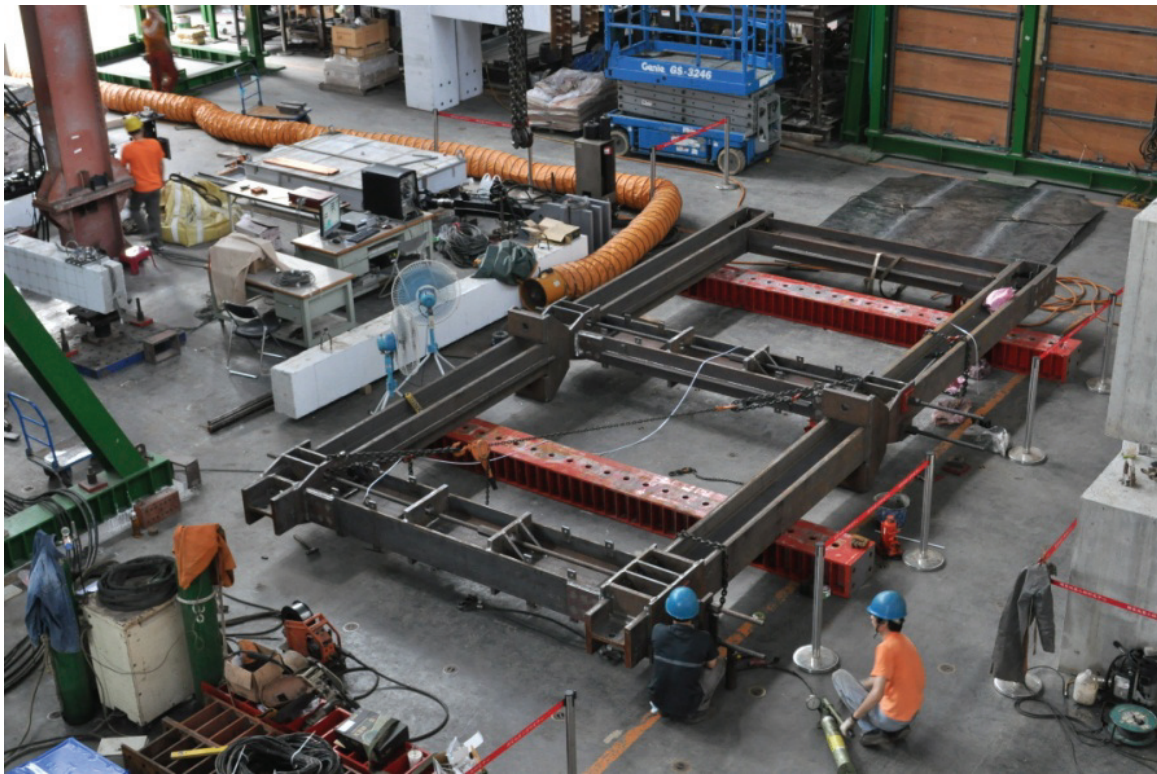


**FIGURE 9-1b Specimen NZ construction: Step 2 – install temporary HBE PT bars**

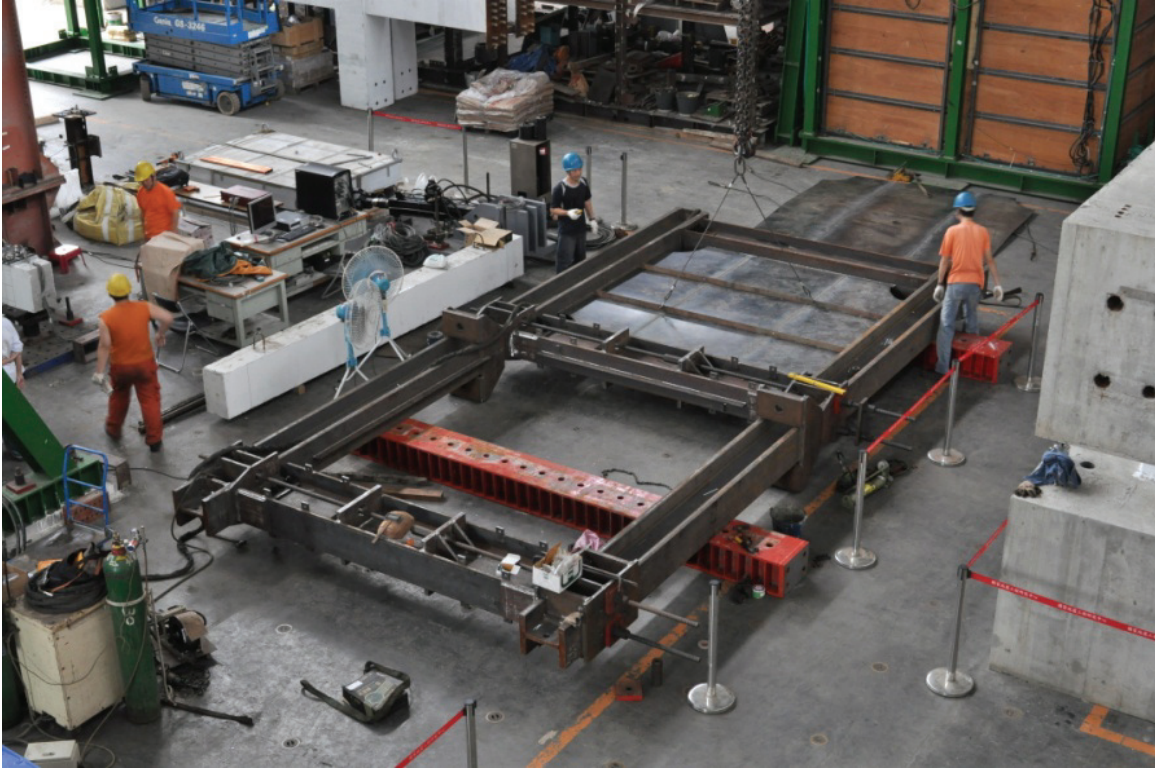


**FIGURE 9-1c Specimen NZ construction: Step 3 – install web plates**



**FIGURE 9-1d Specimen NZ construction: Step 4 – remove temporary HBE PT bars**

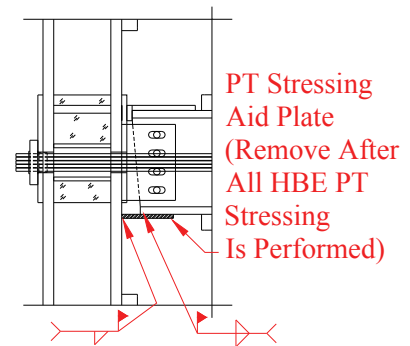


**FIGURE 9-1e Specimen NZ construction: Step 5 – install HBE PT strands**



### 9.3 Test Setup

The SC-SPSW test specimen was laterally braced by an existing steel modular frame and anchorage system provided by NCREE. The steel modular frame provided out-of-plane restraint but allowed the SC-SPSW specimen to move in-plane by sliding on an alignment interface having contact points located on the lateral bracing frame columns at the location of the specimen's HBE flanges. The schematic of the test setup is shown in figure 9-2 and the actual in-place setup prior to testing in figure 9-3. As shown, the lateral bracing frames consist of an assembly of steel wide-flange sections and are provided on each side of the test specimen. Contact bearing points of the SC-SPSW test frame to the lateral bracing frames were provided by a T-brace connection. The T-brace sections (150mmx20mm flange, 80mmx25mm web and 1000 mm in length each) were provided at each ends of the HBE top and bottom flanges and bolted to steel connecting plates (130mmx70mmx15mm) on the HBEs. These steel connecting plates were welded to the inside of the HBE flanges and two connecting plates at each T-brace location were provided at 400 mm on center. The bearing connection contact points of the lateral bracing frames to the test specimen was provided at the lateral brace frame column locations where a steel bearing plates were attached to the lateral brace frame columns. These bearing plates were adjustable and positioned to be in contact with the T-brace sections located on the HBEs. Lubricating grease was provided on the surface of the T-brace and the bearing plate to minimize friction between the sliding interfaces. Bracing points described were provided at the top HBE and middle HBE locations.

The anchorage of the VBEs to the strong floor was provided by the use of an existing 1240mmx1200mmx100mm steel bearing plate connection designated as NCREE Plate 140-A. This bearing plate was anchored to the strong floor with post-tensioned all-thread bars and had a pre-allocated array of existing threaded tapped holes for anchorage of the VBE pedestal base connection. For erection tolerances, oversized holes were used in the base anchorage connection of the VBE pedestal base to the Plate 140-A. To prevent undesired slip during testing, the VBE pedestal base anchorage bolts attached to Plate 140-A was designed as slip-critical bolts.

Lateral loading of the test specimen was provided by direct attachment of the actuator to the top level of the test specimen; the lateral bracing system only served to provide out-of-plane

stability. However due to the presence of the PT anchorage on the outside of the VBE flanges, the VBE detail at the actuator connection had to be modified to accommodate the actuator connection in combination with the PT anchorage detail. To facilitate this, a transfer beam attached to the outside of the top of the West VBE flange was provided at the actuator connection location. The HBE PT anchorage was extended to the outside of the transfer beam to facilitate PT stressing and the transfer beam was fabricated length wise perpendicular to the test frame to accommodate an actuator connection. Consequently, to avoid eccentrically loading the test specimen, two actuators were provided, one on each side of the HBE PT anchorage.

The assembly of the test setup consisted of three general steps, namely:

- 1) Positioning the test specimen in place. In this step, with the South elevation lateral bracing frame and the VBE base pedestals already in place after the previous Specimen FR tests, because Specimen FR and NZ are identical in dimensions, all that was required was to move Specimen NZ from the staging area where it had been constructed (discussed in Section 9.2) and hoisted in place on top of the VBE base pedestals.
- 2) Completing lateral restraint system. In this step, the North elevation lateral bracing frame was moved in place and contact at bearing points of the lateral bracing frames to the test specimen T-braces was made by adjusting the bearing plates located on the lateral brace frame column locations mentioned above.
- 3) Installation of VBE PT Rods. Once the test specimen was securely braced by the lateral bracing frames, the VBE PT rods were installed and stressed. As was the case for the HBE PT, the stressing sequence of the VBE PT was not known during design of the test specimens, and the VBES were conservatively designed for the worst-case stressing sequence, which consists of stressing each VBE PT rod in full to its target initial PT force one at a time, leading to a temporary eccentric loading of the VBES. However, for the NCREE test, it turned-out that all of the VBE PT rods were stressed simultaneously. A target initial VBE PT force of approximately 15% of the yield strength of the PT rods was provided. This initial VBE PT force value had been selected during design to ensure that the VBE PT force demand at 4.5% drift remained below the capacity of the 200 metric-ton (440 kips) load cells used at the VBE PT locations. The stressing of the PT

rods to the target initial PT force was achieved by monitoring forces in the VBE PT loads cells.

Note that the test specimen was not checked for out-of-plane plumb prior to stressing the VBE PT rods. Since the South elevation bracing frame and VBE pedestals were already in place from the previous Specimen FR test (which was plumbed), this was an understandable oversight. Given that the dimensions of Specimen FR and NZ are not identical due to fabrication tolerances and natural member cambers, in hindsight, checking for out-of-plumb should have been done prior to VBE PT stressing. Thus, after the VBE PT stressing operations had been completed, the frame was then checked for out-of-plumb by dropping a plumb bob from the outside center of the VBE flange to the VBE base. It was determined that the West VBE was plumb but that the East VBE was out-of-plumb by approximately 1 cm, leaning to the South. The extent of this out-of-plumb of the East VBE was less than the height/500 tolerance for out-of-plumb specified by current building codes and standards and could have been deemed acceptable. However, the East VBE was adjusted to vertical plumb (by adjustment of the top level lateral framing brace bearing plate). Doing so however, affected the East VBE initially applied PT forces, resulting in an increase and decrease in PT force in the PT rods located on the South and North web of the East VBE, respectively (note that the West VBE PT rods were not affected by this operation). As a consequence, to balance the PT forces, further adjustments of the VBE PT forces were made to approximately match the original initial target forces at each VBE PT rod location. Since the VBE PT consisted of threaded bar, this made for a relatively simple adjustment for PT re-stressing. For this purpose, the South and North VBE web PT force respectively at the East VBE was reduced and increased accordingly by adjustment of the vertical PT bar threaded anchor nut.

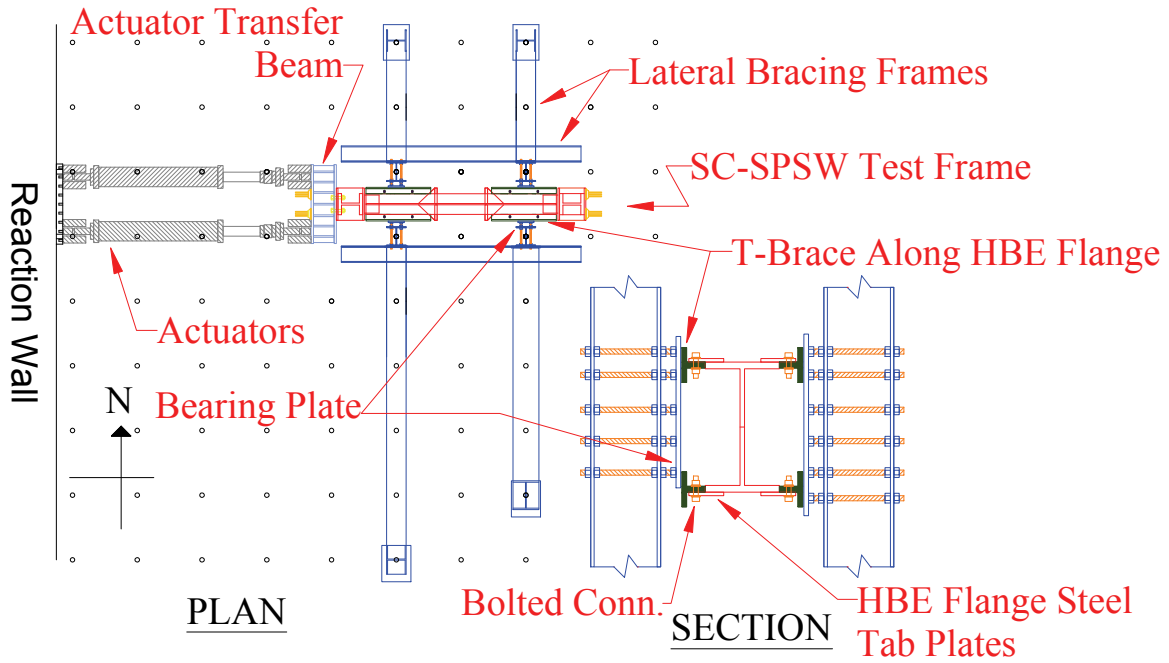


**FIGURE 9-2a Test setup plan**

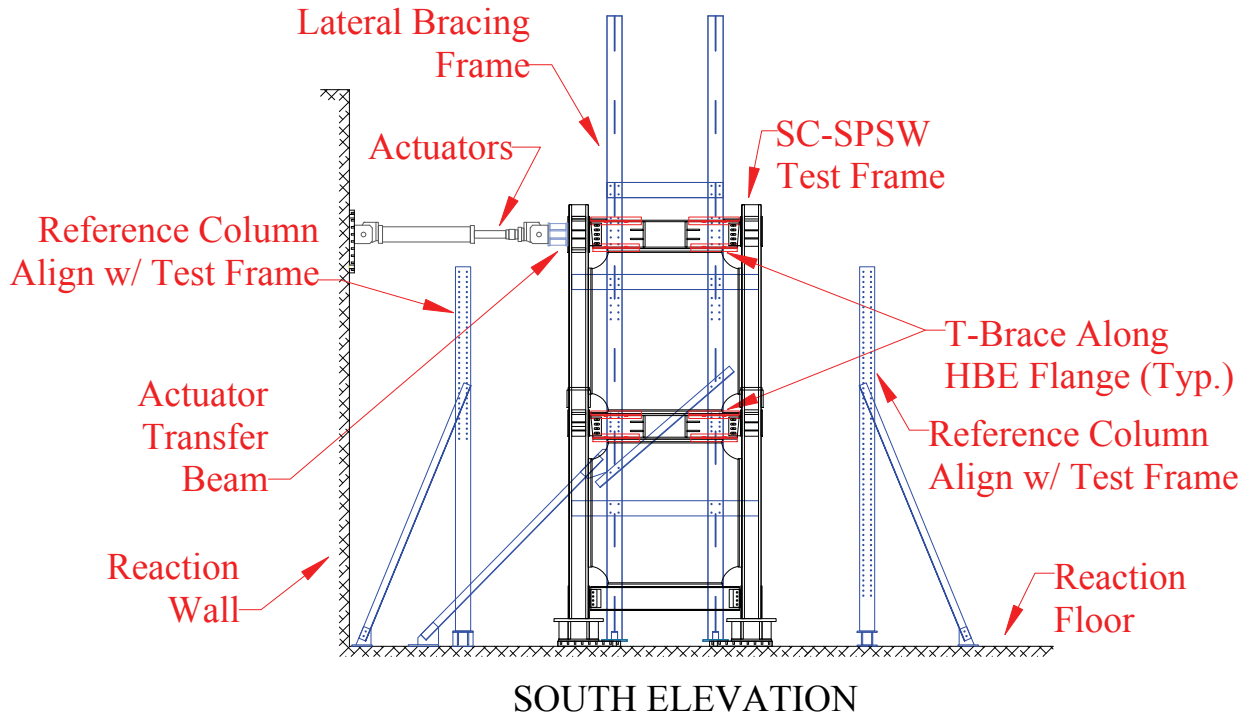


**FIGURE 9-2b Test setup elevation**



**FIGURE 9-3 Test setup final**

#### **9.4 Instrumentation**

Instrumentation was provided to record particular aspects of local and global responses. Sensors included displacement transducers, load cells, and strain gages. Layout of the displacement transducers is shown in figure 9-4 and a combination of different types of displacement transducers was used. In particular, linear potentiometers were provided at the HBE and VBE flange locations to calculate relative end joint rotations, string pots were provided at the HBE levels to record lateral frame displacements, dial gages were provided at the base of the VBE connections to monitor its displacement relative to the foundation (if unintended bolt slippage was to occur), and linear variable differential transformers (LVDTs) were provided along the infill panel web to measure the approximate axial deformation of the infill web plates. The use of a particular type of displacement transducer at a particular location was dependent on the anticipated magnitude of the relative displacement to measure, distance of the measured points to

its reference point, and the desired precision tolerance. Additionally, an LVDT (sensor name *Tempo*) was provided approximately 120 mm (4.7 in.) below the centerline of the top level HBE just below the actuator. The purpose of this sensor was to facilitate the displacement control of the actuator during the PSD earthquake simulation tests. In other words, the real displacement of the actuator,  $\Delta_{actuator}$ , during the test was controlled to trace the recorded *Tempo* measurement such that  $\Delta_{actuator} = (HeightActuator/HeightTemp) * \Delta_{Tempo}$ . This LVDT was attached to a fixed reference column (see figure 9-2b) to measure the true displacement of the test specimen (note that readings from the displacement transducer inside the actuator also include the displacement of the reaction wall at the actuator support, and could not be used for this purpose). Note that all the string pots provided to measure frame displacements were also attached to a fixed reference column. Load cells were provided at all PT locations on the HBEs and VBEs to record PT forces, per the layout shown in figure 9-5.

Although the boundary frame was designed to remain essentially elastic, strain gage sensors were still provided to monitor localized strain effects at the ends of the boundary frame members to monitor the possible occurrence of yielding at specific locations, and to obtain flexural and axial force demands on the HBE boundary frame. The strain gage layout is shown in figure 9-6. Gages were placed on the inside of boundary frame flanges to help protect them during construction of the test setup. To provide some data redundancy and to allow calculations of axial forces and in-plane and out-of-plane moments, at any given cross-section of interest (where strain gages were provided), there were two gages on each flange, located one on each side of the web (for a total of 4 gages at a single location). Quarter bridge circuit wiring was used for all gages such that each gage is independent of each other.

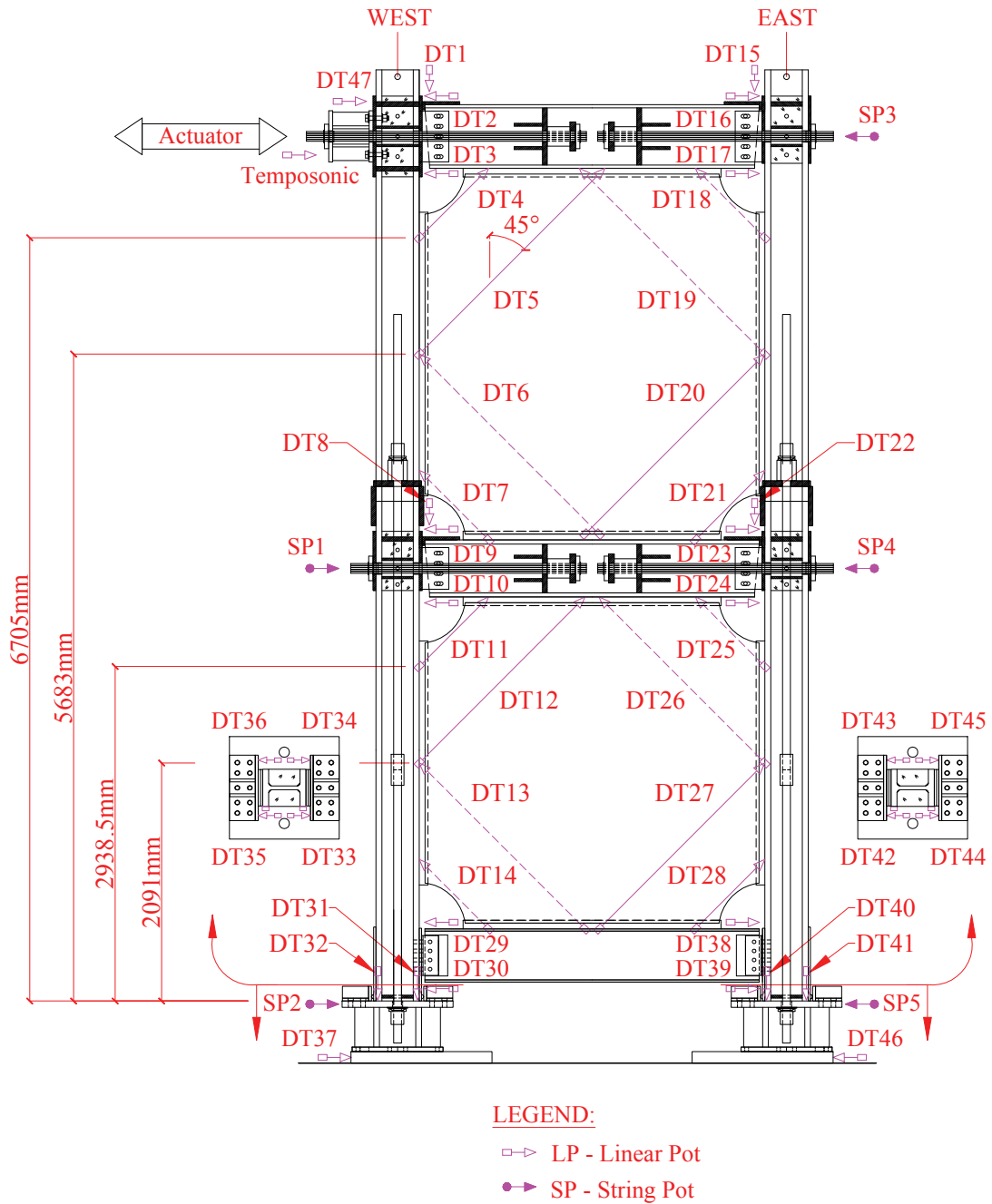


**FIGURE 9-4 Displacement transducers**

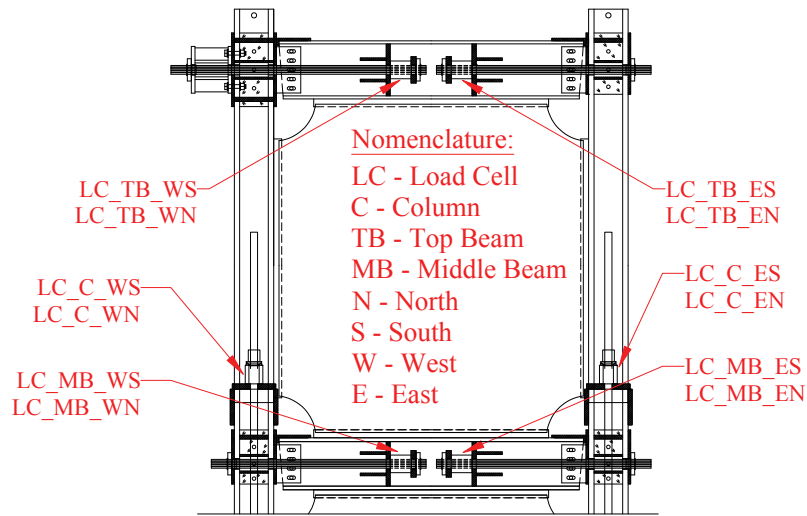


**FIGURE 9-5 PT load cells**

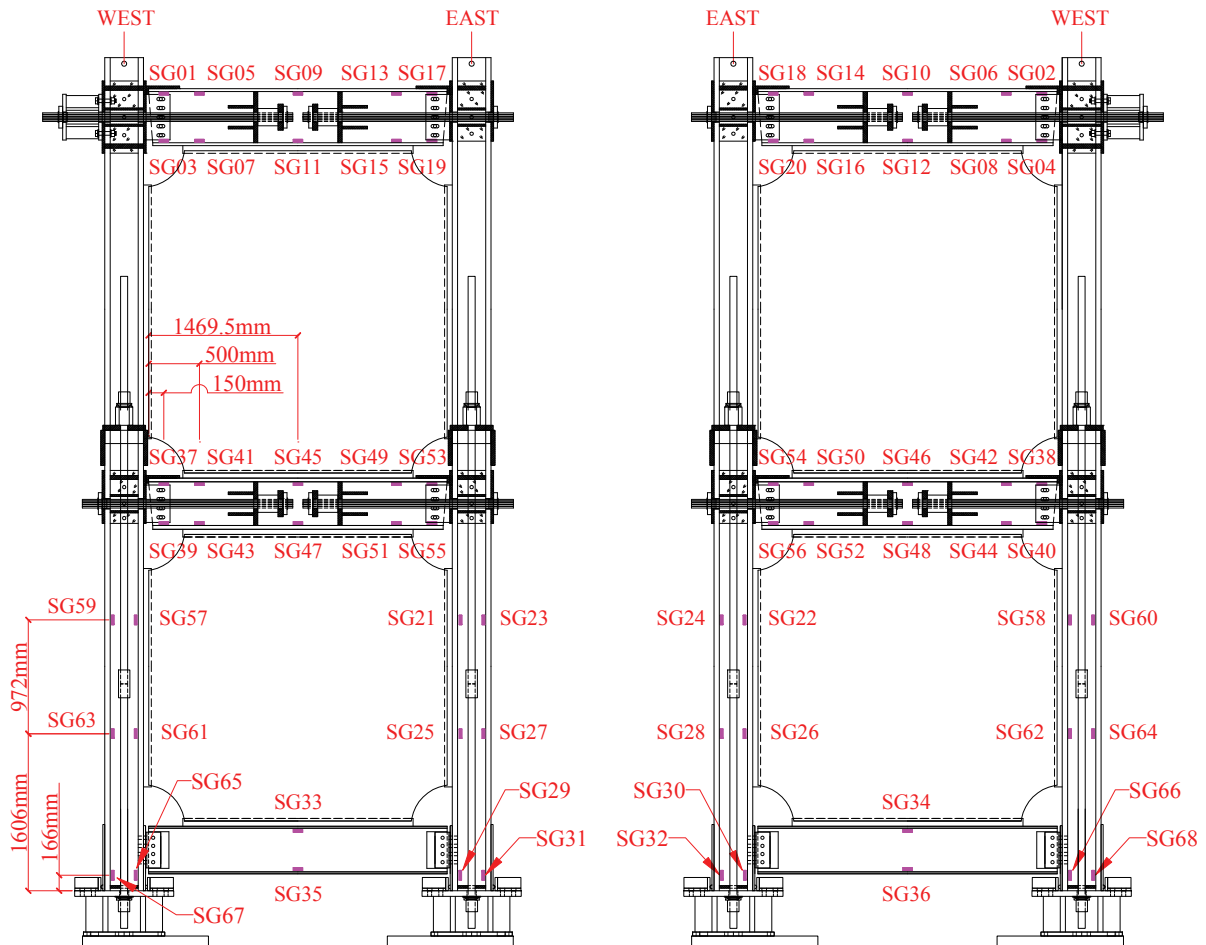


**FIGURE 9-6 Boundary frame strain gages**



## 9.5 Pseudo-Dynamic Loading Procedure

The PSD tests were performed using a closed-loop framework using the Newmark explicit algorithm (Newmark 1959) as the integrator for solving the incremental equations of motion. For the experimental tests, only the response of the SC-SPSW test frame was used in the PSD tests; no additional numerical modeling of the prototype building was included. The test frame was designed based on a seismic tributary mass representing a typical lateral frame in the prototype building. The purpose of the NCREE tests was to investigate behavior of a full scale SC-SPSW frame and the exclusion of numerical modeling of additional prototype building components is reasonable for this purpose.

In the explicit form of the Newmark difference equations, the parameters defining the variation of accelerations over each time step are provided such that the parameters  $\gamma = 0.5$  but  $\beta$  is set to zero. The explicit form eliminates the need to iterate on a basic variable, as the target displacement (which is the basic variable used here) is computed only using data from the current time step, which is attractive for use in PSD testing. The algorithm used to solve the incremental equation of motion response of the test specimen through each time step during the PSD tests is as follows:

- Step 1. Calculate displacement  $u(i+1) = u_i + (\dot{u}_i)(\Delta t) + 0.5(\ddot{u}_i)(\Delta t)^2$
- Step 2. Command actuator to impose displacement  $u(i+1)$  on the test specimen
- Step 3. At displacement of step 2, measure actuator force  $p_r(i+1)$
- Step 4. Calculate acceleration  $\ddot{u}(i+1)$  and velocity  $\dot{u}(i+1)$  by simultaneously solving the two equations *a)*  $m[\ddot{u}(i+1)] + c[\dot{u}(i+1)] + p_r(i+1) = -m[\ddot{u}_g(i+1)]$  and *b)*  $\dot{u}(i+1) = \dot{u}(i) + 0.5[\ddot{u}(i) + \ddot{u}(i+1)]\Delta t$
- Step 5. Let  $u(i) = u(i+1)$ ,  $\dot{u}(i) = \dot{u}(i+1)$ , and  $\ddot{u}(i) = \ddot{u}(i+1)$  and repeat steps 1 to 5

A presentation of the underlying theory of PSD testing and numerical integration techniques is available elsewhere (e.g., Tsai et al. 2006). The loading protocol and selected ground motion accelerograms were presented in Section 8. Using the numerical integration algorithm described

above within the closed-loop framework, an incremental time step of 0.01 seconds was used to obtain the estimated response of the test specimen subjected to the GM load protocol. It is noted that after subjecting the test specimen to each GM record (including free vibration), the initial displacement, velocity and acceleration conditions (obtained in the last time step of calculation for the previously applied GM record) were reset to zero prior to PSD testing using the subsequent GM record. This was done to reflect the assumption that the prototype building would be at full rest conditions prior to the next seismic event. Note that although the initial conditions were reset to zero, all residual sensor measurements and any residual lateral frame drifts were preserved from the previously applied GM record for inclusion in the subsequent GM record.

## **9.6 Free Vibration Tests**

Prior to the start of the PSD earthquake simulations, a free vibration test was conducted to obtain initial dynamic properties. Of interest was determination of the approximate elastic fundamental period of the test specimen and the approximate total initial equivalent viscous damping in the system (i.e., test frame setup combined with inherent damping of the test frame). Additionally, after completion of the PSD and inelastic cyclic tests, the infill web plate panels were cut-out and removed, and free vibration tests were conducted on the remaining bare PT boundary frame to obtain period and damping information. For these bare frame tests, two conditions were investigated. The first free vibration test condition was conducted without any modifications to the lateral bracing test setup. Secondly, to investigate the effects of the lateral bracing system on the test specimen response (if any), the lateral bracing contact points on the test specimen were loosened just enough to allow the test specimen to essentially move freely between the lateral bracing frames.

Note that the free vibration test was simulated. An initial top level displacement was physically applied to the test specimen by the actuators and released in the numerical model followed by the PSD simulation of the free vibration response. Additionally no numerical damping was included in the equations of motion for determining the free vibration response. The purpose of the free vibration tests was to identify the approximate equivalent viscous damping present in the test specimen and setup. In other words, if the test setup were friction free and the damping

coefficient was set to zero in the equations of motion, there would be no motion decay of the test specimen during the PSD test and it would be in free vibration indefinitely. Observed decay in motion during the PSD free vibration test (when numerical damping is set to zero) is therefore attributed to friction in various parts of the test set-up, and can be quantified in the form of an equivalent viscous damping.

Free vibration response for the cases described above is shown in figure 9-7 and the corresponding calculated dynamic properties are summarized in figure 9-8, where  $U_0$  is the initial displacement imposed at the roof level of the test specimen. The free vibration tests are labeled as Elastic SPSW, BF and BF Released (BF-R), respectively, corresponding to the free vibration test prior to the start of the PSD earthquake simulations, the test on bare frame without any changes to the test setup, and the bare frame test allowing for essentially free movement between the lateral bracing frames (as described above and in Section 8.5). For the free vibration response, decay in the amplitude of motion and the time between successive peaks can respectively be used to calculate equivalent viscous damping and natural period of the system. These dynamic properties were calculated using the logarithmic decrement procedure using the peaks shown in the roof displacement response plot. Note that the free vibration responses shown in figure 9-7, which are the actual ones recorded during the tests, exhibit a vertical offset in the roof displacement time history. To calculate damping using the logarithmic decrement method, the plots were shifted vertically to remove the offsets.

Results in figure 9-7 show a noticeable difference in initial response of the Elastic SPSW and bare frame (i.e., BF and BF-R) free vibration tests. Namely, in the tests BF and BF-R after release of the initial displacement, it takes the test specimen a few cycles to find its steady state free vibration response; this is identified as the linear elastic portion of the base shear vs. roof displacement response. Without the presence of the stiffness of the infill web plate a whipping behavior is observed which is not readily present in the Elastic SPSW free vibration response. The exact reason for this initial whipping behavior could not be identified. Consequently, the peaks used to calculate dynamic properties using the logarithmic decrement procedure for the bare frame tests were based on the peaks measured after this whipping response was no longer present. Additionally for the Elastic SPSW test, it appears that, after approximately 6 seconds of

free vibrations, there is no further damping of response in the system. However, in fact, a damping ratio of approximately 0.4% can be calculated from the data in this region of decay, and it is noted that the amplitude of motion decay in this region is approximately 1 mm (i.e., essentially zero). One possible explanation for the near zero damping in this later stage of vibration might be that the response at such low amplitude only consisted of free slippage and play in the connections of the test setup, resulting in the actuator is simply displacing without truly engaging free vibration of the test specimen itself.

As indicated in figure 9-8, a damping ratio of approximately 4% was calculated to exist in the test setup (which includes inherent damping in the test specimen). This number falls within the range of 2% to 5% damping typically assumed for building structures. Consequently for the PSD tests, no additional numerical damping was provided (i.e., the damping coefficient in the equations of motions was set to zero). For the BF test, a decreased damping ratio of approximately 2% was calculated, which appears reasonable as one would expect a reduction in damping with the removal of the infill web plate. However for the BF-R test, after loosening the bearing points of the lateral bracing frames in contact with the test specimen, a damping ratio of approximately 4.6% was calculated; which actually is larger than the calculated damping ratio for the Elastic SPSW test. The reasoning for this is unclear and it appears to be incorrect as one would intuitively expect the damping ratio to be similar to or less than the previous test BF. One explanation is that the whipping effect mentioned above has had a corrupting influence on the data, leading to a calculated damping ratio that is not representative of the true steady state free vibration response of the test specimen.

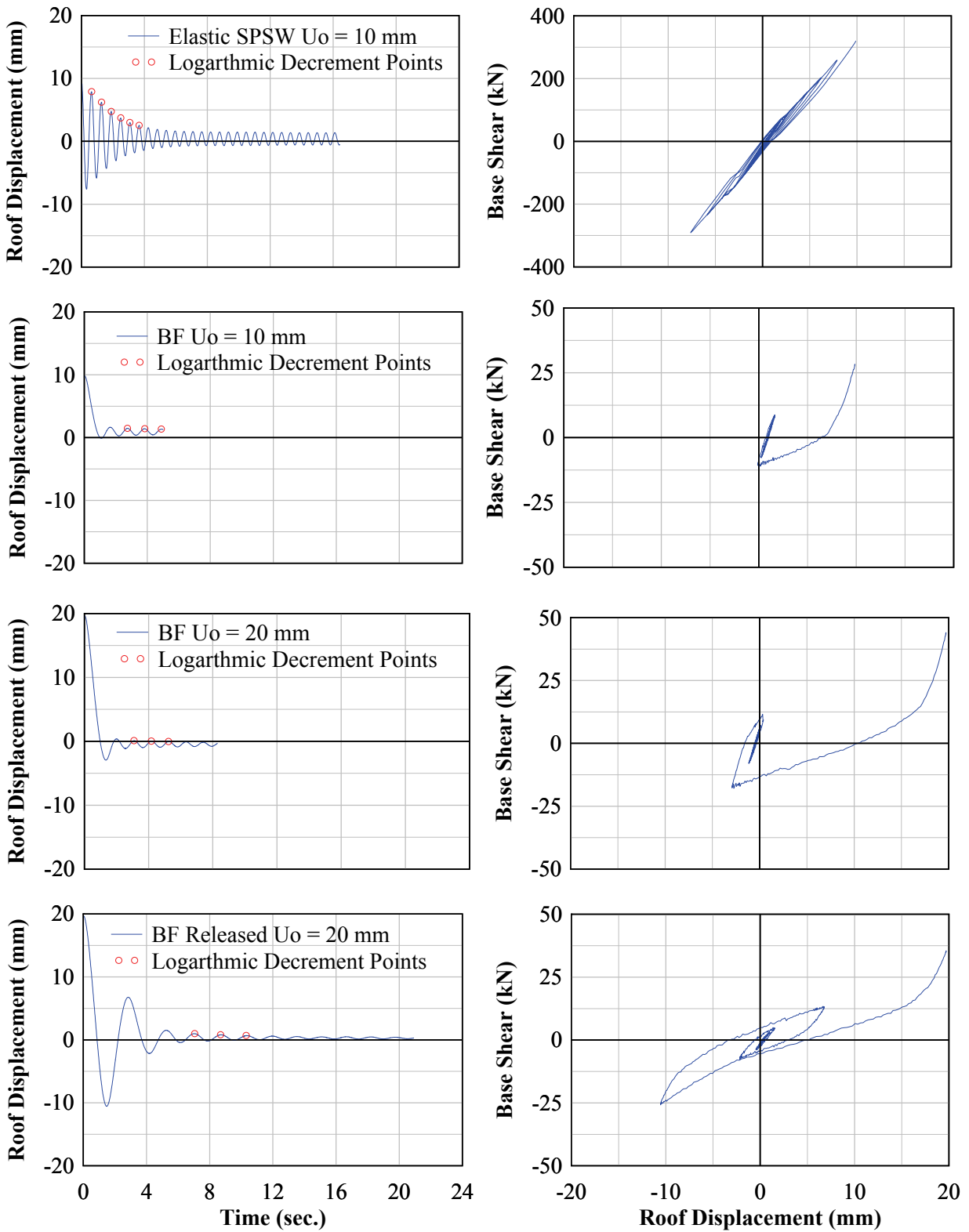
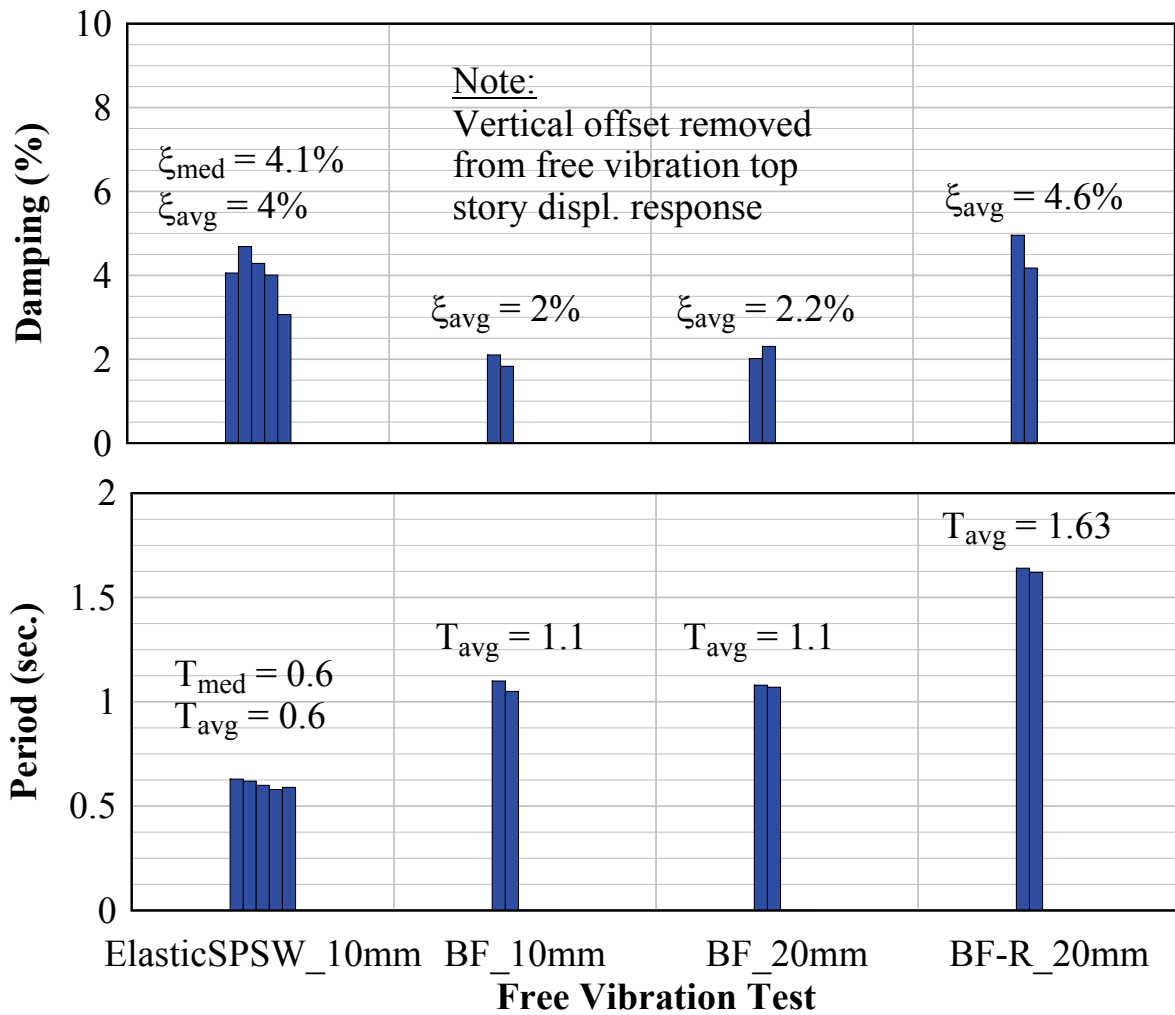


FIGURE 9-7 PSD Free vibration tests



**FIGURE 9-8 Test specimen dynamic properties**

The fundamental natural period of the Elastic SPSW, BF, and BF-R frames was calculated to be approximately 0.6, 1.1, and 1.6 seconds, respectively. The OpenSees analytical model developed to predict response prior to the tests gave a fundamental natural period of 0.53 and 1.73 seconds for the Elastic SC-SPSW and bare frame, respectively. The analytical value for the Elastic SC-SPSW period is within approximately 10 percent of the experimentally determined value, which is reasonable. For the bare frame tests, the period corresponding to test BF-R better matches the analytical prediction than test BF. Considering that the analytical model is free of influence from lateral supports (i.e., restraining effects, if any, of the lateral bracing system are not included in the analytical model), the BF-R period of 1.6 seconds is more reasonable to compare with the

OpenSees analytical prediction than the BF period (which should have more restraint from the lateral bracing system and thus be stiffer as reflected by the smaller period obtained in the free vibration tests).

## **9.7 Experimental Observations**

Periodic pauses during the PSD tests were taken to survey the test specimen. Given the full scale size of the test specimen, visual observations was made by a team of UB, UW and NTU graduate students working together in addition to NCREE staff. In total, 10 persons made observations collectively during each “hold points” such as to collect visual observation data in an efficient and timely manner.

Note that such experimental observations for the bare frame tests are not reported, because they were minimal given that the primary purpose of those tests was to collect global response data on the PT boundary frame response, which was expected to be entirely elastic. However, observations were made on separation of the HBE flange to VBE flange as it occurred, and will be described later. Also note that all the displacement transducers located on the flanges of the boundary frame (used to calculate relative joint rotations) and the diagonal displacement transducers (used to record infill web plate axial deformations) were removed during the process of cutting-out the infill web panels as to not damage them; and were not re-installed for reasons noted earlier.

### **9.7.1 Experimental Observations – PSD Tests**

The concatenated record of all ground motions used in the PSD tests (including the pauses in excitation to allow for free vibration of the specimen after each test) is plotted in figure 9-9. The resulting roof drift response is shown in figure 9-10, with observation hold points as noted. The nomenclature convention used to label the hold points consists of a first part that identifies the seismic hazard (identifying the GM), a second part indicating whether the hold point occurred during a positive (P) or negative (N) drift, or at a point of residual drift (R), followed by a number ordering all the hold points in sequence within their group. For example, “10/50N2” corresponds to the second negative drift hold point during the 10/50 seismic hazard GM. Table 9-1 provides a summary of key observations common to all observation hold points, in terms of

infill plate tearing, boundary element yielding, and HBE-to-VBE gap openings. Other observations specific to particular hold points are presented in the rest of this section. Note that the following acronyms are used for this purpose: TB = top HBE, MB = middle HBE, and BB = bottom HBE are used.

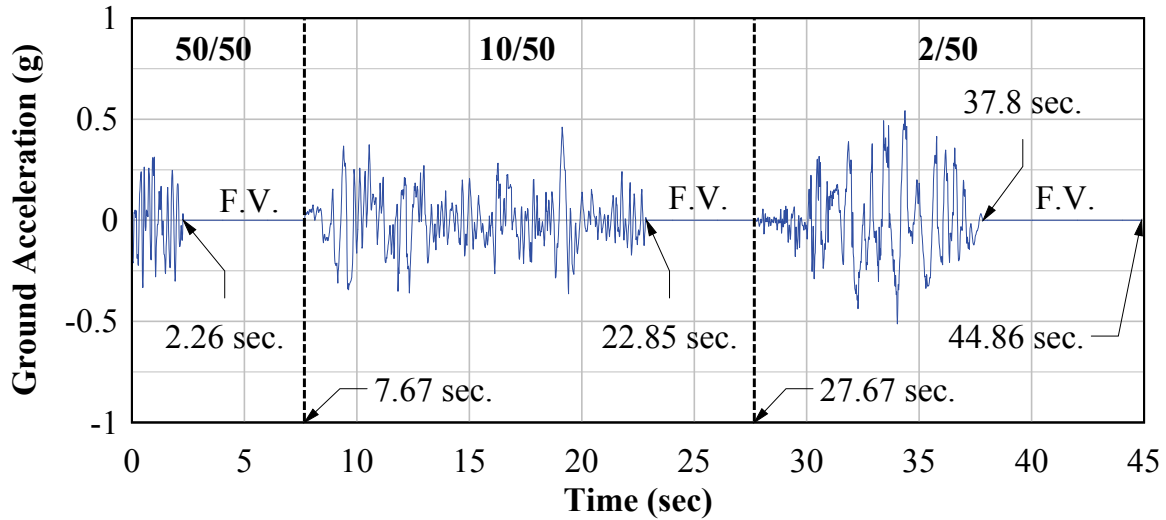


**FIGURE 9-9 PSD ground motion loading protocol**

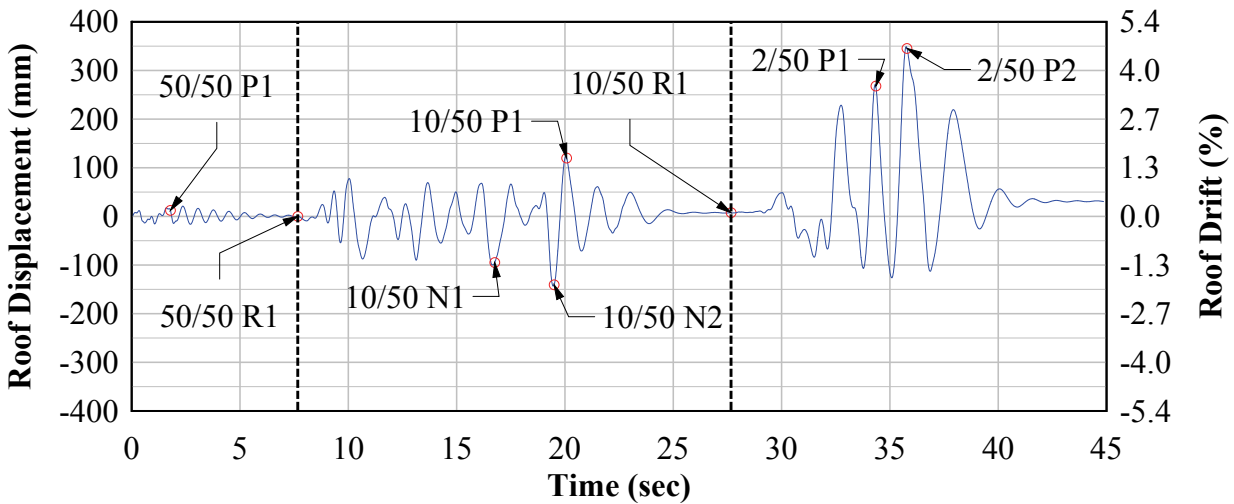


**FIGURE 9-10 PSD roof drift observation hold points**



**TABLE 9-1 NCREE test observations**

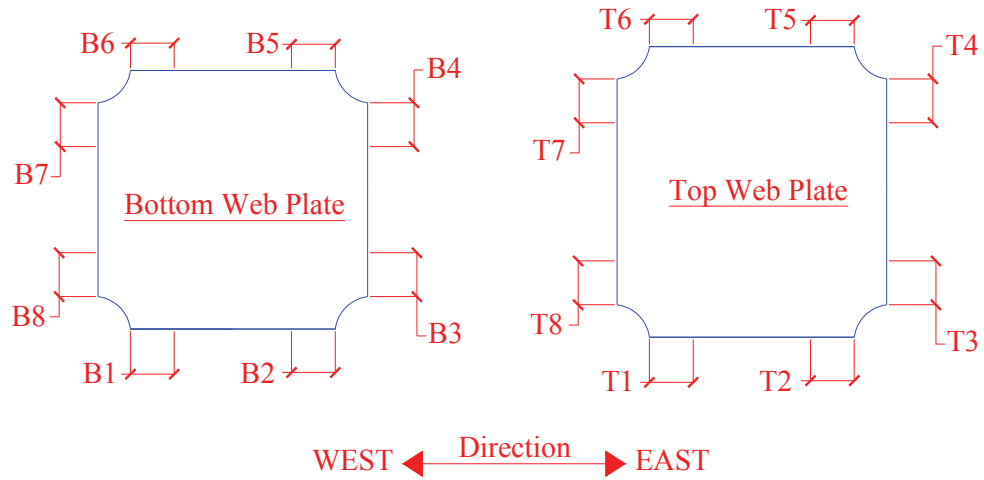
Test Hold Point	<sup>1</sup> Time (sec)	Infill Plate Tearing			Boundary Element Yielding				<sup>2</sup> HBE-toVBE Gap		
		No	Yes	<sup>3</sup> Ref.	No	Mild	Moderate	<sup>3</sup> Ref.	No	Yes	<sup>3</sup> Ref.
50/50P1	1.79	✓			✓				✓		
50/50R1	7.67	✓			✓				✓		
10/50N1	16.76		✓	Fig. 9.11	✓				✓		
10/50N2	19.5		✓	Fig. 9.11		✓		Sec. 9.7.1		✓	Fig. 9.13
10/50P1	20.08		✓	Fig. 9.11		✓		Sec. 9.7.1			
10/50R1	27.67		✓	Fig. 9.11		✓		Sec. 9.7.1			
2/50P1	34.35		✓	Fig. 9.11		✓		Sec. 9.7.1		✓	Fig. 9.13
2/50P2	35.79		✓	Fig. 9.11		✓		Sec. 9.7.1		✓	Fig. 9.13
-2.5% Drift	-		✓	Fig. 9.12							
-3.0% Drift	-		✓	Fig. 9.12		✓		Sec. 9.7.2		✓	Fig. 9.13
-3.5% Drift	-		✓	Fig. 9.12		✓		Sec. 9.7.2		✓	Fig. 9.13
-4.0% Drift	-		✓	Fig. 9.12		✓		Sec. 9.7.2		✓	Fig. 9.13
-4.5% Drift	-		✓	Fig. 9.12		✓		Sec. 9.7.2		✓	Fig. 9.13

<sup>1</sup>Total cumulative time from start of 50/50 test

<sup>2</sup>HBE-to-VBE flange separation occurrence

<sup>3</sup>Reference figure or chapter section for detailed information

NOTE: only key observations are provided in table, for additional observations see Section 9.7



Web Plate Tearing Legend

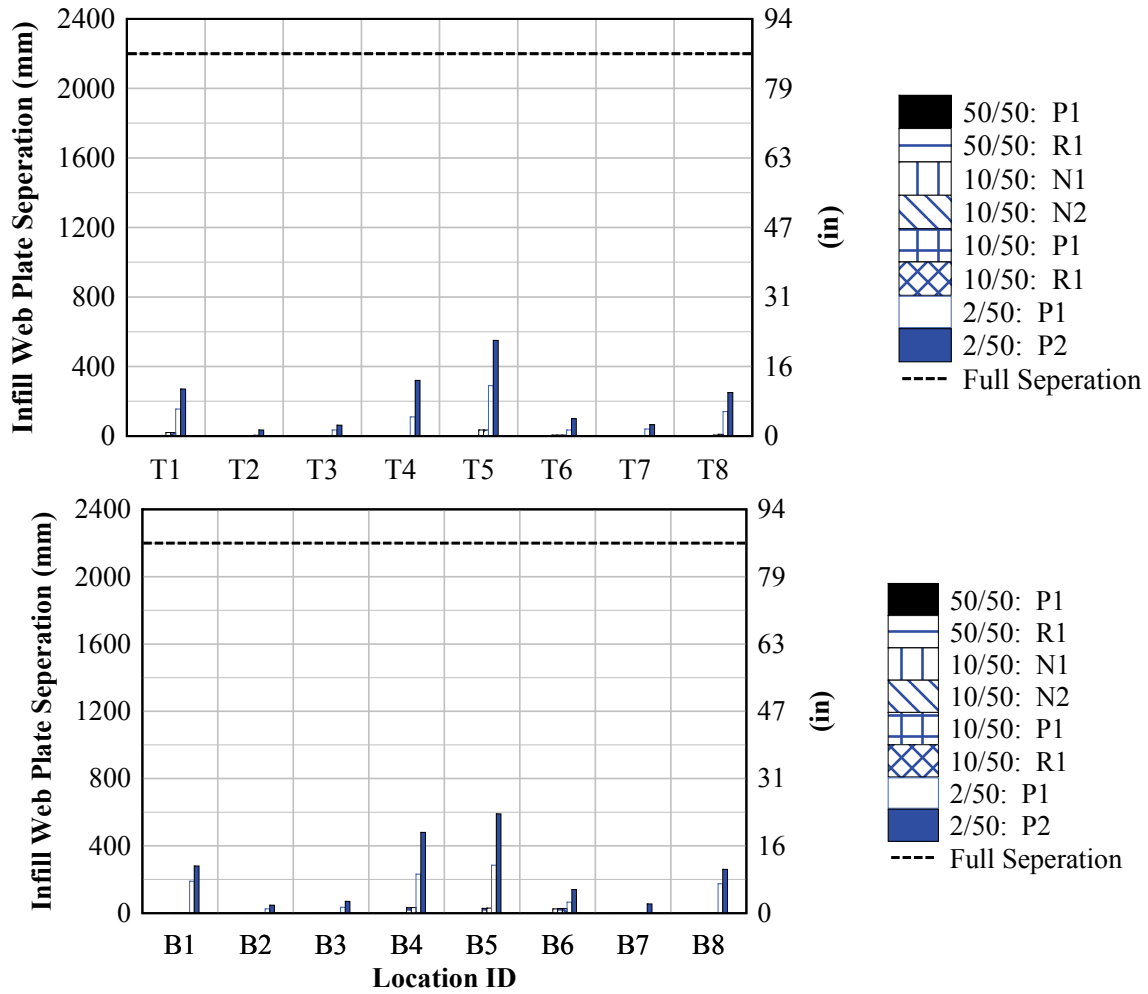
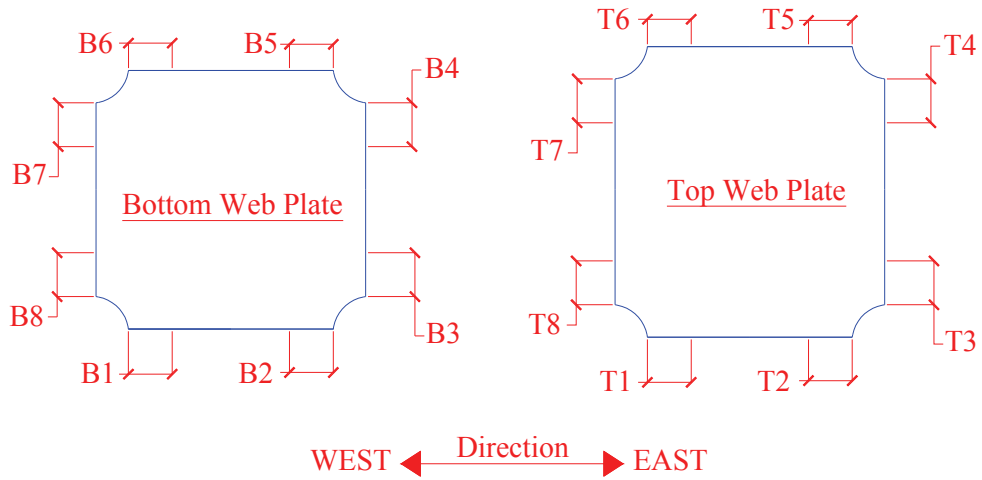


**FIGURE 9-11 Infill web plate tearing – PSD tests**



Web Plate Tearing Legend

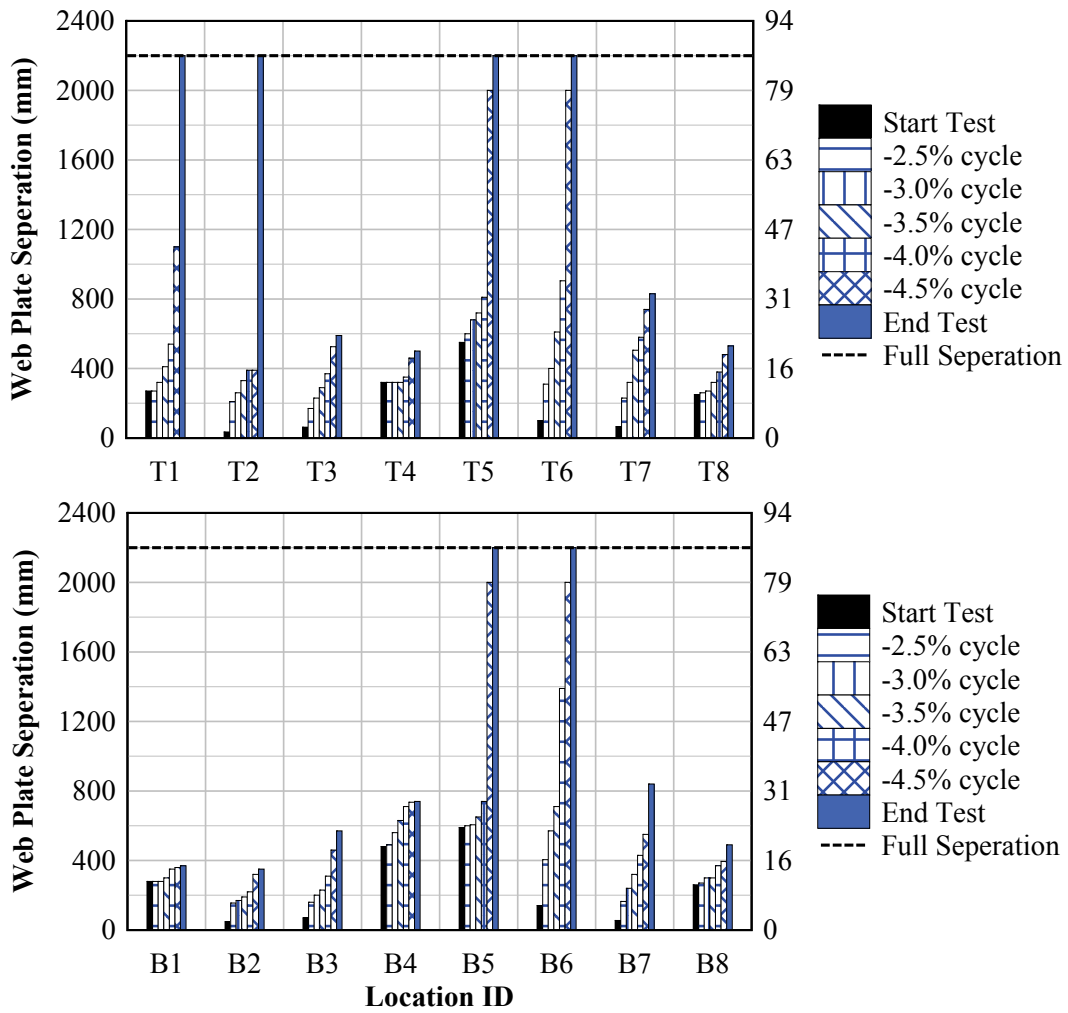


**FIGURE 9-12 Infill web plate – inelastic cyclic tests**

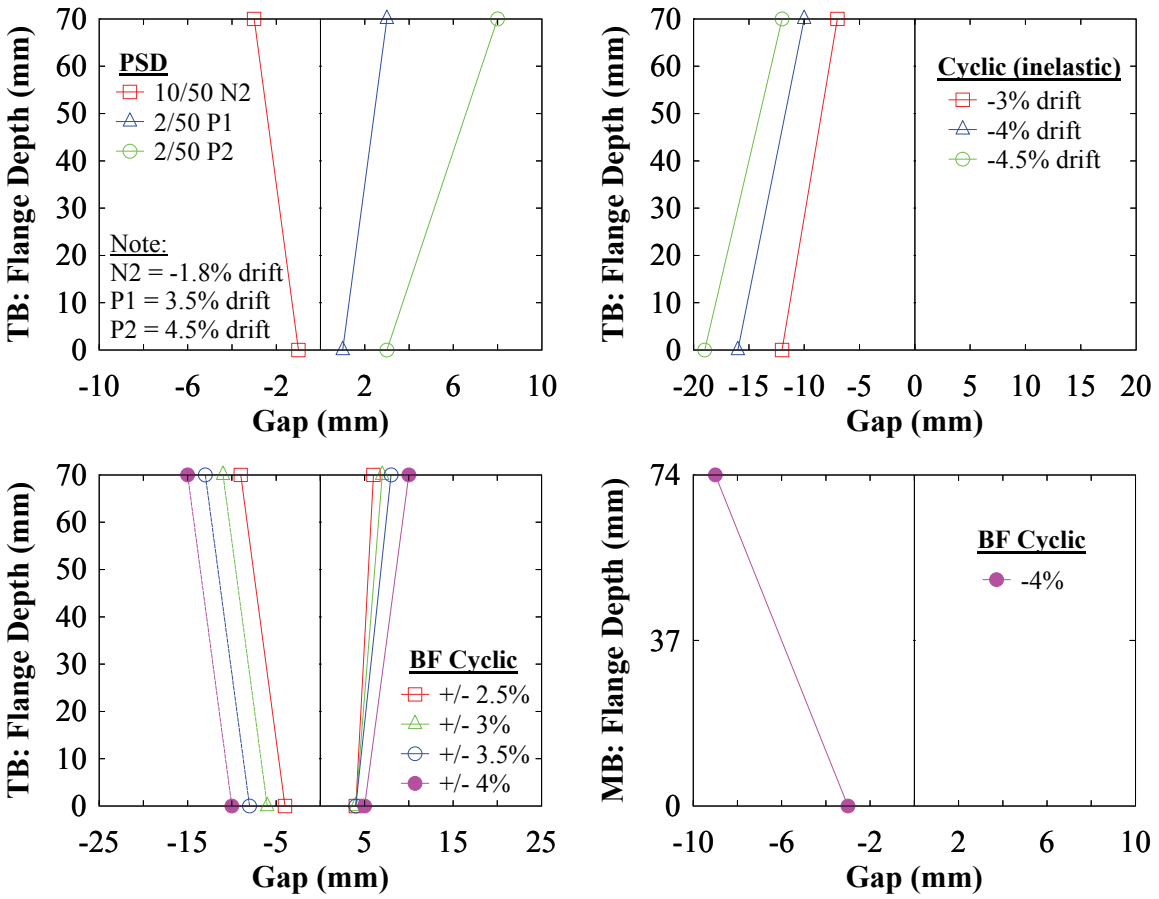


**FIGURE 9-13 HBE-to-VBE flange separation**

**50/50P1:** The boundary frame remained elastic. There were approximately 3 web buckles visible at Level 1 infill web plate and approximately 2 buckles visible at Level 2 infill web plate. These web plate buckles appeared to be elastic buckling.

**50/50R1:** At the end of the 50/50 GM test, it was observed that the boundary frame remained elastic. There was some minor buckling visible at the Levels 1 and 2 infill web plates; but less so at Level 2. Although some residual infill web plate buckling was present, it was minor and the web plate essentially remained elastic. Some minor flaking in the white wash paint at Level 1 infill web plate was also observed as an indication of buckling (i.e., elastic buckling) of the infill plate. Additionally the TB bolts at the shear plate connection were essentially aligned vertically, indicating that the frame returned back to its original position prior to the GM loading.

The MB bolts on the West end were essentially aligned vertically; however on the East end, the bolts were observed to be aligned at a slight angle.

**10/50N1:** At this observation hold point, approximately 7 inelastic buckles and 6 inelastic buckles were observed at the Levels 1 and 2 infill web plates. Additionally, there was minor white wash flaking present at the radius corner locations of the infill web plates at the top corners of Levels 1 and 2 infill web plates, and approximately 1 mm long tears at the B1, B2, B3 and B8 locations shown on figure 9-11 (note that the tears are not visible on figure 9-11 since they were so small). There was also presence of minor yield lines at the top flange South side of the TB at the PT anchorage locations.

**10/50N2:** At this observation hold point, approximately 8 and 7 inelastic buckles were present at the Levels 1 and 2 infill web plates respectively. The presence of minor yield lines were observed at: 1) The top flange South side of the TB at the PT anchorage locations; 2) The top flange North side of the TB at the East PT anchorage location; 3) The TB North side web at the West end PT anchorage location; 4) The West and East VBE webs near the toe of the radius of the web and flanges, on the inside flange location; and 5) The top of the double-angle shear connection at the West and East ends of the BB (which pulled-out from the VBE, by approximately 4 mm). It was also observed that the PT strands on the MB West end were fully relaxed (i.e., no PT force). Note that at this PT location on the North elevation side, a steel shim was added between the load cell and the bottom support angle rail; since the PT was at full slack, the centerline of the PT load cell was shifting from the centerline of the PT strand bundle.

**10/50P1:** It was observed that the East end PT strands at the TB and MB were in tension and not fully relaxed. Additional minor yielding occurred at the TB PT anchor locations on the webs and top flange locations. At the VBE base rocking connection, a vertical gap opening at the base of the West VBE (i.e., lifting of the West flange) was measured to be approximately 4 mm.

**10/50R1:** At the end of the 10/50 GM test, additive to the previous observations, minor yielding at the top of the fish plate located on the East VBE at Level 1 was observed. Additionally a residual deformation of approximately 1 mm pull-out from the face of the VBE flange was measured at the BB double-angle shear connections.

**2/50P1:** At this observation hold point, at the VBE base rocking connection, a vertical gap opening (i.e., lifting of the West VBE flanges) at the base of the West VBE and base of the East VBE was measured to be approximately 20 mm and 10 mm respectively. Additionally, the East end PT strands on the MB and TB were fully relaxed and the PT anchor plates located on the HBE webs had twisted. This rotation of the PT anchor plate was first observed at the 10/50N2 observation hold point noted above, but was not as noticeable.

Twisting of the PT anchorage (see figure 9-14) likely occurred because when the PT strands became fully relaxed, they were not free to slide in compression, and was stiff enough to elastically buckle laterally. Guiding plates and angles (see figure 9-14) had been installed to prevent the load cell from falling off from the anchor plates in that fully relaxed position and to guide the system back into place upon re-tensioning (i.e., when initial PT forces were regained as the closing gap re-opens) of the PT strands as the SC-SPSW cycled back. These guiding plates and angles were unable to resist the unexpected forces resulting from the strand buckling and produced twisting of the anchor plate at the load cells in the process. However, this twisting did not seem to affect the response of the test specimen.

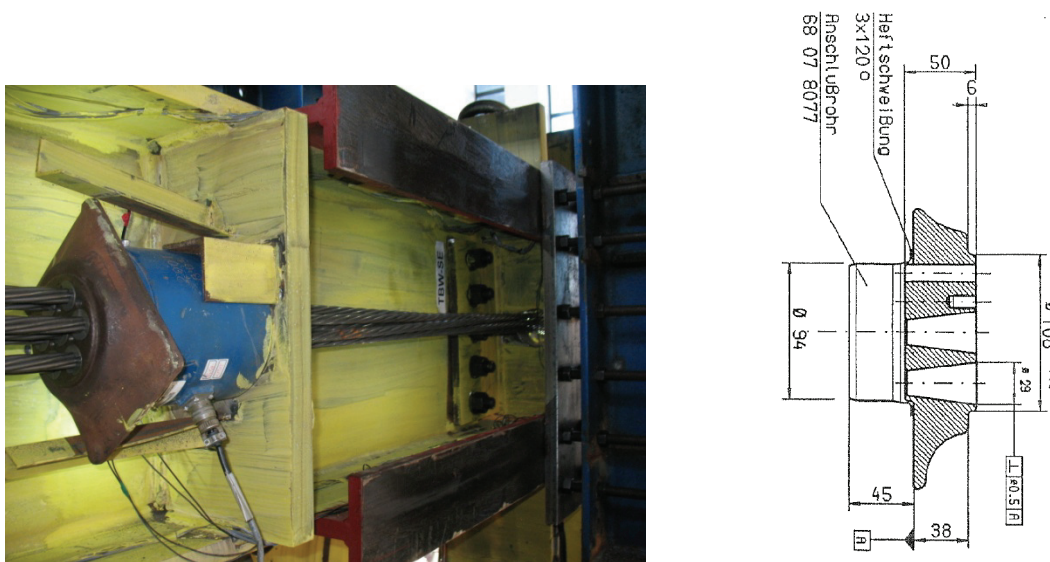


**FIGURE 9-14 PT anchorage plate: observed twisting and detail (DSI Int.)**

**2/50P2:** At this observation hold point, the East end PT strands on the MB and TB were fully relaxed and the corresponding PT anchor plates on the HBE were twisting (for reasons noted above). Additionally, the displacement transducer DT25 (provided to measure infill web plate deformations) was removed as the infill web plate was touching it due to infill web plate buckling. It was also observed that the bolt washers at the HBE shear plate connections were scraping against the HBE webs due to the relative movement of the HBE-to-VBE joint from gap opening and closing. At the VBE base location, the vertical gap opening (i.e., lifting of the West VBE flanges) at the West and East VBE was measured to be approximately 22 mm and 13 mm respectively. Additional minor yield lines were observed at the top flanges and web of the TB near the PT anchorage locations. Finally, the top of the double-angle shear connection at the West end of the BB pulled-out from the VBE by approximately 10mm and the bottom of the double-angle shear connection at the East end of the BB pulled-out from the VBE by approximately 3 mm.

Photos of typical notable observations for the 2/50 GM test are shown in figure 9-15a. In particular the HBE-to-VBE flange separation is shown at the top HBE along with photos of minor local yielding at the PT HBE anchor locations as noted above. Additionally some inelastic deformation (i.e., rounding at the edges) at the HBE flange bearing can be observed in photo (b) in that figure.

### **9.7.2 Experimental Observations – Inelastic Cyclic Tests**

**-2.5% Drift:** Observations are all as noted in table 9-1.

**-3.0% Drift:** It was observed that the PT strands at the West end of MB were fully relaxed and the PT anchor plate on the South elevation rotated approximately 60 degrees. At the VBE base location, a vertical gap opening (i.e., lifting of the East VBE flanges) of approximately 15 mm and 17 mm was measured at the base of the West and East VBE respectively. Additionally, at the double-angle shear plate connections of the BB, approximately 5 mm pull-out at the top and approximately 10 mm pull-out at the bottom from the VBE flange was measured at the West and East end respectively.

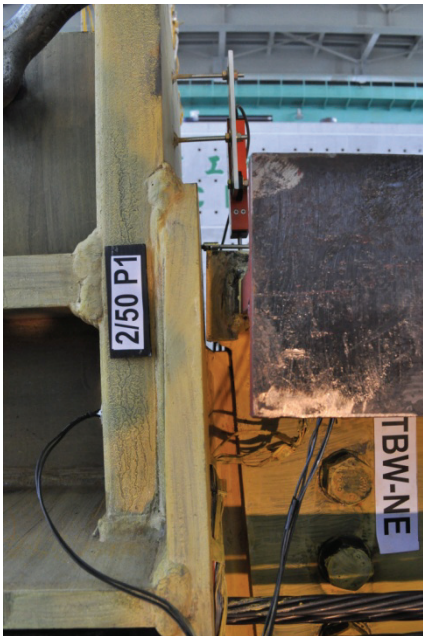
**-3.5% Drift:** Observations are all as noted in table 9-1.

**-4.0% Drift:** At the double-angle shear plate connections of the BB approximately 6 mm pull-out at the top and approximately 12 mm pull-out at the bottom from the VBE flange was measured at the West and East end respectively.

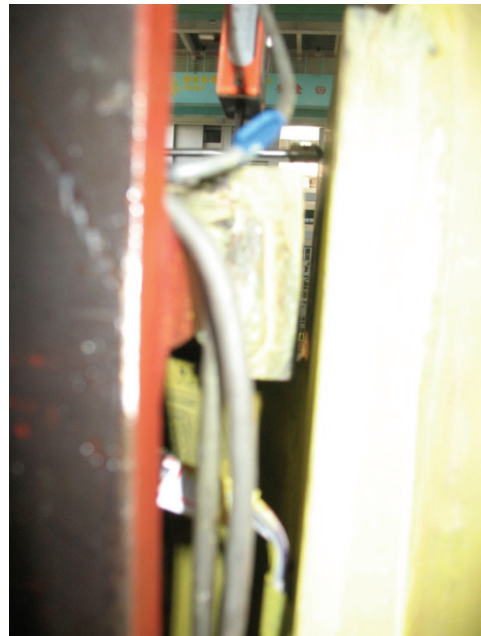
**-4.5% Drift:** The PT strands at West end of MB were fully relaxed. Some additional minor yield lines on the TB web on the South elevation at the East PT anchor location were observed. The displacement transducer DT19 (provided to measure infill web plate deformations) was removed as infill web plate was almost in contact due to infill web plate buckling deformation. Finally at the VBE base location, a vertical gap opening (i.e., lifting of the East VBE flanges) of the base of the West VBE and base of the East VBE was measured to be approximately 16 mm and 20 mm respectively.

Photos of typical notable observations at the conclusion of the inelastic cyclic test are shown in figure 9-15b. Photo (a) shows some residual deformation (i.e., due to rounding at the edges) at the HBE top flange due to rocking by observation of the noticeable gap between the HBE-to-VBE flange contact points. Photo (b) is a typical infill web plate tearing condition from the boundary frame. Photo (c) shows that the HBE shear plate bolts were scraping against the shear plate to accommodate gap rotation. It is also noted that the scraping progressively increases in intensity from the top of the HBE flange to the bottom most bolt; which is representative of rotation from the top flange only with gap opening/closing demand at the bottom flange of the HBE. Photo (d) shows the residual deformation to accommodate joint rotation at the BB double-angle shear connections.





(a) HBE Flange Separation



(b) HBE Flange Separation



(c) Local Yielding HBE Flange



(d) Local Yielding HBE Web

**FIGURE 9-15a 2/50 GM select test photos**



(a) Typ. Flange Bearing Deformation



(b) Typ. Infill Web Plate Tearing



(c) Typ. HBE Shear Plate



(d) Typ. Double Angle Yielding

**FIGURE 9-15b End of test select photos**

## **9.8 PSD Experimental Results**

The PSD experimental results are presented in this section. However, where appropriate, selected experimental results of the inelastic cyclic tests (presented in full in Section 9.9) are included for comparison to help illuminate response behavior that may not be readily apparent by observation of the PSD response alone.

### **9.8.1 PSD Global Response**

The design objectives for the global response of the test specimens, presented in Section 8, were based on meeting certain target performance objectives (POs). The global response of the test specimens can be expressed in terms of base shear vs. roof drift, and roof drift vs. time, shown in the plots of figure 9-16. Note that in the roof drift history plots, provided for convenience, the end of the GM record (also corresponding to the start of free vibration) is identified by a vertical dashed line. Additionally, the threshold for full recentering ( $\pm 0.2\%$  drift) is identified by the horizontal dashed lines at the end of each PSD test.

From observation of the global response plots, for the 50/50 GM, the test specimen remained essentially elastic, with minor infill web plate yielding indicated by the formation of minor hysteresis loops. The maximum base shear was approximately 600 kN (135 kips) and the maximum roof drift approximately 0.3%. For the 10/50 GM, the maximum base shear was approximately 1200 kN (270 kips) and the maximum roof drift approximately 2%. From observation of the residual drift at the end of the PSD 10/50 GM test, recentering was achieved. For the 2/50 GM, the maximum base shear was approximately 1300 kN (290 kips) and the maximum roof drift approximately 4.7%. At the end of the PSD 2/50 GM test, the residual drift was approximately 0.4% indicating that full recentering was not achieved (but it was not a target PO for this seismic hazard). However, note that a residual drift of 0.4% in comparison to the 0.2% recentering threshold is not significantly far off and would be sufficient to meet the PO for collapse prevention at the MCE seismic hazard. From these experimental results, it is observed that all design objectives were achieved.

Additionally, it is observed from the 10/50 and 2/50 GM hysteresis response, similarly to what was observed in the UB tests for a infill web plate configuration, that some compression strength

is present in the infill web plate by evidenced by the fact that there are drift excursions at which the base shear is not zero at the zero drift location. However, as was also observed in the UB shake-table tests, the compression stiffness of the infill web plates does not appear to have a significant influence on frame recentering for dynamic loadings. This is believe to be a consequence of the many smaller cycles of excitations that follow the larger cycles during which the compression strut effect of the infill web plate occurs; these smaller cycles occur in absence of the compression strut, which facilitates recentering of the frame. Additionally, for the 2/50 GM, it is observed that the hysteresis response is not symmetrical and is drift dominated in the positive direction. Although this is not something unusual (as the displacement history of the ground motion is not necessarily symmetric), this was also observed in the preliminary analytical results presented in Section 8.

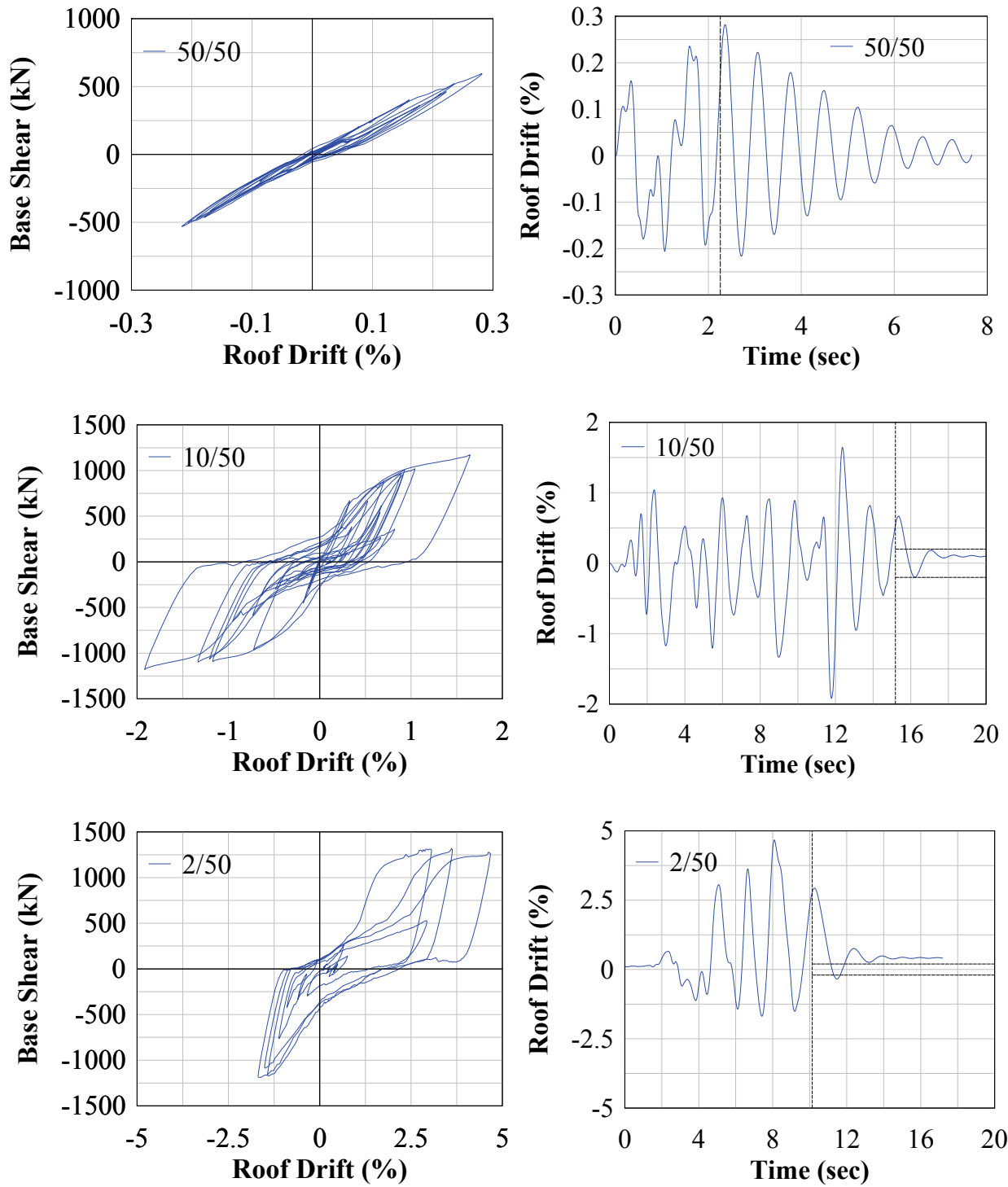


FIGURE 9-16 PSD global response

## **9.8.2 PSD Local Response**

Local response of the test specimen can provide valuable insights on the behavior of SC-SPSW that can be used to inform design at the component level of an SC-SPSW system. Information recorded by the instrumentation is used here to present response histories on PT forces, relative joint rotations, interstory deformations, and strain demands on the boundary frame. Note that in the information presented below, a positive drift corresponds to a frame sway in an Eastward direction (i.e., actuator pushing the specimen away from the strong wall) and a negative drift corresponds to a frame sway in the Westward direction (i.e., actuator pulling the specimen towards the strong wall).

### **9.8.2.1 Boundary Frame Post-Tension Response**

The HBE PT force and HBE end gap rotation response is shown in figure 9-17. It is observed that the response at the top and middle HBEs is similar, as it should be, since the test specimen is loaded by only one actuator at the top level HBE. In the positive drift direction, the PT at the closing joint (East end) reduces and eventually becomes fully relaxed as the frame drift increases. For the particular test specimen under investigation, this occurred at approximately 2.6% interstory drift. However, in the negative drift direction, the response of the PT at the closing joint (West end) did not match the typically expected response of NewZ-BREAKSS connection. The reason for this discrepancy is an artifact of the loading test setup used. The actuators are attached and load the test specimen by pushing and pulling the top of the West VBE. As a result, in the negative drift direction, the actuators effectively load the frame by pulling on the HBE PT strands. In practice, the PT response in the negative drift direction would be similar to that in the positive drift direction as the loading of the SC-SPSW would be provided by the floor/roof diaphragm to the HBEs directly (as was done in the UB tests).

It is also observed that the loading and unloading of the PT force is nonlinear even though the PT strands themselves are elastic. This is due to the effects of the infill web plates. For example, in the positive drift direction upon unloading at the end of the drift excursion, there is a small transition where the PT force remains relatively constant. At that point, the infill web plate is providing some lateral stiffness due to the compression stiffening of the temporary deformed “corrugated plate” shape of the infill web plate. Once this is compression strut effect is

overcome by infill web plate buckling, the PT force then unloads in accordance with the kinematics of the HBE-to-VBE joint. As such, the HBE PT response indicates that the boundary frame HBE-to-VBE joint connections do not open and close freely, and that partial restraint is sometimes provided by the presence of the infill web plate. Additionally, it is observed that the corresponding HBE gap rotation vs. interstory drift plots also exhibit nonlinear response. Similar to the PT force response just described, this effect is due to the infill web plate. Finally, note that when the HBE PT force at the closing joint becomes fully relaxed, it does not significantly affect the recentering response of the SC-SPSW system.

The VBE PT force and VBE base gap rotation response is shown in figure 9-18. The rocking connection at the base of the VBES is a flange rocking configuration with kinematics comparable to that of a typical HBE-to-VBE flange rocking joint (presented in Section 3). In this configuration the bottom of the VBE and VBE base pedestal in the current detail are respectively analogous to the HBE and VBE in the typical flange rocking detail. As expected, based on the HBE PT response presented above, the VBE PT response is also nonlinear in a manner that can be attributed due to the presence of the infill web plate. However, the VBE PT response is peculiar in that there is a notable lateral shift between the West and East VBE response curves (i.e., they do not lay directly on top of each other). This is due to the influence of the frame overturning moment on VBE axial forces. For example, it is observed that for a positive drift, the PT force in the West VBE increases almost immediately as would be expected, but the PT force in the East VBE decreases before it increases. For this positive drift condition, the East VBE is in compression due to overturning. Consequently, this compression force must be overcome before the gap opening at the base of the East VBE can form, resulting in the observed response.

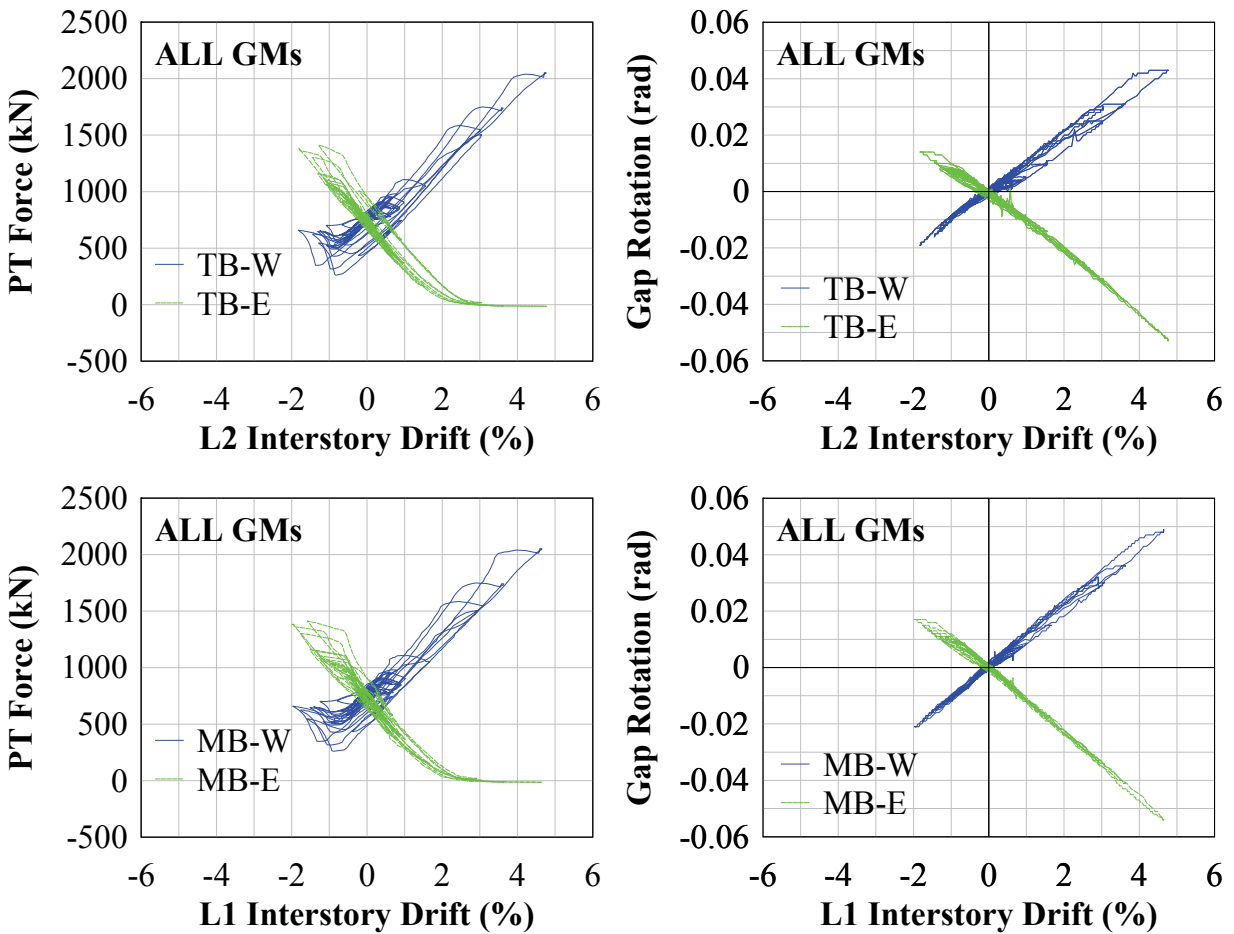


FIGURE 9-17 HBE PT force versus interstory drift and gap rotation versus interstory drift

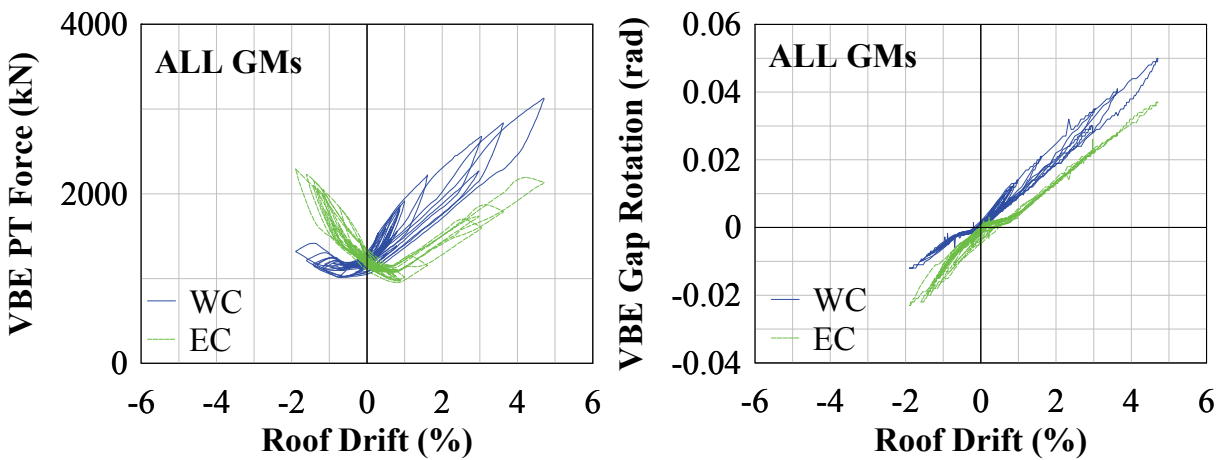
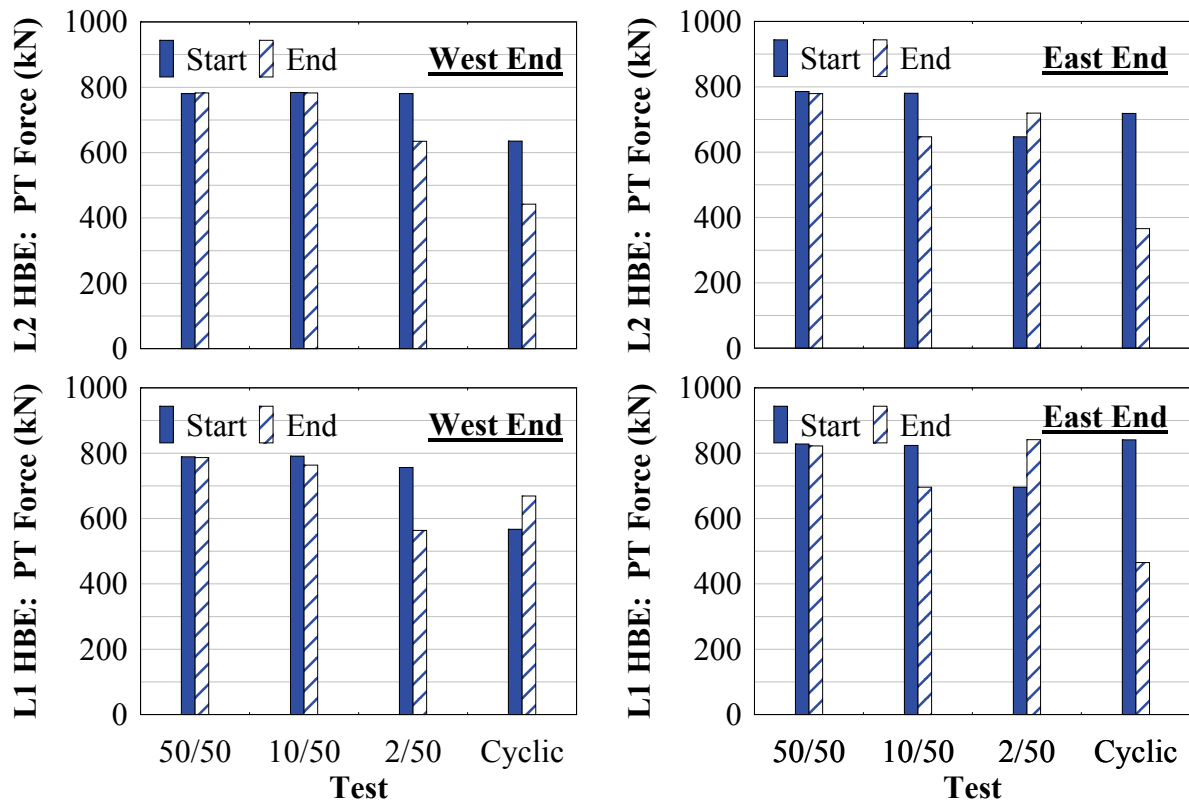


FIGURE 9-18 VBE PT force versus roof drift and gap rotation versus interstory drift



PT force losses due to anchor wedge seating and strand relaxation were observed during subsequent tests. Figure 9-19 shows the HBE PT force at the start and end of each test. For the PT located at the West end of the HBEs, it is observed that for the 50/50 and 10/50 GM tests no noticeable loss of PT was observed. For the 2/50 GM, a reduction of PT force of approximately 20-25% was observed. For the inelastic cyclic test, a further reduction of approximately 30% was observed at the top HBE. At the middle HBE, the PT force actually increased approximately 18% from the start of the cyclic tests. This increase is due to the twisting of the PT strands that was observed; which had a residual turn-buckle tensioning effect on the PT strands. Of particular interest, from the start of the 50/50 to the end of the 2/50 PSD tests, a cumulative loss of approximately 20-30% was observed. For comparison, from the start of the 50/50 to the end of the inelastic cyclic test a cumulative loss of approximately 55% was observed at the top HBE and approximately 15% at the middle HBE. However, at the middle HBE this included the tensioning effect due to PT strand twisting which did not occur at the top HBE (i.e., the loss of the middle HBE PT force would have likely been similar to the top HBE if the twisting of the strands had been avoided).



**FIGURE 9-19 HBE initial PT force history**

For the HBE PT located at the East end of the HBEs, no noticeable loss effects were observed for the 50/50; however, a loss of approximately 15-20% was observed after the 10/50 GM test. Recall that the East end PT did become fully relaxed at large drift levels during the 10/50 GM test. By contrast, the HBE West end PT always remained in tension due to the actuator pulling on the West VBE in the negative drift direction for the 10/50 GM loading condition. Additionally the twisting effect observed on the East end was more prominent which generated larger PT tension forces (as a result of a turn-buckle tensioning effect) leading to larger PT force losses due to PT relaxation and anchor wedge seating. Consequently, it appears to be for these reasons that a loss in PT force was observed at the East end but not at the West end location for the 10/50 GM test. For the 2/50 GM test an increase of approximately 10-20% was observed due to the twisting-tensioning effects of the PT strands noted above. For the inelastic cyclic test, a reduction of approximately 50-55% loss was observed. Of particular interest, from the start of the 50/50 to the end of the 2/50 PSD tests, a cumulative loss of approximately 5-10% was observed; however this included the strand twisting-tensioning effect during the 2/50 GM test. For comparison, from the start of the 50/50 to the end of the inelastic test, a cumulative loss of approximately 45-55% was observed. Note that in hindsight, much of the observed PT losses can be avoided in future applications by using alternate details that would eliminate the above problems.

PT force losses at the VBEs are shown in figure 9-20. The cumulative PT force loss from the start of the 50/50 GM test to the end of the inelastic cyclic test is approximately 5-10%; which is insignificant compared to the HBE losses. Some reasons that could contribute to the differences are that for the VBEs: 1) rods were used versus strands, although strands are better suited for HBEs as they behave more like tension-only members than rods which have to buckle elastically when in compression; 2) the PT rods are anchored with threaded nuts versus HBE monostrands which rely on anchor wedges which contribute to some PT loss effects in monostrands, and; 3) rods are less susceptible to PT force loss due to relaxation compared to monostrands as rods consist of a single cross-sectional area whereas monostrands are made up of individual steel wires bundled together to form a single monostrand.

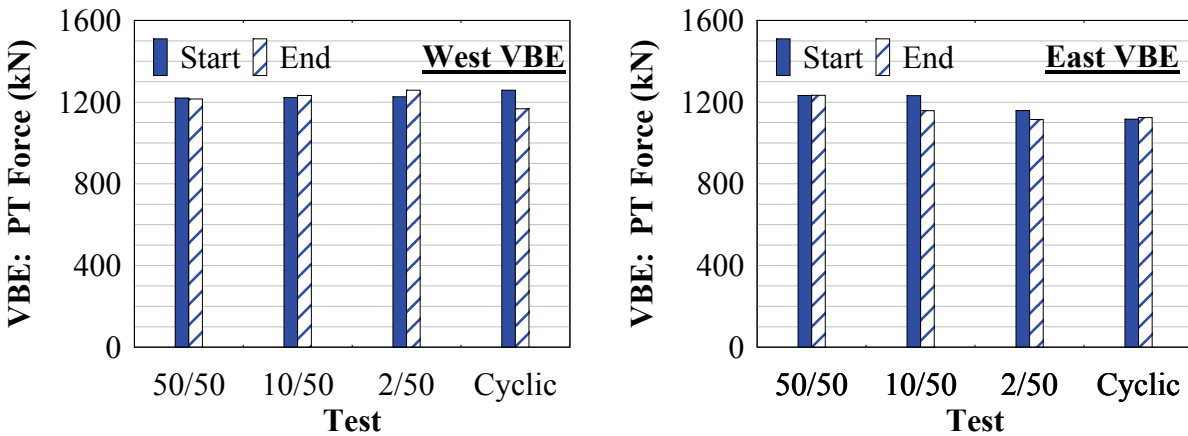


**FIGURE 9-20 VBE initial PT force history**

### 9.8.2.2 Boundary Frame Strain Gage Response

The strain gages were installed prior to the installation of the boundary frame PT elements. Consequently, at the start of the PSD tests, there were some initial strain readings as a result of the HBE and VBE initial PT forces. Additionally, it was determined that there were also initial strain readings present that were not credible (maybe due to corrupting electrical noise and/or calibration error, to name a few). To minimize the influence of these “ghost” strains, the strain readings presented here are relative strains, obtained by subtracting out the initial strain reading at the start of each test. Thus, the resulting quantities calculated using the relative strains (i.e.,  $\Delta\varepsilon$ ) are those due to change in strain effects during the PSD loading and are not the actual total values.

#### 9.8.2.2.1 Boundary Frame Strain Gage Response - VBEs

The strain versus VBE base gap rotation at the bottom, middle and top locations along the height of West VBE at the ground level are shown in figure 9-21. Recall that the base of the VBE is a flange rocking connection. Accordingly, for an Eastward drift the base of the VBE rocks about the East flange (with corresponding lifting of the West flange due to formation of a vertical gap opening), and vice versa for a Westward drift. At the VBE bottom location, it is observed that the strain on the lifting flange is approximately zero as indicated by the flat line portion of the strain response (with results reflecting this behavior dependent on the drift direction). This is logical since there are no external forces at the boundary surface at the lifting flange location.

Note that for the East flange strain gage, the flat line portion indicating zero strain should be located near zero (similar to what is observed by the West flange strain gage); the offset observed in the plot reflects the fact (described in previous section) that the real strain values on the East flange are offset by that amount.

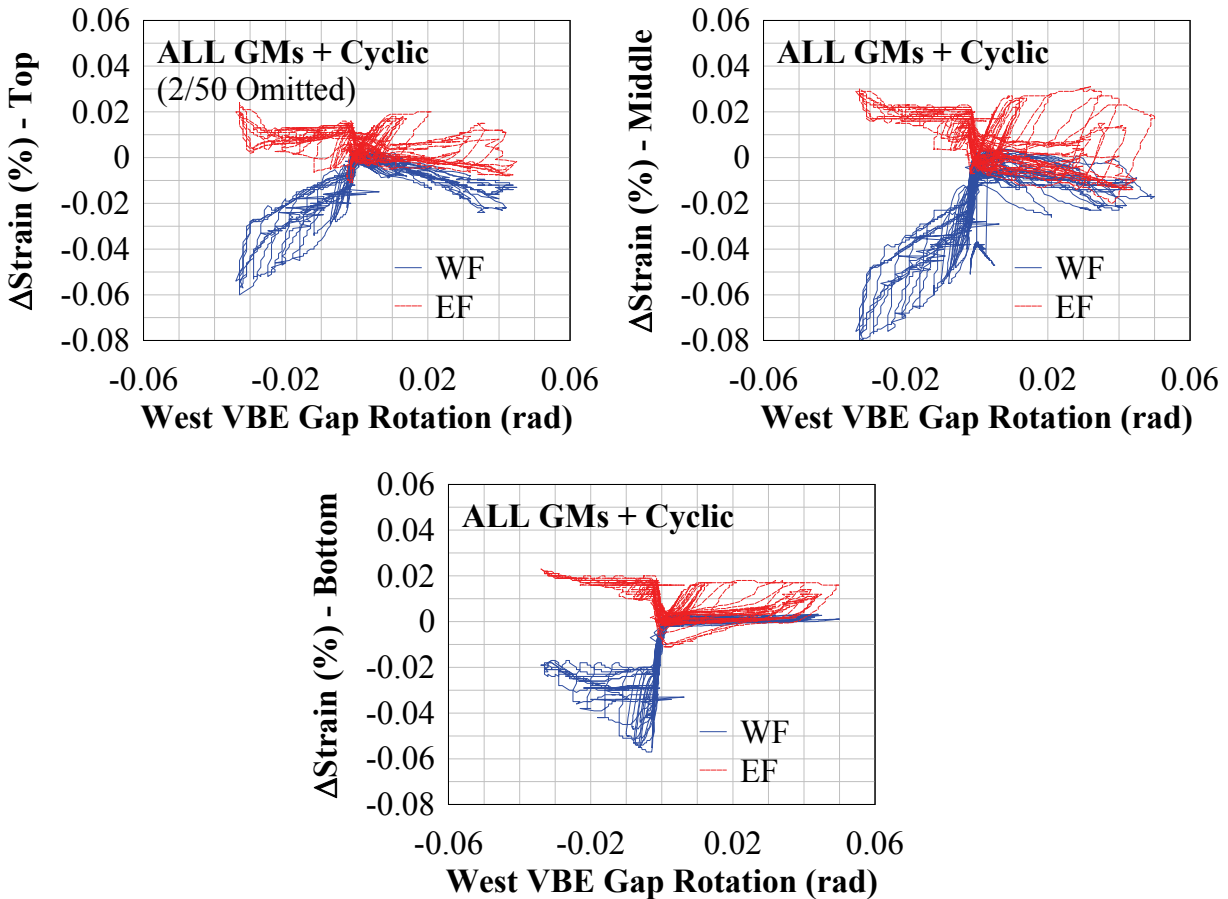


**FIGURE 9-21 West VBE:  $\Delta$ Strains versus gap rotation**

Additionally, it is observed that the strain gage response is nonlinear. The nonlinearity is due to the effects of infill web plate yielding and localized deformation at the rocking point. In particular, the resulting hysteresis loops is primarily due to the action of the infill web plate, and the decrease in strain (for an increase in gap rotation) is due to the effects of localized deformations at the rocking contact point. To further clarify this last point, note that just prior to the vertical gap opening, the compression stress field is concentrated along the flange. As the vertical gap forms and the bearing rocking point becomes more rounded due to localized

deformation, upon rotation about that point, the compression stress field trajectory changes, leading to a reduction in strains at the rocking flange location, this is shown schematically in figure 9-22. Furthermore, it is observed that the effects of the stress trajectory changes are more prominent in the West flange than the East flange location. This is logical since the outside of the VBE columns will experience larger compression forces due to overturning (and hence larger rounding deformation effects at the rocking point). To validate this behavior, a finite element analysis of that local detail would need to be performed (this is not within the current scope of work and could be investigated in future research). The strains along the VBE flange at the middle and top locations follow similar trends, but the effects of the localized deformation at the rocking bearing point are understandably not dominant and nonlinear response is primarily due to the action of the infill web plate. Note that, even at distances relatively far removed from the bottom of the VBE, strains on the lifting flange are not as high as on the rocking flange.

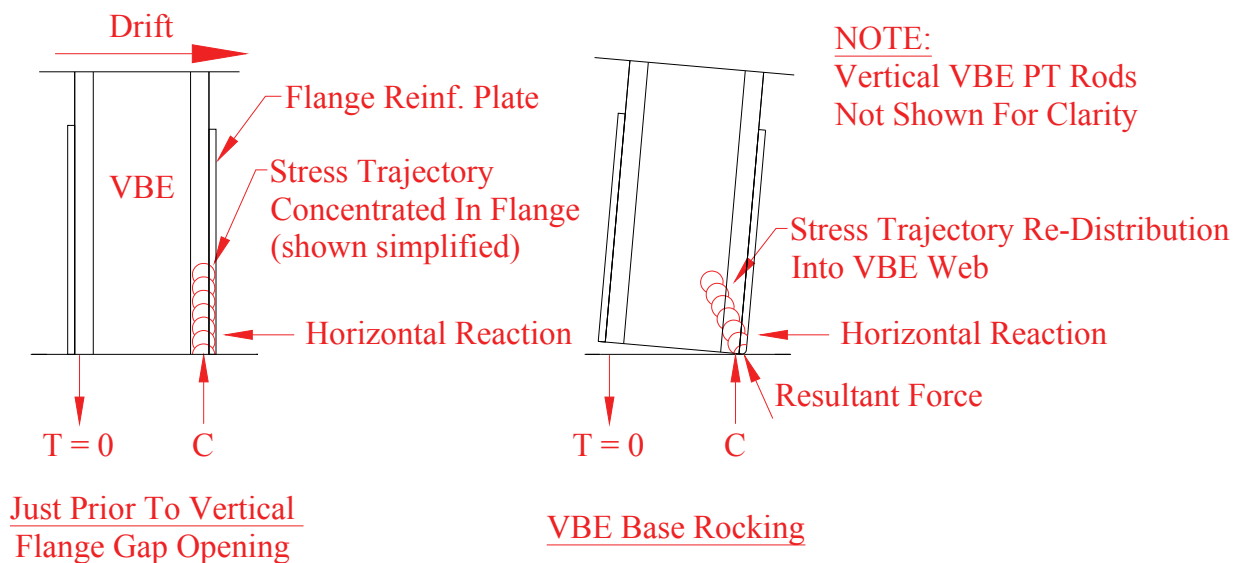


**FIGURE 9-22 Strain effect schematic due to localized flange deformation**

#### 9.8.2.2.2 Boundary Frame Strain Gage Response – HBEs

The strains at the end and sixth point locations of the top HBE are shown in figure 9-23. and figure 9-24, respectively. The strains at the end and sixth point locations of the middle HBE are shown in figures 9-25 and 9-26 respectively. The sixth point locations are the gages located at a distance of 500 mm from the ends of the HBEs shown on figure 9-6. Additionally, note that

some plots do not include both top flange and bottom flange data; with the missing data due to strain gage failures or errors. Also note that strains are presented for both the PSD tests and the inelastic cyclic tests for reasons presented earlier.

First observation is that the GM strain response plots exhibit more hysteresis than the inelastic cyclic plots. This is because additional energy dissipation through hysteretic response of the infill web plate is only achieved when drift exceeds the maximum value reached during previous cycles of response. In other words, during the inelastic cyclic test, the web plate had already been stretched up to the previous GM drift levels and little energy dissipation occurs for drifts up to that point.

Of particular interest is the strain response at the HBE top flanges at the ends of the HBES (where in contact with the VBE flanges at the HBE-to-VBE rocking point). It can be observed that the strains at a certain drift level become zero (shown by the horizontal segment of the strain response plot). Note that at these locations the real strain values can be obtained by shifting the strain response plot vertically such that the horizontal segment corresponds to zero strain. These horizontal segments of the strain response plots occur when the top flange of the HBE is no longer in contact with the VBE flange, as they separate. The occurrence of this gap was physically observed during the PSD and inelastic cyclic tests as noted in Sections 9.7.1 and 9.7.2. This phenomenon can be explained by reviewing the kinematics of the test specimen and is discussed in detail in Section 9.11; only general observations are made here.

It is observed that, for an Eastward drift, the top HBE at the opening joint (i.e., HBE West end) is always in contact with the VBE as expected. Separation always occurs at the closing joint. For a Westward drift, separation occurs sooner and the horizontal segment in the strain history diagram is more defined. This difference is a result of how the test specimen is loaded. Recall that in the Eastward drift direction the actuators are pushing on the frame, and in the Westward drift direction the actuators are pulling on the PT strands (as a result of pulling on the VBE). Consequently, for the Westward drift, the pulling of the PT strands produces an additive effect to the kinematic effects described in Section 9.11, leading to the differences noted in the strain histories. For comparison, at the middle HBE, for an Eastward drift, the HBE is always in contact with the VBEs. In the Westward drift direction, although it appears that the HBE is

always in contact with the VBEs by observation of the strain data, this cannot definitively be concluded as it is apparent that some drifting of the strain data has occurred distorting the response. However, in that last case, it was physically observed that at -4% drift, separation did occur as shown in figure 9-13. It is also observed that the top flange strains at the ends of the HBE at the opening joint locations increase in compression for an increase joint rotation as would be expected. However upon reaching a certain strain level, for a further increase in joint rotation a decrease in compression strain occurred, leading to a dipping/reduction effect of the response curve. This is a similar behavior observed for the strains at the base of the VBEs, and occurs here for the same reasons presented earlier (Section 9.8.2.2.1). From observations of the strain gage response at the interior sixth point locations away from the ends of the HBE (figures 9-24 and 9-26), this dipping effect was not observed in the strain histories recorded, as the stress and strain distributions are more uniform there.

From the strain data at both the middle and top HBEs it is also observed that the strain on the bottom flanges at the ends of the HBEs is essentially zero. This is logical, because there are no external loads applied at the boundary surface at these locations. However, note that there is an end HBE moment created by the eccentricity of the bearing force at the HBE-to-VBE rocking point, and that, consequently, strains would be expected on the bottom flange as a result of this eccentric moment if strain distribution was linear. However the data show otherwise. Additionally, the bottom strain gage values recorded at the sixth point locations are interestingly also essentially zero, which is counter intuitive. The strain gage data indicate that the distribution of stresses and strains in the HBE of frames with rocking connections is complex, and that the classic linear strain distribution does not occur up to a significant distance from the HBE ends. To better understand the actual internal stress/strain distribution, finite element analyses would need to be performed (again, beyond the current scope of work and could be investigated in future research).

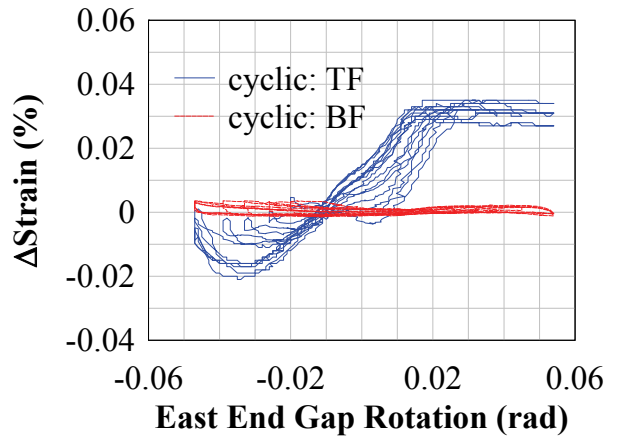
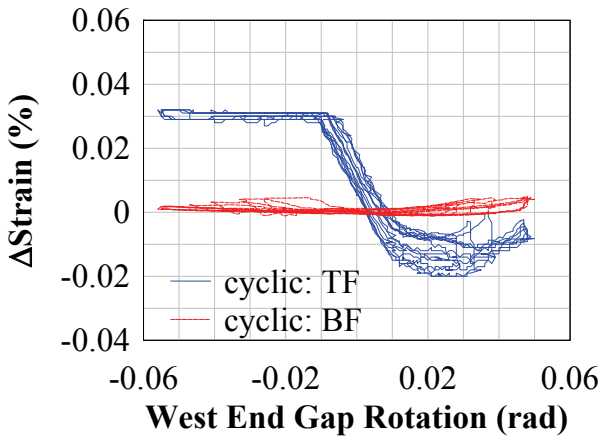
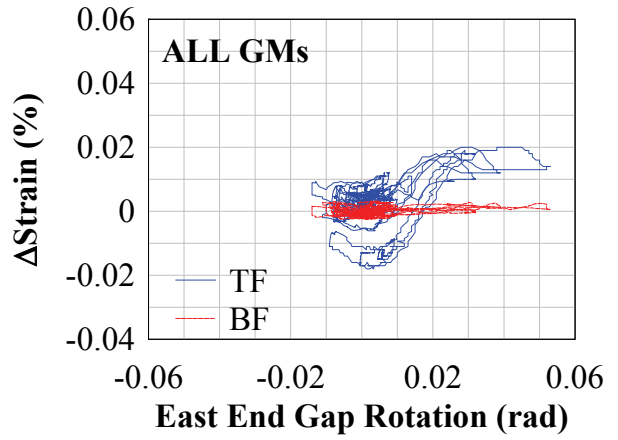
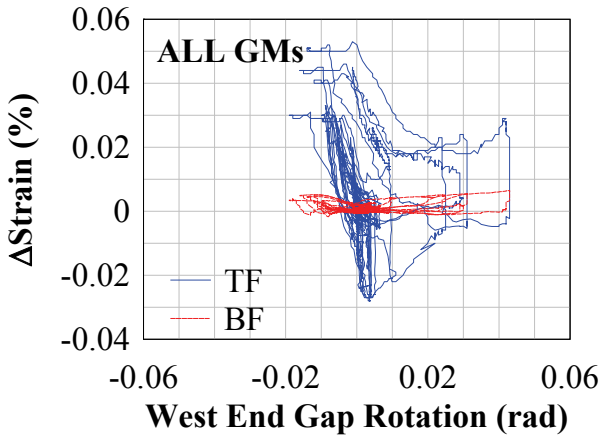


**FIGURE 9-23 Level 2 HBE: End ΔStrains versus gap rotation**



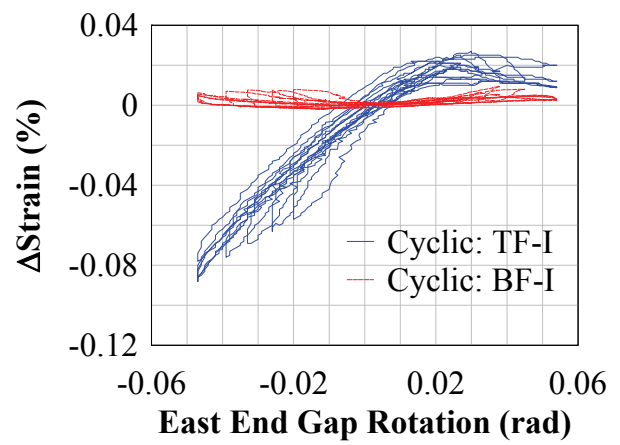
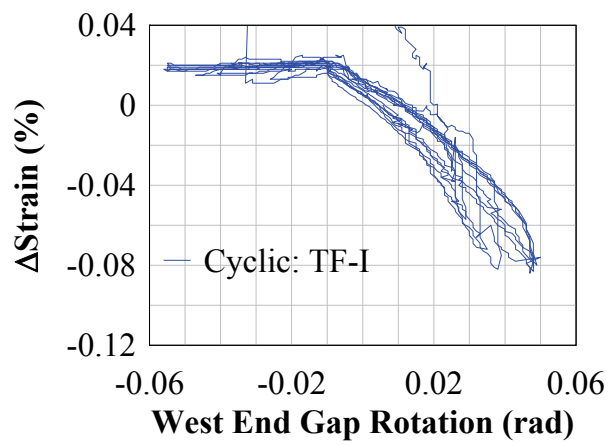
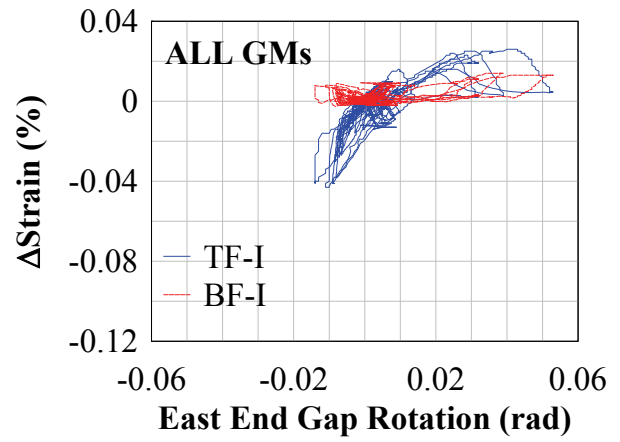
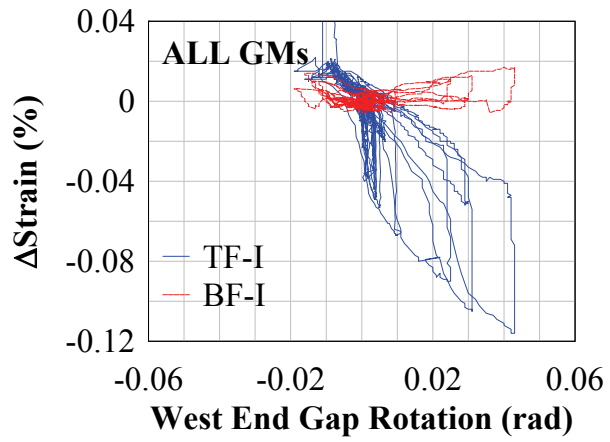


**FIGURE 9-24 Level 2 HBE: 1/6 point ΔStrains versus gap rotation**

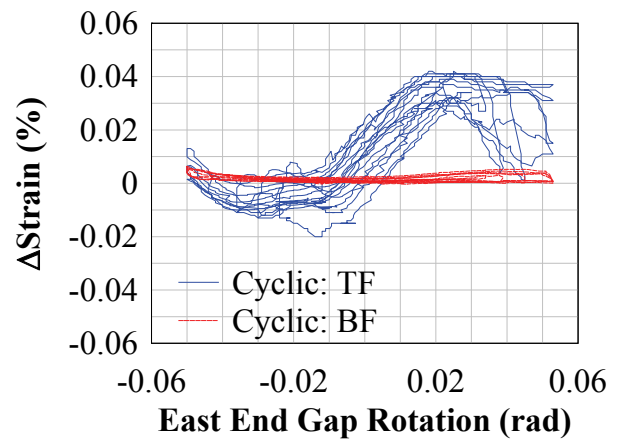
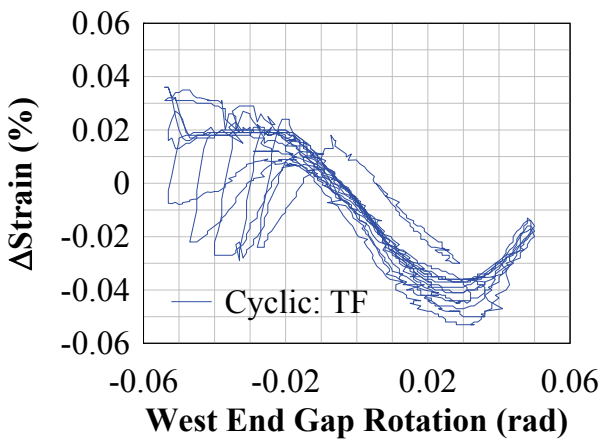
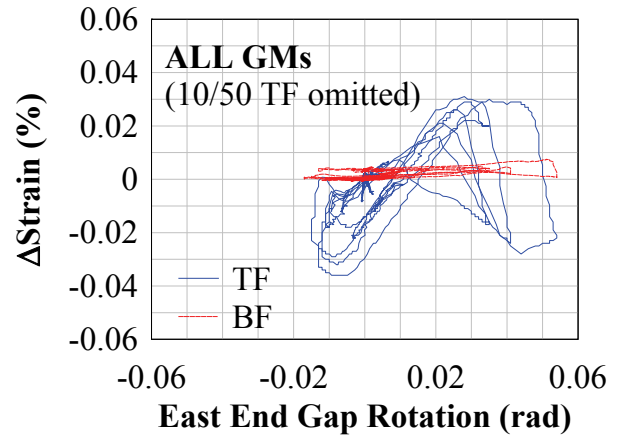
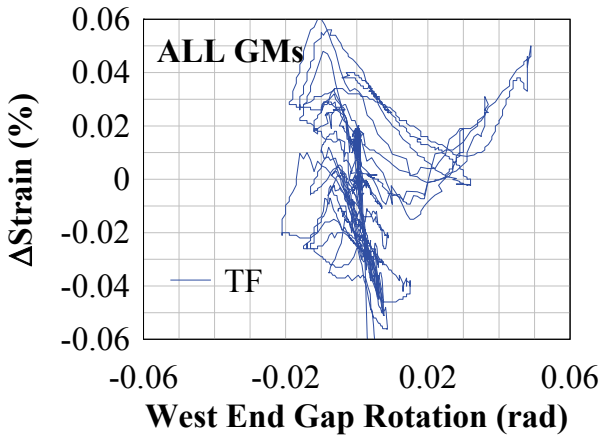


**FIGURE 9-25 Level 1 HBE: End  $\Delta$ Strains versus gap rotation**

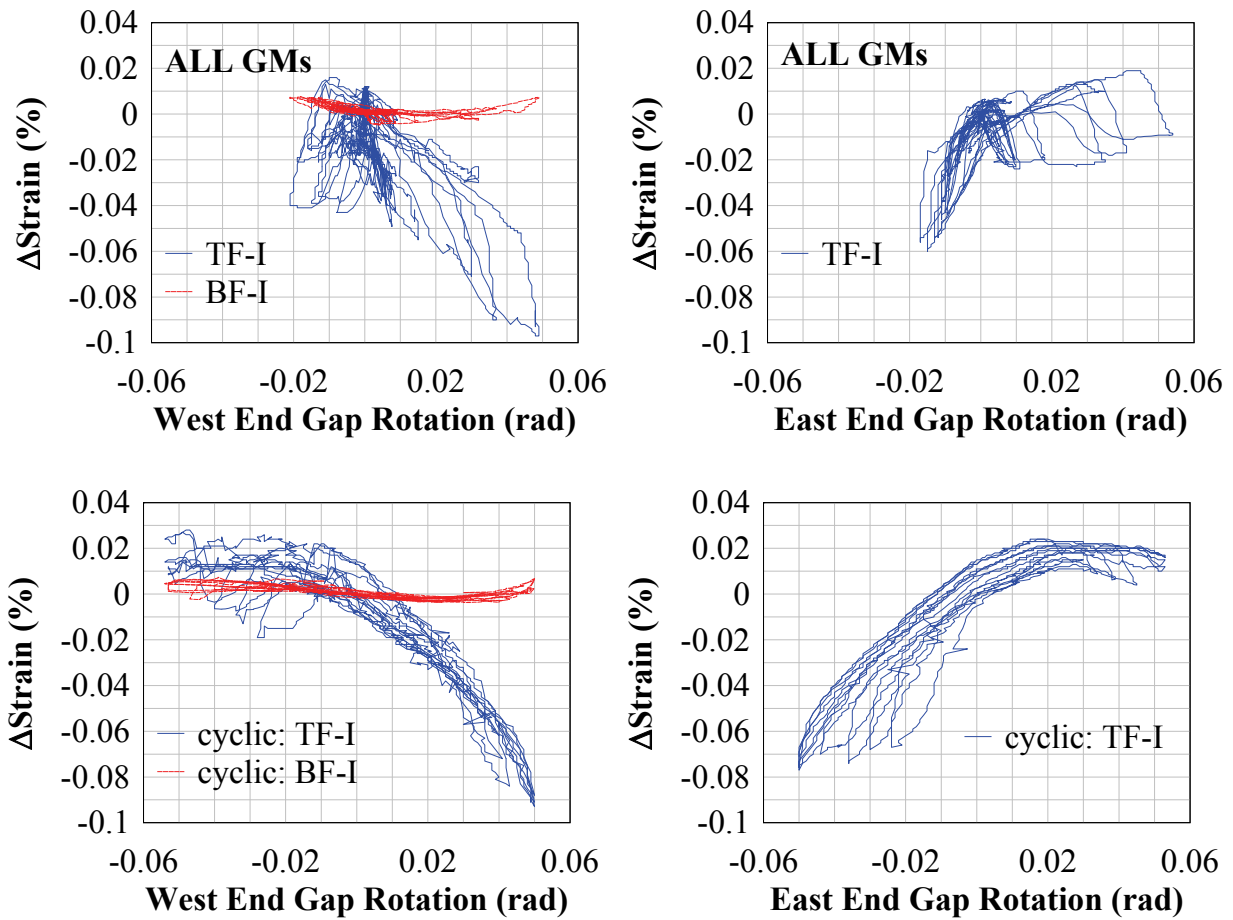


FIGURE 9-26 Level 1 HBE: 1/6 point ΔStrains versus gap rotation

### 9.8.2.3 Boundary Frame Axial and Moment Demands

The axial and moment demands on the boundary frame members using  $\Delta\varepsilon$  is presented here. Accordingly, the results are presented for relative axial forces and moments on the boundary frame members from the start of each test (i.e., by subtracting out the initial strain readings at the start of the test for reasons noted earlier).

Note that to approximate the total axial force and moment demands on boundary frame members, one could superimpose the effects of the initial PT force to those calculated from strain gage results using  $\Delta\varepsilon$  values, since the PT force value is known at the start of the test (i.e., obtained from the PT load cell readings). However, this approach is appropriate only for the flange rocking HBE-to-VBE details for which the PT load cell reading corresponds directly to

the PT axial force along the entire length of the member and that the moment demand due to the initial PT force at the start of the PSD test is essentially zero (i.e., since the HBE member is in full contact with the VBE and resulting in no moment demands due to PT force eccentricities at the HBE-to-VBE contact point). On the other hand, for the NewZ-BREAKSS connection, the PT load cell reading does not correspond directly to the PT axial force along the length of the HBE (i.e., since the HBE-to-VBE contact point is only at the top flange of the HBE and the PT is anchored at the centroid of the HBE, recall Fig. 3-58). It is therefore not possible to accurately obtain the actual PT force at the HBE-to-VBE contact flange location. As a consequence, the HBE axial force and moment due to the eccentric PT force at the HBE-to-VBE contact point cannot be accurately calculated. For these reasons, axial and moment demands along the boundary frame elements are presented based on  $\Delta\varepsilon$  only. Since the boundary frame is designed to remain essentially elastic, observations using  $\Delta\varepsilon$  (i.e., change of moment and axial force) along the boundary frame members will still provide useful insight on the seismic response of the test specimen without significant distortion when compared to that using total strain values.

#### **9.8.2.3.1 Boundary Frame Axial and Moment Demands - VBEs**

The corresponding relative VBE axial force and moment demands for the bottom of the West and East VBEs are shown in figure 9-27. The axial force response at the base of the VBEs reflects the interaction of the axial PT forces and the axial forces of the overturning moments (described in Section 9.8.2.1). Correspondingly, there is also a shift in the moment demand at the base of the West and East VBEs (i.e., they do not lay directly on top of each other) as a result of this interaction. Furthermore, it is observed that at the extreme VBE rocking points of the test specimen (i.e., West flange of the West VBE and East flange of the East VBE) there is a larger reduction in demand (more noticeable in the axial force plots) at these locations consequently to the local deformation at the rocking contact point (as mentioned earlier).

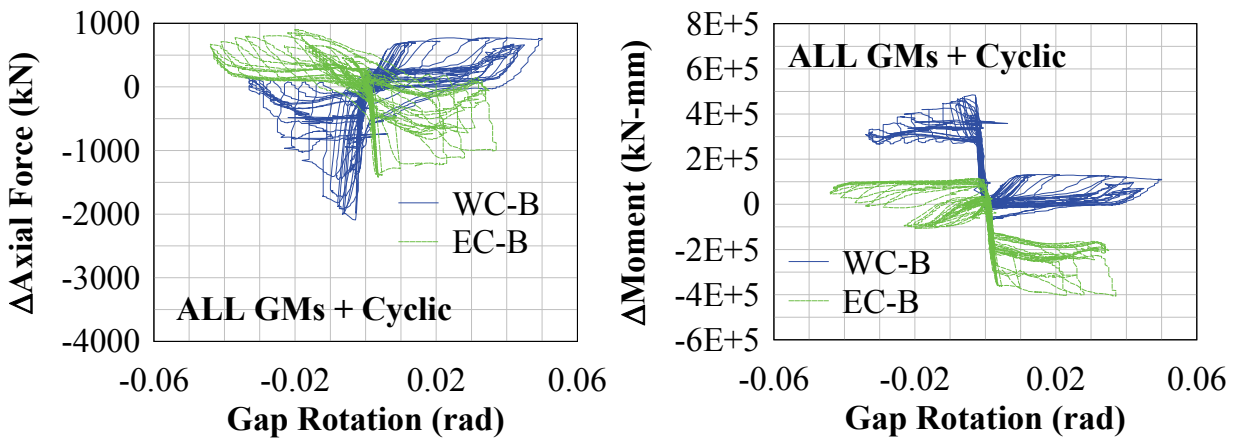


FIGURE 9-27 VBE bottom:  $\Delta$ Axial force and  $\Delta$ Moment versus gap rotation

### 9.8.2.3.2 Boundary Frame Axial and Moment Demands - HBEs

The relative axial and moment demands at the ends and sixth point locations for the top HBE are shown in figures 9-28 and 9-29 and the middle HBE shown in figures 9-30 and 9-31 respectively. The same observations made for the strain response at these locations are also applicable here to the axial force and moment response, since these are obtained by a linear combination of the strain values. Additionally, note that for the response at the ends of the HBE, the real response would be the one obtained by shifting the response curve vertically to align the horizontal segment of the axial and moment curves with the zero point in the vertical axis direction; the plots as shown provide only the changes in response from the start of each PSD test, for reasons described earlier. The axial force and moment distribution along the length of the top HBE and middle HBE are shown in figure 9-32. Note that the moment curves corresponding to the strain gage locations are connected by linear segments. Although the real moment diagram does not vary linearly along the length of the HBE, the linear segments are only provided as reference lines between each point. Also note that for the NewZ-BREAKSS frame, the moment discontinuities at the PT anchorage location on the HBE cannot be accurately captured with the current strain gage distribution on the HBEs; with this in mind, observations on the resulting axial force and moment diagrams are presented below.

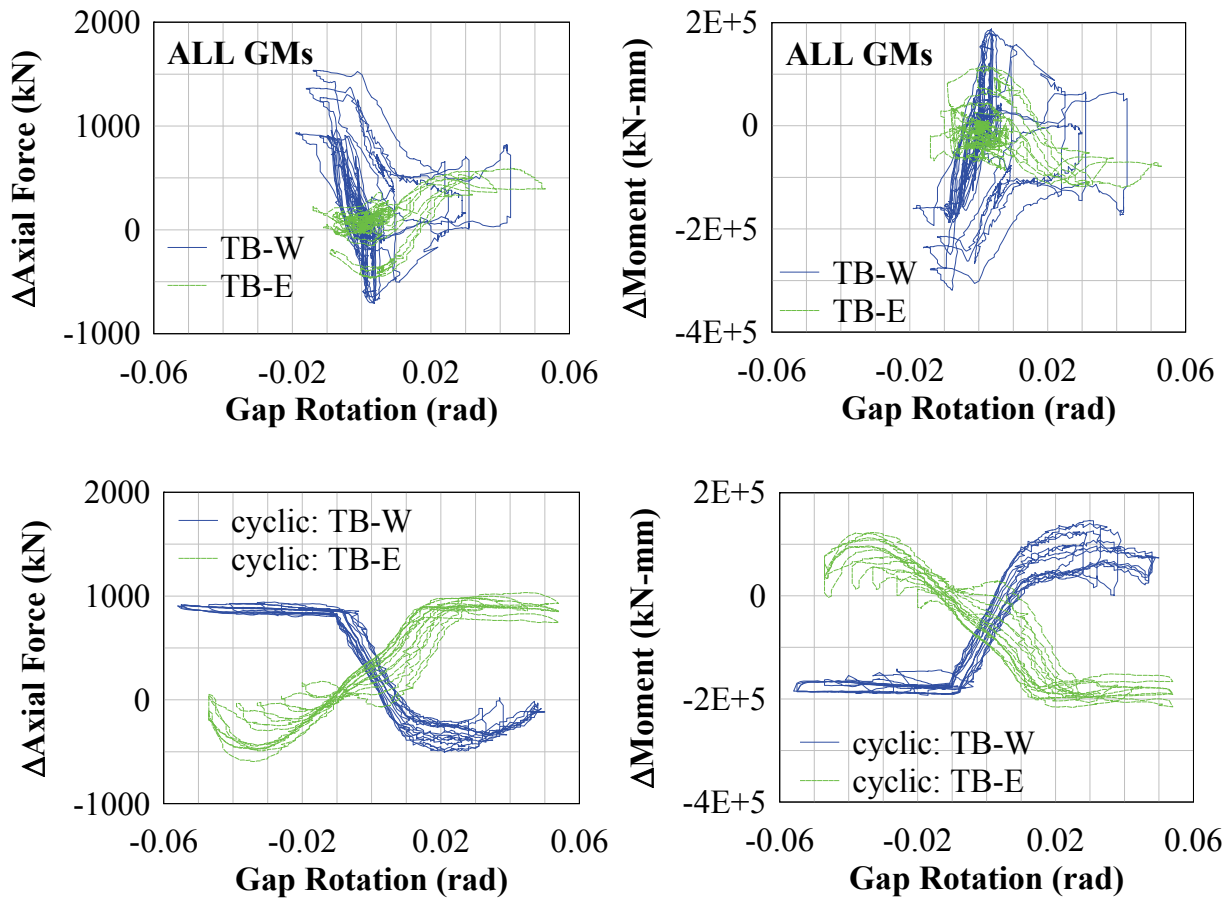


FIGURE 9-28 Level 2: HBE end  $\Delta$ Axial force and end  $\Delta$ Moment versus gap rotation

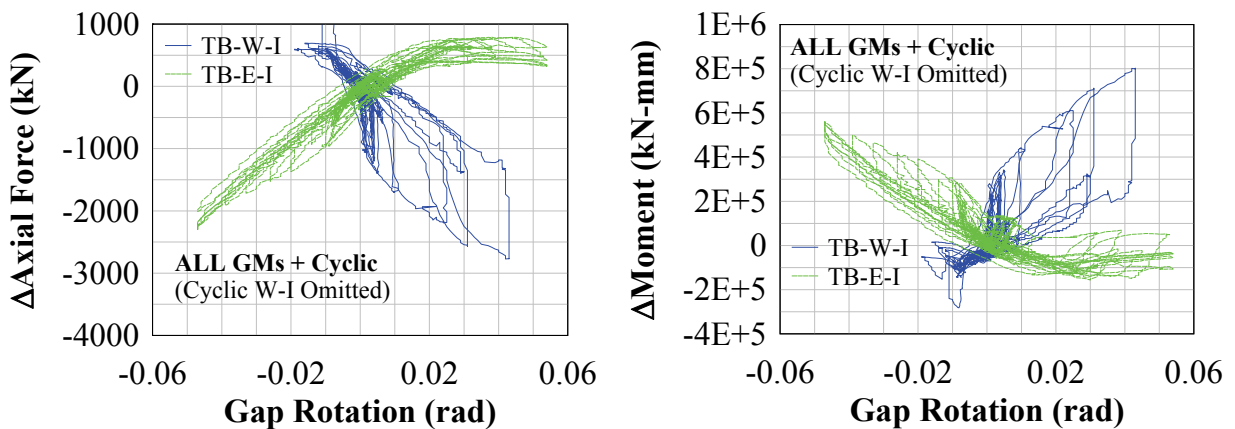


FIGURE 9-29 Level 2: HBE 1/6 point  $\Delta$ Axial force and interior  $\Delta$ Moment versus gap rotation

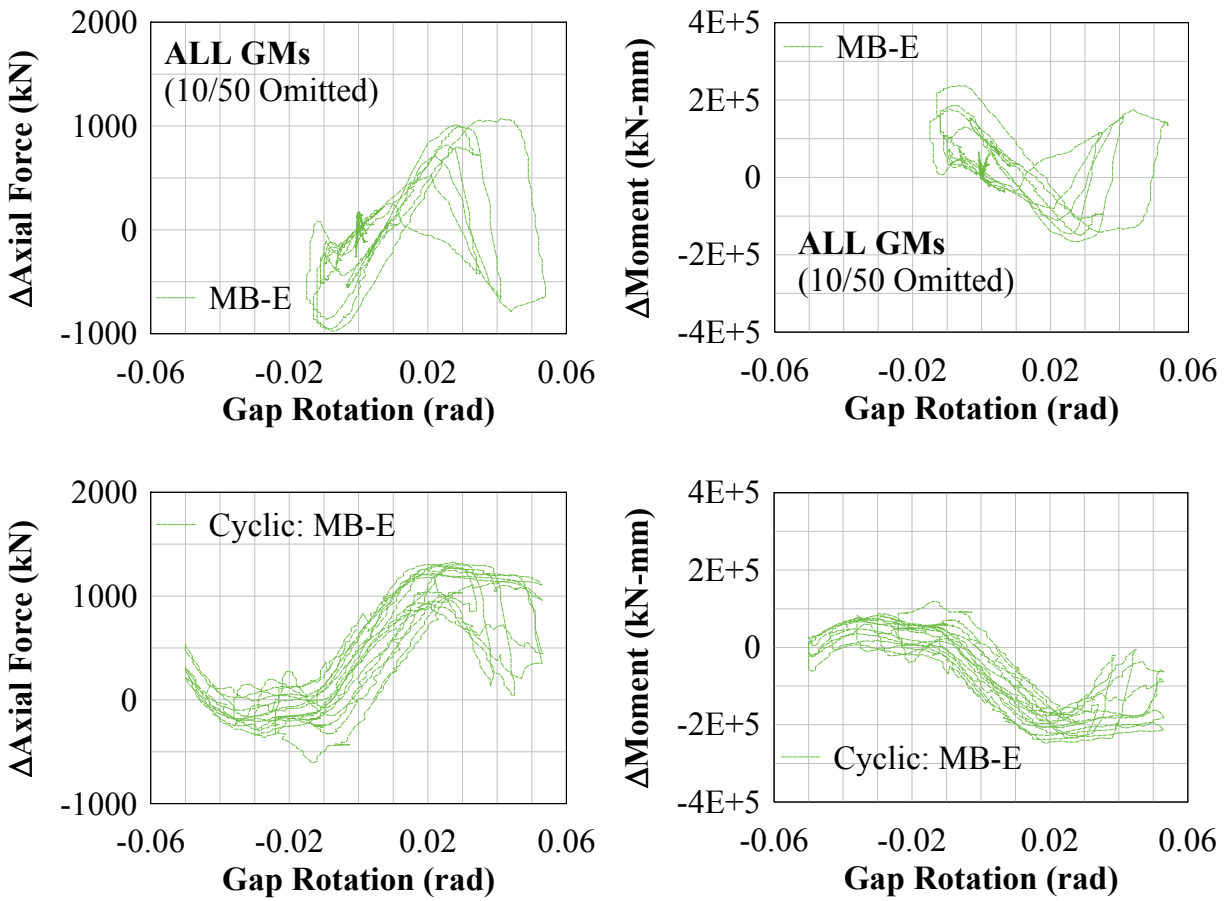


FIGURE 9-30 Level 1: HBE end  $\Delta$ Axial force and end  $\Delta$ Moment versus gap rotation

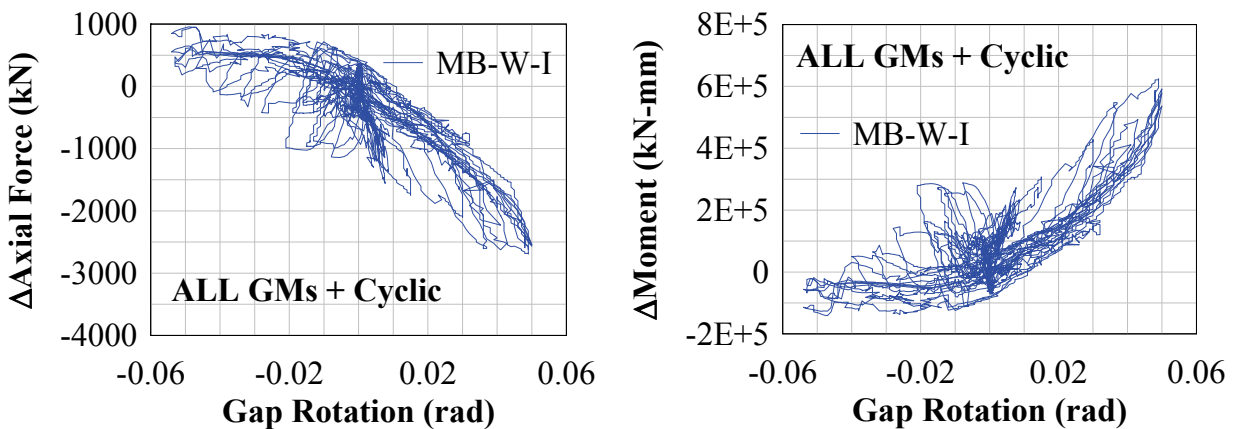
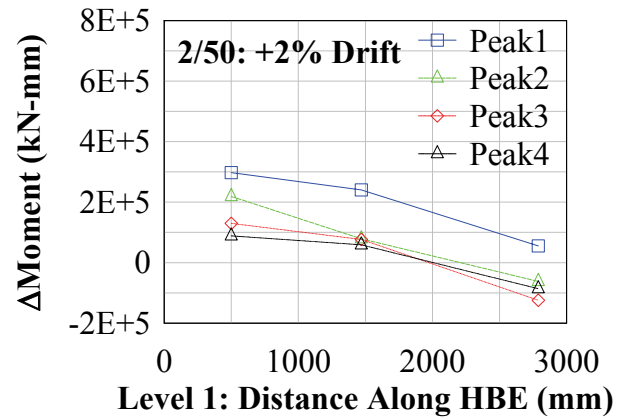
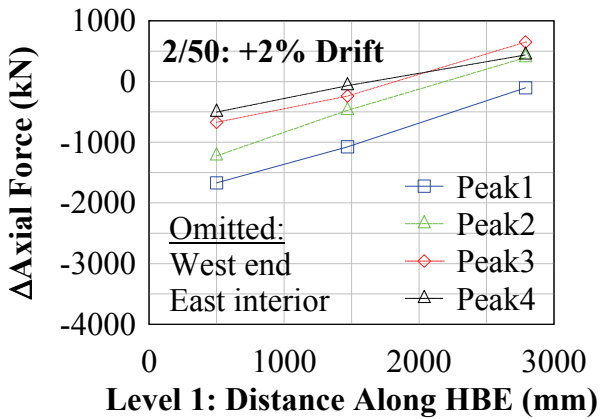
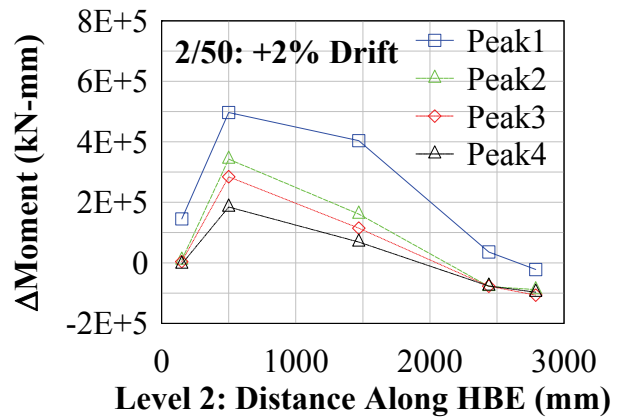
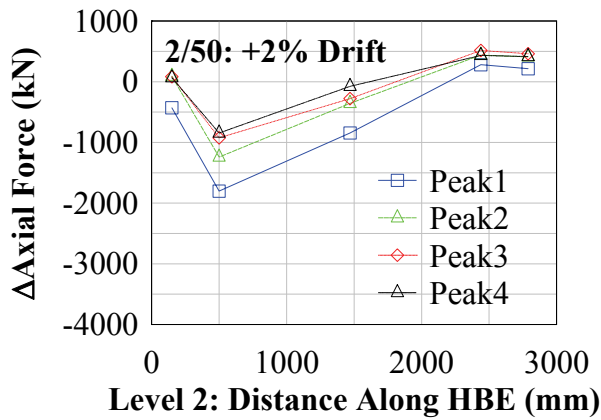
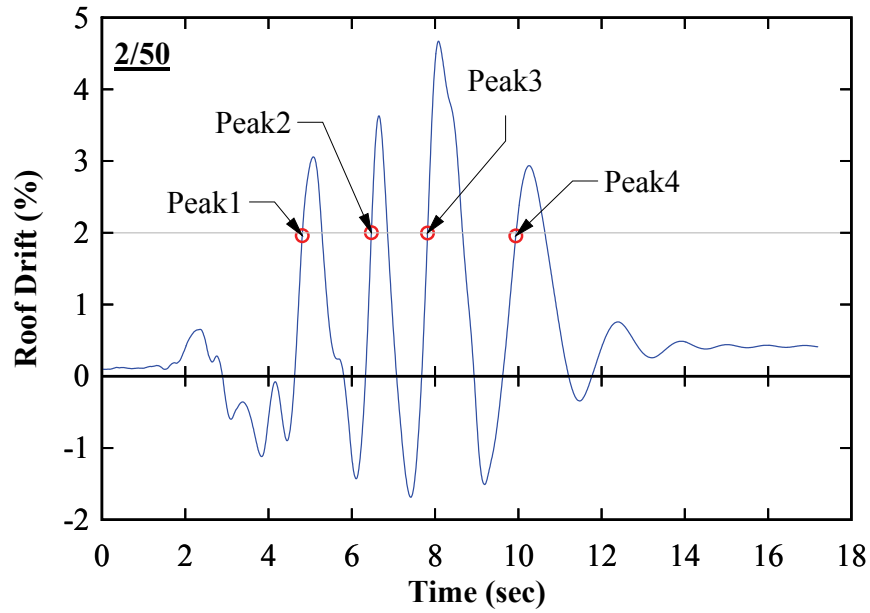


FIGURE 9-31 Level 1: HBE 1/6 point  $\Delta$ Axial force and interior  $\Delta$ Moment versus gap rotation



**FIGURE 9-32 HBE: ΔAxial force and ΔMoment distribution**



Arbitrarily choosing a positive 2% roof drift condition (corresponding to the maximum target drift for the 10/50 design earthquake event), the axial force and moment distribution shown in figure 9-32 are shown for four consecutive roof drift peaks which pass through a 2% roof drift as shown in the roof drift plot in the figure. The first peak corresponding to the point at which the frame reaches positive 2% roof drift for the first time and the fourth peak being the fourth time at positive 2% roof drift. Prior to providing general observations, it is noted that the axial force at the West end of the HBE appears to be incorrect and should be the largest in magnitude. Recall that at the ends of the HBEs when acting as the opening joint (i.e., the condition when the compression strains should be at a maximum) there is a reduction in compression strain demand on the bearing flange as observed in the dipping effect of the response plots noted earlier. Consequently, the axial forces at the ends of the HBEs indicate the appearance of a lower demand than what actually is present. Accordingly at the ends of the HBE, although the strains are real for the distribution of strain gages provided, the calculated axial force and moment demands is not necessarily representative of the actual demand. The strain gage distribution at the end locations are representative of a localized response due to the presence of local deformation at the HBE-to-VBE bearing contact point; additional strain gages along the depth of the member would be required to obtain a better representation of the actual axial force and moment demands at the HBE ends. Being cognizant of the strain response at the ends of the HBEs, general observations of the relative axial and moment demands are made subsequently.

Results allow observation of the reduction in infill web plate strength as it is stretched repeatedly through the same drift excursion. This is evident by the reduction in axial and moment demands on the HBE for subsequent peaks. With the exception of the West end location on the HBE as noted above, the response of the axial force along the HBEs shows a reduction in axial force demand. This is an appropriate response as the axial force should decrease (from West to East end for an Eastward drift condition) as the effects of the infill web plate will reduce the axial force at the West end HBE rocking point. Additionally the axial force on the East end of the HBE also reduces as a result of a reduction in PT force due to loss of PT elongation as a consequence of the closing joint. By comparison of the top and middle axial force diagrams, it is observed that the axial force demand from the PT is dominant compared to the axial force demand from the infill web plate. That is, at the middle HBE, axial force effects from the infill

web plate cancel out (since the same infill web plate thickness is used above and below and there is no actuator present at this location providing any story force demand). Thus the axial force diagram at the middle HBE is dominated by the PT effect which is comparable in force magnitudes to the top HBE axial force diagram. At the top HBE, the infill web plate is shown to have a dominant effect by observing the moment demands as affected by the vertical component of the infill web plate pulling on the HBE. In contrast, at the middle HBE, the moment demand is smaller and due to the dominant effects of the PT as the moment demands of the infill web plates above and below cancel out.

#### **9.8.2.4 Boundary Frame Infill Web Plate Displacement Transducers**

The displacement response history recorded by the diagonal displacement transducers (DTs) placed to measure the approximate axial deformations (at 45 degree) of the infill web plate are shown in figure 9-33 for the 2/50 GM. The plots provided are in terms of percentage strain calculated by dividing the recorded DT displacement values along the axis of the DT by the undeformed length between the DT anchor points. Only results for the diagonal DTs for which positive axial displacements corresponding to an Eastward drift are shown (for location of the DT sensor see figure 9-4); similar observations can be made for the DTs oriented in the opposite direction. For the current purpose, it is only necessary to know whether the sensors are located near a corner or at an interior location, and the plots are labeled accordingly. Note that the positive strain values are the primary response of interest (rather than the negative strain values when the infill web plate buckles), as the positive strain values correspond to the development of a diagonal tension field in the infill, which leads to larger stress demands on the connection of the infill web plate to the boundary frame. Three comparisons are made at each floor level: first, a comparison of the corner and adjacent interior DT at the opening joint; second, a comparison of the corner DT at the opening joint and the corner DT at the opposite infill web plate corner at the lower closing joint, and; third, a comparison of the interior DTs.

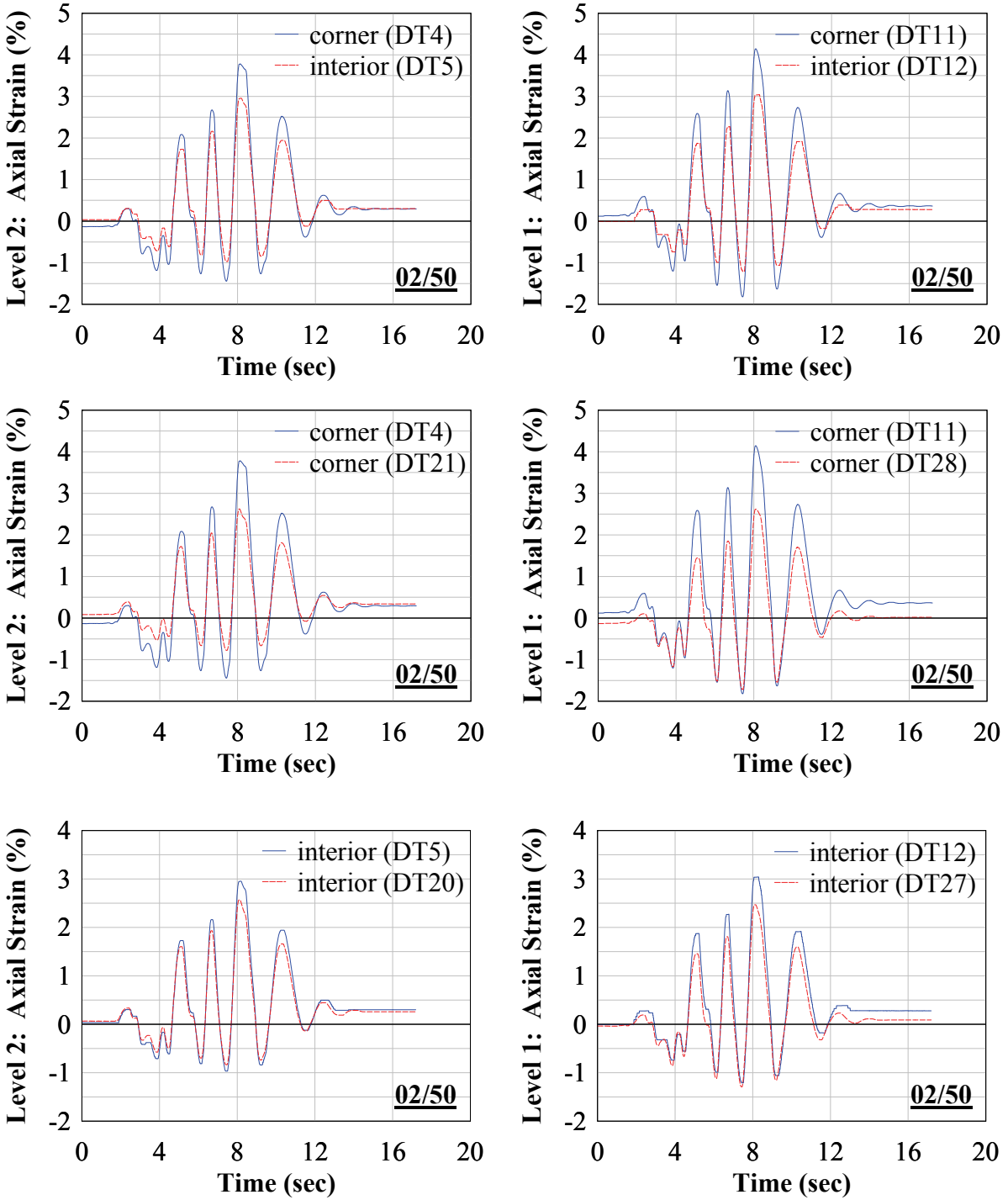


**FIGURE 9-33 Infill web plate axial deformation response**

Results show that the axial tensile strains are higher at the corners. Additionally, the closer the location to the corner of the opening joint, the larger the tensile strains are in the infill web plate. This response is in agreement with the theoretical formulation derived in Section 3 defining the relationship of the infill web plate tensile strains at rocking joint connections. Figure 9-34 compares the cumulative (i.e., all GM responses superimposed) experimentally obtained DTs versus interstory drift with the ones derived from the theoretical formulation (3-106). Results are in good agreement. Note that the actual values of the infill web plate strains at the location of the DTs will be different since the actual distribution of strains within the web plate is more complex than that represented by the placement of a single diagonally placed DT sensor. However, the DT sensor information presented should accurately represent the kinematics of the global deformation of the infill plate, and accordingly should provide a reasonable approximation of the infill web plate strain at that location.

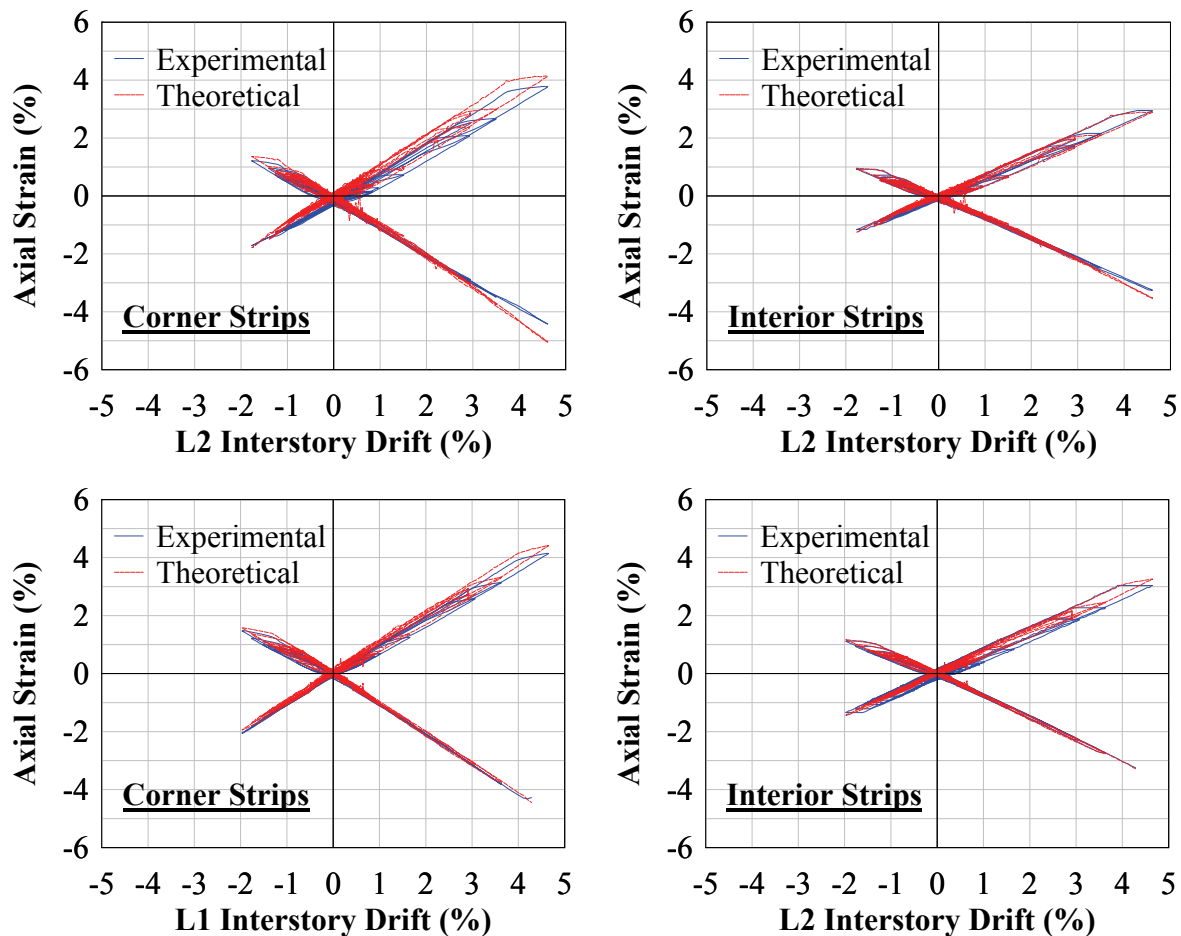


**FIGURE 9-34 Experimental versus theoretical**

## **9.9 Inelastic Cyclic and Bare Frame Cyclic Experimental Results**

### **9.9.1 Cyclic Global Response**

Global hysteretic response in terms of base shear versus roof drift, along with the cyclic loading history, is shown in figure 9-35. For the inelastic cyclic test, the response of the PSD test is superimposed for reference. It is observed that the base shear in the positive drift direction is approximately 10% larger than that in the negative drift direction and is a reflection in part of the loading setup discussed earlier (i.e., although the test was conducted in displacement control, the resulting base shear demand was different in each direction, because Eastward drifts were achieved by pushing on the frame, and Westward drifts by pulling on the HBE PT, which affected the base shear strength contribution from the PT boundary frame). Results show that for repeated cycles after the PSD cumulative damage to the infill web plate, the infill web plate still provides some energy dissipation. Additionally, lateral load resistance remained significant, with the base shear strength at positive 4% drift and 4.5% only reduced by approximately 25% and 50% respectively from the previous PSD tests (note that at these drifts, approximately 25-30% of this cyclic strength comes from the bare frame alone). Additionally, some compression strength is present in the infill web plate as evidenced by the fact that there are drift excursions during which the base shear is not zero at the zero drift location (i.e., indicated by the “fatness” of the hysteresis curve at the zero drift location). Similarly to what was observed in the UB quasi-static tests for an infill web plate configuration, recentering is not achieved when a residual drift exists at the zero base shear location.

For the bare frame tests, the base shear strength contribution from the PT boundary frame is approximately 20% of the total base shear strength (at 2% drift) obtained in the PSD tests. Comparing results of the bare frame tests with and without lateral frame release shows no significant difference. This suggests that the lateral bracing frame does not provide any significant “clamping force” that could have affected the results. In other words, the measured energy dissipation is provided by the infill web plate and the possible contribution due to sliding friction between the lateral bracing frames is negligible. However it is noted that some energy dissipation (attributed to friction in the boundary frame connections) although negligible, is provided by the bare frame, as is it is observed that the base shear versus roof drift response curve is not completely linear elastic.

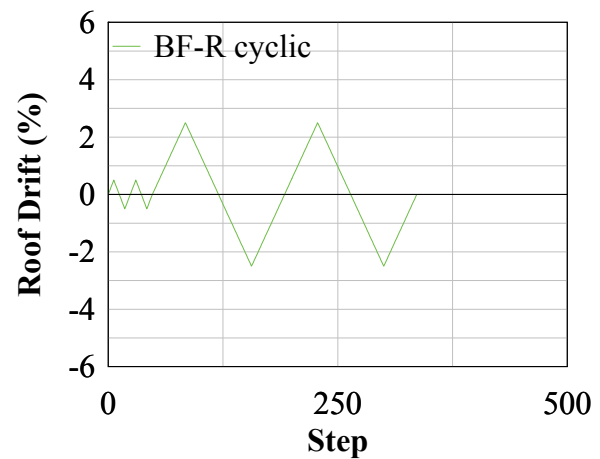
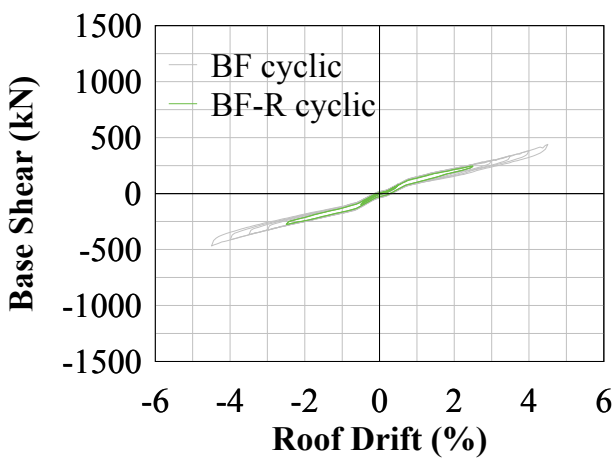
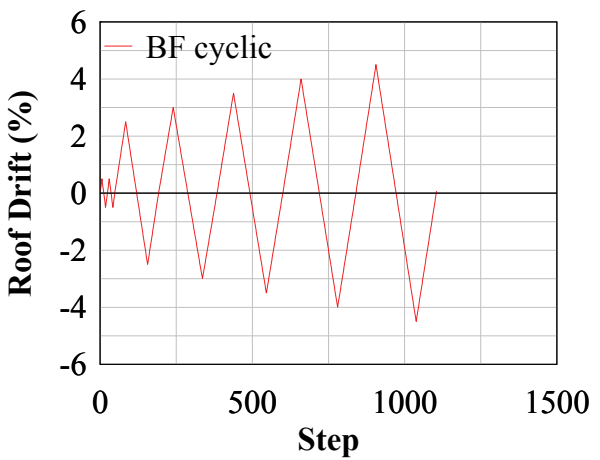
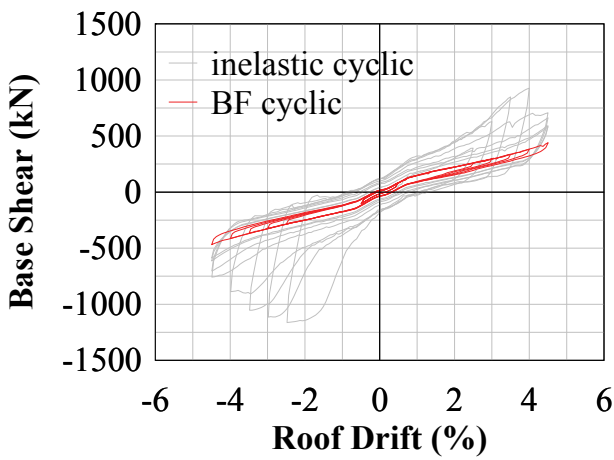
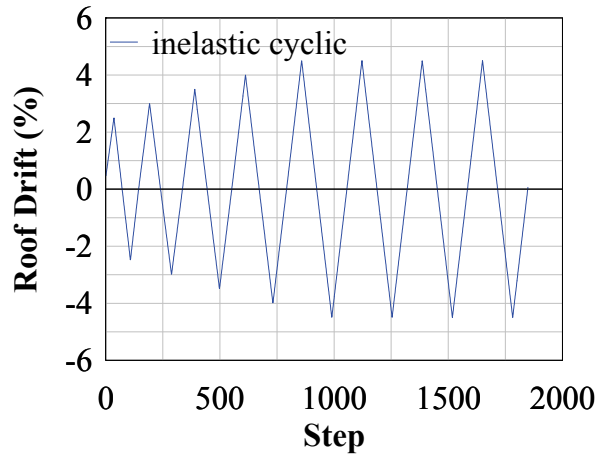
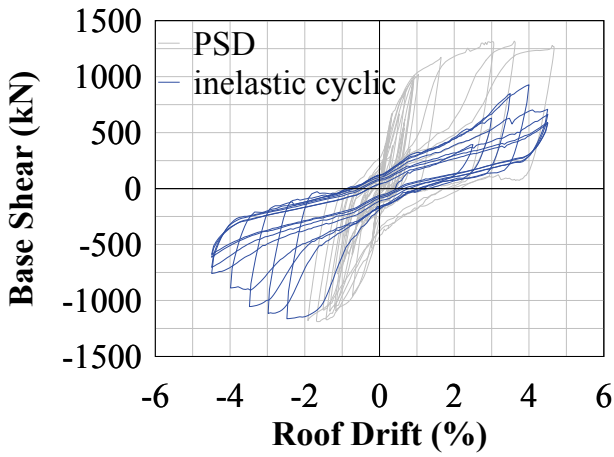


FIGURE 9-35 Cyclic global response

### 9.9.2 Cyclic Local Response

Since many local response values of interest from the inelastic cyclic tests have been presented earlier together with the PSD results, and because all DTs were removed prior to cutting out the infill web plates and were not put back in place for the bare frame tests (as mentioned earlier), the instrumentation remaining on the bare frame tests mainly served to record global response behavior. Only selected response plots for the bare frame test without modification of the lateral bracing frame (i.e., BF plots) are provided here to further highlight some observations made during the PSD tests.

The PT force response is shown in figure 9-36. Results show that response was essentially linear elastic in the absence of infill web plates. As before, the pulling effect on the HBE PT by the actuator in the negative drift direction is noticeable, as well as the lateral shifting effect of the VBE PT response due to the VBE axial forces from the frame overturning moment.

The total strain response at the ends of the HBEs is shown in figures 9-37 and 9-38 for the top HBE and middle HBE respectively. Note that the strains are plotted as total strains and not incremental strains as was done for presentation of the PSD test results (note that for this purpose, the vertical offset error as presented earlier in the strain gage data was removed showing the “correct” strain response, since here, only the strain gage response is shown and no moment and axial force demands are presented). It is observed that a gap between the HBE and VBE flanges forms once the frame reaches a certain drift level, as indicated by the horizontal segment of the strain response plot. This indicates that this separation phenomena is not significantly influenced by the infill web plates. It is also observed that this separation also occurred for the middle HBE in the negative drift direction, which was not the case when the infill web plate was present (suggesting that presence of the infill web plate does provide some restraint against HBE-to-VBE flange separation).

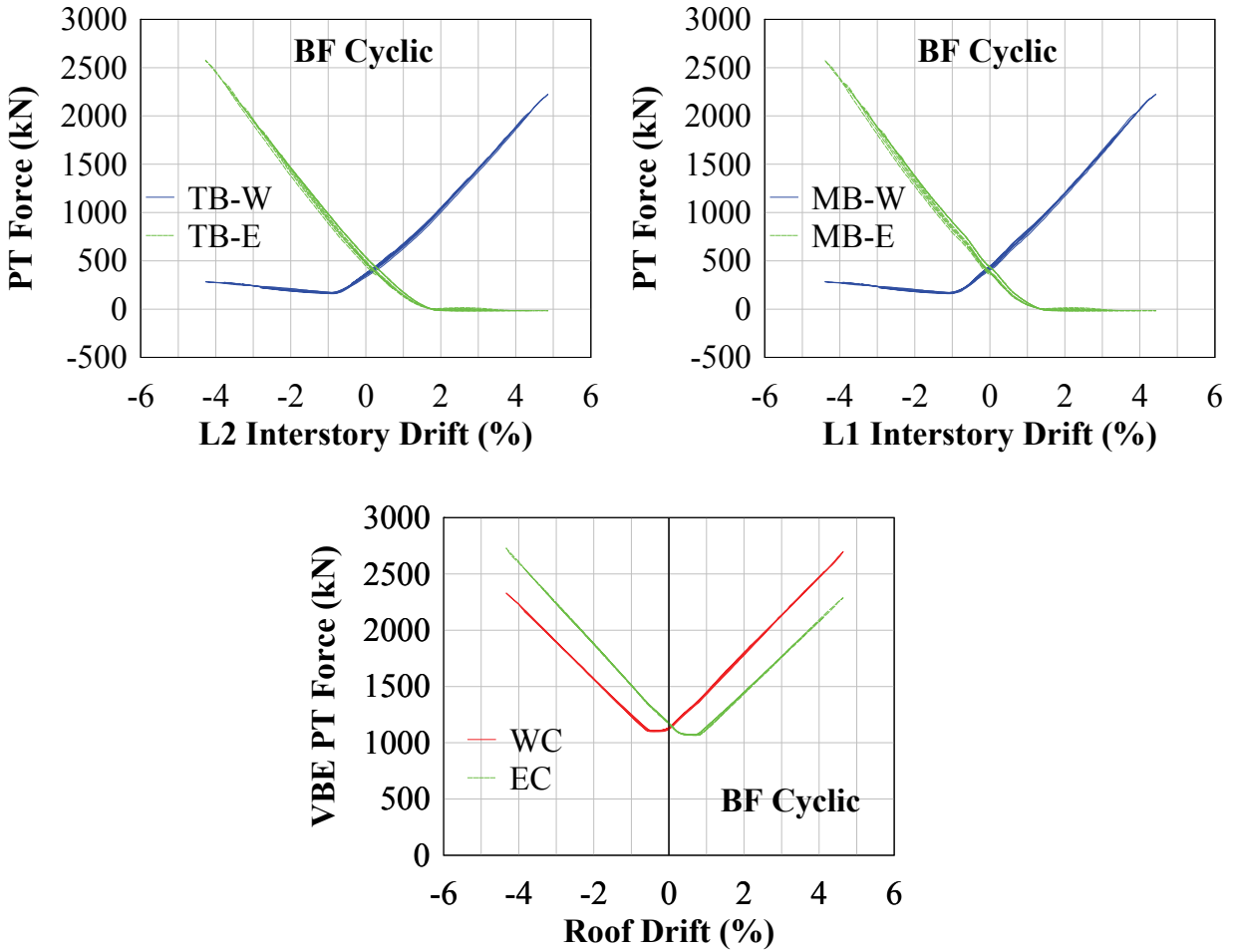


FIGURE 9-36 Cyclic PT force response



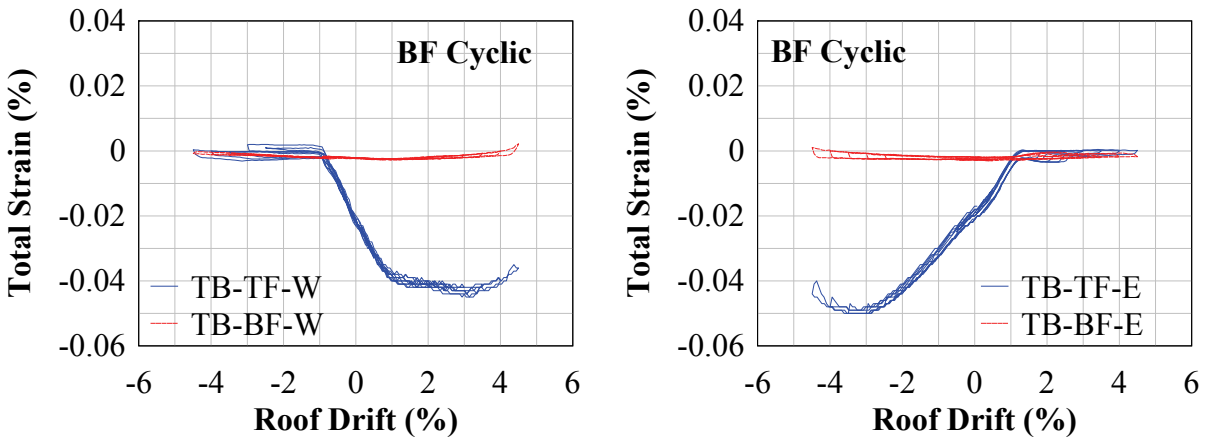


FIGURE 9-37 L2 HBE: end total strains versus roof drift

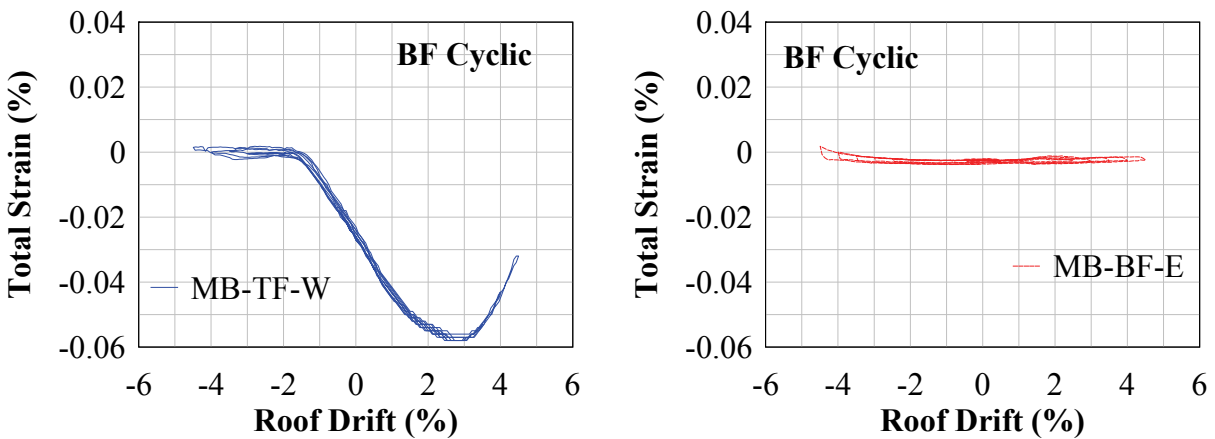


FIGURE 9-38 L1 HBE: end total strains versus roof drift

Finally, the same reduction in compression strain as a result of the dipping effect, previously observed during the PSD tests and inelastic cyclic tests, also occurred for the bare frame. This provides evidence that this previously observed behavior is not due to effects of the infill web plate (since in the bare frame test the infill web plate is not present). Rather, it is due to a complex localized behavior that occurs at the bearing contact point of the HBE-to-VBE rocking connection presented earlier (Section 9.8.2.2.1).

## 9.10 Experimental versus Analytical Comparisons

The experimentally obtained PSD global responses are shown in figure 9-39 along with analytical results from OpenSees analyses for comparison, where the curves labeled “OS TO” and “OS TC” corresponds to “OpenSees Tension-Only” and “OpenSees Tension-Compression” strip models (which will be clarified subsequently). The corresponding PSD incremental dynamic response (IDR) showing resulting peak maximum absolute base shears and roof drifts is shown in figure 9-40. Each point on the IDR curve represents the absolute global response value for a given GM. There are three separate PSD IDR curves shown: 1) The one labeled “PSD maximums” reports the absolute maximum base shear and roof drift regardless of time occurrence. In this case, it is possible that the maximum base shear and roof drift did not necessarily happen at the same time; 2) The curve labeled “PSD maximum shear” reports the maximum absolute base shear with the corresponding roof drift when it was reached, and; 3) The curve labeled “PSD maximum drift” reports the maximum absolute roof drift with the corresponding base shear when it was reached. It is observed that for the 50/50 and 10/50 the maximum response occurs at the same time; whereas for the 2/50 response the absolute maximums occur at different times. For design purposes, of interest are the PSD maximums; the PSD maximum shear and drift plots are provided for reference.

The analytical plots shown are provided for damping of 1% and 5%. For reference, recall that the experimental initial damping was estimated to be approximately 4% for the SC-SPWS specimen (based on results from the Elastic SC-SPSW PSD free vibration tests) and approximately 2% for the bare frame. Additionally, two sets of OpenSees analyses results are presented for comparison with the experimental response. The first set was obtained using a tension-only hysteretic model for the infill web plate strips, as typically done to model SPSWs; these are the analytical results presented earlier in Section 8. The second set of OpenSees IDR plots uses a combined tension-compression hysteretic model for the infill web plate strips presented by Clayton (2013), which considers some compression strength of the infill web plate. The tension-compression model used for these PSD analyses was calibrated such that the cyclic static pushover analysis approximately matched the experimentally obtained inelastic cyclic response. As expected, analysis results obtained using the tension-compression model show smaller drift demands than the tension-only model, as a consequence of the additional energy

dissipation provided by the compression strength of the infill web plate. Yet, the tension-compression model base shear demands are not significantly different from those obtained from the tension-only model, because the compression strength contribution is small compared to the strength of the infill web plate strips in tension. Additionally, for the 5% damping case, results from the tension-only and tension-compression model analyses are closer to each other than for the 1% damped condition, which is logical since more inelastic response would be expected for the 1% damping case, leading to larger differences due to nonlinear response.

In other comparisons, it is observed that the analytical results, in general, conservatively overestimate the experimental response. The drift demands at the 50/50 level are more comparable than those at the 10/50 and 2/50; this should be expected as the response was essentially elastic at the 50/50 GM test. However it is observed that the PSD and OpenSees elastic secant stiffness at the 50/50 GM test are noticeably different. Recall that the initial elastic period of the OpenSees model and the experimental elastic period estimated from the Elastic SC-SPSW free vibration test were also different (by approximately 10 percent). Additionally, for the 10/50 and 2/50 GMs, the differences between the analytical and experimental response become more noticeable as a result of the greater inelastic response at larger drifts. Note that the analytical models used were not able to capture infill web plate separation (i.e., tearing) from the boundary frame, and that for the 10/50 and 2/50 GM response, some infill web plate separation occurred. Tearing of the infill web plate from the boundary frame during the tests can be observed by the strength degradation of the hysteresis loops on the experimental base shear versus roof drift response curves.

The above modeling differences provide some explanation why the analytical time-history response does not accurately match that for the test specimen (figure 9-39). However, the analytical results do provide a reasonable approximation of the peak response, depending on appropriate assumptions on damping. Overall, the analysis results suggests, that using the tension-only model and small damping provides an upperbound response that may be suitable for design purposes.

The cyclic static analytical and experimental results are shown in figure 9-41. The PSD results are also shown for reference (since the cumulative infill web plate damage from the PSD tests

was present prior to the start of the inelastic cyclic test). Additionally, the analytical static response is based on the OpenSees tension-compression model using an infill web plate compression strength equal to approximately 20% of its tensile yield strength. This value was obtained by iterations, to match the inelastic cyclic response at the zero drift axis location. It is observed that the corresponding PSD response at the zero drift axis location is noticeably different than the path of the inelastic cyclic test. It is interesting to note that this change in load path only occurred at the 2/50 GM. For the 10/50 GM, the load path at the zero drift axis location closely matches that for the inelastic cyclic test. Additionally, at approximately 4% positive drift, there is a dip on the unload path at the 2/50 GM test that does not occur anywhere else. In particular, it does not occur in the cyclic tests or in the corresponding negative drift direction during the 2/50 GM test. The reason for this is not entirely clear, but may be related to the dynamic response during the PSD tests.

Another notable difference observed is that the stiffness of the analytical cyclic response is larger than the experimental PSD response. However, this is not unexpected as the analytical time-history analysis and the experimental PSD results showed similar results (as well as analytical and experimental comparisons of the free vibration tests in Section 9.6). Additionally, it is observed that the boundary frame stiffness of the analytical model is larger than the boundary frame test specimen; this indicates that the differences in analytical and experimental results presented are also partly due to the modeling of the boundary frame itself (i.e., they are not only dependent on the assumed properties of the nonlinear model of the infill web plate). Finally, similar to the PSD tests, also observed is the strength degradation of the experimental base shear versus roof drift response; an indication of the infill web plate tearing from the boundary frame. Except for the noted differences, contrary to the analytical dynamic time-history comparisons, the static analyses provide global response results that compare reasonably well to the experimental.

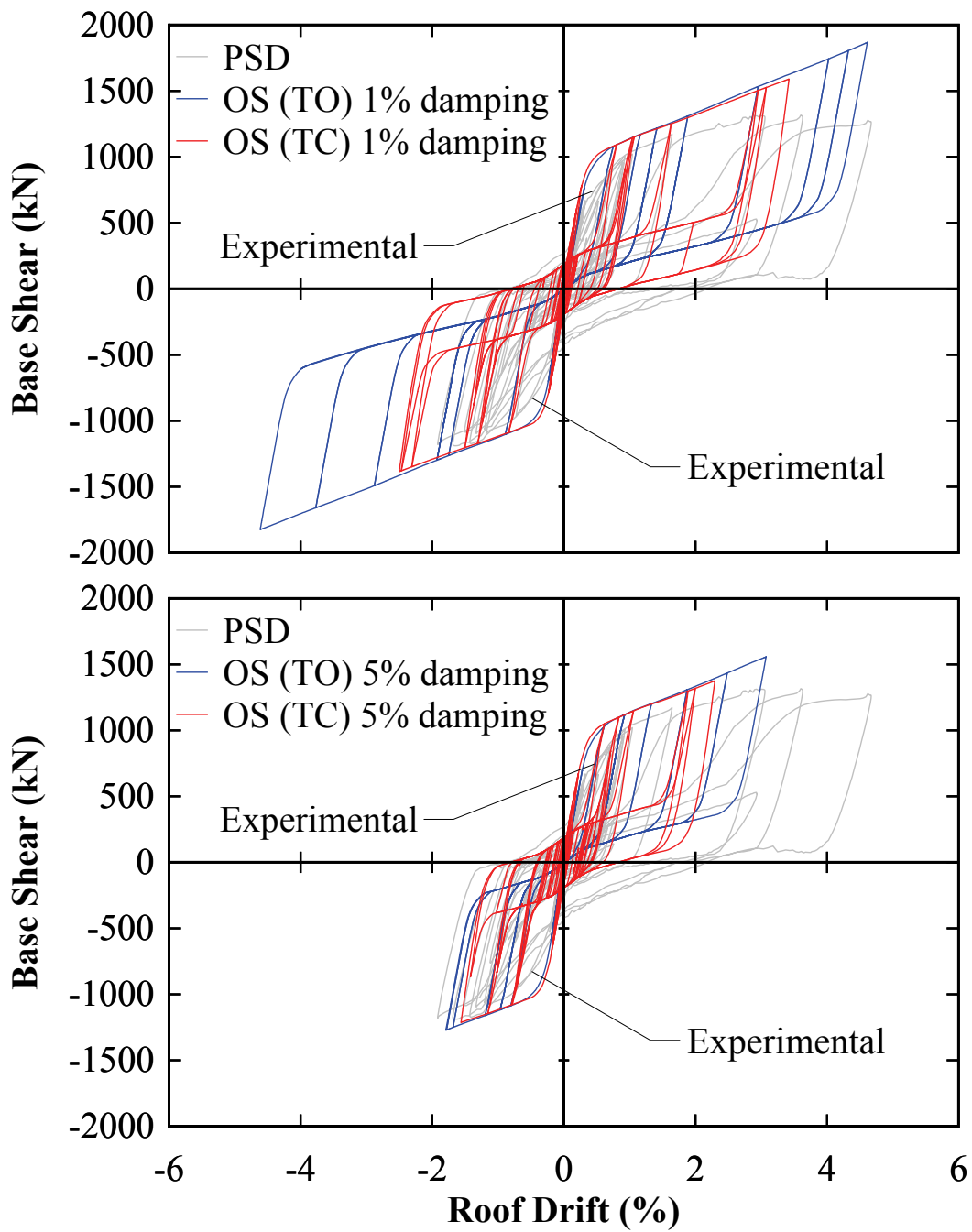


**FIGURE 9-39 PSD global response: experimental versus analytical**

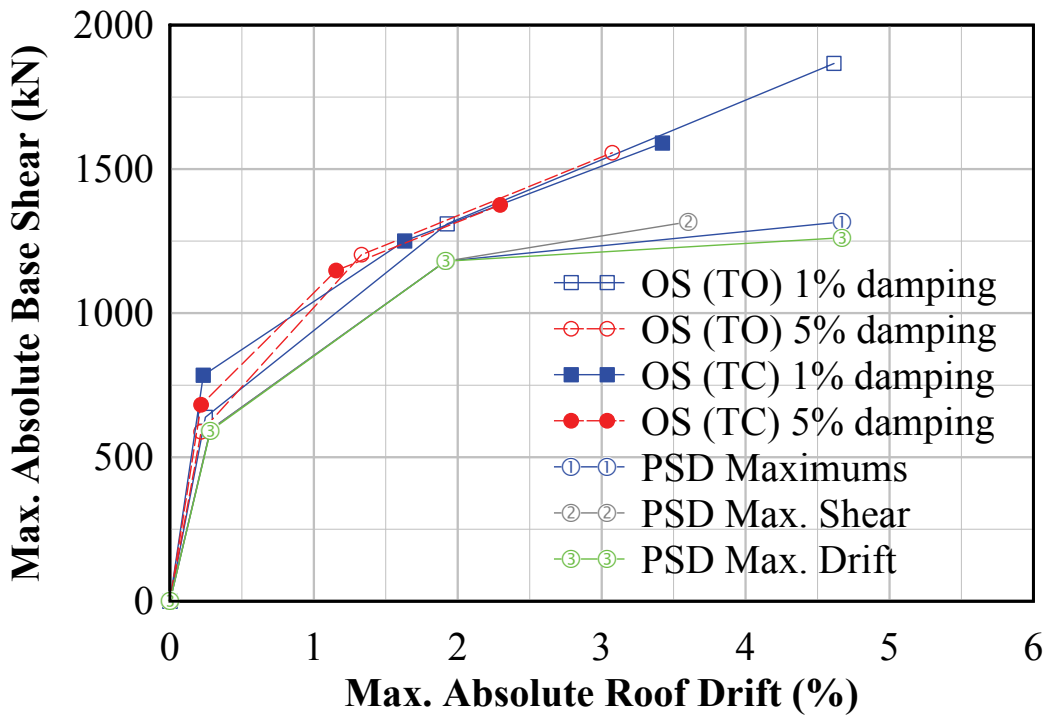


FIGURE 9-40 Incremental dynamic response: experimental versus analytical

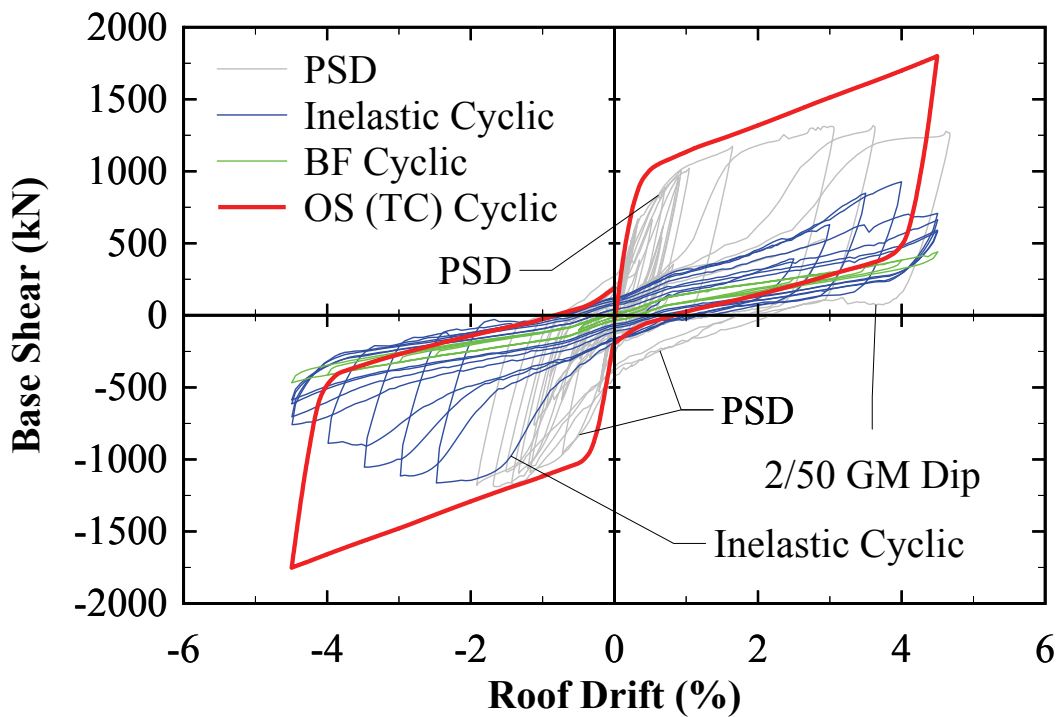


FIGURE 9-41 Cyclic pushover response: experimental versus analytical

## 9.11 PT Boundary Frame Expansion – Derivation of Beam-Growth

In the experimental results using the NewZ-BREAKSS rocking connection, as mentioned above, separation of the HBE from the VBE was observed. Although this flange separation was not detrimental to the response of the SC-SPSW system, it was puzzling. Further investigation (reported in this section) determined that this phenomenon was due to expansion of the PT boundary frame (i.e., beam-growth), as explained below.

Even though the NewZ-BREAKSS rocking connection was developed to eliminate beam-growth by having only a single HBE flange in contact to the VBE at each frame joint, it remains that the NewZ-BREAKSS connection can rock about the top and bottom edge of that HBE flange, and since it is a rocking mechanism, beam-growth will develop. Compared to connections that rock about both the top and bottom HBE flanges, the magnitude of beam-growth is significantly less and frames with flexible VBEs may be able to bend sufficiently to accommodate beam-growth affects and prevent separation of the HBE-to-VBE flange. For stiff VBEs, this may not be the case (as it was for the Specimen NZ test).

The combination of rigid frame behavior, presence of beam-growth and loss in HBE-to-VBE PT clamping force at the closing joint resulted in the HBE-to-VBE flange separation observed during the tests. Even for the bare frame tests, beam-growth effects were also observed, albeit at large drifts. Given that the infill web plate was removed in those tests, this confirms that for frames with HBE-to-VBE rocking connections, beam-growth is a function of the boundary frame geometry and its associated kinematics during drift.

At first, a graphical approach (by drawing to scale using computer aided drafting) followed to check this behavior, and the resulting frame geometry of the test specimen is shown in figure 9-42 at 4.5% roof drift. Note that the frame in its deformed position shown assumes rigid frame behavior, ignores PT force effects on the frame, and the HBEs only move in the horizontal direction. It then follows, for the Eastward drift shown in Fig 9.42, that the rotation at the West VBE and East VBE will differ by an incremental amount  $\Delta\theta$  as a result of beam-growth where the additional parameters in the figure are defined as follows:  $\theta$  is the VBE rotation at a known drift level;  $h1$  and  $h2$  are the heights from the VBE base to the lower rocking contact point of

interest on the middle and top HBE, respectively, and;  $D1$  and  $D2$  are the rocking depth lever arm of the middle and top HBE, respectively. Consequently, as a result of beam-growth and for conditions noted earlier, the graphical approach confirms complete separation of the HBE-to-VBE flange at the top HBE closing joint. At this location, the graphical solution indicates that the gap above and below the top flange of that HBE should be approximately 7 mm and 4 mm, respectively. In figure 9-13, values of approximately 8 mm and 3 mm were measured during the PSD tests at 4.5% drift, which is in good agreement with the values obtained graphically.

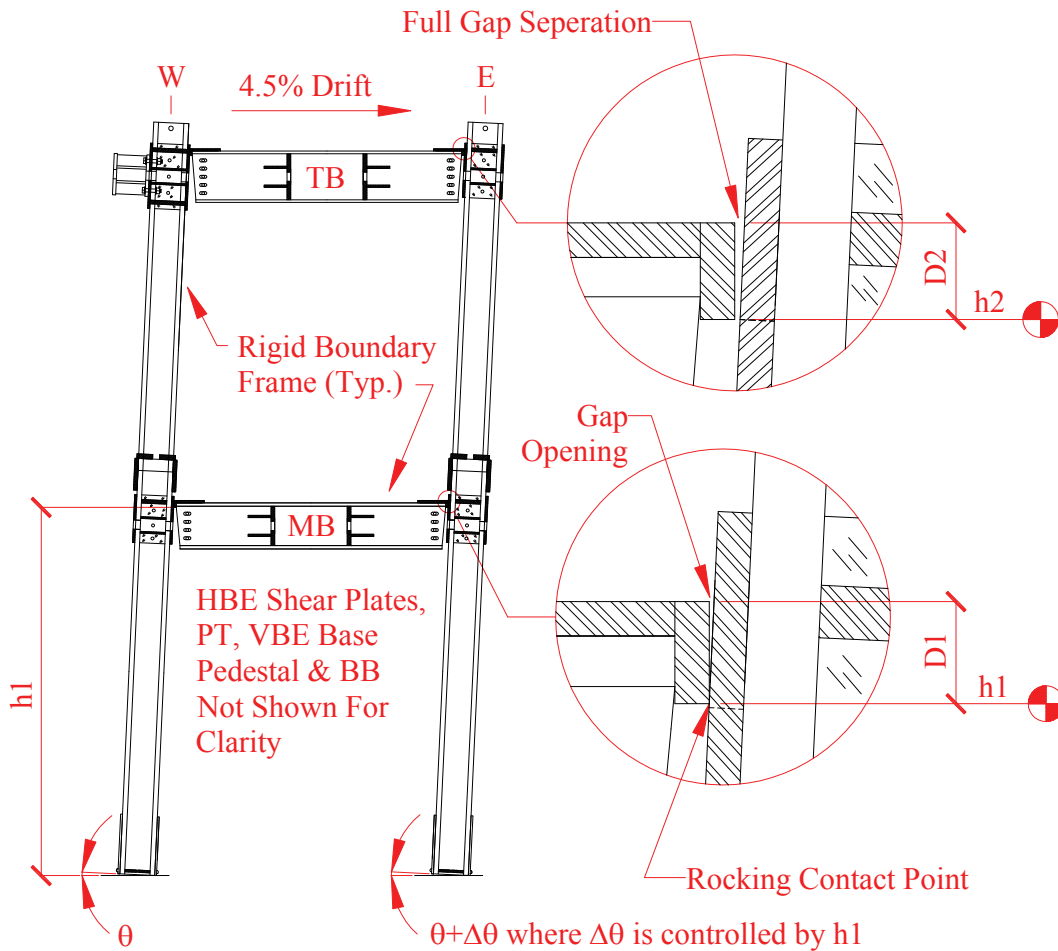


**FIGURE 9-42 Frame beam-growth schematic**

More practical from a design perspective, analytical formulations were developed to provide the same results directly from calculations. The relationship for beam-growth demand can be obtained by reviewing the free-body-diagram shown in figure 9-43 where:  $h1$  is the height from



the VBE base to the bottom most rocking contact point of interest;  $L_{HBE}$  is the length of the HBE;  $\Delta L1$  is the horizontal length due to drift rotation  $\theta$ ;  $\Delta L2$  is the horizontal length due to the drift gap opening  $\theta$  at the opening joint,  $d_{VBE}$  is the depth of the VBE which is shown in a position before and after rotation of the VBE;  $DI$  is the flange rocking depth rotation lever arm;  $\Delta V$ ,  $\Delta H1$  and  $\Delta H2$  are incremental dimensions dependent on the VBE base rotation at the VBE location effected by  $\theta+\Delta\theta$ ;  $x$  is the length parameter used to define  $\theta+\Delta\theta$  for subsequent derivation. From the parameters defined, the quantity  $\Delta H2$  is the key parameter needed to define the real relationship of beam-growth (for the conditions noted above) and represents the change in length reduction in the bottom of the parallelogram that takes into account the VBE base rotation  $\theta+\Delta\theta$ .

Note that the subsequent derivation is based on using a two-story frame with NewZ-BREAKSS rocking connections for illustration purposes. However, the formulations can be applied to a frame of any height and any rocking connection because: a) the height just above ground level controls the kinematic equations, and b) the parameter associated with the type of rocking connection affecting beam-growth is only dependent on the depth of the rocking point rotation lever arm. Additionally, in this analytical approach, the following simplifications and assumptions was made: 1) the boundary frame is taken as rigid members; 2) the rocking contact points are at the extreme edge of the HBE-to-VBE flange bearing point shown by the “Rocking Contact Point” indicated in figure 9-43; 3) local deformation effects at the rocking contact points are neglected; 4) elevation of the HBEs remain unchanged for a given VBE rotation during drift; 5) the HBE-to-VBE joints are frictionless and no PT clamping force is present allowing the joint to rotate and move freely, and; 6) at each VBE location, the line created by joining the points of HBE flange rocking and VBE base rocking points are parallel to the longitudinal axis of the associated VBE.

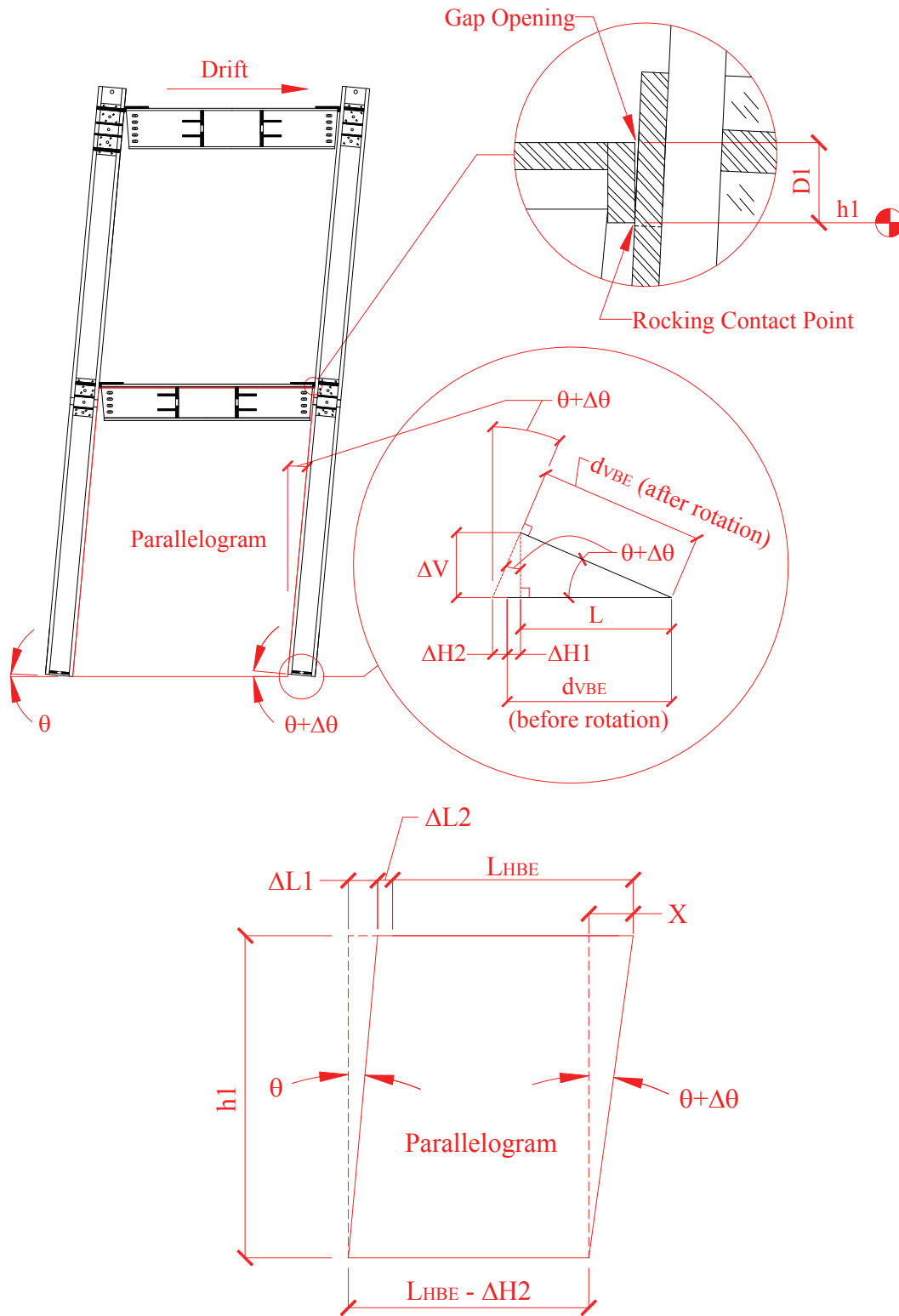


**FIGURE 9-43** Frame beam-growth kinematics

The formulation of a relationship for beam-growth first requires the development of an equation for the incremental VBE rotation  $\Delta\theta$ . This proceeds by first obtaining all of the incremental dimensions at the base of the affected VBE shown in the close-up detail in figure 9-43. It then follows, from geometry, the vertical displacement at the VBE flange due to rotation is:

$$\Delta V = d_{VBE} [\sin(\theta + \Delta\theta)] \quad (9-1)$$

Next, the length of the horizontal projection of the base of the rotated VBE is found to be:

$$L = d_{VBE} [\cos(\theta + \Delta\theta)] \quad (9-2)$$

The additional unknown parameter needed to completely define the kinematics at the base of the VBE is  $\Delta H$ . Derivation of the expression for this term is done in three steps. First,  $\Delta H$  is equal to the sum of  $\Delta H1$  and  $\Delta H2$  such that:

$$\Delta H = \Delta H1 + \Delta H2 \quad (9-3)$$

second, expanding (9-3) into an expression in terms of  $\tan\theta$  shown directly in figure 9-43 leads to:

$$\Delta H = (\Delta V) [\tan(\theta + \Delta\theta)] \quad (9-4)$$

third, substituting (9-1) into (9-4) leads to:

$$\Delta H = d_{VBE} [\tan(\theta + \Delta\theta) \sin(\theta + \Delta\theta)] \quad (9-5)$$

Towards derivation of an expression for  $\Delta\theta$ , the horizontal projection of the base of the rotated VBE extending beyond the footprint of the VBE prior to rotation needs to be established (i.e.,  $\Delta H2$ ), which can be calculated as:

$$\begin{aligned}\Delta H2 &= (\Delta H + L) - d_{VBE} \\ &= d_{VBE} \left[ \tan(\theta + \Delta\theta) \sin(\theta + \Delta\theta) + \cos(\theta + \Delta\theta) - 1 \right]\end{aligned}\quad (9-6)$$

It is observed that the inside surface of the deformed frame displacement can be bounded by a parallelogram from which the geometry  $\theta + \Delta\theta$  can be determined, from which  $\Delta\theta$  can then be calculated for any known value of  $\theta$  (i.e., typically by selecting a target drift). From the free-body-diagram of the parallelogram in figure 9-43 for all remaining derivation steps, it follows:

The horizontal length due to frame drift is:

$$\Delta L1 = h1(\tan \theta) \quad (9-7)$$

The incremental horizontal length due to HBE-to-VBE gap opening is:

$$\Delta L2 = D1(\tan \theta) \quad (9-8)$$

Next, solving for  $\tan(\theta + \Delta\theta)$  and substituting (9-6), (9-7) and (9-8) for  $\Delta H2$ ,  $\Delta L1$  and  $\Delta L2$ , respectively, into (9-9) leads to:

$$\begin{aligned}\tan(\theta + \Delta\theta) &= \frac{x}{h1} \\ &= \frac{(\Delta L1 + \Delta L2 + L_{HBE}) - (L_{HBE} - \Delta H2)}{h1} \\ &= \frac{\Delta L1 + \Delta L2 + \Delta H2}{h1} \\ &= \frac{(h1 + D1) [\tan(\theta)] + d_{VBE} [\tan(\theta + \Delta\theta) \sin(\theta + \Delta\theta) + \cos(\theta + \Delta\theta) - 1]}{h1}\end{aligned}\quad (9-9)$$

Solving (9-9) for  $\tan(\theta)$  leads to the following relationship defining beam-growth:

$$\tan(\theta) = \frac{\tan(\theta + \Delta\theta) [h1 - d_{VBE} \{ \sin(\theta + \Delta\theta) \}] + d_{VBE} [1 - \cos(\theta + \Delta\theta)]}{h1 + D1} \quad (9-10)$$

In the above equation, all parameters have been defined previously and are known except for  $\Delta\theta$ . One approach to solve (9-10) consists of iterating on the value of  $\Delta\theta$  until convergence. Once the parameter  $\Delta\theta$  is known, the beam-growth at each floor level can then be calculated.

Although the solution for  $\Delta\theta$  will converge fairly quickly, an alternate simplified formulation can be used that provides an approximate solution without iteration. It is obtained by realizing that the reduction in length of the bottom of the parallelogram due to  $\Delta H2$  (from the VBE base rotation) is insignificant. It then follows that, by letting  $\Delta H2 = 0$  in the above derivation, the expression for  $\tan(\theta + \Delta\theta)$  simplifies to:

$$\tan(\theta + \Delta\theta) \cong \frac{h1 + D1}{h1} [\tan(\theta)] \quad (9-11)$$

Given the insignificance of  $\Delta H2$ , the approximate solution to obtain  $\Delta\theta$  using (9-11) will be within a percent accuracy compared to that using the exact relationship shown in (9-10) that requires more computational effort. Once  $\Delta\theta$  is known the calculation of beam-growth demand at each level can be obtained. To illustrate the calculation of beam-growth and the distribution along the frame height, using the frame shown in figure 9-42 as an example, the calculations are made with the following assumptions:

- The story heights at each level are equal to  $h$ .
- The rocking depth  $D1 = D2 = D$ .
- The height to the bottom gap opening  $h1$  is equal to  $h$  to keep calculations simple for illustration purposes. This will lead to an approximate solution since  $h1$  at the ground level is actually  $h1 = h - D$  if story heights are equal.

The following calculations are then made:

- Step 1. Calculate the gap adjustment  $\delta = (\Delta\theta)(h1)$  due beam-growth at the middle HBE. Since the adjustment is required at the middle HBE level, the bottom of flange gap

opening is zero (i.e., in bearing contact with the VBE flange). The top of flange gap opening is equal to  $(D)(\theta+\Delta\theta)$ .

- Step 2. Calculate the gap openings at the top HBE. The bottom of flange gap is equal to  $(\Delta\theta)(2h)$ ; this represents the incremental gap opening required due to beam-growth. The top of flange gap is equal to  $(\Delta\theta)(2h)+(\theta+\Delta\theta)(D)$ ; the first component represents the incremental gap opening required due to beam-growth (also is the gap opening at the bottom of flange) and the latter component is the gap opening due to the joint rotation.

Note that if additional stories were present, beam-growth at each subsequent level above would increase proportional to the height of the bottom of flange level at that location only. For example, if there was an additional floor level in the example shown, the bottom of the flange gap would be equal to  $(\Delta\theta)(3h)$ , and the top of flange gap would equal to  $(\Delta\theta)(3h)+(\theta+\Delta\theta)(D)$ . That is the component due to the gap opening due to the joint rotation remains constant and only the incremental gap opening due to beam-growth increases with story height. Additionally, to capture the beam-growth behavior about the top flange in the analytical model response, the alternate HBE-to-VBE model presented in Section 8 would be required. However, this would be at the expense of additional computational run time, as a result of doubling the amount of nonlinear compression-only springs required to model the rocking behavior of the top flanges.

Two alternative modifications to the NewZ-BREAKSS rocking flange detail used in the test specimen could be made to further reduce the effects due to beam-growth observed in the experiments. A first modification would be to provide a semi-spherical bearing plate (similar to what was used at the base of the VBE for these tests) at the end of the HBE flange and reinforcement plates, as shown in figure 9-44a. This option would seek to completely eliminate beam-growth, and thus eliminate HBE-to-VBE flange separation. Alternatively, the second option would be to provide additional PT elements near the bottom of the top flange, as shown in figure 9-44b. This option would not eliminate beam-growth, but compensate for it by increasing the clamping force to reduce (maybe eliminate) HBE-to-VBE flange separation by bending the VBE's back into contact. An additional benefit of this latter option is that it would also increase the recentering potential of the PT boundary frame. A combination of both proposed

modifications presented could also both be incorporated, to further enhance the performance of the NewZ-BREAKSS connection.

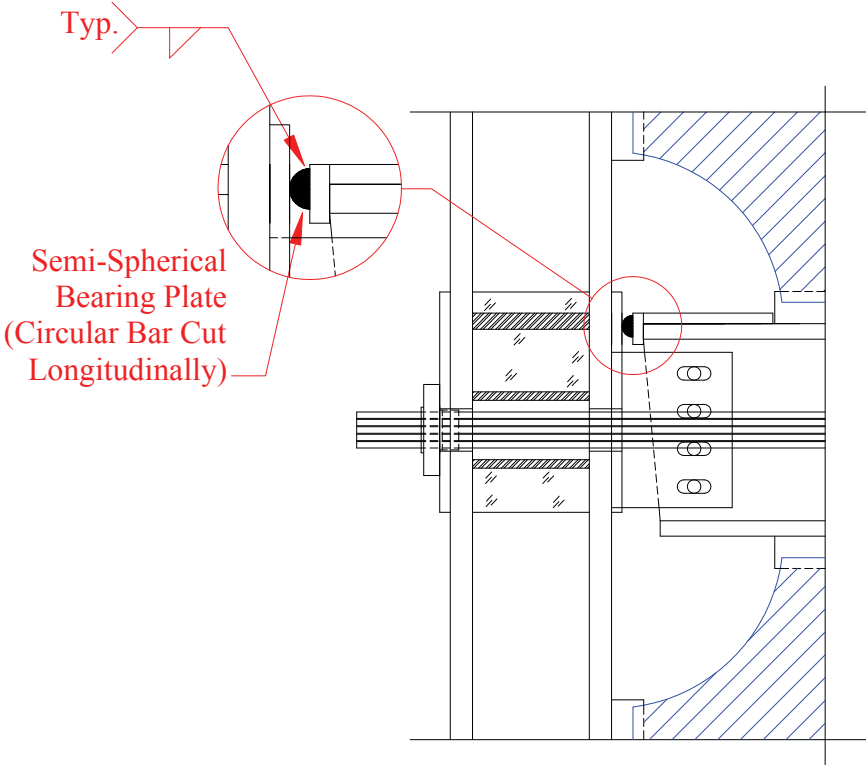


**FIGURE 9-44a NewZ-BREAKSS connection Alt. detail 1**

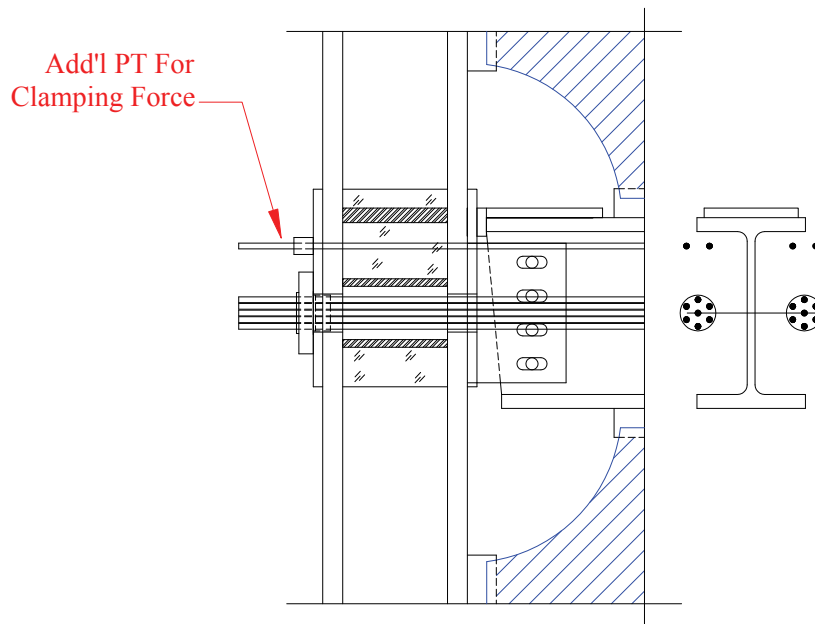


**FIGURE 9-44b NewZ-BREAKSS connection Alt. detail 2**

### **9.12 Comparison of UB Shake-Table and NCREE PSD Specimen Response**

It is of interest to compare results from the NCREE PSD tests with those from the UB shake-table tests. For this purpose, only the UB NewZ-BREAKSS specimen with infill web plate is considered (as results from all other UB shake-table test specimens cannot be compared due to detailing parameters that are not common with the NCREE specimen). The experimental incremental dynamic response curves, obtained for each specimen by creating an envelope of peak force-displacement values obtained from each earthquake excitation to which it was subjected, are shown in figure 9-45 for both test specimens. Note that for the UB curve, the label for each individual point represents the amplitude-scaled percent of the shake-table reference GM; for the NCREE curve, the labels used are those that have already been defined earlier. It is observed that the response of the two specimens differs significantly. In particular the normalized base shear demands are much higher and the roof drifts are much smaller for the UB specimen. To provide perspective on this difference in specimen response for the NCREE and UB tests, two key design parameters are identified.



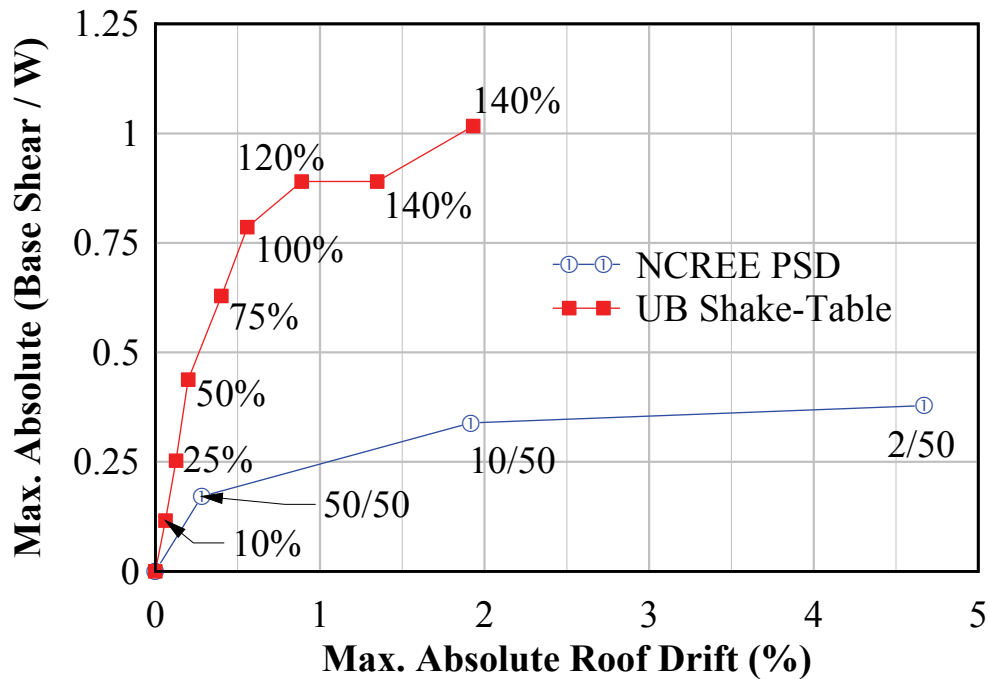


**FIGURE 9-45 UB versus NCREE - incremental dynamic response**

First, the Design Basis Earthquake (DBE) acceleration response spectra for which the selection of GMs was based on are compared. As shown in figure 9-46, for the elastic period range anticipated for both specimens, the maximum spectral acceleration demand for the UB specimen is approximately 50% larger than that for the NCREE specimen. Consequently, the GMs used between the two different test phases are not directly comparable (in that they target a much different spectral acceleration response), and in part contribute to the differences in specimen response observed between the two test phases.

Second, the prototype building parameters are significantly different between the two test phases. The NCREE specimen is based on the three-story SAC building but modified for a two-story frame (see Section 8.2). For the UB quasi-static tests, the specimens were also designed based on the three-story SAC building (see Section 4), but for the UB shake-table tests, while the quasi-static specimens were the same (i.e., were re-used by replacing their infill web plates), the prototype building to which they corresponded had to be modified based on the constraints of the existing test setup and capacity of the shake table (see Section 4.3.3). Of particular significance as a result of this, the tributary seismic mass of the prototype frame for the shake-table tests was

reduced compared to that for which the test specimens were originally designed (i.e., the frame tributary seismic mass was based on the three-story SAC building for the quasi-static tests, but not so anymore for the shake-table tests).

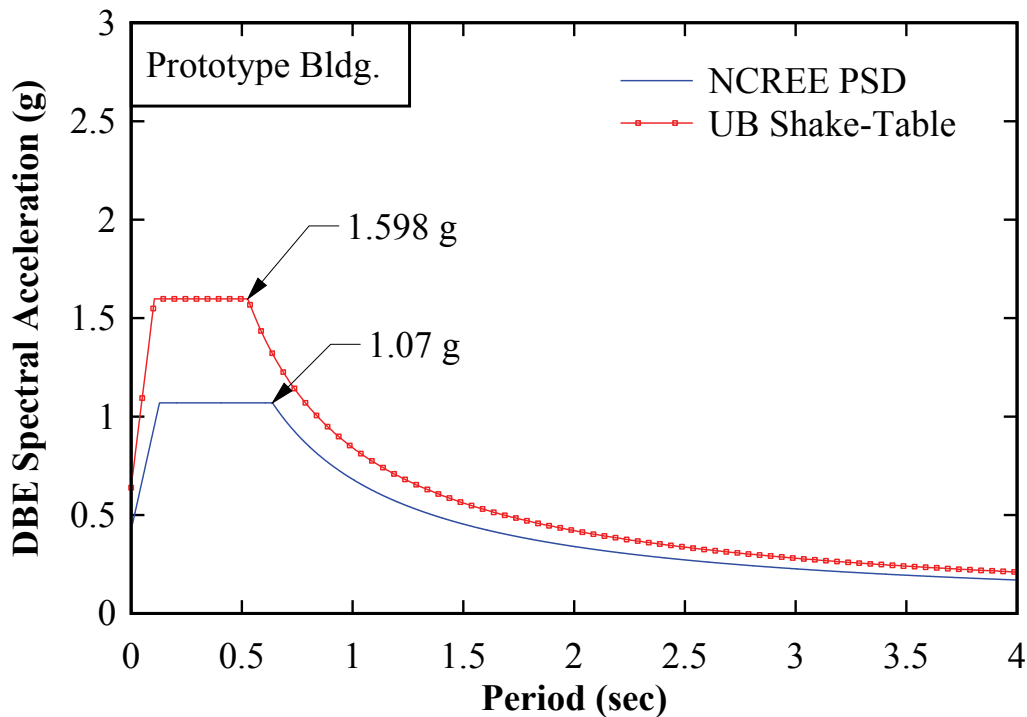


**FIGURE 9-46 UB versus NCREE - DBE response spectra**

To further clarify the effects of the prototype building parameters on the observed experimental results, an estimate of the actual response modification factor,  $R$ , can be obtained for each specimen by performing a spectral analysis (see Section 4.3.4); the results are shown in figure 9-47 and figure 9-48 for the NCREE and UB specimen respectively. Note that the spectral capacity curve shown is for the total capacity of the specimen. Also provided for reference are the spectral capacity curves for the individual contribution of the infill web plate and the PT bare frame; it can be seen that for SC-SPSWs, the capacity contribution of the PT boundary frame is not significant compared to that provided by the infill web plate. Additionally, for the NCREE test, only the 10/50 GM spectral demand is presented as this represents the design level earthquake. For the NCREE specimen, assuming 2% equivalent viscous damping, it is observed that  $R = 1.66/0.3 = 5.53$ . In contrast,  $R = 2.41/0.74 = 3.25$  for the UB specimen. In other words,

the estimated response modification factor of the NCREE specimen is approximately 1.7 that of the UB specimen. As a consequence, more inelastic action would be expected from the NCREE specimen, leading to larger drift demands and smaller base shears at those drifts (in proportion to the strength that would be required for elastic response). Likewise, the UB test specimen would be expected to respond with less severe inelastic response (compared to the NCREE specimen), leading to smaller drift demands and larger base shear demands (in proportion to the strength that would be required for elastic response). This largely explains the differences observed between the NCREE and UB shake-table tests.

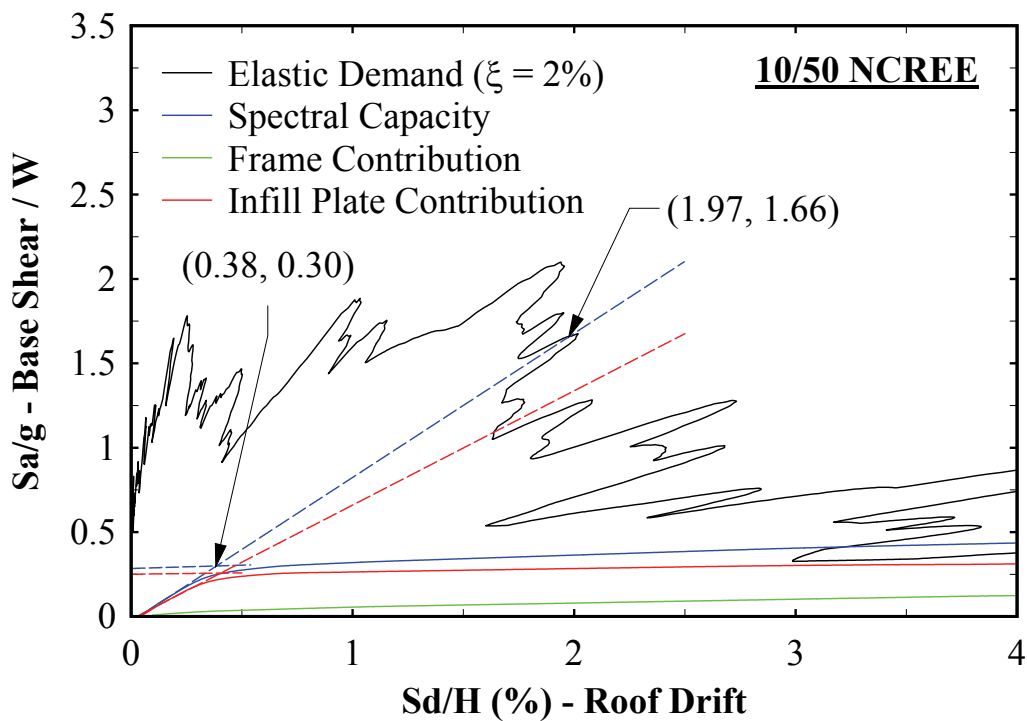
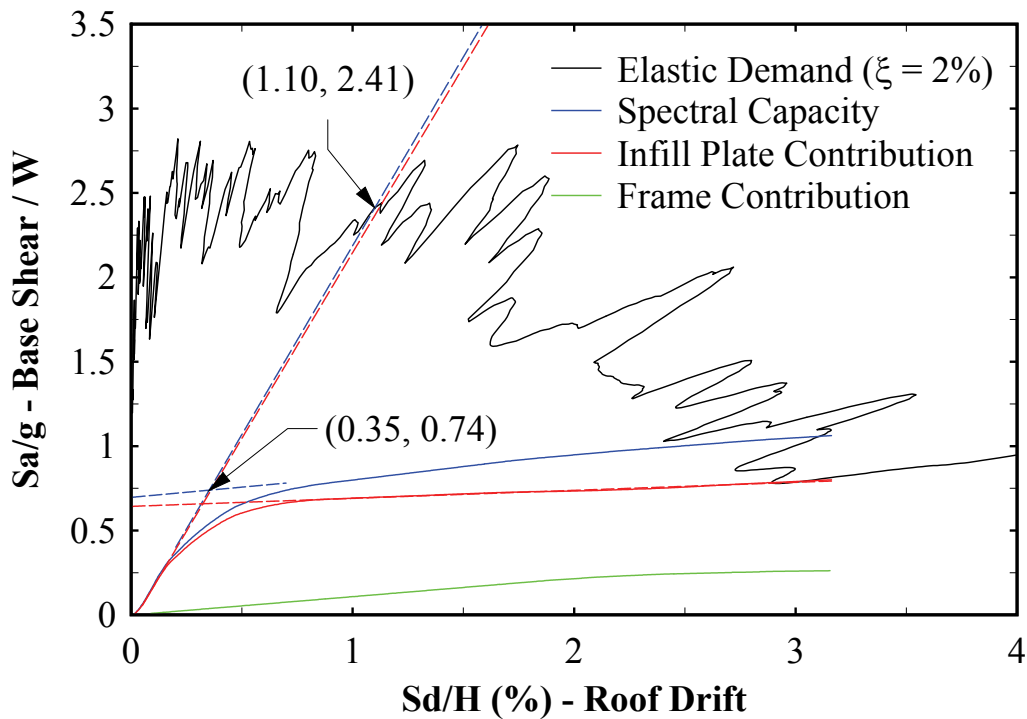


FIGURE 9-47 NCREE PSD spectral response



**FIGURE 9-48 UB shake-table spectral response (scaled specimen)**

### 9.13 Summary

The NCREE tests provided an additional proof-of-concept that SC-SPSW frames can be a viable lateral force resisting system. An alternative VBE PT base rocking connection was also investigated. These tests were conducted on a full-scale SC-SPSW specimen subjected to multiple seismic hazard levels for buildings in areas of high seismicity using the PSD testing procedure. The test specimen met all target performance objectives. In particular, similarly to what was observed in the UB shake-table tests, recentering was found to occur and wasn't affected by the temporary compression stiffening of the infill web plate, contrary to what had been observed in prior static tests. Additional knowledge on the fundamental behavior of the NewZ-BREAKSS rocking connection was gained with respect to possible beam-growth effects. This has led to a better understanding of beam-growth, equations that could be used to inform design, and optional alternate details that could be used to further enhance the NewZ-BREAKSS connection.

## SECTION 10

### SUMMARY, CONCLUSIONS, AND RECOMMENDATIONS

#### 10.1 Summary

An innovative self-centering steel plate shear wall (SC-SPSW) has been proposed. The SC-SPSW combines the advantages of high initial stiffness and substantial energy dissipation provided by SPSW infill web plates, provides frame self-centering capability through the use of post-tensioned (PT) rocking frame joint connections, and concentrates hysteretic energy dissipation to replaceable infill web plates. Unlike conventional LFRS where cumulative inelastic deformations could lead to significant residual drifts and hysteretic energy dissipation elements are not necessarily easy to replace after they have yielded, the proposed SC-SPSW is intended to self-center and concentrates hysteretic energy to easily replaceable infill web plates only, allowing the SC-SPSW to recover to its near pre-earthquake condition, after a moderate to significant earthquake.

Three different HBE-to-VBE joint connections were investigated for the beam (i.e., HBE) and column (i.e., VBE) joint connections of the boundary frame of the SC-SPSW. Namely, an HBE-to-VBE joint that: 1) rocks about the top and bottom HBE flanges; 2) rocks about the HBE centerline, and; 3) rocks about the HBE top flanges only (called the NewZ-BREAKSS connection), and abbreviated as the FR, CR, and NZ connection/frame for short. The latter two connections, CR and NZ, were investigated to eliminate beam-growth (i.e., PT frame expansion) that is associated with the FR connection. Based on capacity design principles, the kinematics of each SC-SPSW configuration was investigated assuming full yielding of infill web plates and elastic rigid body response of the PT boundary frame, leading to fundamental closed-form equations based on detailed free body diagrams. More specifically:

- Expressions that describe the moment, shear, and axial demands along the length of the HBES has been provided. Also related, expressions were derived for the PT force response considering the interaction of the axial stiffness of the PT elements with consideration of flexible HBES (i.e., PT force losses due to axial shortening).

- An expression describing the infill web plate tensile strains due to frame drift has been provided, considering the fact that an HBE-to-VBE rocking connection increases the tensile strains on the infill web plate. That is, in addition to the tensile strains resulting from a panel sway yield mechanism, compounding strain effects are also present due to the formation of a gap at the HBE-to-VBE joint. Use of a corner cut-out in the infill plate is essential at the HBE-to-VBE joint detail to avoid large tensile strains at the infill web plate corner locations, which could lead to a premature un-zippering effect of the infill web plate tearing from the boundary frame; the equations provided account for this behavior. Comparisons made using the derived equation with experimental results from the UB shake-table and NCREE PSD tests, were in good agreement.
- An expression describing the effects of beam-growth for boundary frames detailed with rocking connections has been provided. This equation predicts the amount of beam-growth that could occur along the height of the frame, if no restraining effects are present (i.e., diaphragm restraint, PT clamping force, etc.). With an understanding of the potential beam-growth demands by calculation, this information could be used to determine the additional interstory deformations on the VBEs for design. Furthermore, the calculated values could also be used to facilitate design and detailing of diaphragm connections for frames with rocking joints susceptible to beam-growth effects.

A multi-facility experimental program was developed and conducted to validate the SC-SPSW behavior. For this purpose, one-third scale three-story frames were tested at the Structural Engineering and Earthquake Simulation Laboratory (SEESL) at the University at Buffalo (UB) and conducted in two phases. First, a total of nine quasi-static cyclic tests were conducted consisting of the FR, CR and NZ frames with three configurations each (i.e., infill web plate, PT boundary frame only, and infill web strips). Secondly, a total of seven dynamic shake-table tests were conducted consisting of the FR and NZ frames with three configurations for the FR frame and four configurations for the NZ frame. All configurations matched that of the quasi-static tests, except for the fourth configuration of the NZ frame that consisted of a bolted perforated infill web plate at Level 1 (Levels 2 & 3 remained unchanged from previous infill web plate configurations); this fourth configuration was investigated in collaboration with researchers at the Ecole Polytechnique of Montreal. A final complementary test was performed at the National

Center for Research on Earthquake Engineering (NCREE) in Taiwan, where a full scale single-bay two-story specimen, detailed with the NewZ-BREAKSS connection, was subjected to an earthquake excitation loading using the pseudo-dynamic testing method. This frame also used an alternative VBE PT base rocking connection.

Analytical models were developed in both SAP2000 and OpenSees. The former is a commercially available software program used in common practice by design professionals. The latter is an open-source code mainly used by the research community. The fundamental equations presented for HBE strength demands were validated by nonlinear pushover analyses of simple frames. These equations (describing the moment, shear, and axial demands along the length of HBEs) also provided a means to check the analytical computer models. Pushover analyses were conducted identifying differences in frame response between the PT boundary frames detailed with different HBE-to-VBE rocking joints along with parametric pushover analyses investigating the effects due to the PT parameters (i.e., total number of strands, the initial PT force provided, etc.). Similar analyses were conducted for PT boundary frames with a VBE PT base rocking connection. Nonlinear static cyclic and nonlinear time history analyses were conducted and compared with experimental results. These latter analytical models included a tension-only hysteretic model for the infill web plate (typically assumed for modeling of SPSWs) and a tension-compression hysteretic model that includes some compression strength of the infill web plate.

## **10.2 Conclusions**

The experimental results show that SC-SPSWs systems can be a viable alternative LFRS appropriate for buildings in regions of high seismicity. The quasi-static tests provided behavior differences between the infill web strip and infill web plate configurations, as well as with the response of the PT boundary frame by itself. Some key highlights from these quasi-static cyclic tests are presented as follows:

- 1) In general, infill web plate separation from the boundary frame started to develop at approximately 2% roof drift (a drift magnitude expected for a design level earthquake), propagating from the plate corners. This provides some indication that the  $R/d$  ratio of

1.0 (see Fig. 3.86) used in the HBE-to-VBE joint detail for the infill web plate corners, performed reasonably well to delay the effects of initial web plate tearing from the boundary frame.

- 2) It was observed that some compression strength is developed by the infill web plates due to the random folding of the plate as it is pushed through the zero drift point after some cycles. This compression strength, by calibration with analytical models and experimental results, was found to be approximately 10% of the yield strength of the infill web plate. Note that an additional 10% compression strength was found to be needed (for a total of 20% used in the analytical model) to accurately model the experimental response, and attributed to the effect of friction between the various parts of the specimens, and between these specimens and their experimental set-up. In particular, it was observed that this compression strength contributes to energy dissipation during repeated drift cycles (contrary to the tension-only behavior typically assumed). However, the compression strength observed has an effect on frame re-centering for static cyclic loadings (although does not have any significant effect on recentering under dynamic earthquake excitations as indicated below).
- 3) Infill web strips essentially behaved as tension-only members. Furthermore, infill web strips were not susceptible to tearing from the boundary frame compared to infill web plates (e.g., roof drifts up to 9% were achieved without tearing). It was also observed that infill web strips only provided energy dissipation for increased axial yielding beyond the previous inelastic excursion, in a characteristic tension-only behavior. As expected for SC-SPSW with infills having this tension-only behavior, recentering was achieved.
- 4) Compared to frame FR and NZ, frame CR was more susceptible to unbalanced PT force effects (as a result of PT force losses) due to the inherent instability of the HBE-to-VBE pinned joints in the absence of PT elements. As a consequence, larger residual drifts could occur for frame CR if the PT force at each end of the HBEs is significantly unbalanced.
- 5) The PT boundary frame(s) remained essentially elastic. Between test setups, only the infill web plates/strips were removed and replaced for subsequent tests. This validated the structural fuse concept for this system (i.e., reusability of the PT boundary frame and the use of replaceable hysteretic energy dissipating elements).



The shake-table tests conducted have provided key insights into the seismic response of SC-SPSW systems. In particular, recentering was found to not be sensitive to the compression stiffening of the infill web plate, contrary to what had been initially observed during the static tests. Frame recentering was achieved for all shake-table tests conducted. In part, this is because of the many smaller cycles of excitations that follow the larger cycles after temporary compression strut effect developed (i.e., due to the buckled plate taking the form of a sort of corrugated shape when drifts exceed previously achieved values). Furthermore, it was shown that an alternative bolted connection with a perforated infill web plate to the boundary frame could be incorporated in the SC-SPSW when relying on the clamping force of bolts to connect thin infill plates. It was also observed that the compression strut effect of a solid infill web plate was reduced by providing perforated holes in the web plate. Additionally, no bolt slip was observed in this specimen having perforated infill web plate bolted to the boundary frame.

The NCREE test provided an additional proof-of-concept that SC-SPSW systems can be a viable LFRS for earthquake loadings. Similar to what was observed in the UB shake-table tests, the PT boundary frame remained essentially elastic and recentering was achieved. Additionally, through this full scale test, it was observed that some beam-growth does develop for the NewZ-BREAKSS rocking connection, contrary to what was initially assumed (although significantly reduced compared to other rocking connections, such as that used for frame FR). This has led to a better understanding of beam-growth; equations that could be used to inform design were developed, and optional modifications to the NewZ-BREAKSS detail were proposed to eliminate beam-growth effects.

### **10.3 Recommendations for Future Research**

Detailed free body diagrams developed and presented in this report provide valuable insights on the basic fundamental kinematic behavior of SC-SPSWs. Along with the fundamental equations presented (suitable for use as design tools) and results of the experimental investigation, much information on the behavior of SC-SPSWs has been provided. These are initial steps towards practical implementation. However, much remains to be done. Some possible areas of further research are presented below.

- a) **Beam-Growth Free Connections and Diaphragm Interaction:** The CR and NZ connections investigated in this research are intended to eliminate diaphragm interaction effects; but their effectiveness for that purpose remains to be validated through experiments. Experimental system testing of SC-SPSWs detailed with these connections, including effects of slab diaphragm restraint, would be informative. Additionally, the research results from the NCREE full scale test showed that the NZ connection did develop some beam-growth, which led to a suggested modified NZ connection having a semi-spherical end bearing plate located at the HBE flange rocking point. This modification should eliminate the beam-growth observed with the original detail. However, experimental testing is required to validate this.
- b) **Alternative VBE Base Connections:** In developing an alternate LFRS that is essentially damage free, with the exception of the replaceable infill web plates, the base of the VBEs were detailed with pinned connections (to ensure plastic hinging does not develop at those locations) in the current research presented. However, this requires non-standard detailing. To facilitate the use of more conventional detailing, alternative VBE base connections could be explored through experimental and analytical investigation, using semi-rigid to rigid base connections representative of “typical” LFRS column base connections. In doing so, particular attention would need to be given to the effect on frame recentering and implications on the reduced resiliency of the SC-SPSW should yielding occur (or be allowed) at the base of the VBEs.
- c) **Alternative Post-Tension Material:** The use of fiber reinforced polymers (FRP) PT reinforcement as an alternative to conventional PT steel strands could be explored. FRP has a lower modulus of elasticity than steel, allowing for larger axial tensile strains. This would benefit the NZ and CR frames in particular, as the PT strands are much shorter than those for the FR frame. Additionally, FRP is corrosion resistant, which could be appealing in certain applications.
- d) **Improvements to Current Strip Modeling Techniques:** This research revealed that solid infill web plates do not exhibit a purely tension-only behavior (as typically assumed in common analyses of SPSWs). The experimental results show that frame recentering is not significantly affected by this for earthquake loadings. Although analytical results were presented, including some compression effects of the infill web plate, the modeling

technique used assumed a constant compression strength, which does not necessarily reflect the actual inelastic response of the infill web plate. Future research could further investigate whether improvements on analytical strip models are necessary from a research or design perspective, and the potential significance on seismic performance of the new uniaxial material models recently proposed by other researchers (based on limited calibration of cyclic tests and finite element analyses). Substantiated evidence validating these newly proposed material definitions compared with experimental results with frames subjected to dynamic earthquake loadings would be desirable.

- e) **Finite Element Modeling on Local Response:** There were several localized phenomena that were observed from the experimental results, including: particular strain response at the ends of the HBEs at the HBE-to-VBE flange rocking points, infill web plate tensile strain distribution, and effects leading to tearing of the infill web plate from the boundary frame. Finite element models could be developed to better understand these localized phenomena.
- f) **Determination of Seismic Performance Factors:** In order to facilitate potential implementation into future code standards, a FEMA P695 study would need to be performed for the proposed SC-SPSW, with consideration of different archetype frames (i.e., different panel aspect ratios, number of stories, etc.), to evaluate the appropriate seismic performance factors (i.e.,  $R$ ,  $\Omega_o$ , and  $C_d$ ) for consideration by future editions of ASCE-7. Additionally, it would be desirable to perform such analyses for all three HBE-to-VBE rocking joints investigated in this research for comparison.



## SECTION 11

### REFERENCES

AISC (2005a). "Specification for Structural Steel Buildings." ANSI/AISC 360-05, American Institute of Steel Construction, Chicago, IL.

AISC (2005b). "Seismic Provisions for Structural Steel Buildings." ANSI/AISC 341-05, American Institute of Steel Construction, Chicago, IL.

AISC (2010a). "Specification for Structural Steel Buildings." ANSI/AISC 360-10, American Institute of Steel Construction, Chicago, IL.

AISC (2010b). "Seismic Provisions for Structural Steel Buildings." ANSI/AISC 341-10, American Institute of Steel Construction, Chicago, IL.

ASCE (2010). "Minimum Design Loads for Buildings and Other Structures." ASCE/SEI 7-10. American Society of Civil Engineers, Reston, VA.

American Society for Testing and Materials (ASTM). "Standard Methods for Tension Testing of Metallic Materials." *ASTM Designation E8*.

ATC (1992). "Guidelines for Seismic Testing of Components of Steel Structures." Applied Technology Council, Report 24.

Berman, J. W., and Bruneau, M. (2003). "Plastic Analysis and Design of Steel Plate Shear Walls." *Journal of Structural Engineering*, ASCE, Vol. 129, No. 11, pp. 1448-1456.

Berman, J., and Bruneau, M. (2008). "Capacity Design of Vertical Boundary Elements in Steel Plate Shear Walls." *Engineering Journal*, AISC, First Quarter pp. 57-71.

Bruneau, M., Uang, C. M., and Sabelli, R. (2011). "Ductile Design of Steel Structures, 2nd Edition", McGraw-Hill, New York, NY.

Cheok, G., and Lew, H. (1991). "Performance of 1/3-Scale Model Precast Concrete Beam-Column Connections Subjected to Cyclic Inelastic Loads – Report No. 2." *NISTIR 4589*, National Institute of Standards and Technology, NIST, Gaithersburg, MD, June.

Cheok, G., Stone, W.C., and Lew, H. (1993). "Performance of 1/3-Scale Model Precast Concrete Beam-Column Connections Subjected to Cyclic Inelastic Loads – Report No. 3." *NISTIR 5246*, National Institute of Standards and Technology, NIST, Gaithersburg, MD, August.

Cheok, G., and Stone, W.C. (1994). "Performance of 1/3-Scale Model Precast Concrete Beam-Column Connections Subjected to Cyclic Inelastic Loads – Report No. 4." *NISTIR 5436*, National Institute of Standards and Technology, NIST, Gaithersburg, MD, June.

Chi, H., and Liu, J. (2012). "Seismic Behavior of Post-Tensioned Column Base for Steel Self-Centering Moment-Resisting Frame." *Journal of Constructional Steel Research*, 78, pp. 117-130.

Chopra, A.K. (2007). "Earthquake dynamics of structures: Theory and Applications to Earthquake Engineering", 3rd Ed., Prentice Hall, Upper saddle River, NJ.

Christopoulos, C. (2002). "Self-Centering Post-Tensioned Energy Dissipating (PTED) Steel Frames for Seismic Regions", Ph.D. dissertation, Department of Structural Engineering, University of California San Diego, La Jolla, CA.

Christopoulos, C., Filiatrault, A., Uang, C.M., and Folz, B. (2002). "Posttensioned Energy Dissipating Connections for Moment-Resisting Steel Frame." *Journal of Structural Engineering*, ASCE, Vol. 128, No. 9, pp. 1111-1120.

Christopoulos, C., Tremblay, R., Kim, H.-J., and Lacerte, M. (2008). "Self-Centering Energy Dissipative Bracing System for the Seismic Resistance of Structures: Development and Validation." *Journal of Structural Engineering*, ASCE, Vol. 134, No. 1, pp. 96-107.

Clayton, P.M., Berman, J.W., and Lowes, L.N. (2012). "Seismic Design and Performance of Self-Centering Steel Plate Shear Walls." *Journal of Structural Engineering*, ASCE, Vol. 138, No. 1, pp. 22-30.

Clayton, P.M. (2013). "Self-centering Steel Plate Shear Wall: Subassembly and Full-scale Testing." Ph.D. dissertation, Dept. of Civil and Environmental Engineering, University of Washington, Seattle, WA.

Clifton, G.C. (1996). "Development of Perimeter Moment-Resisting Steel Frames Incorporating Semi-Rigid Elastic Joints", New Zealand National Society for Earthquake Engineering Conference, 1996; pp. 177-184.

Clifton, G.C. (2005). "Semi-Rigid Joints for Moment Resisting Steel Framed Seismic Resisting Systems." Ph.D. dissertation, Department of Civil and Environmental Engineering, University of Auckland, New Zealand.

Clifton, G. C., MacRae, G. A., Mackinven, H., Pampanin, S., and Butterworth, J. (2007). "Sliding Hinge Joints and Subassemblies for Steel Moment Frames", Proceedings of the New Zealand Society of Earthquake Engineering Annual Conference, Paper 19, Palmerston North, New Zealand.

CSA (2009), Design of Steel Structures, CAN/CSA-S16-09, Canadian Standards Association, Willowdale, Ontario, Canada.

CSI (2009). "SAP2000: Static and Dynamic Finite Element Analysis of Structures (Version 14.1.0)," Computers and Structures Inc., Berkeley, CA.

- Dowden, D.M., and Bruneau, M. (2011). "NewZ-BREAKSS: Post-tensioned Rocking Connection Detail Free of Beam Growth." *Engineering Journal*, AISC, Second Quarter, pp. 153-158.
- Dowden, D.M., Purba, R., and Bruneau, M. (2012). "Behavior of Self-centering Steel Plate Shear Walls and Design Considerations." *Journal of Structural Engineering*, ASCE, Vol. 138, No. 1, pp. 11-21.
- Driver, R. G., Kulak, G. L., Kennedy, D. J. L., and Elwi, A. E. (1997). "Seismic Behavior of Steel Plate Shear Walls." *Structural Engineering Report 215*, Department of Civil Engineering, University of Alberta, Edmonton, Alberta, Canada.
- Driver, R. G., Kulak, G. L., Kennedy, D. J. L., and Elwi, A. E. (1998). "Cyclic Tests of Four-Story Steel Plate Shear Wall." *Journal of Structural Engineering*, ASCE, Vol. 124, No. 2, pp. 112-120.
- FEMA (2000). "State of the Art Report on Systems Performance of Steel Moment Frames Subject to Earthquake Ground Shaking." *Rep. No. 355c*, SAC Joint Venture for the Federal Emergency Management Agency, Washington, D.C.
- Garlock, M. (2002). "Design, Analysis, and Experimental Behavior of Seismic Resistant Post-Tensioned Steel Moment Frames." Ph.D. dissertation, Department of Civil and Environmental Engineering, Lehigh University, Bethlehem, PA.
- Garlock, M., Ricles J.M., and Sause R. (2003). "Cyclic Load Tests and Analysis of Bolted Top-and-Seat Angle Connections." *Journal of Structural Engineering*, ASCE, Vol. 129, No. 12, pp. 1615-1625.
- Garlock, M., Ricles J.M., and Sause R. (2005). "Experimental Studies of Full-Scale Posttensioned Steel Connections." *Journal of Structural Engineering*, ASCE, Vol. 131, No. 3, pp. 438-448.
- Garlock, M., and Li, J. (2008). "Steel Self-Centering Moment Frames with Collector Beam Floor Diaphragms", *Journal of Constructional Steel Research*, Vol. 64, No. 5, pp. 526-538.
- Iyama, J., Seo, C-Y., Ricles, J., and Sause R. (2009). "Self-centering MRFs with bottom flange friction devices under earthquake loading", *Journal of Constructional Steel Research*, Vol. 65, pp. 314-325.
- Kim, H.-J., and Christopoulos, C. (2008). "Friction Damped Posttensioned Self-Centering Steel Moment-Resisting Frames." *Journal of Structural Engineering*, ASCE, Vol. 134, No. 11, pp. 1768-1779.
- Kim, H.-J., and Christopoulos, C. (2009). "Seismic Design Procedure and Seismic Response of Post-tensioned Self-centering Steel Frames." *Earthquake Engineering and Structural Dynamics*, Vol. 38, pp. 355-376.

- Kulak, G.L., Kennedy, D.J.L., Driver, R.G., and Medhekar, M. (2001). "Steel Plate Shear Walls – An Overview." *Engineering Journal*, AISC, Vol. 38, No. 1, pp. 50-62.
- Kusumastuti, D. (2005). "A Versatile Experimentation Model for Study of Structures Near Collapse: Applications to Seismic Evaluation of Irregular Structures." PhD dissertation, Dept. of Civil and Environmental Engineering, University at Buffalo, Buffalo, NY.
- Li, C.-H., Lee, H.-C., Tsai, K.-C., and Lin, C.-H. (2012). "Experimental Investigation on Seismic Behavior and Design of Bottom Boundary Column in Steel Plate Shear Walls." Proc., 15th World Conference on Earthquake Engineering, Lisbon, Portugal.
- Lubell, A.S., Prion, H.G.L., Ventura, C.E., and Rezai, M. (2000). "Unstiffened Steel Plate Shear Wall Performance Under Cyclic Loading." *Journal of Structural Engineering*, ASCE, Vol. 126, No. 4, pp. 453-460.
- MacRae, G.A., and Priestley, M.J.N. (1994). "Precast Post-tensioned UngROUTED Concrete Beam-Column Subassemblage Tests." Structural System Research Report, *SSRP 94/10*, University of California at San Diego, La Jolla, CA, 124 pp.
- MacRae, G.A., Clifton, G.C., Mackinven, H., Mago, N., Butterworth, J., and Pampanin, S. (2008). "The Sliding Hinge Joint Moment Connection." *Bulletin of the New Zealand Society for Earthquake Engineering*, Vol. 43, No. 3, pp. 202-212.
- Mazzoni, S., McKenna, F., Scott, M.H., and Fenves, G.L. (2009). *Open system for earthquake engineering simulation user command-language manual – OpenSees version 2.0*, Pacific Earthquake Engineering Research Center, University of California, Berkeley, Berkeley, CA.
- Mesa, A.D.A. (2010). "Developments of Advanced Solutions for Seismic Resisting Precast Concrete Frames." Ph.D. dissertation, Department of Civil and Natural Resources Engineering, University of Canterbury, Christchurch, New Zealand.
- Newmark, N.M. (1959). "A Method of Computation for Structural Dynamics." *Journal of Engineering Mechanics*, Vol. 85, No. 3, pp. 67-94.
- Pampanin, S., Priestley, M.J.N., and Sritharan, S. (1999). "Frame Direction Modeling of the Five-Story PRESSS precast tall building." *Rep. No. SSRP 99/20*, University of California San Diego, La Jolla, CA.
- Papageorgiou, A., Halldorsson, B., and Dong, G. (1999). "Target Acceleration Spectra Compatible Time Histories." *TARSCHTHS-User's manual*, Engineering Seismology Laboratory, State University of New York, Buffalo, NY.
- Petty, G.D. (1999). "Evaluation of a Friction Component for a Post-tensioned Steel Connection." M.S. thesis, Department of Civil and Environmental Engineering, Lehigh University, Bethlehem, PA.



Qu, B., Bruneau, M., Lin, C.H., and Tsai, K.C. (2008). "Testing of Full Scale Two-story Steel Plate Shear Walls with Reduced Beam Section Connections and Composite Floors." *Journal of Structural Engineering*, ASCE, Vol. 134, No. 3, pp. 364-373.

Reinhorn, A.M. (1997). "Inelastic Analysis Techniques in Seismic Evaluation." "Seismic Design Methodologies for the Next Generation of Codes", P. Fajfar & H. Krawinkler eds., Balkema, Rotterdam.

Ricles J.M., Sause R., Peng, S., and Lu, L. (2002). "Experimental Evaluation of Earthquake Resistant Posttensioned Steel Connections." *Journal of Structural Engineering*, ASCE, Vol. 128, No. 7, pp. 850-859.

Rojas, P.R. (2003). "Seismic Analysis, Design, and Evaluation of Post-Tensioned Friction Damped Connections for Steel Moment Resisting Frames." Ph.D. Thesis, Department of Civil and Environmental Engineering, Lehigh University, Bethlehem, PA.

Rojas, P., Ricles, J.M., and Sause, R. (2005). "Seismic Performance of Post-tensioned Steel Moment Resisting Frames With Friction Devices." *Journal of Structural Engineering*, ASCE, Vol. 131, No. 4, pp. 529-540.

Sabelli, R., and Bruneau, M., (2007). "Steel Plate Shear Walls." AISC Steel Design Guide 20, American Institute of Steel Construction, Inc., Chicago, Ill.

Shishkin, J.J., Driver, R.G., and Grondin, G.Y. (2005). "Analysis of Steel Plate Shear Walls Using the Modified Strip Model." *Structural Engineering Report No. 261*, Department of Civil Engineering, University of Alberta, Edmonton, Alberta, Canada.

Shishkin, J.J., Driver, R.G., and Grondin, G.Y. (2009). "Analysis of Steel Plate Shear Walls Using the Modified Strip Model." *Journal of Structural Engineering*, ASCE, Vol. 135, No. 11, pp. 1357-1366.

Sritharan, S., Priestley, M.J.N., Seible, F., and Igarashi, A. (2000). "A Five-Story Precast Concrete Test Building for Seismic Conditions - Overview." Proc., 12th World Conference on Earthquake Engineering, Auckland, New Zealand.

Stanton, J.F., Stone, W.C., and Cheok, G.S. (1997). "A Hybrid Reinforced Frame for Seismic Regions." *PCI Journal*, Vol. 42, No. 2, pp. 20-32.

Thorburn, L.J., Kulak, G.L., and Montgomery, C.J. (1983). "Analysis of Steel Plate Shear Walls." *Structural Engineering Report No. 107*, Department of Civil Engineering, University of Alberta, Edmonton, Alberta, Canada.

Timler, P.A., and Kulak, G.L. (1983). "Experimental Study of Steel Plate Shear Walls." *Structural Engineering Report No. 114*, Department of Civil Engineering, University of Alberta, Edmonton, Alberta, Canada.

Timler, P.A., Ventura, C.E., Prion, H., and Anjam, R. (1998). "Experimental and Analytical Studies of Steel Plate Shear Walls as Applied to the Design of Tall Buildings." *Struct. Des. Tall Build.*, 7, pp. 233-249.

Tsai, K.C., Lin, C.H., Lin, Y.C., Hsieh, W.D., and Qu, B. (2006). "Substructural Hybrid Tests of Full Scale Two-story Steel Plate Shear Wall." *Technical Report NCREE-06-017*, National Center for Research on Earthquake Engineering. Taipei, Taiwan (in Chinese).

Vargas, R.E. (2006). "Analytical and Experimental Investigation of the Structural Fuse Concept." Ph.D. dissertation, Dept. of Civil and Environmental Engineering, University at Buffalo, Buffalo, NY.

Vian, D., and Bruneau, M. (2005). "Steel Plate Shear Walls for Seismic Design and Retrofit of Building Structures." *Tech. Rep. No. MCEER-05-0010*, Multidisciplinary Center for Earthquake Engineering Research, State Univ. of New York at Buffalo, Buffalo, NY.

Wagner, H. (1931). "Flat Sheet Metal Girders with Very Thin Webs, Part III: Sheet Metal Girders with Spars Resistant to Bending – The Stress in Uprights – Diagonal Tension Fields." *Technical Memorandum No. 606*, National Advisory Committee for Aeronautics, Washington, D.C.

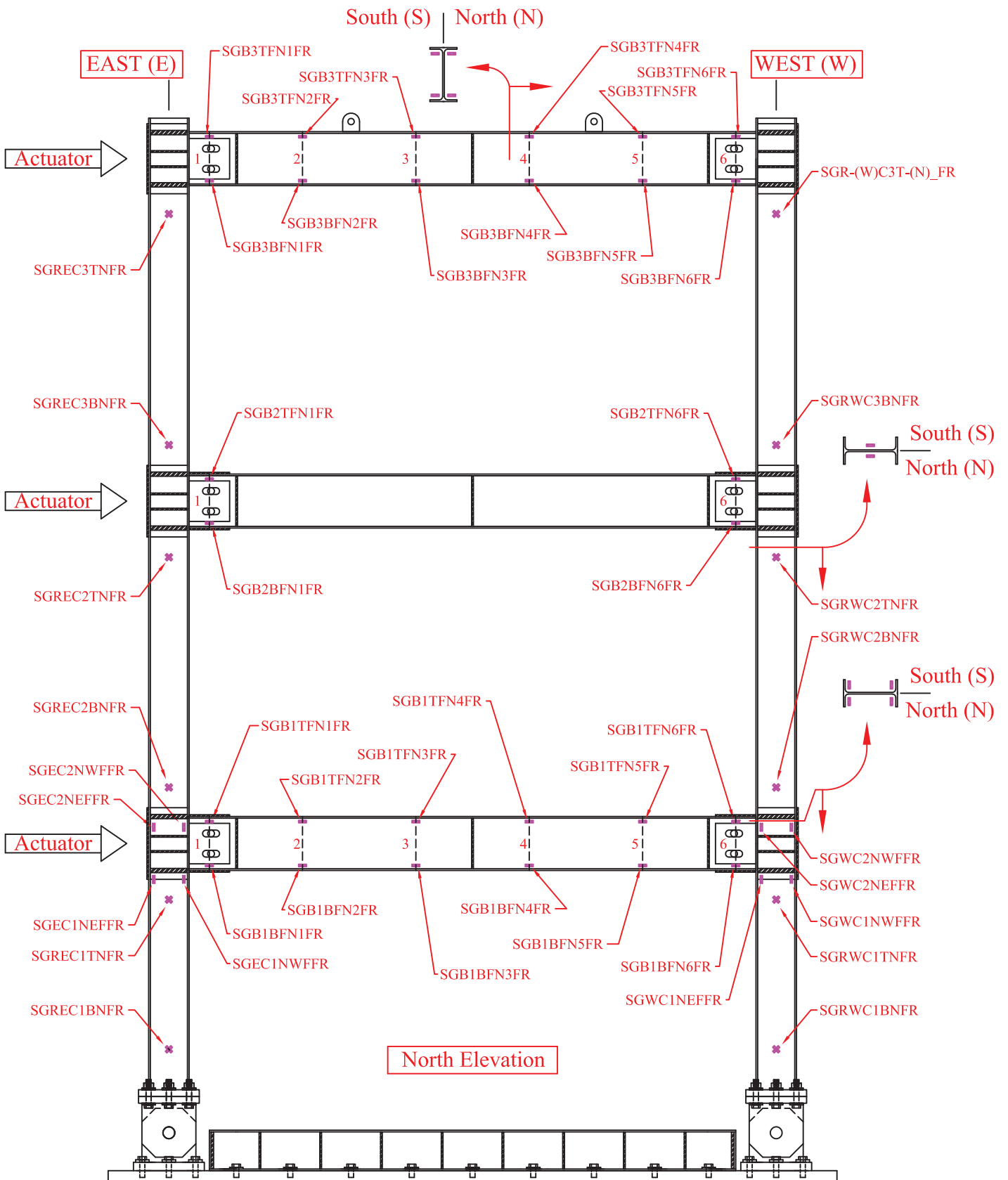
Webster, D.J. (2013). "The Behavior of Un-stiffened Steel Plate Shear Wall Web Plates and their Impact on the Vertical Boundary Elements." Ph.D. dissertation, Dept. of Civil and Environmental Engineering, University of Washington, Seattle, WA.

Winkley, T.B. (2011). "Self-centering Steel Plate Shear Walls: Large Scale Experimental Investigation." M.S. thesis, Dept. of Civil and Environmental Engineering, University of Washington, Seattle, WA.

Wolski, M., Ricles, J.M., and Sause, R. (2009). "Experimental Study of a Self-Centering Beam-Column Connection with Bottom Flange Friction Device." *Journal of Structural Engineering*, ASCE, Vol. 135, No. 5, pp. 479-488.

## **APPENDIX A1**

### **QUASI-STATIC TESTING INSTRUMENTATION DRAWINGS**



**LEGEND:**

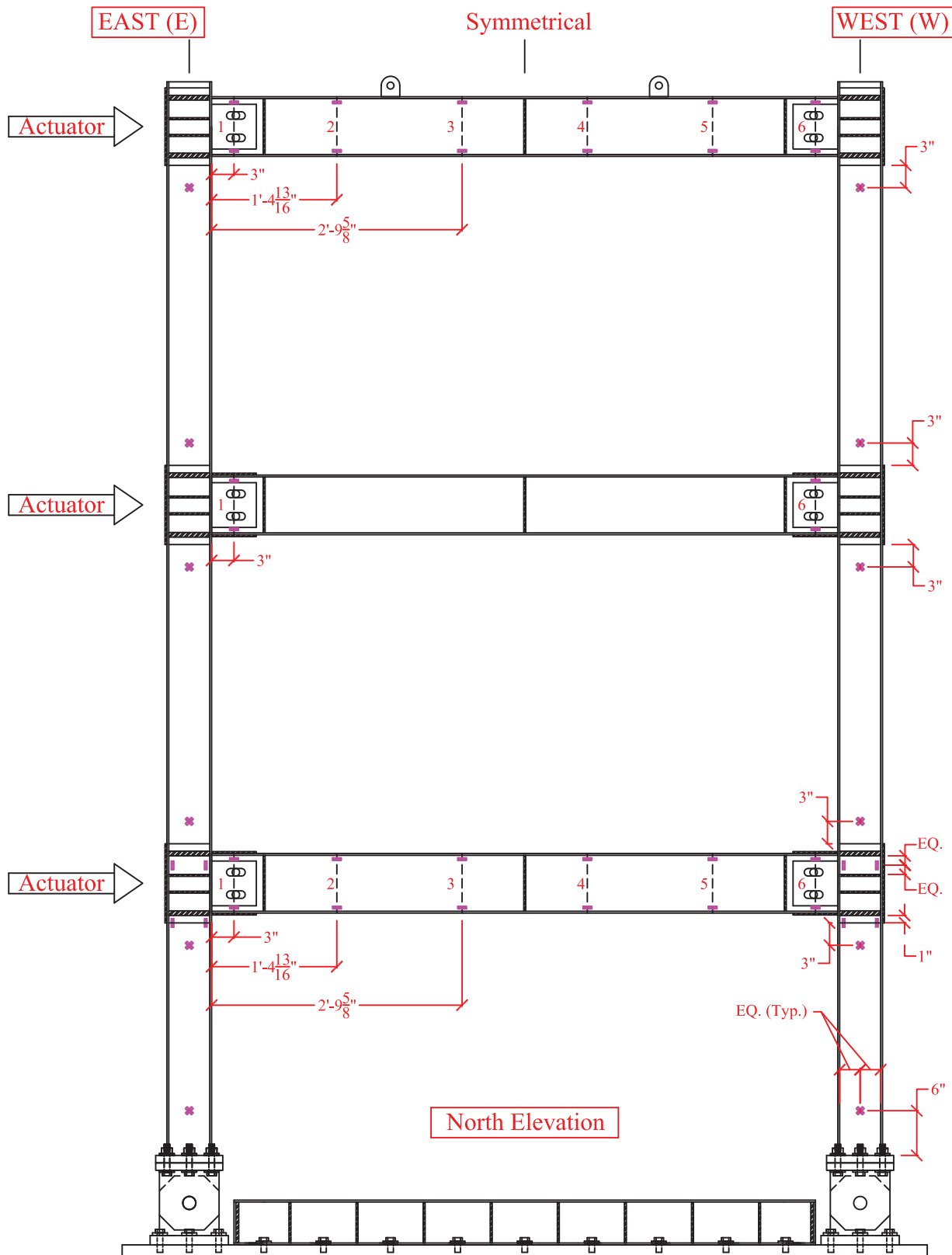
- Uniaxial Strain Gage (SG)
- \* Shear Rosette Strain Gage (SGR)

**NOTE:**

All Strain Gages On Steel Frame Are To Be Self-Temperature-Compensated (S-T-C)

588

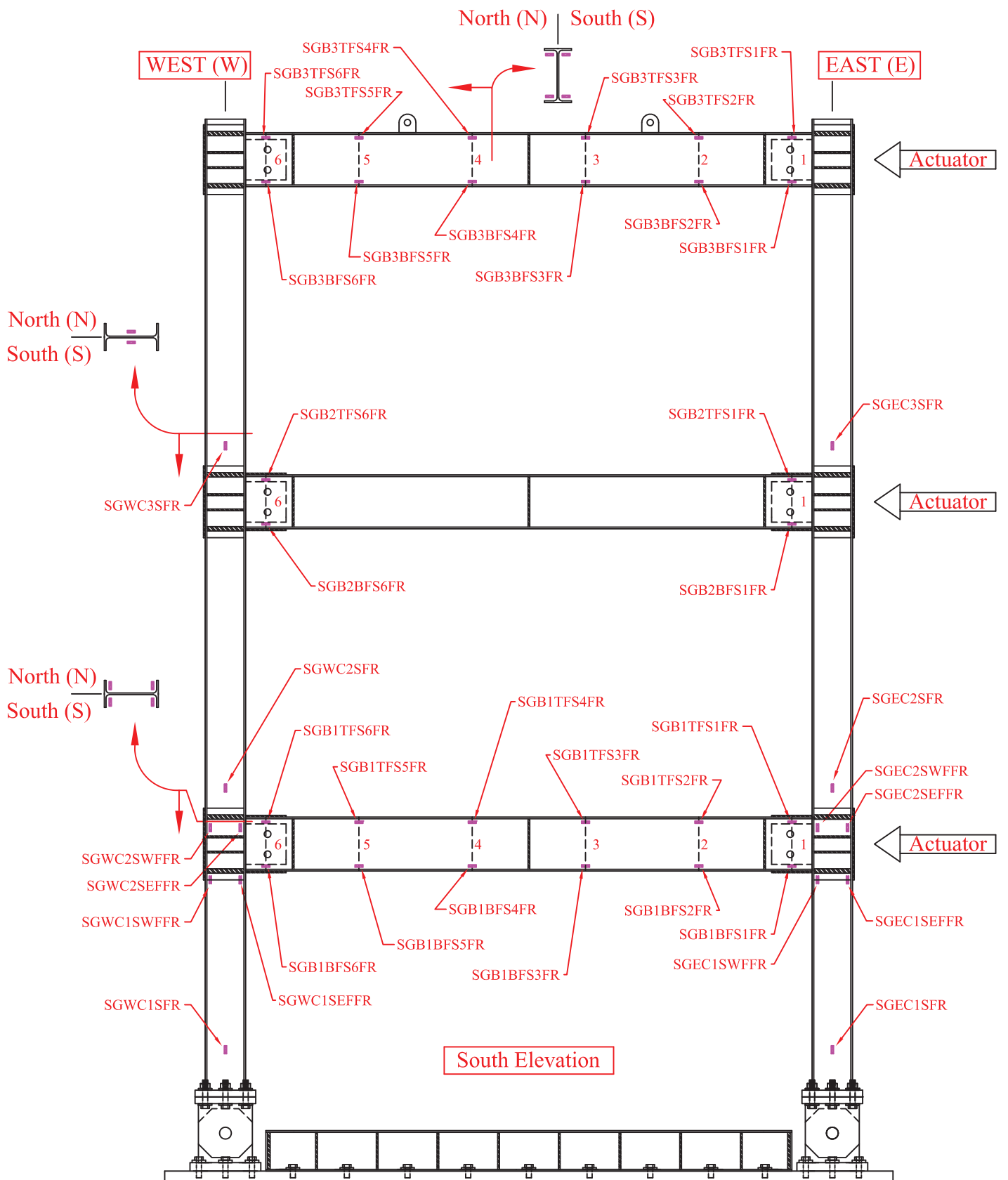
<b>University at Buffalo</b>			<b>DRWG:</b>
<b>PROJECT:</b> NEESR-SG Self-Centering Steel Plate Shear Walls		<b>CONTENT:</b> Boundary Frame 1 Strain Gages	1-1a/11
<b>BY:</b> Daniel M. Dowden	<b>REVISION:</b>	<b>DATE:</b>	<b>SCALE:</b> 3/5" = 1'-0"



**LEGEND:**

- Uniaxial Strain Gage (SG)
- \* Shear Rosette Strain Gage (SGR)

<b>University at Buffalo</b>			<b>DRWG:</b>
<b>PROJECT:</b> NEESR-SG Self-Centering Steel Plate Shear Walls		<b>CONTENT:</b> BF-1 Strain Gage Dims.	1-1a dim/11
<b>BY:</b> Daniel M. Dowden	<b>REVISION:</b>	<b>DATE:</b>	<b>SCALE:</b> 3/5" = 1'-0"



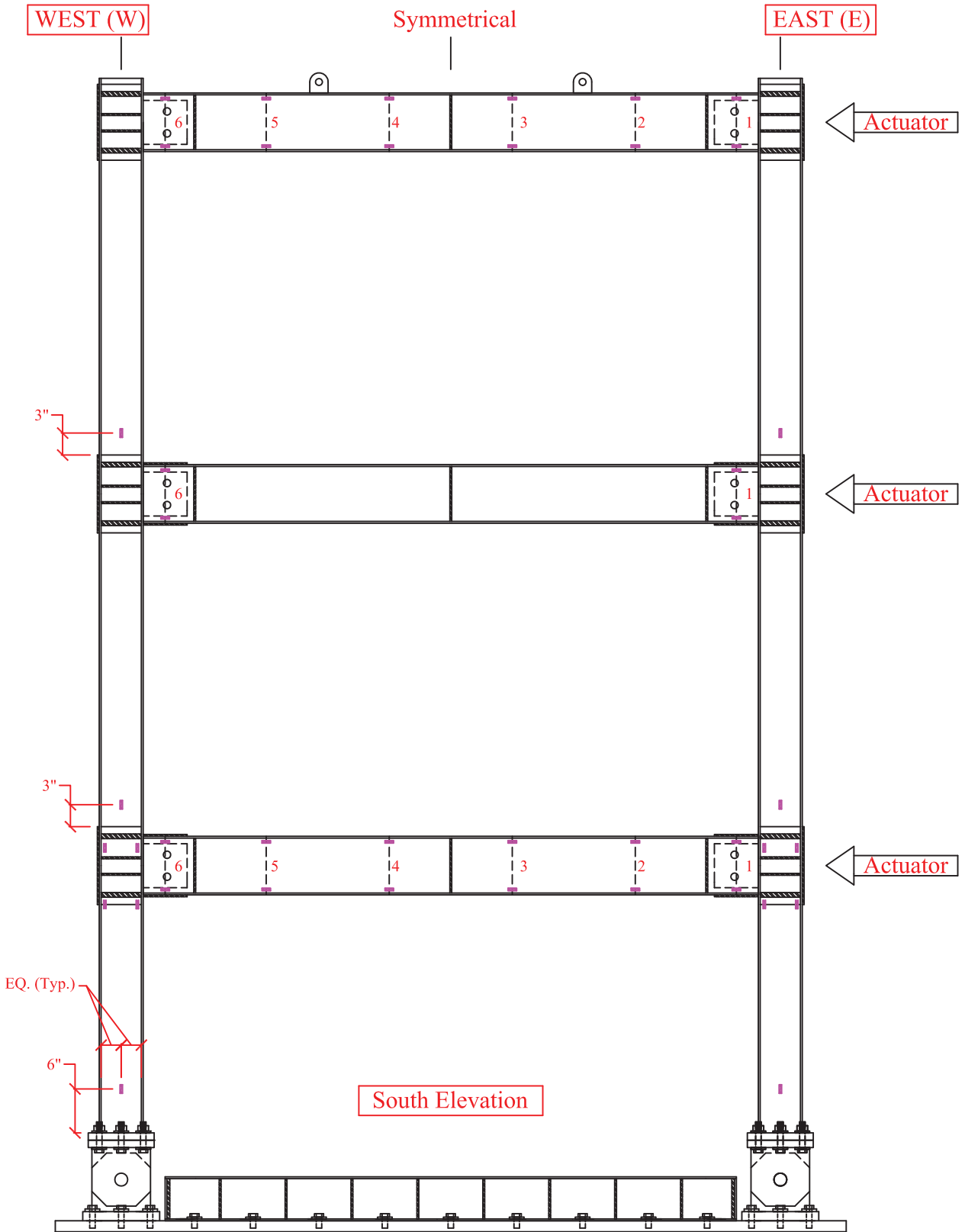
**LEGEND:**

- Uniaxial Strain Gage (SG)

**NOTE:**

All Strain Gages On Steel Frame Are To Be Self-Temperature-Compensated (S-T-C)

<b>University at Buffalo</b>			<b>DRWG:</b>
<b>PROJECT:</b> NEESR-SG Self-Centering Steel Plate Shear Walls		<b>CONTENT:</b> Boundary Frame 1 Strain Gages	1-1b/11
<b>BY:</b> Daniel M. Dowden	<b>REVISION:</b>	<b>DATE:</b>	<b>SCALE:</b> 3/5" = 1'-0"



**LEGEND:**

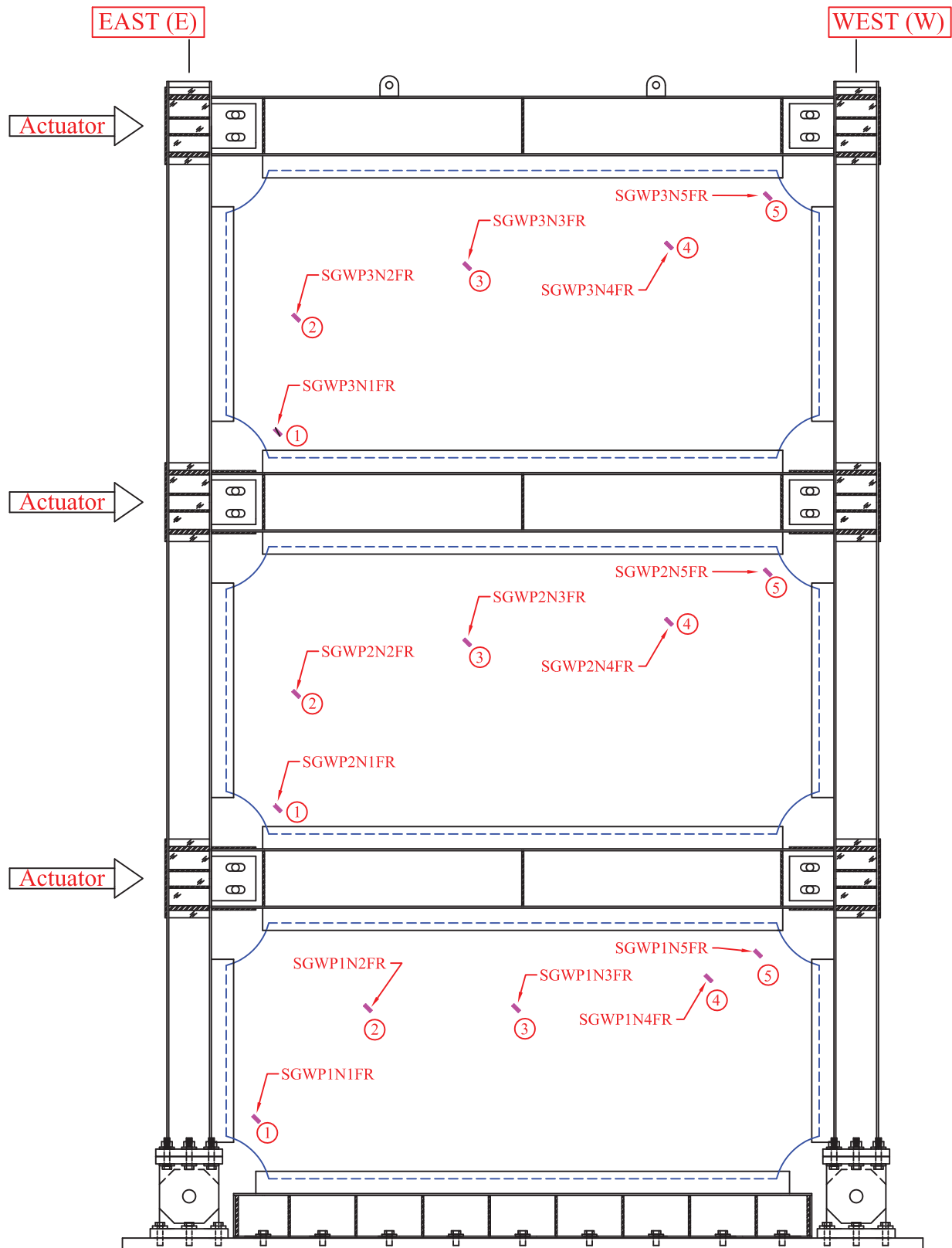
- Uniaxial Strain Gage (SG)

**NOTES:**

For Dimensions Not Shown See 1a dim/I1

591

<b>University at Buffalo</b>			<b>DRWG:</b>
<b>PROJECT:</b> NEESR-SG Self-Centering Steel Plate Shear Walls		<b>CONTENT:</b> BF-1 Strain Gage Dims.	1-1b dim/I1
<b>BY:</b> Daniel M. Dowden	<b>REVISION:</b>	<b>DATE:</b>	<b>SCALE:</b> 3/5" = 1'-0"



**LEGEND:**

- Uniaxial Strain Gage (SG)

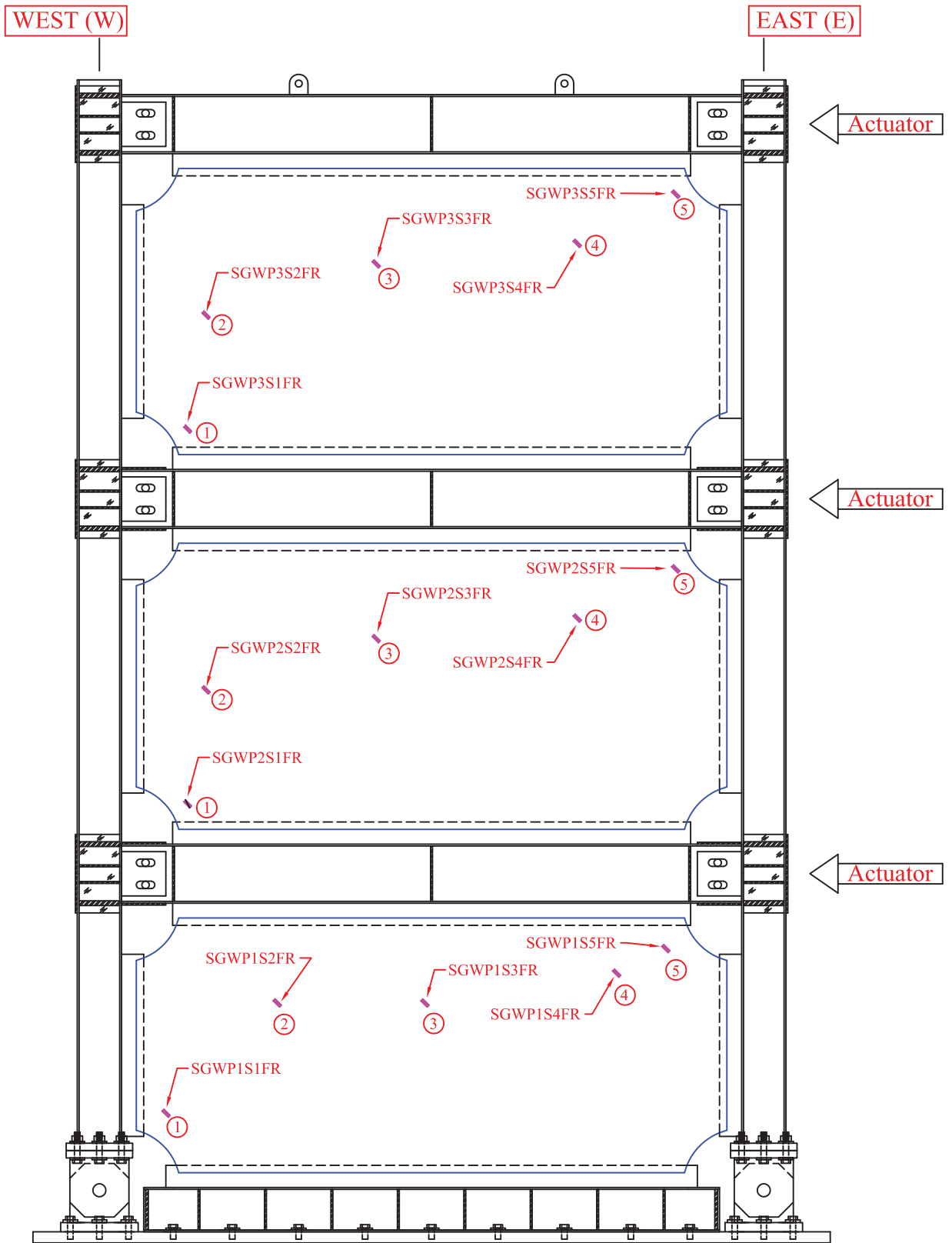
North Elevation

**NOTE:**

For Strain Gage Dimension Layout See 1-3 dim/I1

<b>University at Buffalo</b>			<b>DRWG:</b>
<b>PROJECT:</b> NEESR-SG Self-Centering Steel Plate Shear Walls		<b>CONTENT:</b> Frame 1 Web Plate Strain Gages	1-3a/11
<b>BY:</b> Daniel M. Dowden	<b>REVISION:</b>	<b>DATE:</b>	<b>SCALE:</b> 3/5" = 1'-0"





**LEGEND:**

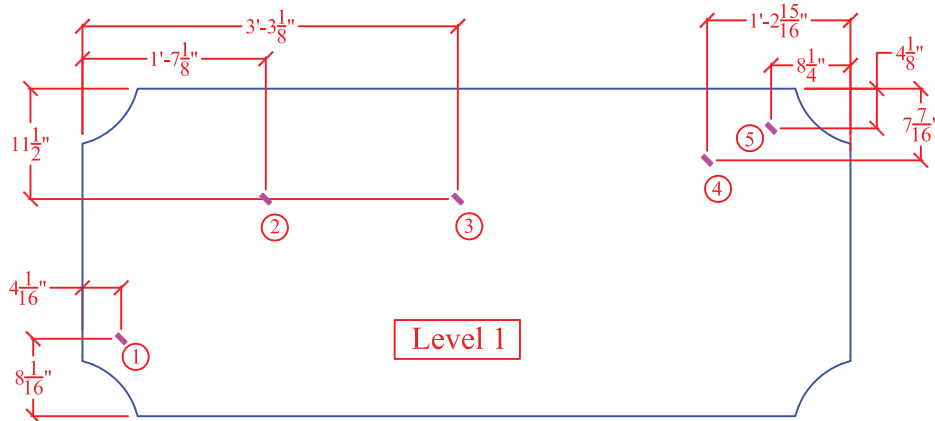
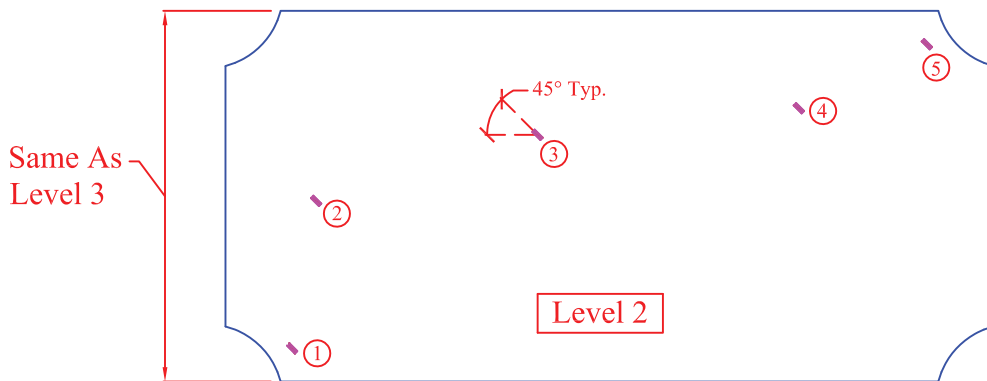
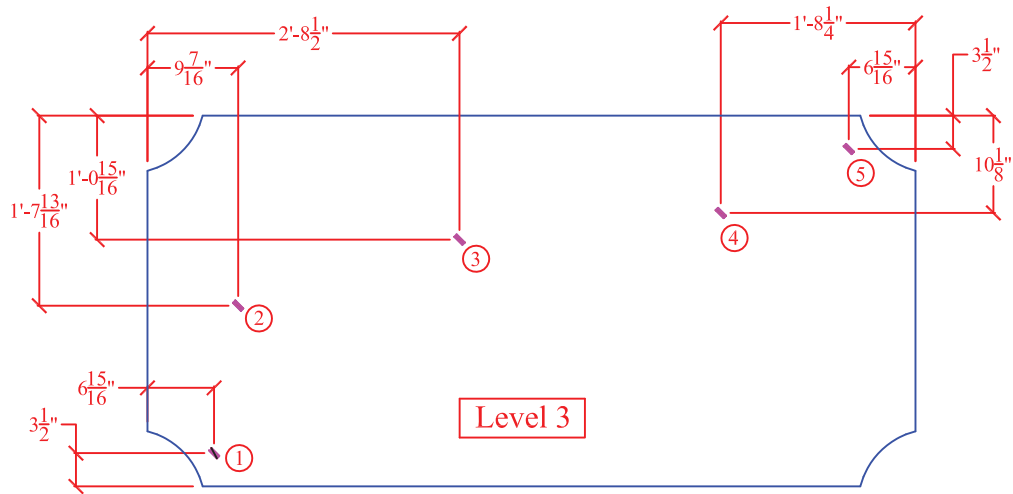
- Uniaxial Strain Gage (SG)

South Elevation

**NOTE:**

For Strain Gage Dimension Layout See 1-3 dim/I1

<b>University at Buffalo</b>			<b>DRWG:</b>
<b>PROJECT:</b> NEESR-SG Self-Centering Steel Plate Shear Walls		<b>CONTENT:</b> Frame 1 Web Plate Strain Gages	1-3b/I1
<b>BY:</b> Daniel M. Dowden	<b>REVISION:</b>	<b>DATE:</b>	<b>SCALE:</b> 3/5" = 1'-0"



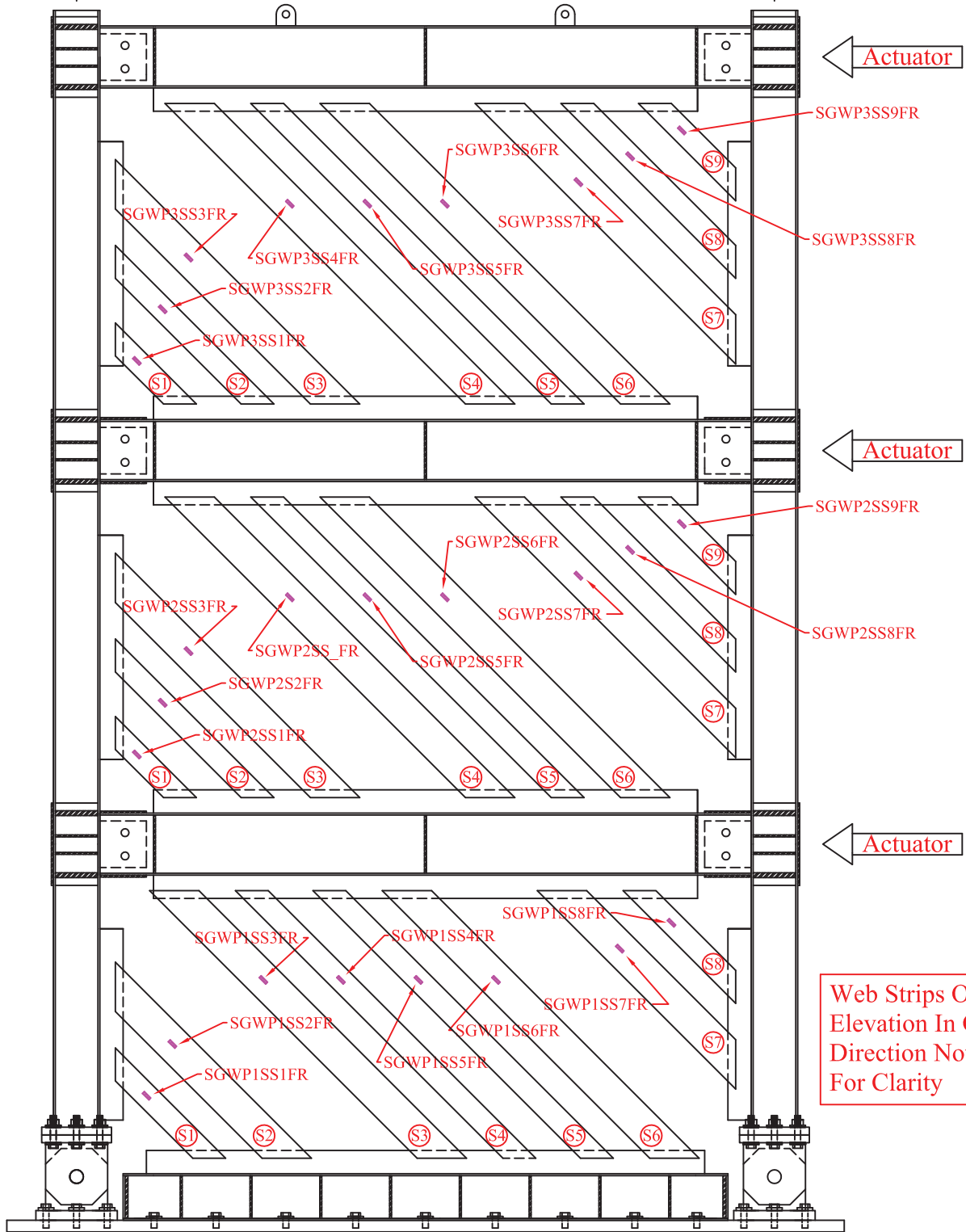
**NOTE:**  
Strain Gage Dimension Layout  
For Frame 2 & 3 Similar

**LEGEND:**  
- Uniaxial Strain Gage (SG)

<b>University at Buffalo</b>			<b>DRWG:</b>
<b>PROJECT:</b> NEESR-SG Self-Centering Steel Plate Shear Walls		<b>CONTENT:</b> Web Plate Strain Gage Dims.	1-3 dim/I1
<b>BY:</b> Daniel M. Dowden	<b>REVISION:</b>	<b>DATE:</b>	<b>SCALE:</b> 3/5" = 1'-0"

WEST (W)

EAST (E)



**LEGEND:**

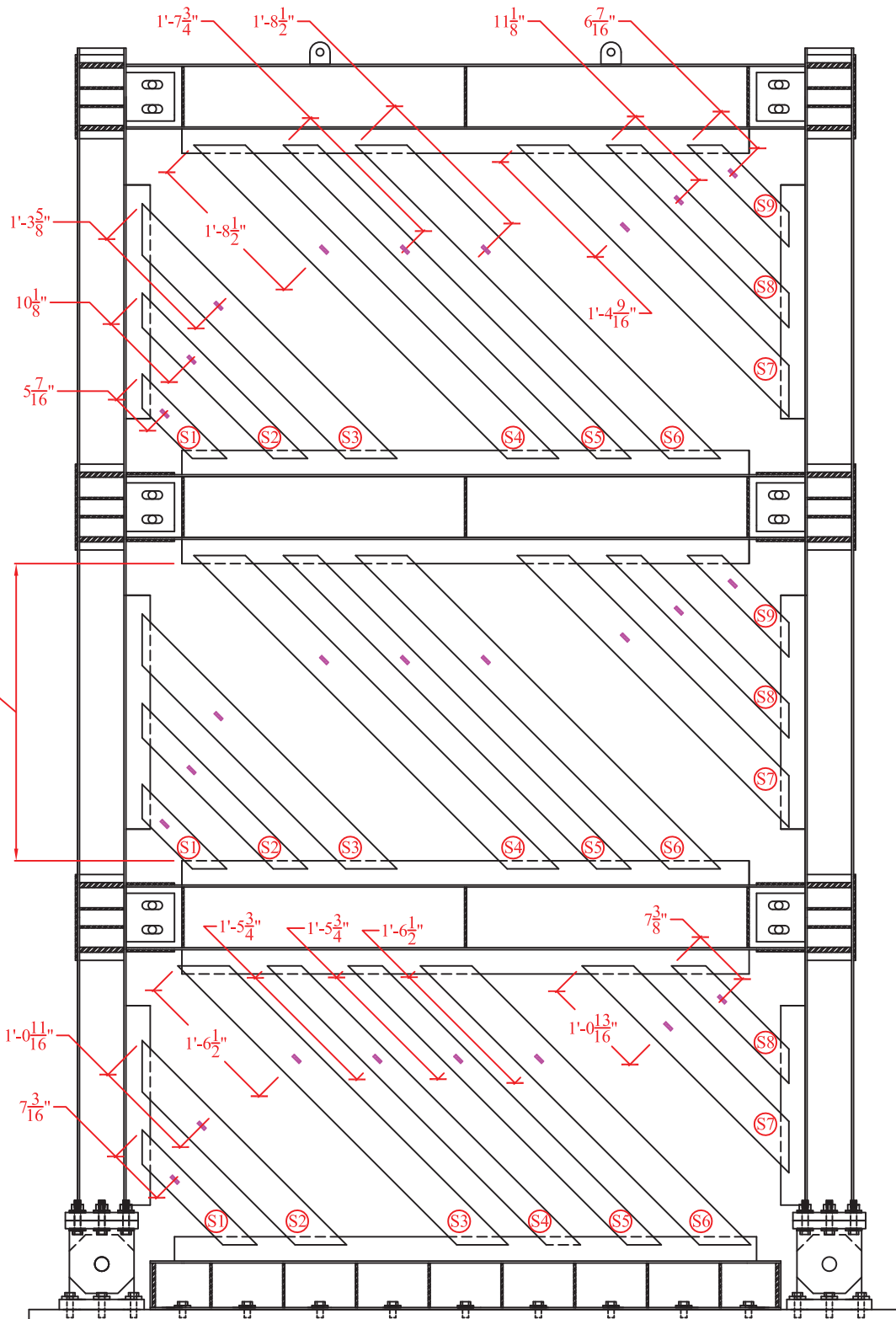
- Uniaxial Strain Gage (SG)

South Elevation

**NOTE:**

For Strain Gage Dimension Layout See 1-2 dim/I1

<b>University at Buffalo</b>			<b>DRWG:</b>
<b>PROJECT:</b> NEESR-SG Self-Centering Steel Plate Shear Walls		<b>CONTENT:</b> Frame 1 Web Strip Strain Gages	1-2b/I1
<b>BY:</b> Daniel M. Dowden	<b>REVISION:</b>	<b>DATE:</b>	<b>SCALE:</b> 3/5" = 1'-0"



Same As  
Level 3

**NOTE:**

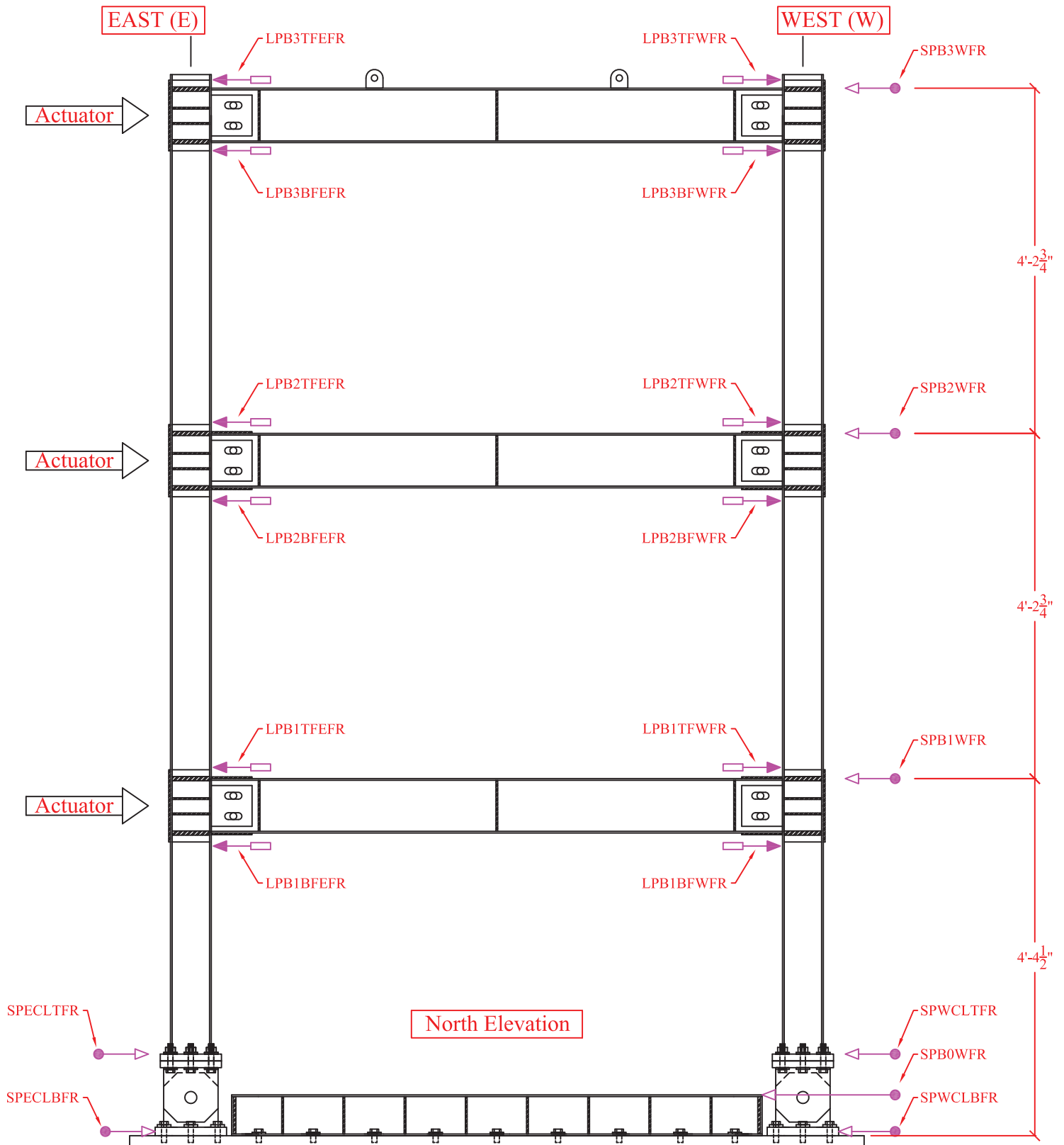
1) Strain Gage Dimension  
Layout For Frame 2 & 3 Similar

**LEGEND:**

- Uniaxial Strain Gage (SG)

596

<b>University at Buffalo</b>			<b>DRWG:</b>
<b>PROJECT:</b> NEESR-SG Self-Centering Steel Plate Shear Walls		<b>CONTENT:</b> Web Strip Strain Gage Dims.	1-2 dim/I1
<b>BY:</b> Daniel M. Dowden	<b>REVISION:</b>	<b>DATE:</b>	<b>SCALE:</b> 3/5" = 1'-0"

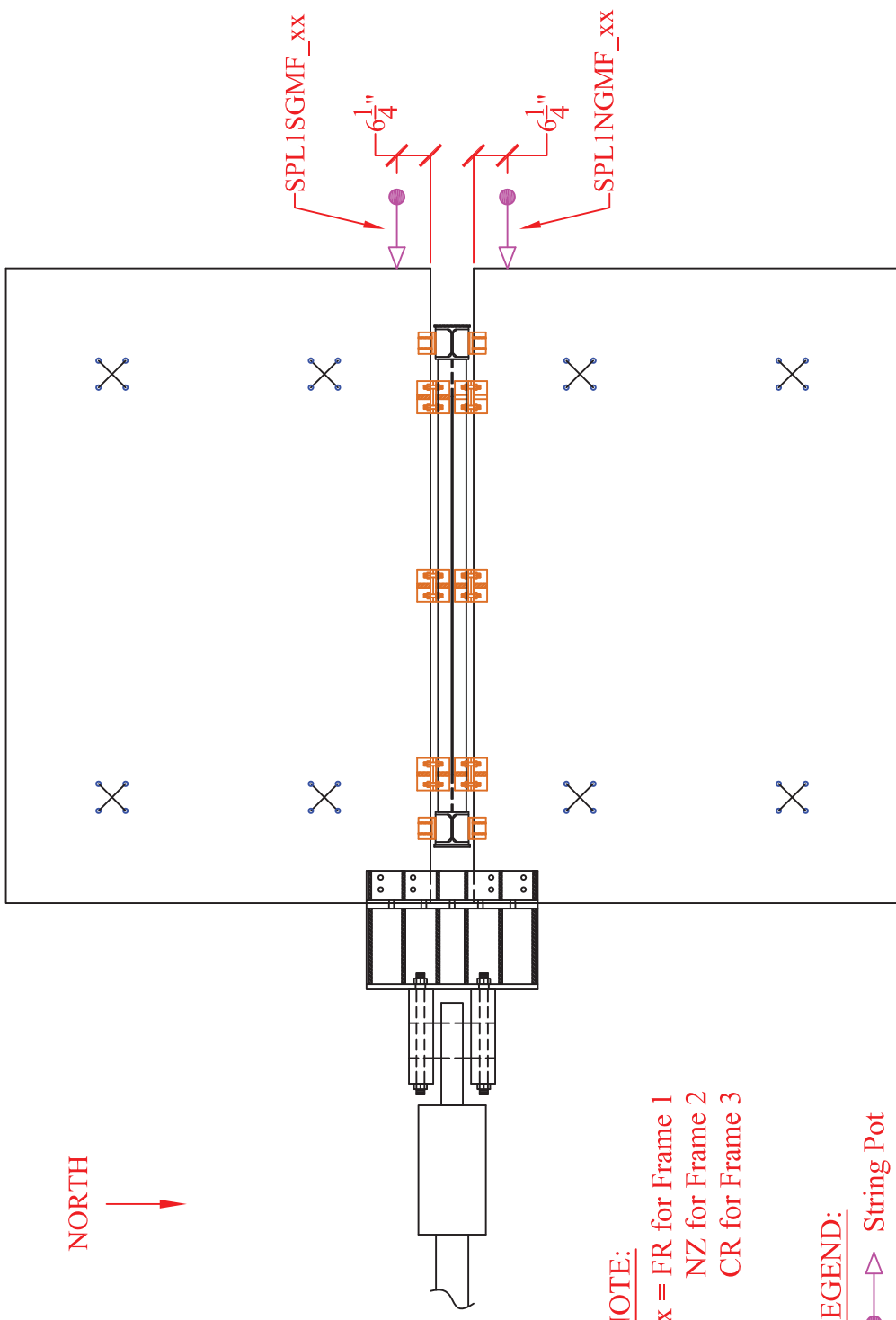


**LEGEND:**

-  LVDT
-  String Pot

<b>University at Buffalo</b>			<b>DRWG:</b>
<b>PROJECT:</b> NEESR-SG Self-Centering Steel Plate Shear Walls		<b>CONTENT:</b> Frame 1 - Disp. Transducers	1/12
<b>BY:</b> Daniel M. Dowden	<b>REVISION:</b>	<b>DATE:</b>	<b>SCALE:</b> 3/5" = 1'-0"

NORTH  

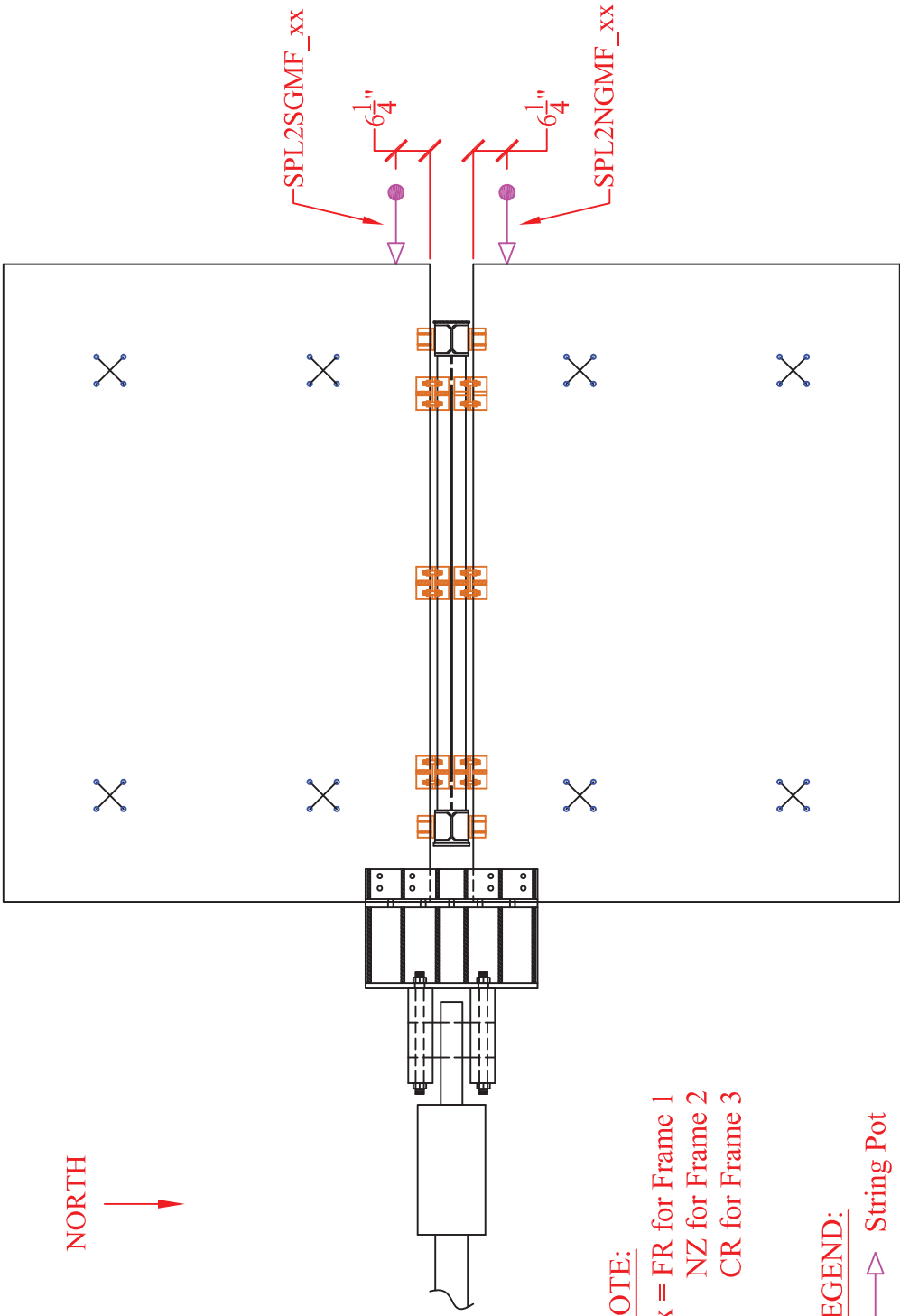
NOTE:  
 xx = FR for Frame 1  
 NZ for Frame 2  
 CR for Frame 3

LEGEND:  
 String Pot

Level 1 - Plan

<b>University at Buffalo</b>		<b>DRWG:</b>
<b>PROJECT:</b> NEESR-SG Self-Centering Steel Plate Shear Walls	<b>CONTENT:</b> GMF Disp. Transducers - Level 1	4/12
<b>BY:</b> Daniel M. Dowden	<b>REVISION:</b>	<b>SCALE:</b> 3/8" = 1'-0"
	<b>DATE:</b>	

NORTH  

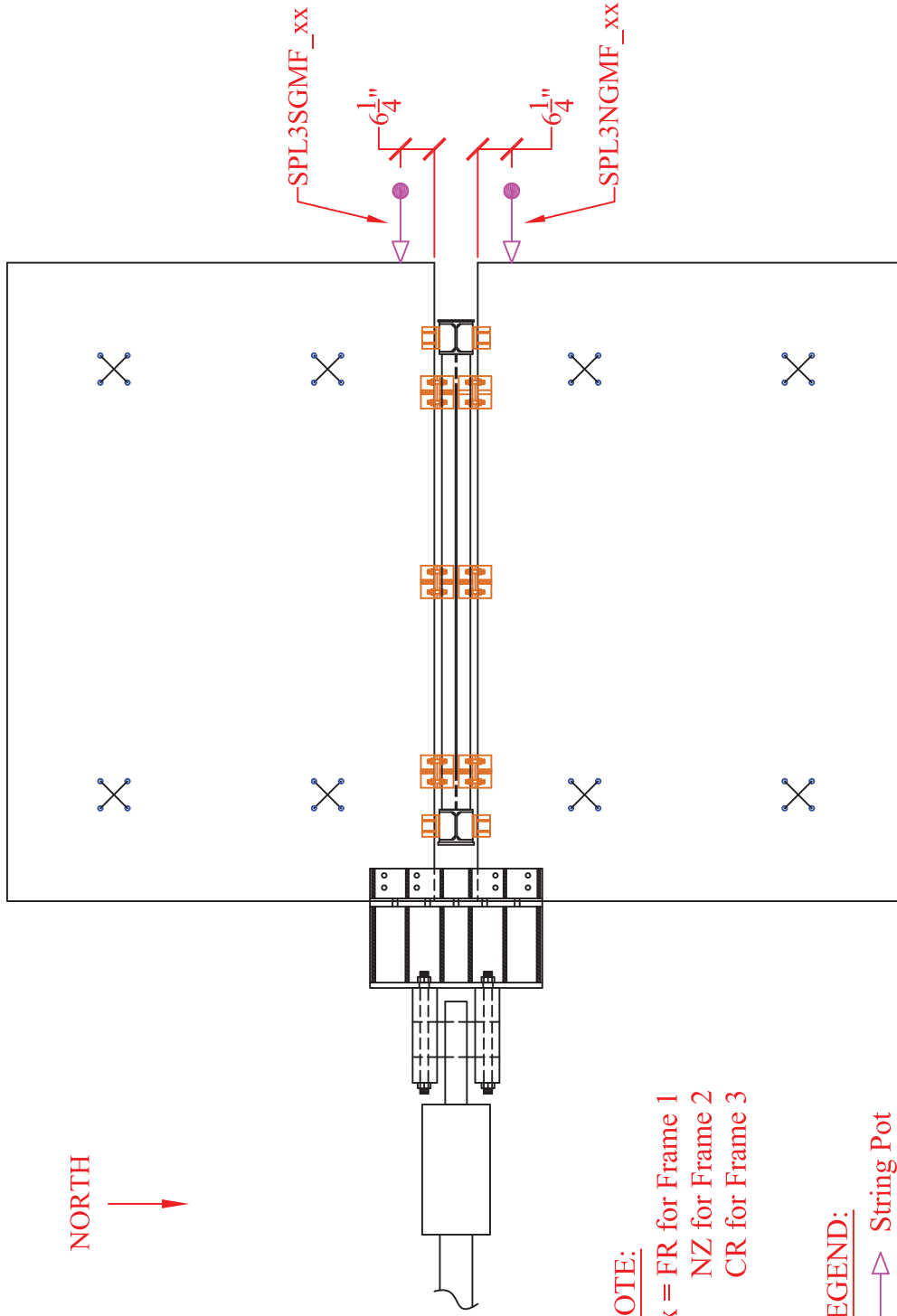
**NOTE:**  
 xx = FR for Frame 1  
 NZ for Frame 2  
 CR for Frame 3

**LEGEND:**  
 String Pot

Level 2 - Plan

<b>University at Buffalo</b>		<b>DRWG:</b>
<b>PROJECT:</b> NEESR-SG Self-Centering Steel Plate Shear Walls	<b>CONTENT:</b> GMF Disp. Transducers - Level 2	5/12
<b>BY:</b> Daniel M. Dowden	<b>REVISION:</b>	<b>SCALE:</b> 3/8" = 1'-0"
	<b>DATE:</b>	

NORTH  

NOTE:

xx = FR for Frame 1  
 NZ for Frame 2  
 CR for Frame 3

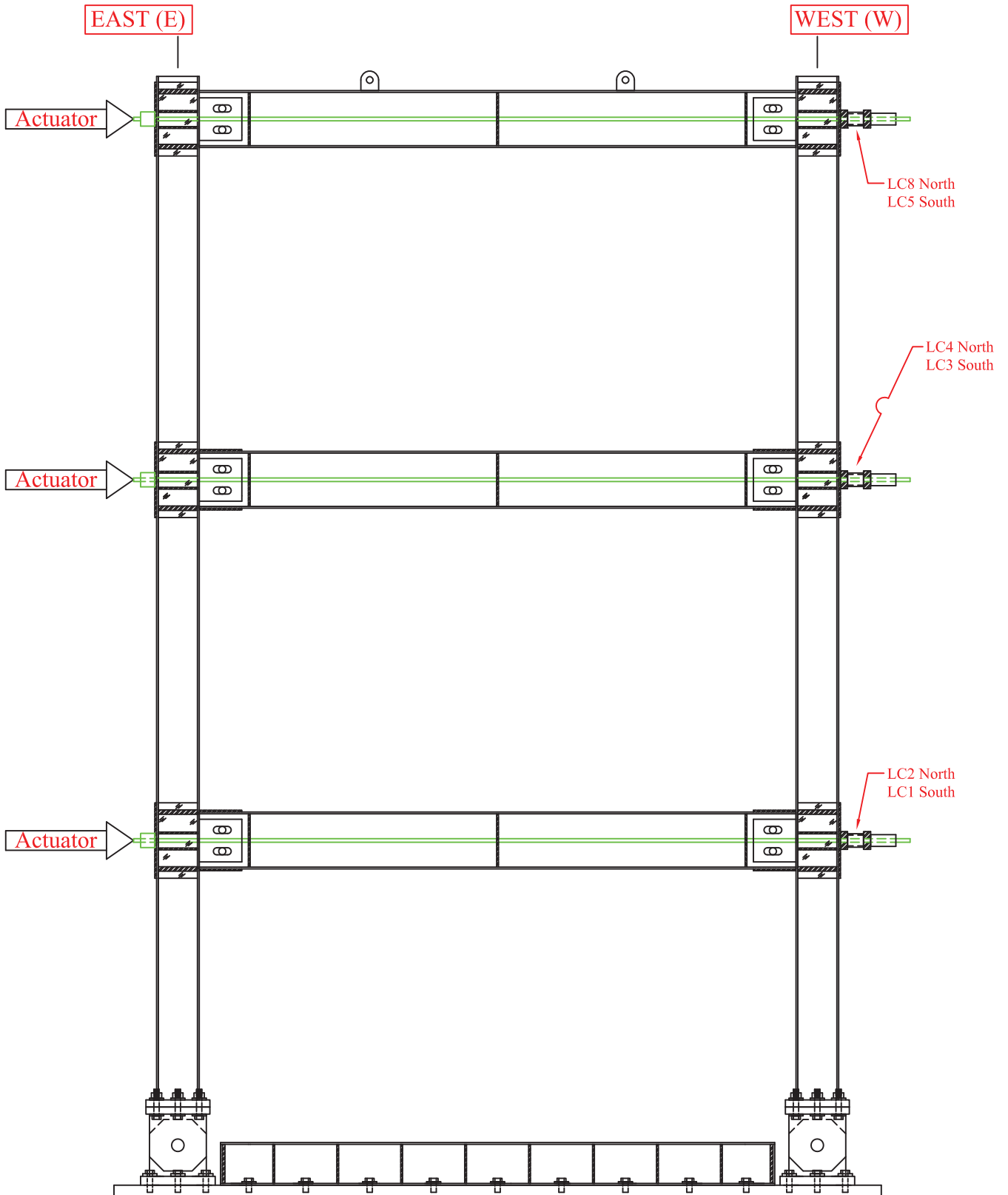
LEGEND:

 String Pot

Level 3 - Plan

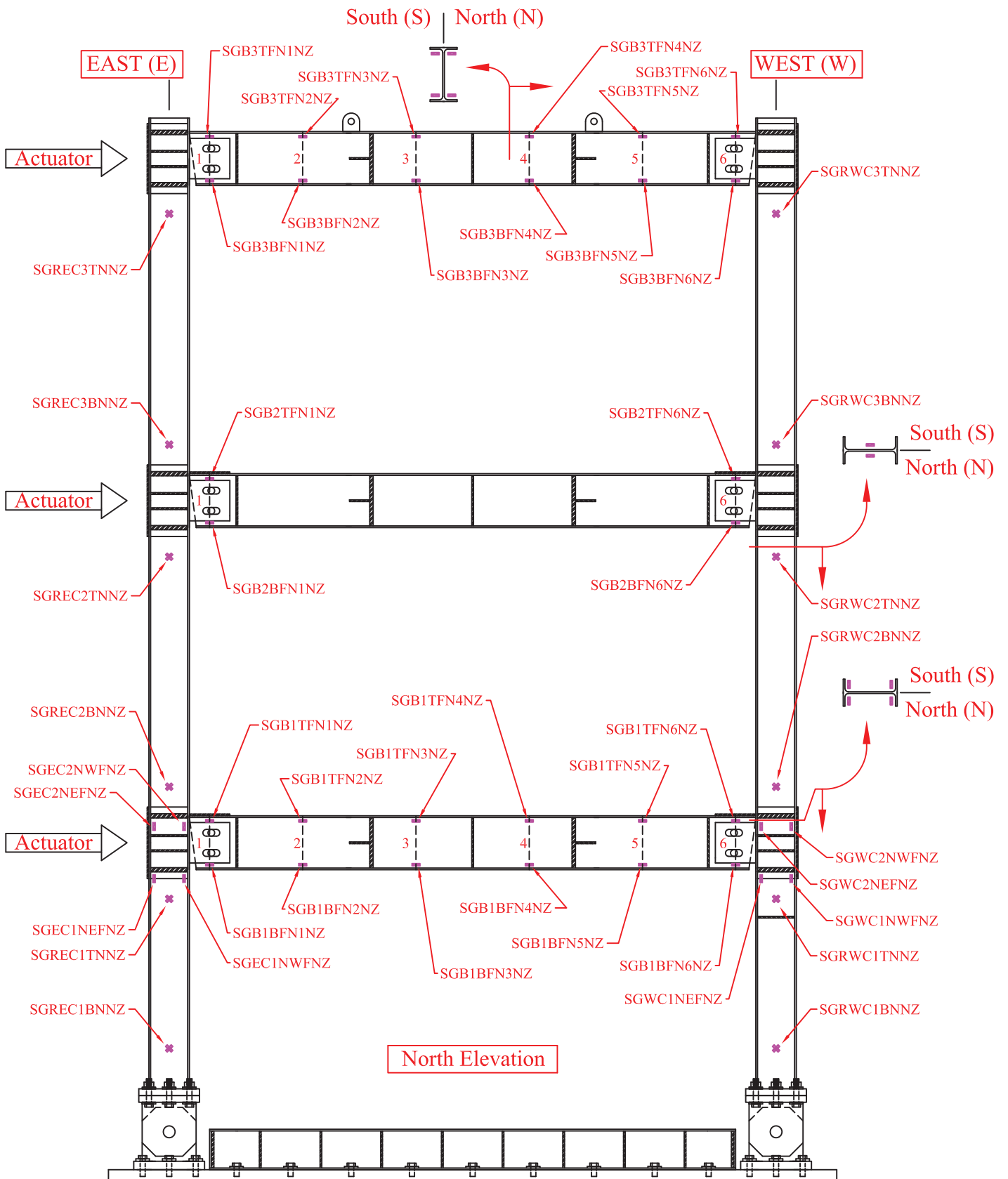
<b>University at Buffalo</b>		<b>DRWG:</b>
<b>PROJECT:</b> NEESR-SG Self-Centering Steel Plate Shear Walls	<b>CONTENT:</b> GMF Disp. Transducers - Level 3	6/12
<b>BY:</b> Daniel M. Dowden	<b>REVISION:</b>	<b>SCALE:</b> 3/8" = 1'-0"
	<b>DATE:</b>	





North Elevation

<b>University at Buffalo</b>			<b>DRWG:</b>
<b>PROJECT:</b> NEESR-SG Self-Centering Steel Plate Shear Walls		<b>CONTENT:</b> Frame 1 Load Cells	1/13
<b>BY:</b> Daniel M. Dowden	<b>REVISION:</b>	<b>DATE:</b>	<b>SCALE:</b> 3/5" = 1'-0"



North Elevation

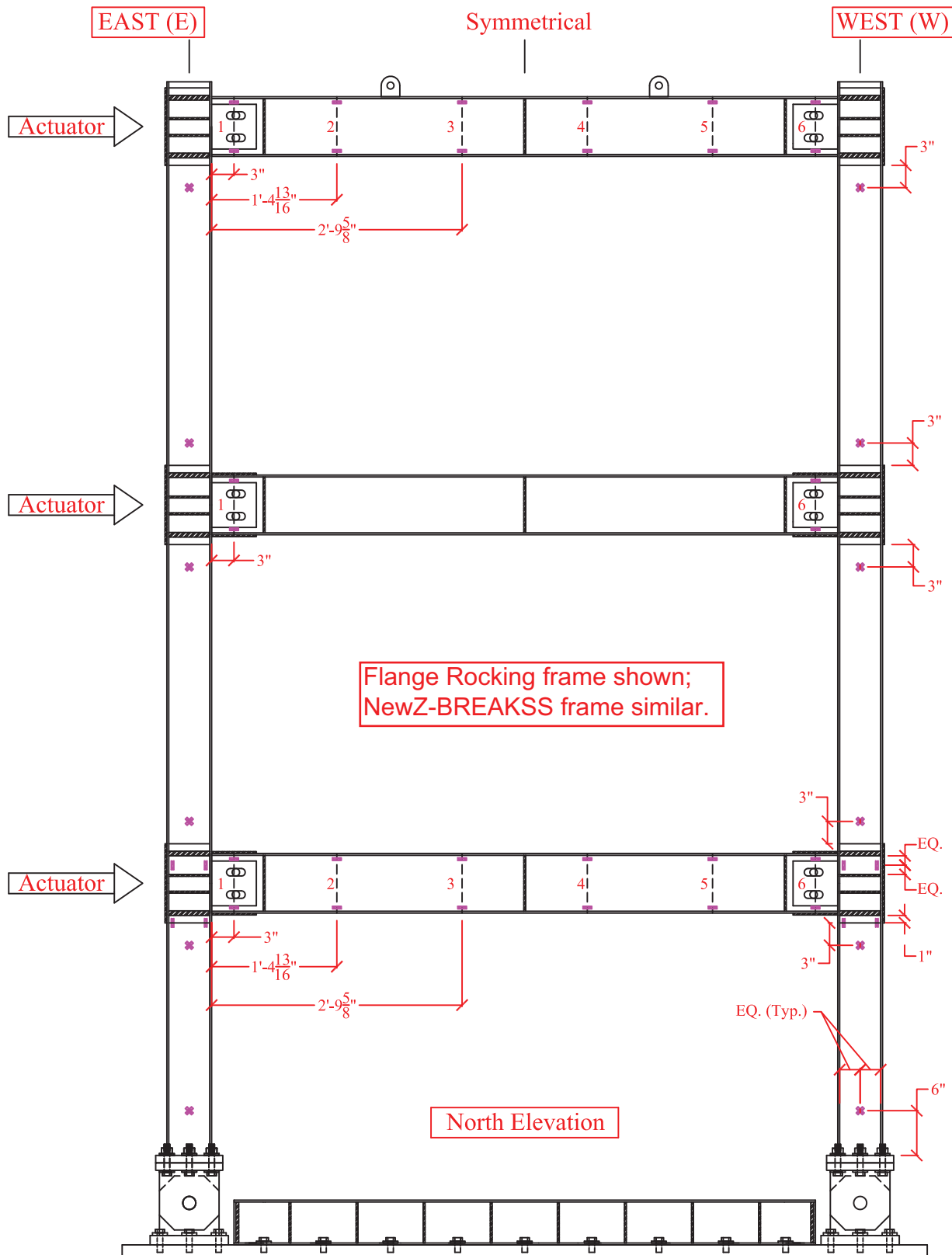
**NOTE:**

1) For Strain Gage Dimension Layout See 1a dim/I1 Sim.

**LEGEND:**

- Uniaxial Strain Gage (SG)
- \* Shear Rosette Strain Gage (SGR)

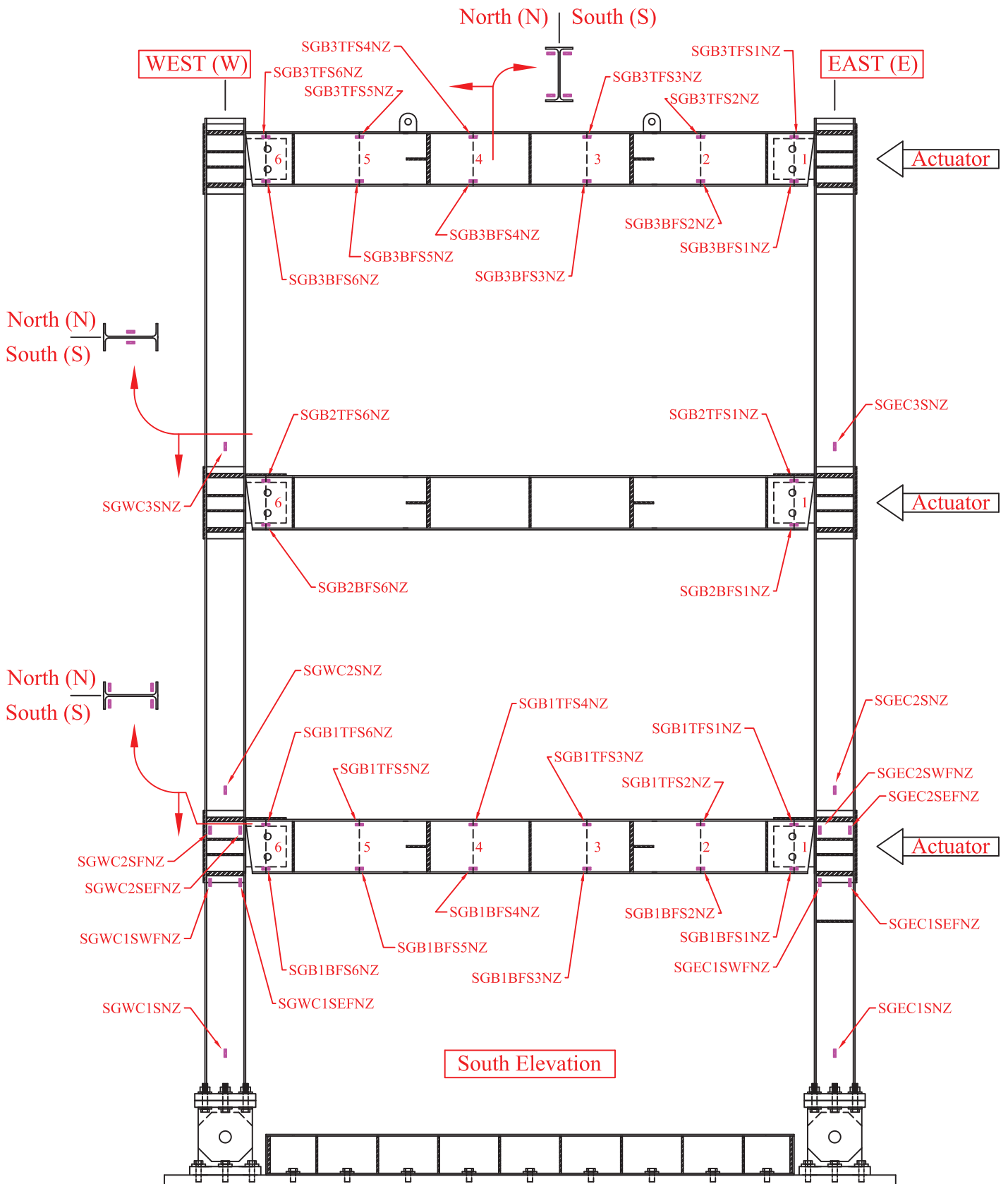
<b>University at Buffalo</b>			<b>DRWG:</b>
<b>PROJECT:</b> NEESR-SG Self-Centering Steel Plate Shear Walls		<b>CONTENT:</b> Boundary Frame 2 Strain Gages	2-1a/I1
<b>BY:</b> Daniel M. Dowden	<b>REVISION:</b>	<b>DATE:</b>	<b>SCALE:</b> 3/5" = 1'-0"



**LEGEND:**

- Uniaxial Strain Gage (SG)
- \* Shear Rosette Strain Gage (SGR)

<b>University at Buffalo</b>			<b>DRWG:</b>
<b>PROJECT:</b> NEESR-SG Self-Centering Steel Plate Shear Walls		<b>CONTENT:</b> BF-1 Strain Gage Dims.	
<b>BY:</b> Daniel M. Dowden		<b>REVISION:</b>	<b>DATE:</b>
			<b>SCALE:</b> 3/5" = 1'-0"



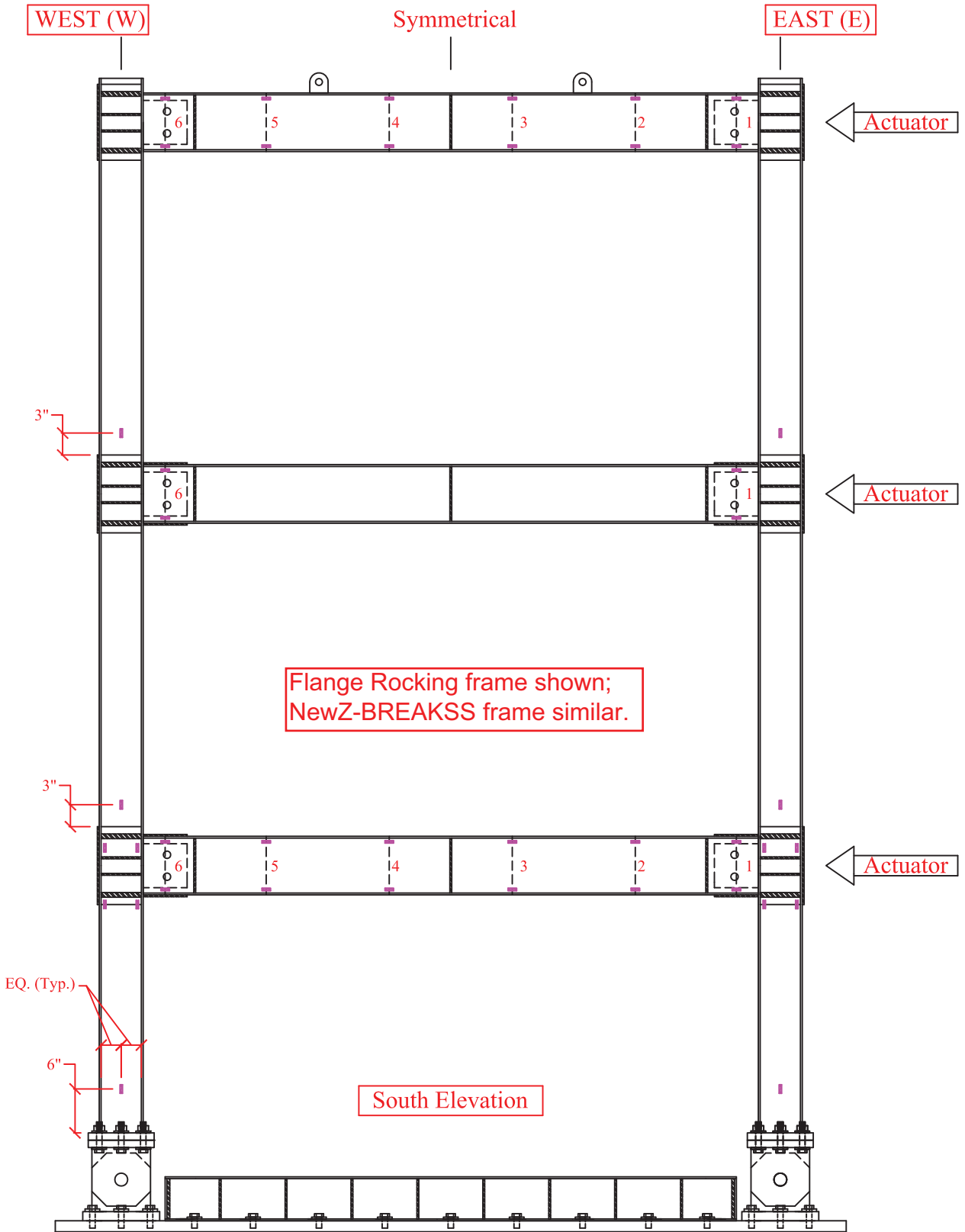
**NOTE:**

1) For Strain Gage Dimension Layout See 1b dim/I1 Sim.

**LEGEND:**

- Uniaxial Strain Gage (SG)

<b>University at Buffalo</b>			<b>DRWG:</b>
<b>PROJECT:</b> NEESR-SG Self-Centering Steel Plate Shear Walls		<b>CONTENT:</b> Boundary Frame 2 Strain Gages	2-1b/I1
<b>BY:</b> Daniel M. Dowden	<b>REVISION:</b>	<b>DATE:</b>	<b>SCALE:</b> 3/5" = 1'-0"



**LEGEND:**

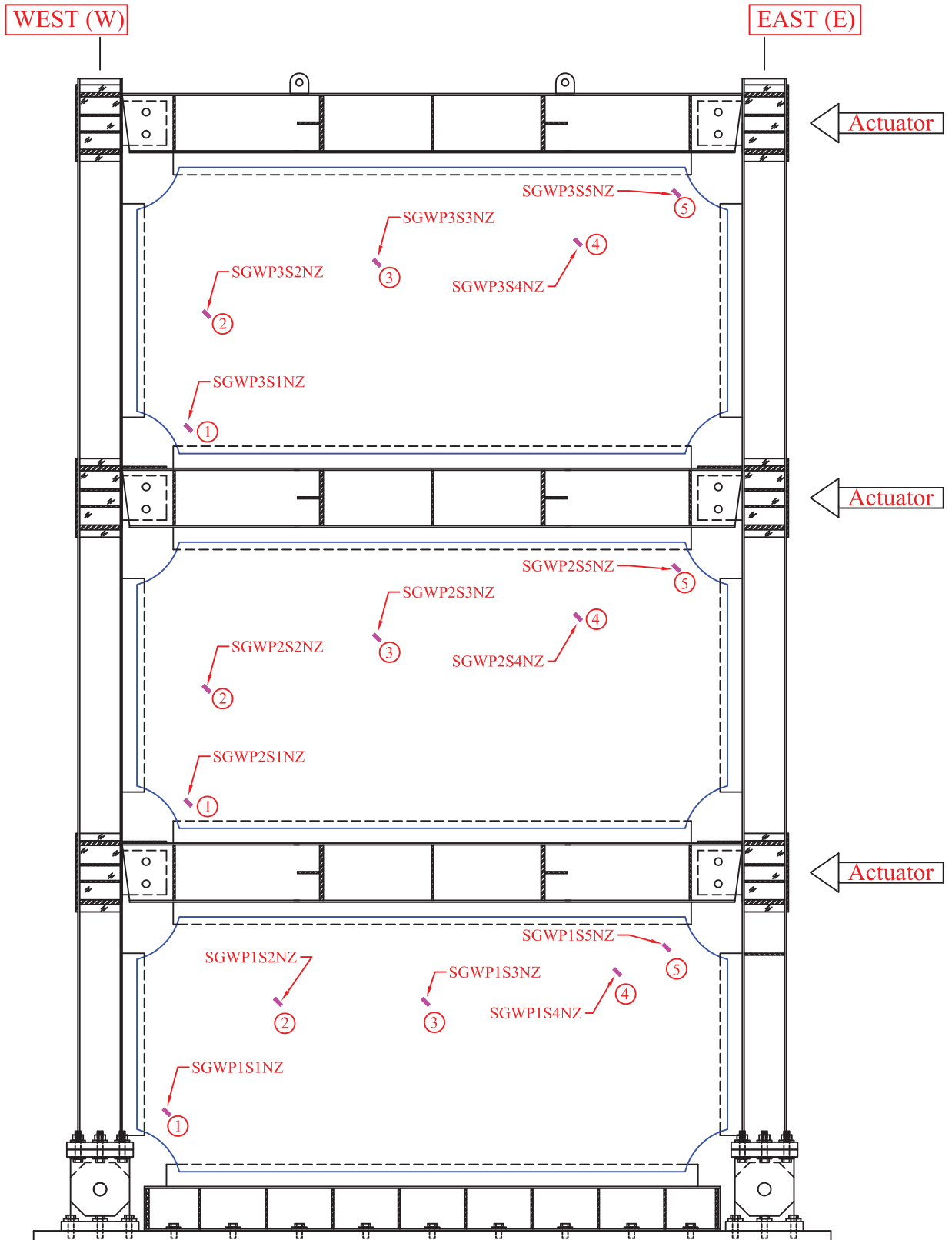
- Uniaxial Strain Gage (SG)

**NOTES:**

For Dimensions Not Shown See 1a dim/I1

605

<b>University at Buffalo</b>			<b>DRWG:</b>
<b>PROJECT:</b> NEESR-SG Self-Centering Steel Plate Shear Walls		<b>CONTENT:</b> BF-1 Strain Gage Dims.	1-1b dim/I1
<b>BY:</b> Daniel M. Dowden	<b>REVISION:</b>	<b>DATE:</b>	<b>SCALE:</b> 3/5" = 1'-0"



**LEGEND:**

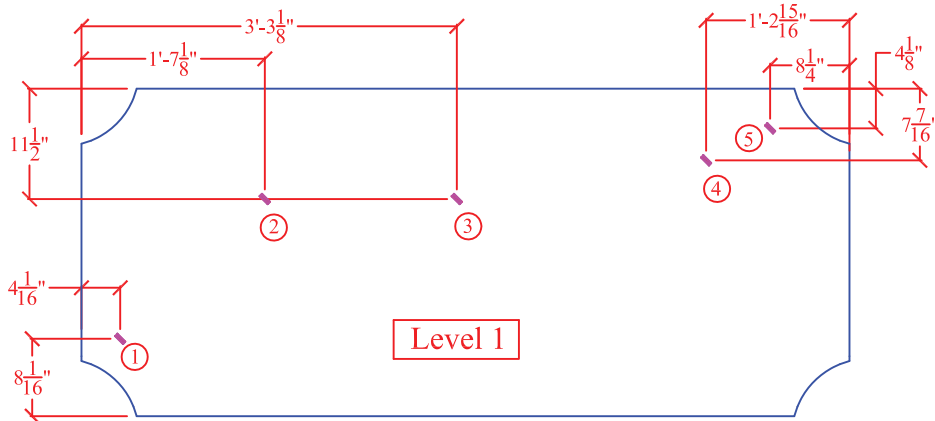
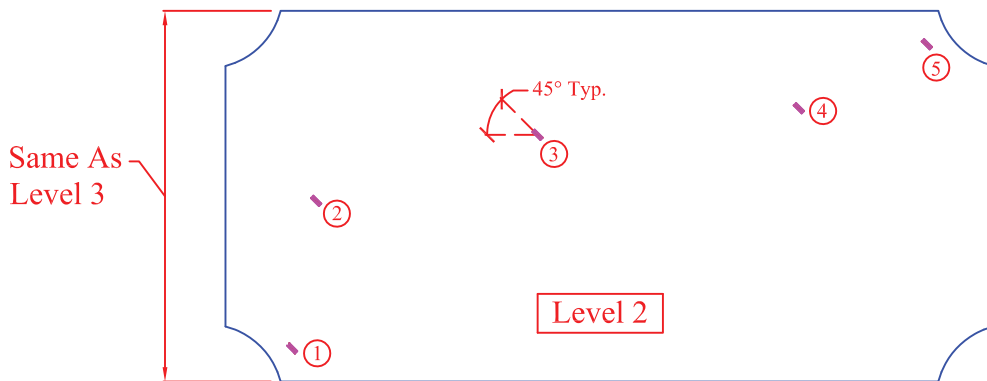
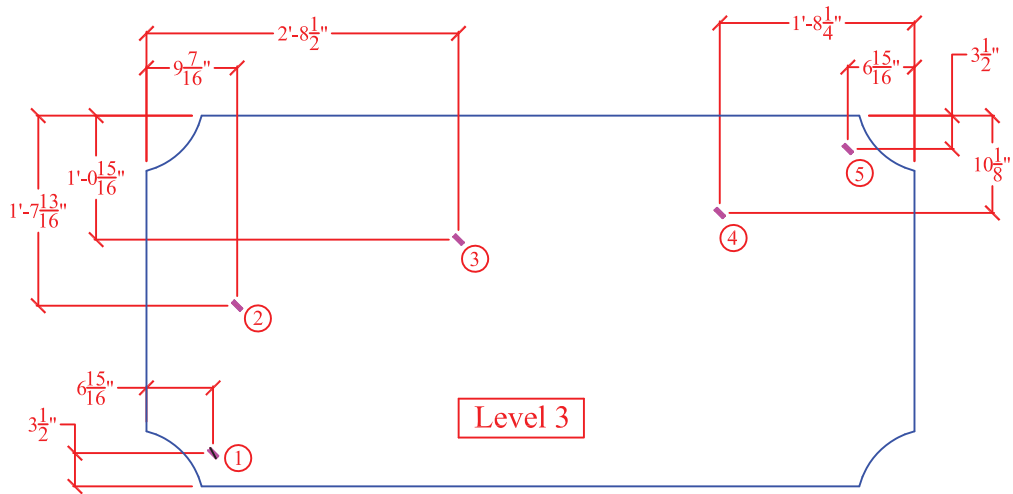
- Uniaxial Strain Gage (SG)

South Elevation

**NOTE:**

For Strain Gage Dimension Layout See 1-3 dim/I1 Sim.

<b>University at Buffalo</b>			<b>DRWG:</b>
<b>PROJECT:</b> NEESR-SG Self-Centering Steel Plate Shear Walls		<b>CONTENT:</b> Frame 2 Web Plate Strain Gages	2-3b/I1
<b>BY:</b> Daniel M. Dowden	<b>REVISION:</b>	<b>DATE:</b>	<b>SCALE:</b> 3/5" = 1'-0"



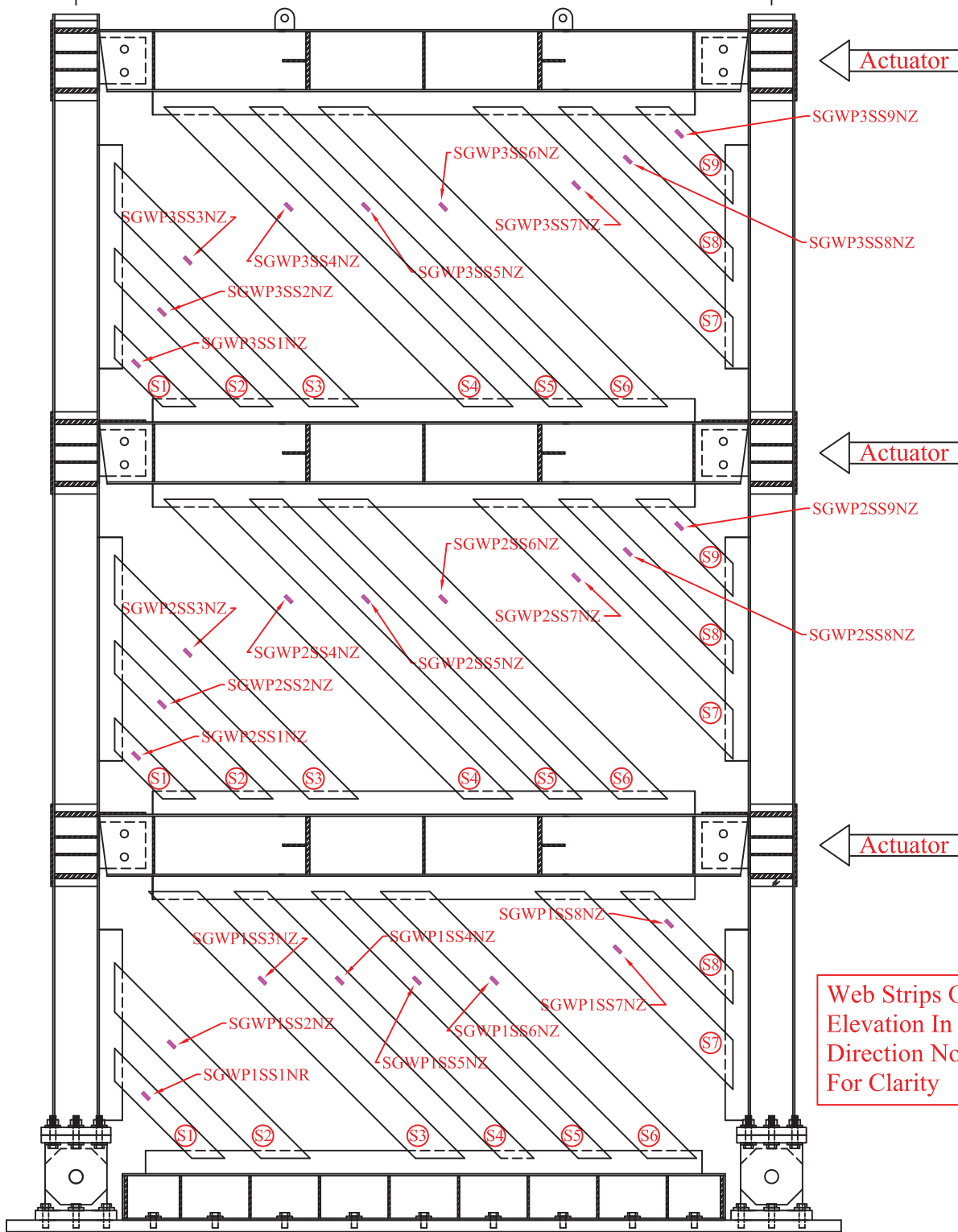
**NOTE:**  
Strain Gage Dimension Layout  
For Frame 2 & 3 Similar

**LEGEND:**  
- Uniaxial Strain Gage (SG)

<b>University at Buffalo</b>			<b>DRWG:</b>
<b>PROJECT:</b> NEESR-SG Self-Centering Steel Plate Shear Walls		<b>CONTENT:</b> Web Plate Strain Gage Dims.	1-3 dim/I1
<b>BY:</b> Daniel M. Dowden	<b>REVISION:</b>	<b>DATE:</b>	<b>SCALE:</b> 3/5" = 1'-0"

WEST (W)

EAST (E)



**LEGEND:**

- Uniaxial Strain Gage (SG)

South Elevation

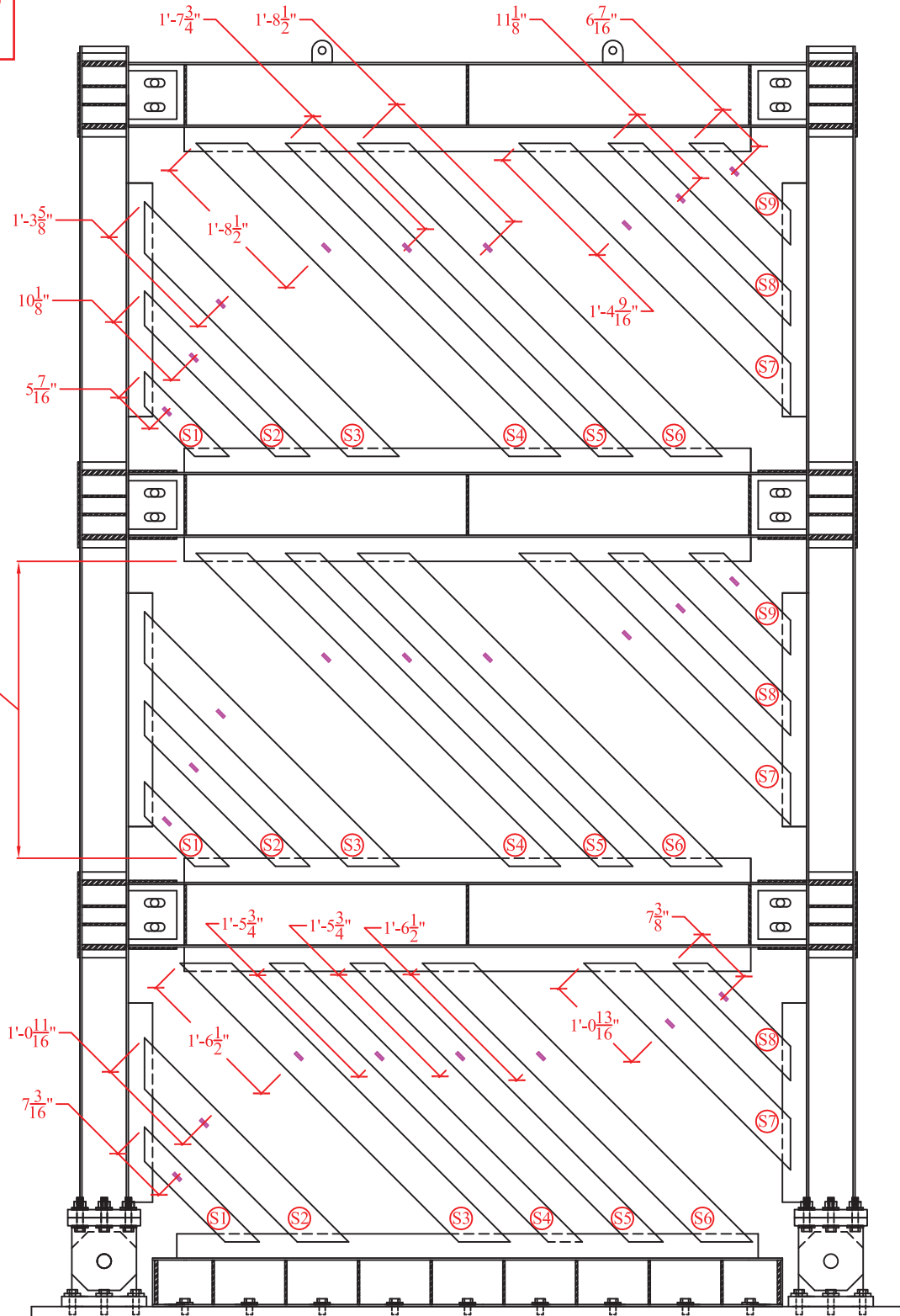
**NOTE:**

For Strain Gage Dimension Layout See 1-2 dim/I1 Sim.

<b>University at Buffalo</b>			<b>DRWG:</b>
<b>PROJECT:</b> NEESR-SG Self-Centering Steel Plate Shear Walls		<b>CONTENT:</b> Frame 2 Web Strip Strain Gages	2-2b/I1
<b>BY:</b> Daniel M. Dowden	<b>REVISION:</b>	<b>DATE:</b>	<b>SCALE:</b> 3/5" = 1'-0"



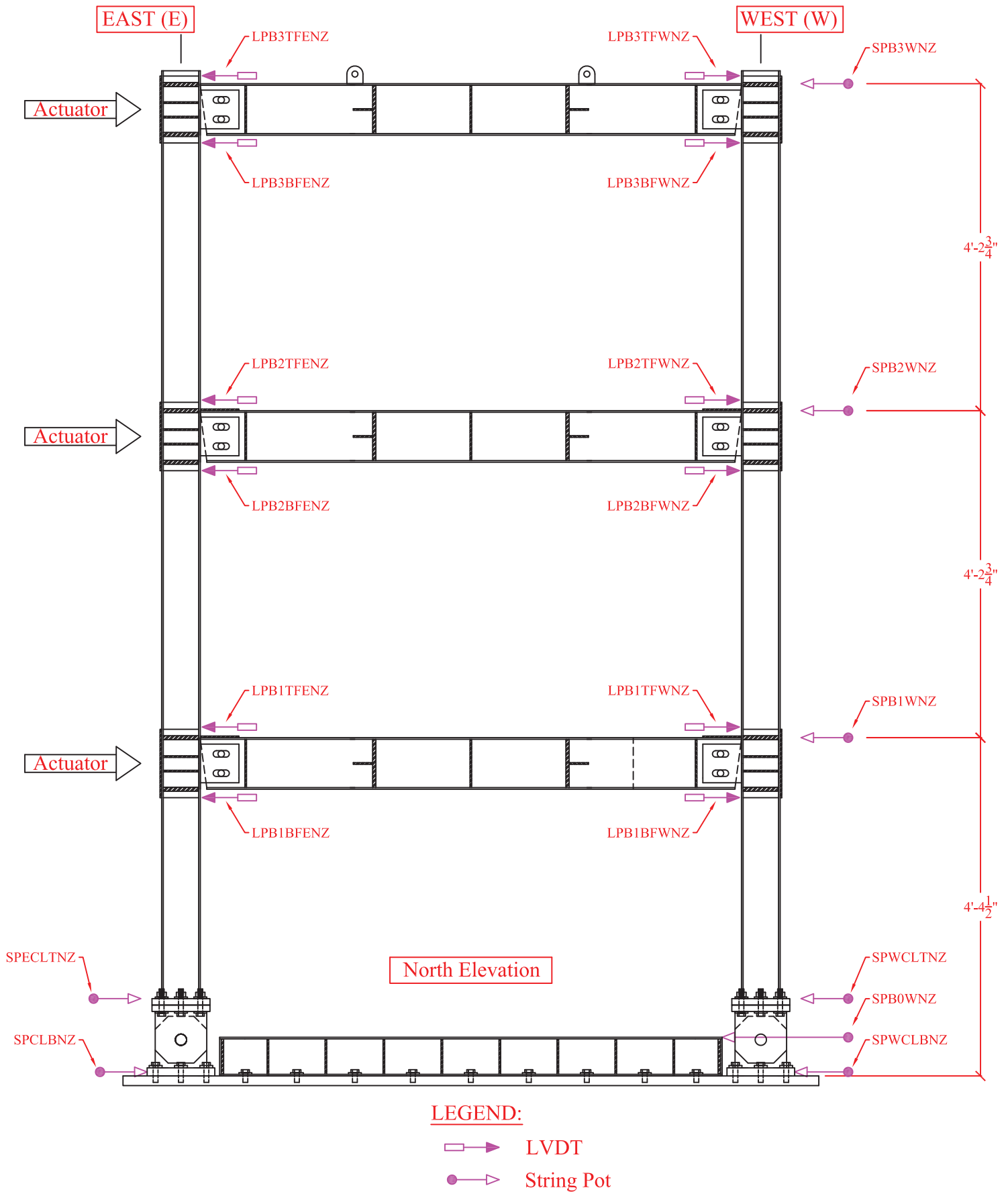
Flange Rocking frame shown;  
NewZ-BREAKSS frame similar.



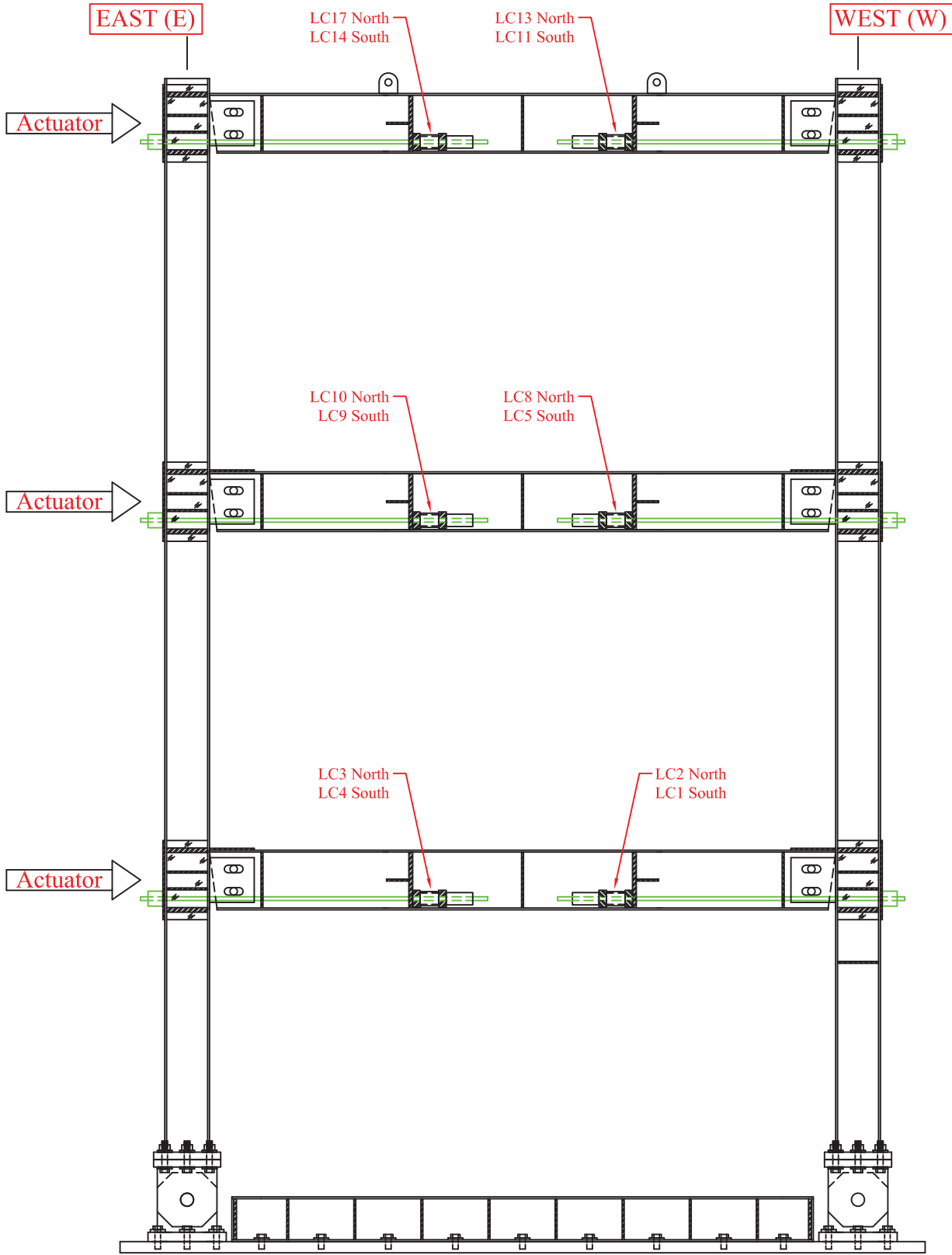
**NOTE:**  
1) Strain Gage Dimension  
Layout For Frame 2 & 3 Similar

**LEGEND:**  
- Uniaxial Strain Gage (SG)

<b>University at Buffalo</b>			<b>DRWG:</b>
<b>PROJECT:</b> NEESR-SG Self-Centering Steel Plate Shear Walls		<b>CONTENT:</b> Web Strip Strain Gage Dims.	1-2 dim/I1
<b>BY:</b> Daniel M. Dowden	<b>REVISION:</b>	<b>DATE:</b>	<b>SCALE:</b> 3/5" = 1'-0"

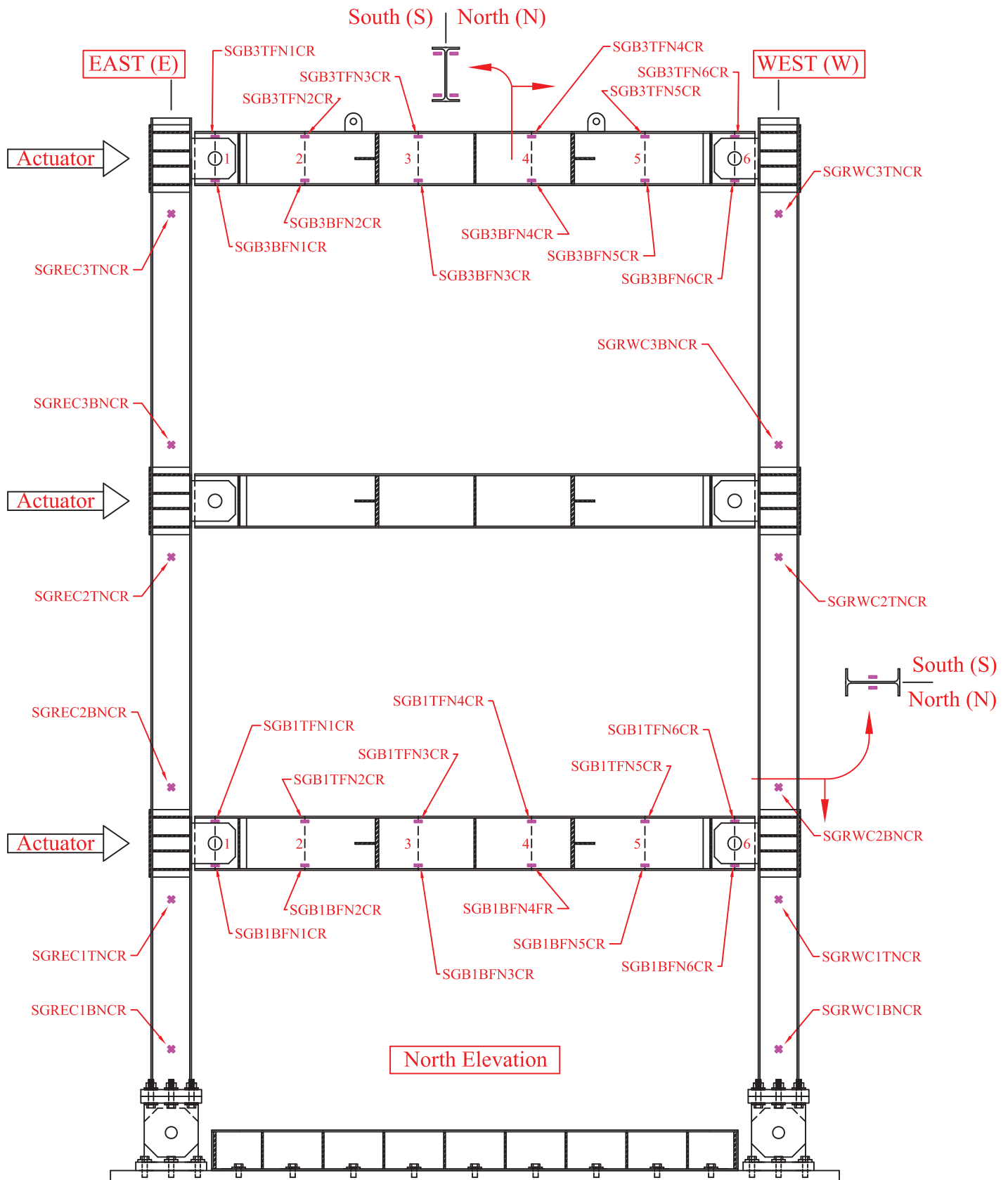


<b>University at Buffalo</b>			<b>DRWG:</b>
<b>PROJECT:</b> NEESR-SG Self-Centering Steel Plate Shear Walls		<b>CONTENT:</b> Frame 2 - Disp. Transducers	2/12
<b>BY:</b> Daniel M. Dowden	<b>REVISION:</b>	<b>DATE:</b>	<b>SCALE:</b> 3/5" = 1'-0"



North Elevation

<b>University at Buffalo</b>			<b>DRWG:</b>
<b>PROJECT:</b> NEESR-SG Self-Centering Steel Plate Shear Walls		<b>CONTENT:</b> Frame 2 Load Cells	2/13
<b>BY:</b> Daniel M. Dowden	<b>REVISION:</b>	<b>DATE:</b>	<b>SCALE:</b> 3/5" = 1'-0"

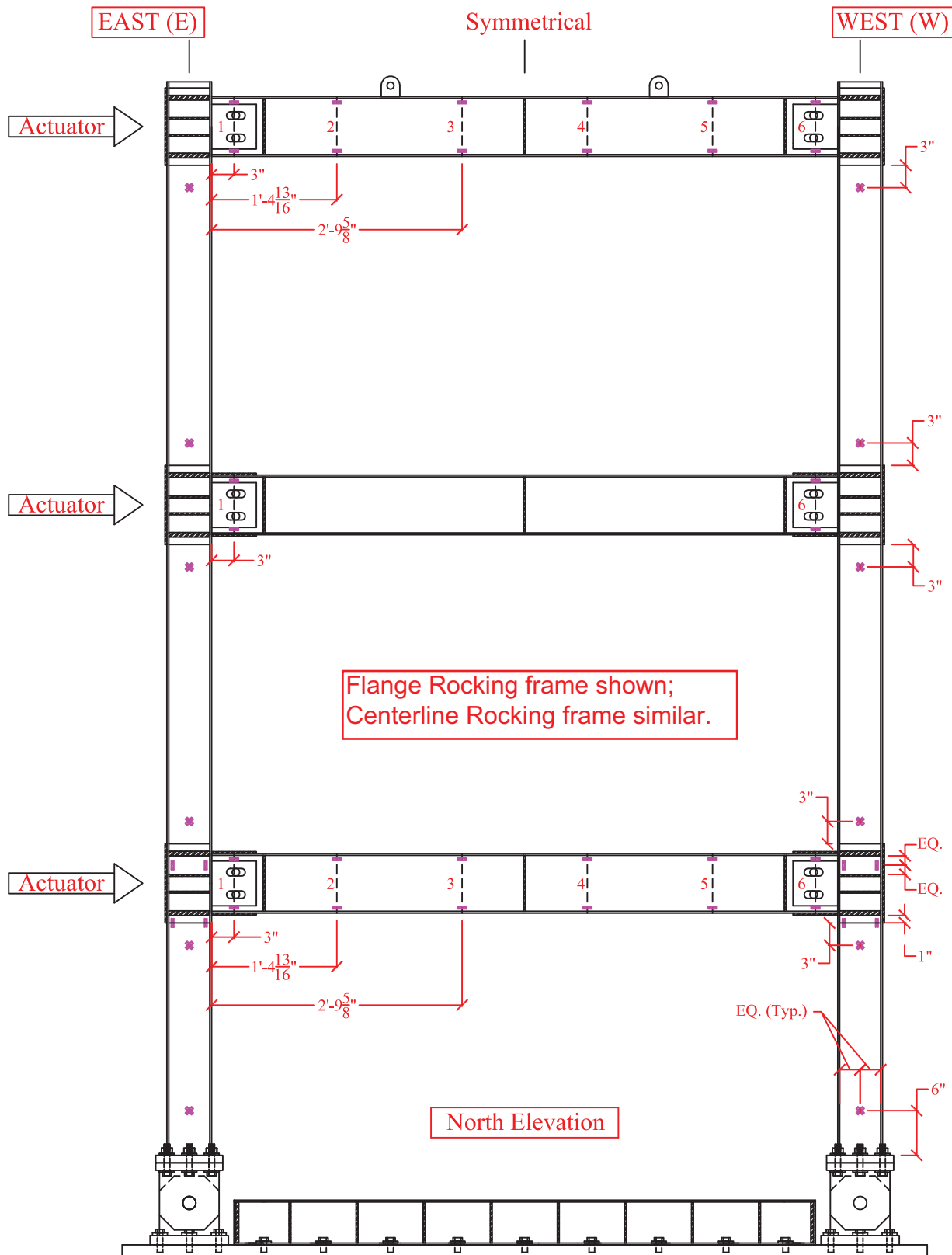


**NOTE:**  
 1) For Strain Gage Dimension Layout See 1a dim/I1 Sim.

**LEGEND:**  
 - Uniaxial Strain Gage (SG)  
 \* Shear Rosette Strain Gage (SGR)

612

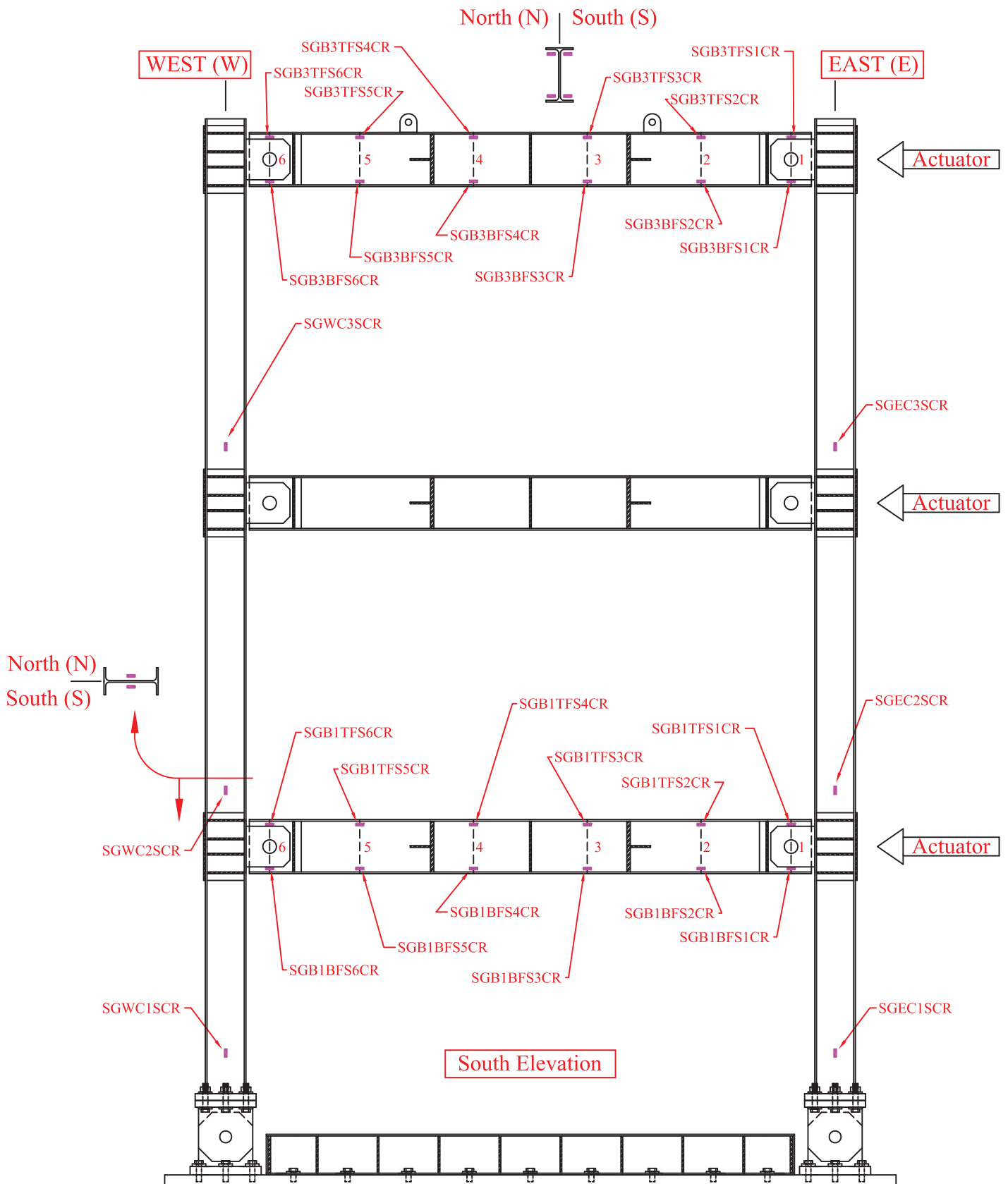
<b>University at Buffalo</b>			<b>DRWG:</b>
<b>PROJECT:</b> NEESR-SG Self-Centering Steel Plate Shear Walls		<b>CONTENT:</b> Boundary Frame 3 Strain Gages	3-1a/I1
<b>BY:</b> Daniel M. Dowden	<b>REVISION:</b>	<b>DATE:</b>	<b>SCALE:</b> 3/5" = 1'-0"



**LEGEND:**

- Uniaxial Strain Gage (SG)
- \* Shear Rosette Strain Gage (SGR)

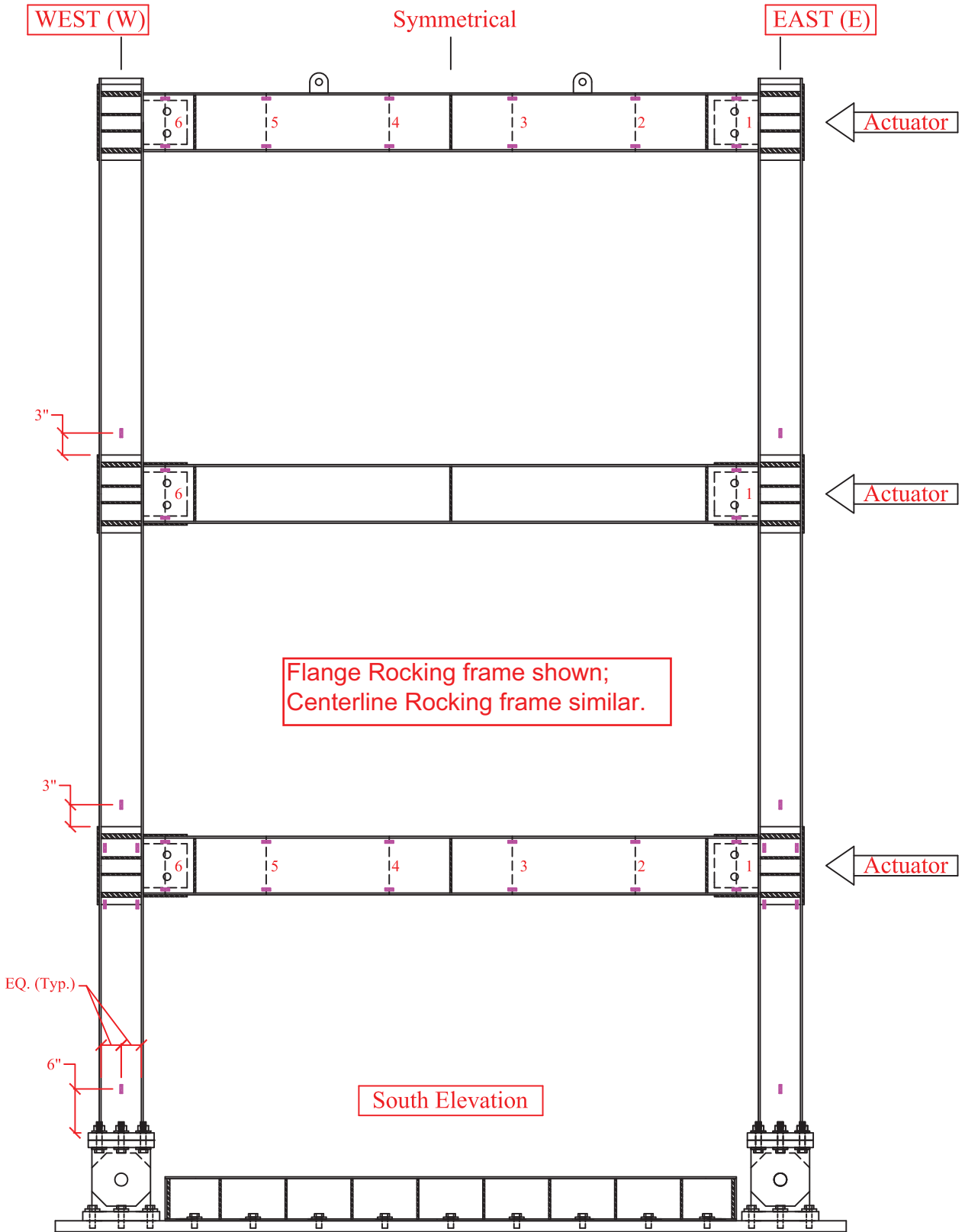
<b>University at Buffalo</b>			<b>DRWG:</b>
<b>PROJECT:</b> NEESR-SG Self-Centering Steel Plate Shear Walls		<b>CONTENT:</b> BF-1 Strain Gage Dims.	1-1a dim/11
<b>BY:</b> Daniel M. Dowden	<b>REVISION:</b>	<b>DATE:</b>	<b>SCALE:</b> 3/5" = 1'-0"



**NOTE:**  
 1) For Strain Gage Dimension  
 Layout See 1a dim/I1 Sim.

**LEGEND:**  
 - Uniaxial Strain Gage (SG)

<b>University at Buffalo</b>			<b>DRWG:</b>
<b>PROJECT:</b> NEESR-SG Self-Centering Steel Plate Shear Walls		<b>CONTENT:</b> Boundary Frame 3 Strain Gages	3-1b/I1
<b>BY:</b> Daniel M. Dowden	<b>REVISION:</b>	<b>DATE:</b>	<b>SCALE:</b> 3/5" = 1'-0"



**LEGEND:**

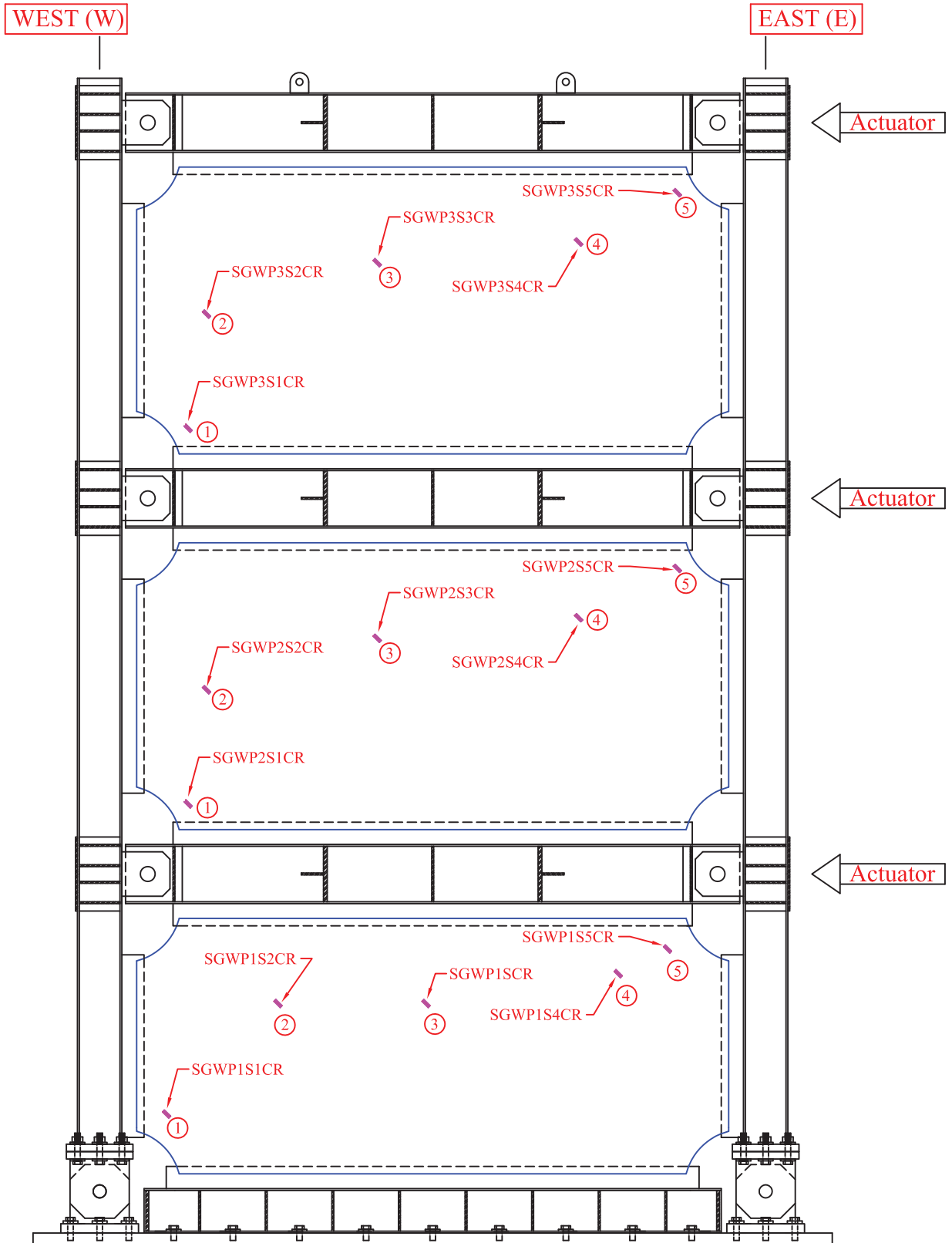
- Uniaxial Strain Gage (SG)

**NOTES:**

For Dimensions Not Shown See 1a dim/I1

615

<b>University at Buffalo</b>			<b>DRWG:</b>
<b>PROJECT:</b> NEESR-SG Self-Centering Steel Plate Shear Walls		<b>CONTENT:</b> BF-1 Strain Gage Dims.	1-1b dim/I1
<b>BY:</b> Daniel M. Dowden	<b>REVISION:</b>	<b>DATE:</b>	<b>SCALE:</b> 3/5" = 1'-0"



**LEGEND:**

- Uniaxial Strain Gage (SG)

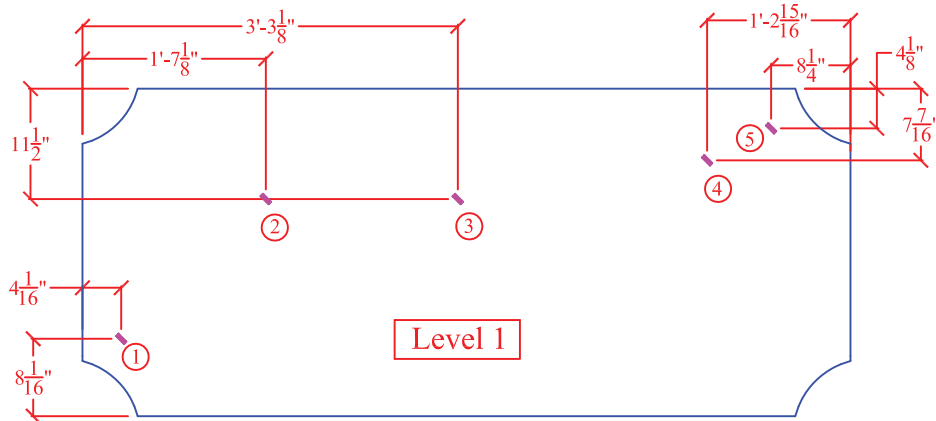
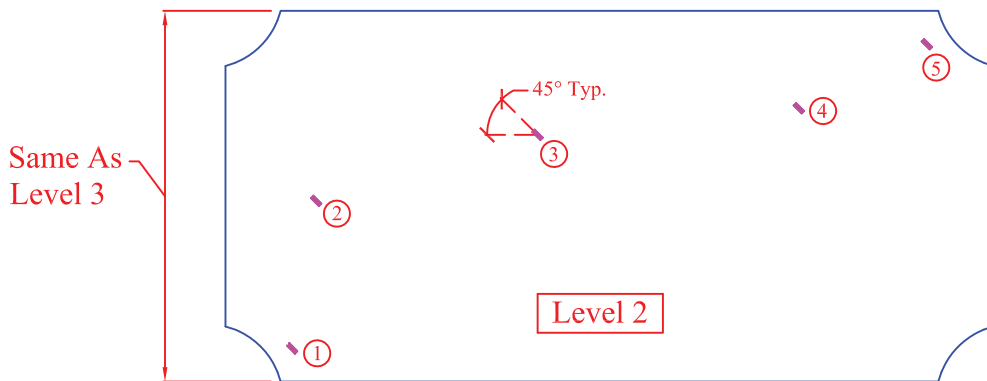
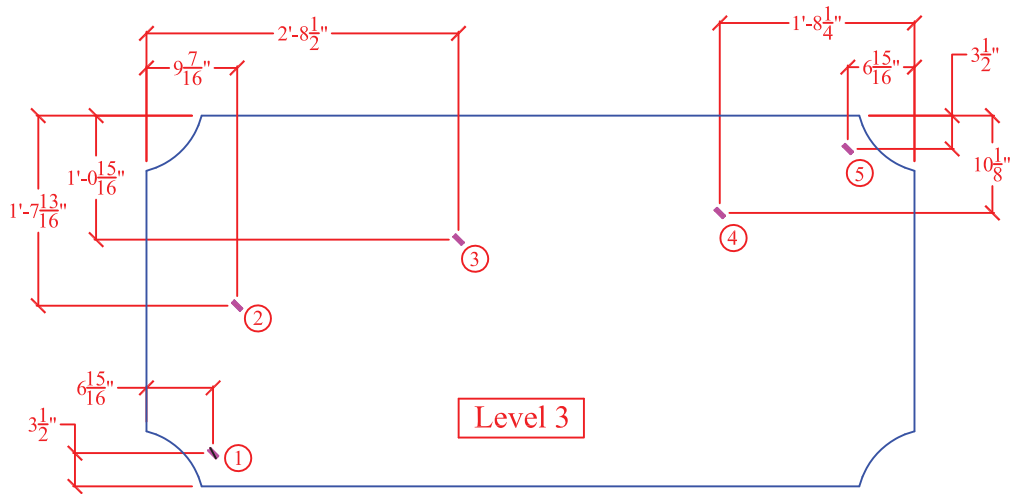
South Elevation

**NOTE:**

For Strain Gage Dimension Layout See 1-3 dim/I1 Sim.

<b>University at Buffalo</b>			<b>DRWG:</b>
<b>PROJECT:</b> NEESR-SG Self-Centering Steel Plate Shear Walls		<b>CONTENT:</b> Frame 3 Web Plate Strain Gages	3-3b/I1
<b>BY:</b> Daniel M. Dowden	<b>REVISION:</b>	<b>DATE:</b>	<b>SCALE:</b> 3/5" = 1'-0"

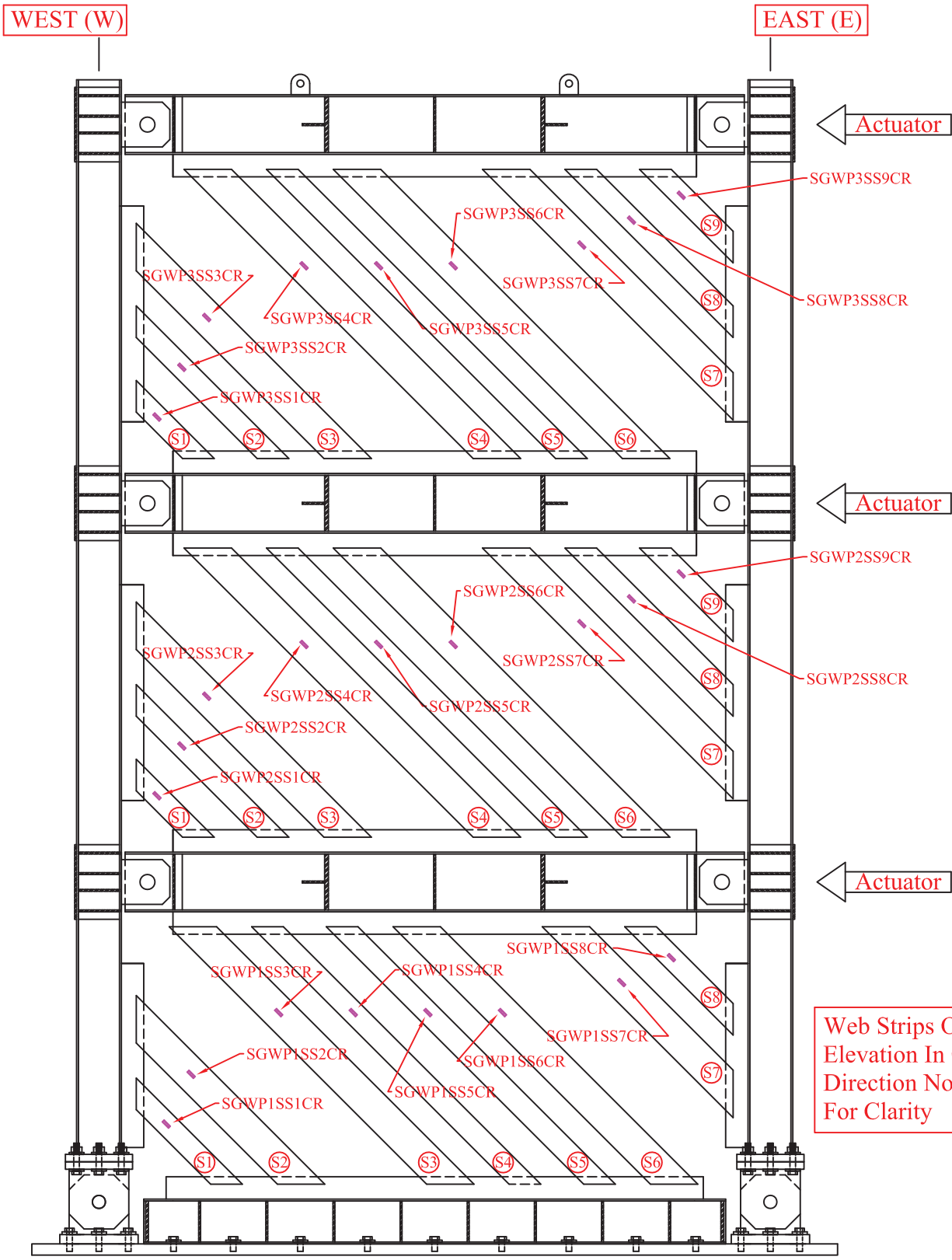




**NOTE:**  
Strain Gage Dimension Layout  
For Frame 2 & 3 Similar

**LEGEND:**  
- Uniaxial Strain Gage (SG)

<b>University at Buffalo</b>			<b>DRWG:</b>
<b>PROJECT:</b> NEESR-SG Self-Centering Steel Plate Shear Walls		<b>CONTENT:</b> Web Plate Strain Gage Dims.	1-3 dim/I1
<b>BY:</b> Daniel M. Dowden	<b>REVISION:</b>	<b>DATE:</b>	<b>SCALE:</b> 3/5" = 1'-0"



**LEGEND:**

- Uniaxial Strain Gage (SG)

South Elevation

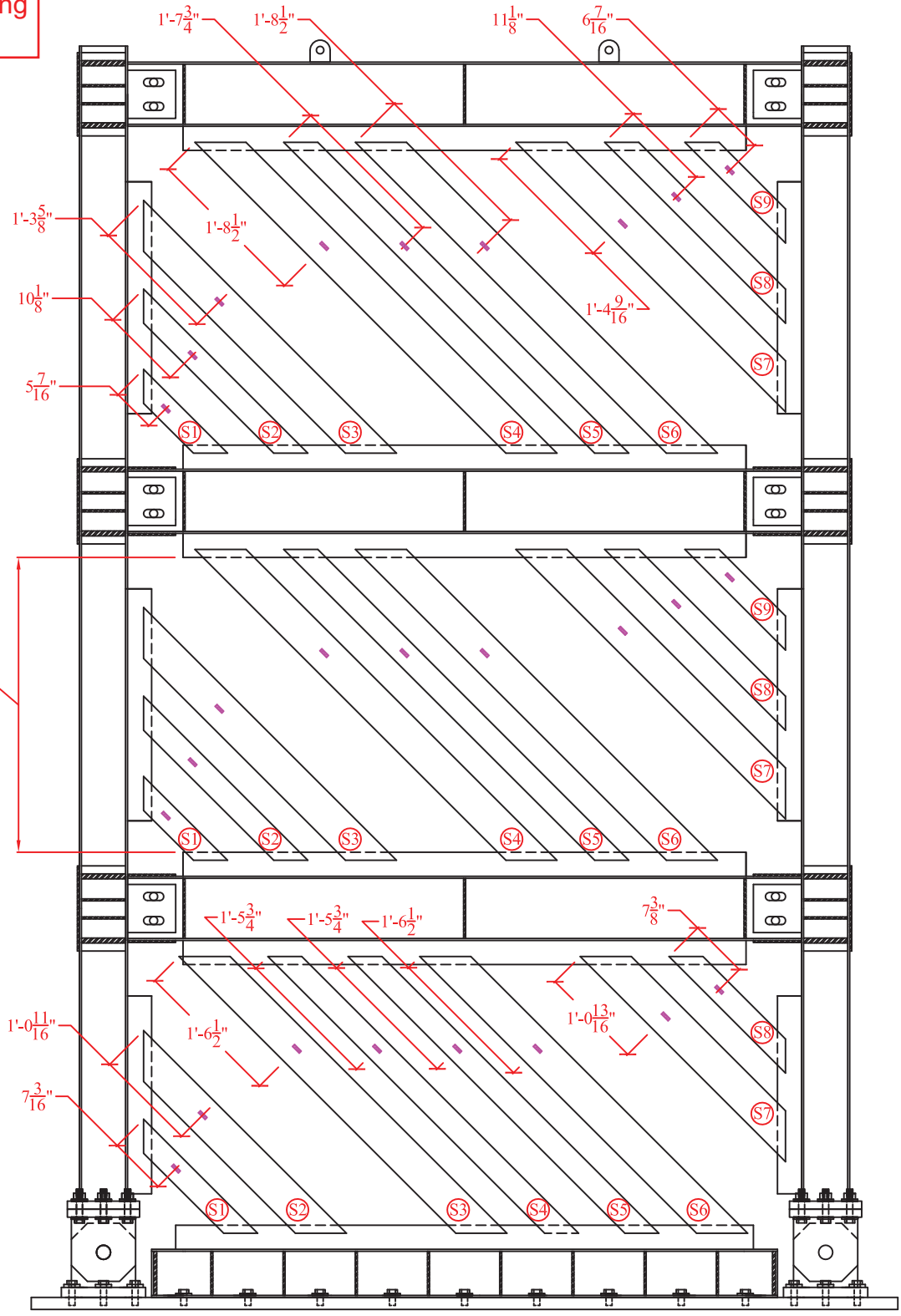
**NOTE:**

For Strain Gage Dimension Layout See 1-2 dim/I1 Sim.

<b>University at Buffalo</b>			<b>DRWG:</b>
<b>PROJECT:</b> NEESR-SG Self-Centering Steel Plate Shear Walls		<b>CONTENT:</b> Frame 3 Web Strip Strain Gages	3-2b/I1
<b>BY:</b> Daniel M. Dowden	<b>REVISION:</b>	<b>DATE:</b>	<b>SCALE:</b> 3/5" = 1'-0"

Flange Rocking  
frame shown;  
Centerline Rocking  
frame similar.

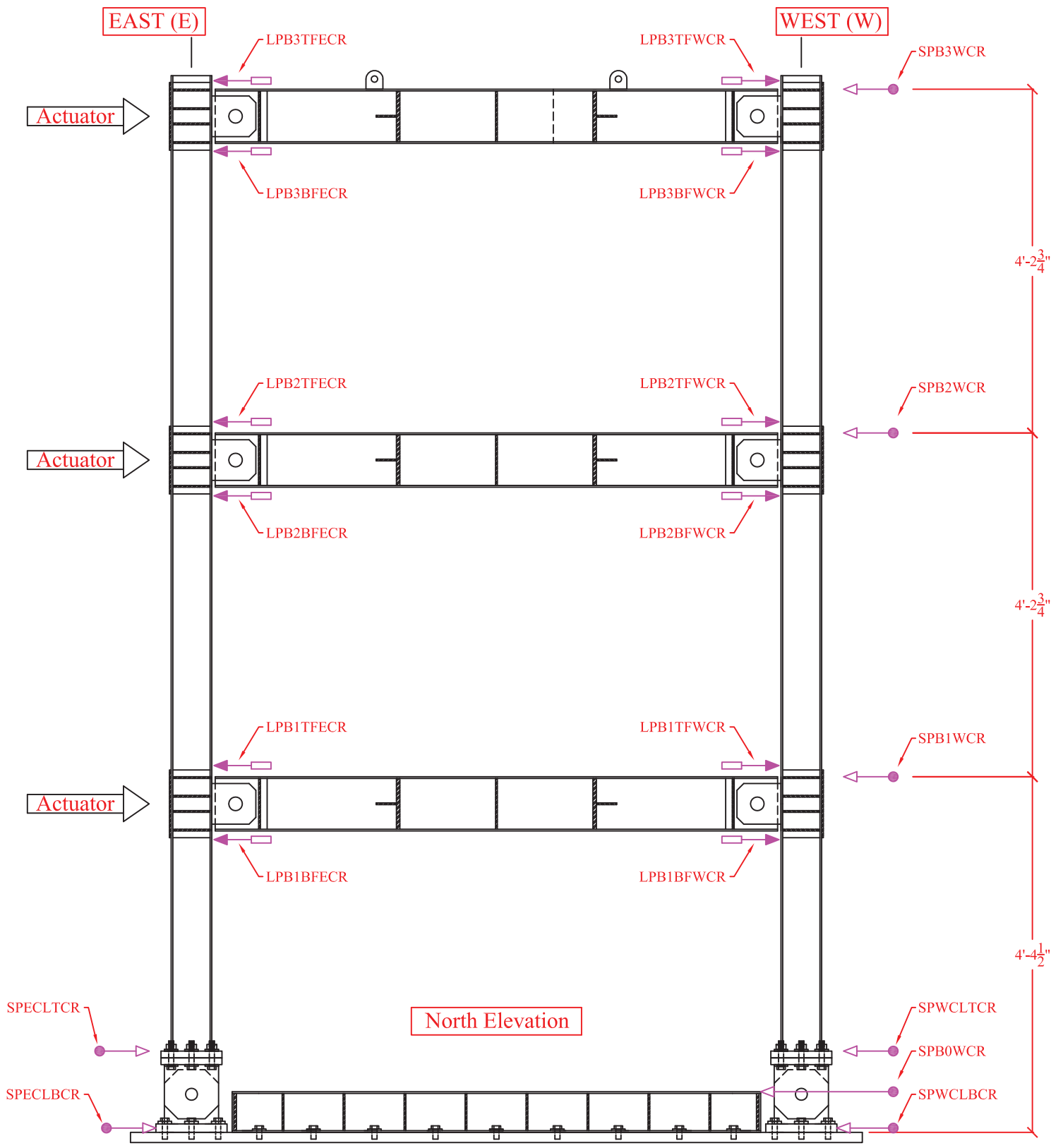
Same As  
Level 3



**NOTE:**  
1) Strain Gage Dimension  
Layout For Frame 2 & 3 Similar

**LEGEND:**  
- Uniaxial Strain Gage (SG)

<b>University at Buffalo</b>			<b>DRWG:</b>
<b>PROJECT:</b> NEESR-SG Self-Centering Steel Plate Shear Walls		<b>CONTENT:</b> Web Strip Strain Gage Dims.	1-2 dim/I1
<b>BY:</b> Daniel M. Dowden	<b>REVISION:</b>	<b>DATE:</b>	<b>SCALE:</b> 3/5" = 1'-0"

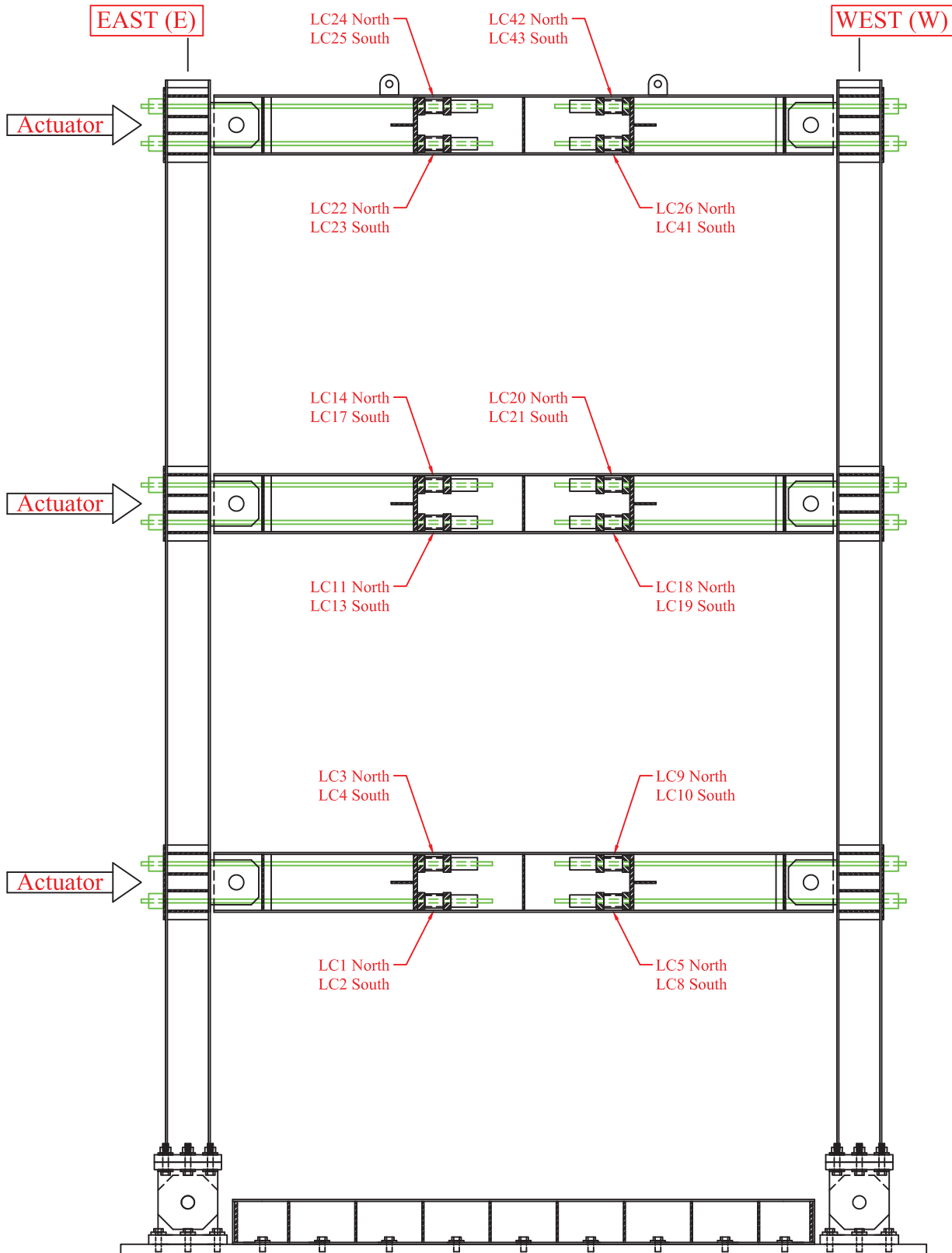


**LEGEND:**

-  Linear Potentiometer
-  String Pot

620

<b>University at Buffalo</b>			<b>DRWG:</b>
<b>PROJECT:</b> NEESR-SG Self-Centering Steel Plate Shear Walls		<b>CONTENT:</b> Frame 3 - Disp. Transducers	3/12
<b>BY:</b> Daniel M. Dowden	<b>REVISION:</b>	<b>DATE:</b>	<b>SCALE:</b> 3/5" = 1'-0"



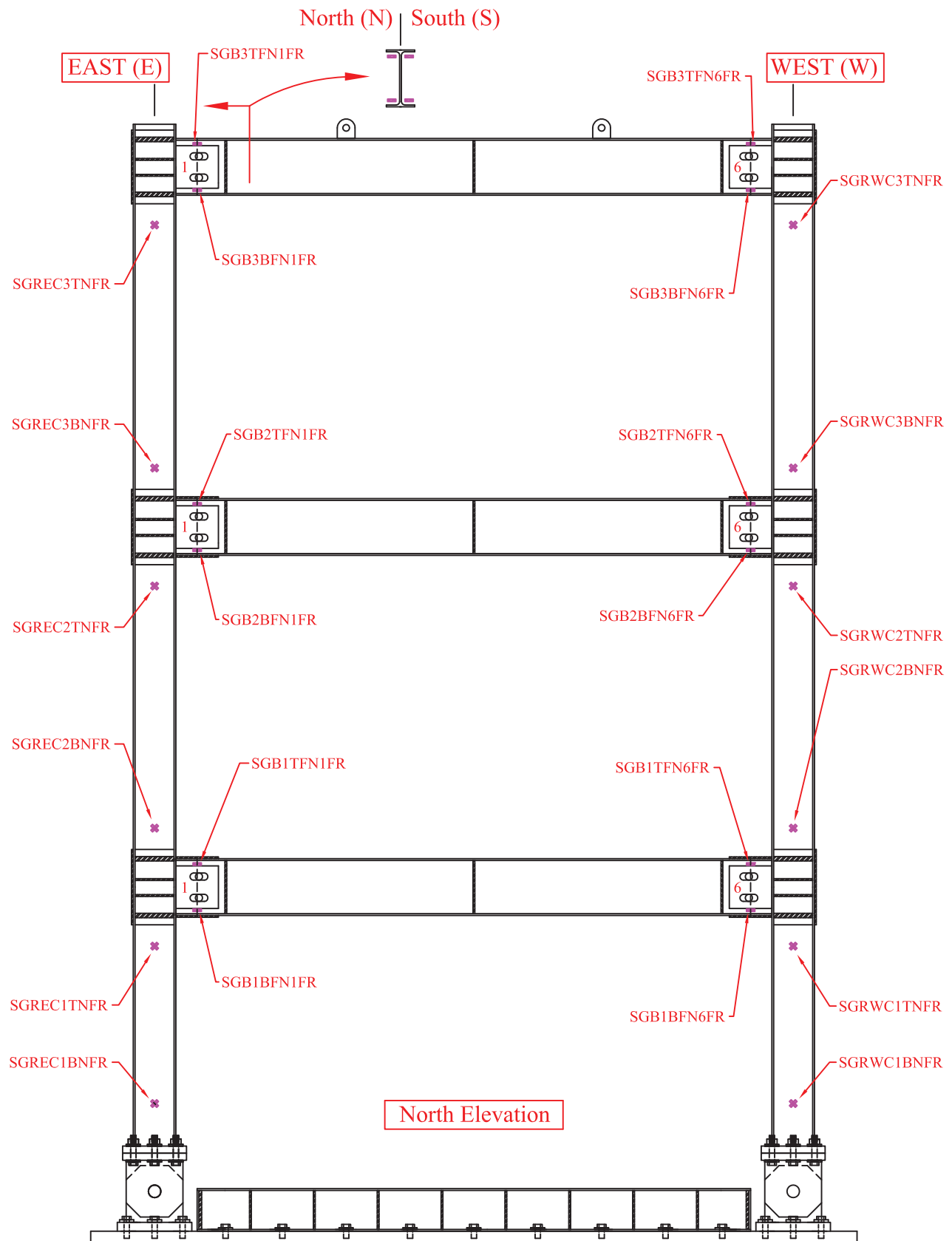
North Elevation

<b>University at Buffalo</b>			<b>DRWG:</b>
<b>PROJECT:</b> NEESR-SG Self-Centering Steel Plate Shear Walls		<b>CONTENT:</b> Frame 3 Load Cells	3/13
<b>BY:</b> Daniel M. Dowden	<b>REVISION:</b>	<b>DATE:</b>	<b>SCALE:</b> 3/5" = 1'-0"



## **APPENDIX A2**

### **SHAKE-TABLE TESTING INSTRUMENTATION DRAWINGS**

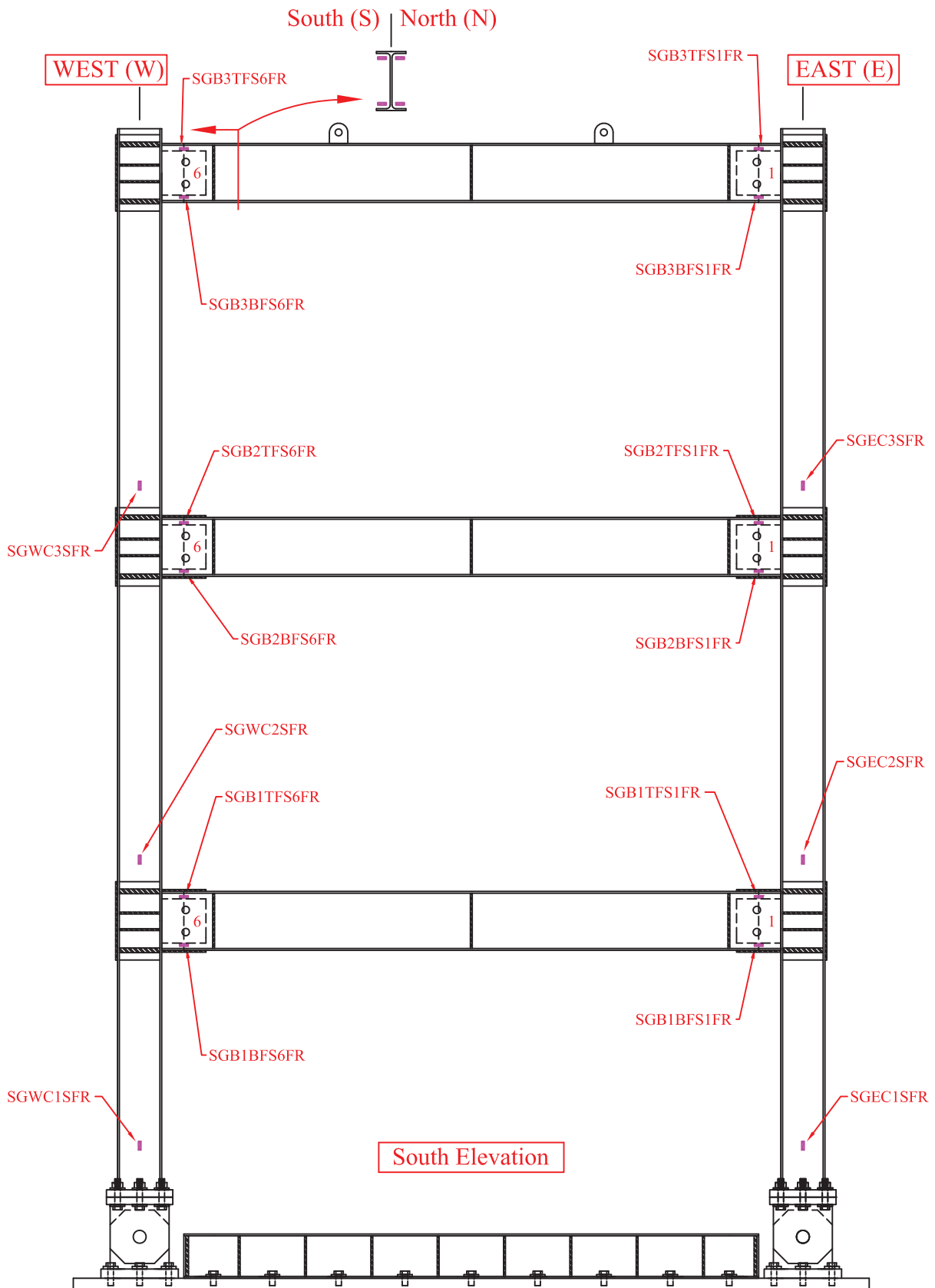


**LEGEND:**

- Uniaxial Strain Gage (SG)
- \* Shear Rosette Strain Gage (SGR)

<b>University at Buffalo - Shake Table Tests</b>			<b>DRWG:</b>
<b>PROJECT:</b> NEESR-SG Self-Centering Steel Plate Shear Walls		<b>CONTENT:</b> Boundary Frame 1 Strain Gages	1-1a/11
<b>BY:</b> Daniel M. Dowden	<b>REVISION:</b>	<b>DATE:</b>	<b>SCALE:</b> 3/5" = 1'-0"





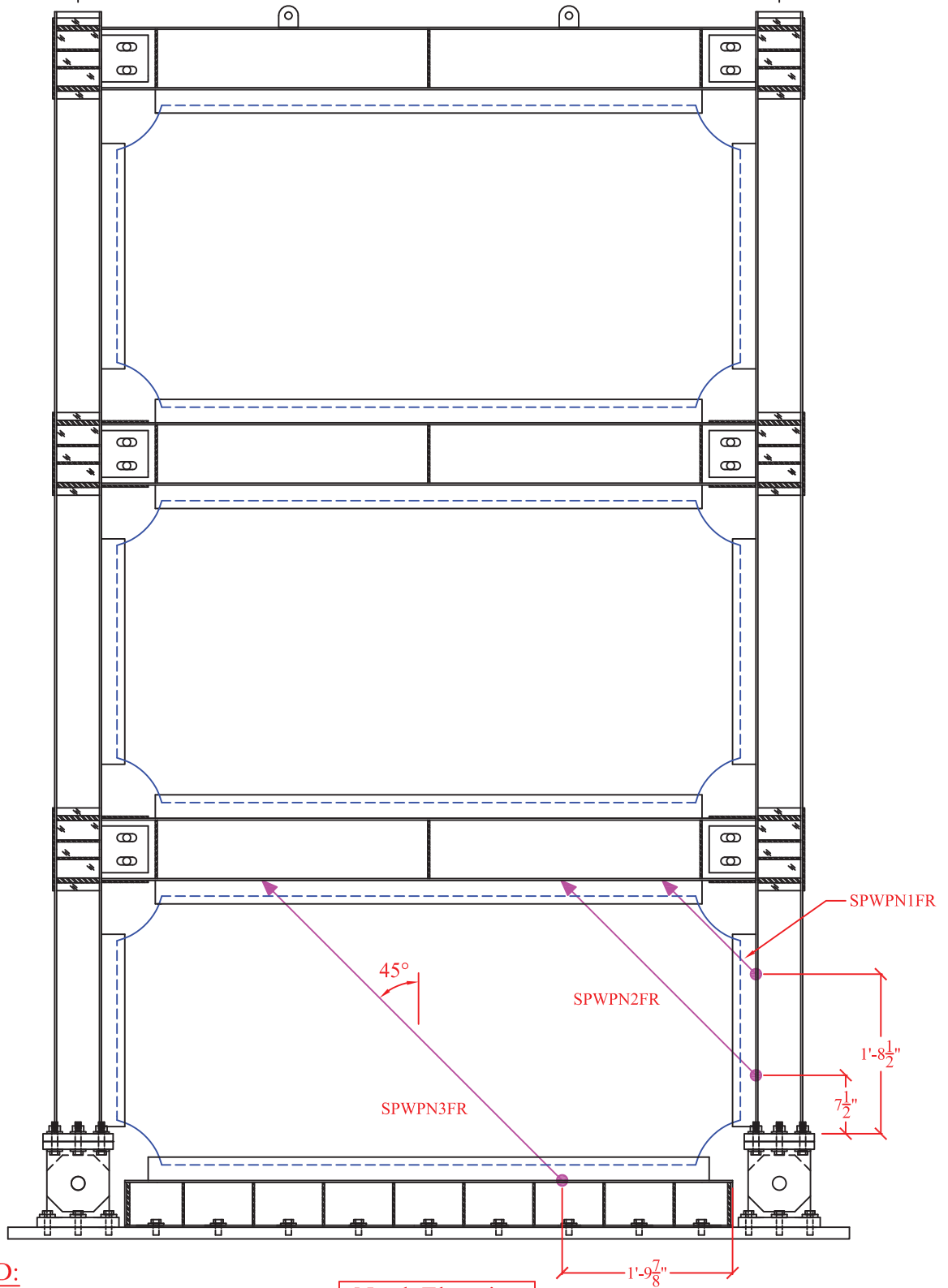
**LEGEND:**

- Uniaxial Strain Gage (SG)

<b>University at Buffalo - Shake Table Tests</b>			<b>DRWG:</b>
<b>PROJECT:</b> NEESR-SG Self-Centering Steel Plate Shear Walls		<b>CONTENT:</b> Boundary Frame 1 Strain Gages	1-1b/11
<b>BY:</b> Daniel M. Dowden	<b>REVISION:</b>	<b>DATE:</b>	<b>SCALE:</b> 3/5" = 1'-0"

EAST (E)

WEST (W)

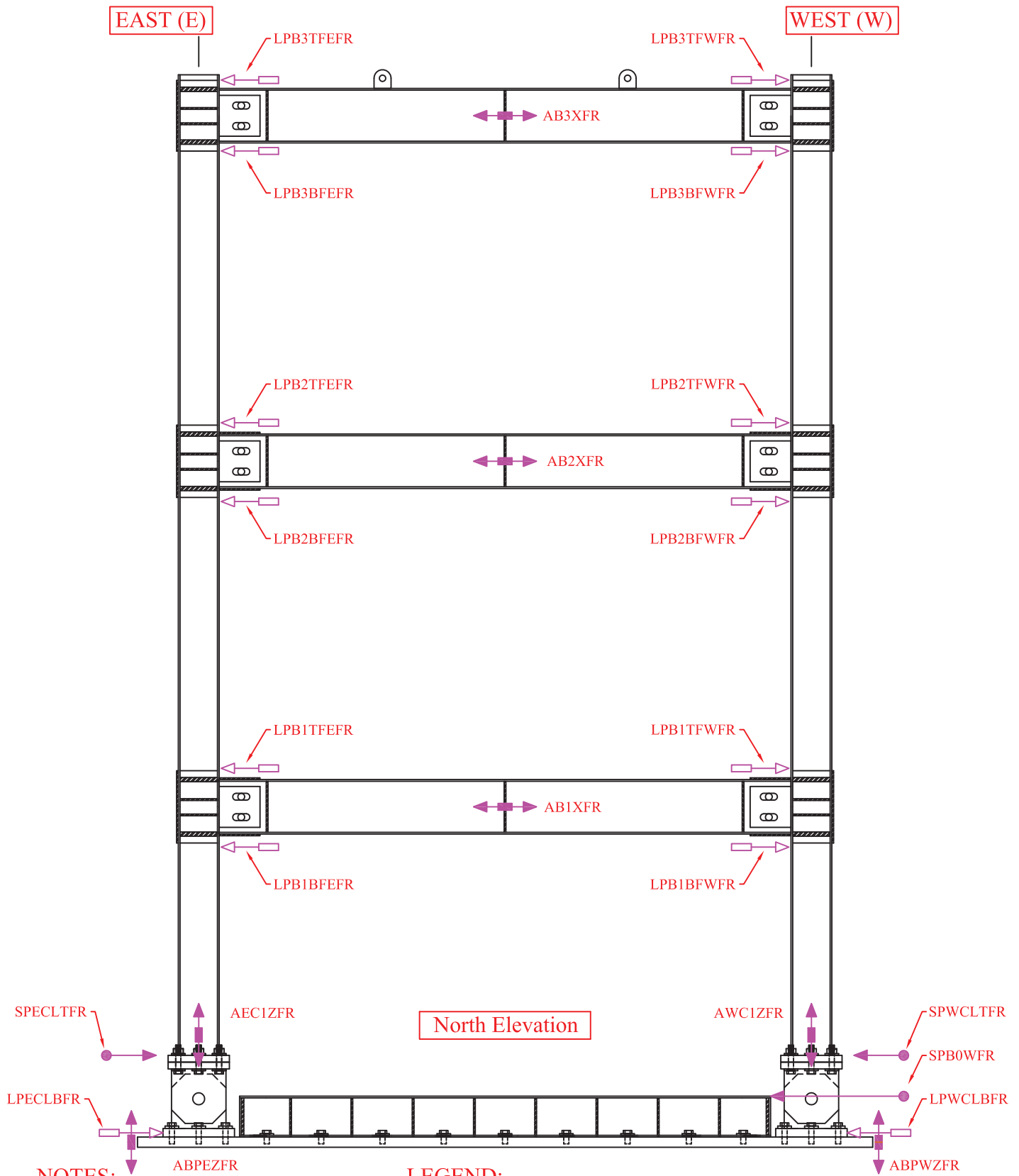


LEGEND:

● → String Pot

North Elevation

<b>University at Buffalo - Shake Table Tests</b>			<b>DRWG:</b>
<b>PROJECT:</b> NEESR-SG Self-Centering Steel Plate Shear Walls		<b>CONTENT:</b> Frame 1 Web Plate String Pots	1-2/11
<b>BY:</b> Daniel M. Dowden	<b>REVISION:</b>	<b>DATE:</b>	<b>SCALE:</b> 3/5" = 1'-0"






North Elevation

NOTES:

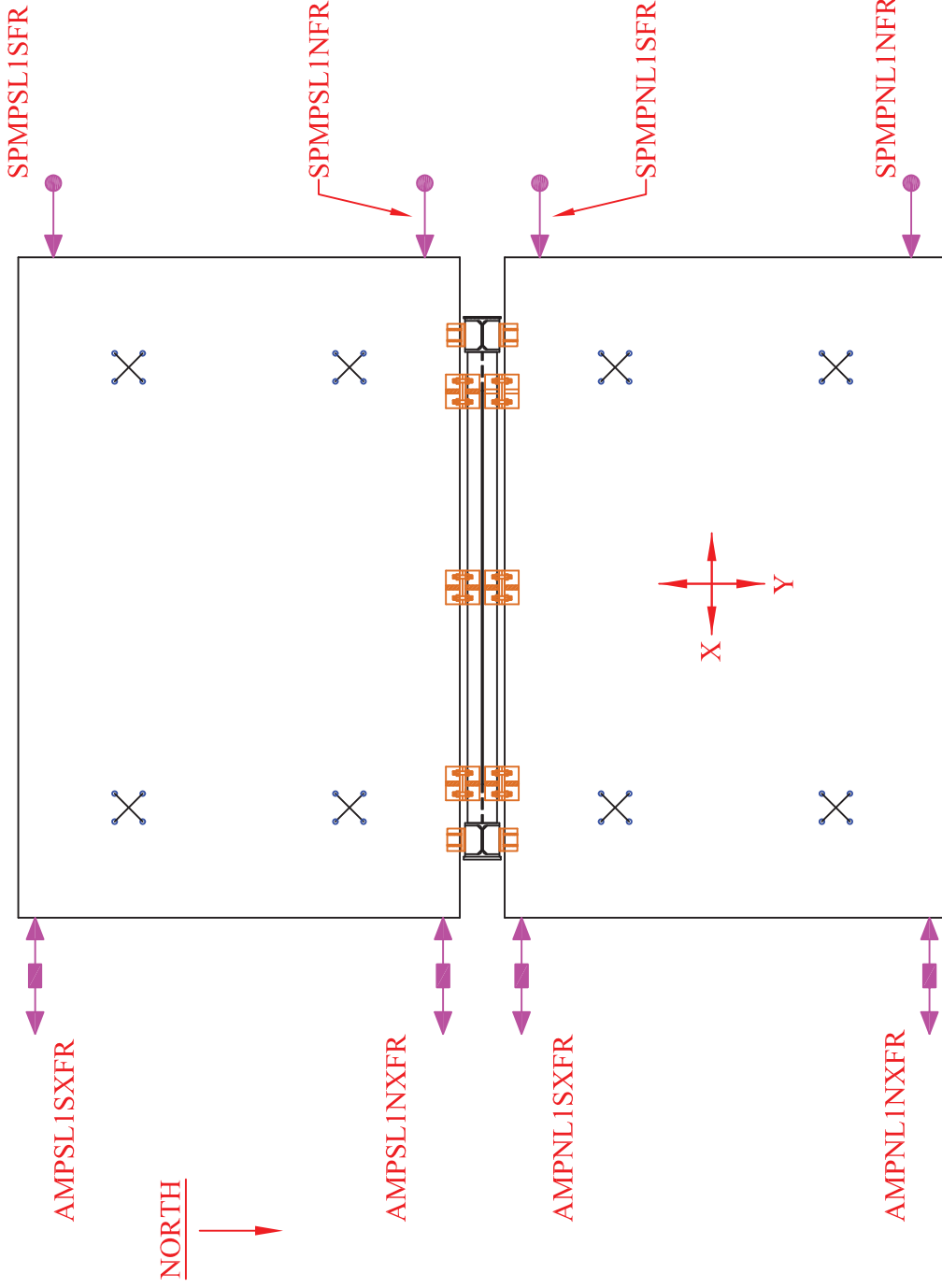
- 1) SPB0WFR not required for Bare Frame Test
- 2) Infill Web Plates Not Shown For Clarity

LEGEND:

-  Linear Potentiometer
-  String Pot
-  Accelerometer (X = Long., Y = Transverse, Z = Vertical)

627

<b>University at Buffalo - Shake Table Tests</b>			<b>DRWG:</b>
<b>PROJECT:</b> NEESR-SG Self-Centering Steel Plate Shear Walls		<b>CONTENT:</b> Frame 1 - Sensors	1-1/12
<b>BY:</b> Daniel M. Dowden	<b>REVISION:</b>	<b>DATE:</b>	<b>SCALE:</b> 3/5" = 1'-0"

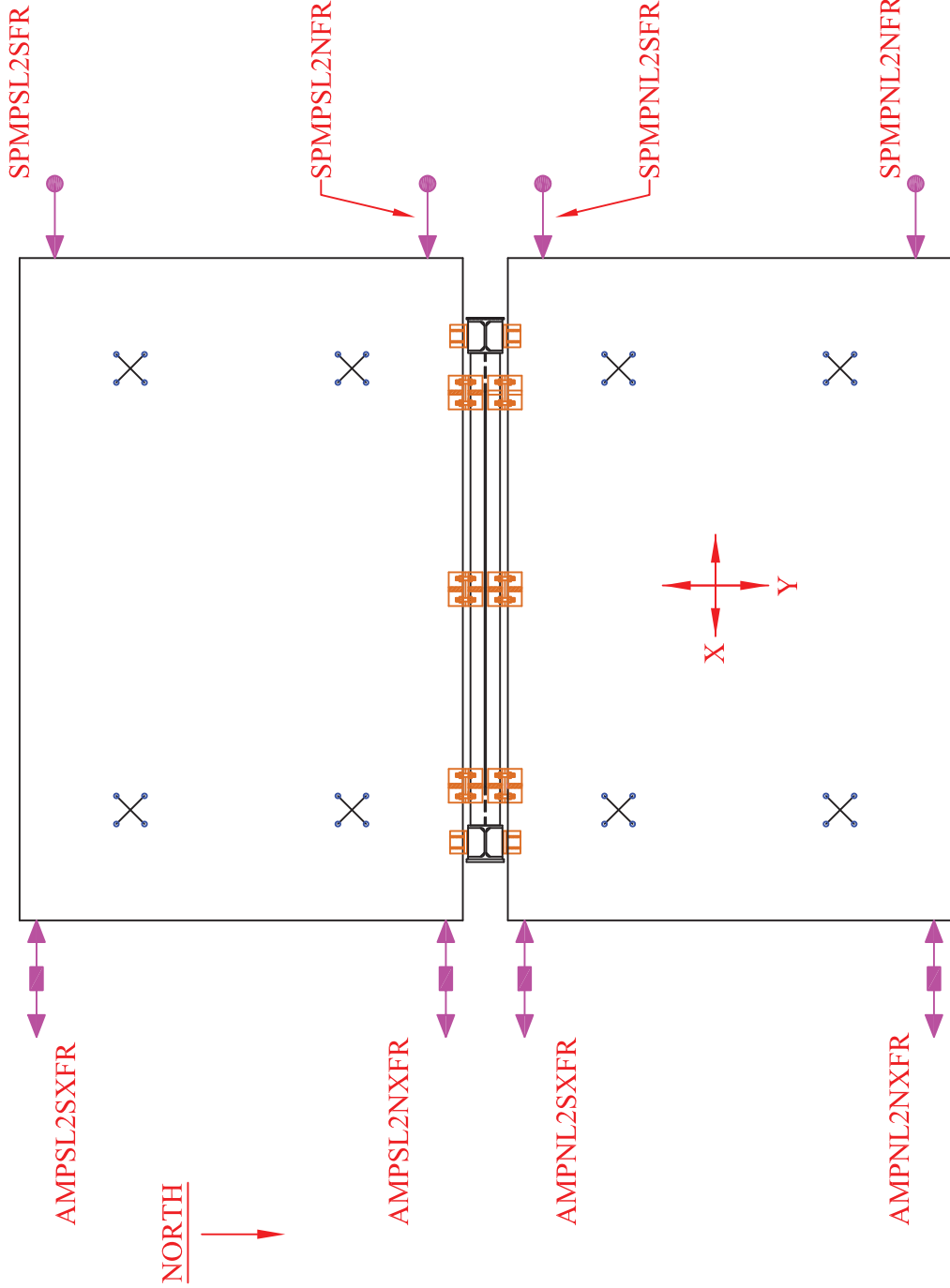


**LEGEND:**

- String Pot
- ↔ Accelerometer (X = Long., Y = Transverse, Z = Vertical)

Level 1 - Plan

<b>University at Buffalo - Shake Table Tests</b>		<b>DRWG:</b>
<b>PROJECT:</b> NEESR-SG Self-Centering Steel Plate Shear Walls	<b>CONTENT:</b> GMF Sensors - Frame 1: Level 1	1-2/12
<b>BY:</b> Daniel M. Dowden	<b>REVISION:</b>	<b>SCALE:</b> 3/8" = 1'-0"
	<b>DATE:</b>	

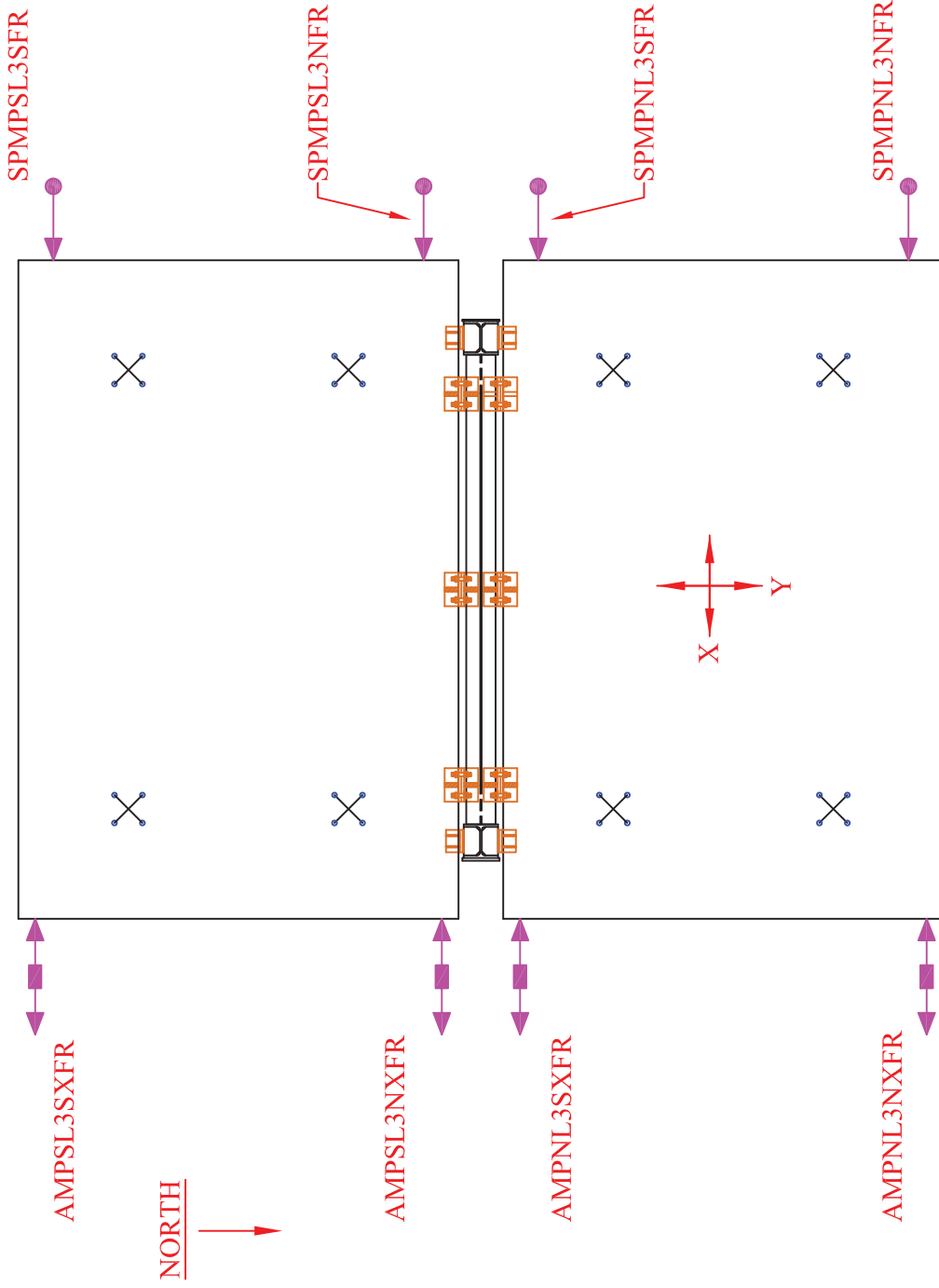


**LEGEND:**

- String Pot
- ↔ Accelerometer (X = Long., Y = Transverse, Z = Vertical)

Level 2 - Plan

<b>University at Buffalo - Shake Table Tests</b>		<b>DRWG:</b>
<b>PROJECT:</b> NEESR-SG Self-Centering Steel Plate Shear Walls	<b>CONTENT:</b> GMF Sensors - Frame 1: Level 2	1-3/12
<b>BY:</b> Daniel M. Dowden	<b>REVISION:</b>	<b>SCALE:</b> 3/8" = 1'-0"
	<b>DATE:</b>	

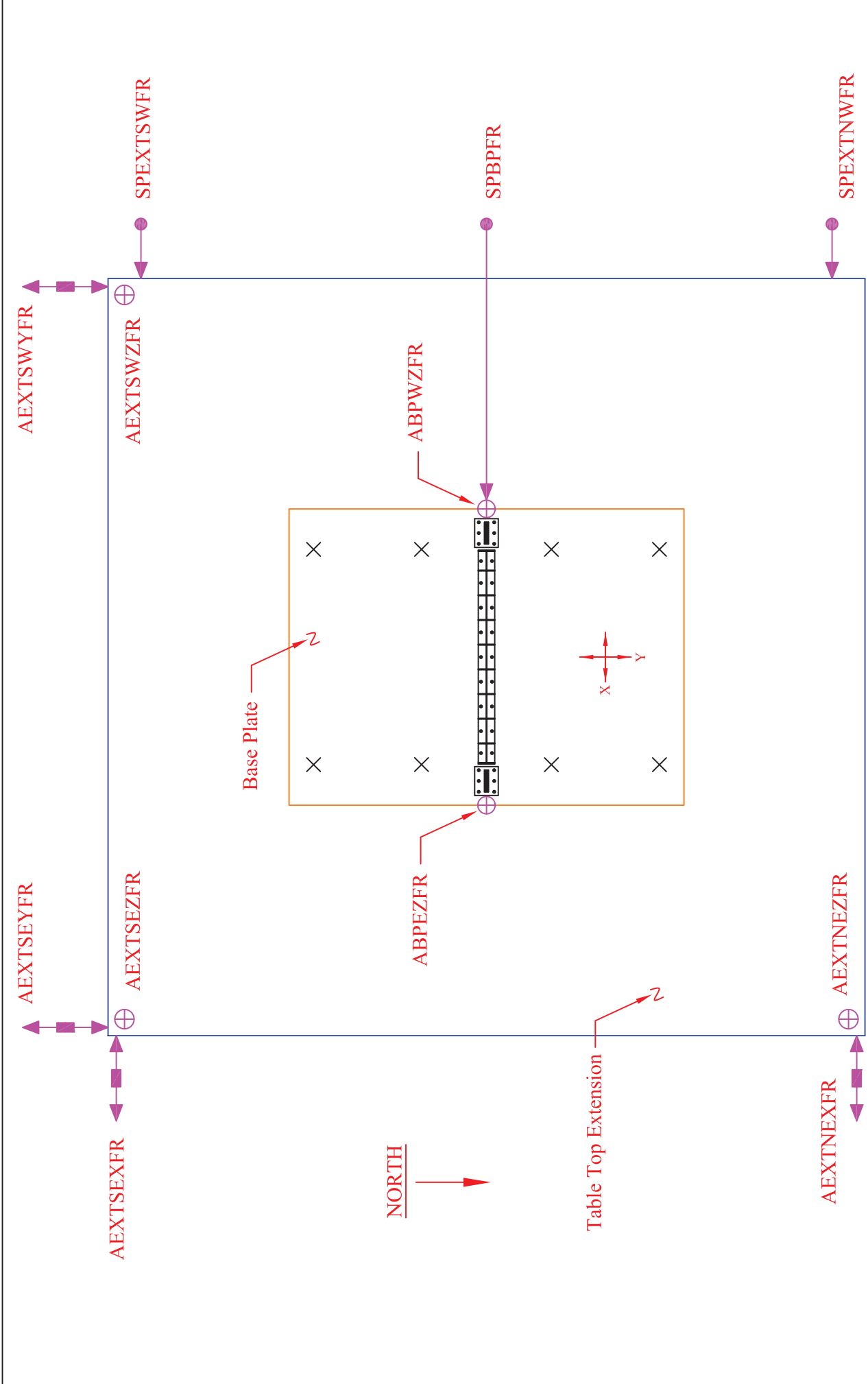


**LEGEND:**

- String Pot
- ↔ Accelerometer (X = Long., Y = Transverse, Z = Vertical)

Level 3 - Plan

<b>University at Buffalo - Shake Table Tests</b>		<b>DRWG:</b>
<b>PROJECT:</b> NEESR-SG Self-Centering Steel Plate Shear Walls	<b>CONTENT:</b> GMF Sensors - Frame 1: Level 3	1-4/12
<b>BY:</b> Daniel M. Dowden	<b>REVISION:</b>	<b>SCALE:</b> 3/8" = 1'-0"
	<b>DATE:</b>	

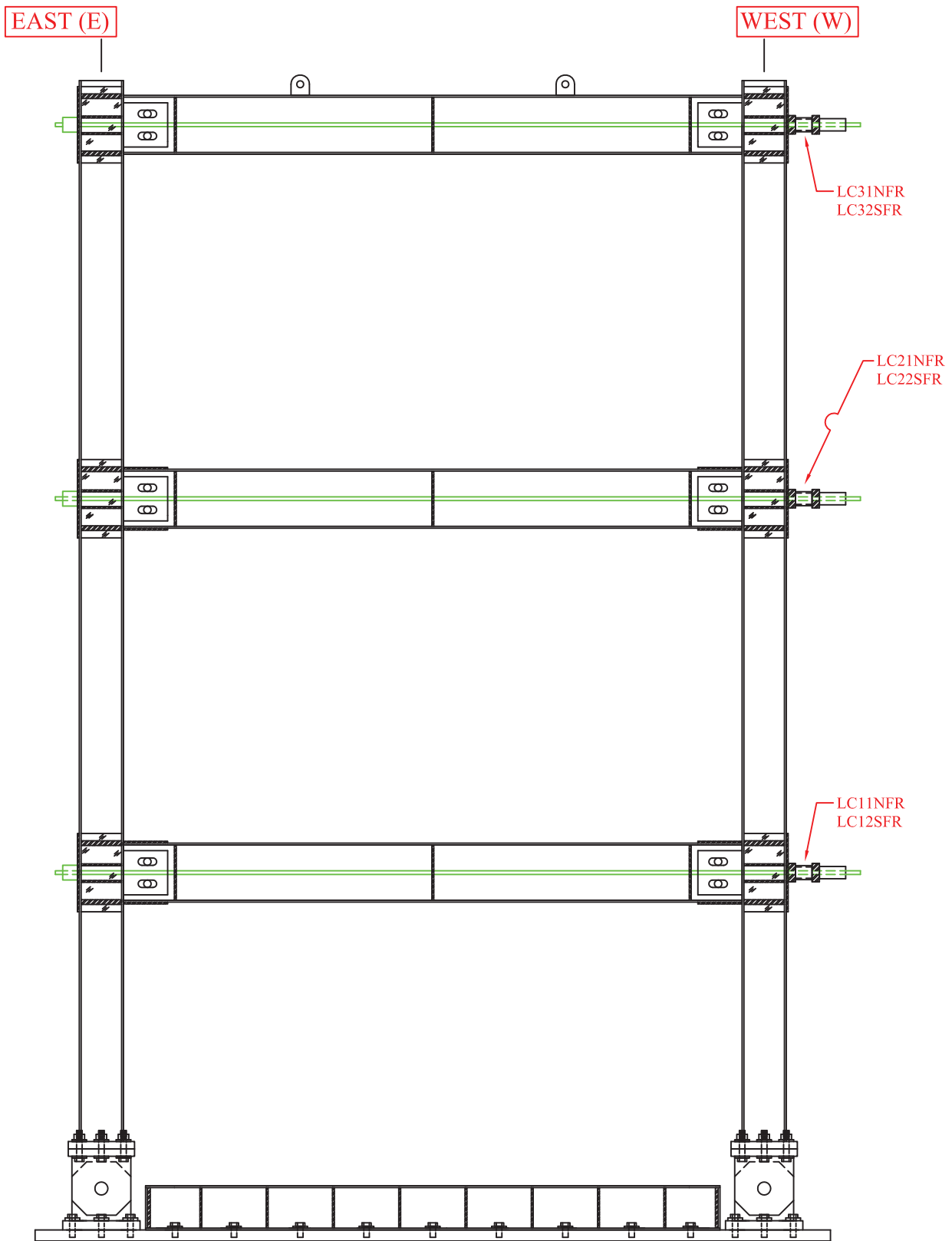


**PLAN VIEW**

**LEGEND:**

- ◄—■—► Accelerometer (X = Long., Y = Transverse, Z = Vertical)
- ⊕ Accelerometer (Vertical)
- String Pot

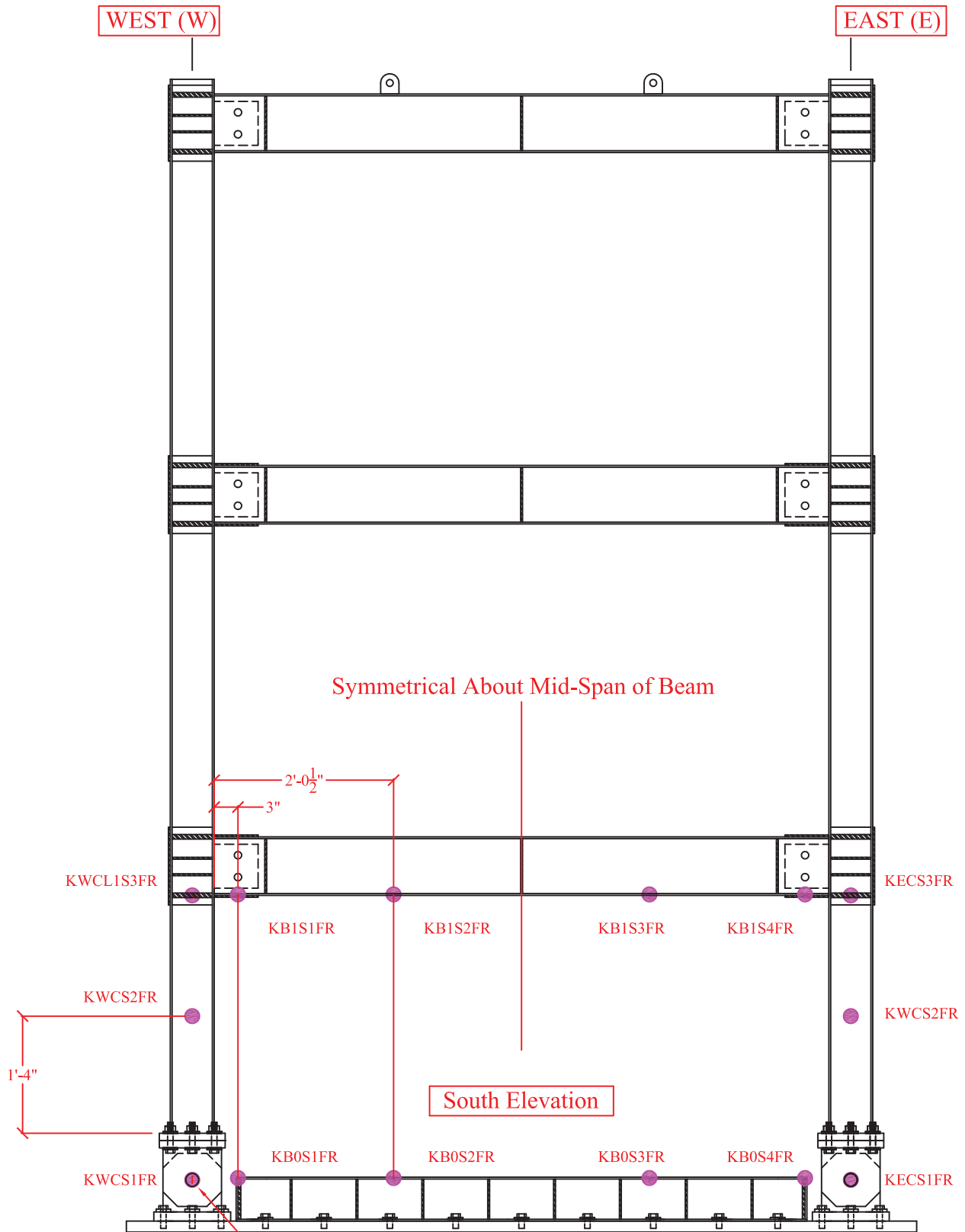
<b>University at Buffalo - Shake Table Tests</b>		<b>DRWG:</b>
<b>PROJECT:</b> NEESR-SG Self-Centering Steel Plate Shear Walls	<b>CONTENT:</b> Shake Table Ext. & Base Plate Sensors	1-5/12
<b>BY:</b> Daniel M. Dowden	<b>REVISION:</b>	<b>SCALE:</b> 1/4" = 1'-0"
	<b>DATE:</b>	



North Elevation

<b>University at Buffalo - Shake Table Tests</b>			<b>DRWG:</b>
<b>PROJECT:</b> NEESR-SG Self-Centering Steel Plate Shear Walls		<b>CONTENT:</b> Frame 1 - Load Cells	1/13
<b>BY:</b> Daniel M. Dowden	<b>REVISION:</b>	<b>DATE:</b>	<b>SCALE:</b> 3/5" = 1'-0"





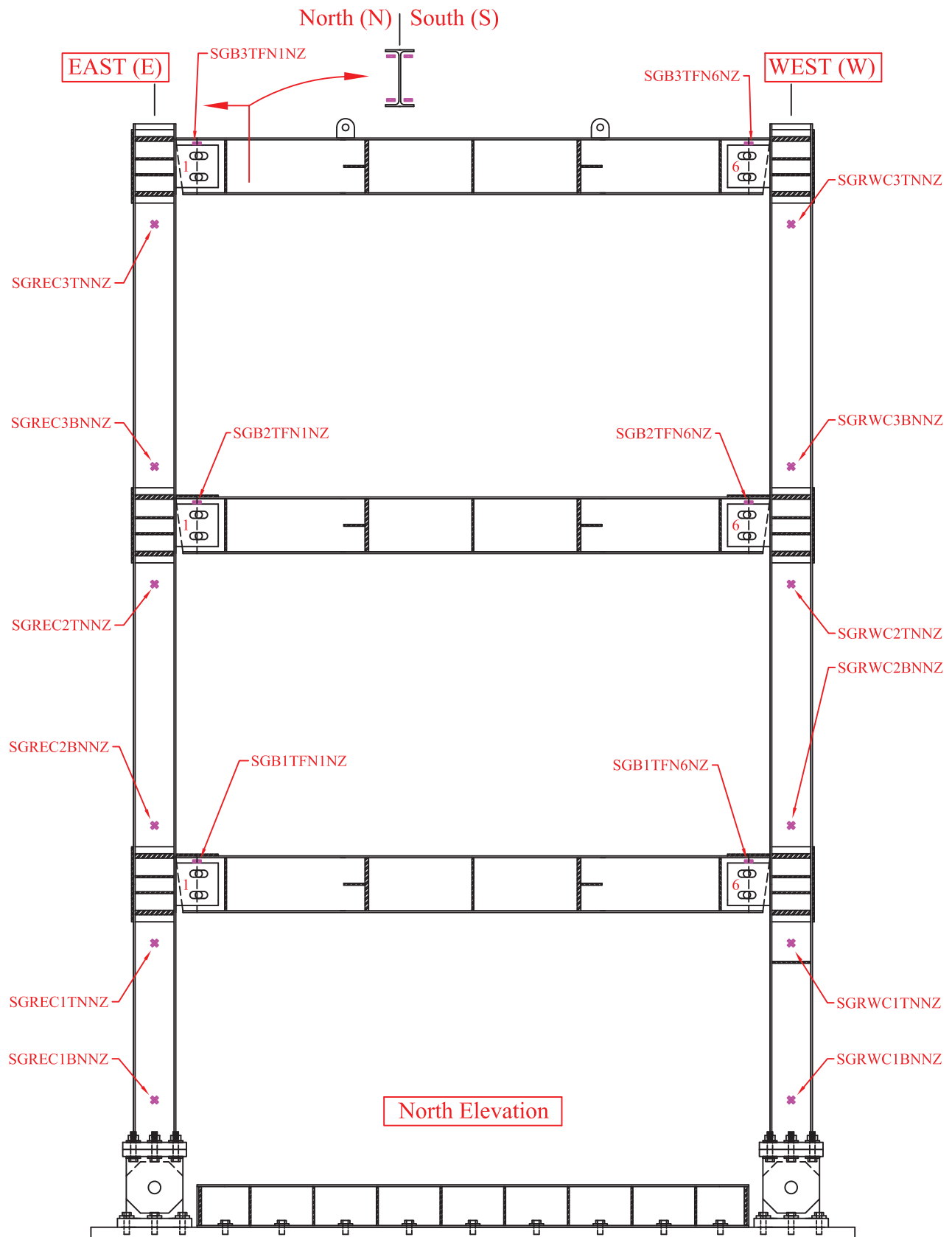
**NOTES:**  
 Infill Web Plates Not  
 Shown For Clarity

Krypton Sensor  
 On Clevis Pin

**LEGEND:**

● Krypton

<b>University at Buffalo - Shake Table Tests</b>			<b>DRWG:</b>
<b>PROJECT:</b> NEESR-SG Self-Centering Steel Plate Shear Walls		<b>CONTENT:</b> Frame 1 - Krypton Sensors	1/14
<b>BY:</b> Daniel M. Dowden	<b>REVISION:</b>	<b>DATE:</b>	<b>SCALE:</b> 3/5" = 1'-0"

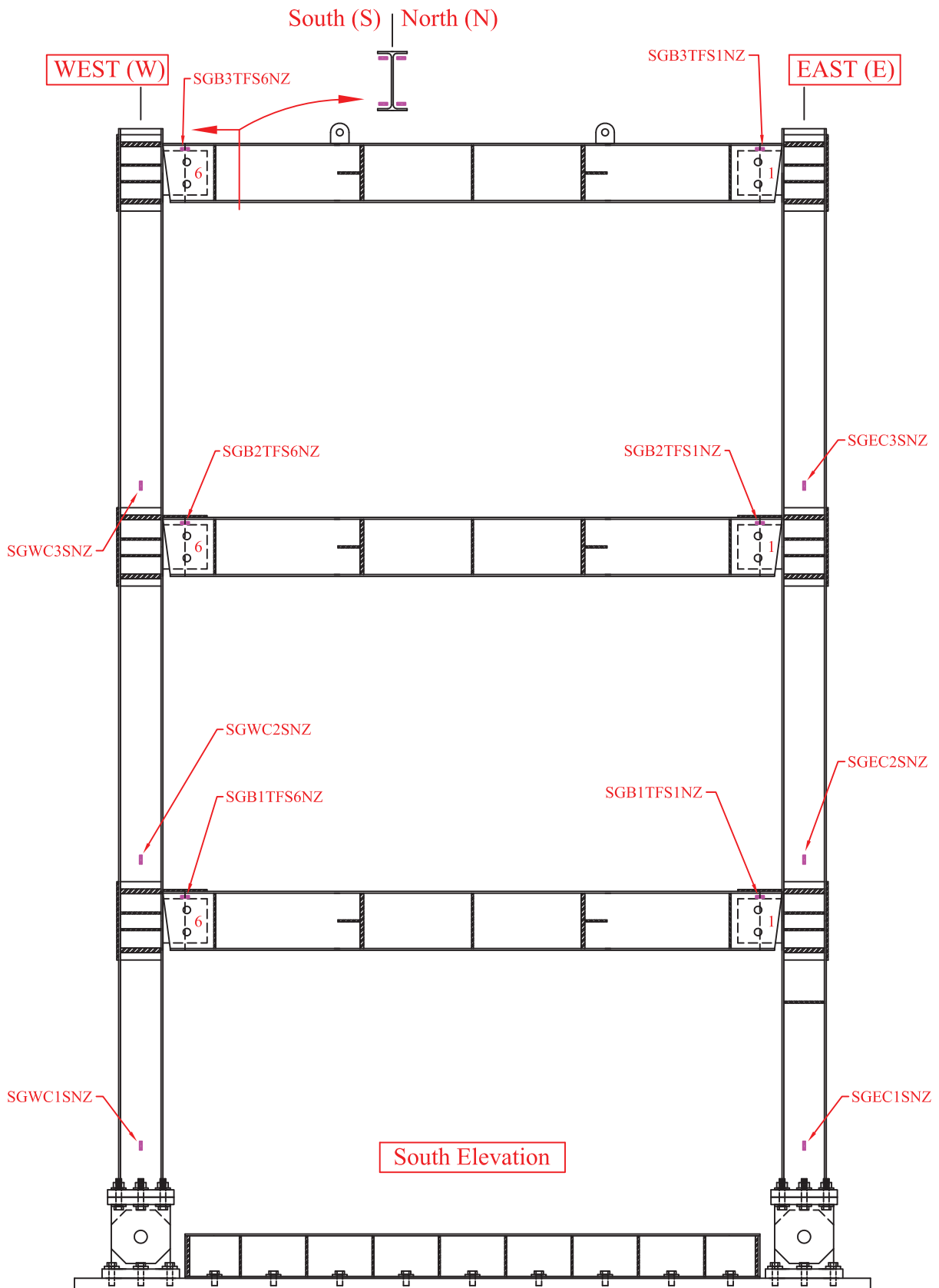


**LEGEND:**

- Uniaxial Strain Gage (SG)
- \* Shear Rosette Strain Gage (SGR)

634

<b>University at Buffalo</b>			<b>DRWG:</b>
<b>PROJECT:</b> NEESR-SG Self-Centering Steel Plate Shear Walls		<b>CONTENT:</b> Boundary Frame 2 Strain Gages	2-1a/I1
<b>BY:</b> Daniel M. Dowden	<b>REVISION:</b>	<b>DATE:</b>	<b>SCALE:</b> 3/5" = 1'-0"



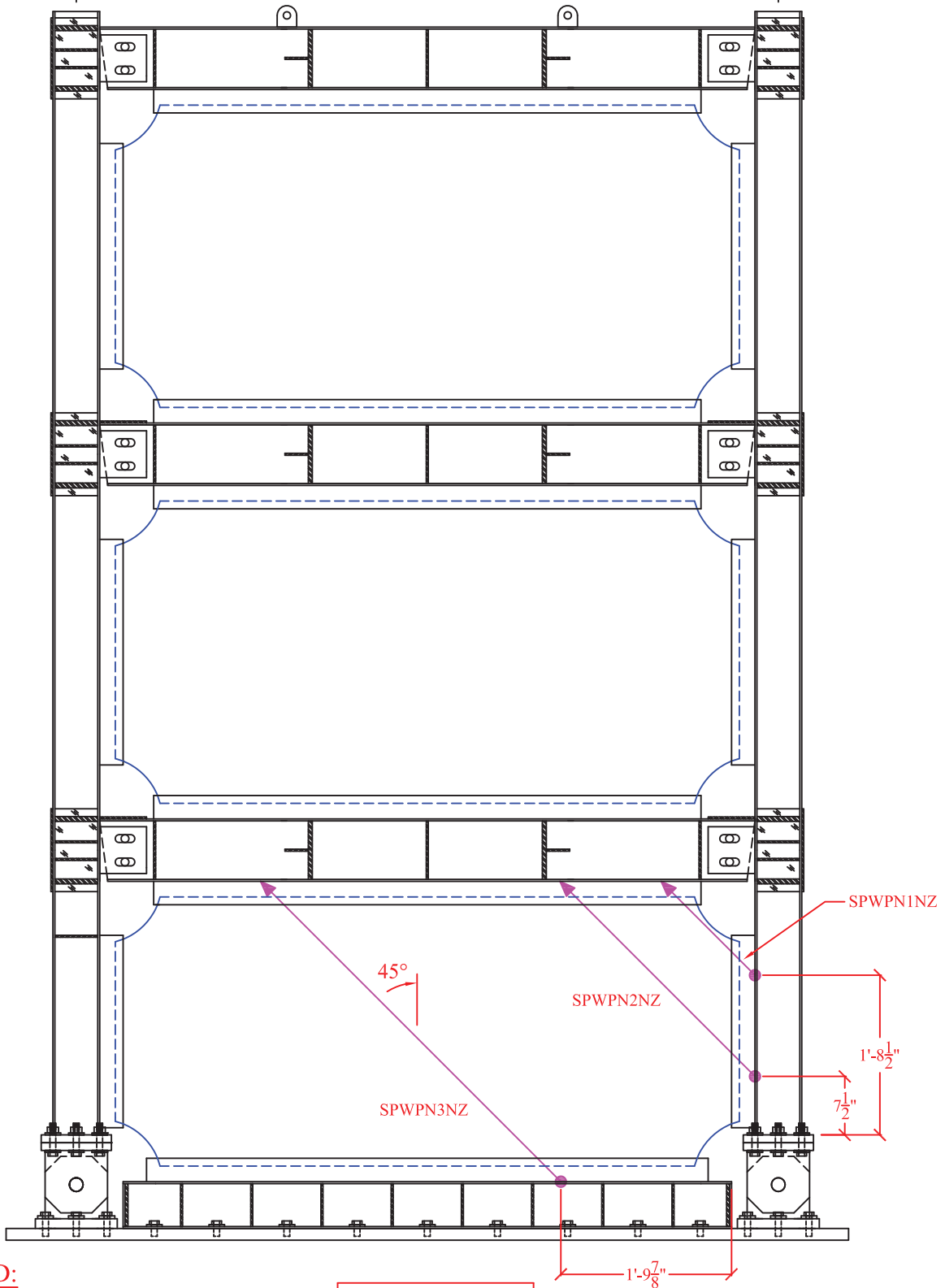
**LEGEND:**

- Uniaxial Strain Gage (SG)

<b>University at Buffalo</b>			<b>DRWG:</b>
<b>PROJECT:</b> NEESR-SG Self-Centering Steel Plate Shear Walls		<b>CONTENT:</b> Boundary Frame 2 Strain Gages	2-1b/11
<b>BY:</b> Daniel M. Dowden	<b>REVISION:</b>	<b>DATE:</b>	<b>SCALE:</b> 3/5" = 1'-0"

EAST (E)

WEST (W)



North Elevation

LEGEND:

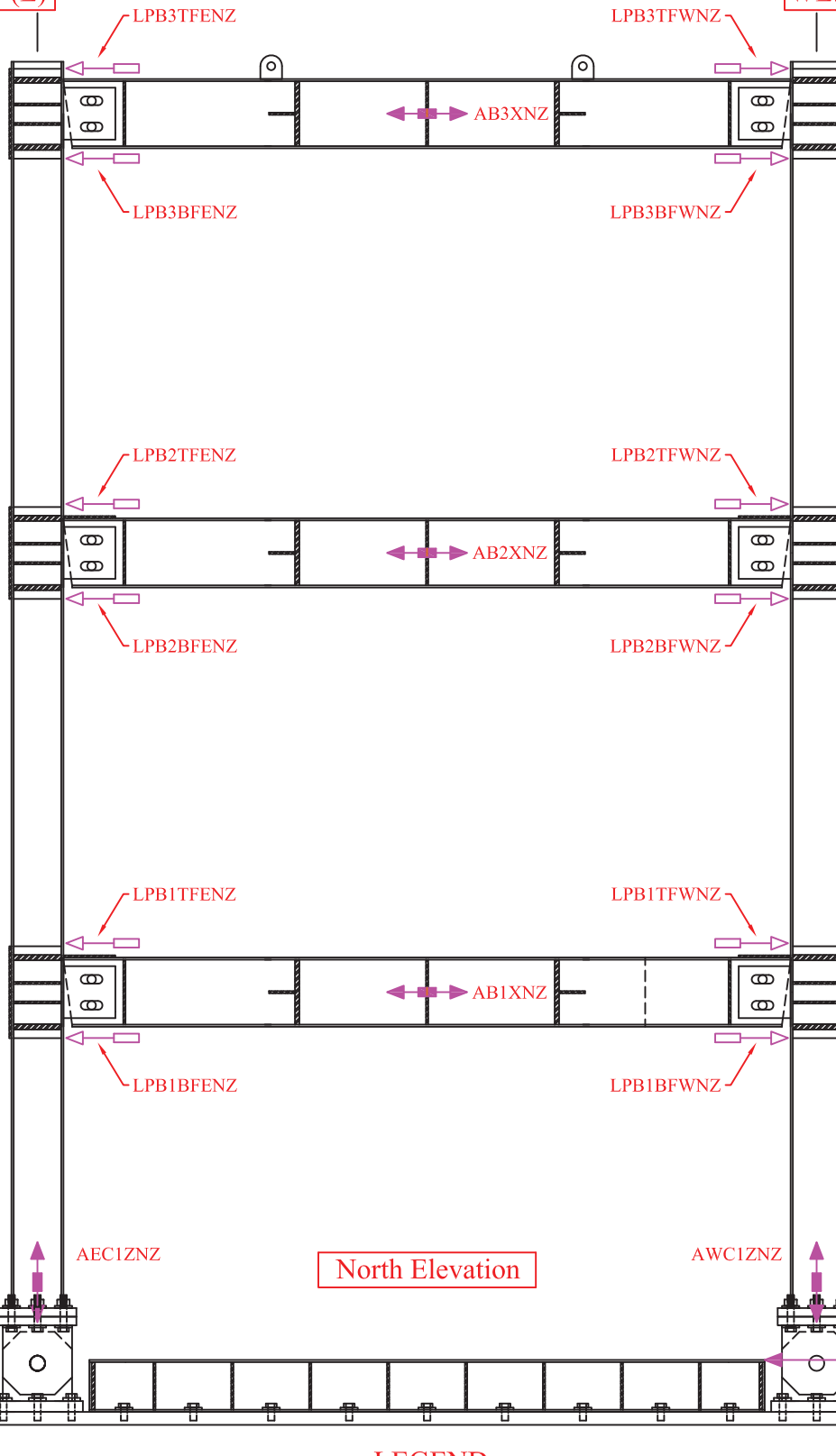
● → String Pot

636

<b>University at Buffalo</b>			<b>DRWG:</b>
<b>PROJECT:</b> NEESR-SG Self-Centering Steel Plate Shear Walls		<b>CONTENT:</b> Frame 2 Web Plate String Pots	2-2/11
<b>BY:</b> Daniel M. Dowden	<b>REVISION:</b>	<b>DATE:</b>	<b>SCALE:</b> 3/5" = 1'-0"

EAST (E)

WEST (W)



North Elevation

**NOTES:**

1) SPB0WNZ not required for Bare Frame Test

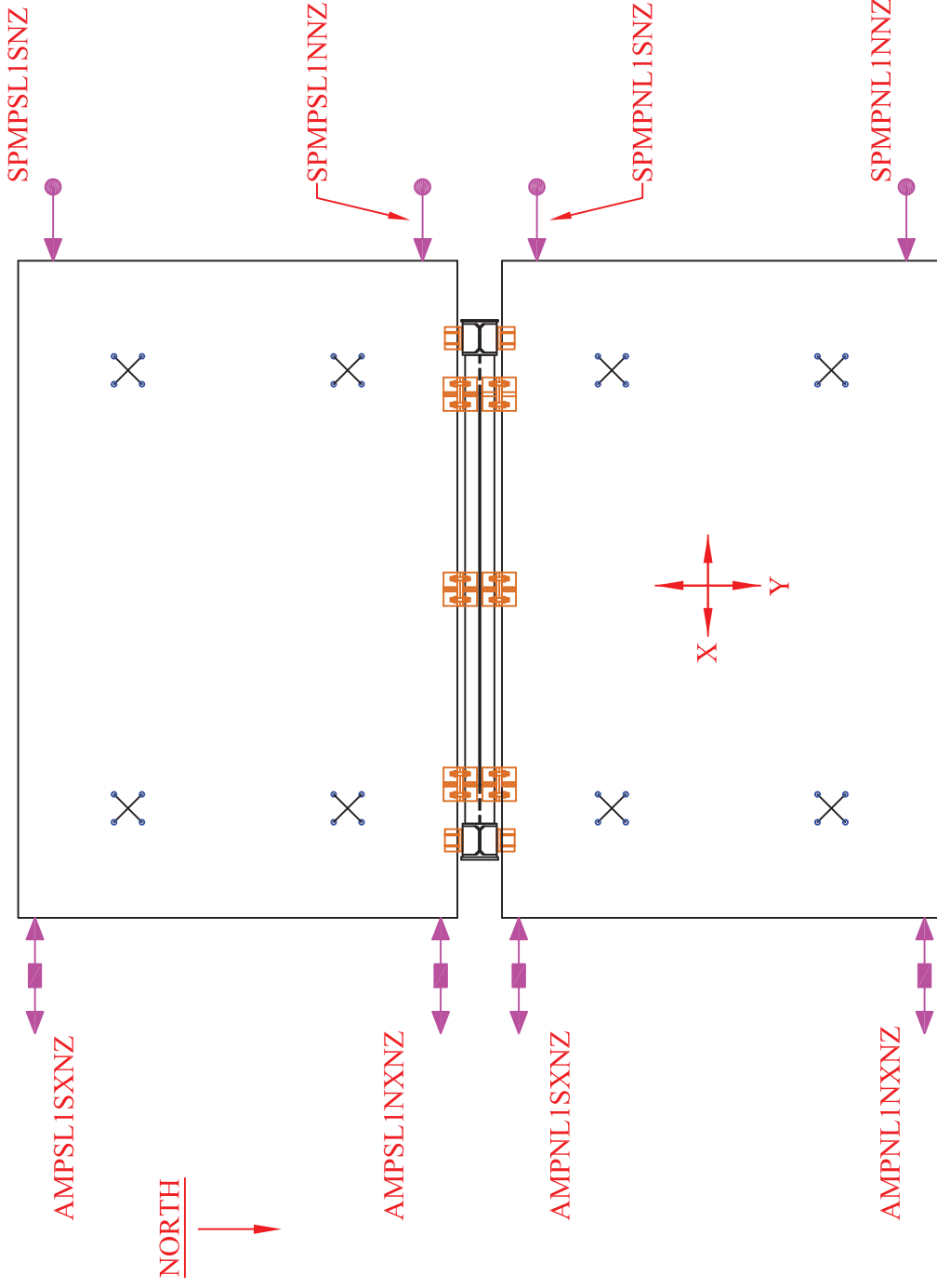
2) Infill Web Plates Not Shown For Clarity

**LEGEND:**

-  Linear Potentiometer
-  String Pot
-  Accelerometer

637

<b>University at Buffalo - Shake Table Tests</b>			<b>DRWG:</b>
<b>PROJECT:</b> NEESR-SG Self-Centering Steel Plate Shear Walls		<b>CONTENT:</b> Frame 2 - Sensors	2-1/2
<b>BY:</b> Daniel M. Dowden	<b>REVISION:</b>	<b>DATE:</b>	<b>SCALE:</b> 3/5" = 1'-0"

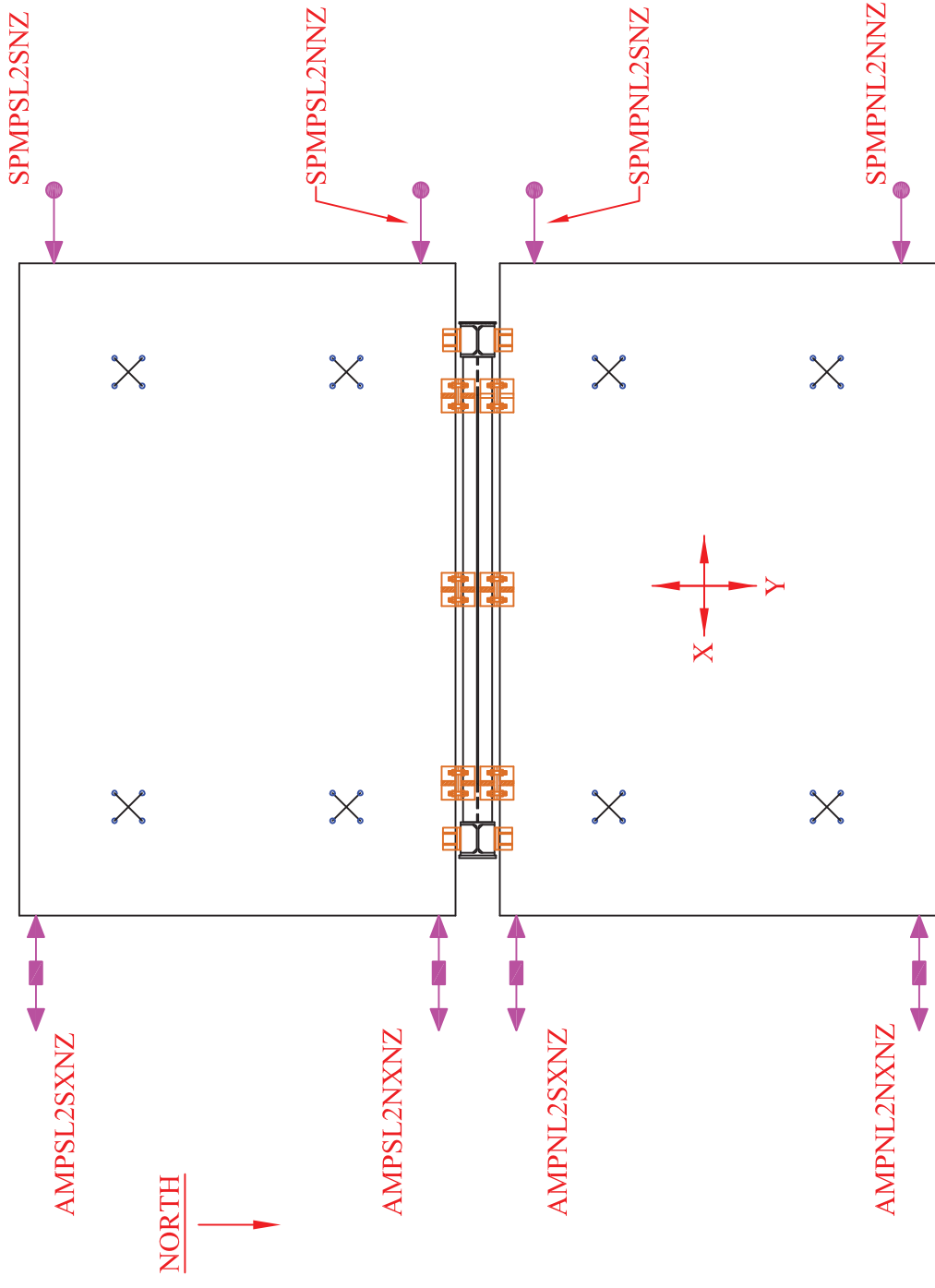


**LEGEND:**

- String Pot
- ◄► Accelerometer (X = Long., Y = Transverse, Z = Vertical)

Level 1 - Plan

<b>University at Buffalo - Shake Table Tests</b>		<b>DRWG:</b>
<b>PROJECT:</b> NEESR-SG Self-Centering Steel Plate Shear Walls	<b>CONTENT:</b> GMF Sensors - Frame 2: Level 1	2-2/12
<b>BY:</b> Daniel M. Dowden	<b>REVISION:</b>	<b>SCALE:</b> 3/8" = 1'-0"
	<b>DATE:</b>	

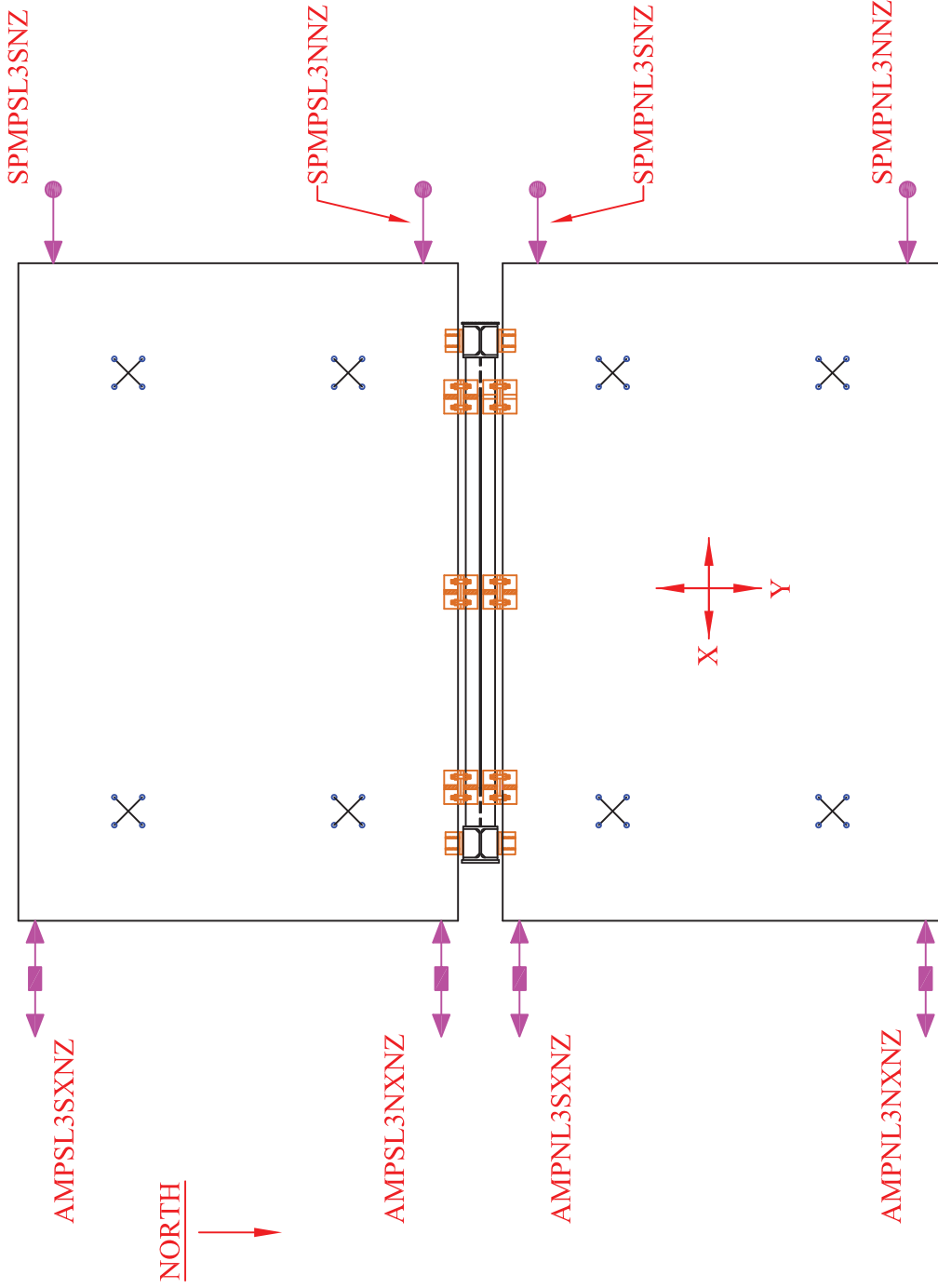


LEGEND:

- String Pot
- ◄► Accelerometer (X = Long., Y = Transverse, Z = Vertical)

Level 2 - Plan

<b>University at Buffalo - Shake Table Tests</b>		<b>DRWG:</b>
<b>PROJECT:</b> NEESR-SG Self-Centering Steel Plate Shear Walls	<b>CONTENT:</b> GMF Sensors - Frame 2: Level 2	2-3/12
<b>BY:</b> Daniel M. Dowden	<b>REVISION:</b>	<b>SCALE:</b> 3/8" = 1'-0"
	<b>DATE:</b>	



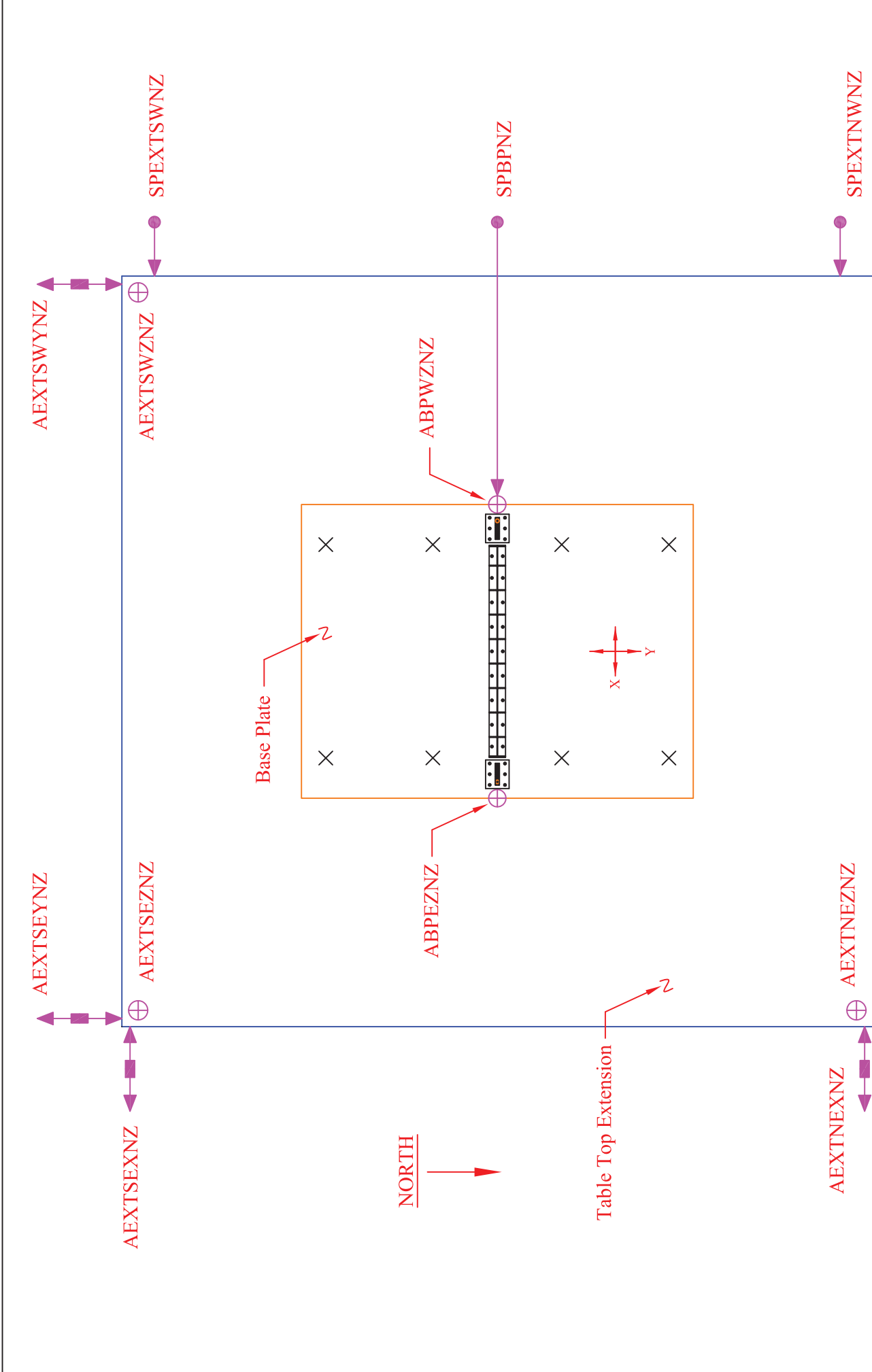
**LEGEND:**

- String Pot
- ↔ Accelerometer (X = Long., Y = Transverse, Z = Vertical)

Level 3 - Plan

<b>University at Buffalo - Shake Table Tests</b>		<b>DRWG:</b>
<b>PROJECT:</b> NEESR-SG Self-Centering Steel Plate Shear Walls	<b>CONTENT:</b> GMF Sensors - Frame 2: Level 3	2-4/12
<b>BY:</b> Daniel M. Dowden	<b>REVISION:</b>	<b>SCALE:</b> 3/8" = 1'-0"
	<b>DATE:</b>	



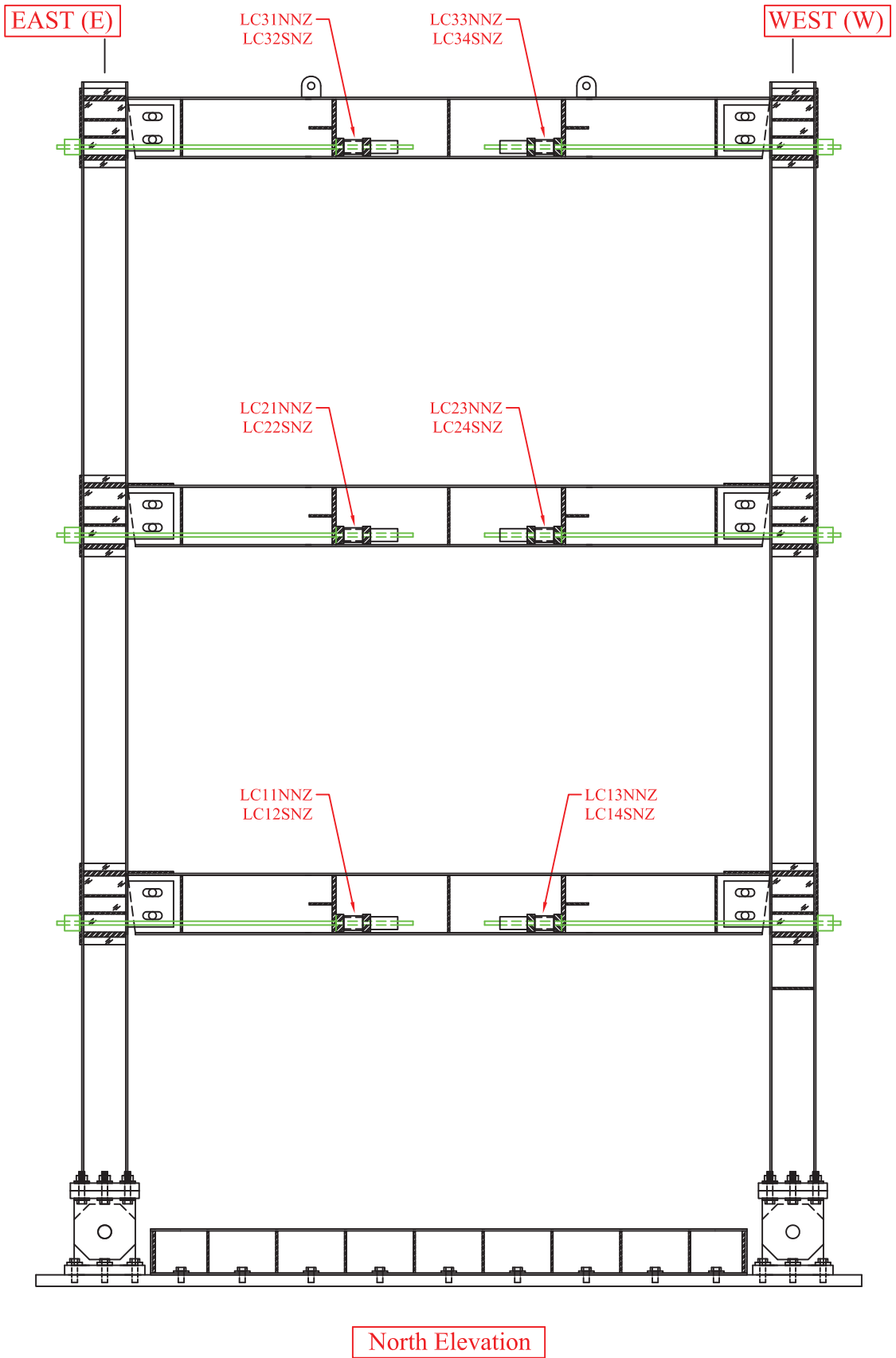


**LEGEND:**

- ◄—► Accelerometer (X = Long., Y = Transverse, Z = Vertical)
- ⊕ Accelerometer (Vertical)
- String Pot

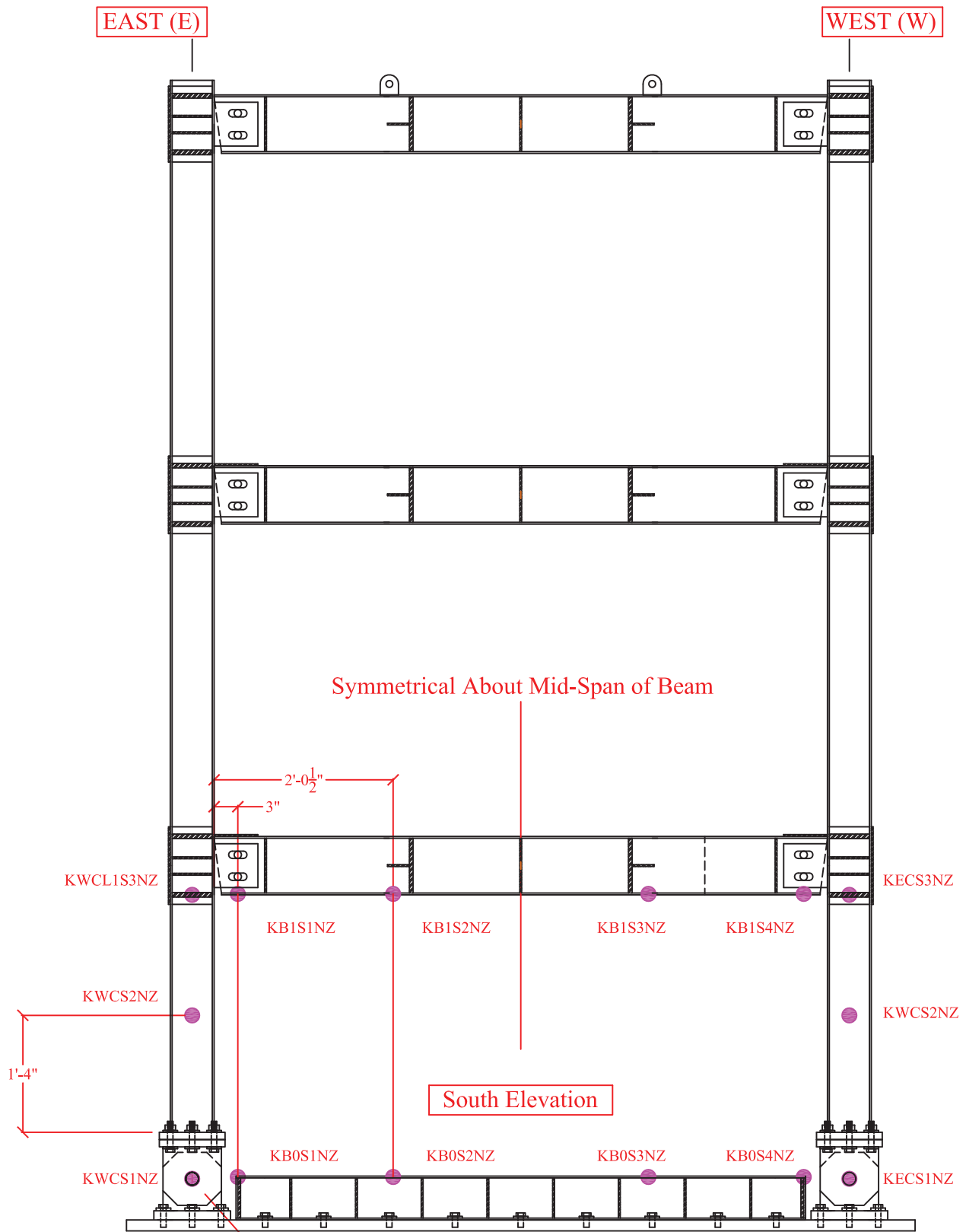
**PLAN VIEW**

<b>University at Buffalo - Shake Table Tests</b>		<b>DRWG:</b>	2-5/12
<b>PROJECT:</b> NEESR-SG Self-Centering Steel Plate Shear Walls	<b>CONTENT:</b> Shake Table Ext. & Base Plate Sensors	<b>SCALE:</b>	1/4" = 1'-0"
<b>BY:</b> Daniel M. Dowden	<b>REVISION:</b>	<b>DATE:</b>	



North Elevation

<b>University at Buffalo - Shake Table Tests</b>			<b>DRWG:</b>
<b>PROJECT:</b> NEESR-SG Self-Centering Steel Plate Shear Walls		<b>CONTENT:</b> Frame 2 - Load Cells	2/13
<b>BY:</b> Daniel M. Dowden	<b>REVISION:</b>	<b>DATE:</b>	<b>SCALE:</b> 3/5" = 1'-0"



**NOTES:**  
 Infill Web Plates Not  
 Shown For Clarity

Krypton Sensor  
 On Clevis Pin

**LEGEND:**

● Krypton

<b>University at Buffalo - Shake Table Tests</b>			<b>DRWG:</b>
<b>PROJECT:</b> NEESR-SG Self-Centering Steel Plate Shear Walls		<b>CONTENT:</b> Frame 2 - Krypton Sensors	2/14
<b>BY:</b> Daniel M. Dowden	<b>REVISION:</b>	<b>DATE:</b>	<b>SCALE:</b> 3/5" = 1'-0"



## APPENDIX B

### SUPPORTING INFORMATION ON QUASI-STATIC TEST FRAME FR ACTUATOR INTERACTION

#### B.1 General

This appendix section provides additional supporting information investigating the actuator interaction effects observed with the quasi-static tests FRW, FRB, and FRS. The global response in terms of base shear versus roof drift (figure 6-15) and story shear versus interstory drifts (figure 6-16) were presented in Chapter 6. From these experimental results, an apparent negative stiffness was observed. Recall that these tests were conducted using displacement control of all three actuators. Furthermore, also recall that after the FRB test (i.e., bare frame) was complete, a combined force-and-displacement actuator control was conducted on the bare frame, which then eliminated the apparent negative stiffness effects observed (figures 6-1 and 6-2). This provided some indication that the force readings of the actuator load cells were correct along with the associated channel numbers (i.e., the possibility of error in the data acquisition system was unlikely the culprit). However, looking at the results for FRW, FRB, and FRS, one may question how the negative stiffness could be possible, since this indicates that for a given direction of lateral frame displacement, the resultant summation of the actuator forces is in the opposing direction (in other words, how could story shears be acting in a direction opposed to the story drift). The information presented below is intended to illustrate that this can indeed be the case.

#### B.2 Investigation by Calculation

Figure B-1 provides the peak positive base shear and corresponding roof drift at select displacement steps for frame FRS. Also superimposed on that figure is the corresponding response of frame FRB. The difference in response for frame FRS and FRB is then the approximate contribution from the infill web strips only. It is observed that the base shear contribution of the infill web strips increases for an increased displacement step (i.e., is a positive response), which is as expected. In contrast, the contribution of the PT boundary frame component decreases (i.e., is a negative response), which is counter intuitive. However, most importantly, this identifies that it is the contribution of the PT boundary frame (in response to the

original displacement control actuator loading scheme) that is responsible for the negative stiffness effect observed in the FRW and FRS tests.

A simple calculation is provided here to demonstrate this “negative stiffness” peculiarity by idealizing frame FRB as a cantilever beam. For this purpose, the actuator forces at the 3% roof drift displacement step are arbitrarily selected from the history shown in figure B-2. Note that because the actuator force at Level 3 is small compared to the actuators at Levels 1 and 2, calculation in the simplified example only consider the actuators forces at Levels 1 and 2 (but superimposing the Level 3 actuator forces at these locations, to maintain the total base shear at this displacement step such that  $F_2 = 32 \text{ kips} - 4 \text{ kips}/2 = 30 \text{ kips}$  and  $F_1 = -36 \text{ kips} - 4 \text{ kips}/2 \text{ kips} = -38 \text{ kips}$ ). The calculations and results provided in figure B-3 show that a positive deflected shape (with positive displacements at both “levels”) is obtained even though the resultant actuator force of 8 kips (for this calculation) is acting in the opposing direction. The same phenomena occurs when the entire bare frame is used (instead of a simplified beam), but closed-form calculations are not as easily obtained. However, flexure of the VBEs is the contributing factor that induces the negative stiffness effects, as part of the total system equilibrium.

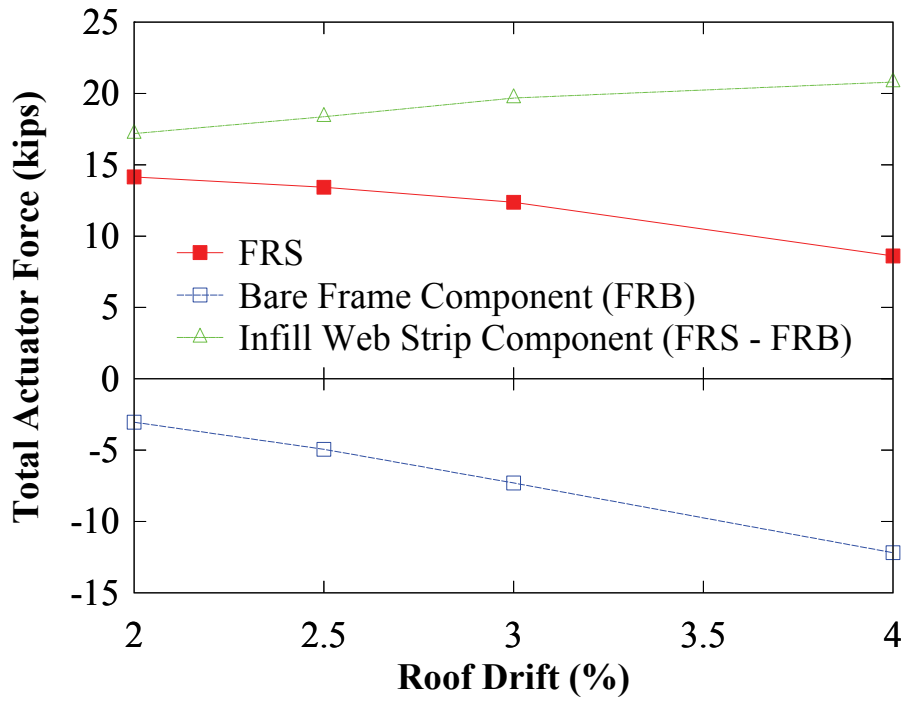


FIGURE B-1 Select actuator force and roof drift peak response

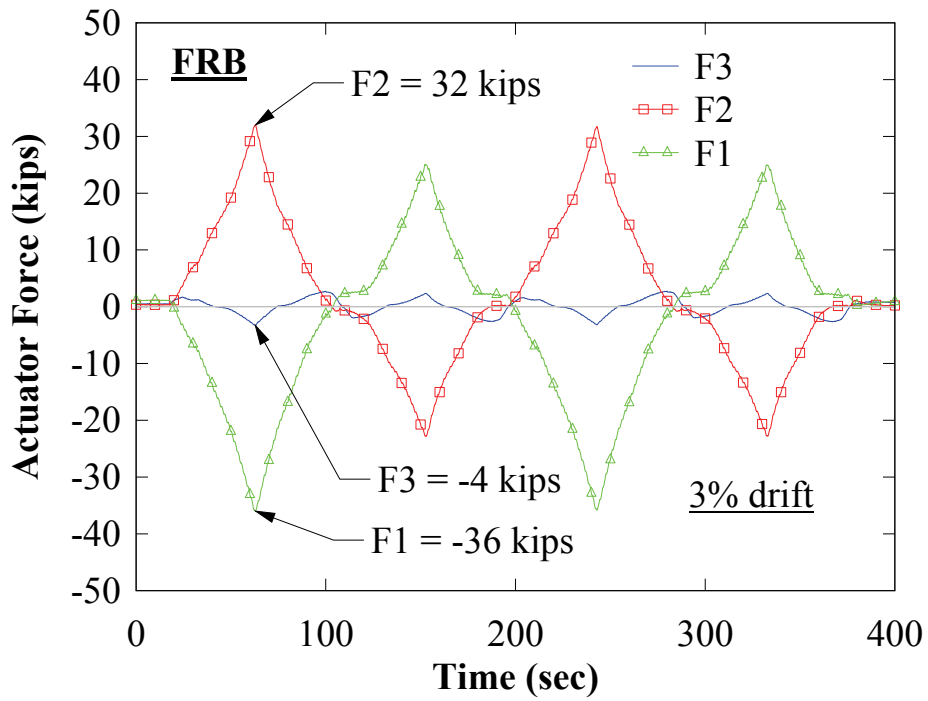
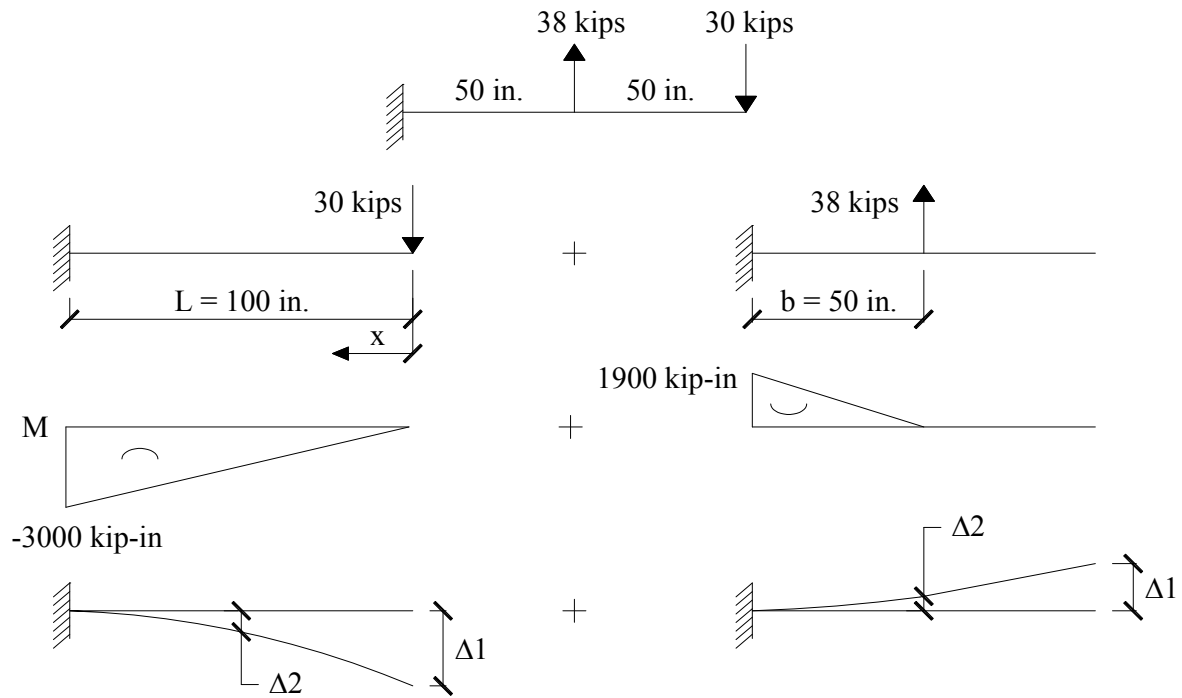


FIGURE B-2 Frame FRB: Actuator response history – 3% roof drift displacement step



$$\Delta 1 = \frac{PL^3}{3EI}$$

$$= \frac{(30)(L)^3}{3EI} = \frac{10L^3}{EI}$$

$$\Delta 2 = \frac{P}{6EI} (2L^3 - 3L^2x + x^3)$$

$$= \frac{30}{6EI} \left[ 2L^3 - 3(L^2) \left( \frac{L}{2} \right) + \left( \frac{L}{2} \right)^3 \right] = \frac{25L^3}{8EI}$$

$$\Delta 1 = \frac{Pb^2}{6EI} (3L - b)$$

$$= \frac{38 \left( \frac{L}{2} \right)^2}{6EI} \left( 3L - \frac{L}{2} \right) = \frac{190L^3}{48EI}$$

$$\Delta 2 = \frac{Pb^3}{3EI}$$

$$= \frac{38 \left( \frac{L}{2} \right)^3}{3EI} = \frac{38L^3}{24EI}$$

Combined (Frame FRB)

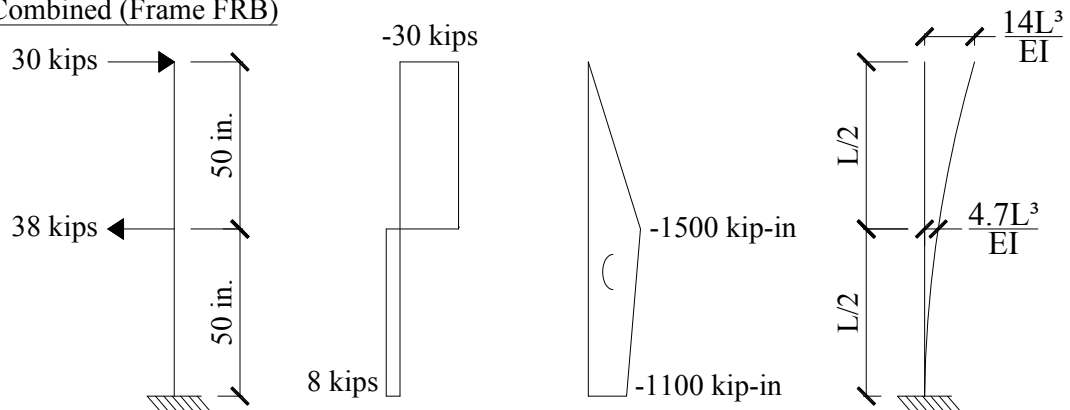


FIGURE B-3 Frame FRB - simplified calculation



## MCEER Technical Reports

MCEER publishes technical reports on a variety of subjects written by authors funded through MCEER. These reports are available from both MCEER Publications and the National Technical Information Service (NTIS). Requests for reports should be directed to MCEER Publications, MCEER, University at Buffalo, State University of New York, 133A Ketter Hall, Buffalo, New York 14260. Reports can also be requested through NTIS, P.O. Box 1425, Springfield, Virginia 22151. NTIS accession numbers are shown in parenthesis, if available.

- NCEER-87-0001 "First-Year Program in Research, Education and Technology Transfer," 3/5/87, (PB88-134275, A04, MF-A01).
- NCEER-87-0002 "Experimental Evaluation of Instantaneous Optimal Algorithms for Structural Control," by R.C. Lin, T.T. Soong and A.M. Reinhorn, 4/20/87, (PB88-134341, A04, MF-A01).
- NCEER-87-0003 "Experimentation Using the Earthquake Simulation Facilities at University at Buffalo," by A.M. Reinhorn and R.L. Ketter, not available.
- NCEER-87-0004 "The System Characteristics and Performance of a Shaking Table," by J.S. Hwang, K.C. Chang and G.C. Lee, 6/1/87, (PB88-134259, A03, MF-A01). This report is available only through NTIS (see address given above).
- NCEER-87-0005 "A Finite Element Formulation for Nonlinear Viscoplastic Material Using a Q Model," by O. Gyebe and G. Dasgupta, 11/2/87, (PB88-213764, A08, MF-A01).
- NCEER-87-0006 "Symbolic Manipulation Program (SMP) - Algebraic Codes for Two and Three Dimensional Finite Element Formulations," by X. Lee and G. Dasgupta, 11/9/87, (PB88-218522, A05, MF-A01).
- NCEER-87-0007 "Instantaneous Optimal Control Laws for Tall Buildings Under Seismic Excitations," by J.N. Yang, A. Akbarpour and P. Ghaemmaghami, 6/10/87, (PB88-134333, A06, MF-A01). This report is only available through NTIS (see address given above).
- NCEER-87-0008 "IDARC: Inelastic Damage Analysis of Reinforced Concrete Frame - Shear-Wall Structures," by Y.J. Park, A.M. Reinhorn and S.K. Kunnath, 7/20/87, (PB88-134325, A09, MF-A01). This report is only available through NTIS (see address given above).
- NCEER-87-0009 "Liquefaction Potential for New York State: A Preliminary Report on Sites in Manhattan and Buffalo," by M. Budhu, V. Vijayakumar, R.F. Giese and L. Baumgras, 8/31/87, (PB88-163704, A03, MF-A01). This report is available only through NTIS (see address given above).
- NCEER-87-0010 "Vertical and Torsional Vibration of Foundations in Inhomogeneous Media," by A.S. Veletsos and K.W. Dotson, 6/1/87, (PB88-134291, A03, MF-A01). This report is only available through NTIS (see address given above).
- NCEER-87-0011 "Seismic Probabilistic Risk Assessment and Seismic Margins Studies for Nuclear Power Plants," by Howard H.M. Hwang, 6/15/87, (PB88-134267, A03, MF-A01). This report is only available through NTIS (see address given above).
- NCEER-87-0012 "Parametric Studies of Frequency Response of Secondary Systems Under Ground-Acceleration Excitations," by Y. Yong and Y.K. Lin, 6/10/87, (PB88-134309, A03, MF-A01). This report is only available through NTIS (see address given above).
- NCEER-87-0013 "Frequency Response of Secondary Systems Under Seismic Excitation," by J.A. HoLung, J. Cai and Y.K. Lin, 7/31/87, (PB88-134317, A05, MF-A01). This report is only available through NTIS (see address given above).
- NCEER-87-0014 "Modelling Earthquake Ground Motions in Seismically Active Regions Using Parametric Time Series Methods," by G.W. Ellis and A.S. Cakmak, 8/25/87, (PB88-134283, A08, MF-A01). This report is only available through NTIS (see address given above).
- NCEER-87-0015 "Detection and Assessment of Seismic Structural Damage," by E. DiPasquale and A.S. Cakmak, 8/25/87, (PB88-163712, A05, MF-A01). This report is only available through NTIS (see address given above).

- NCEER-87-0016 "Pipeline Experiment at Parkfield, California," by J. Isenberg and E. Richardson, 9/15/87, (PB88-163720, A03, MF-A01). This report is available only through NTIS (see address given above).
- NCEER-87-0017 "Digital Simulation of Seismic Ground Motion," by M. Shinozuka, G. Deodatis and T. Harada, 8/31/87, (PB88-155197, A04, MF-A01). This report is available only through NTIS (see address given above).
- NCEER-87-0018 "Practical Considerations for Structural Control: System Uncertainty, System Time Delay and Truncation of Small Control Forces," J.N. Yang and A. Akbarpour, 8/10/87, (PB88-163738, A08, MF-A01). This report is only available through NTIS (see address given above).
- NCEER-87-0019 "Modal Analysis of Nonclassically Damped Structural Systems Using Canonical Transformation," by J.N. Yang, S. Sarkani and F.X. Long, 9/27/87, (PB88-187851, A04, MF-A01).
- NCEER-87-0020 "A Nonstationary Solution in Random Vibration Theory," by J.R. Red-Horse and P.D. Spanos, 11/3/87, (PB88-163746, A03, MF-A01).
- NCEER-87-0021 "Horizontal Impedances for Radially Inhomogeneous Viscoelastic Soil Layers," by A.S. Veletsos and K.W. Dotson, 10/15/87, (PB88-150859, A04, MF-A01).
- NCEER-87-0022 "Seismic Damage Assessment of Reinforced Concrete Members," by Y.S. Chung, C. Meyer and M. Shinozuka, 10/9/87, (PB88-150867, A05, MF-A01). This report is available only through NTIS (see address given above).
- NCEER-87-0023 "Active Structural Control in Civil Engineering," by T.T. Soong, 11/11/87, (PB88-187778, A03, MF-A01).
- NCEER-87-0024 "Vertical and Torsional Impedances for Radially Inhomogeneous Viscoelastic Soil Layers," by K.W. Dotson and A.S. Veletsos, 12/87, (PB88-187786, A03, MF-A01).
- NCEER-87-0025 "Proceedings from the Symposium on Seismic Hazards, Ground Motions, Soil-Liquefaction and Engineering Practice in Eastern North America," October 20-22, 1987, edited by K.H. Jacob, 12/87, (PB88-188115, A23, MF-A01). This report is available only through NTIS (see address given above).
- NCEER-87-0026 "Report on the Whittier-Narrows, California, Earthquake of October 1, 1987," by J. Pantelic and A. Reinhorn, 11/87, (PB88-187752, A03, MF-A01). This report is available only through NTIS (see address given above).
- NCEER-87-0027 "Design of a Modular Program for Transient Nonlinear Analysis of Large 3-D Building Structures," by S. Srivastav and J.F. Abel, 12/30/87, (PB88-187950, A05, MF-A01). This report is only available through NTIS (see address given above).
- NCEER-87-0028 "Second-Year Program in Research, Education and Technology Transfer," 3/8/88, (PB88-219480, A04, MF-A01).
- NCEER-88-0001 "Workshop on Seismic Computer Analysis and Design of Buildings With Interactive Graphics," by W. McGuire, J.F. Abel and C.H. Conley, 1/18/88, (PB88-187760, A03, MF-A01). This report is only available through NTIS (see address given above).
- NCEER-88-0002 "Optimal Control of Nonlinear Flexible Structures," by J.N. Yang, F.X. Long and D. Wong, 1/22/88, (PB88-213772, A06, MF-A01).
- NCEER-88-0003 "Substructuring Techniques in the Time Domain for Primary-Secondary Structural Systems," by G.D. Manolis and G. Juhn, 2/10/88, (PB88-213780, A04, MF-A01).
- NCEER-88-0004 "Iterative Seismic Analysis of Primary-Secondary Systems," by A. Singhal, L.D. Lutes and P.D. Spanos, 2/23/88, (PB88-213798, A04, MF-A01).
- NCEER-88-0005 "Stochastic Finite Element Expansion for Random Media," by P.D. Spanos and R. Ghanem, 3/14/88, (PB88-213806, A03, MF-A01).

- NCEER-88-0006 "Combining Structural Optimization and Structural Control," by F.Y. Cheng and C.P. Pantelides, 1/10/88, (PB88-213814, A05, MF-A01).
- NCEER-88-0007 "Seismic Performance Assessment of Code-Designed Structures," by H.H-M. Hwang, J-W. Jaw and H-J. Shau, 3/20/88, (PB88-219423, A04, MF-A01). This report is only available through NTIS (see address given above).
- NCEER-88-0008 "Reliability Analysis of Code-Designed Structures Under Natural Hazards," by H.H-M. Hwang, H. Ushiba and M. Shinozuka, 2/29/88, (PB88-229471, A07, MF-A01). This report is only available through NTIS (see address given above).
- NCEER-88-0009 "Seismic Fragility Analysis of Shear Wall Structures," by J-W Jaw and H.H-M. Hwang, 4/30/88, (PB89-102867, A04, MF-A01).
- NCEER-88-0010 "Base Isolation of a Multi-Story Building Under a Harmonic Ground Motion - A Comparison of Performances of Various Systems," by F-G Fan, G. Ahmadi and I.G. Tadjbakhsh, 5/18/88, (PB89-122238, A06, MF-A01). This report is only available through NTIS (see address given above).
- NCEER-88-0011 "Seismic Floor Response Spectra for a Combined System by Green's Functions," by F.M. Lavelle, L.A. Bergman and P.D. Spanos, 5/1/88, (PB89-102875, A03, MF-A01).
- NCEER-88-0012 "A New Solution Technique for Randomly Excited Hysteretic Structures," by G.Q. Cai and Y.K. Lin, 5/16/88, (PB89-102883, A03, MF-A01).
- NCEER-88-0013 "A Study of Radiation Damping and Soil-Structure Interaction Effects in the Centrifuge," by K. Weissman, supervised by J.H. Prevost, 5/24/88, (PB89-144703, A06, MF-A01).
- NCEER-88-0014 "Parameter Identification and Implementation of a Kinematic Plasticity Model for Frictional Soils," by J.H. Prevost and D.V. Griffiths, not available.
- NCEER-88-0015 "Two- and Three- Dimensional Dynamic Finite Element Analyses of the Long Valley Dam," by D.V. Griffiths and J.H. Prevost, 6/17/88, (PB89-144711, A04, MF-A01).
- NCEER-88-0016 "Damage Assessment of Reinforced Concrete Structures in Eastern United States," by A.M. Reinhorn, M.J. Seidel, S.K. Kunnath and Y.J. Park, 6/15/88, (PB89-122220, A04, MF-A01). This report is only available through NTIS (see address given above).
- NCEER-88-0017 "Dynamic Compliance of Vertically Loaded Strip Foundations in Multilayered Viscoelastic Soils," by S. Ahmad and A.S.M. Israil, 6/17/88, (PB89-102891, A04, MF-A01).
- NCEER-88-0018 "An Experimental Study of Seismic Structural Response With Added Viscoelastic Dampers," by R.C. Lin, Z. Liang, T.T. Soong and R.H. Zhang, 6/30/88, (PB89-122212, A05, MF-A01). This report is available only through NTIS (see address given above).
- NCEER-88-0019 "Experimental Investigation of Primary - Secondary System Interaction," by G.D. Manolis, G. Juhn and A.M. Reinhorn, 5/27/88, (PB89-122204, A04, MF-A01).
- NCEER-88-0020 "A Response Spectrum Approach For Analysis of Nonclassically Damped Structures," by J.N. Yang, S. Sarkani and F.X. Long, 4/22/88, (PB89-102909, A04, MF-A01).
- NCEER-88-0021 "Seismic Interaction of Structures and Soils: Stochastic Approach," by A.S. Veletsos and A.M. Prasad, 7/21/88, (PB89-122196, A04, MF-A01). This report is only available through NTIS (see address given above).
- NCEER-88-0022 "Identification of the Serviceability Limit State and Detection of Seismic Structural Damage," by E. DiPasquale and A.S. Cakmak, 6/15/88, (PB89-122188, A05, MF-A01). This report is available only through NTIS (see address given above).
- NCEER-88-0023 "Multi-Hazard Risk Analysis: Case of a Simple Offshore Structure," by B.K. Bhartia and E.H. Vanmarcke, 7/21/88, (PB89-145213, A05, MF-A01).

- NCEER-88-0024 "Automated Seismic Design of Reinforced Concrete Buildings," by Y.S. Chung, C. Meyer and M. Shinozuka, 7/5/88, (PB89-122170, A06, MF-A01). This report is available only through NTIS (see address given above).
- NCEER-88-0025 "Experimental Study of Active Control of MDOF Structures Under Seismic Excitations," by L.L. Chung, R.C. Lin, T.T. Soong and A.M. Reinhorn, 7/10/88, (PB89-122600, A04, MF-A01).
- NCEER-88-0026 "Earthquake Simulation Tests of a Low-Rise Metal Structure," by J.S. Hwang, K.C. Chang, G.C. Lee and R.L. Ketter, 8/1/88, (PB89-102917, A04, MF-A01).
- NCEER-88-0027 "Systems Study of Urban Response and Reconstruction Due to Catastrophic Earthquakes," by F. Kozin and H.K. Zhou, 9/22/88, (PB90-162348, A04, MF-A01).
- NCEER-88-0028 "Seismic Fragility Analysis of Plane Frame Structures," by H.H-M. Hwang and Y.K. Low, 7/31/88, (PB89-131445, A06, MF-A01).
- NCEER-88-0029 "Response Analysis of Stochastic Structures," by A. Kardara, C. Bucher and M. Shinozuka, 9/22/88, (PB89-174429, A04, MF-A01).
- NCEER-88-0030 "Nonnormal Accelerations Due to Yielding in a Primary Structure," by D.C.K. Chen and L.D. Lutes, 9/19/88, (PB89-131437, A04, MF-A01).
- NCEER-88-0031 "Design Approaches for Soil-Structure Interaction," by A.S. Veletsos, A.M. Prasad and Y. Tang, 12/30/88, (PB89-174437, A03, MF-A01). This report is available only through NTIS (see address given above).
- NCEER-88-0032 "A Re-evaluation of Design Spectra for Seismic Damage Control," by C.J. Turkstra and A.G. Tallin, 11/7/88, (PB89-145221, A05, MF-A01).
- NCEER-88-0033 "The Behavior and Design of Noncontact Lap Splices Subjected to Repeated Inelastic Tensile Loading," by V.E. Sagan, P. Gergely and R.N. White, 12/8/88, (PB89-163737, A08, MF-A01).
- NCEER-88-0034 "Seismic Response of Pile Foundations," by S.M. Mamoon, P.K. Banerjee and S. Ahmad, 11/1/88, (PB89-145239, A04, MF-A01).
- NCEER-88-0035 "Modeling of R/C Building Structures With Flexible Floor Diaphragms (IDARC2)," by A.M. Reinhorn, S.K. Kunnath and N. Panahshahi, 9/7/88, (PB89-207153, A07, MF-A01).
- NCEER-88-0036 "Solution of the Dam-Reservoir Interaction Problem Using a Combination of FEM, BEM with Particular Integrals, Modal Analysis, and Substructuring," by C-S. Tsai, G.C. Lee and R.L. Ketter, 12/31/88, (PB89-207146, A04, MF-A01).
- NCEER-88-0037 "Optimal Placement of Actuators for Structural Control," by F.Y. Cheng and C.P. Pantelides, 8/15/88, (PB89-162846, A05, MF-A01).
- NCEER-88-0038 "Teflon Bearings in Aseismic Base Isolation: Experimental Studies and Mathematical Modeling," by A. Mokha, M.C. Constantinou and A.M. Reinhorn, 12/5/88, (PB89-218457, A10, MF-A01). This report is available only through NTIS (see address given above).
- NCEER-88-0039 "Seismic Behavior of Flat Slab High-Rise Buildings in the New York City Area," by P. Weidlinger and M. Ettouney, 10/15/88, (PB90-145681, A04, MF-A01).
- NCEER-88-0040 "Evaluation of the Earthquake Resistance of Existing Buildings in New York City," by P. Weidlinger and M. Ettouney, 10/15/88, not available.
- NCEER-88-0041 "Small-Scale Modeling Techniques for Reinforced Concrete Structures Subjected to Seismic Loads," by W. Kim, A. El-Attar and R.N. White, 11/22/88, (PB89-189625, A05, MF-A01).
- NCEER-88-0042 "Modeling Strong Ground Motion from Multiple Event Earthquakes," by G.W. Ellis and A.S. Cakmak, 10/15/88, (PB89-174445, A03, MF-A01).

- NCEER-88-0043 "Nonstationary Models of Seismic Ground Acceleration," by M. Grigoriu, S.E. Ruiz and E. Rosenblueth, 7/15/88, (PB89-189617, A04, MF-A01).
- NCEER-88-0044 "SARCF User's Guide: Seismic Analysis of Reinforced Concrete Frames," by Y.S. Chung, C. Meyer and M. Shinozuka, 11/9/88, (PB89-174452, A08, MF-A01).
- NCEER-88-0045 "First Expert Panel Meeting on Disaster Research and Planning," edited by J. Pantelic and J. Stoyke, 9/15/88, (PB89-174460, A05, MF-A01).
- NCEER-88-0046 "Preliminary Studies of the Effect of Degrading Infill Walls on the Nonlinear Seismic Response of Steel Frames," by C.Z. Chrysostomou, P. Gergely and J.F. Abel, 12/19/88, (PB89-208383, A05, MF-A01).
- NCEER-88-0047 "Reinforced Concrete Frame Component Testing Facility - Design, Construction, Instrumentation and Operation," by S.P. Pessiki, C. Conley, T. Bond, P. Gergely and R.N. White, 12/16/88, (PB89-174478, A04, MF-A01).
- NCEER-89-0001 "Effects of Protective Cushion and Soil Compliancy on the Response of Equipment Within a Seismically Excited Building," by J.A. HoLung, 2/16/89, (PB89-207179, A04, MF-A01).
- NCEER-89-0002 "Statistical Evaluation of Response Modification Factors for Reinforced Concrete Structures," by H.H-M. Hwang and J-W. Jaw, 2/17/89, (PB89-207187, A05, MF-A01).
- NCEER-89-0003 "Hysteretic Columns Under Random Excitation," by G-Q. Cai and Y.K. Lin, 1/9/89, (PB89-196513, A03, MF-A01).
- NCEER-89-0004 "Experimental Study of 'Elephant Foot Bulge' Instability of Thin-Walled Metal Tanks," by Z-H. Jia and R.L. Ketter, 2/22/89, (PB89-207195, A03, MF-A01).
- NCEER-89-0005 "Experiment on Performance of Buried Pipelines Across San Andreas Fault," by J. Isenberg, E. Richardson and T.D. O'Rourke, 3/10/89, (PB89-218440, A04, MF-A01). This report is available only through NTIS (see address given above).
- NCEER-89-0006 "A Knowledge-Based Approach to Structural Design of Earthquake-Resistant Buildings," by M. Subramani, P. Gergely, C.H. Conley, J.F. Abel and A.H. Zaghaw, 1/15/89, (PB89-218465, A06, MF-A01).
- NCEER-89-0007 "Liquefaction Hazards and Their Effects on Buried Pipelines," by T.D. O'Rourke and P.A. Lane, 2/1/89, (PB89-218481, A09, MF-A01).
- NCEER-89-0008 "Fundamentals of System Identification in Structural Dynamics," by H. Imai, C-B. Yun, O. Maruyama and M. Shinozuka, 1/26/89, (PB89-207211, A04, MF-A01).
- NCEER-89-0009 "Effects of the 1985 Michoacan Earthquake on Water Systems and Other Buried Lifelines in Mexico," by A.G. Ayala and M.J. O'Rourke, 3/8/89, (PB89-207229, A06, MF-A01).
- NCEER-89-R010 "NCEER Bibliography of Earthquake Education Materials," by K.E.K. Ross, Second Revision, 9/1/89, (PB90-125352, A05, MF-A01). This report is replaced by NCEER-92-0018.
- NCEER-89-0011 "Inelastic Three-Dimensional Response Analysis of Reinforced Concrete Building Structures (IDARC-3D), Part I - Modeling," by S.K. Kunnath and A.M. Reinhorn, 4/17/89, (PB90-114612, A07, MF-A01). This report is available only through NTIS (see address given above).
- NCEER-89-0012 "Recommended Modifications to ATC-14," by C.D. Poland and J.O. Malley, 4/12/89, (PB90-108648, A15, MF-A01).
- NCEER-89-0013 "Repair and Strengthening of Beam-to-Column Connections Subjected to Earthquake Loading," by M. Corazao and A.J. Durrani, 2/28/89, (PB90-109885, A06, MF-A01).
- NCEER-89-0014 "Program EXKAL2 for Identification of Structural Dynamic Systems," by O. Maruyama, C-B. Yun, M. Hoshiya and M. Shinozuka, 5/19/89, (PB90-109877, A09, MF-A01).

- NCEER-89-0015 "Response of Frames With Bolted Semi-Rigid Connections, Part I - Experimental Study and Analytical Predictions," by P.J. DiCorso, A.M. Reinhorn, J.R. Dickerson, J.B. Radzimirski and W.L. Harper, 6/1/89, not available.
- NCEER-89-0016 "ARMA Monte Carlo Simulation in Probabilistic Structural Analysis," by P.D. Spanos and M.P. Mignolet, 7/10/89, (PB90-109893, A03, MF-A01).
- NCEER-89-P017 "Preliminary Proceedings from the Conference on Disaster Preparedness - The Place of Earthquake Education in Our Schools," Edited by K.E.K. Ross, 6/23/89, (PB90-108606, A03, MF-A01).
- NCEER-89-0017 "Proceedings from the Conference on Disaster Preparedness - The Place of Earthquake Education in Our Schools," Edited by K.E.K. Ross, 12/31/89, (PB90-207895, A012, MF-A02). This report is available only through NTIS (see address given above).
- NCEER-89-0018 "Multidimensional Models of Hysteretic Material Behavior for Vibration Analysis of Shape Memory Energy Absorbing Devices, by E.J. Graesser and F.A. Cozzarelli, 6/7/89, (PB90-164146, A04, MF-A01).
- NCEER-89-0019 "Nonlinear Dynamic Analysis of Three-Dimensional Base Isolated Structures (3D-BASIS)," by S. Nagarajaiah, A.M. Reinhorn and M.C. Constantinou, 8/3/89, (PB90-161936, A06, MF-A01). This report has been replaced by NCEER-93-0011.
- NCEER-89-0020 "Structural Control Considering Time-Rate of Control Forces and Control Rate Constraints," by F.Y. Cheng and C.P. Pantelides, 8/3/89, (PB90-120445, A04, MF-A01).
- NCEER-89-0021 "Subsurface Conditions of Memphis and Shelby County," by K.W. Ng, T-S. Chang and H-H.M. Hwang, 7/26/89, (PB90-120437, A03, MF-A01).
- NCEER-89-0022 "Seismic Wave Propagation Effects on Straight Jointed Buried Pipelines," by K. Elhmadi and M.J. O'Rourke, 8/24/89, (PB90-162322, A10, MF-A02).
- NCEER-89-0023 "Workshop on Serviceability Analysis of Water Delivery Systems," edited by M. Grigoriu, 3/6/89, (PB90-127424, A03, MF-A01).
- NCEER-89-0024 "Shaking Table Study of a 1/5 Scale Steel Frame Composed of Tapered Members," by K.C. Chang, J.S. Hwang and G.C. Lee, 9/18/89, (PB90-160169, A04, MF-A01).
- NCEER-89-0025 "DYNA1D: A Computer Program for Nonlinear Seismic Site Response Analysis - Technical Documentation," by Jean H. Prevost, 9/14/89, (PB90-161944, A07, MF-A01). This report is available only through NTIS (see address given above).
- NCEER-89-0026 "1:4 Scale Model Studies of Active Tendon Systems and Active Mass Dampers for Aseismic Protection," by A.M. Reinhorn, T.T. Soong, R.C. Lin, Y.P. Yang, Y. Fukao, H. Abe and M. Nakai, 9/15/89, (PB90-173246, A10, MF-A02). This report is available only through NTIS (see address given above).
- NCEER-89-0027 "Scattering of Waves by Inclusions in a Nonhomogeneous Elastic Half Space Solved by Boundary Element Methods," by P.K. Hadley, A. Askar and A.S. Cakmak, 6/15/89, (PB90-145699, A07, MF-A01).
- NCEER-89-0028 "Statistical Evaluation of Deflection Amplification Factors for Reinforced Concrete Structures," by H.H.M. Hwang, J-W. Jaw and A.L. Ch'ng, 8/31/89, (PB90-164633, A05, MF-A01).
- NCEER-89-0029 "Bedrock Accelerations in Memphis Area Due to Large New Madrid Earthquakes," by H.H.M. Hwang, C.H.S. Chen and G. Yu, 11/7/89, (PB90-162330, A04, MF-A01).
- NCEER-89-0030 "Seismic Behavior and Response Sensitivity of Secondary Structural Systems," by Y.Q. Chen and T.T. Soong, 10/23/89, (PB90-164658, A08, MF-A01).
- NCEER-89-0031 "Random Vibration and Reliability Analysis of Primary-Secondary Structural Systems," by Y. Ibrahim, M. Grigoriu and T.T. Soong, 11/10/89, (PB90-161951, A04, MF-A01).

- NCEER-89-0032 "Proceedings from the Second U.S. - Japan Workshop on Liquefaction, Large Ground Deformation and Their Effects on Lifelines, September 26-29, 1989," Edited by T.D. O'Rourke and M. Hamada, 12/1/89, (PB90-209388, A22, MF-A03).
- NCEER-89-0033 "Deterministic Model for Seismic Damage Evaluation of Reinforced Concrete Structures," by J.M. Bracci, A.M. Reinhorn, J.B. Mander and S.K. Kunnath, 9/27/89, (PB91-108803, A06, MF-A01).
- NCEER-89-0034 "On the Relation Between Local and Global Damage Indices," by E. DiPasquale and A.S. Cakmak, 8/15/89, (PB90-173865, A05, MF-A01).
- NCEER-89-0035 "Cyclic Undrained Behavior of Nonplastic and Low Plasticity Silts," by A.J. Walker and H.E. Stewart, 7/26/89, (PB90-183518, A10, MF-A01).
- NCEER-89-0036 "Liquefaction Potential of Surficial Deposits in the City of Buffalo, New York," by M. Budhu, R. Giese and L. Baumgrass, 1/17/89, (PB90-208455, A04, MF-A01).
- NCEER-89-0037 "A Deterministic Assessment of Effects of Ground Motion Incoherence," by A.S. Veletsos and Y. Tang, 7/15/89, (PB90-164294, A03, MF-A01).
- NCEER-89-0038 "Workshop on Ground Motion Parameters for Seismic Hazard Mapping," July 17-18, 1989, edited by R.V. Whitman, 12/1/89, (PB90-173923, A04, MF-A01).
- NCEER-89-0039 "Seismic Effects on Elevated Transit Lines of the New York City Transit Authority," by C.J. Costantino, C.A. Miller and E. Heymsfield, 12/26/89, (PB90-207887, A06, MF-A01).
- NCEER-89-0040 "Centrifugal Modeling of Dynamic Soil-Structure Interaction," by K. Weissman, Supervised by J.H. Prevost, 5/10/89, (PB90-207879, A07, MF-A01).
- NCEER-89-0041 "Linearized Identification of Buildings With Cores for Seismic Vulnerability Assessment," by I-K. Ho and A.E. Aktan, 11/1/89, (PB90-251943, A07, MF-A01).
- NCEER-90-0001 "Geotechnical and Lifeline Aspects of the October 17, 1989 Loma Prieta Earthquake in San Francisco," by T.D. O'Rourke, H.E. Stewart, F.T. Blackburn and T.S. Dickerman, 1/90, (PB90-208596, A05, MF-A01).
- NCEER-90-0002 "Nonnormal Secondary Response Due to Yielding in a Primary Structure," by D.C.K. Chen and L.D. Lutes, 2/28/90, (PB90-251976, A07, MF-A01).
- NCEER-90-0003 "Earthquake Education Materials for Grades K-12," by K.E.K. Ross, 4/16/90, (PB91-251984, A05, MF-A05). This report has been replaced by NCEER-92-0018.
- NCEER-90-0004 "Catalog of Strong Motion Stations in Eastern North America," by R.W. Busby, 4/3/90, (PB90-251984, A05, MF-A01).
- NCEER-90-0005 "NCEER Strong-Motion Data Base: A User Manual for the GeoBase Release (Version 1.0 for the Sun3)," by P. Friberg and K. Jacob, 3/31/90 (PB90-258062, A04, MF-A01).
- NCEER-90-0006 "Seismic Hazard Along a Crude Oil Pipeline in the Event of an 1811-1812 Type New Madrid Earthquake," by H.H.M. Hwang and C-H.S. Chen, 4/16/90, (PB90-258054, A04, MF-A01).
- NCEER-90-0007 "Site-Specific Response Spectra for Memphis Sheahan Pumping Station," by H.H.M. Hwang and C.S. Lee, 5/15/90, (PB91-108811, A05, MF-A01).
- NCEER-90-0008 "Pilot Study on Seismic Vulnerability of Crude Oil Transmission Systems," by T. Ariman, R. Dobry, M. Grigoriu, F. Kozin, M. O'Rourke, T. O'Rourke and M. Shinozuka, 5/25/90, (PB91-108837, A06, MF-A01).
- NCEER-90-0009 "A Program to Generate Site Dependent Time Histories: EQGEN," by G.W. Ellis, M. Srinivasan and A.S. Cakmak, 1/30/90, (PB91-108829, A04, MF-A01).
- NCEER-90-0010 "Active Isolation for Seismic Protection of Operating Rooms," by M.E. Talbott, Supervised by M. Shinozuka, 6/8/9, (PB91-110205, A05, MF-A01).

- NCEER-90-0011 "Program LINEARID for Identification of Linear Structural Dynamic Systems," by C-B. Yun and M. Shinozuka, 6/25/90, (PB91-110312, A08, MF-A01).
- NCEER-90-0012 "Two-Dimensional Two-Phase Elasto-Plastic Seismic Response of Earth Dams," by A.N. Yiagos, Supervised by J.H. Prevost, 6/20/90, (PB91-110197, A13, MF-A02).
- NCEER-90-0013 "Secondary Systems in Base-Isolated Structures: Experimental Investigation, Stochastic Response and Stochastic Sensitivity," by G.D. Manolis, G. Juhn, M.C. Constantinou and A.M. Reinhorn, 7/1/90, (PB91-110320, A08, MF-A01).
- NCEER-90-0014 "Seismic Behavior of Lightly-Reinforced Concrete Column and Beam-Column Joint Details," by S.P. Pessiki, C.H. Conley, P. Gergely and R.N. White, 8/22/90, (PB91-108795, A11, MF-A02).
- NCEER-90-0015 "Two Hybrid Control Systems for Building Structures Under Strong Earthquakes," by J.N. Yang and A. Daniellians, 6/29/90, (PB91-125393, A04, MF-A01).
- NCEER-90-0016 "Instantaneous Optimal Control with Acceleration and Velocity Feedback," by J.N. Yang and Z. Li, 6/29/90, (PB91-125401, A03, MF-A01).
- NCEER-90-0017 "Reconnaissance Report on the Northern Iran Earthquake of June 21, 1990," by M. Mehrain, 10/4/90, (PB91-125377, A03, MF-A01).
- NCEER-90-0018 "Evaluation of Liquefaction Potential in Memphis and Shelby County," by T.S. Chang, P.S. Tang, C.S. Lee and H. Hwang, 8/10/90, (PB91-125427, A09, MF-A01).
- NCEER-90-0019 "Experimental and Analytical Study of a Combined Sliding Disc Bearing and Helical Steel Spring Isolation System," by M.C. Constantinou, A.S. Mokha and A.M. Reinhorn, 10/4/90, (PB91-125385, A06, MF-A01). This report is available only through NTIS (see address given above).
- NCEER-90-0020 "Experimental Study and Analytical Prediction of Earthquake Response of a Sliding Isolation System with a Spherical Surface," by A.S. Mokha, M.C. Constantinou and A.M. Reinhorn, 10/11/90, (PB91-125419, A05, MF-A01).
- NCEER-90-0021 "Dynamic Interaction Factors for Floating Pile Groups," by G. Gazetas, K. Fan, A. Kaynia and E. Kausel, 9/10/90, (PB91-170381, A05, MF-A01).
- NCEER-90-0022 "Evaluation of Seismic Damage Indices for Reinforced Concrete Structures," by S. Rodriguez-Gomez and A.S. Cakmak, 9/30/90, PB91-171322, A06, MF-A01).
- NCEER-90-0023 "Study of Site Response at a Selected Memphis Site," by H. Desai, S. Ahmad, E.S. Gazetas and M.R. Oh, 10/11/90, (PB91-196857, A03, MF-A01).
- NCEER-90-0024 "A User's Guide to Strongmo: Version 1.0 of NCEER's Strong-Motion Data Access Tool for PCs and Terminals," by P.A. Friberg and C.A.T. Susch, 11/15/90, (PB91-171272, A03, MF-A01).
- NCEER-90-0025 "A Three-Dimensional Analytical Study of Spatial Variability of Seismic Ground Motions," by L-L. Hong and A.H.-S. Ang, 10/30/90, (PB91-170399, A09, MF-A01).
- NCEER-90-0026 "MUMOID User's Guide - A Program for the Identification of Modal Parameters," by S. Rodriguez-Gomez and E. DiPasquale, 9/30/90, (PB91-171298, A04, MF-A01).
- NCEER-90-0027 "SARCF-II User's Guide - Seismic Analysis of Reinforced Concrete Frames," by S. Rodriguez-Gomez, Y.S. Chung and C. Meyer, 9/30/90, (PB91-171280, A05, MF-A01).
- NCEER-90-0028 "Viscous Dampers: Testing, Modeling and Application in Vibration and Seismic Isolation," by N. Makris and M.C. Constantinou, 12/20/90 (PB91-190561, A06, MF-A01).
- NCEER-90-0029 "Soil Effects on Earthquake Ground Motions in the Memphis Area," by H. Hwang, C.S. Lee, K.W. Ng and T.S. Chang, 8/2/90, (PB91-190751, A05, MF-A01).



- NCEER-91-0001 "Proceedings from the Third Japan-U.S. Workshop on Earthquake Resistant Design of Lifeline Facilities and Countermeasures for Soil Liquefaction, December 17-19, 1990," edited by T.D. O'Rourke and M. Hamada, 2/1/91, (PB91-179259, A99, MF-A04).
- NCEER-91-0002 "Physical Space Solutions of Non-Proportionally Damped Systems," by M. Tong, Z. Liang and G.C. Lee, 1/15/91, (PB91-179242, A04, MF-A01).
- NCEER-91-0003 "Seismic Response of Single Piles and Pile Groups," by K. Fan and G. Gazetas, 1/10/91, (PB92-174994, A04, MF-A01).
- NCEER-91-0004 "Damping of Structures: Part I - Theory of Complex Damping," by Z. Liang and G. Lee, 10/10/91, (PB92-197235, A12, MF-A03).
- NCEER-91-0005 "3D-BASIS - Nonlinear Dynamic Analysis of Three Dimensional Base Isolated Structures: Part II," by S. Nagarajaiah, A.M. Reinhorn and M.C. Constantinou, 2/28/91, (PB91-190553, A07, MF-A01). This report has been replaced by NCEER-93-0011.
- NCEER-91-0006 "A Multidimensional Hysteretic Model for Plasticity Deforming Metals in Energy Absorbing Devices," by E.J. Graesser and F.A. Cozzarelli, 4/9/91, (PB92-108364, A04, MF-A01).
- NCEER-91-0007 "A Framework for Customizable Knowledge-Based Expert Systems with an Application to a KBES for Evaluating the Seismic Resistance of Existing Buildings," by E.G. Ibarra-Anaya and S.J. Fenves, 4/9/91, (PB91-210930, A08, MF-A01).
- NCEER-91-0008 "Nonlinear Analysis of Steel Frames with Semi-Rigid Connections Using the Capacity Spectrum Method," by G.G. Deierlein, S-H. Hsieh, Y-J. Shen and J.F. Abel, 7/2/91, (PB92-113828, A05, MF-A01).
- NCEER-91-0009 "Earthquake Education Materials for Grades K-12," by K.E.K. Ross, 4/30/91, (PB91-212142, A06, MF-A01). This report has been replaced by NCEER-92-0018.
- NCEER-91-0010 "Phase Wave Velocities and Displacement Phase Differences in a Harmonically Oscillating Pile," by N. Makris and G. Gazetas, 7/8/91, (PB92-108356, A04, MF-A01).
- NCEER-91-0011 "Dynamic Characteristics of a Full-Size Five-Story Steel Structure and a 2/5 Scale Model," by K.C. Chang, G.C. Yao, G.C. Lee, D.S. Hao and Y.C. Yeh, 7/2/91, (PB93-116648, A06, MF-A02).
- NCEER-91-0012 "Seismic Response of a 2/5 Scale Steel Structure with Added Viscoelastic Dampers," by K.C. Chang, T.T. Soong, S-T. Oh and M.L. Lai, 5/17/91, (PB92-110816, A05, MF-A01).
- NCEER-91-0013 "Earthquake Response of Retaining Walls; Full-Scale Testing and Computational Modeling," by S. Alampalli and A-W.M. Elgamal, 6/20/91, not available.
- NCEER-91-0014 "3D-BASIS-M: Nonlinear Dynamic Analysis of Multiple Building Base Isolated Structures," by P.C. Tsopelas, S. Nagarajaiah, M.C. Constantinou and A.M. Reinhorn, 5/28/91, (PB92-113885, A09, MF-A02).
- NCEER-91-0015 "Evaluation of SEAOC Design Requirements for Sliding Isolated Structures," by D. Theodossiou and M.C. Constantinou, 6/10/91, (PB92-114602, A11, MF-A03).
- NCEER-91-0016 "Closed-Loop Modal Testing of a 27-Story Reinforced Concrete Flat Plate-Core Building," by H.R. Somaprasad, T. Toksoy, H. Yoshiyuki and A.E. Aktan, 7/15/91, (PB92-129980, A07, MF-A02).
- NCEER-91-0017 "Shake Table Test of a 1/6 Scale Two-Story Lightly Reinforced Concrete Building," by A.G. El-Attar, R.N. White and P. Gergely, 2/28/91, (PB92-222447, A06, MF-A02).
- NCEER-91-0018 "Shake Table Test of a 1/8 Scale Three-Story Lightly Reinforced Concrete Building," by A.G. El-Attar, R.N. White and P. Gergely, 2/28/91, (PB93-116630, A08, MF-A02).
- NCEER-91-0019 "Transfer Functions for Rigid Rectangular Foundations," by A.S. Veletsos, A.M. Prasad and W.H. Wu, 7/31/91, not available.

- NCEER-91-0020 "Hybrid Control of Seismic-Excited Nonlinear and Inelastic Structural Systems," by J.N. Yang, Z. Li and A. Daniellians, 8/1/91, (PB92-143171, A06, MF-A02).
- NCEER-91-0021 "The NCEER-91 Earthquake Catalog: Improved Intensity-Based Magnitudes and Recurrence Relations for U.S. Earthquakes East of New Madrid," by L. Seeber and J.G. Armbruster, 8/28/91, (PB92-176742, A06, MF-A02).
- NCEER-91-0022 "Proceedings from the Implementation of Earthquake Planning and Education in Schools: The Need for Change - The Roles of the Changemakers," by K.E.K. Ross and F. Winslow, 7/23/91, (PB92-129998, A12, MF-A03).
- NCEER-91-0023 "A Study of Reliability-Based Criteria for Seismic Design of Reinforced Concrete Frame Buildings," by H.H.M. Hwang and H-M. Hsu, 8/10/91, (PB92-140235, A09, MF-A02).
- NCEER-91-0024 "Experimental Verification of a Number of Structural System Identification Algorithms," by R.G. Ghanem, H. Gavin and M. Shinozuka, 9/18/91, (PB92-176577, A18, MF-A04).
- NCEER-91-0025 "Probabilistic Evaluation of Liquefaction Potential," by H.H.M. Hwang and C.S. Lee," 11/25/91, (PB92-143429, A05, MF-A01).
- NCEER-91-0026 "Instantaneous Optimal Control for Linear, Nonlinear and Hysteretic Structures - Stable Controllers," by J.N. Yang and Z. Li, 11/15/91, (PB92-163807, A04, MF-A01).
- NCEER-91-0027 "Experimental and Theoretical Study of a Sliding Isolation System for Bridges," by M.C. Constantinou, A. Kartoum, A.M. Reinhorn and P. Bradford, 11/15/91, (PB92-176973, A10, MF-A03).
- NCEER-92-0001 "Case Studies of Liquefaction and Lifeline Performance During Past Earthquakes, Volume 1: Japanese Case Studies," Edited by M. Hamada and T. O'Rourke, 2/17/92, (PB92-197243, A18, MF-A04).
- NCEER-92-0002 "Case Studies of Liquefaction and Lifeline Performance During Past Earthquakes, Volume 2: United States Case Studies," Edited by T. O'Rourke and M. Hamada, 2/17/92, (PB92-197250, A20, MF-A04).
- NCEER-92-0003 "Issues in Earthquake Education," Edited by K. Ross, 2/3/92, (PB92-222389, A07, MF-A02).
- NCEER-92-0004 "Proceedings from the First U.S. - Japan Workshop on Earthquake Protective Systems for Bridges," Edited by I.G. Buckle, 2/4/92, (PB94-142239, A99, MF-A06).
- NCEER-92-0005 "Seismic Ground Motion from a Haskell-Type Source in a Multiple-Layered Half-Space," A.P. Theoharis, G. Deodatis and M. Shinozuka, 1/2/92, not available.
- NCEER-92-0006 "Proceedings from the Site Effects Workshop," Edited by R. Whitman, 2/29/92, (PB92-197201, A04, MF-A01).
- NCEER-92-0007 "Engineering Evaluation of Permanent Ground Deformations Due to Seismically-Induced Liquefaction," by M.H. Baziar, R. Dobry and A-W.M. Elgamel, 3/24/92, (PB92-222421, A13, MF-A03).
- NCEER-92-0008 "A Procedure for the Seismic Evaluation of Buildings in the Central and Eastern United States," by C.D. Poland and J.O. Malley, 4/2/92, (PB92-222439, A20, MF-A04).
- NCEER-92-0009 "Experimental and Analytical Study of a Hybrid Isolation System Using Friction Controllable Sliding Bearings," by M.Q. Feng, S. Fujii and M. Shinozuka, 5/15/92, (PB93-150282, A06, MF-A02).
- NCEER-92-0010 "Seismic Resistance of Slab-Column Connections in Existing Non-Ductile Flat-Plate Buildings," by A.J. Durrani and Y. Du, 5/18/92, (PB93-116812, A06, MF-A02).
- NCEER-92-0011 "The Hysteretic and Dynamic Behavior of Brick Masonry Walls Upgraded by Ferrocement Coatings Under Cyclic Loading and Strong Simulated Ground Motion," by H. Lee and S.P. Prawel, 5/11/92, not available.
- NCEER-92-0012 "Study of Wire Rope Systems for Seismic Protection of Equipment in Buildings," by G.F. Demetriades, M.C. Constantinou and A.M. Reinhorn, 5/20/92, (PB93-116655, A08, MF-A02).

- NCEER-92-0013 "Shape Memory Structural Dampers: Material Properties, Design and Seismic Testing," by P.R. Witting and F.A. Cozzarelli, 5/26/92, (PB93-116663, A05, MF-A01).
- NCEER-92-0014 "Longitudinal Permanent Ground Deformation Effects on Buried Continuous Pipelines," by M.J. O'Rourke, and C. Nordberg, 6/15/92, (PB93-116671, A08, MF-A02).
- NCEER-92-0015 "A Simulation Method for Stationary Gaussian Random Functions Based on the Sampling Theorem," by M. Grigoriu and S. Balopoulou, 6/11/92, (PB93-127496, A05, MF-A01).
- NCEER-92-0016 "Gravity-Load-Designed Reinforced Concrete Buildings: Seismic Evaluation of Existing Construction and Detailing Strategies for Improved Seismic Resistance," by G.W. Hoffmann, S.K. Kunnath, A.M. Reinhorn and J.B. Mander, 7/15/92, (PB94-142007, A08, MF-A02).
- NCEER-92-0017 "Observations on Water System and Pipeline Performance in the Limón Area of Costa Rica Due to the April 22, 1991 Earthquake," by M. O'Rourke and D. Ballantyne, 6/30/92, (PB93-126811, A06, MF-A02).
- NCEER-92-0018 "Fourth Edition of Earthquake Education Materials for Grades K-12," Edited by K.E.K. Ross, 8/10/92, (PB93-114023, A07, MF-A02).
- NCEER-92-0019 "Proceedings from the Fourth Japan-U.S. Workshop on Earthquake Resistant Design of Lifeline Facilities and Countermeasures for Soil Liquefaction," Edited by M. Hamada and T.D. O'Rourke, 8/12/92, (PB93-163939, A99, MF-E11).
- NCEER-92-0020 "Active Bracing System: A Full Scale Implementation of Active Control," by A.M. Reinhorn, T.T. Soong, R.C. Lin, M.A. Riley, Y.P. Wang, S. Aizawa and M. Higashino, 8/14/92, (PB93-127512, A06, MF-A02).
- NCEER-92-0021 "Empirical Analysis of Horizontal Ground Displacement Generated by Liquefaction-Induced Lateral Spreads," by S.F. Bartlett and T.L. Youd, 8/17/92, (PB93-188241, A06, MF-A02).
- NCEER-92-0022 "IDARC Version 3.0: Inelastic Damage Analysis of Reinforced Concrete Structures," by S.K. Kunnath, A.M. Reinhorn and R.F. Lobo, 8/31/92, (PB93-227502, A07, MF-A02).
- NCEER-92-0023 "A Semi-Empirical Analysis of Strong-Motion Peaks in Terms of Seismic Source, Propagation Path and Local Site Conditions, by M. Kamiyama, M.J. O'Rourke and R. Flores-Berrones, 9/9/92, (PB93-150266, A08, MF-A02).
- NCEER-92-0024 "Seismic Behavior of Reinforced Concrete Frame Structures with Nonductile Details, Part I: Summary of Experimental Findings of Full Scale Beam-Column Joint Tests," by A. Beres, R.N. White and P. Gergely, 9/30/92, (PB93-227783, A05, MF-A01).
- NCEER-92-0025 "Experimental Results of Repaired and Retrofitted Beam-Column Joint Tests in Lightly Reinforced Concrete Frame Buildings," by A. Beres, S. El-Borgi, R.N. White and P. Gergely, 10/29/92, (PB93-227791, A05, MF-A01).
- NCEER-92-0026 "A Generalization of Optimal Control Theory: Linear and Nonlinear Structures," by J.N. Yang, Z. Li and S. Vongchavalitkul, 11/2/92, (PB93-188621, A05, MF-A01).
- NCEER-92-0027 "Seismic Resistance of Reinforced Concrete Frame Structures Designed Only for Gravity Loads: Part I - Design and Properties of a One-Third Scale Model Structure," by J.M. Bracci, A.M. Reinhorn and J.B. Mander, 12/1/92, (PB94-104502, A08, MF-A02).
- NCEER-92-0028 "Seismic Resistance of Reinforced Concrete Frame Structures Designed Only for Gravity Loads: Part II - Experimental Performance of Subassemblages," by L.E. Aycaardi, J.B. Mander and A.M. Reinhorn, 12/1/92, (PB94-104510, A08, MF-A02).
- NCEER-92-0029 "Seismic Resistance of Reinforced Concrete Frame Structures Designed Only for Gravity Loads: Part III - Experimental Performance and Analytical Study of a Structural Model," by J.M. Bracci, A.M. Reinhorn and J.B. Mander, 12/1/92, (PB93-227528, A09, MF-A01).

- NCEER-92-0030 "Evaluation of Seismic Retrofit of Reinforced Concrete Frame Structures: Part I - Experimental Performance of Retrofitted Subassemblages," by D. Choudhuri, J.B. Mander and A.M. Reinhorn, 12/8/92, (PB93-198307, A07, MF-A02).
- NCEER-92-0031 "Evaluation of Seismic Retrofit of Reinforced Concrete Frame Structures: Part II - Experimental Performance and Analytical Study of a Retrofitted Structural Model," by J.M. Bracci, A.M. Reinhorn and J.B. Mander, 12/8/92, (PB93-198315, A09, MF-A03).
- NCEER-92-0032 "Experimental and Analytical Investigation of Seismic Response of Structures with Supplemental Fluid Viscous Dampers," by M.C. Constantinou and M.D. Symans, 12/21/92, (PB93-191435, A10, MF-A03). This report is available only through NTIS (see address given above).
- NCEER-92-0033 "Reconnaissance Report on the Cairo, Egypt Earthquake of October 12, 1992," by M. Khater, 12/23/92, (PB93-188621, A03, MF-A01).
- NCEER-92-0034 "Low-Level Dynamic Characteristics of Four Tall Flat-Plate Buildings in New York City," by H. Gavin, S. Yuan, J. Grossman, E. Pekelis and K. Jacob, 12/28/92, (PB93-188217, A07, MF-A02).
- NCEER-93-0001 "An Experimental Study on the Seismic Performance of Brick-Infilled Steel Frames With and Without Retrofit," by J.B. Mander, B. Nair, K. Wojtkowski and J. Ma, 1/29/93, (PB93-227510, A07, MF-A02).
- NCEER-93-0002 "Social Accounting for Disaster Preparedness and Recovery Planning," by S. Cole, E. Pantoja and V. Razak, 2/22/93, (PB94-142114, A12, MF-A03).
- NCEER-93-0003 "Assessment of 1991 NEHRP Provisions for Nonstructural Components and Recommended Revisions," by T.T. Soong, G. Chen, Z. Wu, R-H. Zhang and M. Grigoriu, 3/1/93, (PB93-188639, A06, MF-A02).
- NCEER-93-0004 "Evaluation of Static and Response Spectrum Analysis Procedures of SEAOC/UBC for Seismic Isolated Structures," by C.W. Winters and M.C. Constantinou, 3/23/93, (PB93-198299, A10, MF-A03).
- NCEER-93-0005 "Earthquakes in the Northeast - Are We Ignoring the Hazard? A Workshop on Earthquake Science and Safety for Educators," edited by K.E.K. Ross, 4/2/93, (PB94-103066, A09, MF-A02).
- NCEER-93-0006 "Inelastic Response of Reinforced Concrete Structures with Viscoelastic Braces," by R.F. Lobo, J.M. Bracci, K.L. Shen, A.M. Reinhorn and T.T. Soong, 4/5/93, (PB93-227486, A05, MF-A02).
- NCEER-93-0007 "Seismic Testing of Installation Methods for Computers and Data Processing Equipment," by K. Kosar, T.T. Soong, K.L. Shen, J.A. HoLung and Y.K. Lin, 4/12/93, (PB93-198299, A07, MF-A02).
- NCEER-93-0008 "Retrofit of Reinforced Concrete Frames Using Added Dampers," by A. Reinhorn, M. Constantinou and C. Li, not available.
- NCEER-93-0009 "Seismic Behavior and Design Guidelines for Steel Frame Structures with Added Viscoelastic Dampers," by K.C. Chang, M.L. Lai, T.T. Soong, D.S. Hao and Y.C. Yeh, 5/1/93, (PB94-141959, A07, MF-A02).
- NCEER-93-0010 "Seismic Performance of Shear-Critical Reinforced Concrete Bridge Piers," by J.B. Mander, S.M. Waheed, M.T.A. Chaudhary and S.S. Chen, 5/12/93, (PB93-227494, A08, MF-A02).
- NCEER-93-0011 "3D-BASIS-TABS: Computer Program for Nonlinear Dynamic Analysis of Three Dimensional Base Isolated Structures," by S. Nagarajaiah, C. Li, A.M. Reinhorn and M.C. Constantinou, 8/2/93, (PB94-141819, A09, MF-A02).
- NCEER-93-0012 "Effects of Hydrocarbon Spills from an Oil Pipeline Break on Ground Water," by O.J. Helweg and H.H.M. Hwang, 8/3/93, (PB94-141942, A06, MF-A02).
- NCEER-93-0013 "Simplified Procedures for Seismic Design of Nonstructural Components and Assessment of Current Code Provisions," by M.P. Singh, L.E. Suarez, E.E. Matheu and G.O. Maldonado, 8/4/93, (PB94-141827, A09, MF-A02).
- NCEER-93-0014 "An Energy Approach to Seismic Analysis and Design of Secondary Systems," by G. Chen and T.T. Soong, 8/6/93, (PB94-142767, A11, MF-A03).

- NCEER-93-0015 "Proceedings from School Sites: Becoming Prepared for Earthquakes - Commemorating the Third Anniversary of the Loma Prieta Earthquake," Edited by F.E. Winslow and K.E.K. Ross, 8/16/93, (PB94-154275, A16, MF-A02).
- NCEER-93-0016 "Reconnaissance Report of Damage to Historic Monuments in Cairo, Egypt Following the October 12, 1992 Dahshur Earthquake," by D. Sykora, D. Look, G. Croci, E. Karaesmen and E. Karaesmen, 8/19/93, (PB94-142221, A08, MF-A02).
- NCEER-93-0017 "The Island of Guam Earthquake of August 8, 1993," by S.W. Swan and S.K. Harris, 9/30/93, (PB94-141843, A04, MF-A01).
- NCEER-93-0018 "Engineering Aspects of the October 12, 1992 Egyptian Earthquake," by A.W. Elgamal, M. Amer, K. Adalier and A. Abul-Fadl, 10/7/93, (PB94-141983, A05, MF-A01).
- NCEER-93-0019 "Development of an Earthquake Motion Simulator and its Application in Dynamic Centrifuge Testing," by I. Krstelj, Supervised by J.H. Prevost, 10/23/93, (PB94-181773, A-10, MF-A03).
- NCEER-93-0020 "NCEER-Taisei Corporation Research Program on Sliding Seismic Isolation Systems for Bridges: Experimental and Analytical Study of a Friction Pendulum System (FPS)," by M.C. Constantinou, P. Tsopelas, Y-S. Kim and S. Okamoto, 11/1/93, (PB94-142775, A08, MF-A02).
- NCEER-93-0021 "Finite Element Modeling of Elastomeric Seismic Isolation Bearings," by L.J. Billings, Supervised by R. Shepherd, 11/8/93, not available.
- NCEER-93-0022 "Seismic Vulnerability of Equipment in Critical Facilities: Life-Safety and Operational Consequences," by K. Porter, G.S. Johnson, M.M. Zadeh, C. Scawthorn and S. Eder, 11/24/93, (PB94-181765, A16, MF-A03).
- NCEER-93-0023 "Hokkaido Nansei-oki, Japan Earthquake of July 12, 1993, by P.I. Yanev and C.R. Scawthorn, 12/23/93, (PB94-181500, A07, MF-A01).
- NCEER-94-0001 "An Evaluation of Seismic Serviceability of Water Supply Networks with Application to the San Francisco Auxiliary Water Supply System," by I. Markov, Supervised by M. Grigoriu and T. O'Rourke, 1/21/94, (PB94-204013, A07, MF-A02).
- NCEER-94-0002 "NCEER-Taisei Corporation Research Program on Sliding Seismic Isolation Systems for Bridges: Experimental and Analytical Study of Systems Consisting of Sliding Bearings, Rubber Restoring Force Devices and Fluid Dampers," Volumes I and II, by P. Tsopelas, S. Okamoto, M.C. Constantinou, D. Ozaki and S. Fujii, 2/4/94, (PB94-181740, A09, MF-A02 and PB94-181757, A12, MF-A03).
- NCEER-94-0003 "A Markov Model for Local and Global Damage Indices in Seismic Analysis," by S. Rahman and M. Grigoriu, 2/18/94, (PB94-206000, A12, MF-A03).
- NCEER-94-0004 "Proceedings from the NCEER Workshop on Seismic Response of Masonry Infills," edited by D.P. Abrams, 3/1/94, (PB94-180783, A07, MF-A02).
- NCEER-94-0005 "The Northridge, California Earthquake of January 17, 1994: General Reconnaissance Report," edited by J.D. Goltz, 3/11/94, (PB94-193943, A10, MF-A03).
- NCEER-94-0006 "Seismic Energy Based Fatigue Damage Analysis of Bridge Columns: Part I - Evaluation of Seismic Capacity," by G.A. Chang and J.B. Mander, 3/14/94, (PB94-219185, A11, MF-A03).
- NCEER-94-0007 "Seismic Isolation of Multi-Story Frame Structures Using Spherical Sliding Isolation Systems," by T.M. Al-Hussaini, V.A. Zayas and M.C. Constantinou, 3/17/94, (PB94-193745, A09, MF-A02).
- NCEER-94-0008 "The Northridge, California Earthquake of January 17, 1994: Performance of Highway Bridges," edited by I.G. Buckle, 3/24/94, (PB94-193851, A06, MF-A02).
- NCEER-94-0009 "Proceedings of the Third U.S.-Japan Workshop on Earthquake Protective Systems for Bridges," edited by I.G. Buckle and I. Friedland, 3/31/94, (PB94-195815, A99, MF-A06).

- NCEER-94-0010 "3D-BASIS-ME: Computer Program for Nonlinear Dynamic Analysis of Seismically Isolated Single and Multiple Structures and Liquid Storage Tanks," by P.C. Tsopelas, M.C. Constantinou and A.M. Reinhorn, 4/12/94, (PB94-204922, A09, MF-A02).
- NCEER-94-0011 "The Northridge, California Earthquake of January 17, 1994: Performance of Gas Transmission Pipelines," by T.D. O'Rourke and M.C. Palmer, 5/16/94, (PB94-204989, A05, MF-A01).
- NCEER-94-0012 "Feasibility Study of Replacement Procedures and Earthquake Performance Related to Gas Transmission Pipelines," by T.D. O'Rourke and M.C. Palmer, 5/25/94, (PB94-206638, A09, MF-A02).
- NCEER-94-0013 "Seismic Energy Based Fatigue Damage Analysis of Bridge Columns: Part II - Evaluation of Seismic Demand," by G.A. Chang and J.B. Mander, 6/1/94, (PB95-18106, A08, MF-A02).
- NCEER-94-0014 "NCEER-Taisei Corporation Research Program on Sliding Seismic Isolation Systems for Bridges: Experimental and Analytical Study of a System Consisting of Sliding Bearings and Fluid Restoring Force/Damping Devices," by P. Tsopelas and M.C. Constantinou, 6/13/94, (PB94-219144, A10, MF-A03).
- NCEER-94-0015 "Generation of Hazard-Consistent Fragility Curves for Seismic Loss Estimation Studies," by H. Hwang and J-R. Huo, 6/14/94, (PB95-181996, A09, MF-A02).
- NCEER-94-0016 "Seismic Study of Building Frames with Added Energy-Absorbing Devices," by W.S. Pong, C.S. Tsai and G.C. Lee, 6/20/94, (PB94-219136, A10, A03).
- NCEER-94-0017 "Sliding Mode Control for Seismic-Excited Linear and Nonlinear Civil Engineering Structures," by J. Yang, J. Wu, A. Agrawal and Z. Li, 6/21/94, (PB95-138483, A06, MF-A02).
- NCEER-94-0018 "3D-BASIS-TABS Version 2.0: Computer Program for Nonlinear Dynamic Analysis of Three Dimensional Base Isolated Structures," by A.M. Reinhorn, S. Nagarajaiah, M.C. Constantinou, P. Tsopelas and R. Li, 6/22/94, (PB95-182176, A08, MF-A02).
- NCEER-94-0019 "Proceedings of the International Workshop on Civil Infrastructure Systems: Application of Intelligent Systems and Advanced Materials on Bridge Systems," Edited by G.C. Lee and K.C. Chang, 7/18/94, (PB95-252474, A20, MF-A04).
- NCEER-94-0020 "Study of Seismic Isolation Systems for Computer Floors," by V. Lambrou and M.C. Constantinou, 7/19/94, (PB95-138533, A10, MF-A03).
- NCEER-94-0021 "Proceedings of the U.S.-Italian Workshop on Guidelines for Seismic Evaluation and Rehabilitation of Unreinforced Masonry Buildings," Edited by D.P. Abrams and G.M. Calvi, 7/20/94, (PB95-138749, A13, MF-A03).
- NCEER-94-0022 "NCEER-Taisei Corporation Research Program on Sliding Seismic Isolation Systems for Bridges: Experimental and Analytical Study of a System Consisting of Lubricated PTFE Sliding Bearings and Mild Steel Dampers," by P. Tsopelas and M.C. Constantinou, 7/22/94, (PB95-182184, A08, MF-A02).
- NCEER-94-0023 "Development of Reliability-Based Design Criteria for Buildings Under Seismic Load," by Y.K. Wen, H. Hwang and M. Shinozuka, 8/1/94, (PB95-211934, A08, MF-A02).
- NCEER-94-0024 "Experimental Verification of Acceleration Feedback Control Strategies for an Active Tendon System," by S.J. Dyke, B.F. Spencer, Jr., P. Quast, M.K. Sain, D.C. Kaspari, Jr. and T.T. Soong, 8/29/94, (PB95-212320, A05, MF-A01).
- NCEER-94-0025 "Seismic Retrofitting Manual for Highway Bridges," Edited by I.G. Buckle and I.F. Friedland, published by the Federal Highway Administration (PB95-212676, A15, MF-A03).
- NCEER-94-0026 "Proceedings from the Fifth U.S.-Japan Workshop on Earthquake Resistant Design of Lifeline Facilities and Countermeasures Against Soil Liquefaction," Edited by T.D. O'Rourke and M. Hamada, 11/7/94, (PB95-220802, A99, MF-E08).

- NCEER-95-0001 “Experimental and Analytical Investigation of Seismic Retrofit of Structures with Supplemental Damping: Part 1 - Fluid Viscous Damping Devices,” by A.M. Reinhorn, C. Li and M.C. Constantinou, 1/3/95, (PB95-266599, A09, MF-A02).
- NCEER-95-0002 “Experimental and Analytical Study of Low-Cycle Fatigue Behavior of Semi-Rigid Top-And-Seat Angle Connections,” by G. Pekcan, J.B. Mander and S.S. Chen, 1/5/95, (PB95-220042, A07, MF-A02).
- NCEER-95-0003 “NCEER-ATC Joint Study on Fragility of Buildings,” by T. Anagnos, C. Rojahn and A.S. Kiremidjian, 1/20/95, (PB95-220026, A06, MF-A02).
- NCEER-95-0004 “Nonlinear Control Algorithms for Peak Response Reduction,” by Z. Wu, T.T. Soong, V. Gattulli and R.C. Lin, 2/16/95, (PB95-220349, A05, MF-A01).
- NCEER-95-0005 “Pipeline Replacement Feasibility Study: A Methodology for Minimizing Seismic and Corrosion Risks to Underground Natural Gas Pipelines,” by R.T. Eguchi, H.A. Seligson and D.G. Honegger, 3/2/95, (PB95-252326, A06, MF-A02).
- NCEER-95-0006 “Evaluation of Seismic Performance of an 11-Story Frame Building During the 1994 Northridge Earthquake,” by F. Naeim, R. DiSulio, K. Benuska, A. Reinhorn and C. Li, not available.
- NCEER-95-0007 “Prioritization of Bridges for Seismic Retrofitting,” by N. Basöz and A.S. Kiremidjian, 4/24/95, (PB95-252300, A08, MF-A02).
- NCEER-95-0008 “Method for Developing Motion Damage Relationships for Reinforced Concrete Frames,” by A. Singhal and A.S. Kiremidjian, 5/11/95, (PB95-266607, A06, MF-A02).
- NCEER-95-0009 “Experimental and Analytical Investigation of Seismic Retrofit of Structures with Supplemental Damping: Part II - Friction Devices,” by C. Li and A.M. Reinhorn, 7/6/95, (PB96-128087, A11, MF-A03).
- NCEER-95-0010 “Experimental Performance and Analytical Study of a Non-Ductile Reinforced Concrete Frame Structure Retrofitted with Elastomeric Spring Dampers,” by G. Pekcan, J.B. Mander and S.S. Chen, 7/14/95, (PB96-137161, A08, MF-A02).
- NCEER-95-0011 “Development and Experimental Study of Semi-Active Fluid Damping Devices for Seismic Protection of Structures,” by M.D. Symans and M.C. Constantinou, 8/3/95, (PB96-136940, A23, MF-A04).
- NCEER-95-0012 “Real-Time Structural Parameter Modification (RSPM): Development of Innervated Structures,” by Z. Liang, M. Tong and G.C. Lee, 4/11/95, (PB96-137153, A06, MF-A01).
- NCEER-95-0013 “Experimental and Analytical Investigation of Seismic Retrofit of Structures with Supplemental Damping: Part III - Viscous Damping Walls,” by A.M. Reinhorn and C. Li, 10/1/95, (PB96-176409, A11, MF-A03).
- NCEER-95-0014 “Seismic Fragility Analysis of Equipment and Structures in a Memphis Electric Substation,” by J-R. Huo and H.H.M. Hwang, 8/10/95, (PB96-128087, A09, MF-A02).
- NCEER-95-0015 “The Hanshin-Awaji Earthquake of January 17, 1995: Performance of Lifelines,” Edited by M. Shinozuka, 11/3/95, (PB96-176383, A15, MF-A03).
- NCEER-95-0016 “Highway Culvert Performance During Earthquakes,” by T.L. Youd and C.J. Beckman, available as NCEER-96-0015.
- NCEER-95-0017 “The Hanshin-Awaji Earthquake of January 17, 1995: Performance of Highway Bridges,” Edited by I.G. Buckle, 12/1/95, not available.
- NCEER-95-0018 “Modeling of Masonry Infill Panels for Structural Analysis,” by A.M. Reinhorn, A. Madan, R.E. Valles, Y. Reichmann and J.B. Mander, 12/8/95, (PB97-110886, MF-A01, A06).
- NCEER-95-0019 “Optimal Polynomial Control for Linear and Nonlinear Structures,” by A.K. Agrawal and J.N. Yang, 12/11/95, (PB96-168737, A07, MF-A02).

- NCEER-95-0020 "Retrofit of Non-Ductile Reinforced Concrete Frames Using Friction Dampers," by R.S. Rao, P. Gergely and R.N. White, 12/22/95, (PB97-133508, A10, MF-A02).
- NCEER-95-0021 "Parametric Results for Seismic Response of Pile-Supported Bridge Bents," by G. Mylonakis, A. Nikolaou and G. Gazetas, 12/22/95, (PB97-100242, A12, MF-A03).
- NCEER-95-0022 "Kinematic Bending Moments in Seismically Stressed Piles," by A. Nikolaou, G. Mylonakis and G. Gazetas, 12/23/95, (PB97-113914, MF-A03, A13).
- NCEER-96-0001 "Dynamic Response of Unreinforced Masonry Buildings with Flexible Diaphragms," by A.C. Costley and D.P. Abrams, 10/10/96, (PB97-133573, MF-A03, A15).
- NCEER-96-0002 "State of the Art Review: Foundations and Retaining Structures," by I. Po Lam, not available.
- NCEER-96-0003 "Ductility of Rectangular Reinforced Concrete Bridge Columns with Moderate Confinement," by N. Wehbe, M. Saiidi, D. Sanders and B. Douglas, 11/7/96, (PB97-133557, A06, MF-A02).
- NCEER-96-0004 "Proceedings of the Long-Span Bridge Seismic Research Workshop," edited by I.G. Buckle and I.M. Friedland, not available.
- NCEER-96-0005 "Establish Representative Pier Types for Comprehensive Study: Eastern United States," by J. Kulicki and Z. Prucz, 5/28/96, (PB98-119217, A07, MF-A02).
- NCEER-96-0006 "Establish Representative Pier Types for Comprehensive Study: Western United States," by R. Imbsen, R.A. Schamber and T.A. Osterkamp, 5/28/96, (PB98-118607, A07, MF-A02).
- NCEER-96-0007 "Nonlinear Control Techniques for Dynamical Systems with Uncertain Parameters," by R.G. Ghanem and M.I. Bujakov, 5/27/96, (PB97-100259, A17, MF-A03).
- NCEER-96-0008 "Seismic Evaluation of a 30-Year Old Non-Ductile Highway Bridge Pier and Its Retrofit," by J.B. Mander, B. Mahmoodzadegan, S. Bhadra and S.S. Chen, 5/31/96, (PB97-110902, MF-A03, A10).
- NCEER-96-0009 "Seismic Performance of a Model Reinforced Concrete Bridge Pier Before and After Retrofit," by J.B. Mander, J.H. Kim and C.A. Ligozio, 5/31/96, (PB97-110910, MF-A02, A10).
- NCEER-96-0010 "IDARC2D Version 4.0: A Computer Program for the Inelastic Damage Analysis of Buildings," by R.E. Valles, A.M. Reinhorn, S.K. Kunnath, C. Li and A. Madan, 6/3/96, (PB97-100234, A17, MF-A03).
- NCEER-96-0011 "Estimation of the Economic Impact of Multiple Lifeline Disruption: Memphis Light, Gas and Water Division Case Study," by S.E. Chang, H.A. Seligson and R.T. Eguchi, 8/16/96, (PB97-133490, A11, MF-A03).
- NCEER-96-0012 "Proceedings from the Sixth Japan-U.S. Workshop on Earthquake Resistant Design of Lifeline Facilities and Countermeasures Against Soil Liquefaction, Edited by M. Hamada and T. O'Rourke, 9/11/96, (PB97-133581, A99, MF-A06).
- NCEER-96-0013 "Chemical Hazards, Mitigation and Preparedness in Areas of High Seismic Risk: A Methodology for Estimating the Risk of Post-Earthquake Hazardous Materials Release," by H.A. Seligson, R.T. Eguchi, K.J. Tierney and K. Richmond, 11/7/96, (PB97-133565, MF-A02, A08).
- NCEER-96-0014 "Response of Steel Bridge Bearings to Reversed Cyclic Loading," by J.B. Mander, D-K. Kim, S.S. Chen and G.J. Premus, 11/13/96, (PB97-140735, A12, MF-A03).
- NCEER-96-0015 "Highway Culvert Performance During Past Earthquakes," by T.L. Youd and C.J. Beckman, 11/25/96, (PB97-133532, A06, MF-A01).
- NCEER-97-0001 "Evaluation, Prevention and Mitigation of Pounding Effects in Building Structures," by R.E. Valles and A.M. Reinhorn, 2/20/97, (PB97-159552, A14, MF-A03).
- NCEER-97-0002 "Seismic Design Criteria for Bridges and Other Highway Structures," by C. Rojahn, R. Mayes, D.G. Anderson, J. Clark, J.H. Hom, R.V. Nutt and M.J. O'Rourke, 4/30/97, (PB97-194658, A06, MF-A03).



- NCEER-97-0003 "Proceedings of the U.S.-Italian Workshop on Seismic Evaluation and Retrofit," Edited by D.P. Abrams and G.M. Calvi, 3/19/97, (PB97-194666, A13, MF-A03).
- NCEER-97-0004 "Investigation of Seismic Response of Buildings with Linear and Nonlinear Fluid Viscous Dampers," by A.A. Seleemah and M.C. Constantinou, 5/21/97, (PB98-109002, A15, MF-A03).
- NCEER-97-0005 "Proceedings of the Workshop on Earthquake Engineering Frontiers in Transportation Facilities," edited by G.C. Lee and I.M. Friedland, 8/29/97, (PB98-128911, A25, MR-A04).
- NCEER-97-0006 "Cumulative Seismic Damage of Reinforced Concrete Bridge Piers," by S.K. Kunnath, A. El-Bahy, A. Taylor and W. Stone, 9/2/97, (PB98-108814, A11, MF-A03).
- NCEER-97-0007 "Structural Details to Accommodate Seismic Movements of Highway Bridges and Retaining Walls," by R.A. Imbsen, R.A. Schamber, E. Thorkildsen, A. Kartoum, B.T. Martin, T.N. Rosser and J.M. Kulicki, 9/3/97, (PB98-108996, A09, MF-A02).
- NCEER-97-0008 "A Method for Earthquake Motion-Damage Relationships with Application to Reinforced Concrete Frames," by A. Singhal and A.S. Kiremidjian, 9/10/97, (PB98-108988, A13, MF-A03).
- NCEER-97-0009 "Seismic Analysis and Design of Bridge Abutments Considering Sliding and Rotation," by K. Fishman and R. Richards, Jr., 9/15/97, (PB98-108897, A06, MF-A02).
- NCEER-97-0010 "Proceedings of the FHWA/NCEER Workshop on the National Representation of Seismic Ground Motion for New and Existing Highway Facilities," edited by I.M. Friedland, M.S. Power and R.L. Mayes, 9/22/97, (PB98-128903, A21, MF-A04).
- NCEER-97-0011 "Seismic Analysis for Design or Retrofit of Gravity Bridge Abutments," by K.L. Fishman, R. Richards, Jr. and R.C. Divito, 10/2/97, (PB98-128937, A08, MF-A02).
- NCEER-97-0012 "Evaluation of Simplified Methods of Analysis for Yielding Structures," by P. Tsopelas, M.C. Constantinou, C.A. Kircher and A.S. Whittaker, 10/31/97, (PB98-128929, A10, MF-A03).
- NCEER-97-0013 "Seismic Design of Bridge Columns Based on Control and Repairability of Damage," by C-T. Cheng and J.B. Mander, 12/8/97, (PB98-144249, A11, MF-A03).
- NCEER-97-0014 "Seismic Resistance of Bridge Piers Based on Damage Avoidance Design," by J.B. Mander and C-T. Cheng, 12/10/97, (PB98-144223, A09, MF-A02).
- NCEER-97-0015 "Seismic Response of Nominally Symmetric Systems with Strength Uncertainty," by S. Balopoulou and M. Grigoriu, 12/23/97, (PB98-153422, A11, MF-A03).
- NCEER-97-0016 "Evaluation of Seismic Retrofit Methods for Reinforced Concrete Bridge Columns," by T.J. Wipf, F.W. Klaiber and F.M. Russo, 12/28/97, (PB98-144215, A12, MF-A03).
- NCEER-97-0017 "Seismic Fragility of Existing Conventional Reinforced Concrete Highway Bridges," by C.L. Mullen and A.S. Cakmak, 12/30/97, (PB98-153406, A08, MF-A02).
- NCEER-97-0018 "Loss Assessment of Memphis Buildings," edited by D.P. Abrams and M. Shinozuka, 12/31/97, (PB98-144231, A13, MF-A03).
- NCEER-97-0019 "Seismic Evaluation of Frames with Infill Walls Using Quasi-static Experiments," by K.M. Mosalam, R.N. White and P. Gergely, 12/31/97, (PB98-153455, A07, MF-A02).
- NCEER-97-0020 "Seismic Evaluation of Frames with Infill Walls Using Pseudo-dynamic Experiments," by K.M. Mosalam, R.N. White and P. Gergely, 12/31/97, (PB98-153430, A07, MF-A02).
- NCEER-97-0021 "Computational Strategies for Frames with Infill Walls: Discrete and Smeared Crack Analyses and Seismic Fragility," by K.M. Mosalam, R.N. White and P. Gergely, 12/31/97, (PB98-153414, A10, MF-A02).

- NCEER-97-0022 "Proceedings of the NCEER Workshop on Evaluation of Liquefaction Resistance of Soils," edited by T.L. Youd and I.M. Idriss, 12/31/97, (PB98-155617, A15, MF-A03).
- MCEER-98-0001 "Extraction of Nonlinear Hysteretic Properties of Seismically Isolated Bridges from Quick-Release Field Tests," by Q. Chen, B.M. Douglas, E.M. Maragakis and I.G. Buckle, 5/26/98, (PB99-118838, A06, MF-A01).
- MCEER-98-0002 "Methodologies for Evaluating the Importance of Highway Bridges," by A. Thomas, S. Eshenaur and J. Kulicki, 5/29/98, (PB99-118846, A10, MF-A02).
- MCEER-98-0003 "Capacity Design of Bridge Piers and the Analysis of Overstrength," by J.B. Mander, A. Dutta and P. Goel, 6/1/98, (PB99-118853, A09, MF-A02).
- MCEER-98-0004 "Evaluation of Bridge Damage Data from the Loma Prieta and Northridge, California Earthquakes," by N. Basoz and A. Kiremidjian, 6/2/98, (PB99-118861, A15, MF-A03).
- MCEER-98-0005 "Screening Guide for Rapid Assessment of Liquefaction Hazard at Highway Bridge Sites," by T. L. Youd, 6/16/98, (PB99-118879, A06, not available on microfiche).
- MCEER-98-0006 "Structural Steel and Steel/Concrete Interface Details for Bridges," by P. Ritchie, N. Kauh and J. Kulicki, 7/13/98, (PB99-118945, A06, MF-A01).
- MCEER-98-0007 "Capacity Design and Fatigue Analysis of Confined Concrete Columns," by A. Dutta and J.B. Mander, 7/14/98, (PB99-118960, A14, MF-A03).
- MCEER-98-0008 "Proceedings of the Workshop on Performance Criteria for Telecommunication Services Under Earthquake Conditions," edited by A.J. Schiff, 7/15/98, (PB99-118952, A08, MF-A02).
- MCEER-98-0009 "Fatigue Analysis of Unconfined Concrete Columns," by J.B. Mander, A. Dutta and J.H. Kim, 9/12/98, (PB99-123655, A10, MF-A02).
- MCEER-98-0010 "Centrifuge Modeling of Cyclic Lateral Response of Pile-Cap Systems and Seat-Type Abutments in Dry Sands," by A.D. Gadre and R. Dobry, 10/2/98, (PB99-123606, A13, MF-A03).
- MCEER-98-0011 "IDARC-BRIDGE: A Computational Platform for Seismic Damage Assessment of Bridge Structures," by A.M. Reinhorn, V. Simeonov, G. Mylonakis and Y. Reichman, 10/2/98, (PB99-162919, A15, MF-A03).
- MCEER-98-0012 "Experimental Investigation of the Dynamic Response of Two Bridges Before and After Retrofitting with Elastomeric Bearings," by D.A. Wendichansky, S.S. Chen and J.B. Mander, 10/2/98, (PB99-162927, A15, MF-A03).
- MCEER-98-0013 "Design Procedures for Hinge Restrainers and Hinge Sear Width for Multiple-Frame Bridges," by R. Des Roches and G.L. Fenves, 11/3/98, (PB99-140477, A13, MF-A03).
- MCEER-98-0014 "Response Modification Factors for Seismically Isolated Bridges," by M.C. Constantinou and J.K. Quarshie, 11/3/98, (PB99-140485, A14, MF-A03).
- MCEER-98-0015 "Proceedings of the U.S.-Italy Workshop on Seismic Protective Systems for Bridges," edited by I.M. Friedland and M.C. Constantinou, 11/3/98, (PB2000-101711, A22, MF-A04).
- MCEER-98-0016 "Appropriate Seismic Reliability for Critical Equipment Systems: Recommendations Based on Regional Analysis of Financial and Life Loss," by K. Porter, C. Scawthorn, C. Taylor and N. Blais, 11/10/98, (PB99-157265, A08, MF-A02).
- MCEER-98-0017 "Proceedings of the U.S. Japan Joint Seminar on Civil Infrastructure Systems Research," edited by M. Shinozuka and A. Rose, 11/12/98, (PB99-156713, A16, MF-A03).
- MCEER-98-0018 "Modeling of Pile Footings and Drilled Shafts for Seismic Design," by I. PoLam, M. Kapuskar and D. Chaudhuri, 12/21/98, (PB99-157257, A09, MF-A02).

- MCEER-99-0001 "Seismic Evaluation of a Masonry Infilled Reinforced Concrete Frame by Pseudodynamic Testing," by S.G. Buonopane and R.N. White, 2/16/99, (PB99-162851, A09, MF-A02).
- MCEER-99-0002 "Response History Analysis of Structures with Seismic Isolation and Energy Dissipation Systems: Verification Examples for Program SAP2000," by J. Scheller and M.C. Constantinou, 2/22/99, (PB99-162869, A08, MF-A02).
- MCEER-99-0003 "Experimental Study on the Seismic Design and Retrofit of Bridge Columns Including Axial Load Effects," by A. Dutta, T. Kokorina and J.B. Mander, 2/22/99, (PB99-162877, A09, MF-A02).
- MCEER-99-0004 "Experimental Study of Bridge Elastomeric and Other Isolation and Energy Dissipation Systems with Emphasis on Uplift Prevention and High Velocity Near-source Seismic Excitation," by A. Kasalanati and M. C. Constantinou, 2/26/99, (PB99-162885, A12, MF-A03).
- MCEER-99-0005 "Truss Modeling of Reinforced Concrete Shear-flexure Behavior," by J.H. Kim and J.B. Mander, 3/8/99, (PB99-163693, A12, MF-A03).
- MCEER-99-0006 "Experimental Investigation and Computational Modeling of Seismic Response of a 1:4 Scale Model Steel Structure with a Load Balancing Supplemental Damping System," by G. Pekcan, J.B. Mander and S.S. Chen, 4/2/99, (PB99-162893, A11, MF-A03).
- MCEER-99-0007 "Effect of Vertical Ground Motions on the Structural Response of Highway Bridges," by M.R. Button, C.J. Cronin and R.L. Mayes, 4/10/99, (PB2000-101411, A10, MF-A03).
- MCEER-99-0008 "Seismic Reliability Assessment of Critical Facilities: A Handbook, Supporting Documentation, and Model Code Provisions," by G.S. Johnson, R.E. Sheppard, M.D. Quilici, S.J. Eder and C.R. Scawthorn, 4/12/99, (PB2000-101701, A18, MF-A04).
- MCEER-99-0009 "Impact Assessment of Selected MCEER Highway Project Research on the Seismic Design of Highway Structures," by C. Rojahn, R. Mayes, D.G. Anderson, J.H. Clark, D'Appolonia Engineering, S. Gloyd and R.V. Nutt, 4/14/99, (PB99-162901, A10, MF-A02).
- MCEER-99-0010 "Site Factors and Site Categories in Seismic Codes," by R. Dobry, R. Ramos and M.S. Power, 7/19/99, (PB2000-101705, A08, MF-A02).
- MCEER-99-0011 "Restrainer Design Procedures for Multi-Span Simply-Supported Bridges," by M.J. Randall, M. Saiidi, E. Maragakis and T. Isakovic, 7/20/99, (PB2000-101702, A10, MF-A02).
- MCEER-99-0012 "Property Modification Factors for Seismic Isolation Bearings," by M.C. Constantinou, P. Tsopelas, A. Kasalanati and E. Wolff, 7/20/99, (PB2000-103387, A11, MF-A03).
- MCEER-99-0013 "Critical Seismic Issues for Existing Steel Bridges," by P. Ritchie, N. Kauh and J. Kulicki, 7/20/99, (PB2000-101697, A09, MF-A02).
- MCEER-99-0014 "Nonstructural Damage Database," by A. Kao, T.T. Soong and A. Vender, 7/24/99, (PB2000-101407, A06, MF-A01).
- MCEER-99-0015 "Guide to Remedial Measures for Liquefaction Mitigation at Existing Highway Bridge Sites," by H.G. Cooke and J. K. Mitchell, 7/26/99, (PB2000-101703, A11, MF-A03).
- MCEER-99-0016 "Proceedings of the MCEER Workshop on Ground Motion Methodologies for the Eastern United States," edited by N. Abrahamson and A. Becker, 8/11/99, (PB2000-103385, A07, MF-A02).
- MCEER-99-0017 "Quindío, Colombia Earthquake of January 25, 1999: Reconnaissance Report," by A.P. Asfura and P.J. Flores, 10/4/99, (PB2000-106893, A06, MF-A01).
- MCEER-99-0018 "Hysteretic Models for Cyclic Behavior of Deteriorating Inelastic Structures," by M.V. Sivaselvan and A.M. Reinhorn, 11/5/99, (PB2000-103386, A08, MF-A02).

- MCEER-99-0019 "Proceedings of the 7<sup>th</sup> U.S.- Japan Workshop on Earthquake Resistant Design of Lifeline Facilities and Countermeasures Against Soil Liquefaction," edited by T.D. O'Rourke, J.P. Bardet and M. Hamada, 11/19/99, (PB2000-103354, A99, MF-A06).
- MCEER-99-0020 "Development of Measurement Capability for Micro-Vibration Evaluations with Application to Chip Fabrication Facilities," by G.C. Lee, Z. Liang, J.W. Song, J.D. Shen and W.C. Liu, 12/1/99, (PB2000-105993, A08, MF-A02).
- MCEER-99-0021 "Design and Retrofit Methodology for Building Structures with Supplemental Energy Dissipating Systems," by G. Pekcan, J.B. Mander and S.S. Chen, 12/31/99, (PB2000-105994, A11, MF-A03).
- MCEER-00-0001 "The Marmara, Turkey Earthquake of August 17, 1999: Reconnaissance Report," edited by C. Scawthorn; with major contributions by M. Bruneau, R. Eguchi, T. Holzer, G. Johnson, J. Mander, J. Mitchell, W. Mitchell, A. Papageorgiou, C. Scaethorn, and G. Webb, 3/23/00, (PB2000-106200, A11, MF-A03).
- MCEER-00-0002 "Proceedings of the MCEER Workshop for Seismic Hazard Mitigation of Health Care Facilities," edited by G.C. Lee, M. Ettouney, M. Grigoriu, J. Hauer and J. Nigg, 3/29/00, (PB2000-106892, A08, MF-A02).
- MCEER-00-0003 "The Chi-Chi, Taiwan Earthquake of September 21, 1999: Reconnaissance Report," edited by G.C. Lee and C.H. Loh, with major contributions by G.C. Lee, M. Bruneau, I.G. Buckle, S.E. Chang, P.J. Flores, T.D. O'Rourke, M. Shinozuka, T.T. Soong, C-H. Loh, K-C. Chang, Z-J. Chen, J-S. Hwang, M-L. Lin, G-Y. Liu, K-C. Tsai, G.C. Yao and C-L. Yen, 4/30/00, (PB2001-100980, A10, MF-A02).
- MCEER-00-0004 "Seismic Retrofit of End-Sway Frames of Steel Deck-Truss Bridges with a Supplemental Tendon System: Experimental and Analytical Investigation," by G. Pekcan, J.B. Mander and S.S. Chen, 7/1/00, (PB2001-100982, A10, MF-A02).
- MCEER-00-0005 "Sliding Fragility of Unrestrained Equipment in Critical Facilities," by W.H. Chong and T.T. Soong, 7/5/00, (PB2001-100983, A08, MF-A02).
- MCEER-00-0006 "Seismic Response of Reinforced Concrete Bridge Pier Walls in the Weak Direction," by N. Abo-Shadi, M. Saiidi and D. Sanders, 7/17/00, (PB2001-100981, A17, MF-A03).
- MCEER-00-0007 "Low-Cycle Fatigue Behavior of Longitudinal Reinforcement in Reinforced Concrete Bridge Columns," by J. Brown and S.K. Kunnath, 7/23/00, (PB2001-104392, A08, MF-A02).
- MCEER-00-0008 "Soil Structure Interaction of Bridges for Seismic Analysis," I. PoLam and H. Law, 9/25/00, (PB2001-105397, A08, MF-A02).
- MCEER-00-0009 "Proceedings of the First MCEER Workshop on Mitigation of Earthquake Disaster by Advanced Technologies (MEDAT-1), edited by M. Shinozuka, D.J. Inman and T.D. O'Rourke, 11/10/00, (PB2001-105399, A14, MF-A03).
- MCEER-00-0010 "Development and Evaluation of Simplified Procedures for Analysis and Design of Buildings with Passive Energy Dissipation Systems, Revision 01," by O.M. Ramirez, M.C. Constantinou, C.A. Kircher, A.S. Whittaker, M.W. Johnson, J.D. Gomez and C. Chrysostomou, 11/16/01, (PB2001-105523, A23, MF-A04).
- MCEER-00-0011 "Dynamic Soil-Foundation-Structure Interaction Analyses of Large Caissons," by C-Y. Chang, C-M. Mok, Z-L. Wang, R. Settgast, F. Waggoner, M.A. Ketchum, H.M. Gonnermann and C-C. Chin, 12/30/00, (PB2001-104373, A07, MF-A02).
- MCEER-00-0012 "Experimental Evaluation of Seismic Performance of Bridge Restrainers," by A.G. Vlassis, E.M. Maragakis and M. Saiid Saiidi, 12/30/00, (PB2001-104354, A09, MF-A02).
- MCEER-00-0013 "Effect of Spatial Variation of Ground Motion on Highway Structures," by M. Shinozuka, V. Saxena and G. Deodatis, 12/31/00, (PB2001-108755, A13, MF-A03).
- MCEER-00-0014 "A Risk-Based Methodology for Assessing the Seismic Performance of Highway Systems," by S.D. Werner, C.E. Taylor, J.E. Moore, II, J.S. Walton and S. Cho, 12/31/00, (PB2001-108756, A14, MF-A03).

- MCEER-01-0001 "Experimental Investigation of P-Delta Effects to Collapse During Earthquakes," by D. Vian and M. Bruneau, 6/25/01, (PB2002-100534, A17, MF-A03).
- MCEER-01-0002 "Proceedings of the Second MCEER Workshop on Mitigation of Earthquake Disaster by Advanced Technologies (MEDAT-2)," edited by M. Bruneau and D.J. Inman, 7/23/01, (PB2002-100434, A16, MF-A03).
- MCEER-01-0003 "Sensitivity Analysis of Dynamic Systems Subjected to Seismic Loads," by C. Roth and M. Grigoriu, 9/18/01, (PB2003-100884, A12, MF-A03).
- MCEER-01-0004 "Overcoming Obstacles to Implementing Earthquake Hazard Mitigation Policies: Stage 1 Report," by D.J. Alesch and W.J. Petak, 12/17/01, (PB2002-107949, A07, MF-A02).
- MCEER-01-0005 "Updating Real-Time Earthquake Loss Estimates: Methods, Problems and Insights," by C.E. Taylor, S.E. Chang and R.T. Eguchi, 12/17/01, (PB2002-107948, A05, MF-A01).
- MCEER-01-0006 "Experimental Investigation and Retrofit of Steel Pile Foundations and Pile Bents Under Cyclic Lateral Loadings," by A. Shama, J. Mander, B. Blabac and S. Chen, 12/31/01, (PB2002-107950, A13, MF-A03).
- MCEER-02-0001 "Assessment of Performance of Bolu Viaduct in the 1999 Duzce Earthquake in Turkey" by P.C. Roussis, M.C. Constantinou, M. Erdik, E. Durukal and M. Dicleli, 5/8/02, (PB2003-100883, A08, MF-A02).
- MCEER-02-0002 "Seismic Behavior of Rail Counterweight Systems of Elevators in Buildings," by M.P. Singh, Rildova and L.E. Suarez, 5/27/02. (PB2003-100882, A11, MF-A03).
- MCEER-02-0003 "Development of Analysis and Design Procedures for Spread Footings," by G. Mylonakis, G. Gazetas, S. Nikolaou and A. Chauncey, 10/02/02, (PB2004-101636, A13, MF-A03, CD-A13).
- MCEER-02-0004 "Bare-Earth Algorithms for Use with SAR and LIDAR Digital Elevation Models," by C.K. Huyck, R.T. Eguchi and B. Houshmand, 10/16/02, (PB2004-101637, A07, CD-A07).
- MCEER-02-0005 "Review of Energy Dissipation of Compression Members in Concentrically Braced Frames," by K.Lee and M. Bruneau, 10/18/02, (PB2004-101638, A10, CD-A10).
- MCEER-03-0001 "Experimental Investigation of Light-Gauge Steel Plate Shear Walls for the Seismic Retrofit of Buildings" by J. Berman and M. Bruneau, 5/2/03, (PB2004-101622, A10, MF-A03, CD-A10).
- MCEER-03-0002 "Statistical Analysis of Fragility Curves," by M. Shinozuka, M.Q. Feng, H. Kim, T. Uzawa and T. Ueda, 6/16/03, (PB2004-101849, A09, CD-A09).
- MCEER-03-0003 "Proceedings of the Eighth U.S.-Japan Workshop on Earthquake Resistant Design of Lifeline Facilities and Countermeasures Against Liquefaction," edited by M. Hamada, J.P. Bardet and T.D. O'Rourke, 6/30/03, (PB2004-104386, A99, CD-A99).
- MCEER-03-0004 "Proceedings of the PRC-US Workshop on Seismic Analysis and Design of Special Bridges," edited by L.C. Fan and G.C. Lee, 7/15/03, (PB2004-104387, A14, CD-A14).
- MCEER-03-0005 "Urban Disaster Recovery: A Framework and Simulation Model," by S.B. Miles and S.E. Chang, 7/25/03, (PB2004-104388, A07, CD-A07).
- MCEER-03-0006 "Behavior of Underground Piping Joints Due to Static and Dynamic Loading," by R.D. Meis, M. Maragakis and R. Siddharthan, 11/17/03, (PB2005-102194, A13, MF-A03, CD-A00).
- MCEER-04-0001 "Experimental Study of Seismic Isolation Systems with Emphasis on Secondary System Response and Verification of Accuracy of Dynamic Response History Analysis Methods," by E. Wolff and M. Constantinou, 1/16/04 (PB2005-102195, A99, MF-E08, CD-A00).
- MCEER-04-0002 "Tension, Compression and Cyclic Testing of Engineered Cementitious Composite Materials," by K. Kesner and S.L. Billington, 3/1/04, (PB2005-102196, A08, CD-A08).

- MCEER-04-0003 "Cyclic Testing of Braces Laterally Restrained by Steel Studs to Enhance Performance During Earthquakes," by O.C. Celik, J.W. Berman and M. Bruneau, 3/16/04, (PB2005-102197, A13, MF-A03, CD-A00).
- MCEER-04-0004 "Methodologies for Post Earthquake Building Damage Detection Using SAR and Optical Remote Sensing: Application to the August 17, 1999 Marmara, Turkey Earthquake," by C.K. Huyck, B.J. Adams, S. Cho, R.T. Eguchi, B. Mansouri and B. Houshmand, 6/15/04, (PB2005-104888, A10, CD-A00).
- MCEER-04-0005 "Nonlinear Structural Analysis Towards Collapse Simulation: A Dynamical Systems Approach," by M.V. Sivaselvan and A.M. Reinhorn, 6/16/04, (PB2005-104889, A11, MF-A03, CD-A00).
- MCEER-04-0006 "Proceedings of the Second PRC-US Workshop on Seismic Analysis and Design of Special Bridges," edited by G.C. Lee and L.C. Fan, 6/25/04, (PB2005-104890, A16, CD-A00).
- MCEER-04-0007 "Seismic Vulnerability Evaluation of Axially Loaded Steel Built-up Laced Members," by K. Lee and M. Bruneau, 6/30/04, (PB2005-104891, A16, CD-A00).
- MCEER-04-0008 "Evaluation of Accuracy of Simplified Methods of Analysis and Design of Buildings with Damping Systems for Near-Fault and for Soft-Soil Seismic Motions," by E.A. Pavlou and M.C. Constantinou, 8/16/04, (PB2005-104892, A08, MF-A02, CD-A00).
- MCEER-04-0009 "Assessment of Geotechnical Issues in Acute Care Facilities in California," by M. Lew, T.D. O'Rourke, R. Dobry and M. Koch, 9/15/04, (PB2005-104893, A08, CD-A00).
- MCEER-04-0010 "Scissor-Jack-Damper Energy Dissipation System," by A.N. Sigaher-Boyle and M.C. Constantinou, 12/1/04 (PB2005-108221).
- MCEER-04-0011 "Seismic Retrofit of Bridge Steel Truss Piers Using a Controlled Rocking Approach," by M. Pollino and M. Bruneau, 12/20/04 (PB2006-105795).
- MCEER-05-0001 "Experimental and Analytical Studies of Structures Seismically Isolated with an Uplift-Restraint Isolation System," by P.C. Roussis and M.C. Constantinou, 1/10/05 (PB2005-108222).
- MCEER-05-0002 "A Versatile Experimentation Model for Study of Structures Near Collapse Applied to Seismic Evaluation of Irregular Structures," by D. Kusumastuti, A.M. Reinhorn and A. Rutenberg, 3/31/05 (PB2006-101523).
- MCEER-05-0003 "Proceedings of the Third PRC-US Workshop on Seismic Analysis and Design of Special Bridges," edited by L.C. Fan and G.C. Lee, 4/20/05, (PB2006-105796).
- MCEER-05-0004 "Approaches for the Seismic Retrofit of Braced Steel Bridge Piers and Proof-of-Concept Testing of an Eccentrically Braced Frame with Tubular Link," by J.W. Berman and M. Bruneau, 4/21/05 (PB2006-101524).
- MCEER-05-0005 "Simulation of Strong Ground Motions for Seismic Fragility Evaluation of Nonstructural Components in Hospitals," by A. Wanitkorkul and A. Filiatrault, 5/26/05 (PB2006-500027).
- MCEER-05-0006 "Seismic Safety in California Hospitals: Assessing an Attempt to Accelerate the Replacement or Seismic Retrofit of Older Hospital Facilities," by D.J. Alesch, L.A. Arendt and W.J. Petak, 6/6/05 (PB2006-105794).
- MCEER-05-0007 "Development of Seismic Strengthening and Retrofit Strategies for Critical Facilities Using Engineered Cementitious Composite Materials," by K. Kesner and S.L. Billington, 8/29/05 (PB2006-111701).
- MCEER-05-0008 "Experimental and Analytical Studies of Base Isolation Systems for Seismic Protection of Power Transformers," by N. Murota, M.Q. Feng and G-Y. Liu, 9/30/05 (PB2006-111702).
- MCEER-05-0009 "3D-BASIS-ME-MB: Computer Program for Nonlinear Dynamic Analysis of Seismically Isolated Structures," by P.C. Tsopelas, P.C. Roussis, M.C. Constantinou, R. Buchanan and A.M. Reinhorn, 10/3/05 (PB2006-111703).
- MCEER-05-0010 "Steel Plate Shear Walls for Seismic Design and Retrofit of Building Structures," by D. Vian and M. Bruneau, 12/15/05 (PB2006-111704).

- MCEER-05-0011 "The Performance-Based Design Paradigm," by M.J. Astrella and A. Whittaker, 12/15/05 (PB2006-111705).
- MCEER-06-0001 "Seismic Fragility of Suspended Ceiling Systems," H. Badillo-Almaraz, A.S. Whittaker, A.M. Reinhorn and G.P. Cimellaro, 2/4/06 (PB2006-111706).
- MCEER-06-0002 "Multi-Dimensional Fragility of Structures," by G.P. Cimellaro, A.M. Reinhorn and M. Bruneau, 3/1/06 (PB2007-106974, A09, MF-A02, CD A00).
- MCEER-06-0003 "Built-Up Shear Links as Energy Dissipators for Seismic Protection of Bridges," by P. Dusicka, A.M. Itani and I.G. Buckle, 3/15/06 (PB2006-111708).
- MCEER-06-0004 "Analytical Investigation of the Structural Fuse Concept," by R.E. Vargas and M. Bruneau, 3/16/06 (PB2006-111709).
- MCEER-06-0005 "Experimental Investigation of the Structural Fuse Concept," by R.E. Vargas and M. Bruneau, 3/17/06 (PB2006-111710).
- MCEER-06-0006 "Further Development of Tubular Eccentrically Braced Frame Links for the Seismic Retrofit of Braced Steel Truss Bridge Piers," by J.W. Berman and M. Bruneau, 3/27/06 (PB2007-105147).
- MCEER-06-0007 "REDARS Validation Report," by S. Cho, C.K. Huyck, S. Ghosh and R.T. Eguchi, 8/8/06 (PB2007-106983).
- MCEER-06-0008 "Review of Current NDE Technologies for Post-Earthquake Assessment of Retrofitted Bridge Columns," by J.W. Song, Z. Liang and G.C. Lee, 8/21/06 (PB2007-106984).
- MCEER-06-0009 "Liquefaction Remediation in Silty Soils Using Dynamic Compaction and Stone Columns," by S. Thevanayagam, G.R. Martin, R. Nashed, T. Shenthan, T. Kanagalingam and N. Ecemis, 8/28/06 (PB2007-106985).
- MCEER-06-0010 "Conceptual Design and Experimental Investigation of Polymer Matrix Composite Infill Panels for Seismic Retrofitting," by W. Jung, M. Chiewanichakorn and A.J. Aref, 9/21/06 (PB2007-106986).
- MCEER-06-0011 "A Study of the Coupled Horizontal-Vertical Behavior of Elastomeric and Lead-Rubber Seismic Isolation Bearings," by G.P. Warn and A.S. Whittaker, 9/22/06 (PB2007-108679).
- MCEER-06-0012 "Proceedings of the Fourth PRC-US Workshop on Seismic Analysis and Design of Special Bridges: Advancing Bridge Technologies in Research, Design, Construction and Preservation," Edited by L.C. Fan, G.C. Lee and L. Ziang, 10/12/06 (PB2007-109042).
- MCEER-06-0013 "Cyclic Response and Low Cycle Fatigue Characteristics of Plate Steels," by P. Dusicka, A.M. Itani and I.G. Buckle, 11/1/06 (PB2007-106987).
- MCEER-06-0014 "Proceedings of the Second US-Taiwan Bridge Engineering Workshop," edited by W.P. Yen, J. Shen, J-Y. Chen and M. Wang, 11/15/06 (PB2008-500041).
- MCEER-06-0015 "User Manual and Technical Documentation for the REDARS<sup>TM</sup> Import Wizard," by S. Cho, S. Ghosh, C.K. Huyck and S.D. Werner, 11/30/06 (PB2007-114766).
- MCEER-06-0016 "Hazard Mitigation Strategy and Monitoring Technologies for Urban and Infrastructure Public Buildings: Proceedings of the China-US Workshops," edited by X.Y. Zhou, A.L. Zhang, G.C. Lee and M. Tong, 12/12/06 (PB2008-500018).
- MCEER-07-0001 "Static and Kinetic Coefficients of Friction for Rigid Blocks," by C. Kafali, S. Fathali, M. Grigoriu and A.S. Whittaker, 3/20/07 (PB2007-114767).
- MCEER-07-0002 "Hazard Mitigation Investment Decision Making: Organizational Response to Legislative Mandate," by L.A. Arendt, D.J. Alesch and W.J. Petak, 4/9/07 (PB2007-114768).
- MCEER-07-0003 "Seismic Behavior of Bidirectional-Resistant Ductile End Diaphragms with Unbonded Braces in Straight or Skewed Steel Bridges," by O. Celik and M. Bruneau, 4/11/07 (PB2008-105141).

- MCEER-07-0004 "Modeling Pile Behavior in Large Pile Groups Under Lateral Loading," by A.M. Dodds and G.R. Martin, 4/16/07(PB2008-105142).
- MCEER-07-0005 "Experimental Investigation of Blast Performance of Seismically Resistant Concrete-Filled Steel Tube Bridge Piers," by S. Fujikura, M. Bruneau and D. Lopez-Garcia, 4/20/07 (PB2008-105143).
- MCEER-07-0006 "Seismic Analysis of Conventional and Isolated Liquefied Natural Gas Tanks Using Mechanical Analogs," by I.P. Christovasilis and A.S. Whittaker, 5/1/07, not available.
- MCEER-07-0007 "Experimental Seismic Performance Evaluation of Isolation/Restraint Systems for Mechanical Equipment – Part 1: Heavy Equipment Study," by S. Fathali and A. Filiatrault, 6/6/07 (PB2008-105144).
- MCEER-07-0008 "Seismic Vulnerability of Timber Bridges and Timber Substructures," by A.A. Sharma, J.B. Mander, I.M. Friedland and D.R. Allicock, 6/7/07 (PB2008-105145).
- MCEER-07-0009 "Experimental and Analytical Study of the XY-Friction Pendulum (XY-FP) Bearing for Bridge Applications," by C.C. Marin-Artieda, A.S. Whittaker and M.C. Constantinou, 6/7/07 (PB2008-105191).
- MCEER-07-0010 "Proceedings of the PRC-US Earthquake Engineering Forum for Young Researchers," Edited by G.C. Lee and X.Z. Qi, 6/8/07 (PB2008-500058).
- MCEER-07-0011 "Design Recommendations for Perforated Steel Plate Shear Walls," by R. Purba and M. Bruneau, 6/18/07, (PB2008-105192).
- MCEER-07-0012 "Performance of Seismic Isolation Hardware Under Service and Seismic Loading," by M.C. Constantinou, A.S. Whittaker, Y. Kalpakidis, D.M. Fenz and G.P. Warn, 8/27/07, (PB2008-105193).
- MCEER-07-0013 "Experimental Evaluation of the Seismic Performance of Hospital Piping Subassemblies," by E.R. Goodwin, E. Maragakis and A.M. Itani, 9/4/07, (PB2008-105194).
- MCEER-07-0014 "A Simulation Model of Urban Disaster Recovery and Resilience: Implementation for the 1994 Northridge Earthquake," by S. Miles and S.E. Chang, 9/7/07, (PB2008-106426).
- MCEER-07-0015 "Statistical and Mechanistic Fragility Analysis of Concrete Bridges," by M. Shinozuka, S. Banerjee and S-H. Kim, 9/10/07, (PB2008-106427).
- MCEER-07-0016 "Three-Dimensional Modeling of Inelastic Buckling in Frame Structures," by M. Schachter and AM. Reinhorn, 9/13/07, (PB2008-108125).
- MCEER-07-0017 "Modeling of Seismic Wave Scattering on Pile Groups and Caissons," by I. Po Lam, H. Law and C.T. Yang, 9/17/07 (PB2008-108150).
- MCEER-07-0018 "Bridge Foundations: Modeling Large Pile Groups and Caissons for Seismic Design," by I. Po Lam, H. Law and G.R. Martin (Coordinating Author), 12/1/07 (PB2008-111190).
- MCEER-07-0019 "Principles and Performance of Roller Seismic Isolation Bearings for Highway Bridges," by G.C. Lee, Y.C. Ou, Z. Liang, T.C. Niu and J. Song, 12/10/07 (PB2009-110466).
- MCEER-07-0020 "Centrifuge Modeling of Permeability and Pinning Reinforcement Effects on Pile Response to Lateral Spreading," by L.L. Gonzalez-Lagos, T. Abdoun and R. Dobry, 12/10/07 (PB2008-111191).
- MCEER-07-0021 "Damage to the Highway System from the Pisco, Perú Earthquake of August 15, 2007," by J.S. O'Connor, L. Mesa and M. Nykamp, 12/10/07, (PB2008-108126).
- MCEER-07-0022 "Experimental Seismic Performance Evaluation of Isolation/Restraint Systems for Mechanical Equipment – Part 2: Light Equipment Study," by S. Fathali and A. Filiatrault, 12/13/07 (PB2008-111192).
- MCEER-07-0023 "Fragility Considerations in Highway Bridge Design," by M. Shinozuka, S. Banerjee and S.H. Kim, 12/14/07 (PB2008-111193).



- MCEER-07-0024 "Performance Estimates for Seismically Isolated Bridges," by G.P. Warn and A.S. Whittaker, 12/30/07 (PB2008-112230).
- MCEER-08-0001 "Seismic Performance of Steel Girder Bridge Superstructures with Conventional Cross Frames," by L.P. Carden, A.M. Itani and I.G. Buckle, 1/7/08, (PB2008-112231).
- MCEER-08-0002 "Seismic Performance of Steel Girder Bridge Superstructures with Ductile End Cross Frames with Seismic Isolators," by L.P. Carden, A.M. Itani and I.G. Buckle, 1/7/08 (PB2008-112232).
- MCEER-08-0003 "Analytical and Experimental Investigation of a Controlled Rocking Approach for Seismic Protection of Bridge Steel Truss Piers," by M. Pollino and M. Bruneau, 1/21/08 (PB2008-112233).
- MCEER-08-0004 "Linking Lifeline Infrastructure Performance and Community Disaster Resilience: Models and Multi-Stakeholder Processes," by S.E. Chang, C. Pasion, K. Tatebe and R. Ahmad, 3/3/08 (PB2008-112234).
- MCEER-08-0005 "Modal Analysis of Generally Damped Linear Structures Subjected to Seismic Excitations," by J. Song, Y-L. Chu, Z. Liang and G.C. Lee, 3/4/08 (PB2009-102311).
- MCEER-08-0006 "System Performance Under Multi-Hazard Environments," by C. Kafali and M. Grigoriu, 3/4/08 (PB2008-112235).
- MCEER-08-0007 "Mechanical Behavior of Multi-Spherical Sliding Bearings," by D.M. Fenz and M.C. Constantinou, 3/6/08 (PB2008-112236).
- MCEER-08-0008 "Post-Earthquake Restoration of the Los Angeles Water Supply System," by T.H.P. Tabucchi and R.A. Davidson, 3/7/08 (PB2008-112237).
- MCEER-08-0009 "Fragility Analysis of Water Supply Systems," by A. Jacobson and M. Grigoriu, 3/10/08 (PB2009-105545).
- MCEER-08-0010 "Experimental Investigation of Full-Scale Two-Story Steel Plate Shear Walls with Reduced Beam Section Connections," by B. Qu, M. Bruneau, C-H. Lin and K-C. Tsai, 3/17/08 (PB2009-106368).
- MCEER-08-0011 "Seismic Evaluation and Rehabilitation of Critical Components of Electrical Power Systems," S. Ersoy, B. Feizi, A. Ashrafi and M. Ala Saadeghvaziri, 3/17/08 (PB2009-105546).
- MCEER-08-0012 "Seismic Behavior and Design of Boundary Frame Members of Steel Plate Shear Walls," by B. Qu and M. Bruneau, 4/26/08 . (PB2009-106744).
- MCEER-08-0013 "Development and Appraisal of a Numerical Cyclic Loading Protocol for Quantifying Building System Performance," by A. Filiatrault, A. Wanitkorkul and M. Constantinou, 4/27/08 (PB2009-107906).
- MCEER-08-0014 "Structural and Nonstructural Earthquake Design: The Challenge of Integrating Specialty Areas in Designing Complex, Critical Facilities," by W.J. Petak and D.J. Alesch, 4/30/08 (PB2009-107907).
- MCEER-08-0015 "Seismic Performance Evaluation of Water Systems," by Y. Wang and T.D. O'Rourke, 5/5/08 (PB2009-107908).
- MCEER-08-0016 "Seismic Response Modeling of Water Supply Systems," by P. Shi and T.D. O'Rourke, 5/5/08 (PB2009-107910).
- MCEER-08-0017 "Numerical and Experimental Studies of Self-Centering Post-Tensioned Steel Frames," by D. Wang and A. Filiatrault, 5/12/08 (PB2009-110479).
- MCEER-08-0018 "Development, Implementation and Verification of Dynamic Analysis Models for Multi-Spherical Sliding Bearings," by D.M. Fenz and M.C. Constantinou, 8/15/08 (PB2009-107911).
- MCEER-08-0019 "Performance Assessment of Conventional and Base Isolated Nuclear Power Plants for Earthquake Blast Loadings," by Y.N. Huang, A.S. Whittaker and N. Luco, 10/28/08 (PB2009-107912).

- MCEER-08-0020 “Remote Sensing for Resilient Multi-Hazard Disaster Response – Volume I: Introduction to Damage Assessment Methodologies,” by B.J. Adams and R.T. Eguchi, 11/17/08 (PB2010-102695).
- MCEER-08-0021 “Remote Sensing for Resilient Multi-Hazard Disaster Response – Volume II: Counting the Number of Collapsed Buildings Using an Object-Oriented Analysis: Case Study of the 2003 Bam Earthquake,” by L. Gusella, C.K. Huyck and B.J. Adams, 11/17/08 (PB2010-100925).
- MCEER-08-0022 “Remote Sensing for Resilient Multi-Hazard Disaster Response – Volume III: Multi-Sensor Image Fusion Techniques for Robust Neighborhood-Scale Urban Damage Assessment,” by B.J. Adams and A. McMillan, 11/17/08 (PB2010-100926).
- MCEER-08-0023 “Remote Sensing for Resilient Multi-Hazard Disaster Response – Volume IV: A Study of Multi-Temporal and Multi-Resolution SAR Imagery for Post-Katrina Flood Monitoring in New Orleans,” by A. McMillan, J.G. Morley, B.J. Adams and S. Chesworth, 11/17/08 (PB2010-100927).
- MCEER-08-0024 “Remote Sensing for Resilient Multi-Hazard Disaster Response – Volume V: Integration of Remote Sensing Imagery and VIEWS™ Field Data for Post-Hurricane Charley Building Damage Assessment,” by J.A. Womble, K. Mehta and B.J. Adams, 11/17/08 (PB2009-115532).
- MCEER-08-0025 “Building Inventory Compilation for Disaster Management: Application of Remote Sensing and Statistical Modeling,” by P. Sarabandi, A.S. Kiremidjian, R.T. Eguchi and B. J. Adams, 11/20/08 (PB2009-110484).
- MCEER-08-0026 “New Experimental Capabilities and Loading Protocols for Seismic Qualification and Fragility Assessment of Nonstructural Systems,” by R. Retamales, G. Mosqueda, A. Filiatrault and A. Reinhorn, 11/24/08 (PB2009-110485).
- MCEER-08-0027 “Effects of Heating and Load History on the Behavior of Lead-Rubber Bearings,” by I.V. Kalpakidis and M.C. Constantinou, 12/1/08 (PB2009-115533).
- MCEER-08-0028 “Experimental and Analytical Investigation of Blast Performance of Seismically Resistant Bridge Piers,” by S.Fujikura and M. Bruneau, 12/8/08 (PB2009-115534).
- MCEER-08-0029 “Evolutionary Methodology for Aseismic Decision Support,” by Y. Hu and G. Dargush, 12/15/08.
- MCEER-08-0030 “Development of a Steel Plate Shear Wall Bridge Pier System Conceived from a Multi-Hazard Perspective,” by D. Keller and M. Bruneau, 12/19/08 (PB2010-102696).
- MCEER-09-0001 “Modal Analysis of Arbitrarily Damped Three-Dimensional Linear Structures Subjected to Seismic Excitations,” by Y.L. Chu, J. Song and G.C. Lee, 1/31/09 (PB2010-100922).
- MCEER-09-0002 “Air-Blast Effects on Structural Shapes,” by G. Ballantyne, A.S. Whittaker, A.J. Aref and G.F. Dargush, 2/2/09 (PB2010-102697).
- MCEER-09-0003 “Water Supply Performance During Earthquakes and Extreme Events,” by A.L. Bonneau and T.D. O’Rourke, 2/16/09 (PB2010-100923).
- MCEER-09-0004 “Generalized Linear (Mixed) Models of Post-Earthquake Ignitions,” by R.A. Davidson, 7/20/09 (PB2010-102698).
- MCEER-09-0005 “Seismic Testing of a Full-Scale Two-Story Light-Frame Wood Building: NEESWood Benchmark Test,” by I.P. Christovasilis, A. Filiatrault and A. Wanitkorkul, 7/22/09 (PB2012-102401).
- MCEER-09-0006 “IDARC2D Version 7.0: A Program for the Inelastic Damage Analysis of Structures,” by A.M. Reinhorn, H. Roh, M. Sivaselvan, S.K. Kunnath, R.E. Valles, A. Madan, C. Li, R. Lobo and Y.J. Park, 7/28/09 (PB2010-103199).
- MCEER-09-0007 “Enhancements to Hospital Resiliency: Improving Emergency Planning for and Response to Hurricanes,” by D.B. Hess and L.A. Arendt, 7/30/09 (PB2010-100924).

- MCEER-09-0008 "Assessment of Base-Isolated Nuclear Structures for Design and Beyond-Design Basis Earthquake Shaking," by Y.N. Huang, A.S. Whittaker, R.P. Kennedy and R.L. Mayes, 8/20/09 (PB2010-102699).
- MCEER-09-0009 "Quantification of Disaster Resilience of Health Care Facilities," by G.P. Cimellaro, C. Fumo, A.M. Reinhorn and M. Bruneau, 9/14/09 (PB2010-105384).
- MCEER-09-0010 "Performance-Based Assessment and Design of Squat Reinforced Concrete Shear Walls," by C.K. Gulec and A.S. Whittaker, 9/15/09 (PB2010-102700).
- MCEER-09-0011 "Proceedings of the Fourth US-Taiwan Bridge Engineering Workshop," edited by W.P. Yen, J.J. Shen, T.M. Lee and R.B. Zheng, 10/27/09 (PB2010-500009).
- MCEER-09-0012 "Proceedings of the Special International Workshop on Seismic Connection Details for Segmental Bridge Construction," edited by W. Phillip Yen and George C. Lee, 12/21/09 (PB2012-102402).
- MCEER-10-0001 "Direct Displacement Procedure for Performance-Based Seismic Design of Multistory Woodframe Structures," by W. Pang and D. Rosowsky, 4/26/10 (PB2012-102403).
- MCEER-10-0002 "Simplified Direct Displacement Design of Six-Story NEESWood Capstone Building and Pre-Test Seismic Performance Assessment," by W. Pang, D. Rosowsky, J. van de Lindt and S. Pei, 5/28/10 (PB2012-102404).
- MCEER-10-0003 "Integration of Seismic Protection Systems in Performance-Based Seismic Design of Woodframed Structures," by J.K. Shinde and M.D. Symans, 6/18/10 (PB2012-102405).
- MCEER-10-0004 "Modeling and Seismic Evaluation of Nonstructural Components: Testing Frame for Experimental Evaluation of Suspended Ceiling Systems," by A.M. Reinhorn, K.P. Ryu and G. Maddaloni, 6/30/10 (PB2012-102406).
- MCEER-10-0005 "Analytical Development and Experimental Validation of a Structural-Fuse Bridge Pier Concept," by S. El-Bahey and M. Bruneau, 10/1/10 (PB2012-102407).
- MCEER-10-0006 "A Framework for Defining and Measuring Resilience at the Community Scale: The PEOPLES Resilience Framework," by C.S. Renschler, A.E. Frazier, L.A. Arendt, G.P. Cimellaro, A.M. Reinhorn and M. Bruneau, 10/8/10 (PB2012-102408).
- MCEER-10-0007 "Impact of Horizontal Boundary Elements Design on Seismic Behavior of Steel Plate Shear Walls," by R. Purba and M. Bruneau, 11/14/10 (PB2012-102409).
- MCEER-10-0008 "Seismic Testing of a Full-Scale Mid-Rise Building: The NEESWood Capstone Test," by S. Pei, J.W. van de Lindt, S.E. Pryor, H. Shimizu, H. Isoda and D.R. Rammer, 12/1/10 (PB2012-102410).
- MCEER-10-0009 "Modeling the Effects of Detonations of High Explosives to Inform Blast-Resistant Design," by P. Sherkar, A.S. Whittaker and A.J. Aref, 12/1/10 (PB2012-102411).
- MCEER-10-0010 "L'Aquila Earthquake of April 6, 2009 in Italy: Rebuilding a Resilient City to Withstand Multiple Hazards," by G.P. Cimellaro, I.P. Christovasilis, A.M. Reinhorn, A. De Stefano and T. Kirova, 12/29/10.
- MCEER-11-0001 "Numerical and Experimental Investigation of the Seismic Response of Light-Frame Wood Structures," by I.P. Christovasilis and A. Filiatrault, 8/8/11 (PB2012-102412).
- MCEER-11-0002 "Seismic Design and Analysis of a Precast Segmental Concrete Bridge Model," by M. Anagnostopoulou, A. Filiatrault and A. Aref, 9/15/11.
- MCEER-11-0003 "Proceedings of the Workshop on Improving Earthquake Response of Substation Equipment," Edited by A.M. Reinhorn, 9/19/11 (PB2012-102413).
- MCEER-11-0004 "LRFD-Based Analysis and Design Procedures for Bridge Bearings and Seismic Isolators," by M.C. Constantinou, I. Kalpakidis, A. Filiatrault and R.A. Ecker Lay, 9/26/11.

- MCEER-11-0005 “Experimental Seismic Evaluation, Model Parameterization, and Effects of Cold-Formed Steel-Framed Gypsum Partition Walls on the Seismic Performance of an Essential Facility,” by R. Davies, R. Retamales, G. Mosqueda and A. Filiatrault, 10/12/11.
- MCEER-11-0006 “Modeling and Seismic Performance Evaluation of High Voltage Transformers and Bushings,” by A.M. Reinhorn, K. Oikonomou, H. Roh, A. Schiff and L. Kempner, Jr., 10/3/11.
- MCEER-11-0007 “Extreme Load Combinations: A Survey of State Bridge Engineers,” by G.C. Lee, Z. Liang, J.J. Shen and J.S. O’Connor, 10/14/11.
- MCEER-12-0001 “Simplified Analysis Procedures in Support of Performance Based Seismic Design,” by Y.N. Huang and A.S. Whittaker.
- MCEER-12-0002 “Seismic Protection of Electrical Transformer Bushing Systems by Stiffening Techniques,” by M. Koliou, A. Filiatrault, A.M. Reinhorn and N. Oliveto, 6/1/12.
- MCEER-12-0003 “Post-Earthquake Bridge Inspection Guidelines,” by J.S. O’Connor and S. Alampalli, 6/8/12.
- MCEER-12-0004 “Integrated Design Methodology for Isolated Floor Systems in Single-Degree-of-Freedom Structural Fuse Systems,” by S. Cui, M. Bruneau and M.C. Constantinou, 6/13/12.
- MCEER-12-0005 “Characterizing the Rotational Components of Earthquake Ground Motion,” by D. Basu, A.S. Whittaker and M.C. Constantinou, 6/15/12.
- MCEER-12-0006 “Bayesian Fragility for Nonstructural Systems,” by C.H. Lee and M.D. Grigoriu, 9/12/12.
- MCEER-12-0007 “A Numerical Model for Capturing the In-Plane Seismic Response of Interior Metal Stud Partition Walls,” by R.L. Wood and T.C. Hutchinson, 9/12/12.
- MCEER-12-0008 “Assessment of Floor Accelerations in Yielding Buildings,” by J.D. Wieser, G. Pekcan, A.E. Zaghi, A.M. Itani and E. Maragakis, 10/5/12.
- MCEER-13-0001 “Experimental Seismic Study of Pressurized Fire Sprinkler Piping Systems,” by Y. Tian, A. Filiatrault and G. Mosqueda, 4/8/13.
- MCEER-13-0002 “Enhancing Resource Coordination for Multi-Modal Evacuation Planning,” by D.B. Hess, B.W. Conley and C.M. Farrell, 2/8/13.
- MCEER-13-0003 “Seismic Response of Base Isolated Buildings Considering Pounding to Moat Walls,” by A. Masroor and G. Mosqueda, 2/26/13.
- MCEER-13-0004 “Seismic Response Control of Structures Using a Novel Adaptive Passive Negative Stiffness Device,” by D.T.R. Pasala, A.A. Sarlis, S. Nagarajaiah, A.M. Reinhorn, M.C. Constantinou and D.P. Taylor, 6/10/13.
- MCEER-13-0005 “Negative Stiffness Device for Seismic Protection of Structures,” by A.A. Sarlis, D.T.R. Pasala, M.C. Constantinou, A.M. Reinhorn, S. Nagarajaiah and D.P. Taylor, 6/12/13.
- MCEER-13-0006 “Emilia Earthquake of May 20, 2012 in Northern Italy: Rebuilding a Resilient Community to Withstand Multiple Hazards,” by G.P. Cimellaro, M. Chiriatti, A.M. Reinhorn and L. Tirca, June 30, 2013.
- MCEER-13-0007 “Precast Concrete Segmental Components and Systems for Accelerated Bridge Construction in Seismic Regions,” by A.J. Aref, G.C. Lee, Y.C. Ou and P. Sideris, with contributions from K.C. Chang, S. Chen, A. Filiatrault and Y. Zhou, June 13, 2013.
- MCEER-13-0008 “A Study of U.S. Bridge Failures (1980-2012),” by G.C. Lee, S.B. Mohan, C. Huang and B.N. Fard, June 15, 2013.
- MCEER-13-0009 “Development of a Database Framework for Modeling Damaged Bridges,” by G.C. Lee, J.C. Qi and C. Huang, June 16, 2013.

- MCEER-13-0010 “Model of Triple Friction Pendulum Bearing for General Geometric and Frictional Parameters and for Uplift Conditions,” by A.A. Sarlis and M.C. Constantinou, July 1, 2013.
- MCEER-13-0011 “Shake Table Testing of Triple Friction Pendulum Isolators under Extreme Conditions,” by A.A. Sarlis, M.C. Constantinou and A.M. Reinhorn, July 2, 2013.
- MCEER-13-0012 “Theoretical Framework for the Development of MH-LRFD,” by G.C. Lee (coordinating author), H.A. Capers, Jr., C. Huang, J.M. Kulicki, Z. Liang, T. Murphy, J.J.D. Shen, M. Shinozuka and P.W.H. Yen, July 31, 2013.
- MCEER-13-0013 “Seismic Protection of Highway Bridges with Negative Stiffness Devices,” by N.K.A. Attary, M.D. Symans, S. Nagarajaiah, A.M. Reinhorn, M.C. Constantinou, A.A. Sarlis, D.T.R. Pasala, and D.P. Taylor, September 3, 2014.
- MCEER-14-0001 “Simplified Seismic Collapse Capacity-Based Evaluation and Design of Frame Buildings with and without Supplemental Damping Systems,” by M. Hamidia, A. Filiatrault, and A. Aref, May 19, 2014.
- MCEER-14-0002 “Comprehensive Analytical Seismic Fragility of Fire Sprinkler Piping Systems,” by Siavash Soroushian, Emmanuel “Manos” Maragakis, Arash E. Zaghi, Alicia Echevarria, Yuan Tian and Andre Filiatrault, August 26, 2014.
- MCEER-14-0003 “Hybrid Simulation of the Seismic Response of a Steel Moment Frame Building Structure through Collapse,” by M. Del Carpio Ramos, G. Mosqueda and D.G. Lignos, October 30, 2014.
- MCEER-14-0005 “Seismic Performance of Steel Plate Shear Walls Considering Various Design Approaches,” by R. Purba and M. Bruneau, October 31, 2014.
- MCEER-14-0006 “Air-Blast Effects on Civil Structures,” by Jinwon Shin, Andrew S. Whittaker, Amjad J. Aref and David Cormie, October 30, 2014.
- MCEER-14-0007 “Seismic Performance Evaluation of Precast Girders with Field-Cast Ultra High Performance Concrete (UHPC) Connections,” by G.C. Lee, C. Huang, J. Song, and J. S. O’Connor, July 31, 2014.
- MCEER-14-0008 “Post-Earthquake Fire Resistance of Ductile Concrete-Filled Double-Skin Tube Columns,” by Reza Imani, Gilberto Mosqueda and Michel Bruneau, December 1, 2014.
- MCEER-14-0009 “Cyclic Inelastic Behavior of Concrete Filled Sandwich Panel Walls Subjected to In-Plane Flexure,” by Y. Alzeni and M. Bruneau, December 19, 2014.
- MCEER-14-0010 “Analytical and Experimental Investigation of Self-Centering Steel Plate Shear Walls,” by D.M. Dowden and M. Bruneau, December 19, 2014.



**EARTHQUAKE ENGINEERING TO EXTREME EVENTS**

University at Buffalo, The State University of New York

133A Ketter Hall ■ Buffalo, New York 14260-4300

Phone: (716) 645-3391 ■ Fax: (716) 645-3399

Email: [mceer@buffalo.edu](mailto:mceer@buffalo.edu) ■ Web: <http://mceer.buffalo.edu>



**University at Buffalo** *The State University of New York*

ISSN 1520-295X